MECHANICAL PROPERTIES OF FUNCTIONALLY GRADED MATERIALS: CARBON GRADIENT INSIDE INTERSTITIAL FREE STEEL

By

ELISA CANTERGIANI, M.Sc., B.Sc.

Thesis submitted to the
Faculty of Graduate and Postdoctoral Studies
in partial fulfillment of the requirements
for the Doctorate in Philosophy degree in Mechanical Engineering

Ottawa-Carleton Institute for
Mechanical and Aerospace Engineering

University of Ottawa
© Elisa Cantergiani, Ottawa, Canada, 2016

DOCTOR OF PHILOSOPHY (2016) University of Ottawa

(Department of Mechanical Engineering) Ottawa, Ontario

TITLE: Mechanical Properties of Functionally Graded Materials: Carbon Gradient inside Interstitial Free Steel

AUTHOR: Elisa Cantergiani, M.Sc., B.Sc.

SUPERVISOR: Dr. Arnaud Weck

NUMBER OF PAGES: LXXVII, 473 (without appendices), 685 (including appendices)

Abstract

In the last decade aluminium started to be considered as an alternative to steel to produce car body panels, especially considering the strict demands to decrease fuel consumption which require vehicle weight reduction. In order to keep their leading role, steel companies have to produce stronger materials to reduce the thickness of steel sheets used in cars and are now considering non-conventional steel making processes.

The purpose of this PhD research was to investigate the possibility of strengthening thin sheets of interstitial free steel (IF steel) by using carbon rich films deposited on the steel surface using Physical Vapour Deposition (PVD). These films then act as a carbon reservoir which upon heat treatment release carbon in the IF steel and strengthen it.

Coated tensile coupons 200 μm thick were annealed at different temperatures under high vacuum. Tensile tests show that a 100 MPa increase in yield stress can be obtained after annealing at 430 ˚C for 1h in high vacuum. The effects of annealing environment, film thickness and prestrain on carbon diffusion were also investigated. It was shown that carbon diffusion from the film to the IF steel substrate is limited by the film transformation into cementite at temperatures equal or higher than 530 ˚C.

All tensile curves showed a plastic instability known as Lüders plateau, which is undesirable as it results in surface markings on the deformed part. FEM analyses were performed to find ways to suppress the Lüders plateau, proving that increasing strain-hardening or having a graded instead of uniform carbon content through thickness can suppress or limit Lüdering.

The possibility of creating a through thickness gradient of microstructure was investigated as it could suppress Lüdering and result in higher strength. For these tests, FeC coated coupons were induction heated to 820 ˚C followed by water quenching. After only 2 minutes of heat treatment the yield stress was increased by 250 MPa and the ultimate tensile strength reached 400 MPa. With an annealing of 4 minutes, the Lüders plateau was fully suppressed and the microstructure consisted in ferrite grains and TiC nanocarbides. This work demonstrates that FeC films can be effectively used to diffuse carbon into steel and that a significant increase in mechanical properties can be obtained after a heat treatment of only a few minutes.

Preface

The majority of the work presented in this PhD thesis was performed in the Department of Mechanical Engineering at the University of Ottawa between May 2011 and August 2015. In particular, all the experimental design, diffusion simulations, annealing treatments, metallography, digital image correlation, mechanical testing, finite element simulations, induction heating, fracture studies and programs used to perform laser ablation and holes were performed by the author.

The only work that was performed outside the University of Ottawa includes PVD depositions, done at the University of British Columbia; transmission electron microscope (TEM) investigations done at the University of Rouen (France) and at INSA Lyon (France). Thermoelectric power measurements (TEP) were performed by Dr. Jean-Louis Uriarte at ArcelorMittal but the specimens were prepared by the author.

Three dimensional atom probe tomography (APT) tests and results presented in this PhD thesis were performed at the University of Rouen. The samples and data analyses were obtained with the help of Dr. Amélie Fillon when the author went to the University of Rouen for a research stay (September/October 2013).

The help of Mr. John Hopkins for the sealing of the glass ampoules used for induction heating experiments is acknowledged. The electron backscattered diffraction (EBSD) analyses were performed by Chris Butcher at the Brockhouse Institute for Materials Research at the Canadian Centre for Electron Microscopy. For EBSD, the author prepared the specimens and decided what steps to follow to obtain relevant data from EBSD. Grazing X-ray tests shown in chapter 8 were performed by Dr. Ilia Korobkov at the University of Ottawa. All the SEM imaging and EDS were performed by the author, except the EDS on specimens annealed at 710 ˚C – 1h which were performed by Dr. Mohammed Yandouzi at the University of Ottawa. Dr. Yun Liu from the Bioscience department at the University of Ottawa performed the SEM imaging of the specimens shown in chapter 8, however the author was present during the imaging and the author performed all the specimen preparation and the EDS.

Depth measurements of laser ablation shown in chapter 9 were performed by Emna Benfredj at the École de Technologie Supérieure in Montreal. The PhD author performed all laser experiments.

Acknowledgements

First I would like to thank my supervisor Dr. Arnaud Weck for his guidance through the whole project and for its patience in reading and reviewing the thesis. I also would like to thank him for giving me the opportunity of working on a side project related to fracture and tomography of bones from spring 2012 to fall 2012 which gave me a precious experience at Argonne National Laboratory.

I would like as well to thank Dr. Colin Scott for his invaluable support and very good technical advices related to heat treatment and explanation of mechanical properties. I am very grateful to Prof. Xavier Sauvage and Dr. Amélie Fillon from the University of Rouen for giving me the chance to spend some time in their group to learn about atom probe tomography, even if the specimen preparation almost drove me to craziness. I wish to thank also Prof. Chad Sinclair and Dr. Ben Lawrence for performing the PVD depositions. I am grateful to Dr. Jean-Louis Uriarte for performing the TEP measurements and to Prof. Michel Perez for discussions of the obtained results.

Dr. Mohammed Yandouzi and Dr. Yun Liu are acknowledged for giving me access to the SEM and for their great help and advices.

Many thanks to Paul Burberry for teaching me how to use the EDM machine to cut tensile coupons, to Leo Denner for all the technical support in the lab and for the amusing conversations and to Frantz Celestin for listening to me every time I needed an advice.

During all these years I spent in Canada, I had the opportunity to meet people from different countries and I would like to thank all of them for their support and for all the very interesting conversations related to science and not, which opened my mind. Special thanks to all the colleagues which were part of the FROG group: Marina Pushkareva, Hourieh Exir, Yusha Lan, Mishaal Azhar, Mahyar Asadi, Trevor Meunier and Steven Knapp. It was really a pleasure to share the lab life with all of you. I was also very happy to share a lot of discussions about material science and life with Rubén Fernández Urrutia and Leon Guo. During the summers of these years, several coop students were part of the lab. On purpose, I wish to thank Jean-François Croteau for all the good conversations ranging from astronomy up to politics during the long and very boring polishing preparation of specimens. A special thanks also to the students Franck Tchuente, Leticia Goes and Antoine Olivier for their really great companionship.

Finally, I would like to thank my family and friends for their support, understanding, patience and friendship. Special thanks to my parents Gloria and Giancarlo for their unconditioned support. A special thanks to all my best friends Stefania, Yu Jing, Richard, Massimo, Maria Cristina and Thomas for listening to me every time I needed a good word, a life advice and encouragement in pursuing the journey of my life.

Table of Contents

Abstract ..... **iii**

Preface ..... **iv**

Acknowledgements ..... **v**

List of Figures ..... **xvii**

List of Figures in Appendices ..... **xlvii**

List of Tables ..... **lxiv**

List of Tables in Appendices ..... **lxx**

Chapter 1 : Introduction **1**

1.1. Main Contributions 2

Chapter 2 : Literature Review **4**

2.1. What is a Functionally Graded Material? 4

2.2. Main Industrial Applications of Functionally Graded Materials 5

2.3. Functionally Graded Materials Processing 6

2.4. Constitutive Processes 7

2.4.1. Powder Densification Processes 7

2.5. Transport Based Processes 9

2.5.1. Bake Hardening and Case Hardening of Steel 9

2.5.2. Case Hardening 10

2.6. Diffusion of Carbon 12

2.7. Microstructure Characterization of FGM 18

2.7.1. Carbides Analyses 18

2.8. Mechanical Response of Functionally Graded Fe-C 19

2.8.1. Local Mechanical Properties 19

2.8.2. Hardness Test 21

2.8.3. X-ray Diffraction for Local Stress State 25
2.9. Global Mechanical Properties 28
2.9.1. Tensile Properties 28
2.10. Piobert-Lüders Effect 32
2.11. Piobert-Lüders Effect Modelling 39
2.12. Modelling and Fracture of Functionally Graded Materials 43
2.13. Summary from Literature Review 58
Chapter 3 : Research Proposal 60
3.1. Scope of the Project 60
3.1.1. $Fe_{1-x}C_x$ Films 62
3.1.2. Fabrication and Characterization of a Functionally Graded Material 64
3.2. Modelling of Lüders Bands 64
3.3. Experimental Studies of Fracture in Graded Materials 66
Chapter 4 : Experimental Procedures 67
4.1. Methods used for Iron-Carbon Film Deposition 67
4.2. Fabrication of Tensile Coupons and Annealing Procedure 69
4.3. Annealing Treatment 70
4.3.1. Annealing Treatment in High Vacuum 70
4.3.2. Annealing Treatment in Argon 72
4.4. Polishing Procedure 74
4.5. Etching 75
4.6. Method used for Hardness Measurement 76
4.6.1. Vickers and Knoop Microhardness Tests 76
4.6.2. Tensile Test 80
4.7. Methods used for Lüders Bands Analyses: Digital Image Correlation 84

4.8. Scanning Electron Microscopy and Transmission Electron Microscopy 87

4.9. Method used for evaluating carbon concentration 88

4.9.1. Atom Probe Tomography (APT) 88

4.9.2. Thermo Electric Power Measurements (TEP) 92

Chapter 5 : Experimental Results of Diffusion from FeC Films 96

5.1. Simulation of carbon diffusion through thickness 96

5.2. Hardness Measurements 99

5.3. Tensile Tests 101

5.3.1. Tensile Tests on coupons coated both sides with 500 nm FeC amorphous film 103

5.3.2. Tensile Tests on coupons coated both sides with 500 nm thick FeC amorphous film annealing in argon atmosphere 118

5.3.3. Tensile Tests on coupons coated on both sides with FeC amorphous film and annealed in air 122

5.4. Ductility of coupons coated with FeC film after annealing 124

5.5. Characterization of tensile coupons: FeC film crystallization 125

5.6. Characterization of tensile coupons: annealing at 710 ˚C – 1h 139

5.6.1. Energy Dispersive X-ray Spectroscopy (EDS) 140

5.6.2. Thermoelectric Power Measurements (TEP) 148

5.6.3. Atom Probe Tomography (APT) 150

5.6.4. Considerations about annealing at 710 ˚C 159

5.7. Influence of FeC film thickness on mechanical properties 159

5.8. Further tests to confirm modelling prediction 170

5.9. Digital Image Correlation (DIC) 177

5.10. Discussion of Chapter 5 190

Chapter 6 :Finite Element Simulations of Lüders Bands 195

6.1. Parametric study of the influence of linear softening on Lüders length 197

6.1.1. Influence of the upper yield stress on Lüders length 197

6.1.2. Influence of the slope of the linear softening on the Lüders length 200

6.2. Results of the parametric study of the influence of linear softening on Lüders length 203

6.3. Influence of uniform and graded carbon profiles on Lüders propagation 205

6.4. Investigations of solutions to suppress Lüders plateau 208

6.4.1. Influence of stiffness 208

6.4.2. Change in thickness of the central layer 210

6.4.3. Results of change in stiffness and in thickness for a central layer without Lüders plateau 214

6.4.4. Influence of strain hardening on Lüders propagation 218

6.4.5. Influence of Intervoids spacing on Lüeder propagation 221

6.5. Influence of voids volume fraction on Lüders propagation 225

6.6. Conclusions 227

Chapter 7 : Prestrain and Strain Ageing of Interstitial Free Steel coated with FeC Film 229

7.1. Influence of pre-strain on carbon diffusion 229

7.2. Pre-strained IF steel coated with FeC film 232

7.2.1 Experimental Results of pre-strained IF steel coated with FeC film 232

7.2.2. Experimental Results of pre-strained uncoated IF steel 240

7.3. Strain-ageing of IF steel coated with FeC film 245

7.4. Conclusions 251

Chapter 8 : Flash Annealing of Interstitial Free Steel coated with FeC film 256

8.1. Flash annealing procedure with the annealing furnace 257

8.2. Flash annealing using induction heating 267

8.2.1. Induction Heating in steel processing....268
8.2.2. Experimental Approach for Induction Heating on IF steel 268
8.2.3. Results from Induction Heating Experiments: carbon gradient through the thickness of the Interstitial Free steel 272
8.2.4. Results from Induction Heating Experiments....281
8.2.5. Scanning Electron Microscope (SEM) analyses of induction heated microstructures: one side coated coupons 300
8.2.6. Scanning Electron Microscope (SEM) analyses of induction heated microstructures: both sides coated coupons....307
8.2.7. EBSD and TEM analyses on Induction Heated Specimens 314
8.3. Structure of the FeC film during Induction Heating....319
8.4. Induction Heating on Pre-strained Tensile coupons 323
8.5. Discussion and Conclusions....327
8.5.1. One side coated coupons 329
8.5.2. Both sides coated coupons....331
Chapter 9 : Fracture Studies on Carbon Graded Interstitial Free Steel....338
9.1. Carbon gradient along gauge length 338
9.1.1. Prediction of carbon diffusion for half coated gauge length 338
9.1.2. Vickers Hardness Measurements....345
9.2. Femtosecond Laser Drilling of Holes 353
9.3. Tensile tests....356
9.4. Void Growth Analyses....360
9.4.1. Void Growth Analyses for coupons with holes along the gauge length....367
9.4.2. Carbon gradient along gauge width....381
9.5. Laser Ablation....388
9.6. Characterization of carbon gradient....394

9.7. Laser parameters and hole configuration 401

9.8. Results of specimens containing voids and having carbon gradient along the gauge width 404

9.8.1. Results of tensile tests and Digital Image Correlation (DIC) 404

9.8.2. Extraction of void growth from tensile tests 413

9.9. Results of void growth for specimens having carbon gradient along the gauge width 413

9.9.1. Results for specimens having a 500 μm ablation in the centre 413

9.9.2. Results for specimens having 500 μm of film left in the centre 417

9.9.3. Results for specimens having uniform carbon content along gauge width 419

9.9.4. Results for uncoated and not-annealed specimens of IF steel 422

9.10. Void Growth fitting with theoretical models 423

9.11. Conclusions 428

Chapter 10 : Use of different films as reservoir for diffusion 433

10.1. Diffusion of Carbon and Manganese into IF steel from FeMnC films 433

10.1.1. Importance of Manganese for steels 433

10.1.2. Experimental Results 435

10.1.3. Discussion of experimental results on FeMnC coated coupons 441

10.2. Carbon films 446

Chapter 11 : Conclusions and Future Work 449

11.1. Conclusions 449

11.2. Future Work 452

Bibliography 455

Appendices 474

Appendix A: Vickers and Knoop Microhardness 475

Appendix B: Atom Probe Tomography.....477

B.1 Introduction to Atom Probe Tomography.....477

B.2 Atom Probe Tomography.....478

B.2.1 Set-up of an Atom Probe chamber.....481

B.2.2 Spectrum obtained from an Atom Probe Tomography analysis.....482

B.2.3 Three dimensional reconstruction of Atom Probe Tomography Data.....483

B.3 Specimen requirements for Atom Probe Tomography 487

B.3.1 Methods to obtain specimens for Atom Probe Tomography.....488

B.3.2 Focused Ion Beam and Lift-Out Method.....491

Appendix C: Thermoelectric Power Measurements 497

C.1 Thermoelectric power measurements (TEP).....497

Appendix D: Tensile Tests 500

D.1 Calibration of the tensile machine 500

D.2 Tensile Tests 500

D.2.1 Dimensions of tested coupons 500

D.3 Tensile Tests on coupons coated both sides with FeC film and annealed in argon atmosphere.....505

D.4 Tensile Tests on coupons coated both sides with FeC film and Nickel cap layer annealed in Argon atmosphere 507

D.5 Tensile Tests on coupons cleaned using HCl and coated both sides with FeC amorphous film.....518

D.6 Annealing of both sides coated coupons in air 531

D.7 Comparison between theoretical yield stresses and experimental yield stresses...532

D.8 Stoichiometric calculation of FeC film crystallization 532

D.8.1 Stoichiometric calculation considering carbon concentration variation in the film.....532

D.8.2 Stoichiometric calculation considering tolerance of film thickness 534

D.9 Coupons having different FeC film thickness.....535

D.9.1 Tensile tests on coupons having different film thicknesses.....535

D.9.2 Stoichiometric calculation considering variation of film thickness 537

D.9.3 Stoichiometric calculations considering carbon concentration and film thickness variations for coupons having different nominal FeC film thicknesses 546

D.10 Annealing in high vacuum at 630 ºC of both sides coated coupons for times longer than 1h 552

D.11 Annealing in high vacuum at 430 ºC for several hours 553

D.12 Annealing of one side coated coupons.....553

D.13 Digital Image Correlation on specimens annealed in high vacuum.....554

D.14 Grain size analyses on diffusion annealed coupons.....555

D.15 Scanning Electron Microscope Images of specimens annealed in high vacuum in the furnace 557

Appendix E: Finite Element Method 559

E.1 Mesh Influence on Lüders bands simulation 559

E.2 Evolution of artificial energy and internal energy for FEM simulations of Lüdering 559

Appendix F: Pre-strain Results 568

Appendix G: Flash Annealing 572

G.1 Sealing of quartz ampoules.....572

G.2 Calculation of time required for flash annealing in the furnace 573

G.3 Theory of Induction Heating.....575

G.4 Mechanical Properties of induction heated one side coated coupons.....577

G.4.1 Calculation of strain-hardening exponent for one side coated coupons 580

G.5 Mechanical Properties of induction heated both sides coated coupons 581

G.5.1 Calculation of strain-hardening exponent for both sides coated coupons 582

G.5.2 EDS and BSE on induction heated specimens 584

G.4.3 Tensile Test of pre-strained and induction heated coupons.....595

Appendix H: Fracture Studies Results 596

H.1 Tensile tests of coupons having carbon gradient along the gauge length.....596

H.2 Void Growth analyses of coupons with holes along the gauge length 598

H.2.1 Void growth as function of true strain extracted in the gauge length.....598

H.2.2 Void Growth as function of the local true strain at the sides of the voids..... 616

H.3 Theoretical prediction of carbon gradient through width 622

H.3.1 Carbon Gradient obtained for annealing times shorter than 1h.....628

H.4 Vickers Hardness for coupons having carbon gradient along the width.....630

H.5 Tensile tests of coupons having carbon gradient on the width 642

H.6 Void growth analyses.....646

H.6.1 Void growth of specimens having FeC film removed in the center 646

H.6.2 Void growth of specimens having FeC film removed on the sides 658

H.6.3 Void growth of specimens having FeC film removed in the center and uniform carbon distribution 663

H.6.4 Void growth of uncoated specimens.....671

H.7 McClintok Fitting.....676

H.7.1 McClintok fitting for specimens having FeC film removed in the center.....676

H.7.2 McClintok fitting for specimens having FeC film removed on the sides.....678

H.7.3 McClintok fitting for specimens having FeC film removed in the center and uniform carbon distribution 678

H.7.4 McClintok fitting for uncoated coupons.....679

H.8 McClintok fitting neglecting Lüdering.....680

Appendix I: IF steel coated with FeMnC Films.....682

List of Figures

Figure 2-1 - Material structures and properties of ordinary composite and functionally graded materials [2] 5
Figure 2-2 - Separation of ceramics and metals by thermal stress [2].....5
Figure 2-3 - Functionally graded materials: processing methods and their classification [8]..8
Figure 2-4 - Schematic mechanism of carbosulphide and carbide formation in titanium IF steels [13].....11
Figure 2-5 - Interstices in ferrite and austenite: (a) one unit cell of bcc ferrite: the iron atoms are not shown for clarity, only octahedral and tetrahedral sites are shown. (b) Octahedral sites in austenite [24] 14
Figure 2-6 - Stabilization processing of Ti-only ULC steel and Ti+Nb ULC steel [35].....18
Figure 2-7 - TEM micrograph showing the in-situ transformation of TiS into $Ti_4C_2S_2$ [36].19
Figure 2-8 - Solid solution strengthening of bcc iron. The effects of different substitutional solute contents (wt%) on the yield strength are shown [33].....20
Figure 2-9 - Yield strength as function of interstitial contents [33] 21
Figure 2-10 - Tensile curves for steels having different carbon content and microstructures [37].....21
Figure 2-11 - Nanoindentation load-depth curves [37] 22
Figure 2-12 - Hardness as function of depth for different materials [37].....22
Figure 2-13 - Variation of micro-Vickers hardness with depth. Three different indent loads show little effect of indentation size [45] 24
Figure 2-14 - Schematic description of all combined softening and hardening effects due to carbon addition [50].....27
Figure 2-15 - Schematic description of the stress necessary to move edges and screws at a constant velocity in Fe and FeC; T_p is the onset of the plateau (260K in FeC) [50].....27
Figure 2-16 - Schematic definition of bake hardening (BH) [61] 31
Figure 2-17 - Results from uniaxial test on steel strip; (a) stress and strain histories recorded, (b) x-t diagram of evolution of deformation front [64] 39
Figure 2-18 - Lateral displacement of strip axis as function of axial displacement δ [79].....41
Figure 2-19 - Local plastic law used to simulate Lüders band in FEM [99] 42

Figure 2-20 - Propagating crack orientation with respect to direction of property variation in FGM (reproduced from a figure reported in ref. [108]) 45
Figure 2-21 - Crack-tip kinking [104] 46
Figure 2-22 - Fracture toughness versus normalized crack length [109] 48
Figure 2-23 - Crack tip interference for FGMs (a, b), for a bimaterial (c) and for a homogeneous glass-epoxy composite (d) [108] 51
Figure 2-24 - FGM model for impact load simulation (figure adapted from image shown in ref. [114]).....53
Figure 2-25 - Change in potential energy due to an increase of the yield stress [115] 55
Figure 2-26 - Plastic zone for a crack in a hard material, parallel to an interface to a soft material. The crack will change its path and curve towards the interface [115] 56
Figure 3-1 - Schematic view of the substrate of IF steel coated both sides with the carbon containing coating.....60
Figure 3-2 - Iron-Carbon diagram [123].....61
Figure 3-3 - Crystallization temperatures and products of $Fe_{1-x}C_x$ films with varying carbon concentration [125], [126] 63
Figure 3-4 - Layout to analyze influence of stiffness on Lüders propagation.....65
Figure 3-5 - Layout of the model to analyze influence of stiffness and thickness but with Lüders created with a gradient.....65
Figure 4-1 - PVD chamber used for film deposition at UBC [127] 68
Figure 4-2 - Schematic view of the thickness of Gracos specimen.....68
Figure 4-3 - (a) IF steel coated both sides with 500nm FeC film; (b) uncoated IF steel.....69
Figure 4-4 - Dimensions of tensile coupon in mm 69
Figure 4-5 - Picture of a tensile coupon obtained with EDM.....69
Figure 4-6 - Wire-EDM cutting of tensile coupons used for Gracos project (University of Ottawa) 70
Figure 4-7 - Temperature vs time curve for annealing treatment at 530 ˚C 71
Figure 4-8 - Turbopump system for the high vacuum annealing at the University of Ottawa 72
Figure 4-9 - System used to perform annealing in argon 73
Figure 4-10 - Schematic view of reference indent used for Knoop hardness measurements.77

Figure 4-11 - Knoop reference indent made on the not-polished surface of a piece of IF steel strip coated both sides with 500 nm thick FeC film and annealed at 430 ˚C - 1h in high vacuum.....79
Figure 4-12 - Knoop reference indent made on the surface of a piece of IF steel strip coated both sides with 500 nm thick FeC film and annealed at 430 ˚C - 1h in high vacuum, the surface has been polished using 4000SiC paper.....79
Figure 4-13 - Knoop reference indent made on the surface of a piece of IF steel strip coated both sides with 500 nm thick FeC film and annealed at 430 ˚C - 1h in high vacuum, the surface has been polished using 1 µm diamond suspension and OPS.....80
Figure 4-14 - Schematic view of an engineering stress-strain curve showing Lüdering.....82
Figure 4-15 - First tensile machine used for Gracos project 83
Figure 4-16 - Another tensile machine used for tensile tests of the Gracos Project.....84
Figure 4-17 - Surface of a Gracos coupon prepared for DIC testing.....86
Figure 4-18 - Fracture surface of specimen annealed in high vacuum at 430 ˚C - 1h.....87
Figure 4-19 - Examples of applications in Atom Probe Tomography (APT) [148].....89
Figure 4-20 - Main peaks of iron isotopes obtained from APT of an IF steel sample coated both sides with 500 nm FeC film and annealed at 530 ˚C – 1h in high vacuum.....90
Figure 4-21 - Peaks of isotopes found in an IF steel sample coated both sides with 500 nm FeC film and annealed at 530 ˚C – 1h in high vacuum 91
Figure 4-22 - Peak of hydrogen for an IF steel sample coated both sides with 500 nm FeC film and annealed at 530 ˚C – 1h in high vacuum.....92
Figure 4-23 - Principle of the TEP measurements [149].....93
Figure 4-24 - Experimental procedure used for the quantitative evaluation of the amount of interstitial atoms in solid solution using TEP measurements [32] 94
Figure 5-1 - Carbon profile through thickness predicted by the solution of the second Fick's law considering heating and cooling stages with isothermal plateau: in the x axis the position through thickness is reported, where 0 indicates the center of the coupon, while in the y axis the carbon concentration is shown in at% 98
Figure 5-2 - Knoop Hardness profile through thickness of IF steel coated both sides with 500 nm thick FeC film and annealed in high vacuum at different temperatures. The Knoop values have been obtained applying a load of 100g for 10s. In the X axis thedistance from

the centre is reported, while the Y axis shows the Knoop hardness values. In the X axis, 0 µm corresponds to the centre of the specimen, while the value of 100 µm corresponds to the coated surface if the IF steel 100
Figure 5-3 - Time and temperature profiles for the different annealing treatments implemented in the vacuum furnace at the University of Ottawa 102
Figure 5-4 - Engineering stress-strain curves for coupons coated both sides with 500 nm FeC and tested at a speed of 2.5 µm/s 104
Figure 5-5 - FeC film behaviour for a not-annealed IF coupon during a tensile test (images taken with optical microscope at magnification 10X).....105
Figure 5-6 - Engineering stress-strain curves for samples annealed at 330 ºC for 1h, tested at 2.5 µm/s 106
Figure 5-7 - FeC film behaviour during a tensile test for a both side coated IF coupon annealed at 330 ˚C - 1h in high vacuum (images taken with optical microscope at magnification 10X).....107
Figure 5-8 - Carbon profile created trough thickness for diffusion at 330 ˚C for 1h and 4 days.....108
Figure 5-9 - Engineering stress-strain curves for samples annealed at 330 ºC for 4 days, tested at the same speed of 2.5 µm/s 108
Figure 5-10 - Engineering stress-strain curves for samples annealed at 430 ºC for 1h in high vacuum, tested at the same speed of 2.5 µm/s.....109
Figure 5-11 - FeC film behaviour during a tensile test for a both side coated IF coupon annealed at 430 ˚C - 1h in high vacuum (images taken with optical microscope at magnification 10X).....110
Figure 5-12 - Engineering stress-strain curves for samples annealed at 530 ºC for 1h in high vacuum, tested at the same speed of 2.5 µm/s.....111
Figure 5-13 - FeC film behaviour during a tensile test for a both side coated IF coupon annealed at 530 ˚C - 1h in high vacuum (images taken with optical microscope at magnification 10X).....112
Figure 5-14 - Engineering stress-strain curves for samples annealed at 630 ºC for 1h, tested at the same speed of 2.5 µm/s.....113

Figure 5-15 - Engineering stress-strain curves for samples E-7, E-8 and E-9 annealed at 630 ºC for 1h, tested at the same speed of 2.5 µm/s and used for DIC analyses.....113
Figure 5-16 - FeC film behaviour during a tensile test for a both side coated IF coupon annealed at 630 ˚C - 1h in high vacuum (pictures taken with optical microscope at magnification 10X).....114
Figure 5-17 - Engineering stress-strain curves for coupons coated both sides with 500 nm FeC amorphous film and annealed in high vacuum at 710 ˚C - 1h.....115
Figure 5-18 - Engineering stress-strain curves for coupons coated both sides with 500 nm FeC amorphous film and annealed in high vacuum at 710 ˚C - 1h.....115
Figure 5-19 - FeC film behaviour during a tensile test for a both side coated IF coupon annealed at 710 ˚C - 1h in high vacuum (images taken with optical microscope at magnification 10X).....116
Figure 5-20 - Global comparison of engineering stress-strain curves for annealing in high vacuum at different temperatures for 1h.....117
Figure 5-21 - Global comparison of engineering stress-strain curves for annealing in high vacuum at different temperatures for 1h of uncoated IF coupons.....118
Figure 5-22 - Engineering stress-strain curves for coupons coated both sides with a 500 nm thick FeC amorphous film and annealed in argon at 430 ˚C - 1h.....119
Figure 5-23 - Engineering stress-strain curves for coupons coated both sides with a 500 nm thick FeC amorphous film and annealed in argon at 530 ˚C - 1h.....120
Figure 5-24 - Engineering stress-strain curves for coupons coated both sides with a 500 nm thick FeC amorphous film and annealed in argon at 630 ˚C - 1h.....121
Figure 5-25 - Engineering stress-strain curves for coupons coated both sides with a 500 nm thick FeC amorphous film and annealed in argon at 710 ˚C - 1h.....121
Figure 5-26 - Comparison of the average yield stress values obtained by annealing in high vacuum and argon.....122
Figure 5-27 - Engineering stress-strain curves for coupons coated both sides with a 500 nm thick FeC amorphous film. Annealing performed in air at 530 ˚C - 1h for specimens A and B and at 630 ºC - 1h in air for specimen C.....123
Figure 5-28 - Fracture surface of tensile coupon coated both sides with 500 nm thick FeC film and annealed at 430 ˚C - 1h in high vacuum.....125

Figure 5-29 - Contour of the fracture surface defined with Image J for a tensile coupon coated both sides with 500 nm thick FeC film annealed at 430 ˚C – 1h in high vacuum 125
Figure 5-30 - Comparison between yield stress expected theoretically and yield stress obtained experimentally for annealing in high vacuum at different temperatures for 1h of specimens coated both sides with 500 nm FeC film.....127
Figure 5-31 - SEM images of the surface of a both sides coated coupon annealed in high vacuum at 330 ºC - 1h.....128
Figure 5-32 - SEM images of the surface of a both sides coated coupon annealed in high vacuum at 430 ºC - 1h.....128
Figure 5-33 - SEM images of the surface of a both sides coated coupon annealed in high vacuum at 530 ºC - 1h.....129
Figure 5-34 - SEM images of the surface of a both sides coated coupon annealed in high vacuum at 630 ºC - 1h.....129
Figure 5-35 - SEM images of the surface of a both sides coated coupon annealed in high vacuum at 710 ºC - 1h.....130
Figure 5-36 - TEM Image: cross view of IF substrate coated with 500 nm of FeC film as deposited. The SAED pattern obtained from the film is included in the figure. A is the Pt cap layer, B is the FeC film and C is the IF substrate (courtesy of Dr. Amelié Fillon).....131
Figure 5-37 - TEM Image: cross view of IF substrate coated with 500 nm of FeC film and annealed at 430 ˚C in high vacuum. The SAED pattern obtained from the film is included in the figure (courtesy of Dr. Amelié Fillon).....131
Figure 5-38 - TEM Image: cross view of IF substrate coated with 500 nm of FeC film and annealed at 530 ˚C in high vacuum. The SAED pattern obtained from the film is included in the figure (courtesy of Dr. Amelié Fillon).....132
Figure 5-39 - X-ray diffraction analyses performed on FeC film (30 at% carbon content) deposited on silicon substrate (Co K-alpha radiation was used) (courtesy of Dr. Amélie Fillon) 133
Figure 5-40 - Comparison between theoretical yield stress and experimental yield stress considering FeC film crystallization.....136

Figure 5-41 - Comparison between theoretical yield stress and experimental yield stress considering FeC film crystallization – error bars were calculated considering both carbon content variations and film thickness variation 137
Figure 5-42 - Fracture surface of a coated and not-annealed tensile coupon 140
Figure 5-43 - Fracture surface of an uncoated tensile tested coupon annealed at 710 ˚C – 1h. Spectrum 1 indicates the first analyzed particle 141
Figure 5-44 - Fracture surface of tensile coupon coated both sides and annealed at 430 ˚C – 1h in high vacuum. Spectra 1, 2 and 3 indicate the particles whose composition was analyzed 142
Figure 5-45 - Fracture surface of tensile coupon coated both sides and annealed at 530 ˚C – 1h in high vacuum. Spectra 1, 2 and 3 (a) and 4, 5 (b) indicate particles whose composition was analyzed 143
Figure 5-46 - Fracture surface of tensile coupon coated both sides and annealed at 630 ˚C – 1h in high vacuum. Spectra 1 and 2 indicate the particles whose composition was analyzed 144
Figure 5-47 - Fracture surface of tensile coupon coated both sides and annealed at 710 ˚C – 1h in high vacuum. Spectra 1 and 2 indicate the particles whose composition was analyzed (specimen F-9) 145
Figure 5-48 - Fracture surface of tensile coupon coated both sides and annealed at 710 ˚C – 1h in high vacuum. Spectra 1 and 2 indicate the particles whose composition was analyzed (specimen F-10) 145
Figure 5-49 - Fracture surface of tensile coupon coated both sides and annealed at 710 ˚C – 1h in high vacuum (specimen F-10). Spectra 3, 4 and 5 indicate the particles whose composition was analyzed 146
Figure 5-50 - Fracture surface of tensile coupon coated both sides and annealed at 710 ˚C – 1h in high vacuum. Spectra 1, 2 and 3 indicate the particles whose composition was analyzed 147
Figure 5-51 - Carbon concentration from TEP measurements as function of annealing temperature for uncoated and both sides coated coupons 150
Figure 5-52 - Iron atom distribution obtained by APT from a tip of uncoated and not-annealed IF steel 151

Figure 5-53 - Phosphorus and titanium distributions obtained inside a tip of uncoated and not-annealed IF steel.....152
Figure 5-54 - Carbon and titanium distribution for a 500 nm both sides coated IF steel annealed at 530 ˚C -1h (reconstructed volume 80 x 80 x 450 nm^3) 153
Figure 5-55 - Phosphorus and aluminium distribution for a 500 nm both sides coated IF steel annealed at 530 ˚C -1h (reconstructed volume 80 x 80 x 450 nm^3) 153
Figure 5-56 - Carbon and titanium atoms distribution for a specimen coated both sides and annealed at 710 ˚C – 1h (analyzed volume 48 nm x 48 nm x 70 nm).....155
Figure 5-57 - Carbon and titanium atoms distribution for a specimen coated both sides and annealed at 710 ˚C – 1h (analyzed volume 77 nm x 77 nm x 210 nm).....156
Figure 5-58 - Distribution of Ti, C and O or S atoms in a both sides coated IF specimen annealed at 710 ˚C – 1h 158
Figure 5-59 - Engineering stress-strain curves for coupons coated both sides with 50 nm thick FeC amorphous film: sample 50 - A was not annealed, while samples 50 - B and 50 - C were annealed at 530 ˚C - 1h in high vacuum 160
Figure 5-60 - Microscope picture of the surface of coupons coated both sides with 50 nm annealed at 530 ˚C - 1h in high vacuum.....161
Figure 5-61 - Engineering stress-strain curves for coupons coated both sides with 100 nm thick FeC amorphous film: sample 100 - A was not annealed, while sample 100 - B was annealed at 530 ˚C-1h in high vacuum.....162
Figure 5-62 - Microscope picture of the surface of coupons coated both sides with 100 nm annealed at 530 ˚C - 1h in high vacuum.....163
Figure 5-63 - Engineering stress-strain curves for coupons coated both sides with 200 nm thick FeC amorphous film: sample 200 - A was not annealed, while sample 200 - B and 200 - C were annealed at 530 ˚C - 1h in high vacuum 164
Figure 5-64 - Microscope picture of the surface of coupons coated both sides with 200 nm annealed at 530 ˚C - 1h in high vacuum.....165
Figure 5-65 - Engineering stress-strain curves for coupons coated both sides with 300 nm thick FeC amorphous film 166
Figure 5-66 - Engineering stress-strain curves for coupons coated both sides with 400 nm thick FeC amorphous film 167

Figure 5-67 - Engineering stress-strain curves for coupons coated both sides with different thicknesses of FeC amorphous film and annealed in high vacuum at 530 ˚C - 1h.....168
Figure 5-68 - Comparison of theoretical yield stress and experimental yield stress for coupons coated with different thicknesses of FeC film.....169
Figure 5-69 - Comparison of theoretical yield stress and experimental yield stress for coupons coated with different thicknesses of FeC film considering carbon content uncertainty and film thickness uncertainty.....170
Figure 5-70 - Engineering stress-strain curves for specimens coated both sides with 500nm thick FeC film and annealed at 630˚C-5h in high vacuum.....171
Figure 5-71 - Evolution of the carbon concentration through thickness for a coupon coated both sides and annealed at 430 ˚C for different times.....172
Figure 5-72 - Engineering stress-strain curves for specimens coated both sides with 500 nm thick FeC film and annealed at 430 ˚C - 10h in high vacuum.....173
Figure 5-73 - Knoop microhardness curve for specimen coated both sides with 500 nm FeC film and annealed at 430 ˚C - 10h in high vacuum. The hardness curve has been added to the Knoop microhardness previously shown in section 5.2. for other heat treatments.....174
Figure 5-74 - Engineering stress-strain curves for coupons coated one side with 500 nm thick FeC film and annealed at 530 ˚C - 1h in high vacuum. OS means one side coated while A and B indicate two different specimens that were tested.....175
Figure 5-75 - Engineering stress-strain curves for coupons coated one side with 500 nm thick FeC film and annealed at 630 ˚C - 1h in high vacuum.....176
Figure 5-76 - Comparison between theoretical yield stress and experimental yield stress for one side coated coupons.....177
Figure 5-77 - Lüders plateau detail of the engineering stress-strain curves for samples C-4 (a, b, c, d) and C-5 (e, f, g, h) annealed at 430 ˚C - 1h in high vacuum.....178
Figure 5-78 - Propagation of Lüders bands for sample C-4 coated both sides with 500 nm thick FeC film and annealed at 430 ˚C - 1h in high vacuum.....179
Figure 5-79 - Velocity profile of Lüders bands in sample C-4 coated both sides with 500 nm FeC film and annealed at 430 ˚C - 1h.....180
Figure 5-80 - Lüders plateau detail of the engineering stress-strain curves for samples D-3 (a, b, c, d) and D-4 (e, f, g, h) annealed at 530 ˚C - 1h in high vacuum.....181

Figure 5-81 - Propagation of Lüders bands for sample D-3 coated both sides with 500 nm thick FeC film and annealed at 530 ˚C - 1h in high vacuum 181
Figure 5-82 - Velocity profile of Lüders bands in sample D-3 coated both sides with 500 nm FeC film and annealed at 530 ˚C - 1h 182
Figure 5-83 - Lüders plateau detail of the engineering stress-strain curves for samples E-9 (a, b, c, d) E-8 (e, f, g, h) and E-7 (i, l, m, n) annealed at 630 ˚C - 1h in high vacuum 183
Figure 5-84 - Propagation of Lüders bands for sample E-9 coated both sides with 500 nm thick FeC film and annealed at 630 ˚C - 1h in high vacuum 184
Figure 5-85 - Lüders plateau detail of the engineering stress-strain curves for sample F-11 (a, b, c, d) and sample F-12 (e, f, g, h) annealed at 710 ˚C - 1h in high vacuum 185
Figure 5-86 - Propagation of Lüders bands for sample F-11 coated both sides with 500 nm thick FeC film and annealed at 710 ˚C - 1h in high vacuum 185
Figure 5-87 - Propagation of Lüders bands (points e and f of the stress-strain curve) for sample F-12 coated both sides with 500 nm thick FeC film and annealed at 710 ˚C - 1h in high vacuum.....186
Figure 5-88 - Stress drop at the start of the Lüders plateau propagation as function of annealing temperature.....187
Figure 5-89 - Diffused carbon content, Lüders length and Lüders bands speed as function of annealing temperature.....189
Figure 5-90 - Comparison of yield stress (YS) and Ultimate Tensile Strength (UTS) for uncoated and annealed IF steel coupons and coated and annealed IF steel coupons 191
Figure 6-1 - Sketch showing the increase or decrease of the upper point corresponding to the upper yield stress 197
Figure 6-2 - Plastic behaviour with linear softening implemented in ABAQUS to analyze the influence of different yield stresses on Lüders propagation.....199
Figure 6-3 - Detail of the implemented linear softening for the plastic behaviour 200
Figure 6-4 - Sketch showing the change of linear slope in the softening implemented to simulate Lueder plateau. Upper yield stress (point A) and Lüders strain (point B) are kept constant.....201
Figure 6-5 - Detail of the implemented linear softening behaviour for the series of simulations having different linear slopes 202

Figure 6-6 - Detail of the implemented linear softening for the plastic behaviour showing the change of slope 202
Figure 6-7 - Engineering stress-strain obtained by simulation of Lüders plateau by using a linear softening where the upper yield stress was changed 203
Figure 6-8 - Engineering stress-strain curves obtained by changing slope of the linear softening 204
Figure 6-9 - Artificial energy evolution expressed as percentage of the internal energy during the simulation of change in slope of the linear softening 205
Figure 6-10 - Schematic view of the thickness of the tensile coupon simulated to investigate the influence of a gradient of mechanical properties on Lüders propagation.....206
Figure 6-11 - Plastic behaviour implemented in ABAQUS to simulate the influence of graded and constant carbon content on Lüders propagation 207
Figure 6-12 - Comparison of stress-strain curves obtained simulating Lüders propagation in a specimen having carbon gradient through thickness and a specimen having uniform carbon content through thickness 207
Figure 6-13 - Thickness of the tensile coupon implemented in ABAQUS to simulate influence of stiffness of central layer having no plateau on Lüders propagation.....208
Figure 6-14 - Stress-strain curve detail of the plastic behaviour implemented in ABAQUS in order to simulate the influence of stiffness on the Lüders propagation.....210
Figure 6-15 - Stress-strain curve detail of the plastic behaviour implemented in ABAQUS in order to simulate the influence of thickness of a central layer having no plateau on the Lüders propagation 212
Figure 6-16 - Thickness of a tensile coupon implemented in ABAQUS to simulate influence of thickness of central layer having no Lüdering. Outer layers have both yield stress and Lüders length gradient 212
Figure 6-17 - Plastic properties implemented in the outer layers to simulate a graded structure having Lüders plateau.....213
Figure 6-18 - Influence of stiffness of a central layer having no Lüders behaviour on Lüders propagation 214
Figure 6-19 - Schematic view of engineering stress-strain curves for a “sandwiched” material having Lüders on the outer layers and no Lüders on the central layer.....215

Figure 6-20 - Magnified view of the upper yield stress for simulations showing the influence of stiffness on Lüders propagation 216
Figure 6-21 - Influence of change of thickness of a central layer on Lüders plateau length. Central layer without Lüdering, while outer layers have Lüdering with no gradient.....217
Figure 6-22 - Influence of change of thickness of a central layer on Lüders plateau length. Central layer without Lüdering, while outer layers have Lüdering with a graded configuration.....218
Figure 6-23 - Schematic view of the configuration implemented in ABAQUS to prove the influence of strain-hardening.....219
Figure 6-24 - Plastic properties implemented in layer 3 to simulate the influence of strain-hardening on Lüders propagation 220
Figure 6-25 - Engineering stress-strain curves obtained changing the strain-hardening behaviour 220
Figure 6-26 - Sketch of the thickness of tensile coupon used to simulate influence of voids on Lüders propagation 221
Figure 6-27 - Sketch of the simulated voids configuration. Void applied in the gauge length of the specimen.....222
Figure 6-28 - Sketch of void dimensions.....222
Figure 6-29 - Stress-strain curves obtained simulating the influence of intervoid spacing on Lüders propagation 223
Figure 6-30 - Lüders bands localization in tensile coupon having voids with interspace of 50 μm.....224
Figure 6-31 - Lüders bands localization in tensile coupon having voids with interspace of 70 μm.....224
Figure 6-32 - Lüders bands localization in tensile coupon having voids with interspace of 100 μm.....224
Figure 6-33 - Sketch of the void configuration used to simulate the influence of volume fraction on Lüders propagation.....226
Figure 6-34 - Influence of different volume fractions of voids on Lüders propagation.....226
Figure 7-1 - Increase of yield stress obtained for different pre-strain levels at 50 ˚C of ageing temperature [168].....230

Figure 7-2 - Increase of yield stress obtained for different ageing temperatures for 1% pre-strain [168].....230
Figure 7-3 - Stress-strain curve for low carbon steel strained to point A, unloaded, and then restrained immediately (curve a) and after ageing (curve b) [170] 232
Figure 7-4 - Quantities evaluated during the tensile pre-strain and after the diffusion heat treatment 233
Figure 7-5 - Pre-strain engineering stress-strain curves of specimens A and B which will be annealed at 430 ˚C - 1h in high vacuum after the deposition of the FeC film on both sides233
Figure 7-6 - Engineering stress-strain curves of specimens A and B after pre-strain and annealing at 430 ˚C - 1h in high vacuum after the deposition of the FeC film on both sides 234
Figure 7-7 - Pre-strain engineering stress-strain curves of specimens D and G which will be annealed at 530 ˚C - 1h in high vacuum after the deposition of the FeC film on both sides235
Figure 7-8 - Engineering stress-strain curves of specimens D and G after pre-strain and annealing at 530 ˚C - 1h in high vacuum after the deposition of the FeC film on both sides 235
Figure 7-9 - Pre-strain engineering stress-strain curves of specimens C and E which will be annealed at 630 ˚C - 1h in high vacuum after the deposition of the FeC film on both sides236
Figure 7-10 - Engineering stress-strain curves of specimens C and E after pre-strain and annealing at 630 ˚C - 1h in high vacuum after the deposition of the FeC film on both sides 236
Figure 7-11 - Pre-strain engineering stress-strain curves of specimens H and L which will be annealed at 710 ˚C - 1h in high vacuum after the deposition of the FeC film on both sides237
Figure 7-12 - Engineering stress-strain curves of specimens H and L after pre-strain and annealing at 710 ˚C - 1h in high vacuum after the deposition of the FeC film on both sides 237
Figure 7-13 - Comparison of increase of strength for pre-strained and coated coupons and coated but not pre-strained coupons 239
Figure 7-14 - Comparison of engineering stress-strain curves for pre-strained and both sides coated coupons (500nm FeC film) after annealing at different temperatures for 1h in high vacuum.....240

Figure 7-15 - Engineering stress-strain curves of specimens A16, A 11, A13 and A18 after pre-strain 241
Figure 7-16 - Engineering stress-strain curves of specimens A16, A 11, A13 and A18 after pre-strain and annealing at different temperatures for 1h.....241
Figure 7-17 - Comparison of yield stress after pre-strain, annealing and reloading for coated coupons and not-coated coupons. For each temperature the plotted value is an average of the measured values. 242
Figure 7-18 - Microstructure of the gauge length of uncoated and 15% prestrain coupons of IF steel 245
Figure 7-19 - Engineering stress-strain curves of loading and unloading of coupons coated both sides with 500 nm thick FeC film annealed at different temperatures for 1h. Coupons where tested until the end of the Lüders plateau. 247
Figure 7-20 - Engineering stress-strain curves of specimens coated both sides with 500 nm thick FeC film annealed at different temperatures and aged at 170 ˚C for 20 min 247
Figure 7-21 - Sketch of the quantities measured before and after strain ageing 248
Figure 8-1 - Sketch showing the sealing of IF steel samples inside quartz ampoules.....257
Figure 8-2 - Microstructure of the specimen coated one side and “flash annealed” at 950˚C for 2min and 30s. Etching performed with 4% vol. Nital solution. Images taken with optical microscope (magnification 20X). The images show zones with different grain sizes present in the same specimen after flash annealing. 260
Figure 8-3 - Microstructure of the specimen coated one side and “flash annealed” at 950˚C for 2min and 30s. Etching performed with 2% vol. Nital solution and after with 10% sodium metabisulfite ($Na_2S_2O_5$) solution. Images taken with optical microscope (magnification 20X). The images show zones with different grain sizes present in the same specimen after flash annealing 261
Figure 8-4 - Microstructure of the specimen coated one side and “flash annealed” at 950˚C for 1min and 55s: (a) and (b) etching performed with 4% vol. Nital solution (magnification 10X), (c) and (d) etching performed with 10% sodium metabisulphide (magnification 20X) 262

Figure 8-5 - Schematic view of the IF steel specimen cold mounted in resin, showing the different zones where hardness and images of the microstructure were taken for the specimen “flash annealed” at 950 ˚C for 2 min and 30 seconds 263
Figure 8-6 - Vickers hardness through thickness of specimens coated one side with 500 nm FeC film and “flash annealed” at 950 ˚C for 2 min - 30 s and 1 min - 55 s respectively. Vickers hardness of a piece of IF steel not coated and not annealed is reported for comparison. Error bars are shown for clarity only for some curves. For the other curves error bars are of the same order of magnitude of the bars already shown in the graph 264
Figure 8-7 - Microstructure of zone A (a) and zone B (b) of the specimen of IF steel coated one side with 500 nm thick FeC film and” flash annealed” at 950 ˚C for 2 min and 30 s ...265
Figure 8-8 - Microstructure of zone C of the specimen of IF steel coated one side with 500 nm thick FeC film and” flash annealed” at 950 ˚C for 2 min and 30 s 265
Figure 8-9 - Microstructure of zone A of the specimen of IF steel coated one side with 500 nm thick FeC film and” flash annealed” at 950 ˚C for 1 min and 55 s 266
Figure 8-10 - Microstructure of zone C of the specimen of IF steel coated one side with 500 nm thick FeC film and” flash annealed” at 950 ˚C for 1 min and 55 s 266
Figure 8-11 - Set-up of induction heating experiment.....270
Figure 8-12 - Heat treatment cycle used for induction heating experiments.....271
Figure 8-13 - Vickers hardness of one-side coated coupon and uncoated coupon both induction heated at 1150 ºC for 1 second and then at 820 ˚C for 30 seconds. Each point in the curve corresponds to at least 10 measurements. Error bars representing the standard deviation are shown 273
Figure 8-14 - Thickness of the one side coated coupon. Bottom side was coated with 500 nm FeC film before performing induction heating at 1150 ºC for 1 s and then at 820 ˚C for 30 s: (a) view of the whole thickness; (b) close view of the grains close to the coated side of the specimen 274
Figure 8-15 - Thickness of the one side coated coupon. Bottom side was coated with 500 nm FeC film before performing induction heating at 1150 ºC for 1 s and 820 ˚C for 30 s: (a) view of the grains close to the coated surface; (b) close view of the grains close to the uncoated side of the specimen 275

Figure 8-16 - Etching of the one side coated coupon with 1% vol. Nital and 15% sodium metabisulphite. The FeC coated side is on the bottom of the picture while the not-coated side is at the top of the picture 276
Figure 8-17 – Forward Scatter Detector (FSD) Image of the area analyzed by EBSD of the one side coated IF coupon induction heated at 1150 ºC for 1 s and then at 820 ˚C for 30 s 276
Figure 8-18 - Phase map obtained by EBSD analysis on a one side coated coupon induction heated at 1150 ºC for 1 s and then at 820 ˚C for 30 s 277
Figure 8-19 - Etching with 4% vol Nital solution of the uncoated coupon induction heated at 1150 ºC for 1 s and then at 820 ˚C for 30 s: (a) whole thickness, (b) view close to one of the edges 278
Figure 8-20 - Etching of the uncoated and induction heated coupon with 15% sodium metabisulphite.....278
Figure 8-21 - Vickers hardness through thickness for one side coated coupons induction heated at 1100 ºC - 1150ºC for 1 second and then induction heated at 820 ˚C for 30 seconds and 4 minutes. Vickers hardness of uncoated and not-annealed IF steel and for uncoated IF steel induction heated at 1100 ºC - 1150ºC for 1 second and then induction heated at 820 ˚C for 30 seconds, 1 minute and 4 minutes. 279
Figure 8-22 - Engineering stress-strain curves of a not-annealed IF steel and of uncoated coupons induction heated at 1100 ºC – 1150 ºC for 1 second and then induction heated at 820 ºC for different times 282
Figure 8-23 - Microstructure of the uncoated IF steel induction heated at 1100 ºC – 1150 ºC for 1 second and then induction heated at 820 ºC – 2 minutes (etching performed with 4% vol Nital solution).....283
Figure 8-24 - Microstructure of the uncoated IF steel induction heated at 1100 ºC – 1150 ºC for 1 second and then induction heated at 820 ºC for 4 minutes (etching performed with 4% vol Nital solution): (a) whole thickness, (b) closer view.....284
Figure 8-25 – Etching with sodium metabisulphite for uncoated coupons induction heated at 1100 ºC – 1150 ºC for 1 second and then induction heated at 820 ºC for 2 min (a) and for 4 min (b) 284
Figure 8-26 - Engineering stress-strain curves for coupons coated on one side with 500 nm thick FeC film and induction heated at different temperatures and for different times. The

specimens induction heated at 820 ºC were first heated at 1100 ºC -1150 ºC for 1 second and then the temperature was lowered at 820 ºC.....285
Figure 8-27 - Etching of specimen one side coated, induction heated at 1100 ºC – 1150 ºC for 1 second and then induction heated at 820 ˚C for 30 seconds 288
Figure 8-28 - Microstructure of the specimen coated on one side and induction heated at 1100 ºC – 1150 ºC for 1 second and then induction heated at 820˚C for 2 minutes 289
Figure 8-29 - Microstructure of the specimen coated on one side and induction heated at 1100 ºC – 1150 ºC for 1 second and then induction heated at 820 ˚C for 4 minutes 289
Figure 8-30 - Microstructure of the specimen coated on one side and induction heated at 1100 ˚C for 4 minutes.....290
Figure 8-31 - Engineering stress-strain curves for tensile coupons coated both sides with 500 nm FeC film induction heated at 820 ˚C for different time and compared with one uncoated coupon of IF steel induction heated for 2 minutes and one both sides coated coupon annealed in furnace at 820 ºC for 2 minutes. The specimens induction heated at 820 ºC were first heated at 1100 - 1150 ºC for 1 second and then the temperature was lowered at 820 ºC 291
Figure 8-32 - Vickers hardness through thickness for one side and both sides coated coupons induction heated at 1100 ºC – 1150 ºC for 1 second and then induction heated at 820 ˚C for different times. Vickers hardness of uncoated and not annealed IF steel is included for reference 294
Figure 8-33 - Microstructure of both sides coated tensile coupon induction heated at 1100 ºC – 1150 ºC for 1 second and then induction heated at 820 ˚C: (a) 1 minute coupon and (b) 2 minutes coupon.....295
Figure 8-34 – Microstructure of a both sides coated tensile coupon induction heated at 1100 ºC – 1150 ºC for 1 second and then induction heated at 820 ˚C for 2 minutes (etching performed with Nital solution for 7 seconds and with sodium metabisulphite solution for 15 seconds) 296
Figure 8-35 - Microstructure of tensile coupon coated both sides, induction heated at 1100 ºC – 1150 ºC for 1 second and then induction heated at 820 ˚C for 2 minutes (etching with 4% vol Nital solution and 12% sodium metabisulfite solution. Magnification 50X) 297

Figure 8-36 – Microstructures of both sides coated coupons induction heated at 1100 ºC – 1150 ºC for 1 second and then induction heated at 820 ºC for 4 minutes (a) and for 8 minutes (b) (etching with 4% vol Nital solution) (Magnification 50X).....298
Figure 8-37 - Microstructure of tensile coupon coated both sides, induction heated at 1100 ºC – 1150 ºC for 1 second and then induction heated at 820 ˚C for 4 minutes (etching with 4% vol Nital solution and 12% sodium metabisulfite solution. Magnification 50X) 298
Figure 8-38 - Microstructure of a both sides coated coupon which was induction heated at 1100 ºC – 1150 ºC for 1 second and then induction heated at 820 ˚C for 8 minutes. (Etching performed using 4% vol Nital solution and 11% sodium metabisulfite solution. Magnification 50X) 299
Figure 8-39 - Overall view of the microstructure of uncoated not-annealed IF steel. Etching performed with 4% vol Nital solution before placing the specimen in the SEM chamber (magnification 550X).....300
Figure 8-40 - Detail of the etched microstructure of uncoated not-annealed IF steel (magnification 2000X).....301
Figure 8-41 - Detail of grain boundaries of uncoated and not-annealed IF steel (magnification 5000X).....301
Figure 8-42 - Overall view of the microstructure of uncoated coupon induction heated at 1100 ºC – 1150 ºC for 1 second and then at 820 ˚C – 30 s (magnification 450X).....302
Figure 8-43 - Detail of the etched microstructure of uncoated coupon induction heated at 1100 ºC – 1150 ºC for 1 second and then at 820 ˚C – 30 s (magnification 2000X).....302
Figure 8-44 - Detail of grain boundaries for etched microstructure of uncoated coupon induction heated at 1100 ºC – 1150 ºC for 1 second and then at 820 ˚C – 30 s (magnification 5000X) 303
Figure 8-45 - Overall view of the microstructure of one side coated coupon induction heated at 1100 ºC – 1150 ºC for 1 second and then at 820 ˚C – 30 s. The microstructure is close to the coated edge (magnification 750X).....303
Figure 8-46 - Detail of the etched microstructure of one side coated coupon induction heated at 1100 ºC – 1150 ºC for 1 second and then at 820 ˚C – 30 s. Grains are close to the coated edge (magnification 4000X). The arrows indicate thick grain boundaries and grain boundaries made by more lines 304

Figure 8-47 - Detail of the etched microstructure of one side coated coupon induction heated at 1100 ºC – 1150 ºC for 1 second and then at 820 ˚C – 30 s. Grains are in the middle of the thickness of the specimen (magnification 4000X). The arrows indicate thick grain boundaries and grain boundaries made by more lines.....304
Figure 8-48 - Detail of the etched microstructure of one side coated coupon induction heated at 1100 ºC – 1150 ºC for 1 second and then at 820 ˚C – 30 s. Grains are close to the uncoated edge (magnification 4000X).....305
Figure 8-49 - Overall view of the microstructure of one side coated coupon induction heated at 1100 ºC – 1150 ºC for 1 second and then at 820 ˚C – 4 minutes (magnification 650X)..306
Figure 8-50 - Detail of the etched microstructure of one side coated coupon induction heated at 1100 ºC – 1150 ºC for 1 second and then at 820 ˚C – 4 minutes (magnification 2000X) 306
Figure 8-51 - Overall view of the microstructure of both sides coated coupond induction heated at 1100 ºC – 1150 ºC for 1 second and then at 820 ˚C – 1 minute (magnification 550X).....307
Figure 8-52 - Detail of the etched microstructure of both sides coated coupon induction heated at 1100 ºC – 1150 ºC for 1 second and then at 820 ˚C – 1 minute (magnification 2000X).....308
Figure 8-53 - Detail of the etched microstructure of both sides coated coupon induction heated at 1100 ºC – 1150 ºC for 1 second and then at 820 ˚C – 1 minute (magnification 5000X).....308
Figure 8-54 - Detail of the etched microstructure of both sides coated coupon induction heated at 1100 ºC – 1150 ºC for 1 second and then at 820 ˚C – 1 minute (etching with 4% vol Nital solution for 5 seconds. Magnification 5000X).....309
Figure 8-55 - Overall view of the microstructure of both sides coated coupon induction heated at 1100 ºC – 1150 ºC for 1 second and then at 820 ˚C –2 minutes (magnification 1000X).....310
Figure 8-56 - Detail of the etched microstructure of both sides coated coupon induction heated at 1100 ºC – 1150 ºC for 1 second and then at 820 ˚C – 2 minutes (magnification 5000X).....311

Figure 8-57 - Overall view of the microstructure of both sides coated coupon induction heated at 1100 ºC – 1150 ºC for 1 second and then at 820 ˚C – 4 minutes (magnification 1000X) 311
Figure 8-58 - Overall view of another zone of the microstructure of both sides coated coupon induction heated at 1100 ºC – 1150 ºC for 1 second and then at 820 ˚C – 4 minutes (magnification 2000X).....312
Figure 8-59 - Detail of the etched microstructure of both sides coated coupon induction heated at 1100 ºC – 1150 ºC for 1 second and then at 820 ˚C – 4 minutes (magnification 5000X) 312
Figure 8-60 - Overall view of the microstructure of both sides coated coupon induction heated at 1100 ºC – 1150 ºC for 1 second and then at 820 ˚C – 4 minutes (magnification 550X) 313
Figure 8-61 - Detail of the etched microstructure of both sides coated coupon induction heated at 1100 ºC – 1150 ºC for 1 second and then at 820 ˚C – 8 minutes (magnification 5000X) 314
Figure 8-62 - Steps followed to prepare TEM specimens from induction heated coupons .315
Figure 8-63 - TEM bright field image obtained in one grain of a specimen induction heated at 1100 ºC – 1150 ºC for 1 second and then at 820 ˚C for 2 minutes 315
Figure 8-64 - TEM bright field image obtained in another grain of a specimen induction heated at 1100 ºC – 1150 ºC for 1 second and at 820 ˚C for 2 minutes: SAED pattern for carbides is shown 316
Figure 8-65 - Bright field STEM images of specimen induction heated at 1100 ºC – 1150 ºC for 1 second and then at 820 ºC for 2 minutes (a) and (b). Dislocations and precipitates are visible in both images. (c) zones where EDS spectra were acquired 316
Figure 8-66 - EDS spectra obtained from nanosized carbides found for specimen induction heated at 1100 ºC – 1150 ºC for 1 second and at 820 ºC for 2 minutes 317
Figure 8-67 - Brigth field STEM images (a) and (b) showing dislocations and carbides obtained for the specimen induction heated at 1100 ºC – 1150 ºC for 1 second and at 820 ºC for 4 minutes 318

Figure 8-68 - EDS spectra obtained for specimen induction heated at 1100 ºC – 1150 ºC for 1 second and at 820 ºC for 4 minutes: (a) shows the zones where the spectra were extracted; (b) shows the spectrum detected for a TiC carbide 318
Figure 8-69 – EDS spectra obtained for specimen induction heated at 1100 ºC – 1150 ºC for 1 second and at 820 ºC for 4 minutes: spectra 3 and 4 were detected from TiC carbides, while spectrum 5 was obtained from the ferrite matrix.....319
Figure 8-70 - Grazing X-Ray analyses of the FeC film induction heated at 1100 ºC – 1150 ºC for 1 second and at 820 ˚C for 1 minute.....320
Figure 8-71 - Grazing X-Ray analyses of the FeC film induction heated at 1100 ºC – 1150 ºC for 1 second and at 820 ˚C for 1 minute and 820 ˚C for 4 minutes analyzed from 24˚ to 64˚ 321
Figure 8-72 - Schematic view of the quantities evaluated for induction heating after a pre-strained coupon.....324
Figure 8-73 - Prestrain engineering stress—strain curves for two specimens before performing induction heating 324
Figure 8-74 - Engineering stress-strain curves for 16.5% pre-strained coupon coated both side with 500 nm thick FeC film and induction heated at 1100 ºC – 1150 ºC for 1 second and then at 820 ˚C – 2 min (A).....325
Figure 8-75 - Engineering stress-strain curves for 16.5% pre-strained coupon coated both side with 500 nm thick FeC film and induction heated at 1100 ºC – 1150 ºC for 1 second and then at 820 ˚C – 4 min (B).....326
Figure 8-76 - Engineering stress-strain curves for 16.5% pre-strained coupon coated both side with 500 nm thick FeC film and induction heated at 1100 ºC – 1150 ºC for 1 second and then at 820 ˚C – 8 min (C).....326
Figure 8-77 - Schematic view of microstructure evolution for one-side coated coupon during induction heating at 1100 ºC – 1150 ºC for 1 second and then induction heated at 820 ºC – 30 seconds.....330
Figure 8-78 - Schematic view of microstructure evolution for both-sides coated coupon during induction heating at 1100 ºC – 1150 ºC for 1 second and then induction heated at 820 ºC – 1 minute 332

Figure 8-79 - Variation in the difference of Gibbs free energy between ferrite and austenite as function of temperature and magnetic field intensity (calculated from molecular field model and [200]) [199] 333
Figure 8-80 - Ferrite plus pearlite microstructure obtained after continuous cooling in absence of magnetic field (microstructure revealed after etching with Nital solution) [199] 334
Figure 9-1 - Schematic view of a tensile coupon having the gauge length half coated with a FeC film (500 nm – 30 at%) on one side 338
Figure 9-2 - Assumption made in order to simulate carbon diffusion for half masked tensile coupons 340
Figure 9-3 - Schematic view through thickness of the one side coated portion of the gauge length 340
Figure 9-4 - Carbon concentration through thickness for tensile coupon coated one side and annealed at 630 ˚C and 530 ˚C for 1h 340
Figure 9-5 - Optical microscope pictures of the interface between coated and not-coated zone of the gauge length of a tensile coupon: (a) magnification 5X and (b) magnification 10X . 342
Figure 9-6 - Schematic view of the measurements taken on a tensile coupon having half gauge length coated and half not coated. B indicates the upper corner, L the end of the first fillet radii, C is the interface, D is the start of the second fillet radii and K is the other upper corner 343
Figure 9-7 - Expected carbon gradient along the gauge length– annealing at 630 ˚C – 1h in high vacuum 344
Figure 9-8 - Schematic view of how Vickers hardness has been performed to assess the shape of the gradient 344
Figure 9-9 - Vickers measurements along the half coated gauge length for specimen 5 after heat treatment at 630 ˚C – 1h in high vacuum without polishing 346
Figure 9-10 - Vickers measurements along the uncoated gauge length on the uncoated side for specimen 5 after heat treatment at 630 ˚C – 1h in high vacuum: two measurements were taken close to the edges (A and B) and two measurements were taken in the center of the gauge width 346

Figure 9-11 - Vickers measurements after polishing along the half coated gauge length for specimen 5 after heat treatment at 630 ˚C – 1h in high vacuum: two measurements (A and B) were taken close to the edges of the coupon, while two measurements were taken in the center of the coupon.....347
Figure 9-12 - Vickers measurements along the half coated gauge length for specimen 6 after heat treatment at 630 ˚C – 1h in high vacuum without polishing.....347
Figure 9-13 - Vickers measurements along the uncoated gauge length for specimen 6 after heat treatment at 630 ˚C – 1h in high vacuum.....348
Figure 9-14 - Vickers measurements after polishing along the half coated gauge length for specimen 6 after heat treatment at 630 ˚C – 1h in high vacuum 348
Figure 9-15 - Vickers measurements along the half coated gauge length and the uncoated side for specimen 10 after heat treatment at 630 ˚C – 1h in high vacuum after polishing...349
Figure 9-16 - Vickers measurements after polishing along the half coated gauge length for specimen 10 after heat treatment at 630 ˚C for 5 days in high vacuum 350
Figure 9-17 - Vickers measurements after polishing along the uncoated gauge length for specimen 10 after heat treatment at 630 ˚C for 5 days in high vacuum 350
Figure 9-18 - Vickers measurements along the half coated gauge length and the uncoated side (flipped side) for specimen 11 after heat treatment at 630 ˚C – 1h in high vacuum without polishing 351
Figure 9-19 - Vickers measurements along the half coated gauge length and the uncoated side (flipped side) for specimen 11 after heat treatment at 630 ˚C – 1h in high vacuum after polishing 351
Figure 9-20 - Sketch of the holes configuration drilled along the gauge length 353
Figure 9-21 - Laser set-up used for lasing of holes and DIC features on tensile coupons. The yellow line shows the path followed by the laser beam up to the top of the microscope objective.....355
Figure 9-22 - Examples of features for DIC analyses applied with laser on tensile coupons 355
Figure 9-23 - Engineering stress-strain curves for specimen having holes along the axis of the gauge length.....356

Figure 9-24 - Lüders band propagation during tensile test of carbon graded specimen number 5: (a) starting of the nucleation of the Lüders band along the gauge length (couple of holes 9 and 10 are at the end of the graded zone, while couple 11 is in a no carbon zone); (b) progressing of the Lüders band in the graded zone from couple of hole number 10 until couple of hole number 6. (Couple of holes 6 was at the interface between FeC coated zone and uncoated zone) 357
Figure 9-25 - Lüders band propagation during tensile test of carbon graded specimen number 6: Starting of the nucleation of the Lüders band (a). Couple of holes 9 and 10 are inside the graded zone, while couple 11 and 12 are inside the uncoated zone. (b) progressing of the Lüders band in the graded zone of specimen 6 from couple of holes number 9 until couple of holes number 6, which is at the end of the graded zone and the voids above this couple are in the FeC coated zone. 358
Figure 9-26 - Lüders band propagation during tensile test of carbon graded specimen number 10: Starting of the nucleation of the Lüders band during tensile testing of specimen 10 having uniform carbon content along the gauge length (a) Couple of voids 5 is at the interface of the coated FeC zone and the uncoated zone. (b) progressing of the Lüders band in the uniform zone of specimen 10 359
Figure 9-27 - Uniform deformation of specimen 7 without carbon 360
Figure 9-28 - Hole configuration at the starting of the tensile test for specimen number 5 showing carbon gradient along the gauge length 361
Figure 9-29 - Hole configuration at the starting of the tensile test for specimen number 6 showing carbon gradient along the gauge length 361
Figure 9-30 - Hole configuration at the starting of the tensile test for uncoated IF steel (specimen 7).....362
Figure 9-31 - Hole configuration at the starting of the tensile test for uncoated IF steel (specimen 8).....362
Figure 9-32 - Hole configuration at the starting of the tensile test for specimen number 10 having uniform carbon distribution along the gauge length.....363
Figure 9-33 - Schematic view of evolution of voids dimensions during a uniaxial tensile test [206].....363

Figure 9-34 - Example of thresholding of an image of voids: (a) 8-bit image of couple of voids; (b) thresholded image of couple of voids 364
Figure 9-35 - Schematic view of extraction of the average true far field strain for uncoated and not-annealed IF steel (specimen 7) 365
Figure 9-36 - Schematic view of the extraction of the true far field strain for coupons having a carbon gradient along the gauge length. The number of analyzed couple is also reported for specimen number 5 366
Figure 9-37 - Schematic view of the extraction of the local true far field strain at the side of the voids for coupons having a carbon gradient along the gauge length. The number of analyzed couple is also reported for specimen number 5 366
Figure 9-38 - Local true strain versus true far field strain for couple 8 of holes on uncoated and not-annealed IF steel (specimen 7) 367
Figure 9-39 - Slope of the local true strain versus true far field strain for couple 8 of holes on uncoated and not-annealed IF steel (specimen 7).....368
Figure 9-40 - Slope of the local true strain versus the local true far field strain for couple 8 of holes on specimen number 7 having carbon gradient along the gauge length 368
Figure 9-41 - Local true strain versus true far field strain for couple number 4 of voids for specimen number 5 having carbon gradient along the gauge length.....369
Figure 9-42 - Slope of the local true strain versus the local true far field strain for couple 4 of holes on specimen number 5 having carbon gradient along the gauge length 369
Figure 9-43 - Slope of the local true strain versus the true far field strain taken along the whole gauge length for couple 4 of holes on specimen number 5.....370
Figure 9-44 - Local true strain versus true far field strain for couple number 4 of voids for specimen number 6 having carbon gradient along the gauge length.....370
Figure 9-45 - Slope of the local true strain versus the true far field strain taken in the whole gauge length for couple 4 of holes on specimen number 6 having carbon gradient along the gauge length.....371
Figure 9-46 - Slope of the local true strain versus the local true far field strain for couple 4 of holes on specimen number 6 having carbon gradient along the gauge length 371
Figure 9-47 - Local true strain versus true far field strain for couple number 5 of voids for specimen number 10 having uniform carbon distribution along the gauge length.....372

Figure 9-48 - Slope of the local true strain versus the true far field strain taken in the whole gauge length for couple 5 of holes on specimen number 10 having uniform carbon distribution along the gauge length.....372
Figure 9-49 - Slope of the local true strain versus the local true far field strain for couple 5 of holes on specimen number 10 having uniform carbon distribution along the gauge length 373
Figure 9-50 - Local true strain as function of the local true far field strain extracted at the side of the voids for couples 4 and 6 of specimen 5 having carbon gradient along the gauge length 374
Figure 9-51 - Slope of the local true strain versus the local true far field strain at the sides of the voids for couples 4 and 6 on specimen number 5 having carbon gradient along the gauge length 374
Figure 9-52 - McClintok fitting of the void growth of uncoated specimen 7.....378
Figure 9-53 - McClintok fitting of the void growth of specimen 5 having carbon gradient along gauge length.....379
Figure 9-54 - McClintok fitting of the void growth of specimen 6 having carbon gradient along gauge length.....379
Figure 9-55 - McClintok fitting of the void growth of specimen 10 having uniform carbon distribution along gauge length 381
Figure 9-56 - Ablation configurations to obtain carbon gradient along the gauge width of tensile coupons after annealing.....382
Figure 9-57 - 500 µm removal of the FeC film in the center of the tensile coupon.....383
Figure 9-58 – 500 µm of FeC film left at the center of the gauge width.....383
Figure 9-59 - Diffusion paths followed by carbon in coupons which have undergone laser ablation of FeC film.....383
Figure 9-60 - Carbon gradient obtained along a gauge width in a zone where 500 µm coating was removed.....384
Figure 9-61 - Change in carbon concentration profile through thickness for annealing at 530 ˚C for different times 386
Figure 9-62 - Carbon gradient obtained along a gauge width in a zone where 500 µm coating was removed for annealing times shorter than 1h 387

Figure 9-63 - Carbon gradient obtained along a gauge width in a zone where 250 μm coating was removed on the side of the gauge width 387
Figure 9-64 - Path followed by the laser beam to create the rectangular ablated zone 388
Figure 9-65 - Optical microscope pictures of the ablated zone E 3 and E 4 389
Figure 9-66 - (a) Scanning of the ablated square with a 3D confocal laser microscope; (b) scanning of the ablated surface showing the points where the measurements were taken...390
Figure 9-67 - Tensile coupon with ablated zone in the centre of the gauge width (area of the ablated zone is 9 mm x 0.5 mm).....392
Figure 9-68 - Tensile coupon with ablated zone in the outer sides of the gauge width (area of the ablated zone is 9 mm x 0.5 mm). 0.5 mm of coated width left in the centre of the specimen 392
Figure 9-69 - Optical microscope picture of tensile coupons ablated with femtosecond laser 392
Figure 9-70 - Annealing time required to obtain a uniform carbon content in a specimen having an ablated zone of 500 μm width which was previously diffused at 530 ˚C for 1h .394
Figure 9-71 - Specimen with 500 μm ablated zone in the middle of the gauge width with hardness patterns schematically shown by dots.....394
Figure 9-72 - Vickers hardness through width for specimen EC 1 where 500 μm were ablated in the centre of the gauge width 395
Figure 9-73 - Vickers hardness of specimen EC 2 after polishing of the surface 396
Figure 9-74 - Vickers hardness of specimen EC 9 after annealing in high vacuum at 530 ˚C for 12h.....397
Figure 9-75 - Vickers hardness of specimen EC 10 after annealing in high vacuum at 530 ˚C for 12h.....397
Figure 9-76 - Vickers hardness of specimen EC 12 after annealing in high vacuum at 530 ˚C for 12h.....398
Figure 9-77 - Hardness measurements of an uncoated not-annealed coupon of IF steel (specimen GW1).....399
Figure 9-78 - Hardness measurements of an uncoated not-annealed coupon of IF steel (specimen GW2).....399
Figure 9-79 - Sketch of the quantities measured for the voids.....402

Figure 9-80 - Void configuration along the gauge width of a specimen where 500 μm of FeC film were ablated in the centre (specimen EC 3).....404
Figure 9-81 - Engineering stress-strain curves for tensile coupons having a gradient of carbon obtained by removing 500 μm of FeC film at the centre of the coupon.....405
Figure 9-82 - Specimen EC 1: (a) starting of Lüders bands nucleation far from voids; (b) propagation of the band.....406
Figure 9-83 - Specimen EC 3: (a) starting of Lüders bands nucleation far from voids; (b) propagation of the bands in the voids zone.....406
Figure 9-84 - Specimen EC 5: (a) starting of Lüders bands nucleation at voids; (b) propagation of the bands.....407
Figure 9-85 - Lüders bands propagation for specimen EC 6: (a) nucleation of the bands at the fillet radii; (b) bottom band propagating along the gauge length.....407
Figure 9-86 - Specimen EC 11: (a) starting of Lüders bands far from the voids; (b) coalescence of Lüders bands close to the voids.....408
Figure 9-87 - Engineering stress-strain curves for tensile coupons having a gradient of carbon obtained by leaving 500 μm of FeC film at the centre of the coupon.....408
Figure 9-88 - Specimen EC 2: (a) starting of Lüders bands nucleation at voids; (b) propagation of the bands in the voids zone.....409
Figure 9-89 - Specimen EC 4: (a) starting of Lüders bands nucleation far from voids; (b) propagation of the bands in the voids zone.....410
Figure 9-90 - Engineering stress-strain curves for tensile coupons having a uniform distribution of carbon along the gauge width.....410
Figure 9-91 - Lüders bands nucleation for specimen EC 9 Lüders bands nucleation for specimen EC 10.....411
Figure 9-92 – (a) Lüders bands propagation for specimen EC 12; (b) bands crossing the voids.....412
Figure 9-93 - Engineering stress-strain curves for uncoated and not-annealed tensile coupons.....412
Figure 9-94 - Local true strain versus true far field strain for bottom couple of holes of specimen EC 1.....414

Figure 9-95 - Linear slope of local true strain versus true far field strain of the bottom couple of holes for specimen EC 1 414
Figure 9-96 - Local true strain versus true far field strain for bottom couple of holes of specimen EC 2 417
Figure 9-97 - Linear slope of local true strain versus true far field strain of the bottom couple of holes for specimen EC 2 417
Figure 9-98 - Local true strain versus true far field strain for bottom couple of holes of specimen EC 9 419
Figure 9-99 - Linear slope of local true strain versus true far field strain of the bottom couple of holes for specimen EC 9 420
Figure 9-100 - Local true strain versus true far field strain for left couple of holes of specimen GW 1 422
Figure 9-101 - Linear slope of local true strain versus true far field strain of the left couple of holes for uncoated and not-annealed specimen GW 1 422
Figure 9-102 - McClintok fitting of the void growth for top holes in specimen EC 1 having 500 µm FeC film removed in the center of the tensile coupon 425
Figure 9-103 - McClintok fitting of the void growth for top holes in specimen EC 2 425
Figure 9-104 - McClintok fitting of the void growth for top holes in specimen EC 9 426
Figure 9-105 - McClintok fitting of the void growth for right holes in specimen GW 1 426
Figure 9-106 - McClintok fitting of specimen EC 3 after Lüdering removal in the curves describing void growth 427
Figure 9-107 - McClintok fitting of specimen EC 2 after Lüdering removal in the curves describing void growth 428
Figure 9-108 - Comparison of engineering stress-strain curves of coupons with carbon ablated in the center of the gauge width and uncoated IF steel 430
Figure 9-109 – Comparison of engineering stress-strain curves of a coupon having carbon gradient and a coupon having a uniform carbon distribution 431
Figure 10-1 - Engineering stress-strain curves of coupons coated both sides with 500 nm thick FeMnC film and annealed at 530 ˚C – 1h in high vacuum 436
Figure 10-2 - Engineering stress-strain curves of coupons coated both sides with 500 nm thick FeMnC film and annealed at 630 ˚C – 1h in high vacuum 437

Figure 10-3 - Engineering stress-strain curves of coupons coated both sides with 500 nm thick FeMnC film and annealed at 1000 ˚C – 1h in high vacuum.....437
Figure 10-4 - Engineering stress-strain curves of coupons coated both sides with 500 nm thick FeMnC film and annealed at 1000 ˚C – 10h in high vacuum.....438
Figure 10-5 - Images of microstructure of tensile coupons A coated on both sides with 500 nm thick FeMnC film and annealed at 530 ˚C – 1h in high vacuum: (a) whole thickness (magnification 20X); (b) closer view at one edge (magnification 50X) 439
Figure 10-6 - Images of microstructure of tensile coupons B coated on both sides with 500 nm thick FeMnC film and annealed at 630 ˚C – 1h in high vacuum: (a) whole thickness (magnification 20X); (b) closer view (magnification 50X).....439
Figure 10-7 - Images of microstructure of tensile coupon B coated on both sides with 500 nm thick FeMnC film and annealed at 1000 ˚C – 1h in high vacuum: (a) whole thickness (magnification 20X); (b) closer view (magnification 50X).....440
Figure 10-8 - Images of microstructure of tensile coupon A coated on both sides with 500 nm thick FeMnC film and annealed at 1000 ˚C – 10h in high vacuum: (a) whole thickness (magnification 20X); (b) closer view (magnification 50 X).....441
Figure 10-9 - TEM image and SAED pattern of as-deposited FeMnC film 445
Figure 10-10 - TEM image and SAED pattern of FeMnC film at 360 ˚C after 5 minutes...446
Figure 10-11 - Comparison of mechanical properties of a coupon coated one side (OS) with 150 nm amorphous carbon film with mechanical properties obtained for one side coated coupon (OS) with 500 nm FeC film and annealed in high vacuum. The curve for annealing in air at 530 ˚C – 1h of a both sides (BS) coated coupon with 500 nm thick FeC film is also reported 447

List of Figures in Appendices

Figure A. 1 - Vickers indenter [140] 475
Figure A. 2 - Knoop indenter [140].....476

Figure B. 1 - Schematic view of the field ion microscopy (FIM) process [223].....477
Figure B. 2 - Ratio between the field applied to the specimen (F) and the evaporation field (F_e) versus the temperature. The two modes, high-voltage pulse method and laser method, used to obtain evaporation are illustrated [224] 479
Figure B. 3 - Schematic view of the pulse behaviour during time for the high-pulse method 480
Figure B. 4 - Set-up of atom probe tomography [148].....482
Figure B. 5 - Schematic view of field evaporation during atom probe tomography: L is the perpendicular direction between the tip and the center of the detector, however some ions will hit the detector not in the center, so L must be recalculated by using the Pythagore correction [225] 483
Figure B. 6 - Schematic view of the trajectory followed by an atom during its evaporation [148].....484
Figure B. 7 - View of the roll-up effect (a) and of its trajectory aberrations (b) [148] 486
Figure B. 8 - Trajectory aberrations due to a change in surface curvature for the presence of low-field and high-field precipitates [148].....487
Figure B. 9 - Eectropolishing curve showing the current density between anode and cathode as function of the applied voltage. The optimal voltage range for polishing occurs between points B and C [148].....488
Figure B. 10 - Slices to be used to prepare tips for Atom Probe Tomography 489
Figure B. 11 - Schematic view of experimental set-up for microelectropolishing [226].....490
Figure B. 12 - Microelectropolishing schematic view.....490
Figure B. 13 - Sharp tip obtained by electropolishing method (20X) [148].....491
Figure B. 14 - Deposition of Pt protective layer on the IF steel.....492
Figure B. 15 - Cross-section view of the milled wedge. The trapezoidal cuts are clearly visible while the wedge of interest is coated with the Pt protective layer.....492

Figure B. 16 - Micromanipulator is placed adjacent to the free end of the wedge.....493
Figure B. 17 - Micromanipulator is welded on the free end of the wedge and the other end of the wedge is cut to completely extract the bar of material from the bulk 493
Figure B. 18 - Slices of the wedge are cut and welded on the posts before performing the final annular milling (a), detail of the deposited slice on the tip support (b) 494
Figure B. 19 - Steps of FIB preparation of tips for Atom Probe Tomography: (a) the material to be analysed is placed on a metallic pre-tip, (b) and (c) SEM annular milling of the tip; (d) final shape of the tip that can be analyzed in APT 495
Figure B. 20 - Milling of a tip by using an annular milling pattern, where x represents a feature of interest to be kept in the final APT tip. The size of the inner diameter is progressively decreased from (a) to (c), while the beam current is decreased [148] 495

Figure C. 1 - Experimental procedure used for the quantitative evaluation of the amount of interstitial atoms in solid solution using TEP measurements [32] 499

Figure D. 1 - Schematic view of the thickness of tensile coupons of IF steel coated both sides with a 500 nm thick amorphous FeC film protected from oxidation or decarburization with 20 nm Nickel cap layer on both sides.....508
Figure D. 2 - Engineering stress-strain curves obtained for coupons coated both sides with a 500 nm thick FeC amorphous film and 20 nm Nickel cap layer annealed at 430 ˚C - 1h in argon 510
Figure D. 3 - Surface of the tensile coupon coated with 500 nm thick FeC amorphous film and 20 nm Nickel cap layer after annealing in argon at 530 ˚C - 1h.....511
Figure D. 4 - Engineering stress-strain curves obtained for coupons coated both sides with a 500 nm thick FeC amorphous film and 20 nm Nickel cap layer annealed at 530 ˚C - 1h in argon 511
Figure D. 5 - Engineering stress-strain curves obtained for coupons coated both sides with a 500 nm thick FeC amorphous film and 20 nm Nickel cap layer annealed at 630 ˚C - 1h in argon 512
Figure D. 6 - Surface of the tensile coupon NiAr-6 coated with 500 nm thick FeC amorphous film and 20 nm Nickel cap layer after annealing in argon at 630 ˚C - 1h 513

Figure D. 7 - Engineering stress-strain curves obtained for coupons coated both sides with a 500 nm thick FeC amorphous film and 20 nm Nickel cap layer annealed at 710 ˚C - 1h in argon 514
Figure D. 8 - Surface of the tensile coupon NiAr-10 coated with 500 nm thick FeC amorphous film and 20 nm Nickel cap layer after annealing in Argon at 710 ˚C - 1h 515
Figure D. 9 - Global comparison of engineering stress-strain curves for coupons coated both sides with 500 nm thick FeC film and 20 nm Ni cap layer after annealing in argon 515
Figure D. 10 - Graph of the upper yield stress for annealing in argon at different temperatures for 1h of coupons coated both sides with 500 nm FeC film and of coupons coated both sides with 500 nm FeC film and 20 nm Nickel cap layer 516
Figure D. 11 - Energy filtering TEM of the interface between IF substrate and as deposited FeC film (courtesy of Dr. Amélie Fillon).....519
Figure D. 12 - Engineering stress-strain curves for coupons coated both sides with a 500 nm thick FeC amorphous film after cleaning with HCl solution. Annealing performed in high vacuum at 430˚C - 1h 521
Figure D. 13 - Lüders bands propagation and exfoliation of the film for a coupon annealed at 430 ˚C - 1h cleaned with HCl before applying the FeC film.....522
Figure D. 14 - Engineering stress-strain curves for coupons coated both sides with a 500 nm thick FeC amorphous film after cleaning with HCl solution. Annealing performed in high vacuum at 530˚C - 1h 523
Figure D. 15 - Microscope pictures of the FeC film for a coupon annealed at 530 ˚C - 1h cleaned with HCl before applying the FeC film.....524
Figure D. 16 - Engineering stress-strain curves for coupons coated both sides with a 500 nm thick FeC amorphous film after cleaning with HCl solution. Annealing performed in high vacuum at 630 ˚C - 1h 525
Figure D. 17 - Microscope pictures of the FeC film for a coupon annealed at 630˚C-1h cleaned with HCl before applying the FeC film.....526
Figure D. 18 - Engineering stress-strain curves for coupons coated both sides with a 500 nm thick FeC amorphous film after cleaning with HCl solution. Annealing performed in high vacuum at 710 ˚C - 1h 527

Figure D. 19 - Microscope pictures of the FeC film for a coupon annealed at 710 ˚C - 1h cleaned with HCl before applying the FeC film.....528
Figure D. 20 - Comparison of engineering stress-strain curves obtained at different temperatures on coupons cleaned with HCl and coated on both sides with 500 nm FeC film. Annealing was performed in high vacuum.....529
Figure D. 21 - Comparison of the upper yield stress obtained on coupon cleaned with Nital and on coupon cleaned with HCl.....529
Figure D. 22 - Comparison between theoretical yield stress considering FeC transformation and yield stresses obtained with annealing in high vacuum with coupons cleaned with Nital before PVD deposition or cleaned with HCl before the PVD deposition 531
Figure D. 23 - Velocity profile of Lüders bands in sample E-9 coated both sides with 500 nm FeC film and annealed at 630 ˚C - 1h.....554
Figure D. 24 - Velocity profile of Lüders bands in sample F-12 coated both sides with 500 nm FeC film and annealed at 710 ˚C - 1h.....555
Figure D. 25 - Microstructures of both sides coated coupons annealed in the furnace in argon at different temperatures for 1h 556
Figure D. 26 - SEM images of grain boundaries in both sides coated coupons annealed in high vacuum at different temperatures for 1h.....557

Figure E. 1 - Study of mesh influence on Lüders bands propagation.....559
Figure E. 2 - Artificial energy evolution expressed as percentage of the internal energy during the simulation of change in yield stress under the same slope of the linear softening 560
Figure E. 3 - Comparison of internal energy and artificial energy evolution for simulations of graded mechanical properties and uniform mechanical properties 561
Figure E. 4 - Artificial energy evolution during the simulation of graded mechanical properties and uniform mechanical properties through thickness, expressed as percentage of the internal energy 561
Figure E. 5 - Artificial energy evolution expressed as percentage of the internal energy during the simulation of change of Young's modulus of a central layer having no Lüdering 562

Figure E. 6 - Comparison of internal energy and artificial energy evolution for simulations having changes of thickness of the central layer (ratio 1:1 and ratio 1.5:1) and uniform mechanical properties in the outer layers 563
Figure E. 7 - Comparison of internal energy and artificial energy evolution for simulations having changes of thickness of the central layer (ratio 2:1 and ratio 2.5:1) and uniform mechanical properties in the outer layers 563
Figure E. 8 - Artificial energy evolution during the simulation expressed as percentage of the internal energy for change of thickness of the central layer and uniform material properties in the outer layers.....564
Figure E. 9 - Comparison of internal energy and artificial energy evolution for simulations having changes of thickness of the central layer (ratio 1:1 and ratio 1.5:1) and graded mechanical properties in the outer layers 565
Figure E. 10 - Comparison of internal energy and artificial energy evolution for simulations having changes of thickness of the central layer (ratio 2:1 and ratio 2.5:1) and graded mechanical properties in the outer layers 565
Figure E. 11 - Artificial energy evolution during the simulation expressed as percentage of the internal energy for change of thickness of the central layer and gradient of material properties in the outer layers.....566
Figure E. 12 - Artificial energy evolution during the simulation expressed as percentage of the internal energy for change of strain hardening 566
Figure E. 13 - Artificial energy evolution during the simulation expressed as percentage of the internal energy for change of voids interspacing.....567
Figure E. 14 - Artificial energy evolution during the simulation expressed as percentage of the internal energy for change of voids volume fraction.....567

Figure F. 1 - Pre-strain engineering stress-strain curves of specimens A15 and A16 which will be annealed at 430 ˚C - 1h in high vacuum 568
Figure F. 2 - Engineering stress-strain curves of specimens A15 and A16 after pre-strain and annealing at 430 ˚C - 1h in high vacuum.....568
Figure F. 3 - Pre-strain engineering stress-strain curves of specimens A11 and A17 which will be annealed at 530 ˚C - 1h in high vacuum 569

Figure F. 4 - Engineering stress-strain curves of specimens A11 and A17 after pre-strain and annealing at 530 ˚C - 1h in high vacuum.....569
Figure F. 5 - Pre-strain engineering stress-strain curves of specimens A12 and A13 which will be annealed at 630 ˚C - 1h in high vacuum.....570
Figure F. 6 - Engineering stress-strain curves of specimens A12 and A13 after pre-strain and annealing at 630 ˚C - 1h in high vacuum.....570
Figure F. 7 - Pre-strain engineering stress-strain curves of specimens A14 and A18 which will be annealed at 710 ˚C - 1h in high vacuum.....571
Figure F. 8 - Engineering stress-strain curves of specimens A14 and A18 after pre-strain and annealing at 710 ˚C - 1h in high vacuum.....571

Figure G. 1 - Sequence of steps showing the sealing of the quartz ampoule containing the IF steel specimen.....573
Figure G. 2 - Magnetic domain configurations during the magnetization of a ferromagnetic material (redrawn from a figure published in ref. [15]).....577
Figure G. 3 - ln (σ_{True}) versus ln (ε_{True}) for tensile coupons coated on one side with 500 nm thick FeC film and annealed using furnace and induction heating at different times and temperatures. IH means induction heating. 580
Figure G. 4 - ln (σ_{True}) versus ln (ε_{True}) for tensile coupons coated on both sides with 500 nm thick FeC film and annealed using furnace and induction heating at different times and temperatures. IH means induction heating 583
Figure G. 5 - EDS performed inside a grain of a specimen induction heated at 1100 ºC – 1150 ºC for 1 seconds and then at 820 ˚C – 1 minute 585
Figure G. 6 - EDS performed inside grains of a specimen induction heated at 1100 ºC – 1150 ºC for 1 seconds and then at 820 ˚C – 1 minute 586
Figure G. 7 - EDS performed at grain boundaries of a specimen induction heated at 1100 ºC – 1150 ºC for 1 seconds and then at 820 ˚C – 1 minute 586
Figure G. 8 - EDS performed at grain boundaries of a specimen induction heated at 1100 ºC – 1150 ºC for 1 seconds and then at 820 ˚C – 1 minute 587
Figure G. 9 - EDS performed inside two grains of a specimen induction heated at 1100 ºC – 1150 ºC for 1 seconds and then at 820 ˚C – 2 minutes.....588

Figure G. 10 - EDS performed at grain boundaries for a specimen induction heated at 1100 ºC – 1150 ºC for 1 seconds and then at 820 ˚C – 2 minutes.....588
Figure G. 11 - EDS performed inside grains for a specimen induction heated at 1100 ºC – 1150 ºC for 1 seconds and then at 820 ˚C – 4 minutes.....589
Figure G. 12 - EDS performed inside a grain and at a grain boundary for a specimen induction heated at 1100 ºC – 1150 ºC for 1 seconds and then at 820 ˚C – 4 minutes 590
Figure G. 13 - BSE image obtained in one zone close to one edge of a both sides coated coupon induction heated at 1100 ºC – 1150 ºC for 1 seconds and then at 820 ˚C for 2 minutes.....591
Figure G. 14 - BSE image obtained in another zone of a both sides coated coupon induction heated at 1100 ºC – 1150 ºC for 1 seconds and then at 820 ˚C for 2 minutes.....591
Figure G. 15 - BSE image obtained in a zone close to the edge of a both sides coated coupon induction heated at 1100 ºC – 1150 ºC for 1 seconds and then at 820 ˚C for 4 minutes.....592
Figure G. 16 - BSE image obtained in another zone of a both sides coated coupon induction heated at 1100 ºC – 1150 ºC for 1 seconds and then at 820 ˚C for 4 minutes.....592
Figure G. 17 - Phase maps obtained on coupons induction heated at 1100 ºC – 1150 ºC for 1 seconds and then at 820 ˚C for 2 minutes (a) and 4 minutes (b) 594
Figure G. 18 - Local misorientation and band contrast maps on coupons induction heated at 1100 ºC – 1150 ºC for 1 seconds and then at 820 ˚C for 2 minutes (a) and 4 minutes (b)...595

Figure H. 1 - Local true strain versus true far field strain for couple of holes number 6 on uncoated and not-annealed IF steel (specimen 7).....598
Figure H. 2 - Slope of the local true strain versus true far field strain extracted in the whole gauge length for couple of holes number 6 on uncoated and not-annealed IF steel (specimen 7).....599
Figure H. 3 - Slope of the local true strain versus the local true far field strain for couple of holes number 6 on specimen number 7 having carbon gradient along the gauge length 599
Figure H. 4 - Local true strain versus true far field strain for couple of holes number 5 on uncoated and not-annealed IF steel (specimen 7).....600

Figure H. 5 - Slope of the local true strain versus true far field strain extracted in the whole gauge length for couple of holes number 5 on uncoated and not-annealed IF steel (specimen 7) 600
Figure H. 6 - Slope of the local true strain versus the local true far field strain for couple of holes number 6 on specimen number 7 having carbon gradient along the gauge length 601
Figure H. 7 - Local true strain versus true far field strain for couple of holes number 6 for specimen number 5 having carbon gradient along the gauge length 601
Figure H. 8 - Slope of the local true strain versus the true far field strain extracted in the whole gauge length for couple of holes number 6 on specimen number 5 having carbon gradient along the gauge length 602
Figure H. 9 - Slope of the local true strain versus the local true far field strain for couple of holes number 6 on specimen number 5 having carbon gradient along the gauge length 602
Figure H. 10 - Local true strain versus true far field strain for couple of holes number 8 for specimen number 5 having carbon gradient along the gauge length 603
Figure H. 11 - Slope of the local true strain versus the true far field strain extracted in the whole gauge length for couple of holes number 8 on specimen number 5 having carbon gradient along the gauge length 604
Figure H. 12 - Slope of the local true strain versus the local true far field strain for couple of holes number 8 on specimen number 5 having carbon gradient along the gauge length 604
Figure H. 13 - Local true strain versus true far field strain for couple of holes number 11 for specimen number 5 having carbon gradient along the gauge length 605
Figure H. 14 - Slope of the local true strain versus the true far field strain extracted in the whole gauge length for couple of holes number 11 on specimen number 5 having carbon gradient along the gauge length 605
Figure H. 15 - Slope of the local true strain versus the local true far field strain for couple of holes number 11 on specimen number 5 having carbon gradient along the gauge length ... 606
Figure H. 16 - Local true strain versus true far field strain for couple of holes number 5 for specimen number 6 having carbon gradient along the gauge length 607
Figure H. 17 - Slope of the local true strain versus the true far field strain extracted in the whole gauge length for couple of holes number 5 on specimen number 6 having carbon gradient along the gauge length 607

Figure H. 18 - Slope of the local true strain versus the local true far field strain for couple of holes 5 on specimen number 6 having carbon gradient along the gauge length 608
Figure H. 19 - Local true strain versus true far field strain for couple of holes number 7 for specimen number 6 having carbon gradient along the gauge length.....608
Figure H. 20 - Slope of the local true strain versus the true far field strain extracted in the whole gauge length for couple of holes number 7 on specimen number 6 having carbon gradient along the gauge length.....609
Figure H. 21 - Slope of the local true strain versus the local true far field strain for couple of holes number 7 on specimen number 6 having carbon gradient along the gauge length 609
Figure H. 22 - Local true strain versus true far field strain for couple of holes number 12 for specimen number 6 having carbon gradient along the gauge length.....610
Figure H. 23 - Slope of the local true strain versus the true far field strain extracted in the whole gauge length for couple of holes number 12 on specimen number 6 having carbon gradient along the gauge length.....610
Figure H. 24 - Slope of the local true strain versus the local true far field strain for couple of holes number 12 on specimen number 6 having carbon gradient along the gauge length ...611
Figure H. 25 - Local true strain versus true far field strain for couple of holes number 7 for specimen number 10 having uniform carbon distribution along the gauge length.....612
Figure H. 26 - Slope of the local true strain versus the true far field strain extracted in the whole gauge length for couple of holes number 7 on specimen number 10 having uniform carbon distribution along the gauge length.....612
Figure H. 27 - Slope of the local true strain versus the local true far field strain for couple of holes number 7 on specimen number 10 having uniform carbon distribution along the gauge length 613
Figure H. 28 - Local true strain versus true far field strain for couple of holes number 10 for specimen number 10 having uniform carbon distribution along the gauge length.....613
Figure H. 29 - Slope of the local true strain versus the true far field strain taken in the whole gauge length for couple of holes number 10 on specimen number 10 having uniform carbon distribution along the gauge length.....614

Figure H. 30 - Slope of the local true strain versus the local true far field strain for couple of holes number 10 on specimen number 10 having uniform carbon distribution along the gauge length.....614
Figure H. 31 - Local true strain versus true far field strain for couple number of holes number 12 for specimen number 10 having uniform carbon distribution along the gauge length 615
Figure H. 32 - Slope of the local true strain versus the true far field strain taken in the whole gauge length for couple of holes number 12 on specimen number 10 having uniform carbon distribution along the gauge length.....615
Figure H. 33 - Slope of the local true strain versus the local true far field strain for couple of holes number 12 on specimen number 10 having uniform carbon distribution along the gauge length.....616
Figure H. 34 - Local true strain as function of the local true far field strain extracted at the side of the voids for couples 8 and 11 of specimen 5 having carbon gradient along the gauge length 617
Figure H. 35 - Slope of the local true strain versus the local true far field strain at the sides of the voids for couples 8 and 11 on specimen number 5 having carbon gradient along the gauge length.....617
Figure H. 36 - Local true strain as function of the local true far field strain extracted at the side of the voids for couples 4 and 5 of specimen 6 having carbon gradient along the gauge length 618
Figure H. 37 - Slope of the local true strain versus the local true far field strain at the sides of the voids for couples 4 and 5 on specimen number 6 having carbon gradient along the gauge length 618
Figure H. 38 - Local true strain as function of the local true far field strain extracted at the side of the voids for couples 7 and 12 of specimen 6 having carbon gradient along the gauge length 619
Figure H. 39 - Slope of the local true strain versus the local true far field strain at the sides of the voids for couples 7 and 12 on specimen number 6 having carbon gradient along the gauge length.....619

Figure H. 40 - Local true strain as function of the local true far field strain extracted at the side of the voids for couples 5 and 7 of specimen 10 having uniform carbon distribution along the gauge length 620
Figure H. 41 - Slope of the local true strain versus the local true far field strain at the sides of the voids for couples 5 and 7 on specimen number 10 having uniform carbon distribution along the gauge length 620
Figure H. 42 - Local true strain as function of the local true far field strain extracted at the side of the voids for couples 10 and 12 of specimen 10 having uniform carbon distribution along the gauge length 621
Figure H. 43 - Slope of the local true strain versus the local true far field strain at the sides of the voids for couples 10 and 12 on specimen number 10 having uniform carbon distribution along the gauge length 621
Figure H. 44 - Carbon gradient obtained along a gauge width in a zone where 333 µm coating was removed 622
Figure H. 45 - Carbon gradient obtained along a gauge width in a zone where 500 µm coating was removed 624
Figure H. 46 - Carbon gradient obtained along a gauge width in a zone where 600 µm coating was removed 625
Figure H. 47 - Carbon gradient obtained along a gauge width in a zone where 500 µm coating was removed close to one edge of the width 627
Figure H. 48 - Hardness through with for specimen EC 1 before polishing 630
Figure H. 49 - Vickers hardness of specimen EC 3 without polishing of the surface.....631
Figure H. 50 - Vickers hardness of specimen EC 3 after polishing of the surface.....632
Figure H. 51 - Vickers hardness of specimen EC 5 without polishing of the surface.....632
Figure H. 52 - Vickers hardness of specimen EC 5 after polishing of the surface.....633
Figure H. 53 - Vickers hardness of specimen EC 6 without polishing of the surface.....633
Figure H. 54 - Vickers hardness of specimen EC 6 after polishing of the surface.....634
Figure H. 55 - Vickers hardness of specimen EC 11 without polishing of the surface.....634
Figure H. 56 - Vickers hardness of specimen EC 11 after polishing of the surface.....635
Figure H. 57 - Vickers hardness of specimen EC 2 without polishing of the surface.....635
Figure H. 58 - Vickers hardness of specimen EC 4 without polishing of the surface.....636

Figure H. 59 - Vickers hardness of specimen EC 4 after polishing of the surface.....636
Figure H. 60 - Vickers hardness of specimen EC 7 without polishing of the surface.....637
Figure H. 61 - Vickers hardness of specimen EC 7 after polishing of the surface.....637
Figure H. 62 - Vickers hardness of specimen EC 13 without polishing of the surface.....638
Figure H. 63 - Vickers hardness of specimen EC 13 after polishing of the surface.....638
Figure H. 64 - Vickers hardness of specimen EC 9 without polishing of the surface after annealing in high vacuum at 530 ˚C – 1h.....639
Figure H. 65 - Vickers hardness of specimen EC 9 after polishing of the surface and annealing at 530 ˚C -1h in high vacuum.....640
Figure H. 66 - Vickers hardness of specimen EC 10 without polishing of the surface after annealing in high vacuum at 530 ˚C – 1h.....640
Figure H. 67 - Vickers hardness of specimen EC 10 after polishing of the surface and annealing at 530 ˚C -1h in high vacuum.....641
Figure H. 68 - Vickers hardness of specimen EC 12 without polishing of the surface after annealing in high vacuum at 530 ˚C – 1h.....641
Figure H. 69 - Vickers hardness of specimen EC 12 after polishing of the surface and annealing at 530 ˚C -1h in high vacuum.....642
Figure H. 70 - Starting of the deformation for uncoated and not-annealed specimen (GW 1); progressing of the deformation for uncoated and not-annealed specimen (GW 1).....644
Figure H. 71 - Starting of the deformation for uncoated and not-annealed specimen (GW 2) progressing of the deformation for uncoated and not-annealed specimen (GW 2).....644
Figure H. 72 - Local true strain versus true far field strain for central couple of holes of specimen EC 1.....647
Figure H. 73 - Linear slope of local true strain versus true far field strain of the central couple of holes for specimen EC 1.....647
Figure H. 74 - Local true strain versus true far field strain for top couple of holes of specimen EC 1.....648
Figure H. 75 - Linear slope of local true strain versus true far field strain of the top couple of holes for specimen EC 1.....648
Figure H. 76 - Local true strain versus true far field strain for bottom couple of holes of specimen EC 3.....649

Figure H. 77 - Linear slope of local true strain versus true far field strain of the bottom couple of holes for specimen EC 3 649
Figure H. 78 - Local true strain versus true far field strain for central couple of holes of specimen EC 3 650
Figure H. 79 - Linear slope of local true strain versus true far field strain of the central couple of holes for specimen EC 3 650
Figure H. 80 - Local true strain versus true far field strain for top couple of holes of specimen EC 3 651
Figure H. 81 - Linear slope of local true strain versus true far field strain of the top couple of holes for specimen EC 3 651
Figure H. 82 - Local true strain versus true far field strain for bottom couple of holes of specimen EC 5 652
Figure H. 83 - Linear slope of local true strain versus true far field strain of the bottom couple of holes for specimen EC 5 652
Figure H. 84 - Local true strain versus true far field strain for central couple of holes of specimen EC 5 653
Figure H. 85 - Linear slope of local true strain versus true far field strain of the central couple of holes for specimen EC 5 653
Figure H. 86 - Local true strain versus true far field strain for top couple of holes of specimen EC 5 654
Figure H. 87 - Linear slope of local true strain versus true far field strain of the top couple of holes for specimen EC 5 654
Figure H. 88 - Local true strain versus true far field strain for bottom couple of holes of specimen EC 11 655
Figure H. 89 - Linear slope of local true strain versus true far field strain of the bottom couple of holes for specimen EC 11 655
Figure H. 90 - Local true strain versus true far field strain for central couple of holes of specimen EC 11 656
Figure H. 91 - Linear slope of local true strain versus true far field strain of the central couple of holes for specimen EC 11 656

Figure H. 92 - Local true strain versus true far field strain for top couple of holes of specimen EC 11 657
Figure H. 93 - Linear slope of local true strain versus true far field strain of the central couple of holes for specimen EC 11 657
Figure H. 94 - Local true strain versus true far field strain for central couple of holes of specimen EC 2 658
Figure H. 95 - Linear slope of local true strain versus true far field strain of the central couple of holes for specimen EC 2 658
Figure H. 96 - Local true strain versus true far field strain for top couple of holes of specimen EC 2 659
Figure H. 97 - Linear slope of local true strain versus true far field strain of the top couple of holes for specimen EC 2 659
Figure H. 98 - Local true strain versus true far field strain for left couple of holes of specimen EC 4 660
Figure H. 99 - Linear slope of local true strain versus true far field strain of the left couple of holes for specimen EC 4 660
Figure H. 100 - Local true strain versus true far field strain for central couple of holes of specimen EC 4 661
Figure H. 101 - Linear slope of local true strain versus true far field strain of the central couple of holes for specimen EC 4 661
Figure H. 102 - Local true strain versus true far field strain for right couple of holes of specimen EC 4 662
Figure H. 103 - Linear slope of local true strain versus true far field strain of the right couple of holes for specimen EC 4.....662
Figure H. 104 - Local true strain versus true far field strain for central couple of holes of specimen EC 9 663
Figure H. 105 - Linear slope of local true strain versus true far field strain of the central couple of holes for specimen EC 9 663
Figure H. 106 - Local true strain versus true far field strain for top couple of holes of specimen EC 9 664

Figure H. 107 - Linear slope of local true strain versus true far field strain of the top couple of holes for specimen EC 9 664
Figure H. 108 - Local true strain versus true far field strain for bottom couple of holes of specimen EC 10 665
Figure H. 109 - Linear slope of local true strain versus true far field strain of the bottom couple of holes for specimen EC 10 665
Figure H. 110 - Local true strain versus true far field strain for central couple of holes of specimen EC 10 666
Figure H. 111 - Linear slope of local true strain versus true far field strain of the central couple of holes for specimen EC 10 666
Figure H. 112 - Local true strain versus true far field strain for top couple of holes of specimen EC 10 667
Figure H. 113 - Linear slope of local true strain versus true far field strain of the top couple of holes for specimen EC 10 667
Figure H. 114 - Local true strain versus true far field strain for left couple of holes of specimen EC 12 668
Figure H. 115 - Linear slope of local true strain versus true far field strain of the left couple of holes for specimen EC 12 668
Figure H. 116 - Local true strain versus true far field strain for central couple of holes of specimen EC 12 669
Figure H. 117 - Linear slope of local true strain versus true far field strain of the central couple of holes for specimen EC 12 669
Figure H. 118 - Local true strain versus true far field strain for right couple of holes of specimen EC 12 670
Figure H. 119 - Linear slope of local true strain versus true far field strain of the right couple of holes for specimen EC 12 670
Figure H. 120 - Local true strain versus true far field strain for central couple of holes for uncoated and not annealed specimen GW 1 671
Figure H. 121 - Linear slope of local true strain versus true far field strain of the central couple of holes for uncoated and not-annealed specimen GW 1 671

Figure H. 122 - Local true strain versus true far field strain for right couple of holes for uncoated and not annealed specimen GW 1 672
Figure H. 123 - Linear slope of local true strain versus true far field strain of the right couple of holes for uncoated and not-annealed specimen GW 1 672
Figure H. 124 - Local true strain versus true far field strain for bottom couple of holes of specimen GW 2.....673
Figure H. 125 - Linear slope of local true strain versus true far field strain of the bottom couple of holes for specimen GW 2 673
Figure H. 126 - Local true strain versus true far field strain for central couple of holes of specimen GW 2.....674
Figure H. 127 - Linear slope of local true strain versus true far field strain of the central couple of holes for specimen GW 2 674
Figure H. 128 - Local true strain versus true far field strain for top couple of holes of specimen GW 2.....675
Figure H. 129 - Linear slope of local true strain versus true far field strain of the top couple of holes for specimen GW 2 675
Figure H. 130 - McClintok fitting of the void growth for top holes in specimen EC 3 676
Figure H. 131 - McClintok fitting of the void growth for top holes in specimen EC 5 677
Figure H. 132 - McClintok fitting of the void growth for top holes in specimen EC 11 677
Figure H. 133 - McClintok fitting of the void growth for top holes in specimen EC 4 678
Figure H. 134 - McClintok fitting of the void growth for top holes in specimen EC 10 678
Figure H. 135 - McClintok fitting of the void growth for right holes in specimen EC 12...679
Figure H. 136 - McClintok fitting of the void growth for top holes in specimen GW 2.....679
Figure H. 137 - McClintok fitting of specimen EC 1 after Lüdering removal in the curves describing void growth 680
Figure H. 138 - McClintok fitting of specimen EC 4 after Lüdering removal in the curves describing void growth 680
Figure H. 139 - McClintok fitting of specimen EC 5 after Lüdering removal in the curves describing void growth 681
Figure H. 140 - McClintok fitting of specimen EC 11 after Lüdering removal in the curves describing void growth 681

Figure I. 1 - Optical microscope pictures of the surface of the film for a coupon annealed at 530 ˚C – 1h in high vacuum and coated with 500 nm thick FeMnC film on both sides.....683
Figure I. 2 - Optical microscope pictures of the surface of the film for a coupon annealed at 630 ˚C – 1h in high vacuum and coated with 500 nm thick FeMnC film on both sides.....684
Figure I. 3 - Optical microscope pictures of the surface of the film for a coupon annealed at 1000 ˚C – 1h in high vacuum and coated with 500 nm thick FeMnC film on both sides....685

List of Tables

Table 2-1 - Summary of main diffusion coefficient values measured for diffusion of carbon into ferrite 16
Table 2-2 - Summary of influence of different parameters on Lüders propagation 34
Table 4-1 - Calculation of the material removed during polishing with OPS diamond suspension for a piece of IF steel coated both sides with 500 nm FeC film and annealed at 430 ˚C - 1h in high vacuum 78
Table 5-1 - Relation between yield stress and Knoop hardness found for specimens of IF steel coated both sides with 500 nm thick FeC film and annealed at different temperatures in high vacuum.....101
Table 5-2 - Composition of the interstitial free steel (IF steel) used for the Gracos project 101
Table 5-3 - Vacuum level at the starting and ending of heat treatments 102
Table 5-4 - List of tensile tested coupons 103
Table 5-5 - List of tensile tested coupons annealed in argon 119
Table 5-6 - Summary of the reduction in area calculated for coupon having different film thicknesses and annealed at different temperatures 125
Table 5-7 - Iron and carbon atoms for FeC film of 500 nm thickness 134
Table 5-8 - Composition of particles detected on the fracture surface of a coated and not-annealed IF coupon after tensile testing 140
Table 5-9 - Composition obtained for particles present on the fracture surface of an uncoated tensile coupon annealed at 710 ˚C – 1h 141
Table 5-10 - Composition obtained for particles present on the fracture surface of a both sides coated tensile coupon annealed at 430 ˚C – 1h.....142
Table 5-11 - Composition obtained for particles present on the fracture surface of a both sides coated tensile coupon annealed at 530 ˚C – 1h.....143
Table 5-12 - Composition obtained for particles present on the fracture surface of a both sides coated tensile coupon annealed at 630 ˚C – 1h.....144
Table 5-13 - Composition obtained for particles present on the fracture surface of a both sides coated tensile coupon annealed at 710 ˚C – 1h (specimen F-9) 145
Table 5-14 - Composition obtained for particles present on the fracture surface of a both sides coated tensile coupon annealed at 710 ˚C – 1h (specimen F-10) 146

Table 5-15 - Composition obtained for particles present on the fracture surface of a both sides coated tensile coupon annealed at 710 ˚C – 1h and having low yield stress 147
Table 5-16 - Comparison of C/Ti ratio for particles containing sulphur at different annealing temperatures 148
Table 5-17 - Thermoelectric power results on both sides coated IF steel annealed at different temperatures in high vacuum 149
Table 5-18 - APT composition of uncoated and not-annealed IF steel 152
Table 5-19 - APT composition of both sides coated IF steel annealed at 530 ˚C – 1h in high vacuum – specimen taken at the centre of the thickness 153
Table 5-20 - APT composition of both sides coated IF steel annealed at 530 ˚C – 1h in high vacuum – specimen close to the FeC film/IF substrate interface 154
Table 5-21 - APT composition of both sides coated IF steel annealed at 710 ˚C – 1h – specimen taken at the centre of the thickness 155
Table 5-22 - APT composition of probe 2 and 3: both sides coated IF steel annealed at 710 ˚C – 1h – specimens taken at the centre of the thickness 156
Table 5-23 - APT composition of probe 4: both sides coated IF steel annealed at 710 ˚C – 1h – specimens taken at the centre of the thickness 157
Table 5-24 - Values of vacuum during annealing of coupons coated both sides with different FeC film thicknesses and annealed at 530 ˚C - 1h.....160
Table 5-25 - Summary of the specimens tested with different film thicknesses after annealing at 530 ºC – 1h in high vacuum.....160
Table 5-26 - Lüders bands speed for specimens coated both sides with 500 nm FeC film and annealed at different temperatures in high vacuum 189
Table 6-1 - Summary of plastic behaviour implemented in the first series of simulations ..199
Table 6-2 - Summary of plastic behaviour implemented in the second series of simulations 201
Table 6-3 - Results obtained by simulating Lüders plateau by applying linear softening ...204
Table 6-4 - Mechanical properties implemented to compare the influence of graded and constant carbon content through thickness on Lüders propagation.....206
Table 6-5 - Mechanical properties implemented in ABAQUS to simulate the influence of stiffness on the Lüders propagation.....209

Table 6-6 - Mechanical properties implemented in ABAQUS to simulate the influence of thickness of a central layer having no plateau on the Lüders propagation 211
Table 6-7 - Mechanical properties implemented in ABAQUS to simulate the influence of thickness of a central layer having no Lüdering when the outer layers have a gradient of yield stress and of Lüders plateau length.....213
Table 6-8 - Mechanical properties and Lüders length obtained by varying the stiffness of the central layer 215
Table 6-9 - Mechanical properties and Lüders length obtained by varying the thickness of a central layer without Lüders, while outer layers show Lüders with uniform mechanical properties distribution.....217
Table 6-10 - Mechanical properties and Lüders length obtained by varying the thickness of a central layer without Lüders, while outer layers show Lüdering with a graded mechanical properties 218
Table 6-11 - Mechanical properties implemented to assess the influence of strain-hardening on Lüders propagation 219
Table 6-12 - Mechanical properties implemented in the tensile coupon to simulate influence of voids on Lüders propagation 221
Table 6-13 - Geometrical configurations of the voids implemented in the FEM simulations 222
Table 7-1 - Strengthening obtained by pre-strain and diffusion for specimens coated both sides with 500 nm FeC amorphous film and annealed at 430 ˚C - 1h in high vacuum.....234
Table 7-2 - Strengthening obtained by pre-strain and diffusion for specimens coated both sides with 500 nm FeC amorphous film and annealed at 530 ˚C - 1h in high vacuum.....236
Table 7-3 - Strengthening obtained by pre-strain and diffusion for specimens coated both sides with 500 nm FeC amorphous film and annealed at 630 ˚C - 1h in high vacuum.....237
Table 7-4 - Strengthening obtained by pre-strain and diffusion for specimens coated both sides with 500 nm FeC amorphous film and annealed at 710 ˚C - 1h in high vacuum.....238
Table 7-5 - Summary of stresses obtained for pre-strained not-coated IF coupons annealed in high vacuum at different temperatures 242
Table 7-6 - Level of vacuum during ageing treatment in high vacuum at 170 ˚C for 20 min 246

Table 7-7 - Values of the engineering stress-strain curves before aging but after the heat treatment in high vacuum of coupons coated both sides with 500 nm thick FeC film at different temperatures for 1h 249
Table 7-8 - Values of the engineering stress-strain curves after aging at 170 ˚C for 20 min 249
Table 7-9 - Increase of strength and reduction of Lüders plateau length after strain-ageing 249
Table 7-10 - Separation of the contribution to strengthening coming from Cottrell atmosphere formation and precipitation plus grain boundary segregation for not-prestrained IF steel coated on both sides with 500 nm thick FeC film. 252
Table 7-11 - Separation of the contribution to strengthening coming from Cottrell atmosphere formation and precipitation plus grain boundary segregation for prestrained IF steel coated on both sides with 500 nm thick FeC film.....254
Table 8-1 - Correlation of surface colors and temperature for carbon steels [183].....269
Table 8-2 - Measurement of temperature of induction heating treatment with thermocouple and with pyrometer.....270
Table 8-3 – Depth affected by carbon diffusion in austenite.....280
Table 8-4 - Depth affected by carbon diffusion in austenite through grain boundaries.....281
Table 8-5 - List of tests performed on one side coated coupon annealed in high vacuum using a furnace or induction heating for different temperatures and times 285
Table 8-6 - Strain hardening exponent values for specimen coated on one side with 500 nm FeC film and induction heated (IH) or annealed in furnace (HV) at different temperatures and different times. For some specimens two values of n have been indicated since the first n represents the strain-hardening exponent right after Lüders bands propagation is finished, while the second value of *n* represents the normal hardening until UTS is reached.....287
Table 8-7 - List of specimens coated both sides induction heated (IH) for different times or annealed in furnace in high vacuum (HV).....291
Table 8-8 - Strain hardening exponent values for specimen coated both sides with 500 nm FeC film and induction heated or annealed in furnace at different temperatures and different times.....292

Table 8-9 - Area reduction measured in coupons coated both sides with 500 nm thick FeC film.....293
Table 8-10 - Comparison between experimental position of the peaks and their theoretically expected position for specimen induction heated at 1100 ºC – 1150 ºC for 1 second and then at 820 ˚C for 1 minute.....322
Table 8-11 - Comparison between experimental position of the peaks and their theoretically expected position for specimen induction heated at 1100 ºC – 1150 ºC for 1 second and then at 820 ˚C for 4 minutes.....322
Table 8-12 - Numerical values of mechanical properties of prestrained coupons induction heated at 1100 ºC – 1150 ºC for 1 second and then at 820 ˚C for different times.....327
Table 9-1 - Carbon concentration through thickness considering only one side coated coupon 341
Table 9-2 - Size and steepness of the obtained carbon gradient for one side half coated coupons.....352
Table 9-3 – Femtosecond laser parameters used to machine holes along the gauge length of tensile coupons.....354
Table 9-4 - Dimensions of the holes measured by optical microscope after laser machining and polishing.....354
Table 9-5 - Summary of void growth obtained for all the specimens having holes along the gauge length. (*) for the average of this specimens, the value of 1.8 has been discarded ...375
Table 9-6 - Values of strain hardening exponent extracted from stress-strain curves of coupons having holes along the gauge length 377
Table 9-7 - Simulation of ablated configurations.....383
Table 9-8 - Summary of the simulated ablated configurations – (*) details reported in Appendix H.....385
Table 9-9 - Summary of the laser parameters used to perform ablation 389
Table 9-10 - Average depth and corresponding standard deviation for the different ablated zones: (*) indicates ablations which are acceptable for the creation of graded coupons 391
Table 9-11 - Summary of the performed ablation configurations and heat treatments 393
Table 9-12 - Comparison between theoretical and experimentally obtained carbon gradient; (*) indicates specimens showing high difference between expected and obtained gradient 400

Table 9-13 - Femtosecond laser parameters used to machine holes along the gauge width of tensile coupons.....402
Table 9-14 - Voids dimensions measured from pictures taken with optical microscope.....403
Table 9-15 – Summary of the void growth obtained for specimen ablated 500 μm at the center of the gauge width.....415
Table 9-16 - Summary of the void growth obtained for specimens having 500 μm of FeC film left at the center of the gauge width.....418
Table 9-17 - Summary of the void growth obtained for specimens having uniform carbon distribution along the gauge width 421
Table 9-18 - Summary of the void growth obtained for uncoated and not-annealed specimens 423
Table 9-19 – Strain-hardening exponent for specimens having holes along the gauge width 424
Table 10-1 - Dimensions of tensile coupons coated both sides with 500 nm thick FeMnC films. (*) indicates specimens which were DIC tested and the thickness was measured before the application of the DIC coating.....435
Table 10-2 - Reduction in area for specimens annealed at different temperatures and time in high vacuum after coating on both sides with 500 nm FeMnC films.....438
Table 10-3 - Comparison of mechanical properties obtained from FeC films and FeMnC films 442
Table 10-4 - Diffusion depth of manganese during annealing of FeMnC coated IF steel annealed at 530 ˚C and 630 ˚C for 1h in high vacuum.....443
Table 10-5 - Diffusion depth of manganese during annealing of FeMnC coated IF steel annealed at 1000 ˚C for 1h and for 10h in high vacuum 444
Table 10-6 - Strain–hardening exponents values evaluated for FeMnC coated tensile coupons.....444
Table 10-7 - Mechanical properties of tensile coupons coated one side with 150 nm thick carbon film annealed in air at 530 ˚C – 1h. Mechanical properties obtained with FeC films are reported for comparison.....448

List of Tables in Appendices

Table D- 1 - Calibration of the tensile machine 500
Table D- 2 - Dimensions of tensile coupons coated both sides and not-annealed and of tensile coupons coated both sides and annealed at 330 ºC – 1h in high vacuum 501
Table D- 3 - Dimensions of tensile coupons coated both sides and annealed at 330 ºC – 4 days or at 430 ºC or 530 ºC – 1h in high vacuum.....502
Table D- 4 - Dimensions of tensile coupons coated both sides and annealed at 630 ºC – 1h or at 710 ºC-1h in high vacuum 502
Table D- 5 - Dimensions of uncoated tensile coupons annealed at different temperatures for 1h in high vacuum 503
Table D- 6 - Values of mechanical properties for both sides coated and not annealed samples tested at a speed of 2.5µm/s.....503
Table D- 7 - Values of mechanical properties for both sides coated samples annealed at 330 ºC for 1h and tested at a speed of 2.5 µm/s 503
Table D- 8 - Values of mechanical properties for both sides coated samples annealed at 330 ºC for 4 days and tested at a speed of 2.5 µm/s 503
Table D- 9 - Values of mechanical properties for both sides coated samples annealed at 430 ºC for 1h and tested at a speed of 2.5 µm/s 504
Table D- 10 - Values of mechanical properties for both sides coated samples annealed at 530 ºC for 1h and tested at a speed of 2.5 µm/s 504
Table D- 11 - Values of mechanical properties for both sides coated samples annealed at 630 ºC for 1h and tested at a speed of 2.5 µm/s 504
Table D- 12 - Values of mechanical properties for both sides coated samples annealed at 710 ˚C for 1h and tested at a speed of 2.5 µm/s 505
Table D- 13 - Values of mechanical properties of not-coated IF coupons annealed at different temperatures for 1h in high vacuum 505
Table D- 14 - Dimensions of tensile coupons coated both sides and annealed at different temperatures for 1h in argon atmosphere 506
Table D- 15 - Mechanical properties obtained for annealing in argon at 430 ˚C-1h.....506
Table D- 16 - Mechanical properties obtained for annealing in argon at 530 ˚C-1h.....506

Table D- 17 - Mechanical properties obtained for annealing in argon at 630 ˚C-1h.....507
Table D- 18 - Mechanical properties obtained for annealing in argon at 710 ˚C-1h.....507
Table D- 19 - Summary of tensile coupon coated both sides with FeC film and Nickel cap layer annealed at different temperatures in argon.....508
Table D- 20 - Summary of the dimensions of the tensile coupons coated both sides with FeC film and Nickel cap layer.....509
Table D- 21 - Mechanical properties obtained for annealing in argon at 430 ˚C - 1h of coupons coated both sides with 500 nm thick FeC and 20 nm Nickel cap layer 509
Table D- 22 - Mechanical properties obtained for annealing in argon at 530 ˚C - 1h of coupons coated both sides with 500 nm thick FeC and 20 nm Nickel cap layer 510
Table D- 23 - Mechanical properties obtained for annealing in argon at 630 ˚C - 1h of coupons coated both sides with 500 nm thick FeC and 20 nm Nickel cap layer 513
Table D- 24 - Mechanical properties obtained for annealing in argon at 710 ˚C - 1h of coupons coated both sides with 500 nm thick FeC and 20 nm Nickel cap layer 514
Table D- 25 - Comparison of upper yield stress for annealing in argon at different temperatures for 1h of coupons coated both sides with 500 nm FeC film and of coupons coated both sides with 500 nm FeC film and 20 nm Nickel cap layer 516
Table D- 26 - Comparison of diffusion coefficient of carbon into ferrite and nickel for different annealing temperatures 517
Table D- 27 - Vacuum levels during annealing in high vacuum of specimens cleaned with HCl before deposition of the FeC film 519
Table D- 28 - Dimensions of coupons coated with a 500 nm thick FeC film on both sides after a cleaning with HCl solution of the IF core and annealed at different temperatures for 1h in high vacuum 520
Table D- 29 - Mechanical properties obtained for annealing in high vacuum at 430 ˚C - 1h of coupons coted both sides with 500 nm thick FeC and cleaned using HCl solution 520
Table D- 30 - Mechanical properties obtained for annealing in high vacuum at 530 ˚C - 1h of coupons coted both sides with 500nm thick FeC and cleaned using HCl solution 523
Table D- 31 - Mechanical properties obtained for annealing in high vacuum at 630 ˚C - 1h of coupons coted both sides with 500nm thick FeC and cleaned using HCl solution 525

Table D- 32 - Mechanical properties obtained for annealing in high vacuum at 710 ˚C - 1h of coupons coted both sides with 500 nm thick FeC and cleaned using HCl solution 527
Table D- 33 - Dimensions of coupons coated with a 500 nm thick FeC film on both sides annealed at 530 ˚C - 1h in air.....531
Table D- 34 - Mechanical properties obtained for two coupons annealed in air at 530 ˚C - 1h and one coupon annealed in air at 630 ˚C - 1h. All coupons were coated both sides with 500 nm thick FeC amorphous film 532
Table D- 35 - Expected theoretical yield stress and experimentally obtained yield stress. (*) indicates that for these temperatures, the coupons having lower yield stress were discarded to minimize the standard deviation.....532
Table D- 36 - Carbon atoms and iron atoms in the FeC film considering 27 at% of carbon as nominal content 532
Table D- 37 - Carbon atoms and iron atoms in the FeC film considering 33 at% of carbon as nominal content 533
Table D- 38 - Carbon atoms and iron atoms in the FeC film considering a film thickness of 520 nm and a 34.3 at% of carbon content 534
Table D- 39 - Carbon atoms and iron atoms in the FeC film considering a film thickness of 480 nm and a 26 at% of carbon content 535
Table D- 40 - Dimensions of coupons coated both sides with different FeC film thicknesses 536
Table D- 41 - Mechanical properties obtained for coupons coated both sides with 50 nm thick FeC amorphous film: specimen 50 - A (not annealed), specimen 50 - B and 50 - C (annealed in high vacuum at 530 ˚C-1h) 536
Table D- 42 - Mechanical properties obtained for coupons coated both sides with 100 nm thick FeC amorphous film: specimen 100 - A (not annealed), specimen 100 - B (annealed in high vacuum at 530 ˚C-1h).....536
Table D- 43 - Mechanical properties obtained for coupons coated both sides with 200 nm thick FeC amorphous film: specimen 200 - A (not annealed), specimen 200 - B and 200 - C (annealed in high vacuum at 530 ˚C-1h) 537
Table D- 44 - Mechanical properties obtained for coupons coated both sides with 300 nm thick FeC amorphous film, specimen 300 - C and 300 - D were DIC tested 537

Table D- 45 - Mechanical properties obtained for coupons coated both sides with 400 nm thick FeC amorphous film, specimen 400 - C and 400 - D were DIC tested 537
Table D- 46 - Iron and carbon atoms for FeC film of 400 nm thickness 538
Table D- 47 - Iron and carbon atoms for FeC film of 300 nm thickness 538
Table D- 48 - Iron and carbon atoms for FeC film of 200 nm thickness 539
Table D- 49 - Iron and carbon atoms for FeC film of 100 nm thickness 539
Table D- 50 - Iron and carbon atoms for FeC film of 50 nm thickness 540
Table D- 51 - Comparison between calculated yield stress and experimental yield stress considering different film thicknesses. The values marked as (x) are calculated considering that all the carbon available can be diffused even if its amount is higher than the solubility limit at 530 ˚C - 1h (which is equal to 0.0260 at%). The value marked as (xx) is calculated considering that only the solubility limit of carbon at 530 ˚C can be effectively diffused ..541
Table D- 52 - Iron and carbon atoms for FeC film of 400 nm thickness and 27 at % of carbon 541
Table D- 53 - Iron and carbon atoms for FeC film of 300 nm thickness and 27 at % of carbon 542
Table D- 54 - Iron and carbon atoms for FeC film of 200 nm thickness and 27 at % of carbon 542
Table D- 55 - Iron and carbon atoms for FeC film of 100 nm thickness and 27 at % of carbon 543
Table D- 56 - Iron and carbon atoms for FeC film of 50 nm thickness and 27 at % of carbon 543
Table D- 57 - Iron and carbon atoms for FeC film of 400 nm thickness and 33 at % of carbon 544
Table D- 58 - Iron and carbon atoms for FeC film of 300 nm thickness and 33 at % of carbon 544
Table D- 59 - Iron and carbon atoms for FeC film of 200 nm thickness and 33 at % of carbon 545
Table D- 60 - Iron and carbon atoms for FeC film of 100 nm thickness and 33 at % of carbon 545

Table D- 61 - Iron and carbon atoms for FeC film of 50 nm thickness and 33 at % of carbon 546
Table D- 62 - Uncertainty associated to the film thickness for different nominal values of FeC film thicknesses.....546
Table D- 63 - Iron and carbon atoms considering film thickness variation of ± 17 nm on a nominal thickness of 400 nm.....547
Table D- 64 - Iron and carbon atoms considering film thickness variation of ± 12 nm on a nominal thickness of 300 nm.....548
Table D- 65 - Iron and carbon atoms considering film thickness variation of ± 8 nm on a nominal thickness of 200 nm.....549
Table D- 66 - Iron and carbon atoms considering film thickness variation of ± 4 nm on a nominal thickness of 100 nm.....550
Table D- 67 - Iron and carbon atoms considering film thickness variation of ± 2 nm on a nominal thickness of 50 nm.....551
Table D- 68 - Dimensions of coupons coated both sides with 500 nm FeC film and annealed at 630˚C - 5h in high vacuum 552
Table D- 69 - Mechanical properties of coupons coated both sides with 500 nm FeC film and annealed at 630 ˚C - 5h in high vacuum.....552
Table D- 70 - Geometrical dimensions of coupons coated both sides with 500 nm FeC film and annealed at 430 ˚C - 10h in high vacuum 553
Table D- 71 - Mechanical properties obtained during tensile test of tensile coupons coated both sides with 500 nm FeC film annealed at 430 ˚C - 10h in high vacuum 553
Table D- 72 - Dimensions of coupons coated on one side with 500 nm FeC film and annealed at 530 ˚C - 1h or 630 ºC – 1h in high vacuum.....553
Table D- 73 - Mechanical properties obtained for specimens coated on one side with 500 nm thick FeC film and annealed at 530 ˚C - 1h in high vacuum.....554
Table D- 74 - Mechanical properties of a coupon coated only on one side with 500 nm thick FeC film and annealed at 630 ˚C - 1h in high vacuum.....554

Table G- 1 - Values recorded by the thermocouple inserted in the furnace inside the quartz ampoule.....575

Table G- 2 - Vickers hardness values through thickness for one side coated coupons and for uncoated coupons induction heated at 1100 ºC – 1150 ºC for 1 seconds and then at 820 ˚C for different times. Vickers hardness of an uncoated and not-annealed IF steel is reported as reference 578
Table G- 3 - Dimensions of tensile coupons coated only on one side with 500 nm FeC film and annealed in high vacuum (HV) using furnace or induction heating (IH) for different temperatures and times 579
Table G- 4 - Mechanical properties obtained for one side coated coupons annealed in furnace or induction heated at different temperatures and times (YS means yield stress, while UTS is the ultimate tensile strength).....579
Table G- 5 - Dimensions of tensile coupons coated on both sides with 500 nm FeC film and annealed in high vacuum (HV) using furnace or induction heating (IH) for different temperatures and times 581
Table G- 6 - Mechanical properties obtained for both sides coated coupons annealed in furnace or induction heated at different temperatures and times (YS means yield stress, while UTS is the ultimate tensile stress) 582
Table G- 7 - Vickers microhardness of one side and both sides coated coupons induction heated at 1100 ºC – 1150 ºC for 1 seconds and then at 820 ˚C for different times 584
Table G- 8 - Carbon concentration obtained during EDS performed in a specimen induction heated at 1100 ºC – 1150 ºC for 1 seconds and then at 820 ˚C for 1 minute.....587
Table G- 9 - Carbon content measured by EDS inside grains and at grain boundaries for a specimen induction heated at 1100 ºC – 1150 ºC for 1 seconds and then at 820 ˚C for 2 minutes.....589
Table G- 10 - Carbon content measured by EDS inside grains and at grain boundaries for a specimen induction heated at 1100 ºC – 1150 ºC for 1 seconds and then at 820 ˚C for 4 minutes.....590
Table G- 11 - Dimension of specimens before performing 16-17% pre-strain.....595

Table H- 1 - Dimensions of tensile coupons having holes lased along the gauge length.....596
Table H- 2 - Mechanical properties of specimens having holes along the gauge length 596

Table H- 3 - Carbon concentration and yield stress gradient created by ablating 333 μm in the centre of the tensile coupon. AV indicates the concentration in the center of the width, while AV 10 reports the concentration at the interface between ablated and not-ablated zones 623
Table H- 4 - Carbon concentration and yield stress gradient created by ablating 500 μm in the centre of the tensile coupon 624
Table H- 5 - Carbon concentration and yield stress gradient created by ablating 600 μm in the centre of the tensile coupon 626
Table H- 6 - Carbon concentration and yield stress gradient created by ablating 500 μm close to one edge of the tensile coupon 627
Table H- 7 - Values of diffused carbon for heat treatments performed at 530 ˚C for 20 min, 25 min and 30 min 629
Table H- 8 - Carbon concentration and yield stress gradient created by ablating 500 μm in the centre of the specimen and by performing annealing at 530 ˚C for 25 minutes and 30 minutes.....629
Table H- 9 - Gradient of yield stress obtained by removing 250 μm of FeC film on the sides of the tensile coupon and leaving 500 μm at the centre of the coupon.....630
Table H- 10 - Dimensions of tested specimens having holes on the gauge width (EC 6 and EC 13 had no voids) 642
Table H- 11 - Summary mechanical properties for tensile coupons having a gradient of carbon obtained by removing 500 μm of FeC film at the centre of the coupon.....643
Table H- 12 - Summary mechanical properties for tensile coupons having a gradient of carbon obtained by leaving 500 μm of FeC film at the centre of the coupon 643
Table H- 13 - Summary mechanical properties for tensile coupons having a uniform distribution of carbon along the gauge width 643
Table H- 14 - Summary mechanical properties for uncoated and not-annealed tensile coupons 644

Table I- 1 - Mechanical properties of tensile coupons coated both sides with 500 nm thick FeMnC film and annealed at 530 ˚C – 1h in high vacuum.....682

Table I- 2 - Mechanical properties of tensile coupons coated both sides with 500 nm thick FeMnC film and annealed at 630 ˚C – 1h in high vacuum.....682
Table I- 3 - Mechanical properties of tensile coupons coated both sides with 500 nm thick FeMnC film and annealed at 1000 ˚C – 1h in high vacuum.....684
Table I- 4 - Mechanical properties of tensile coupons coated both sides with 500 nm thick FeMnC film and annealed at 1000 ˚C – 10h in high vacuum.....685

Chapter 1 : Introduction

This PhD thesis is part of a research project called Gracos (Graded Composite Steels) whose main scope is the production of carbon graded packaging steels. New demands exist to produce packaging and automotive steels with higher strength but still high formability to obtain thinner cans and thinner car body panels that can save material and lower the weight of the final product. The traditional process used to strengthen this type of ultra-low carbon steels is bake-hardening. As it will be discussed in the literature review, bake hardening is a low temperature heat treatment, which is done after the steel has been formed, in order to segregate carbon to dislocations. This segregation causes an increase in yield stress in the final product. However, the increase in yield stress that can be obtained with this thermal treatment is limited because the initial amount of carbon in the packaging steel must remain low; otherwise the material would age at room temperature causing the appearance of a plastic instability known as Lüders plateau. Lüders plateau should be avoided (especially in outer car body panels) since it causes the appearance of striations on the surface of the steel which compromises its lacquering and paintability. Starting from this background, the company Arcelor-Mittal, who is partially funding the Gracos project, is interested in developing a new method to further increase the strength of packaging steels. The main idea is to use a carbon rich vapour deposited coating on the surface of the steel which can act as carbon reservoir during heat treatment. It is expected that by properly choosing the heat treatment temperature and time, carbon can be diffused into the steel sheet to obtain different concentration profiles through thickness. The configuration chosen in this thesis is to have a carbon gradient through thickness with high levels of carbon in the near-surface region of the steel sheet which will increase the strength and no carbon in the core of the sheet which will prevent or limit the appearance of Lüders bands.

The Gracos project is a collaboration between the University of Ottawa, the University of Rouen, the University of British Columbia (UBC) and INSA Lyon. Study and production of the Physical Vapour Deposited carbon coating was performed at UBC, while annealing and successive testing and modelling of mechanical properties of the steel sheet was performed by the University of Ottawa. Analyses of the carbon coating transformation during annealing and measurements of the final carbon content in the steels after annealing were

performed in collaboration with the University of Rouen using Atom Probe Tomography experiments.

1.1. Main Contributions

The main contributions and originality of the work presented by this PhD thesis are summarized in this section. Chapter 5 describes all the results obtained by diffusion annealing of carbon from FeC film. The new contributions given by these results are:

- Carbon diffusion has been successfully obtained from FeC film to strengthen Interstitial Free (IF) steel;
- Investigations related to film thickness and annealing environment are reported in the same chapter in order to assess the maximum strengthening that can be obtained with diffusion of carbon from FeC films;

In Chapter 6, finite element modelling of Lüdering is described. The new results and investigations done in this work are:

- Lüdering can be limited or suppressed by having a carbon gradient instead of a uniform distribution of carbon;
- Lüdering can be limited by increasing the strain-hardening of the material;
- The steel which shows Lüders instability can be "sandwiched" with another material having no Lüders plateau to suppress the plastic instability;
- Influence of void interspacing and of void volume fraction on Lüders plateau was assessed;

Chapter 7 shows the influence that pre-strain has on carbon diffusion from FeC film; in particular, if the specimens are subjected to high levels of pre-strain, the strengthening caused by carbon diffusion is lowered. In the same chapter, strain-ageing experiments were performed to separate the contributions due to strengthening from the different mechanisms (such as segregation of carbon at grain boundaries, formation of Cottrell atmosphere and precipitation).

Chapter 8 proposes a completely new processing method to obtain high strength Interstitial Free (IF) steel by using induction heating as annealing technology to promote diffusion of carbon from FeC films. The results shown in this chapter are very promising for both

packaging and automotive applications due to the high mechanical properties obtained in very short annealing times.

In Chapter 9, the influence of carbon gradient (i.e. yield stress gradient) on void growth is investigated experimentally. Two configurations were studied, the first one with a carbon gradient along the gauge length of the coupon (isostress condition) and the other with carbon gradient along the width (isostrain condition). The main results obtained from this work are:

- In isostress condition, void growth is higher in holes placed in a no-carbon zone since they accumulate most of the deformation and reach a critical strain earlier than voids placed in zones containing carbon;
- In isostrain condition, the material fails in the couple of voids inserted in zones containing carbon since they will quickly reach the critical stress to obtain failure;
- During these tests, it was also proven that Lüdering accelerates void growth;

Finally Chapter 10 reports some preliminary work done on FeMnC film and on 100% amorphous carbon films. However, from these first experiments, the diffusion of substitutional atoms from Physically Vapour Deposited (PVD) films does not seem to be possible. More promising is the diffusion of carbon from 100% carbon containing films, even if some considerations about thickness and its adhesion to the IF substrate are necessary before proceeding with further experiments.

Chapter 2 : Literature Review

2.1. What is a Functionally Graded Material?

Functionally graded materials (FGMs) are inhomogeneous materials having a spatial gradient that is properly tailored to have a specific behaviour of mechanical, thermal or electrical properties. According to a definition given by Gasik [1]: "A functionally graded material is a material with engineered gradients of composition, structure and/or specific properties aiming to become superior over the homogeneous materials composed of the same or similar constituents". Figure 2-1 shows the difference in composition and properties between a "traditional" composite, which has a well-defined interface between the components, and a functionally graded material having a gradual change in microstructure [2]. More precisely, a functionally graded material has properties that change gradually moving from one end to the other end, while a traditional composite has properties which are homogeneous in space and are an average of the properties of the main constituents. The difference of thermal expansion at the interface of the two different materials can cause detachment in a "traditional" composite (Figure 2-2), while an FGM is able to reduce thermal stress by almost 30% avoiding damage at the interface [2]. There are many ways to classify functionally graded materials, for example referring to their constituents (metallic-metallic, metallic-ceramic or ceramic-ceramic), or to the method used to create the property gradient (induced in situ by chemical reaction or created using mechanical methods, etc…). In other situations, the classification can be done depending on the kind of gradient that has been created (physical gradient as porosity gradient, or a chemical gradient such as a concentration variation of an element) or referring to gradient distribution (mono-, bi- or three-dimensional) [3]. In 1990 Ilschner demonstrated that some properties of the FGMs are more dependent on the chemical composition than on the structure (for example, the modulus, the thermal conductivity, the electrical resistance and the specific heat), but other properties are strongly dependent on the structure of the composite (for example tensile resistance, fracture toughness, optical and magnetic properties) [4].

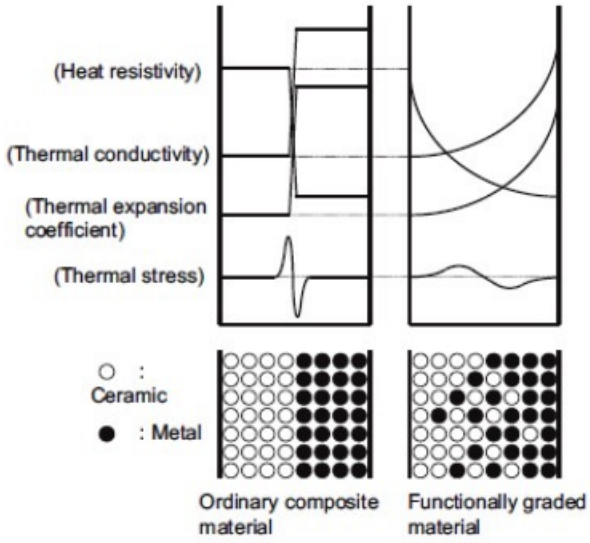

Figure 2-1 - Material structures and properties of ordinary composite and functionally graded materials [2]

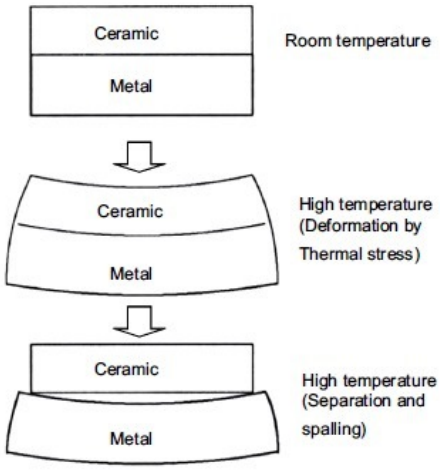

Figure 2-2 - Separation of ceramics and metals by thermal stress [2]

2.2. Main Industrial Applications of Functionally Graded Materials

The main reason for the development of functionally graded materials was the development of structural materials which have to be able to act as thermal barrier for space programs [5]. The idea to overcome the problem was the development of new composite using ceramic materials which are heat resistant on the side of the high temperatures and having metals with high thermal conductivity, high toughness on the side of the low temperature [5]. Other

researches aimed at the production of Functionally Graded Materials for high efficiency thermoelectric/thermionic hybrid direct energy conversion system (HYDECS) [5].

The Graded Structure can be referred not only as the mixture of two different materials, but it can also be related to the creation of a gradient of porosity inside a metal. For example, Titanium alloys with porosity gradient have been applied for light weight structures in aircraft components. Moreover, many graded materials are present in nature such as bamboo and human bones, while artificial graded materials are very useful to satisfy the requirement of biocompatibility [2]. For dental implants which are used as a root to fix artificial teeth, compositional graded materials made of titanium and hydroxyapatite are used as constituents because the first one meets the structural criteria of stiffness and toughness while hydroxyapatite is compatible with human bones [2].

2.3. Functionally Graded Materials Processing

There are many methods to produce functionally graded materials, but it is possible to classify them in two main groups: constructive processes and transport based processes. According to Suresh and Mortensen, “constructive processes can construct the functional graded material layer by layer, starting from a proper distribution of constituents of the functional graded materials” [6]. For this reason these techniques are called constructive processes, because the gradients can be really designed in space. The change of composition can be tailored based on the final requirements that the material has to fulfill and the variation of composition can be controlled by computer during the production process, keeping under control the feeding of the different materials that will constitute the final functionally graded composite [6].

The other class of processing methods is that of transport based processes. These techniques are based on natural transport phenomena to create a gradient inside the final component. The principal transport mechanisms that are used are the flow of fluid, the diffusion of atomic species, or the conduction of heat to create gradients in the microstructure and on composition [6]. In Figure 2-3, all the processes available for FGM production are summarized and classified in two different classes. More recently, the functionally graded materials concept has been extended to create metallic graded structures [7]. One of the main techniques which are used to produce graded metal matrix composites (MMCs) is based on

the exploitation of external force fields such as gravitational, centrifugal, thermal, magnetic or electrical [7]. This kind of approach has been used to create W-Mo-Ti graded structures and to produce graded structure of SiC particles in aluminium matrix or again to reinforce aluminium alloys with nickel coated graphite particles [7]. Another technique mainly used to produce graded coatings of plates is the electrophoretic deposition process (EPD), where powders are electrically charged through interaction with the suspension medium and they can migrate under the influence of an electric field applied to the suspension [7]. A very new class of graded materials are called "Gasars", which are materials having a high ordered porosity that can be used in heat exchangers, filters, fluid substance separators and stainless steel for biomedical applications [7]. However, transport phenomena have to be kept into account also for the constructive processes, because they tend to erase gradients incorporated early in the FGM process cycle [6]. For this reason it is important to consider the time and velocity scales for heat, solute and liquid transport for an FGM production technique [6]. Diffusion mechanisms in the solid state are able to create functional gradients in composition inside interstitial systems with reasonable processing times [6]. This is the basis for the carburization and nitridation of steel [6].

2.4. Constitutive Processes

2.4.1. Powder Densification Processes

Powder processes start from a preform body that contains the desired gradient as volume fraction of the different phases (i.e. ceramic and metallic phases). The preform body needs then to be densified using techniques such as cold pressing, pressure-less sintering, hot isostatic pressing or hot pressing in a closed die [6]. There can be two classes of powder consolidation processes: the single-phase densification and the two phase densification [6]. To avoid high residual deformation at the end of the consolidation process it is very important that the two phases densify at the same speed [6]. The achievement of uniform sintering rate across a wide range of volume fractions of two phases is considerably challenging, because the sintering rates vary significantly with the nature and the properties of each phase, in particular ceramics densify slower than metals. Another method is based on

using sintering promoters to increase the sintering rate of the ceramics or adding additives that can lower the sintering temperature of the ceramic phase [6].

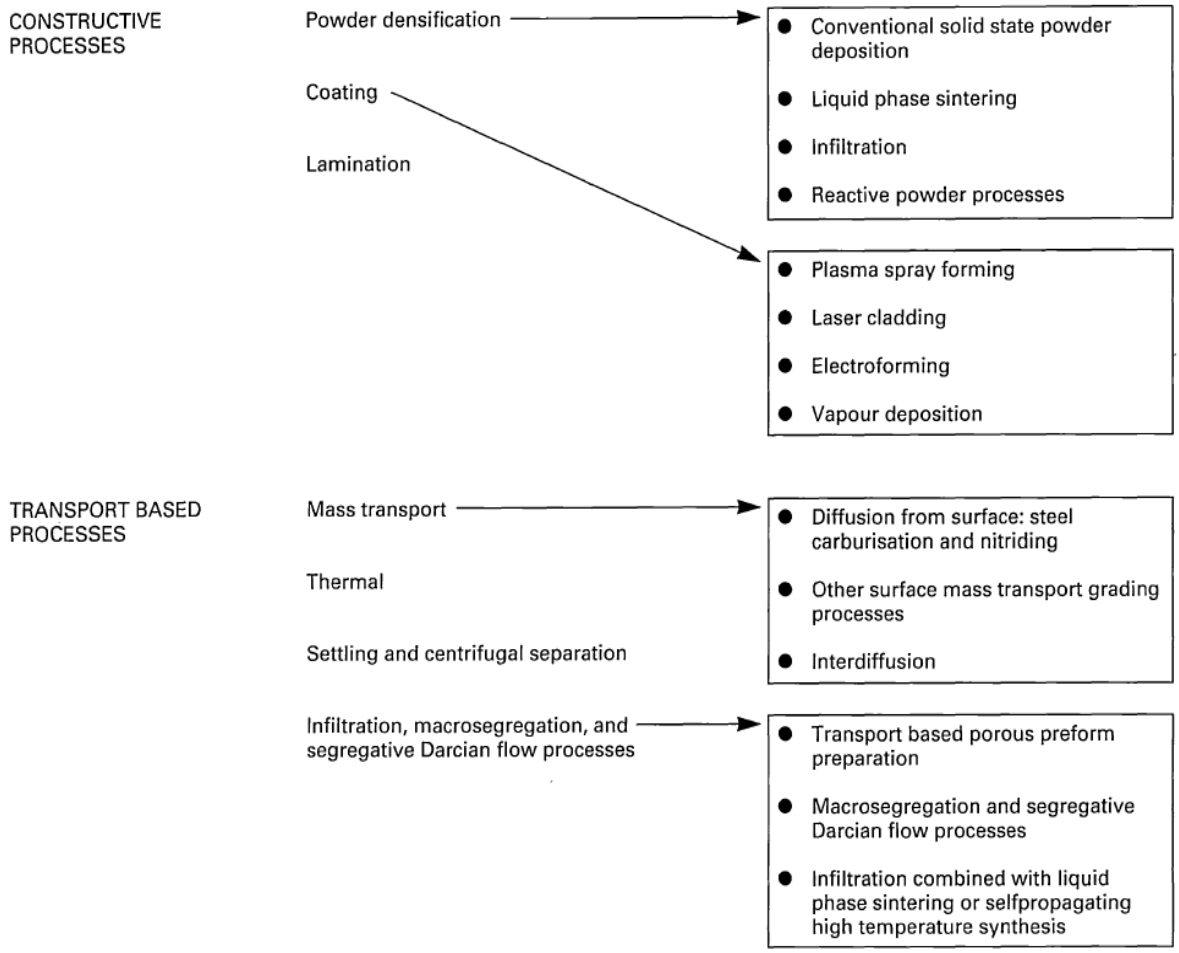

Figure 2-3 - Functionally graded materials: processing methods and their classification [8] (copyright © The Institute of Materials, Minerals and Mining, reprinted by permission of Taylor & Francis Ltd.)

Another concern on the powder consolidation process is the formation of the preform body, because the gradient of composition must be created before the densification process takes place. The most common technique to obtain unidirectional gradients is to prepare and stack discrete layers of uniform composition. The main limitation of this technique is the steepness of the gradients that can be created given that the layers must have a minimum thickness to be stacked [6]. In order to obtain unidirectional gradients, many automated techniques have been designed which can create gradients both across the thickness and across the width of a strip [6]. Different techniques have been developed for obtaining three-dimensional FGM powder preforms [6]. Another process to obtain FGMs from powders includes liquid

sintering which has been applied successfully for the production of "WO based cermets" [6] and of functionally graded cemented carbonitrides [9]. Another technique involving powders is the infiltration method which consists in the formation of a preform of the more refractory phase. Such preform has a gradient of porosity and is then infiltrated with the less refractory phase in its molten state. This technique has been used to produce FGMs of Alumina-Calcium Hexaluminate (CA_6) [10].

Other processes are defined as "reactive powder processes" which are distinguished in two main classes: the first one is called "reactive sintering" or "self-ignition processing method" and it happens when the powder compact is heated uniformly until it reacts at a high rate so that the synthesis can take place [6], [11]. A second class of reactive processes is called "self-propagating high temperature synthesis (SHS), where the reaction is ignited in one location of the powder compact; if the reaction is self-sustaining it will propagate in the whole sample [6]. Moreover, coating processes have been developed to create graded layers that act as transition between a bulk and an outer coating that has to protect the bulk from harsh conditions of temperature, corrosion or erosion [6]. Some techniques used to produce graded coatings are plasma spray forming [6], [12], laser cladding [6] and vapour deposition [6].

2.5. Transport Based Processes

An example of FGM obtained through mass transport is the surface hardening of steel by transport of carbon and nitrogen atoms to create a harder external surface and generate a gradual transition to a tougher and softer core. Carbon and nitrogen are interstitial atoms and they can be supplied using several sources such as gas, solid compounds or salt baths [6]. The outer layer, which is rich in carbon, will be transformed in martensite and its hardness is therefore high, while the core will be softer [6]. Other techniques to migrate solid particles involve settling and centrifugal separation [6].

2.5.1. Bake Hardening and Case Hardening of Steel

The strengthening influence of interstitial carbon atoms is well known from bake hardening processes (150 – 200 °C) for 20 minutes [13]. During this treatment, interstitial solute atoms migrate to the dislocations which have been produced during the forming process. The

strength increase obtained in these steels is due to interstitial atoms (carbon atoms) migrating and pinning dislocations. This "cloud" of carbon atoms locking dislocations is known as Cottrell atmosphere. Once the dislocations have been pinned, there is an increase in yield stress and the appearance of a Lüders plateau. Further details on the stress-strain behaviour of materials showing discontinuous yielding will be given in section 2.10. The bake hardening process is diffusion controlled because carbon atoms have to migrate through the iron lattice and this is influenced by temperature, time, and by the initial carbon concentration of the steel [13]. Bake hardening is usually used to strengthen Ultra-Low Carbon (ULC) steels, while Interstitial Free steels (IF steels) cannot in general be strengthened using this method since no carbon is "free" to migrate to dislocations unless higher amounts of this element are added initially in the steel. Indeed, inside IF steels, all the interstitial elements are removed from solution by addition of carbide and nitride formers such as aluminum, titanium, niobium and also vanadium [13]. Depending on the alloying elements used, there are several "families" of interstitial free steel. Here the attention is focused on Titanium IF steels because their composition is similar to the IF steel used for the Gracos Project. To guarantee full stabilization of the interstitial elements, titanium must be added according to the stoichiometric ratio [13]:

$$\%Ti = 4(\%C) + 3.42(\%N) + 1.5(\%S) \qquad \text{(eq. 2-1)}$$

In reality, Titanium is added in higher quantity to ensure complete stabilization of carbon avoiding ageing of the steel at room temperature. The precipitates that can be formed by Ti are shown in Figure 2-4 [13]. TiN particles formed during the slab casting act as nucleation sites for the precipitation of TiS and $Ti_4C_2S_2$. The remaining carbon is precipitated as TiC. Then, during the reheating of the slab only TiS and TiN remain as precipitates and during the cooling of the strip through the austenite-ferrite transformation TiS is transformed in $Ti_4C_2S_2$ by the absorption of titanium and carbon [13]. IF steels are already applied in the automotive sector since they show excellent drawability and high ductility which makes them suitable to obtain complex shapes as single piece.

2.5.2. Case Hardening

Surface heat treatments of steel are used to increase its hardness in the outer zones keeping a tough core. Two approaches have been developed; the first one consists in taking medium-carbon steels and hardening their surface through a heat treatment such as flame hardening

or induction hardening [14]. The second approach is to diffuse carbon into the surface layers of low-carbon steel using carburizing techniques which are often called case-hardening processes [14].

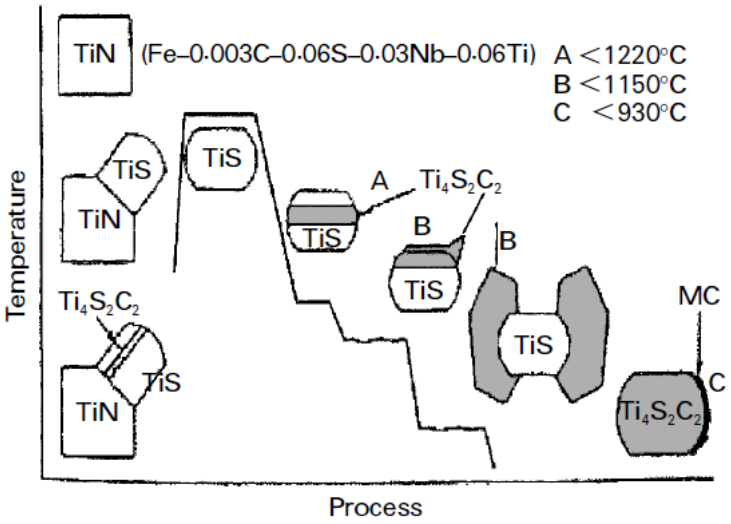

Figure 2-4 - Schematic mechanism of carbosulphide and carbide formation in titanium IF steels [13]

There is a wide variety of carburizing treatments depending on the medium used to diffuse carbon. For example, pack carburizing is a process where the parts to be carburized are placed in a heat resistant container with a solid carburizing medium such as charcoal [14]. The parts within the container are heated at a temperature comprised in a range between 875 ˚C and 925 ˚C and they are kept at high temperature for 8 hours, even if higher temperatures and longer times might be used to increase the depth of case [14]. Other carburizing techniques use a liquid medium such as bath of fused salts containing sodium cyanide and sodium carbonate [14]. The bath has to be heated to a temperature between 870 ˚C and 955 ˚C while the time ranges between 5 minutes up to 1h. According to Campbell, “these baths offer accurate temperature control; however, they contain cyanides which are extremely poisonous” [14]. Another category of carburization processes is the one which uses gases such as methane, propane and butane. Again, high temperatures are necessary, in fact the part is heated at least to 900 ˚C for 3 to 4 hours in a carbon rich atmosphere which is usually a mixture of carbon monoxide and water vapour and the case depth range between 0.5 and 1.5 mm [14]. Another recent technique is vacuum carburization which is performed at temperatures between 845 ˚C and 1040 ˚C. The part is heated at these temperatures in a rough vacuum (0.1 - 0.3 torr) to prevent oxidation and then the chamber is backfilled to a

partial pressure of hydrocarbon gas which is the supplier of the carbon which will diffuse in the part [14].

2.6. Diffusion of Carbon

Diffusion is a mass transport mechanism that happens in solids, liquids, and gases. In solids the diffusion occurs thanks to the movement of point defects such as vacancies and interstitial atoms. The solid solutions can be substitutional or interstitial [15]. According to Callister, "in the case of interstitial solid solutions, even small atoms are bigger than the dimension of the interstitial lattice site and they will introduce some lattice strains on the adjacent atoms" [15].

An important parameter for diffusion is the temperature because it influences directly the value of the diffusion coefficient *D*, in particular they are related through an Arrhenius equation [15]:

$$D = D_0 \exp\left(-\frac{Q_d}{RT}\right) \qquad \text{(eq. 2-2)}$$

where:

D = diffusion coefficient (m^2/s);

D_0 = a temperature independent preexponential (m^2/s);

Q_d = activation energy for diffusion (J/mol);

R = gas constant (8.31 J/mol K);

T = absolute temperature (K);

In literature, different value of *D* for diffusion of C in alpha iron are found. From Callister [15] the value of D_0 for carbon diffusing in alpha iron is 6.2×10^{-7} m^2/s and the activation energy Q_d is estimated to be 80 kJ/mol. Wilkinson [16] gives a value of D_0 = 2.20 cm^2/s and a value for Q_d = 122 kJ/mol, while C.G.Homan [17] gives the following expression for the coefficient of diffusion D_C:

$$D_C = 0.008 \times \exp(-19800/RT) \qquad \text{(eq. 2-3)}$$

where, the activation energy is 19800 cal/mol.

Bokshtein et al. [18] have shown that the diffusion of carbon in iron is strongly dependent on the grain boundaries, and stated that diffusivity along grain boundaries is four orders of

magnitude higher than within the grains. In their research the authors mentioned that at 550 °C the diffusion coefficients along the grain boundaries and within the bulk of the grains are $D_b = 1.5x10^{-7}$ cm^2/s and $D_g = 5x10^{-11}$ cm^2/s respectively [18]. In 1950 Wert studied the diffusion of carbon in alpha iron in the range of temperatures from -35 °C to 200 °C [19]. In his study he suggested that pre-exponential factor D_0 is equal to 0.02 cm^2/s while the activation energy Q is equal to 84.10 kJ/mol. In another work Wert and Zener [20] tried to measure values for the pre-exponential factor D_0 for interstitial diffusion of C and N in alpha iron. The values stated in this article are $D_0 = 0.008$ cm^2/s and Q = 82.843 kJ/mol. In 1959, starting from the results of Wert, Doremus was measuring the activation energy and the diffusion coefficient for precipitation of carbon in α-iron [21]. He found that the activation energy is 17.1 kcal/mole which is lower than the one measured using relaxation methods, which is close to 19.8-20 kcal/mole [21]. In 1969, Lord tried to measure the coefficient of diffusion of C in α-iron using ultrasonic measurements and calculated a diffusion coefficient of $D_c = 4.52x10^{-9}$ cm^2/s at 408 °C and a diffusion coefficient of $D_c = 8.85x10^{-9}$ cm^2/s at 430 °C [22]. The author mentioned that the best fit of the linear portion of the curve is obtained if $D_0 = 0.0033$ cm^2/s and Q = 19.3 kcal/mol. The increase of diffusivity at higher temperatures is attributed to carbon atoms that occupy tetrahedral interstitial sites.

McLellan and Wasz in 1992 analyzed statistically all the available data related to diffusion of C in BCC iron and confirmed that the diffusion cannot be explained by a single linear Arrhenius expression. The plot of D versus 1/T has a positive departure from the linear behaviour as the temperature approaches the α-γ transition [23]. McLellan and Wasz have fitted the diffusion data below 360 K with the Arrhenius type equation with $D_0 = 4.876x10^{-7}$ m^2/s and Q = 80.64 kJ/mol.

It is important to consider the interactions between carbon atoms because they determine the probability that another interstitial adjacent site can be occupied [24]. In his paper, Bhadeshia [24] has reviewed the carbon-carbon interaction in austenite and ferrite and the interaction of carbon atoms with defects such as vacancies and interstitials defects which can be studied by applying the quasichemical theory. In Figure 2-5 the interstitial sites for ferrite and austenite are shown; carbon mainly occupies octahedral interstices in both cases [24]. Because of the different crystal lattice the C-C interaction energy in austenite and ferrite is different, equal to 8250 J/mol (or 0.086 eV) for the austenite and 150000 J/mol (or 1.54 eV)

for C-C pair in ferrite [24]. This difference in net interaction energy is explained by the fact that the closest approach distance of carbon atoms in austenite is 0.252 nm, while the closest approach distance of carbon atoms in ferrite is 0.143 nm [24]. According to Bhadeshia [24], "the larger C-C interaction in ferrite is due to the smaller spacing of adjacent interstitial sites compared to the one of austenite. These repulsive forces between carbon atoms affect the migration of carbon with respect to the motion up or down a concentration gradient". In ferrite the adjacent sites are so close (a/2) that electrostatic, thermodynamic and elastic strain interactions completely exclude them from occupation [24]. Instead, in austenite the distance for a pair of interstitial sites is equal to the lattice parameter "a" so that adjacent sites can be occupied [24]. Associations between carbon atoms have been studied extensively in ferrite [24]. Similar clusters are not investigated for austenite because the strain interactions between carbon atoms are much smaller than the ones in ferrite [24].

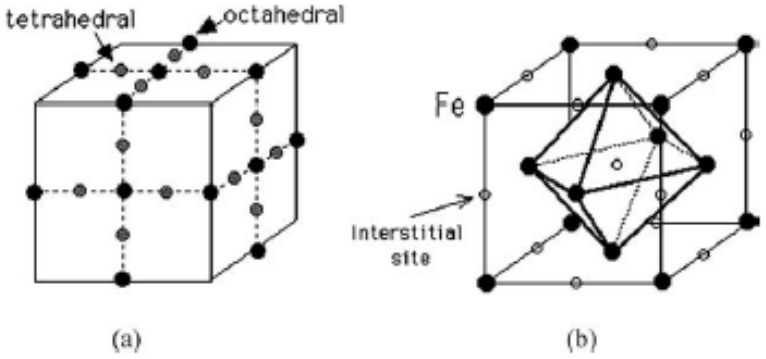

Figure 2-5 - Interstices in ferrite and austenite: (a) one unit cell of bcc ferrite: the iron atoms are not shown for clarity, only octahedral and tetrahedral sites are shown. (b) Octahedral sites in austenite [24]

This happens because the carbon atom causes an isotropic strain in austenite whereas it leads to tetragonal distortion in ferrite [24]. Density functional theory calculations have been performed to find out the most likely path that the carbon uses to diffuse. It was found that the minimum energy path of carbon diffusion from an octahedral site to another octahedral site is through a tetrahedral site inside bcc iron [25]. In these calculations it was also proven that in bcc iron, the stable phase at low temperature places the carbon in the octahedral sites [25]. In order to calculate the value of the diffusion coefficient for C in α-iron, another study was performed by Agren in his work on computer simulation of austenite/ferrite

transformation [26]. Agren underlined that at temperatures lower than 500 °C the diffusion of carbon in ferrite is well described by the following Arrhenius equation (units of cm^2/s):

$$D_C^{\alpha} = 0.02 \times \exp(-10115/T) \qquad \text{(eq. 2-4)}$$

However, at higher temperatures there is discrepancy between the above equation and experimental data. Agren has derived an equation that can fit the data for the diffusion coefficient in the whole range of temperatures but at low temperatures the equation will just reduce to the Arrhenius type equation shown above [26]. In the context of this thesis, the value of the diffusion coefficient used by Rebishung and Scott to simulate diffusion of carbon into IF steel will be used, where D_0 is equal to 0.0062 cm^2/s and the activation energy Q = 80350 J/mol [27]. Similar values for D_0 and for the activation energy were reported by McLellan and Wasz [23]. A summary of all the values indicated for carbon diffusion into ferrite are reported in Table 2-1.

Value of D_0 [cm^2/s]	Value of Q [kJ/mol]	Reference	Notes
0.02	84.10	C.A. Wert [19] (1950)	Measured using relaxation method for T between -35 ˚C and 200 ˚C – polycrystalline iron
0.008	82.88 (or 19800 cal/mol)	C.G. Homan [17] (1964)	Measured using relaxation methods for T between 616 ˚C and 844 ˚C- polycrystalline iron
0.008	82.843	Wert and Zener [20] (1949)	Measured using relaxation method for T between -35 ˚C and 200 ˚C – polycrystalline iron
$\sim 10^{-3}$	71.58 (or 17100 cal/mol)	R.H. Doremus [21] (1959)	Activation energy measured by carbon precipitation for aging T from 0 ˚C to 170 ˚C
0.0033	80.79 (or 19300 cal/mol)	McLellan, Chraska [28] (1971)	Fitting data obtained for T between -50 ˚C to 450 ˚C using relaxation methods
0.00488	80.64	McLellan, Wasz [23] (1993)	Analyzed statistically all the available data related to diffusion of C in BCC iron
0.0062	80	Callister [15]	Summarizing results taken from: "E. A. Brandes and G. B. Brook (Editors), *Smithells Metals Reference Book*, Tth edition, Butterworth-Heinemann, Oxford, 1992
0.0062	80.35	Rebishung and Scott [27]	Used to describe the diffusion of C into IF steel the range of T 430 ˚C – 530 ˚C

Table 2-1 - Summary of main diffusion coefficient values measured for diffusion of carbon into ferrite

For accurate modelling of the diffusion process it is necessary to know how the solubility limit of carbon inside ferrite varies as temperature increases. Researchers have evaluated the amount of carbon as a function of the carburization temperature measuring the variation of

electrical resistivity [29]. Many researchers [26], [27], [30] have summarized in their papers the better known relations to calculate the solubility limit of carbon in α-iron.

The change in the amount of carbon in solid solution is often verified by means of internal friction measurements, by measuring the Snoek peak which depends on the quantity of atoms in solid solution [30]. However, values obtained with this method are strongly influenced by the texture and by small addition of alloying elements. For this reason, in 2001 and 2003 Lavaire suggested TEP measurements for the evaluation of the amount of interstitial elements in solid solution in ferrite matrix [31] and in ultra and extra low carbon steels [32]. This technique can be used only if the amount of interstitial atoms does not exceed $15x10^{-3}$ wt% [31] and TEP measurements are very sensitive to modifications of the electronic or elastic properties of the iron lattice induced by defects [32].

Merlin et al. measured the solubility limit of carbon in the range 500 °C – 750 °C in an Al-killed steel performing thermoelectric power (TEP) measurements on the material [30]. Moreover, carbon atoms can interact with substitutional atoms even if they do not form precipitates; for example phosphor and manganese can stabilize a higher amount of interstitial atoms in ferrite [30]. Other authors [31] investigated the influence of substitutional atoms such as Mn, Cr, Si, P and Al on the solubility limit of carbon in bcc ferrite performing internal friction measurements and infrared analyses and they concluded that Mn, Cr and Al do not affect the carbon solubility limit, which is instead increased by the presence of P and Si [31]. Gladman [33] suggests the following relation to evaluate the solubility of carbon in ferrite:

$$\log[C] = -\frac{2710}{T} + 1.07 \qquad \text{(eq.2-5)}$$

where *[C]* is the carbon concentration in wt% and *T* is the absolute temperature expressed in K, but in the context of this project the relation proposed by Rebischung and Scott [27] will be used. In their work, the solubility limit is expressed in at% as:

$$C_{ss} = 11.67 \times \exp(-40600/RT) \qquad \text{(eq. 2-6)}$$

2.7. Microstructure Characterization of FGM

2.7.1. Carbides Analyses

In the previous paragraphs, interstitial free steels used for bake hardening treatments have been described and the role of titanium has already been introduced. However more detailed studies have been performed on the action of Ti inside steel. In particular it was found that Ti influences the grain size of ferrite [34]. In 1997 Hua et al. were able to reveal the mechanism of carbon stabilization by titanium inside Ultra Low Carbon steels (ULC) [35] by performing TEM analyses and atom probe field ion microscopy to follow the evolution of precipitation of carbides and particles during the hot strip mill rolling [35]. Their results are summarized in Figure 2-6 where M indicates Ti for ULC steels stabilized with Ti, or it indicates Ti or Nb for ULC steels stabilized with both Ti and Nb. The letter H represents the compound $Ti_4C_2S_2$ [35].

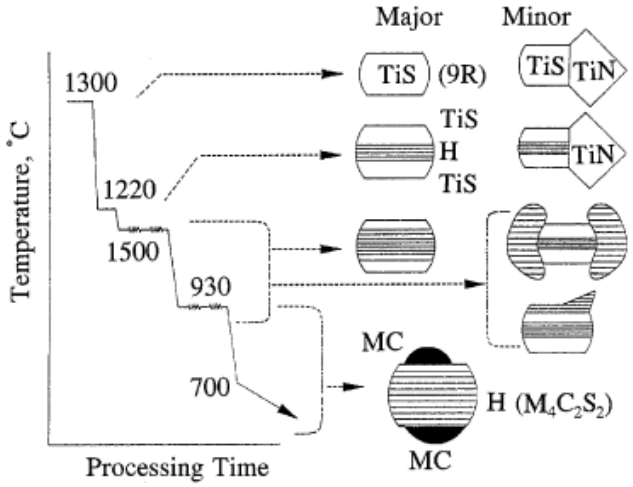

Figure 2-6 - Stabilization processing of Ti-only ULC steel and Ti+Nb ULC steel [35]

In a more recent study [36] thermoelectric power measurements (TEP) and transmission electron microscopy (TEM) have been performed to follow the evolution of precipitation in hot-rolled Ti added interstitial free steels sheets during different annealing treatments. TEM observation of IF steels which have undergone the batch-annealing (BA) treatment have shown that there is dissolution of TiS precipitates and an increase in number of $Ti_4C_2S_2$ and Ti-Fe-P particles as well as a coarsening of TiC particles [36]. According to these TEM observations, $Ti_4C_2S_2$ particles are formed by an in-situ transformation of TiS caused by the diffusion of Ti and C as shown in Figure 2-7 [36]. For a continuous annealing (CA)

treatment there is first a partial dissolution of TiS and a high precipitation of TiC and $Ti_4C_2S_2$ and finally precipitations of small Ti-S-C complexes which have a high Ti/S ratio (>>2) [36]. Another TEM study analyzed the effect of titanium addition on sulphides in low carbon and low manganese steels heated for 1 min at 1350 ˚C and then fractured at 800 ºC or 900 ˚C proving that complexes of iron titanium sulphides are associated with manganese iron sulphides [29].

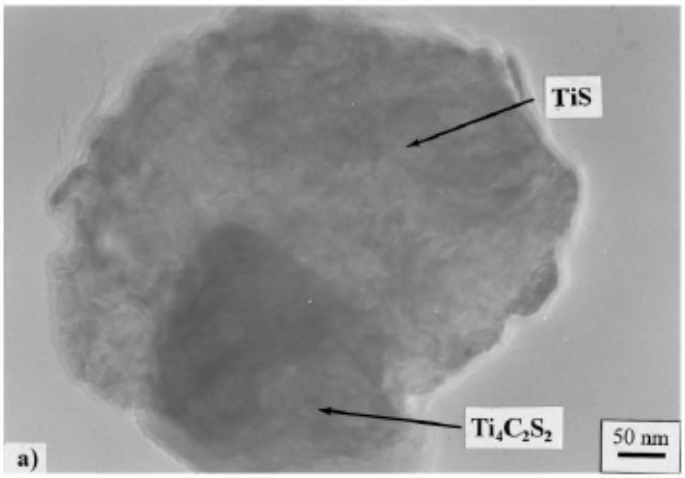

Figure 2-7 - TEM micrograph showing the in-situ transformation of TiS into $Ti_4C_2S_2$ [36]

2.8. Mechanical Response of Functionally Graded Fe-C

2.8.1. Local Mechanical Properties

The addition of carbon causes an increase in hardness and yield stress in steels as a consequence of the interaction of dislocations with interstitial atoms. The solid solution hardening effect of various substitutional solutes in bcc iron is shown in Figure 2-8, where the change in yield strength is plotted as a function of wt% of solute [33]. For microalloyed steels it was assumed that the solid solution strengthening is expressed by a linear relationship at low concentrations:

$$\Delta y_i = k_i \cdot c_i \qquad \text{(eq. 2-7)}$$

where, Δy_i is the increase in strength caused by the ith solute, c_i is the concentration of the ith solute (wt%) and k_i is the strengthening coefficient for the ith solute, as different solutes have different strengthening coefficients [33]. Figure 2-8 shows that the yield strength is a function of the solute content and if the attention is focused just on carbon and nitrogen

content, the dependence of yield strength versus the interstitial atoms concentration is as shown in Figure 2-9 [33].

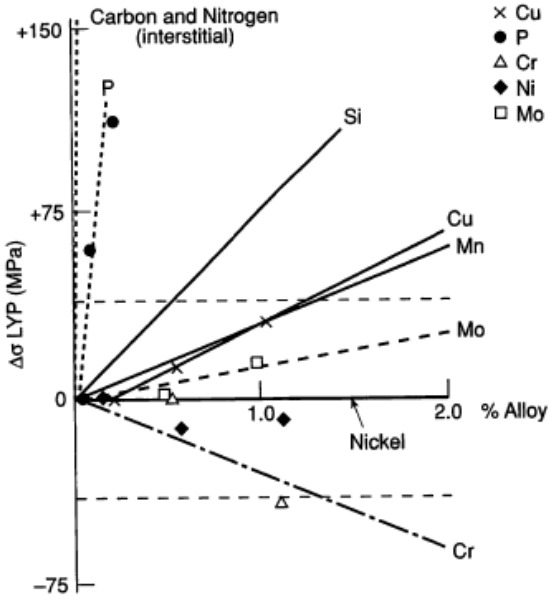

Figure 2-8 - Solid solution strengthening of bcc iron. The effects of different substitutional solute contents (wt%) on the yield strength are shown [33]

The strengthening coefficient expressing the influence of interstitial atoms of carbon or nitrogen on the yield strength is around 5544 MPa/wt% [33]. In ref. [33] strengthening coefficients and ferrite lattice distortion effects are shown for a number of solutes based on both at% and wt%.

In another study [37], Rodríguez and Gutierrez performed tensile tests of various steels having different microstructures and carbon contents. Results are shown in Figure 2-10, where it is evident that both yield stress and tensile strength increase with the carbon content of the sample. In particular the yield stress of martensitic steels is in the range from 1052 MPa to 1632 MPa, while perlitic steels are close to 670 MPa [37].

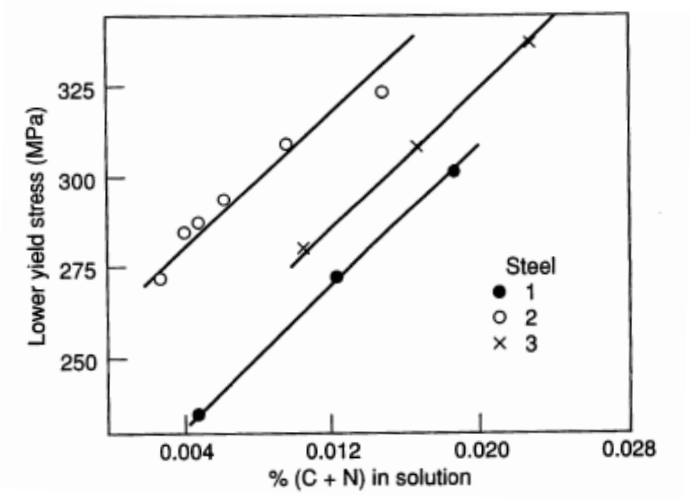

Figure 2-9 - Yield strength as function of interstitial contents [33]

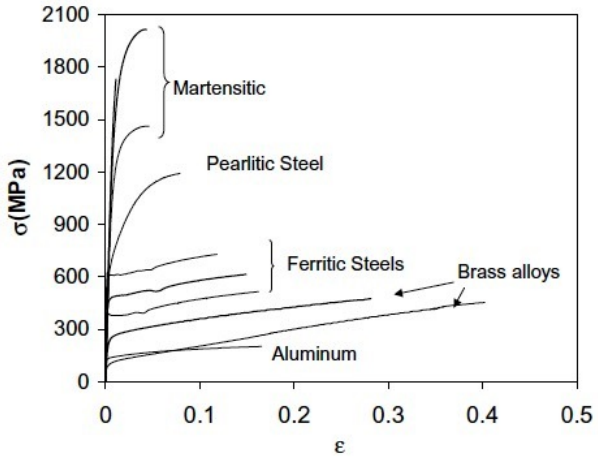

Figure 2-10 - Tensile curves for steels having different carbon content and microstructures [37]

2.8.2. Hardness Test

When it is necessary to gain information at sub-micron scale as in the case of graded materials, nanohardness tests are often used where the nanoindenter continuously measures the load and displacement as it is pushed against the specimen. The hardness is obtained as a function of indent depth dividing the load by the projected contact area of the indenter tip. The compliance is calculated from the slope of the load-displacement curve upon unloading, and then the elastic modulus can be calculated from the compliance [38].

Tests are often performed using a Berkovitch diamond indenter and the resolution is usually around 0.2 μN for the load and 0.2 nm for the depth [38]. However, nanohardness measurements are affected by the "Indentation Size Effect", which means that there is an

increase in nanohardness as the indentation depth decreases [37]. During nanohardness measurements, load-depth curves are obtained as shown in Figure 2-11 and at each depth the elastic modulus *E* and the nanohardness *H* can be calculated using the Oliver and Pharr method [39]. If the mean value of nanohardness is plotted versus the depth of indentation, the behaviour is the one shown in Figure 2-12. Rodríguez and Gutierrez have related the nanohardness value with tensile properties using Tabor's expression for large indentation depths [37].

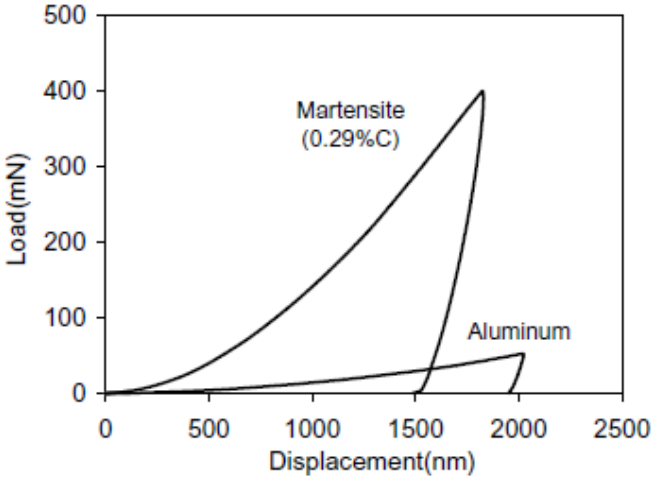

Figure 2-11 - Nanoindentation load-depth curves [37]

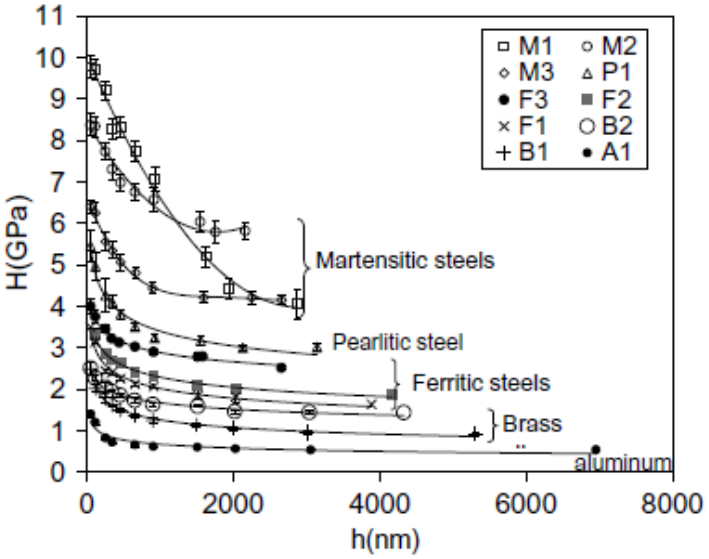

Figure 2-12 - Hardness as function of depth for different materials [37]

However, there is a better relationship that keeps into account the indentation size effect as follows:

$$\frac{H}{H_0} = \sqrt{1 + \left(\frac{h^*}{h}\right)} \qquad \text{(eq. 2-8)}$$

where, H is the nominal hardness measured for a certain depth, h and h^* are characteristic depths which depend on the shape of the indenter and the material, while H_0 is the hardness corresponding to an infinite depth and that arises only from statistically stored dislocations [37]. Recently, Yang and Vehoff [40] studied the influence of grain size on nanohardness measurements, since grain boundaries can lock or slow down dislocation motion delaying the spreading of the plastic zone.

Various studies of nanohardness for non-homogeneous materials are published and available in literature. Usually these measurements are done to test mechanical properties of thin films, for example of plasma sprayed WC-Co coatings [41]. Again, nanohardness measurements have been applied successfully to compare tetrahedral amorphous carbon films (ta-C films) and hydrogenated amorphous carbon films (a-C:H films) [42]. An example of nanohardness measurements made on graded structures is the one done in layered structures. In literature, nanohardness data for Ag/Ni multilayered films are reported where it was proven that hardness is affected by stress state, microstructure, interfaces and the bilayer repeat length [38].

Another technique to evaluate mechanical properties of graded structures is Vickers microhardness which helps in describing the obtained graded profiles [43]. Nazari et al. were able to obtain experimentally and to model the Vickers microhardness profile for graded steels obtained using the electroslag remelting technique [43]. In their work, the authors proposed an expression that takes into account the gradual variation of density of dislocations due to the gradual variation in microstructure from austenite to ferrite [43]. In a research work made by Suresh et al. [44] experiments and simulations of spherical indentation were performed on materials having a gradient of Young modulus; the author developed a new expression to describe Hertzian contact in FGMs fitting experimental data for graded γ-TiAl/Y-TZP and graded Ni-Al_2O_3 [44]. Vickers hardness testing was used to study the hardness of Plastically Graded Materials (PGMs). Very often carburization

treatment in these materials determines a variation of carbide volume fraction with depth which is responsible for variation in hardness and plastic response over the case hardened region [45]. Branch et al. measured the Vickers hardness variation in a case-hardened Pyrowear 675 and as reported in Figure 2-13 they observed that hardness varies linearly from 930 HV at the surface to 433 HV over a depth of 2 mm after which the hardness remains constant in the core region [45]. In the same article, the authors give the following relationship between yield stress and hardness:

$$\frac{H}{\sigma_y} = \frac{2}{3}\left\{\left(1-\frac{1}{n}\right)+\left(\frac{3}{4}+\frac{1}{n}\right)\left(\frac{1}{3}\frac{E}{\sigma_y}\cot\alpha\right)^n\right\} \qquad \text{(eq. 2-9)}$$

where, α is the equivalent half cone angle for Vickers indenter, E is the Young Modulus, n is the strain hardening exponent, H is the hardness value and σ_y is the yield stress [45].

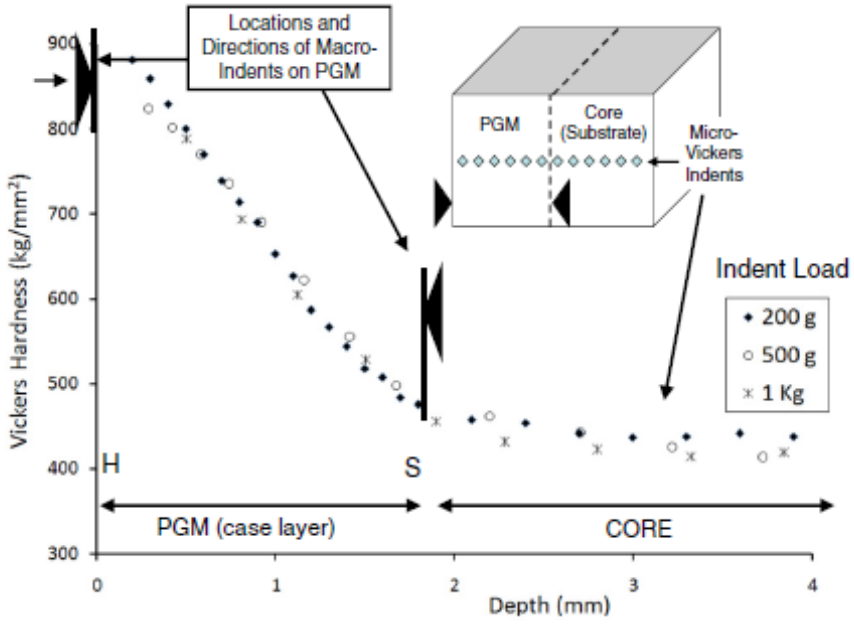

Figure 2-13 - Variation of micro-Vickers hardness with depth. Three different indent loads show little effect of indentation size [45]

In order to assess the plastic profile caused by a Vickers indent, FEM simulations have been performed by Branch et al. where it was proven that the profile is affected by the gradient [45]. According to Branch [45], "if the indent is made on the harder surface towards the softer one the profile is deeper and narrower than the case where the indent is made on the

softer surface towards the harder one". From the processing point of view the methods described so far require sectioning and polishing of the material through the cross section of the hardness gradient. However, Klecka et al. proposed a novel method for predicting the hardness gradient profile using only surface indentations taken at a range of different loads [46]. Bhattacharya and Nix first [47] and later Nayebi et al. [48] proposed a relationship to describe the variation of Brinell hardness for a material having a gradient of yield stress.

Many researchers used Finite Element Method (FEM) to study the influence of plasticity gradient in indentation. Choi, Dao and Suresh have studied the indentation response for a material having a linear variation of yield strength to obtain a dimensionless function that can be used to predict the hardness behaviour [49]. They have shown that the highest Von Mises stress occurs below the surface for the increasing yield stress gradient condition, while for homogeneous material and for the decreasing yield stress gradient the highest Von Mises stress appears on the surface directly in contact with the indenter [49]. As reported by Choi et al. [49] "under the same load, the plastic zone is larger for the decreasing gradient of yield stress and smaller for the increasing gradient of yield stress compared to the plastic zone of the homogeneous material".

2.8.3. X-ray Diffraction for Local Stress State

In order to investigate the effect of carbon in iron, TEM in situ observations were performed to assess how the dislocation motion and profile change when interstitial atoms are present in iron. It was proven that carbon added in iron has an hardening effect at temperatures lower than 150 K, while it has a softening effect at temperatures between 150 - 300 K and again an hardening effect at temperatures higher than 300 K (Figure 2-14) [50].

Hardening at temperatures lower than 150 K is not the result of higher internal stresses due to interstitial atoms and it is neither the result of pinning effect of carbon atoms on screw dislocations; instead it is caused by a strengthening of the sessile-glissile energy barrier [50]. Softening at intermediate temperatures is due to the vanishing of the peak of activation area that is present in pure Fe and then hardening at higher temperature is caused by an inversion of screw/edge mobility ratio and pinning of edge dislocations by interstitial atoms [50]. The mobility of edge dislocations is much higher than that of screw dislocations at temperatures lower than room temperature [50]. Moreover, contrary to edge dislocations, the motion of

screw dislocations is in general not much influenced by local pinning [50]. The situation changes at higher temperatures where dislocations with large edge components become less mobile than screw dislocations and as shown in Figure 2-15 the curves of the stress required to move the two types of dislocations at constant velocity intersect at 300K. Given that the motion of complete dislocation loops requires the motion of both types of dislocations in series, the yield stress will be controlled by the most difficult one, which mean the screw one at low temperatures and the edge mechanism above 300 K [50]. Similar results were found in 1974 by Quesnel and Meshi [51] who determined yield stress and strain rate sensitivity in the range of temperatures 78 K – 318 K for pure and carburized single crystals of iron. Many researchers also analyzed the energy of interaction between edge and screw dislocations with interstitial carbon atoms. It was already mentioned that the interstitial atoms diffuse to dislocations because the strain energy of the crystal will be lowered [52], [53]. Cottrell and Bilby calculated a reduction of 10% of the strain energy of a dislocation when it is surrounded by carbon atmosphere, but other researchers mentioned that this energy reduction is only on the order of a few tenths of 1% [52]. Moreover, according to Cochardt et al., Cottrell and Bilby in their calculations made the simplified assumption that the carbon atoms strain the iron unit cell only in an hydrostatic way but according to this, carbon atoms would segregate only near edge dislocations while in reality, carbon atoms diffuse to screw dislocations as well [52]. Cochardt et al. showed that the strain energy is reduced by 20% for a screw dislocation and by half of this for an edge dislocation if they are surrounded by interstitial atoms at a concentration of saturation [52].

However, the interaction between the interstitial atoms and the dislocations decreases if the temperature is increased, so carbon atoms are bound to a dislocation line only when their interaction energy is larger than the thermal energy [52].

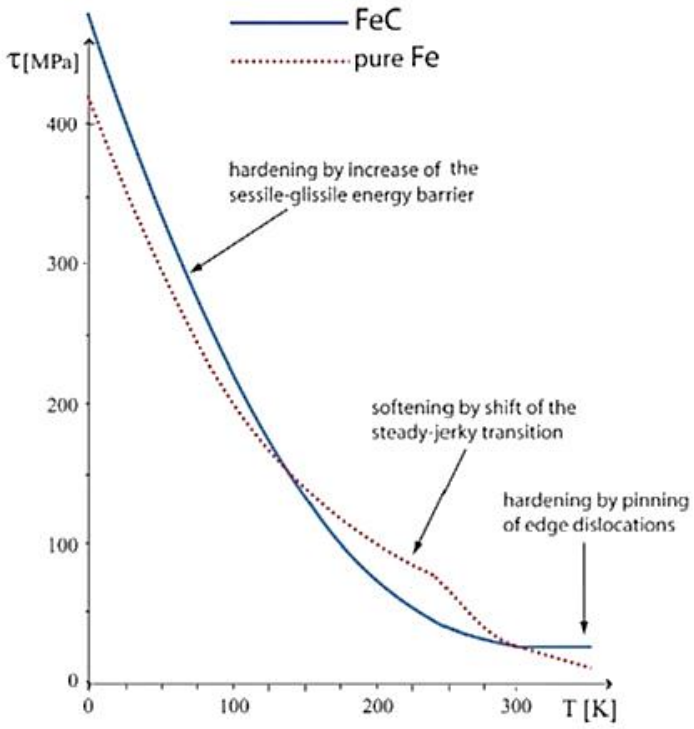

Figure 2-14 - Schematic description of all combined softening and hardening effects due to carbon addition [50]

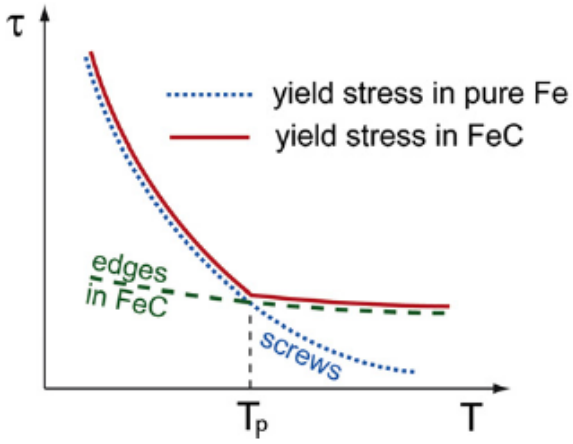

Figure 2-15 - Schematic description of the stress necessary to move edges and screws at a constant velocity in Fe and FeC; T_p is the onset of the plateau (260K in FeC) [50]

In another study [54], a model to calculate the probabilistic distribution of carbon atoms near an edge dislocation in alpha-iron was built. The model allows estimating the interaction between the atoms and the dislocation using the isotropic elasticity theory, keeping into

account both size and shape variations caused in the bcc lattice by the carbon atoms [54]. Using this model, Nandedkar et al. proved that "the stress necessary to move a dislocation away from carbon atoms atmosphere decreases linearly with decreasing C concentration but it increases less than linearly with increasing carbon concentration" [54]. According to the same paper, the dislocation unpinning from the interstitial atoms will not happen by movement of the whole dislocation but by a process of nucleation and growth of bowed-out sections of dislocation [54]. In a more recent study, Cochhardt's theory presented in reference [52] was used to evaluate the diffusion of carbon atoms towards edge and screw dislocations [53]. In this study, it was concluded that an edge dislocation can accommodate 86% of the carbon atoms predicted for a screw dislocation; this happens because in the edge dislocation the atoms are not located only in a single row below the slip plane but they are spread at different angles and they are also slightly above the slip plane [53].

In another study, experiments were conducted on Ti-ULC bake hardenable steels in order to understand the influence of dislocation density on the strain aging process [55]. From the tensile results for the different aging temperatures and times, it was proven that the increase of yield stress increases with aging time until it reaches a maximum, and then it remains constant [55]. Moreover, the maximum increase in yield stress is the same for all levels of prestrain, which means that dislocation density is not influencing the Cottrell atmosphere formation [55]. In the same study, De et al. used Hartley's modified Cottrell-Bilby relationship to prove that pre-strain is not influencing the kinetics of aging [55].

2.9. Global Mechanical Properties

2.9.1. Tensile Properties

In this paragraph the effect of carbon content on stress-strain curves will be discussed. The typical engineering stress-strain curve for low carbon steel has the deformation that is not homogeneous because of the presence of Lüders plateau.

The Lüders plateau has been found not only in low carbon steels but also in polycrystalline molybdenum and aluminum alloys. It is usually associated with the presence of interstitial or substitutional atoms [56]. Interstitial atoms cause distortion of the iron lattice. This distortion will interact with the dislocation movement. In particular, the dislocation will be pinned by those atoms; which is the reason why it is necessary to reach an upper yield stress to start

plastic deformation. When the stress corresponding to the upper yield point has been reached, dislocations are unpinned and slip can occur at a lower stress. If dislocations are strongly pinned, the drop in stress is explained by the formation of new dislocations that have to be generated to allow for plastic flow [56].

More information about the Lüders plateau will be provided in the next paragraph. Winchell and Cohen proposed a relationship between the stress acting on a dislocation line of length L and the concentration of carbon atoms which is:

$$\tau_f = K \frac{X_C^{1/3}}{\sqrt{L}} \qquad \text{(eq. 2-10)}$$

where, τ_f is the flow stress in shear, X_C is the atom fraction of carbon and K is a constant [57]. Researchers have also tried to understand if interstitial atoms are the reason for the variation of flow stress with temperature. The increase of flow stress as temperature decreases is more marked in bcc than in fcc metals; Fleischer and Friedel believe that the variation of flow stress with temperature is due to thermally activated unpinning of dislocations [57]. Roberts and Owen measured the variation of 0.2% proof stress with carbon content and temperature; they proved that the flow stress at constant temperature increases with concentration of solute, and that the flow stress at constant solute content increases markedly with decreasing temperature [57]. For a constant temperature the variation of flow stress in shear with atomic fraction of carbon is represented by the following relationship:

$$\tau_f = \tau_i + m X_C^n \qquad \text{(eq. 2-11)}$$

where, τ_i is the flow stress in shear of iron without interstitial atoms, m is the slope, X_C is the carbon concentration and n is an exponent equal to 0.5 [57].

In 1966 Stein and Low [58] studied the effect of carbon and temperature on the yield stress of iron single crystals proving that for a given temperature the yield stress increases by increasing the carbon content. The authors proved that the variation of yield stress caused by a given change in carbon content increases with decreasing temperature [58]. Stein and Low supported the theory of Fleischer who proposed the following expression to evaluate the change in yield stress caused by tetragonal defects:

$$\left(\tau - \tau_p\right) = \frac{G\sqrt{C}}{A_0} \qquad \text{(eq. 2-12)}$$

where, τ is the increased flow stress due to the impurities strain-hardening and τ_p is the flow stress for the iron containing less than 0.005 ppm carbon and it would also include the Peierls-Nabarro force [58]. When the temperature increases, dislocations are expected to move more easily from the action of interstitial atoms because of thermal fluctuations [58]. These thermal fluctuations have a high influence on lowering the flow stress because tetragonal distortions caused by interstitial carbons have stress fields that decrease rapidly with distance [58]. However, the yield stress temperature dependence is not only due to impurities; indeed the strong orientation dependence of the yield stress indicates that either dislocation-dislocation interaction or Peierls-Nabarro stress may play a role [58].

Itabashi and Kawata studied the influence of carbon on high strain rate tensile properties for carbon steels [59]. In case of the lower strain rate, yield phenomena tend to disappear or to attenuate as the carbon content is increased [59]. At high strain rates corresponding to dynamic impacts, the yielding behaviour is more pronounced than the quasi-static strain rate conditions and the upper yield point is higher than the one for low strain rates [59]. In a study made by Chen et al., the plastic properties of low carbon steel sheets, which have undergone different rolling conditions, were analyzed during uniaxial tensile tests and plain-strain tensile tests [60]. In the same reference, it is mentioned that Lüders plateau can be removed by performing a temper-rolling treatment to cold-work the steel sheets; but if the material is stocked and allowed to strain-age then the Lüders will reappear [60]. Other useful information related to the effect of carbon on the tensile properties are found for steels used for bake hardening, in particular models have been developed to predict the diffusion and the segregation of carbon atoms to dislocations [61]. It was already mentioned earlier that the bake hardening process is a strain aging process where the strength of steel is increased by performing a heat treatment in the range of 100 ˚C - 200 ˚C for less than 1 hour during which carbon atoms present in solid solution interact with the dislocations [61]. In order to study the mechanical properties of bake hardened steels, tensile coupons are usually loaded to 2% of pre-strain which is an amount of strain similar to industrial operations; then the specimen is baked at 170 ˚C for 20 minutes [61]. After this treatment the specimen can be tensile tested and the bake hardening (BH) is defined as the difference between the lower yield

stress after the heat treatment and the flow stress at the pre-strain, as shown in Figure 2-16 [61].

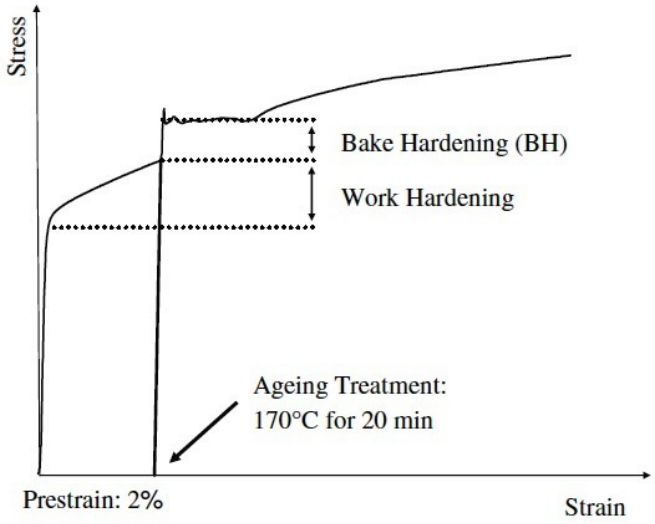

Figure 2-16 - Schematic definition of bake hardening (BH) [61]

In order to describe the phenomenon of bake hardening, which is due to the formation of Cottrell atmospheres, Ballarin et al. proposed a model based on the solute carbon content, on the dislocation density and on the kinetics of strain aging [61]. Furthermore, the pre-strain also has an influence on the second step of aging since if the dislocation density increases, more carbon atoms will be necessary to saturate them leaving a lower concentration of atoms in solution available for precipitation [61]. It is known that Lüdering is undesirable in forming processes since it creates surface irregularities called stretcher strains. In order to avoid this problem during forming, the sheet metal is usually subjected to a final light pass from 0.5% to 1.5% reduction, which is called temper rolling or skin pass [62]. According to the information reported in the complete technology book on hot rolling of steel [62], "the width of rolled products may range up to 5 m and be as thin as 0.0025 mm".

Other studies that are helpful for the Gracos project involve the analysis of the tensile behaviour of graded steels. Graded steels can be produced by electroslag remelting obtaining steels where layers of ferrite, austenite, bainite and martensite are present [63]. The final structure can be composed of ferrite-bainite-austenite (called $\alpha\beta\gamma$), or structures such as ferrite/bainite/austenite/bainite/ferrite ($\alpha\beta\gamma\beta\alpha$) and austenite/martensite/austenite ($\gamma M\gamma$) [63]. The tensile behaviour of these graded steels is modelled starting from the values of microhardness and yield strength of the main phases [63].

2.10. Piobert-Lüders Effect

Some introduction about the Lüders plateau was given in section 2.9.1. Here, details about its modelling, its behaviour and relation with material microstructure will be provided. The main theory explaining the Lüders plateau is the one of Cottrell and Bilby [64], [65] according to which the plateau is caused by the pinning of dislocations by interstitial atoms. The energy of interaction between dislocations and interstitial atoms for a bcc lattice is quite high (0.5 eV) which causes an effective pinning at room temperature, provided that the concentration of interstitial atoms is larger than 10 ppm [66]. A theory supported by Johnston and Gilman suggests that the load drop is due to the multiplication of dislocations which decreases the stress required to move them [64]. When the yielding is discontinuous, the strain rate is much higher than the strain rate in the situation of homogeneous yielding [67]. Before that a Lüders band can propagate, the local stress at the band front must reach the upper yield stress which can be a lot higher than the stress required to propagate the band (lower yield stress) [67]. For this reason, it is usually assumed that there is a stress concentration at the Lüders front which separates the elastic and plastic portions of the specimen so that locally the upper yield stress is reached and at the Lüders edge the plastic deformation may occur for unlocking of dislocations, for the activation of new dislocations sources or by the multiplication of mobile dislocations [67]. “In the machining of metals, Lüders strain is something to avoid because it causes the appearance of a texture in the form of “orange peel” on the surface of the metal” [68]. Kubin and Estrin [69] believe that the Lüders plateau is directly related to the activity of dislocations, so at low strains, the multiplication of mobile dislocations always prevails and for this reason the deformation will not be uniform and slip bands will form [69]. As soon as the hardening starts to build up and the mobile dislocations saturate, the deformation tends to become more uniform while slip will be activated in other areas of the specimen to compensate for the loss activity of dislocations in the saturated region [69]. The Lüders plateau is the result of the spreading of this slip activity and the front velocity is directly related to the dislocation velocity at the front [69]. In particular, no propagation is observed if the multiplication rate of dislocations is lower than a certain critical value [69]. Before Kubin and Estrin, Hahn [70] supported the theory of Johnston and Gilman, suggesting that the velocity of multiplication of dislocations

had a deep influence on Lüders bands and that the pinning effect due to interstitial atoms was not enough to explain the phenomenon. The growth of the band is explained considering that dislocations generated within the band are "injected small distance to the surrounding matrix" as suggested by Hahn [70]. In this way the rate of deformation of the zones adjacent to the band front are enhanced and this non-uniform yielding is stable if the deformation contributed by the material outside the band remains small compared with the contribution of the growing band [70]; otherwise, if the material outside the band deforms rapidly, then the stress-strain curve will have the shape of uniform yielding [70]. Again according to Hahn, the yield drop is not related to the unlocking, which would influence more the upper yield stress, but it is related to dislocation density and multiplication [70]. The influence of the strain rate on the upper yield stress (σ_{UY}) has also been studied by Hahn who proposed the following relation [70]:

$$\log\left(\sigma_{UY}\right) = \log A + \frac{1}{n}\log \dot{\varepsilon} \qquad \text{(eq. 2-13)}$$

where, A is a parameter depending on the Burger's vector, on the density of dislocations and on the resolved shear stresses (see [70] for further details) and n is a constant. The yield point behaviour is also influenced by temperature [70] because strain aging and stress-induced ordering of interstitial atoms close to dislocations are responsible for the strengthening effect encountered in some temperature ranges [70]. In his work, Hahn also derived relationships to calculate the speed of the band front and the stress at any point of the band [70]; in particular the speed of the band front (u) is expressed as:

$$\dot{\varepsilon}\, l = u\varepsilon_L \qquad \text{(eq. 2-14)}$$

where, l is the gauge length, ε_L is the Lüders strain and $\dot{\varepsilon}$ is the strain rate [70]. Lüders bands propagation is influenced by many factors; for simplicity, some of the results reported in literature are summarized in Table 2-2.

Parameter	Lüders Feature	Reference
Increase of strain rate	Increase of Lüders speed and Lüders strain	[71], [72]
Increase of strain rate	Number of load drops increases	[71]
Increase of strain rate	For aluminium alloy lower yield stress of Lüders plateau decreases	[73]
Decrease of strain rate	Magnitude of serrations inside bands increases for alloy AA5182	[73]
Increase of cold working	eliminates yield drop but if specimen is aged, yield appears again	[70]
Grain size refinement	Speed of bands is reduced	[74]
Grain size refinement	Higher upper yield stress, lower yield stress and higher Lüders strain	[75], [76], [64], [77], [78], [66], [65], [79]
Increase of compliance of the testing machine	Decrease of number of load drops	[71]
Increase of testing temperature	Number of load drops decreases and then increases	[71]
Increase of testing temperature at constant strain rate	Lüders strain first increases and then decreases	[71]
Decrease of testing temperature	Lüders strain increases; difference between upper yield stress and lower yield stress increases	[67]
Carbide forming elements (Ti, Va, Cr)	Lower upper yield stress	[80]
Quenching from 700˚C	Favours homogeneous yielding	[75]

Table 2-2 - Summary of influence of different parameters on Lüders propagation

In another paper, Sleeswyk and Verel suggest that Hahn's concept of injection of dislocations ahead of the Lüders front applies to the nucleation of the band but it is not right to explain the steady state propagation of the front [81]. According to this paper, dislocations multiplication happening at the band front is responsible for band propagation [81]. Hart [74] proposed a uniaxial strain model for the Lüders band propagation suggesting an exponential stress-strain relationship in the Lüders band, and reported that the speed of propagation of the band depends on the initial stress, proposing a relation between width and speed of the band [74]. If the band has a low speed then it will be very sharp, while if the speed is high the band will be very broad and it might not even reach the steady-state condition [74]. Factors that are believed to influence Lüders strain also include strain rate,

degree of segregation of interstitials to dislocations and grain boundaries [77], [82], testing temperature and prior mechanical treatment [67]. The grain size also influences the type of band pattern, and it was pointed out that complex bands raise the mean value of the lower yield stress making the curve less smooth compared with situations where a simple band is nucleated and propagated [80], [82]. Moreover, every time there is a new formation of a band, there is also a stress drop in the stress-strain curve [80]. According to the same study, in large grained material there is no appreciable surface kink. However, in a more recent study, it was shown that when the work hardening of the material is increased, Lüders plateau can decrease its length even if the grain structure is refined and that an increase of carbon content does not necessarily lead to an increase in Lüders length if the carbon is present as fine dispersed cementite particles in a ferrite matrix instead of being in solid solution [83]. Butler studied how the grain size affects the speed of two Lüders fronts, one propagating from each grip, he showed that an increase of grain size causes an increase in the speed of the fronts [82], and he proved that both the yield stress and Lüders strain decrease if the grain size is increased [82]. Butler also showed that having different grain sizes in various zones of the specimen will cause the band fronts formed at the two ends of the specimen to propagate with different speeds [82]. In his work Butler proposes an equation to estimate the Lüders strain knowing the crosshead speed of the tensile machine v_C, the speed of the Lüders front $\bar{v}_L$ and the number of Lüders bands n [82]:

$$\varepsilon_L = \left(\frac{v_C}{n * \bar{v}_L} \right) \qquad \text{(eq. 2-15)}$$

The following relation between the stress σ_L at the end of the Lüders elongation and the Lüders strain ε_L was used by Butler [82]:

$$\sigma_L = A + B\log(\varepsilon_L) \qquad \text{(eq. 2-16)}$$

with A and B constants. He also proposed a relation which correlates the average front velocity v_L, the Lüders stress σ_L and the absolute temperature T:

$$\log(\bar{v}_L) = C - (D/\sigma_L T) \qquad \text{(eq. 2-17)}$$

with constant C changing primarily with the grain size and constant D changing mainly with the composition of the steel [82]. Fisher and Rogers confirmed the validity of the above relation doing a creep test and found that the fronts move at a uniform velocity for a given

stress and at a given temperature, but move more rapidly when the stress or temperature are raised [84]. Shear stress is present at the front of the band and according to Butler the change in shear direction occurs to minimize the misalignment of the specimen caused by the kinking of the front, which increases with strain [82].

It has been suggested that the occurrence of the Lüders effect is linked to the structure of the grain boundaries; so that processes which lead to grain boundaries free of defects result in Lüders effect, whereas treatments giving a high density of grain boundary dislocations remove or at least reduce the Lüders effect [73]. For Conrad [85], the rate controlling mechanism for yielding and flow of iron and steels at low temperatures ($T < 0.2\ T_m$) is the thermally activated overcoming of the Peierls-Nabarro stress. In another study, Conrad and Stone supported the idea that the velocity of the bands depends only on the effective stress and is not dependent on specimen length, on the cross-head velocity or on the number of fronts [86]. Moreover, in the same study Conrad and Stone suggested that the drop in stress which happens when two bands meet might be due to the fact that the stress fields ahead of the band fronts reinforce each other giving a rapid multiplication of dislocations [86]. Van Rooyen proposed the following relationship between the stress drop and the Lüders strain:

$$(\sigma_2 - \sigma_1) = k * \varepsilon_L^m \qquad \text{(eq. 2-18)}$$

where, σ_2-σ_1 is the yield stress drop, k and m are material constants and ε_L is the Lüders strain [67]. If a specimen has been subjected to cyclic loading before tensile testing, then the surface plastic strain which is due to the initial stages of cyclic loading will cause a reduction in dislocation locking, and this will decrease the upper yield stress necessary to start band propagation [67]. Delwiche and Moon [87] analyzed the orientation assumed by Lüders front propagating in specimens of mild steel having different parallelogram cross sections; they concluded that the most stable orientation of the Lüders front is the one which maximises the bending stress produced by the distortion of the specimen and that the Lüders front spreads within a plane where the shear stress is maximum [87]. Other researchers analyzed the influence of the shape and geometry of the specimen on the type of band pattern [80], [76], [82]. In a study conducted by Van Rooyen [67] it is stated that the propagation of Lüders band causes a certain bending in the specimen with the bending stress increasing with the Lüders strain, and that if these bending stresses are high then new bands can be nucleated in the front of the main propagating one. However, restrictions of the specimen inside the

aligned grips of the tensile machine require the shear kink to be minimized [82]. The minimization happens by specimen bending adjacent to the front; if the bending stresses are too high the shear kink is minimized, nucleating further Lüders bands [82]. During Lüders bands analysis the speed of the bands, the angle of their front with respect to the tensile direction, the in-plane kinking of the strips, as well as the formation of stress valleys on the plateau are checked. It was suggested that stress drops on the plateau can occur when more than one front is propagating through the gauge length and when these fronts coalesce [74]. If multiple bands are formed, the speed of each front decreases and the lower yield stress has no more the shape of a plateau but it shows load drops [88]. Butler made experiments forming various Lüders bands in the gauge length of specimens and he proved that an increase of the number of Lüders fronts propagating causes a decrease of lower yield stress, a decrease of Lüders strain ε_L and consequently an increase in the total speed of the front [88]. The stress drop caused by multiple nucleation of Lüders front may be related to the increased number of dislocations taking part in the deformation; in this way the same strain rate can be maintained moving the dislocation at lower speed [88]. Besides, the local strain rate in the Lüders band can be two orders of magnitude higher than the external strain rate [66], while other authors state that the true rate of yielding in the bands is three orders of magnitude higher than in uniform yielding [68]. The appearance of Lüders bands is strictly related to the microstructure of the steel; in carbon steels with ferrite-pearlite structure the plateau does not form because concentrated Cottrell atmospheres of carbon atoms are not present at dislocation sources on ferrite-cementite phase boundaries [68]. The Lüders plateau is also absent in bainite-martensite structures because of the elevated density of free dislocations [68]. In another research paper, it is mentioned that the orientation and morphology of Lüders band is influenced by the type of loading as pure tension, pure torsion or a combination of torsion and tension [65]. However, in all loading conditions the Lüders front takes the inclination of the plane where the shear stress has its maximum, but when the loading condition is a mixture of tension and torsion then two Lüders fronts having different inclinations and speeds of propagation can appear [65].

For AA5182 aluminium alloy it was shown that for recrystallized specimens, the increase of cold rolling causes an increase in Lüders elongation [89], since dislocations are mostly annealed out so the small amount of dislocations left can move very easily when a stress is

applied. However, in the last portion of the plateau serrations appear because even if the dislocation density is low, the moving dislocations interact with Mg solute atoms getting locked and then unlocked [89]. In another study Shaw et al. [79] performed tensile tests on NiTi shape memory alloy strips and found that the shear deformation associated with the bands is responsible for the kinking of the strips. According to Shaw, the amount of kinking depends on " the aspect ratio of the specimen itself, on the axial position of the front, on the axial stress and on the boundary conditions used " [79]. Kinking of the band causes the rise of a moment in the specimen; however, the kinking effect and the moment associated with it can be reduced if two fronts are propagating instead of just one front [64]. However, if the extent of kinking is high and it cannot be sustained, then a switch of the direction of the inclined band can happen and the propagation is more as a criss-cross or finger-like pattern [79]. If the propagation is not uniform and some islands of non-deformed material are left behind, then the band front can change its shape from the inclined one to a more symmetrical V shape which causes a drop of stress and a drop in moment [64]. In their work, Kyriakides et al. used the following expression to calculate the speed of the Lüders front:

$$c = \frac{\dot{\delta}}{n\Delta\varepsilon_L} \qquad \text{(eq. 2-19)}$$

where $\dot{\delta}$ is the displacement rate applied during the tensile test, $\Delta\varepsilon_L$ is the Lüders strain and n is the number of fronts [64]. Moreover, the authors measured the position of the middle point of each front and they plotted it versus time as shown in Figure 2-17 (b). The linear distribution indicates that the velocity of propagation of the front is constant [64]. They also clarified that once the Lüders band has started, the strain remains unchanged in the non-deformed zones until the deformation front reaches them, causing a jump in strain as shown in Figure 2-17 (a) [64], [73]. The area that has experienced Lüders strain earlier shows higher local strains than the areas which experienced Lüders strain later [65]. In FEM simulations Kyriakides and Miller simulated Lüders plateau propagation using an up-down-up stress profile and they concluded that the stress fluctuations in the Lüders plateau double when the mesh is coarse and also the width of the front is mesh dependent [64].

More recently other techniques such as neutron diffraction [78], acoustic emission power spectral analyses (AE) [66], [90]. digital infrared thermography (DIT) [73], [91] and digital

image correlation (DIC) have been used to study plastic instabilities in iron and aluminium. The information obtained about Lüders plateau through tensile tests has been correlated to the geometry of microhardness and hardness indentations performing profilometer and optical measurements [92]. In their study Haggag and Lucas developed a set of equations to fit true stress-true strain curves with the data obtained with hardness tests [92]. Moreover, in their study Haggag and Lucas showed that the Lüders strain depends on the aging temperature [92] and they pointed out that the lower yield stress σ_{yl} , the strain hardening exponent n and the Lüders strain ε_L are related by Morrison's equation:

$$\ln\left(\frac{K}{\sigma_{ly}}\right) = \varepsilon_L - n\ln(\varepsilon_L) \qquad \text{(eq. 2-20)}$$

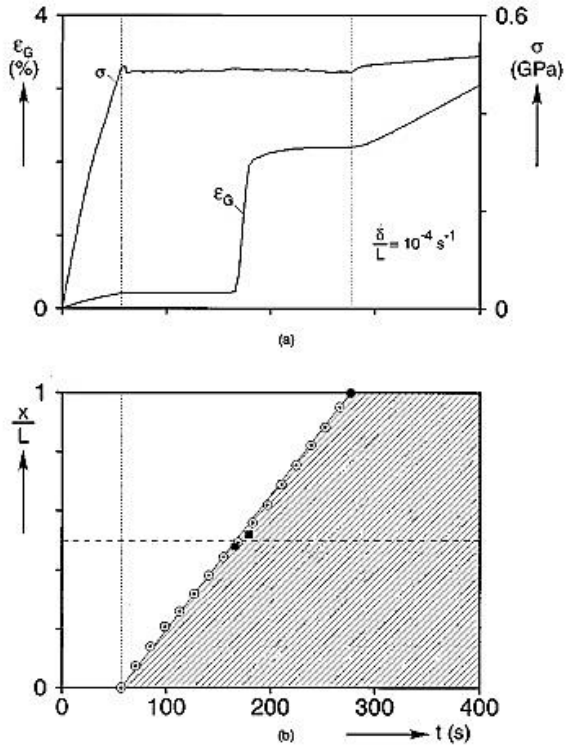

Figure 2-17 - Results from uniaxial test on steel strip; (a) stress and strain histories recorded, (b) x-t diagram of evolution of deformation front [64]

2.11. Piobert-Lüders Effect Modelling

As reported recently, Lüders plateau and localized plastic instabilities are not only present in ultra-low carbon steels but they also occur in shape memory alloys such as polycrystalline

NiTi alloy which is capable of stress-induced transformations between two solid states called austenite and martensite [79], [93]. To model Lüders plateau behaviour, it is usually assumed that the material behaves as a finitely deforming J_2-type elastoplastic solid having an up-down-up stress profile [79], [93]. Hallai and Kyriakides have shown that outer strips made of a material which hardens uniformly can constrain the Lüders deformation of the central layer shortening the Lüders plateau [93]. In the same study, Hallai and Kyriakides performed a parametric study to see how the shape of the curve changes depending on the thickness of the outer strips compared with the thickness of the inner core [93]. A similar study was performed by Weck et al. [94] where a layer of the high magnesium aluminum alloy AA5083, which is known for having Lüders bands and PLC effect, has been cladded between two layers of low magnesium aluminum alloy AA5005 which do not shown any plastic instabilities. Other studies focused their attention on the propagation of Lüders bands under axial compression loads, observing how the plastic instabilities propagate and influence the buckling behaviour [95]. In the FEM simulation the plastic instability is very often initiated introducing a local geometrical imperfection for example as a small indent along one side of the strip [79], [95].

In FEM analyses, the kinking effect can also be evaluated measuring the transverse displacement of the axis of the strip as a function of the net axial displacement [79] . Usually, three-dimensional plots with net axial displacement δ, transverse displacement of the axis of the specimen v and the axial position x are made to follow the evolution of the kinking effect, as shown in Figure 2-18 [79]. As the deformation in the band grows, the kinking reaches a maximum value but then it decreases again because it is counterbalanced by the axial load which tends to keep the strips aligned [79]. Lüders band propagation was also studied in hot-finished steel pipes subjected to pure bending, where the plastic instability interacts with other effects such as ovalization of the cross section and wrinkling due to the bending of the pipe [96], [97].

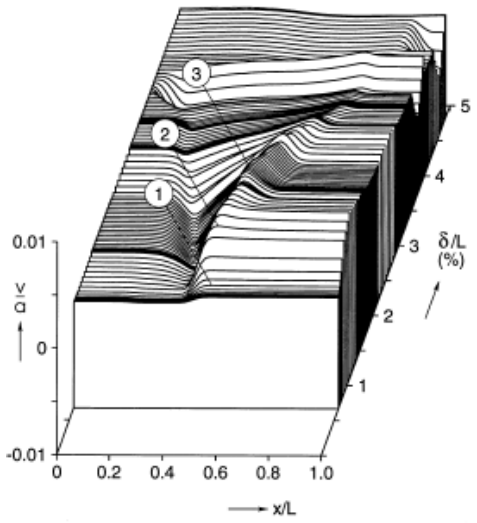

Figure 2-18 - Lateral displacement of strip axis as function of axial displacement δ [79]

In another study, the propagation of Lüders band in welded low carbon steel was investigated at the mesoscale level analyzing the effect of grain boundaries, free surfaces and interfaces between the different zones of a weld on the propagation of the bands [98]. FEM can be used to simulate nucleation and propagation of Lüders band during mechanical tests. However, as it can be concluded from what has been reported so far, it is clear that Lüders bands are a complex phenomenon that relates to macroscopic parameters such as specimen shape, loading rate, etc. and is also related to the microstructure of the specimen such as grain size, dislocations density, etc. Figure 2-19 shows a stress-strain curve that can be used to simulate the Lüders phenomenon. This curve is composed of two straight lines where the point A represents the stress that has to be overcome to unlock or multiply the dislocations, the yield drop between points A and B represents how easily the band propagates through the grain boundaries, and the part BC is the usual strain-hardening behaviour [99]. In the work of Belotteau et al. [100], the influence of parameters such as meshing, behaviour law and boundary conditions were investigated in the FEM simulation of Lüders propagation. In the results, the authors showed that [100]:

- a stress drop happens in the plateau when bands are nucleated or two fronts meet;
- larger is the softening (difference between upper and lower yield stresses σ_{max}-σ_{min}) and longer is the plateau;
- the position of ε_{min} (Lüders strain) does not seem to influence Lüders length;

- finer meshes cause longer plateau and higher stress levels;
- irregular meshes cause more discontinuous band propagation;

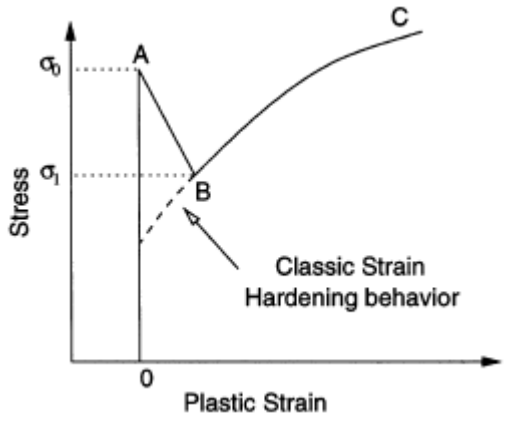

Figure 2-19 - Local plastic law used to simulate Lüders band in FEM [99]

In the same study, the influence of artificial defects was investigated and the authors analyzed two different types of defects, the first one being a geometrical defect which is created displacing a node of the mesh, while the second type of defect is a behaviour defect which is created assigning a lower yield stress in the element of the mesh [100]. They concluded that the type of defect can modify the stress plateau level, but a geometrical defect is more severe than a behavioural defect and causes an earlier localization which will cause a higher and longer plateau [100].

In their work, Belotteau et al. [100] also analyzed the influence of the boundary conditions, looking at the behaviour of Lüders band in a situation where the transverse displacements are set free and repeating the calculation for a situation where the transverse displacements are locked. In another study, Sun et al. performed FEM simulations on tensile coupon shapes concluding that the number of Lüders bands which are formed during a test is influenced by the level of stress concentration existing at the ends of the specimen, so in ideal conditions double bands should originate at the same time from both ends; however, in a real tensile test, this is not often observed because of the differences in the force applied by the two grips and geometrical imperfections of specimen that introduce a stress concentration which influences the nucleation of the bands [101].

A study of the interaction between crack propagation and Lüders was also done, performing FEM simulations on pipelines subjected to bending [102]. When Lüders plateau is present, it

decreases the stress necessary for crack opening at the tip of the crack and at the same time it increases the plastic strain close to the tip and the stress triaxiality, promoting ductile fracture [102]. In another study the interaction between Lüders plateau and Bauschinger effect was analyzed and it was proven that the yield points are absent or present after aging treatment, depending on whether the strain is reversed or not [103].

2.12. Modelling and Fracture of Functionally Graded Materials

Some models used to describe mechanical properties of functionally graded materials include self-consistent models, the Mori-Tanaka model and the Tamura-Tomota-Ozawa model [104], [105], [106]. More precisely, the Mori-Tanaka model gives good predictions of the properties when there is a well-defined matrix and the inclusions are spherical, and there is a short transition zone between one phase and the other compared to the thickness of the specimen (distinct threshold) [105]. On the other hand, the self-consistent model is preferred when there is a skeletal microstructure which does not have a distinct threshold and the zone of gradation has a high extension compared to the thickness of the specimen [105]. The evaluation of the stress intensity factors for the functionally graded materials was done using finite element analyses, considering an exponential variation of the elastic modulus E [107] described by:

$$E(x) = E_1 e^{\beta x} \qquad \text{(eq. 2-21)}$$

where E_1 is the elastic modulus at the starting point, β is a parameter describing the spatial variation of the properties and x is the coordinate [107]. It is known that in the case of plane strain, the stress intensity factor is related to the strain energy release rate by the following equation:

$$K_I^2 = \frac{GE_{tip}}{1-\nu^2} \qquad \text{(eq. 2-22)}$$

where G is the strain energy release rate defined as the variation of strain energy for a certain area and ν is Poisson's ratio [107]. Then, it is also known that for homogeneous materials the strain energy release rate equals the J-integral and that the J-integral is path independent. For homogeneous material $G=J$ where the J-integral is defined as:

$$J = \int_{\Gamma} \left(Wn_1 - \sigma_{ij} n_i \frac{\partial u_j}{\partial x_1} \right) ds \qquad \text{(eq. 2-23)}$$

where W is the deformation energy per unit volume, $\sigma_{ij}n_i$ is the tension vector perpendicular to the contour chosen around the crack tip and pointing in the outside direction, u is the displacement in the x direction and ds is an infinitesimal element of the contour. This definition of J-integral is path dependent for non-homogeneous materials [107]. For this reason, in a non-homogeneous material the G is different from J, but it is still possible to give a definition of the J-integral that is path independent [107]. For a non-homogeneous material the J-integral contains a term of the derivative of W with respect to the position x. So, the new expression of the J-integral is:

$$\tilde{J} = \int_{\Gamma} \left(Wn_1 - \sigma_{ij} n_i \frac{\partial u_j}{\partial x_1} \right) ds - \int_{A} W_{,1} q dA \qquad \text{(eq. 2-24)}$$

This definition for the J-integral is path independent [107]. Regarding the crack growth, the theoretical models used to predict the behaviour of the FGMs are based on the exponential variation of the elastic properties, where the shear modulus is often expressed as:

$$\mu(x, y) = \mu_0 e^{(\beta x + \gamma y)} \qquad \text{(eq. 2-25)}$$

where, β and γ define the spatial variations of the material along the x- and y- directions respectively [108]. The exponential gradation is used because the exponential function is easy to manipulate and gives a good approximation of step-wise gradient, especially when the change of properties is steep compared to the thickness of the functionally graded material [108]. As shown in Figure 2-20 the coordinates x and y are universally described as being aligned in direction parallel to and normal to the crack face, with the crack tip at the origin.

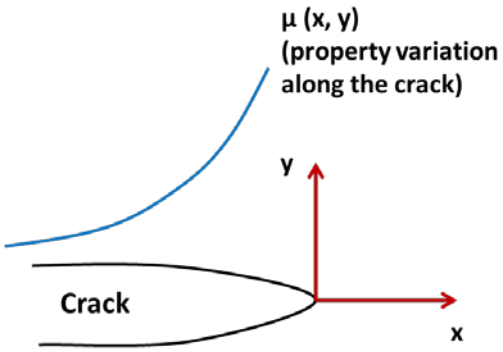

Figure 2-20 - Propagating crack orientation with respect to direction of property variation in FGM (reproduced from a figure reported in ref. [108])

When a dynamic crack growth situation is considered, the variation of the density has to be taken into account. On the other hand, Poisson's ratio was found to be less important in the study of the fracture behaviour [108].

Eischen derived the in-plane displacement fields u_x and u_y for the case of a nonhomogeneous material with elastic properties described by MacLaurin series expansion [108]. However, in general crack extension in FGMs can follow two different scenarios:

- first scenario: crack is perpendicular to the direction of the gradient. The crack growth mode is mixed and the crack deflects from the original orientation;
- second scenario: crack is parallel to the gradient and the crack propagates following a mode I condition.

When the crack tends to kink, many theories can predict the kinking angle and the stress intensity factors at the kinked crack tip. A first criterion is the one related to the maximum energy release rate which suggests that the crack growth occurs along the direction which provides the maximum energy release rate [104]. Another criterion is the maximum circumferential stress theory which assumes that the crack propagation direction corresponds to the one at which the circumferential stress reaches the maximum [104]. Numerical methods are usually used to evaluate the stress intensity factor at the tip of a kinked crack; however, if the kinked crack is small, it is still possible to calculate the stress intensity factor starting from the one of the main crack. Cottrell and Rice (1980) assumed that the stress intensity factors at the kinked crack tip can be expressed as [104]:

$$K_I^* = C_{11}(\phi)K_I + C_{12}(\phi)K_{II} \qquad \text{(eq. 2-26)}$$

$$K_{II}^{*} = C_{21}(\phi)K_I + C_{22}(\phi)K_{II} \quad \text{(eq. 2-27)}$$

where, K_I^* and K_{II}^* are the stress intensity factors at the kinked crack-tip, while K_I and K_{II} are the stress intensity factors at the main crack tip, ϕ is the kink angle and C_{11}, C_{12}, C_{21}, C_{22} are functions of $sin(\phi)$ [104].

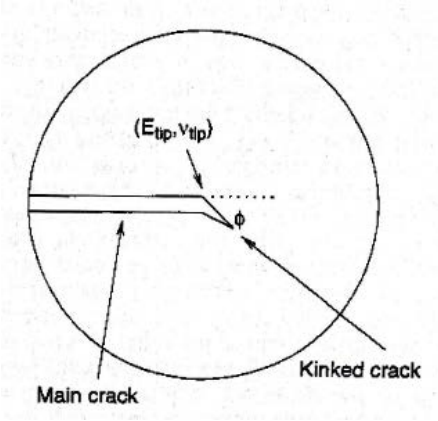

Figure 2-21 - Crack-tip kinking [104]

In literature, a strong effect of the material gradient was observed on the kink angle when the crack tip is situated in the middle of the FGM, but the effect becomes small when the crack tip lies near the boundaries of the FGM [104].

Concerning the fracture toughness, the first theoretical models for FGM fracture toughness have been based on ceramic-metals FGMs that were the first type of FGM to be developed. Experimentally it was observed that surface cracking starting at the ceramic side is the most common failure mode of a metal-ceramic FGM when it is subjected to a thermal shock. A type of failure which is less influenced by the gradient of properties is found when the cracking propagates perpendicular to the material gradient direction which corresponds to delamination and the crack grows along the interface [109]. This can become a common failure mode when FGMs have a highly layered structure. From a theoretical point of view, the equations for the evaluation of the fracture toughness were developed considering the case of a crack growing in the gradient direction and it is assumed that the crack will grow from the ceramic-rich region into the metal-rich region [109]. The simplest approach to evaluate the fracture toughness is to use a rule of mixture, even if this method can lead to an overestimation, since the fracture toughness of a metal in the bulk form is much larger than that for the corresponding particulates dispersed in a brittle matrix [109]. If the crack grows

from the ceramic to the metallic phase without any debonding and if the metal behaves in a brittle manner, the rule of mixture can be used to evaluate the critical energy release rate giving the following expression [109]:

$$G_{IC}(x) = V_m(x)G_{IC}^{metal} + (1 - V_m(x))G_{IC}^{ceram} \quad \text{(eq. 2-28)}$$

where, G_{IC}^{metal} is the critical energy release rate of the metal while G_{IC}^{ceram} is the critical energy release rate of the ceramic, and $V_m(x)$ is the volume fraction of the metal. Then the following relations correlate the energy release rate with the stress-intensity factor if the material is in plane strain [109]:

$$G_{IC}(x) = \frac{1-\nu^2(x)}{E(x)} K_{IC}^2 \quad \text{(eq. 2-29)}$$

$$G_{IC}^{metal} = \frac{1-\nu_1^2}{E_1}(K_{IC}^{metal})^2 \quad \text{(eq. 2-30)}$$

$$G_{IC}^{ceram} = \frac{1-\nu_0^2}{E_0}(K_{IC}^{ceram})^2 \quad \text{(eq. 2-31)}$$

where E_0, ν_0 are Young's modulus and Poisson's ratio of the ceramic and E_1 and ν_1 are Young's modulus and Poisson's ratio of the metal. Substituting the three previous expressions in the equation for the rule of mixture the following expression is obtained [109]:

$$\frac{K_{IC}(x)}{K_{IC}^{ceram}} = \left\{ \frac{E(x)}{1-\nu^2(x)} \left[V_m(x) * \frac{1-\nu_1^2}{E_1} * \left(\frac{K_{IC}^{metal}}{K_{IC}^{ceram}} \right)^2 + \left(1 - V_m(x)\right) \frac{1-\nu_0^2}{E_0} \right] \right\}^{1/2} \quad \text{(eq. 2-32)}$$

From the above equation it can be seen that the fracture toughness varies with the spatial coordinate x and when the crack grows from the ceramic layer to the metallic one, the fracture toughness is expected to rise. However, eq. 2-32 overestimates the value of the fracture toughness because it considers the fracture toughness of the metallic material in the bulk form, which is much larger than the real metallic toughness when brittle particles are dispersed in it [109]. Moreover, in FGMs which have transition from brittle to ductile materials other toughening mechanisms such as crack bridging become important to describe

the fracture behaviour of the composite. However, it must be clarified that this phenomenon applies to FGMs only if the grain size of the metal is much larger than that of the ceramic [109]. With this phenomenon, it is assumed that the metal is not plastically deformed elsewhere. In order to calculate the fracture toughness or R-curve due to bridging, it is necessary to relate the bridging stress with the crack opening displacement of the bridging zone.

Figure 2-22 shows how the fracture toughness value changes if it is calculated using the rule of mixture or if it is calculated taking into account crack-bridging phenomenon when the crack grows from the ceramic-rich region into the metal-rich region [109]. Clearly, the rule of mixture overestimate the toughness; moreover in the case of crack-bridging one can see that the initial crack size a_0 strongly influences the slope of the R-curve especially during the initial stage of crack growth [109]. However, as reported by Jin [109] "the curves for the crack-bridging tend to reach the same value once that the crack has grown so that the bridging zone is fully developed". Jin [109] also reported that "when the metal volume fractions become large, the crack bridging may not be the major mechanism influencing the fracture toughness, because other mechanisms such as microcracking, extensive plastic deformation of the metal and debonding between ceramic and metal may occur in a region around the crack-tip". One of the easiest ways to obtain FGM specimens at laboratory scale having a gradient in stiffness is to exploit the degradation of polymers when they are subjected by UV radiation [110].

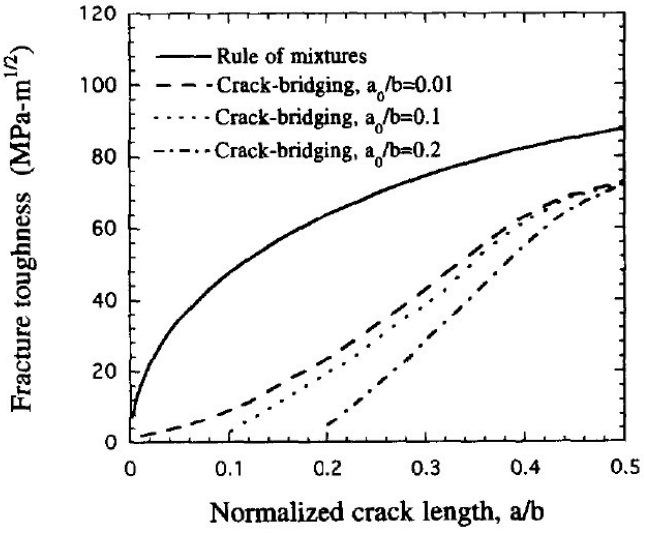

Figure 2-22 - Fracture toughness versus normalized crack length [109]

Lambros et al. [110] performed some experiments using specimens of ethylene carbon monoxide copolymer (ECO) which is susceptible to UV radiation. They studied the fracture toughness for the Mode I fracture and obtained different behaviours for the energy release rate G as function of the time of exposure to UV radiation [110]. They verified that the energy release rate increases after crack initiation for all the specimens, but as irradiation time increases the curves shift to lower values of G [110]. The increase in irradiation time decreases the ductility of the material and so the influence of plasticity on the fracture at the crack tip will not be evident [110]. Then, using the following relation, the energy release rate G and stress intensity factor K_I can be related [110]:

$$J = G = \frac{K_I^2}{E} \qquad \text{(eq. 2-33)}$$

Another experimental study to measure the fracture toughness was done using FGMs of Ti/TiB [111]. However, it is well known that the test for fracture toughness requires the generation of a short and sharp pre-crack at the notch-tip, but only for metals there are accepted and tested procedures, but no clear procedures for FGMs [111].

Suresh and Brockenbrough suggested using axial tensile compression tests for FGMs containing a ceramic phase to create pre-cracking, but the notch of the Ti/TiB FGM was created in the most brittle layer by cyclically loading the material in reverse four-point bending [111]. The authors saw that as soon as the crack starts to propagate in the layers having higher contents of the metallic phase, there is an increase in the fracture toughness. If the samples are tested without any pre-crack, the crack growth is quite unstable and fast. If the sample is pre-cracked using the axial compression technique, it has a stable crack growth but the value obtained for the fracture toughness is only 70% of the value obtained testing samples that have been pre-cracked with the reverse four point bending method [111]. The compression technique creates many microcracks compared to four point bending that will cause a decrease in fracture toughness [111]. For this reason, it is important to point out that the mechanism used for pre-cracking is influencing the measured toughness value [111]. The toughness of the FGMs is strictly dependent on the microstructure, because mechanisms such as particle debonding, crack bridging and crack deflection can be dominant and they increase the toughness value.

Another area of experimental fracture analysis is the one linked with optical methods. On the work of Rousseau et al. [108], the optical approach was used on materials having a variation of Young's modulus. It is implicit that other factors such as variation in fracture toughness can play a role in guiding the behaviour of the crack. Optical investigations were performed for both cracks perpendicular to the gradient and parallel to the gradient directions [108], [112]. The first optical fracture analyses were carried out using an interferometer on FGMs of epoxy resin and glass particles [108].

The behaviour of FGMs was compared with the case of a homogeneous epoxy/glass composite and with a bimaterial (see Figure 2-23) [108]. Rousseau [108] reported that "as soon as the crack moves towards the region with higher elastic modulus, the stress field at the crack-tip becomes slightly asymmetric towards the most compliant region. The FGMs are superior compared to the fracture performance of a bimaterial". According to Rousseau [108] "even if in the bimaterial there is a high asymmetry of the stress field at the crack-tip, this is not enough to have many crack kinking phenomena to delay the fracture". As a crack extends in the FGMs, the material asymmetry gives rise to crack kinking which increases as soon as the crack is situated closer to the compliant end of the material [108]. Analysis with an interferometer was also used to analyze the crack tip stress field when the plane of the latter lies in the direction of gradation. When the crack is located on the stiff side of the gradient (decreasing gradient for the elastic modulus) the frontal fringe lobes tend to expand, while if the crack is on the compliant side the effect is opposite. These differences on the stress field lobes at the crack tip are reflected in different values for the stress intensity factor. So for identical geometry and loading, the functional graded material with decreasing gradient ($E2/E1<1$) has a 40% increase in stress intensity factor when compared with the situation of the increasing gradient ($E2/E1>1$) [108], [112]. However, one must keep in mind that for the two configurations the elastic modulus at the crack tip is different. When each functionally graded material is compared with the corresponding homogeneous material, the FGM having an increasing gradient performs better than its counterpart, whereas the FGM having a decreasing gradient performs poorly compared with the homogeneous material [112]. Crack growth experiments were also performed for the case of the crack located on the stiffer side and for the crack located on the more compliant side [112], proving that the FGM having the crack on the more compliant side has lower crack tip toughness but is able

to sustain a higher load before fracturing than the FGM having a crack on the stiff side [112]. The FGM with increasing gradient (*E2/E1*>1) tends to have a faster crack growth and so higher K_I with increasing elastic modulus gradation [108]. Dynamic loading tests were performed using both epoxy-glass FGMs and polymeric material degraded by UV radiation. Given that the results showed the same behaviour for the fracture, it was concluded by Rousseau [108] that the elastic modulus variation has "the precedence over the microstructural difference to explain the dynamic fracture behaviour". Another imaging technique used to study fracture propagation is the 2D digital image correlation (DIC) and the photoelastic method [108]. The specimen is coated with a photoelastic coating and it is monitored during the test using a circular polariscope. This analysis will give the maximum in plane shear strains [108]. Using all the optical techniques mentioned above, it was seen that when the crack is placed in the direction of gradation under quasi static conditions, the FGM is capable of sustaining higher loads with the crack located on the compliant side of the FGM than when it is placed on the stiffer side of the FGM.

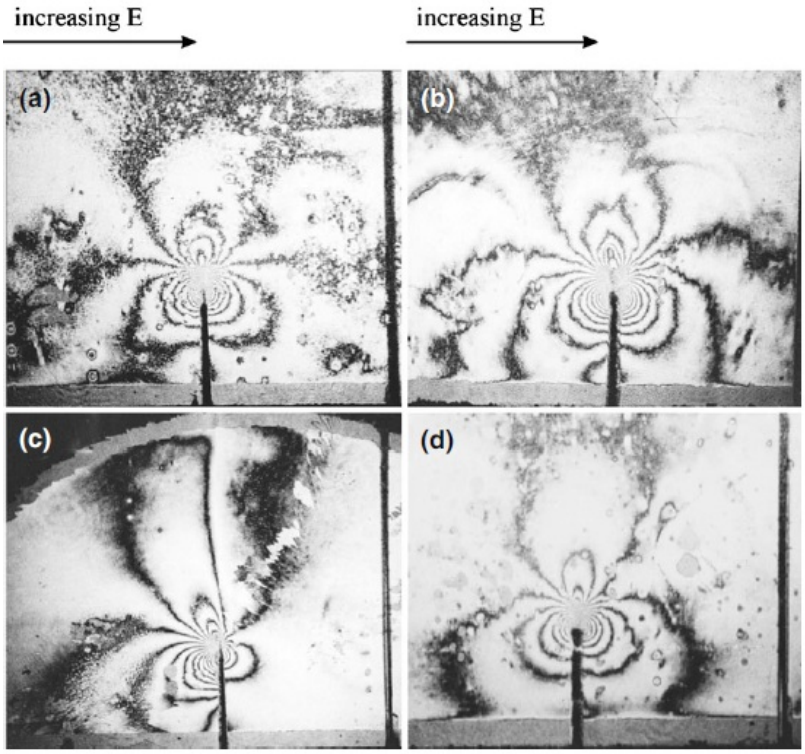

Figure 2-23 - Crack tip interference for FGMs (a, b), for a bimaterial (c) and for a homogeneous glass-epoxy composite (d) [108]

Under dynamic conditions however, locating the crack on the more compliant side of the material promotes faster and easier propagation than when the crack is on the stiffer side [113]. Moreover, when there is a dynamic load the effect of the elastic modulus variation takes precedence over the local microstructure [113].

Considering the difficulties in creating FGM specimens that can be used in laboratory for fracture tests and taking into account that even though some measurements can be made, the quantitative interpretation of test data is difficult because of the small size of the specimens; it becomes desirable to reproduce the fracture propagation using finite element modelling. In the case of a ceramic-metal FGM, simulations are based on the simulation of elastic-plastic crack propagation. A first approach is the surface separation model. This method is based on the use of cohesive elements that follow appropriate traction-displacement relations to achieve the separation of the surfaces of the crack [114]. Based on this model, when the crack is starting from the elastic phase (the ceramic one) and crossing the elastic-plastic phase (the ceramic-metal graded region) the separation energy increases as more energy is required to propagate fracture in the ductile phase [114]. In a finite element simulation, the influence of the cohesive elements is limited by setting their thickness to less than 1% of the size of adjacent elements. Moreover, the initial stiffness of the cohesive elements is set close to that of the bulk material to avoid these elements altering stiffness of the structure. There are other models which are used to simulate impact loads on FGMs with a high velocity rod. Usually, impact loads generate multiple cracks at arbitrary locations which then grow along arbitrary directions [114]. The modelling reproduces the case of a FGM layer that is placed at the top of a metal substrate as shown in Figure 2-24 [114]. To simulate crack propagation, cohesive elements are distributed along the element boundaries within a rectangular region underneath the rod impact. According to Wang [114], “the most difficult part for dynamic simulations is the stability of calculation which is influenced by various factors such as element size, shapes and the traction-separation law of cohesive elements”. Instability increases further under a compression load compared with a tensile one, because under a compression load the elements tend to overlap. Usually in simulations the crack propagation directions are classified in two types: the first one tends to propagate in the horizontal direction while the other tends to propagate downward in the material [114]. As reported by Wang [114], “the first type of cracks has more influence coming from Mode I of fracture,

while the other type is generally dominated by Mode II. These cracks dominated by Mode II fracture have small normal separation because for them the shear stresses are dominant". The fracture behaviour depends on material gradation through the thickness and usually a power law relation is chosen to perform the modeling of cracks propagation [114].

From the finite element simulations it was proven that as soon as more ceramic phase is present the cracks propagate more downward in the material, and that this behaviour is related to the changes of toughness through the thickness [114]. Some additional simulations were carried out to understand how the presence of cracking influences the values of the energy, and it was proven that the cracking alters the energy absorption characteristics of the material [114]. Another point that must be kept in mind during these simulations is that the toughness for the Mode I fracture and for the Mode II fracture is not the same. A parameter "*q*" can be defined as the ratio between the separation energies for Mode II and Mode I. A larger *q* slows crack initiation, but once cracking begins, the propagation is accompanied by larger plastic flow. This confirms that the cracks have a large influence on energy absorption even if the separation energy is small.

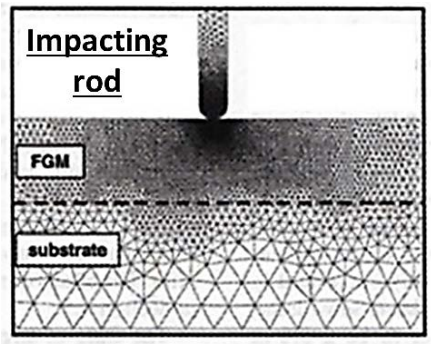

Figure 2-24 - FGM model for impact load simulation (figure adapted from image shown in ref. [114])

Investigations were made to understand the influence of the yield stress gradient on crack propagation; in particular according to Kolednik [115] "the near-tip crack driving force is increased if the yield stress increases in the crack growth direction and vice versa ". Kolednik [115] also pointed out that "ideally, when a crack originates in the more compliant material and then it evolves toward the interface of the stiffer material, the local stress intensity at the crack tip decreases and it is equal to zero at the interface". On the other hand,

again according to Kolednik [115] “if the crack starts on the stiffer material and then propagates toward the more compliant material, at the interface the local stress will rise to infinite”.

In 1992 Suresh et al. did some fatigue loading experiments on bimaterials made of ferritic and austenitic steels [115]. In this study, elastic properties such as Young’s modulus and Poisson’s ratio were the same for both materials and the yield stress was also similar, but the strain hardening coefficient was higher for the austenitic steel than for the ferritic steel [115]. During this study the propagation of a crack perpendicular to the interface was studied and it was seen that when the crack makes a soft-hard transition approaching the interface starting from the ferritic steel, which is less stiff than the austenitic steel, the crack growth rate decreases and the crack almost stops before reaching the interface [115]. On the other hand, when a crack approaches the interface starting from the stiffer material (hard-soft transition), the crack crosses the interface and it does not stop. A model was proposed to explain this behaviour of the crack propagation in presence of a gradient of yield stress and it was seen that compared with the traditional formulation of the J-integral there is the addition of another term to the expression of the J-integral [115]. Rice (1968) showed that the potential energy for a load-controlled test is represented by the area above the load-displacement curve (Q-q) [115]. More in detail, from the results of Rice [115] it was stated that “the potential energy for a linear elastic material depends on the load *Q*, on the crack length *a*, on the Young’s modulus *E* and on the geometry of the specimen”. For a non-linear elastic body having a yield stress gradient, the potential energy will also depend on the yield stress value. The value of σ_y also affects the radius of the pseudo-plastic zone r_y, but many models assume for simplicity that the radius of the plastic zone is small compared with the dimension of the crack and of the specimen dimensions. If the crack increases its length by an amount Δa while the load Q and the yield stress are kept constant, there is a decrease in the potential energy and the J-integral is related to this decrease by the following expression [115]:

$$J = -\frac{1}{B}\frac{\partial P}{\partial a}\Big|_Q \qquad \text{(eq. 2-34)}$$

Kolednik [115] specified that “this expression is a measure of the crack driving force, but it is valid only if the other parameters (*E*, geometry and yield stress) are constant during the crack extension. On the other hand, if the yield stress is increased by a certain amount $\Delta\sigma_y$

while Q, a, E and the geometry are kept constant, the energy of the specimen will increase by the amount ΔP_y (see Figure 2-25)" [115]. For this reason if the yield stress in the specimen changes during the crack propagation, it is necessary to consider also the following term [115]:

$$C_y = -\frac{1}{B}\frac{\partial P}{\partial \sigma_y}\Big|_{Q,a}\frac{d\sigma_y}{da} \qquad \text{(eq. 2-35)}$$

So the total change of potential energy in a material that has a yield stress gradient is the sum of the two previous terms:

$$C_{tot} = -\frac{1}{B}\frac{dP}{da}\Big|_{Q,geometry} = J + C_y \qquad \text{(eq. 2-36)}$$

Different relationships are found in literature for C_y depending on the geometry and on the plastic zone dimension [115]. According to this model, an additional term C_y appears when there is a gradient of yield stress and the term is positive. This term enhances the effective crack driving force if the yield stress decreases along the crack growth direction.

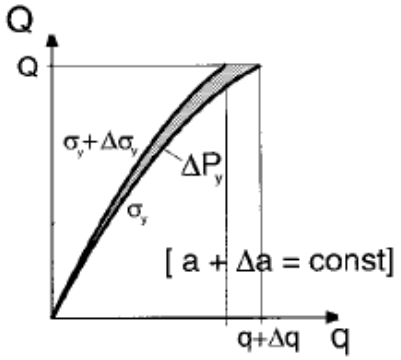

Figure 2-25 - Change in potential energy due to an increase of the yield stress [115]

On the contrary, an increase in yield stress along the crack growth direction will cause C_y to be negative and this decreases the effective crack driving force. Furthermore, the term C_y is directly proportional to the gradient of yield stress and to the size of the plastic zone and to the far field applied load [115]. Experimental observations were done for fatigue cracks on interfaces between ferritic and austenitic steel by Suresh et al. Soft or hard interlayers can act

as effective obstacles for cracks but only if the thickness of the interlayer is of the order of the plastic zone radius of the softer material, or larger [115].

Another situation occurs when the crack grows parallel to the interface between the hard and the soft material, Figure 2-26 [115].

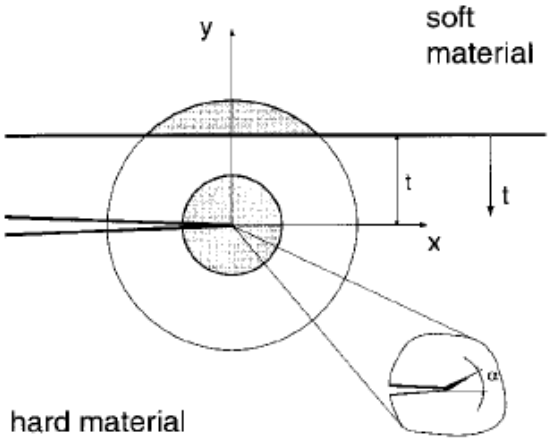

Figure 2-26 - Plastic zone for a crack in a hard material, parallel to an interface to a soft material. The crack will change its path and curve towards the interface [115]

Kolednik [115] specified that "if the case of a crack in a hard material is considered, meandering cracks can appear. If the distance "t" between the interface and the crack is higher than the size of the plastic zone in the soft material, the crack will always feel the same potential energy and it will steadily grow at the same distance from the interface. On the other hand, if the distance "t" from the crack to the interface is lower than the size of the plastic zone in the soft material, the crack will feel a smaller potential energy, and it will kink toward the interface and it will cross the interface to reach a condition of less potential energy" [115]. Again according to Kolednik [115], "two limitations of this developed model are that it doesn't take into account the strain hardening exponent of materials, but it is clear that a yield stress gradient term will be induced on an interface of two material having equal yield stress but different strain hardening exponents. Another drawback of the model is that the plastic zone is assumed to have a circular shape around the centre of the crack-tip". Shukla et al. wrote a review summarizing both theoretical and experimental approach describing dynamical crack growth in FGMs [116]. In their review, they proposed a theoretical formulation for a transient solution of a crack which propagates at an arbitrary

angle compared to the direction followed by the gradient of the material [116]. From their experiments, Shukla et al. verified that if the crack is propagating towards a zone having higher toughness, it will require the release of more strain energy to maintain a constant velocity, and the stress intensity factor will increase with the crack length [116].

Mohandesi et al. performed studies about fracture toughness in graded steels obtained using plain carbon steel and austenitic stainless steel as electroslag remelting electrodes [117]. They proposed a model supported by experimental measurements, to calculate fracture toughness depending on the type, volume fraction and position of the phases formed [117]. In particular, they supposed that the fracture toughness follows a rule of mixture [117]. In another study made by Nazari et al. the fracture toughness of similar microstructures, obtained again with electroslag remelting technology, was evaluated in both crack divider and crack arrester configuration [118]. As already mentioned before, in the crack divider configuration the crack propagates orthogonal to the direction of gradation while for the crack arrester configuration, the crack propagates parallel to the direction of gradation [118]. The authors concluded that in crack divider configuration, the type of phases and their volume fraction are primary factors which affect the toughness, while for the crack arrester configuration it is the position of the crack tip and its distance from the bainite or from the martensite layers that affect the toughness value [118]. Rousseau and Tippur studied the mixed mode deformation at the crack tip evaluating the influence of the elastic gradient and of the crack location on the stress intensity factor, on the energy release rate and on the mode mixity when the crack is applied orthogonal to the elastic gradient [119]. Analyzing the optical image they observed that the fringe pattern for an FGM is similar to the one encountered for a homogeneous material, and concluded that the FGM stress intensity factor increases as the crack is relocated from the stiff side to the compliant side of the gradient; this result seems valid for all crack lengths [119]. They also proved that the kinking angle is larger if the initial crack is propagating in the compliant region [119]. Other studies were dedicated to the fracture of ceramic/metal functionally graded coatings [120], [121]. The elastic properties of the coating varied through thickness and from FEM analyses performed by Bao and Wang, it was demonstrated that the effect of gradation on crack propagation is not high for mechanical loading while it plays a major role for thermal loading [120]. The authors saw that if the crack density is small, the energy release rate increases monotonically

but if the crack density is high then the curve of the energy release rate has a peak; this means that the crack is not easy to propagate and it can stop at a certain length [120]. Bao and Cai studied the delamination cracking of ceramic/metal functionally graded coatings applied on a metallic substrate [121]. In this study the authors analyzed the influence of coating gradation, location of the crack and ratio between the thickness of the coating and the substrate on the energy release rate [121]. When a high thermal expansion mismatch between the coating and the substrate was present, delamination or spalling of the coating occurred, but FGM coatings have the potential to reduce thermal expansion mismatch [121]. Indeed, the fracture driving force decreases if the gradation degree is high [121].

A FEM study related to void growth and coalescence in materials having yield stress gradient was made by Li et al. [122]. In particular, the authors used an axysimmetric cylindrical cell model containing a spherical void and from the computational results they concluded that the yield stress gradient brings faster void growth rates and lower void coalescence strain. Indeed, in the homogeneous materials the critical shapes of voids are independent on the yield stress of matrix, but the graded distribution of yield stress leads to a higher plastic strain in the softer matrix zone; this has an influence on the critical void shape [122]. More precisely, Li et al. [122] established that "for low stress triaxiality levels, the aspect ratio of the voids is low in graded materials compared to what happens in homogeneous materials and this will cause an earlier coalescence of voids; however, the effect of gradient on the void shapes decreases if the stress triaxiality is increased".

2.13. Summary from Literature Review

The literature review presented in this chapter has shown that most of the studies concerning graded materials are related to ceramic-metallic systems, and that only few studies involved metallic graded microstructures. For the creation of a carbon gradient inside steel, case hardening is the main technique used. The easiest way to strengthen the steel is to introduce carbon in solid solution or in the form of precipitates. The effect of carbon on the yield stress of the steels and its interaction with dislocations are well documented in literature. The plastic instability (Lüdering) associated to carbon in solid solution has been deeply investigated. In particular, the testing temperature, strain rate, grain size, percentage of cold

working and stiffness of the tensile machine are just some of the parameters whose influence on Lüdering has been studied. However, no clear effect of carbon gradient on Lüders propagation was found. Concerning fracture, most of the studies are related to the propagation of cracks in materials having gradient of Young modulus. Furthermore, many investigations rely mainly on simulations, while few experiments are reported. A lack of experimental studies on void growth and coalescence in materials having carbon gradient was highlighted. The influence of Lüdering on void growth and coalescence has been only investigated by modelling, while no experimental study has been found.

Chapter 3 : Research Proposal

3.1. Scope of the Project

In the literature review, the two main processes to increase the strength of steels (case hardening and bake hardening) were reviewed. The main disadvantage of these two processes is that for bake hardening it is necessary to have a careful control of the steel composition to ensure that the amount of carbon is not too high to start aging at room temperature compromising the ductility of the steel; but at the same time the amount of carbon in solution must be high enough to guarantee pinning of the dislocations during heating at 170 °C. On the other hand, case hardening is not an advantageous process considering the high temperatures and time that have to be used to increase the carbon content inside steel and it is not currently applied to steel sheets.

The new approach that the Gracos project (Graded Composite Steels) wants to develop is the diffusion of carbon inside Interstitial Free (IF) steel using a carbon rich film as carbon reservoir. The film, which is amorphous and contains both iron and carbon, is deposited using a Physical Vapour Deposition (PVD) process. After the PVD process, the coated IF steel is annealed at temperatures up to 700 °C to cause diffusion of carbon and to increase yield strength and tensile strength. Figure 3-1 shows a schematic view of the substrate of IF steel coated on both sides with a carbon containing layer. The main scope of the company Arcelor-Mittal, which is supporting the project, is to use the improved interstitial free steel for packaging applications or even for automotive panels. The technique used to increase the mechanical response of the material should therefore be cost efficient.

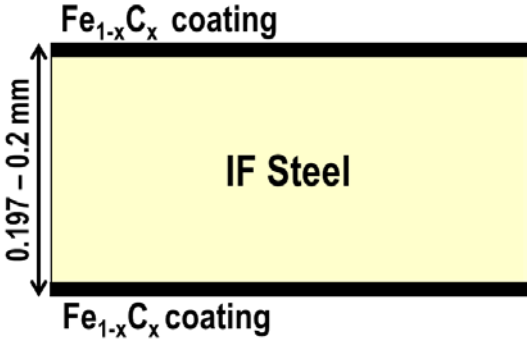

Figure 3-1 - Schematic view of the substrate of IF steel coated both sides with the carbon containing coating

In this PhD work, modelling of carbon diffusion and mechanical testing (tensile test, hardness measurements) will be performed. The diffusion of carbon into the IF steel substrate will occur in the ferrite zone of the Fe-Fe_3C equilibrium diagram, which was used as reference to evaluate solubility limit of carbon into ferrite for all the annealing temperatures of the experiments presented in Chapter 5. The Fe-Fe_3C equilibrium phase diagram is shown in Figure 3-2. Other objectives of this work involve the understanding of how carbon gradient influences Lüders bands propagation, yield stress and fracture.

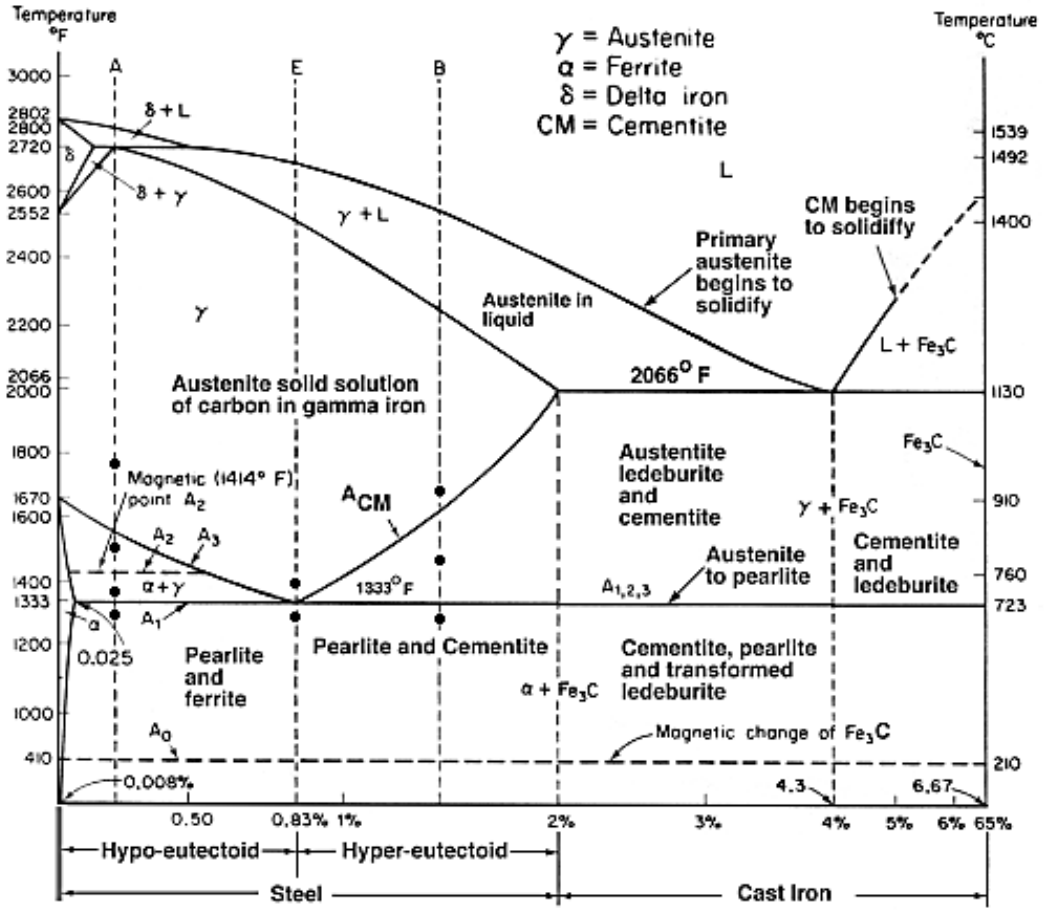

Figure 3-2 - Iron-Carbon diagram [123]

In another set of experiments, PVD films containing iron, manganese and carbon are deposited on the surface of the IF steel. This set of tests should verify if substitutional elements can be diffused into the IF substrate by using PVD films. Manganese was selected since it is often used in steel industry to obtain TWIP steels which show a good combination of tensile strength and ductility. Finally, one specimen of IF steel coated with a film

containing 100% of carbon is tested to analyze how the diffusion and the mechanical properties change when no iron is present in the deposited film.

3.1.1. $Fe_{1-x}C_x$ Films

Iron/carbon and iron carbides/carbon films have been widely studied because of their magnetic properties. Most of the work regarding iron/carbon film was done by Dr. Bauer-Grosse and her group. A common way used to produce metal/non-metal films is the sputtering of a composite target in a neutral atmosphere, or the sputtering of a metallic target in a reactive atmosphere [124]. The composition and the microstructure of the deposited film are dependent on the substrate temperature, pressure and composition of the target [124]. Bauer-Grosse et al. obtained $Fe_{1-x}C_x$ films performing triode sputtering of different composite targets but keeping constants all the other parameters of the process [124]. In particular, sputtering of a metallic target in a reactive atmosphere which contains methane is widely used because the film composition and structure can be modified controlling the gas ratio CH_4/Ar in a more flexible way than the use of composite target [124]. The studies performed in these films have shown that the carbon content inside the film is proportional to the methane partial pressure and the film becomes amorphous if *x* is increased [124]. Bauer-Grosse et al. [124] have also performed annealing treatment to evaluate the thermal stability of FeC films and to study the products of transformations occurring during heat treatment [124].

The structure of the deposited film can be influenced by the energy level at the surface of the growing film, which depends on temperature, sputtering distance, substrate and target voltages and concentration of gases in the sputtering atmosphere. The graph in Figure 3-3 summarizes the products of thermal decomposition for different initial levels of carbon in the amorphous $Fe_{1-x}C_x$ films [125]. The three forms of amorphous film are listed on the bottom, while the types of carbides that can be formed are shown along the top [125].

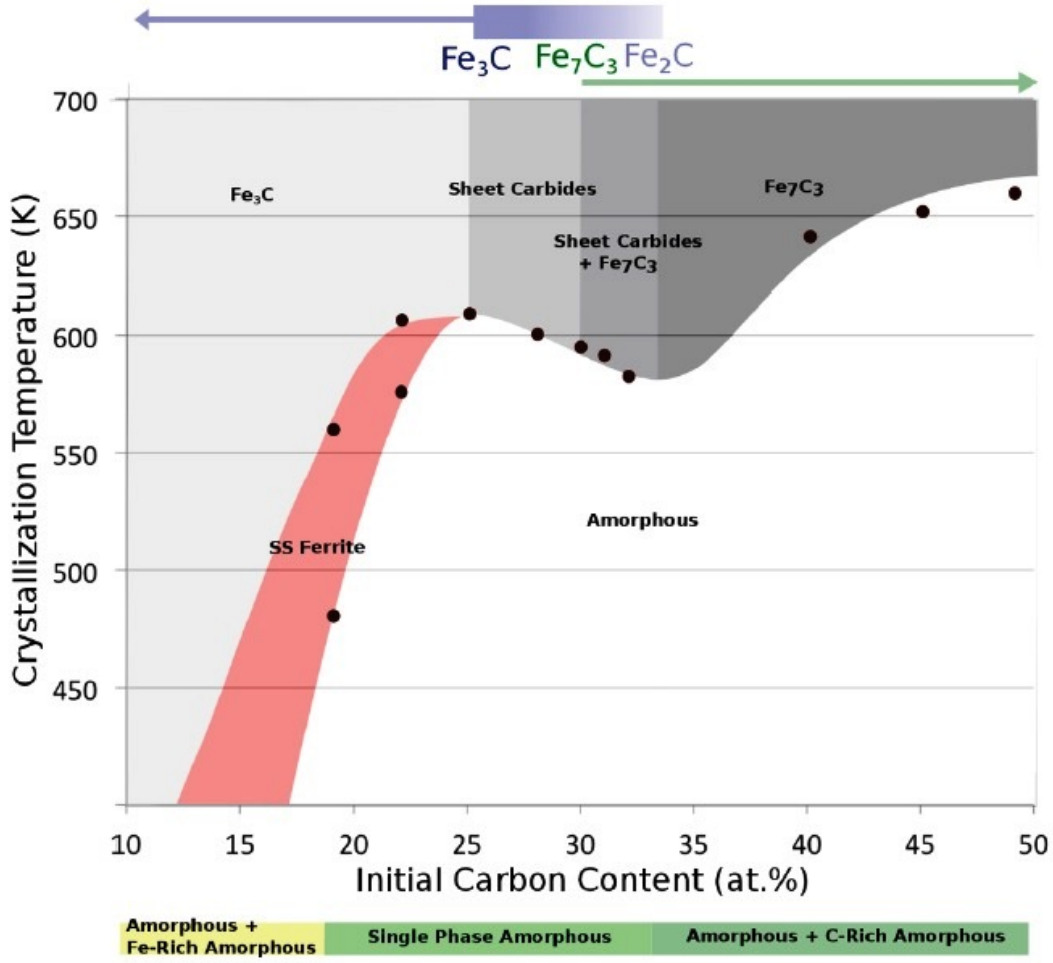

Figure 3-3 - Crystallization temperatures and products of $Fe_{1-x}C_x$ films with varying carbon concentration [125], [126]

$Fe_{1-x}C_x$ can be applied using Physical Vapour Deposition (PVD) technique. PVD is a process by which a material is deposited on a substrate using a method which physically removes atoms from a target material. A PVD system comprises a vacuum or near vacuum chamber and a target which provides the material for the deposition. The plasma-based sputtering systems use small amounts of inert gas, usually argon, to conduct current and to sputter atoms from the target to the substrate. The atoms of the inert gas are ionized and they hit the target surface at high energy ejecting atoms from the target itself by momentum transfer [127]. An increase of pressure of the inert gas allows larger numbers of ions to be sputtered but with the increase in pressure there is also a higher probability that the sputtered species interact with the inert gas which decreases the deposition rate compared to what can be obtained using evaporation processes [127].

PVD was chosen as deposition technique since it allows quite fast deposition rates and a precise control of the composition, microstructure and thickness of the film [128]. As reported by B. Lawrence [129]: “this deposition technique relies on several variables such as target composition, working pressure of the system, distance between substrate and target, sputtering atmospheres and voltages of both target and substrate”. PVD units are of particular interest for steel companies since they can produce coatings on steel surfaces continuously in few minutes [129], [130].

3.1.2. Fabrication and Characterization of a Functionally Graded Material

One purpose of this work is to prove that FeC film can be used to carburize steel sheets by performing heat treatments at temperatures lower than the one used for case-hardening. Moreover, the carburization obtained from FeC films can result in strengthening levels higher than what is obtained with bake-hardening.

Another objective is to obtain carbon gradients in the IF steel by properly tailoring the diffusion of carbon from FeC films. Carbon graded structures are of particular interest since they can have a high amount of carbon close to the coated surfaces and no carbon at the core of the IF sheet. This can increase markedly the strength of the steel, without compromising its ductility. Furthermore, given the same level of strength, carbon graded structures could be beneficial compared to uniform carbon distributions since they could reduce Lüdering.

Carbon gradients are obtained by using different annealing procedures and the final mechanical properties are assessed through tensile testing, while the carbon distribution is characterized by using Vickers microhardness. Other techniques such as Atom Probe Tomography (APT) can be used to characterize the presence of precipitates in the IF matrix, while Electron Back-Scattered Diffraction (EBSD) and Transmission Electron Microscope (TEM) can be used to identify the presence of different phases or precipitates caused by phase transformations.

3.2. Modelling of Lüders Bands

Many studies were performed on understanding the influence of grain size, gauge length and tensile machine stiffness on Lüders behaviour; but there is no study showing the influence of voids on Lüders bands propagation. For this reason, we propose to carry out FEM studies to

understand how the volume fraction of 2D cylindrical holes can increase or decrease the speed of band propagation. In particular, two separate studies were undertaken:

- the first one keeps constant the interspacing of voids but changes the volume fraction;
- the second one varies the spacing between voids but the volume fraction stays constant.

The objective of these studies is to understand how voids can slow Lüders band propagation. These FEM simulations can be carried out on a tensile coupon having a C-gradient through thickness and having the same geometrical dimension as the Gracos coupons.

Furthermore, studies made on plastic instabilities in NiTi shape memory alloy have shown that it is possible to suppress the propagation of the bands if the alloy is coupled with a strip of material which has no plastic instability [93]. However, only the influence of strip thickness on the plastic instability propagation was analyzed. The model proposed in this section aims at studying the influence of thickness and stiffness of a layer showing no plastic instability when it is coupled with two outer layers having Lüdering. A schematic view of the structure through thickness is shown in Figure 3-4.

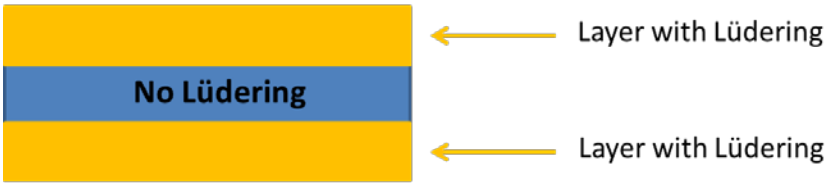

Figure 3-4 - Layout to analyze influence of stiffness on Lüders propagation

Another model was proposed to verify the influence of thickness of the central layer, when it is coupled with outer layers having Lüders plateau but with gradients of yield stress and Lüders length which decrease moving from the outer surface towards the interface with the central layer as shown schematically in Figure 3-5.

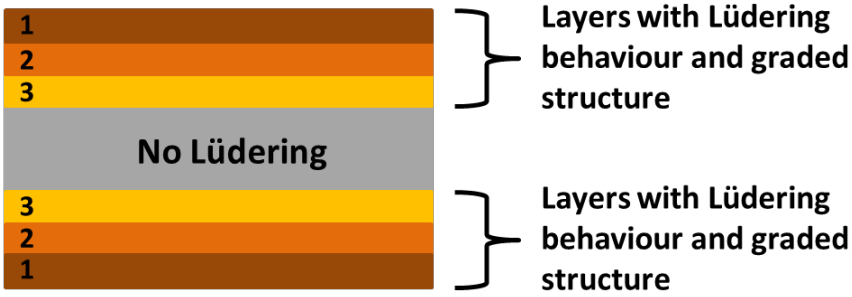

Figure 3-5 - Layout of the model to analyze influence of stiffness and thickness but with Lüders created with a gradient

It has already been mentioned earlier that Lüders bands can be simulated using a linear softening between the upper yield stress and the lower yield stress as mentioned in ref. [131] and shown in Figure 2-19. A parametric study is presented to analyze the influence of upper yield stress and slope of the lineat softening on Lüders plateau length. In this PhD work, another objective is to assess the influence of strain-hardening on Lüdering since no FEM simulation was found in literature.

In this section, modelling of Lüdering at the macroscale has been presented, however, it would be interesting to run simulations where the nucleation of dislocations can be controlled to see how this can influence load drop and speed of the bands in situations where the density of dislocations is low and their multiplication is hindered.

3.3. Experimental Studies of Fracture in Graded Materials

In literature, there is no experimental work about fracture on materials having gradient of yield stress or of strain hardening. Most of the knowledge has been obtained using models. In order to experimentally investigate fracture on graded steels, short annealing treatments (for example 530 ˚C, 30 minutes) could be performed on Gracos coupons to maximise the carbon gradient between the outer surface and the steel core. Another flash annealing can be performed at 950 ˚C for few minutes followed by a rapid quench which could result in a gradient of microstructure with the formation of martensite or bainite close to the coated surfaces. Once the gradient has been obtained, different pattern of holes can be lased in the gauge length using femtosecond laser and the behaviour of the graded material can be compared with the one of homogeneous material. In particular, the configurations of holes studied by Weck et al. [132] could be used. It is difficult to study the effect of yield stress gradient on fracture with a through thickness gradient on just 200 μm of thickness. For this reason, a carbon gradient (i.e. yield stress gradient) through the width or through the gauge length of a tensile sample would allow visualizing markedly its effect on the growth and linkage of voids placed through the gradient. For this reason, in Chapter 9, experimental fracture studies of coupons having carbon gradient along the gauge length or along the gauge width are presented.

Chapter 4 : Experimental Procedures

4.1. Methods used for Iron-Carbon Film Deposition

The most common techniques to transfer material atom by atom from a source to a substrate are Physical Vapour Deposition (PVD) and Chemical Vapour Deposition (CVD). Description of their working principles is written in detail in [133], [128]. In the next chapter only the PVD technique used in the Gracos project will be briefly described.

PVD is the process used at the University of British Columbia (UBC) in Vancouver to deposit $Fe_{1-x}C_x$ films on the substrate of IF steel. The methods used at UBC to deposit iron-carbon films use AC magnetron sputtering and provide two ways to control the amount of carbon in the film: the first method uses a voltage bias, while the second uses an atmosphere of methane [127]. A DC voltage can be applied and this is the situation defined as "bias voltage" [127]. A picture of the deposition chamber used at UBC for the coating of the Gracos specimens is shown in Figure 4-1. The target is made of an Armco iron disc with holes which is placed on a sheet of graphite [127]. Once the sample drum has been loaded, the vacuum chamber is pumped down to $3x10^{-6}$ Torr and when this pressure has been reached, a small flow of argon is introduced to maintain the plasma (a higher pressure is not used because it would interfere with sputtering increasing the film porosity [127]). During the process Argon is continuously pumped in and then out to maintain the atmosphere pure and eliminate water vapour or other gases evaporating from the chamber walls and off the sample drum [127]. The sputtering rate of iron is higher than that of carbon so if no bias voltage is applied the carbon content in the film will be only 8 at% [127]. A method to regulate the carbon content in the film is the application of a biased voltage [127]. Indeed, films produced using a bias voltage of -600 V and methane had a final carbon content of 30 at.% [127].

Figure 4-2 gives a schematic cross sectional view of the thickness of a specimen used in the Gracos project. The IF steel core is coated on both sides with the carbon containing PVD coating. The total thickness of the coated specimen is 200 µm while the coating on each side has a thickness of 500 nm which means the IF steel core has a thickness of 199 µm.

However, to simplify the modelling the thickness is still considered being 200 µm without distinction between coating and core.

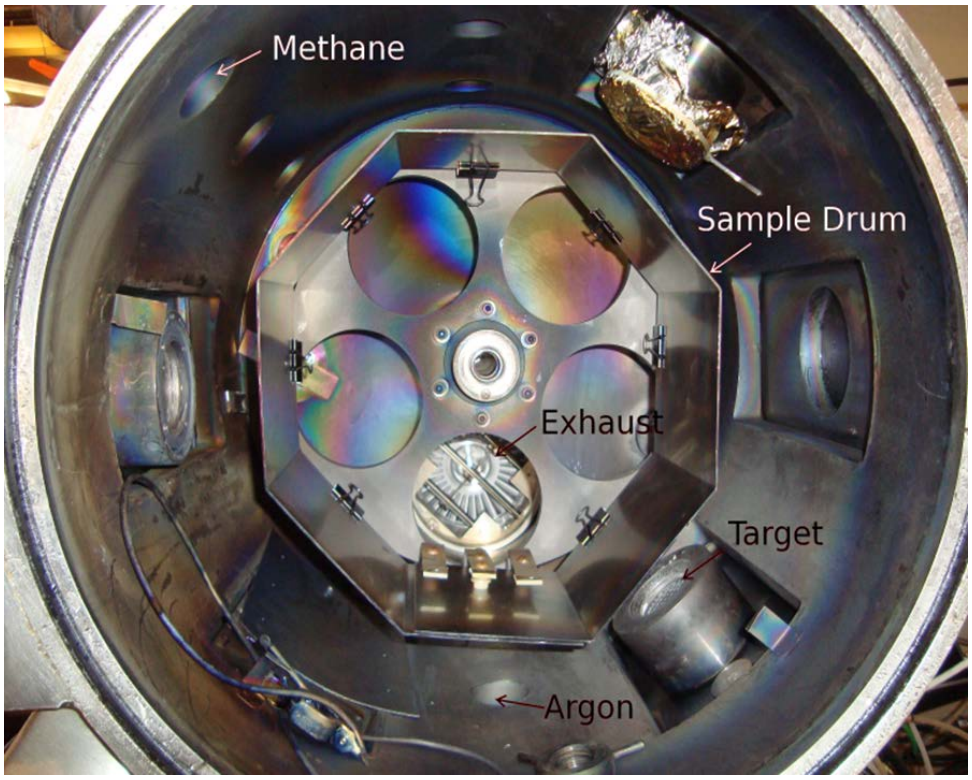

Figure 4-1 - PVD chamber used for film deposition at UBC [127]

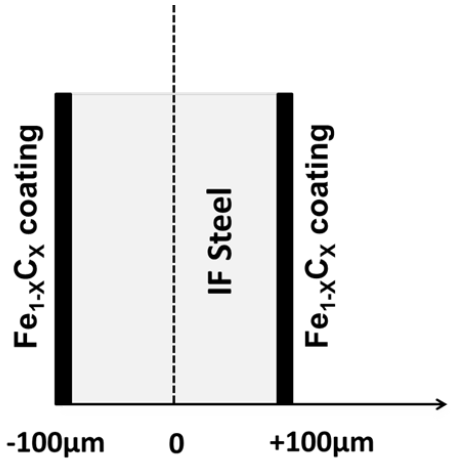

Figure 4-2 - Schematic view of the thickness of Gracos specimen

Figure 4-3 shows the appearance of the coated and uncoated IF steel to human eyes.

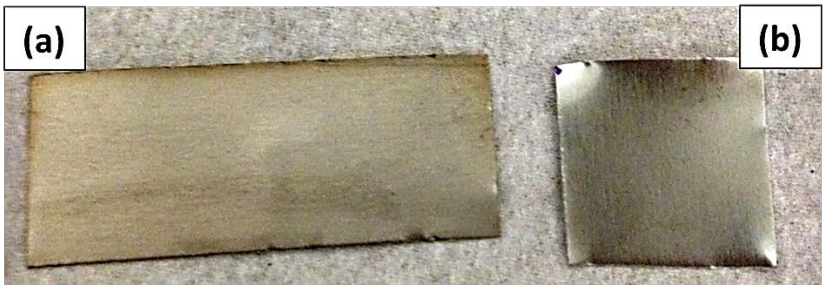

Figure 4-3 - (a) IF steel coated both sides with 500nm FeC film; (b) uncoated IF steel

4.2. Fabrication of Tensile Coupons and Annealing Procedure

Tensile coupons have the dimensions shown in Figure 4-4. Given the thickness of the steel sheet (around 0.197 mm) and the small dimensions of the coupons, the best technique to machine them is electro-discharging machining (EDM). Once cut, they were shipped at UBC for the PVD coating. As defined by Krar [134], "Electrical discharge machining (EDM) is a process used to remove metals by means of electric spark erosion". According to literature [135], EDM has the advantage of being a non-contact process compared to milling. For this reason, EDM will not generate directly cutting forces on the workpiece and it can be used to obtain complex shapes in thin metallic sheets [135]. Details about EDM machining are reported in [134], [135] and [136]. An image of an uncoated coupon of IF steel after EDM machining is shown in Figure 4-5, while Figure 4-6 shows the cutting of the coupons at the University of Ottawa.

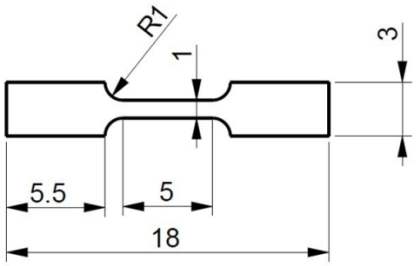

Figure 4-4 - Dimensions of tensile coupon in mm

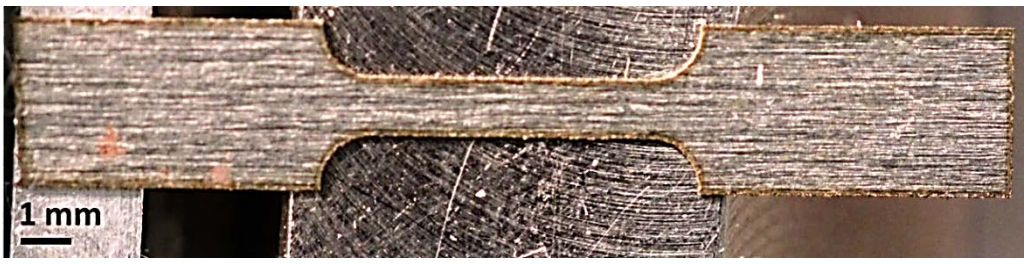

Figure 4-5 - Picture of a tensile coupon obtained with EDM

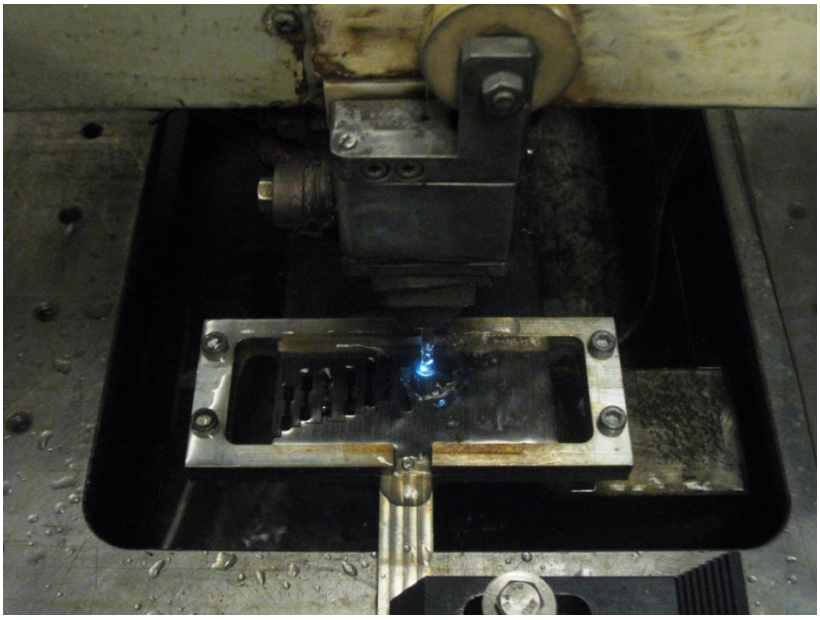

Figure 4-6 - Wire-EDM cutting of tensile coupons used for Gracos project (University of Ottawa)

4.3. Annealing Treatment

For the experimental work performed in this thesis, annealing treatments have been performed to diffuse carbon from the FeC film into the IF steel substrate. Various environments have been investigated, including high vacuum, argon and air. Another series of annealing has been performed in high vacuum followed by a rapid quench. In the following paragraphs the technique and equipment used for annealing will be described.

4.3.1. Annealing Treatment in High Vacuum

After PVD coating of FeC film at the University of British Columbia (UBC), tensile coupons were shipped back to the University of Ottawa where annealing treatments were carried out.

The high vacuum furnace consists of an alumina tube and two pumps: a rough pump and a diffusion pump. The specimens were placed inside an alumina crucible which was then placed at the center of the tube where a thermocouple is located. The valve of the rough pump is then opened to obtain a vacuum of 10^{-4}-10^{-5} Torr inside the tube. The valve of the rough pump is then closed and the valve of the diffusion pump is opened to reach a final high vacuum value of 10^{-6} Torr. When this level of vacuum is reached, the temperature for the isothermal annealing is then set. An example of heat treatment in high vacuum

performed at an isothermal temperature of 530 ˚C for 1h is shown in Figure 4-7. The heating rate is 12 ˚C/min, but it can be increased, while the cooling rate is 12 ˚C/min and drops at 3 ˚C/min below 400 ˚C.

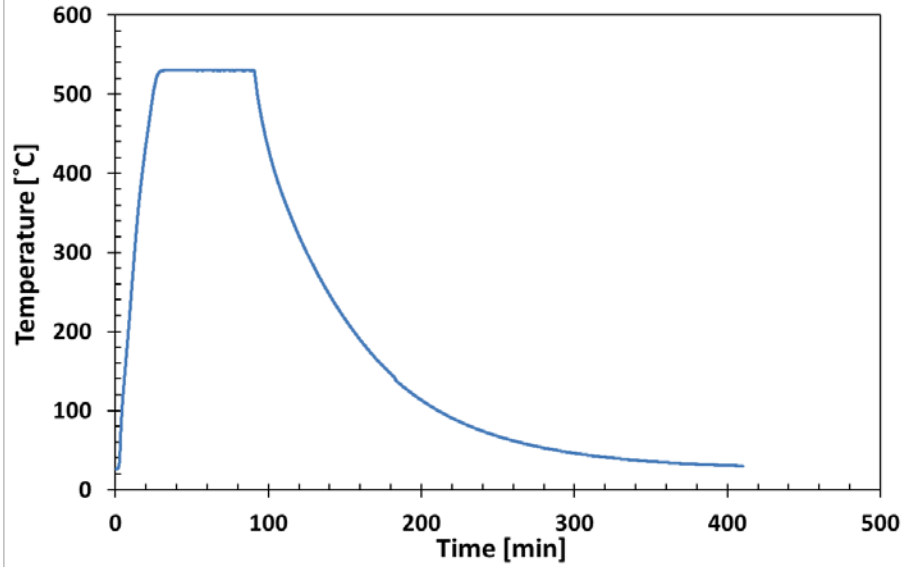

Figure 4-7 - Temperature vs time curve for annealing treatment at 530 ˚C

Since May 2013 the system made of the two pumps was replaced with a system made of a unique turbopump (HiPace) which allows reaching a vacuum level of $1x10^{-7}$ Torr in less time. The whole system is shown in Figure 4-8, where the ceramic tube is connected to the HiPace turbopump. Once annealed, the coupons are tensile tested at a speed of 2.3 - 2.5 µm/s.

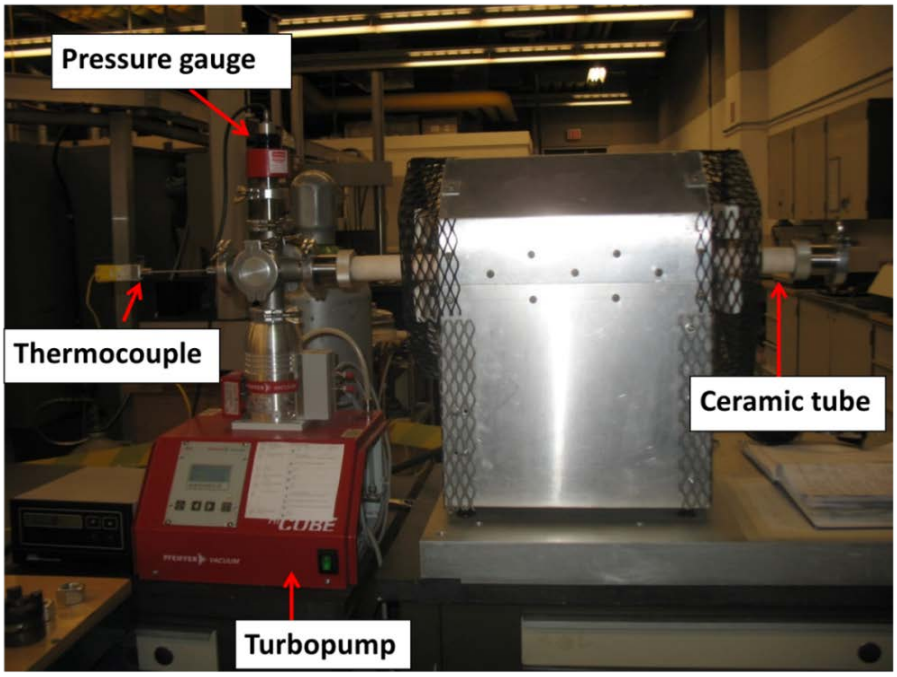

Figure 4-8 - Turbopump system for the high vacuum annealing at the University of Ottawa

4.3.2. Annealing Treatment in Argon

In order to perform this heat treatment, an argon gas cylinder is connected at one end of the alumina tube as shown in Figure 4-9 (a). The container with the specimens to be annealed is then placed at the center of the ceramic tube. The other end of the tube is connected to a cross which has multiple connections, one with a valve to the rough pump and the other with a valve that can vent the system. Before starting the flow of Argon, a rough vacuum of 10^{-3}-10^{-4} Torr is created inside the ceramic tube. When this vacuum is reached, the valve of the pump is closed and argon is allowed to flow through the system. In order to visually quantify the flow of argon, a bubbler was used. A picture of the whole system is shown in Figure 4-9 (a) and (b).

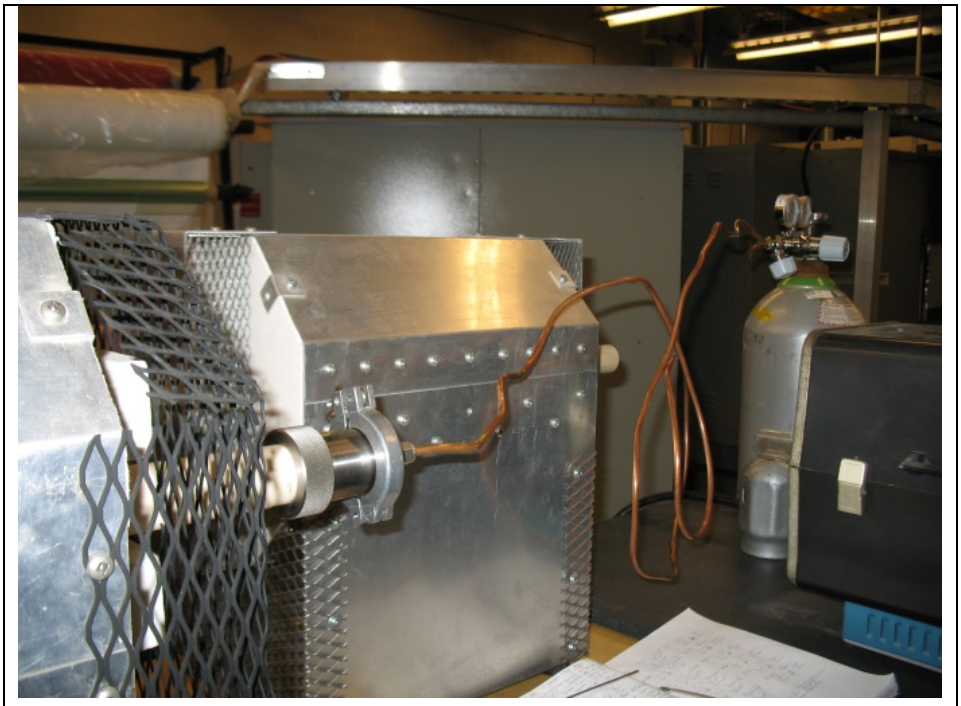

(a) Connection between ceramic tube and argon gas cylinder

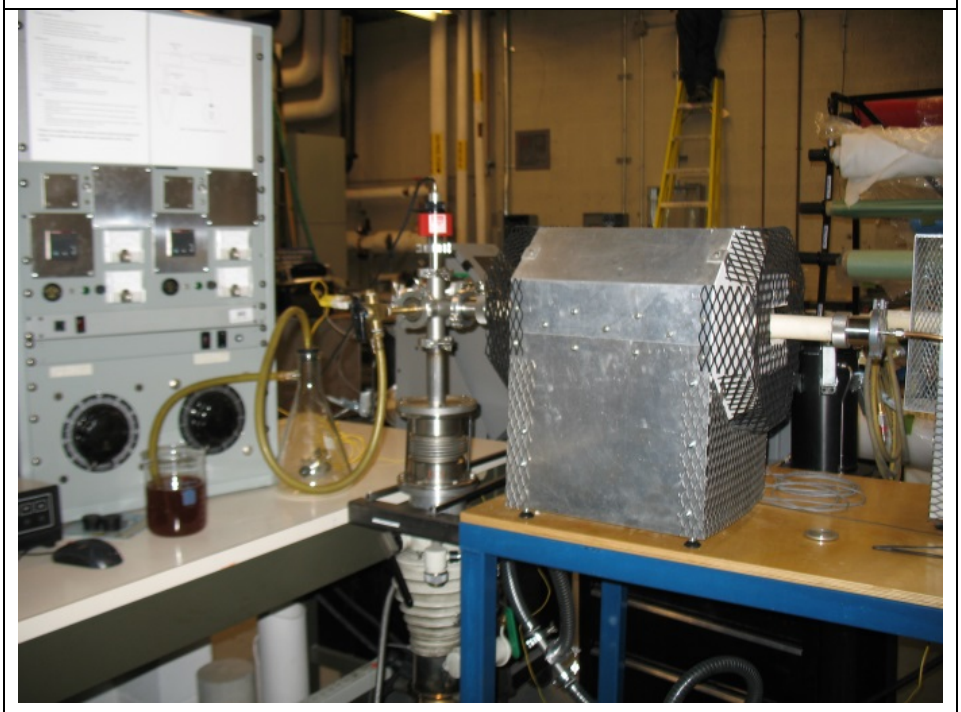

(b) Complete system to perform annealing in argon atmosphere

Figure 4-9 - System used to perform annealing in argon

The argon used for the annealing was argon grade 5.3 supplied by Linde and its composition was the following: H_2O<1 ppm, N_2<8 ppm, O_2<2 ppm, THC<0.5 ppm [137]

4.4. Polishing Procedure

Polishing is a fundamental process to prepare specimens that have to be used for metallographic analyses and to prepare surfaces that are indented to measure hardness. In this paragraph some general information about how polishing was performed are reported. As reported by Higgins [138], "for metallographic analyses to reveal the microstructure and for hardness it is important to have a surface which appears flat and scratch-free when placed under a microscope". If the specimen is difficult to hold on the polishing paper, it can be mounted using either cold mounting or hot mounting [138]. Both cold and hot mounting are based on polymerization reaction which produce a hard plastic which retains the piece of metal to be polished and analyzed. Cold mounting uses epoxy resin which can cure at room temperature if it is mixed with a certain amount of hardener, without the use of heat. This method is used when the heat necessary to harden the resin in the hot mounting would affect the microstructure of the specimen. The first part of surface preparation is called *grinding* because it uses very rough SiC paper (from 200 to 600 grit) to remove the resin on the top of the metal and water is flushed between the specimen and the SiC paper [138]. Lubrification with water is important to cool the surface of the polished specimen and to wash away the debris formed by the wearing process [138] - [139]. For rough grit, light pressure should be used during polishing since they can scratch deeply the surface of the specimen [138] - [139].

After the grinding step is performed using SiC paper and water, the polishing procedure continues using polishing clothes and diamond polishing solutions. Usually, these solutions are made of a suspension of diamond particles and are applied to the polishing pads to lubricate it [138]. The solutions are classified depending on the size of diamond particles dispersed in it and the sizes range from 9 μm until 0.05 μm. Below are some important factors to keep into account during grinding and polishing [138]:

- Cool down the surface of the specimen during grinding;
- Ensure cleanliness of the surface of the specimen at every step of the grinding;
- Apply low pressure during all steps of grinding and polishing.

According to another reference [139], grinding and polishing plastically deform a layer of the surface of the metal and the depth of this deformed layer depends both on material

properties and polishing conditions. In particular, the abrasion rate depends on hardness, on the work-hardening rate of the material to be polished and on the coefficient of friction created between the metallic surface and the polishing cloth or the SiC paper [139]. The full depth of the plastically deformed layer is never less than 50 times the depth of the surface scratches [139]. The depth of this deformed layer is inversely proportional to the hardness of the polished metal.

Cleaning of the specimen surface between every stage of polishing is very important to prevent carrying over of abrasives. The specimen can be cleaned using ultrasonic cleaning methods which are very efficient and reliable [139]. According to Samuels [139]: "after the cleaning it is very important to dry properly the surface to avoid the formation of stains"; one of the technique suggested in literature is based on washing the specimen under a stream of hot water, then rinsing it with a volatile solvent and finally drying it with an air blast" [139]. The solvent can be ethanol or acetone so it will not leave stains.

The polishing procedure used for the Gracos project is described here. If the specimen is cold mounted in resin, the first grinding is made using papers not rougher than 500grit SiC paper. The sequence of grinding starts with 500grit, then 1000grit, then 2400grit and finally 4000grit SiC paper. During each step, cold water is used as lubricant. Polishing papers with grit size above 4000grit SiC are used for less than 5 minutes, while the 4000grit SiC is used for 10 or even 20 minutes. As successive polishing steps, 3µm and after 1µm diamond polishing solutions are used, while the final step is made with OPS 0.05µm polishing solution or with OPU 0.05µm polishing solution. During this final stage, the solution is diluted with water. Between each step of grinding and polishing the specimen is cleaned in the ultrasonic bath for 5 minutes, and it is washed with ethanol and dried using an air blower.

4.5. Etching

Etching is used when grain size measurements have to be performed or when it is necessary to make metallographic investigation to know which microstructures are present in the specimen. Before being etched, the specimen has to be properly polished removing the plastically deformed layer and scratches. Moreover, the specimen must be absolutely clean; otherwise it will stain during etching. Once it has been properly cleaned, the specimen is etched by being plunged into the etching reagent and agitated for several seconds. It is then

rinsed in water to wash away the etching reagent. The etching solution and time depend on the microstructure that has to be revealed. Some alloys can be etched in a few seconds, while some stainless steels require up to 30 minutes to be properly etched. After etching and washing with water, the specimen is cleaned with ethanol and it must be dried evenly and quickly otherwise localized attack will appear [138]. The most well-known etching reagents for iron, steels and cast-irons are Nital and Picral. Nital is obtained mixing 2 cm^3 of nitric acid and 98 cm^3 of ethanol. Nital is able to etch pearlite, martensite, tempered martensite and bainite and it also attacks very well the grain boundaries of ferrite [138].

Picral is composed of 4 g of picric acid and 96 cm^3 of ethanol. It is very suitable for etching pearlite and spheroidized structures, but it does not attack the ferrite grain boundaries. It is used for completely ferritic cast irons [138].

4.6. Method used for Hardness Measurement

An important mechanical property, which is often measured and that is highly affected by changes in microstructure (or carbon diffusion in our case), is hardness. It is defined as resistance to localized plastic deformation. Hardness tests have a small indenter which is forced against the surface of a material. According to the definition reported by Callister [15] "the test is performed by applying a given load for a certain time for a given indenter geometry". The size of the indent is measured and from it the hardness value is calculated. Again, as specified by Callister [15] ,"if the material is soft, the indent will be big and deep and lower will be the hardness number, and vice versa if the material is hard". In our project, given the size of the carbon diffusion which takes place over distances at the microscale, microindentation hardness tests such as Vickers and Knoop are of particular interest.

4.6.1. Vickers and Knoop Microhardness Tests

For each test a very small diamond indenter having a pyramidal geometry is forced into the surface of the specimen. The applied loads can go from 1g to a maximum of 1 Kg. the resulting indent is observed under a microscope and the dimensions of its diagonals are measured. Details about how to calculate hardness in both cases are shown in Appendix A. The surface of the specimen that needs to be measured with microindentation has to be carefully prepared, so during every grinding and polishing step, the plastically damaged layer caused by the previous polishing step has to be removed. Vickers and Knoop are both

useful to measure the hardness of microscale regions and according to the manual of the indenter [140], “microhardness testing is appropriate for carburized materials to track hardness changes related to microstructural modifications of the hardness”.

Knoop test is more suitable to obtain the hardness of thin coatings and thin metal sheets since the depth of the indentation is smaller compared to Vickers. However Knoop is more sensitive to surface smoothness and to the surface finish of the specimen [140].

In order to verify that the carbon profile obtained experimentally by diffusion is close to the predicted profile, Knoop microhardness indentation has been performed. Knoop is preferred compared to Vickers because it has lower penetration depth, for this reason the carbon profile can be discerned more precisely. Hardness is first taken at the surface of the coated specimen once it has been annealed, then the piece of steel is polished to remove the FeC film using 0.05 µm OPS diamond solution. Once the coating is removed, another series of indents is performed, where 10 measurements are carried out with a 50 g load, 18 measurements are obtained by using the 100 g load and 15 measurements using the 200 g load. The material is then polished with 4000 SiC paper to remove approximately 10 µm of material, and it is polished with the 1 µm diamond polishing solution to remove 3 µm and finally polished with 0.05 µm OPS to remove another 7 µm before performing another series of indents. The procedure is repeated until the center of the material is reached. We found that this polishing procedure does not influence the hardness results if the Knoop hardness is taken at loads equal or higher than 100 g for 10 s. Before each polishing step, three reference indents are made on the piece of material and their change in shape is measured during polishing to measure the amount of material removed as shown in Figure 4-10.

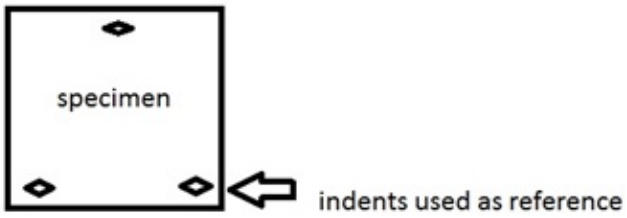

Figure 4-10 - Schematic view of reference indent used for Knoop hardness measurements

Before each polishing step, at least three reference indents are placed on the specimen and their depth is calculated by taking the dimension of the largest diagonal and dividing it by

30. The change in dimension that the diagonals undergo because of polishing is tracked periodically by using the optical microscope and the amount of material removed is calculated in the following way. Three indents are placed on the surface before polishing (they are called I_1, I_2, and I_3) and their depth is evaluated by dividing the main diagonal (d_1) by 30 as shown in Table 4-1. The dimension of the main diagonal is measured after polishing and the depth is again evaluated by dividing the length of the diagonal by 30. Once the depth of removed material is calculated for each diagonal, the average is calculated. According to Table 4-1 the material removed after the polishing procedure is (4.56+5.09+4.31)/3 = 4.65 µm. This approach is adopted to measure the material removed after each polishing step. Examples of pictures of the reference indents during each step of polishing are reported in Figure 4-11, Figure 4-12 and Figure 4-13.

Ref. indent	**Dim. main diagonal [µm]**	**Depth of the indent before polishing [µm]**	**Dim. main diagonal after polishing [µm]**	**Depth of the indent after polishing [µm]**	**Material removed [µm]**
I_1	289.796	(289.796/30) = 9.66	153.070	(153.070/30) = 5.10	(9.66-5.10) = 4.56
I_2	195.780	(195.780/30) = 6.53	43.216	(43.216/30) = 1.44	(6.53-1.44) = 5.09
I_3	231.710	(231.710/30) = 7.72	102.434	(102.434/30) = 3.41	(7.72-3.41) = 4.31

Table 4-1 - Calculation of the material removed during polishing with OPS diamond suspension for a piece of IF steel coated both sides with 500 nm FeC film and annealed at 430 ˚C - 1h in high vacuum

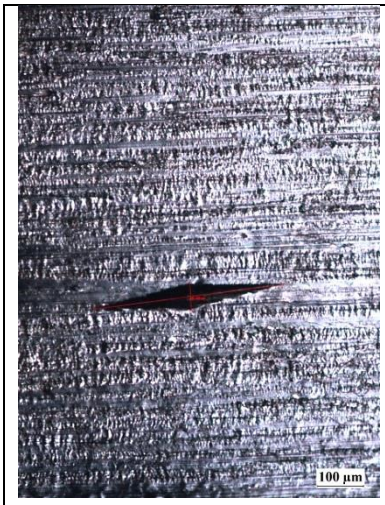		
Reference indent I_1 made on a not-polished surface	Reference indent I_2 made on a not-polished surface	Reference indent I_3 made on a not-polished surface

Figure 4-11 - Knoop reference indent made on the not-polished surface of a piece of IF steel strip coated both sides with 500 nm thick FeC film and annealed at 430 ˚C - 1h in high vacuum

Reference indent I_1 made on a surface polished using 4000SiC paper	Reference indent I_2 made on a surface polished using 4000SiC paper	Reference indent I_3 made on a surface polished using 4000SiC paper

Figure 4-12 - Knoop reference indent made on the surface of a piece of IF steel strip coated both sides with 500 nm thick FeC film and annealed at 430 ˚C - 1h in high vacuum, the surface has been polished using 4000SiC paper

	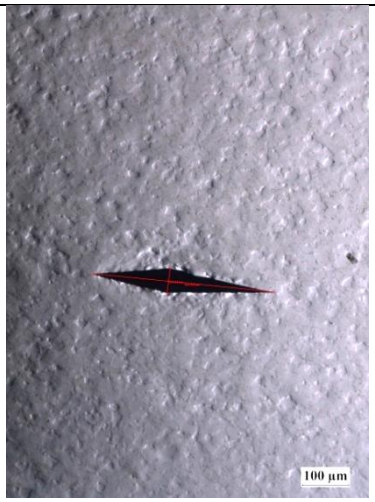	
Reference indent I_1 on a surface polished using 1µm diamond suspension and OPS	Reference indent I_2 made on a surface polished using 1µm diamond suspension and OPS	Reference indent I_3 made on a surface polished using 1µm diamond suspension and OPS

Figure 4-13 - Knoop reference indent made on the surface of a piece of IF steel strip coated both sides with 500 nm thick FeC film and annealed at 430 ˚C - 1h in high vacuum, the surface has been polished using 1 µm diamond suspension and OPS

4.6.2. Tensile Test

In the Gracos project, tensile tests are fundamental to assess changes in mechanical properties caused by carbon diffusion or by modification of the microstructure. In the following paragraph, the quantities and the information that can be obtained from a tensile test will be explained.

During a tensile test, the specimen is pulled only in the axial direction until fracture. A “dog bone” shape is used so that during testing, the deformation is confined in the central region (which has a uniform cross section along its length), and also to reduce the likelihood of fracture at the ends of the specimen [15]. During the test, the tensile machine elongates the specimen at a constant rate and the applied load and resulting elongation are instantaneously measured using a load cell and an extensometer. The output of a tensile test is load (usually in N) versus displacement (usually expressed in mm) and from these values the engineering stress and strain can be calculated. The engineering stress is defined as:

$$\sigma_{eng} = \frac{F}{A_0} \qquad \text{(eq. 4-1)}$$

where, F is the instantaneous load applied perpendicular to the cross-section of the specimen and A_0 is the original cross-sectional area before any load is applied. The engineering stress is usually expressed in MPa (N/mm^2) [15].

The engineering strain is defined as:

$$\varepsilon_{eng} = \frac{l_i - l_0}{l_0} = \frac{\Delta l}{l_0} \qquad \text{(eq. 4-2)}$$

where, l_i is the instantaneous length measured during the test, while l_0 is the initial gauge length of the tensile coupon.

If the engineering stress-strain curve is plotted, the first part is linear so that the stress is directly proportional to the applied strain according to the relation $\sigma = E\varepsilon$, where E is the elastic modulus or Young's modulus. For interstitial free steel the Young's modulus is 200-210 GPa. In the second part of the curve, plastic deformation occurs and the relation between engineering stress and strain is no longer linear. If the transition between elastic and plastic behaviour happens gradually, then the yield stress is evaluated following a convention. According to this procedure explained by Callister [15], "the yield stress is found constructing a straight line parallel to the elastic portion of the stress-strain curve at a strain offset of 0.002 and intersecting the engineering stress-strain curve". The stress corresponding to the intersection between this line and the engineering stress-strain curve is defined as the yield stress (σ_{ys}).

For specimens showing Lüders plateau, three values of yield stresses are usually indicated, the first one is the upper yield stress which is the starting of the plastic deformation ($\sigma_{YS\ Upper}$ in Figure 4-14) , the second one is the lower yield stress ($\sigma_{YS\ Lower}$ in Figure 4-14) , which is defined as the yield stress taken at the end of the Lüders plateau and finally an average of the stress in the plateau is also extracted (*AV* in Figure 4-14).

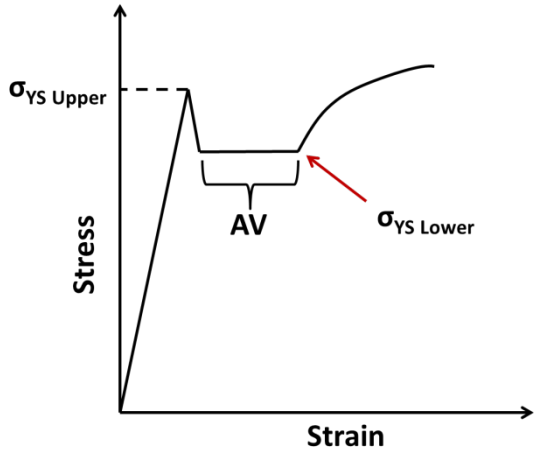

Figure 4-14 - Schematic view of an engineering stress-strain curve showing Lüdering

Once yielding has started, the stress necessary to continue plastic deformation in metals increases up to a maximum which is called ultimate tensile strength (UTS) and then the engineering stress decreases to the fracture point. "All the deformation up to the UTS is uniform along the gauge length, but at the UTS a small constriction or neck begins to form and all the subsequent deformation is localized at the neck until the fracture occurs" [56].

Instead of the engineering stress-strain curve, the true stress-strain curve provides a more accurate representation of the material behaviour. The true stress and the true strain are defined by taking into account the instantaneous change in geometry of the specimen during the tensile test. The true stress (σ_T) and the true strain (ε_T) are defined as [56]:

$$\sigma_T = \frac{F}{A_i} \qquad \varepsilon_T = \ln\left(\frac{l_i}{l_0}\right) \qquad \text{(eq. 4-3)}$$

where, F is the applied load, A_i is the instantaneous cross-sectional area (in the neck if the specimen is necking), l_i is the instantaneous length of the specimen while l_0 is the initial gauge length. If no volume change occurs during deformation, then $A_0 l_0 = A_i l_i$ and as a result the true strain can be also written as $\varepsilon_T = ln(A_0/A_i)$. Relations can be obtained between true stress and engineering stress and true strain and engineering strain. The relation between true stress and engineering stress and strain can be obtained as [56]:

$$\sigma_T = \left(\frac{F}{A_i}\right) = \left(\frac{F}{A_i}\right) \times \left(\frac{A_0}{A_0}\right) = \sigma_{eng} \times \left(\frac{A_0}{A_i}\right) = \sigma_{eng} \times \left(\frac{l_i}{l_0}\right)$$

Considering the definition of the engineering strain:

$\frac{l_i}{l_0} = (\varepsilon_{eng} + 1)$ and substituting this in the expression of the true stress, the following equation is obtained:

$$\sigma_T = \sigma_{eng} \times \left(\frac{l_i}{l_0}\right) = \sigma_{eng} \times (1 + \varepsilon_{eng}) \qquad \text{(eq. 4-4)}$$

The relation between the true strain and the engineering strain is given by the following expression:

$$\varepsilon_T = \ln\left(\frac{l_i}{l_0}\right) = \ln(1 + \varepsilon_{eng}) \qquad \text{(eq. 4-5)}$$

Eq. 4-4 and eq.4-5 are only valid until necking of the tensile coupon.

Another mechanical property that can be obtained from the engineering stress-strain curve is the ductility, which is a measure of the degree of plastic deformation that can be sustained by the specimen before fracture. Ductility can be expressed quantitatively either as percent of elongation or percent of reduction in area as shown by the following expressions [56]:

$$\%EL = \left(\frac{l_f - l_0}{l_0}\right) \times 100 \quad \%RA = \left(\frac{A_0 - A_f}{A_0}\right) \times 100 \qquad \text{(eq. 4-6)}$$

where, l_f is the fracture length, l_0 is the initial gauge length, A_0 is the initial cross-sectional area, A_f is the cross-sectional area at fracture.

In the Gracos project, two tensile machines have been used (see Figure 4-15 and Figure 4-16). For both of them the strain rate used was 5×10^{-4} s^{-1}. Details of the calibration of the tensile machine shown in Figure 4-15 are reported in Appendix D (section D.1). The same calibration procedure was applied also for the tensile machine shown in Figure 4-16.

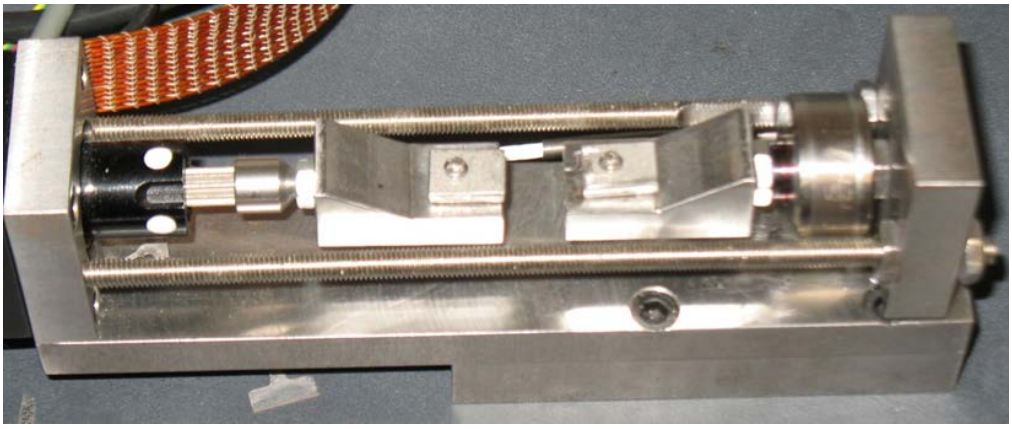

Figure 4-15 - First tensile machine used for Gracos project

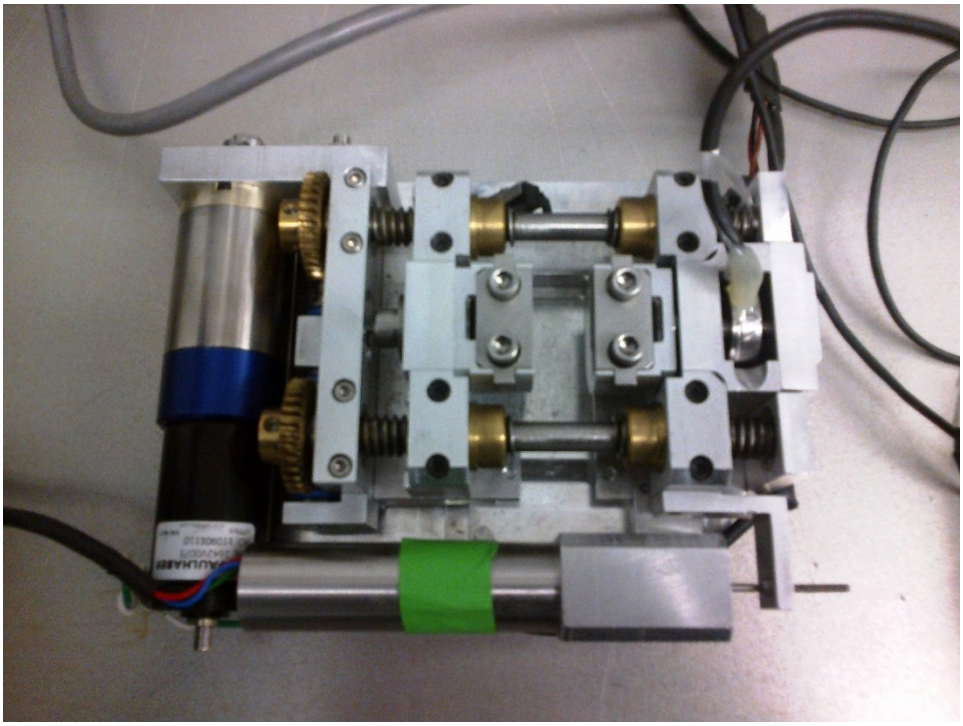

Figure 4-16 - Another tensile machine used for tensile tests of the Gracos Project

4.7. Methods used for Lüders Bands Analyses: Digital Image Correlation

Once carbon has diffused into the IF steel, it is expected that the tensile coupons will show Lüdering since some of the diffused carbon will pin the dislocations present in the material causing the appearance of the plastic instability. The speed and pattern of the bands can be experimentally detected using Digital Image Correlation (DIC). “Digital Image Correlation is an optical technique which measures displacement and strain fields on a surface of a deforming specimen” [141]. “This technique is particularly useful to study non-uniformity in the local strain due to the presence of grain boundaries, or inclusions or to the presence of holes and crack tips” [142]. “DIC uses a camera or an optical microscope to record digital images of both undeformed and deformed surfaces of the specimen. The pictures are digitized assigning a light intensity to each pixel using a scale of gray where 0 corresponds to black while 255 corresponds to white” [142]. The digitized images have to be related using a correlation algorithm. First of all, the image of the undeformed state is subdivided into subsets and each subset contains a certain number of pixels which represent a certain

level of gray. Successively, the coordinate of the center of these subsets are defined and in order to calculate the local displacement at the surface of the material, the DIC matches the subsets of each image by recognition of the gray level distribution [141]. In particular, in order to quantify the degree of gray similarity of the same subset between one image and the other, a correlation coefficient is defined. The equation of this correlation coefficient is given below.

$$C_L\left(u, v, \frac{\partial u}{\partial r}, \frac{\partial u}{\partial s}, \frac{\partial v}{\partial r}, \frac{\partial v}{\partial s}\right) = 1 - \frac{\sum_{i=1}^{i=N}\sum_{j=1}^{j=M} I_u\left(r_i, s_j\right) * I_d\left(r_i + u_L; s_j + v_L\right)}{\sqrt{\sum_{i=1}^{i=N}\sum_{j=1}^{j=M} I_u^2\left(r_i, s_j\right) * \sum_{i=1}^{i=N}\sum_{j=1}^{j=M} I_d^2\left(r_i + u_L; s_j + v_L\right)}} \quad \text{(eq. 4-7)}$$

where u_L and v_L are defined as:

$$u_L = u + \frac{\partial u}{\partial r}\left(r_L - r_C\right) + \frac{\partial u}{\partial s}\left(s_L - s_C\right) \quad \text{(eq. 4-8)}$$

$$v_L = v + \frac{\partial v}{\partial r}\left(r_L - r_C\right) + \frac{\partial v}{\partial s}\left(s_L - s_C\right) \quad \text{(eq. 4-9)}$$

where u and v are the displacements of a subset's centerpoint located at coordinate (r_C, s_C) and u_L and v_L are the displacements of an arbitrary point (r_L, s_L) within the subset. I_u and I_d are the subset intensity patterns taken from the undeformed and deformed image respectively [142]. The cross-correlation coefficient is minimized to estimate the center displacements u and v for each subset. From this procedure displacement vectors are obtained and are used to calculate strains ε_{xx}, ε_{yy}, γ_{xy}.

In order to follow the deformation at the macroscale during the test, the surface of the specimen has to be prepared by depositing speckles of ink using an air-brush. Once the pattern of ink-speckles has been applied (see Figure 4-17) a camera is used to take pictures every 2 seconds during the tensile test. The pictures are successively loaded in the "Davis" software from "LaVision" which discretizes each image in smaller subsection each one containing a certain amount of speckles [143]. The displacement of the speckles for each subsection is followed for each picture to calculate the displacements vectors.

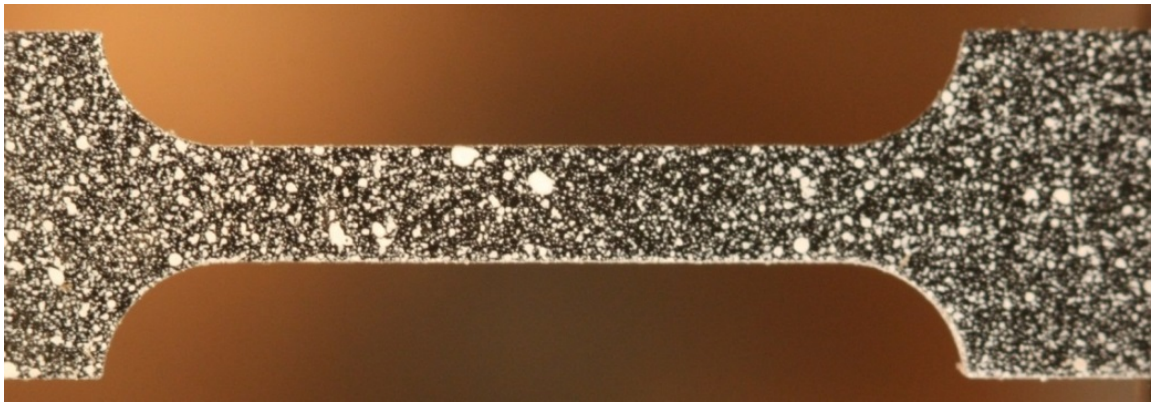

Figure 4-17 - Surface of a Gracos coupon prepared for DIC testing

According to literature, the type of speckle pattern can influence strongly the accuracy of strain measurements. For example, speckles created spraying powder on the specimen surface underestimate the strain for large deformations because the particles of powder are not adherent to the surface of the deforming specimen. If large deformation have to be followed using DIC, then it is better to apply painted speckle pattern which are very adherent to the specimen and that can follow the deformation of its surface. However, for strains lower than 10% both powders and painted speckle can be acceptable and the type of speckle pattern does not influence the strain measurements [141]. Other researchers use titanium powders (average diameter 5 µm) mixed with plastic liquid (Collodion, 2% in amylacetate), which is then applied to the specimen surface. When the liquid is dried, a plastic film with random pattern of powders is left on the specimen surface. This film is very flexible and very adherent to the surface while the density of particle distribution can be controlled by changing the density of particles inside the liquid [142].

From the DIC results it is possible to measure speed and inclination of the Lüders bands and the kinking caused by their propagation and to clearly correlate it with the features found in the Lüders plateau during the tensile test. For the Gracos coupons the surface is first polished with 0.05 µm OPS to remove the FeC film and then it is uniformly painted with a layer of black ink and then white ink speckles are sprayed on it. It is very important to have good adhesion between the ink coating and the specimen during the whole tensile test otherwise deformation will not be measured accurately.

Another technique used to study Lüdering is finite element methods. Lüders bands nucleation and the influence of stiffness, strain hardening behaviour and void pattern on bands propagation can be modelled at the macroscale using the FEM code ABAQUS.

However, it is not possible to easily model the plastic instability seen in the experimental stress-strain curves, using the procedure described in [131]. This happens because there is no clear relationship between Lüders strain and carbon content if the carbon amount is lower than 0.15 mass% [83], while upper yield stress and UTS can clearly be related to carbon content. For this reason, it might be difficult to create a model in ABAQUS to predict exactly the stress-strain curve obtained experimentally for this project.

4.8. Scanning Electron Microscopy and Transmission Electron Microscopy

After a tensile test, the cross-section area of the tensile coupon is observed to calculate the reduction in area and to evaluate the ductility of the specimen. Scanning Electron Microscopy (SEM) is used to take a sequence of pictures of the fracture surface as shown Figure 4-18. The area of the cross-section is calculated using the open source software ImageJ [144], [145].

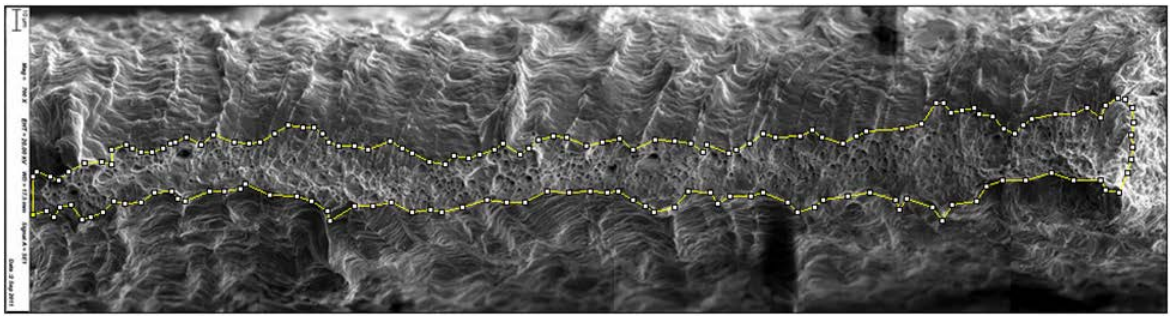

Figure 4-18 - Fracture surface of specimen annealed in high vacuum at 430 ˚C - 1h

Scanning electron microscopy (SEM) is also used to look at the surface of the specimen to see if the film is still adherent to the IF core after the tensile test. Energy dispersive x-ray spectrometry (EDS) was used to characterize carbide particles found in dimples of the fracture surface. EDS allows performing a qualitative x-ray analysis to determine the composition of one precipitate.

Another analysis which can be performed using a SEM is electron-backscattered diffraction (EBSD). This technique is particularly useful when the phases which compose a microstructure have to be identified. EBSD in the SEM is used for two main purposes [146]:

- The measurement of individual orientations in a grain giving information about the local microtexture;
- Identification of micrometer or submicrometer crystalline phases.

In the Gracos project, EBSD was performed on specimens which have been annealed using an induction heating treatment. In these specimens a mixture of ferrite and austenite is thought to be present in the microstructure and to fully characterize the microstructure it is necessary to evaluate the volume fraction of the two phases.

In order to better image the interface between the IF core and the as-deposited FeC film, Transmission Electron Microscopy (TEM) was used. TEM allowed not only for better imaging but also to follow the in-situ crystallization of the FeC film upon annealing. TEM analyses were carried out at the University of Rouen and at INSA-Lyon.

4.9. Method used for evaluating carbon concentration

4.9.1. Atom Probe Tomography (APT)

Atom probe tomography (APT), which is an atom probe microscopy technique (APM), provides three-dimensional mapping of materials at atomic-scale resolution and it can give information about chemical composition and the atomic structure of matter [147] [148]. The detection range of APT in terms of concentrations goes from 1 ppm up to 1% while its spatial resolution goes from 30 pm to 100 nm [148]. Figure 4-19 summarizes some typical applications of APT which include:

- Revealing details of atomic architecture within solid solutions;
- Characterizing gradient in chemical composition within and between second phase precipitate particles and the host matrix;
- Texture mapping.

Atom probe tomography was used in the Gracos project to measure the amount of carbon into the IF steel for specimens annealed at 530 ˚C - 1h and to understand the different behaviour obtained for specimens annealed at 710 ˚C - 1h. The experiments in the Gracos project were performed by the author in collaboration with Dr. Amélie Fillon and Professor X. Sauvage at the Université de Rouen (France).

The technique consist in applying a high difference of voltage between a sharp tip of the material that needs to be analyzed and an electrode. The voltage signal was pulsed at 30 kHz

for the ECOWATAP system. ECOWATAP is the name with which the wide angle atom probe is indicated at the Université de Rouen. The pulse of the voltage has to be properly set to ensure that enough electric field is created at the tip to cause evaporation of atoms.

Once an atom is evaporated, it is accelerated towards a detector. When the atom hits the detector, the coordinates of the impact is recorded. The type of atom is determined by its mass to charge ratio, which is related to the time of flight and to the distance between tip and detector by the following equation:

$$M = \frac{m}{n} = \frac{2eV}{v^2} = 2eV * \left(\frac{ToF}{L}\right)^2 \qquad \text{(eq. 4-10)}$$

where, m is the atomic mass of the ion, n is its charge, v is its velocity, "e" the charge of the electron and V is the total voltage applied to trigger the evaporation. The velocity "v" of the ion can be calculated as the distance between the tip of the analyzed material and detector (L) divided by the time of flight (ToF). From the time of flight a mass to ratio spectrum is obtained.

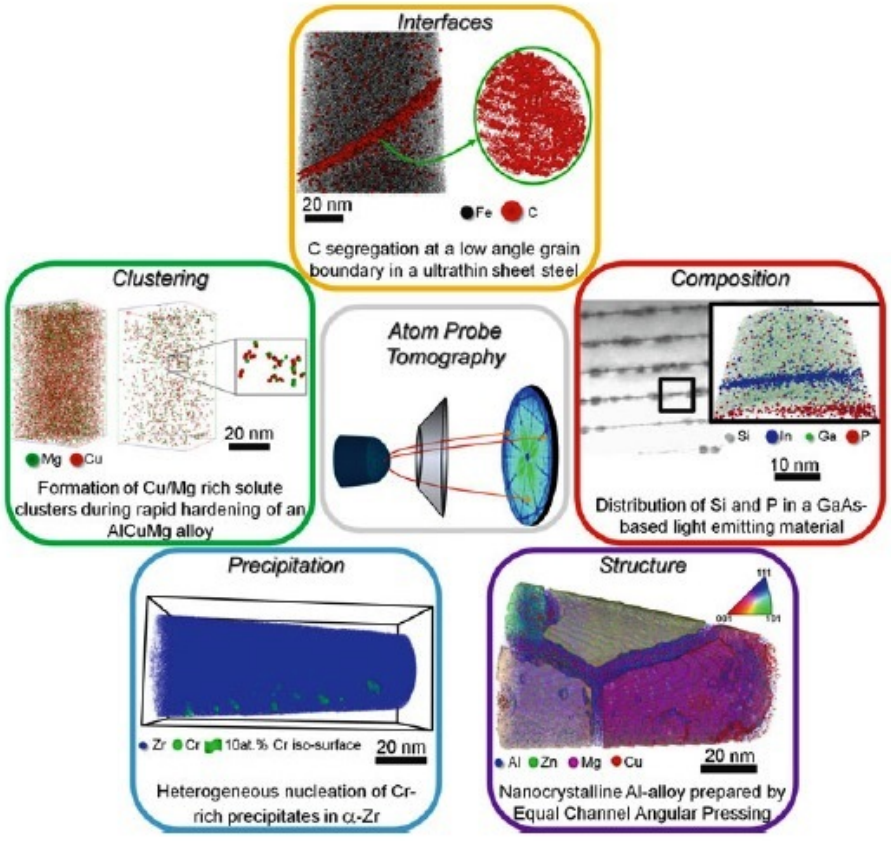

Figure 4-19 - Examples of applications in Atom Probe Tomography (APT) **[148]**

The analyses of the mass to ratio spectra and the 3D volume reconstruction were performed using the GPM 3d Software developed at the Université de Rouen. In particular, before identifying the peaks of the different elements, it is important to shift the spectrum so that the peak of hydrogen is at 1 and in our case the peak of iron (which is the main element) is placed at a mass to charge ratio (*m/n*) of 28 as expected. The position of the main peak of iron is adjusted to be at 28 by modifying the flight length (i.e. the actual distance which was covered by the evaporated atom). After the main peak is set in proper position, then the peak of hydrogen has to be checked, if it is not at 1, then it is necessary to modify the "t_0 value", which indicates the starting time of the evaporation of the atoms. Once the mass to ratio spectra has been properly adjusted, the identification of the atomic species can be performed. In Figure 4-20 the two main peaks of iron are shown, while Figure 4-21 and Figure 4-22 show other zones of the mass to charge spectrum for a specimen coated both sides with 500 nm FeC film and annealed at 530 ˚C - 1h in high vacuum. The evaporated species include several elements. The isotopes of aluminium, phosphor, nitrogen and titanium come from the IF substrate while the carbon is mainly due to the diffusion from the FeC film. More detailed results from different specimens will be shown in Chapter 5.

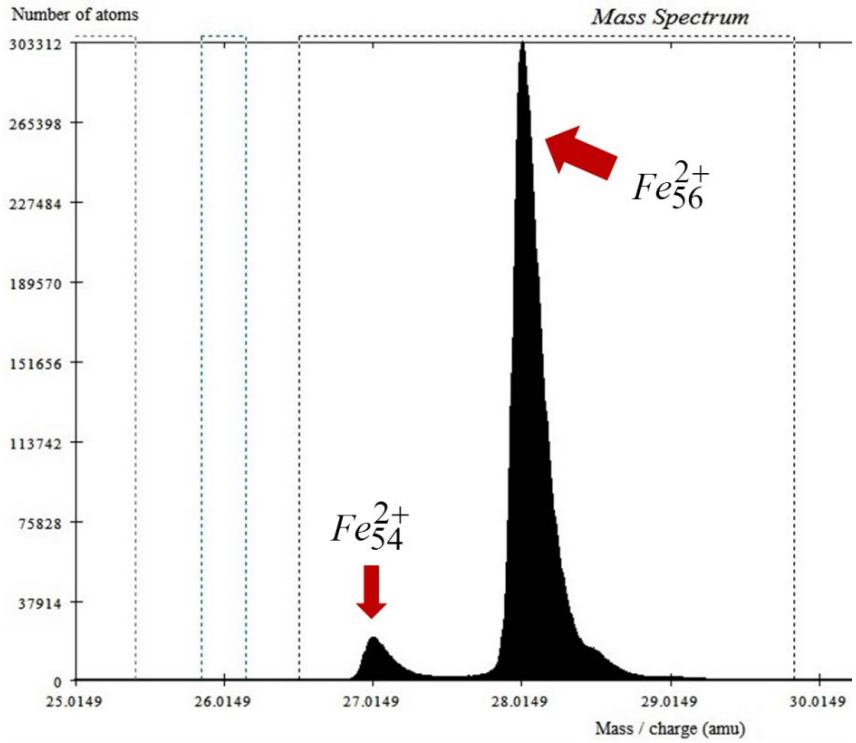

Figure 4-20 - Main peaks of iron isotopes obtained from APT of an IF steel sample coated both sides with 500 nm FeC film and annealed at 530 ˚C – 1h in high vacuum

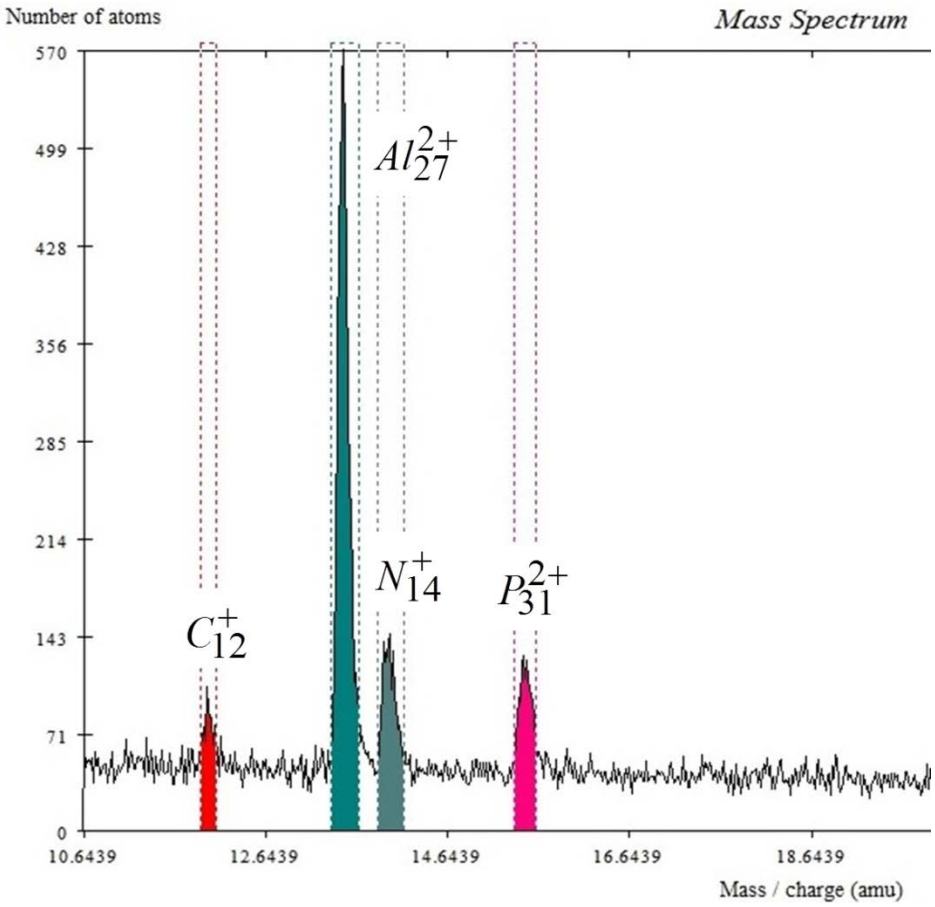

Figure 4-21 - Peaks of isotopes found in an IF steel sample coated both sides with 500 nm FeC film and annealed at 530 ˚C – 1h in high vacuum

Once the intervals of the isotopes for the different elements have been identified, the GPM software gives automatically the concentrations of the elements in at%, however, from the given concentration, it is necessary to subtract the noise. Once the noise has been removed, true concentration of the chemical species is obtained. More details regarding APT and techniques used for specimen preparation are included in Appendix B.

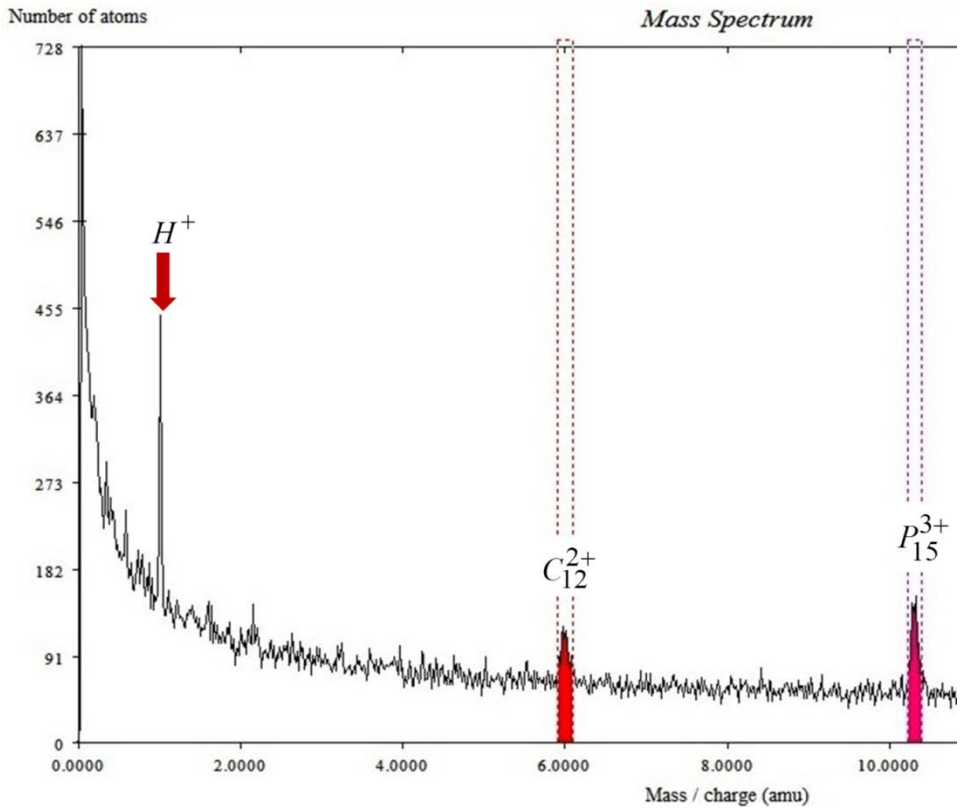

Figure 4-22 - Peak of hydrogen for an IF steel sample coated both sides with 500 nm FeC film and annealed at 530 ˚C – 1h in high vacuum

4.9.2. Thermo Electric Power Measurements (TEP)

While atom probe tomography can give a confirmation of the different carbon concentration at the interface and in the core of the sheet and can provide composition measurements of precipitates at nanometric scale; thermo electrical power (TEP) measurements can be used to confirm the amount of carbon which diffuses at dislocations into the whole IF sheet.

This technique is based on the measurement of the thermoelectric power, which is calculated by detecting the induced thermoelectric voltage caused by the application of a temperature difference across the material [149]. A schematic view of the setup of the experiments is shown in Figure 4-23 and it consists in pressing the metallic sample between two blocks of a reference metal (usually pure copper) [150]. One of the blocks is set at 15 ˚C while the other block is at 25 ˚C so that a slight difference of temperature is created across the specimen. This temperature difference will result in a voltage difference at the contacts between the specimen and the blocks (B segments in Figure 4-23) as result of the Seebeck effect [150].

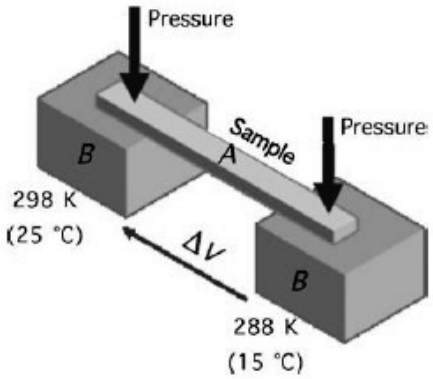

Figure 4-23 - Principle of the TEP measurements [149]

The TEP (S_{AB}) of the circuit B/A/B shown in Figure 4-23 is defined as the ratio between the difference of voltage (ΔV) over the applied difference of temperature (ΔT). However S_{AB} is the relative TEP value of metal A with respect to metal B and it is equal to the difference between the absolute TEP of both metals (S_A^* and S_B^*) [149].

$$S_{AB} = \left(S_A^* - S_B^*\right) = \frac{\Delta V}{\Delta T} \qquad \text{(eq. 4-11)}$$

A procedure to evaluate the concentration of interstitial atoms (carbon) in a ferrite matrix is described in detail in [32]. This procedure is schematically shown in Figure 4-24 and it is made by two steps. The first step consists in cold-working the material to introduce a sufficient density of dislocations to trap all the interstitial solutes. After this step, the TEP variation of the cold rolled specimen is measured compared to the initial state of the material. The second step involves a static strain ageing treatment of 30 min at 120 ˚C which will cause the segregation of all the interstitial atoms to the dislocations [31]- [32]. The TEP variation between the cold-rolled state and the aged state is then measured to assess the concentration of interstitial elements [32]. This protocol was also used to measure the interstitial carbon content in the Gracos specimens. The measurements were performed by Dr. Jean-Louis Uriarte at the ArcelorMittal Research Center in Maizières. The initial TEP state of the specimens was first assessed, followed by a 70% cold rolling. During this stage, dislocations are introduced in the material which will be used later to pin the solute atoms.

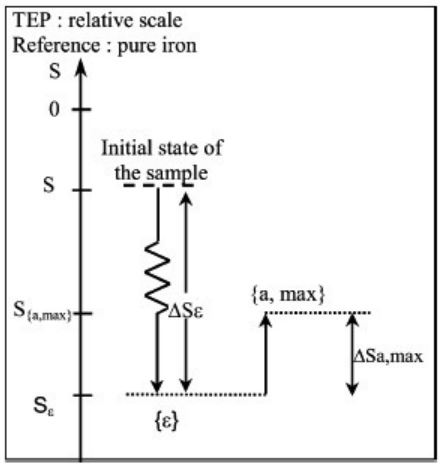

Figure 4-24 - Experimental procedure used for the quantitative evaluation of the amount of interstitial atoms in solid solution using TEP measurements [32]

The percentage of cold working is established in order to achieve a saturation stage. For our specimens, the value of 70% was used because this value ensures saturation for ultra-low carbon steels (ULC) and for this reason it is considered acceptable also for our specimens. After cold rolling, lower TEP values are measured, due to the introduction of fresh dislocations (ΔS_ε) in Figure 4-24. A thermal treatment is then performed in order to pin the dislocations with the solute carbon atoms. The time and temperature of the heat treatment have to be chosen in order to ensure no recovery of dislocations is taking place. From ageing experiments it is known that in order to diffuse carbon atoms at dislocations, a heat treatment at 120 ˚C for 30 minutes is sufficient to ensure saturation of dislocations and to avoid precipitation. After the heat treatment, the TEP values increase compared to the value measured after cold rolling. In Figure 4-24, the TEP measured after the treatment is indicated as ($\Delta S_{a,\,max}$).

The percentage of carbon in solid solution can then be calculated as:

$$[C_{ss}(TEP)](wt\%) = \frac{\Delta S_{a,\max}}{|P_C|} \qquad \text{(eq. 4-12)}$$

The proportionality factor P_C is calculated as:

$$|P_C| = \frac{\alpha_C \cdot S_C}{\rho} \qquad \text{(eq. 4-13)}$$

where, α_C and S_C are the specific resistivity and the specific TEP of carbon in solution of the pure metal, whilst ρ is the resistivity of the material [151]. The value of P_C for our interstitial

free steel was evaluated knowing that a mild steel used as reference has a resistivity of 11.41 μΩ cm and that its P_c is 45 μV/(K wt%) [151]. The resistivity of our steel was calculated based on the composition of the steel by using the following equation:

$$\rho = 9.9 + 6\cdot[Mn] + 12\cdot[Si] + 14\cdot[P] - 10\cdot[S] + 2.9\cdot[Ni] + 5.5\cdot[Cr] + \\ + 2.8\cdot[Mo] + 6.4\cdot[Ti] + 3.9\cdot[Cu] + 13\cdot[Al] \quad \text{(eq. 4-14)}$$

A similar equation with less element in solid solution is reported in ref. [151]. The value obtained for the resistivity of the IF steel used in the Gracos project was 10.66 μΩ cm, so the P_C for the studied IF steel will be:

$$P_{C_{IFsteel}} = \left(\frac{45\times 11.41}{10.66}\right) = 48\mu V/(Kwt\%) \quad \text{(eq. 4-15)}$$

Further details are given in Appendix C, while the list of tested specimens and the results of the measured carbon concentration are reported in Chapter 5. Once P_C is known, the concentration of carbon in solid solution can by evaluated using (eq. 4-14). The value of concentration is expressed in mass ppm. To obtain the total concentration of carbon a value of 12.6 ppm in mass was added since this carbon was calculated to be in interaction with manganese according to the following formula:

$$[C] = 1.6873\cdot(Mn)^{0.4269} \quad \text{(eq. 4-16)}$$

where, *Mn* is the manganese concentration in the IF steel expressed as (wt%) x 1000.

Chapter 5 : Experimental Results of Diffusion from FeC Films

5.1. Simulation of carbon diffusion through thickness

For the Gracos Project, diffusion of carbon atoms will take place in ferrite where the solubility limit is 0.022 wt% (corresponding to 0.1 at%) at 727 ˚C [152]. Diffusion problems are described by Fick's laws. For the modelling of the diffusion of carbon from the PVD film into the core of interstitial free steel, the expression of the general solution to the second Fick's law was used and proper boundary conditions were set. A first approximation is that diffusion was assumed to happen only in one direction (called *y*). The solution has the following expression [16]:

$$\frac{C(y,t)-C_S}{C_i-C_S}=\frac{4}{\pi}\sum_{n=0}^{+\infty}\left(\frac{(-1)^{n+1}}{2n+1}\right)\cos\left(\frac{2n+1}{2}\pi\frac{y}{L}\right)e^{\left(-\left(\frac{2n+1}{2}\frac{\pi}{L}\right)^2 Dt\right)} \qquad \text{(eq. 5-1)}$$

where:

$C(y,t)$ is the concentration at position y at time t;

C_S is concentration at the surface;

C_i is concentration in the IF steel core;

D is diffusion coefficient;

L is total length along which diffusion occurs;

The initial concentration of carbon inside the deposited coating is 30 at% while the initial carbon concentration inside the IF steel is close to zero. Moreover, the concentration of the film will be supposed constant during the diffusion process. This approximation is considered acceptable given that the carbon concentration inside the film is much higher than the solubility limit of carbon in alpha iron which is 0.022 wt% (corresponding to 0.1 at %) at 727 ˚C according to the Fe-Fe_3C equilibrium phase diagram [152]. Based on these considerations, the boundary conditions can be stated as follows:

- $C_S = C_{ss}$, where C_{ss} is the solubility limit of carbon into ferrite for the chosen annealing temperature for $0 < t < +\infty$. The solubility limit used for the carbon diffusion model was the one obtained from the Fe-Fe_3C equilibrium phase diagram; however, here ferrite is

in equilibrium with an amorphous FeC film, so the solvus could be different. On the other hand, the nucleation of Fe_3C at the interface between amorphous film and substrate is equally possible, justifying the use of the solubility limit of carbon into ferrite obtained from the Fe-Fe_3C equilibrium phase diagram.

- $C_i = 0$ for $t = 0$ and -100 µm < x < 100 µm;

A Matlab program, which solves equation 5-1, was written and once the carbon amount through thickness is known, the expected increase of yield strength can be estimated using the following equation:

$$\Delta\sigma = Mm\sqrt{X_C} \qquad \text{(eq. 5-2)}$$

where, according to the work of Scott et al. [27], [153], M is the Taylor factor equal to 2.5, m is equal to 0.051μ where μ is the shear modulus of iron equal to 82 GPa and X_c is the atomic carbon concentration diffused in the steel. The calculated value for the increase in yield strength can be directly compared with the value obtained from tensile tests to see if the theoretical diffusion model is able to predict correctly the diffusion process.

As a first approximation, it is supposed that the criterion limiting carbon diffusion is its solubility limit in ferrite which is described by eq. 2-6 used by Rebischung and Scott [27]. Moreover, the carbon concentration in the FeC film is not supposed to change since its starting concentration is 30 at% which is higher than the carbon solubility into ferrite at every tested temperature. The diffusion coefficient to be used for diffusion is given by the relation D = 0.0062exp(-80350/(RT)) [cm^2/s] used also by Rebischung and Scott [27]. A Matlab program was written to simulate the 1D diffusion of carbon for isothermal treatments at 330 ˚C, 430 ˚C, 530 ˚C, 630 ˚C, 710 ˚C for 1h. The results are shown in Figure 5-1. It is evident that with increasing temperature, more carbon is expected to diffuse, but what is more important is that the carbon profile through thickness is also expected to change depending on the annealing temperature. Temperatures of 330 ˚C and 430 ˚C show graded carbon profiles, while temperatures of 530 ˚C, 630 ˚C and 710 ˚C show uniform carbon profiles. It will be shown later in the next chapter that tailoring the carbon profile could be particularly important to reach good mechanical properties keeping into account the limitation of plastic instability such as Lüders plateau.

The graph shown in Figure 5-1 is taking into account the diffusion caused by both heating and cooling ramps which are present during the heat treatment performed in the high vacuum furnace as shown in Figure 4-6. The heating rate is 12 ˚C/min, and the cooling rate is 12 ˚C/min initially when the temperature is high (from the isothermal plateau down to 400 ºC) and it then falls to 3 ˚C/min when the temperature is below 400 ˚C.

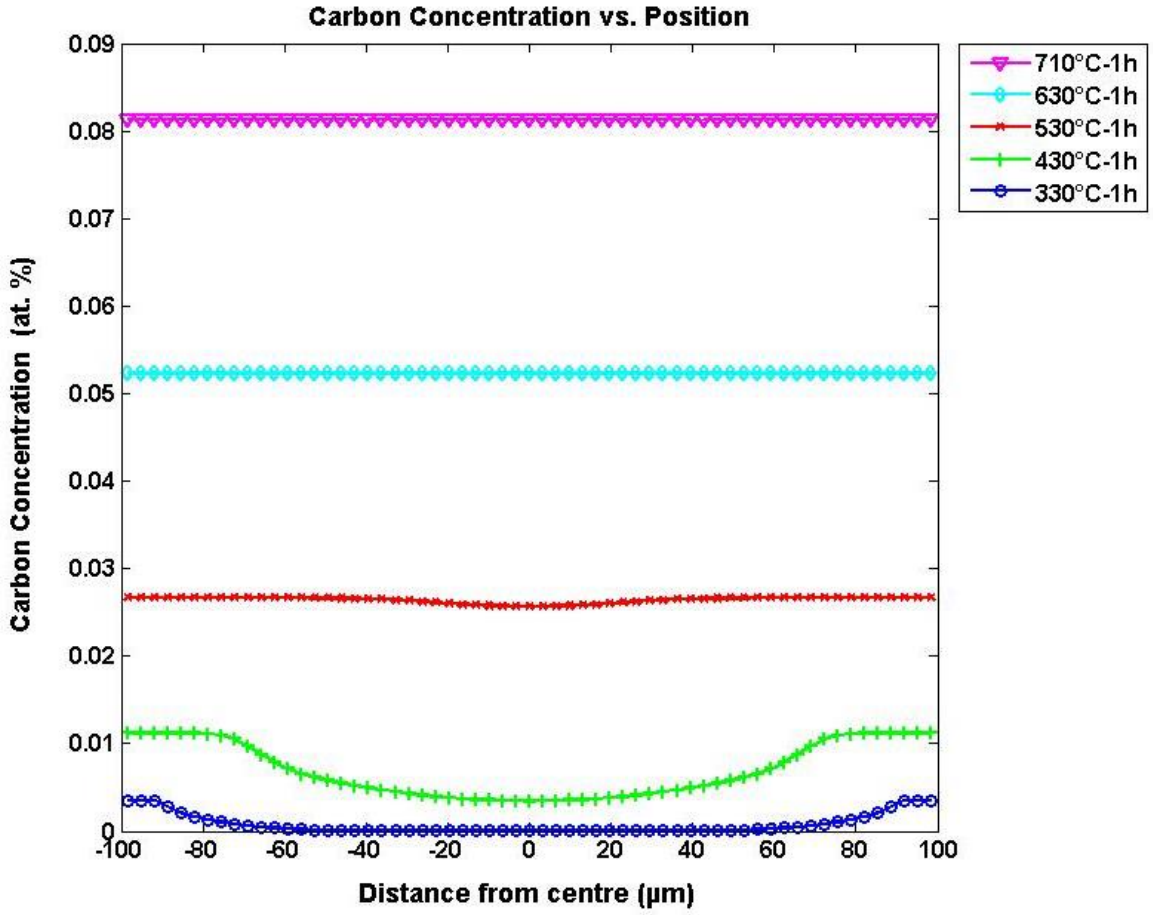

Figure 5-1 - Carbon profile through thickness predicted by the solution of the second Fick's law considering heating and cooling stages with isothermal plateau: in the x axis the position through thickness is reported, where 0 indicates the center of the coupon, while in the y axis the carbon concentration is shown in at%

From Figure 5-1 it is evident that the diffusion caused by the heating and cooling ramp is causing flattening of the profiles close to the coated sides. This is less evident for the profiles obtained for temperatures higher or equal to 530 ˚C - 1h since they will cause a uniform carbon concentration through thickness; however, for annealing at 330 ˚C - 1h and 430 ˚C - 1h, heating and cooling ramps cause a flattening of the carbon profile close to the interface

between coating and IF substrate. One technique to verify experimentally the predicted profiles is to perform hardness through thickness for coupons annealed at different temperatures. The results are shown in the next section.

5.2. Hardness Measurements

In section 5.1, the carbon profiles, which are expected as a consequence of diffusion during isothermal heat treatment in high vacuum for different temperatures, have been presented. In order to verify whether these profiles are indeed obtained experimentally, Knoop hardness was performed on pieces of strip of IF steel which were coated both sides with a 500 nm thick FeC amorphous film and annealed in high vacuum. The hardness was measured only on pieces of strips annealed in high vacuum at 430 ˚C, 530 ˚C, 630 ˚C and 710 ˚C for 1h. The temperature of 330 ˚C - 1h was avoided since the diffusion of carbon at this temperature is not significant and according to the results obtained from tensile tests, it will be shown that no difference in mechanical properties can be discerned compared to a coated and not-annealed IF steel. The procedure of polishing and indentation followed to obtain the measurements has been explained in section 4.6.1 The best results were obtained for loads equal or higher than 100 g applied for 10s since there is no influence from the polishing and the standard deviation for each measurement is reasonably low. The profiles found for the different temperatures are summarized in Figure 5-2. The highest value of hardness is found at the surface of the coated specimens when the film has not been removed by polishing. Moreover, from Figure 5-2 it is clear that the hardness of the coated surface increases as the annealing temperature is raised above 500 ˚C, proving that the FeC amorphous film is also transforming during the heat treatment. In fact, the hardness of the surface at temperatures higher or equal to 530 ˚C is higher than the value found for specimens annealed at 430 ˚C. The hardness of the coated and annealed strips was compared with the hardness of an uncoated IF steel annealed at 530 ˚C - 1h in high vacuum. The annealing of the uncoated IF steel was done to remove the effect of the skin pass in the first 10 μm below the surface.

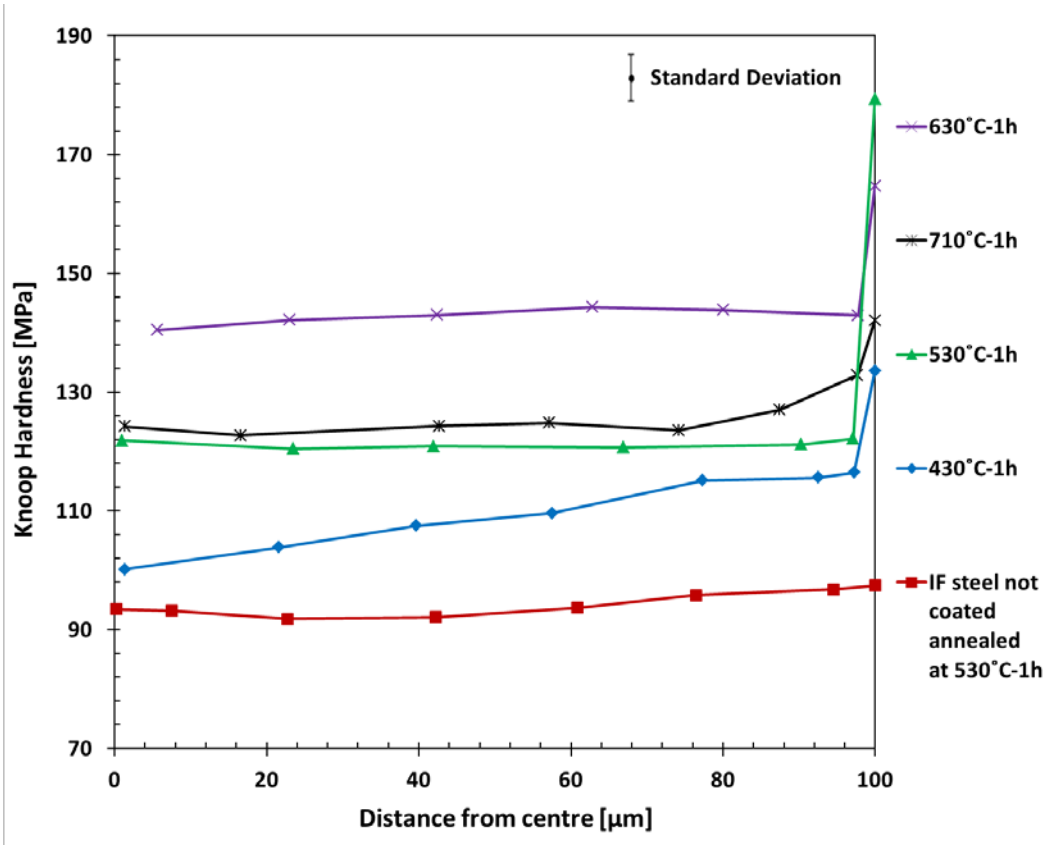

Figure 5-2 - Knoop Hardness profile through thickness of IF steel coated both sides with 500 nm thick FeC film and annealed in high vacuum at different temperatures. The Knoop values have been obtained applying a load of 100g for 10s. In the X axis thedistance from the centre is reported, while the Y axis shows the Knoop hardness values. In the X axis, 0 µm corresponds to the centre of the specimen, while the value of 100 µm corresponds to the coated surface if the IF steel

From the plot it is evident that the hardness increases as the isothermal annealing temperature is raised except for the temperature of 710 ˚C. This is in agreement with the results of the tensile curves shown in the next section. Moreover, the profiles of hardness through thickness are in good agreement with the carbon profiles predicted from the solution of second Fick's law implemented in the 1D diffusion model. Indeed, at 430 ˚C - 1h the carbon profile through thickness is not uniform except for the first 23 µm close to the surface due to the diffusion caused by the heating and cooling ramps. However, for the annealing of 530 ˚C - 1h, 630 ˚C - 1h and 710 ˚C - 1h the profiles are expected to be linear.

According to the ASTM standard for Knoop tests [154] *"there is no generally accepted method for accurate conversion of Knoop or Vickers hardness numbers to other hardness scales or tensile strength values"*. Moreover, according to literature Tabor's relation (HV/YS~3) [155] can be applied between Vickers hardness and the value of yield stress, but

there is no similar relation for Knoop. Based on this, the average Knoop hardness value was related with the yield stress found during the tensile tests for the coupons coated both sides with 500 nm thick FeC film. The ratio between yield stress and Knoop hardness was found to be equal to 2 ± 0.2 (as reported in Table 5-1) for the tested specimens. The average Knoop hardness is calculated without considering the hardness value of the unpolished surface since that value is very high because of the crystallization of the amorphous FeC film at temperatures equal or higher than 530 ˚C.

Annealing	Average Knoop Hardness [MPa]	Average Yield stress from tensile tests [MPa]	Ratio YS/KH
430˚C-1h	110	201	1.8
530˚C-1h	121	259	2.1
630˚C-1h	143	306	2.1
710˚C-1h	126	246	2

Table 5-1 - Relation between yield stress and Knoop hardness found for specimens of IF steel coated both sides with 500 nm thick FeC film and annealed at different temperatures in high vacuum

5.3. Tensile Tests

Tensile coupons of IF steel coated with carbon on both sides were annealed at different temperatures under vacuum to obtain different carbon profiles through thickness. Then, the coupons were tested with a tensile machine at the University of Ottawa. In Figure 5-3, the temperature vs time profiles are reported, while Table 5-3 shows the values of vacuum at the beginning of the heat treatment and at the end of it. Table 5-2 reports the composition of the IF steel, where titanium is added to tie-up the small carbon and nitrogen amount which is present in the steel.

	C	Ti	P	Mn	S	N
x 10^{-3} wt.%	3	55	9	111	12.5	1.8
x 10^{-3} at.%	14	64	16	113	22	7

Table 5-2 - Composition of the interstitial free steel (IF steel) used for the Gracos project

From the composition and according to the following stoichiometric equation which was also reported in section 2.5.1, the amount of titanium necessary to tie-up carbon, nitrogen, and sulphur can be calculated. So using the values reported in Table 5-2, the titanium necessary to tie-up all the interstitial elements and the sulphur would be:

$$\%Ti = 4x(\%C)+3.42x(\%N)+1.5x(\%S) \quad \text{(eq. 5-3)}$$

$$\%Ti = 4x(3x10^{-3})+3.42x(1.8x10^{-3})+1.5x(12.5x10^{-3}) = 0.037 \text{ wt\% of Ti}$$

So there will be (0.055-0.037) = 0.018 wt% of Ti that is not used and that, in theory, could tie-up some of the carbon diffusing from the FeC film.

Annealing Parameters	Vacuum furnace on [torr]	Vacuum furnace off [torr]
330 ºC-1h	$1.1 \cdot 10^{-5}$	$7.6 \cdot 10^{-6}$
430 ºC-1h	$6 \cdot 10^{-6}$	$3 \cdot 10^{-6}$
530 ºC-1h	$3 \cdot 10^{-6}$	$3.3 \cdot 10^{-6}$
630 ºC-1h	$7.4 \cdot 10^{-6}$	$4.6 \cdot 10^{-6}$
710˚C-1h	$2.3x10^{-6}$	$2.3x10^{-6}$

Table 5-3 - Vacuum level at the starting and ending of heat treatments

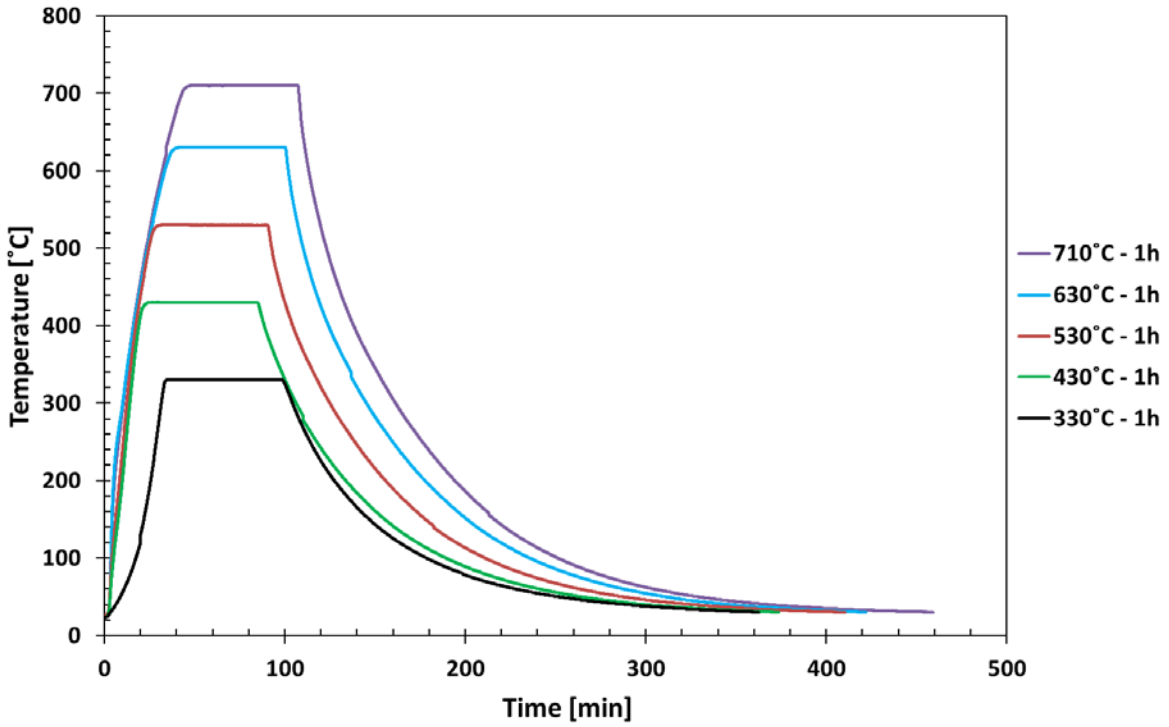

Figure 5-3 - Time and temperature profiles for the different annealing treatments implemented in the vacuum furnace at the University of Ottawa

After annealing, the tensile coupons were tested and the first series of tests was performed using the tensile machine shown in Figure 4-15 in Chapter 4. This tensile machine is made of two arms, one of them is fixed and the other one can move, so the sample is pulled only on one of its ends. On the program of the tensile machine, the speed of the test, the gauge length, the width of the gauge length and the thickness of the specimen have to be set before

starting the test. The thickness of each specimen is measured at least three times before starting the test and an average of the three measurements is taken as the thickness used to calculate the engineering stress-strain curves. Table 5-4 lists all the samples tested for each annealing temperature and time in high vacuum. All the samples were tested at a speed of 2.5 µm/s which corresponds to a strain rate of 5×10^{-4} s^{-1}.

Sample Name	Coating Condition	Heat Treatment
NA 1, NA 2, NA 3, NA 4	Both sides	Not annealed
A-1, A-2, A-3	Both sides	330 ºC -1h
B-1, B-2, B-3	Both sides	330 ºC – 4 days
C-1, C-2, C-3, C-4, C-5	Both sides	430 ºC – 1h
D-1, D-2, D-3, D-4	Both sides	530 ºC – 1h
E-1, E-2, E-3, E-4, E-5, E-6, E-7, E-8, E-9	Both sides	630 ºC – 1h
F-1, F-2, F-3, F-4, F-5, F-6, F-7, F-8, F-9, F-10, F-11, F-12	Both sides	710 ºC – 1h
U1	Uncoated	430 ºC – 1h
U2	Uncoated	530 ºC – 1h
U3	Uncoated	630 ºC – 1h
U4	Uncoated	710 ºC – 1h

Table 5-4 - List of tensile tested coupons

5.3.1. Tensile Tests on coupons coated both sides with 500 nm FeC amorphous film

Not-annealed tensile coupons coated both sides with 500 nm of FeC film were tensile tested to compare their mechanical properties with the ones of annealed and coated coupons. During each tensile test, the load [N] and the displacement [mm] were recorded and the engineering stress-strain curves were calculated. Figure 5-4 shows the corresponding engineering stress-strain curves. All dimensions for each specimen are reported in Appendix D (section D.2).

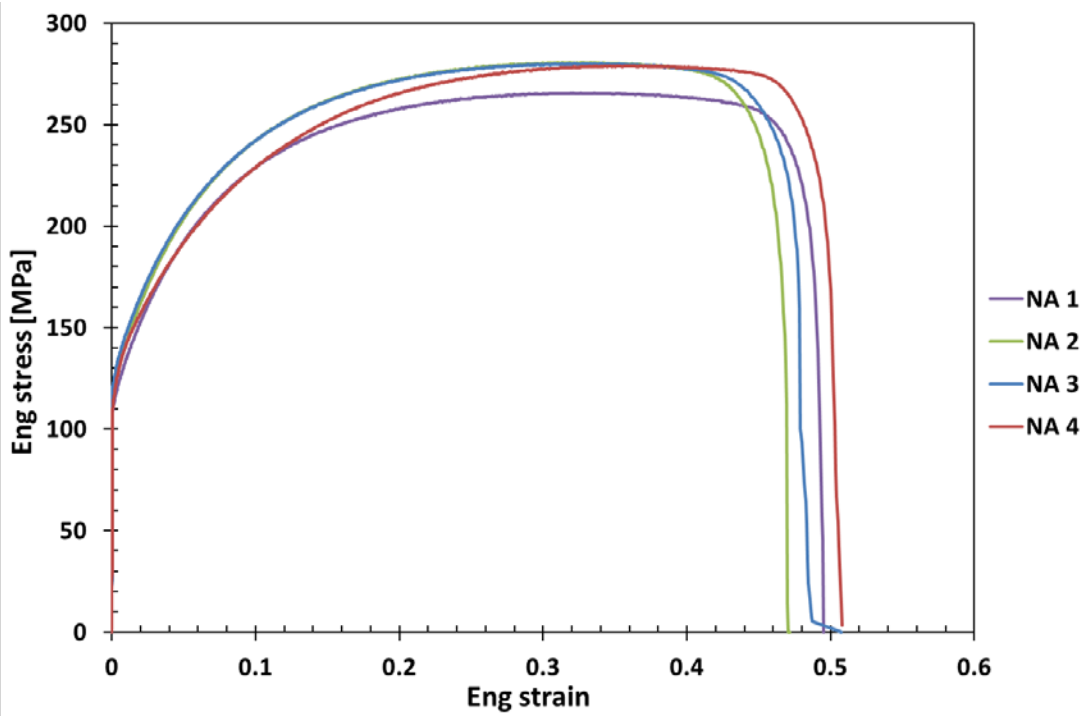

Figure 5-4 - Engineering stress-strain curves for coupons coated both sides with 500 nm FeC and tested at a speed of 2.5 µm/s

From the stress-strain curves, no increase of yield stress and ultimate tensile strength was recorded. Some tensile tests of coated but not-annealed coupons were performed after placing the tensile machine under the optical microscope in order to check the behaviour of the film during the test. For not-annealed samples, a marked exfoliation of the coating occurred during the tensile test.

Since there is no annealing, there is no diffusion occurring between film and substrate and there is no transformation taking place in the film. For this reason, the adhesion between the IF steel and its carbon coating just depends on the parameters of the PVD processing. In Figure 5-5, some pictures taken during a tensile test are reported. From them, it can be seen how the exfoliation develops during the test.

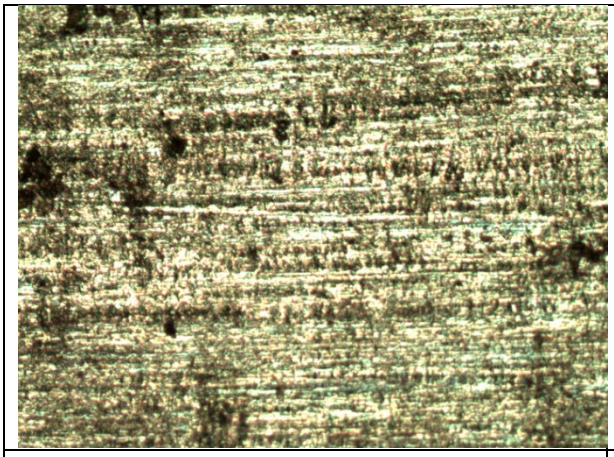

a) Surface of the tensile coupon at the beginning of the tensile test

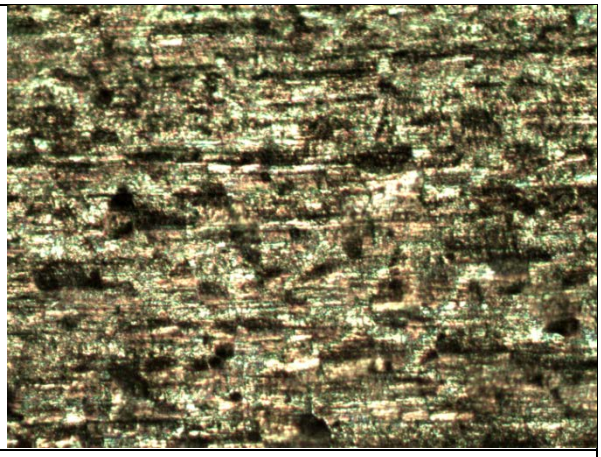

b) Starting of the exfoliation of the surface coating

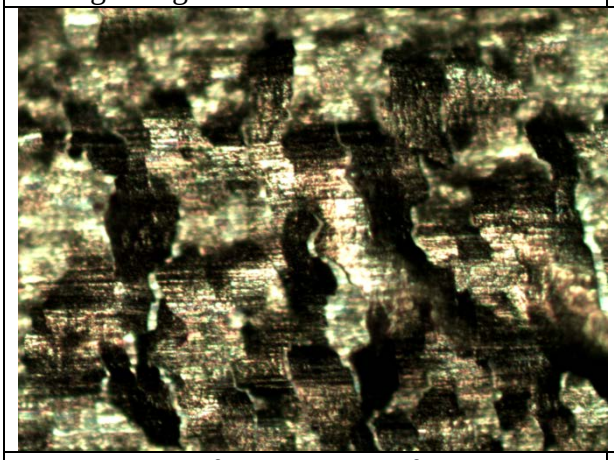

c) Increase of the coating exfoliation

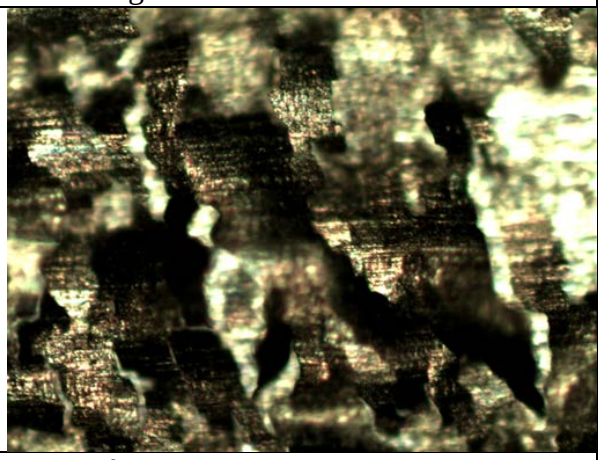

d) Exfoliation still increasing

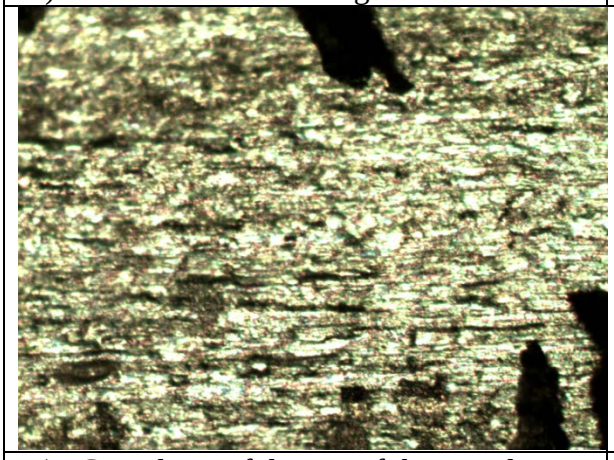

e) Complete exfoliation of the sample

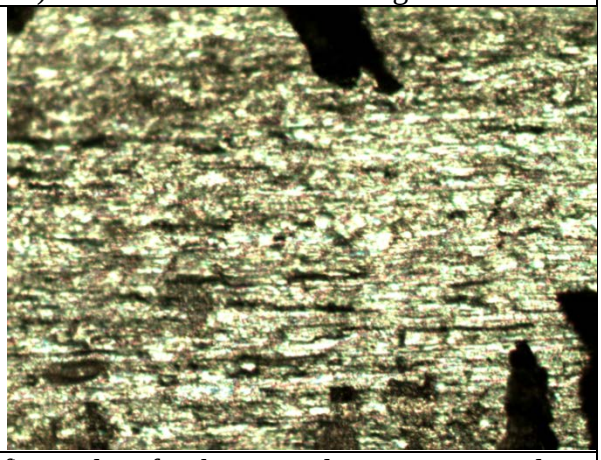

f) End of the tensile test: complete exfoliation of the coating

Figure 5-5 - FeC film behaviour for a not-annealed IF coupon during a tensile test (images taken with optical microscope at magnification 10X)

Coated tensile coupons were then annealed at 330 ˚C - 1h in high vacuum and in Figure 5-6 the tensile curves are shown.

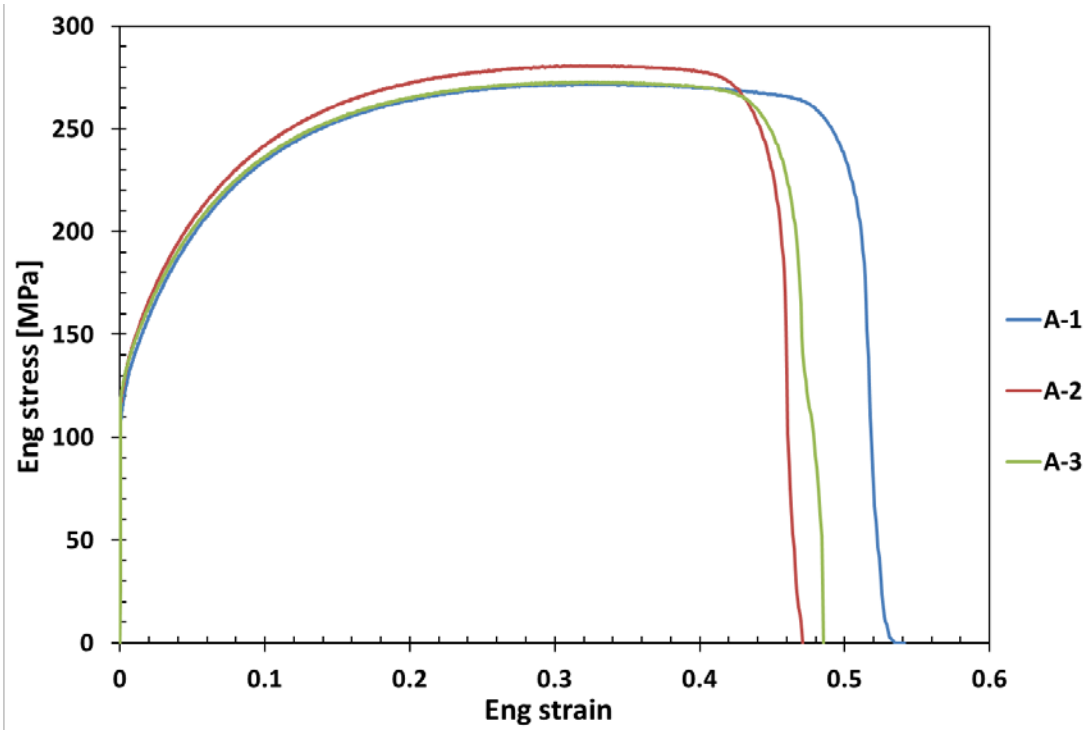

Figure 5-6 - Engineering stress-strain curves for samples annealed at 330 ºC for 1h, tested at 2.5 µm/s

During the tensile test of a coupon annealed at 330 ˚C - 1h in high vacuum, optical microscope pictures were taken to follow the exfoliation of the film as shown in Figure 5-7.

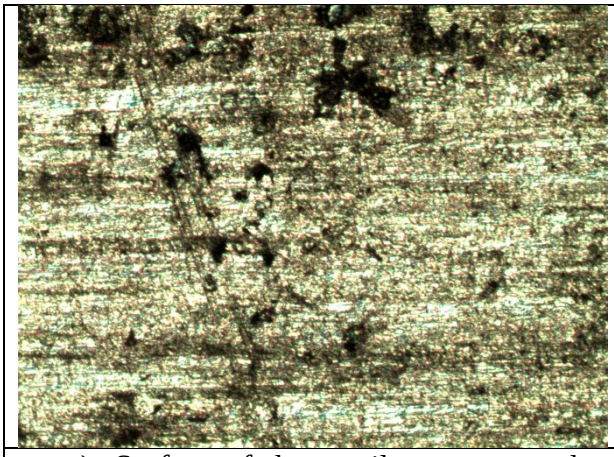

a) Surface of the tensile coupon at the beginning of the tensile test

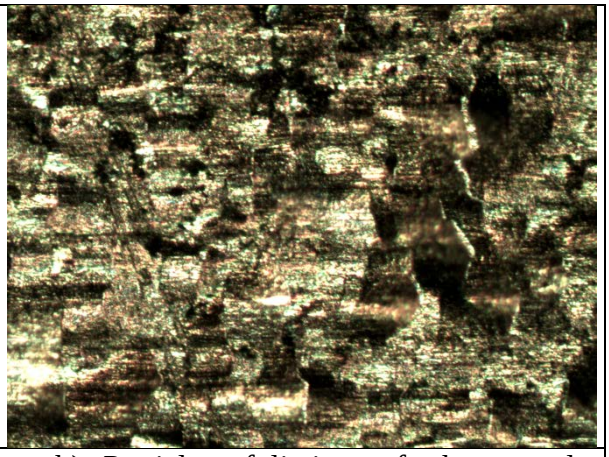

b) Partial exfoliation of the sample during the test

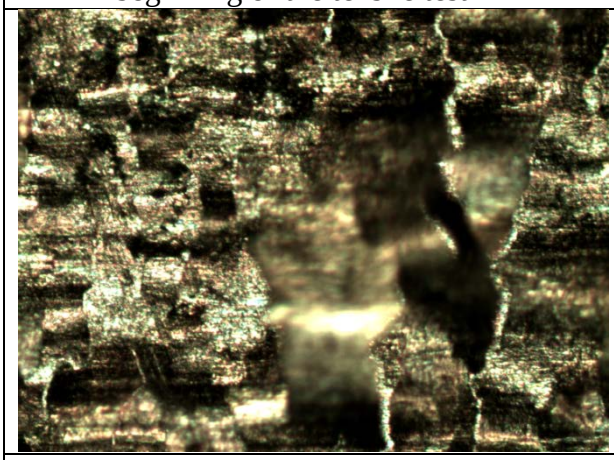

c) Continuation of the exfoliation during the tensile test

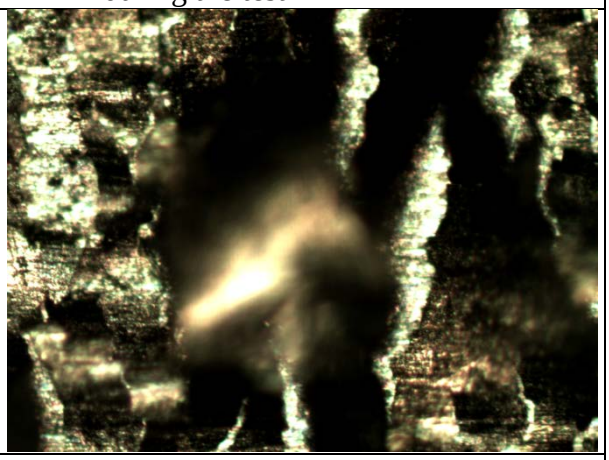

d) Exfoliation during the last part of the tensile test

Figure 5-7 - FeC film behaviour during a tensile test for a both side coated IF coupon annealed at 330 ˚C - 1h in high vacuum (images taken with optical microscope at magnification 10X)

The mechanical properties in terms of stress-strain curves for the samples annealed at 330 ºC for 1h are similar to those found for the not-annealed samples. This means that a heat treatment of 330 ºC for 1h is not sufficient to cause carbon diffusion from the coating into the substrate as expected from the 1D diffusion simulations. Furthermore, the exfoliation of the film during the test is the same as the one obtained for coated but not-annealed coupons meaning that the treatment of 330 ˚C - 1h is not modifying the adhesion between film and substrate which is still only due to the parameters used during PVD deposition.

Tensile tests were performed also on coupons coated both sides with 500 nm thick FeC film and annealed at 330 ˚C for 4 days in high vacuum. According to the 1D simulation of diffusion, 4 days of annealing at 330 ˚C should create a linear carbon profile through

thickness and the diffused carbon concentration should be equal to the solubility limit of carbon into ferrite which is equal to $3.5x10^{-3}$ at% for this temperature. The graph showing the expected carbon profile through thickness is reported in Figure 5-8 while in Figure 5-9 the engineering stress-strain curves are shown.

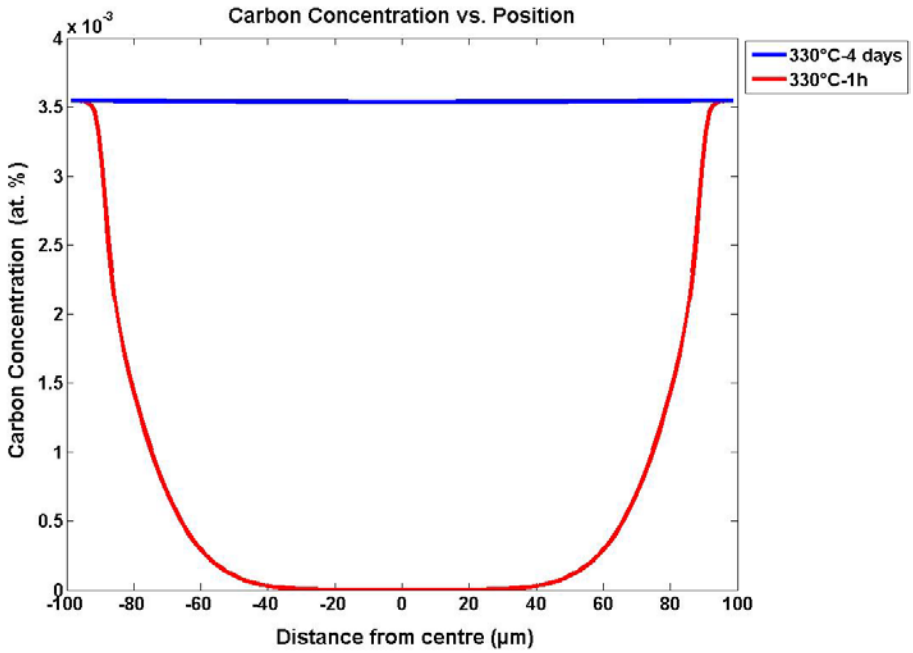

Figure 5-8 - Carbon profile created trough thickness for diffusion at 330 ˚C for 1h and 4 days

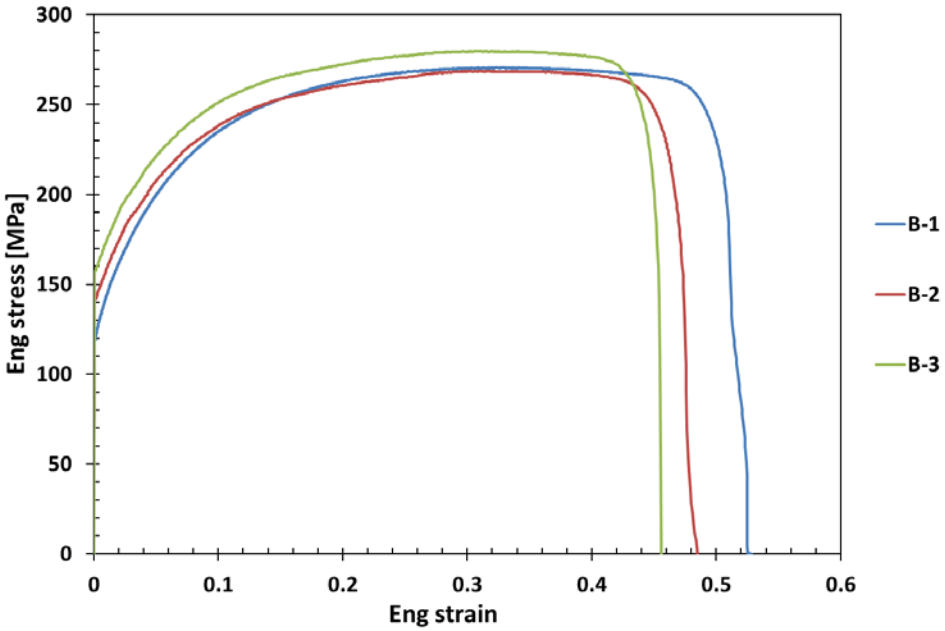

Figure 5-9 - Engineering stress-strain curves for samples annealed at 330 ºC for 4 days, tested at the same speed of 2.5 µm/s

In specimen B-1, no diffusion occurred since there was no improvement of mechanical properties, however, specimen B-2 and B-3 show an increase of yield stress. If an average of the yield stresses of specimen B-2 and B-3 is made without considering specimen B-1, the average stress is 149 MPa. From this value, it is possible to calculate approximately how much carbon was diffused by using the following equation $\Delta\sigma = Mm(X_C)^{1/2}$. The increase of yield stress is calculated as (149-113.7) = 35 MPa which corresponds to 0.00112 at% of carbon. This amount is lower than the carbon which is expected to diffuse at this temperature. This could be due to an overestimation in the modeling of the solubility limit of carbon into ferrite or of the diffusion coefficient of carbon at this temperature.

The annealing temperature was then raised by 100 ˚C and three coupons were annealed at 430 ˚C - 1h in high vacuum. In Figure 5-10 the tensile properties are reported.

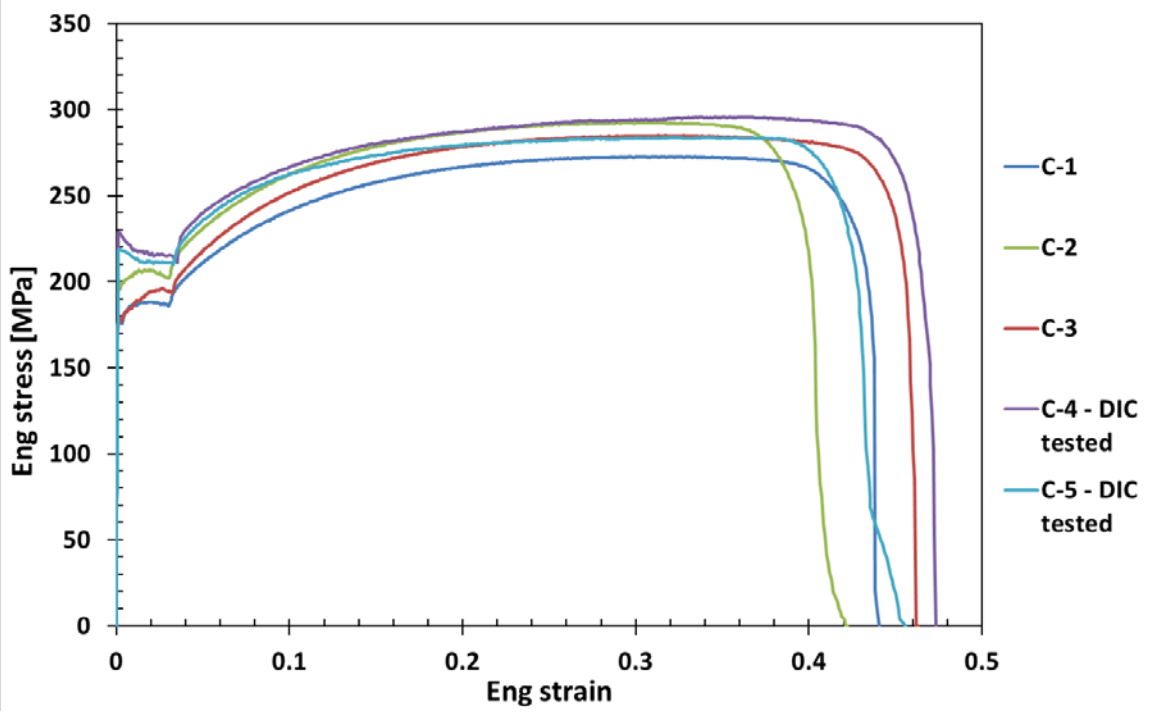

Figure 5-10 - Engineering stress-strain curves for samples annealed at 430 ºC for 1h in high vacuum, tested at the same speed of 2.5 µm/s

From the stress-strain curves shown in Figure 5-10, one can see that carbon diffusion took place during this heat treatment since an increase of yield stress is recorded and the appearance of Lüders plateau confirms that the diffused carbon pins dislocations.

Pictures were taken with the optical microscope during the test and again the tensile coupon showed exfoliation. The images shown in Figure 5-11 were captured at a magnification of 10X and show exfoliation in the gauge length.

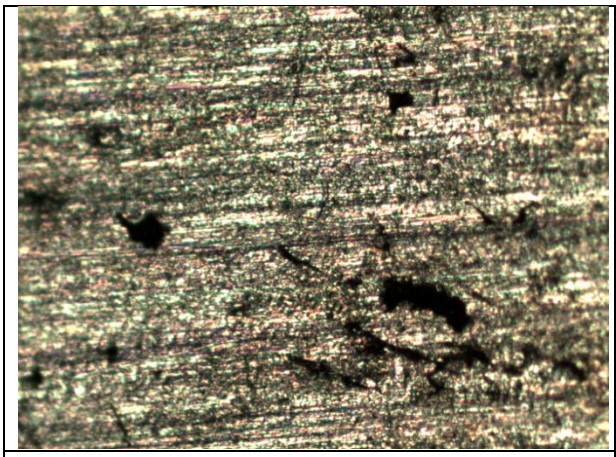

a) Surface of the tensile coupon at the beginning of the tensile test

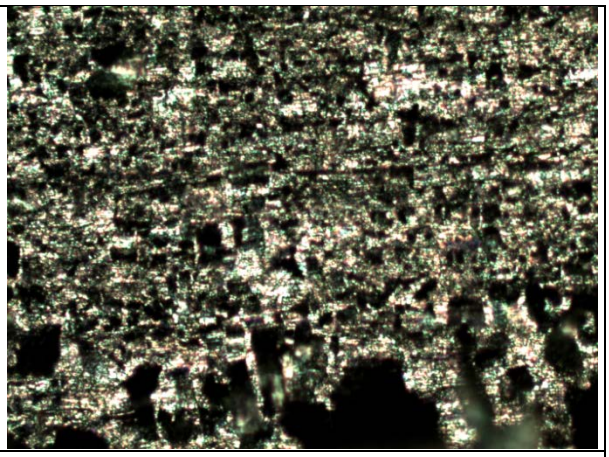

b) Partial exfoliation of the sample during the test

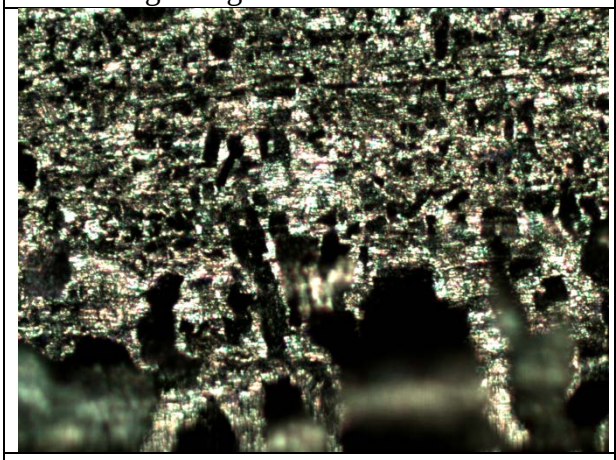

c) Continuation of the exfoliation during the tensile test

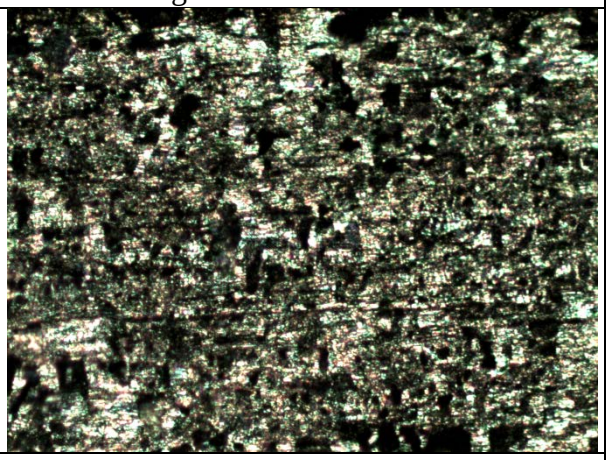

d) Exfoliation at the end of tensile test (another zone of the gauge length)

Figure 5-11 - FeC film behaviour during a tensile test for a both side coated IF coupon annealed at 430 ˚C - 1h in high vacuum (images taken with optical microscope at magnification 10X)

Other tensile coupons were annealed in high vacuum at a temperature of 530 ˚C for 1h and the engineering stress-strain curves are shown in Figure 5-12

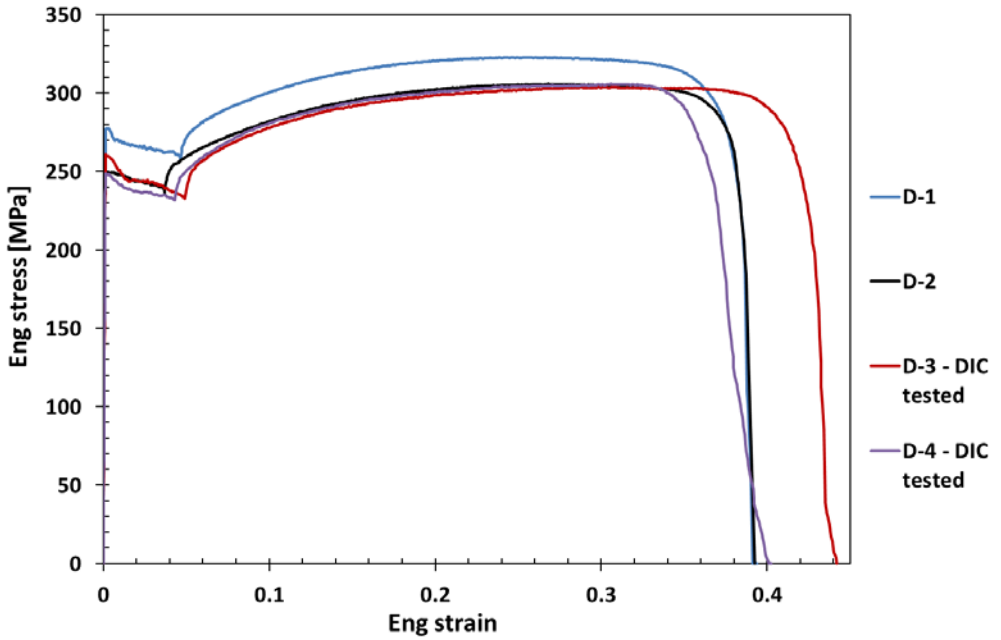

Figure 5-12 - Engineering stress-strain curves for samples annealed at 530 ºC for 1h in high vacuum, tested at the same speed of 2.5 µm/s

Images of the film behaviour during tensile test are reported in Figure 5-13, where it can be seen that the exfoliation starts later compared to the previous tests on coupons annealed at 330 ˚C and 430 ˚C. Moreover, the behaviour cannot be considered an exfoliation but more as a cracking of the FeC film. This indicates that the film at this temperature has undergone some transformation which has strengthened its adherence to the IF substrate. The transformation taking place in the film at this temperature will be shown later in this thesis.

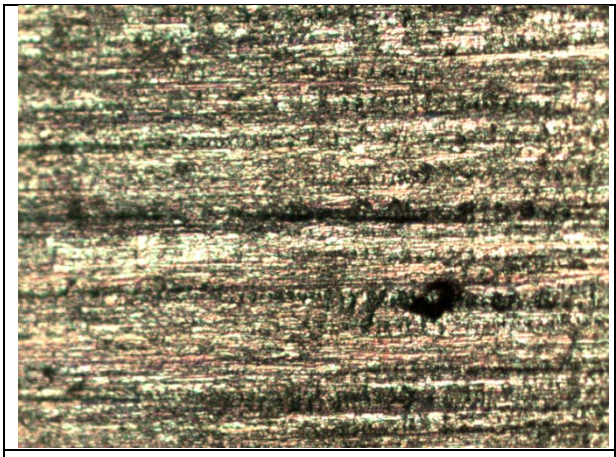

a) Surface of the tensile coupon at the beginning of the tensile test

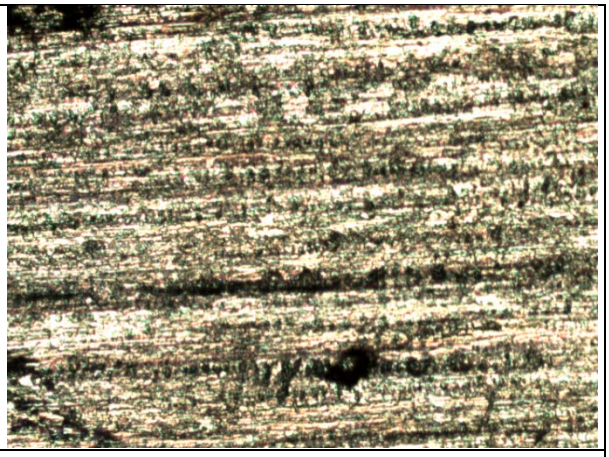

b) No evident exfoliation of the surface coating during the test

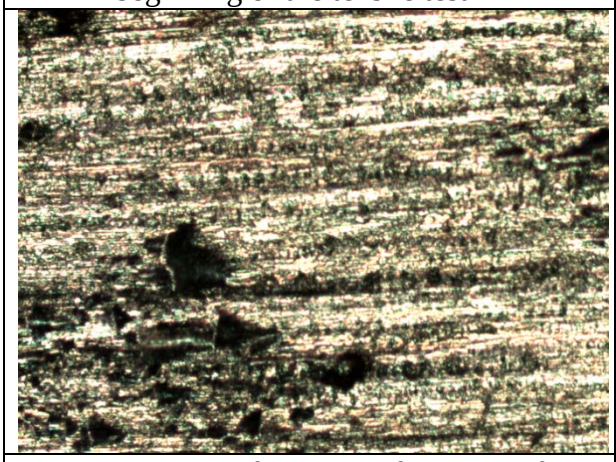

c) Starting of some exfoliation of the carbon coating due to Lüders band propagation

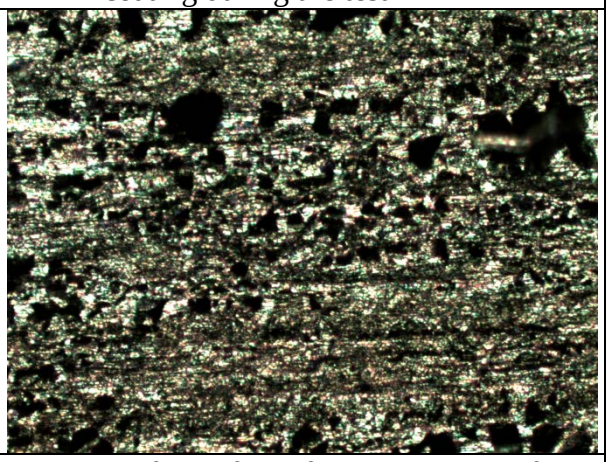

d) Surface of the film at the end of the test

Figure 5-13 - FeC film behaviour during a tensile test for a both side coated IF coupon annealed at 530 ˚C - 1h in high vacuum (images taken with optical microscope at magnification 10X)

According to the tensile curves shown in Figure 5-12, at 530 ºC even more carbon diffusion occurred since the yield stress is higher than what was obtained with annealing at 430 ºC and Lüdering is still present.

Other tensile tests were run on coupons annealed at 630 ˚C - 1h in high vacuum. After this annealing, a higher yield stress is found compared to the values obtained for the annealing at 530 ˚C and 430 ˚C. The behaviour of the FeC film during the tensile test was observed with the optical microscope as shown in Figure 5-16 (a, b, c, d).

The engineering stress-strain curves from specimen E-1 to specimen E-6 are reported in Figure 5-14, while the curves for specimens E-7, E-8 and E-9 are reported for clarity in Figure 5-15.

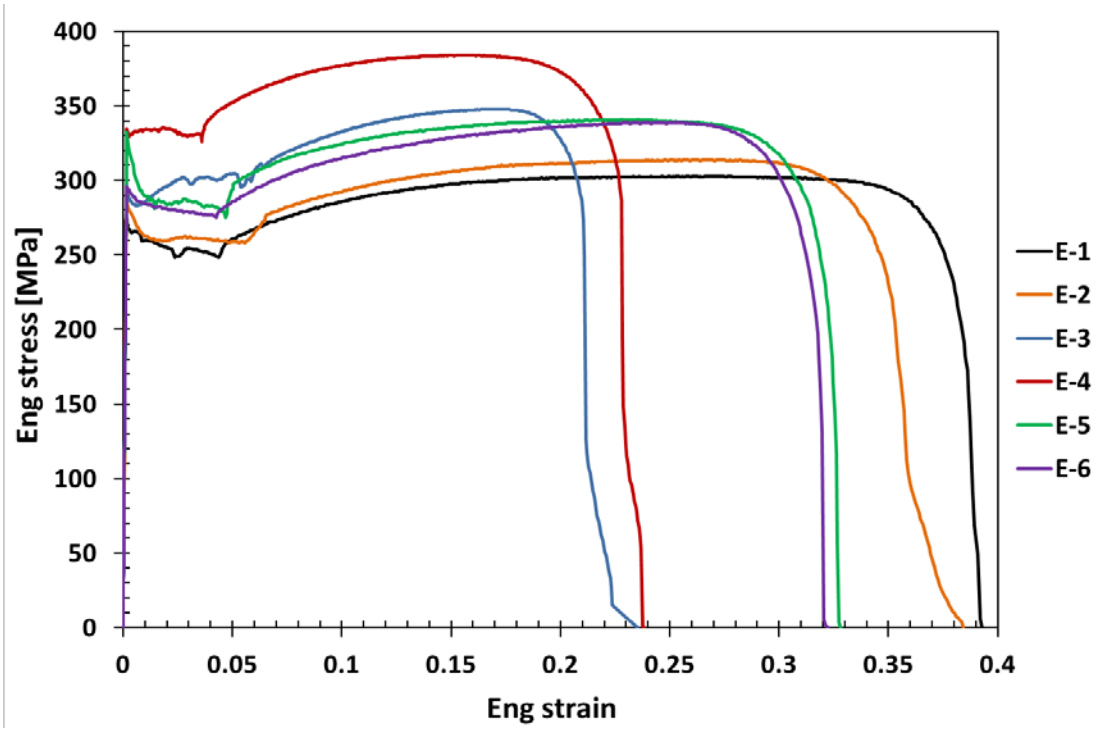

Figure 5-14 - Engineering stress-strain curves for samples annealed at 630 ºC for 1h, tested at the same speed of 2.5 µm/s

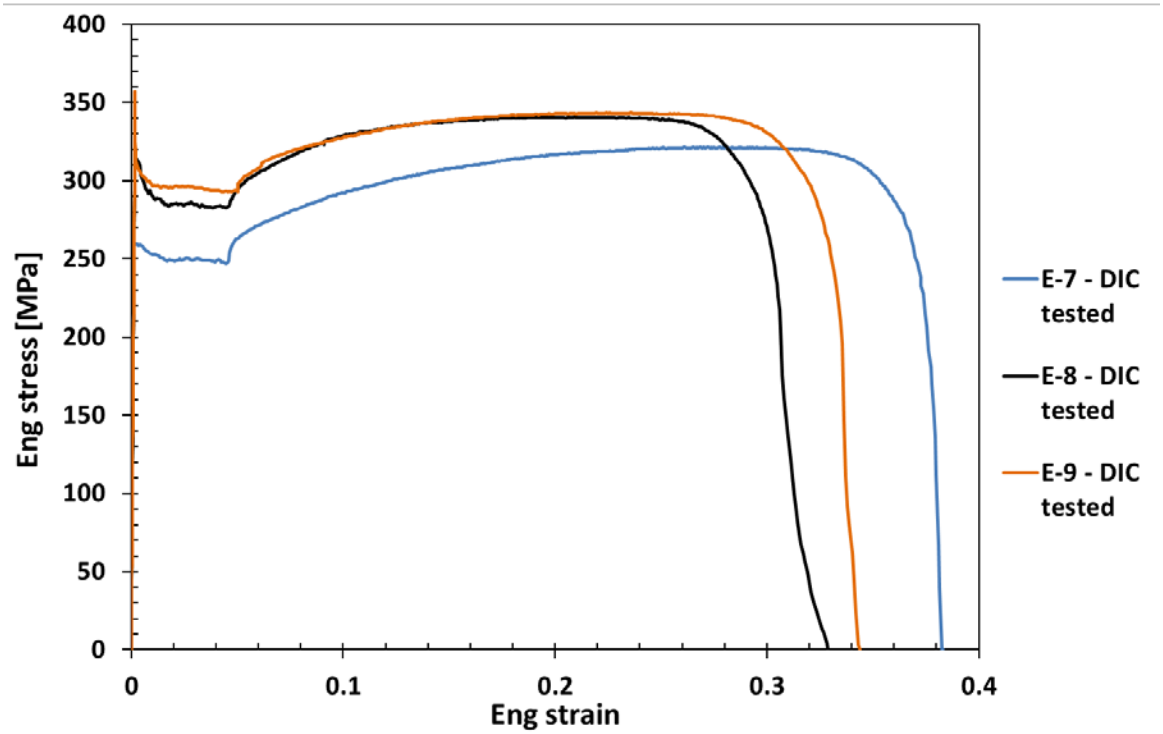

Figure 5-15 - Engineering stress-strain curves for samples E-7, E-8 and E-9 annealed at 630 ºC for 1h, tested at the same speed of 2.5 µm/s and used for DIC analyses

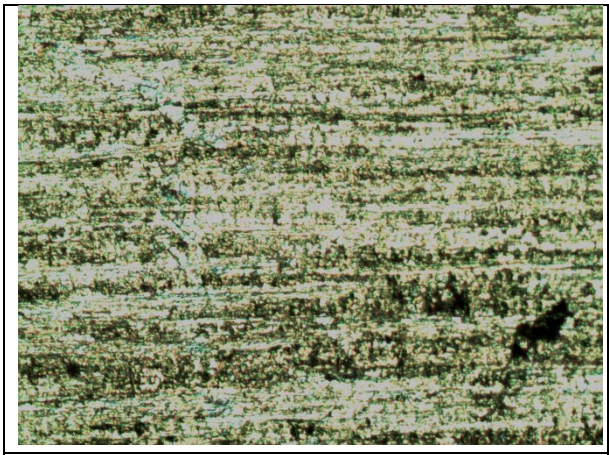

a) Surface of the tensile coupon at the beginning of the tensile test

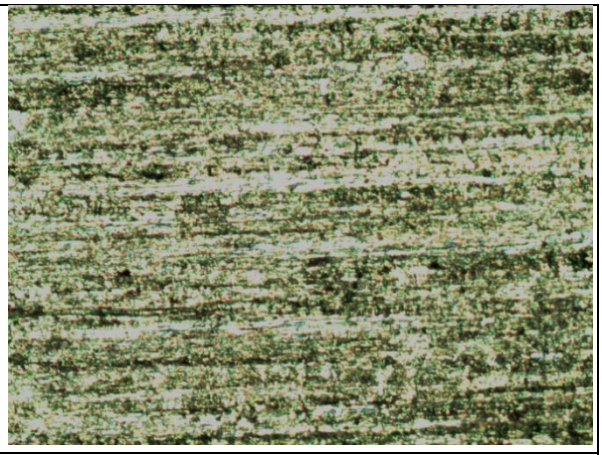

b) Surface of the sample during the test: no exfoliation detected

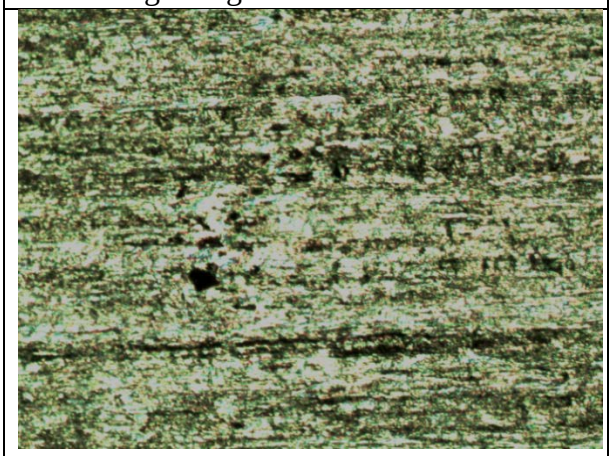

c) Surface of the sample during the last part of the tensile test

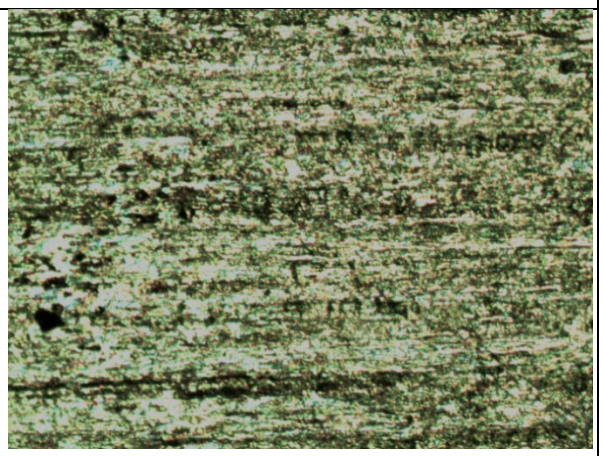

d) Surface at the end of the tensile test

Figure 5-16 - FeC film behaviour during a tensile test for a both side coated IF coupon annealed at 630 ˚C - 1h in high vacuum (pictures taken with optical microscope at magnification 10X)

From curves in Figure 5-14 and Figure 5-15, annealing at 630 ºC causes a further increase in yield stress and a higher ultimate tensile strength is as well recorded, except for few specimens such as sample E-1 and sample E-7. Later in this chapter, it will be shown that this variation of mechanical properties could be due to the variation of ± 3 at% of carbon in the FeC film. Another series of tests was performed by annealing both sides coated tensile coupons with 500 nm amorphous FeC film at 710 ˚C - 1h in high vacuum. The temperature of 710˚C was chosen since it is lower than the eutectoidic temperature of 727 ˚C which separates the fields of ferrite and austenite. In Figure 5-17 a summary of the engineering stress-strain curves is shown. The curves for the specimens from F-8 to F-12 are shown in another graph (Figure 5-18) for clarity.

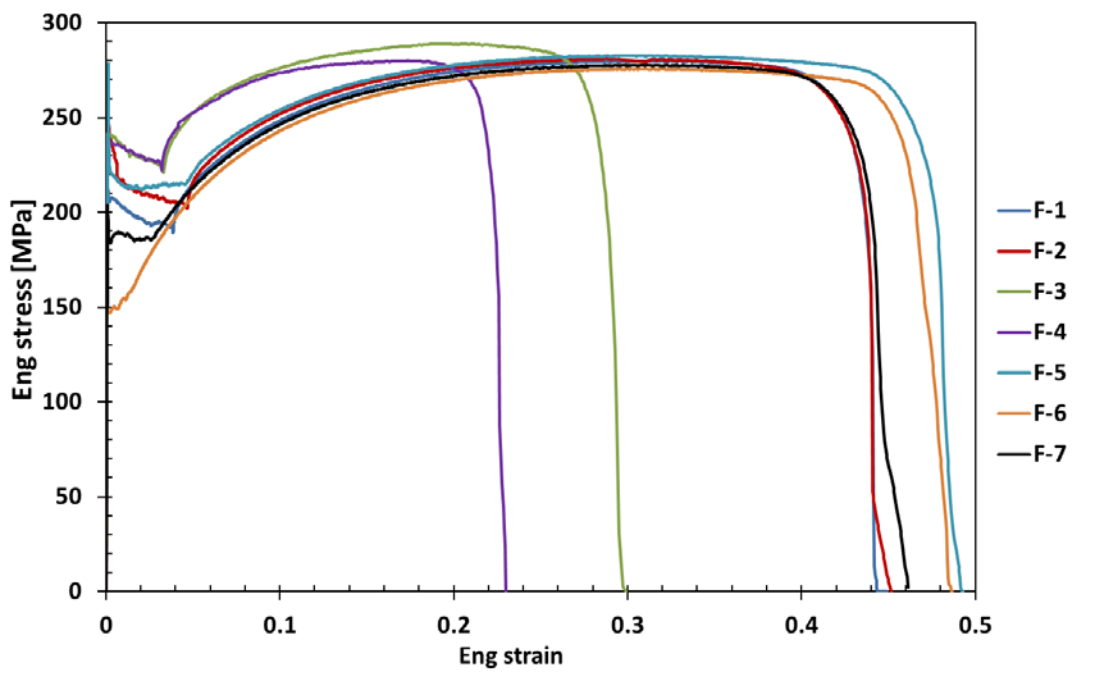

Figure 5-17 - Engineering stress-strain curves for coupons coated both sides with 500 nm FeC amorphous film and annealed in high vacuum at 710 ˚C - 1h

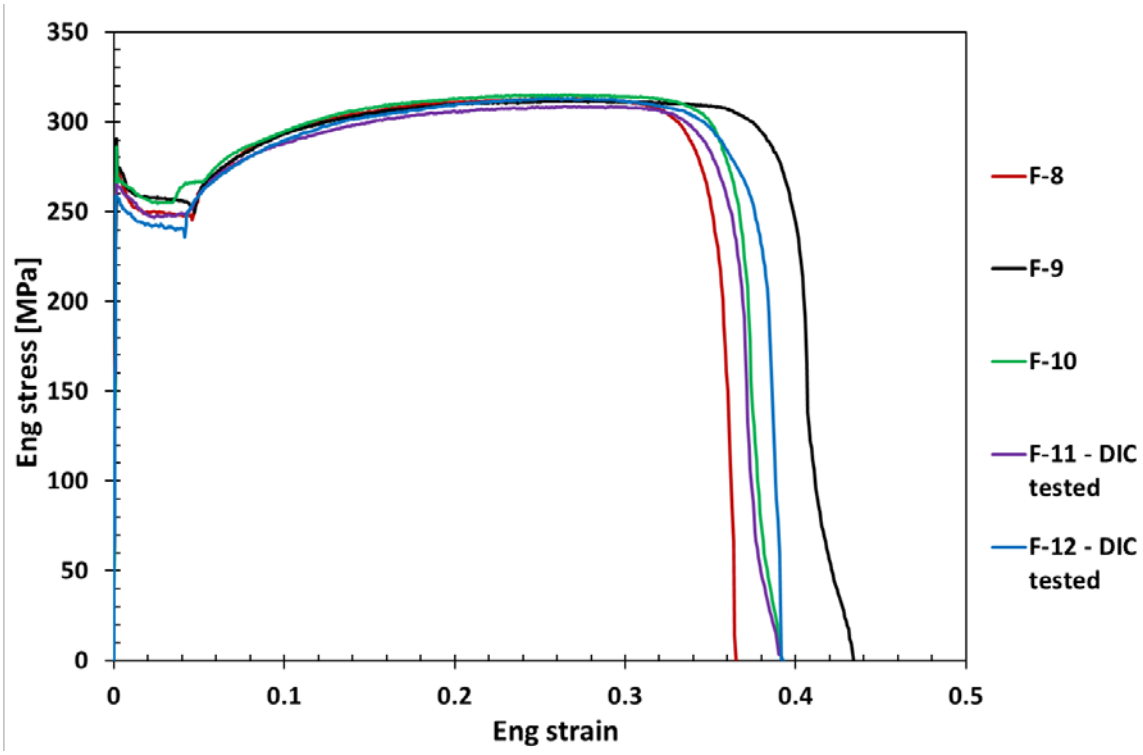

Figure 5-18 - Engineering stress-strain curves for coupons coated both sides with 500 nm FeC amorphous film and annealed in high vacuum at 710 ˚C - 1h

In Figure 5-19, the behaviour of the film during the tensile test for specimen F-7 is shown.

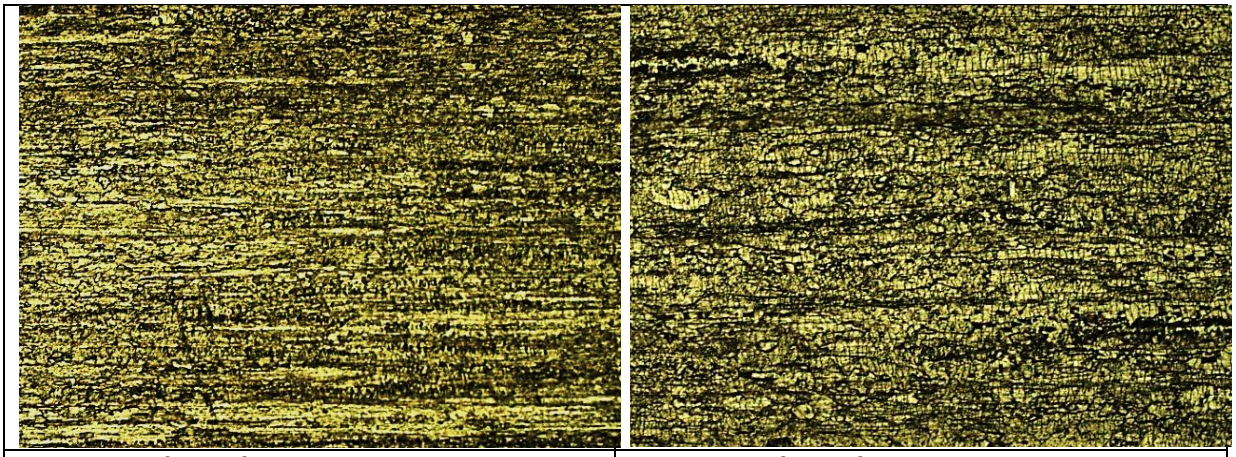

a) Surface of the tensile coupon at the beginning of the tensile test

b) Surface of the tesnile coupons during the test

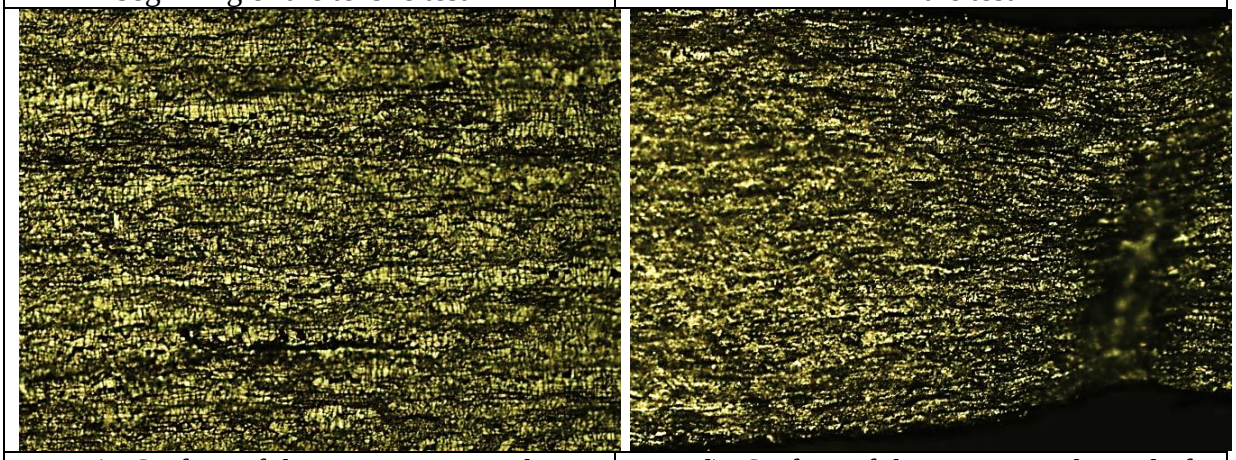

c) Surface of the coupon approaching end of the test

d) Surface of the coupon at the end of test at the necking zone

Figure 5-19 - FeC film behaviour during a tensile test for a both side coated IF coupon annealed at 710 ˚C - 1h in high vacuum (images taken with optical microscope at magnification 10X)

As can be seen from Figure 5-19, after the annealing at 710 ˚C - 1h the FeC film does not exfoliates during the tensile test. Moreover, if the highest engineering stress-strain curve is taken for each annealing temperature, it is possible to see clearly how the increase of yield stress depends on the annealing temperature (Figure 5-20). At 330 ˚C as expected from the 1D diffusion modelling, the amount of carbon diffused is not enough to cause any improvement in mechanical properties. However, starting from 430 ˚C, the yield stress increases as the annealing temperature is raised, except at 710 ˚C where the mechanical properties drop back to the same level as those obtained at 530 ˚C. No difference is detected between a coated and not-annealed IF steel, and an uncoated and not-annealed IF steel, meaning that the FeC film itself is not thick enough to carry any significant load during testing and its amorphous structure is easily exfoliated during testing.

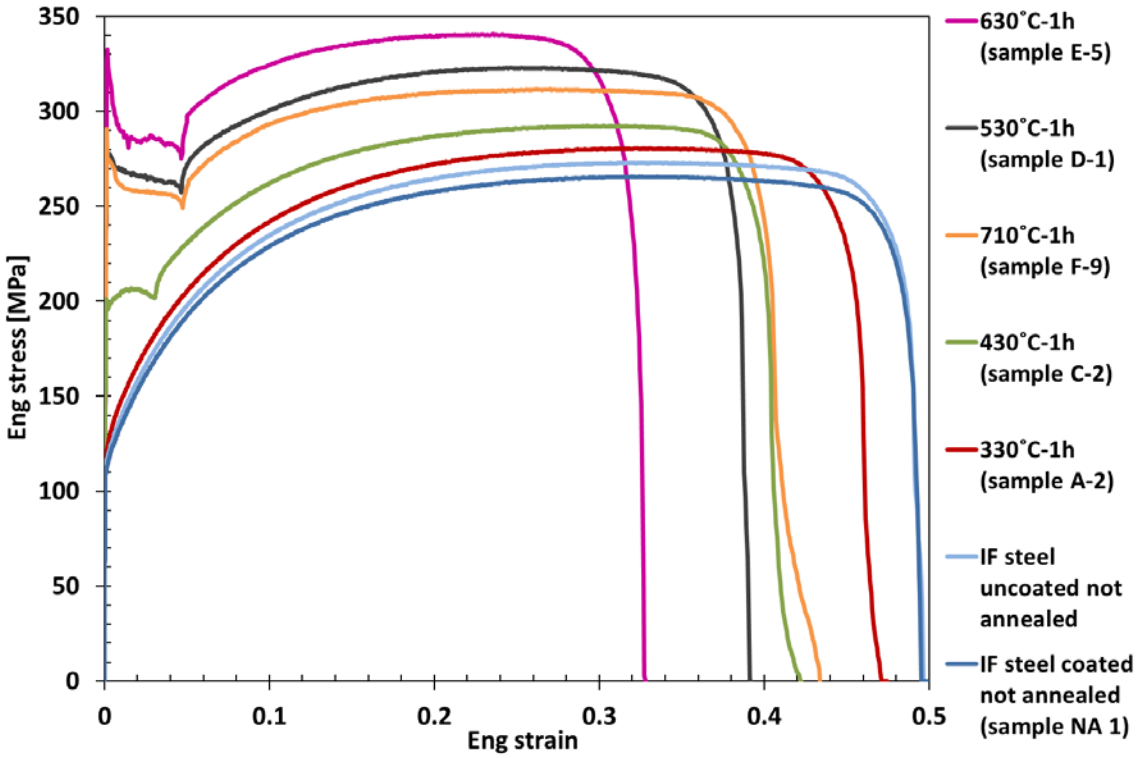

Figure 5-20 - Global comparison of engineering stress-strain curves for annealing in high vacuum at different temperatures for 1h

In order to further prove that the increase of yield stress is due to the diffusion of carbon and not to a transformation of the IF steel substrate, and to prove that for annealing at 710 ˚C - 1h in high vacuum, the decrease in mechanical properties is caused by carbon diffusion, annealing of uncoated IF steel was performed at different temperatures for 1h in high vacuum. A comparison of the engineering stress-strain curves is shown in Figure 5-21. The yield stress is the same for all annealing temperatures and the ultimate tensile strength does not change for coupons annealed at 430 ºC, 530 ºC and 710 ºC, while a slight increase is obtained for annealing at 630 ºC.

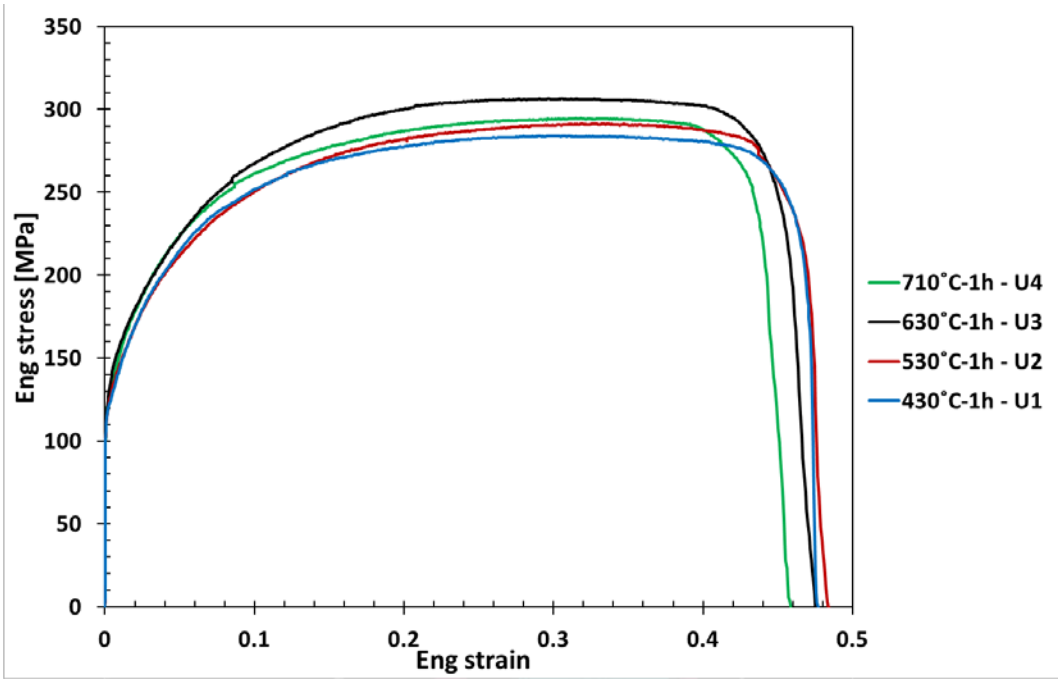

Figure 5-21 - Global comparison of engineering stress-strain curves for annealing in high vacuum at different temperatures for 1h of uncoated IF coupons

5.3.2. Tensile Tests on coupons coated both sides with 500 nm thick FeC amorphous film annealing in argon atmosphere

According to literature [156], vacuum atmosphere can be used to decarburize steel especially if the material is annealed in the range of temperature 600 ˚C - 1000 ˚C. Based on this, it was believed that partial decarburization of the FeC film could as well happen during the diffusion tests that were shown in the previous paragraph. For this reason, a series of tests were performed using a neutral atmosphere to verify whether the final mechanical properties are higher or comparable to those obtained for annealing in high vacuum. For the set of specimens shown in this paragraph, annealings were performed again at 430 ˚C, 530 ˚C, 630 ˚C and 710 ˚C for 1h using the same alumina tube used for the previous annealing but filling it with argon. The set-up of the furnace during these annealing experiments was described in section 4.3.2. Argon grade 5.3 was supplied by Linde with the following composition H_2O<1ppm, N_2<8ppm, O_2<2ppm, THC<0.5ppm [137]. The heating rate and cooling rate during annealing in argon are faster than those obtained during annealing in high vacuum since in argon the heat is transferred by convection while in vacuum it is transferred mainly by irradiation. Based on these considerations, the heating rate for annealing in argon is 19

˚C/min (compared to 12 ˚C/min in high vacuum) and then, the cooling rate is 19 ˚C/min for temperatures above 400 ˚C (compared to 12 ˚C/min in high vacuum) and then it falls to 4 ˚C/min (compared to 3 ˚C/min in high vacuum). Annealing at 330 ˚C - 1h was avoided since no improvement in mechanical properties was found during annealing in high vacuum. In this section the obtained engineering stress-strain curves are shown, while the dimensions of the coupons and the mechanical properties extracted from the stress-strain curves are reported in Appendix D (section D.3). Table 5-5 lists all the coupons that were tested in argon atmosphere, while Figure 5-22 shows the stress-strain curves obtained for annealing at 430 ºC – 1h.

Sample Name	Coating Condition	Heat Treatment
Ar-1, Ar-2, Ar-3	Both sides	430 ºC – 1h - Argon
Ar-4, Ar-5, Ar-6	Both sides	530 ºC – 1h - Argon
Ar-7, Ar-8, Ar-9	Both sides	630 ºC – 1h - Argon
Ar-10, Ar-11, Ar-12	Both sides	710 ºC – 1h - Argon

Table 5-5 - List of tensile tested coupons annealed in argon

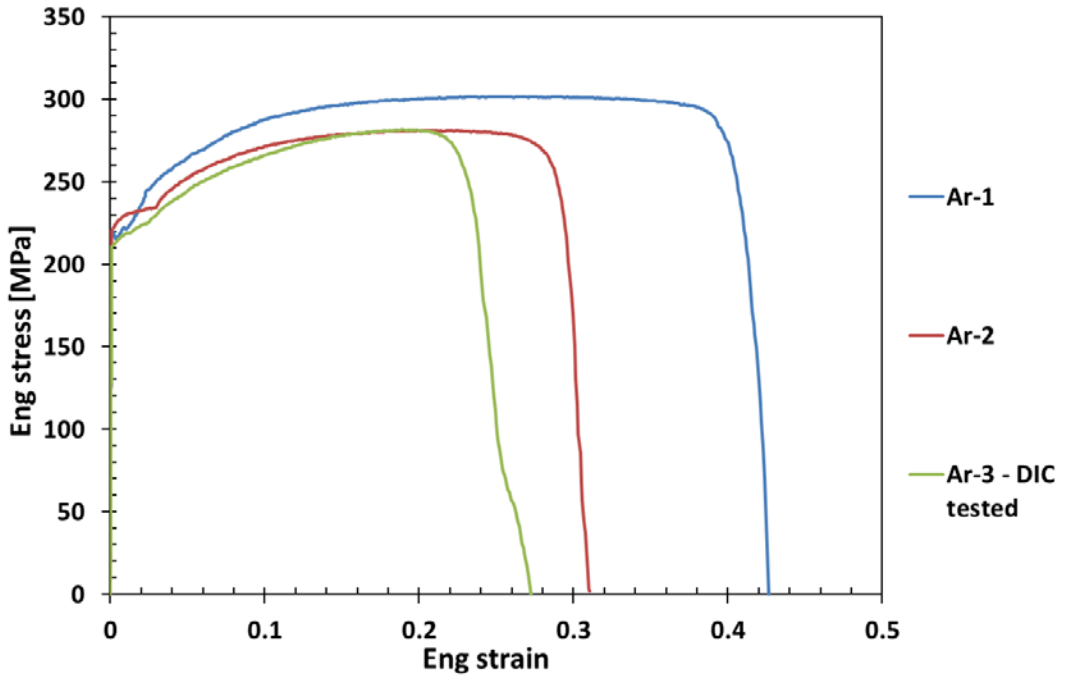

Figure 5-22 - Engineering stress-strain curves for coupons coated both sides with a 500 nm thick FeC amorphous film and annealed in argon at 430 ˚C - 1h

At 430 ºC, carbon has diffused also in argon atmosphere since the yield stress is higher than an uncoated IF steel and Lüdering is as well present. Another set of coupons coated both sides with a 500 nm thick FeC film were annealed in argon at 530 ˚C for 1h (stress-strain curves shown in Figure 5-23).

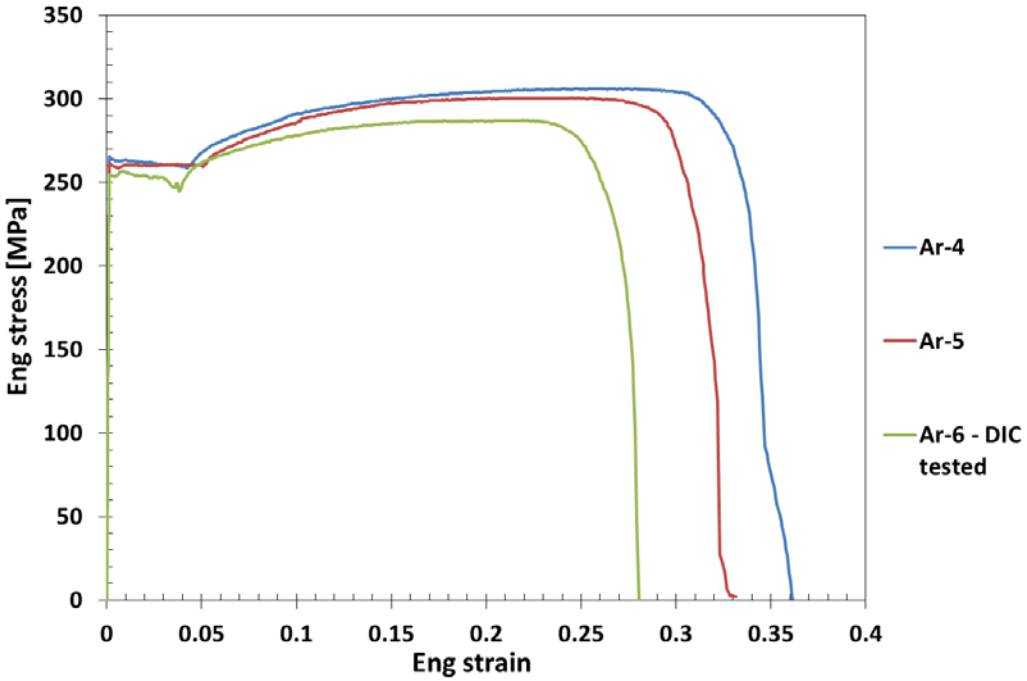

Figure 5-23 - Engineering stress-strain curves for coupons coated both sides with a 500 nm thick FeC amorphous film and annealed in argon at 530 ˚C - 1h

Other sets of coupons coated on both sides with a 500 nm thick FeC were annealed in argon at 630 ˚C for 1h and at 710 ºC for 1h (stress-strain curves shown in Figure 5-24 and in Figure 5-25 respectively).

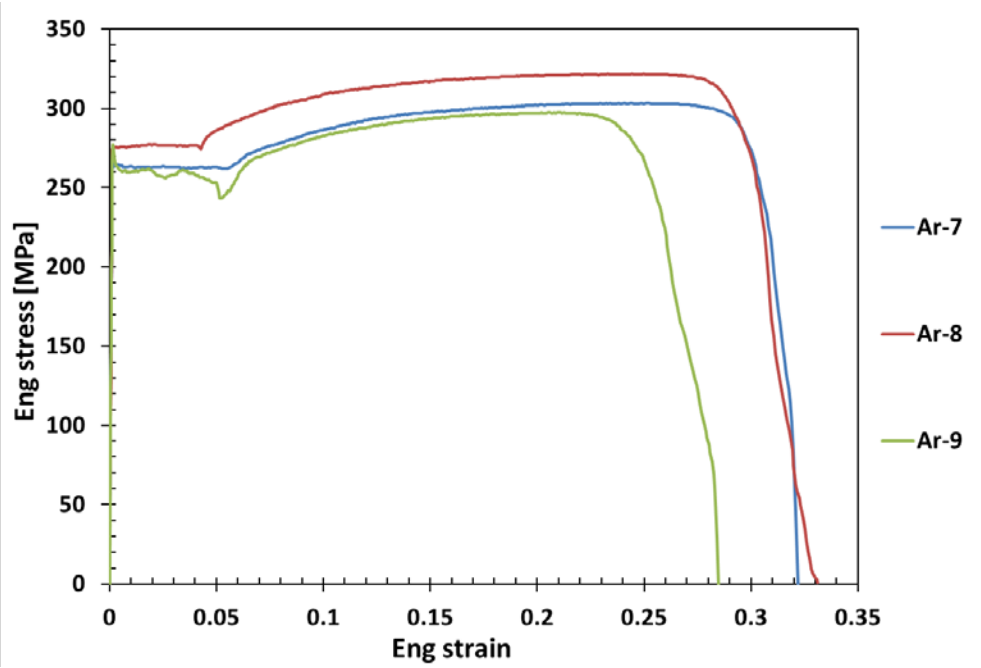

Figure 5-24 - Engineering stress-strain curves for coupons coated both sides with a 500 nm thick FeC amorphous film and annealed in argon at 630 ˚C - 1h

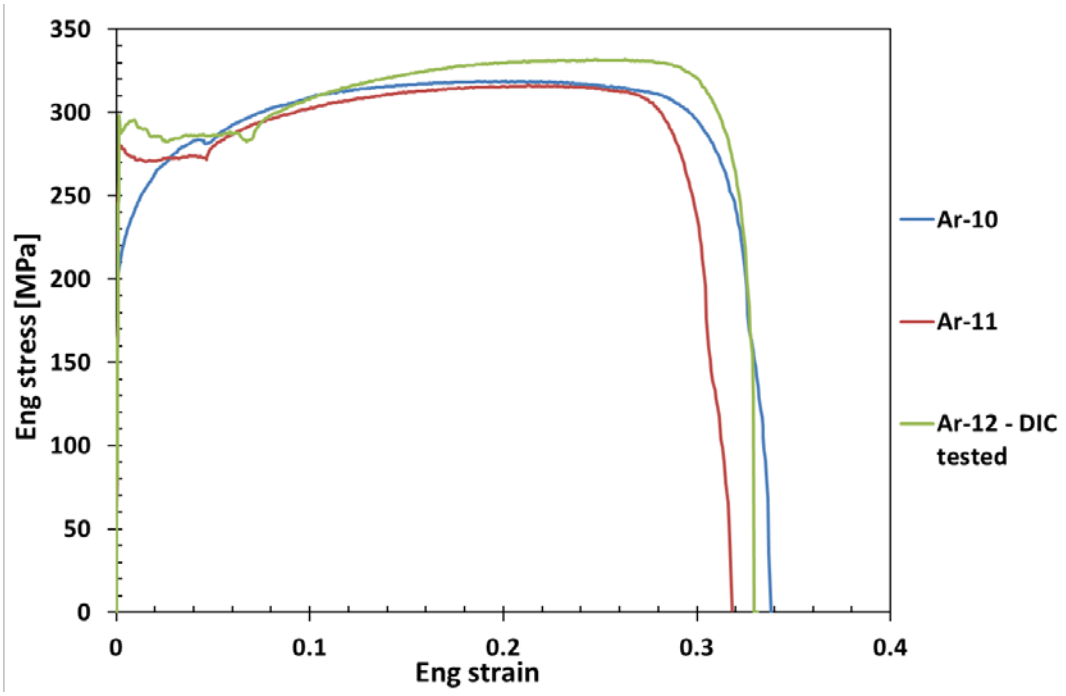

Figure 5-25 - Engineering stress-strain curves for coupons coated both sides with a 500 nm thick FeC amorphous film and annealed in argon at 710 ˚C - 1h

In Figure 5-26 the comparison of the yield stress values obtained by annealing in high vacuum are compared with the values obtained for annealing in argon. The average of the

experimental values is plotted with the error bars associated to the standard deviation obtained experimentally.

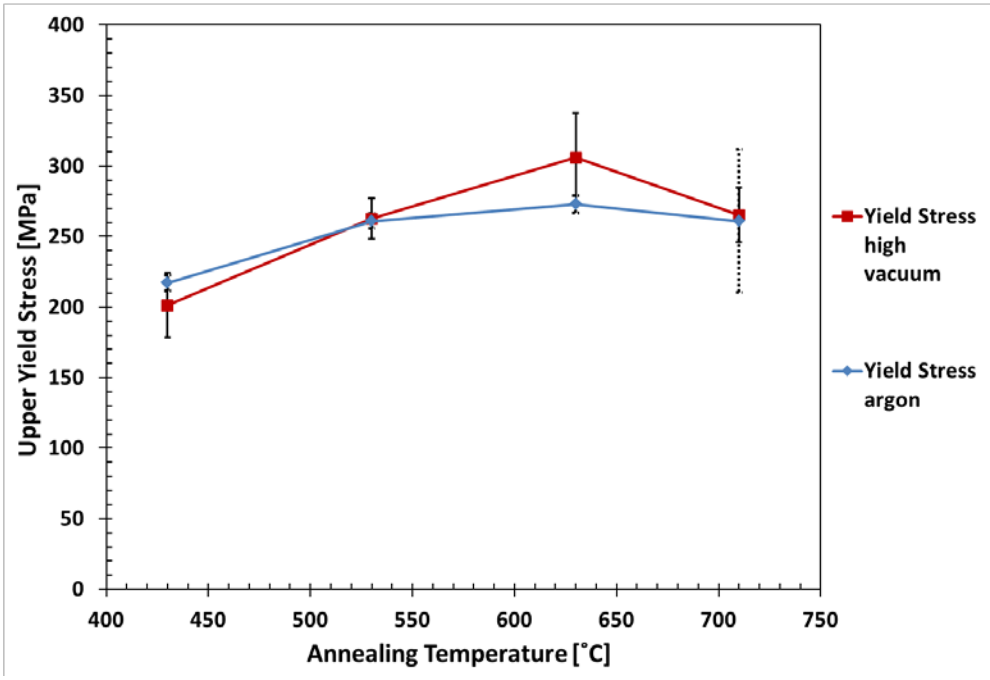

Figure 5-26 - Comparison of the average yield stress values obtained by annealing in high vacuum and argon

Annealings in high vacuum or in argon seem to give the same results for temperatures of 430 ºC and 530 ºC, however, at 630 ºC the yield stress obtained with argon is lower and at 710 ºC the standard deviation for argon is very high compared to the high vacuum. The lower mechanical properties obtained for argon at high temperature are believed to be caused by the few amount of oxygen (O_2<2 ppm) that is present in the argon grade 5.3 and that could be the source of some carburization at these high temperatures.

5.3.3. Tensile Tests on coupons coated on both sides with FeC amorphous film and annealed in air

In order to further verify that the highest strengths are obtained if the annealing is performed in high vacuum, a couple of tensile tests were performed in air. The coupons were cleaned with Nital solution and coated both sides with a 500 nm thick FeC amorphous film and they were placed in the furnace and annealed in air at 530 ˚C for 1h. Another coupon coated both sides with 500 nm thick FeC film was annealed at 630 ˚C - 1h in air. Figure 5-27 plots the

corresponding engineering stress-strain curves, while geometrical dimensions of the specimens and the mechanical properties extracted from tensile tests are reported in Table D-33 and Table D- 34 respectively.

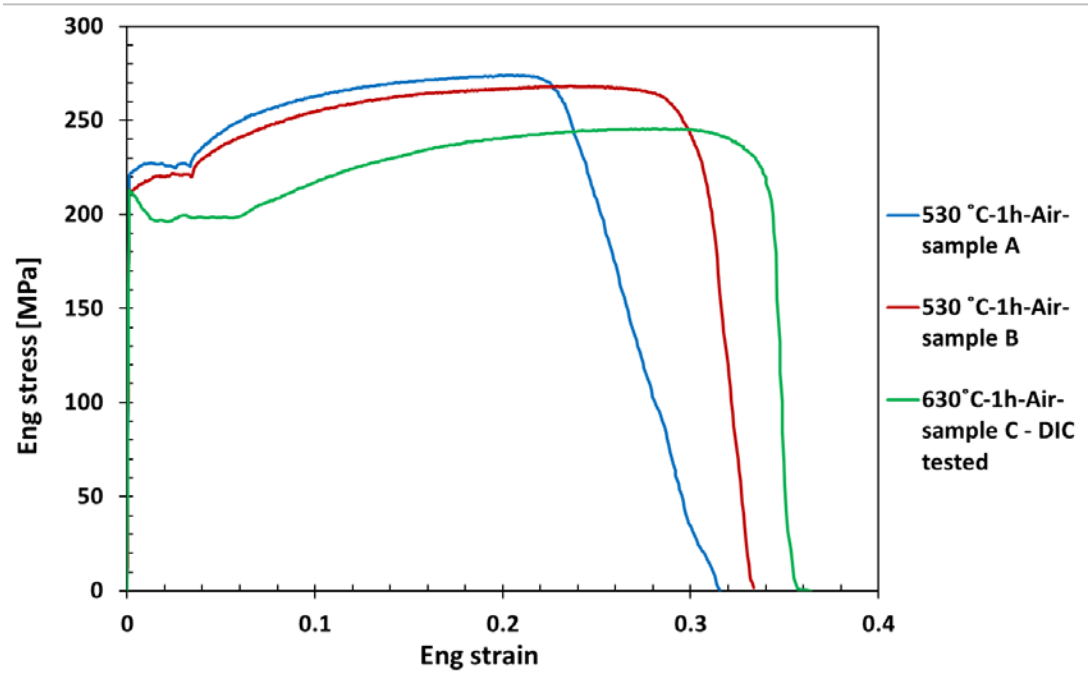

Figure 5-27 - Engineering stress-strain curves for coupons coated both sides with a 500 nm thick FeC amorphous film. Annealing performed in air at 530 ˚C - 1h for specimens A and B and at 630 ºC - 1h in air for specimen C

From Figure 5-27 one can see that the increase in strength is smaller if the heat treatment is performed in air. Indeed, the average increase of yield stress obtained for the annealing in air at 530˚C-1h is only (217 - 113.7) = 103 MPa while in high vacuum for the same specimens, the increase of strength was (259.32 - 113.7) = 146 MPa. The increase of strength is even smaller if the annealing temperature is increased. For the coupon annealed in air at 630˚C-1h the yield stress reaches 213 MPa which is only (213 - 113.7) = 99 MPa higher than the yield stress for a not-annealed IF steel. However, if the same annealing is performed in high vacuum, the yield stress can reach 306 MPa which is (306 - 113.7) = 192 MPa higher than the yield stress of an uncoated IF steel. If the annealing is performed in air, the FeC amorphous film is decarburized and this will lower the amount of carbon that can effectively diffuse towards the IF core. The amount of decarburization is higher if the temperature is raised. The carbon present in the FeC film is expected to react with the oxygen according to the following reactions:

$$C+O_2 \rightarrow CO_2 \quad \text{(eq. 5-4)}$$

$$CO_2+C \rightarrow 2CO \quad \text{(eq. 5-5)}$$

During annealing in air, the amount of oxygen and carbon is higher than the concentration of CO and CO_2, for this reason the above reactions evolve towards the right causing decarburization of the FeC film. According to literature, the same reactions occur during pack carburizing, however they evolve in the left direction ensuring carburization of the part since the ratio between CO and CO_2 present in the carburizing pack is properly controlled [157].

5.4. Ductility of coupons coated with FeC film after annealing

The ductility of tensile coupons coated on both sides with 500 nm FeC film and annealed in high vacuum was calculated by evaluating the reduction in area at the fracture surface. The area of the specimen after fracture was measured by taking a sequence of high magnification images with the SEM, merging them and measuring the area of the fractured surface with Image J (see Figure 5-28 and Figure 5-29). The reduction in area (q) is used as a parameter to evaluate ductility. If this value is high, it means that the coupon sustained locally a lot of deformation before fracturing and the ductility is high, while if the parameter is low, it means that the change of cross-sectional area was limited during the tensile test meaning that the specimen had poor ductility. The reduction in area q is defined as:

$$q = \frac{A_0 - A_f}{A_0} \times 100 \quad \text{(eq. 5-6)}$$

where, A_0 is the initial cross-sectional area of the coupon and A_f is the final cross-sectional area after fracture. A_f is the area measured by using Image J.

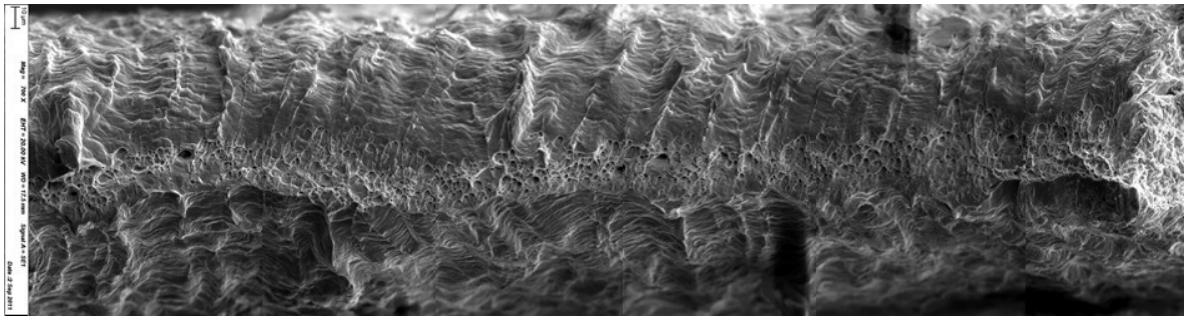

Figure 5-28 - Fracture surface of tensile coupon coated both sides with 500 nm thick FeC film and annealed at 430 ˚C - 1h in high vacuum

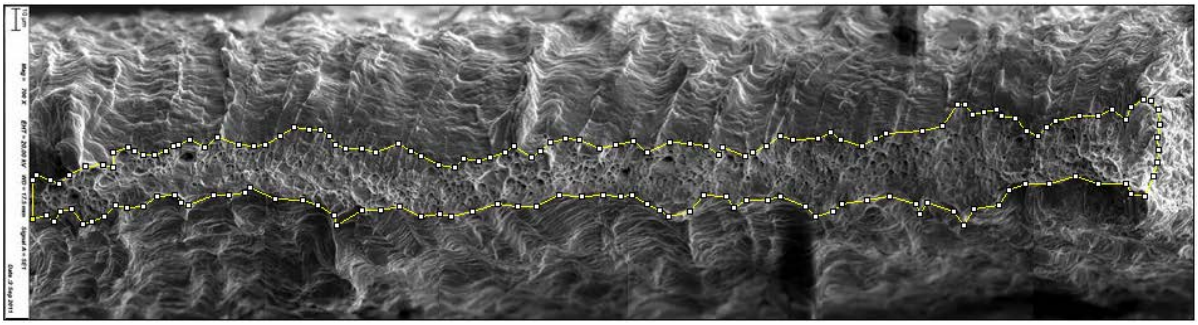

Figure 5-29 - Contour of the fracture surface defined with Image J for a tensile coupon coated both sides with 500 nm thick FeC film annealed at 430 ˚C – 1h in high vacuum

The values obtained are listed in Table 5-6. For each annealing temperature, the reduction in area was above 90% proving that the ductility of the specimen is preserved even if the IF steel has been strengthened. The specimen annealed at 630 ˚C - 1h was the one showing highest increase of yield stress but still its reduction in area is around 92% meaning that the ductility was not affected.

Film Thickness [nm]	Annealing	Reduction in Area (q)
500	330 ˚C - 1h	95.70%
500	430 ˚C - 1h	91.29%
500	530 ˚C - 1h	94.76%
500	630 ˚C - 1h	92.52%
500	710 ˚C - 1h	95.32%

Table 5-6 - Summary of the reduction in area calculated for coupon having different film thicknesses and annealed at different temperatures

5.5. Characterization of tensile coupons: FeC film crystallization

The yield stress obtained experimentally by annealing coated IF coupons can be compared to the theoretical yield stress calculated using the carbon concentration through thickness

predicted from the 1D diffusion model. The carbon content through thickness predicted using the 1D diffusion model for the various annealing temperatures was obtained by writing a subroutine which divides half the thickness of the coupon in 5 sublayers and provides the carbon concentration in each sublayer. The discretization of half the sample thickness in 5 sublayers was representative enough to capture the variation of carbon concentration through thickness. Successively, the increase in yield stress with carbon content was calculated for each sublayer using the equation $\Delta\sigma = Mm(X_C)^{1/2}$, while the yield stress of each sublayer was obtained by adding this increase of yield stress to the yield stress of an uncoated IF steel (113.7 MPa). The average yield stress of the entire sample was then calculated from the yield stress of each layer. The subroutine considers half of the coupon since the carbon profile is expected to be symmetric due to the coating being present on both sides. Numerical values of the theoretically expected yield stresses and of the yield stresses obtained experimentally are shown in Table D- 35 in Appendix D (section D.7). For the specimens annealed at 530 ˚C and at 710 ˚C for 1h, the specimens having the lowest yield stress were discarded from the calculation of the average experimental yield stress to minimize the standard deviation. The comparison between the yield stress predicted by the model and the experimental yield stresses is shown in Figure 5-30. From this graph, the theoretical carbon diffusion predictions are in good agreement with experimental values of yield stress for annealing at 330 ˚C, 430 ˚C , and even 530 ˚C - 1h, but the two curves are diverging for annealing at 630 ˚C - 1h and at 710 ˚C - 1h. Moreover, at 710 ºC there is a decrease in mechanical properties compared to the annealing performed at 630 ˚C - 1h.

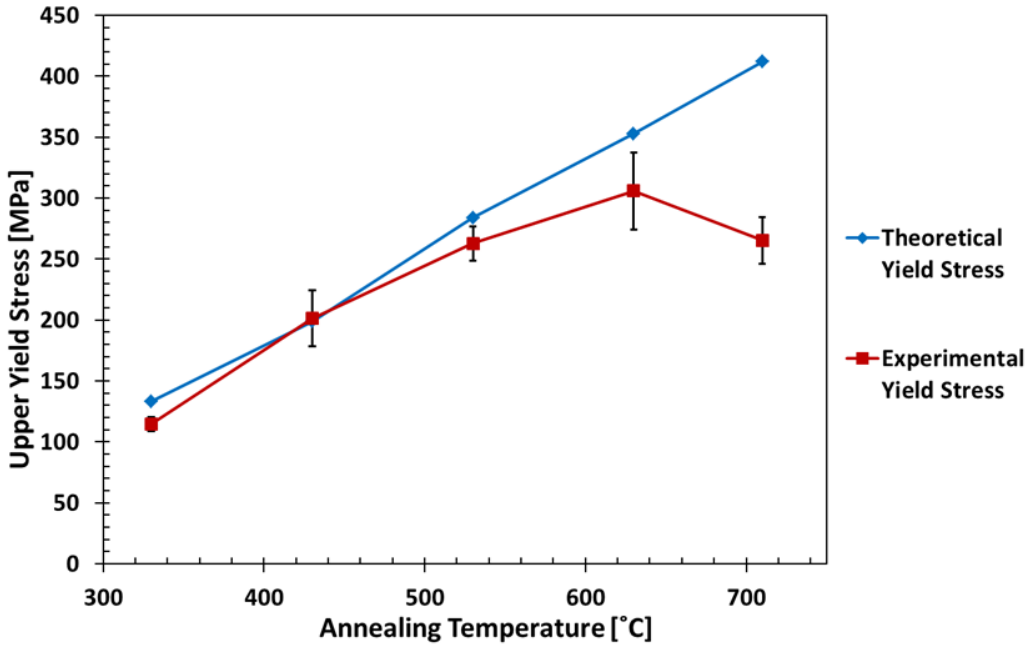

Figure 5-30 - Comparison between yield stress expected theoretically and yield stress obtained experimentally for annealing in high vacuum at different temperatures for 1h of specimens coated both sides with 500 nm FeC film

The reason of the high difference between the theoretical expected yield stress and the experimental one at 630 ˚C and 710 ˚C is related to the crystallization of the FeC film occurring at temperatures above 500 ˚C. In particular, it will be shown later in this paragraph that film crystallization limits the amount of carbon available for diffusion towards the IF substrate and that this amount of carbon is lower than the solubility limit of carbon in ferrite for temperatures of 630 ˚C and 710 ˚C.

It was already shown in the previous sections that during the tensile tests, the film completely exfoliates after annealing at 330 ˚C - 1h and 430 ˚C - 1h, while at temperatures equal or higher than 530 ˚C - 1h the film is adherent to the IF substrate and during testing it cracks but does not exfoliate. Pictures of the tested surfaces of coupons coated both sides with 500 nm FeC film and annealed in high vacuum were taken using scanning electron microscope (SEM) to support the above statements.

- **Surface of coupons annealed in high vacuum at 330 ˚C – 1h after testing**

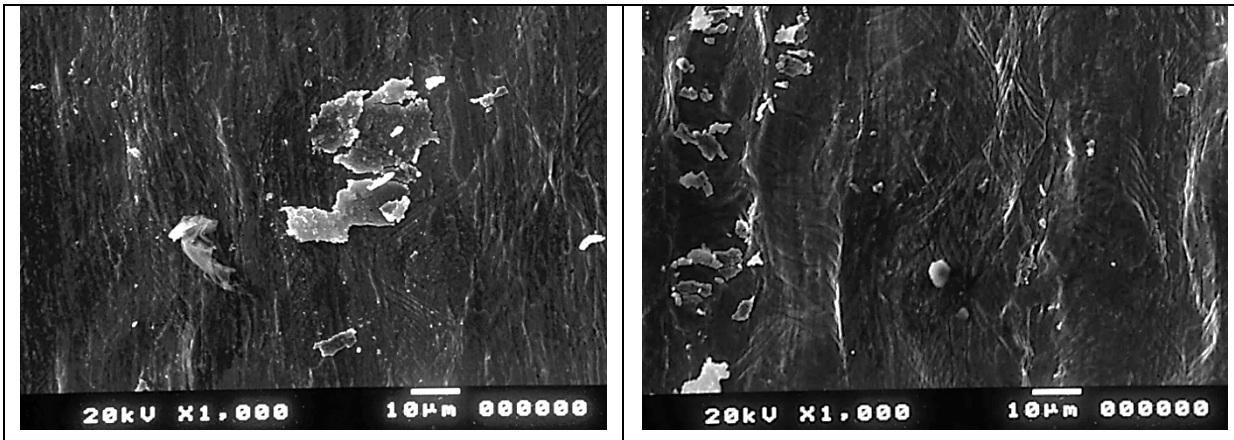

(a) Surface of a tensile coupon annealed at 330˚C - 1h in high vacuum after tensile testing. The image taken far from the fracture surface

(b) Surface of a tensile coupon annealed at 330˚C-1h in high vacuum after tensile testing. The image was taken close to the fracture surface

Figure 5-31 - SEM images of the surface of a both sides coated coupon annealed in high vacuum at 330 ºC - 1h

- **Surface of coupons annealed in high vacuum at 430 ˚C – 1h after testing**

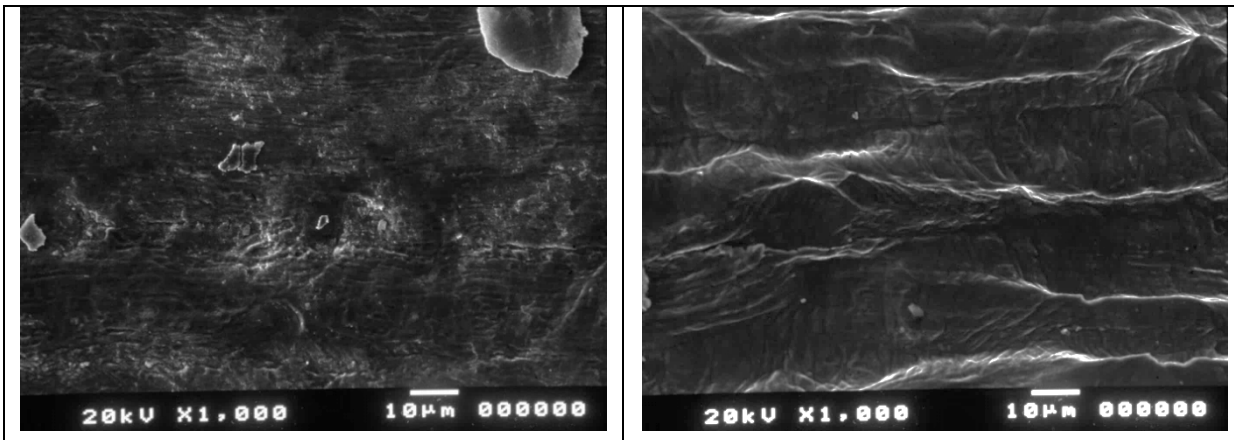

(a) Surface of a tensile coupon annealed at 430˚C - 1h in high vacuum after tensile testing. Image taken far from the fracture surface

(b) Surface of a tensile coupon annealed at 430˚C - 1h in high vacuum after tensile testing. Image taken close to the fracture surface

Figure 5-32 - SEM images of the surface of a both sides coated coupon annealed in high vacuum at 430 ºC - 1h

In Figure 5-31 (a) and in Figure 5-32 (a), some residues of FeC film can be seen after the tensile test, however most of the specimen is exfoliated. The coupon appears completely exfoliated closer to the fracture surface as shown in Figure 5-32 (b) . From Figure 5-33 to Figure 5-35, the film appears still adherent to the IF substrate even after tensile testing. The

coated surface shows only fracturing of the film even close to the fractured surface of the coupon.

- **Surface of coupons annealed in high vacuum at 530 ˚C – 1h after testing**

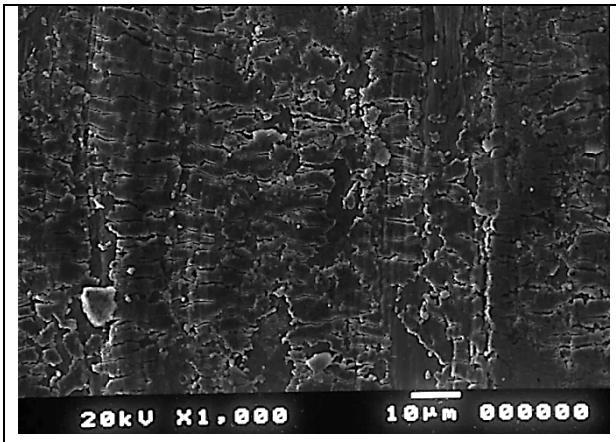

(a) Surface of a tensile coupon annealed at 530˚C - 1h in high vacuum after tensile testing. The image was taken far from the fracture surface

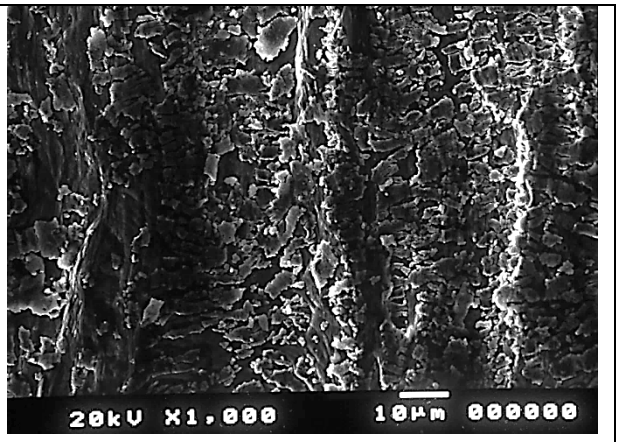

(b) Surface of a tensile coupon annealed at 530˚C - 1h in high vacuum after tensile testing. The image was taken close to the fracture surface

Figure 5-33 - SEM images of the surface of a both sides coated coupon annealed in high vacuum at 530 ºC - 1h

- **Surface of coupons annealed in high vacuum at 630 ˚C – 1h after testing**

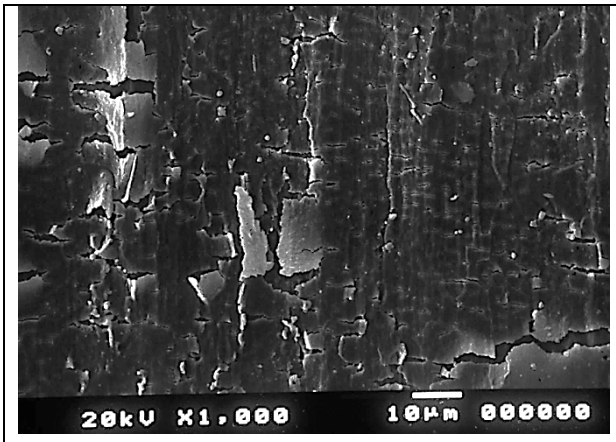

(a) Surface of a tensile coupon annealed at 630˚C - 1h in high vacuum after tensile testing. The image was taken far from the fracture surface

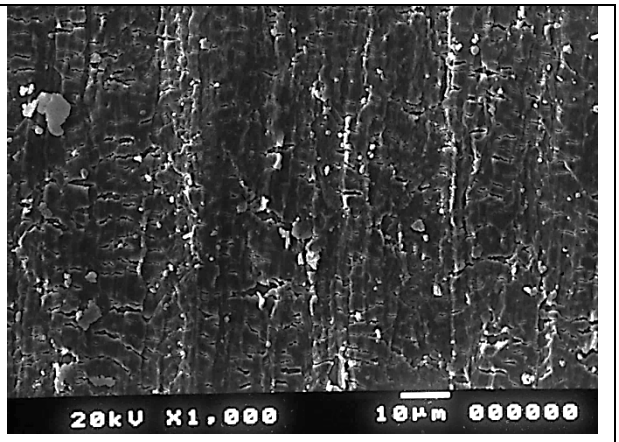

(b) Surface of a tensile coupon annealed at 630˚C - 1h in high vacuum after tensile testing. The image was taken close to the fracture surface

Figure 5-34 - SEM images of the surface of a both sides coated coupon annealed in high vacuum at 630 ºC - 1h

- **Surface of coupons annealed in high vacuum at 710 ˚C – 1h after testing**

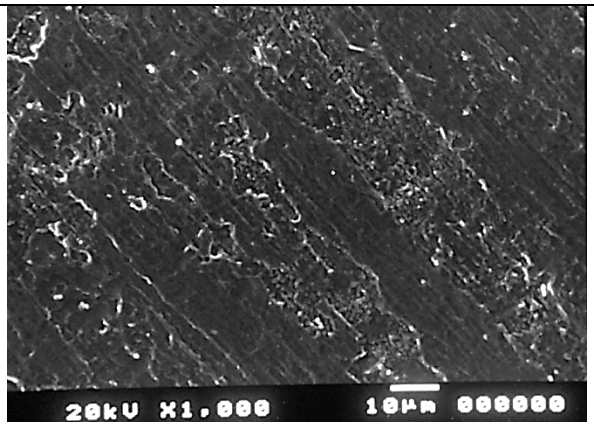

(a) Surface of a tensile coupon annealed at 710 ˚C - 1h in high vacuum after tensile testing. The image was taken far from the fracture surface

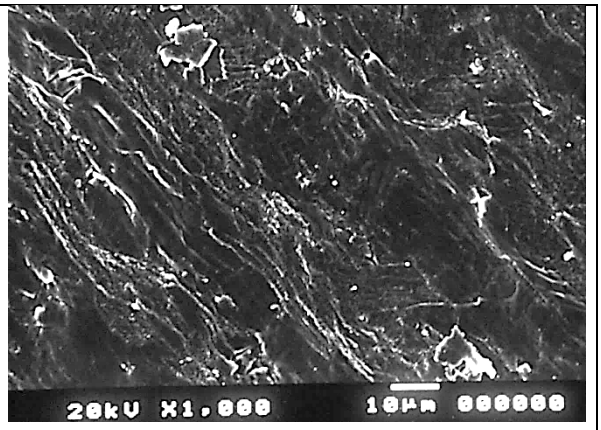

(b) Surface of a tensile coupon annealed at 710˚C - 1h in high vacuum after tensile testing. The image was taken close to the fracture surface

Figure 5-35 - SEM images of the surface of a both sides coated coupon annealed in high vacuum at 710 ºC - 1h

From the SEM images and from the behaviour noticed during tensile tests performed under optical microscope, it was inferred that the FeC film is undergoing some transformation during the annealing. More specifically, it changes its structure if the annealing is performed at temperatures equal or higher than 530 ˚C for 1h. In order to clearly prove this, two pieces of IF steel coated both sides with 500 nm FeC film were prepared. One of them was annealed in high vacuum at 430 ˚C and the other was annealed in high vacuum at 530 ˚C, again both of them for 1h. The specimens were shipped to the University of Rouen (France) and TEM specimens were prepared by using focused ion beam (FIB). The specimens were analyzed under the TEM by Dr. Amélie Fillon. In Figure 5-36 an image of the as-deposited state of the FeC film on the IF substrate is shown. Figure 5-37 shows the diffraction pattern for a specimen annealed at 430 ˚C and in Figure 5-38 the diffraction pattern for a specimen annealed at 530 ˚C is reported.

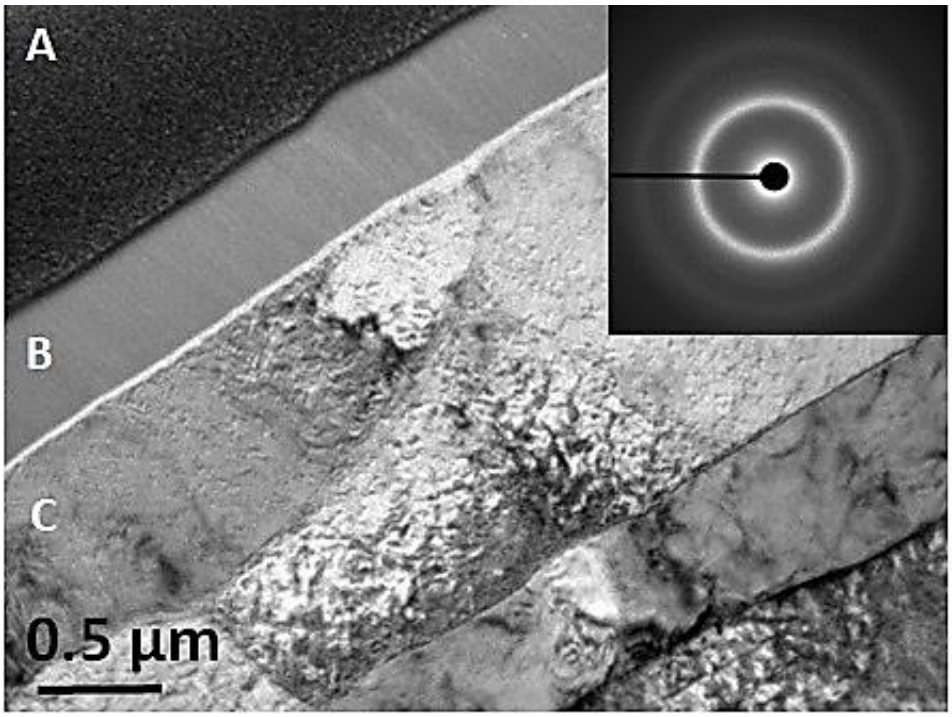

Figure 5-36 - TEM Image: cross view of IF substrate coated with 500 nm of FeC film as deposited. The SAED pattern obtained from the film is included in the figure. A is the Pt cap layer, B is the FeC film and C is the IF substrate (courtesy of Dr. Amelié Fillon)

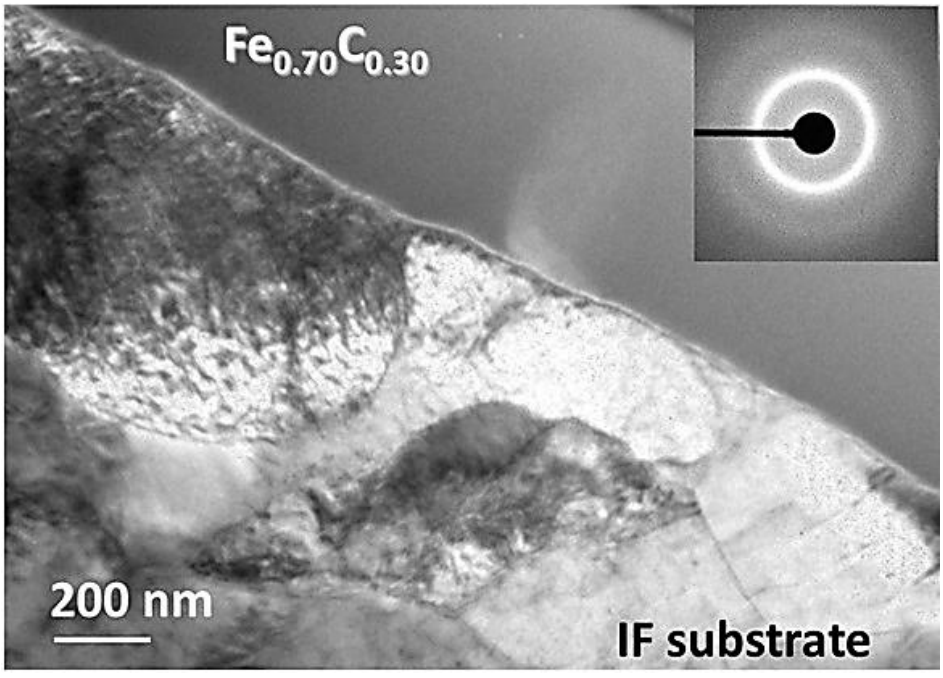

Figure 5-37 - TEM Image: cross view of IF substrate coated with 500 nm of FeC film and annealed at 430 ˚C in high vacuum. The SAED pattern obtained from the film is included in the figure (courtesy of Dr. Amelié Fillon)

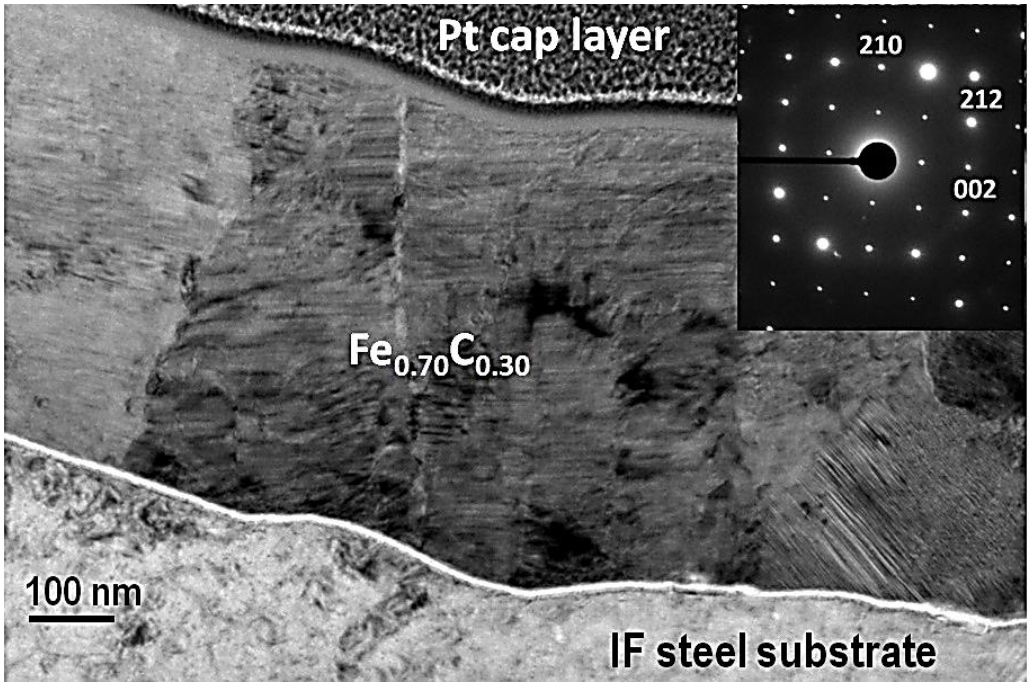

Figure 5-38 - TEM Image: cross view of IF substrate coated with 500 nm of FeC film and annealed at 530 ˚C in high vacuum. The SAED pattern obtained from the film is included in the figure (courtesy of Dr. Amelié Fillon)

From TEM analyses, the FeC film shows the typical halos of an amorphous state when it is just deposited on the IF substrate (see Figure 5-36). After annealing at 430 ˚C for 1h, the film is still amorphous (see Figure 5-37), while raising the annealing temperature at 530 ˚C causes crystallization of the FeC film into cementite (see Figure 5-38). In-situ TEM studies were performed in collaboration with the University of Rouen and INSA-Lyon showing that the FeC film transforms into cementite and that the kinetics of transformation is related to the initial carbon content in the film. In particular, from the in-situ TEM annealing analyses published by Fillon et al. [158] on FeC films, it was proven that films containing 15 at% of carbon start to nucleate first ferrite at low temperature (250 ˚C) and then above 300 ˚C both ferrite and cementite are present. In particular, the matrix takes only 3 minutes to fully crystallize into cementite. Another in-situ TEM annealing was performed on an amorphous FeC film containing 25 at% of carbon and it was found that with this higher amount of carbon only cementite is formed during the crystallization of the film, but no ferrite grains were detected. Moreover, the crystallization into cementite began at around 330˚C and it took around 3-5 minutes. XRD analyses were performed by the University of Rouen on FeC amorphous film containing 30 at% of carbon deposited on silicon wafer and from the XRD

pattern (Figure 5-39) it was shown that the film remains amorphous until 430˚C, where only a couple of peaks of cementite could be identified and they appear broad due to most of the microstructure being still amorphous. At 530 ˚C, more peaks corresponding to cementite are detected and they appear less broad compared to the peaks at 430 ºC, confirming that at or above 530 ºC the crystallization of the film is taking place.

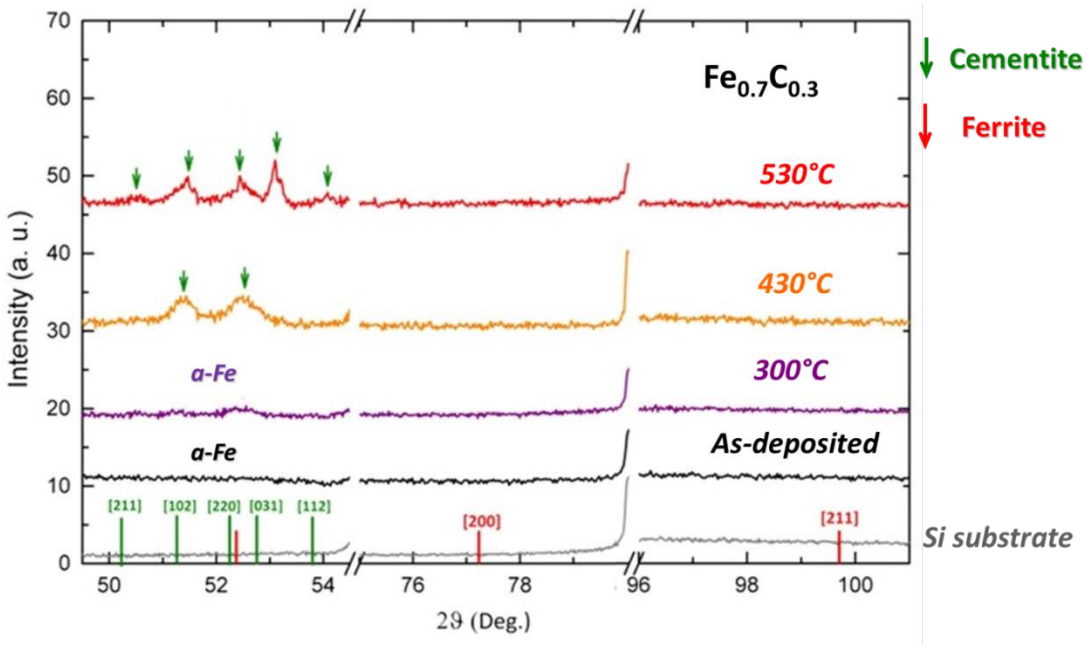

Figure 5-39 - X-ray diffraction analyses performed on FeC film (30 at% carbon content) deposited on silicon substrate (Co K-alpha radiation was used) (courtesy of Dr. Amélie Fillon)

This confirms what was detected during the tensile tests, since the exfoliation of the film was evident for the annealing at 330 ˚C - 1h and 430 ˚C - 1h but starting from 530 ˚C - 1h the film did not exfoliate. Based on these results, it can be concluded that the film is transformed into cementite for annealing at or above 530 ˚C - 1h and a stoichiometric calculation can be performed to calculate how many carbon atoms remain available for diffusion towards the substrate after the film has crystallized. The initial composition of the film is 70 at% of iron and 30 at% of carbon. These quantities are equivalent to the mol% and considering that a mole contains a number of atoms equal to the Avogadro's number 6.022×10^{23} atoms/mol, it is possible to obtain the number of atoms corresponding to 70 at% of Fe and 30 at% of carbon. The values are summarized in Table 5-7.

500nm	Fe	C
at%	70	30
mol%	70	30
Number of atoms	(0.70 x 6.022x 10^{23}) = 4.215x10^{23}	(0.30 x 6.022x 10^{23}) = 1.807x10^{23}

Table 5-7 - Iron and carbon atoms for FeC film of 500 nm thickness

The formation of cementite (Fe_3C) requires 3 atoms of iron and one of carbon so if we assume that all the iron is used to produce cementite, the carbon atoms "consumed" by this crystallization are (4.215x10^{23}/3) = 1.405x10^{23} C atoms. At this point, the amount of carbon available to be diffused into the IF substrate can be calculated by subtracting this quantity from the initial amount of carbon atoms present in the film as: (1.807x10^{23}– 1.405x10^{23}) = 4.02x10^{22} C atoms are thus available to be diffused. This amount can be converted into mol by using the Avogradro's number as: = (4.02x10^{22}/6.022x10^{23}) = 0.0668 mol within the 500 nm thick film. This concentration of carbon atoms has then to be "diluted" into the 200 µm (which means 200x10^3 nm) thick IF substrate. The ratio between the thickness of the substrate and the thickness of the film is (200000/500) = 400. So, the concentration of carbon atoms that can be diffused from the film is given by: (0.0668/400) x 2 x 100 = 0.0334 mol%, where the 2 factor is due to the fact that the specimens are coated both sides. The carbon available for diffusion and strengthening of the substrate, (0.0334 mol% for 500 nm thick FeC film) is just slightly higher than the solubility limit of C into ferrite at 530 ˚C - 1h which would be 0.0260 at%. Considering this, the strengthening of the IF substrate can be calculated by assuming that only the amount of carbon corresponding to the solubility limit at 530 ˚C will diffuse into the substrate. The expected increase of yield stress is therefore: $\Delta\sigma$ = (2.5) x (0.051 x 82000) x $(0.0260/100)^{1/2}$ = 168.6 MPa which added to the 113.7 MPa of the uncoated IF steel gives 282 MPa, while the experimental result is around 263 MPa. The discrepancy between the two values falls inside the standard deviation caused by the uncertainty associated to carbon content in the film and to the uncertainty associated to its thickness as it will be discussed later in detail.

It has to be noted that if all the carbon amount is considered to diffuse into the IF substrate, then the increase of yield stress would be given by: $\Delta\sigma$ = (2.5) x (0.051 x 82000) x $(0.0334/100)^{1/2}$ = 191 MPa that added to 113.7 MPa of the uncoated IF steel, it will give a total yield stress of 305 MPa which is close to the yield stress experimentally found for

specimens coated both sides with 500 nm FeC film and annealed at 630˚C for 1h (YS = 306 MPa), since for this temperature the solubility limit of carbon into ferrite is higher than 0.0334 at%, so all the carbon that remains in the film after its transformation into cementite can be diffused into the substrate.

Taking into account the film crystallization, it is possible to introduce another curve in the graph shown in Figure 5-30, given that the theoretical yield stress can be calculated considering that the maximum amount of carbon that can be diffused above 500 ˚C is 0.0334 at%. Moreover, it is possible to introduce error bars for annealing at 530 ˚C, 630 ˚C and 710 ˚C considering that the variation of carbon content into the film, due to PVD deposition, is ± 3 at%. For annealing at 330 ˚C, 430 ˚C, the solubility limit of carbon into ferrite is always ensured, for this reason the experiments are in good agreement with theoretical prediction from the 1D diffusion model. In order to evaluate the standard deviation caused by the tolerance of ± 3 at% on carbon concentration in the film, the stoichiometric calculations previously illustrated were repeated considering 27 at% of carbon in 500 nm thick FeC film and then considering 33 at% of carbon in 500 nm thick FeC film. The detailed calculations are reported in Appendix D (section D.8).

Figure 5-40 shows the curve of the theoretical yield stress obtained considering the crystallization of the film and the standard deviation given by the error bar. The variation of ± 3 at% of carbon content will have high influence on the diffusion obtained for 630 ˚C and 710 ˚C since for these temperatures the solubility of carbon into ferrite is high, while for 430 ˚C and 330 ˚C, the solubility of carbon into ferrite is so low that it is diffused even if the concentration of carbon in the film is 27 at%. For this reason, the error bars where not indicated for 430 ˚C and 330 ˚C. At 530 ˚C, the maximum amount of carbon which remains in the film is not expected to diffuse completely since this is higher than the solubility of carbon into ferrite at that temperature, which means that the upper portion of the error bar at 530 ˚C in Figure 5-40 will never be obtained.

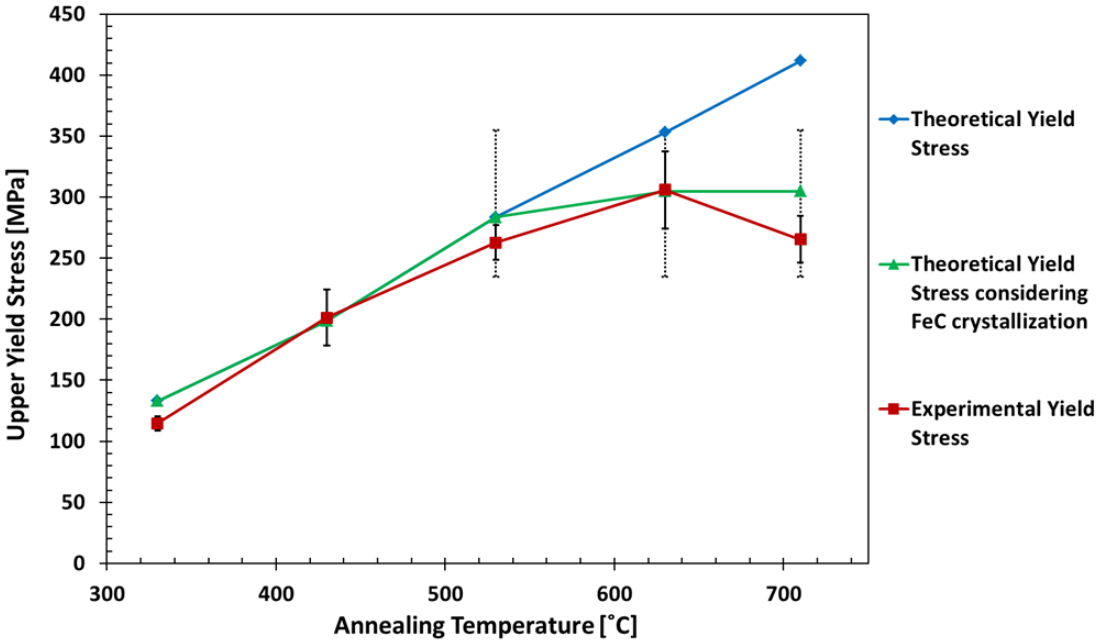

Figure 5-40 - Comparison between theoretical yield stress and experimental yield stress considering FeC film crystallization

However, there is not only variation of carbon content in the film, but there is also an uncertainty associated with film thickness. In particular, the film thickness tolerance is around ± 20 nm considering a deposition rate of 12.2 nm/min with an uncertainty of ± 0.50 nm/min (Ben Lawrence, Thesis Proposal [129]). This uncertainty in thickness will also cause a variation on the carbon content available for diffusion. The error bars shown in Figure 5-40 were calculated again considering the combined effect of film thickness variation and carbon content variation and the results are shown in Figure 5-41. The film thickness variation of ± 20 nm enlarges more the error bars compared to the carbon concentration variation (detailed calculations are shown in Appendix D, section D.8.2). However, it seems that the error bars referred to the experimental standard deviation are well predicted just considering the variation of carbon content in the film. Thus, it can be concluded that this parameter is sufficient to predict the variation of mechanical properties, while the variation in film thickness associated to the PVD deposition is of minor importance.

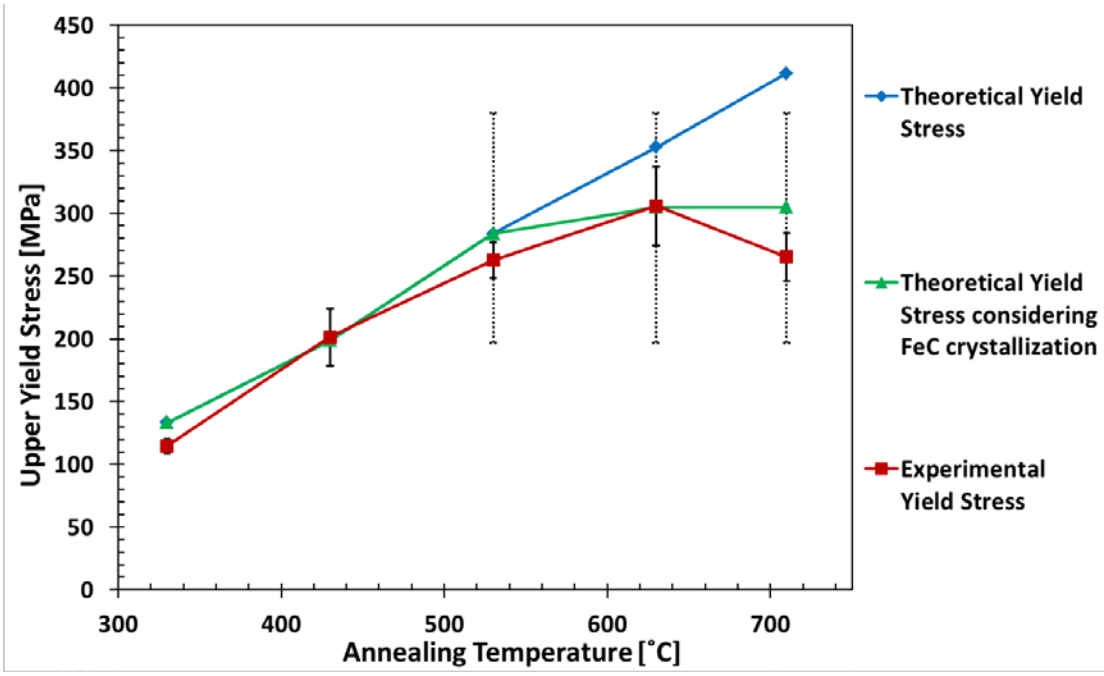

Figure 5-41 - Comparison between theoretical yield stress and experimental yield stress considering FeC film crystallization – error bars were calculated considering both carbon content variations and film thickness variation

From Figure 5-40 and Figure 5-41 it can be seen that taking into account film crystallization and its variation of initial carbon content or the variation of carbon content and film thickness, the experimental results can be well predicted. However, it was noticed that at 710 ˚C – 1h there is a further drop in yield stress compared to the yield stress found at 630 ˚C – 1h and this is not related to the crystallization of the film.

The decrease of yield stress observed at 710 ˚C - 1h is related to carbon diffusion in the IF steel since the same drop is not present in uncoated samples annealed at the same temperature. There are different reasons which could explain this drop; the first one could be that at 710 ˚C some decarburization of the film occurs due to the presence of an oxide layer between the FeC film and the IF substrate caused by the Nital surface cleaning performed before the PVD deposition. However, even changing the cleaning solution and reducing the thickness of the oxide layer, no improvement of diffusion at 710 ºC was recorded (detailed results are reported in Appendix D (section D.5)). Another reason could be due to the formation of TiC precipitates which could deplete the carbon available at dislocation to strengthen the IF steel. The amount of “free” titanium inside the IF steel used in this work is 0.018 wt% (see eq. 5-3) and these titanium atoms could interact with the carbon diffusing at

710 ˚C. The diffusion of titanium into ferrite can be calculated according to the following equation [159]:

$$D = \left(205 \times 10^{-3}\right) \times \exp\left(\frac{-293200}{RT}\right) \qquad \text{(eq. 5-7)}$$

In eq. 5-7 the pre-exponential factor is expressed in m^2/s, while the activation energy is 293200 J/mol and the gas universal constant R is 8.31 J/mol·K.

Using the above equation, the diffusion coefficient for titanium inside iron can be calculated at 710˚C and its value is 5.29×10^{-13} cm^2/s, which is quite low. The diffusion at grain boundaries is faster even for substitutional atoms. However even if for interstitial atoms it was reported that their diffusion through grain boundaries is 3 or 4 order of magnitudes faster [18], it can be inferred as first approximation that substitutional atoms will diffuse slower than this orders so a 2 seems to be a good compromise. So, through the grain boundaries, the diffusion of titanium can be considered 2 order of magnitude faster giving 5.29×10^{-11} cm^2/s, for this reason, it is possible that this titanium has enough mobility at 710 ˚C to form TiC precipitates or to interact with TiS particles already present in the raw IF steel. However, the precipitation of new TiC particles because of the "free" titanium should happen at all temperatures not only at 710˚C, so it is believed that at this temperature there is a coarsening of TiC particles which are already present in the IF substrate or most probably an in-situ transformation of TiS precipitates. Concerning TiS precipitates, other researchers have shown the mechanism of carbon capture by TiS and $Ti_4C_2S_2$ particles in both ultra-low carbon steels and IF steels containing titanium [35], [160], [161], [162], [36]. According to their TEM observations, $Ti_4C_2S_2$ particles are formed by an in-situ transformation of TiS caused by both diffusion of Ti and C. Concerning the coarsening of TiC precipitates, according to the study of Huo et al. [161], the mobility of dislocations inside IF steel can be limited by nanometric TiC precipitates which are present in the initial microstructure of IF steel, but according to their study, these precipitates can coarsen at temperatures above 660 ˚C (933K) and they will not be more effective in limiting dislocations motion. This is probably one reason that could explain why at 710 ˚C the mechanical properties are lower than the one obtained for annealing at 630 ˚C. In the next paragraph, it will be shown that according to EDS, TEP and APT results, annealing at 710 ˚C results in carbon being

"captured" by TiS precipitates present in the raw IF steel or results in the coarsening of TiC precipitates.

The standard deviation found for annealing at 430 ˚C cannot be justified by a full crystallization of the FeC film into cementite since at this temperature most of the film is still amorphous. However, it is possible that some zones of the film could start to crystallize; moreover when the samples are placed in the vacuum furnace, their position might be slightly misaligned from the position of the thermocouple, causing a variation of ± 10 ˚C of temperature which could justify the variation seen for the yield stress at 430 ˚C. At 330 ˚C, the increase of yield stress is lower than what expected, probably the solubility limit of carbon into ferrite or the diffusion coefficient of carbon into ferrite at this temperature were overestimated.

5.6. Characterization of tensile coupons: annealing at 710 ˚C – 1h

In the literature review it was mentioned that TEM observations of IF steels, which have undergone a batch annealing (BA) treatment (10h at 973 K which corresponds to 700 ˚C), showed dissolution of TiS precipitates and an increase in the number of $Ti_4C_2S_2$ and Ti-Fe-P particles and a coarsening of TiC particles [36]. According to these TEM observations, $Ti_4C_2S_2$ particles are formed by an in-situ transformation of TiS caused by the diffusion of Ti and C as shown in Figure 2-7 [36]. From TEP measurements, Carabajar et al. [36] concluded that long heat treatments at temperatures of 873-973 K (600 ˚C – 700 ˚C) can cause a decrease in the amount of carbon because of the precipitation of incoherent titanium carbides or carbosulphides. In order to prove that the capturing of carbon by TiS particles to form $Ti_4C_2S_2$ or the coarsening of TiC are the two main events responsible for a decrease of mechanical properties at 710 ˚C, the following techniques were used:

- Energy Dispersive X-ray Spectroscopy (EDS): by analyzing the fracture surface of the specimens at high magnification, some particles were found and their composition was obtained through EDS analyses;
- Thermoelectric Power measurements (TEP): the amount of carbon in solid solution at dislocations was measured for specimen annealed at 430 ˚C, 530 ˚C, 630 ˚C and 710 ˚C – 1h in the high vacuum furnace;

- Atom Probe Tomography (APT): the amount of carbon in solid solution was measured on several specimens annealed at 530 ˚C and 710 ˚C – 1h in high vacuum and in the uncoated and not-annealed IF steel.

5.6.1. Energy Dispersive X-ray Spectroscopy (EDS)

Initially, EDS analyses were performed on a fracture surface of a coated coupon of IF steel which was not annealed. After tensile testing, some particles were noticed on the fracture surface and their chemical composition was measured. In Figure 5-42 the fracture surface for this coupon is reported. Some particles are visible, however many debris from the FeC film are also noticed on the surface.

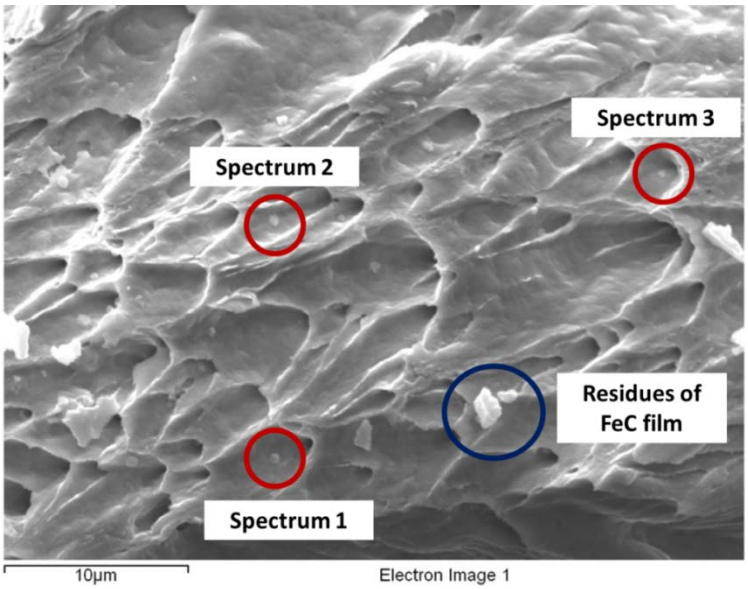

Figure 5-42 - Fracture surface of a coated and not-annealed tensile coupon

Zone	Ti [wt%]	C [wt%]	S [wt%]	O [wt%]	Fe [wt%]
Spectrum 1	3	0	0	0	97
Spectrum 2	4	0	1.4	5	89.6
Spectrum 3	1.5	0	1	0	97.5
Spectrum on residues of FeC film	0	27.2	0	0	72.8

Table 5-8 - Composition of particles detected on the fracture surface of a coated and not-annealed IF coupon after tensile testing

EDS analyses were then performed on the fracture surface of an uncoated coupon of IF steel which had been annealed at 710 ˚C for 1h in high vacuum. Some particles were visible on

the fracture surface and their chemical composition was obtained. In Figure 5-43 one zone of the fracture surface that was analyzed for this specimen is shown and the selected particle is indicated with the name “spectrum 1”. Another area of the fractured surface of the same specimen was selected and the composition of another particle was measured as well as the background composition of the steel (all the numerical values of the obtained compositions are reported in Table 5-9).

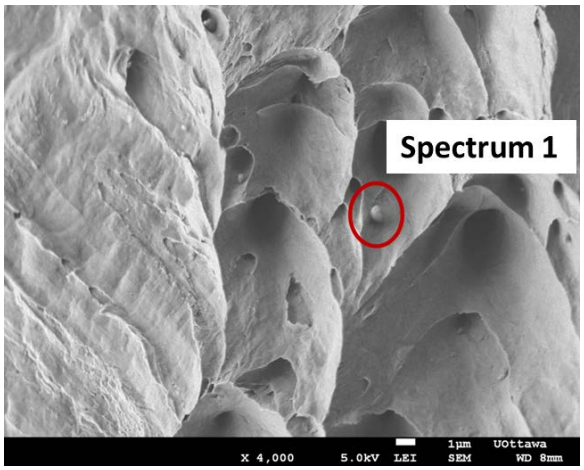

Figure 5-43 - Fracture surface of an uncoated tensile tested coupon annealed at 710 ˚C – 1h. Spectrum 1 indicates the first analyzed particle

Zone	Ti [wt%]	C [wt%]	S [wt%]	Fe [wt%]
Spectrum 1 – particle (Figure 5-43)	51.5	0	48.5	0
Spectrum 2 – particle in another zone of fracture surface	23.2	0	10.5	66.3
Spectrum 3 – Background	0.45	0	0.20	99.35

Table 5-9 - Composition obtained for particles present on the fracture surface of an uncoated tensile coupon annealed at 710 ˚C – 1h

The few particles found on the fracture surface of the coated and not-annealed coupon and of the uncoated coupon annealed at 710 ˚C had mainly titanium and sulphur as chemical elements but, no carbon was detected. The high amount of iron detected in “spectrum 2” in Table 5-9 is due to the particle being quite small so some iron from the background was also measured.

EDS analyses were performed also on few particles seen on the fracture surface of a specimen annealed at 430 ˚C – 1h in high vacuum. An image of the analyzed particles is shown in Figure 5-44, while the chemical composition is reported in Table 5-10.

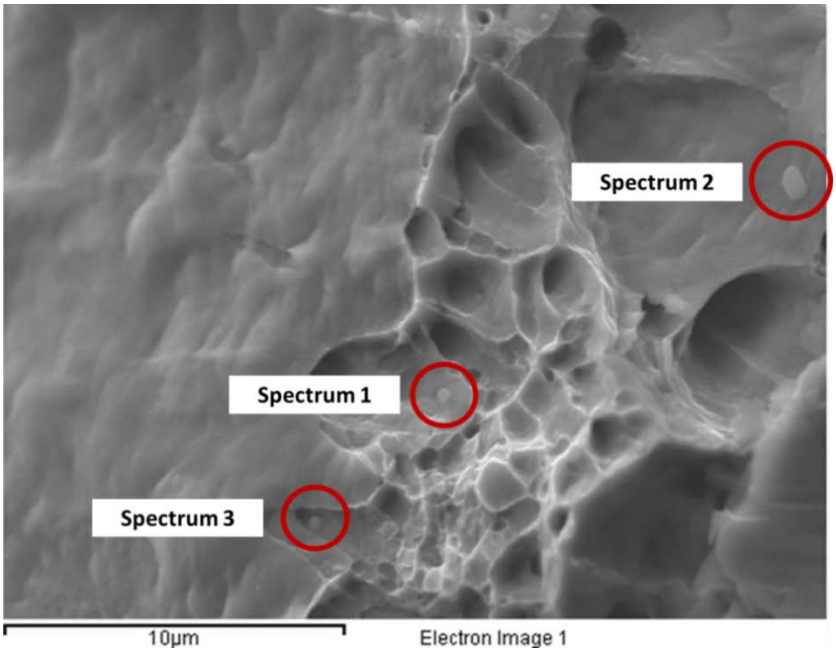

Figure 5-44 - Fracture surface of tensile coupon coated both sides and annealed at 430 ˚C – 1h in high vacuum. Spectra 1, 2 and 3 indicate the particles whose composition was analyzed

Zone	Ti [wt%]	C [wt%]	S [wt%]	Al [wt%]	Si [wt%]	Mn [wt%]	Fe [wt%]
Spectrum 1	4.8	0	5.5	8.4	0	0	81.3
Spectrum 2	13.6	8	14.8	0	0.4	1.2	62
Spectrum 3	0	5	0	0	0	0	95

Table 5-10 - Composition obtained for particles present on the fracture surface of a both sides coated tensile coupon annealed at 430 ˚C – 1h

EDS analyses were performed also on particles found in a specimen annealed at 530 ˚C – 1h in high vacuum.

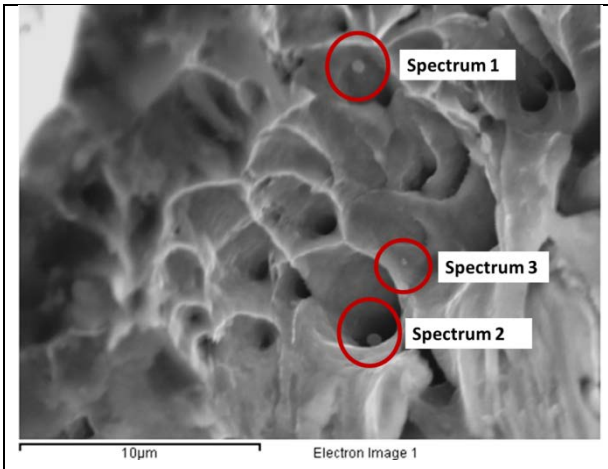

(a) Fracture surface of tensile coupon coated both sides and annealed at 530 ˚C – 1h in high vacuum. Spectrum 1, 2 and 3 indicate the particles whose composition was analyzed

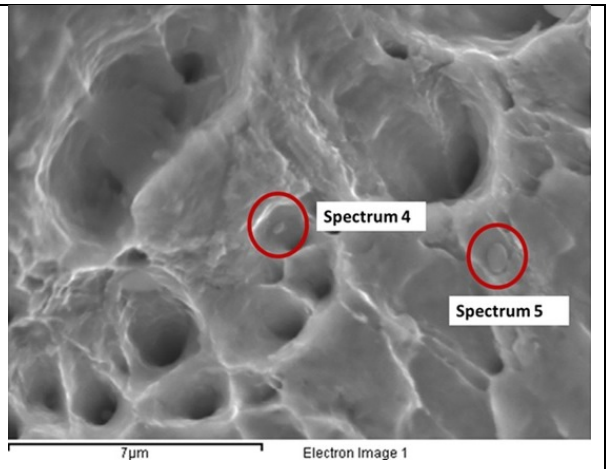

(b) Fracture surface of tensile coupon coated both sides and annealed at 530 ˚C – 1h in high vacuum. Spectrum 4 and 5 indicate the particles whose composition was analyzed

Figure 5-45 - Fracture surface of tensile coupon coated both sides and annealed at 530 ˚C – 1h in high vacuum. Spectra 1, 2 and 3 (a) and 4, 5 (b) indicate particles whose composition was analyzed

Zone	Ti [wt%]	C [wt%]	S [wt%]	Al [wt%]	Si [wt%]	Mn [wt%]	Fe [wt%]
Spectrum 1	4.4	8.8	0	0	0.3	0.5	86
Spectrum 2	4.2	1	0	0	0.1	0.5	94.2
Spectrum 3	0	4.2	0	0	0.1	0	95.7
Spectrum 4	0.7	0.9	0	0.1	0.1	0.3	97.9
Spectrum 5	9.3	2	3.5	0	0.2	0.4	84.6

Table 5-11 - Composition obtained for particles present on the fracture surface of a both sides coated tensile coupon annealed at 530 ˚C – 1h

EDS analyses were performed also on particles found in a specimen annealed at 630 ˚C – 1h in high vacuum.

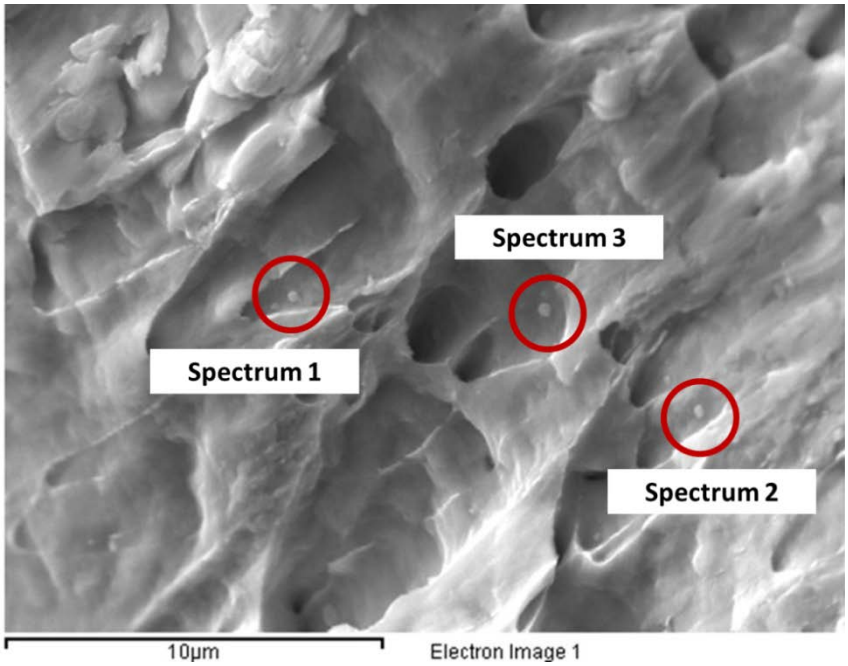

Figure 5-46 - Fracture surface of tensile coupon coated both sides and annealed at 630 ˚C – 1h in high vacuum. Spectra 1 and 2 indicate the particles whose composition was analyzed

Zone	Ti [wt%]	C [wt%]	S [wt%]	Al [wt%]	Si [wt%]	Mn [wt%]	Fe [wt%]
Spectrum 1	3.6	5.7	4.4	0	0	0.9	85.4
Spectrum 2	2	4.7	2.5	0	0	0	90.8
Spectrum 3	8	2.5	8.5	0	0	0	81

Table 5-12 - Composition obtained for particles present on the fracture surface of a both sides coated tensile coupon annealed at 630 ˚C – 1h

Finally EDS analyses were performed on particles found in specimens annealed at 710 ˚C – 1h in high vacuum. In particular for this temperature, one specimen with high yield stress and one specimen with low yield stress were analyzed in order to detect if the number and the composition of the particles seen on the fracture surface could be related to the change in yield stress.

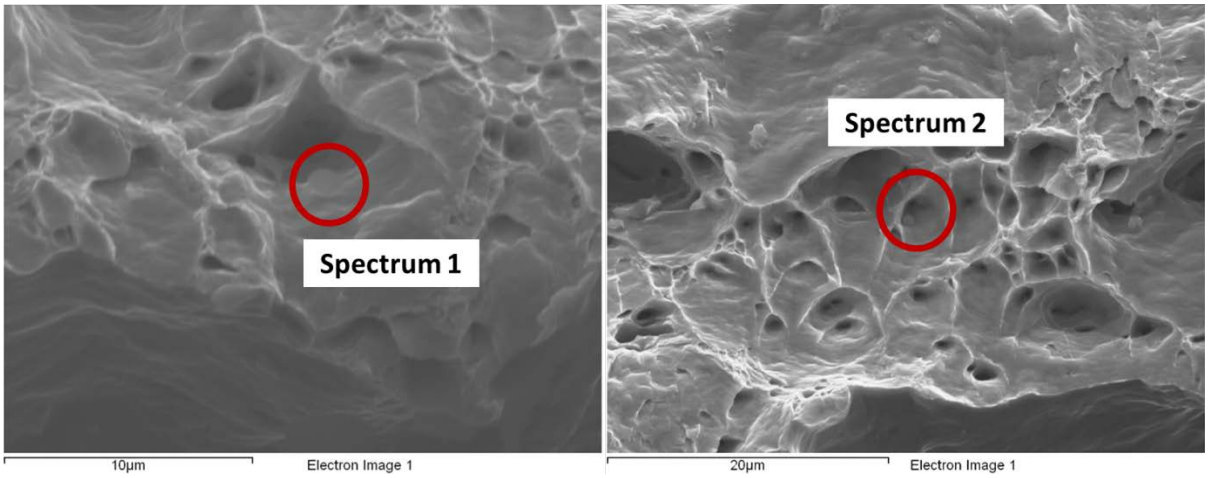

Figure 5-47 - Fracture surface of tensile coupon coated both sides and annealed at 710 ˚C – 1h in high vacuum. Spectra 1 and 2 indicate the particles whose composition was analyzed (specimen F-9)

Zone	Ti [wt%]	C [wt%]	S [wt%]	Mn [wt%]	Fe [wt%]
Spectrum 1	21	0	21.7	3.6	53.7
Spectrum 2	2	0	2	0	96

Table 5-13 - Composition obtained for particles present on the fracture surface of a both sides coated tensile coupon annealed at 710 ˚C – 1h (specimen F-9)

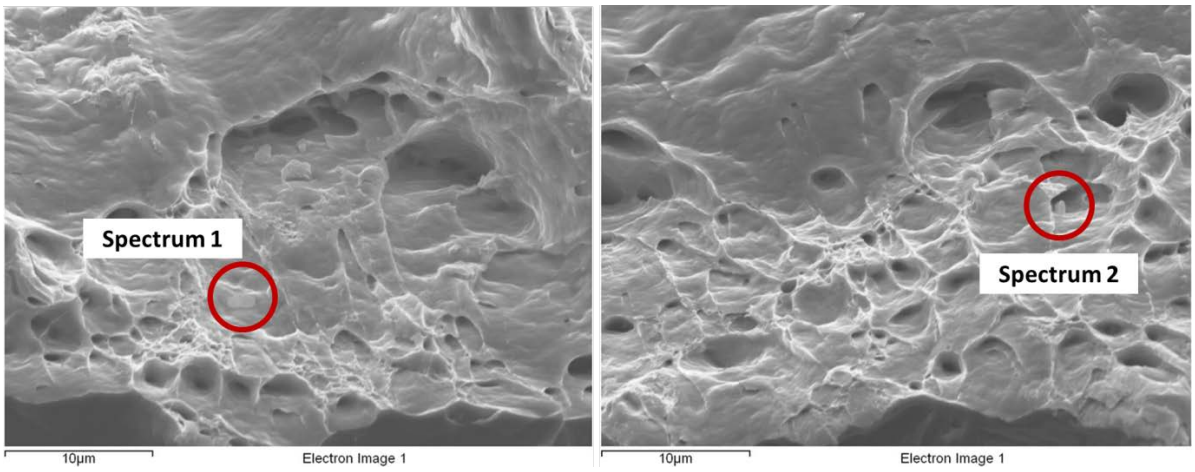

Figure 5-48 - Fracture surface of tensile coupon coated both sides and annealed at 710 ˚C – 1h in high vacuum. Spectra 1 and 2 indicate the particles whose composition was analyzed (specimen F-10)

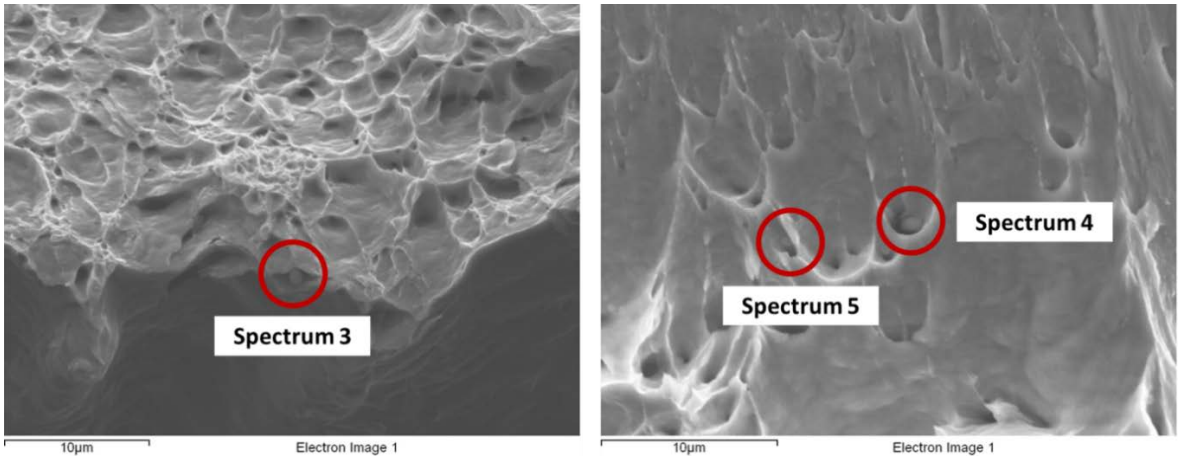

Figure 5-49 - Fracture surface of tensile coupon coated both sides and annealed at 710 ˚C – 1h in high vacuum (specimen F-10). Spectra 3, 4 and 5 indicate the particles whose composition was analyzed

Zone	Ti [wt%]	C [wt%]	S [wt%]	Mn [wt%]	Fe [wt%]
Spectrum 1	8.5	0	8.5	0	83
Spectrum 2	3.8	0	4	1.2	91
Spectrum 3	8	0	8	0	84
Spectrum 4	18.5	0	17	0	64.5
Spectrum 5	5	0	5	0	90

Table 5-14 - Composition obtained for particles present on the fracture surface of a both sides coated tensile coupon annealed at 710 ˚C – 1h (specimen F-10)

Coupons F-9 and F-10 annealed at 710 ºC had the highest yield stress among the coupons annealed at 710 ºC – 1h. In these specimens all particles analysed had no carbon. It is possible that in these coupons, only a coarsening of TiC carbides occurred without any transformation of TiS precipitates into $Ti_4C_2S_2$. However, EDS analyses performed on the fracture surfaces of other specimens annealed at 710 ˚C – 1h in high vacuum and having lower yield stress compared to coupons F-9 and F-10 showed that all particles contained Ti, S and C (see Table 5-15).

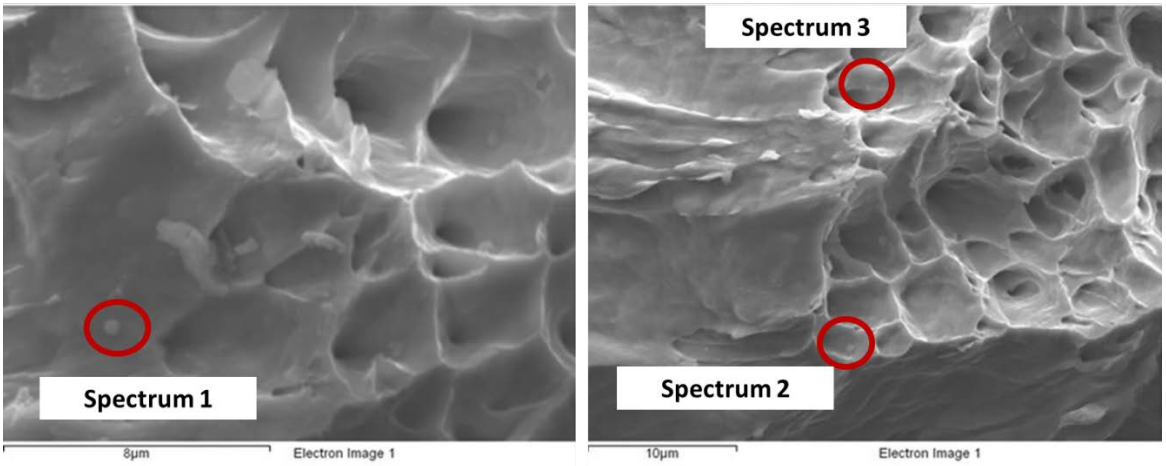

Figure 5-50 - Fracture surface of tensile coupon coated both sides and annealed at 710 ˚C – 1h in high vacuum. Spectra 1, 2 and 3 indicate the particles whose composition was analyzed

Zone	Ti [wt%]	C [wt%]	S [wt%]	Mn [wt%]	Fe [wt%]
Spectrum 1	6	5.4	4	0.6	84
Spectrum 2	5	4.4	3.4	0	87.2
Spectrum 3	3.7	2.9	4	0.8	88.6
Spectrum 4	0.8	2.5	0.5	0	96.2
Spectrum 5	4.2	3.6	2.2	0	90

Table 5-15 - Composition obtained for particles present on the fracture surface of a both sides coated tensile coupon annealed at 710 ˚C – 1h and having low yield stress

If at 710 ˚C, TiS particles capture the diffusing carbon, we would expect that by increasing the annealing temperature, the composition of the precipitates found on the fracture surface will have an increasing C/Ti ratio. In Table 5-16 the C/Ti ratio for the precipitates which contained sulphur has been calculated for each annealing temperature. At 430 ˚C and 530 ˚C, the ratio is always quite lower than 1, while at 630 ˚C some particles start to show a ratio higher than 1, while at 710 ˚C for the specimens having low yield stress, it was found that all the particles which contained sulphur were showing a C/Ti ratio equal to 1. The average C/Ti ratio for 630 ºC and 710 ºC is the same, respectively 1.4 and 1.3. This could prove that the diffusing carbon is interacting with these TiS particles at these temperatures. Moreover, no carbon was found on similar particles for coated but not-annealed coupons and for uncoated coupons annealed at 710 ˚C – 1h.

Sample	Spectrum	Ti [wt%]	C [wt%]	C/Ti ratio
Coated not-annealed IF steel	1	3	0	0
	2	4	0	0
	3	1.5	0	0
Uncoated – annealed at 710 ˚C – 1h	1	51.5	0	0
	2	23.2	0	0
	3	0.45	0	0
Coated annealed at 430 ˚C -1h	1	4.8	0	0
	2	13.6	8	0.59
Coated annealed at 530 ˚C -1h	5	9.3	2	0.21
Coated annealed at 630 ˚C -1h	1	3.6	5.7	1.58
	2	2	4.7	2.35
	3	8	2.5	0.31
Coated annealed at 710 ˚C -1h	1	6	5.4	0.9
	2	5	4.4	0.9
	3	3.7	2.9	0.8
	4	0.8	2.5	3
	5	4.2	3.6	0.86

Table 5-16 - Comparison of C/Ti ratio for particles containing sulphur at different annealing temperatures

One should note that the amount of carbon diffusing into the coupons is quite low and is close to the detection limit of EDS; moreover for most of the specimens, the particles were inside dimples which means that their composition could not be properly determined. For this reason, other techniques were used in order to better characterize specimens annealed at 710 ˚C. Thermoelectric power measurement can record a variation of the carbon in solid solution, while atom probe tomography can detect the presence of precipitates and give information about their composition.

5.6.2. Thermoelectric Power Measurements (TEP)

Thermoelectric power measurements were performed in order to measure the amount of carbon at dislocations as a function of the annealing temperature. The protocol used to perform the measurements was already described in section 4.9.2. Strips of IF steel having dimensions of 1 cm x 10 cm were coated both sides with 500 nm thick FeC film having 30 at% of carbon. For each annealing temperature, three both sides coated specimens were

analyzed. As comparison, one uncoated strip of IF steel was also prepared for each annealing temperature in order to have the TEP value of the raw IF steel as reference. Table 5-17 lists all the specimens analyzed and the measured carbon concentrations.

Annealing condition	**Sample**	**Sample Condition**	**$\Delta S_{a,\,max}$**	**C_{ss} [ppm mass]**	**Carbon concentration [at%]**	**Average [at%]**
430 ˚C – 1h high vacuum	1	Coated both sides	0.046	22.2	0.0103	0.0106
	2		0.047	22.3	0.0104	
	3		0.054	23.7	0.0110	
	4	Uncoated	0.044	21.7	0.0101	0.0101
530 ˚C – 1h high vacuum	1	Coated both sides	0.093	31.8	0.0148	0.0145
	2		0.083	29.7	0.0138	
	3		0.093	32.0	0.0149	
	4	Uncoated	0.051	23.3	0.0108	0.0108
630 ˚C – 1h high vacuum	1	Coated both sides	0.082	29.5	0.0137	0.0138
	2		0.087	30.6	0.0142	
	3		0.079	29.0	0.0135	
	4	Uncoated	0.052	23.5	0.0109	0.0109
710 ˚C – 1h high vacuum	1	Coated both sides	0.067	26.5	0.0123	0.0123
	2		0.063	25.6	0.0119	
	3		0.067	26.4	0.0123	
	4		0.070	27.1	0.0126	
	5	Uncoated	0.044	21.8	0.0101	0.0101

Table 5-17 - Thermoelectric power results on both sides coated IF steel annealed at different temperatures in high vacuum

Once annealed, the specimens were polished using 4000 SiC paper to remove the FeC film. The surface was further polished with a 1 μm diamond polishing solution. In Table 5-17, the values of carbon concentration in solid solution (C_{ss}) expressed in ppm in mass is obtained from TEP, then this value is converted in atomic percent by multiplying for 4.65 (ratio between the atomic mass of iron and the atomic mass of carbon) and by dividing by 10000.

By plotting the average carbon content measured by TEP for the FeC coated strips and for the uncoated strips, the graph shown in Figure 5-51 is obtained. There is a marked increase of carbon at dislocations increasing the temperature from 430 ˚C to 530 ˚C. At 630 ˚C the carbon shows a slight decrease compared to what was measured at 530 ºC, but this variation is inside the experimental error. This could mean that some carbon starts to precipitate, however, the precipitates (most probably TiC) are small and these coupons show the highest

yield stress. However, at 710 ˚C there is a marked drop in the measured amount of carbon, which means that the diffused carbon precipitates even more causing a coarsening of TiC carbides which could justify the decrease in mechanical properties.

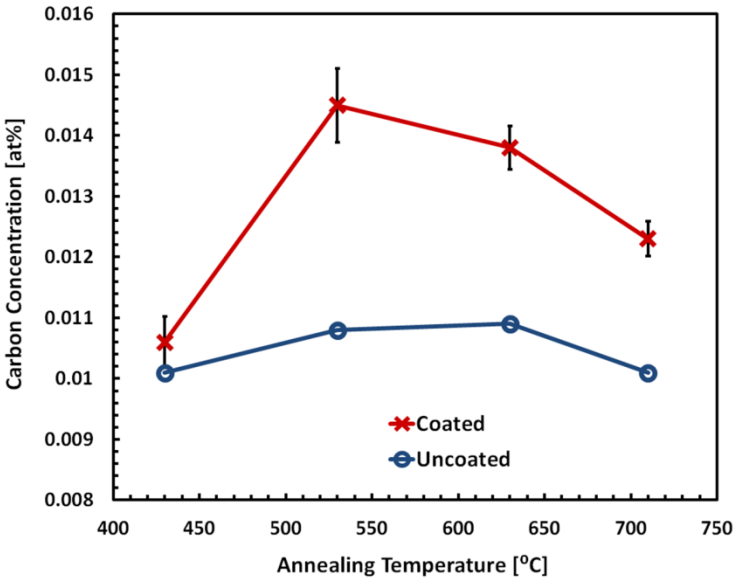

Figure 5-51 - Carbon concentration from TEP measurements as function of annealing temperature for uncoated and both sides coated coupons

From 630 ˚C to 710 ˚C the carbon in solid solution has a drop of 1.5 x 10^{-3} at%, which corresponds to a drop in yield stress of ($\Delta\sigma$ = (2.5) x (0.051x82000) x $(1.5x10^{-3}/100)^{1/2}$ = 40.5 MPa. By subtracting this value from the yield stress which is expected by diffusing the maximum carbon amount of 0.0334 at%, a yield stress of 264 MPa is obtained, which is in agreement with the average yield stress of 260 MPa found experimentally for coupons annealed at 710 ˚C -1h. For this reason, it is believed that the concentration of $1.5x10^{-3}$ at% of carbon is no more at dislocations but it is consumed to coarsen TiC precipitates or to transform TiS into $Ti_4C_2S_2$.

5.6.3. Atom Probe Tomography (APT)

Atom Probe Tomography (APT) was used to measure the concentration of carbon in several specimens. In particular, the following conditions were investigated:

- Uncoated and not-annealed IF substrate;
- IF steel coated on both sides with a 500 nm FeC film and annealed at 530 ˚C – 1h in high vacuum;

- IF steel coated on both sides with a 500 nm FeC film and annealed at 710 ˚C -1h in high vacuum;

Some specimens were taken from the middle of the IF sheet, in which case electropolishing can be used for sample preparation. Specimens close to the FeC film/IF substrate interface were prepared using focused ion beam (FIB). Details about these preparation techniques are reported in Appendix B. The composition of the raw IF steel without any coating and without annealing was first assessed.

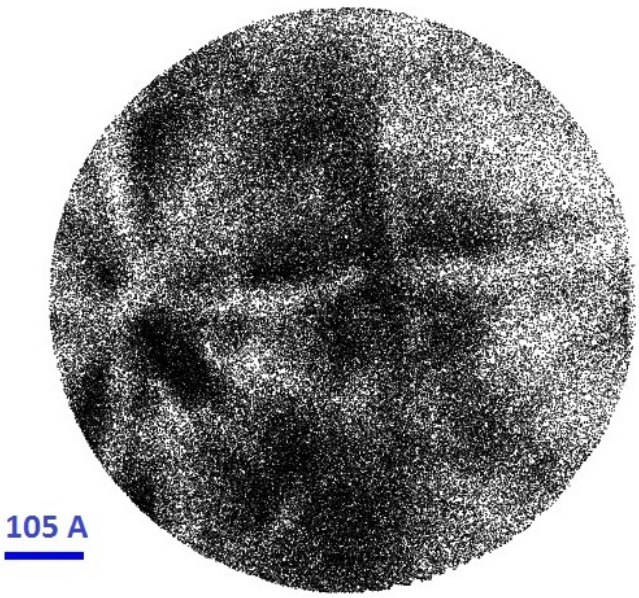

(a) Top view of 10% of the detected iron atoms

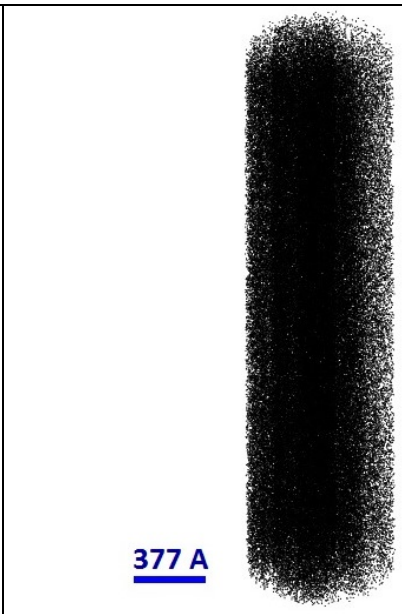

(b) 3D distribution of the detected iron atoms

Figure 5-52 - Iron atom distribution obtained by APT from a tip of uncoated and not-annealed IF steel

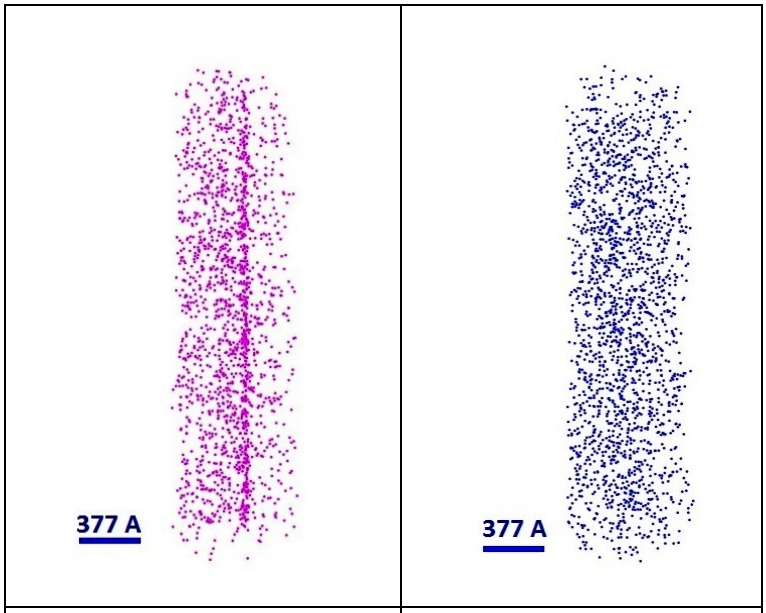

(a) Phosphorus distribution | (b) Titanium distribution

Figure 5-53 - Phosphorus and titanium distributions obtained inside a tip of uncoated and not-annealed IF steel

Fe [at%]	C [at%]	Al [at%]	N [at%]	P [at%]	Ti [at%]	O [at%]
$99.5^{\pm0.01}$	<0.01	$0.08^{\pm0.01}$	$0.019^{\pm0.01}$	$0.033^{\pm0.01}$	$0.035^{\pm0.01}$	$0.36^{\pm0.01}$

Table 5-18 - APT composition of uncoated and not-annealed IF steel

The volume analyzed for the uncoated and not-annealed IF steel had dimensions of 77 nm x 77 nm x 329 nm and contained 3.286 M atoms. The amount of carbon was negligible and no clear peak of this element could be detected from the spectrum of the mass to charge ratio. Titanium, aluminium and phosphorus were detected as main alloying elements. In particular, in the 3D reconstruction, phosphorus is distributed along a line (Figure 5-53 (a)) which means that it is segregated mainly along a grain boundary, while titanium looks uniformly distributed in the whole specimen volume. By looking at the reconstruction from the top of the sample, the evaporation pattern typical of ferrite is detected (Figure 5-52 (a)). The concentration of oxygen measured during the analysis is due to contamination coming from the environment due to specimen preparation and to some humidity present in the evaporation chamber.

- **APT on specimens annealed at 530 ˚C – 1h in high vacuum and coated both sides**

This specimen was prepared with the electropolishing technique since it was taken in the middle of the coated and annealed IF steel. The distribution of carbon atoms and titanium is

reported in Figure 5-54, while the distribution of phosphorus and aluminium is shown in Figure 5-55.

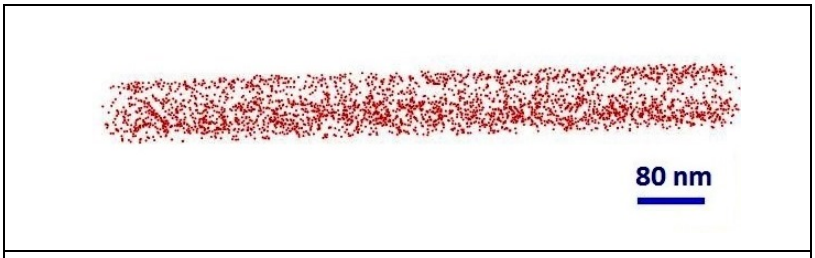

(a) Carbon atoms distribution

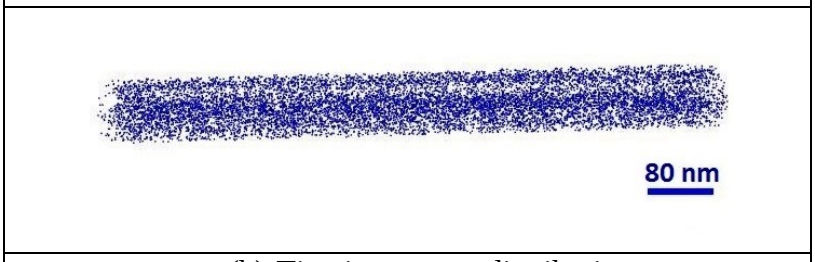

(b) Titanium atoms distribution

Figure 5-54 - Carbon and titanium distribution for a 500 nm both sides coated IF steel annealed at 530 ˚C -1h (reconstructed volume 80 x 80 x 450 nm^3)

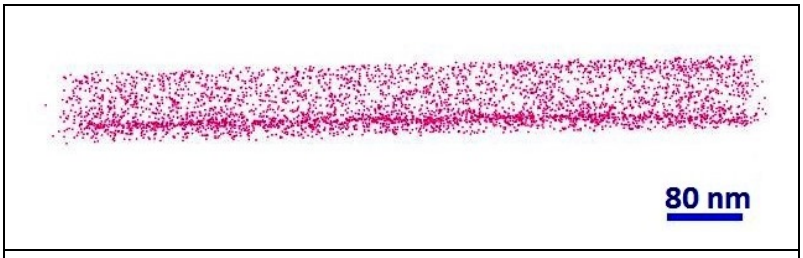

(a) Phosphor atoms distribution

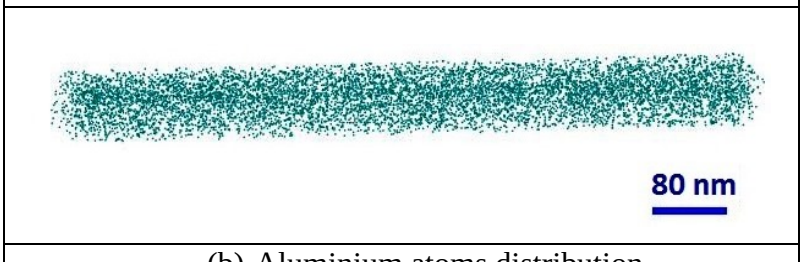

(b) Aluminium atoms distribution

Figure 5-55 - Phosphorus and aluminium distribution for a 500 nm both sides coated IF steel annealed at 530 ˚C -1h (reconstructed volume 80 x 80 x 450 nm^3)

Fe [at%]	C [at%]	Al [at%]	N [at%]	P [at%]	Ti [at%]	O [at%]
$99.81^{\pm 0.01}$	$0.007^{\pm 0.01}$	$0.090^{\pm 0.01}$	$0.017^{\pm 0.01}$	$0.012^{\pm 0.01}$	$0.056^{\pm 0.01}$	-

Table 5-19 - APT composition of both sides coated IF steel annealed at 530 ˚C – 1h in high vacuum – specimen taken at the centre of the thickness

Other two specimens from IF steel coated both sides and annealed at 530 ˚C were prepared close to the coated surface by using FIB. However, both tips flashed and the collected volume included 1 million atoms. Nevertheless, concentration measurements were still extracted and they are summarized in Table 5-20.

Fe [at%]	C [at%]	Al [at%]	N [at%]	P [at%]	Ti [at%]	O [at%]
$99.93^{\pm0.01}$	$0.024^{\pm0.01}$	-	-	$0.01^{\pm0.01}$	$0.01^{\pm0.01}$	$0.03^{\pm0.01}$
$99.87^{\pm0.01}$	$0.036^{\pm0.01}$	-	$0.03^{\pm0.01}$	$0.02^{\pm0.01}$	-	$0.032^{\pm0.01}$

Table 5-20 - APT composition of both sides coated IF steel annealed at 530 ˚C – 1h in high vacuum – specimen close to the FeC film/IF substrate interface

Concerning specimens annealed at 530 ºC – 1h, doing an average of the carbon content obtained with APT, a value of 0.022 at% is obtained, which is in good agreement with the solubility limit of carbon into ferrite for this temperature (0.026 at%). However, the concentration measured in the volume extracted in the center of the specimen has lower carbon than the one obtained in specimens closer to the FeC/IF substrate interface. This does not mean that at 530 ºC – 1h a carbon gradient is formed, since the volume analyzed with APT is very small (below the size of 1 μm^3) and therefore it is not significant enough to make any conclusions about carbon profile through thickness, since only one volume in the center of the coupon was analyzed. In order to assess the whole carbon profile through thickness, Knoop results are more representative. However, APT can provide more accurate information on carbon concentration than EDS and it can detect if this carbon is in solid solution or in the form of precipitates. In all specimens annealed at 530 ºC which were analyzed, no precipitates were detected so all the carbon is probably in solid solution as it can be seen in Figure 5-54.

- **APT on specimens annealed at 710 ˚C – 1h in high vacuum and coated both sides**

The specimen of IF steel annealed at 710 ˚C showed a non-uniform carbon and titanium distribution as shown in the 3D reconstruction in Figure 5-55. In particular, a portion of a carbide is clearly visible and in this zone the number of carbon and titanium atoms seems to be higher than in the matrix. For this reason, the concentration of the atoms was assessed by taking two separates volumes, one containing only the matrix and one containing only the particle. The results of the concentrations of various elements are reported in Table 5-21.

Matrix – annealing 710 ˚C -1h: probe 1						
Fe [at%]	**C [at%]**	**Al [at%]**	**N [at%]**	**P [at%]**	**Ti [at%]**	**O [at%]**
$99.82^{\pm 0.02}$	-	$0.09^{\pm 0.01}$	$0.03^{\pm 0.01}$	$0.04^{\pm 0.01}$	-	-
Precipitate – annealing 710 ˚C – 1h: probe 1						
$33.3^{\pm 2}$	$24.5^{\pm 2}$	-	-	-	$41.6^{\pm 2}$	-

Table 5-21 - APT composition of both sides coated IF steel annealed at 710 ˚C – 1h – specimen taken at the centre of the thickness

From the compositions reported in Table 5-21, it is evident that the concentration of carbon and titanium in the matrix is negligible or close to zero, while most of the atoms for these elements are in the precipitate. In particular, this precipitate could be the results of coarsening of a previous precipitate or the result of TiC precipitation during annealing.

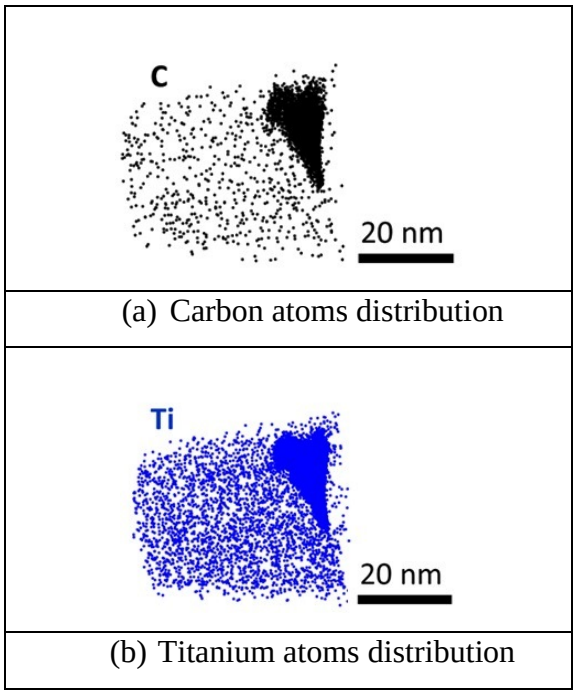

(a) Carbon atoms distribution

(b) Titanium atoms distribution

Figure 5-56 - Carbon and titanium atoms distribution for a specimen coated both sides and annealed at 710 ˚C – 1h (analyzed volume 48 nm x 48 nm x 70 nm)

Two other specimens (probe 2 and 3) annealed at 710 ˚C – 1h were analyzed and both of them were extracted from the middle of the sheet. Probe 2 contained a lot of oxygen because of the electropolishing preparation and because the volume analyzed was only 10 nm x 20 nm x 10 nm, while probe 3 had a volume of 77 nm x 77 nm x 210 nm (its reconstruction is shown in Figure 5-57).

Annealing 710 ˚C -1h: probe 2						
Fe [at%]	**C [at%]**	**Al [at%]**	**N [at%]**	**P [at%]**	**Ti [at%]**	**O [at%]**
$99.89^{\pm 0.02}$	$0.018^{\pm 0.01}$	$0.07^{\pm 0.01}$	$0.008^{\pm 0.01}$	$0.008^{\pm 0.01}$	$0.006^{\pm 0.01}$	-
Annealing 710 ˚C – 1h: probe 3						
$99.73^{\pm 0.01}$	$0.1^{\pm 0.01}$	$0.1^{\pm 0.01}$	$0.018^{\pm 0.01}$	$0.04^{\pm 0.01}$	$0.012^{\pm 0.01}$	-

Table 5-22 - APT composition of probe 2 and 3: both sides coated IF steel annealed at 710 ˚C – 1h – specimens taken at the centre of the thickness

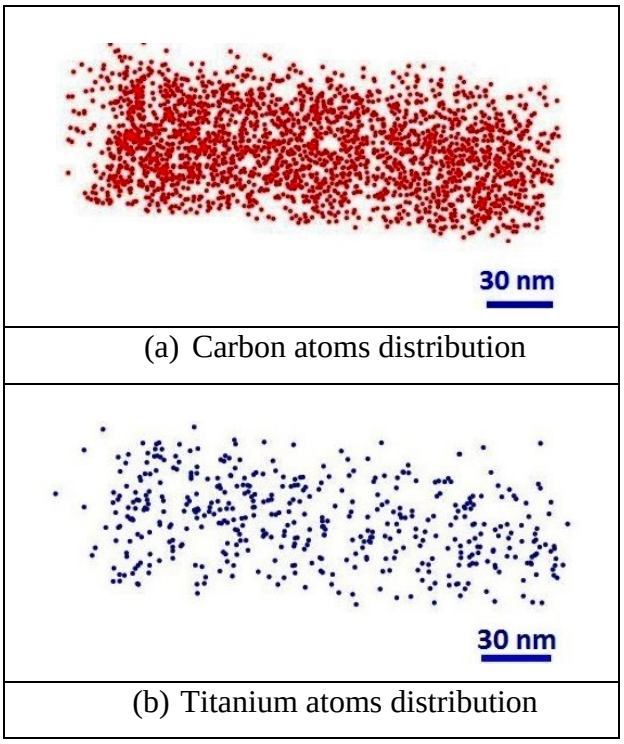

(a) Carbon atoms distribution

(b) Titanium atoms distribution

Figure 5-57 - Carbon and titanium atoms distribution for a specimen coated both sides and annealed at 710 ˚C – 1h (analyzed volume 77 nm x 77 nm x 210 nm)

Both probe 2 and probe 3 did not show any precipitate. Comparing Table 5-21 and Table 5-22 one can see that if precipitates are present, the amount of carbon left in the matrix is negligible, while if precipitates are absent, then the carbon is mainly in the IF matrix.

Another specimen of both sides coated IF steel was annealed at 710 ˚C -1h and analyzed by taking the tip close to the interface between FeC film and IF substrate. The analyzed volume was 48 nm x 48 nm x 70 nm and it showed multiple precipitates. The 3D reconstruction showing the distribution of C, Ti and S is reported in Figure 5-58 (a), and the split distributions of the three atoms are reported in Figure 5-58 (b), (c) and (d).

Matrix – annealing 710 ˚C -1h: probe 4						
Fe [at%]	**C [at%]**	**Al [at%]**	**N [at%]**	**P [at%]**	**Ti [at%]**	**O or S [at%]**
$99.94^{\pm0.01}$	$0.011^{\pm0.01}$	$0.03^{\pm0.01}$	-	-	-	-
Precipitate – annealing 710 ˚C – 1h: probe 4						
$56.5^{\pm4}$	$9.5^{\pm3}$	-	-	$4.8^{\pm0.01}$	$24.4^{\pm3}$	$13^{\pm3}$

Table 5-23 - APT composition of probe 4: both sides coated IF steel annealed at 710 ˚C – 1h – specimens taken at the centre of the thickness

In the mass to charge (*m/n*) ratio spectrum of probe 4, the peak in position 16 was more important here than for the analyses shown for the previous specimens. For this reason, it is believed that some sulphur atoms are contributing to the intensity of this peak. However, the APT experiment performed here does not allow distinguishing between oxygen and sulphur atoms. Indeed, the peak in position 16 could belong to O^+, S^{2+} or even to the evaporation of ion molecules such as nitrogen atoms with 2 H^+, or to silicon atoms with 2 H^+, since contamination of hydrogen atoms cannot be avoided during APT.

It is important to underline that in the 3D volume reconstruction, local magnification effect can occur, especially for small precipitates and especially when there is a marked difference between the evaporation field of the matrix and the precipitates. In particular, the difference in evaporation field will result in a non-realistic shape of the precipitate, which could look like a platelet instead of particles. This will result also in small volume for the precipitate and the composition of the precipitate might not be accurate since the volume of the precipitate is very small. For this reason, the composition indicated in Table 5-23 for the precipitates might not be accurate while the one of the matrix is accurate since it was taken in a bigger volume than the one of the precipitate (discussion with Dr. Amélie Fillon). The average carbon concentration obtained by APT in the matrix for specimens (probe 2, 3 and 4) annealed at 710 ºC – 1h is (0.018+0.1+0.011)/3 = 0.043 at%. This amount falls inside the expected range considering FeC crystallization and ± 3 at% carbon concentration variation in the deposited film, since if the film is 500 nm thick and if it has 33 at% of carbon, the maximum amount of carbon that can be diffused after crystallization will be 0.053 at%.

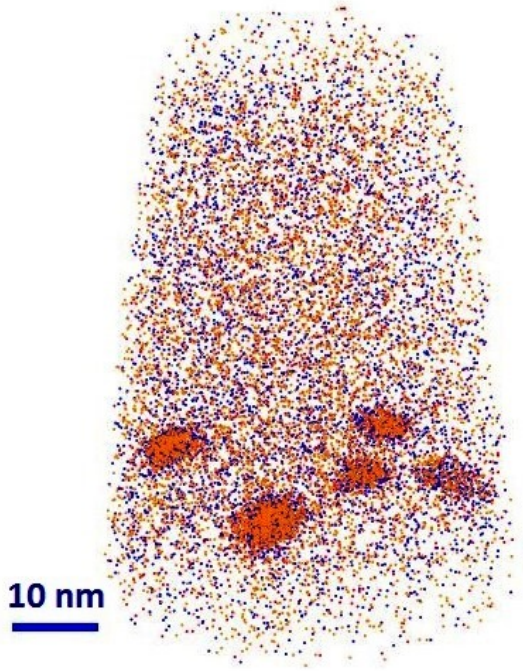

(a) Distribution of C, Ti, S for specimen annealed at 710 ˚C -1h

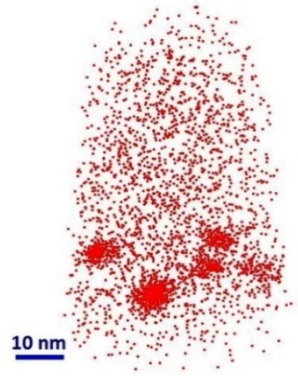

(b) Distribution of C for specimen annealed at 710 ˚C -1h

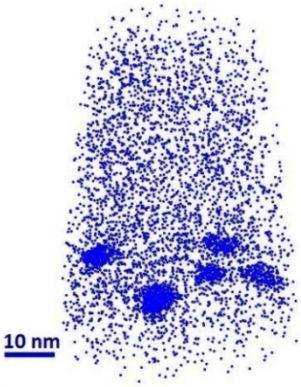

(c) Distribution of Ti for specimen annealed at 710 ˚C -1h

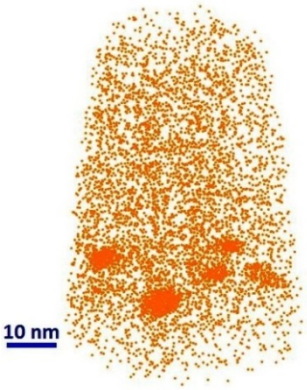

(d) Distribution of S for specimen annealed at 710 ˚C -1h

Figure 5-58 - Distribution of Ti, C and O or S atoms in a both sides coated IF specimen annealed at 710 ˚C – 1h

5.6.4. Considerations about annealing at 710 ˚C

According to the results obtained from EDS it seems that at 710 ˚C some carbon interacts with TiS precipitates. For the same temperature, TEP measurements recorded a decrease of carbon in solid solution at dislocations. The missing carbon at dislocation is probably precipitated or captured by the TiS particles. Moreover, it should be noted, that the same TEP variation is not recorded for the raw IF steel, meaning that the TEP variation measured for the coated specimens is caused by the change in carbon concentration.

Atom probe tomography revealed the presence of precipitates in some of the analyzed volumes at 710 ˚C, while it did not detect any particle for annealing at 530 ˚C or for the raw IF steel. All the precipitates were rich in titanium and carbon, while the percentage of sulphur was difficult to determine due to the overlap of its peak with the peaks of other elements as previously discussed. From these results and from what was reported in literature [36], it is believed that for annealing at 710 ˚C the decrease in mechanical properties compared to the specimens annealed at 630 ˚C could be due to the precipitation of carbon either to coarsen TiC or to trigger the transformation of TiS into $Ti_4C_2S_2$.

5.7. Influence of FeC film thickness on mechanical properties

A series of tensile tests were performed on coupons coated both sides with different thicknesses of FeC film to obtain a relation between the strengthening obtained after diffusion and the carbon content in the film. The tested thicknesses of the film were 50 nm, 100 nm, 200 nm, 300 nm, 400 nm and 500 nm and in every film the nominal amount of carbon was 30 at%. All specimens were annealed in high vacuum at the same temperature of 530 ˚C - 1h because at this temperature a remarkable increase of strength is expected, moreover the carbon profile through thickness is expected to be uniform and it is expected that the amount of carbon which remains available after film crystallization is enough to reach the solubility limit of carbon into ferrite at this temperature.

Table 5-24 reports vacuum levels during the annealing of the different coupons, while Table 5-25 lists all the tested conditions.

Annealing Parameters	Thickness of the FeC amorphous film	Vacuum furnace on [torr]	Vacuum furnace off [torr]
530 ºC-1h	50 nm	$3.5x10^{-5}$	$7x10^{-6}$
	100 nm	$5.4x10^{-6}$	$1x10^{-5}$
	200 nm	$4.6x10^{-6}$	-
	300 nm	$3.2x10^{-6}$	$3.5x10^{-6}$
	400 nm	$3x10^{-6}$	$3.5x10^{-6}$
	500 nm	$3x10^{-6}$	$3.4x10^{-6}$

Table 5-24 - Values of vacuum during annealing of coupons coated both sides with different FeC film thicknesses and annealed at 530 ˚C - 1h

Sample Name	Coating Condition	Film thickness on each side	Heat Treatment
50 - A	Both sides	50 nm	Not annealed
50 - B, 50 - C	Both sides	50 nm	530 ºC-1h
100 - A	Both sides	100 nm	Not annealed
100 - B	Both sides	100 nm	530 ºC-1h
200 - A	Both sides	200 nm	Not annealed
200 - B, 200 - C	Both sides	200 nm	530 ºC-1h
300 - A, 300 - B, 300 - C, 300 - D	Both sides	300 nm	530 ºC-1h
400 - A, 400 - B, 400 - C, 400 - D	Both sides	400 nm	530 ºC-1h

Table 5-25 - Summary of the specimens tested with different film thicknesses after annealing at 530 ºC – 1h in high vacuum

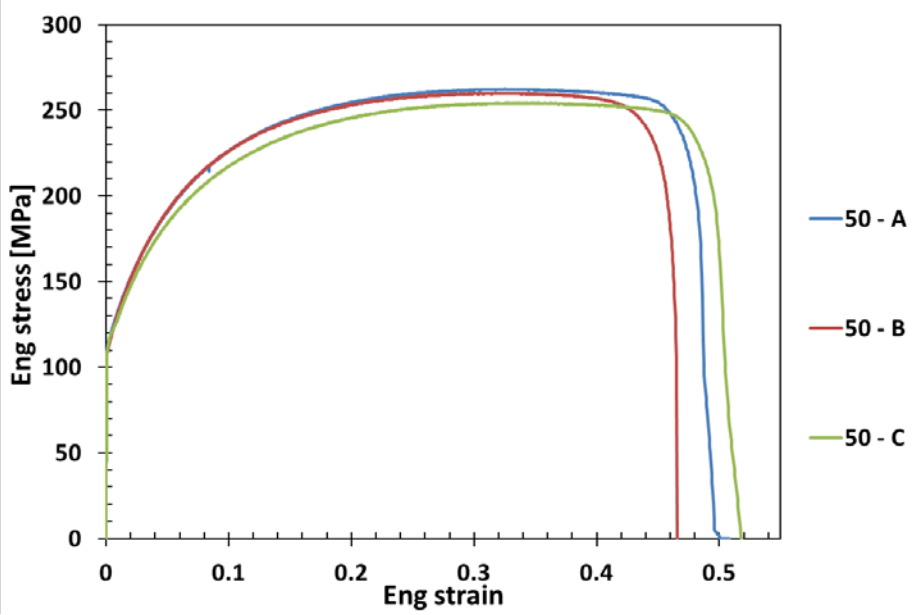

Figure 5-59 - Engineering stress-strain curves for coupons coated both sides with 50 nm thick FeC amorphous film: sample 50 - A was not annealed, while samples 50 - B and 50 - C were annealed at 530 ˚C - 1h in high vacuum

Pictures of the surface of one of the tensile coupons were taken during the tensile test, showing that very low exfoliation of the film occurs during the test. This confirms that for the annealing at 530 ˚C - 1h the film is crystallizing. Pictures are shown in Figure 5-60. Details of the dimension of the tested coupons and values of the mechanical properties extracted from the engineering stress-strain curves are reported in Appendix D (section D.8).

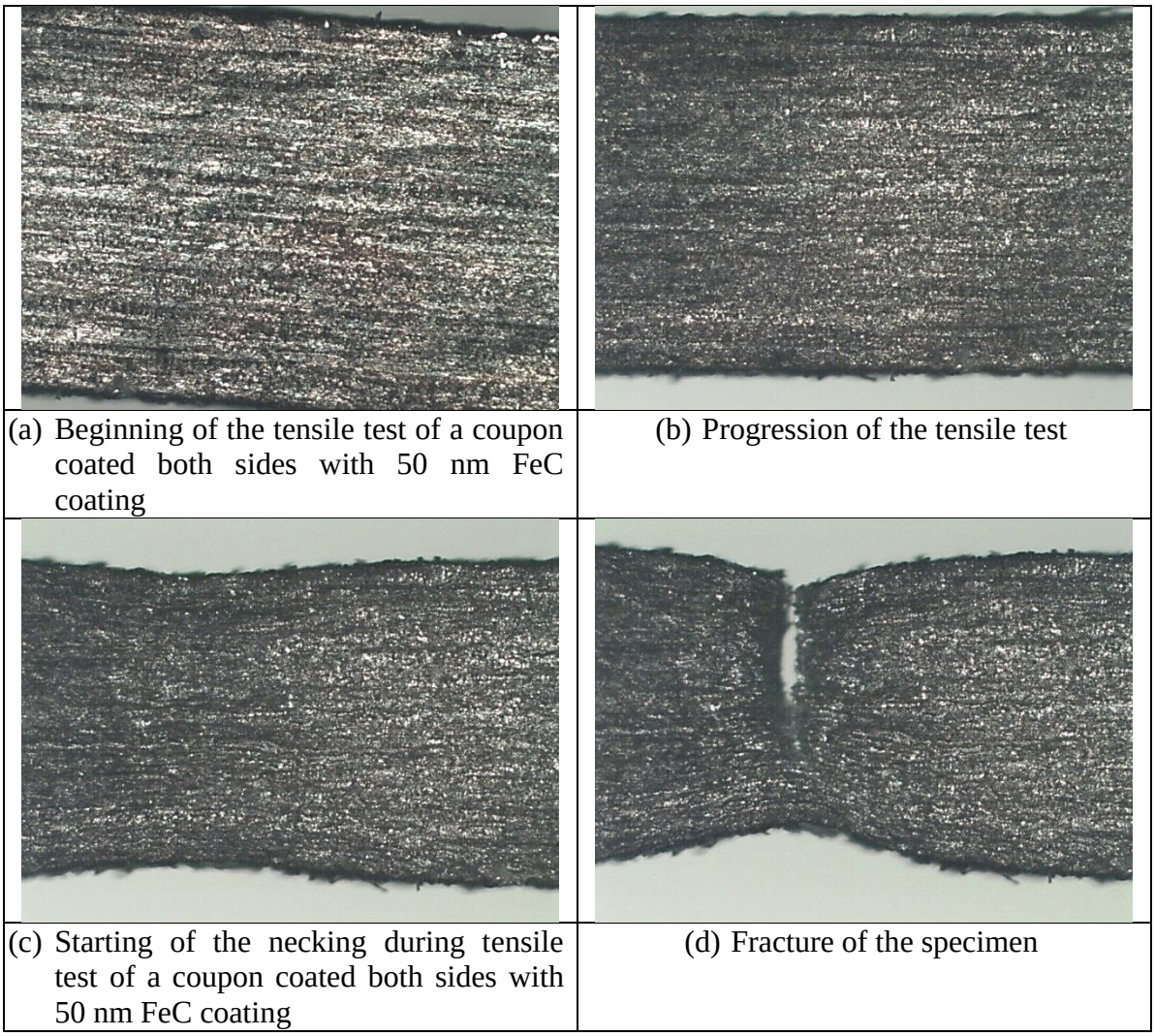

(a) Beginning of the tensile test of a coupon coated both sides with 50 nm FeC coating

(b) Progression of the tensile test

(c) Starting of the necking during tensile test of a coupon coated both sides with 50 nm FeC coating

(d) Fracture of the specimen

Figure 5-60 - Microscope picture of the surface of coupons coated both sides with 50 nm annealed at 530 ˚C - 1h in high vacuum

From Figure 5-59 it is clear that no diffusion is occurring if the film is only 50 nm thick since there is no increase of yield stress or ultimate tensile strength and no Lüders bands propagation was detected. Coupons with 100 nm thick FeC film were then annealed and tested. Engineering stress-strain curves are shown in Figure 5-61. Pictures of the surface during the tensile test were taken for the annealed coupon and they are shown in Figure 5-62.

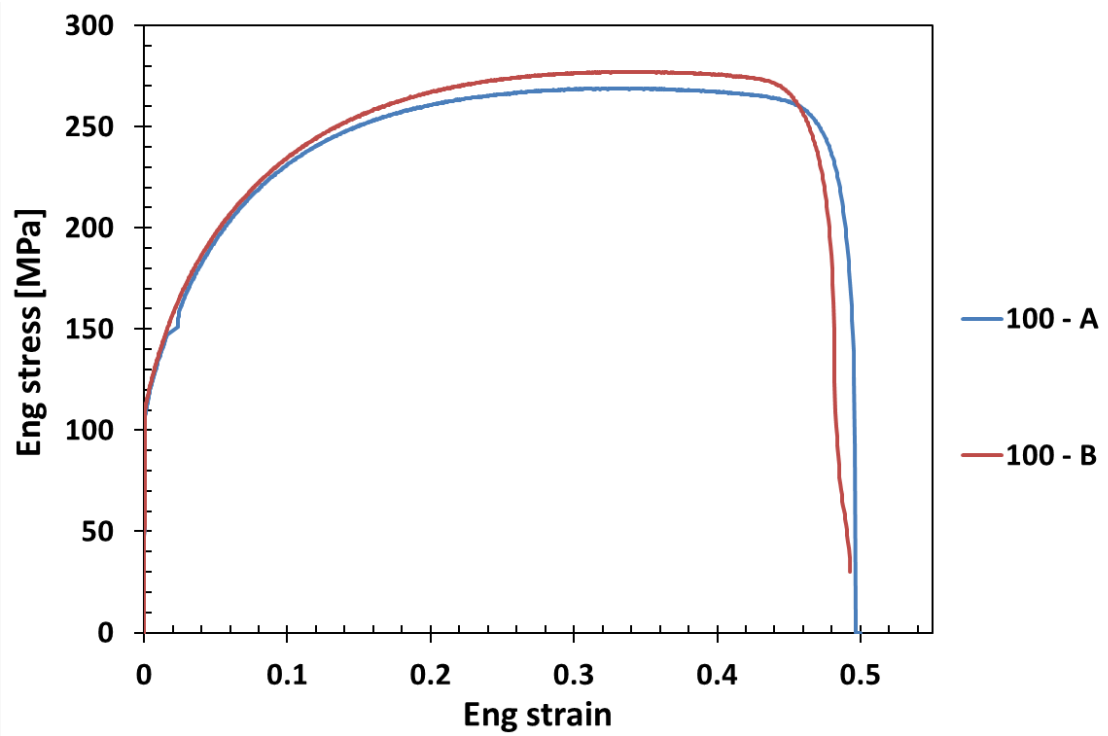

Figure 5-61 - Engineering stress-strain curves for coupons coated both sides with 100 nm thick FeC amorphous film: sample 100 - A was not annealed, while sample 100 - B was annealed at 530 ˚C-1h in high vacuum

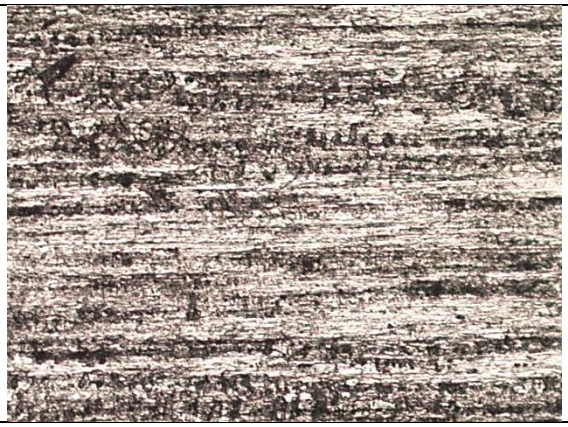

(a) Beginning of the tensile test of a coupon coated both sides with 100 nm FeC coating (magnification 10X)

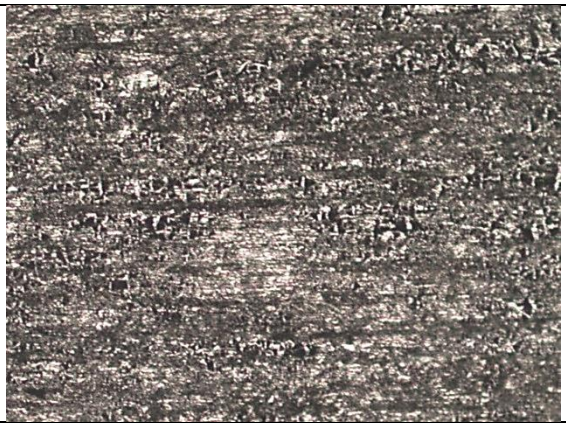

(b) Progression of the tensile test (magnification 10X)

(c) Further surface exfoliation during the tensile test of a coupon coated both sides with 100 nm (magnification 10X)

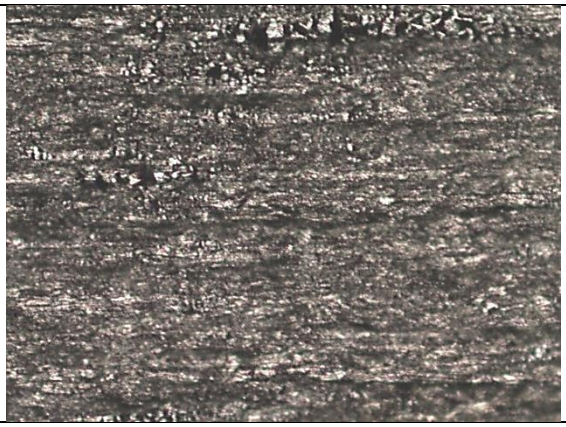

(d) Surface of the coupon at the starting of necking (magnification 10X)

Figure 5-62 - Microscope picture of the surface of coupons coated both sides with 100 nm annealed at 530 ˚C - 1h in high vacuum

From stress – strain curves (Figure 5-61), it is clear that no diffusion occurred even if the thickness of the film was increased to 100 nm on both sides. Moreover, the exfoliation of the film (Figure 5-62) seems higher compared to what was obtained for the 50 nm thick FeC film. This is expected since the thicker is the film the more it is able to carry some stress during the tensile test.

Another serie of coupons was coated with 200 nm thick FeC amorphous film on both sides and annealed in high vacuum at 530 ˚C - 1h. In Figure 5-63 the corresponding engineering stress-strain curves are shown, while optical microscope images of the film behaviour during tensile test are reported in Figure 5-64.

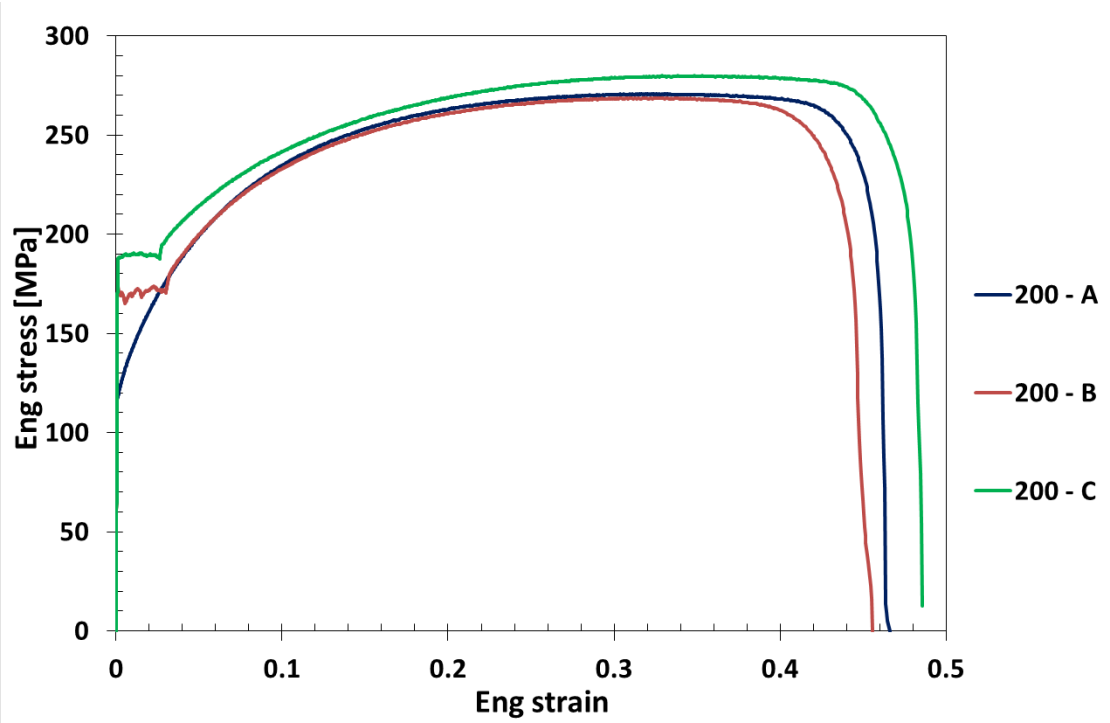

Figure 5-63 - Engineering stress-strain curves for coupons coated both sides with 200 nm thick FeC amorphous film: sample 200 - A was not annealed, while sample 200 - B and 200 - C were annealed at 530 ˚C - 1h in high vacuum

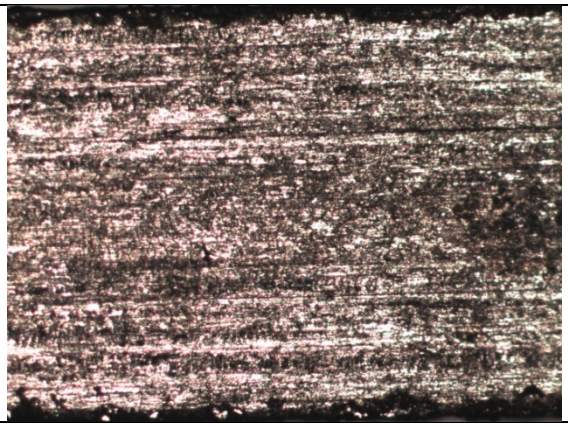

(a) Beginning of the tensile test of a coupon coated both sides with 200nm FeC coating

(b) Progression of the tensile test with starting of exfoliation from the edges of the tensile coupons

(c) Further surface exfoliation during the tensile test of a coupon coated both sides with 200nm

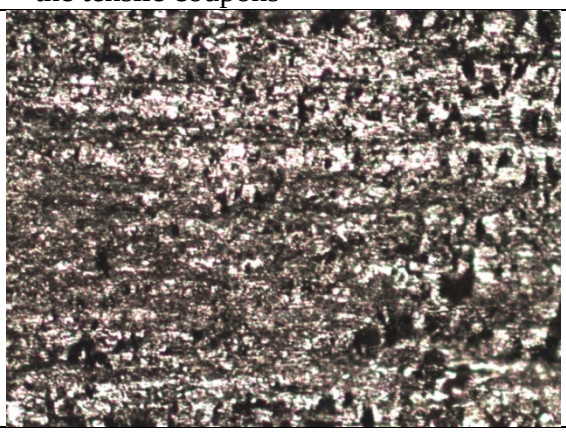

(d) Surface at the end of the tensile test

Figure 5-64 - Microscope picture of the surface of coupons coated both sides with 200 nm annealed at 530 ˚C - 1h in high vacuum

From the tensile curve shown in Figure 5-63 it is evident that when the film is 200 nm thick, some carbon diffusion is occurring and an increase in yield stress followed by the presence of a Lüders plateau are detected. It can therefore be inferred that for this type of isothermal heat treatment under high vacuum, the FeC amorphous film must be at least 200 nm thick in order to improve the mechanical properties of the IF sheet. The exfoliation of the film for these coupons was also higher compared to the ones obtained for coupons coated with 50 nm and 100 nm FeC film and again this can be attributed to the increase in film thickness.

Another series of coupons was coated both sides with 300 nm thick FeC amorphous film and were annealed at 530 ˚C - 1h in high vacuum. In Figure 5-65 the engineering stress-strain

curves are summarized (specimens 300-C and 300-D were tested doing digital image correlation).

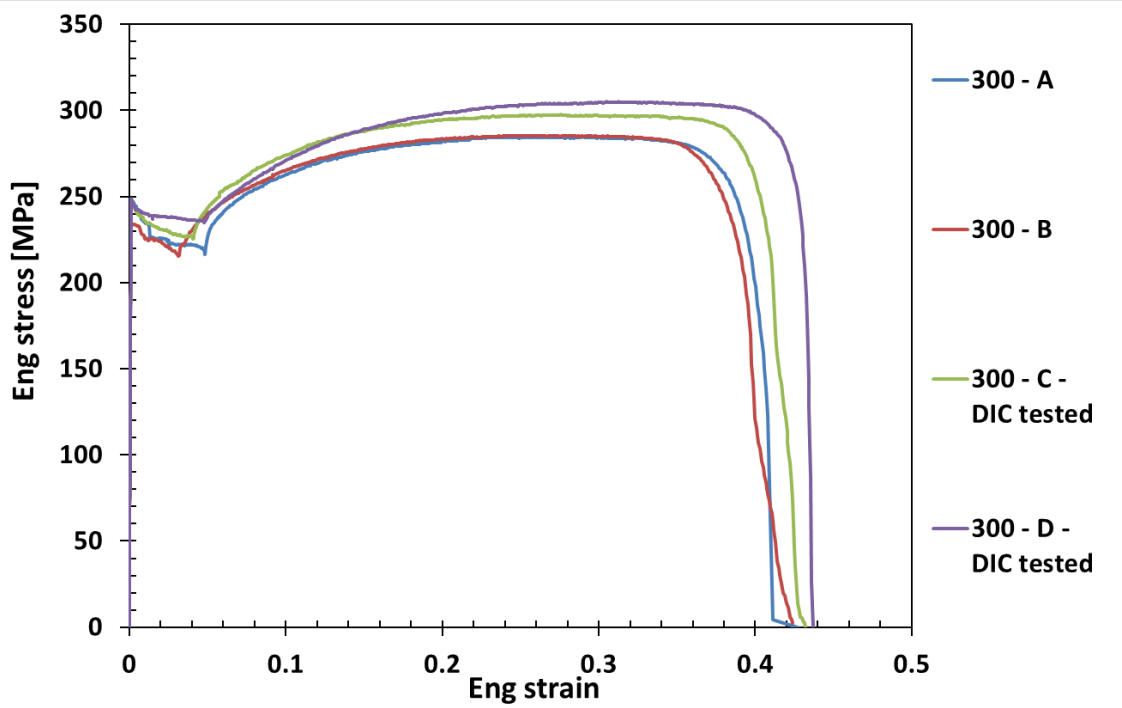

Figure 5-65 - Engineering stress-strain curves for coupons coated both sides with 300 nm thick FeC amorphous film

From these tests (Figure 5-65) it is evident that with a further increase of the film thickness the yield stress reaches even higher values proving that more carbon can be diffused into the substrate. Finally a last series of tests was conducted on coupons coated both sides with 400 nm FeC amorphous film annealed at 530 ˚C - 1h in high vacuum. Figure 5-66 shows the engineering stress-strain curves for these coupons.

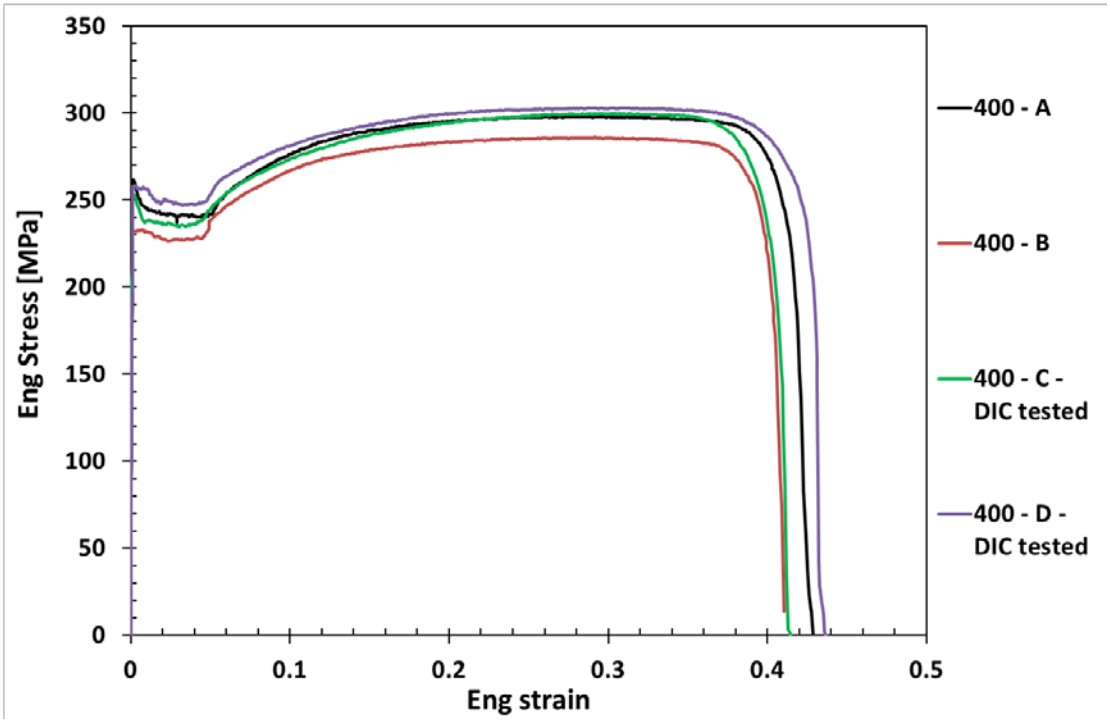

Figure 5-66 - Engineering stress-strain curves for coupons coated both sides with 400 nm thick FeC amorphous film

As it can be evinced from Figure 5-66, the mechanical properties of coupons coated both sides with 400 nm thick FeC amorphous film are higher than what was obtained for coupons coated both sides with 300 nm but lower than what is obtained with 500 nm thick FeC film on both sides. These results further confirm that an increase of film thickness will allow more carbon to diffuse towards the IF core producing higher mechanical properties.

In Figure 5-67, a summary of an engineering stress-strain curve for each film thickness is shown.

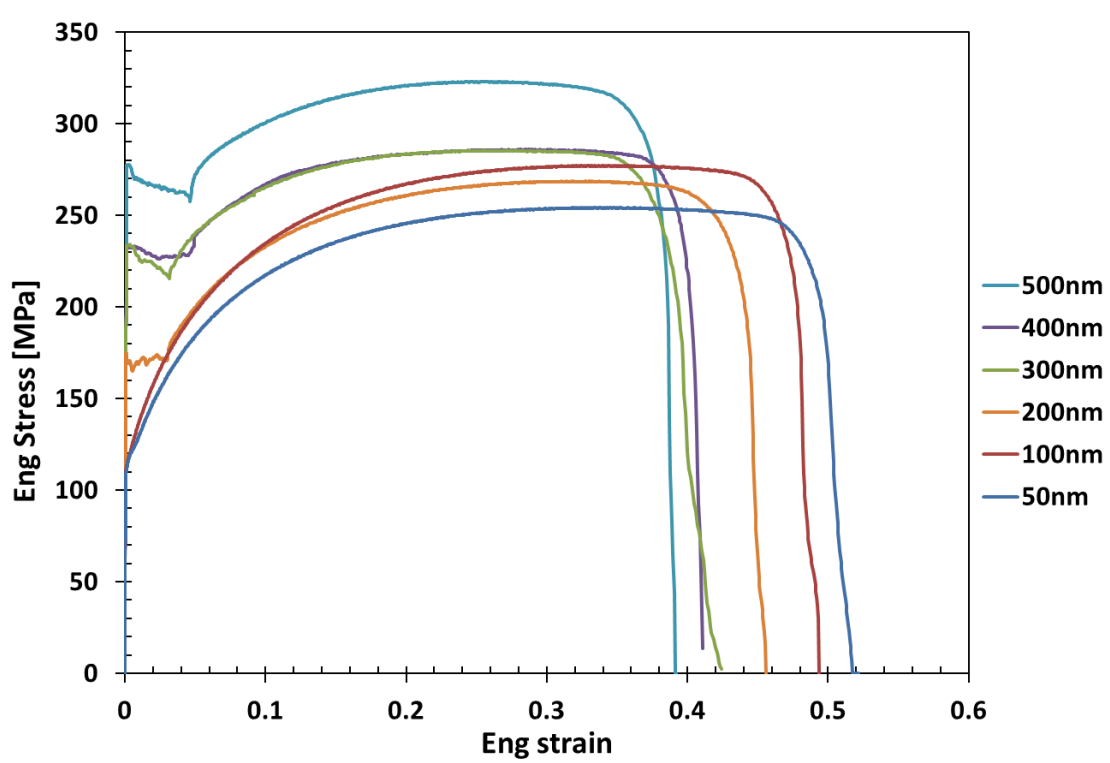

Figure 5-67 - Engineering stress-strain curves for coupons coated both sides with different thicknesses of FeC amorphous film and annealed in high vacuum at 530 ˚C - 1h

The yield stress obtained for different thicknesses of FeC film can be predicted by calculating the carbon which will remain available in the FeC film after the film has transformed into cementite. The same procedure can be applied to evaluate the amount of carbon which remains available for diffusion after the transformation of the film into cementite when the thickness of the film is lower than 500 nm.

The yield stress obtained using stoichiometric calculation, as described in section D.9.2 and section D.9.3 of Appendix D, is compared with the yield stress obtained experimentally after annealing in high vacuum at 530 ˚C - 1h. The comparison between the theoretical yield stress and the experimental yield stress for the different film thicknesses is reported in Figure 5-68. It was found that the yield stress becomes higher as the film thickness is increased by performing tensile tests on coupons annealed at 530 ˚C - 1h in high vacuum. A stoichiometric calculation considering the transformation of the film into cementite has shown that the amount of carbon available to be diffused towards the IF core increases with the thickness of the FeC film.

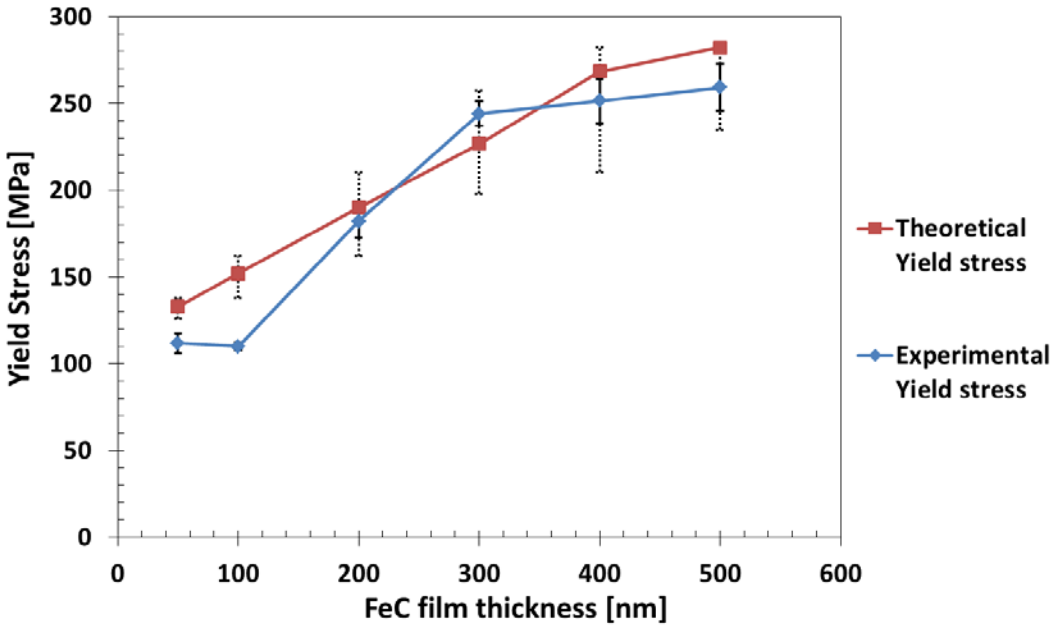

Figure 5-68 - Comparison of theoretical yield stress and experimental yield stress for coupons coated with different thicknesses of FeC film

The points on the curve are obtained considering nominal carbon content in the FeC film of 30 at%, and the error bars, represent the positive and negative shift from the nominal yield stress, due to the ± 3 at% variation in carbon content in the film.

However, it is possible to keep into account also the variation of ± 20 nm in film thickness and to consider the variation of ± 3 at % in carbon content. The graph with the error bars considering both variations is shown in Figure 5-69.

The detailed description of the calculations performed to obtain the error bars shown in Figure 5-69 for the theoretical yield stress are reported in Appendix D (section D.9.3).

As it can be seen from Figure 5-69 the stoichiometric calculations performed by taking into account the ± 3 at% carbon variation and the film thickness uncertainty of ± 20 nm predicts well the experimental yield stress for thicknesses equal to or above 200 nm. For thicknesses above or equal to 200 nm, the experimental yield stress falls inside the error bars. On the other hand, for small thicknesses as 50 nm and 100 nm, the experimental yield stress falls outside of what would be expected theoretically. This could be caused by a carbon amount in the FeC film lower than 27 at% or it is also possible that cementite is not the only carbide formed during the crystallization of the FeC film so that no carbon would be available to be diffused into the IF substrate for these thicknesses.

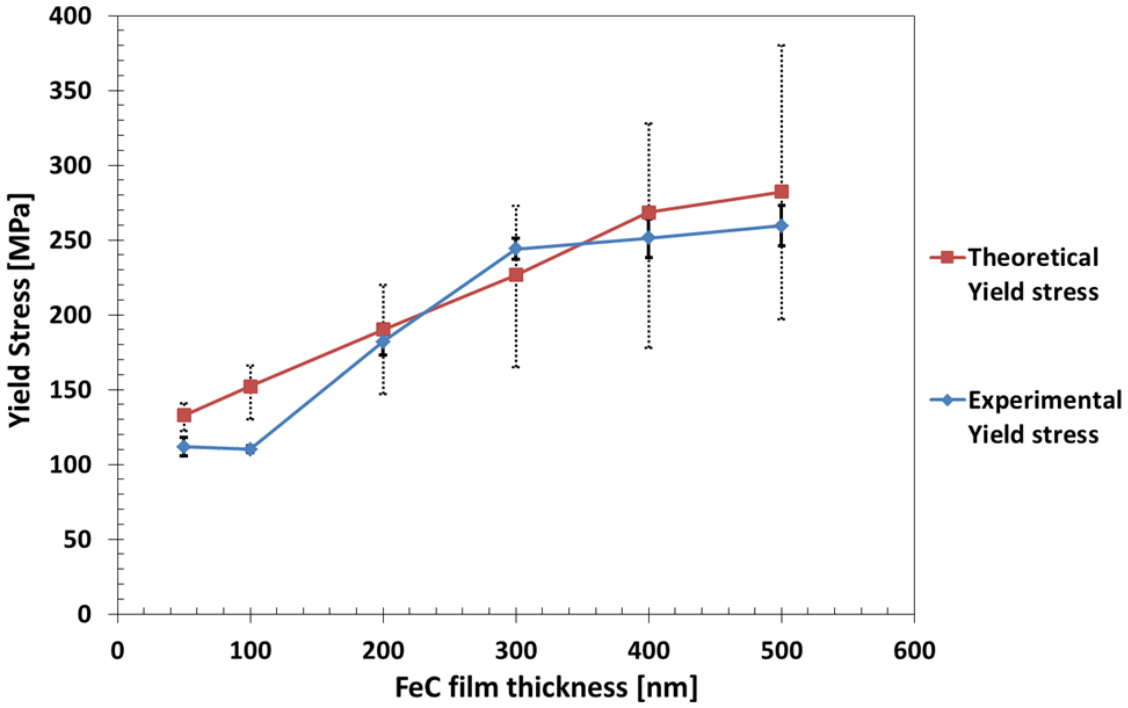

Figure 5-69 - Comparison of theoretical yield stress and experimental yield stress for coupons coated with different thicknesses of FeC film considering carbon content uncertainty and film thickness uncertainty

5.8. Further tests to confirm modelling prediction

From the stoichiometric calculation performed in the previous paragraph it was shown that if the 500 nm thick FeC film contains 30 at% of carbon, the maximum amount of carbon that can be diffused is 0.0334 at%. This amount is lower than the solubility limit of carbon into ferrite at 630 ˚C. However, to prove that no more than this amount can be diffused, an annealing at 630 ˚C for 5h was performed in high vacuum on specimens coated both sides with 500 nm thick FeC film. It was shown that the yield stress of these coupons follows in the same range of coupons annealed at 630 ˚C for just 1h, proving that no more than 0.0334 at% of carbon is available to be diffused.

The engineering stress-strain curves for these coupons are shown in Figure 5-70.

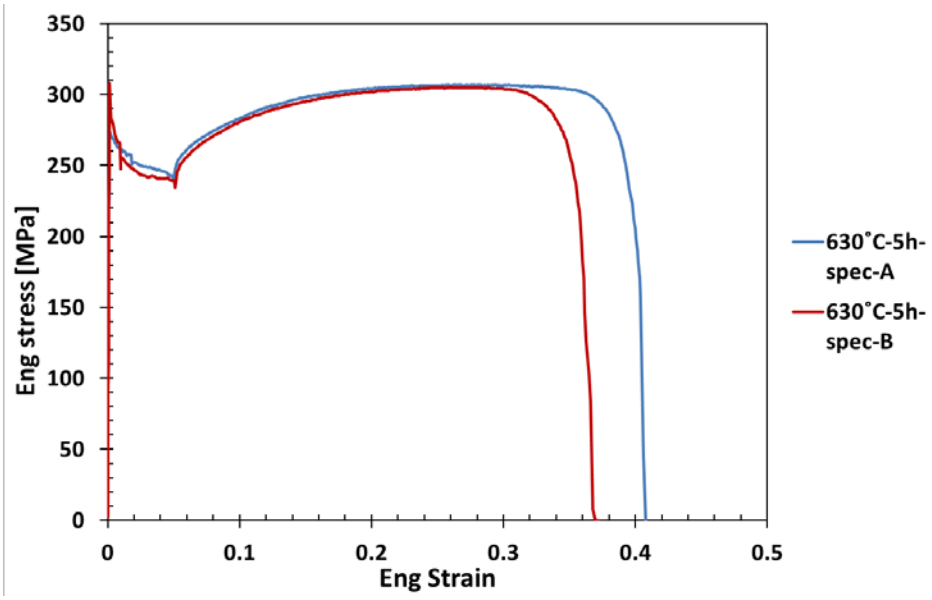

Figure 5-70 - Engineering stress-strain curves for specimens coated both sides with 500nm thick FeC film and annealed at 630˚C-5h in high vacuum

From the values of yield stress, the amount of carbon which has been diffused can be calculated by using the formula $\Delta\sigma = Mm(X_C)^{1/2}$ already introduced in the literature review. From the average upper yield stress of the tensile curves shown in Figure 5-70, an increase of yield stress $\Delta\sigma$ of (290.92 - 113.7) = 177 MPa is measured; where 113.7 MPa is the average yield stress found for not coated and not annealed IF steel. The amount of carbon (X_C) can then be calculated as: $X_C = (\Delta\sigma/Mm)^2$ and the value found is 0.029 at% which is very close to the maximum theoretical amount of carbon (0.0334 at%) that can be diffused at 630 ˚C. If the above calculation is repeated separately for the two specimens, it is found that the amount of carbon diffused in the first specimen is equal to 0.0236 at% by considering a $\Delta\sigma$ of (274.22 - 113.7) = 161 MPa while the carbon diffused in the second specimen is 0.0344at% by calculating a $\Delta\sigma$ of (307.62 - 113.7) = 194 MPa. The difference in mechanical properties found for these two coupons falls within the range of uncertainty of ± 3 at% carbon in the FeC film. Specimens annealed for 5h have an average ultimate tensile strength (UTS) of 307 MPa with a standard deviation of 0.5 MPa, while the coupons annealed for 1h have an average UTS of 337 MPa and standard deviation of 23 MPa. So, after 5h a decrease of UTS is occurring which could be due to some carbon precipitating and coarsening TiC or TiS particles which are already present in the IF steel. It was indeed noticed that the UTS for

annealing at 630 ˚C for 5h is close to the UTS for 710 ˚C -1h so it is believed that the longer annealing time can give enough time for carbon to precipitate.

More analyses and tests were performed to further prove the modelling presented in the previous sections. Using the modelling based on the second Fick's diffusion law, the number of hours necessary to obtain a linear carbon profile through the thickness for an annealing of 430 ˚C was predicted. The results of the modelling are reported in Figure 5-71, where it is clear that for a specimen annealed at 430 ˚C, a linear carbon profile through thickness is obtained after 10h. In order to verify this, two tensile coupons coated both sides with 500 nm thick FeC film were annealed at 430 ˚C for 10h in high vacuum. A piece of IF steel coated both sides with 500 nm thick FeC film was also annealed at 430˚C for 10h in order to verify the microhardness profile through thickness and see if the profile of carbon was uniform through thickness.

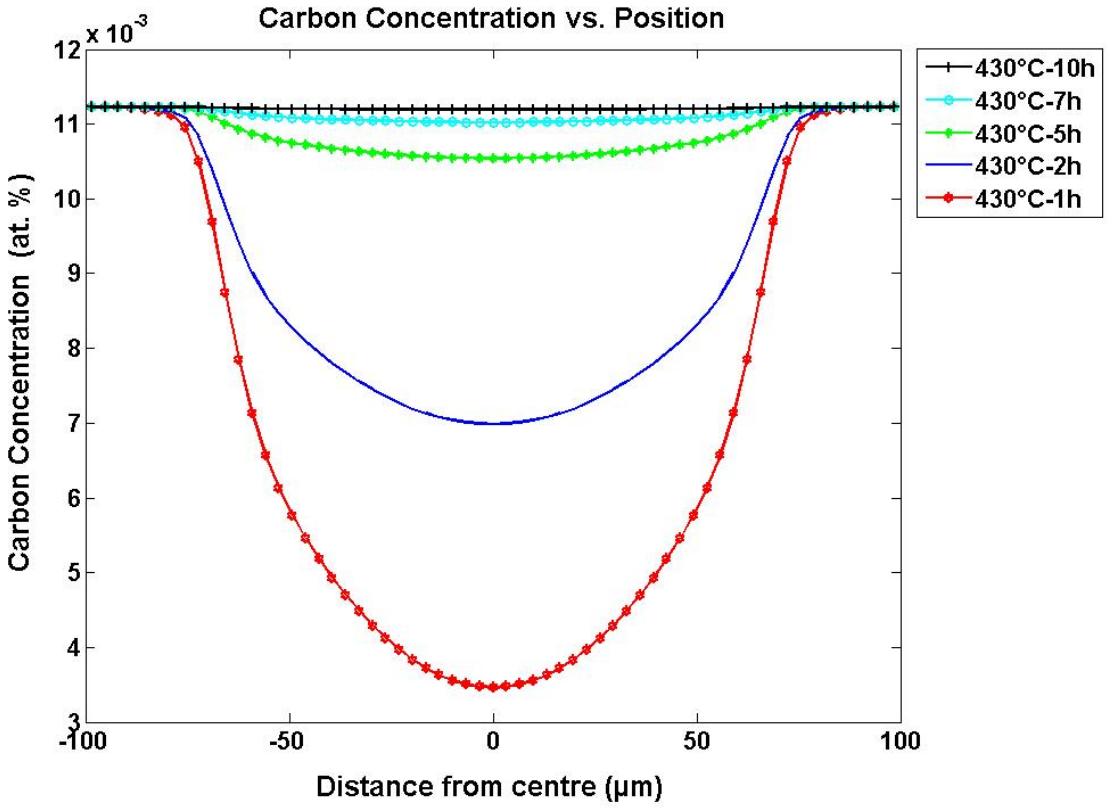

Figure 5-71 - Evolution of the carbon concentration through thickness for a coupon coated both sides and annealed at 430 ˚C for different times

In Figure 5-72 the engineering stress-strain curves for these two coupons are reported.

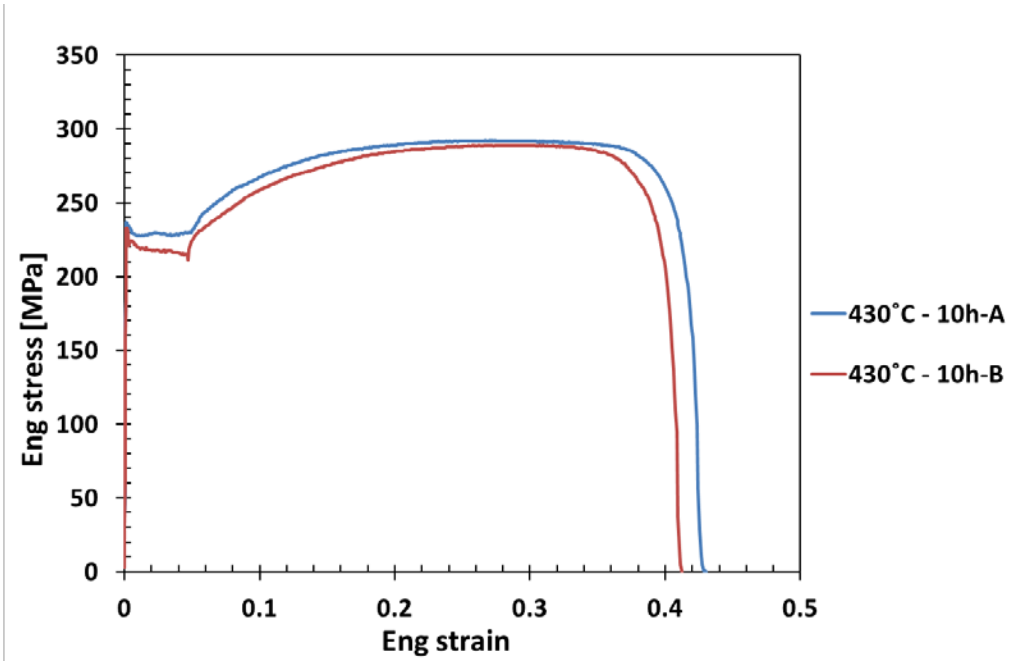

Figure 5-72 - Engineering stress-strain curves for specimens coated both sides with 500 nm thick FeC film and annealed at 430 ˚C - 10h in high vacuum

The average yield stress obtained from the test above is (237 + 233)/2 = 235 MPa and the carbon content which has been diffused can be calculated from the increase of yield stress. The increase of yield stress is $\Delta\sigma$= (235 - 113.7) = 121 MPa which corresponds to 0.0134 at% of carbon (the solubility limit predicted by the model at 430 ˚C is 0.0112 at%). If the calculation is performed separately for each specimen, the amount of carbon diffused in specimen A, where $\Delta\sigma$=(237 - 113.7) = 123 MPa, is 0.0138 at%, while the amount of carbon diffused in specimen B, where $\Delta\sigma$=(233 - 113.7) = 119 MPa, is 0.0129 at%. The carbon profile was then verified through thickness by performing Knoop microhardness tests by following the same procedure described in section 4.6.1. The results of Knoop hardness are shown in Figure 5-73, where it is clear that annealing at 430 ˚C for 10h will cause the carbon profile to become uniform through thickness.

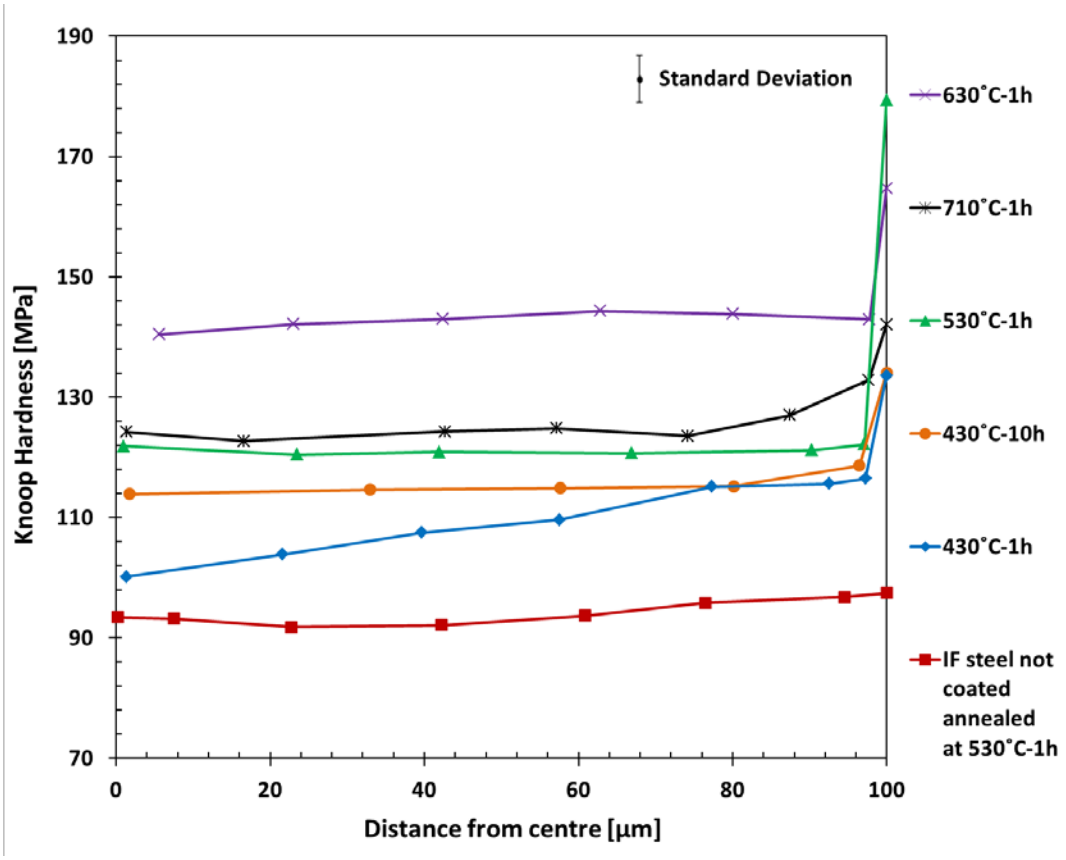

Figure 5-73 - Knoop microhardness curve for specimen coated both sides with 500 nm FeC film and annealed at 430 ˚C - 10h in high vacuum. The hardness curve has been added to the Knoop microhardness previously shown in section 5.2. for other heat treatments

Another series of tests were performed on coupons coated only on one side with 500 nm thick FeC film since it is expected that for them the strengthening should be just half of what is obtained if the specimens are coated both sides. Two coupons coated only on one side were annealed at 530 ˚C - 1h in high vacuum. The engineering stress-strain curves are shown in Figure 5-74.

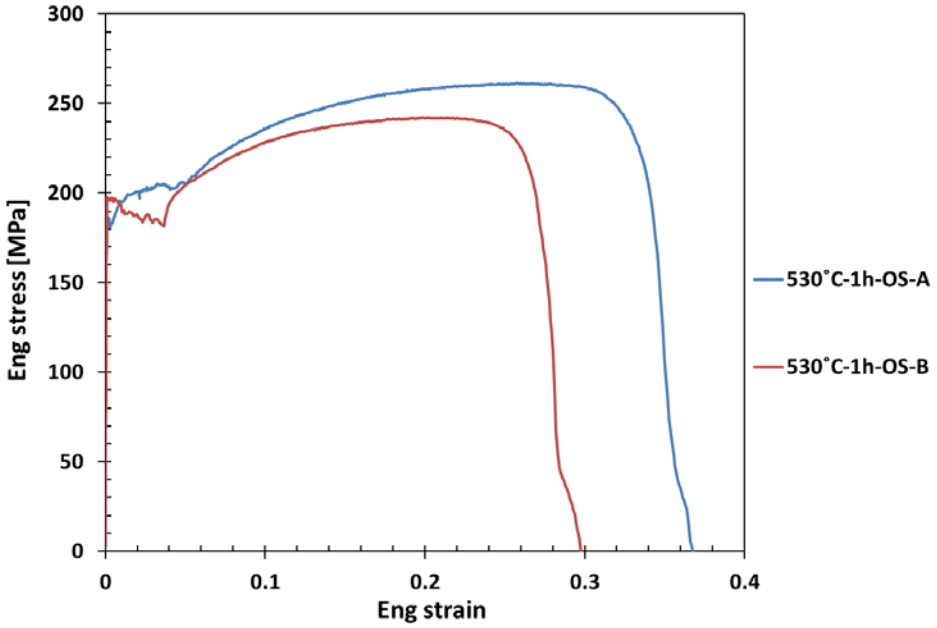

Figure 5-74 - Engineering stress-strain curves for coupons coated one side with 500 nm thick FeC film and annealed at 530 ˚C - 1h in high vacuum. OS means one side coated while A and B indicate two different specimens that were tested

The average increase of yield stress for a specimen coated both sides with 500 nm thick FeC film annealed at 530 ˚C - 1h in high vacuum is $\Delta\sigma$ = (259.32 - 113.7) = 146 MPa, while the average increase of yield stress for a coupon coated only on one side and annealed in the same condition is given by: $\Delta\sigma$ = (193 - 113.7) = 79 MPa which is half of the strengthening obtained using a coating on both sides (146/2) = 73 MPa. The mechanical properties obtained for specimens coated on one side can still be predicted using the equation $\Delta\sigma = Mm(X_c)^{1/2}$, but because the specimen is coated only on one side, the increase of strength will be divided by 2. Thus, for the coupons annealed at 530 ºC, the amount of diffused carbon obtained from the experimental increase of yield stress of 79 MPa will be 0.0057 at%. Theoretically, the amount of diffused carbon for a one side coated coupon, should be given by (0.0334 at% / 2) = 0.0167 at% (where the 0.0334 at% is obtained considering crystallization of FeC film and initial nominal content of 30 at% of carbon in the film and a nominal film thickness of 500 nm). However, if the film contains only 27 at% of carbon, then if the coupon is coated only on one side, the only carbon available to be diffused will be given by (0.01337/2) = 0.0067 at% and this can drop up to 0.0032 at% if the film is thinner than the nominal 500 nm. So for the one side coated coupons annealed at 530 ºC the increase

in strength is half of what is obtained with both sides coated coupons. Moreover, for a one side coated coupon, the discrepancy between the amount of carbon which should diffuse theoretically and the amount of carbon that has been diffused experimentally can be predicted considering both variation of carbon content and film thickness from the nominal values.

Other two tests were performed on coupons coated one side with 500 nm thick FeC film annealed at 630 ˚C - 1h in high vacuum. The engineering stress-strain curves are shown in Figure 5-75.

The average increase of yield stress for these specimens was 125 MPa which is 1.54 times smaller than what was obtained with a both sides coated coupon (which was 192 MPa). The average amount of carbon experimentally diffused in the specimen is 0.0144 at% which is close to the theoretical amount of carbon of 0.0167 at% which is expected to be available for diffusion (again considering FeC crystallization and a nominal carbon content of 30 at% and 500 nm of film thickness).

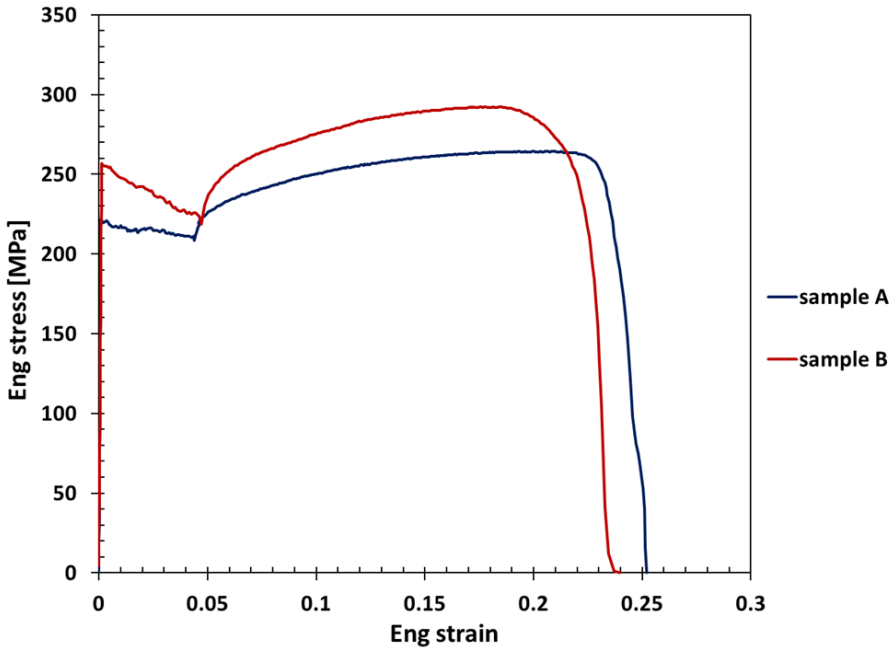

Figure 5-75 - Engineering stress-strain curves for coupons coated one side with 500 nm thick FeC film and annealed at 630 ˚C - 1h in high vacuum

The calculations presented in this section for the one side coated coupons are summarized in Figure 5-76, where the theoretical yield stress is compared with the yield stress obtained

experimentally. The theoretical yield stress is expected to be the same for both temperatures since the carbon available for diffusion is 0.0167 at%, which is lower than solubility of carbon into ferrite for both 530 ºC and 630 ºC. The error bars represent the range of variation considering both the ± 3 at% carbon uncertainty in the film and ± 20 nm uncertainty on its thickness. One can see that the results obtained for coupons annealed at 630 ºC match the nominal values expected theoretically, while the coupons annealed at 530 ºC are close to the yield stress obtained for carbon contents and film thickness lower than the nominal amounts.

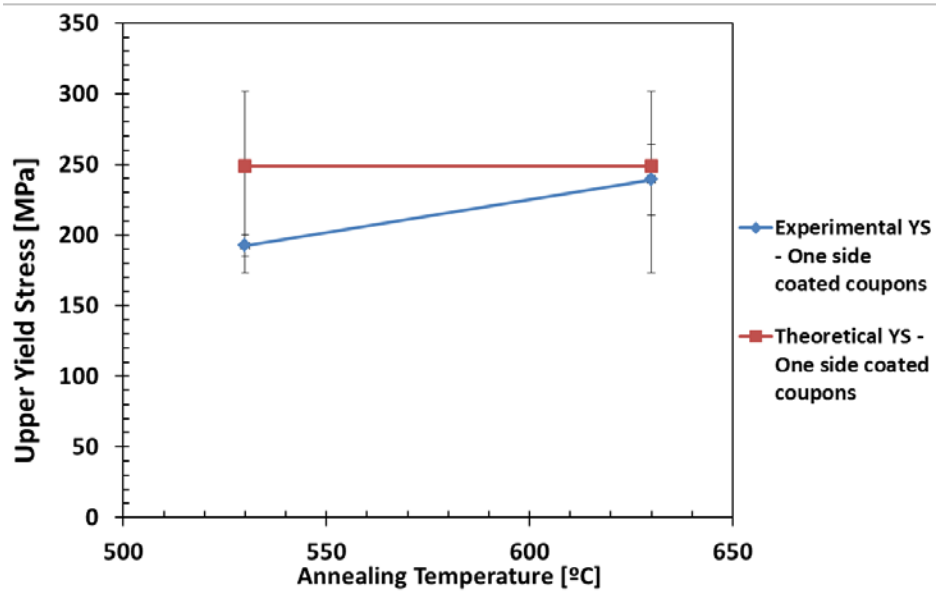

Figure 5-76 - Comparison between theoretical yield stress and experimental yield stress for one side coated coupons

5.9. Digital Image Correlation (DIC)

Digital image correlation (DIC) is a technique that allows following the propagation of Lüders bands in the specimen (see Chapter 4). The information that can be extracted from this analysis includes band pattern, angle of the front of the bands and the speed profile of the front. We will show that the band pattern can be clearly related to the profile of the Lüders plateau seen in the stress-strain curve. In this paragraph, DIC analyses for coupons coated both sides with 500 nm FeC film and annealed in high vacuum at different temperatures are shown.

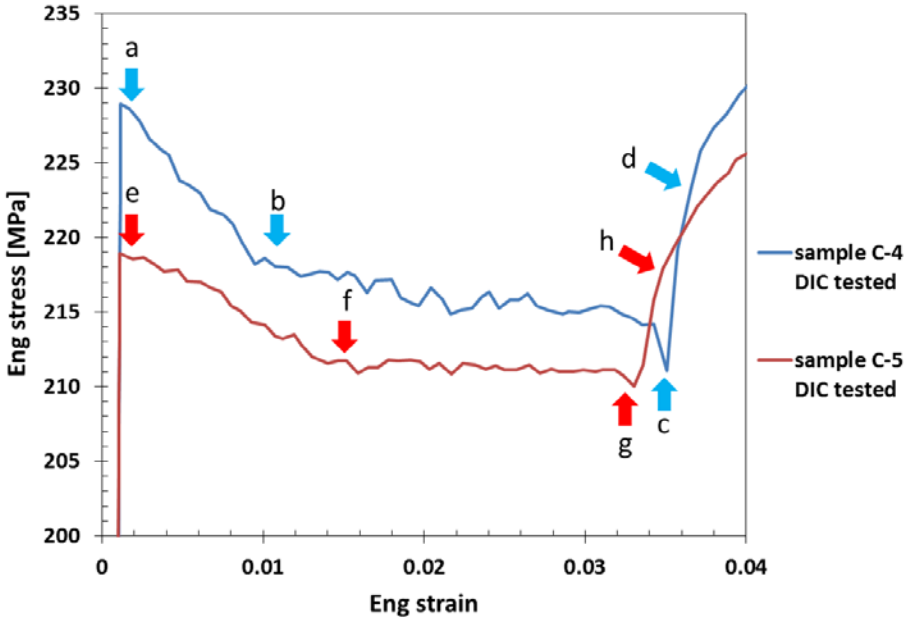

Figure 5-77 - Lüders plateau detail of the engineering stress-strain curves for samples C-4 (a, b, c, d) and C-5 (e, f, g, h) annealed at 430 ˚C - 1h in high vacuum

For sample C-4, the propagation of Lüders bands is shown in Figure 5-78, where in (a) the nucleation of the bands occurred at the radii of curvature and this corresponds to the first drop from the upper yield stress (points from a to b in the engineering stress-strain curve Figure 5-77). Since initially, one band is moving faster than the other, there is a continuous drop of the load before reaching the plateau at point b (Figure 5-77). After this point, the bands propagate with the same speed until they coalesce. When the two fronts meet there will be a further drop in the load which is marked as point c in the stress-strain curve (Figure 5-77) and as image c in Figure 5-78.

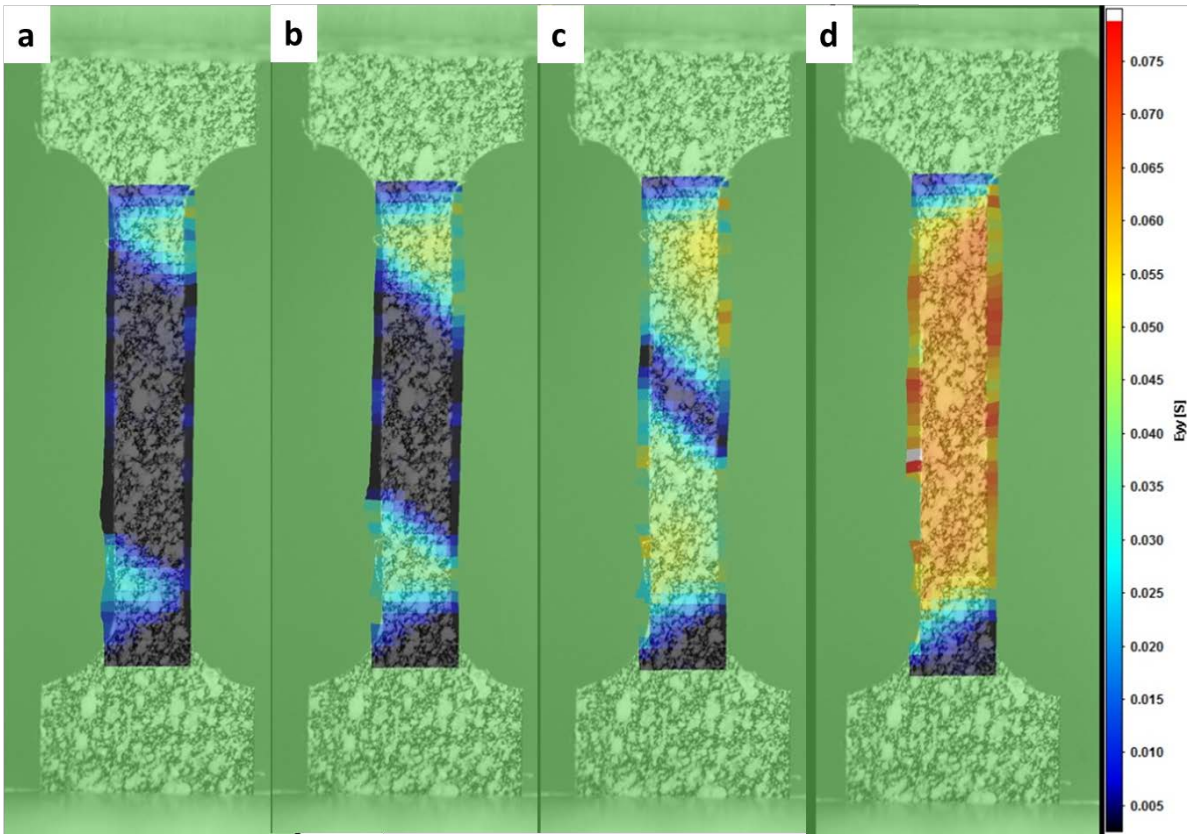

Figure 5-78 - Propagation of Lüders bands for sample C-4 coated both sides with 500 nm thick FeC film and annealed at 430 ˚C - 1h in high vacuum

After the bands have completely propagated through the gauge length, then the material starts the usual strain-hadening behaviour, which is marked as point d in the stress-strain curve (Figure 5-77) and image d in Figure 5-78.

According to the information presented in literature review, it is possible to obtain information on the velocity profile of the bands to see if they are propagating with the same speed or not. The graph that can give this information is obtained by plotting (x/L) versus time, where x is the path covered by the band and L is the total gauge length of the specimen (in this case equal to 5 mm). For sample C-4 annealed at 430 ºC – 1h in high vacuum, the velocity profiles for the two propagating bands is shown in Figure 5-79. One can see that the slope of the two lines is almost the same meaning that the two bands are propagating at the same speed and that for the specimen it is easy to unpin the dislocations from the carbon atoms in the whole gauge length.

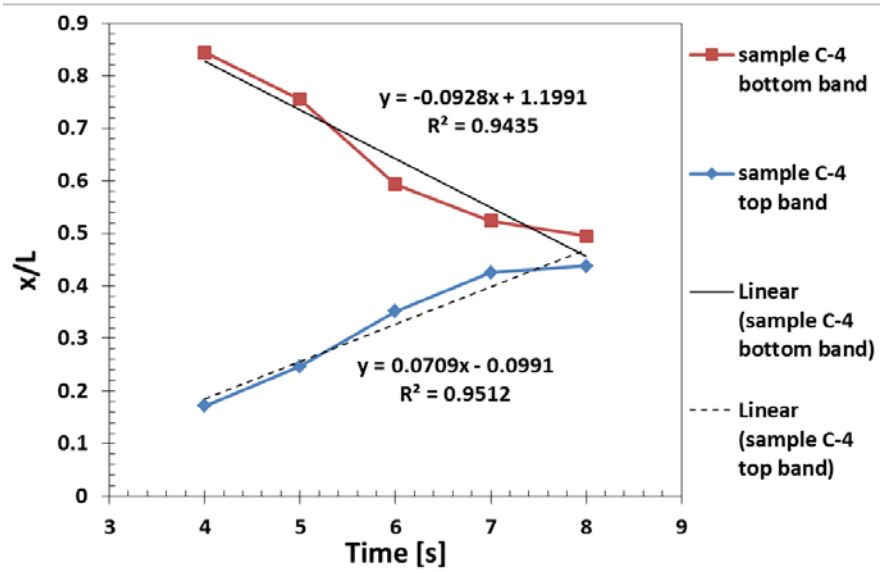

Figure 5-79 - Velocity profile of Lüders bands in sample C-4 coated both sides with 500 nm FeC film and annealed at 430 ˚C - 1h

In Figure 5-80, the Lüders plateau for specimens annealed at 530 ºC – 1h in high vacuum is shown and the sequence of images of Lüders band are reported in Figure 5-81 for specimen D-3. Once again, the nucleation of the bands at the fillet radii is responsible for the load drop from point a to b in the stress-strain curve. However, since the bottom band propagates faster than the top band, there is a continuous drop from point a to point b in the stress-strain curve and also from point b to point c. The band on the bottom has propagated for most of the gauge length, while the top band propagated very slowly and it accelerated only when the bottom band had approached it (image c of Figure 5-81). The two bands then coalesce and a small load drop is registered in the stress-strain curve (point c of Figure 5-80).

The speed at the front of the two bands was extracted by plotting (*x/L*) versus time and it is shown in Figure 5-82, where the bottom band propagates one order of magnitude faster than the top band, which nucleates but it then propagates very slowly and it accelerates only when the bottom band has almost reached it.

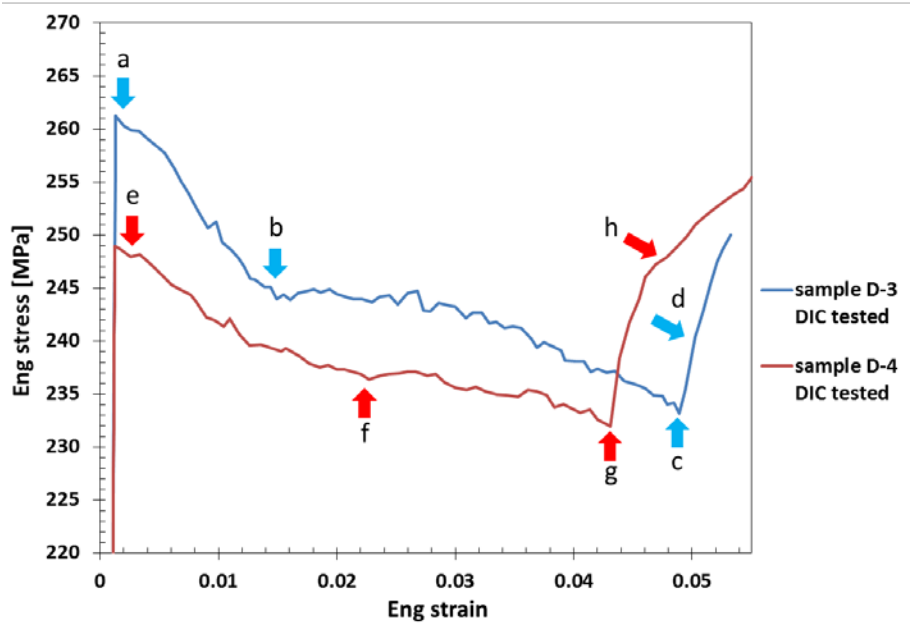

Figure 5-80 - Lüders plateau detail of the engineering stress-strain curves for samples D-3 (a, b, c, d) and D-4 (e, f, g, h) annealed at 530 ˚C - 1h in high vacuum

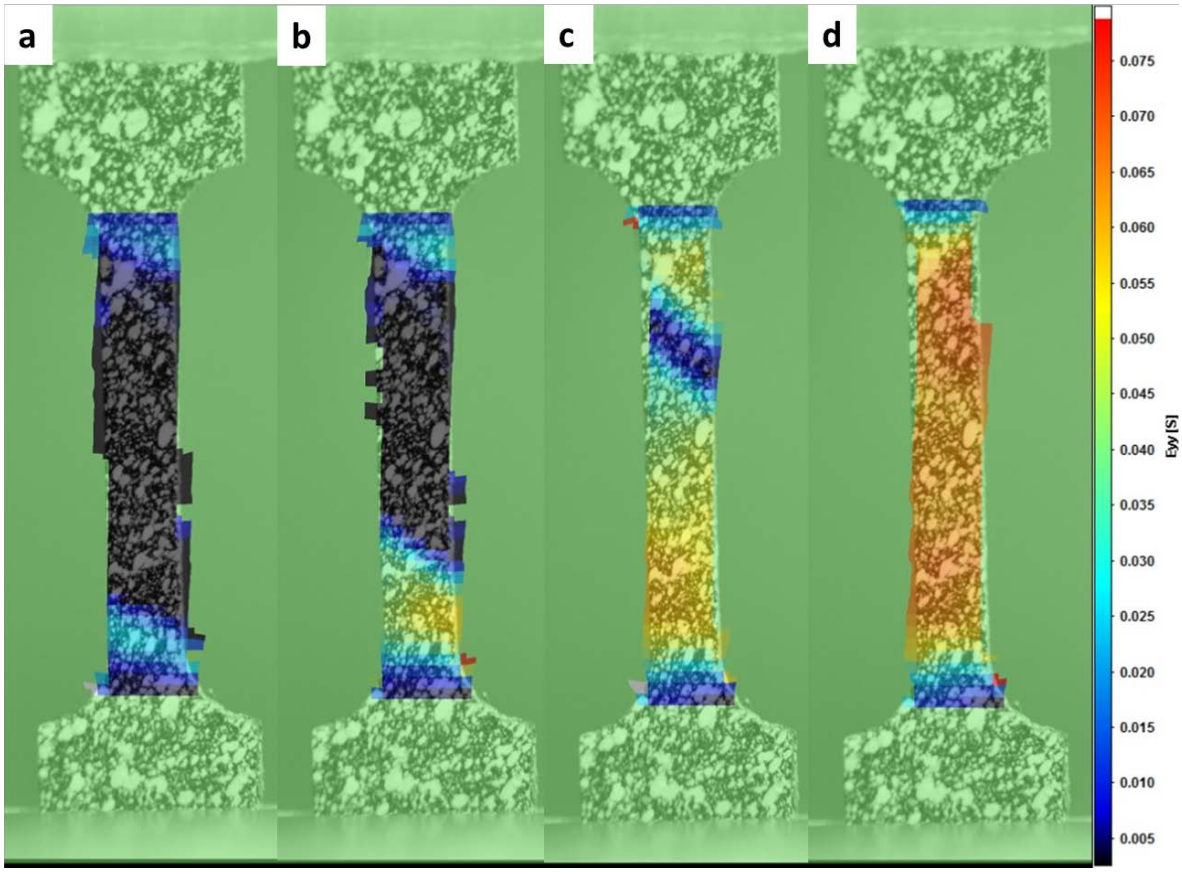

Figure 5-81 - Propagation of Lüders bands for sample D-3 coated both sides with 500 nm thick FeC film and annealed at 530 ˚C - 1h in high vacuum

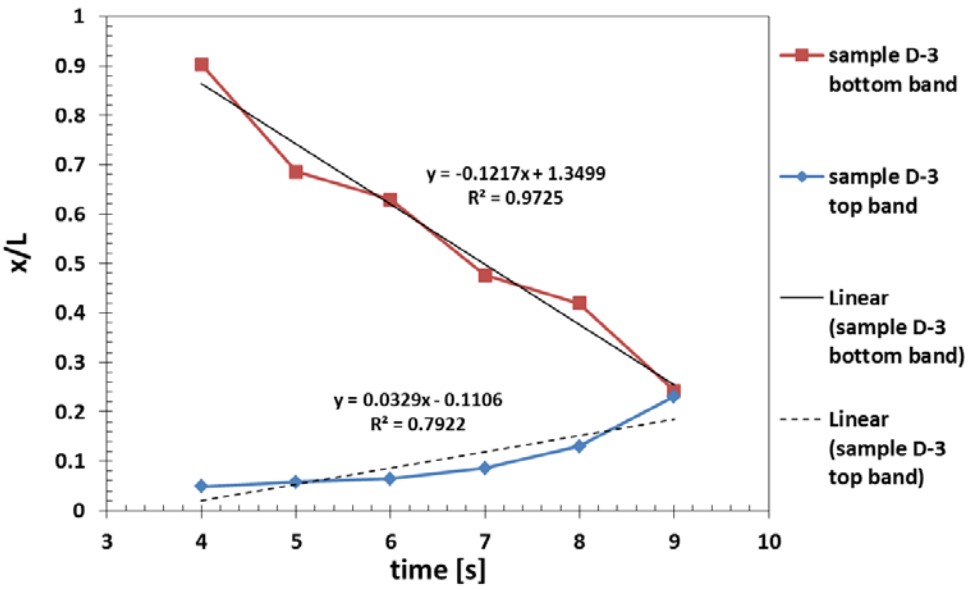

Figure 5-82 - Velocity profile of Lüders bands in sample D-3 coated both sides with 500 nm FeC film and annealed at 530 ˚C - 1h

It should be noted that the load drop at the end of the plateau is less marked when one band is propagating faster than the other band. The drop is completely absent if there is only one band propagating. After the bands have completely propagated along the gauge length, the material starts the usual strain-hadening behaviour, which is marked as point d in the stress-strain plot (Figure 5-80).

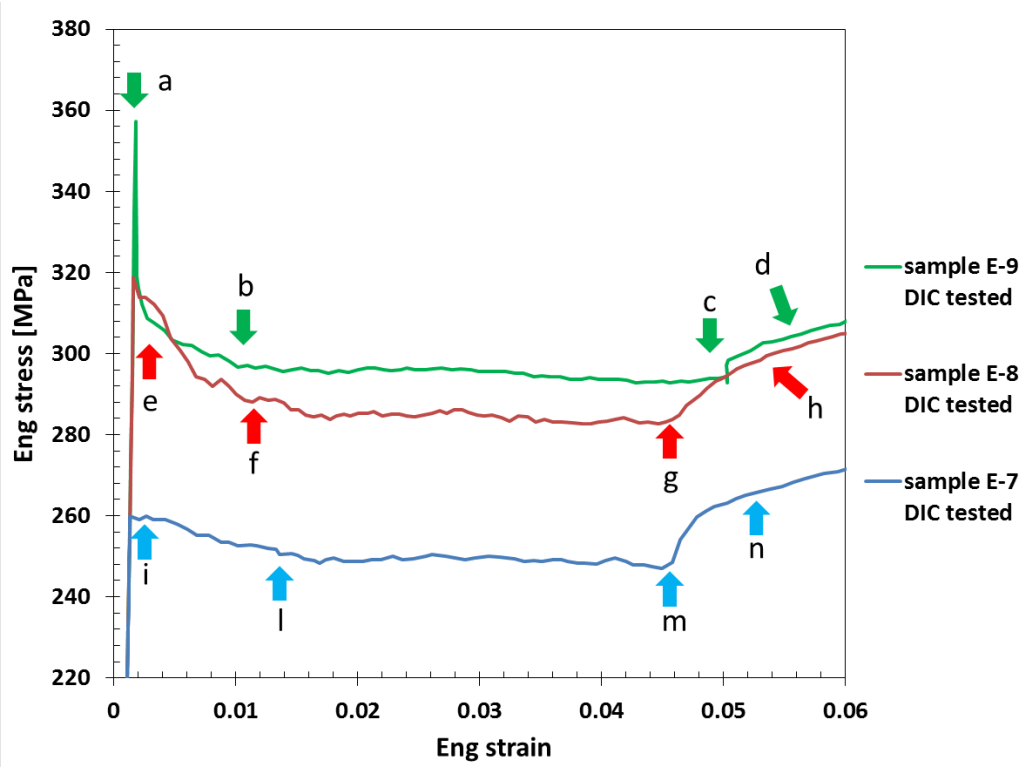

Figure 5-83 - Lüders plateau detail of the engineering stress-strain curves for samples E-9 (a, b, c, d) E-8 (e, f, g, h) and E-7 (i, l, m, n) annealed at 630 ˚C - 1h in high vacuum

In Figure 5-83, three examples of Lüders plateau curves for specimens annealed at 630 ºC - 1h in high vacuum are reported. The sequence of images shown in Figure 5-84 shows the propagation of Lüdering for sample E-9. Compared to the specimens previously reported for annealing at 430 ºC and 530 ºC, samples E-9 shows the nucleation of a single band at one fillet radii. This band is responsible for the load drop from point a to point b in the stress-strain curve (Figure 5-83). Given that no other band is originated inside the gauge length, the Lüders plateau from point b to point c in the stress-strain curve shows no stress drop and propagates smoothly. The figure showing the speed at the band fronts was reported in Appendix D (section D.13).

In Figure 5-85, Lüders plateau details for coupons annealed in high vacuum at 710 ºC are reported.

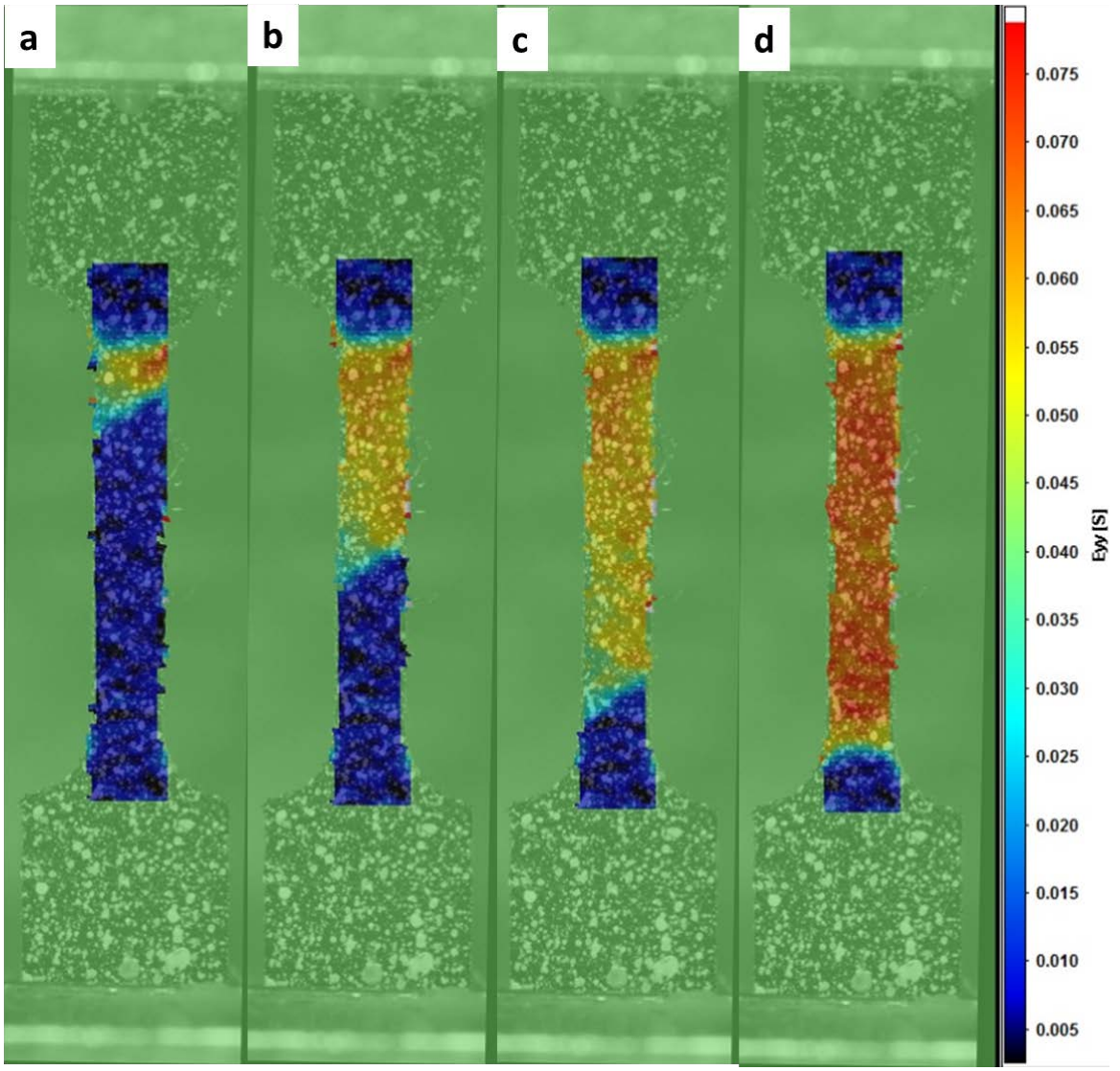

Figure 5-84 - Propagation of Lüders bands for sample E-9 coated both sides with 500 nm thick FeC film and annealed at 630 ˚C - 1h in high vacuum

In Figure 5-86, the nucleation of three bands which are reponsible for the load drop from point a to point b in the stress-strain curve in Figure 5-85 are reported. In the image (b) of Figure 5-86, the coalescence of the two bottom bands occurred and two fronts keep propagating with two opposite inclinations. The opposite inclination of these two fronts limits the lateral kinking of the tensile coupon and it is responsible for a smooth Lüders plateau with no load jumps and no drop at the end of the plateau (point c in the stress-strain curve Figure 5-85).

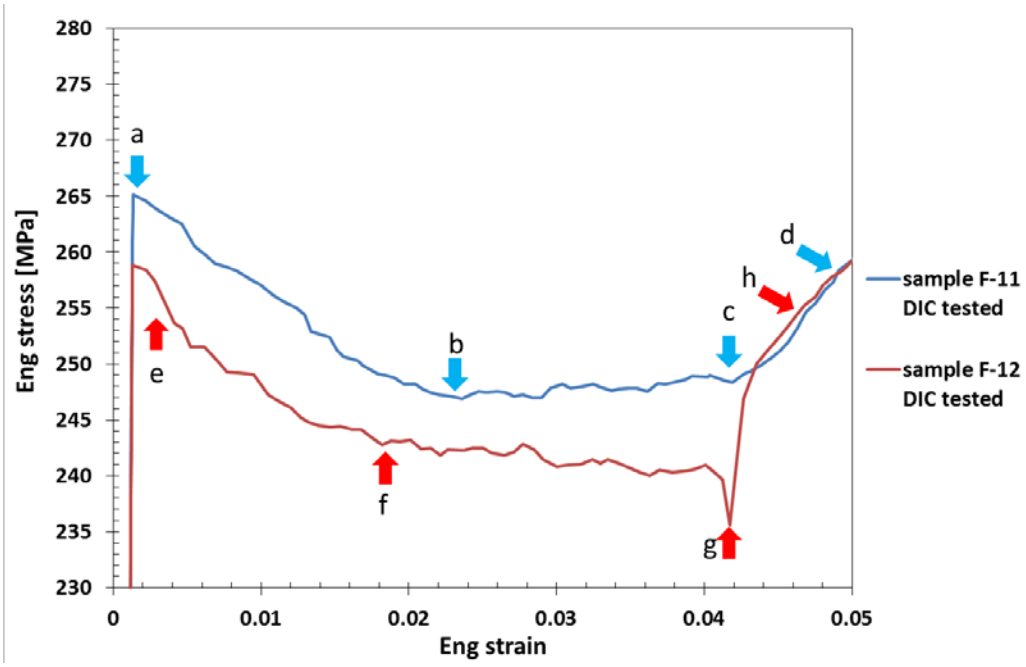

Figure 5-85 - Lüders plateau detail of the engineering stress-strain curves for sample F-11 (a, b, c, d) and sample F-12 (e, f, g, h) annealed at 710 ˚C - 1h in high vacuum

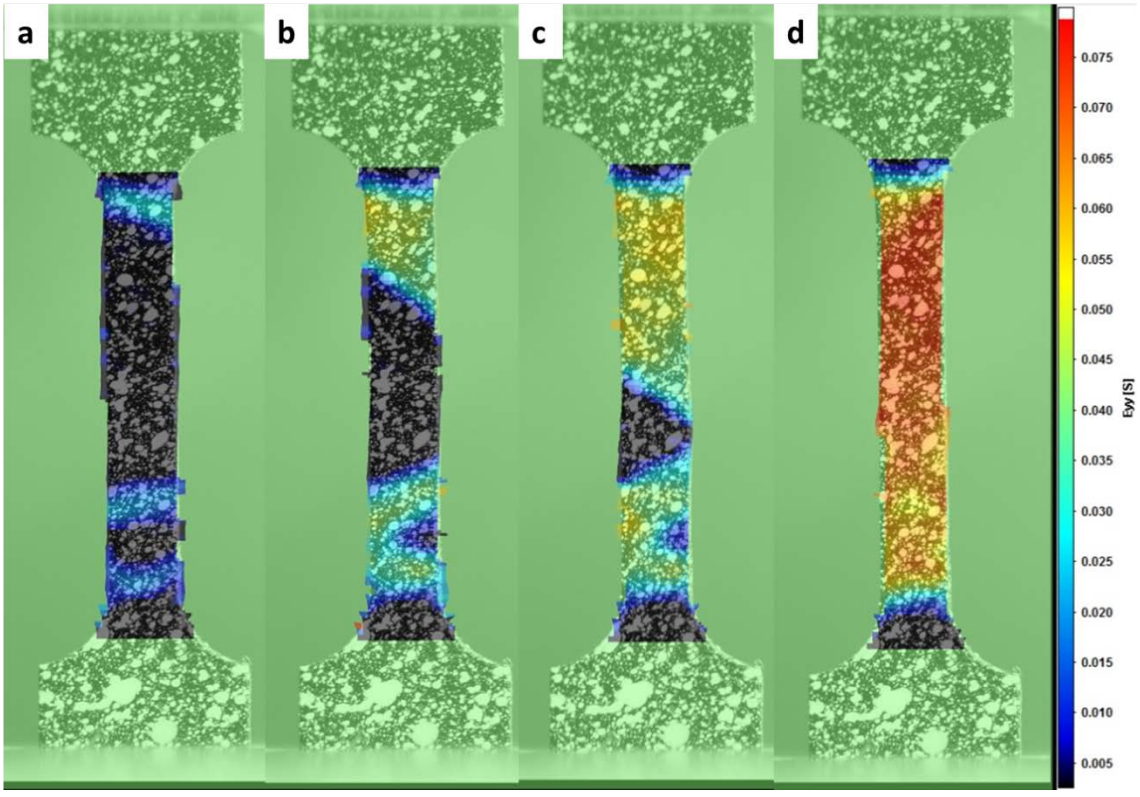

Figure 5-86 - Propagation of Lüders bands for sample F-11 coated both sides with 500 nm thick FeC film and annealed at 710 ˚C - 1h in high vacuum

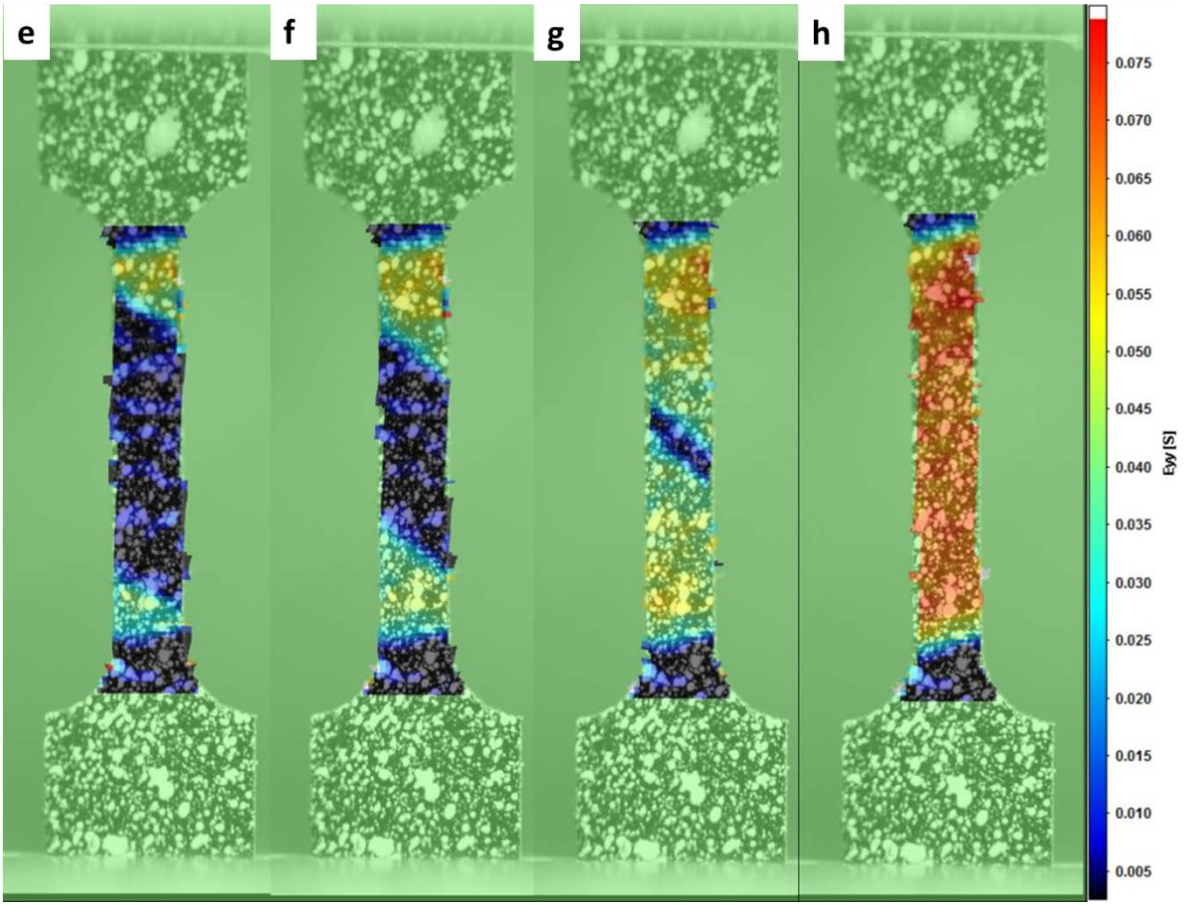

Figure 5-87 - Propagation of Lüders bands (points e and f of the stress-strain curve) for sample F-12 coated both sides with 500 nm thick FeC film and annealed at 710 ˚C - 1h in high vacuum

For sample F-12, which was as well annealed at 710 ºC – 1h in high vacuum, two bands with the same inclination were propagating as shown in the sequence of images in Figure 5-87. The nucleation of two bands occurs at the fillet radii and is reponsible for the load drop from point e to point f in the stress-strain curve in Figure 5-85. The coalescence of the bands will cause a further stress drop (point g in Figure 5-85). The figure showing the speed at the band fronts was reported in Appendix D (section D.13).

The length of the Lüders plateau and speed of propagation of the Lüders bands are related to carbon content at dislocations, to the presence of carbon precipitates inside the specimen and to dislocation multiplication during Lüders bands propagation. If the Lüders plateau is long, it means that the propagation of the bands is slow and that more dislocations need to be formed to propagate the deformation or that precipitates are able to interact with dislocations to slow their motion. Another feature that depends on carbon content is the stress drop from

the upper yield stress to the plateau stress. If this drop is high, it means that all the dislocations are tightly locked by carbon atoms and that they are completely saturated by a high density of carbon atoms. On the contrary, if Lüders plateau starts to propagate without any stress drop, then Cottrell atmosphere contain a low density of carbon atoms and it is easy to unpin dislocations. Moreover, if a Lüders plateau is short, the bands can propagate quite fast, which means that the dislocations are easily unlocked due to the low carbon density of the Cottrell atmospheres or that dislocations can multiply and propagate easily. Calculating an average of the stress drops at the start of the plateau for the specimens shown in Figure 5-77, Figure 5-80, Figure 5-83 and Figure 5-85, it is noticed that the stress drop increases as the amount of diffused carbon is increased as shown in Figure 5-88 except for specimen E-7 annealed at 630 ºC -1h for which the amount of diffused carbon is at the same level as the amount diffused at 530 ºC (most probably because of the low amount of carbon in the FeC film). It was mentioned in literature [71] that the number of drops in the Lüders plateau are influenced by the testing machine compliance, however, all the DIC test were done using the same tensile machine. For this reason, the variation of stress drop shown in Figure 5-88 is not related to the compliance to the testing machine but to the change of carbon content.

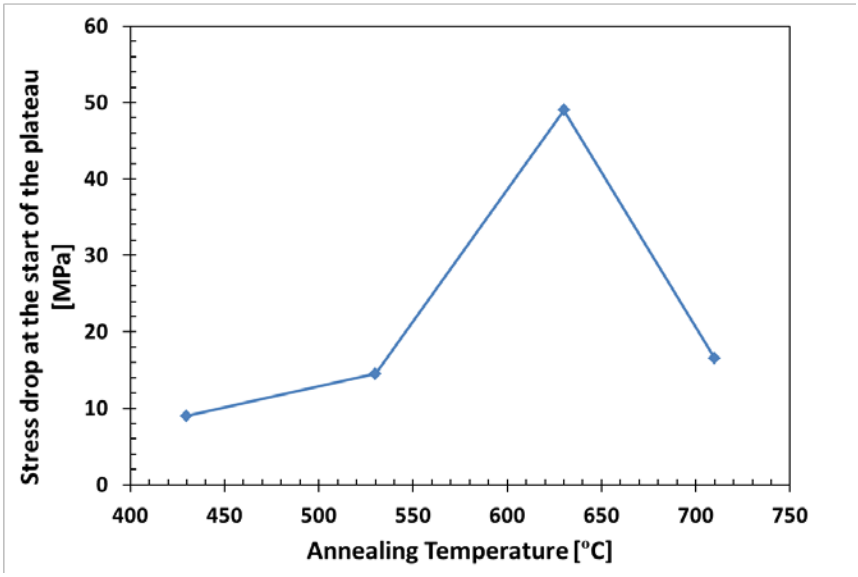

Figure 5-88 - Stress drop at the start of the Lüders plateau propagation as function of annealing temperature

The high stress drop recorded for specimens annealed at 630 ºC means that for this temperature, Cottrell atmospheres have a high density of carbon atoms, moreover,

dislocations require a high stress to be unpinned, due to the formation of nanometric precipitates at dislocations (this is also known as precipitation stage in strain-ageing experiments). For specimens annealed at 710 ºC the level of stress drop is similar to what was found for specimens annealed at 530 ºC. Supposing that at 710 ºC we diffuse the same amount of carbon diffused with annealing at 630 ºC, it is evident that this carbon is not used to form Cottrell atmosphere since dislocations are more easily unpinned compared to annealing at 630 ºC. Another objective of this work was to find a relation between carbon content and the average speed of the bands. According to literature [163] the Lüders strain ε_L is closely related to the velocity of the band front. Calling V the velocity of the tensile machine, then during the time δt, a length of material δl at the band front has covered the length $(1+\varepsilon_L)\times(\delta l)$ as the band passes through it. In the same time, the grip of the tensile machine has moved of a distance $V\delta t$, so:

$$(1+\varepsilon_L)\delta l - \delta l = V\delta t \qquad \text{(eq. 5-8)}$$

from which it can be obtained:

$$\varepsilon_L = V\left(\frac{\delta t}{\delta l}\right) = \frac{V}{v_L} \qquad \text{(eq. 5-9)}$$

where, $v_L = \delta l/\delta t$ is the velocity of the Lüders front. If more than one front is activated, then the Lüders strain is expressed as:

$$\varepsilon_L = \frac{V}{N v_L} \qquad \text{(eq. 5-10)}$$

where N is the number of active fronts. The relation above can be reversed to obtain the speed of the Lüders front since V is known and for the tensile tests previously shown it is equal to 2.5 µm/s. The number of active fronts (N) can be obtained from DIC analyses and the Lüders strain ε_L corresponds to the Lüders plateau length obtained for a stress-strain curve. Based on these considerations, the formula can be written as:

$$v_L = \frac{V}{N\varepsilon_L} \qquad \text{(eq. 5-11)}$$

This equation will give an average speed of the bands, but it will not keep into account if one band is propagating faster than another band.

In Table 5-26, the carbon content and the Lüders bands speed for the specimens analyzed with DIC after annealing at different temperatures for 1h are reported.

Specimen and annealing condition	Carbon content evaluated with the formula $\Delta\sigma=Mm(X_C)^{1/2}$ [at%]	Lüders length	Speed of the Lüders bands [mm/s]
430˚C-1h – specimen C-4	0.01215	0.03391	0.03686
430˚C-1h – specimen C-5	0.01013	0.03195	0.03912
530˚C-1h – specimen D-3	0.01990	0.04761	0.02625
530˚C-1h – specimen D-4	0.01673	0.04183	0.02988
630˚C-1h – specimen E-7	0.01957	0.04363	0.02865
630˚C-1h – specimen E-8	0.03846	0.04302	0.05811
630˚C-1h – specimen E-9	0.05422	0.04850	0.05155
710˚C-1h – specimen F-11	0.02094	0.04055	0.01541
710˚C-1h – specimen F-12	0.01928	0.04043	0.0309

Table 5-26 - Lüders bands speed for specimens coated both sides with 500 nm FeC film and annealed at different temperatures in high vacuum

The carbon content diffused experimentally during annealing in high vacuum is plotted as a function of annealing temperature together with the Lüders plateau length and the Lüders bands speed. The three curves are shown in Figure 5-89.

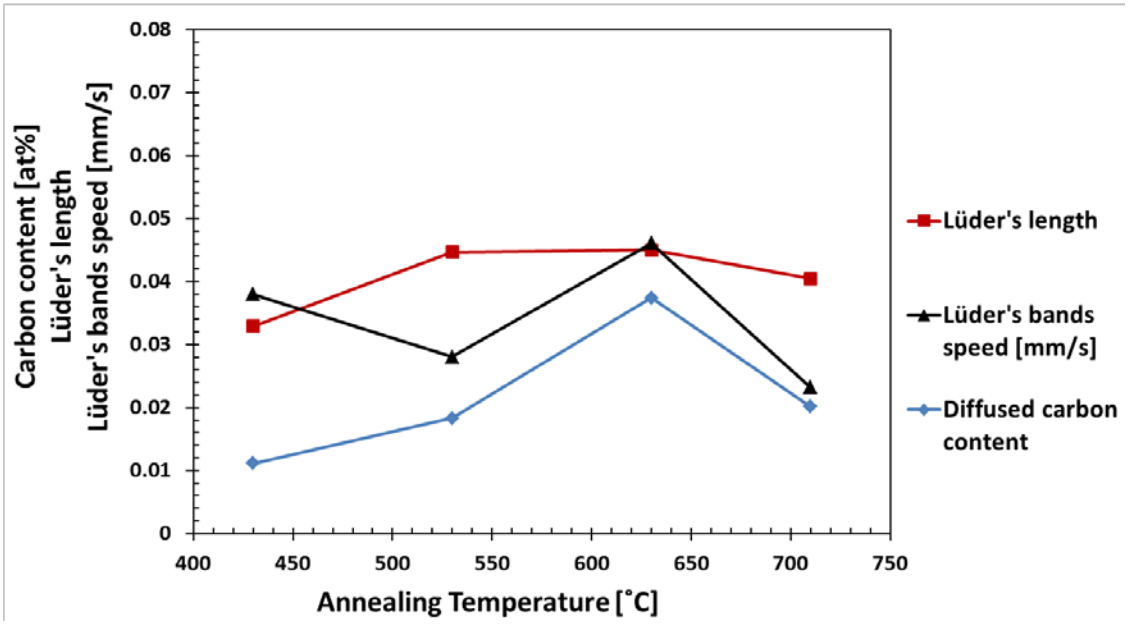

Figure 5-89 - Diffused carbon content, Lüders length and Lüders bands speed as function of annealing temperature

From Figure 5-89 it is evident that as the amount of carbon in the IF steel increases from 430 ˚C to 530 ˚C, the Lüders plateau length increases and the speed of the bands decreases as a consequence, probably due to a high carbon density of Cottrell atmospheres. However, even if going from 530 ˚C to 630 ˚C the carbon content increases, the Lüders length remains the same but the bands speed shows an increase. Going from 630 ˚C to 710 ˚C only a slight decrease of Lüders length is detected. So from this, it is clear that the Lüders plateau length tends to increase as the amount of carbon increases until the Lüders length reaches a plateau. This could mean that at 530 ˚C all Cottrell atmospheres are fully saturated and that the precipitation stage at dislocations started above this temperature. However, no clear relation can be set between the carbon content and the speed of the bands since the speed of the bands is also determined by the multiplications of dislocations.

5.10. Discussion of Chapter 5

In this chapter, the results of diffusion modelling of carbon into IF steel and the mechanical properties obtained after annealing under different conditions have been presented. From the results of the diffusion modelling, the following conclusions can be drawn:

- Annealing at 330 ˚C - 1h does not cause significant carbon diffusion;
- Annealing at 430 ˚C - 1h will cause a gradient of carbon through thickness;
- Annealing at 530 ˚C or above for 1h will create a uniform carbon profile through the thickness of the specimen, with higher temperatures allowing more carbon to diffuse in the IF steel.

From the mechanical tests, the following conclusions can be inferred:

- Annealing of uncoated IF coupons at different temperatures for 1h shows that the mechanical properties of IF steel are stable with a yield stress around 113 MPa, a UTS of 297 MPa and a nominal strain at fracture between 0.45 and 0.50;
- Carbon can be effectively diffused starting from a PVD FeC film with 30 at% carbon having a thickness of 500 nm coated on both sides of an IF steel coupon;
- A coated coupon annealed at 330 ˚C - 1h shows no improvement in mechanical properties compared to an uncoated IF steel. However, an increase of annealing temperature causes an increase of yield stress and ultimate tensile stress except for the annealing at 710 ˚C - 1h where the yield stress falls back to the yield stress obtained when annealing at 530 ˚C -

1h. The appearance of a Lüders plateau at temperatures equal to or above 430 ˚C - 1h confirms the diffusion of carbon in interstitial position from the FeC film into the IF steel core. Yield stress (YS) and ultimate tensile strength (UTS) of uncoated coupons of IF steel annealed in high vacuum can be compared with yield stress and ultimate tensile strength of IF steel coupons coated both sides with 500 nm thick FeC film. The curves showing the evolution of YS and UTS for both configurations at different annealing temperatures are shown in Figure 5-90, where it is evident that the increase of the yield stress is due to carbon diffusion for coated coupons, while the yield stress of uncoated IF steel remains unchanged at the different temperatures. The increase of yield stress found in coupons which have been carbon diffused is due to three main contributions: formation of Cottrell atmospheres which pin dislocations, precipitation of small carbides when Cottrell atmospheres are highly saturated with carbon, and carbon segregation at grain boundaries.

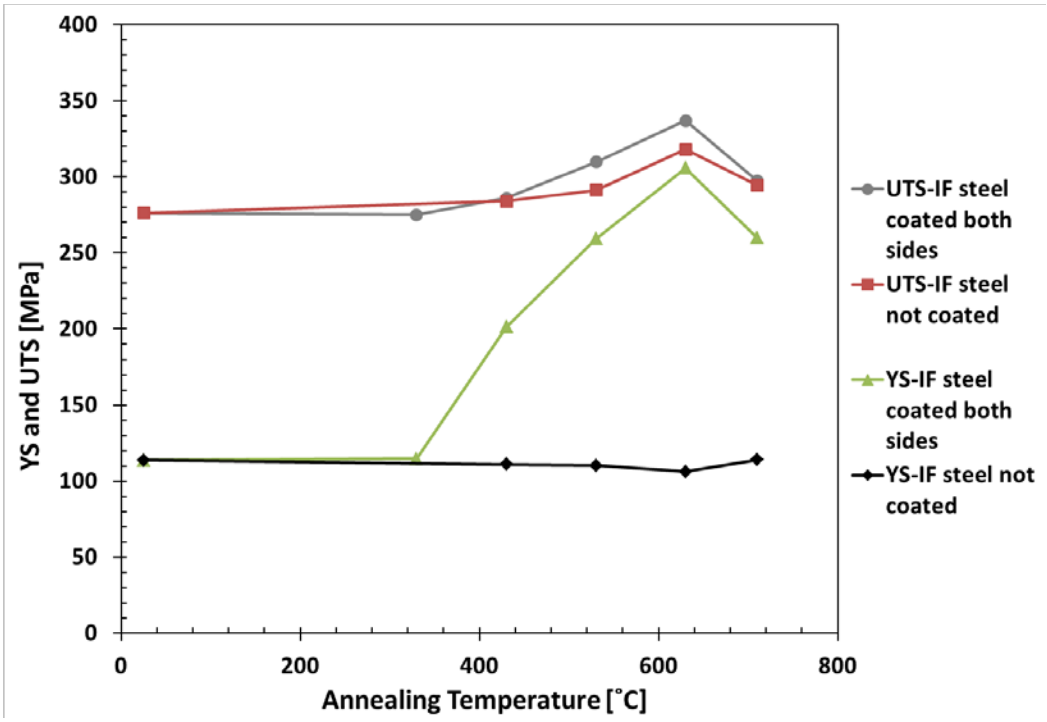

Figure 5-90 - Comparison of yield stress (YS) and Ultimate Tensile Strength (UTS) for uncoated and annealed IF steel coupons and coated and annealed IF steel coupons

In particular, the effect of carbon segregation at grain boundaries on the Hall-Petch coefficient for interstitial free steel has been reported [164]. It was found that the Hall-Petch coefficient is around 150 MPa·μm$^{1/2}$ but it can increase up to 600 MPa·μm$^{1/2}$ by adding

solute carbon up to 60 ppm. The yield stress is very stable for the uncoated coupons, however, for the coated coupons, the yield stress shows a drop at 710 ˚C and since this decrease is not present in uncoated specimens, this proves that carbon diffusion at 710 ˚C is responsible for this yield stress drop. This was related with a decrease of carbon at dislocations (TEP measurements) and with carbon enrichment of TiS particles (EDS and APT measurements).

On the other hand, UTS seems to have a slight increase for annealing at 530 ˚C - 1h and 630 ˚C - 1h for the coated coupons, however, for the other annealing temperature, the UTS of coated coupons is at the same level as that of uncoated coupons. It is also interesting to note the increase of UTS in the uncoated IF steel for annealing at 630 ˚C – 1h. However, no clear cause for this was identified or reported neither in literature nor in this thesis.

In section 5.5, it was calculated that with a nominal amount of carbon in the film of 30 at% and a film thickness of 500 nm on both sides, the carbon which remains available for diffusion after crystallization of the film is 0.0334 at%. This is the maximum amount of carbon that can be diffused after transformation of the film into cementite assuming that no carbon leaves the film before the cementite transformation. This amount is higher than the solubility limit of carbon into ferrite for annealing at 530 ˚C - 1h, so at this temperature, ferrite is saturated. However, the amount of 0.0334 at% is lower than the solubility limit of carbon into ferrite at 630 ˚C and 710 ˚C, which is why at these temperatures, ferrite is not saturated if the film contains 30 at%. On the other hand, if the film contains 33 at%, then even after crystallization, the amount of carbon which remains available for diffusion is 0.0533 at% and this is close to the solubility limit of carbon in ferrite at 630ºC (which is 0.052 at%). If the theoretical yield stresses are plotted with the ones obtained experimentally by taking into account the limited amount of carbon available above 530˚C as a consequence of the film transformation into cementite, a better prediction of the mechanical properties is obtained as shown in Figure 5-41. The error bars were calculated considering both the nominal variation of ± 3 at% carbon in the film and the ± 20 nm variation in film thickness.

The carbon content diffused into the IF steel is equal to the solubility of carbon into ferrite for annealing at 330 ˚C, 430 ˚C and 530 ˚C. However, to confirm that at 630 ºC no more carbon atoms can enter the IF steel sheet and that the solubility limit is not reached (unless the film contains 33 at% of carbon), tensile tests were performed on both sides coated

coupons annealed at 630 ºC for 5 hours. After leaving the specimens for 5h at 630 ˚C, the yield stress is exactly in the same range as the yield stress found for annealing at 630 ˚C - 1h, proving that 0.0334 at% is the maximum amount of carbon that can be diffused as consequence of the crystallization of the film.

The largest increase in mechanical properties is obtained for annealing in high vacuum even if argon was shown to be a good alternative. The worst mechanical properties have been obtained for the annealing in air, since in this case, carbon from the FeC film reacts with oxygen causing decarburization of the FeC coating.

The shape of the carbon profile through thickness predicted from the diffusion model was confirmed by Knoop microhardness tests. The experimental results show that the profile is graded for annealing in high vacuum at 430 ˚C - 1h, while the carbon profile is uniform for annealing in high vacuum at 530 ˚C, 630 ˚C and 710 ˚C for 1h. The profile also becomes uniform if annealing is performed at 430 ˚C for 10h, which was predicted by the model. From the microhardness results, it is confirmed that an increase of annealing temperature brings an increase of hardness except for annealing at 710 ˚C - 1h since the hardness falls back between the hardness of the 530 ˚C - 1h and 630 ˚C - 1h. Knoop microhardness of the coated surface is high for annealing temperatures equal or higher than 530˚C-1h since the FeC film transforms into cementite. The crystallization of the film is detected also during the tensile test, since exfoliation of the film occurs for annealing temperatures of 330 ˚C - 1h and 430 ˚C - 1h, while the FeC film fractures but it does not exfoliate if the annealing temperature is equal to or above 530 ˚C - 1h.

- It was found that the yield stress becomes higher as the film thickness is increased by performing tensile tests on coupons annealed at 530 ˚C – 1h in high vacuum. A stoichiometric calculation considering the transformation of the film into cementite has shown that the amount of carbon available to be diffused towards the IF core increases with film thickness. A comparison between the theoretical yield stress and the experimental yield stress for the different film thicknesses considering both ± 3 at% carbon variation in the film and film thickness variation, are reported in Figure 5-69.
- Finally, it was shown that if the specimens are coated only on one side with 500nm thick FeC film, the increase of yield stress is half of what is obtained with coupons coated on both sides.

From DIC results, it was shown that the stress drop at the starting of Lüdering follows the same trend of the diffused carbon. If the amount of carbon increases, the stress drop will increase as well due to a higher carbon density in Cottrell atmospheres and to a higher stress that has to be reached to unpin dislocations. However, no clear trend could be drawn between speed of the bands and carbon content.

Chapter 6 :Finite Element Simulations of Lüders Bands

Experimental work related to the study of Lüders phenomena was already presented in literature review in paragraph 2.10. In this chapter a review of simulations on Lüdering will be presented.

In literature, many finite element analyses involving Lüders plateau propagation are reported. In particular, Belotteau et al. have analyzed the influence of parameters such as mesh size, behaviour law and boundary conditions on Lüders bands propagation [100]. From their work, Belotteau et al. concluded that there is a stress drop in the Lüders plateau every time a band is nucleated or every time two bands coalesce [100]. In the same study, the influence of artificial defects introduced to generate Lüders band propagation has been assessed [100]. However, no clear influence of stiffness and of strain-hardening on Lüders propagation was reported.

Moreover, in literature, the behaviour of Lüders bands was simulated in materials having no gradient of yield stress. In the scope of this PhD thesis, it is very important to know how a gradient of carbon (which corresponds to a gradient of yield stress) can influence Lüders band propagation since carbon diffusing from the FeC films can create a carbon gradient through the thickness of the IF steel sheet (see for example specimen annealed at 430 ˚C - 1h in vacuum in Chapter 5, or for example specimens coated only on one side with FeC film and induction heated for 30s in Chapter 8). Indeed, considering samples with the same amount of carbon and the same strength, it is currently not known whether having a uniform carbon profile or a graded one will provide the same Lüdering behaviour.

In this chapter, the role of stiffness, strain hardening and gradient of yield stress on Lüders bands propagation is presented. In the following work no artificial defects have been introduced in ABAQUS to propagate the bands since a whole tensile coupon was modeled for each FEM simulation and the fillet radii act as “defects” to nucleate the bands. First, a parametric study was carried out to understand how linear softening, which was proposed by Tsukahara and Iung [131] to simulate Lüders plateau, can influence Lüders bands propagation.

Tsukahara and Iung [131] have shown that Lüders bands can be reproduced in finite element model if a linear "softening" is introduced in the material properties. In particular, a linear relation is used to connect the upper yield stress and the lower yield stress as shown in Figure 2-19 of Chapter 2.

The position of the upper point (upper yield stress) and the slope of the linear softening can influence the final length of the Lüders plateau. In literature there is no data

explaining how the slope of the linear softening and the upper yield stress can influence Lüders length. Moreover Tsukahara and Iung did not relate this linear softening with any physical parameter such as density of dislocations and carbon content. The implementation of the linear softening in ABAQUS is quite straightforward and it can still be used to obtain predictions on the gradient of yield stress and gradient of strain-hardening exponent.

The following three aspects of Lüders band propagation have not been covered in literature:

- Influence of carbon gradient;
- Influence of material stiffness;
- Influence of strain-hardening;

Moreover, no study on the influence of voids on Lüders band propagation is present in literature. In the present work two series of FEM simulations were performed to understand how void spacing and voids volume fraction can slow down or accelerate the propagation of the bands.

Before presenting the simulations and their results, it is important to give some information about the type of finite element used for the mesh and about its stability. First of all, for each "family" of simulations, the number of elements in the mesh was kept constant. All simulations were run using a C3D8R as element of the mesh. This is a 3D solid reduced integration element, which means that there is only one integration point at the center of the element. The advantage of this element compared to a C3D20R or to a C3D8 is that it is less expensive from a computational point of view. However, it can have hourglass problems if the mesh is not fine enough and if hourglass controls are not properly set before starting the analysis. For the FEM simulations which will be presented in the next paragraphs, the hourglass controls were set automatically as "standard", moreover, the mesh along the gauge length (which is the zone of interest) was always properly refined, so that the number of elements was above 90000. This number of elements was set after performing a mesh

dependence study (results shown in section E.1 of Appendix E). From this study, it was shown that for meshes having number of elements equal to 70000 or higher, the Lüders length does not depend markedly on the number of elements. Indeed, from the results presented in Appendix E, the difference in Lüders length between a mesh with 66000 elments and a mesh having 98000 elements is only 2.5%. The seeding size along the gauge length varied between 0.02 up to 0.040. An approach used to see if the simulation has hourglass problems, which could compromise the results, is to compare the evolution of the internal energy with the evolution of the artificial energy during the simulation. The artificial energy is a correction applied if hourglass problems are present. If the artificial energy represents less than 1% of the internal energy, then the simulation has no hourglass instability [165]. The artificial strain energy is obtained by extracting the "ALLAE" parameter for the whole model, while the total strain energy is obtained from the "ALLIE" parameter from the "History outputs" at the end of the simulation [166], [165].

6.1. Parametric study of the influence of linear softening on Lüders length

6.1.1. Influence of the upper yield stress on Lüders length

In the first series of simulations, the influence of the upper yield stress on the Lüders length has been assessed. The slope and the position of the Lüders strain were kept constant and only the upper yield stress was changed as schematically shown in Figure 6-1.

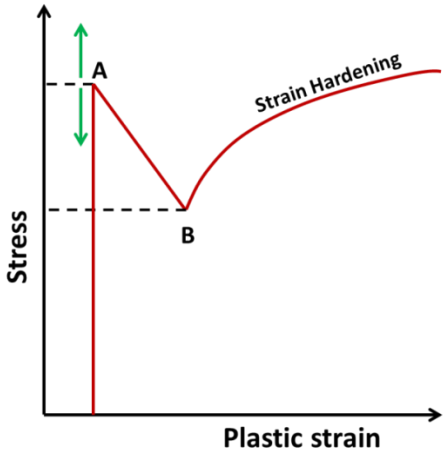

Figure 6-1 - Sketch showing the increase or decrease of the upper point corresponding to the upper yield stress

In the first simulation, the upper yield stress was set to 357 MPa, and the behaviour from upper yield stress to lower yield stress was modelled using the following equation: $\sigma = 357-(6500 \times \varepsilon)$, while the Lüders strain was set to 0.01. The second simulation had exactly the same behaviour for the linear part except for the upper yield stress which was set to 291 MPa, so the equation was $\sigma = 291 - (6500 \times \varepsilon)$, while another simulation had the upper yield stress which was placed at 225 MPa and the softening was described by $\sigma= 225 - (6500 \times \varepsilon)$. Physically, the same slope for each material would indicate that in each situation the material is able to multiply dislocations at the same rate. The strain hardening implemented in each simulation is always described with a Voce hardening behaviour whose parameters are the same for each simulated condition. The Voce equation describes the stress of the strain-hardening part of the stress-strain curve as:

$$\sigma = A - B\exp(-C\varepsilon) \qquad \text{(eq. 6-1)}$$

where, A, B and C are constants and ε is the plastic strain. Voce equation was at first chosen since it is a general hardening law used for aluminum and it can be used also for steel. For steel most of the time, the Kocks-Mecking model is used; however, Voce equation and Kocks-Mecking model can be derived from each other. The value of C controls how fast the material reaches the saturation stress, so if the value of this constant is low, the material will reach early the saturation stress and it will stop to strain-harden at lower strains compared to a situation where the value of C is high. B was always kept constant in all simulations, while A was adjusted depending on the lower yield stress of the Lüders plateau if the material had Lüdering or on the yield stress for materials having no Lüdering. In the simulations performed earlier in the PhD project, a Young's modulus of 220 GPa was chosen since it was believed that this could be a good value for steel. However, it was found that low strength IF steel has usually a Young's modulus of 200 GPa, for this reason; in the more recent simulations the Young's modulus was adjusted to this value.

A summary of the properties implemented for these first three simulations is reported in the following table.

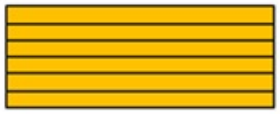 Uniform carbon distribution through thickness	**Upper Yield stress [MPa]**	**Slope of the linear softening**	**Position of the Lüders strain**	**Strain Hardening**
First simulation	357	6500	0.01	$\sigma = 424 - 140\exp(-6x\varepsilon)$
Second simulation	291	6500	0.01	$\sigma = 358 - 140\exp(-6x\varepsilon)$
Third simulation	225	6500	0.01	$\sigma = 292 - 140\exp(-6x\varepsilon)$

Table 6-1 - Summary of plastic behaviour implemented in the first series of simulations

In each simulation, the thickness of the tensile coupon (0.198 mm) was divided in 6 layers (each of them of 0.033 mm thickness). Having 6 layers was a good compromise for the number of materials that needed to be implemented in the simulations (3 material properties in total). Increasing the number of layers would not affect the results of the simulations given the same mechanical properties are implemented. The mechanical properties are the same for each layer (which is why in Table 6-1, a schematic view of the thickness of the specimen is reported showing all the layers with the same color).

For all these simulations Young's Modulus was set at 220 GPa and the implemented plastic behaviour showing a linear softening is shown in Figure 6-2. And a detail of the linear softening is shown in Figure 6-3.

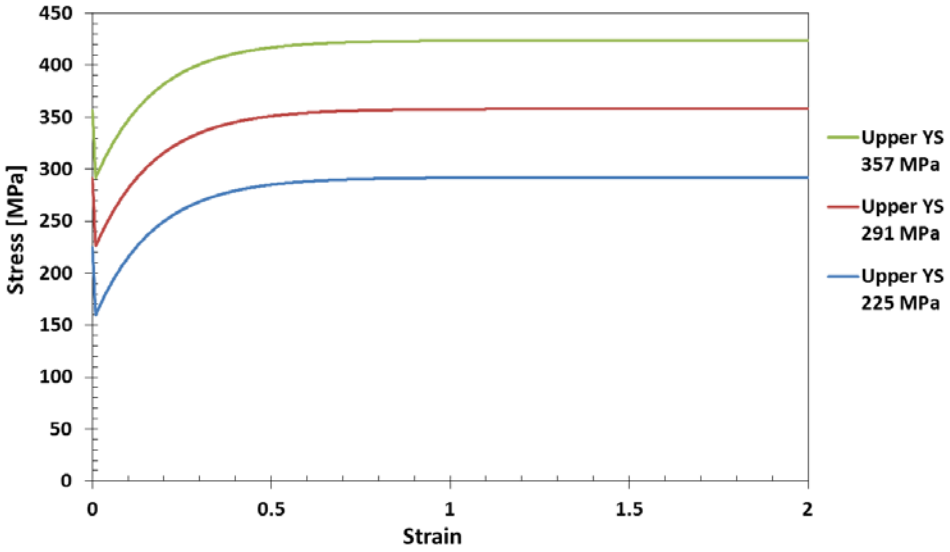

Figure 6-2 - Plastic behaviour with linear softening implemented in ABAQUS to analyze the influence of different yield stresses on Lüders propagation

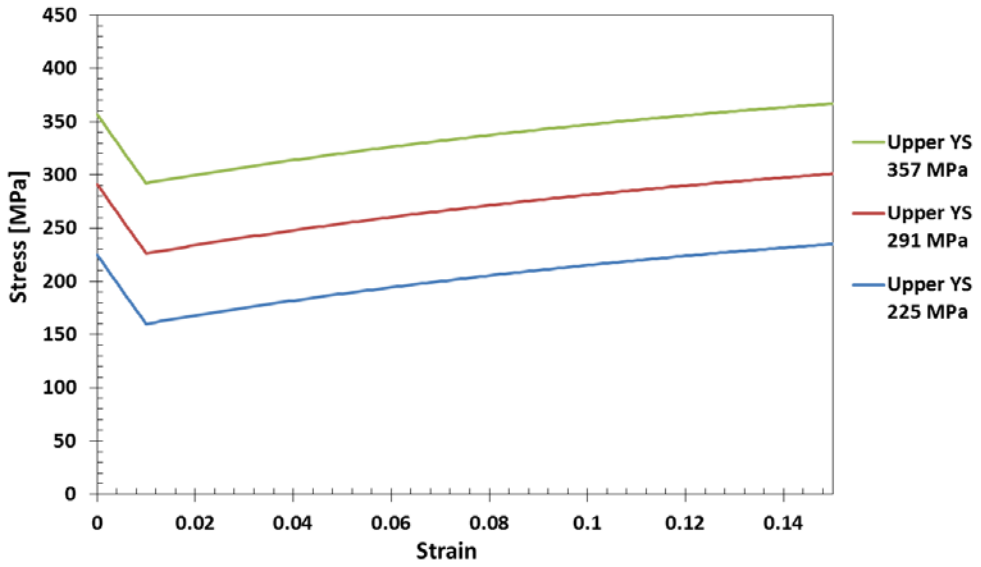

Figure 6-3 - Detail of the implemented linear softening for the plastic behaviour

6.1.2. Influence of the slope of the linear softening on the Lüders length

In another group of simulations, upper yield stress (357 MPa) (point A Figure 6-1) and Lüders strain (0.01) (point B Figure 6-1) were kept constant while the slope of the linear part was changed. Three different simulations have been run to analyze the bands propagation when the following laws are implemented for the linear softening:

- $\sigma = 357-(6500 \times \varepsilon)$
- $\sigma = 357-(4500 \times \varepsilon)$
- $\sigma = 357-(2500 \times \varepsilon)$

Physically having a low linear slope would mean that the material can multiply dislocations more easily and strain harden earlier.

In these simulations, the strain-hardening behaviour was described by the same law for all cases. A schematic view of the implemented plastic behaviour is shown in Figure 6-4 and the numerical data are summarized in Table 6-2.

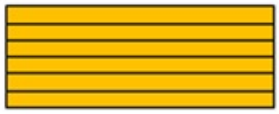 Uniform carbon distribution through thickness	**Upper Yield stress [MPa]**	**Slope of the linear softening**	**Position of the Lüders strain**	**Strain Hardening**
First simulation	357	2500	0.01	$\sigma = 464 - 140\exp(-6x\varepsilon)$
Second simulation	357	4500	0.01	$\sigma = 444 - 140\exp(-6x\varepsilon)$
Third simulation	357	6500	0.01	$\sigma = 424 - 140\exp(-6x\varepsilon)$

Table 6-2 - Summary of plastic behaviour implemented in the second series of simulations

The plastic properties implemented in the above series of simulations are reported in Figure 6-5 while a detailed view of the linear softening is reported in Figure 6-6. Again for this series of simulations, Young's modulus was set to 220 GPa and the thickness of the specimen was divided in 6 layers having the same mechanical properties.

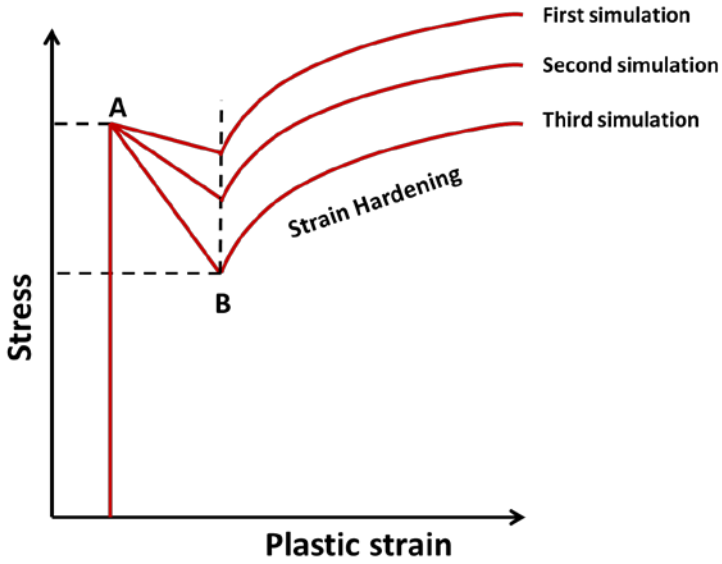

Figure 6-4 - Sketch showing the change of linear slope in the softening implemented to simulate Lueder plateau. Upper yield stress (point A) and Lüders strain (point B) are kept constant

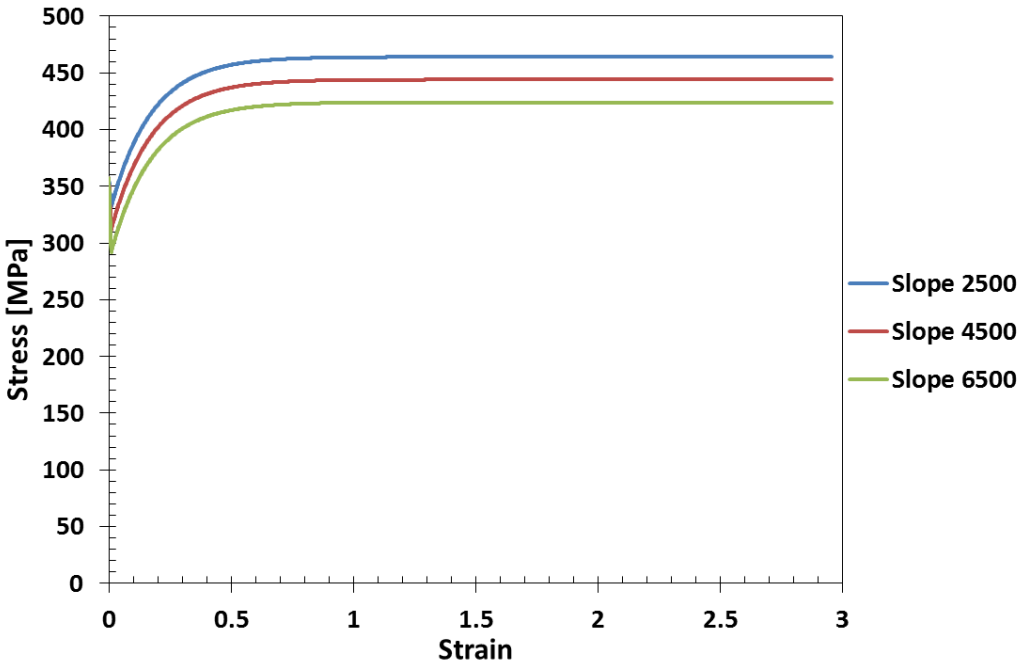

Figure 6-5 - Detail of the implemented linear softening behaviour for the series of simulations having different linear slopes

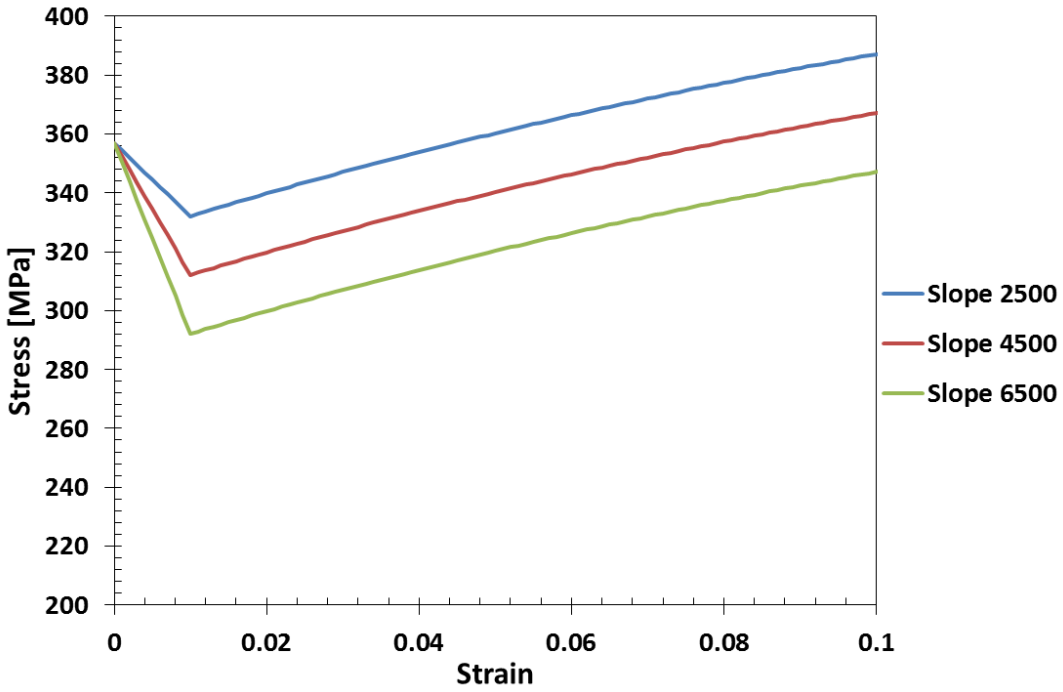

Figure 6-6 - Detail of the implemented linear softening for the plastic behaviour showing the change of slope

6.2. Results of the parametric study of the influence of linear softening on Lüders length

The stress-strain curves in Figure 6-7 show the influence of changing the upper yield stress on the Lüders length. As it can be seen, increasing the upper yield stress shifts the plateau to higher level of stresses but the Lüders length remains the same for all situations since the slope was not modified. The length of the plateau is thus not influenced by a change of stress. Furthermore, the stress drop at the beginning of the Lüders propagation is the same for each simulation. This means that changing the upper yield stress does not play a role in controlling Lüders speed or length but it can only control the stress at which plastic instability will start.

Figure 6-8 shows the influence of the softening slope on the length of the Lüders plateau. If the slope is decreased, the Lüders plateau is shorter even if the Lüders strain implemented in the plastic properties of ABAQUS is not changed. Moreover, the plateau stress rises to higher stresses. From a physical point of view, having a lower slope corresponds having a material which is able to multiply and unpin dislocations easily and to strain harden earlier. In Table 6-3 the numerical values of upper yield stress, plateau stress and Lüders length are reported.

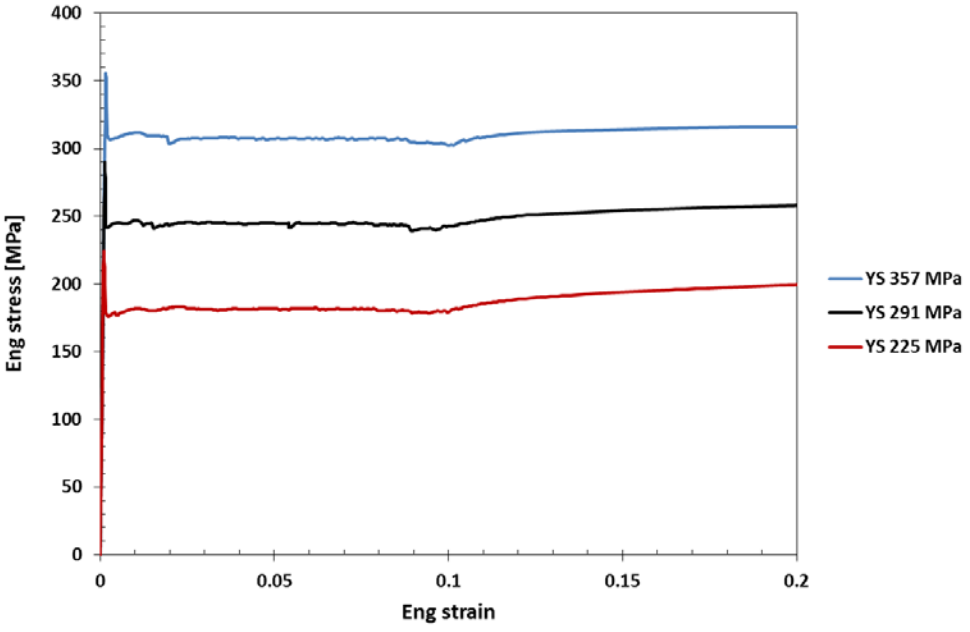

Figure 6-7 - Engineering stress-strain obtained by simulation of Lüders plateau by using a linear softening where the upper yield stress was changed

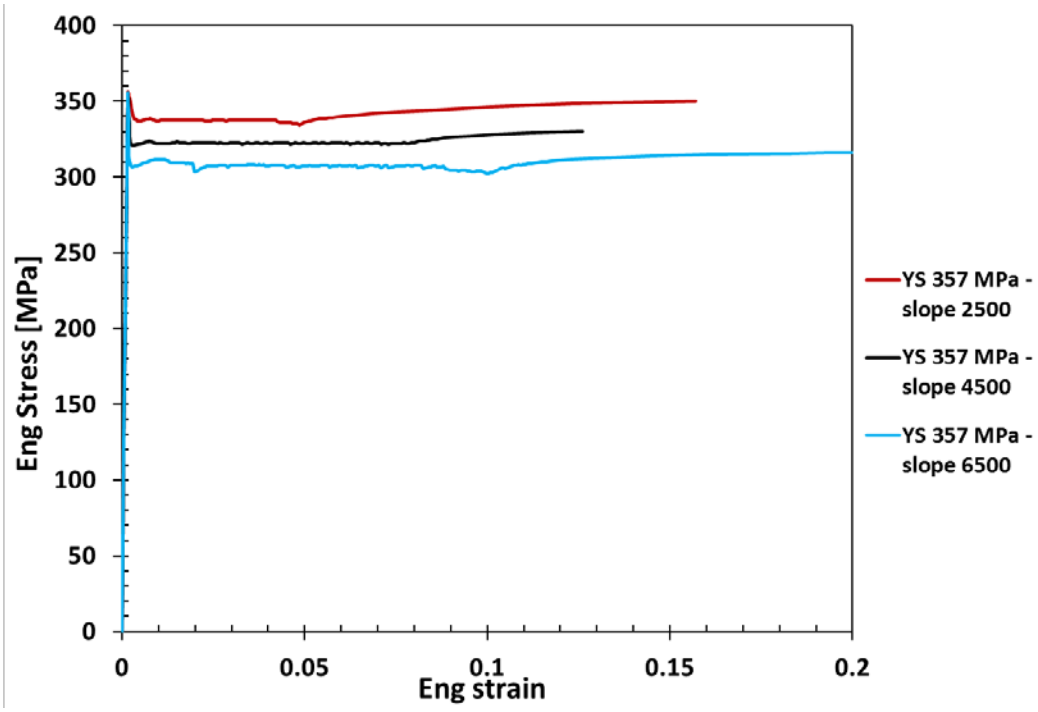

Figure 6-8 - Engineering stress-strain curves obtained by changing slope of the linear softening

Simulation	Upper Yield Stress [MPa]	Average stress Lüders Plateau [MPa]	Lüders length
357 – slope 6500	356	310	0.1
291 – slope 6500	290	245	0.1
225 – slope 6500	224	182	0.1
357 – slope 2500	356	339	0.047
357 – slope 4500	356	325	0.073
357 – slope 6500	356	310	0.1

Table 6-3 - Results obtained by simulating Lüders plateau by applying linear softening

In conclusion, from these preliminary simulations, the influence of the slope of the softening behaviour on Lüders plateau length was assessed and related to the physical behaviour of the material. Having a low slope is equivalent to having a material that strain hardens easily, while changing the upper yield stress has no influence on Lüders length.

All the simulations were run by meshing the tensile coupon with reduced elements C3D8R, for this reason it is important to verify the accuracy of the results by evaluating the ratio between the artificial energy and the internal energy. If no hourglass problems are present, this ratio should remain lower than 1%. The evolution of this ratio for the simulations having different slopes of the linear softening is reported in Figure 6-9 while the evolution of the

artificial energy for the simulation having same slope of the linear softening but different yield stresses are reported in Figure E. 2 Appendix E.

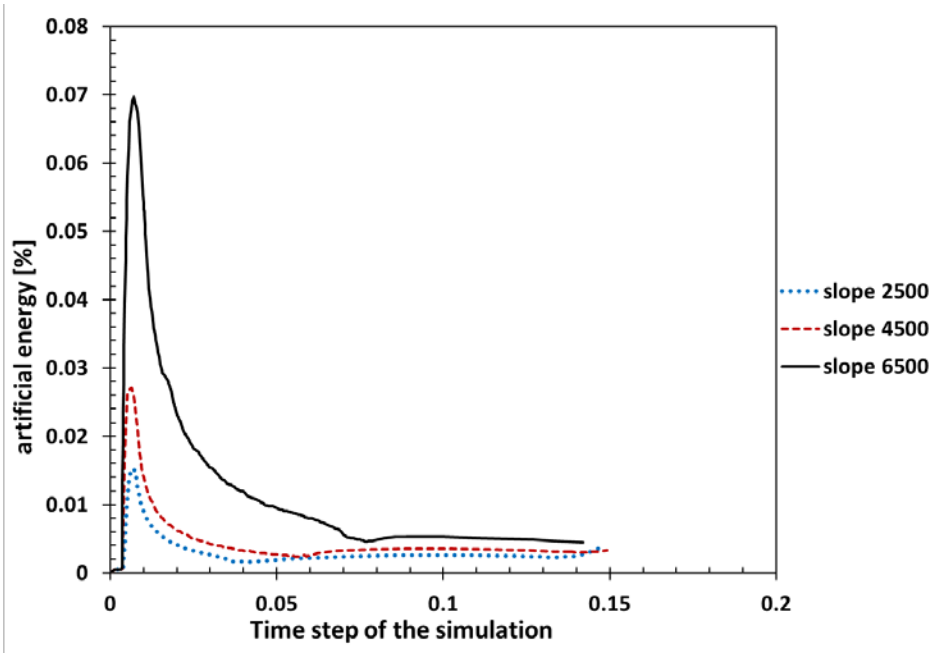

Figure 6-9 - Artificial energy evolution expressed as percentage of the internal energy during the simulation of change in slope of the linear softening

From a physical point of view, having a material with a gradient of yield stress will mean to have a gradient of upper yield stress and of slopes of the linear softening. Indeed, the zone that contains more carbon in solid solution will have denser Cottrell atmospheres which will result in higher yield stress and also longer plateau. For this reason, in the simulations presented in the next sections, the graded structures have been simulated implementing both gradient of yield stress and slopes simultaneously.

6.3. Influence of uniform and graded carbon profiles on Lüders propagation

Once the influence of linear softening on Lüders propagation was assessed, it was decided to verify if a graded carbon content through thickness would help in reducing Lüders length compared to a uniform carbon content. The tensile coupon was modelled in ABAQUS by dividing the thickness in 6 sublayers to be consistent with the geometry implemented in the previous simulations. For the graded configuration, the mechanical properties were different for each layer. The two outer layers (1 and 2 in Figure 6-10) were assumed to have different

yield stresses and slopes of linear softening, while the central layer had no Lüdering and had the strain-hardening behaviour described by the Voce equation.

Figure 6-10 - Schematic view of the thickness of the tensile coupon simulated to investigate the influence of a gradient of mechanical properties on Lüders propagation

The mechanical properties for the different layers are summarized in Table 6-4 and they are plotted in Figure 6-11.

For the simulations with a uniform carbon profile, the mechanical properties implemented are the same for each layer and are an average of the mechanical properties implemented for the graded specimen (which are summarized in Table 6-4). The value of 257 MPa for the yield stress was obtained by doing an average of the yield stresses used for the graded profile. The slope implemented for the linear softening of the uniform profile was also calculated considering an average of the slopes implemented for the linear softening in the graded profile.

Graded Profile	
Layer	**Mechanical Properties**
1	E = 200 GPa, Lüders (upper YS = 357 MPa, slope 7700, Lüders strain 0.01) Strain Hardening: $\sigma = 412 - (140\exp(-6\times\varepsilon))$
2	E = 200 GPa, Lüders (upper YS = 225 MPa, slope 6500, Lüders strain 0.01) Strain Hardening: $\sigma = 292 - (140\exp(-6\times\varepsilon))$
3	E = 200 GPa, No Lüders (upper YS =190 MPa) Strain Hardening: $\sigma = 332 - (140\exp(-6\times\varepsilon))$
Uniform Profile	
Layer	**Mechanical Properties**
1, 2, 3	E = 200 GPa, Lüders (upper YS = 257.33 MPa, slope 7100, Lüders strain 0.01) Strain Hardening: $\sigma = 318 - (140\exp(-6\times\varepsilon))$

Table 6-4 - Mechanical properties implemented to compare the influence of graded and constant carbon content through thickness on Lüders propagation

The results of the simulations are shown in Figure 6-12 where it is evident that for the same mechanical properties (yield stress), having a carbon gradient would help in reducing the

length of Lüders plateau compared with a situation where the same amount of carbon is uniformly distributed along the thickness of the specimen.

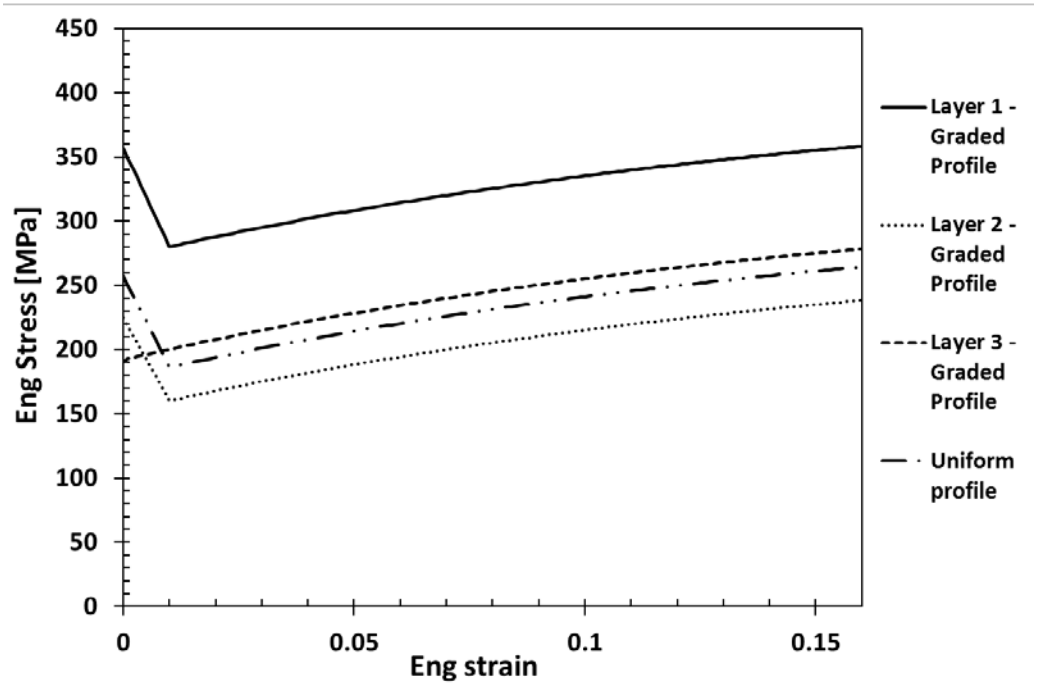

Figure 6-11 - Plastic behaviour implemented in ABAQUS to simulate the influence of graded and constant carbon content on Lüders propagation

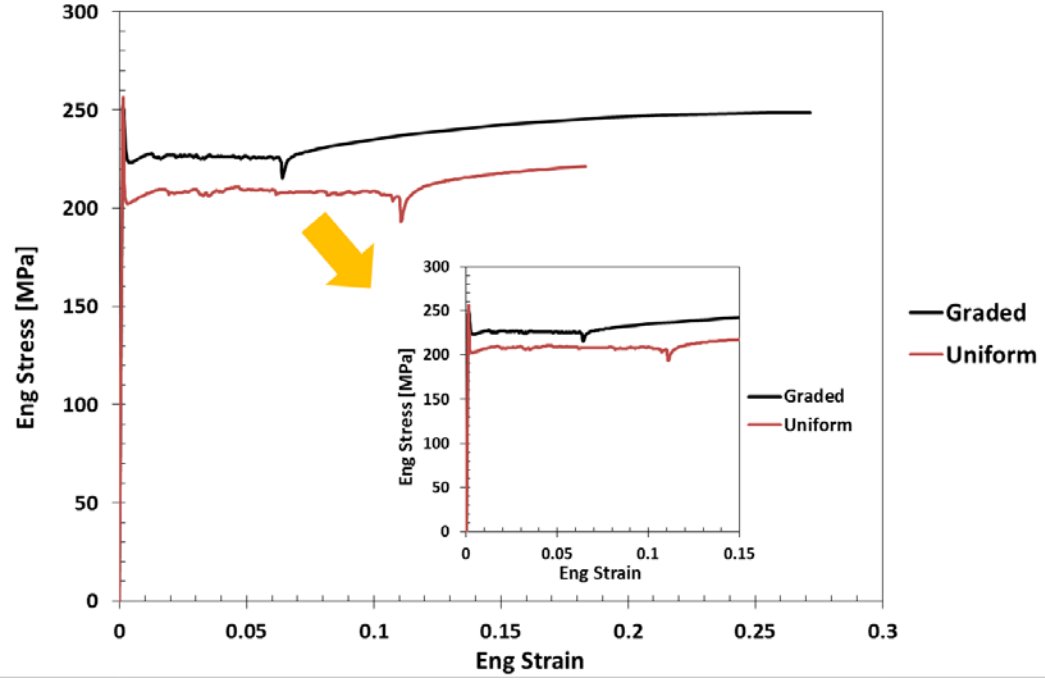

Figure 6-12 - Comparison of stress-strain curves obtained simulating Lüders propagation in a specimen having carbon gradient through thickness and a specimen having uniform carbon content through thickness

From Figure 6-12, the two simulated conditions have the same upper yield stress as expected, while the stress at the plateau is higher for the graded condition than for the uniform profile since for the first configuration, the two central layers (marked with number 3 in Figure 6-10) are strain-hardening without any plastic instability.

6.4. Investigations of solutions to suppress Lüders plateau

In the following paragraph, some solutions which could limit or suppress Lüders plateau will be investigated. A schematic view of the simulated geometry is shown in Figure 6-13. In the first series of simulations, the stiffness of the central layer will be changed to prove its influence on Lüders propagation. In a second series of simulation the thickness of this central layer will be modified to investigate if Lüders propagation can be accelerated or suppressed. This "sandwich" configuration is particularly important because it will give an idea of the dimension that a carbon gradient should have to avoid Lüdering. Moreover, sandwich materials made of steel are under investigation in the automotive and construction sectors [167] so it is important to show what can occur to Lüders plateau when the material showing this plastic instability is coupled with a material which has not such instability.

6.4.1. Influence of stiffness

The CAD model implemented for this series of simulations is made of a full tensile coupon 0.198 mm thick. The sample was divided in 3 layers through thickness (each 0.066 mm thick), with the two outer layers having Lüders plateau and the central one without Lüdering (see Figure 6-13). The stiffness of the outer layers was set at 220 GPa, while the stiffness of the central layer was varied and its influence on the Lüders propagation was assessed. Table 6-5 summarizes the mechanical properties implemented for the different layers.

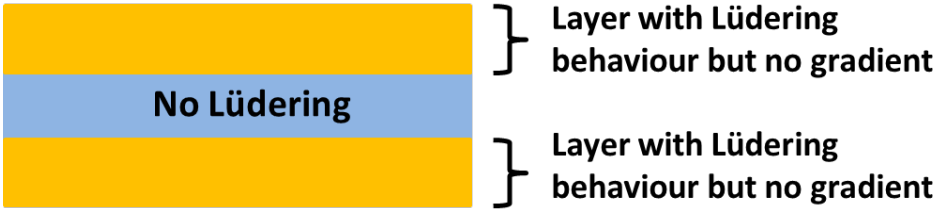

Figure 6-13 - Thickness of the tensile coupon implemented in ABAQUS to simulate influence of stiffness of central layer having no plateau on Lüders propagation

Central Layer	Outer Layers
E = 70 GPa No Lüders	E = 220 GPa Lüders (upper YS = 291 MPa, slope 6400, Lüders strain 0.01) Strain Hardening: $\sigma = 359 - (140 \exp(-6x\varepsilon))$
E = 110 GPa No Lüders	E = 220 GPa Lüders (upper YS = 291 MPa, slope 6400, Lüders strain 0.01) Strain Hardening: $\sigma = 359 - (140 \exp(-6x\varepsilon))$
E = 300 GPa No Lüders	E = 220 GPa Lüders (upper YS = 291 MPa, slope 6400, Lüders strain 0.01) Strain Hardening: $\sigma = 359 - (140 \exp(-6x\varepsilon))$
E = 400 GPa No Lüders	E = 220 GPa Lüders (upper YS = 291 MPa, slope 6400, Lüders strain 0.01) Strain Hardening: $\sigma = 359 - (140 \exp(-6x\varepsilon))$
E = 500 GPa No Lüders	E = 220 GPa Lüders (upper YS = 291 MPa, slope 6400, Lüders strain 0.01) Strain Hardening: $\sigma = 359 - (140 \exp(-6x\varepsilon))$

Table 6-5 - Mechanical properties implemented in ABAQUS to simulate the influence of stiffness on the Lüders propagation

The values of Young modulus chosen in the table above were selected based on possible materials that can be coupled with steel, except the Young moduli of 400 GPa and 500 GPa which are not common for materials. 70 GPa is for aluminium, 110 GPa is for titanium and 300 GPa can be the Young's modulus of a 96% alumina or of commercially pure molybdenum [15]. The plastic behaviour was kept constant in each simulation so that the variation of the Lüders plateau was influenced only by the change in stiffness of the central layer. For the central layer the strain hardening is described by: $\sigma = 480 - 140 \exp(-23 \times \varepsilon)$. The value 23 of the exponent was found by fitting the experimental true stress-strain curve of an IF steel after shifting the curve to higher stresses to simulate a material which could yield at 340 MPa.

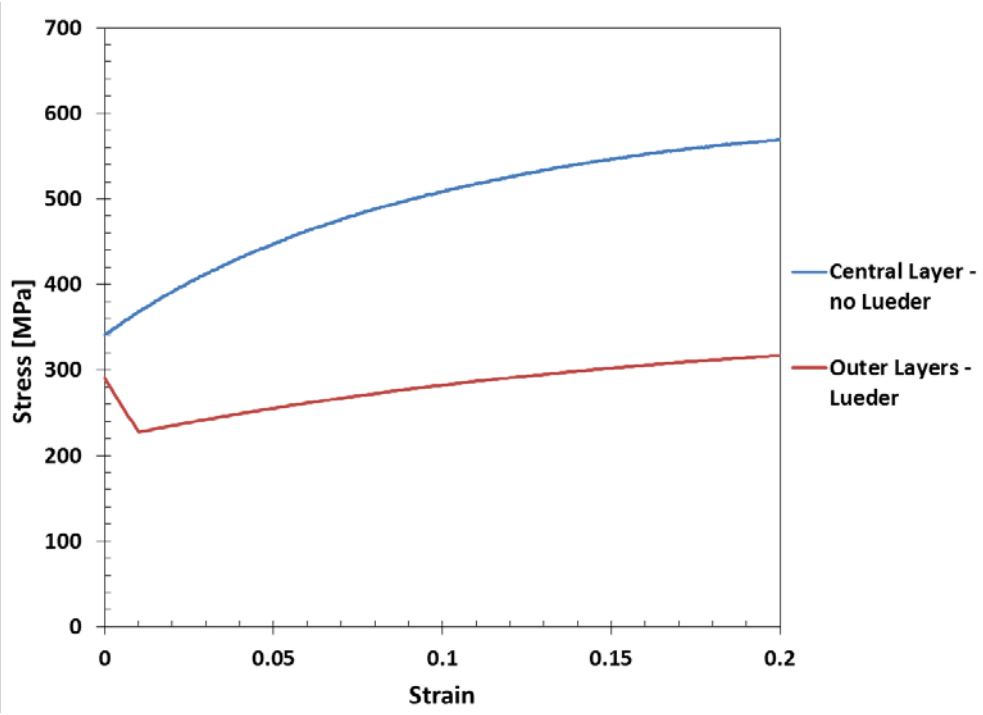

Figure 6-14 - Stress-strain curve detail of the plastic behaviour implemented in ABAQUS in order to simulate the influence of stiffness on the Lüders propagation

6.4.2. Change in thickness of the central layer

The next set of simulations was carried out to find out what the thickness of a central layer should be in order to suppress Lüdering. The full tensile coupon was made of three layers, the central layer had no Lüders behaviour and the stiffness was set at 200 GPa, while the two outer layers had a stiffness of 200 GPa and had Lüders plateau (see Figure 6-13). Details of the mechanical properties implemented in ABAQUS simulations are reported in Table 6-6. The thickness of the central layer was varied and related to the change in Lüders plateau length, while the thickness of the outer layers was kept constant. Table 6-6 summarizes the series of simulations performed, while Figure 6-15 shows the plastic behaviour which was implemented for the layers. For the central layer the following Voce equation was implemented to describe the strain hardening: $\sigma = 480 - 140 \times \exp(-23 \times \varepsilon)$.

Thickness ratio central/outer layers	**Central Layer**	**Outer Layers**
1:2 (0.066/0.132)	E = 200 GPa No Lüders	E = 200 GPa Lüders (upper YS = 291 MPa, slope 6400, Lüders strain 0.01) Strain Hardening: $\sigma = 359 - (140 \times \exp(-6 \times \varepsilon))$
1:1 (0.132/0.132)	E = 200 GPa No Lüders	E = 200 GPa Lüders (upper YS = 291 MPa, slope 6400, Lüders strain 0.01) Strain Hardening: $\sigma = 359 - (140 \times \exp(-6 \times \varepsilon))$
1.5:1 (0.198/0.132)	E = 200 GPa No Lüders	E = 200 GPa Lüders (upper YS = 291 MPa, slope 6400, Lüders strain 0.01) Strain Hardening: $\sigma = 359 - (140 \times \exp(-6 \times \varepsilon))$
2:1 (0.264/0.132)	E = 200 GPa No Lüders	E = 200 GPa Lüders (upper YS = 291 MPa, slope 6400, Lüders strain 0.01) Strain Hardening: $\sigma = 359 - (140 \times \exp(-6 \times \varepsilon))$
2.5:1 (0.33/0.132)	E = 200 GPa No Lüders	E = 200 GPa Lüders (upper YS = 291 MPa, slope 6400, Lüders strain 0.01) Strain Hardening: $\sigma = 359 - (140 \times \exp(-6 \times \varepsilon))$

Table 6-6 - Mechanical properties implemented in ABAQUS to simulate the influence of thickness of a central layer having no plateau on the Lüders propagation

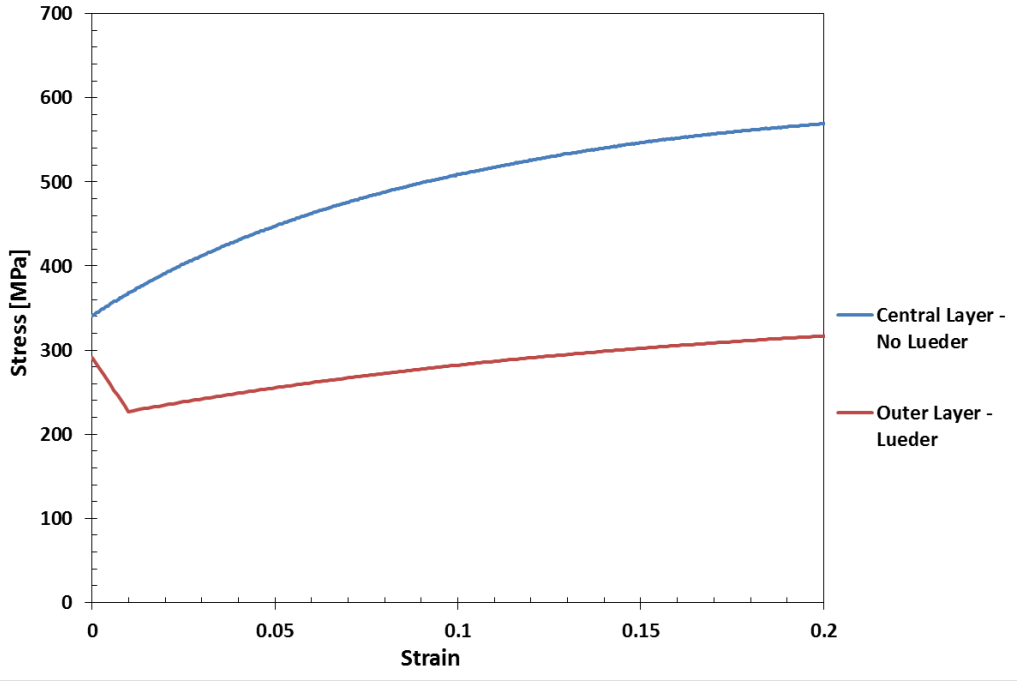

Figure 6-15 - Stress-strain curve detail of the plastic behaviour implemented in ABAQUS in order to simulate the influence of thickness of a central layer having no plateau on the Lüders propagation

The same sequence of simulations was repeated for the situation where the outer layers show a gradient of yield stress and of Lüders length while the central layer was still without any Lüdering. A through thickness schematic view of the tensile coupon is shown in Figure 6-16. For this configuration, only the ratios from 1:1 to 2.5:1 were simulated.

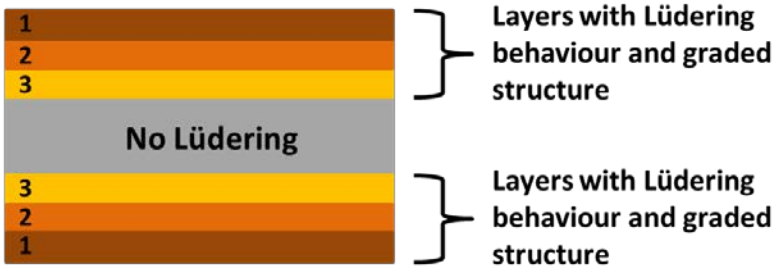

Figure 6-16 - Thickness of a tensile coupon implemented in ABAQUS to simulate influence of thickness of central layer having no Lüdering. Outer layers have both yield stress and Lüders length gradient

The average mechanical properties of the outer layers were still the same as in the case of homogeneous outer layers shown in Figure 6-13. The outer layers have a gradient of yield stress and of Lüders length since the slope of the linear softening of the plastic behaviour,

which is used to simulate Lüders, was changed for each layer and consequently, the stress drop was different for each layer (Figure 6-17). Table 6-7 list the details of the mechanical properties simulated for the graded layers.

Layer	E [GPa]	Lüdering
1	200	Upper yield stress 357 MPa; Slope 7700; Lüders strain 0.01 Strain hardening: $\sigma = (412\text{-}140 \times \exp(-6 \times \varepsilon))$
2	200	Upper yield stress 291 MPa; Slope 6400; Lüders strain 0.01 Strain hardening: $\sigma = (359\text{-}140 \times \exp(-6 \times \varepsilon))$
3	200	Upper yield stress 225 MPa; Slope 5100; Lüders strain 0.01 Strain hardening: $\sigma = (307\text{-}140 \times \exp(-6 \times \varepsilon))$
Central layer (no Lüders)	200	Yield stress: 340 MPa Strain Hardening: $\sigma = 480 - 140 \exp(-23 \times \varepsilon)$

Table 6-7 - Mechanical properties implemented in ABAQUS to simulate the influence of thickness of a central layer having no Lüdering when the outer layers have a gradient of yield stress and of Lüders plateau length

The strain hardening behaviour for the outer graded layers is the same for all of them except for the starting point which depends on the lower yield stress. The plastic behaviour of the central layer is the same as shown in Figure 6-15.

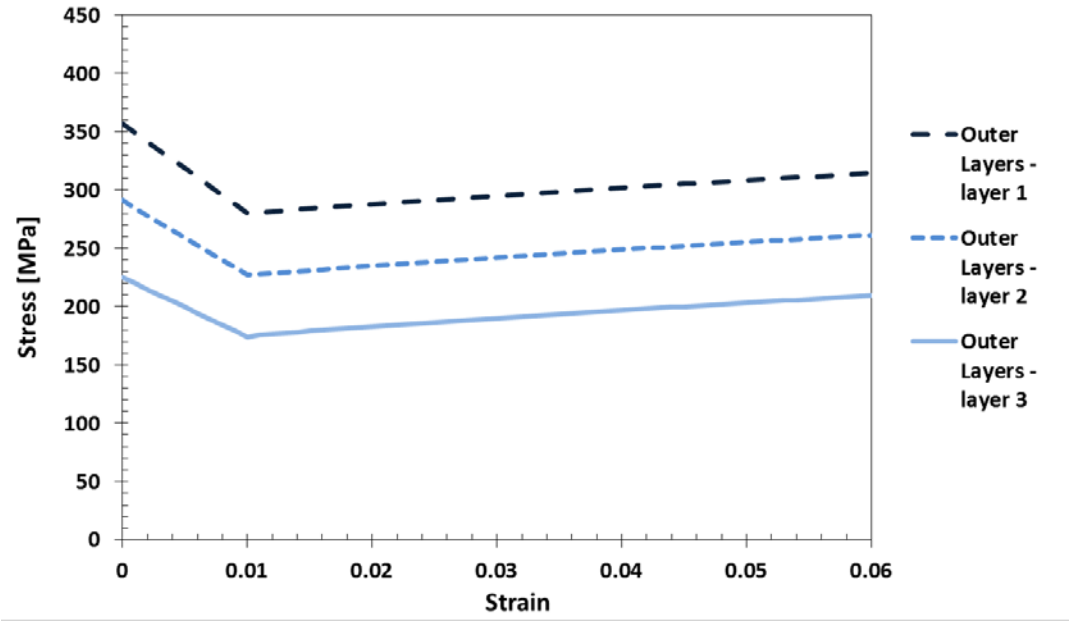

Figure 6-17 - Plastic properties implemented in the outer layers to simulate a graded structure having Lüders plateau

6.4.3. Results of change in stiffness and in thickness for a central layer without Lüders plateau

In Figure 6-18, the engineering stress-strain curves obtained by changing Young's modulus of a central layer having no Lüdering are shown. If the material is stiffer than the outer layers with Lüdering, the plateau does not seem to be influenced by the change in stiffness and its length remains constant. In Figure 6-18, the stress-strain curves for 300 GPa, 400 GPa and 500 GPa are overlapping or there is only a slight shift of the yield drop to lower strains as shown in the magnification of Figure 6-20. However, if the central layer is less stiff than the outer layers, a change in slope in the elastic portion of the curve is found and this delays the start of the plateau and shortens its length.

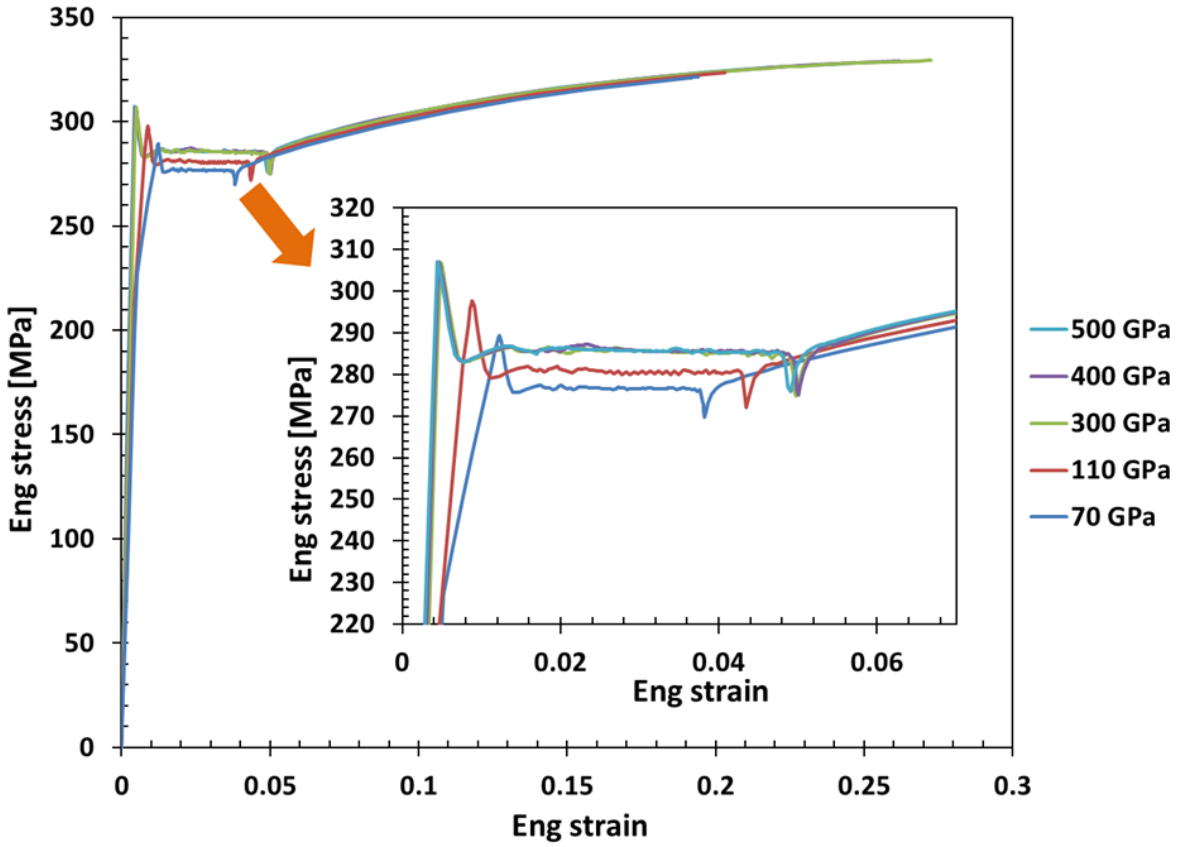

Figure 6-18 - Influence of stiffness of a central layer having no Lüders behaviour on Lüders propagation

The numerical values of the mechanical properties are reported in Table 6-8.

Simulation	Upper Yield Stress [MPa]	Average stress Lüders Plateau [MPa]	Lüders length
70 GPa	289	277	0.02593
110 GPa	298	282	0.03461
300 GPa	307	286	0.04483
400 GPa	307	287	0.04526
500 GPa	307	287	0.044641

Table 6-8 - Mechanical properties and Lüders length obtained by varying the stiffness of the central layer

The results shown in Figure 6-18 can be explained by considering the curves schematically shown in Figure 6-19. In the first two simulations, the Young modulus of the central layer was lower than the Young modulus of the outer layers. This means that the two outer layers will yield at a lower strain than the central layer (and also at a lower stress) (see point A in Figure 6-19). When point A is reached, the outer materials will yield while the central one can still deform elastically, so no Lüders will appear in the stress-strain curve. However, a change in slope will occur since Young's modulus in the central material is lower. Once the central material starts to yield when it reaches point B, then the Lüders band can start to propagate.

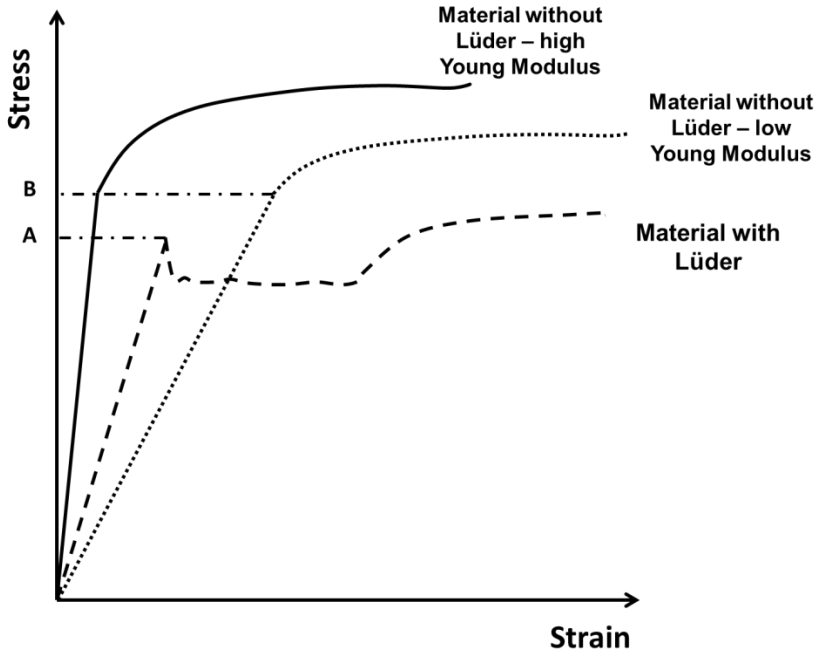

Figure 6-19 - Schematic view of engineering stress-strain curves for a "sandwiched" material having Lüders on the outer layers and no Lüders on the central layer

If the material used as central layer has higher stiffness than the material used in the outer layers, it will start to yield at lower strain and there will be almost no change in the slope of the elastic part of the curve, however, the upper yield stress of the final curve (starting point of the Lüders plateau) will be shifted to lower strains as shown in Figure 6-20 which reports a magnified view of the start of Lüders propagation depending on Young modulus. Moreover for higher stiffnesses, the plateau will be shifted to higher stresses.

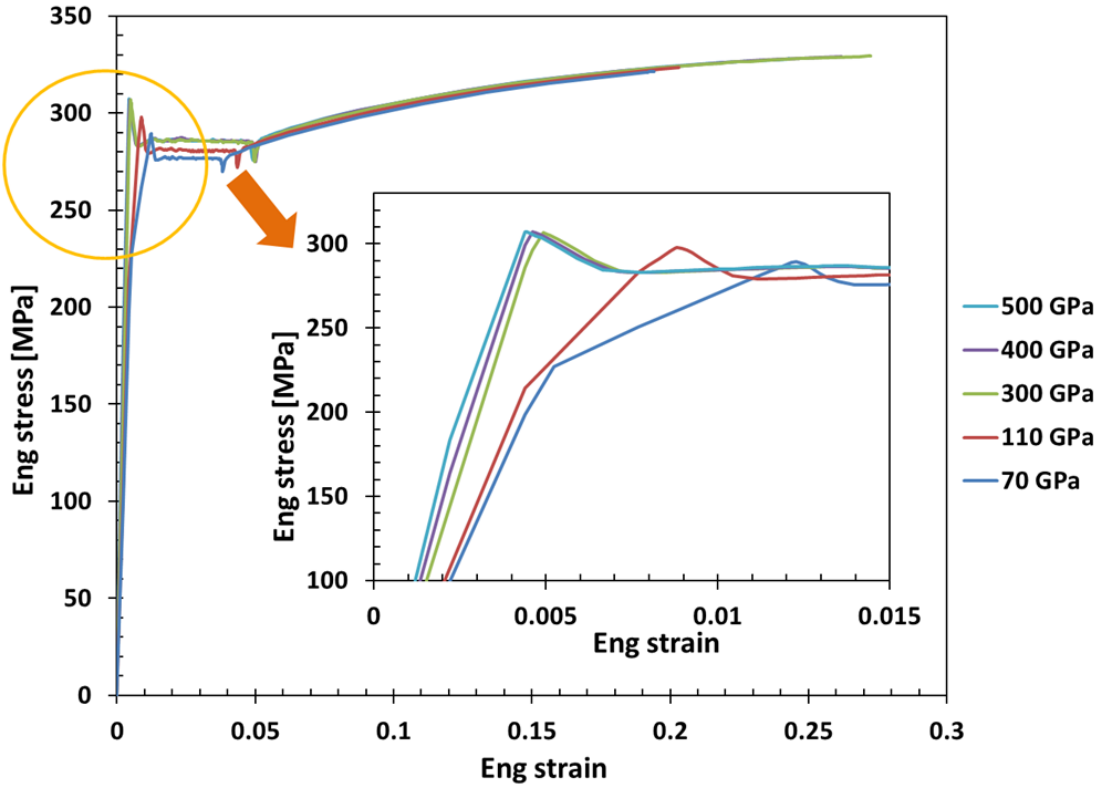

Figure 6-20 - Magnified view of the upper yield stress for simulations showing the influence of stiffness on Lüders propagation

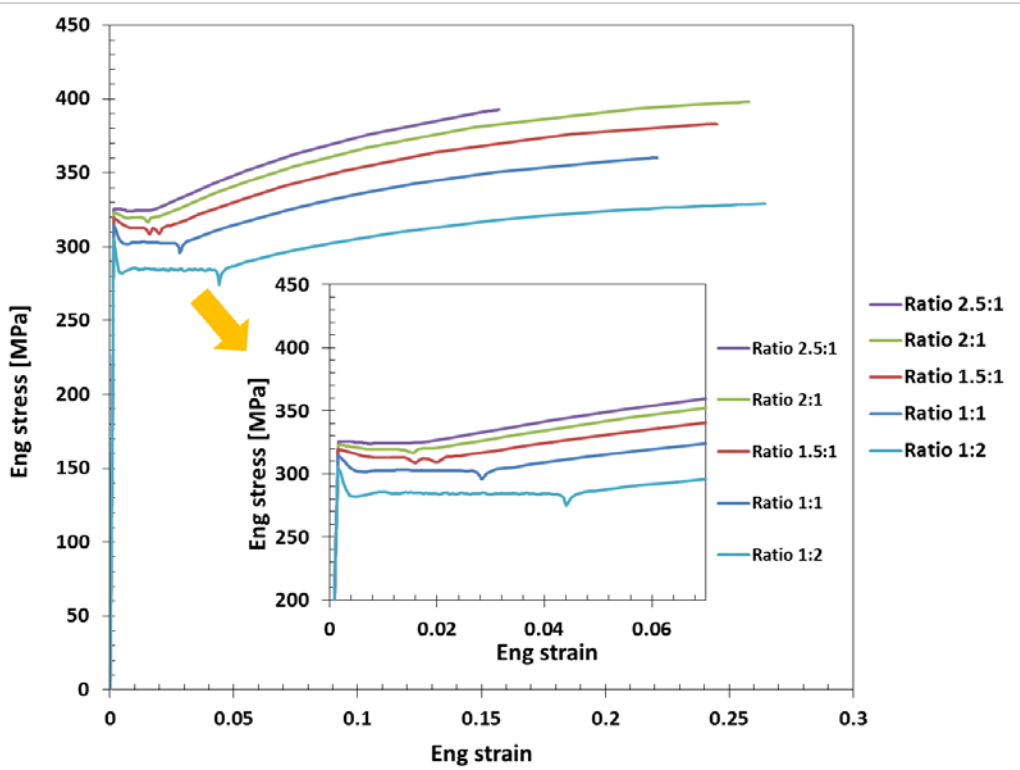

Figure 6-21 - Influence of change of thickness of a central layer on Lüders plateau length. Central layer without Lüdering, while outer layers have Lüdering with no gradient

Simulation	Upper Yield Stress [MPa]	Average stress Lüders Plateau [MPa]	Lüders length
1:2	305	285	0.04248
1:1	314	304	0.02668
1.5:1	319	315	0.01811
2:1	323	322	0.01395
2.5:1	326	325	0.00545

Table 6-9 - Mechanical properties and Lüders length obtained by varying the thickness of a central layer without Lüders, while outer layers show Lüders with uniform mechanical properties distribution

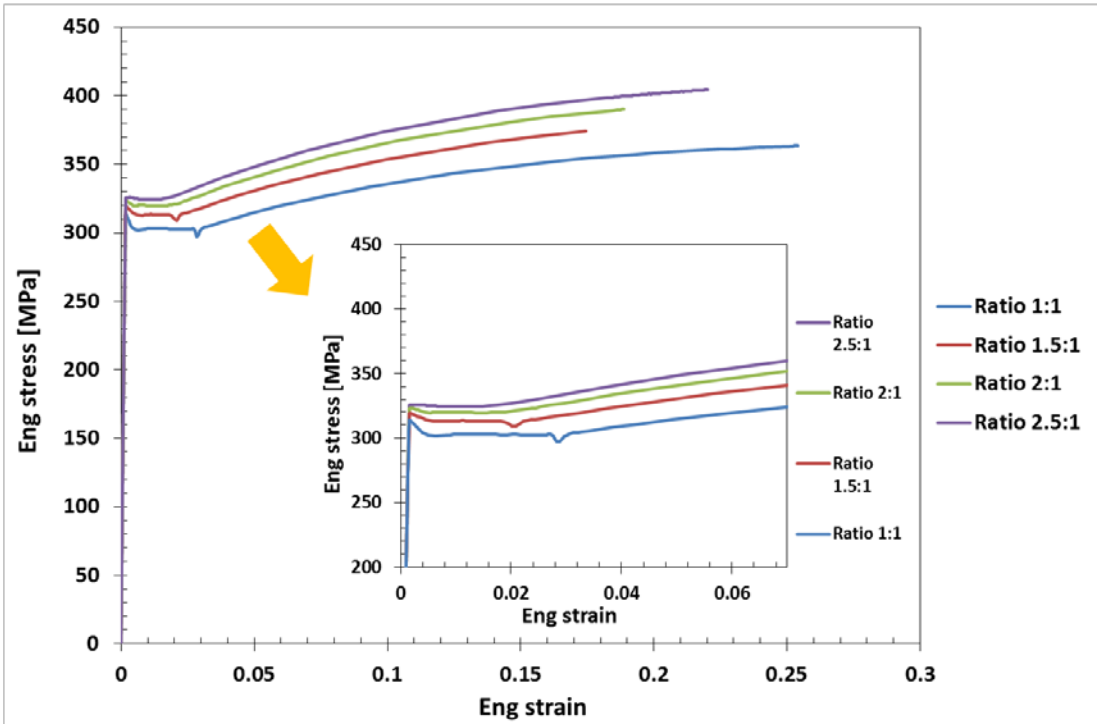

Figure 6-22 - Influence of change of thickness of a central layer on Lüders plateau length. Central layer without Lüdering, while outer layers have Lüdering with a graded configuration

Simulation	Upper Yield Stress [MPa]	Average stress Lüders Plateau [MPa]	Lüders length
1:1	314	305	0.02665
1.5:1	319	315	0.0193
2:1	323	321	0.01298
2.5:1	326	325	0.00606

Table 6-10 - Mechanical properties and Lüders length obtained by varying the thickness of a central layer without Lüders, while outer layers show Lüdering with a graded mechanical properties

As shown in Figure 6-21 and Figure 6-22, if the sandwiched material has a layer without Lüders plateau, if the thickness of this layer is increased, the Lüders plateau can be reduced and eventually suppressed. This behaviour seems to be the same both in case of a uniform Lüdering and a graded Lüdering in the outer layers. This is concluded by comparing Lüders length reported in Table 6-9 and Table 6-10.

6.4.4. Influence of strain hardening on Lüders propagation

If the thickness of the material has to remain unchanged, the other parameter that can be varied to limit or suppress Lüders propagation is strain-hardening. The thickness of the

tensile coupon was divided in six layers each of them having a thickness of 0.033 mm for a total thickness of the coupon of 0.198 mm. Lüdering is present only in the two outer layers marked as 1 and 2 in Figure 6-23, while central layers marked as 3 have a yield stress of 190 MPa but they can strain harden following a Voce equation. Their mechanical properties are summarized in Table 6-11 and the different strain hardening implemented in ABAQUS for layer 3 are shown in Figure 6-24.

Figure 6-23 - Schematic view of the configuration implemented in ABAQUS to prove the influence of strain-hardening

	Central Layers (No Lüders)	**Outer Layers (Lüders)**
First Simulation	E = 200 GPa	**Layer 1:** E= 200 GPa Lüders (upper YS = 357 MPa, slope 7700, Lüders strain 0.01) **Layer 2**: E = 200 GPa Lüders (upper YS = 225 MPa, slope 6500, Lüders strain 0.01)
Second Simulation	E = 200 GPa (initial slope of the plastic part 2.5 times steeper than the first simulation)	
Third Simulation	E = 200 GPa (initial slope of the plastic part 3.5 times steeper than the first simulation)	

Table 6-11 - Mechanical properties implemented to assess the influence of strain-hardening on Lüders propagation

To modify the strain hardening for the different simulations, the slope of the plastic curve of the strain hardening implemented in the first simulation was extracted and then multiplied by a factor of 2.5 for the second simulation and by a factor of 3.5 for the third simulation.

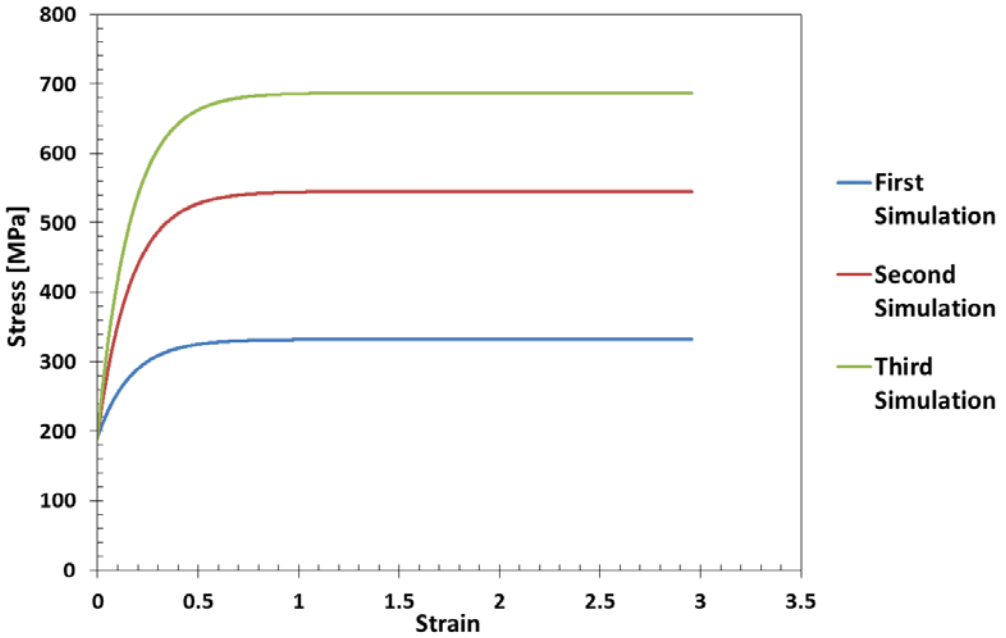

Figure 6-24 - Plastic properties implemented in layer 3 to simulate the influence of strain-hardening on Lüders propagation

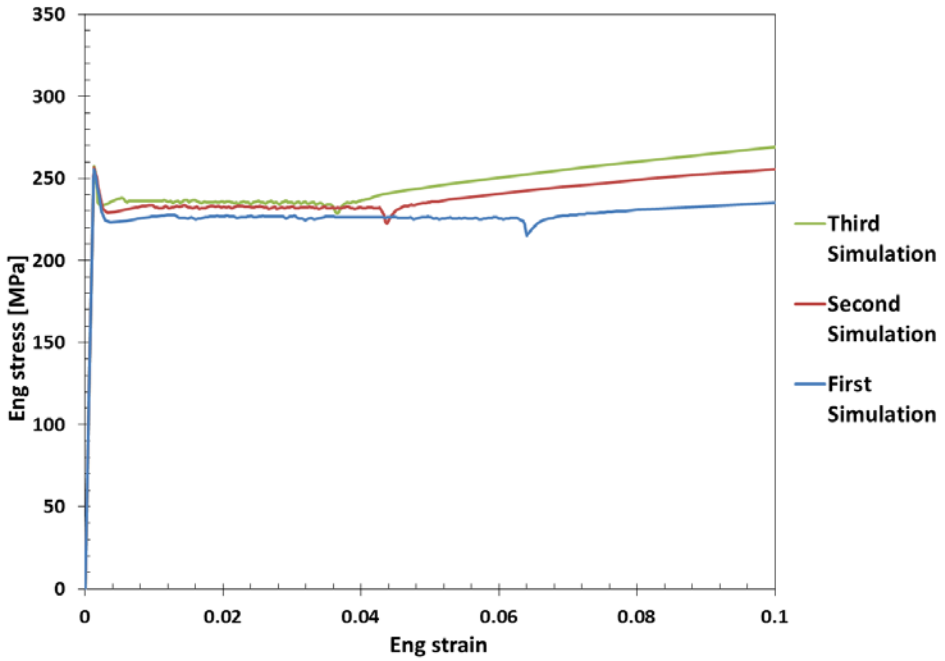

Figure 6-25 - Engineering stress-strain curves obtained changing the strain-hardening behaviour

From the curves shown in Figure 6-25, the influence of strain-hardening is relevant. If the strain-hardening of a material is increasing, the Lüders plateau can be shortened. Physically, this would mean to have a material able to produce high density of dislocations during

plastic deformation. In the next paragraph, the influence of void spacing and void volume fractions on Lüders propagation will be presented.

6.4.5. Influence of Intervoids spacing on Lüeder propagation

In this paragraph, the influence of voids on Lüders propagation will be investigated, since microvoids can be present in materials and no study in literature has been reported yet relating precence of voids and speed or Lüders bands propagation. The simulated tensile coupon has the thickness subdivided in 6 layers (each one with a thickness of 0.033 mm). The two central layers (marked as 3 in Figure 6-26) have no Lüders plateau and they have a yield stress of 190 MPa, while the layers marked as 1 and 2 have Lüdering. Layers 1 and 2 differ both for upper yield stress and for slope of the linear softening implemented in ABAQUS. A summary of the mechanical properties is shown in Table 6-12.

Figure 6-26 - Sketch of the thickness of tensile coupon used to simulate influence of voids on Lüders propagation

	Mechanical Properties
Layer 1	E= 220 GPa (upper YS = 357 MPa, slope 7700, Lüders strain 0.01) (Strain Hardening: $\sigma = 412 - 140 \times \exp(-6 \times \varepsilon)$)
Layer 2	E= 220 GPa (upper YS = 225 MPa, slope 7500, Lüders strain 0.01) (Strain Hardening: $\sigma = 282 - 140 \times \exp(-6 \times \varepsilon)$)
Layer 3	E= 220 GPa (upper YS = 190 MPa, no Lüders) (Strain hardening: $\sigma = 332 - 140 \times \exp(-6 \times \varepsilon)$)

Table 6-12 - Mechanical properties implemented in the tensile coupon to simulate influence of voids on Lüders propagation

The gauge length of the tensile coupon has 4 rows of voids; with each row containing 9 voids (see Figure 6-27). The geometrical dimensions which are of interest are schematically shown in Figure 6-28 and the values for all the run simulations are reported in table Table 6-13.

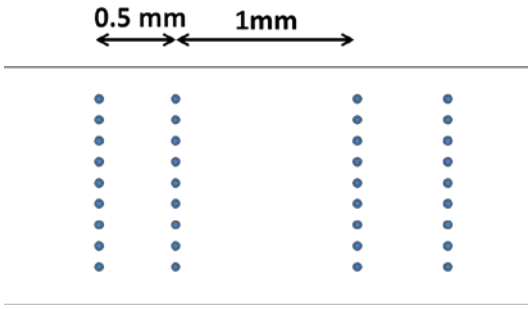

Figure 6-27 - Sketch of the simulated voids configuration. Void applied in the gauge length of the specimen

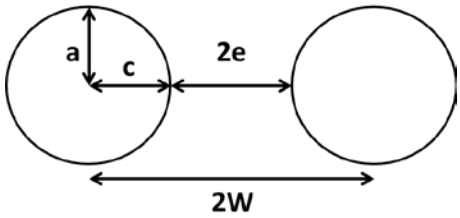

Figure 6-28 - Sketch of void dimensions

Simulation	a [μm]	c [μm]	2e [μm]	2W [μm]
Interspace 0.05 mm	5	5	40	50
Interspace 0.07 mm	5	5	60	70
Interspace 0.1 mm	5	5	90	100

Table 6-13 - Geometrical configurations of the voids implemented in the FEM simulations

The diameter of the voids was set at 10 μm since this dimensions has been used in experimental studies of void growth and coalescence in metals [132]. The value for "2W" was chosen to vary from 50 μm to 100 μm because values close to 50 μm were experimentally investigated by Weck et al. [132], while values of 70 μm and 100 μm were not yet investigated in literature.

The engineering stress-strain curves obtained for the above simulations are shown in Figure 6-29. The engineering stress-strain curves obtained for coupons having voids are compared with a tensile coupon having the same mechanical properties but no voids in the gauge length. From the stress-strain curves it is evident that if no voids are present, the Lueder's plateau is longer than the situation where voids are in the gauge length. If no voids are present, only two Lüders fronts will nucleate, out of which only one will move, requiring more time to cover the whole gauge length before strain-hardening can resume. On the contrary, if voids are present, more fronts can nucleate simultaneously, depending on how

many void rows are placed in the gauge length, and this requires less time to cover the gauge length, which will result in a shorter Lüders plateau. Comparing the curve for the different intervoid spacings, no Lüders length change was recorded. However, the shape of the bands propagating during Lüdering is influenced by the intervoid spacing as can be seen in Figure 6-29. The highly irregular plateau is due to the simultaneous propagation of multiple bands inside the gauge length. Every time two bands coalesce, there is a further stress drop in the plateau. Details of the bands propagation are included in Figure 6-30, Figure 6-31 and Figure 6-32 for intervoid spacings of 50 µm, 70 µm and 100 µm respectively.

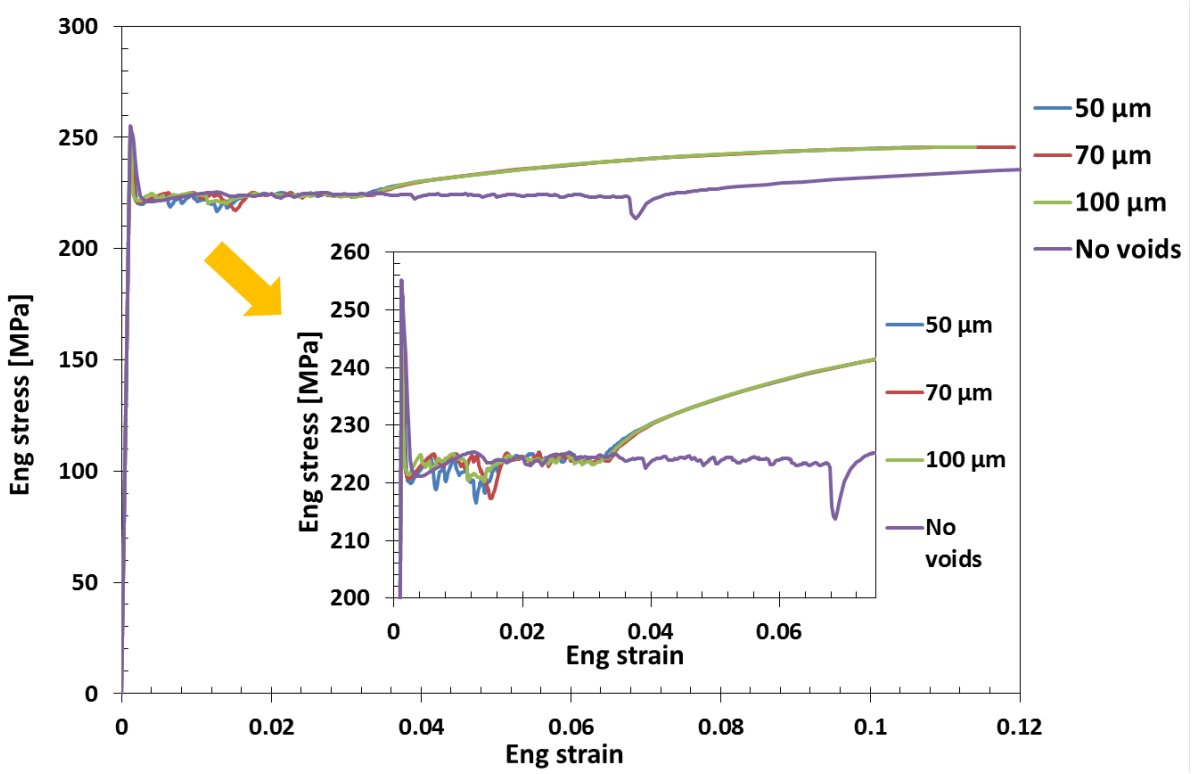

Figure 6-29 - Stress-strain curves obtained simulating the influence of intervoid spacing on Lüders propagation

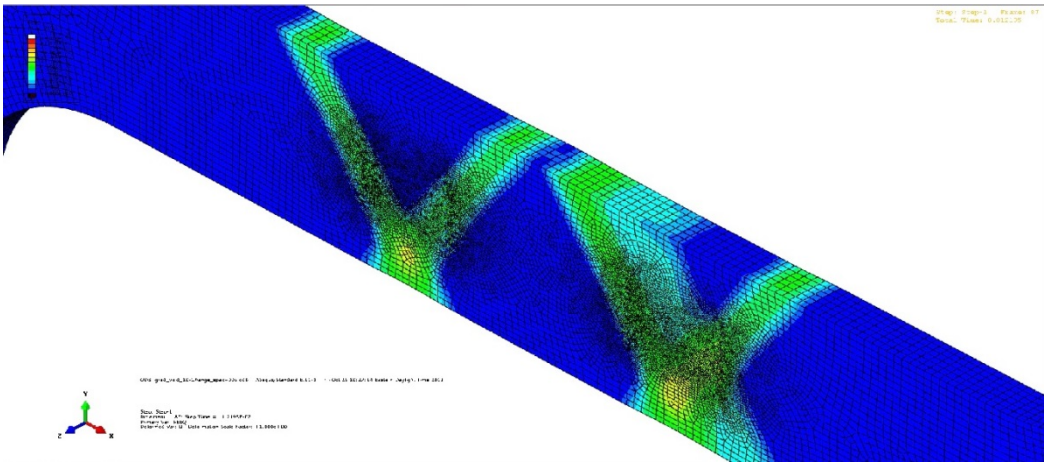

Figure 6-30 - Lüders bands localization in tensile coupon having voids with interspace of 50 µm

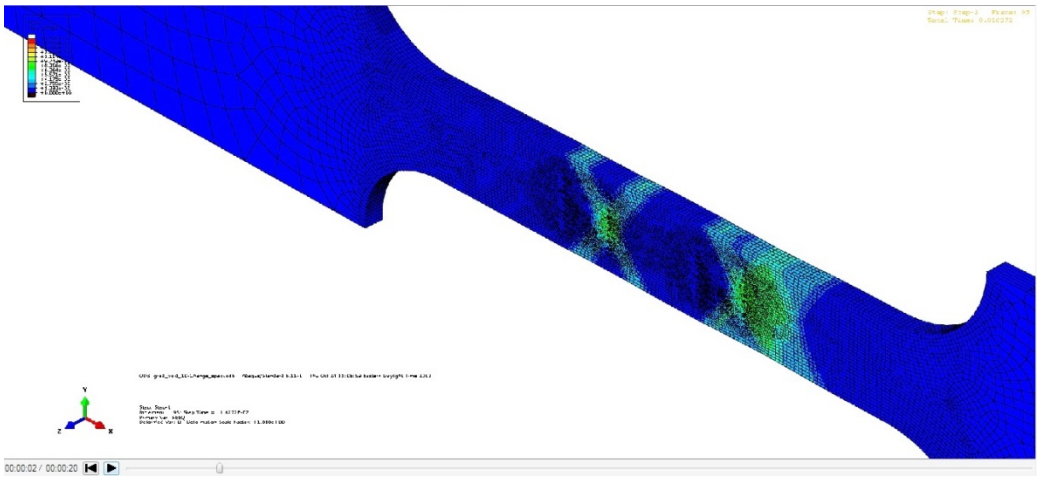

Figure 6-31 - Lüders bands localization in tensile coupon having voids with interspace of 70 µm

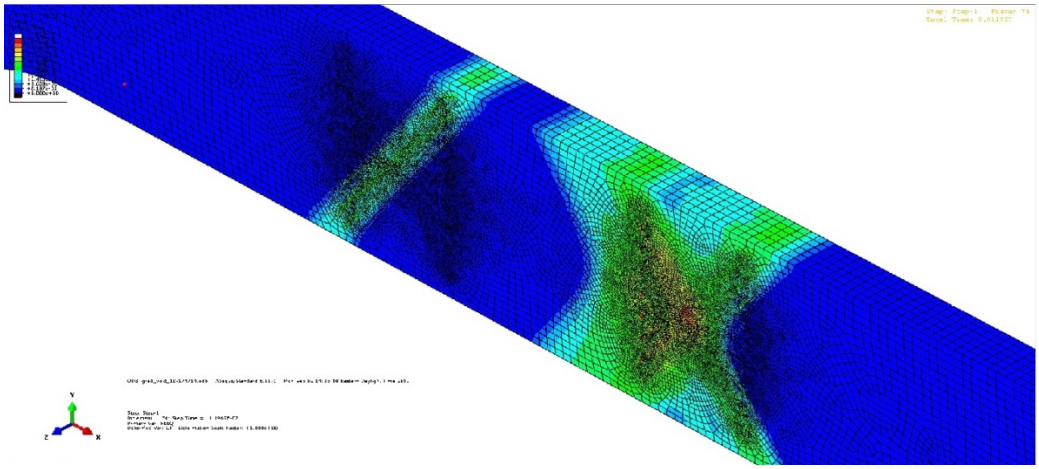

Figure 6-32 - Lüders bands localization in tensile coupon having voids with interspace of 100 µm

For the above simulations the volume fraction of voids can be calculated as the ratio between the volume occupied by the voids and the total volume of the gauge length. The volume fraction is the same for each simulation; only the intervoid spacing was changed. Considering that the voids have a diameter of 10 μm, the volume fraction is given by:

$$V_f = \left[\frac{\pi \times (5)^2 \times (198) \times 9 \times 4}{(198) \times (5000) \times (1000)} \right] \times 100 = 0.057\%$$

In the equation above, 198 μm is the thickness of the tensile coupon, 9 is the number of holes in each row and 4 is the total number of rows in the gauge length. 5000 μm is the total gauge length of the specimen and 1000 μm is its width.

6.5. Influence of voids volume fraction on Lüders propagation

In order to change the volume fraction of voids in the gauge length, there are two options that can be implemented. It is simply possible to add a row of voids so that in the gauge length 5 rows of voids will be present. On the other hand, if one wants to preserve the void pattern to allow for comparison with previous results, the volume fraction has to be changed by modifying the diameter of the holes and by keeping the intervoid spacing constant. This was done by incrementing the void diameter to 40 μm and keeping an intervoid spacing "2e" of 90 μm. The tensile coupon had still 4 rows of voids, each one composed by 7 voids. The results from this simulation will be compared with the results obtained for the configuration presented in the previous paragraph where "2e" was 90 μm but each of the 4 rows was made by 9 voids of 10 μm diameter. The volume fraction for the configuration having voids of 40 μm diameter is given by:

$$V_f = \left[\frac{\pi \times (20)^2 \times (198) \times 7 \times 4}{(198) \times (5000) \times (1000)} \right] \times 100 = 0.70\%$$

The voids were placed with 2W = 130 μm so that 2e = 90 μm. The configuration is schematically shown in Figure 6-33, while the mechanical properties are the same as shown in Table 6-12.

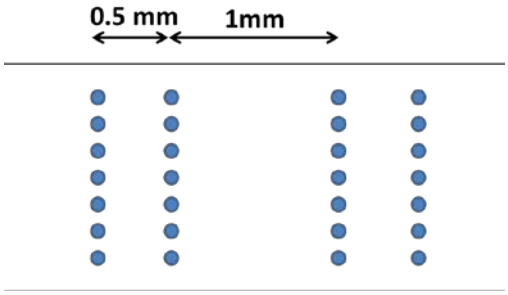

Figure 6-33 - Sketch of the void configuration used to simulate the influence of volume fraction on Lüders propagation

The engineering stress-strain curve obtained for this volume fraction of voids is shown in Figure 6-34 and it is compared with the curve obtained for the specimen having 2W = 100 μm and voids of 10 μm in diameter already presented in paragraph 6.5.

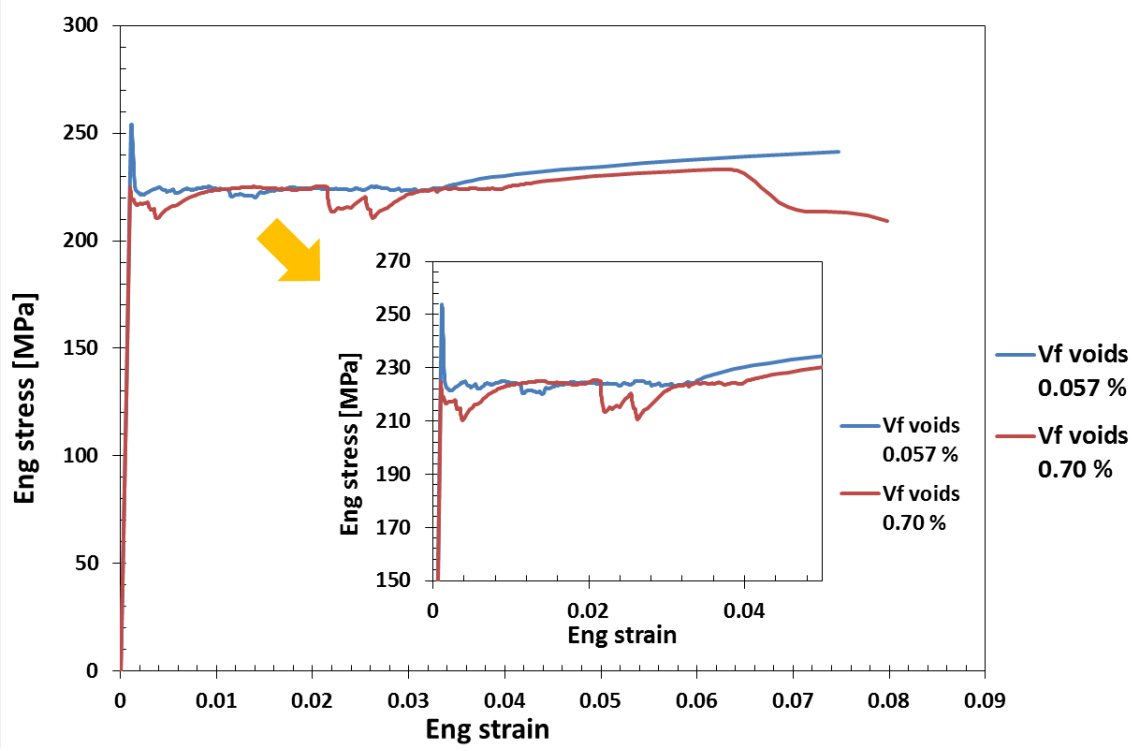

Figure 6-34 - Influence of different volume fractions of voids on Lüders propagation

According to the results shown in Figure 6-34, the Lüders plateau seems to be only slightly longer if the volume fraction of voids is increased. However, increasing the voids volume fraction (making voids with larger diameter) will cause an easier nucleation of the bands at the voids. In fact, the bands start to nucleate at a lower upper yield stress compared to a

situation where the voids are smaller in diameter. Moreover, for bigger voids, the plateau is very unstable with multiple fronts propagating. This causes the presence of stress drops in the plateau and with bigger voids, the material will neck at lower strains without undergoing most of the strain-hardening behaviour.

6.6. Conclusions

From the results presented in this chapter, the following conclusions can be drawn:

- A linear softening in the material behaviour can be used to simulate Lüders plateau, however, the upper yield stress has no influence on its length if the slope and Lüders strain are kept constant;
- The length of the Lüders plateau depends on the slope of the linear softening; in particular, a lower slope corresponds to a shorter plateau, while a steeper slope will result in a longer plateau. From a physical point of view, a lower slope corresponds to a material which will be able to multiply dislocations easily and to propagate faster Lüders bands. In order to simulate a material having a carbon gradient by using the linear softening law, it is required to have both a gradient of yield stress and also a gradient of slope for the linear softening. Indeed, the zone containing higher amount of carbon will have higher yield stress and in general longer plateau, while the zones having less carbon will have lower yield stress and easier unpinning of dislocations which means smaller slope of the linear softening.
- A gradient in mechanical properties through thickness can shorten Lüdering compared to having the same mechanical properties but with uniform properties through thickness;
- One solution to suppress or limit Lüdering is to create a graded structure by placing at the center a material without Lüders and with a lower Young's modulus compared to the outer layers having Lüdering;
- Another option to suppress or limit Lüdering is to increase the thickness of a central layer without Lüdering so that it is at least 2.5 – 3 times thicker than the outer layers showing Lüdering;
- Having a material with a high strain-hardening ability could suppress Lüdering;

- No influence of void interspacing on Lüders length was detected;
- Changing the volume fraction of voids without changing the pattern of voids had only a slight influence on Lüders length. However, both intervoid spacing and volume fraction affect the number of bands that can nucleate and propagate causing stress drops in the plateau and earlier failure.

Chapter 7 : Prestrain and Strain Ageing of Interstitial Free Steel coated with FeC Film

7.1. Influence of pre-strain on carbon diffusion

In this chapter the influence of pre-strain on the strengthening obtained by diffusing carbon from FeC film has been investigated. For steel companies, it is interesting to verify if the interstitial free steel can undergo first the forming process on the samples with FeC film and then do the carbon diffusion strengthening step. For this reason, it is important to verify how the level of strengthening obtained by carbon diffusion in a pre-strained IF steel compares with that found in a not-prestrained IF steel.

In literature the influence of pre-strain on carbon diffusion and on the formation of Cottrell atmosphere has been studied by performing strain-ageing experiments [168]. A strain-ageing experiment is made by pre-straining the material up to a certain point and annealing at a given temperature and time (usually below 200 ˚C for short times up to 20 minutes). From strain ageing experiments performed on Ultra-Low-Carbon steels (ULC steels) De et al. [168] have drawn the following conclusions:

- "The effect of pre-strain on the strain-ageing response was found to be weak" (see Figure 7-1) [168].
- "The kinetic of ageing was determined by means of strength measurements where the increase in yield stress $\Delta\sigma$ due to aging was calculated. $\Delta\sigma$ is defined as (σ_y-σ_f), where σ_y is the upper yield stress after ageing and σ_f is the flow stress at the end of the prestrain" [168]. Both stresses are calculated considering the initial cross-section of the specimen [168].
- For low temperature (below 75 ˚C) there is an incubation period (see Figure 7-2) since the strain-ageing process is time dependent. This time decreases as the ageing temperature is increased;

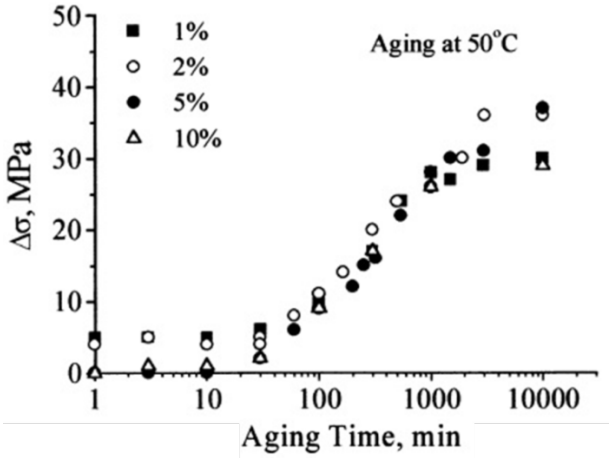

Figure 7-1 - Increase of yield stress obtained for different pre-strain levels at 50 ˚C of ageing temperature [168]

- Yield stress increases with ageing time until the stress field associated with a dislocation is saturated. For 170 ˚C, the saturation point is reached in the first minutes of aging treatment (see Figure 7-2);
- According to literature [168], the time necessary to form carbon atmospheres around dislocations is not affected by the level of pre-strain;

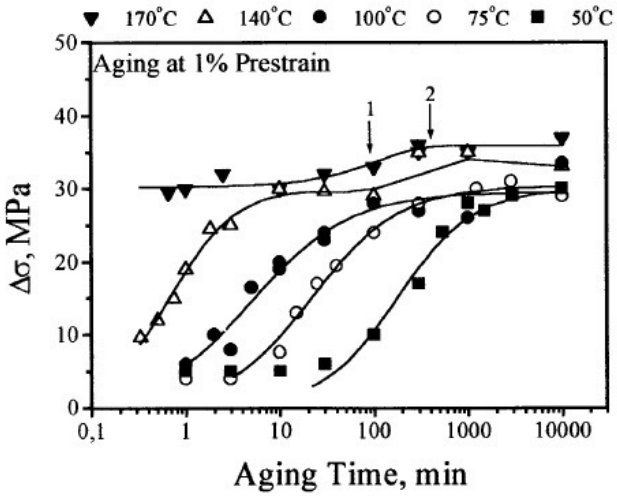

Figure 7-2 - Increase of yield stress obtained for different ageing temperatures for 1% pre-strain [168]

- the second stage of aging can involve low temperature carbides formation, or clustering of C atoms. This second stage can appear at low pre-strain values.
- “The amount of carbon required to form atmospheres close to every dislocation increases as the density of dislocations is augmented. For low pre-strain the density

of dislocations is not high, so the carbon amount is sufficient to saturate all dislocations and the remaining carbon can form clusters or precipitates" [168];

- "Above 5% pre-strain all the carbon is used to completely form Cottrell atmospheres for a steel containing 20 ppm of carbon" [168];
- "The density of atoms required to saturate a dislocation is the same for each dislocation and it does not depend on the dislocation density (which means pre-strain)". "So maximum increase of yield stress at the end of atmosphere formation was the same for all pre-strain levels" [168];
- "If the carbon content in solid solution is increased, more carbon atoms can migrate towards the stress field of dislocations, which means that the stress-fields can be saturated more rapidly" [168];
- The energy of activation for the aging process is not influenced by the pre-strain [168];

Depending on whether the processes of straining and strain-ageing take place simultaneously or in sequence, either dynamic strain ageing (DSA) or static strain aging (SSA) will occur which will result in different mechanical properties. DSA influences plastic deformation and the work hardening behaviour, while SSA has an influence on the yield stress of the material [169].

The quantities that can be evaluated before and after strain ageing are shown in Figure 7-3, where:

- ΔY_1 is the increase in stress due to pre-strain;
- ΔY_2 is the increase in stress due to ageing;
- Y_3 is the total increase of stress ($\Delta Y_1 + \Delta Y_2$);
- ΔU is the change of ultimate tensile strength;
- Δe is the change in total elongation due to straining and ageing;

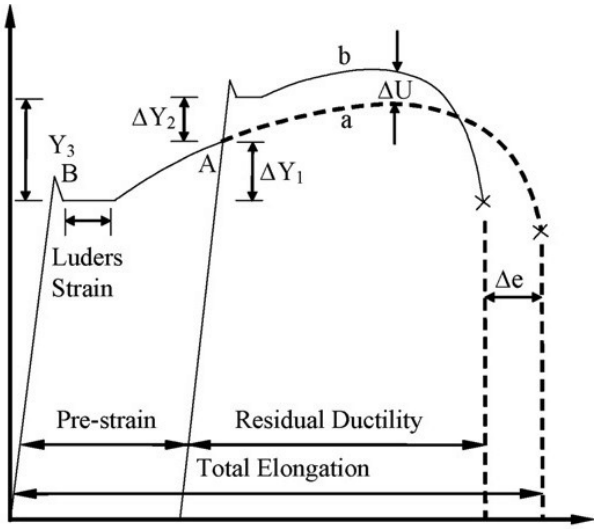

Figure 7-3 - Stress-strain curve for low carbon steel strained to point A, unloaded, and then restrained immediately (curve a) and after ageing (curve b) [170]

7.2. Pre-strained IF steel coated with FeC film

7.2.1 Experimental Results of pre-strained IF steel coated with FeC film

In this PhD thesis, tensile coupons were pre-strained at 15% of nominal pre-strain. They were then shipped to UBC where they were coated on both sides with a 500 nm thick FeC film containing 30 at% of carbon. After the coating process, they were sent back to the University of Ottawa for annealing at different temperatures for 1h under high vacuum and tested in tension until failure. The heat treatment profiles are the same as those performed in chapter 5. Figure 7-4 shows the quantities evaluated during the tensile tests:

- (σ_F -σ_{YS}) is the strengthening due to pre-strain;
- ($\sigma_{YS\ upper} - \sigma_F$) is the strengthening due to carbon diffusion;
- ($L1 - \sigma_F$) is the strengthening due to diffusion considering the average of stress in the Lüders plateau;
- ($L1 - \sigma_{YS}$) is the total strengthening considering the average of stress in the Lüders plateau;
- ($\sigma_{YS\ upper} - \sigma_{YS}$) is the total strengthening obtained from pre-strain and carbon diffusion;

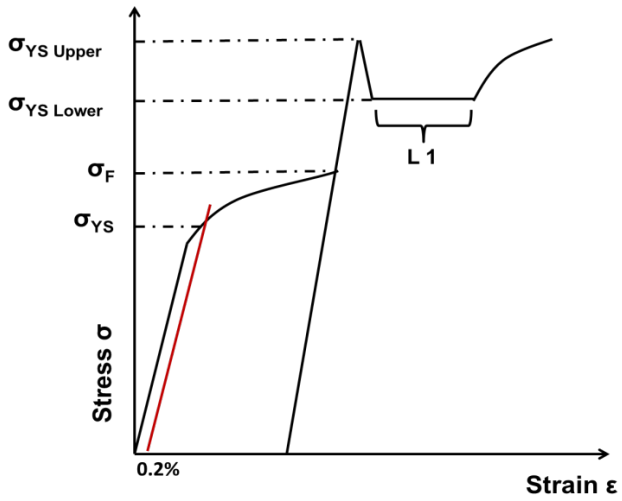

Figure 7-4 - Quantities evaluated during the tensile pre-strain and after the diffusion heat treatment

For the pre-strained specimens annealed at 430 ˚C - 1h the curves of prestrain are shown in the following graph (Figure 7-5) and their tensile curve after annealing are shown in Figure 7-6, while the numerical values of the strengthening obtained by performing prestrain and annealing are reported in Table 7-1. Engineering stress-strain curves and the mechanical properties for prestrained specimens annealed at 530 ˚C, 630 ˚C and 710 ˚C for 1h are also reported.

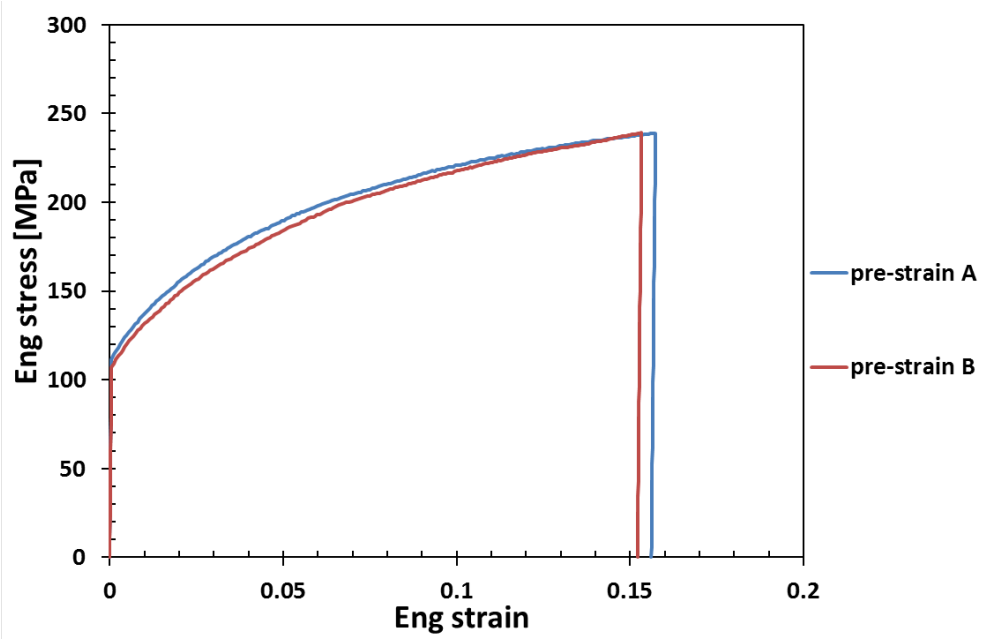

Figure 7-5 - Pre-strain engineering stress-strain curves of specimens A and B which will be annealed at 430 ˚C - 1h in high vacuum after the deposition of the FeC film on both sides

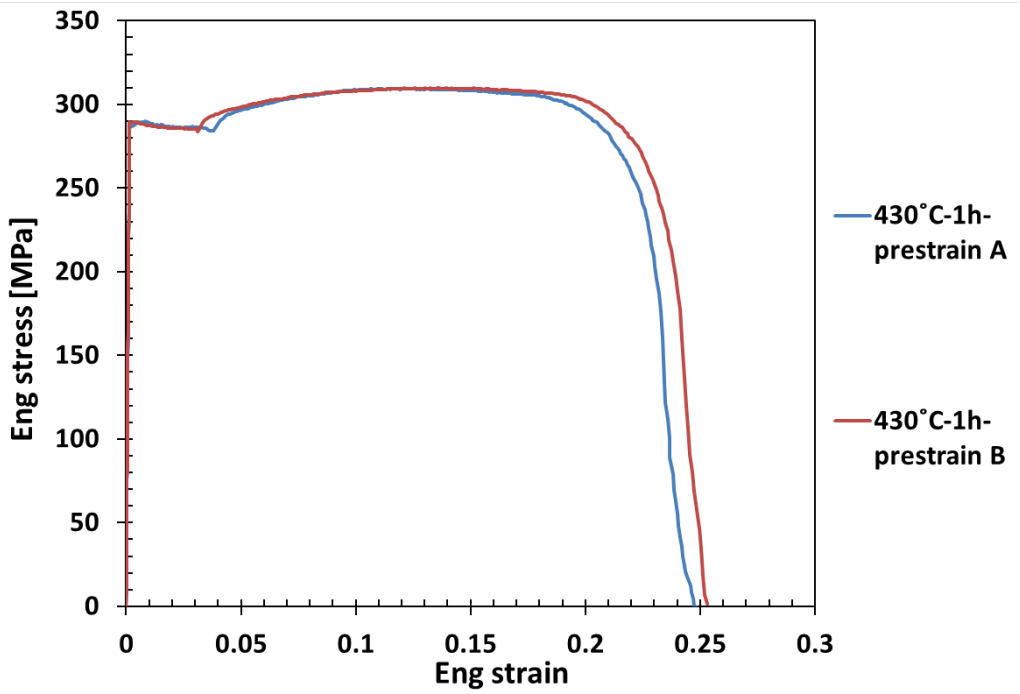

Figure 7-6 - Engineering stress-strain curves of specimens A and B after pre-strain and annealing at 430 ˚C - 1h in high vacuum after the deposition of the FeC film on both sides

Test	(σ_F - σ_{YS}) [MPa]	($\sigma_{YS\ Upper}$ – σ_F) [MPa]	(L1 - σ_F) [MPa]	(L1 - σ_{YS}) [MPa]	($\sigma_{YS\ Upper}$ - σ_{YS}) [MPa]
430˚C-1h-A	127	47	48	176	174
430˚C-1h-B	132	50	48	180	182
Average	130	49	48	178	178

Table 7-1 - Strengthening obtained by pre-strain and diffusion for specimens coated both sides with 500 nm FeC amorphous film and annealed at 430 ˚C - 1h in high vacuum

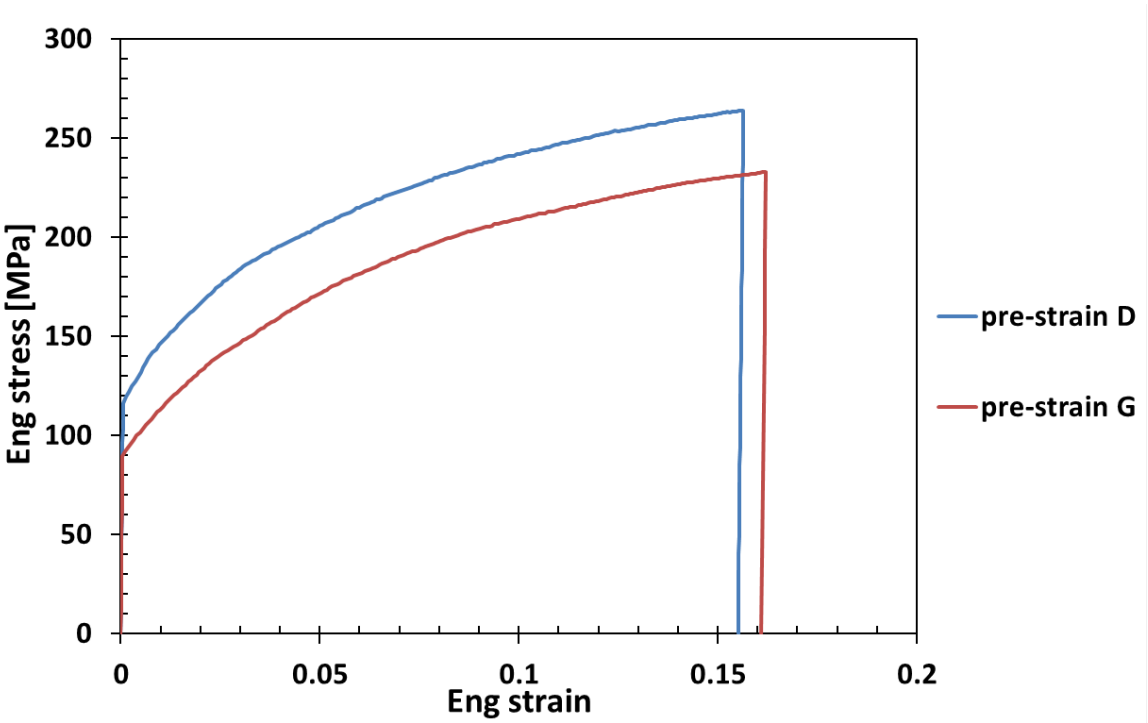

Figure 7-7 - Pre-strain engineering stress-strain curves of specimens D and G which will be annealed at 530 ˚C - 1h in high vacuum after the deposition of the FeC film on both sides

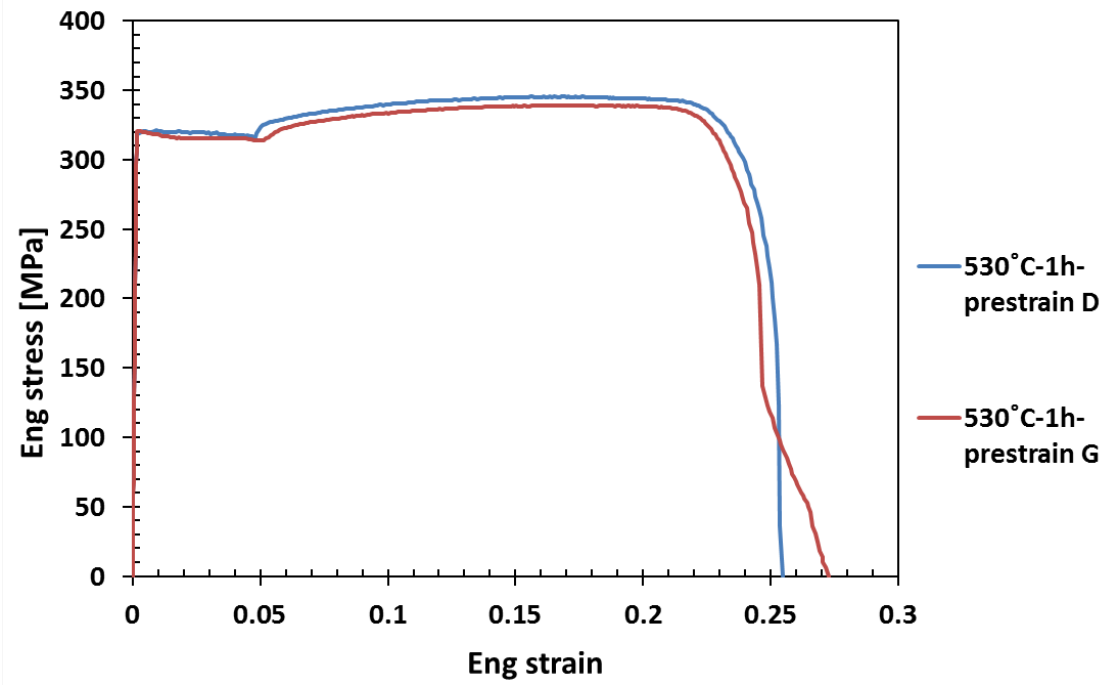

Figure 7-8 - Engineering stress-strain curves of specimens D and G after pre-strain and annealing at 530 ˚C - 1h in high vacuum after the deposition of the FeC film on both sides

Test	(σ_F - σ_{YS}) [MPa]	($\sigma_{YS\ Upper}$ - σ_F) [MPa]	(L1 - σ_F) [MPa]	(L1 - σ_{YS}) [MPa]	($\sigma_{YS\ Upper}$ - σ_{YS}) [MPa]
530˚C-1h-D	148	54	55	203	202
530˚C-1h-G	137	88	83	220	225
Average	143	71	69	212	214

Table 7-2 - Strengthening obtained by pre-strain and diffusion for specimens coated both sides with 500 nm FeC amorphous film and annealed at 530 ˚C - 1h in high vacuum

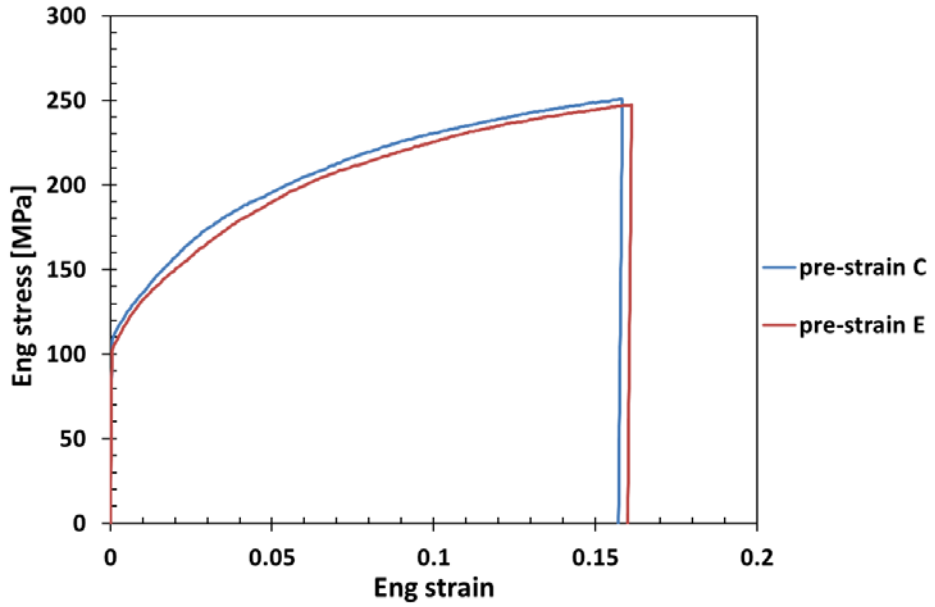

Figure 7-9 - Pre-strain engineering stress-strain curves of specimens C and E which will be annealed at 630 ˚C - 1h in high vacuum after the deposition of the FeC film on both sides

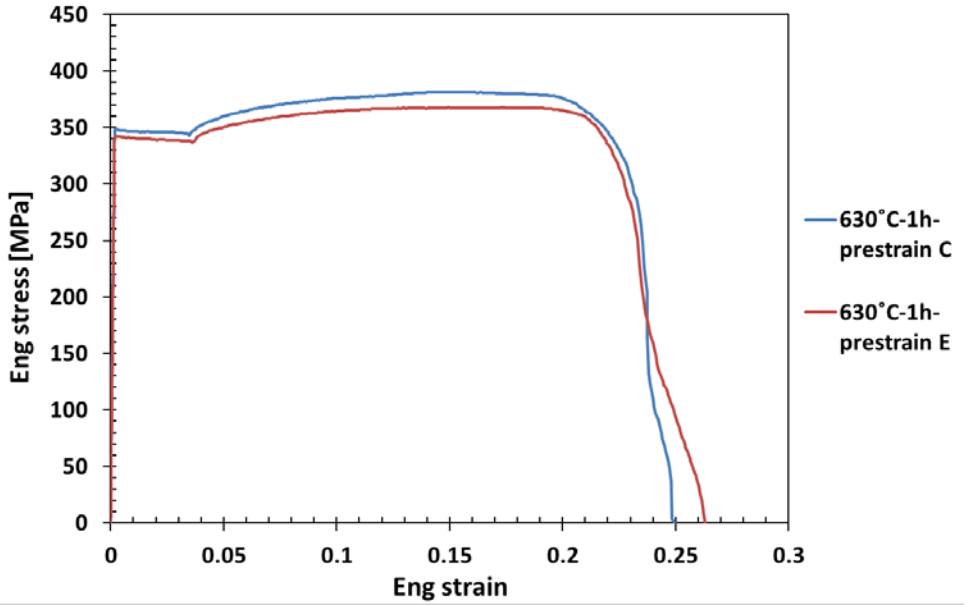

Figure 7-10 - Engineering stress-strain curves of specimens C and E after pre-strain and annealing at 630 ˚C - 1h in high vacuum after the deposition of the FeC film on both sides

Test	(σ_F - σ_{YS}) [MPa]	($\sigma_{YS\ Upper}$ - σ_F) [MPa]	(L1 - σ_F) [MPa]	(L1 - σ_{YS}) [MPa]	($\sigma_{YS\ Upper}$ - σ_{YS}) [MPa]
630˚C-1h-C	143	98	95	238	240
630˚C-1h-E	145	95	92	238	240
Average	144	96	94	238	240

Table 7-3 - Strengthening obtained by pre-strain and diffusion for specimens coated both sides with 500 nm FeC amorphous film and annealed at 630 ˚C - 1h in high vacuum

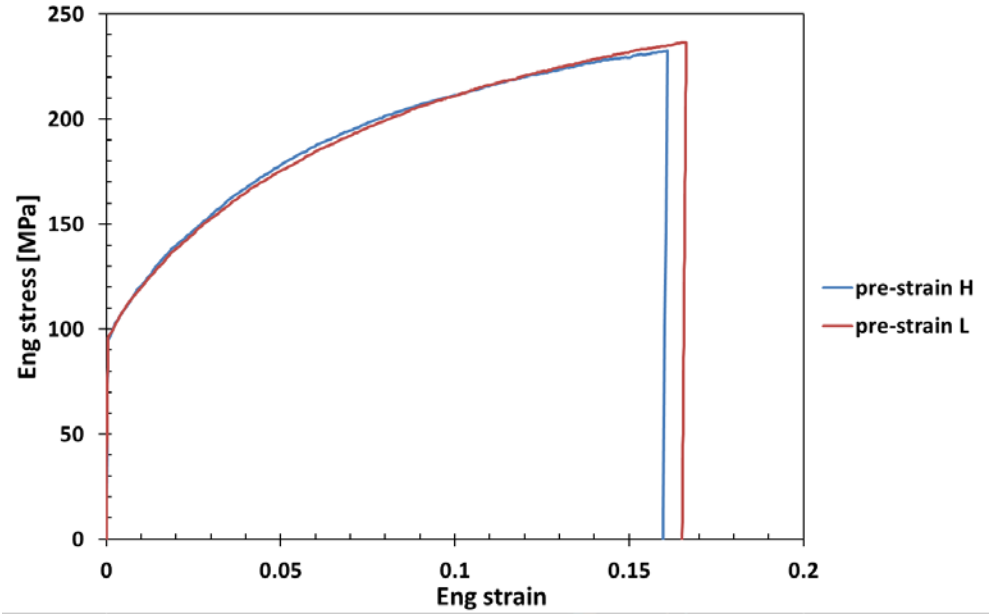

Figure 7-11 - Pre-strain engineering stress-strain curves of specimens H and L which will be annealed at 710 ˚C - 1h in high vacuum after the deposition of the FeC film on both sides

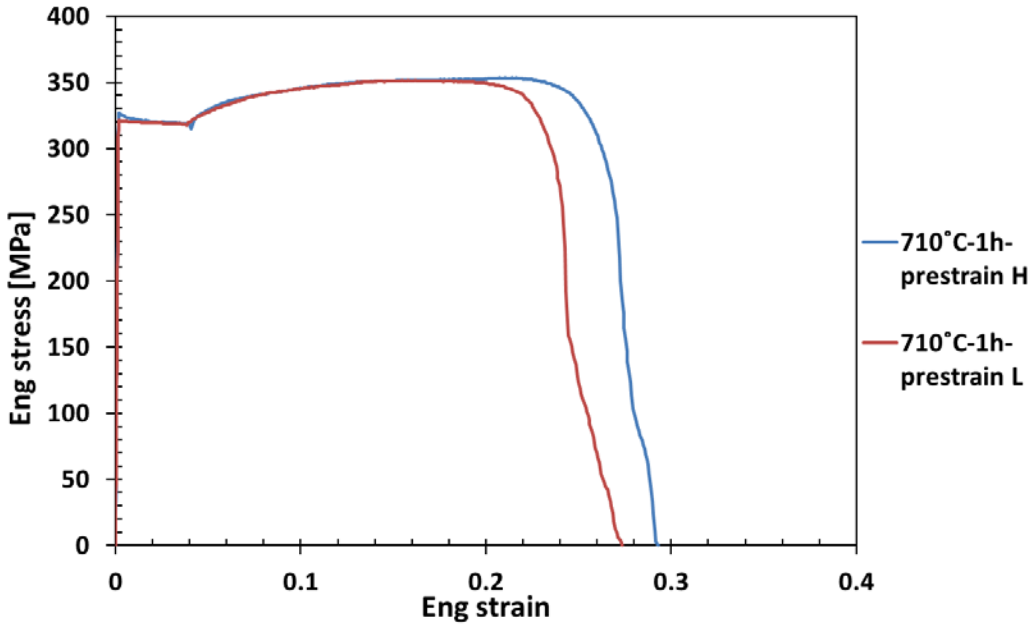

Figure 7-12 - Engineering stress-strain curves of specimens H and L after pre-strain and annealing at 710 ˚C - 1h in high vacuum after the deposition of the FeC film on both sides

Test	(σ_F - σ_{YS}) [MPa]	($\sigma_{YS\ Upper}$ - σ_F) [MPa]	(L1 - σ_F) [MPa]	(L1 - σ_{YS}) [MPa]	($\sigma_{YS\ Upper}$ - σ_{YS}) [MPa]
710˚C-1h-H	130	94	88	218	224
710˚C-1h-L	140	85	83	223	225
Average	135	90	86	221	225

Table 7-4 - Strengthening obtained by pre-strain and diffusion for specimens coated both sides with 500 nm FeC amorphous film and annealed at 710 ˚C - 1h in high vacuum

In Figure 7-13, the strengthening obtained after pre-strain and carbon diffusion is compared with the strengthening obtained for coated and not pre-strained coupons (results presented in chapter 5). The total strengthening in the case of pre-strained and coated coupons (black curve in Figure 7-13) is higher than the strengthening obtained only for carbon diffusion (red curve in Figure 7-13). However, this total strengthening is the sum of two contributions: the first contribution is the increase of yield stress caused by the increase in dislocations density and the second contribution originates from carbon diffusion. On the other hand, for coupons which are not pre-strained, the strengthening is solely due to carbon diffusion. By comparing the strengthening due only to carbon diffusion with and without pre-strain (red and green curves in Figure 7-13), it can be seen that pre-straining decreases the strengthening due to carbon diffusion. Since the diffused carbon amount is the same in both situations (pre-strained and not pre-strained coupons) because the annealing conditions are identical and the thickness and carbon content for the FeC film are the same; it can be concluded that the difference in strengthening is caused by a different density of interstitial atoms at the Cottrell atmospheres. If a coupon is not pre-strained, the two stages of ageing occur. At first the carbon atoms are used to saturate the dislocations and the remaining carbon atoms can form precipitates or clusters around dislocations. However, if the density of dislocations is increased (pre-strained coupons), the number of dislocations that need to be saturated by carbon atoms is increased, leaving less carbon atoms available for the precipitation stage. For this reason, with 15% of pre-strain, the second stage of ageing is compromised. Moreover, for both pre-strained and not-prestrained coupons there will be a similar carbon amount which will segregate at the grain boundaries. This segregation prevents grain growth on pre-strained coupons for annealing above 600 ˚C.

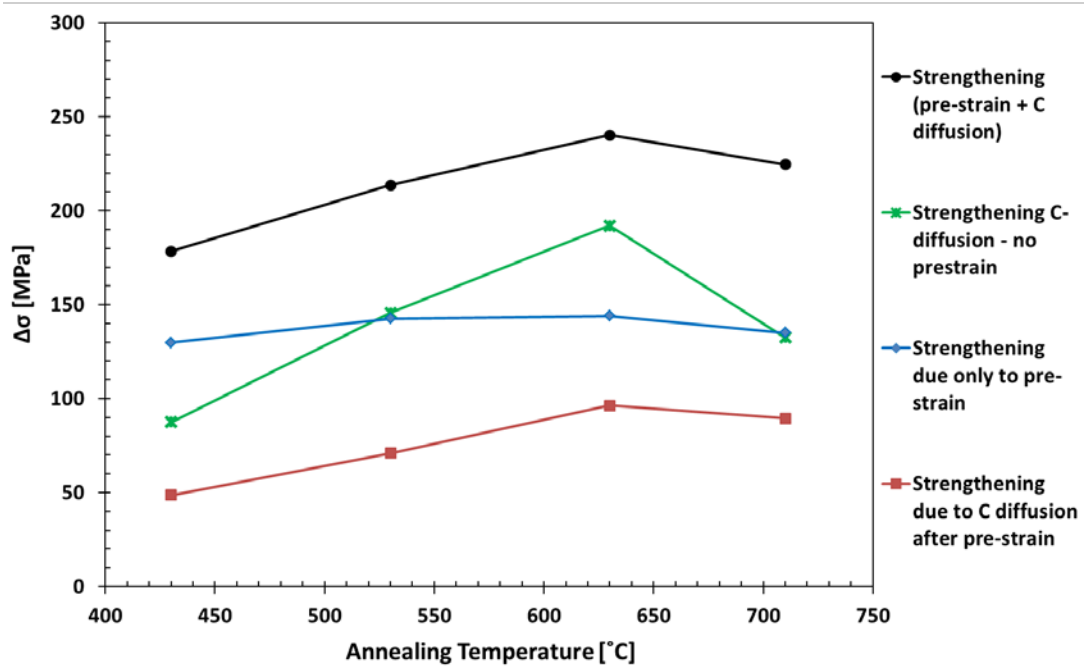

Figure 7-13 - Comparison of increase of strength for pre-strained and coated coupons and coated but not pre-strained coupons

In Figure 7-13 it is interesting to compare the curves of carbon strengthening without pre-strain and carbon strengthening after pre-strain for the annealings at 630 ºC and 710 ºC. If the specimen has not been pre-strained, the strengthening due to carbon will undergo a high drop by increasing the annealing temperature from 630 ºC to 710 ºC; while the same drop is absent or very small if the specimen is pre-strained. This could prove that if the number of dislocations is increased, the carbon will be more distributed and the Cottrell atmospheres will be less dense, preventing the formation of precipitates.

If the engineering stress-strain curves after pre-strain and annealing are plotted in the same graph for the different annealing temperature (Figure 7-14), it can be seen that the strengthening rises as the temperature is increased. However, at 710 ˚C - 1h the mechanical properties are the same as those found at 530 ˚C - 1h, which was as well the case for not pre-strained and coated coupons (results shown in chapter 5).

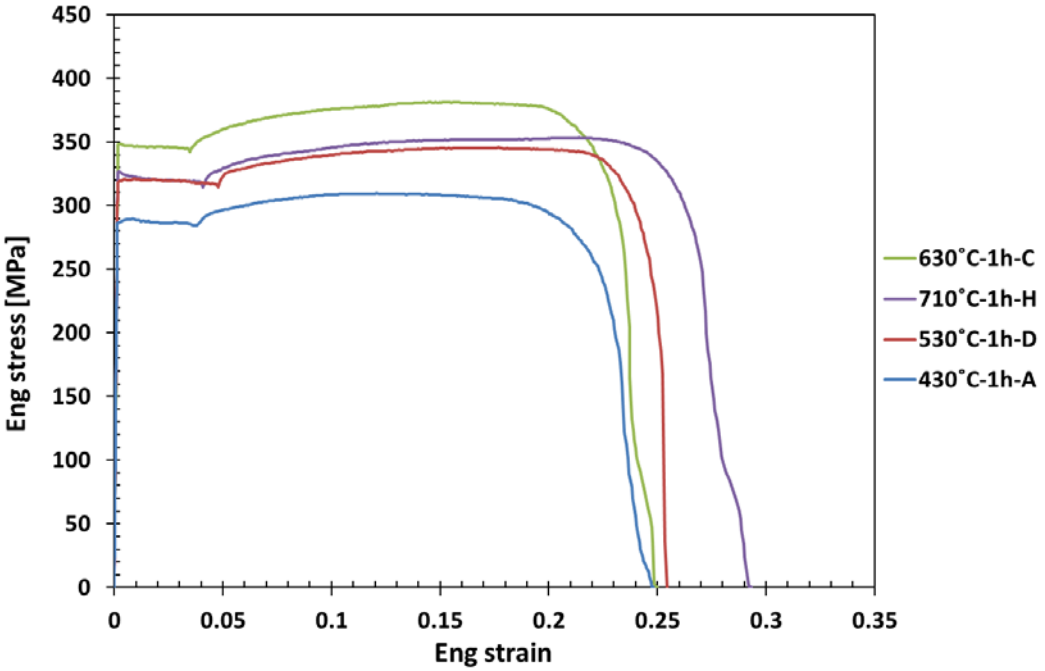

Figure 7-14 - Comparison of engineering stress-strain curves for pre-strained and both sides coated coupons (500nm FeC film) after annealing at different temperatures for 1h in high vacuum

From the curves shown in Figure 7-14, one should note that no peaks is present when the yield stress of Lüdering is reached. This could also confirm the lower carbon density of the Cottrell atmosphere which favors the unpinning of dislocations compared to the tests reported in Chapter 5 for not pre-strained coupons.

7.2.2. Experimental Results of pre-strained uncoated IF steel

In order to highlight the influence of carbon diffusion on the pre-strained coupons, a series of tests were performed on pre-strained and uncoated coupons of IF steel. These coupons were first pre-strained up to 15% and annealed at different temperatures for 1h in high vacuum. Their mechanical properties were compared with the mechanical properties of pre-strained coupons with FeC coating. The specimens are identified with the letter A plus a progressive number. All the pre-strain curves and the engineering stress-strain curves obtained after annealing are reported in detail in Appendix F. In Figure 7-15 only one pre-strain curve for each specimen is shown and in Figure 7-16 only one engineering stress-strain curve after annealing is reported for each temperature.

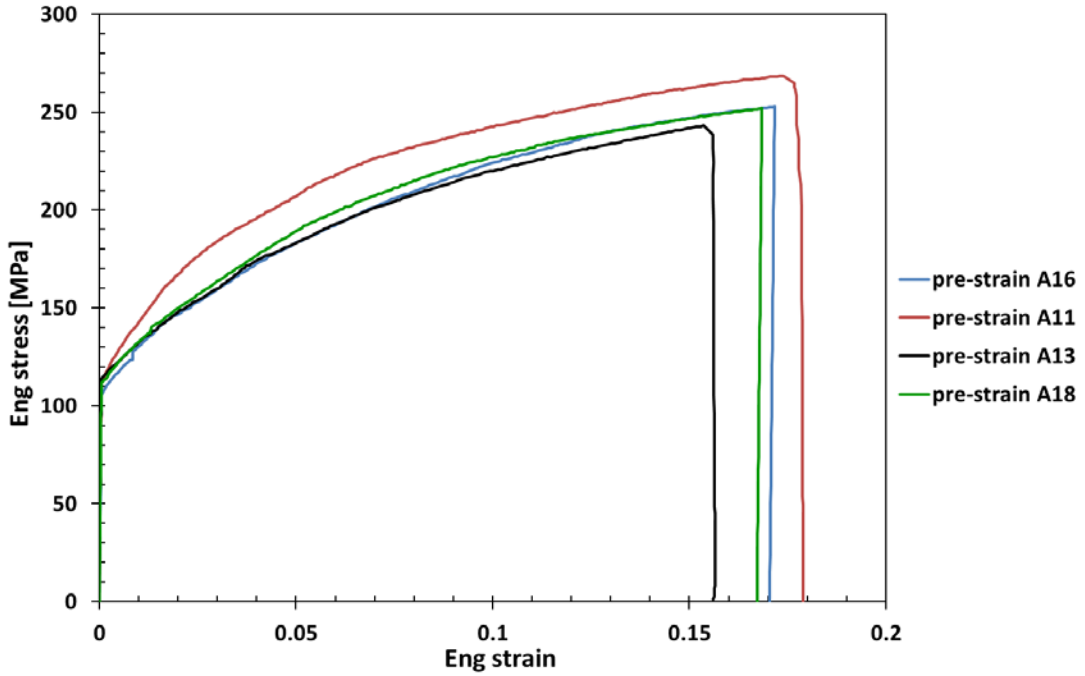

Figure 7-15 - Engineering stress-strain curves of specimens A16, A 11, A13 and A18 after pre-strain

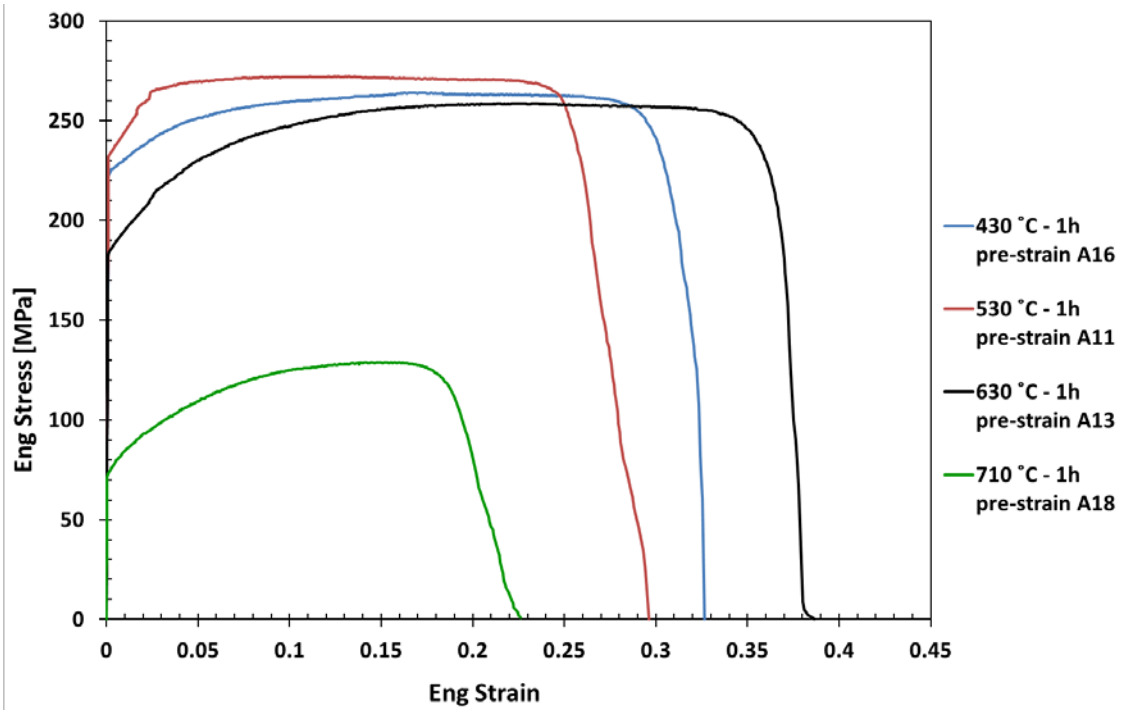

Figure 7-16 - Engineering stress-strain curves of specimens A16, A 11, A13 and A18 after pre-strain and annealing at different temperatures for 1h

In Table 7-5, the level of stress at the end of the pre-strain before unloading (σ_F), the strengthening due to pre-strain (σ_F - σ_{YS}), the yield stress after annealing (σ_{YS2}) and the

difference between the yield stress after annealing and the flow stress of pre-strain before unloading (σ_{YS2} - σ_F) are reported for all uncoated coupons.

Specimen	Strengthening due to pre-strain σ_F - σ_{YS} [MPa]	Flow stress at unloading σ_F [MPa]	Yield stress after heat treatment σ_{YS2} [MPa]	σ_{YS2} - σ_F [MPa]
430˚C-1h-A15	152	270	239	-31
430˚C-1h-A16	147	253	222	-31
530˚C-1h-A11	157	268	232	-36
530˚C-1h-A17	120	234	192	-42
630˚C-1h-A12	151	262	207	-56
630˚C-1h-A13	129	243	183	-60
710˚C-1h-A14	145	252	57	-195
710˚C-1h-A18	140	252	71	-181

Table 7-5 - Summary of stresses obtained for pre-strained not-coated IF coupons annealed in high vacuum at different temperatures

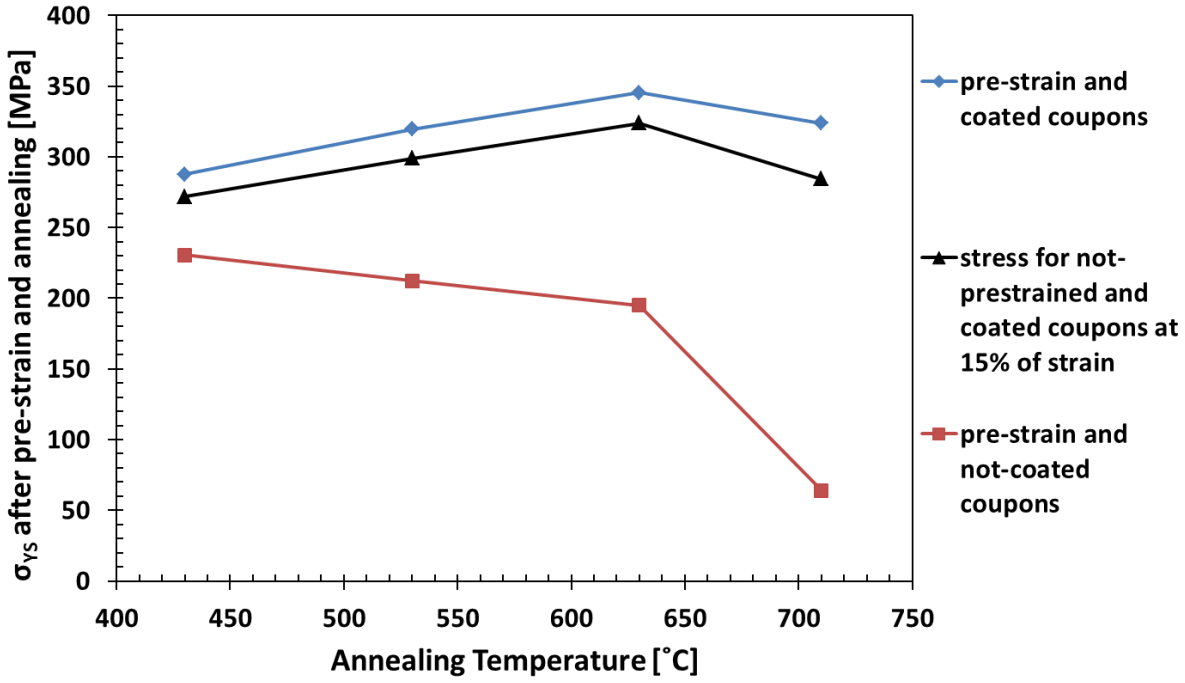

Figure 7-17 - Comparison of yield stress after pre-strain, annealing and reloading for coated coupons and not-coated coupons. For each temperature the plotted value is an average of the measured values.

Pre-straining of crystalline materials causes the formation of three-dimensional arrays of dislocations which are characteristic of the crystal structure of the deformed material. For iron pre-strained at room temperature, as it is the case in our experiments, “the deformation due to pre-strain results in the formation of dense groups of dislocations arranged in walls

surrounding regions (called cells) almost free of dislocations" [171]. The hardening experienced by the material during the plastic deformation is due to the interaction between dislocations due to the higher density of dislocations. However, during plastic deformations such as during a pre-strain, most of the work done by the external load is dissipated as heat but some energy is stored in the deformed material [171]. The pre-strained dislocation cell structure is mechanically stable but it is not thermodynamically stable [56]. This stored energy remains in the material if the temperature is sufficiently low to avoid rearrangement of atoms; however, if the temperature of a heat treatment is high enough, this stored energy can be released since the dislocations will rearrange themselves into lower energy configurations [171]. According to literature, the processes of rearrangement of dislocations require a sufficient thermal activation since they depend on local and long-range diffusion of point defects [171]. This rearrangement of dislocations which occurs when the material is heated to moderate temperatures is known as recovery and it results in a softening of the pre-strained material. "If the pre-strained material is heated even at higher temperatures, then the recovery process can be followed by recrystallization, which involves the nucleation of new grains free from dislocations" [171]. As reported by Dieter [56], "recrystallization is detected by a decrease in strength and an increase in ductility and it is dependent on several factors such as amount of pre-strain, temperature and time of the heat treatment and composition of the steel". Moreover, according to Dieter [56], "the smaller the amount of pre-strain, the higher is the temperature required to cause crystallization and the recrystallization temperature is raised by solid-solution additions".

From Figure 7-17, it is clear that for pre-strained IF coupons coated with FeC film on both sides, the yield stress after annealing in high vacuum and reloading increases as the temperature of the heat treatment is raised since more carbon will diffuse into the IF substrate. Again, at 710 ˚C the mechanical properties drop back to the properties found between 530 ˚C and 630 ˚C. The reason for this can be due to the fact that at 710 ˚C not all the diffusing carbon goes into dislocations but some of it will interact with the free titanium present in the IF steel or with TiS particles to form $Ti_4C_2S_2$. Detailed explanations were given in chapter 5. On the other hand, for pre-strained and not-coated coupons, the yield stress after annealing and reloading is decreasing as the annealing temperature is increased. In particular, a marked drop occurs at 710 ˚C - 1h. This can be explained considering

recovery and recrystallization occurring in the 15% pre-strained IF steel. From these results, it is evident that the diffusion of carbon from the FeC film is preventing the recovery and recrystallization process of pre-strained IF steel considering that carbon will relieve the stress field associated with the dislocations created during the pre-strain phase pinning them and preventing their rearrangement. In Figure 7-11, the engineering flow stress corresponding to 15% of strain for not-prestrained and coated coupons (results shown in chapter 5) is also plotted. Its values are close to the yield stress found for pre-strained and coated coupons.

In order to prove that for the uncoated and pre-strained IF steel, the rearrangement of dislocations is causing recovery and softening (also shown by an increase of grain size as the temperature increases), the microstructures of an uncoated and pre-strained tensile coupon annealed at 430 ˚C – 1h and of one coupon annealed at 710 ˚C – 1h were observed after polishing and etching with 4% Nital. Specimen A 15 (430 ˚C – 1h) and A18 (710 ˚C – 1h) are reported in Figure 7-18. The pictures have been taken in the gauge length since that is the zone that was 15% pre-strained and that is affected by the recovery. No marked change in grain size is detected in the grips since they had no pre-strain.

As it can be seen from Figure 7-18, the grain size does not increase for the annealing at 430 ˚C – 1h in an uncoated 15% pre-strain coupon, however at 710 ˚C – 1h there is a marked grain growth with grains covering the whole thickness of the tensile coupon.

(a) Microstructure of the gauge length of sample A15 uncoated and 15% prestrained annealed at 430 ˚C – 1h in high vacuum

(b) Microstructure of the gauge length of sample A18 uncoated and 15% prestrained annealed at 710 ˚C – 1h in high vacuum

Figure 7-18 - Microstructure of the gauge length of uncoated and 15% prestrain coupons of IF steel

7.3. Strain-ageing of IF steel coated with FeC film

In order to prove that a fraction of the carbon diffused from the FeC film into the IF steel substrate is going into solid solution at dislocations, strain ageing experiments were performed. IF steel coupons coated both sides with 500 nm FeC film were annealed in high vacuum for 1h at temperatures of 430 ˚C, 530 ˚C, 630 ˚C and 710 ˚C. One coupon for each temperature was annealed. The coupons were then tensile tested until the Lüders plateau was overcome and they were then unloaded. It is very important to test the coupon until the end of the Lüders plateau in order for all dislocations to be released from the pinning of carbon atoms. Coupons were then annealed in high vacuum at 170 ˚C for 20 minutes since this is the heat treatment usually performed during bake hardening and it is sufficient to pin dislocations with carbon. The following table summarizes the vacuum levels during the ageing treatment:

Specimen-annealing before ageing	Specimen ageing treatment	Vacuum on [Torr]	Vacuum during plateau [Torr]	Vacuum off [Torr]
430 ˚C - 1h high vacuum	170 ˚C – 20 min	$2.0x10^{-7}$	$4.0x10^{-7}$	$1.0x10^{-7}$
530 ˚C - 1h high vacuum	170 ˚C – 20 min	$2.0x10^{-7}$	$4.0x10^{-7}$	$1.0x10^{-7}$
630 ˚C - 1h high vacuum	170 ˚C – 20 min	$2.0x10^{-7}$	$5.0x10^{-7}$	$1.0x10^{-7}$
710 ˚C - 1h high vacuum	170 ˚C – 20 min	$2.0x10^{-7}$	$5.0x10^{-7}$	$1.0x10^{-7}$

Table 7-6 - Level of vacuum during ageing treatment in high vacuum at 170 ˚C for 20 min

The ageing treatment was performed without removing the FeC film since no carbon can diffuse from the film towards the IF substrate after the main annealing treatments at different temperatures for 1h. Indeed, there will be no carbon diffusing from the FeC film left on the substrate during strain ageing since the adhesion between film and substrate is compromised after the tensile test (this is the case of the specimen annealed at 430 ˚C - 1h in high vacuum). Furthermore, the FeC film is fully transformed into cementite at temperatures equal or higher than 530 ˚C - 1h and is fully stable at 170 ˚C. Moreover, from results presented in chapter 5, it is clear that no carbon diffusion occurs even at 330 ˚C - 1h; as a consequence, it can be concluded that during the annealing at 170 ˚C – 20 min there will be no carbon going from the FeC film into the IF substrate. In Figure 7-19 the engineering stress-strain curves of tensile coupons before the ageing treatment are shown, while the engineering stress-strain curves after the ageing treatment are shown in Figure 7-20.

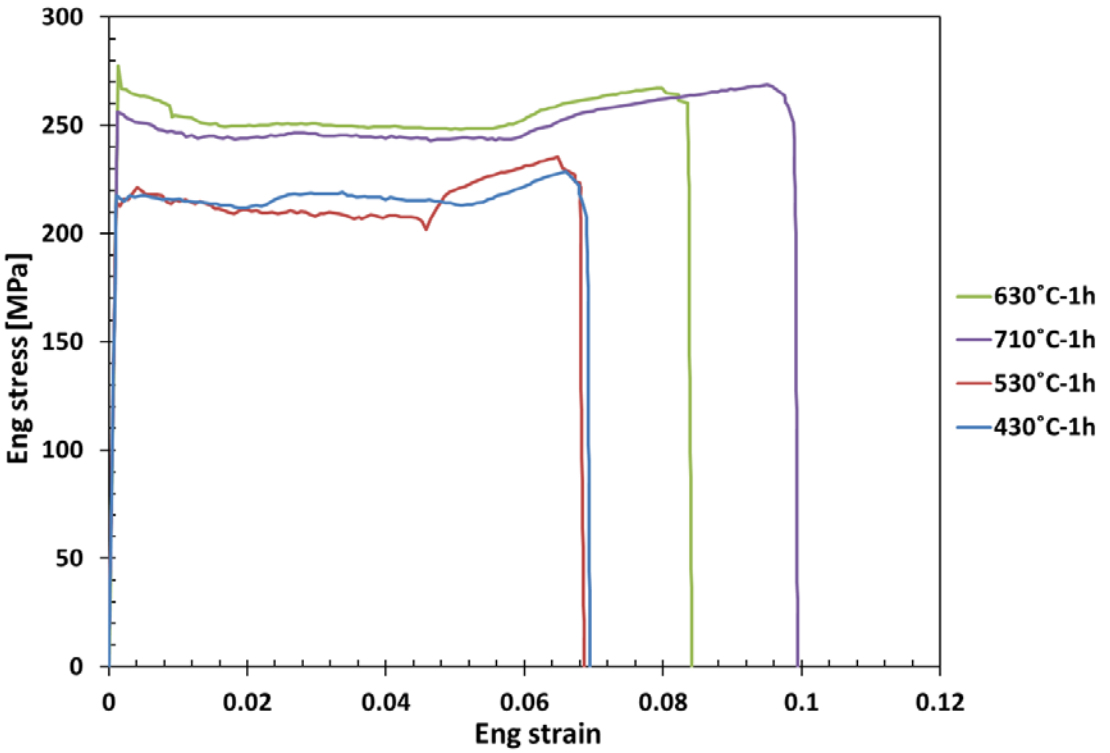

Figure 7-19 - Engineering stress-strain curves of loading and unloading of coupons coated both sides with 500 nm thick FeC film annealed at different temperatures for 1h. Coupons where tested until the end of the Lüders plateau.

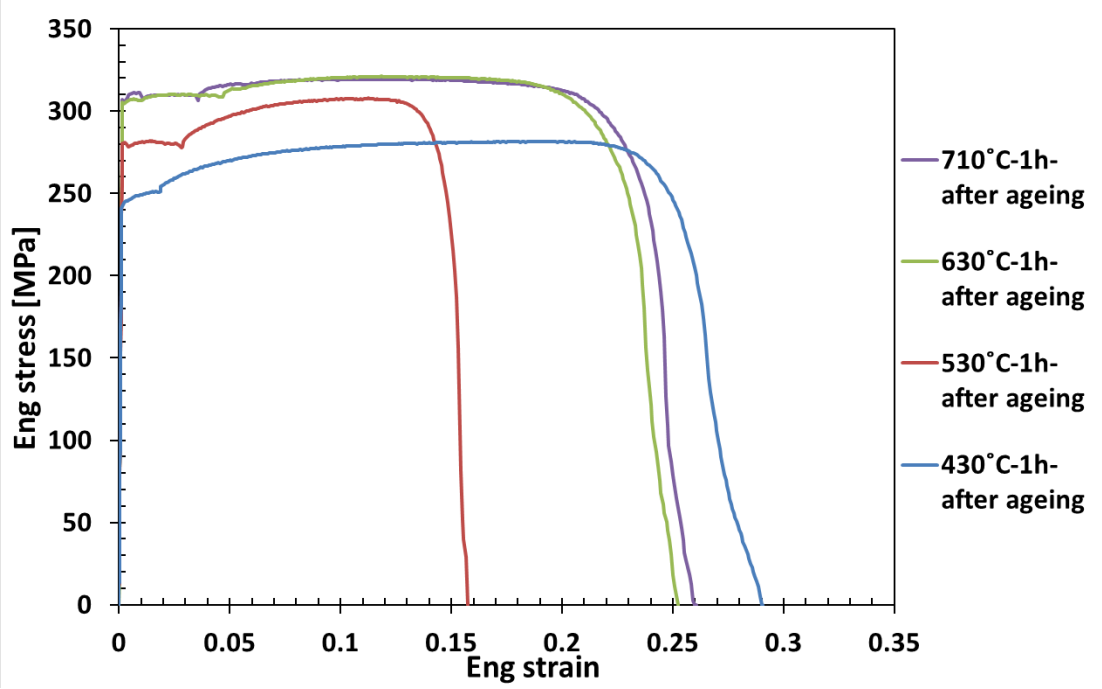

Figure 7-20 - Engineering stress-strain curves of specimens coated both sides with 500 nm thick FeC film annealed at different temperatures and aged at 170 ˚C for 20 min

The quantities measured before and after strain-ageing are shown schematically in Figure 7-21.

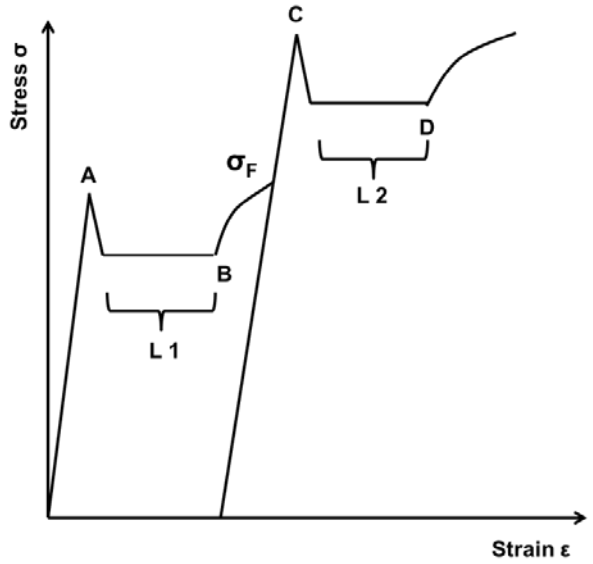

Figure 7-21 - Sketch of the quantities measured before and after strain ageing

where:

- Point *A* represents the coordinate of the upper yield stress before strain-aging;
- Point *B* represents the coordinate of the lower yield stress at the end of the Lüders plateau before strain-aging;
- *L1* is the average of yield stress in the Lüders plateau before strain-aging;
- σ_F represents the flow stress reached before unloading the specimen and performing the aging treatment;
- Point *C* represents the coordinate of the upper yield stress after aging;
- Point *D* represents the coordinate of the lower yield stress at the end of Lüders plateau after aging;
- *L2* is the average of yield stress in the Lüders plateau after aging;

Table 7-7 reports values before strain-ageing.

Specimen-annealing before ageing	Point A	Point B	L1 [MPa]	σ_F [MPa]	Lüders length
430 ˚C - 1h high vacuum	(0.001087; 217 MPa)	(0.05237; 213 MPa)	216	229	0.05128
530 ˚C - 1h high vacuum	(0.00107; 215MPa)	(0.04584; 202 MPa)	211	235	0.04477
630 ˚C - 1h high vacuum	(0.00139; 278 MPa)	(0.0554; 248 MPa)	252	267	0.05401
710 ˚C - 1h high vacuum	(0.00128; 256 MPa)	(0.05717; 244 MPa)	246	269	0.05589

Table 7-7 - Values of the engineering stress-strain curves before aging but after the heat treatment in high vacuum of coupons coated both sides with 500 nm thick FeC film at different temperatures for 1h

The following table reports values after strain-ageing.

Specimen-annealing before ageing	Point C	Point D	L2 [MPa]	Lüders length
430 ˚C - 1h high vacuum	(0.001206; 241 MPa)	(0.01812; 250 MPa)	248	0.01691
530 ˚C - 1h high vacuum	(0.001402; 280 MPa)	(0.02816; 278 MPa)	280	0.02676
630 ˚C - 1h high vacuum	(0.001526; 305 MPa)	(0.04509; 308 MPa)	309	0.04356
710 ˚C - 1h high vacuum	(0.001536; 307 MPa)	(0.03566; 307 MPa)	309	0.03412

Table 7-8 - Values of the engineering stress-strain curves after aging at 170 ˚C for 20 min

Table 7-9 summarizes the increase of stress due to the strain-aging defined as (L2-σ_F) and the decrease of Lüders length.

Specimen-annealing before ageing	Stress increase due to strain ageing (L2-σ_F) [MPa]	Change of Lüders plateau length
430 ˚C - 1h high vacuum	20	-0.03437
530 ˚C - 1h high vacuum	45	-0.01801
630 ˚C - 1h high vacuum	41	-0.01045
710 ˚C - 1h high vacuum	41	-0.02177

Table 7-9 - Increase of strength and reduction of Lüders plateau length after strain-ageing

In order to compare the different specimens after the aging treatment, it is important to remember that the level of pre-strain before the treatment has no influence on the kinetics of carbon diffusion through dislocations [168]. So, having more or less dislocations will not make the diffusion of carbon through ferrite slower or faster. However, the unloading strain of all the specimens was kept almost the same since the level of pre-strain before aging influences the Lüders plateau length after aging. Indeed, from literature [70] it is well proven that if the pre-strain is increased, then more dislocations are created and this will shorten the Lüders plateau for two reasons. The first reason is that the dislocations will be surrounded by less carbon so the "unpinning" process will be easier (absence of marked drop at the starting of the plastic deformation in the stress-strain curves after strain-aging). The second reason is that increasing the density of dislocations will decrease their mean free path and they will start to interact earlier which will result in an earlier hardening of the material. In literature [171], the relation between the shape of the yield drop and the density of mobile dislocations has been discussed, in particular, if there is no mobile dislocation, there will be a marked yield drop at the starting of the plastic behaviour; while the yield drop will decrease if the density of the initially mobile dislocations is increased. This has been proven also from these tests since for all specimens, a shortening of the Lüders plateau was observed when they were reloaded after strain aging as shown in Table 7-9. However, the shortening was higher in the case of the specimen annealed at 430 ˚C - 1h because the carbon in solid solution is not high enough to lock all new dislocations created from the loading before aging. For the specimens annealed at 630 ˚C the shortening of the plateau is low since enough carbon is in solid solution to lock even the newly formed dislocations. However, at 710 ˚C, we see that, even if the increase of stress due to aging (Δy_2) is on the same range as the one found for 530 ˚C and 630 ˚C, the shortening of the Lüders plateau is more pronounced, probably because the carbon in solid solution is not sufficient to lock all the dislocations. This could further prove that for the annealing at 710 ˚C - 1h a portion of the carbon diffusing into the IF steel is used to form TiC precipitates or to increase the size of the $Ti_4C_2S_2$ as already explained in chapter 5.

7.4. Conclusions

When carbon is diffused in ultra-low carbon steels, it can participate in three phenomena which contribute to the final strengthening of the steel:

- Formation of Cottrell atmospheres (first step of aging treatment) [172];
- Formation of low temperature carbides (< 75 ˚C) or ε-carbides (> 75 ˚C) (which is called "precipitation stage" and it corresponds to the second step of aging treatment) [172];
- Grain boundary segregation, which modifies the Hall-Petch coefficient [164].

All these phenomena occur during the diffusion of carbon from FeC film into IF steel, however, the "precipitation stage" is highly dependent on the amount of carbon that surrounds Cottrell atmosphere and for this reason it is influenced by the level of pre-strain. In fact, pre-strains will create less carbon dense Cottrell atmospheres which can hinder the precipitation stage or limit the volume fraction of low temperature carbides.

Soenen et al. proved that the maximum increase in yield stress which can be obtained by Cottrell locking is 30 MPa and that the increase of yield stress is assumed to vary linearly with dislocation saturation [172]. The maximum strengthening due to Cottrell atmosphere can be predicted also by using the information of other two papers. In particular, De et al. [173] reported that the carbon amount necessary to saturate a dislocation density ρ (m^{-2}) in bcc ferrite can be calculated as:

$$[C]_{ppm} = 8.9x10^{-15} \times (\rho) \qquad \text{(eq. 7-1)}$$

Assuming the average dislocation density of a not-prestrained IF steel to be $1x10^{12}$ m^{-2}, the amount of carbon required to saturate these dislocations would be $[C]_{ppm} = (8.9x10^{-15}) x(1x10^{12}) = 8.9x10^{-3}$ ppm, which can be approximated to 0.01 ppm. In the not prestrained IF steels annealed in high vacuum (whose results have been presented in chapter 5), the carbon diffusing into the sample was shown to be much higher than 0.01 ppm. This means that dislocations are saturated and enough carbon is available to form precipitates. As some carbon will be segregated at grain boundaries, it is possible to separate the contribution due to Cottrell atmosphere from the contribution due to precipitation plus carbon segregation by subtracting the 30 MPa of strengthening due to Cottrell atmosphere from the total strengthening as shown in Table 7-10. The total strengthening is the average strengthening experimentally obtained for annealing in high vacuum (see chapter 5).

Specimen	Total strengthening [MPa]	Strengthening due to Cottrell atmosphere [MPa]	Strengthening due to segregation at grain boundaries and to precipitation at dislocations [MPa]
430 ˚C – 1h	88	30	58
530 ˚C – 1h	146	30	116
630 ˚C – 1h	192	30	162
710 ˚C – 1h	146	30	116

Table 7-10 - Separation of the contribution to strengthening coming from Cottrell atmosphere formation and precipitation plus grain boundary segregation for not-prestrained IF steel coated on both sides with 500 nm thick FeC film.

For pre-strained coupons, the density of dislocations that needs to be saturated is increased. The amount of carbon that is necessary to saturate them can be calculated from the engineering pre-strain that has been reached at unloading before the application of the FeC coating. In order to calculate the evolution of dislocation density when the IF steel is prestrained at 15% (eng. prestrain), the Kocks-Mecking model with the modification proposed by Bouaziz [174] can be used. According to this model, the evolution of dislocation as function of true strain is given by:

$$\frac{d\rho}{d\varepsilon} = M\left(\frac{k}{b}\sqrt{\rho} \times e^{\left(-\xi\sqrt{\rho}\right)}\right) \qquad \text{(eq. 7-2)}$$

where, M is a Taylor factor, b is the Burger vector of bcc ferrite, k is a parameter that takes into account the dislocations accumulation and ξ is a parameter related to dislocations annihilation. The equation above must be integrated performing a separation of variables to obtain the expression of dislocation density ρ as function of true strain ε. First of all, Mk/b can be grouped in a single parameter called h since they are all constants, so the equation becomes:

$$\frac{d\rho}{d\varepsilon} = h\sqrt{\rho} \times \exp\left(-\xi\sqrt{\rho}\right) \qquad \text{(eq. 7-3)}$$

and the integral to solve becomes:

$$\int \frac{e^{\xi\sqrt{\rho}}}{h\sqrt{\rho}} d\rho = \int d\varepsilon \qquad \text{(eq. 7-4)}$$

whose primitive is given by $\frac{2}{\xi \times h} e^{\xi\sqrt{\rho}} = \varepsilon + C$ with *C* as integration constant. In order to find the value of the constant of integration *C*, it must be considered that when the strain ε is zero, then the increase in dislocation density ρ is also zero, which gives *C = (2/(ξxh))*. So, the expression will be given by:

$$\frac{2}{\xi \times h} e^{\xi\sqrt{\rho}} = \varepsilon + \frac{2}{\xi \times h} \quad \text{(eq. 7-5)}$$

which can be rearranged to express ρ as function of the true strain ε as:

$$\rho = \rho_0 + \left[\frac{1}{\xi}\ln\left(1 + \frac{\xi \times h \times \varepsilon}{2}\right)\right]^2 \quad \text{(eq. 7-6)}$$

where, ρ_0 is the initial dislocation density, ξ is equal to $2.30\text{x}10^{-7}$ m as suggested by Bouaziz et al. to fit the work hardening curve of an IF steel [174], *h* is equal to $4.35\text{x}10^{8}$ considering a Taylor factor of 2.7, the Burger vector for bcc iron of $2.48\text{x}10^{-10}$ m.

Finally considering an initial dislocation density ρ_0 of $1\text{x}10^{12}$ m^{-2} and considering an engineering pre-strain of 15% which corresponds to a true strain of $\varepsilon_{true} = \ln(1+\varepsilon_{eng}) = \ln(1+0.15) = 0.14$, the dislocation density after prestrain will be:

$$\rho = 1\times10^{12} + \left[\frac{1}{2.30\times10^{-7}}\ln\left(1 + \frac{\left(2.30\times10^{-7}\right)\times\left(4.35\times10^{8}\right)\times\left(0.14\right)}{2}\right)\right]^2 = 8.28\times10^{13}\,m^{-2} \quad \text{(eq. 7-7)}$$

This dislocation density caused by the prestrain can be pinned using the following amount of carbon:

$$[C]_{ppm} = 8.9\text{x}10^{-15} \text{ x } (8.28\text{x}10^{13}) = 0.737 \text{ ppm} \quad \text{(eq. 7-8)}$$

This amount of carbon is almost 74 times higher than the amount of carbon necessary to lock dislocations without prestrain. For pre-strained coupons it is possible to separate the contribution to strengthening due to Cottrell atmosphere and the contribution to strengthening due to carbon segregation and precipitation at dislocations. The values are show in Table 7-11 considering the average of increase of yield stress after carbon diffusion and pre-strain for the specimens shown in section 7.2.1 Again the strengthening due to Cottrell atmosphere is supposed to be 30 MPa.

Specimen 15% prestrain	Total strengthening [MPa]	Strengthening due to Cottrell atmosphere [MPa]	Strengthening due to segregation at grain boundaries and to precipitation at dislocations [MPa]
430 ˚C – 1h	49	30	19
530 ˚C – 1h	71	30	41
630 ˚C – 1h	96	30	66
710 ˚C – 1h	90	30	60

Table 7-11 - Separation of the contribution to strengthening coming from Cottrell atmosphere formation and precipitation plus grain boundary segregation for prestrained IF steel coated on both sides with 500 nm thick FeC film

Comparing the strengthening due to segregation at grain boundaries and to precipitation at dislocations for not-prestrained and pre-strained coated coupons (last column of Table 7-10 and Table 7-11), it is evident that if the dislocation density is increased the strengthening caused by the precipitation of low temperature carbides at the dislocations is compromised. The pre-strain should not influence the segregation of carbon at grain boundaries since there is negligible change in grain size and since the grain boundaries are “filled” by carbon faster than the bulk of the grains given that the diffusion coefficient is 3 or 4 order of magnitudes higher for grain boundaries. For this reason strengthening due to the carbon segregation at grain boundaries is supposed to remain the same both for pre-strained and not- prestrained coupons.

Comparing the mechanical properties of pre-strained uncoated coupons with the pre-strained and coated coupons, carbon segregation at grain boundary at high temperatures (especially 710 ˚C) is important since carbon pins the movement of dislocations avoiding their rearrangement in lower energy configuration and preventing processes such as recovery and grain growth.

Finally, concerning the results shown in section 7.3 for strain-aging experiments performed on carbon diffused coupons, the following conclusions can be drawn:

- All Lüders plateaus are shortened after strain-aging because the pre-strain step increases the dislocations density.
- If we consider the specimen annealed at 430 ˚C - 1h and 530 ˚C - 1h which were both unloaded at the same level of strain, after aging, the Lüders plateau is shorter for the

430 ˚C - 1h than for the 530 ˚C - 1h (see Table 7-8). This is as expected since the specimen annealed at 530 ˚C - 1h contains more carbon than the specimen annealed at 430 ˚C - 1h, so even if the density of dislocation is increased during the first loading, the amount of carbon is still sufficient to lock most of the dislocations. On the other hand, the 430 ˚C - 1h has less carbon and an increase of dislocation density will cause less dense Cottrell atmosphere which will result in easier unpinning of dislocations and shorter plateau;

- The increase of stress measured after the aging treatment is around 40 - 45 MPa for all the specimens annealed at 530 ˚C - 1h, 630 ˚C - 1h and 710 ˚C - 1h (see Table 7-9). Since this strength is caused by carbon in solid solution used to pin dislocations and since this does not seem to change with the annealing temperature, it means that for these specimens, the dislocations were saturated with carbon.

Chapter 8 : Flash Annealing of Interstitial Free Steel coated with FeC film

The aim of this chapter is to investigate the possibility of optimizing the annealing process to obtain similar mechanical properties as those discussed in Chapter 5 but with shorter annealing time. Furthermore, it is believed that more interesting mechanical properties with suppression of Lüders plateau could be produced if a gradient of microstructures could be present through the thickness of the interstitial free (IF) steel. For example, having martensite or bainite close to the coated surfaces and a ferrite core in the center of the IF steel, could probably suppress Lüdering and increase the yield stress (YS) and the ultimate tensile strength (UTS). In order to obtain bainite and martensite, non-equilibrium cooling conditions are necessary. In the work presented in Chapter 5, these microstructures could not be obtained because both heating and cooling rates were very slow (12 ˚C/min for the heating and 12 ˚C/min above 400 ºC during cooling and 2-3 ˚C/min below 400 ºC for the cooling). This slow cooling ensures that enough time is left to obtain the equilibrium compositions predicted by the Fe-Fe_3C diagram. However, it is believed that a quenching in water could lead to the formation of low carbon martensite or low carbon bainite.

Furthermore, in Chapter 5 it was proven that the amount of carbon which could be diffused into the IF steel is limited by the transformation of the FeC film into cementite at temperatures equal or higher than 530 ˚C. This crystallization could be prevented and carbon diffusion could be increased by increasing the heating rate since carbon diffusion could be faster than the kinetics of crystallization of the FeC film. The amount of carbon that can diffuse into the IF substrate is of particular importance since to obtain martensite, a minimum amount of 0.1 wt% must be present, even if most of the commercial carbon steels that can be hardened to martensite contain between 0.5 wt% to 1.4 wt% of carbon [175].

Based on all these considerations, a series of experiments were conducted by performing “flash annealing”. In a first attempt, this procedure called “flash annealing” included a minor increase in heating rate and a major increase in cooling rate; while in a second attempt it included a major increase of both heating and cooling rates.

8.1. Flash annealing procedure with the annealing furnace

In a first attempt, to produce graded microstructures through the thickness of the IF sheet, the heating rate was increased to 46 ˚C/min (0.77 ˚C/s) (which is the maximum rate obtainable with the vacuum furnace used for the tests shown in chapter 5), while the cooling rate was increased to 130 ˚C/s using quenching in water. The heating rates were measured by placing a thermocouple in contact with the specimen during heating and cooling time. However, due to the design of the vacuum furnace it was not possible to perform a fast heating in vacuum and being able to remove fast the specimen to quench it in water, for this reason it was chosen to heat the furnace in air without high vacuum.

Since the specimens must be heat treated in vacuum, to prevent decarburization of the FeC film, as explained in chapter 5, they were sealed under vacuum inside quartz ampoules. These ampoules were used to perform "flash annealing" and during quenching they were smashed in water to quickly release and quench the specimen. The process for obtaining the glass ampoules is shown schematically in Figure 8-1.

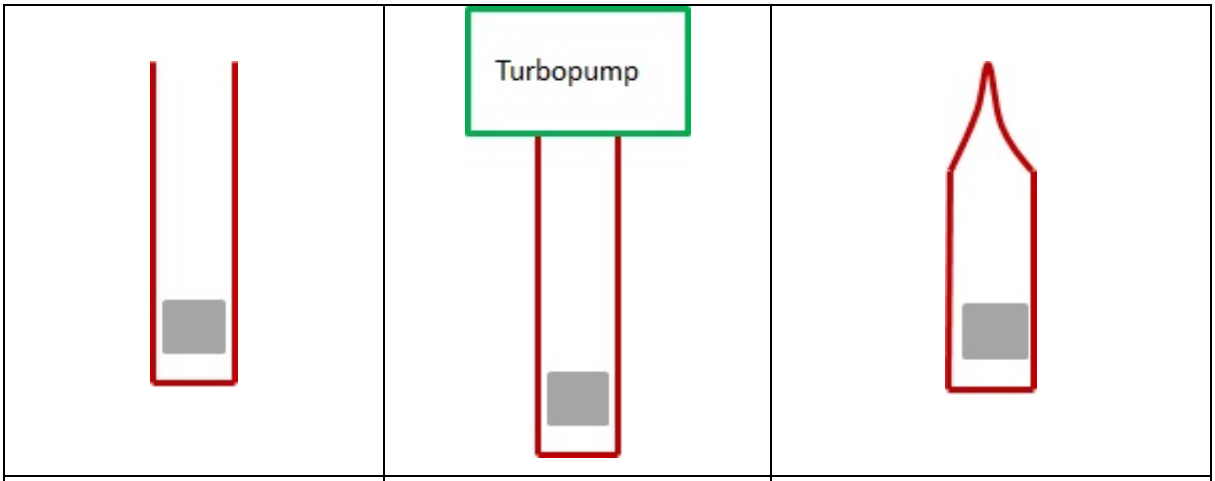

(a) The specimen (either a piece of IF steel or a tensile coupon) is placed inside the glass ampoule	(b) The glass ampoule is connected to the turbopump to obtain the proper level of vacuum	(c) The glass ampoules is sealed with vacuum inside by using an hydrogen-oxygen flame

Figure 8-1 - Sketch showing the sealing of IF steel samples inside quartz ampoules

Quartz was chosen as material for the ampoules since it is highly stable in the range of temperatures from 800 ˚C – 1200 ˚C which should be used to perform "flash annealing" of the coated IF steel. Sequence of images taken during the process of sealing of the glass ampoules are shown section G.1 of Appendix G.

Once the specimen had been sealed under vacuum inside the glass ampoule, the procedure to perform "flash annealing" was the following:

- Heat the furnace in air at 950 ˚C without any specimen inside;
- Leave the furnace for 1h at 950˚C so that all the system is stable at that temperature;
- Insert the glass ampoule containing the steel specimen under vacuum and leave it inside the furnace for 2 minutes and 30 seconds. The IF steel specimen is coated only on one side with 500 nm of FeC film in order to maximize the carbon gradient through thickness.
- Remove quickly the quartz ampoule and smash it with a hammer in water to quench the specimen.

The temperature of 900 ˚C – 950 ˚C was chosen because at that temperature the steel is fully austenitic. The time was chosen based on preliminary results obtained at the University of British Columbia (UBC), where "flash annealing" experiments of 1 min were done by using a Gleeble.

In the "flash annealing" tests performed at the University of Ottawa, the annealing time was increased to 2 min and 30 seconds because it was calculated that 1 minute and 30 seconds are necessary to obtain a temperature close to 900 ˚C in the inner wall of the quartz ampoule. Since the IF steel is placed inside the quartz ampoule, it will be mainly heated by conduction of the heat through the ampoule itself. The quartz ampoule is heated both by conduction and convection by the furnace, however the convection can be neglected since the air is not flowing inside the furnace. Details of the calculations are reported in Appendix G (section G.2).

In summary, by following this procedure, two specimens were tested:

- One specimen coated one side and annealed for 2 minutes and 30 s;
- One specimen coated one side and annealed for 1 minute and 55 seconds. For this specimen the annealing time was reduced to see if a higher carbon gradient through thickness could be obtained.

After the heat treatment, the microstructures of both specimens were analyzed. They were cold mounted and polished to 0.05 μm OPS solution before performing etching with 4% vol. Nital solution. The specimens were etched with Nital for 30 s, then they were rinsed with water, cleaned with ethanol and dried with air. In order to detect the presence of martensite,

an etching with 10% sodium metabisulfite ($Na_2S_2O_5$) solution was performed as well. The 10% sodium metabisulphite was prepared by dissolving 10 g – 12 g into 100 ml of water as described by Bramfitt [176]. Usually before performing the etching with sodium metabisulfite, the surface of the specimen is etched with Nital 2% volume for 5 seconds in order to increase the contrast between the grains. In Figure 8-2 and Figure 8-3 the microstructure of the specimen coated one side with 500 nm FeC film and annealed for 2 min and 30 s and then quenched in water is shown; while in Figure 8-4 the microstructure of the specimen annealed for 1min and 55 s and quenched in water is reported.

According to literature [176], Nital solution will attack ferrite and martensite but not austenite and it is not able to attack carbides even if it can be used to highlight the interface between the carbides and the matrix. On the other hand, sodium metabisulfite belongs to the category of tint etchants. These tint etchants are able to react with the constituents of the microstructure producing different colours. This colour is produced by a chemically deposited film on the surface of the steel, which is caused by sulfur ions which are released when the metabisulfite is placed in aqueous solution [176]. The sodium metabisulfite is able to produce a light coloration which can be enhanced using polarizing filter in the optical microscope. In particular, it will lightly colour ferrite, while it will clearly reveal bainite and as-quenched martensite [177].

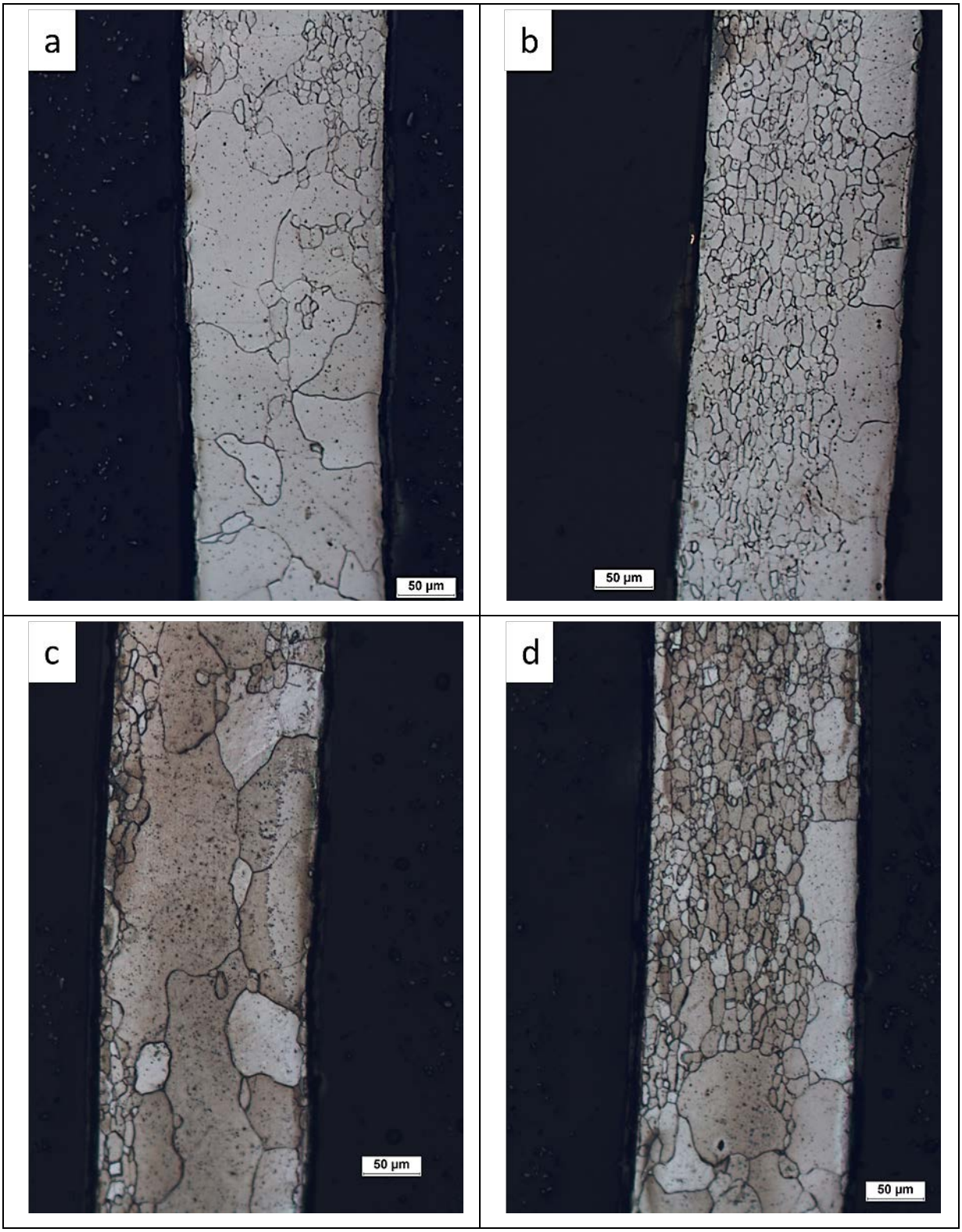

Figure 8-2 - Microstructure of the specimen coated one side and "flash annealed" at 950˚C for 2min and 30s. Etching performed with 4% vol. Nital solution. Images taken with optical microscope (magnification 20X). The images show zones with different grain sizes present in the same specimen after flash annealing.

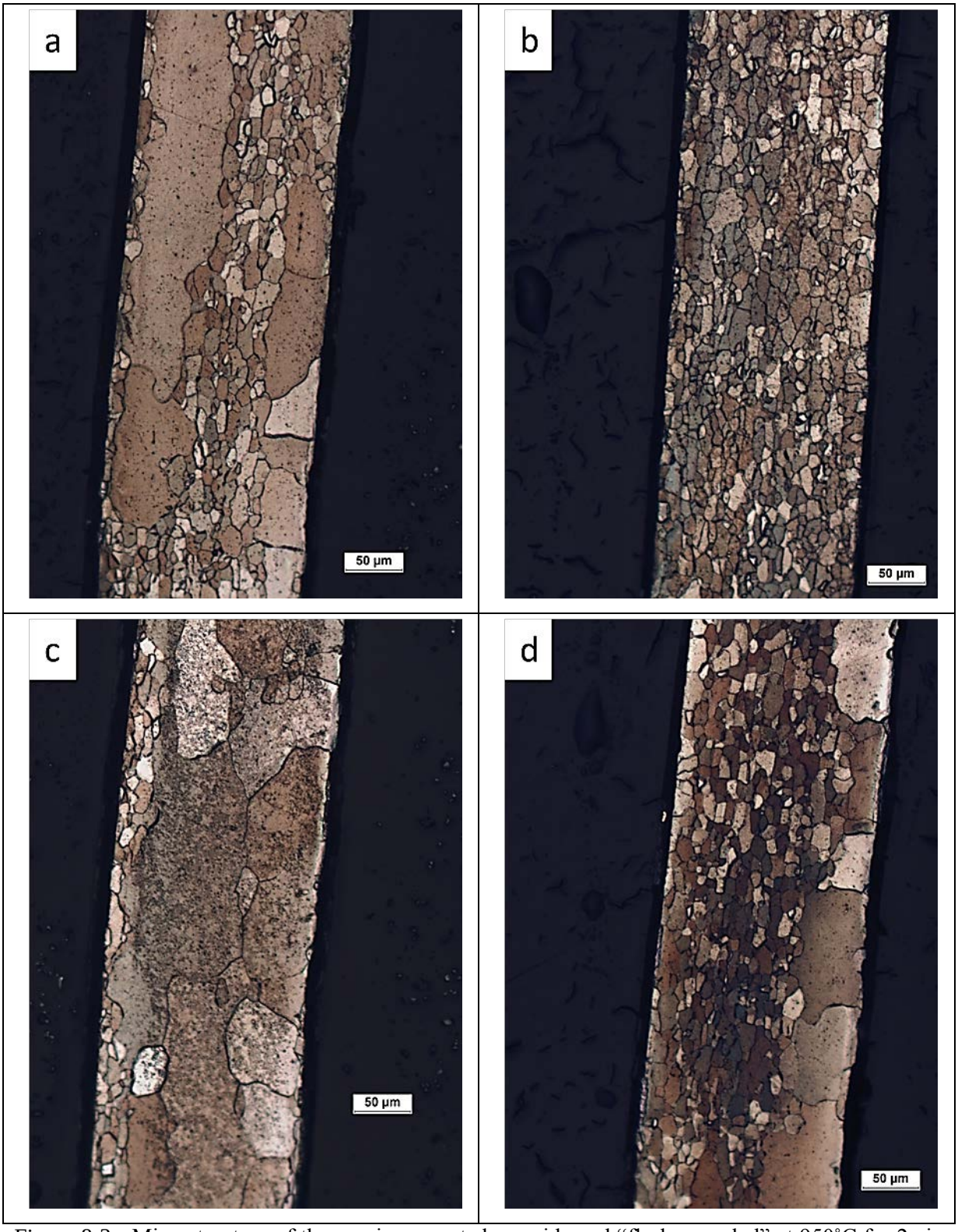

Figure 8-3 - Microstructure of the specimen coated one side and "flash annealed" at 950˚C for 2min and 30s. Etching performed with 2% vol. Nital solution and after with 10% sodium metabisulfite ($Na_2S_2O_5$) solution. Images taken with optical microscope (magnification 20X). The images show zones with different grain sizes present in the same specimen after flash annealing

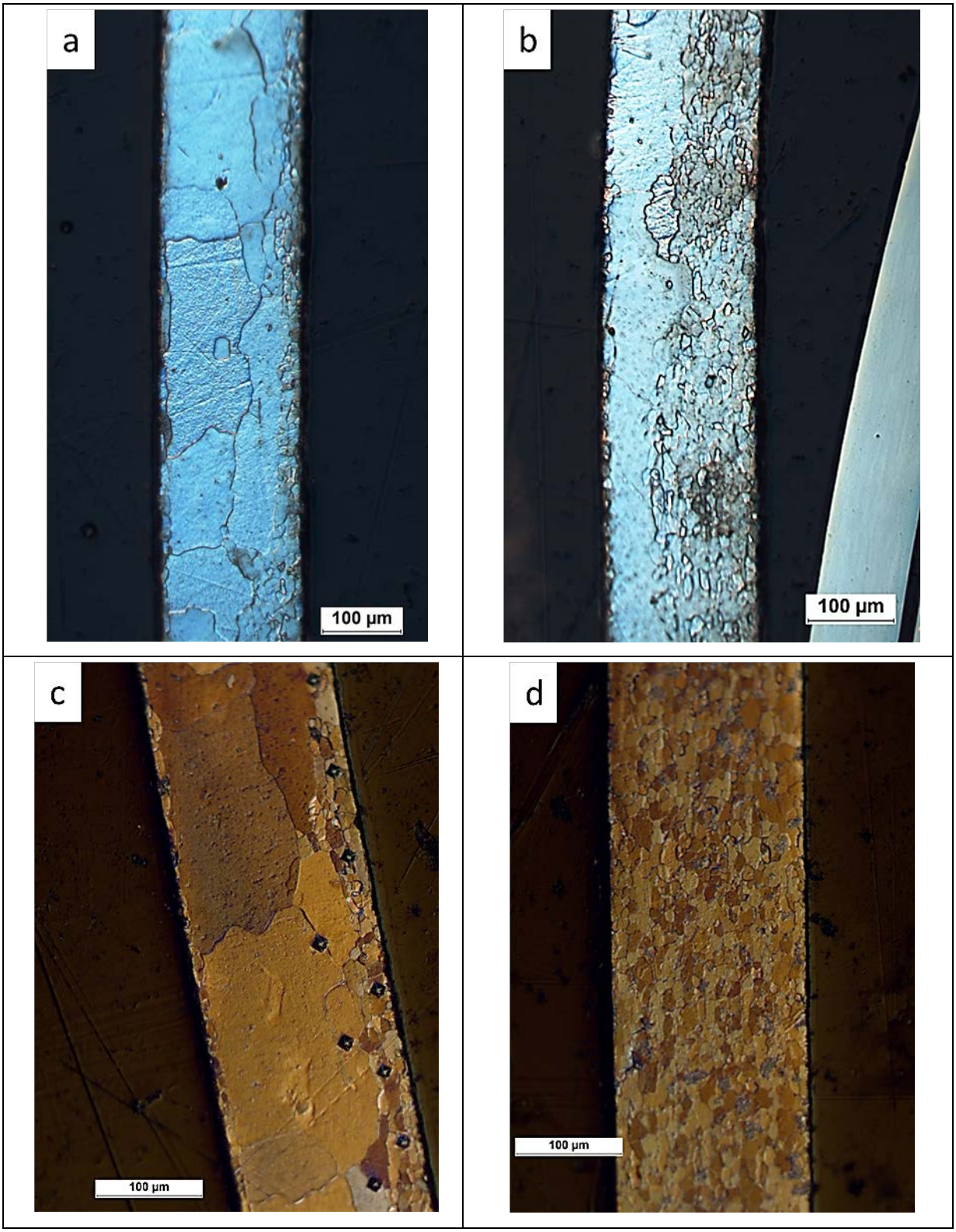

Figure 8-4 - Microstructure of the specimen coated one side and "flash annealed" at 950˚C for 1min and 55s: (a) and (b) etching performed with 4% vol. Nital solution (magnification 10X), (c) and (d) etching performed with 10% sodium metabisulphide (magnification 20X)

From the microstructures shown in Figures 8-2, 8-3 and 8-4 for both specimens, there is through thickness a gradient of grain size, with smaller grains closer to the coated side and bigger grains closer to the uncoated side. However, this microstructure does not seem to be uniform over the whole length of the specimen. Some zones of the thickness are completely made of small grains (see Figure 8-2 (b) and (d) and Figure 8-3 (b) and (d)), while others contain large grains (see Figure 8-2 (a) and (c), Figure 8-3 (c) and Figure 8-4 (c)). Furthermore, etching with sodium metabisulphite did not reveal any lath-like microstructure related to martensite.

Vickers hardness was measured through thickness to probe the presence of a carbon gradient. The specimens were repolished after etching by doing 10 - 15 minutes of 4000 SiC paper, 1h of 1 µm diamond polishing solution and 1h of 0.05 µm OPS suspension. The load applied during Vickers indentation was 25 g for 10 s. Summary of the hardness results are shown in Figure 8-6 for both specimens. Each point on the graph corresponds to 10 Vickers measurements taken at the same distance from the coated edge and then averaged.

The Vickers hardness measurements were taken in different zones along the length of the sample. These zones have been identified as A, B and C for the specimen “flash annealed” at 950 ˚C for 2 min and 30 s and as A and B for the specimen “flash annealed” at 950 ˚C for 1 min and 55 s. Once indented, the specimens were etched in the different zones to relate the Vickers microhardness with the microstructure. A schematic view of the sample of IF steel cold mounted in resin is shown in Figure 8-5.

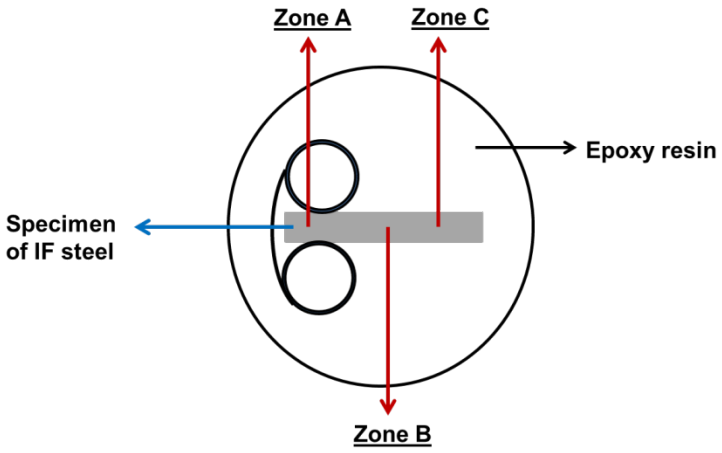

Figure 8-5 - Schematic view of the IF steel specimen cold mounted in resin, showing the different zones where hardness and images of the microstructure were taken for the specimen “flash annealed” at 950 ˚C for 2 min and 30 seconds

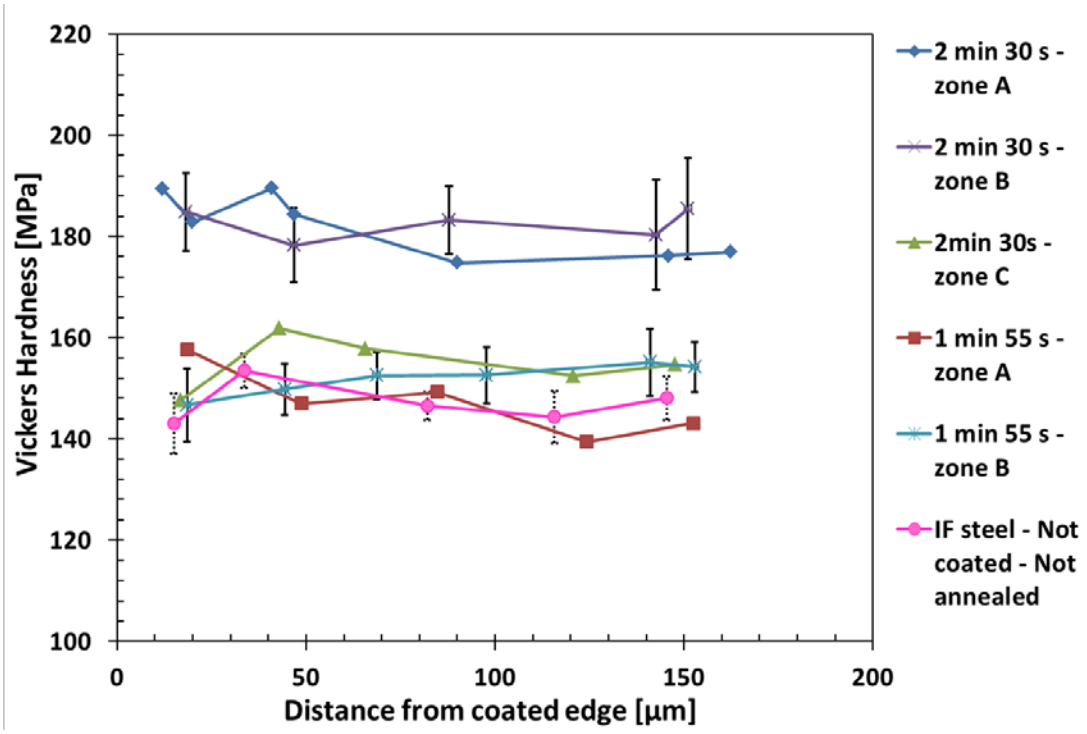

Figure 8-6 - Vickers hardness through thickness of specimens coated one side with 500 nm FeC film and "flash annealed" at 950 ˚C for 2 min - 30 s and 1 min - 55 s respectively. Vickers hardness of a piece of IF steel not coated and not annealed is reported for comparison. Error bars are shown for clarity only for some curves. For the other curves error bars are of the same order of magnitude of the bars already shown in the graph

As can be seen from Figure 8-6 the hardness through thickness for the specimen annealed for 2 minutes and 30 seconds depends also on the zone where it is measured. The specimen showed zones where grain growth was prevented by carbon diffusion and these two zones have higher hardness (zone A and B in Figure 8-7) while zone C showed grain growth and the hardness is lower (Figure 8-8).

The specimen flash annealed for 1 minute and 55 seconds showed small grains close to the coated side (see Figure 8-4 (a), (b), (c)) of the specimen and large grains (see Figure 8-4 (a), (b), (c)) on the uncoated side. However, also for this specimen, the microstructure was not uniform for the whole length of the IF strip. Moreover, its hardness through thickness, measured in two different zones (A and B), overlaps with the hardness of an interstitial free steel uncoated and not annealed. This means that in 1 minute and 55 seconds no relevant diffusion of carbon occurred. Pictures of its microstructure for the zones A and B after etching with Nital and sodium metabisulphite are shown in Figure 8-9 (a) and (b) and zone C in Figure 8-10.

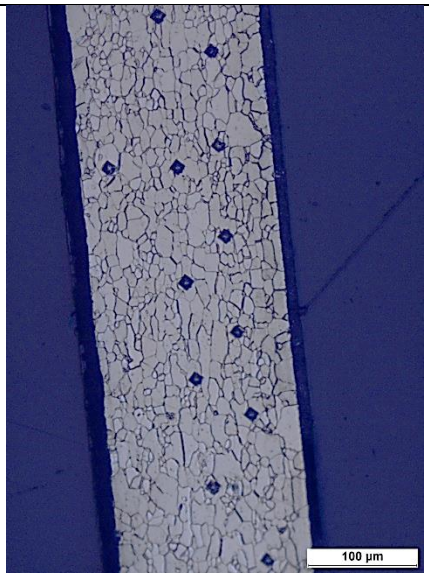

(a) Zone A of the specimen "flash annealed" in the furnace for 2 minutes and 30 seconds. Etching with 4% Nital was performed after indenting

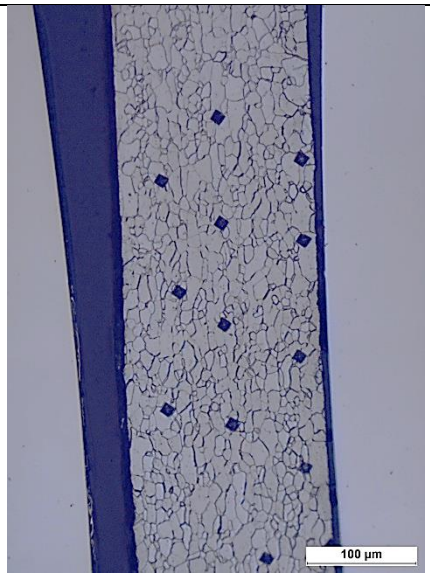

(b) Zone B of the specimen "flash annealed" in the furnace for 2 minutes and 30 seconds. Etching with 4% Nital was performed after indenting

Figure 8-7 - Microstructure of zone A (a) and zone B (b) of the specimen of IF steel coated one side with 500 nm thick FeC film and" flash annealed" at 950 ˚C for 2 min and 30 s

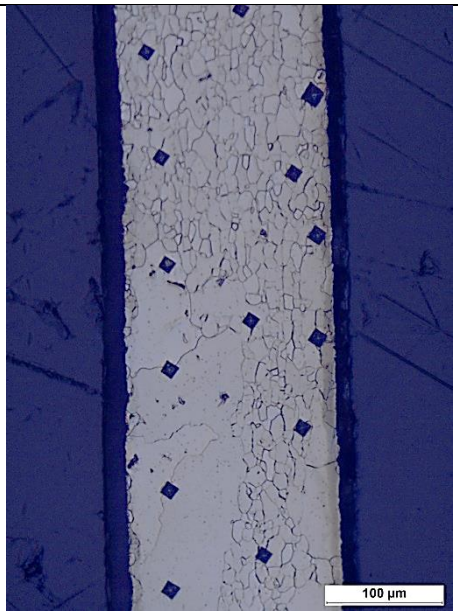

(c) Zone C of the specimen "flash annealed" in the furnace for 2 minutes and 30 seconds. Etching was performed after indenting

Figure 8-8 - Microstructure of zone C of the specimen of IF steel coated one side with 500 nm thick FeC film and" flash annealed" at 950 ˚C for 2 min and 30 s

(a) Zone A of the specimen "flash annealed" in the furnace for 1 minute and 55 seconds. Etching with 4% natal and sodium metabisulphite was performed after indenting (magnification 20X)

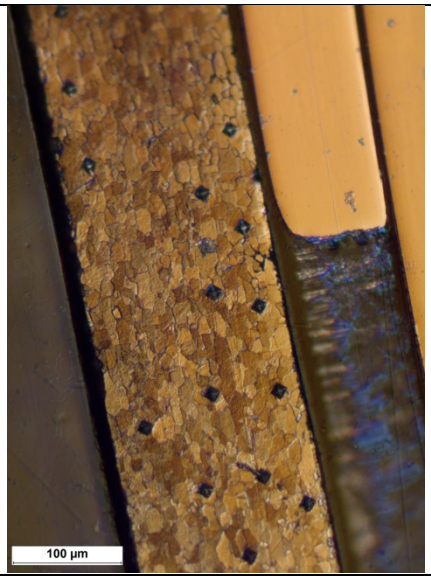

(b) Zone B of the specimen "flash annealed" in the furnace for 1 minute and 55 seconds. Etching with 4% natal and sodium metabisulphite was performed after indenting (magnification 20X)

Figure 8-9 - Microstructure of zone A of the specimen of IF steel coated one side with 500 nm thick FeC film and" flash annealed" at 950 ˚C for 1 min and 55 s

Zone C of the specimen "flash annealed" in the furnace for 1 minute and 55 seconds. Etching with 4% Nital and sodium metabisulphite was performed after indenting (magnification 20X)

Figure 8-10 - Microstructure of zone C of the specimen of IF steel coated one side with 500 nm thick FeC film and" flash annealed" at 950 ˚C for 1 min and 55 s

These results show that with this type of fast annealing performed in the furnace it is difficult to control the final microstructure since grain growth is taking place in some areas of the specimen and not others which resulted in non-uniform properties along the strip. The high variability of microstructure along the IF steel strip is caused by the slow heating rate, since grain growth is dependent on heating rate (especially in the austenite zone) [178]. As expected, if the heating rate is low, more time is allowed for grain growth to occur, compared to fast heating rates [178]. For this reason, it is believed that grain growth could take place before carbon has diffused along the thickness of the IF steel strip, compromising its mechanical properties, especially in one side coated coupons. Based on these observations, it was decided to perform flash annealing using induction heating which would allow higher heating rate and which would give more reproducible results.

In conclusion, from these tests of "flash annealing" performed using the vacuum furnace no marked carbon gradient through the thickness of the IF steel was obtained. However, some carbon diffusion occurred since an improvement in hardness compared to an uncoated and not annealed specimen was recorded in zones A and B for the specimen "flash annealed" at 950 ˚C for 2 minutes and 30 s. It is believed that the cause could be the low heating rate that can be obtained in the furnace when the specimen is sealed inside the quartz ampoule (10 ˚C/s). It was then chosen to use induction heating to obtain higher heating rates, while the quenching is still performed in water.

8.2. Flash annealing using induction heating

The main scope of these experiments was to investigate the possibility of obtaining a gradient of carbon through the thickness of the IF core. By tailoring heating rate and cooling rate a gradient in microstructure could be obtained through the formation of non-equilibrium phases such as bainite or martensite which would result in improved mechanical performances. Moreover, the presence of bainite or martensite through thickness could potentially suppress Lüdering. Some concepts of theory of induction heating are given in Appendix G (section G.3).

8.2.1. Induction Heating in steel processing

Most of the studies concerning the influence of induction heating on steel properties are quite recent. Ahn et al. [179] compared the microstructural evolution and the mechanical properties of low carbon steels tempered using induction heating with the one obtained by doing tempering in salt baths. According to literature [180], the main advantage of induction tempering over furnace tempering is speed; while induction can heat workpieces in minutes or even seconds, the furnaces require hours. Moreover induction tempering is perfect for inline integration and it is already widely employed by automotive companies to temper hardened components such as shafts, bars or joints [180].

Koizumi et al. [181] used super rapid induction heating and quenching to study the evolution and the mechanical properties of Fe-1.4%Cr-1%C perlitic steel.

From an industrial point of view, induction heating is well known for the heat treatments of billet since it can create high heat intensity very quickly, which will result in low processing time with high repeatability and high productivity [182]. Moreover, compared to other heating methods, it is considered more energy efficient with shorter start-up and shut-down times [182]. Induction heating plant can be used even with protective atmospheres in case oxidation of the parts has to be avoided [182].

8.2.2. Experimental Approach for Induction Heating on IF steel

As first approach, a thermocouple type K (Ni-Cr (Cromel)) was used to measure the temperature obtained during an induction heating cycle. The inductance of the induction heater was changed so that, using the thermocouple, it was possible to detect the temperature of 1000 ˚C in 10 s (which would correspond to a heating rate of 100 ˚C/s) by setting the power of the induction heater at 60%. Once the 1000 ˚C was reached, in order to not increase further the temperature, the power was lowered to 21-23% and the temperature in the thermocouple stabilized to 900 ˚C. In literature, it is reported that the color of the surface of some metals (in particular carbon steels) can be related to their temperature [183]. The following table reproduced from the “Handbook of Induction Heating” [183] shows the correlation between the surface colors of carbon steel and temperatures during typical annealing and hardening treatments.

Temperature (˚C)	Color
560-680	Dark red
700-780	Cherry red
800-880	Bright cherry
900-980	Orange red
980-1100	Orange yellow
1100-1250	Bright yellow
1280	White

Table 8-1 - Correlation of surface colors and temperature for carbon steels [183]

For the induction heating tests presented in this chapter, when the thermocouple was measuring 950 ˚C, the color of the piece of steel was bright cherry or orange red. However, the reading of the thermocouple can be inaccurate since the metallic material can be influenced by the magnetic field especially at high frequency. For this reason infrared pyrometers are preferred to measure the temperature. They are capable of measuring the radiation emitted by the heated object and convert it to temperature. First of all, the emissivity of the object has to be set in the pyrometer in order to measure properly the temperature. The emissivity of the Interstitial Free steel used in this PhD project was determined experimentally by using a pyrometer connected to a thermocouple. A piece of IF steel was heated by placing it above a stove, and a thermocouple was measuring its temperature, while in parallel the pyrometer was measuring the emitted radiation. The emissivity of the pyrometer was adjusted automatically to fit the temperature recorded by the thermocouple. The value found for the IF steel is 0.50 and this was used during induction heating measurements. Once the emissivity of the steel was determined, in order to measure the temperature during induction heating, the pyrometer “IGA 15 plus” of “LumaSense technologies” was used. This pyrometer can measure a minimum temperature of 250 ˚C up to a maximum of 1800 ˚C. When placed at a distance of 800 mm from the object whose temperature needs to be measured, the spot size is 4 mm; however, a close-up lens can be installed so that at a measuring distance of 250 mm, and the spot size on the specimen is only 1.25 mm. If the close-up lens is installed, the emissivity needs to be corrected according to the following equation: $EMI = 0.92 \times EMI_{object}$, so for the IF steel used for the experiment, the emissivity needs to be adjusted to $(0.92 \times 0.50) = 0.46$ if the close-up lens has to be used. Based on the measurements performed with the pyrometer, the temperatures shown in Table 8-2 were measured for the induction heating cycle.

Device	60% power	23% power
Thermocouple	950 ˚C in 10 s	900 ˚C
IR pyrometer with close-up lens (EMI = 0.46) – first measurement	1100 ºC - 1150 ˚C in 10 s	820 ˚C
IR pyrometer with close-up lens (EMI = 0.46) – second measurement	1134 ˚C in 10 s	840 ˚C
IR pyrometer without close-up lens (EMI = 0.50)	1196 ˚C in 10 s	780 ˚C

Table 8-2 - Measurement of temperature of induction heating treatment with thermocouple and with pyrometer

Based on the measurements performed with the pyrometer, the heating rate was around 115 ˚C/s and the specimen was held for different times at 820 ˚C. When the power is changed from 60% to 21 - 23%, the temperature drops to 820 ˚C – 830 ˚C in 5 seconds.

The following configurations of specimens were tested following the procedure described above. One series of specimens was coated only on one side with a 500 nm thick FeC film containing 30 at% of carbon, while another series of specimens was coated on both sides with a 500 nm thick FeC film again containing 30 at% of carbon. The power of the induction heater was set to 60% for 10 seconds so that a heating rate of 115 ˚C/s would be obtained; the power was then lowered between 21 - 23% to set the temperature at 820 ˚C. In Figure 8-11 a schematic view of the experimental set-up is shown, while in Figure 8-12 the heating and cooling cycles are reported. Once the specimen had been heat treated, it was quenched in water with a cooling rate of 130 ˚C/s. The cooling rate was measured with a thermocouple brought to 941 ˚C and then quenched in water and reaching 35 ˚C in 7 seconds.

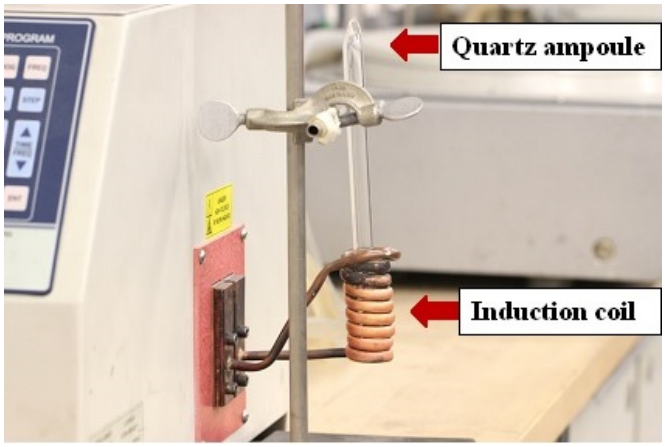

Figure 8-11 - Set-up of induction heating experiment

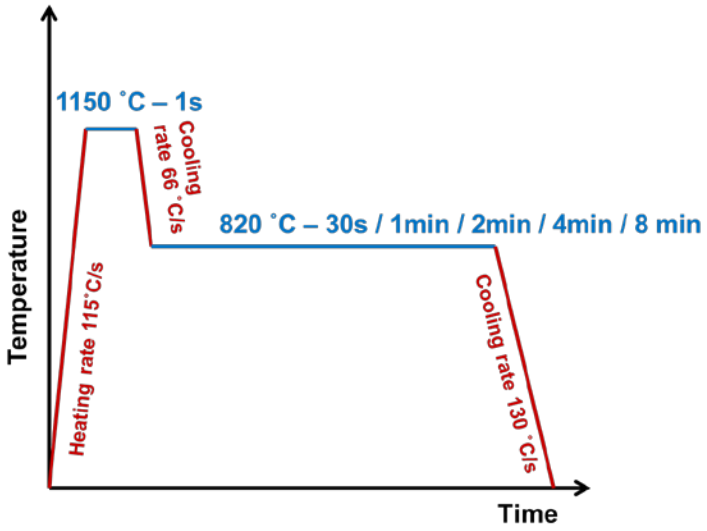

Figure 8-12 - Heat treatment cycle used for induction heating experiments

By knowing the dimensions of the induction coil and the current flowing through it, the magnetic field strength inside a coil can be calculated according to the following equation [15]:

$$H = \frac{N \cdot I}{l} \qquad \text{(eq. 8-1)}$$

Where, N is the number of turn (in our case 8.5), I is the current expressed in Ampere , and l is the length of the coil. In the experiments presented in this chapter, the current was 70 A when the power was set at 60% and it was 50 A when the power was lowered to 22%. So, the magnetic field strength will be:

$$H = \frac{N \cdot I}{l} = \frac{(8.5 \cdot (70))}{72 \cdot 10^{-3}} = 8264 \frac{A}{m} \qquad \text{for the power set at 60\%}$$

$$H = \frac{N \cdot I}{l} = \frac{(8.5 \cdot (50))}{72 \cdot 10^{-3}} = 5903 \frac{A}{m} \qquad \text{for the power set at 22\%}$$

Once the strength of the magnetic field is known, the magnetic flux density in vacuum (inside the quartz ampoule) can be calculated by using the following equation [15]:

$$B_0 = \mu_0 H \qquad \text{(eq. 8-2)}$$

Where, μ_0 is the permeability in vacuum and it is equal to 1.257×10^{-6} henry/m, while H is the magnetic field strength. By doing the calculation for the present induction heating experiments, the intensity of the magnetic field is obtained.

$$B_0 = \mu_0 H = \left(1.257 \cdot 10^{-6}\right) \cdot \left(8264\right) = 0.0104T = 10.4mT \quad \text{for the power set at 60\%}$$

$$B_0 = \mu_0 H = \left(1.257 \cdot 10^{-6}\right) \cdot \left(5903\right) = 0.0074T = 7.4mT \quad \text{for the power set at 22\%}$$

8.2.3. Results from Induction Heating Experiments: carbon gradient through the thickness of the Interstitial Free steel

A piece of IF steel coated on one side with a 500 nm thick FeC film was sealed inside a glass ampoule at a vacuum of 5.6×10^{-6} Torr. The frequency of the induction heating was around 200 KHz and the power was set to 60%. Once a temperature of 1150 ˚C was reached, the power was set at 21%. The specimen was left inside the coil for 30s and quenched in water.

An uncoated piece of IF steel was also prepared following the same annealing procedure after having been sealed under vacuum in a glass ampoule (vacuum level 4.0×10^{-6}Torr). Both specimens were cold mounted and polished to a mirror finishing to perform Vickers Hardness measurements (25 g load for 10s) and to etch the surface to observe the microstructure. The polishing procedure was the following:

- 600 SiC paper to remove the epoxy resin from the specimen (not more than 10 minutes);
- 1500 SiC paper for 10 minutes;
- 4000 SiC for 30 minutes;
- 1 μm diamond suspension for 1h;
- 0.05 μm OPS suspension for 1h;

In Figure 8-13, Vickers hardness measurements taken through thickness for the one side coated coupon and for the uncoated coupon are shown. The gradient of hardness is obvious for the coated coupon, with a hardness ranging from 240 MPa close to the coated side to around 160 MPa for the uncoated side.

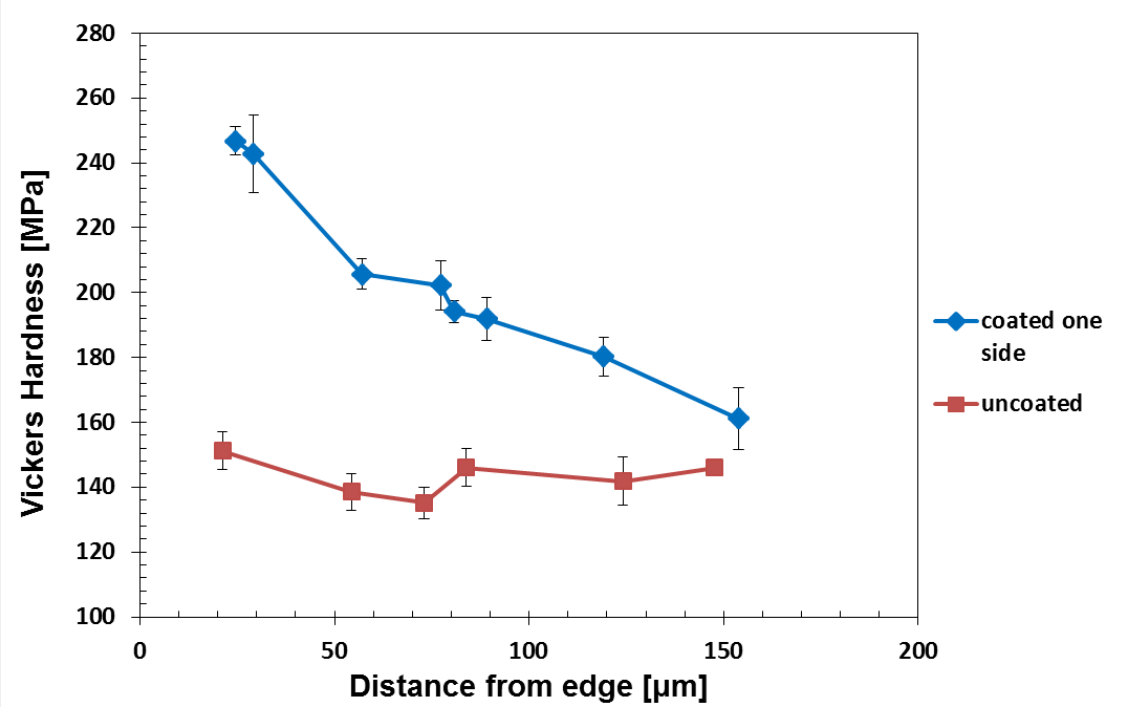

Figure 8-13 - Vickers hardness of one-side coated coupon and uncoated coupon both induction heated at 1150 ºC for 1 second and then at 820 ˚C for 30 seconds. Each point in the curve corresponds to at least 10 measurements. Error bars representing the standard deviation are shown

The microstructure of the one side coated specimen after etching with 4% vol. Nital solution is shown in Figure 8-14 (a), (b) and in Figure 8-15 (a) and (b).

(a) Bottom side was coated with 500 nm FeC film before performing induction heating at 820 ˚C – 30 s. The edge of the top side in the image is not coated. The image has been taken after etching with 4% vol Nital solution for 30 s.

(b) Close view of the Nital etched microstructure of the coated side. The grains close to the coated surface show some dark lines.

Figure 8-14 - Thickness of the one side coated coupon. Bottom side was coated with 500 nm FeC film before performing induction heating at 1150 ºC for 1 s and then at 820 ˚C for 30 s: (a) view of the whole thickness; (b) close view of the grains close to the coated side of the specimen

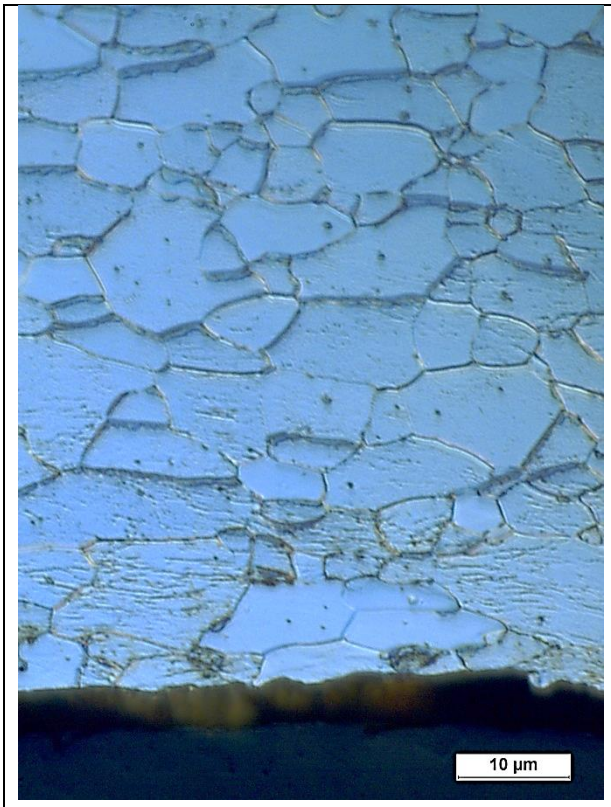

(a) Another close view of the Nital etched microstructure of the coated side. The grains close to the coated surface show some dark lines

(b) Close view of the not coated edge after Nital etch

Figure 8-15 - Thickness of the one side coated coupon. Bottom side was coated with 500 nm FeC film before performing induction heating at 1150 ºC for 1 s and 820 ˚C for 30 s: (a) view of the grains close to the coated surface; (b) close view of the grains close to the uncoated side of the specimen

The same one-side coated specimen was also etched with 15% sodium metabisulphite to look for the presence of martensite or bainite (Figure 8-16). For the one side coated coupon after Nital etching, the grains close to the coated edge revealed some lines which were not present close to the uncoated edge. By etching with the sodium metabisulfite, only a light coloration was obtained and all the grains looked very similar, meaning that the main phase is ferrite and that no retained austenite is present. To further prove this statement, EBSD was performed on this coupon at the center of the thickness by probing an area of 65 µm x 65 µm and setting a step of 0.3 µm for the analysis. The Forward Scatter Detector (FSD) image of the analyzed area is shown in Figure 8-17. The small holes which appear in some of the grains are pitting caused by the OPU polishing solution.

Figure 8-16 - Etching of the one side coated coupon with 1% vol. Nital and 15% sodium metabisulphite. The FeC coated side is on the bottom of the picture while the not-coated side is at the top of the picture

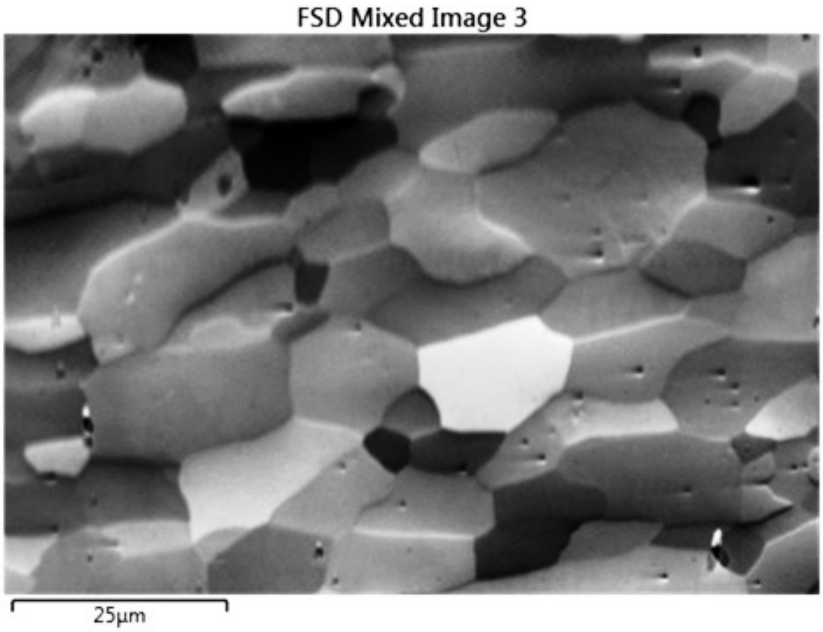

Figure 8-17 – Forward Scatter Detector (FSD) Image of the area analyzed by EBSD of the one side coated IF coupon induction heated at 1150 ºC for 1 s and then at 820 ˚C for 30 s

From the analysis of the phase map (Figure 8-18), the following percentages were identified: 99.43% is bcc ferrite, while 0.04% is fcc austenite. The phase map is shown in the following figure. The few retained austenite seems to be present at grain boundaries.

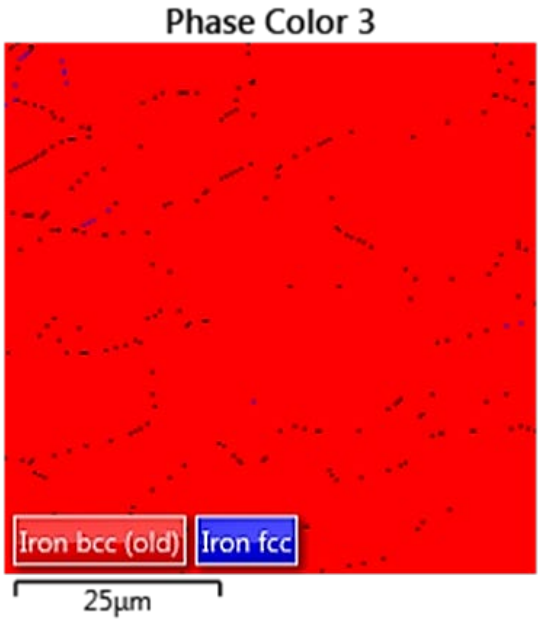

Figure 8-18 - Phase map obtained by EBSD analysis on a one side coated coupon induction heated at 1150 ºC for 1 s and then at 820 ˚C for 30 s

The same etching procedure was applied to analyze the microstructure of the uncoated coupon. The results are shown in Figure 8-19 (a) and (b), and Figure 8-20. With uncoated coupon it is difficult to obtain a good contrast between grains and grain boundaries during etching since there is no carbon that has diffused inside the specimen. Moreover the structure is fairly uniform from one edge to the other. No lines have been detected inside the grains and the microstructure is uniform in the whole thickness. Some grains appear less etched than other grains due to their crystallographic orientation.

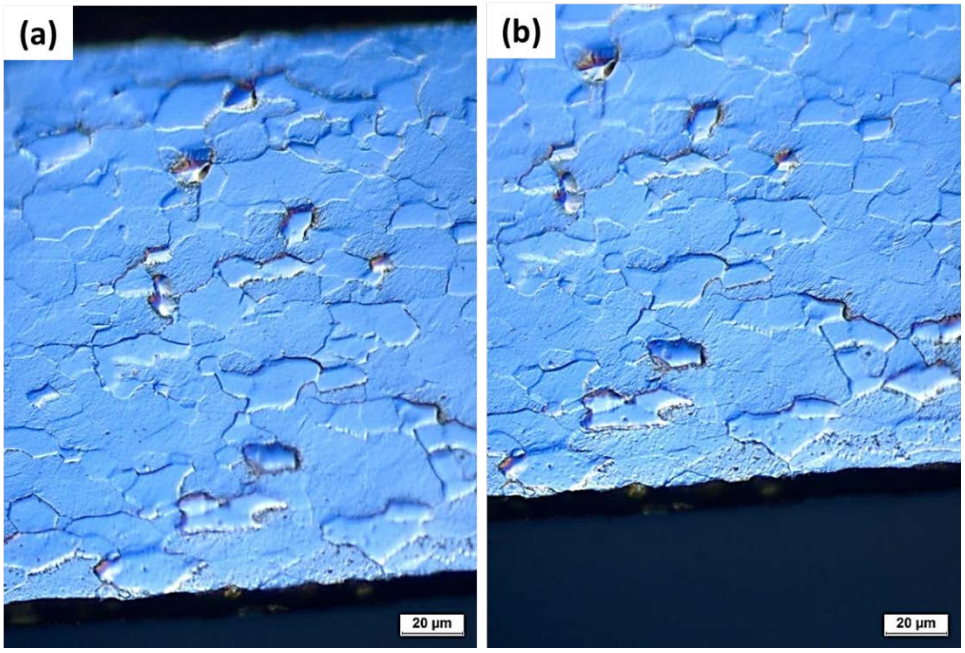

Figure 8-19 - Etching with 4% vol Nital solution of the uncoated coupon induction heated at 1150 ºC for 1 s and then at 820 ˚C for 30 s: (a) whole thickness, (b) view close to one of the edges

Figure 8-20 - Etching of the uncoated and induction heated coupon with 15% sodium metabisulphite

In order to verify that the mechanical properties of the IF substrate do not change during the induction heating, further tests on uncoated coupons of IF steel were performed. In

particular, one sample was induction heated at 1150 ºC for 1 second and then at 820 ˚C for 1 minute, while another specimen was induction heated at 1150 ºC for 1 second and then at 820 ˚C for 4 minutes. After the treatment, the specimens were cold mounted in epoxy resin and the Vickers hardness profile through thickness was assessed after polishing to mirror finish. The values of hardness were compared with the hardness through thickness of an uncoated and not-annealed IF steel. They were compared as well with the hardness obtained for one side coated coupon induction heated first at 1150 ºC for 1 second and then at 820 ˚C for 30 seconds and a one side coated coupon induction heated at 1150 ºC for 1 second and then at 820 ˚C for 4 minutes.

The plot showing the Vickers hardness through thickness is reported in Figure 8-21 for the coated coupon, the coated side is starting on the left of the graph where the hardness is higher. The numerical values plotted in the graph are reported in Appendix G (section G.4, Table G- 2) with the corresponding standard deviation. Each point on the graph represents the average of 10 measurements.

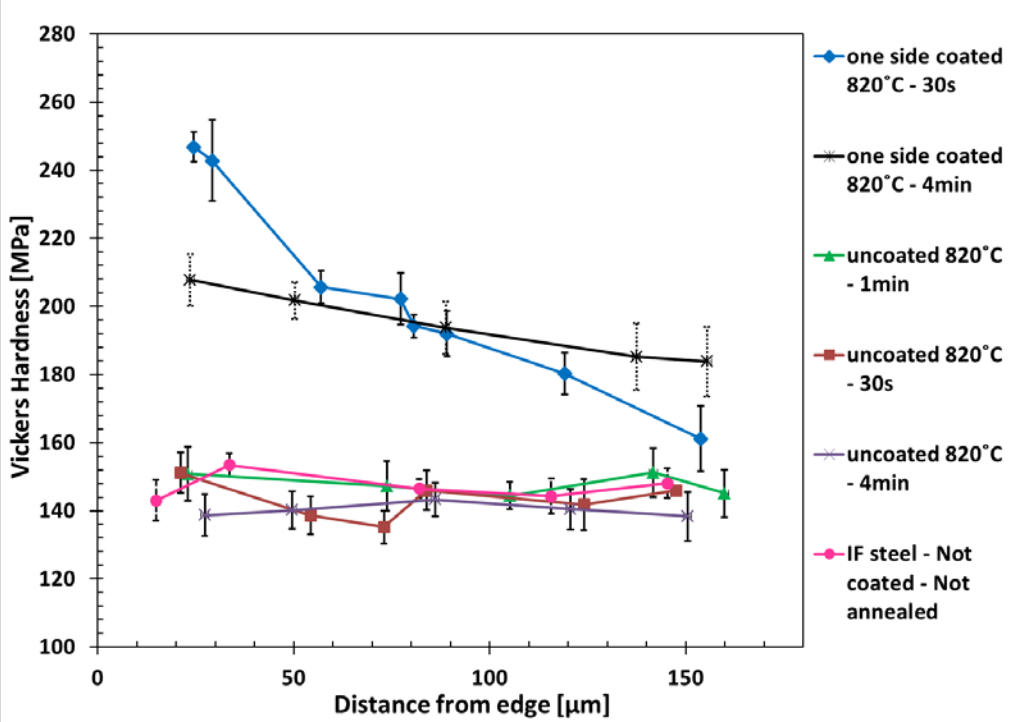

Figure 8-21 - Vickers hardness through thickness for one side coated coupons induction heated at 1100 ºC - 1150ºC for 1 second and then induction heated at 820 ˚C for 30 seconds and 4 minutes. Vickers hardness of uncoated and not-annealed IF steel and for uncoated IF steel induction heated at 1100 ºC - 1150ºC for 1 second and then induction heated at 820 ˚C for 30 seconds, 1 minute and 4 minutes.

From the results presented in Figure 8-21, one can see that the IF steel has mechanical properties which do not change during induction heating, proving that the increase in mechanical properties and the gradient profile observed through thickness is due to carbon diffusion. As expected, the carbon gradient is higher for shorter annealing times of 30 seconds compared to annealing times of 4 minutes, where the carbon has time to diffuse through the bulk of more grains. If the hardness curves shown in Figure 8-22, for specimens induction heated for 30s and 4 minutes are compared, it can be concluded that after 4 minutes, the FeC film is not supplying more carbon since a smoothening of the gradient is occurring due to redistribution of carbon through the whole thickness of the sample.

It is possible to predict the thickness of the specimen that will be affected by carbon diffusion by using the equation $x = \sqrt{D \times t}$, where D is the diffusion coefficient and t is the time of the heat treatment. For the calculation D was considered to be the diffusion coefficient of carbon into austenite which is given by:

$$D = \left(2.3 \times 10^{-5}\right) \times \exp\left(-\frac{\left(148 \times 10^{3}\right)}{(8.31) \times (T)}\right) \qquad \text{(eq. 8-3)}$$

where, the pre-exponential factor is in m^2/s, while the activation energy of $148x10^3$ is in J/mol, R is the gas universal constant and T is the temperature in degree Kelvin. First, the depth affected by carbon diffusion when the specimen is kept at 1150 ˚C for 1 second is obtained. Then, the depth for a temperature equal to 820 ˚C for 30 s, 1 min, 2 min, 4 min and 8 min is calculated. In Table 8-3, the value of the diffusion coefficient of carbon through the austenite grains for the different temperatures and the corresponding diffusion depth are reported. The time "*t*" in equation $x = \sqrt{D \times t}$ must be expressed in seconds.

Temperature - time	**Diffusion coefficient [m^2/s]**	**Depth affected by carbon diffusion [µm]**
1150 ˚C – 1 s	$8.44x10^{-11}$	9.2
820 ˚C – 30 s	$1.93x10^{-12}$	7.6
820 ˚C – 1 min	$1.93x10^{-12}$	10.8
820 ˚C – 2 min	$1.93x10^{-12}$	15.2
820 ˚C – 4 min	$1.93x10^{-12}$	21.5
820 ˚C – 8 min	$1.93x10^{-12}$	30.42

Table 8-3 – Depth affected by carbon diffusion in austenite

One should however note that the values calculated above consider diffusion through the grains, but diffusion can occur faster through grain boundaries. Considering the diffusion coefficient of carbon through grain boundaries of austenite as two orders of magnitude faster than the diffusion coefficient shown above, the depth affected by diffusion will be higher. The values are listed in the following table.

Temperature - time	**Diffusion coefficient [m^2/s]**	**Depth affected by carbon diffusion [μm]**
1150 ˚C – 1 s	$8.44x10^{-9}$	92
820 ˚C – 30 s	$1.93x10^{-10}$	76
820 ˚C – 1 min	$1.93x10^{-10}$	108
820 ˚C – 2 min	$1.93x10^{-10}$	152
820 ˚C – 4 min	$1.93x10^{-10}$	215
820 ˚C – 8 min	$1.93x10^{-10}$	304

Table 8-4 - Depth affected by carbon diffusion in austenite through grain boundaries

8.2.4. Results from Induction Heating Experiments

8.2.4.1. Tensile tests on one side and both sides coated coupons

A first serie of tensile tests was performed on uncoated tensile coupons of IF steel, in particular one uncoated coupon was austenitized at 1150 ºC for 1 second as described by the temperature profile shown in Figure 8-12 and then kept at 820 ºC for 2 minutes, while another uncoated coupon was austenitized following the same procedure but it was kept at 820 ºC for 4 minutes. Both specimens were quenched in water. The resulting engineering stress-strain curves are shown in Figure 8-22. From the curves it is seen that under induction heating, the yield stress of the IF steel substrate is stable and no change is detected; however for a 2 minutes long induction heat treatment, an increase in UTS of 40 MPa was recorded. This increase of UTS value is significant and in the previous experiments it was reached only for annealing in high vacuum furnace of coated coupons at temperatures of 530 ºC – 1h or 710 ºC – 1h. On the other hand, if the induction treatment is prolonged to 4 minutes, the UTS increase is only 18 MPa. This increase is still higher than the standard deviation associated to the UTS of a not-heat treated IF steel (which is ± 8 MPa). To understand the reason for the high UTS obtained after 2 minutes of heat treatment, the microstructure of

both induction heated coupons was analyzed with the optical microscope after etching with 4% vol. Nital solution and after etching with 10-12% sodium metabisulphite.

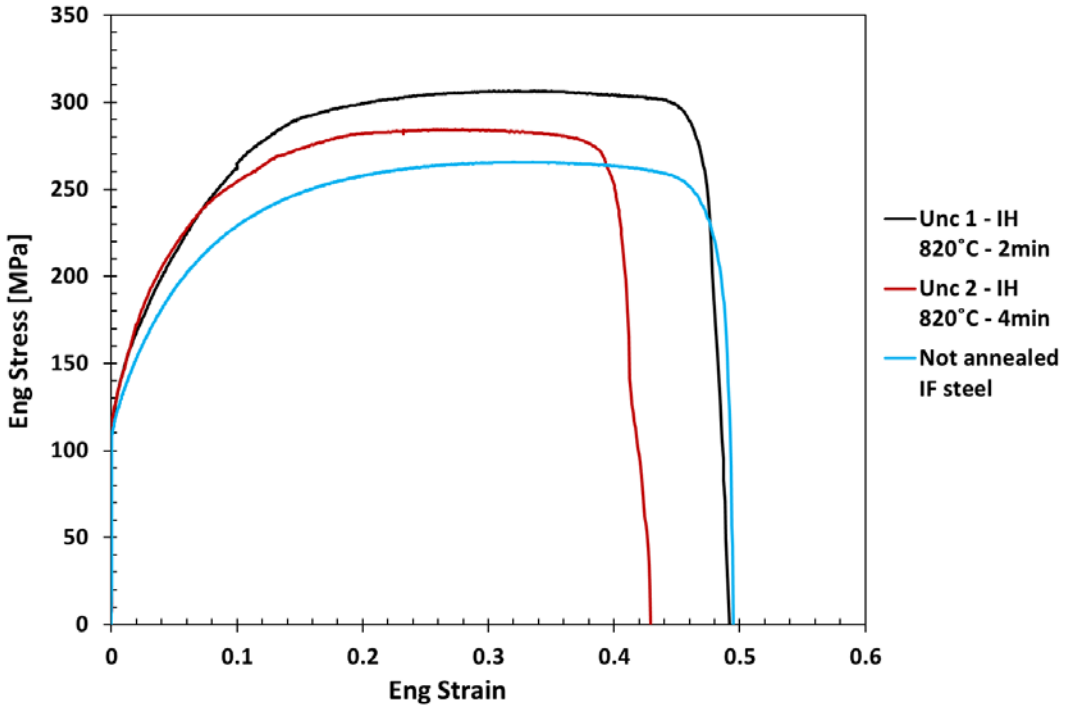

Figure 8-22 - Engineering stress-strain curves of a not-annealed IF steel and of uncoated coupons induction heated at 1100 ºC – 1150 ºC for 1 second and then induction heated at 820 ºC for different times

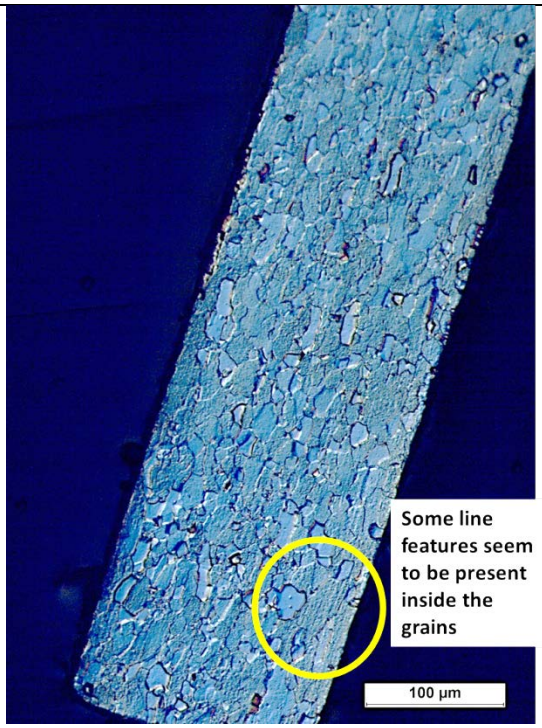

(a) Microstructure of the uncoated IF steel induction heated at 820 ºC for 2 minutes

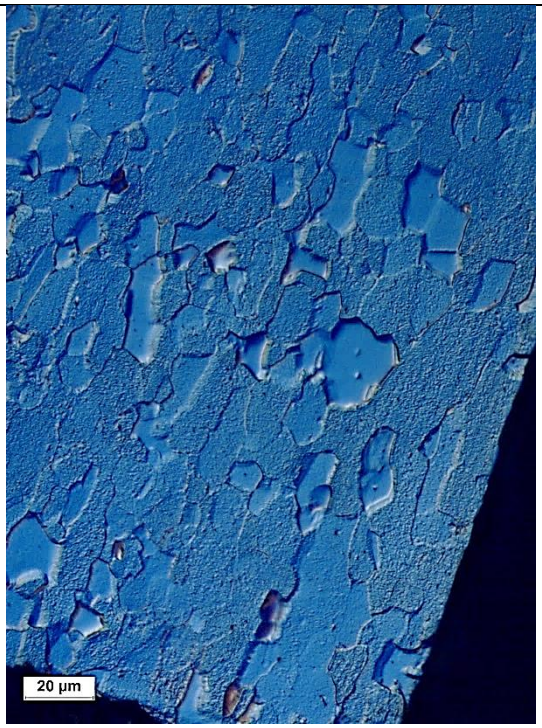

(b) Closer view of the grains marked with a circle in (a)

Figure 8-23 - Microstructure of the uncoated IF steel induction heated at 1100 ºC – 1150 ºC for 1 second and then induction heated at 820 ºC – 2 minutes (etching performed with 4% vol Nital solution)

From the microstructure shown in Figure 8-23, it seems that line features are present in some grains, however, at a closer view they are not easy to identify. Nevertheless, the etched surface looks different from the uncoated IF steel which was induction heated just for 30 s (Figure 8-19 (a) and (b)), since for the 2 minutes coupon, some grains show more roughness after etching as if they had a preferred orientation compared to other grains whose surface looks smoother. In the 30 seconds treatment, the same texture is not discerned.

In the microstructure of the uncoated coupon induction heated at 820 ºC for 4 minutes, no texture could be discerned (Figure 8-24 (a) and (b)). In Figure 8-25 the etching of both coupons with sodium metabisulphite is shown where as expected no martensite or lath structure is found.

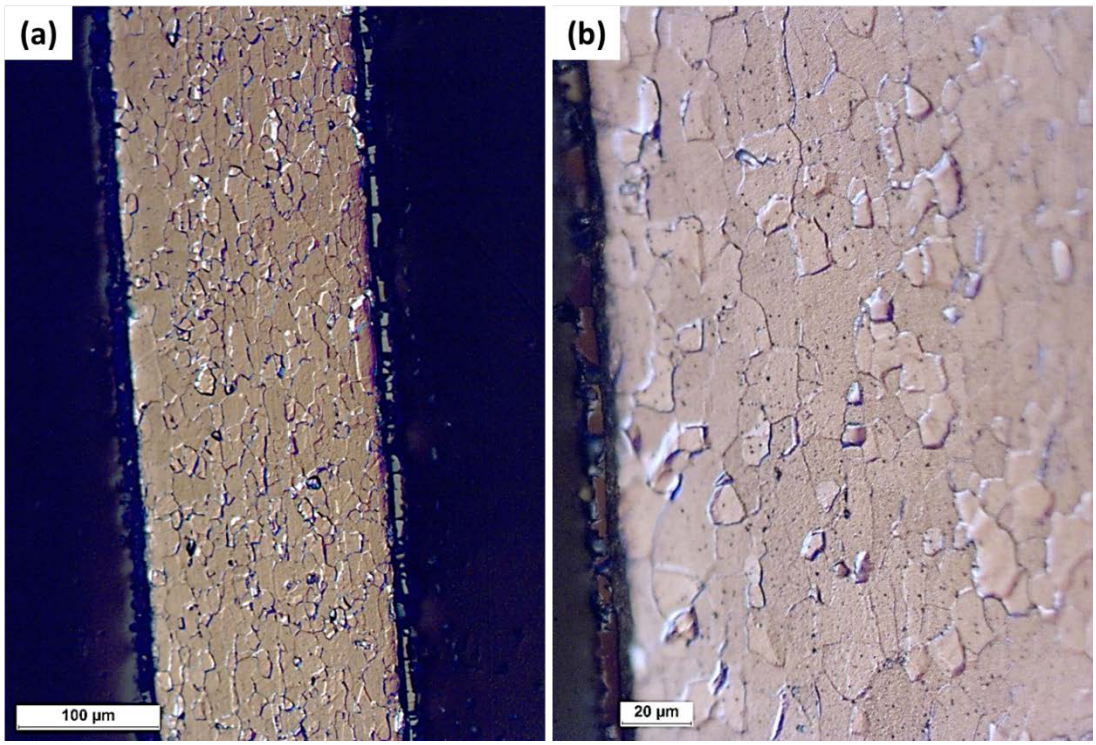

Figure 8-24 - Microstructure of the uncoated IF steel induction heated at 1100 ºC – 1150 ºC for 1 second and then induction heated at 820 ºC for 4 minutes (etching performed with 4% vol Nital solution): (a) whole thickness, (b) closer view

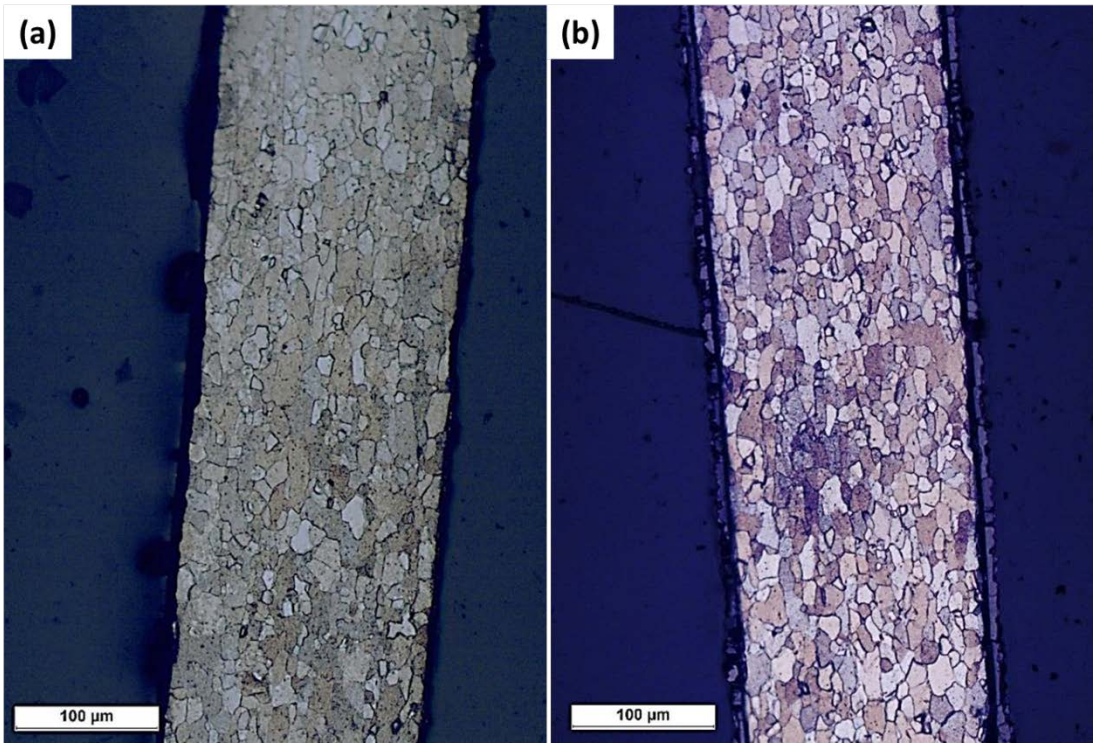

Figure 8-25 – Etching with sodium metabisulphite for uncoated coupons induction heated at 1100 ºC – 1150 ºC for 1 second and then induction heated at 820 ºC for 2 min (a) and for 4 min (b)

Another serie of tensile tests was performed on tensile coupons coated only on one side with 500 nm thick amorphous FeC film and induction heated following the heating and cooling cycle shown in Figure 8-12. The time of isothermal annealing at 820 ˚C was varied for each specimen. The annealing conditions of the specimens are summarized in Table 8-5, while their dimensions are reported in Table G- 3 of section G.4 in Appendix G.

Sample	Annealing Treatment	Heat Treatment environment
IF not annealed	IF steel not annealed	-
HV - A	530 ˚C-1h	High vacuum furnace
IH - A	820 ˚C – 30s	Induction Heating
IH - B	820 ˚C – 2 min	Induction Heating
IH - C	820 ˚C – 4 min	Induction Heating
IH - D	1100 ˚C - 1150 ºC – 4 min	Induction Heating
IH - E	1100 ˚C – 1150 ºC – 4 min	Induction Heating

Table 8-5 - List of tests performed on one side coated coupon annealed in high vacuum using a furnace or induction heating for different temperatures and times

A summary of the engineering stress-strain curves is reported in Figure 8-26, while a summary of the relevant mechanical properties is listed in Appendix G (section G.4, Table G- 4).

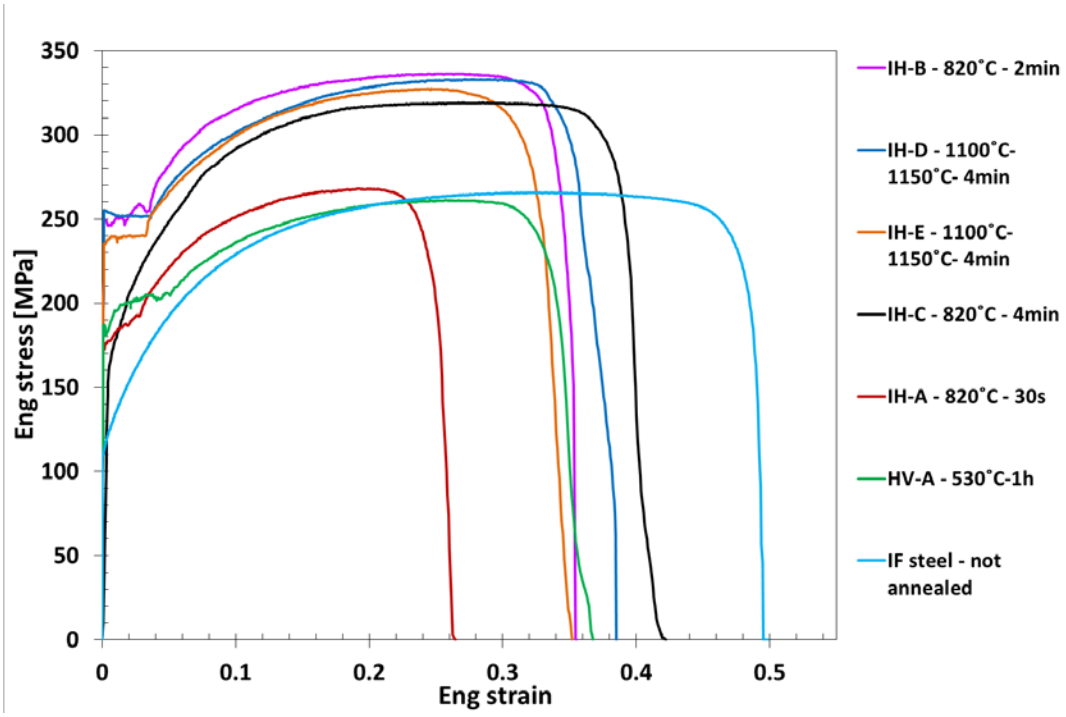

Figure 8-26 - Engineering stress-strain curves for coupons coated on one side with 500 nm thick FeC film and induction heated at different temperatures and for different times. The specimens induction heated at 820 ºC were first heated at 1100 ºC -1150 ºC for 1 second and then the temperature was lowered at 820 ºC

From Figure 8-26, one can see that after 30 seconds of induction heating at 820 ºC, the mechanical properties are the same as those obtained with annealing in high vacuum furnace at 530 ºC for 1h. This proves the high efficiency of induction heating. The highest mechanical properties are obtained for induction heating at 820 ºC for 2 minutes or at 1100 ºC for 4 minutes, for which the yield stress is around 250 MPa and the UTS is between 300 MPa and 350 MPa. It is also interesting to note that if the induction heating at 820 ºC is prolonged to 4 minutes, a decrease in yield stress occurs and Lüdering is suppressed, while a high level of UTS is preserved.

The strain hardening exponent was calculated for each curve shown in Figure 8-26 by calculating the slope of the graph of $ln\ (\sigma_{true})$ versus $ln\ (\varepsilon_{true})$, since it was reported in literature that changes is the value of the strain-hardening exponent are related to the microstructure. In particular, Atkinson [184] reported that a two-stage hardening associated to the Hollomon equation can be related to carbon content and gran size. It was concluded that annealed iron and very low-carbon steels strain harden following Hollomon equation after Lüders plateau has been fully propagated. However, Atkinson [184] suggested that if the grain size is large or the carbon content is high, then the strain hardening will be rapid in the first stage. Mediratta et al. [185] have analyzed the dependence of the multi stage strain-hardening behaviour for ferrite-martensite dual phase steels proving that in the first two stages the value of strain-hardening "*n*" increases with an increase in volume fraction of martensite. Moreover, for the same volume fraction of martensite but with higher values of carbon, they proved that higher values of strain-hardening are measured [185].

The Hollomon equation is considered to be valid to describe the plastic behaviour of carbon steels. The equation relates true stress and true strain as:

$$\sigma_{true} = K \times \left(\varepsilon_{true}\right)^{n} \qquad \text{(eq. 8-4)}$$

where, *n* is the strain hardening exponent and *K* is the strength coefficient. The detailed plots of $ln\ (\sigma_{true})$ versus $ln\ (\varepsilon_{true})$ for the coupons are reported in section G.4.1 of Appendix G.

The numerical values of the strain hardening of the tested coupons are reported in Table 8-6.

Sample	Strain hardening exponent (n)	Strain range (%)
IF steel – not annealed	0.29	2 - 28
530˚C-1h-HV- A	0.66	3.6 - 4.06
	0.23	4.06 – 18.4
820˚C-30s – IH - A	0.26	2.7 – 17.4
820˚C-2min – IH - B	0.42	3.42 – 4.22
	0.23	4.22 – 22.3
820˚C-4min – IH - C	0.25	0.79 – 24.64
1100˚C-4min – IH - D	0.26	3.57 – 24.5
1100˚C-4min – IH - E	0.25	3.11 – 22.05

Table 8-6 - Strain hardening exponent values for specimen coated on one side with 500 nm FeC film and induction heated (IH) or annealed in furnace (HV) at different temperatures and different times. For some specimens two values of n have been indicated since the first n represents the strain-hardening exponent right after Lüders bands propagation is finished, while the second value of *n* represents the normal hardening until UTS is reached

From the values of strain hardening reported in Table 8-6, no clear difference can be noticed between the specimens. They all show similar values. The strain-hardening exponent is higher right after Lüders plateau has propagated since dislocations are multiplied during Lüders propagation causing a marked hardening right after the plateau.

The microstructure of induction heated coupons was observed by etching with 4% vol. Nital solution. The obtained microstructures are summarized in the following figures. In Figure 8-27 (a) and (b), the microstructure of the one side coated coupon induction heated at 820 ˚C for 30 seconds is reported, where holes are clearly visible at the sides of the gauge length. Before starting the induction heating, it was noticed that the specimen had some oxidation on the surface. This would cause local differences in the response to the magnetic field which would cause melting of the oxide during induction heating leaving holes in the final coupon. Another cause of the presence of these holes is the cleaning performed on the surface of the coupons before applying the FeC film using the PVD deposition. If the specimen is left on the Nital solution too long, it is possible that corrosion will occur in some zones at the material surface leaving small pits which will then compromise the mechanical properties.

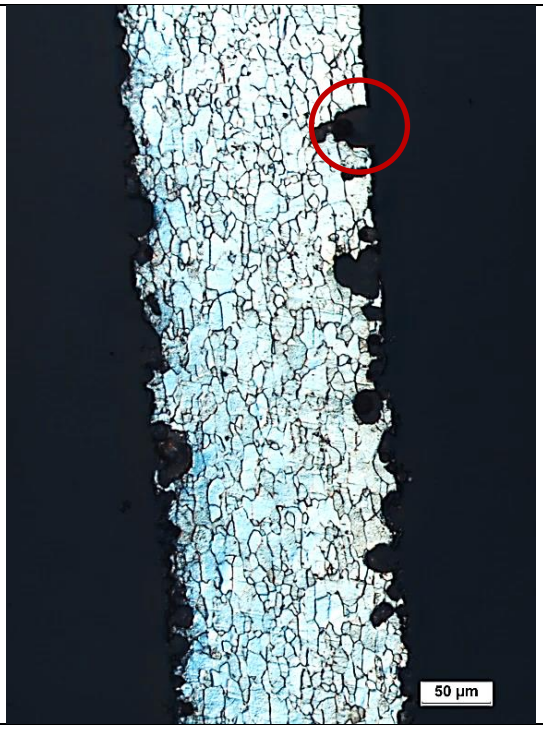

(a) Etching in the grip zone (20X)

(b) Detail of the etching in the grip zone (50X)

Figure 8-27 - Etching of specimen one side coated, induction heated at 1100 ºC – 1150 ºC for 1 second and then induction heated at 820 ˚C for 30 seconds

Figure 8-28 (a) and (b) shows the microstructure of a one side coated coupon induction heated at 820 ºC for 2 minutes, In figure (b), the grain boundary seems to be less attacked by the etchant compared to the bulk of the grains (arrows are indicating some of the grain boundaries). Figure 8-29 (a) and (b) show the microstructure of one side coated coupon induction heated at 820 ºC for 4 minutes, where the grain boundaries look even less attacked by the etchant. However, from the optical microscope pictures no other difference between the specimens could be discerned.

(a) Etching in the grip zone (20X)

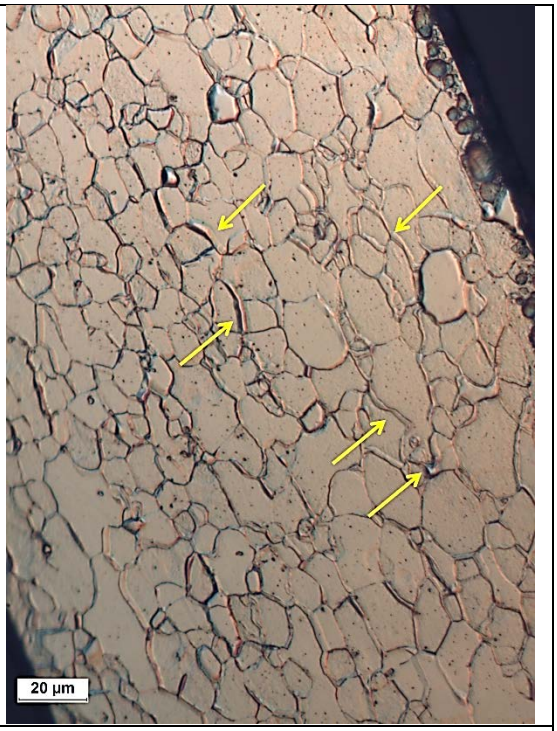

(b) Etching in the grip zone (50X)

Figure 8-28 - Microstructure of the specimen coated on one side and induction heated at 1100 ºC – 1150 ºC for 1 second and then induction heated at 820˚C for 2 minutes

Etching in the grip zone (20X)

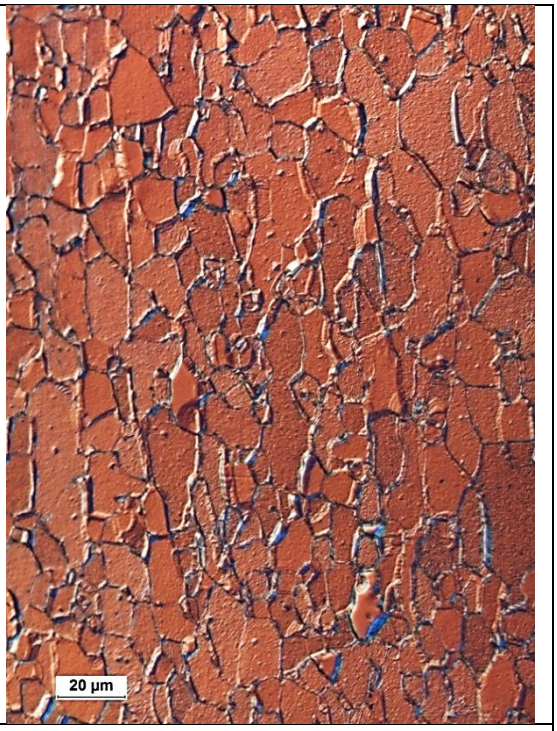

Etching in the grip zone (50X)

Figure 8-29 - Microstructure of the specimen coated on one side and induction heated at 1100 ºC – 1150 ºC for 1 second and then induction heated at 820 ˚C for 4 minutes

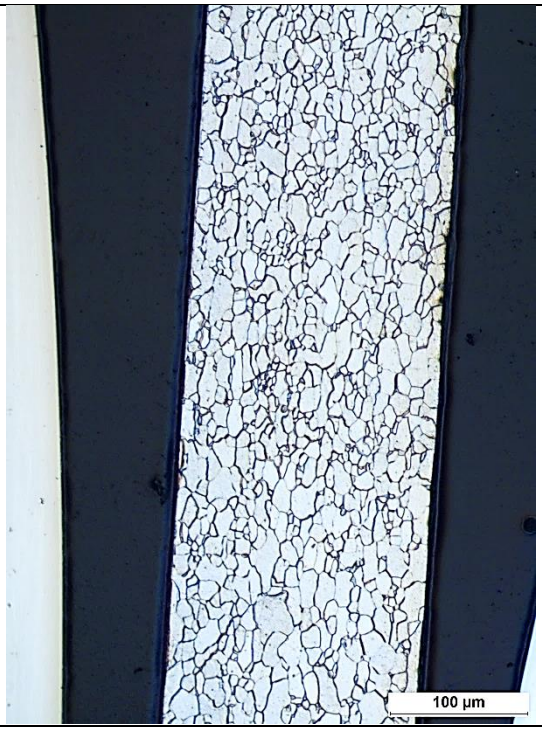

Etching in the grip zone (20X)

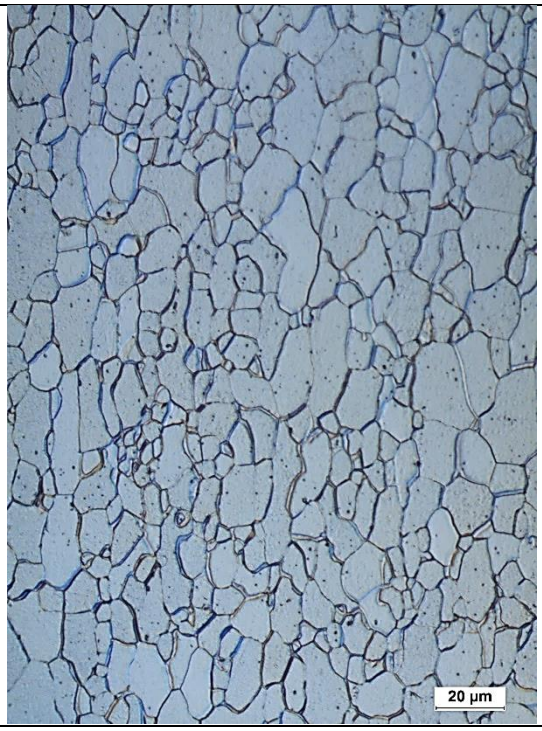

Etching in the grip zone (50X)

Figure 8-30 - Microstructure of the specimen coated on one side and induction heated at 1100 ˚C for 4 minutes

In Figure 8-30 the microstructure of one side coated specimen induction heated at 1100 ºC for 4 minutes is reported. No particular feature could be discerned compared to the previous microstructures. However, one should note that in all microstructures of induction heated coupons, no grain growth was detected proving that a fast heating rate is important to obtain faster diffusion of carbon avoiding grain growth, since the interstitial elements will pin the initial grain boundaries. This was not the case, when the specimens were annealed in the furnace were the heating rate was slow and the kinetic of grain growth was comparable with the speed of carbon diffusion, so that some grain growth could occur before the carbon diffused at the grain boundaries.

Another series of tensile coupons coated on both sides with 500 nm thick FeC film were induction heated. The list and conditions of the tested coupons are reported in Table 8-7, while the engineering stress-strain curves are shown in Figure 8-31. The dimensions of the tested coupons and the values of the mechanical properties are summarized in section G.5 of Appendix G.

Sample	Annealing Treatment	Heat Treatment environment
IF not annealed	IF steel not annealed	-
HV - A	530 ˚C-1h	High Vacuum - furnace
HV - B	820 ˚C – 2 min	High Vacuum furnace
IH – BS - A	820 ˚C – 1 min	Induction Heating
ECD 1L-O	820 ˚C – 2 min	Induction Heating
ECD 1C-K	820 ˚C – 2 min	Induction Heating
IH – BS - B	820 ˚C – 4 min	Induction Heating
IH – BS - C	820 ˚C – 8 min	Induction heated

Table 8-7 - List of specimens coated both sides induction heated (IH) for different times or annealed in furnace in high vacuum (HV)

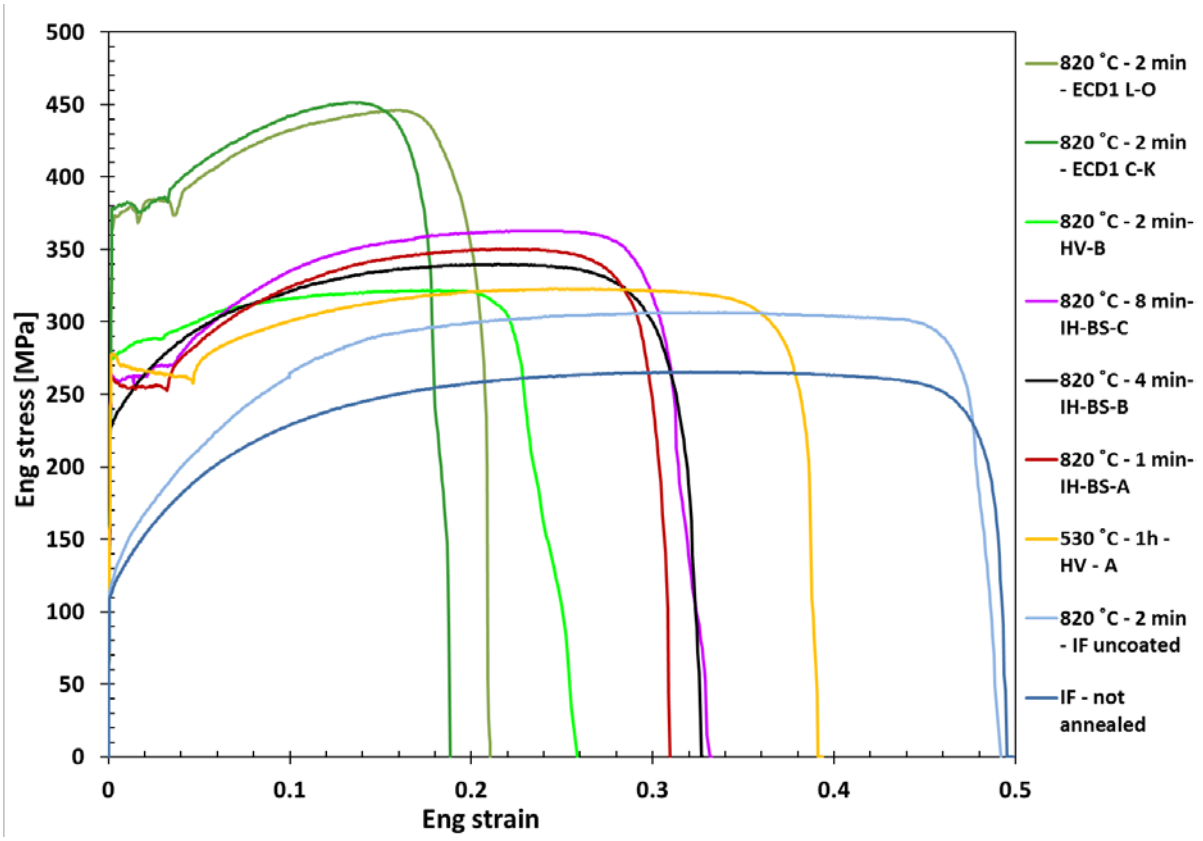

Figure 8-31 - Engineering stress-strain curves for tensile coupons coated both sides with 500 nm FeC film induction heated at 820 ˚C for different time and compared with one uncoated coupon of IF steel induction heated for 2 minutes and one both sides coated coupon annealed in furnace at 820 ºC for 2 minutes. The specimens induction heated at 820 ºC were first heated at 1100 - 1150 ºC for 1 second and then the temperature was lowered at 820 ºC

From Figure 8-31, after 1 minute of induction heating, the increase of yield strength is comparable with the one obtained after annealing in furnace at 530 ºC - 1h. For both sides coated coupons the highest increase of mechanical properties is obtained for 2 minutes of induction heating and after 4 minutes, mechanical properties decrease but Lüdering is

suppressed. If the induction heating time is further increased to 8 minutes, mechanical properties are the same as those obtained after 1 minute. In Figure 8-31, an example of a tensile curve obtained for a both sides coated coupon after annealing at 820 ºC for 2 minutes in the high vacuum furnace is also shown. However, in the furnace it is not possible to austenitize the specimen and then quickly drop the temperature at 820 ºC as it can be done for induction heating experiments. However, if the curves for specimens induction heated for 2 minutes are compared with the curve of the 2 minutes annealed in the furnace, it can be concluded that austenitization of the specimen during carbon diffusion is a key parameter to maximize the strengthening. Moreover, another key factor is the high heating rate obtained with induction heating which could be responsible for a faster carbon diffusion compared to the kinetic of crystallization of the film; while in the high vacuum furnace the two mechanisms are probably occurring with the same kinetics, limiting the diffusion of carbon into the IF substrate.

The stain-hardening exponent *(n)* was calculated for the coupons coated both sides following the same approach previously presented for coupons coated on one side. The values of the strain-hardening exponent are listed in Table 8-8. For some specimens two values of *"n"* have been obtained since the first *"n"* represents the strain-hardening exponent right after Lüders bands propagation is finished, while the second value of *n* represents the normal hardening until UTS is reached.

Sample	Strain hardening exponent (n)	Strain range (%)
IF steel – not annealed	0.29	2 - 28
530˚C-1h – HV-A	0.58	4.55 – 5.06
	0.23	5.06 – 22.03
820˚C-2min – HV-B	0.14	2.82 – 16.73
820˚C-1min – IH-BS-A	0.56	3.17 – 3.62
	0.25	3.62 – 19.55
820˚C-2min – IH – ECD1L-O	0.19	4.1 – 14.54
820˚C-2min – IH – ECD1C-K	0.18	3.48 – 12.66
820˚C-4min – IH-BS-B	0.19	1.50 – 19.32
820˚C-8min – IH-BS-C	0.26	3.48 – 20.87

Table 8-8 - Strain hardening exponent values for specimen coated both sides with 500 nm FeC film and induction heated or annealed in furnace at different temperatures and different times

The reduction in area was calculated for the coupons coated both sides in order to obtain the ductility of the specimen.

Specimen	Reduction in area
530˚C-1h – HV-A	94.76%
820˚C-1min – IH-BS-A	93.43%
820˚C-2min – IH – ECD1L-O	87.53%
820˚C-4min – IH-BS-B	91.83%
820˚C-8min – IH-BS-C	91.78%

Table 8-9 - Area reduction measured in coupons coated both sides with 500 nm thick FeC film

All the values of strain hardening exponent reported in Table 8-8 seem to be close and the slight difference is not enough to justify the presence of any martensite or bainite. From Table 8-9, the reduction in area is still high so the ductility of the specimen is preserved despite their increase in strength. However, the maximum stress before failure is reached at lower strains for specimens induction heated for 2 minutes, meaning that necking starts at lower strains, compared to specimens induction heated for 1 minute, 4 minutes or 8 minutes. Vickers microhardness was measured for both sides coated coupons induction heated first at 1150 ºC for 1 second and then at 820 ˚C for 1 minute, 2 minutes and 4 minutes and the values were compared with the hardness obtained for one side coated coupons and for an uncoated and not-annealed IF steel. The comparison is shown in Figure 8-32. Each point is the average of 10 measurements.

The microstructure of the induction heated and both sides coated coupons was then obtained by performing etching with 4% vol. Nital solution. The obtained microstructures are summarized in section 8.2.4.2.

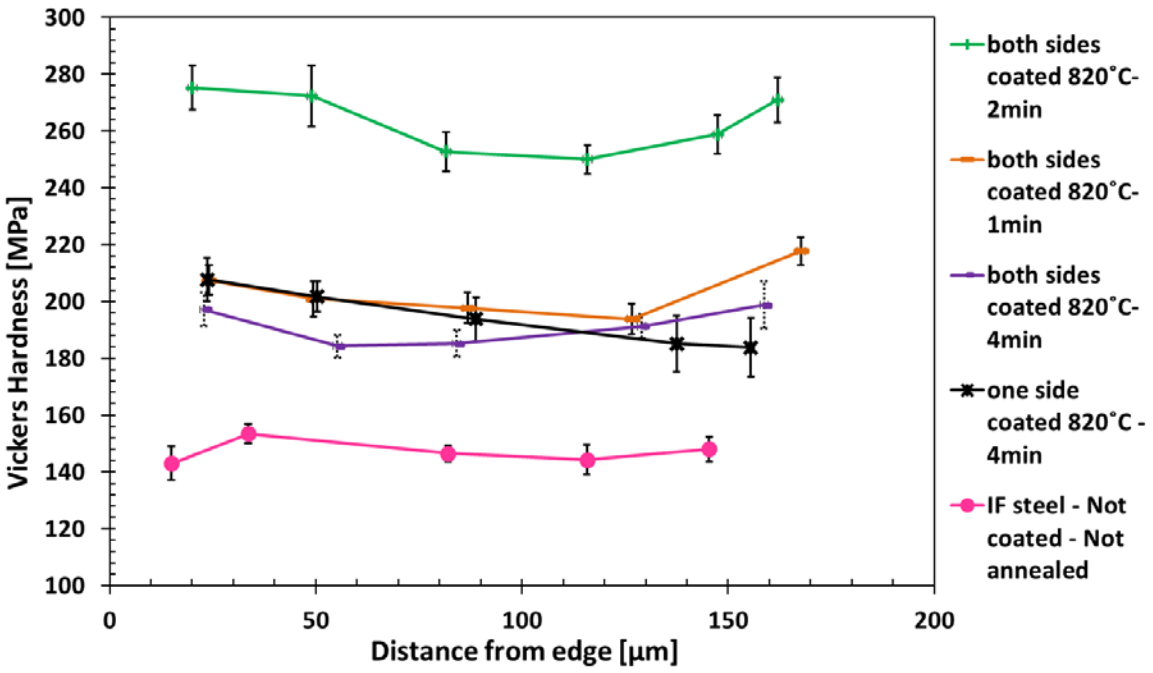

Figure 8-32 - Vickers hardness through thickness for one side and both sides coated coupons induction heated at 1100 ºC – 1150 ºC for 1 second and then induction heated at 820 ˚C for different times. Vickers hardness of uncoated and not annealed IF steel is included for reference

8.2.4.2. Microstructure of both sides coated coupons

Microstructure of coupon coated both sides, induction heated at 1100 ºC - 1150 ºC for 1 second and then induction heated at 820 ˚C for 1 minute

Images of the microstructure of specimens coated both sides and induction heated at 820 ˚C for 1 minute were taken close to the coated edges. It was discovered that the grains close to the coated surfaces had line features that were not present in the grains at the center of the IF steel. The features of grains close to one of the coated surface are shown in Figure 8-33 (a) at a magnification of 50X, while in Figure 8-33 (b), the microstructure of a both sides coated coupon induction heated at 820 ºC for 2 minutes is shown.

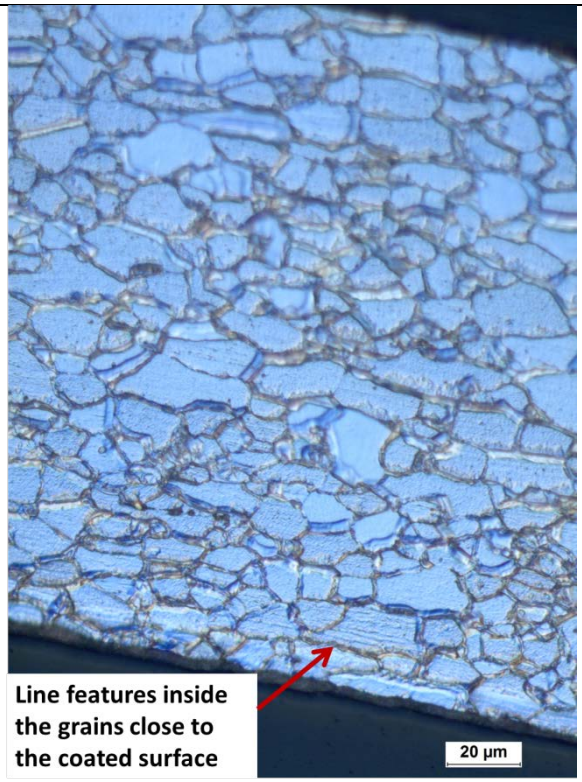

(a) Microstructure of both sides coated coupons which was induction heated at 820 ˚C for 1 minute. Microstructure obtained with 4% vol. Nital solution (Magnification 50X)

(b) Microstructure of a specimen coated both sides and induction heated at 820 ˚C for 2 minutes (Magnification 50X)

Figure 8-33 - Microstructure of both sides coated tensile coupon induction heated at 1100 ºC – 1150 ºC for 1 second and then induction heated at 820 ˚C: (a) 1 minute coupon and (b) 2 minutes coupon

The microstructure of the specimen induction heated for 2 minutes shows the lines in the whole thickness of the specimen. The lines are aligned along the main axis of the tensile coupon and they are continuous from one grain to the next grain.

The 2 minutes induction heated specimen was also etched using 12% sodium metabisulfite aqueous solution. At first a short etching time was used in order to identify the presence of acicular ferrite. The specimen was repolished and etched with 4% vol. Nital solution for only 7 seconds and then immersed in sodium metabisulphite for only 15 seconds. The obtained pictures are shown Figure 8-34 (a) and (b).

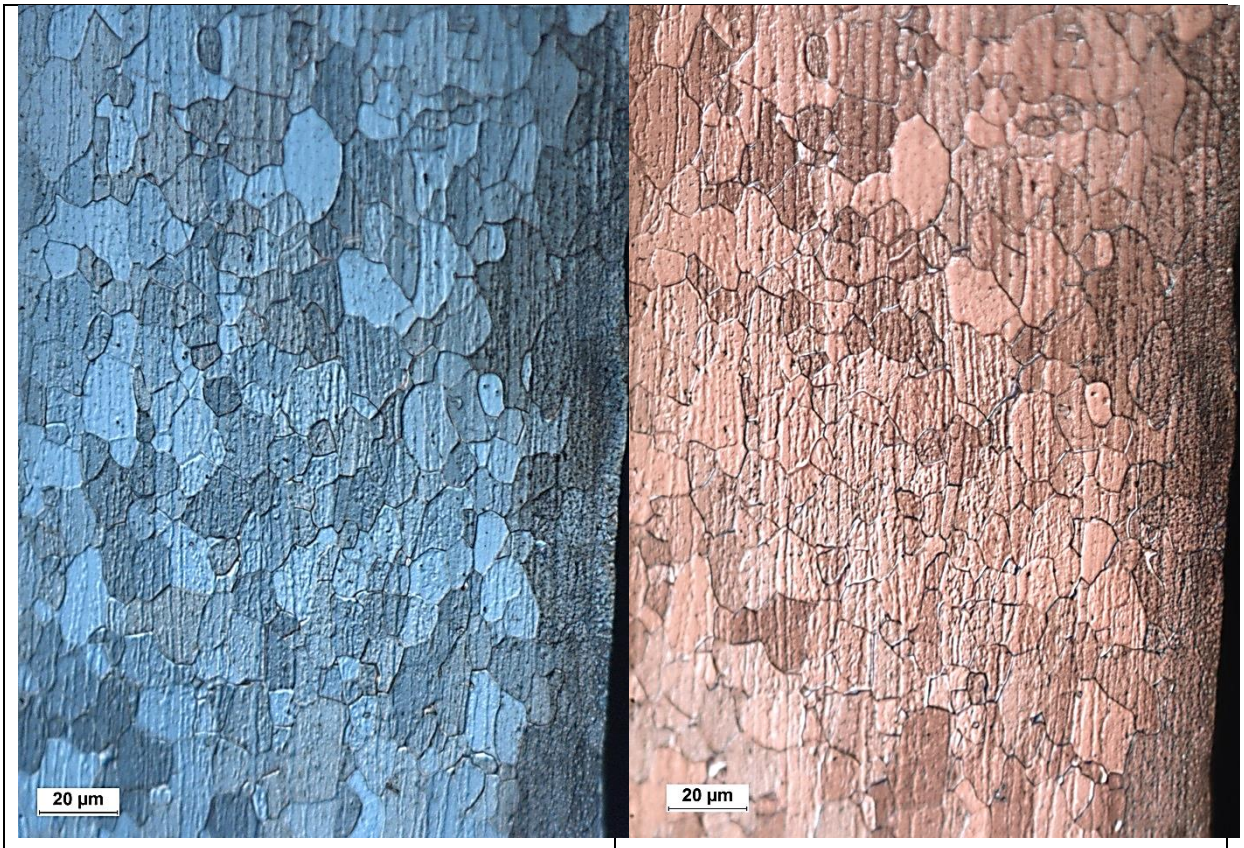

(a) Microstructure after etching for 7s with Nital solution and 15s with sodium metabisulhite using Nomarsky contrast and polarized light (magnification 50X)	(b) Microstructure after etching for 7s with Nital solution and 15s with sodium metabisulhite using Nomarsky contrast without polarized light (magnification 50X)

Figure 8-34 – Microstructure of a both sides coated tensile coupon induction heated at 1100 ºC – 1150 ºC for 1 second and then induction heated at 820 ˚C for 2 minutes (etching performed with Nital solution for 7 seconds and with sodium metabisulphite solution for 15 seconds)

No lath-like structure was detected, however, the lines are still clearly visible and some grains appear darker than others. If the specimen is left into the sodium metabisulphite for longer time, such as 30 or 40 seconds, then some grains will colour more than others and some of them will appear very dark while others will appear white (Figure 8-35). This is caused by the different crystallographic orientations of the grains, however, it was noticed that for the same etching technique, the difference in coloration is not so well defined for uncoated and induction heated coupons. As already mentioned in a previous paragraph, the sodium metabisulphite is expected to lightly colour ferrite but it darkens martensite and bainite.

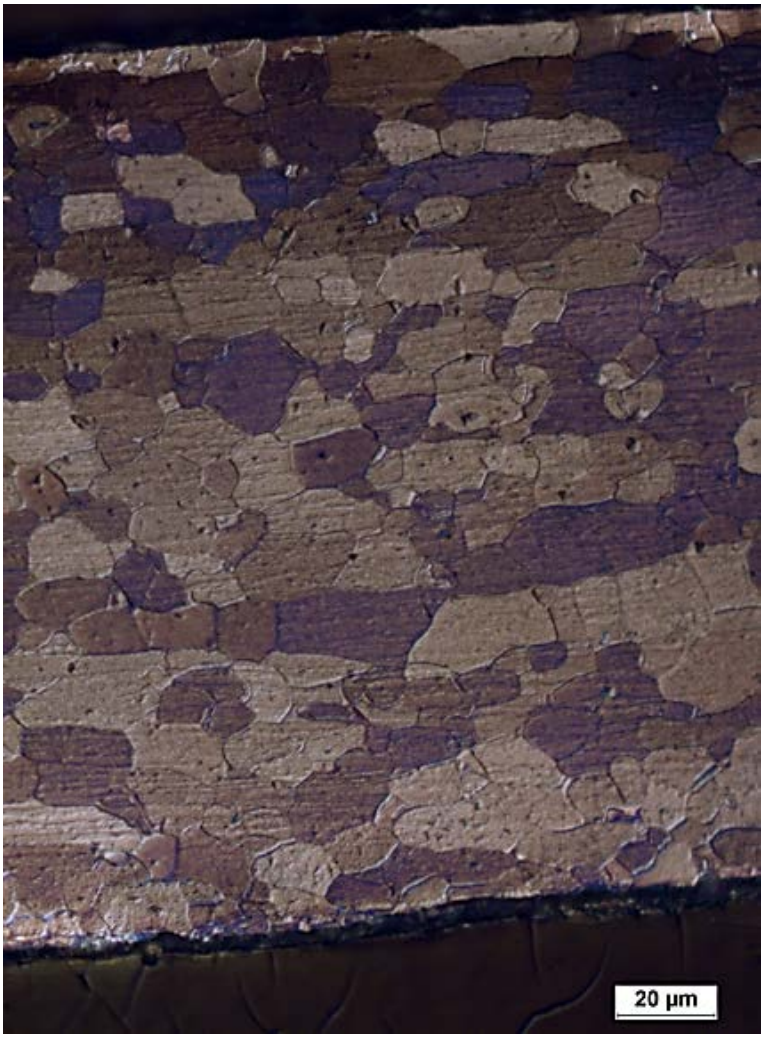

Figure 8-35 - Microstructure of tensile coupon coated both sides, induction heated at 1100 ºC – 1150 ºC for 1 second and then induction heated at 820 ˚C for 2 minutes (etching with 4% vol Nital solution and 12% sodium metabisulfite solution. Magnification 50X)

Microstructure of coupon coated both sides and induction heated at 1100 ºC – 1150 ºC for 1 second and then induction heated at 820 ˚C for 4 minutes

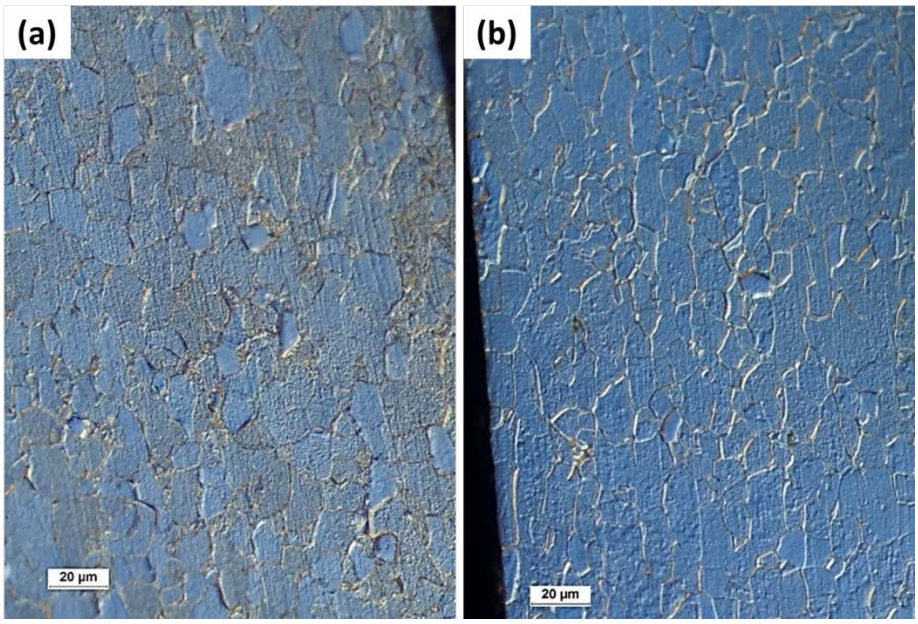

Figure 8-36 – Microstructures of both sides coated coupons induction heated at 1100 ºC – 1150 ºC for 1 second and then induction heated at 820 ºC for 4 minutes (a) and for 8 minutes (b) (etching with 4% vol Nital solution) (Magnification 50X)

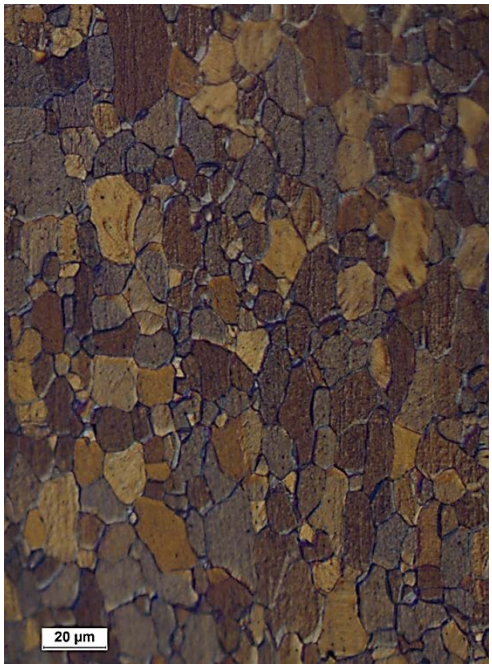

Figure 8-37 - Microstructure of tensile coupon coated both sides, induction heated at 1100 ºC – 1150 ºC for 1 second and then induction heated at 820 ˚C for 4 minutes (etching with 4% vol Nital solution and 12% sodium metabisulfite solution. Magnification 50X)

From Figure 8-36 (a) and Figure 8-37, after 4 minutes of induction heating, the lines are still present in the microstructure but they are less marked and the etching with sodium metabisulphite (Figure 8-37) reveals no highly dark grain as it happened for the 2 minutes but there is another phase which appears as gray. This phase could be ferrite having a different crystallographic orientation compared to other ferritic grains (which appear colored in light brown).

Microstructure of coupon coated both sides and induction heated at 1100 ºC – 1150 ºC for 1 second and then induction heated at 820 ˚C for 8 minutes

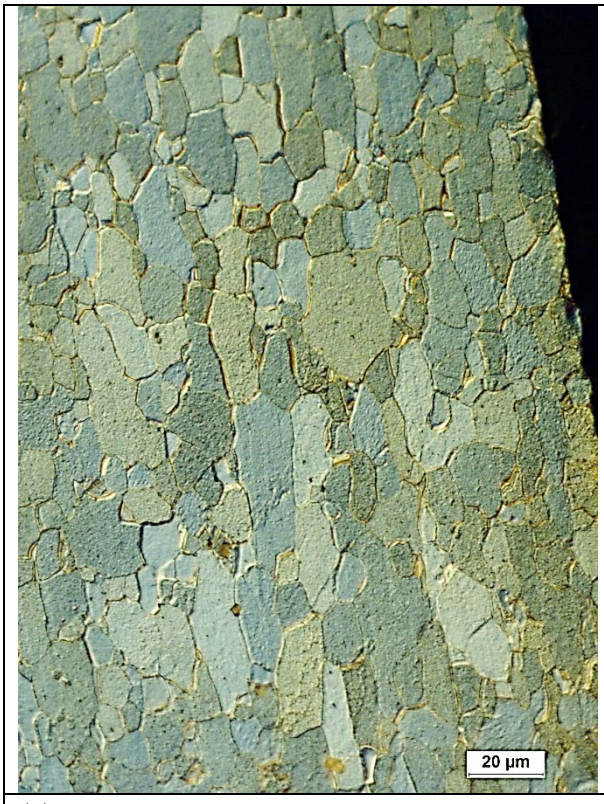

(a) Microstructure of a both sides coated coupon which was induction heated at 820 ˚C for 8 minutes. Etching was performed using 4% vol. Nital and 11% sodium metabisulfite (Magnification 50X)

(b) Microstructure of a both sides coated coupon which was induction heated at 820 ˚C for 8 minutes. Etching was performed using 4% vol. Nital and 11% sodium metabisulfite (Magnification 50X) after change of polarization of light

Figure 8-38 - Microstructure of a both sides coated coupon which was induction heated at 1100 ºC – 1150 ºC for 1 second and then induction heated at 820 ˚C for 8 minutes. (Etching performed using 4% vol Nital solution and 11% sodium metabisulfite solution. Magnification 50X)

For the specimen induction heated for 8 minutes at 820 ˚C, the lines appear less marked and the etching with sodium metabisulphite reveals less contrast between the grains (Figure 8-38 (a) and (b)). There is still the presence of a gray phase which is believed to be ferrite.

From the figures presented above it is clear that there is a difference in the microstructure of the specimens induction heated for different times, however it is hard to quantify and to identify the phases present in the microstructure just by color etching. For this reason further analyses such as EBSD and TEM are required, especially to identify the presence of very fine phases such as low carbon granular bainite. In order to obtain more information, pictures were first taken using the scanning electron microscope on the surfaces of the specimens after they had been etched with 4% vol. Nital solution for 30 seconds. This helped to identify how the grain boundaries evolved during the different times induction heating was applied.

8.2.5. Scanning Electron Microscope (SEM) analyses of induction heated microstructures: one side coated coupons

- **SEM images of not-annealed and uncoated IF steel**

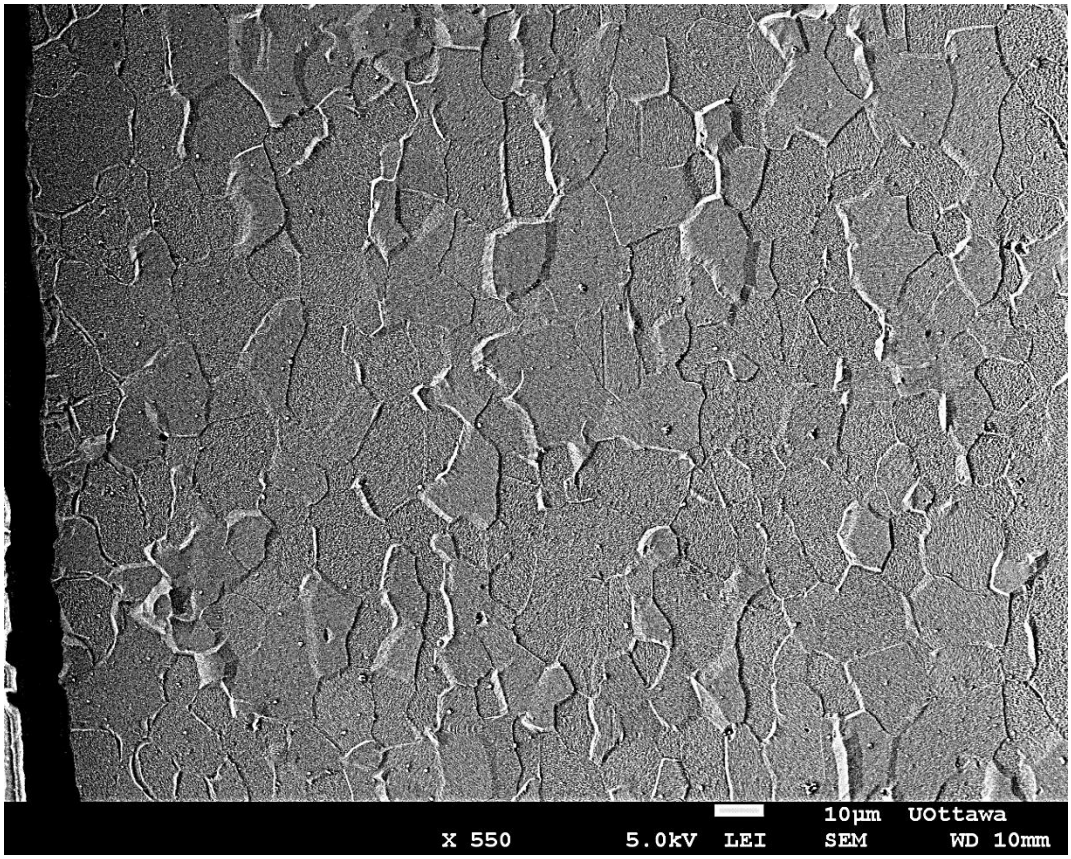

Figure 8-39 - Overall view of the microstructure of uncoated not-annealed IF steel. Etching performed with 4% vol Nital solution before placing the specimen in the SEM chamber (magnification 550X)

From Figure 8-39, one can see that for a not-annealed IF steel, the grain boundaries cannot be easily highlighted even after etching with Nital, since the chemical attack occurs uniformly at most of the grains and grain boundaries. Detailed images of some grains and grain boundaries are shown in Figure 8-40 and Figure 8-41, where the grain boundaries do not appear etched by the Nital solution. Inside the grains, lines caused by the etching are clearly visible, while the small particles are residues left by the OPS polishing solution

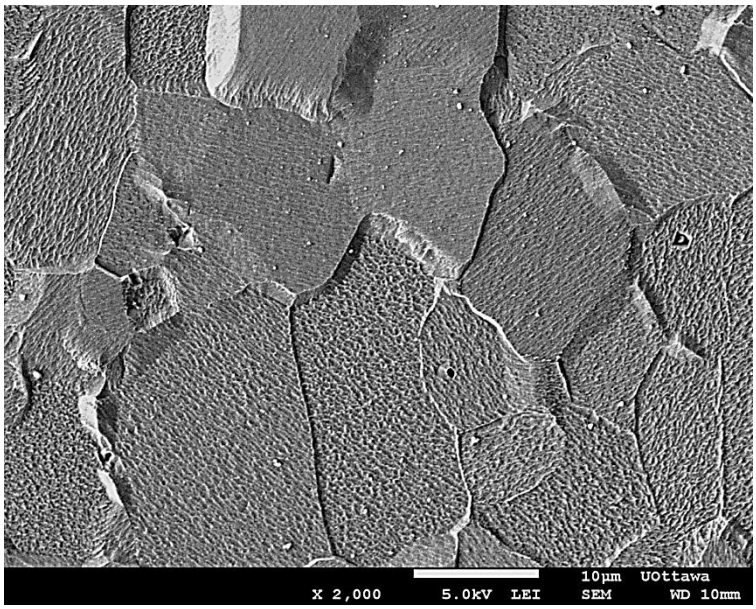

Figure 8-40 - Detail of the etched microstructure of uncoated not-annealed IF steel (magnification 2000X)

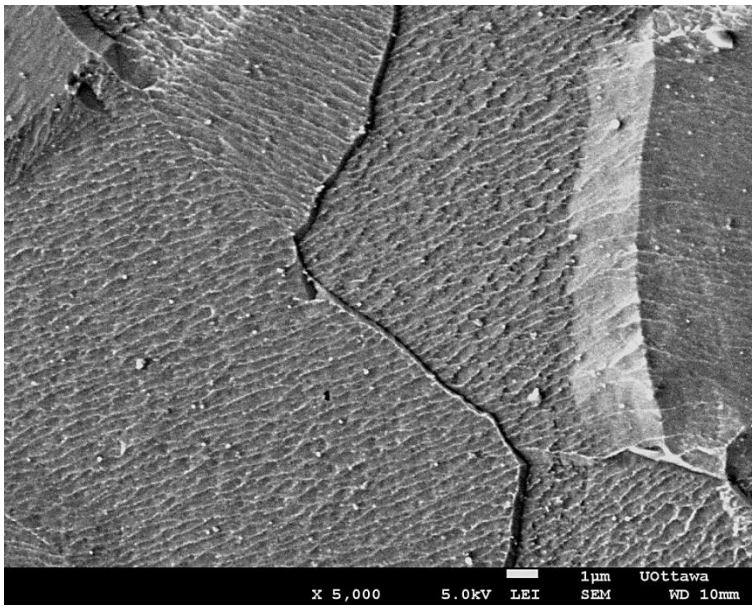

Figure 8-41 - Detail of grain boundaries of uncoated and not-annealed IF steel (magnification 5000X)

- **SEM images of uncoated IF steel induction heated at 1100 ºC - 1150 ºC for 1 second and then at 820 ˚C – 30 seconds**

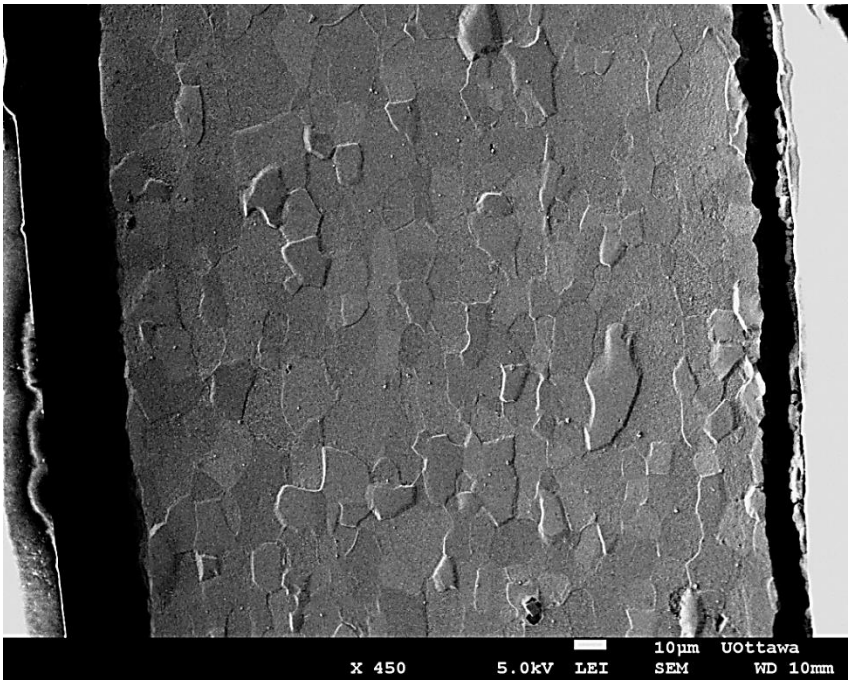

Figure 8-42 - Overall view of the microstructure of uncoated coupon induction heated at 1100 ºC – 1150 ºC for 1 second and then at 820 ˚C – 30 s (magnification 450X)

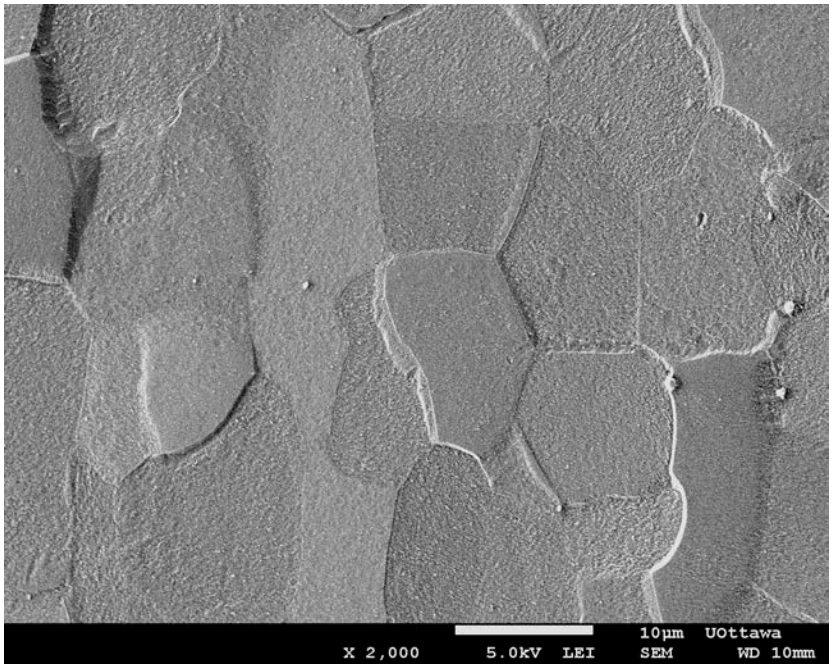

Figure 8-43 - Detail of the etched microstructure of uncoated coupon induction heated at 1100 ºC – 1150 ºC for 1 second and then at 820 ˚C – 30 s (magnification 2000X)

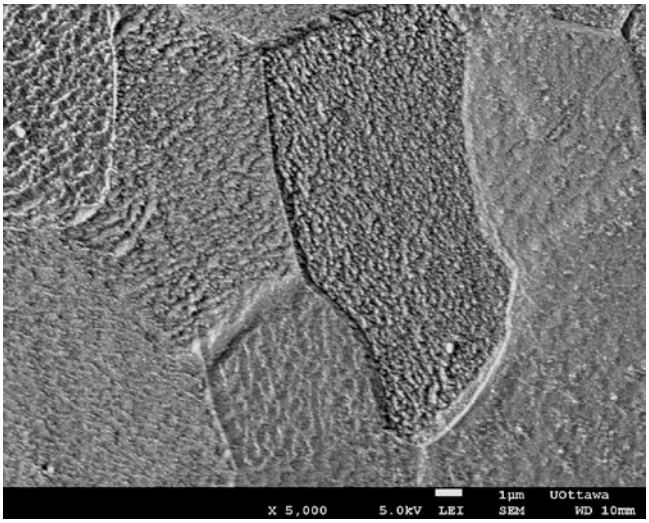

Figure 8-44 - Detail of grain boundaries for etched microstructure of uncoated coupon induction heated at 1100 ºC – 1150 ºC for 1 second and then at 820 ˚C – 30 s (magnification 5000X)

From the microstructures shown in Figures 8-42, 8-43 and 8-44, it can be seen that after 30 seconds of induction heating, the microstructure has no change for an uncoated coupon. The grain boundaries are still difficult to be revealed with etching in Nital.

- **SEM images of one side coated IF steel induction heated at 1100 ºC - 1150 ºC for 1 second and then at 820 ˚C – 30 seconds**

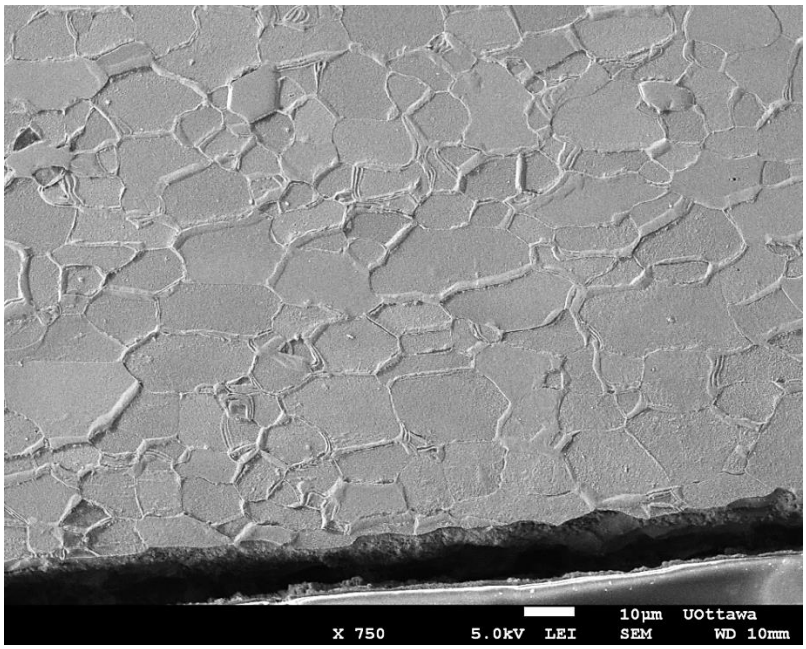

Figure 8-45 - Overall view of the microstructure of one side coated coupon induction heated at 1100 ºC – 1150 ºC for 1 second and then at 820 ˚C – 30 s. The microstructure is close to the coated edge (magnification 750X)

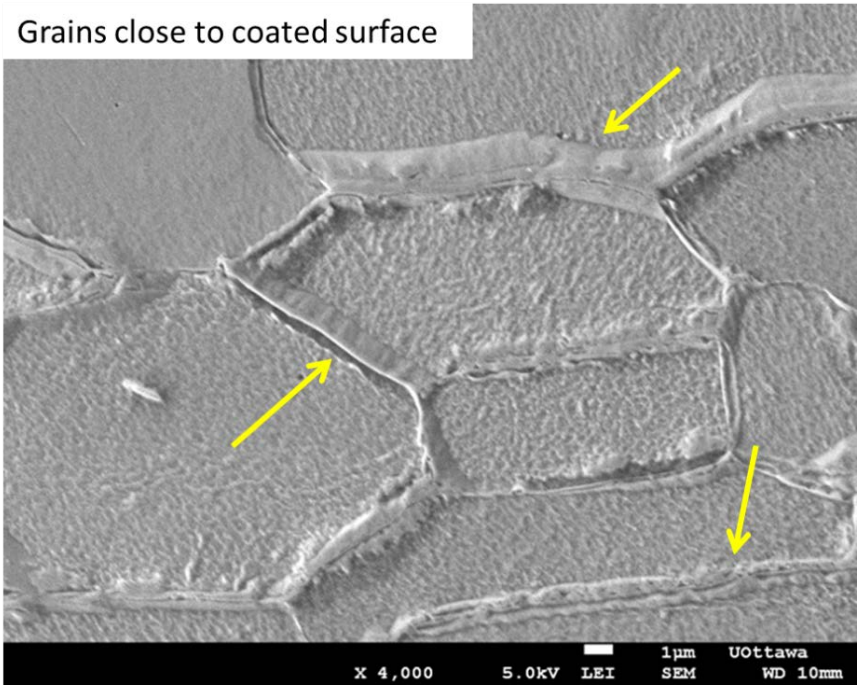

Figure 8-46 - Detail of the etched microstructure of one side coated coupon induction heated at 1100 ºC – 1150 ºC for 1 second and then at 820 ˚C – 30 s. Grains are close to the coated edge (magnification 4000X). The arrows indicate thick grain boundaries and grain boundaries made by more lines

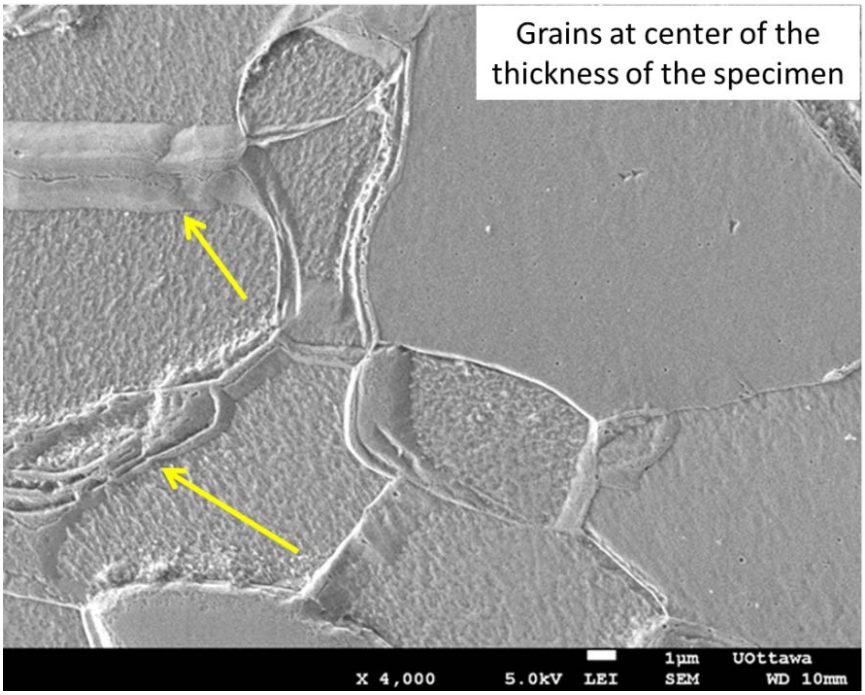

Figure 8-47 - Detail of the etched microstructure of one side coated coupon induction heated at 1100 ºC – 1150 ºC for 1 second and then at 820 ˚C – 30 s. Grains are in the middle of the thickness of the specimen (magnification 4000X). The arrows indicate thick grain boundaries and grain boundaries made by more lines

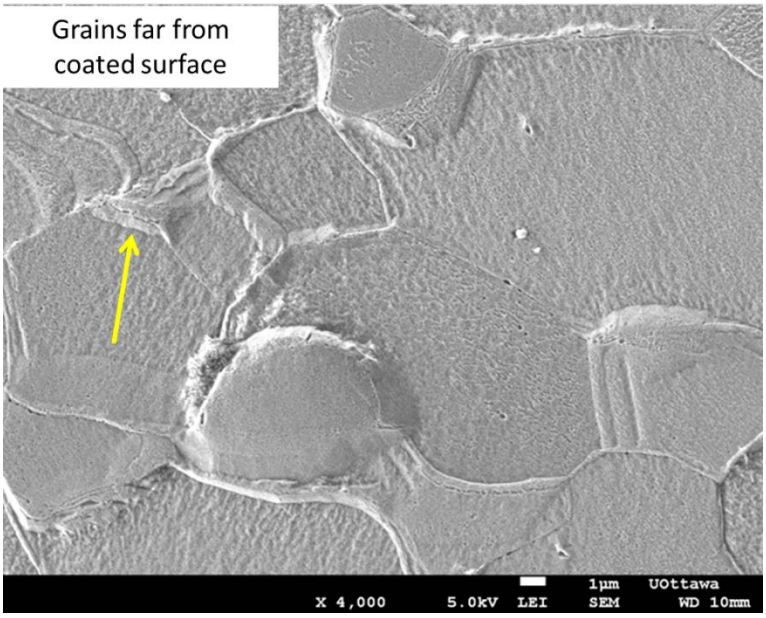

Figure 8-48 - Detail of the etched microstructure of one side coated coupon induction heated at 1100 ºC – 1150 ºC for 1 second and then at 820 ˚C – 30 s. Grains are close to the uncoated edge (magnification 4000X)

For the one side coated coupon induction heated at 820 ˚C for 30 seconds, the grain boundaries are easily revealed by the Nital etch since some carbon diffusion occurred at grain boundaries. Moreover, it seems that they are easier to be revealed close to the coated surface than to the uncoated surface. The grains appear thick and formed by several lines both close to the coated surface and in the middle of the specimen as shown by Figure 8-46 and Figure 8-47. The grain boundaries show several lines, which could represent epitaxial ferrite. This grain boundaries structure is formed when the steel is austenitized and then when it is cooled into the two-phase region, the new ferrite will start to form. However, at the grain boundaries, the old boundaries of previous ferrite and austenite can be visible. Far from the coated surface, some grain boundaries are made by several lines or appear thick while other are not highlighted, meaning that probably the carbon did not cover the whole thickness of the specimen even if diffusion at grain boundaries is faster than through the bulk of the grains.

- **SEM pictures of one side coated IF steel induction heated at 1100 ºC - 1150 ºC for 1 second and then at 820 ˚C – 4 minutes**

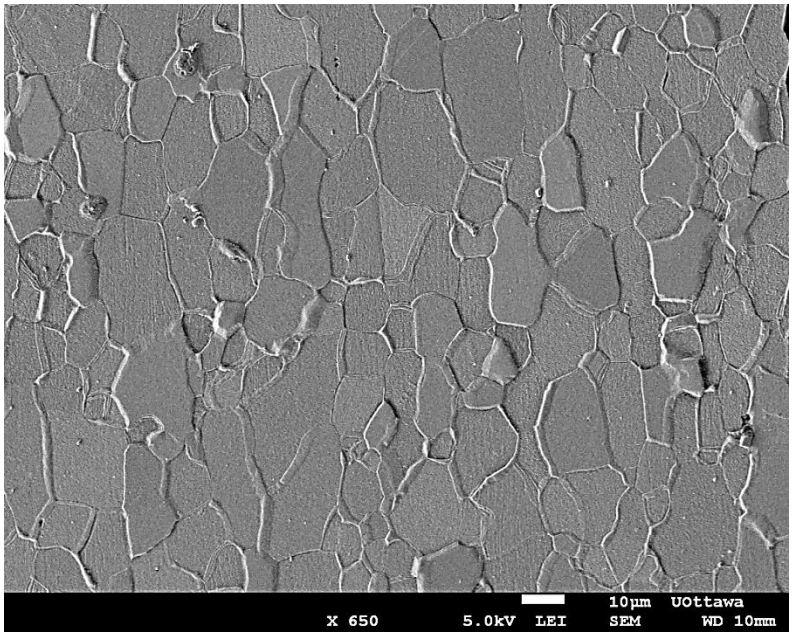

Figure 8-49 - Overall view of the microstructure of one side coated coupon induction heated at 1100 ºC – 1150 ºC for 1 second and then at 820 ˚C – 4 minutes (magnification 650X)

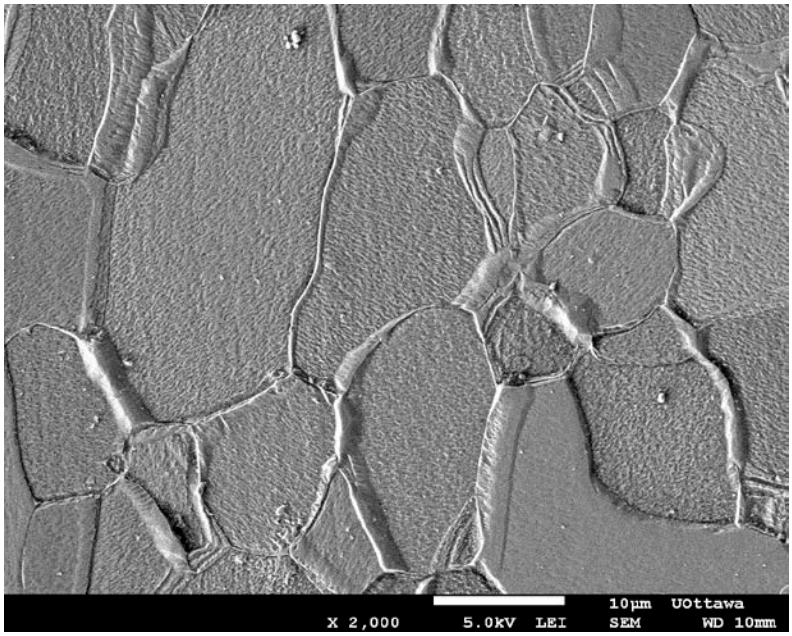

Figure 8-50 - Detail of the etched microstructure of one side coated coupon induction heated at 1100 ºC – 1150 ºC for 1 second and then at 820 ˚C – 4 minutes (magnification 2000X)

From Figure 8-49 the microstructure seems uniform in the whole thickness and the grain boundaries show the same structure that was found for an induction heating of 30 seconds.

8.2.6. Scanning Electron Microscope (SEM) analyses of induction heated microstructures: both sides coated coupons

Half of the tested tensile coupons, which were coated both sides and induction heated for different times, were cold mounted into epoxy resin, polished to mirror finish and etched with 4% Nital solution for 30 seconds before being imaged with SEM. The pictures have been taken in the zone of the grips which is not damaged by the tensile machine, except for the specimens induction heated for 4 minutes where pictures were taken closer to the fillet radii of the gauge length.

- **SEM images of both sides coated IF steel induction heated at 1100 ºC - 1150 ºC for 1 second and then at 820 ˚C – 1 minute**

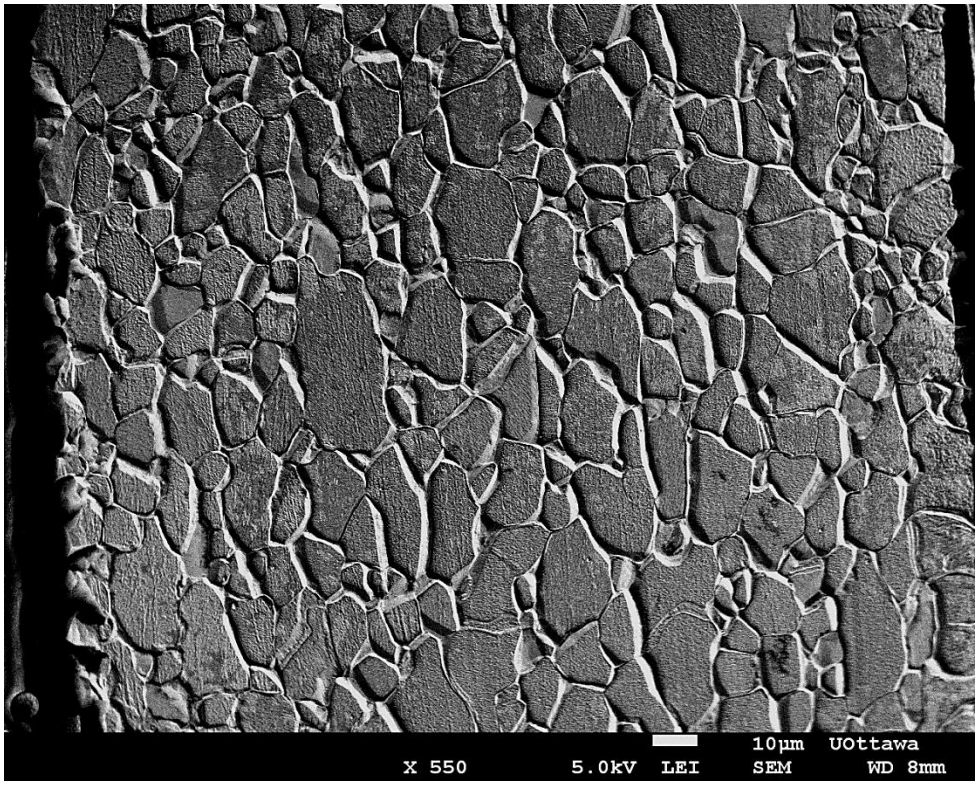

Figure 8-51 - Overall view of the microstructure of both sides coated coupond induction heated at 1100 ºC – 1150 ºC for 1 second and then at 820 ˚C – 1 minute (magnification 550X)

From Figure 8-51, the core of the grains seems to be preferentially attacked compared to grain boundaries. The difference of chemical attack between the core of the grains and the grain boundaries is much higher than other specimens.

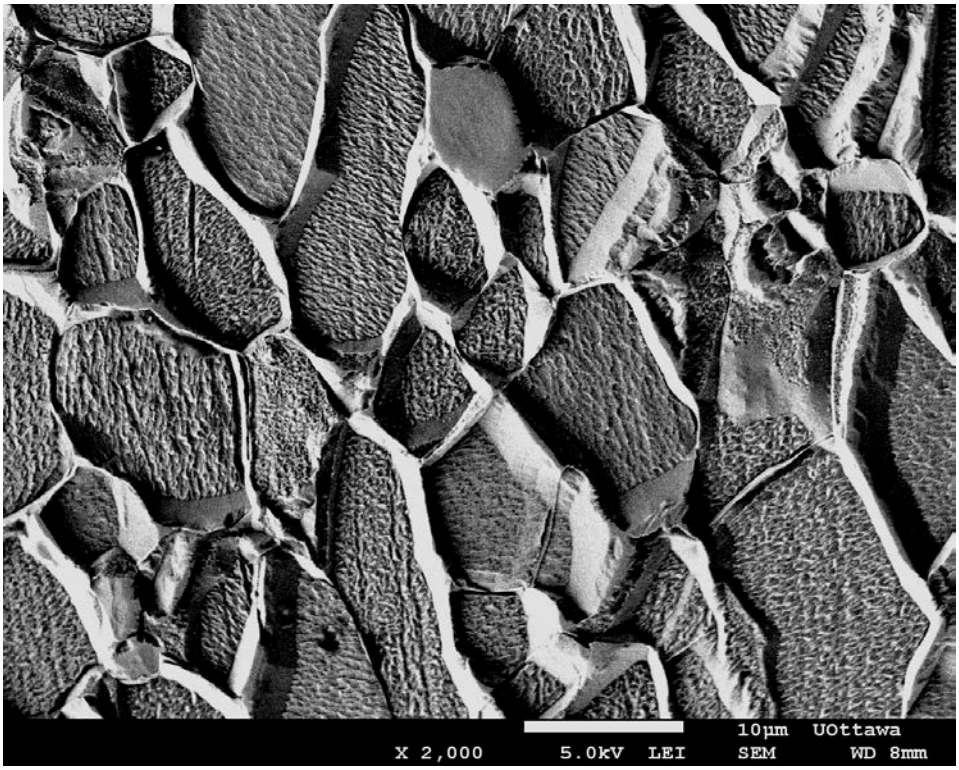

Figure 8-52 - Detail of the etched microstructure of both sides coated coupon induction heated at 1100 ºC – 1150 ºC for 1 second and then at 820 ˚C – 1 minute (magnification 2000X)

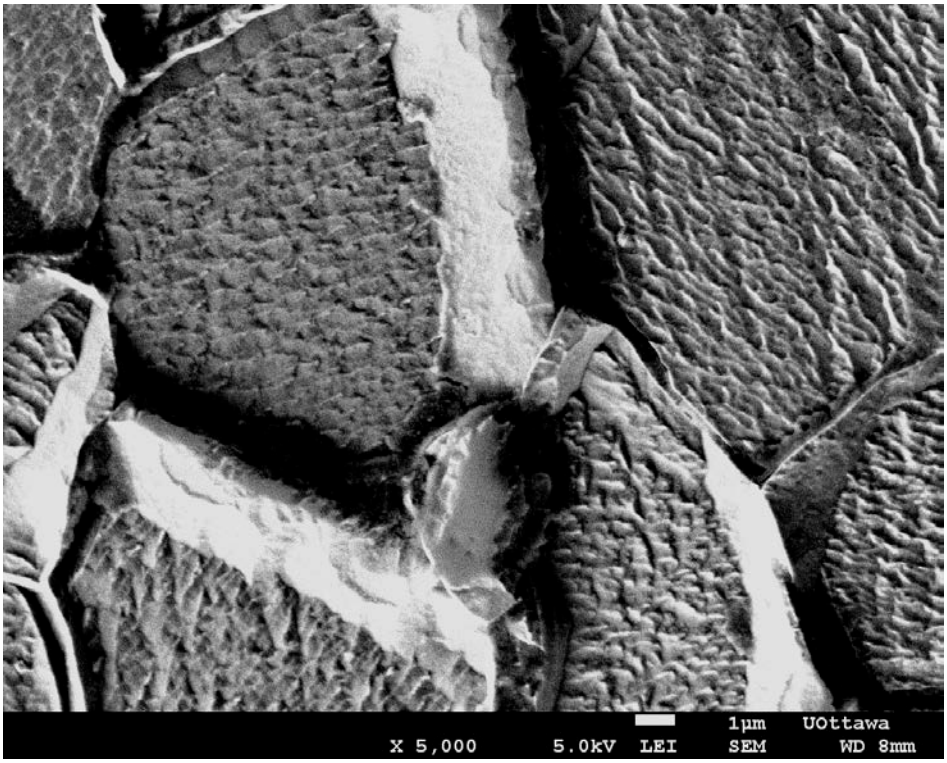

Figure 8-53 - Detail of the etched microstructure of both sides coated coupon induction heated at 1100 ºC – 1150 ºC for 1 second and then at 820 ˚C – 1 minute (magnification 5000X)

From Figure 8-53, it is evident that grains are more etched than grain boundaries. This specimen was the only one who showed so much difference in etching between grains and grain boundaries even if it was etched for 30s with 4% vol. Nital solution as the other specimens. In order to clarify if this microstructure was caused by too much etching, the specimen induction heated for 1 minute was polished again to mirror finish and etched only for 5 seconds with 4% vol. Nital solution and the microstructure was imaged again with SEM. In Figure 8-54 the image of the specimen is shown, where even just after 5 seconds of etching, the grain boundaries are attacked less than the grains. The deposit close to the grain boundaries is due to residues of polishing solution. The high difference in etching between grain boundaries and grains obtained for this specimen could mean that a different phase is present at grain boundaries compared to the core of the grains.

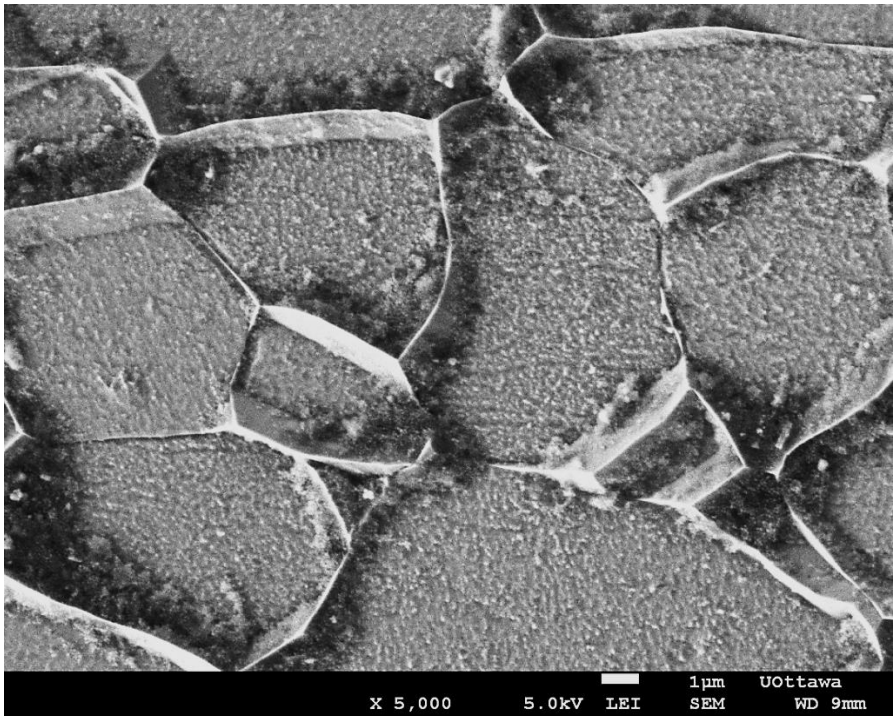

Figure 8-54 - Detail of the etched microstructure of both sides coated coupon induction heated at 1100 ºC – 1150 ºC for 1 second and then at 820 ˚C – 1 minute (etching with 4% vol Nital solution for 5 seconds. Magnification 5000X)

Since the diffusion of carbon is faster through grain boundaries, it is possible that the concentration of carbon in these zones is higher than inside the grains. For this reason, at grain boundaries, a different phase might have been stabilized.

- **SEM images of both sides coated IF steel induction heated at 1100 ºC – 1150 ºC for 1 second and then at 820 ˚C – 2 minutes**

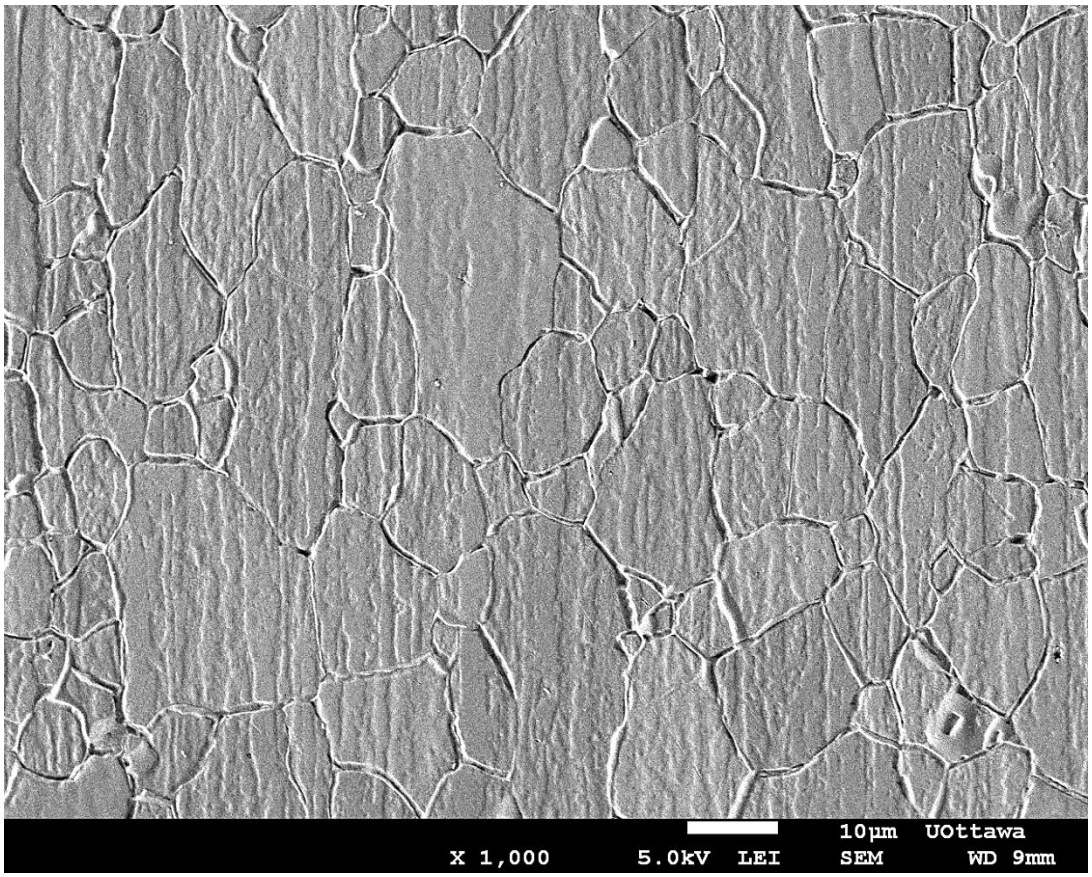

Figure 8-55 - Overall view of the microstructure of both sides coated coupon induction heated at 1100 ºC – 1150 ºC for 1 second and then at 820 ˚C –2 minutes (magnification 1000X)

From Figure 8-55, the microstructure looks very different from what was presented for other specimens. Grain boundaries are revealed but the etching between them and the core of the grains is more uniform. Moreover, lines of another phase can be discerned inside the grains. These lines are running parallel to the main axis of the specimen and they run continuously from one grain to the next one. More detailed view of grains and grain boundaries are reported in Figure 8-56. The grain boundaries appear more attacked by the etchant compared to the grain. This could prove that some carbon has been diffused also inside the bulk of the grains compared to the induction heating performed only for 1 minute.

In Figure 8-57, the microstructure of the specimen induction heated for 4 minutes is shown. Holes are visible at triple junctions of grains since the picture was taken in the gauge length

of a tested tensile coupon. It is also possible that the material got removed during the mechanical polishing or during etching.

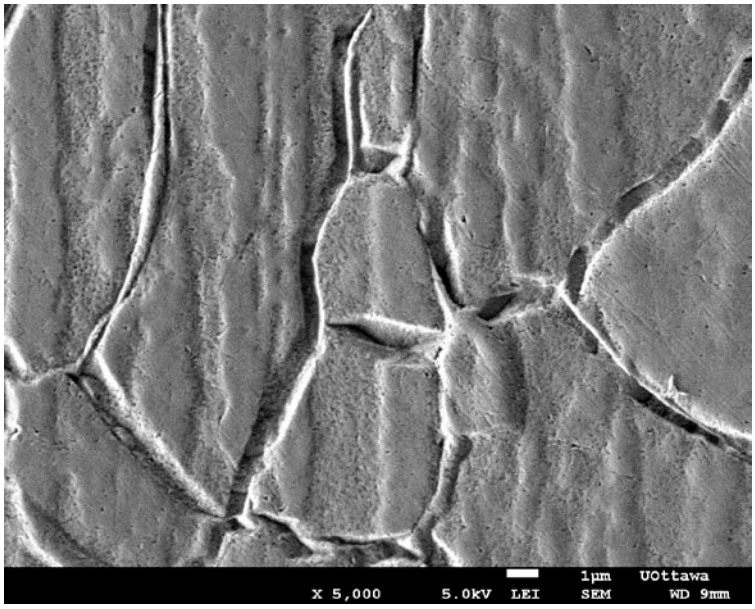

Figure 8-56 - Detail of the etched microstructure of both sides coated coupon induction heated at 1100 ºC – 1150 ºC for 1 second and then at 820 ˚C – 2 minutes (magnification 5000X)

- **<u>SEM images of both sides coated IF steel induction heated at 1100 ºC – 1150 ºC for 1 second and then at 820 ˚C – 4 minutes</u>**

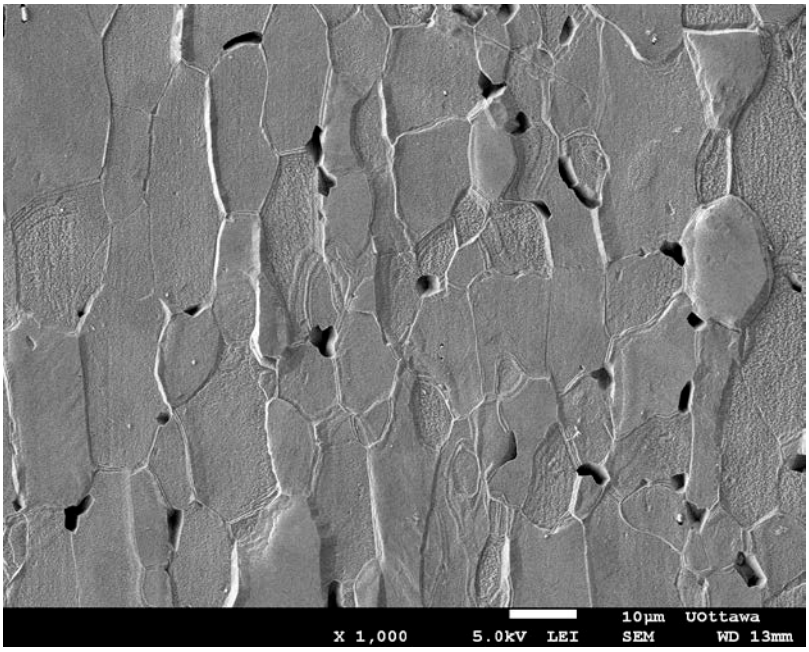

Figure 8-57 - Overall view of the microstructure of both sides coated coupon induction heated at 1100 ºC – 1150 ºC for 1 second and then at 820 ˚C – 4 minutes (magnification 1000X)

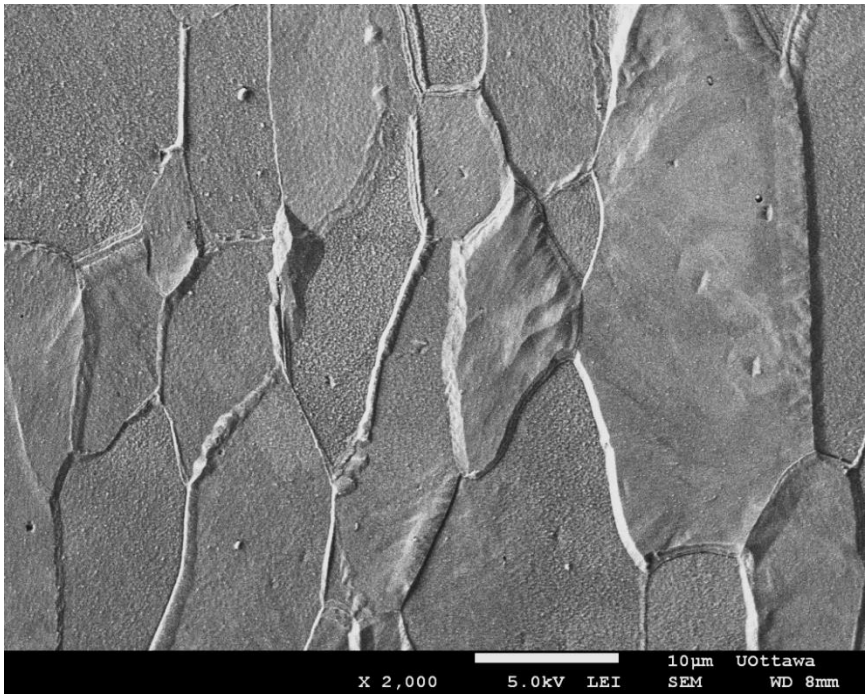

Figure 8-58 - Overall view of another zone of the microstructure of both sides coated coupon induction heated at 1100 ºC – 1150 ºC for 1 second and then at 820 ˚C – 4 minutes (magnification 2000X)

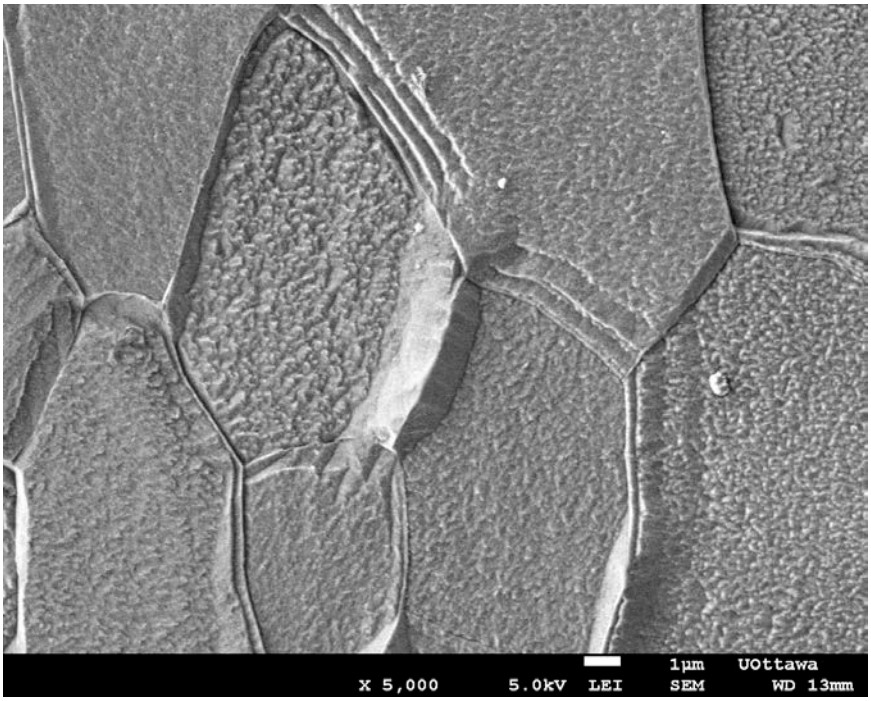

Figure 8-59 - Detail of the etched microstructure of both sides coated coupon induction heated at 1100 ºC – 1150 ºC for 1 second and then at 820 ˚C – 4 minutes (magnification 5000X)

From Figure 8-58 and Figure 8-59, one can see that after 4 minutes of induction heating, the lines which were present inside the grains for the 2 minutes induction heated specimens are no more present and the bulk of the grains are uniformly attacked by the etchant. The grain boundaries show multiple lines; however, their shape looks more marked than the boundaries of the specimen induction heated for 2 minutes,

- **SEM images of both sides coated IF steel induction heated at 1100 ºC – 1150 ºC for 1 second and then at 820 ˚C – 8 minutes**

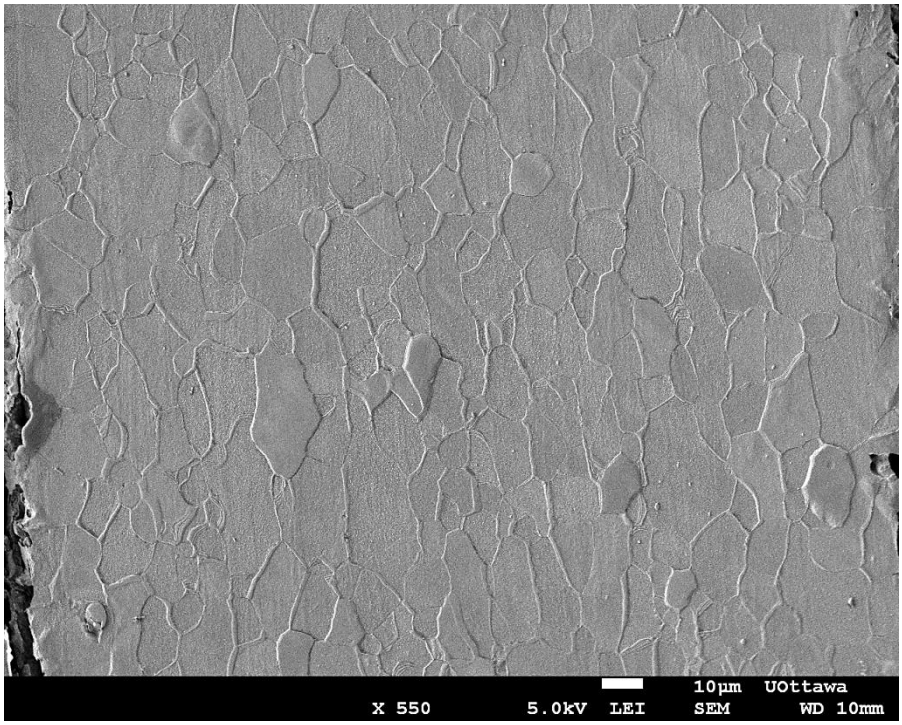

Figure 8-60 - Overall view of the microstructure of both sides coated coupon induction heated at 1100 ºC – 1150 ºC for 1 second and then at 820 ˚C – 4 minutes (magnification 550X)

For the specimen induction heated for 8 minutes the etching between grains and grain boundaries seems to be uniform. No lines are highlighted inside the grains and the grain boundaries have a shape similar to what was found for a one side coated specimen induction heated at 820 ˚C for 30 seconds. Grain boundaries of the specimen coated both sides and induction heated at 820 ˚C for 8 minutes are shown in Figure 8-61, while grain boundaries of the one side coated and induction heated for 30 seconds are shown in Figure 8-47.

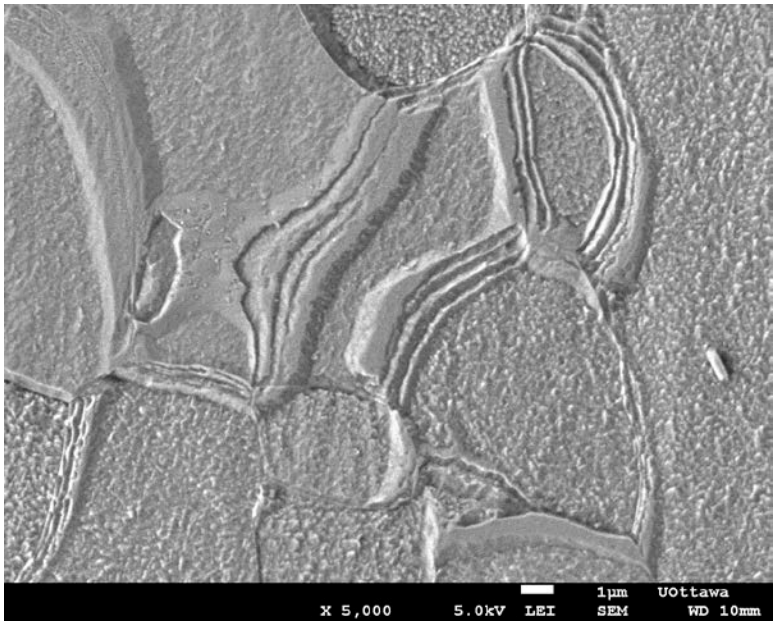

Figure 8-61 - Detail of the etched microstructure of both sides coated coupon induction heated at 1100 ºC – 1150 ºC for 1 second and then at 820 ˚C – 8 minutes (magnification 5000X)

8.2.7. EBSD and TEM analyses on Induction Heated Specimens

The attention was focused on trying to understand what is the main difference between the specimen induction heated for 2 minutes and the one induction heated for 4 minutes, in order to find the reason for the high strength of the first one compared to the absence of Lüdering in the second one. In order to analyze in detail the microstructure, EBSD and TEM analyses were carried out on these specimens. Phase map and band contrast maps were obtained for both specimens from EBSD analyses, however, no clear difference could be discerned between them (results are summarized in section G.4.2.3 of Appendix G). Moreover, if for these specimens, granular bainite, low carbon bainite or martensite-austenite (MA) complex are formed at the grain boundaries, they are not easily detectable with EBSD since the size of the grain boundaries is at the limit of the sensitivity of the system. For this reason, transmission electron microscope (TEM) analyses are the only tool that can help in understanding the obtained microstructures.

8.2.7.1. TEM on Induction Heated Specimens

The specimens for TEM investigations were prepared by Prof. Xavier Sauvage at the University of Rouen (France) following the steps described in Figure 8-62. For specimens induction heated at 1100 ºC – 1150 ºC for 1 second and then at 820 ˚C for 2 minutes,

carbides were found inside the grains (Figure 8-63) and from the SAED pattern (Figure 8-64), it was revealed that these carbides share some orientation with the matrix of ferrite. Moreover, most carbides are arranged in rows and some of them appear elongated.

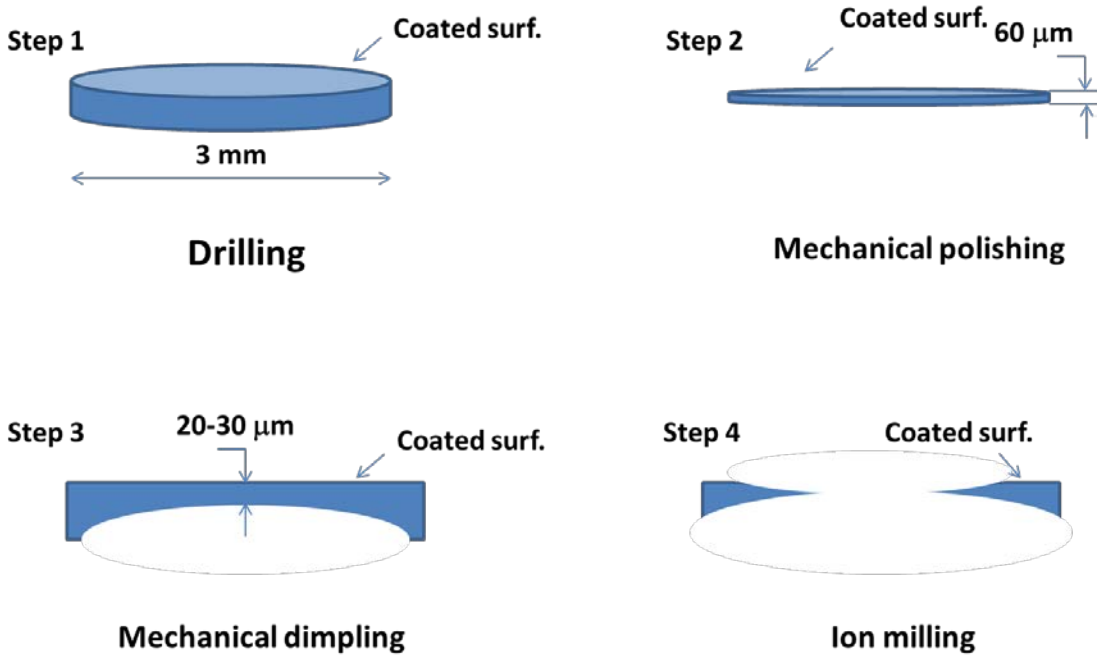

Figure 8-62 - Steps followed to prepare TEM specimens from induction heated coupons

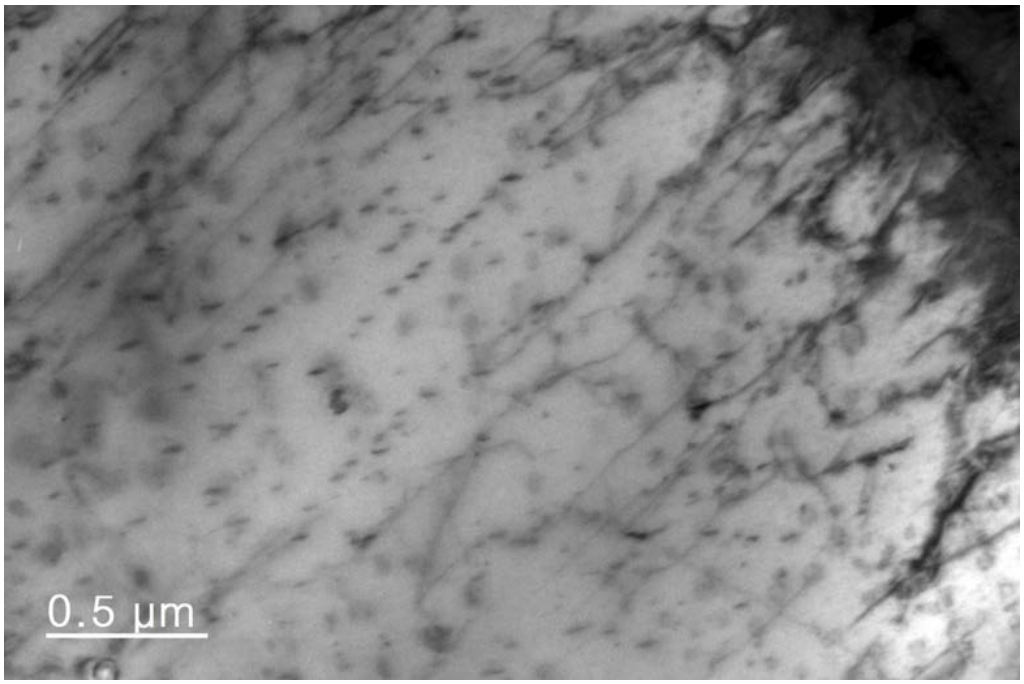

Figure 8-63 - TEM bright field image obtained in one grain of a specimen induction heated at 1100 ºC – 1150 ºC for 1 second and then at 820 ˚C for 2 minutes

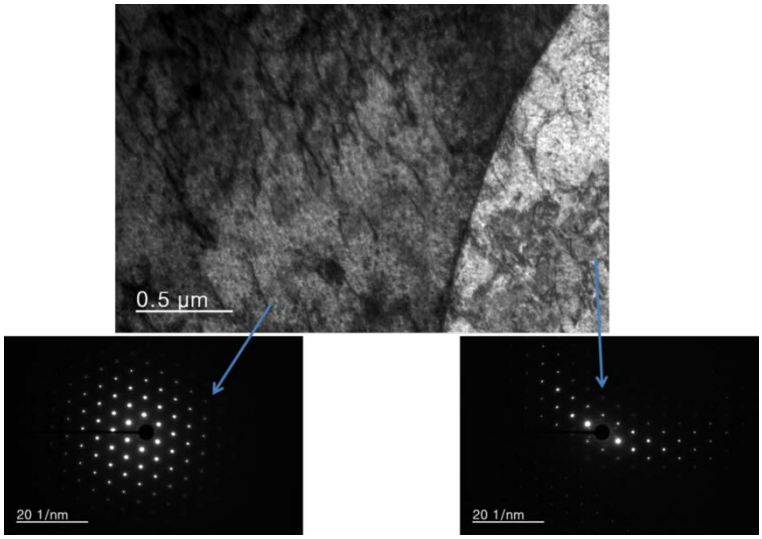

Figure 8-64 - TEM bright field image obtained in another grain of a specimen induction heated at 1100 ºC – 1150 ºC for 1 second and at 820 ˚C for 2 minutes: SAED pattern for carbides is shown

Bright field STEM images were obtained for the same specimen and many dislocations were detected inside the grains togheter with nanosize precipitates (Figure 8-65). From EDS analyses, they were found to be TiC precipitates (Figure 8-66). Despite the S peaks indicated in the image, no S was found in these precipitates.

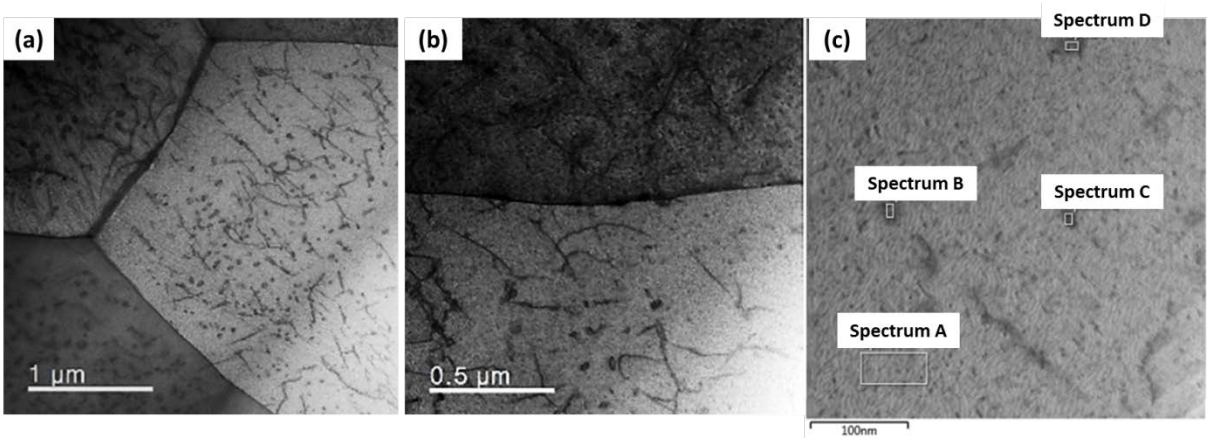

Figure 8-65 - Bright field STEM images of specimen induction heated at 1100 ºC – 1150 ºC for 1 second and then at 820 ºC for 2 minutes (a) and (b). Dislocations and precipitates are visible in both images. (c) zones where EDS spectra were acquired

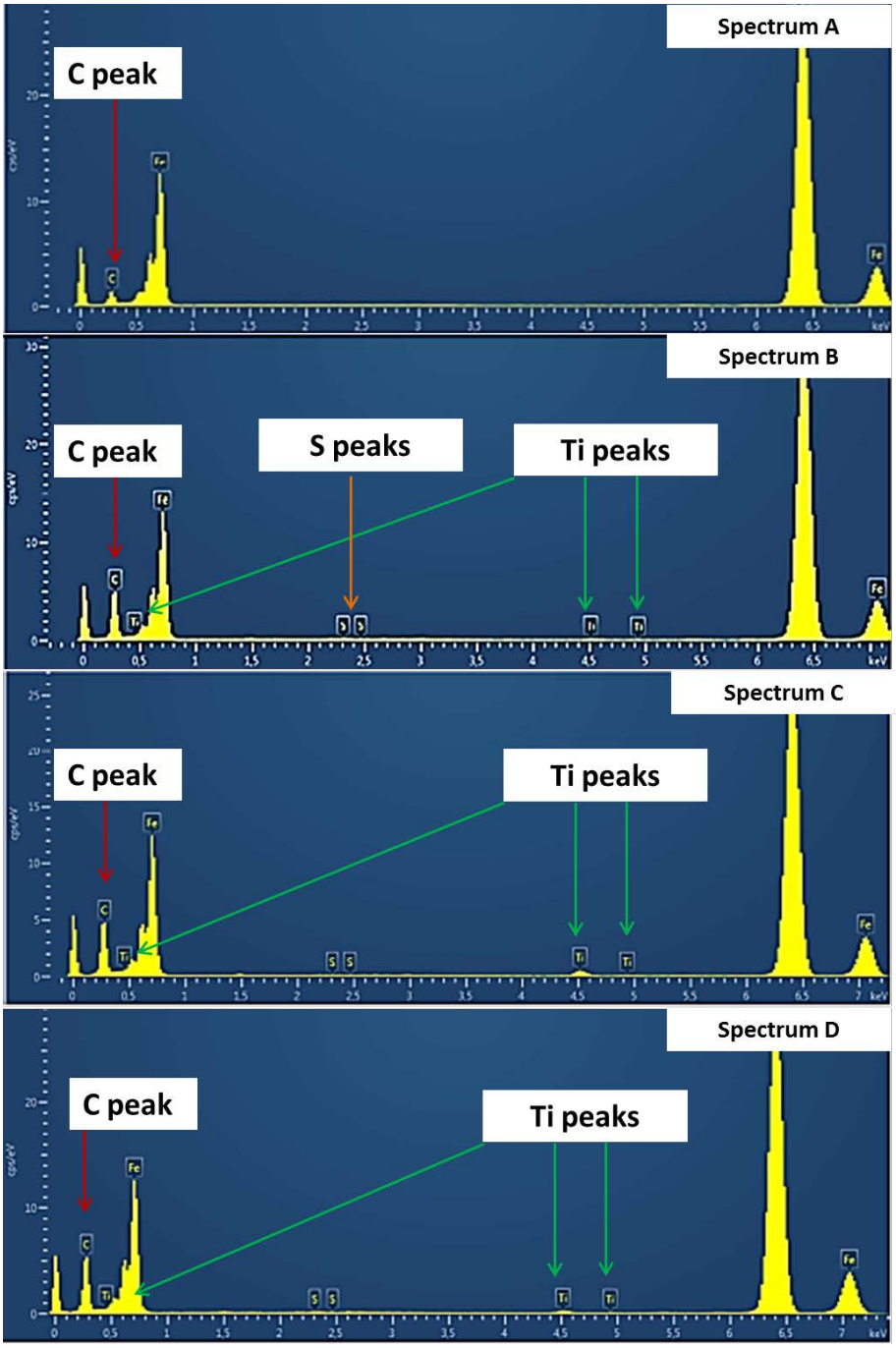

Figure 8-66 - EDS spectra obtained from nanosized carbides found for specimen induction heated at 1100 ºC – 1150 ºC for 1 second and at 820 ºC for 2 minutes

TEM images were extracted in specimens induction heated at 1100 ºC – 1150 ºC for 1 second and then at 820 ºC for 4 minutes and results are shown in Figure 8-67. The specimen has grains with several dislocations and nanoscaled carbides are present as well. Most of the dislocations appear to be connected with carbides. EDS was performed to understand their

composition. Results of the analyzed area are shown in Figure 8-68 and Figure 8-69. Spectra 2, 3 and 4 were obtained from nanosize carbides, while spectrum 5 was obtained from the matrix. Spectra 2, 3 and 4 had peaks of Ti and C proving that these carbides are TiC, while spectrum 5 had only the peaks of iron since the matrix is ferrite.

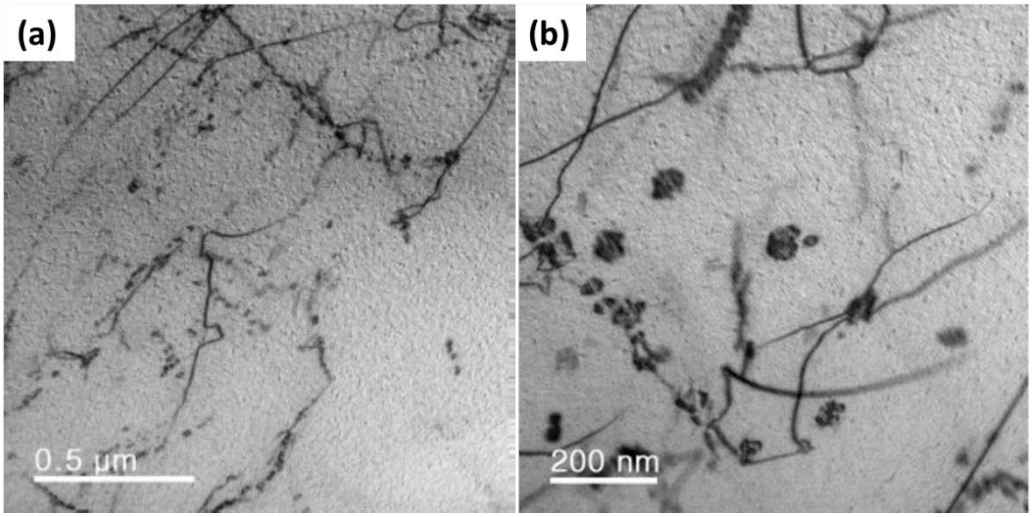

Figure 8-67 - Brigth field STEM images (a) and (b) showing dislocations and carbides obtained for the specimen induction heated at 1100 ºC – 1150 ºC for 1 second and at 820 ºC for 4 minutes

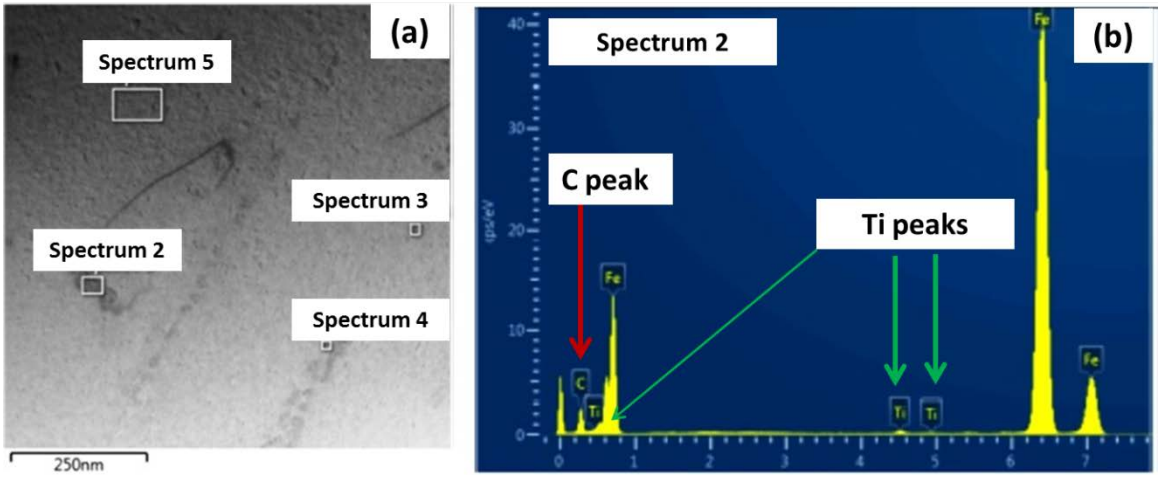

Figure 8-68 - EDS spectra obtained for specimen induction heated at 1100 ºC – 1150 ºC for 1 second and at 820 ºC for 4 minutes: (a) shows the zones where the spectra were extracted; (b) shows the spectrum detected for a TiC carbide

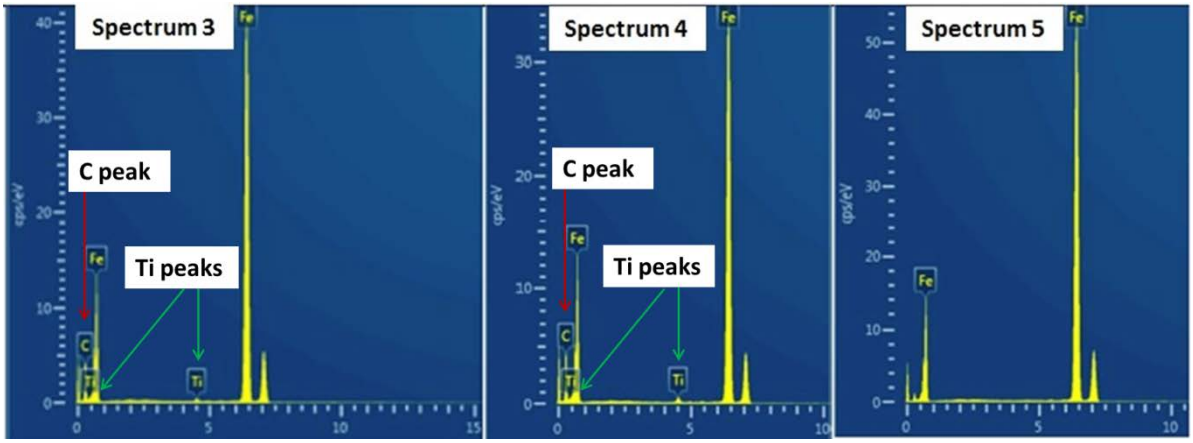

Figure 8-69 – EDS spectra obtained for specimen induction heated at 1100 ºC – 1150 ºC for 1 second and at 820 ºC for 4 minutes: spectra 3 and 4 were detected from TiC carbides, while spectrum 5 was obtained from the ferrite matrix

From TEM analyses, no clear difference was found between the 2 minutes and the 4 minutes induction heated specimens. It was difficult to establish if they differ in terms of density of dislocations, volume fraction of precipitates and size of precipitates since they are not uniformly distributed, especially for the coupon induction heated for 4 minutes.

8.3. Structure of the FeC film during Induction Heating

In chapter 5 it was already shown that during annealings performed in the vacuum furnace, the film is amorphous for temperatures equal or lower than 430 ˚C for 1h, while at or above 530 ˚C for 1h, the FeC film crystallizes into cementite. It was already shown through a stoichiometric calculation that this crystallization limits the carbon available for diffusion into the IF substrate.

From induction heating experiments, it was shown that mechanical properties are improving up to 2 minutes of heat treatment but the yield stress and the UTS decrease after 4 minutes and 8 minutes of heat treatment. This indicates that the film is probably crystallized after 2 minutes of induction heat treatment and that no more carbon is diffusing from the film into the IF substrate; otherwise lath-martensite or high carbon bainite would have been detected inside the microstructure. According to the work made by Bauer-Grosse et al. [125], the FeC films containing 30 at% of carbon are supposed to be crystallized above 700 K (427 ˚C), so at the high temperatures obtained during the induction heating, the film is also expected to crystallize. However, the influence of magnetic field and of high heating rate due to

induction heating was not taken into account during the experiments performed by Bauer-Grosse. Nevertheless, if carbon could diffuse even after 2 minutes of induction heating, the decrease in yield stress obtained after 4 minutes and 8 minutes of heat treatment cannot be justified; since higher diffusion of carbon would facilitate the stabilization of austenite and consequently the formation of bainite or martensite after quenching in water.

In order to further characterize the film, grazing X-ray analyses on the surface of a both sides coated coupon induction heated at 820˚C for 1 minute were performed. In a grazing X-ray experiment, the incident X-ray beam hits the surface at an angle of 1˚ or less ensuring that the probed depth of the sample is around 10 nm [186]. The detector is collecting the beam diffracted from lattice planes perpendicular to the surface of the specimen [186].

Two specimens were analyzed with grazing X-ray, the first one was induction heated at 820 ˚C for 1 minute and the second was induction heated at the same temperature for 4 minutes. The film is expected to be amorphous after 1 minute but it is expected to be crystallized after 4 minutes. For the first scan performed on the 1 minute specimen, the 2Θ angle was run from 2˚ up to 77˚ and the graph is shown in Figure 8-70.

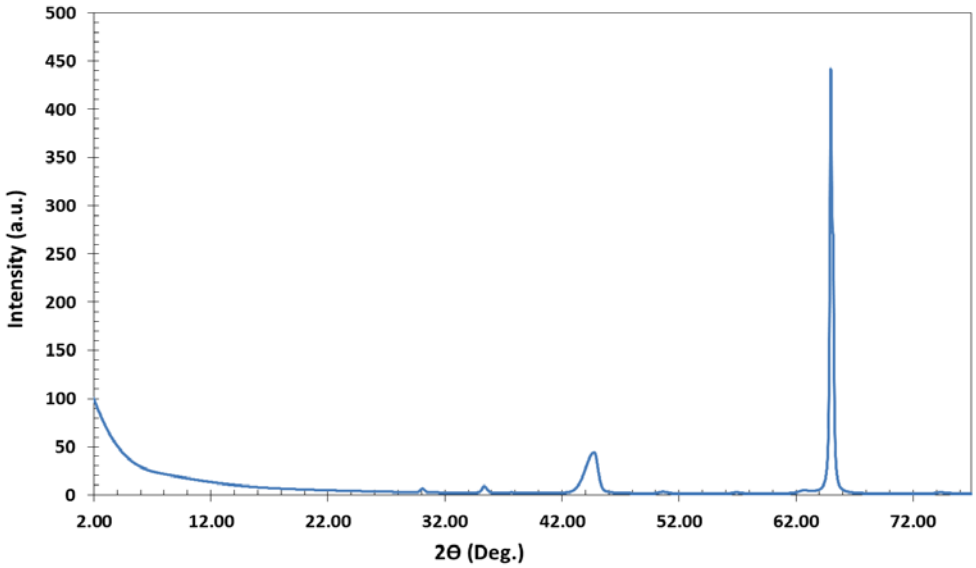

Figure 8-70 - Grazing X-Ray analyses of the FeC film induction heated at 1100 ºC – 1150 ºC for 1 second and at 820 ˚C for 1 minute

In order to better characterize the peaks from 26˚ to 58˚, it was decided to exclude the peak of ferrite at 65˚, for this reason a narrower scan going from 24˚ up to 64˚ was run. The graphs of both specimens inside this range are shown in Figure 8-71. In the same figure, the identification of the peaks is also reported.

The difference in angular position of the peaks between the X-ray obtained for the FeC film in Chapter 5 and the grazing x-ray of the FeC film which was induction heated are due to the different K-alpha radiation used for the analyses. For the FeC film annealed in high vacuum furnace and analyzed with X-ray, the Co K-alpha radiation was used, while for the induction heated FeC film the Cu K-alpha radiation was used. The following table shows the experimental position of the peaks in the plot and the theoretical expected position.

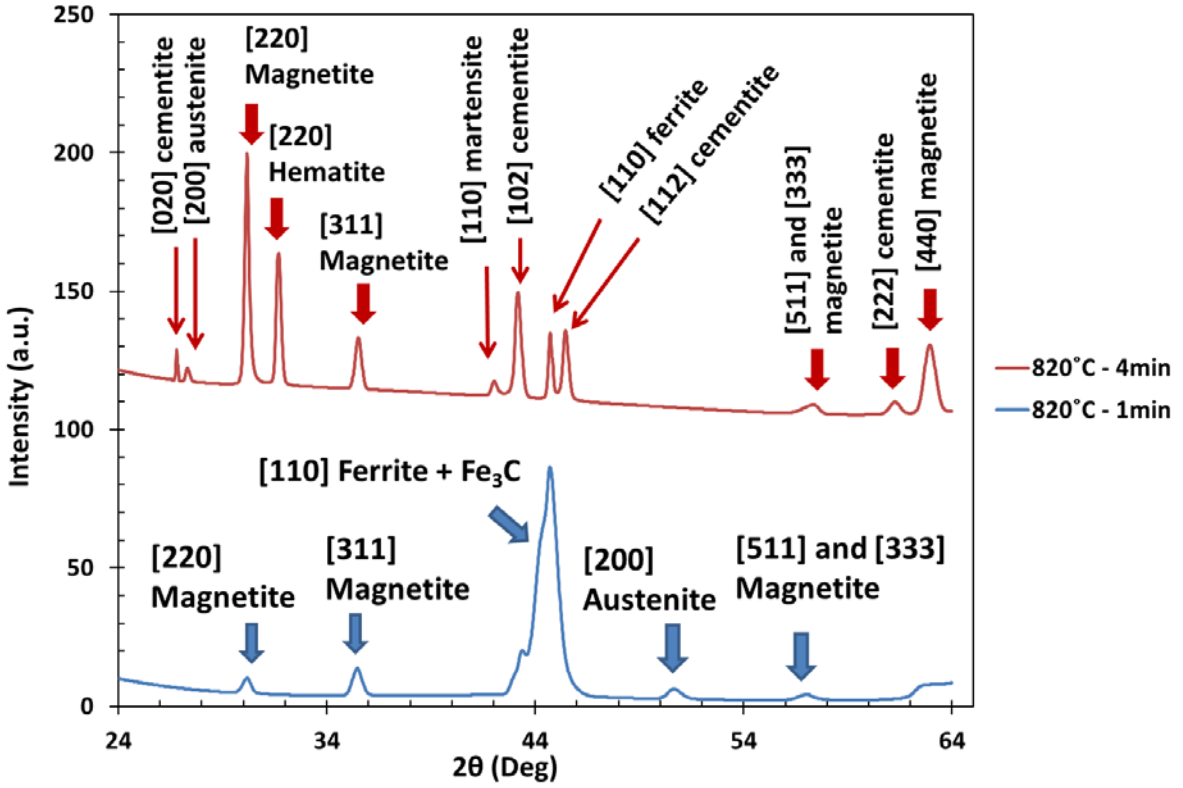

Figure 8-71 - Grazing X-Ray analyses of the FeC film induction heated at 1100 ºC – 1150 ºC for 1 second and at 820 ˚C for 1 minute and 820 ˚C for 4 minutes analyzed from 24˚ to 64˚

Experimental position of the peaks	Phase identified	Expected position of the peak	Reference
30.2˚	[220] magnetite	30.11˚	[187]
35.4˚	[311] magnetite	35.46˚	[187]
43.4˚	[102] cementite or [111] austenite	43.74˚ (for cementite) 43.64˚ (for austenite)	[188] - [189] - [190]
44.7˚	[110] ferrite	44.67˚	[191]
50.6˚	[200] austenite	50.78˚	[190]
57˚	[511], [333] magnetite	57˚	[187]

Table 8-10 - Comparison between experimental position of the peaks and their theoretically expected position for specimen induction heated at 1100 ºC – 1150 ºC for 1 second and then at 820 ˚C for 1 minute

Experimental position of the peaks	Phase identified	Expected position of the peak	Reference
26.8 ˚	[020] cementite	26.4	[188]
27.3 ˚	[200] austenite	27.3˚	[192]
30.2˚	[220] magnetite	30.11˚	[187]
31.7 ˚	[220] hematite	32˚	[193]
35.5˚	[311] magnetite	35.46˚	[187]
42 ˚	[211] cementite	42.88˚	[188]
43.2˚	[102] cementite or [111] austenite	43.74˚ (for cementite) 43.64˚ (for austenite)	[188] - [189] - [190]
44.7˚	[110] ferrite	44.67˚	[191]
45.5 ˚	[112] cementite	45.86˚	[188]
57.3˚	[511], [333] magnetite	57˚	[187]
61.2˚	[222] cementite	61.26˚	[188]
62.9˚	[440] magnetite	62.59˚	[187]

Table 8-11 - Comparison between experimental position of the peaks and their theoretically expected position for specimen induction heated at 1100 ºC – 1150 ºC for 1 second and then at 820 ˚C for 4 minutes

For the specimen induction heated for 1 minute, the peak at position 44.7˚ is very large and asymmetric. This peak could be originated from the following contributions: [110] ferrite plus the contribution of [031] cementite (expected at 44.99˚), [102] cementite (expected at 43.74˚), [211] cementite (expected at 42.88˚), [220] cementite (expected at 44.57˚) and [112] cementite (expected at 45.86˚). Moreover, it is possible that the peak in position 44.7˚ and identified as [110] ferrite could be also [110] martensite. Martensite has peaks at 44.57˚ and at 64.88˚ [190]. From the results presented above, after 1 minute of induction heating at 820 ˚C followed by quenching in water, the film is oxydized (presence of magnetite) and part of it seems to be crystalline (detection of cementite). However, it is difficult to discern if the peak at position 44.7˚ is mainly due to ferrite which transformed into martensite after quenching or if it is mainly due to ferrite plus cementite. The initial carbon content of the film is 30 at% so it is possible that the film after quenching could transform into martensite. For the induction heating of 1 minute, however, the peaks seem broader than after the induction heating of 4 minutes. This indicates that at 4 minutes of heat treatment, the film is crystallized and this limits the amount of carbon available to be diffused towards the IF substrate.

8.4. Induction Heating on Pre-strained Tensile coupons

As already shown in chapter 7 of this PhD thesis, the quantities evaluated during a pre-strain test are represented in Figure 8-72 and are defined as follows:

- $(\sigma_F - \sigma_{YS})$ is the strengthening due to pre-strain;
- $(\sigma_{YS\ upper} - \sigma_F)$ is the strengthening due to carbon diffusion caused by induction heating;
- $(L1 - \sigma_F)$ is the strengthening due to diffusion considering the average of stress in the Lüders plateau. $L1$ is the average stress of the Lüders plateau.
- $(\sigma_{YS\ upper} - \sigma_{YS})$ is the total strengthening;

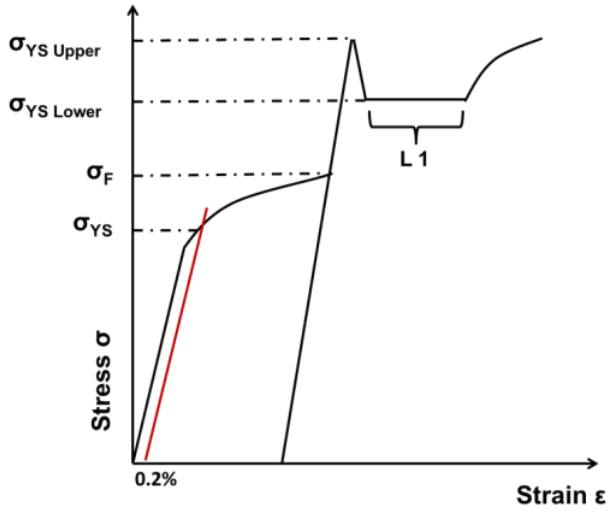

Figure 8-72 - Schematic view of the quantities evaluated for induction heating after a pre-strained coupon

The engineering stress-strain curves for the specimens which underwent induction heating are shown in Figure 8-73.

After prestrain, specimens A, B and C were induction heated at 1100 ºC – 1150 ºC for 1 second and then at 820 ˚C for 2 minutes, 4 minutes and 8 minutes respectively.

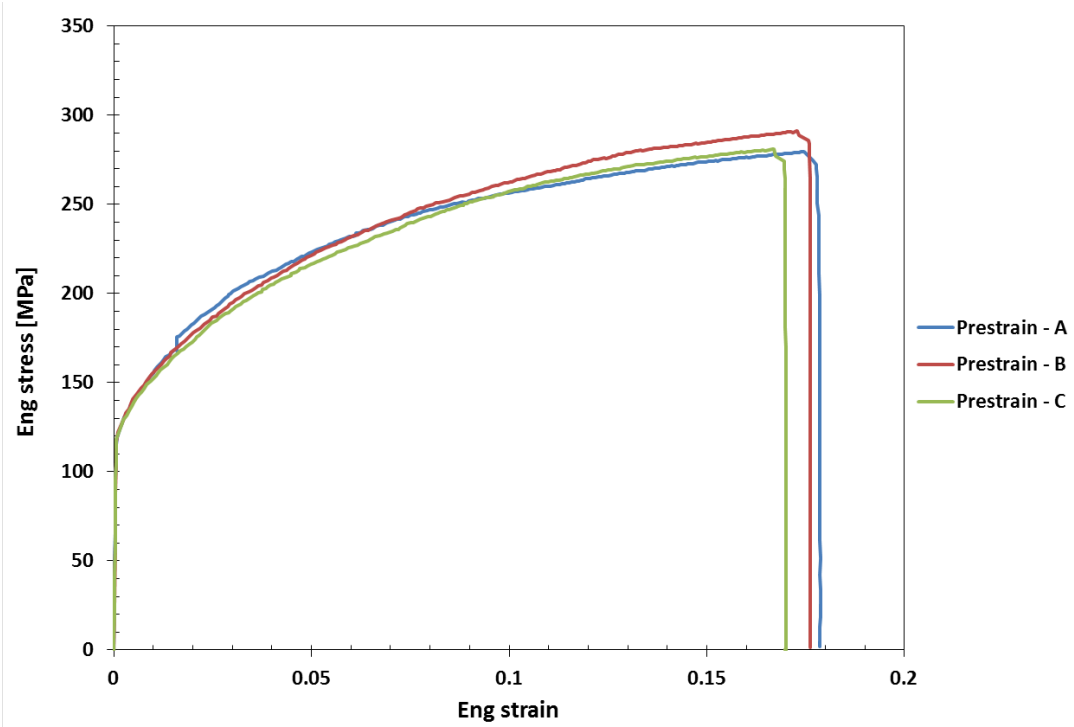

Figure 8-73 - Prestrain engineering stress—strain curves for two specimens before performing induction heating

In the following figures, for each specimen, the pre-strain curve and the curve after pre-strain and induction heating will be shown in the same plot and compared with the curve obtained for the same induction heat treatment but without pre-strain. In the graphs, *Δ1* represents the strengthening obtained with induction heat treatment performed without prestrain, while *Δ2* represents the strengthening obtained from induction heating on a prestrained coupon. Recalling Figure 8-72, *Δ2* is equal to ($\sigma_{YS\ upper} - \sigma_F$).

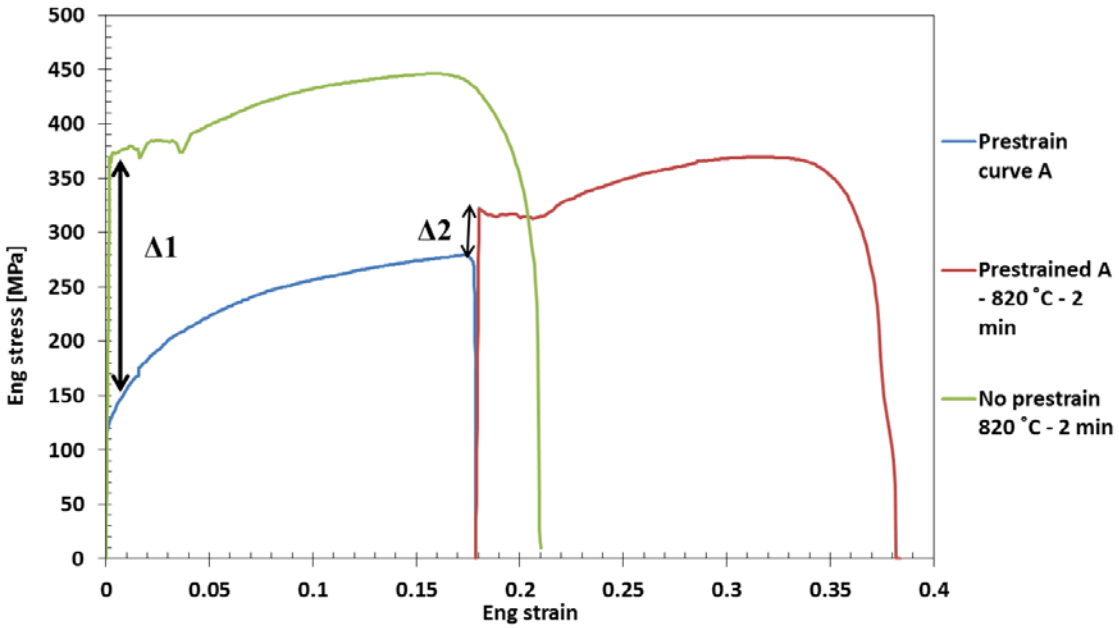

Figure 8-74 - Engineering stress-strain curves for 16.5% pre-strained coupon coated both side with 500 nm thick FeC film and induction heated at 1100 ºC – 1150 ºC for 1 second and then at 820 ˚C – 2 min (A)

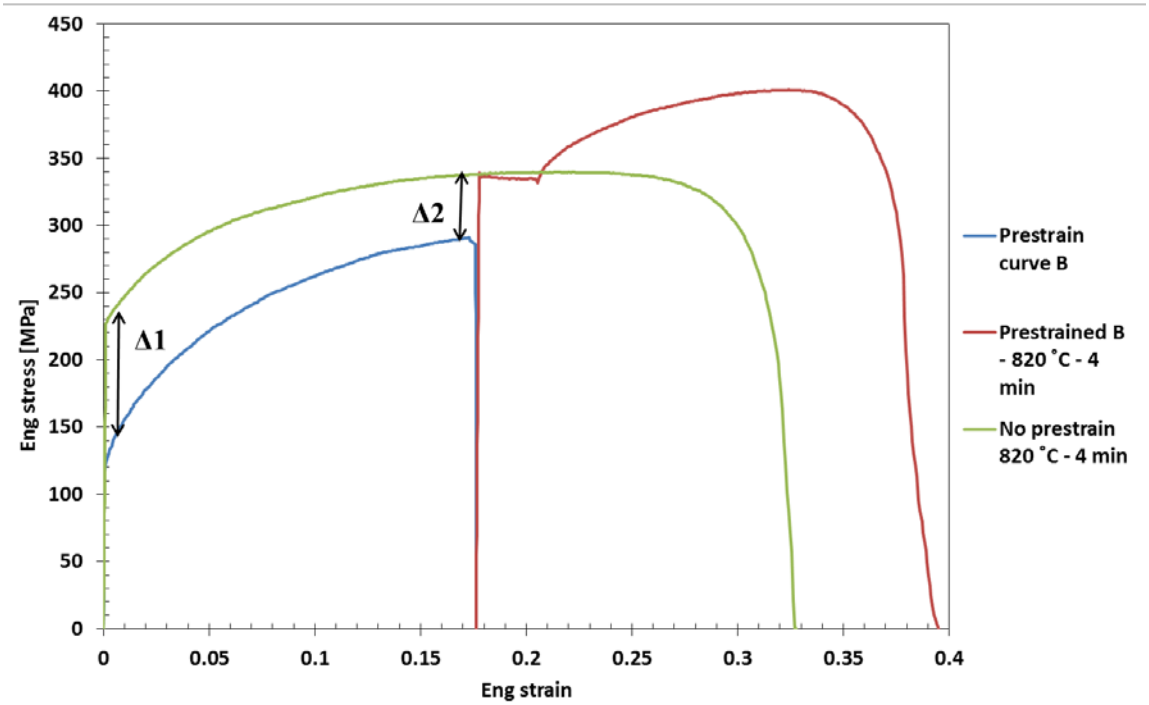

Figure 8-75 - Engineering stress-strain curves for 16.5% pre-strained coupon coated both side with 500 nm thick FeC film and induction heated at 1100 ºC – 1150 ºC for 1 second and then at 820 ˚C – 4 min (B)

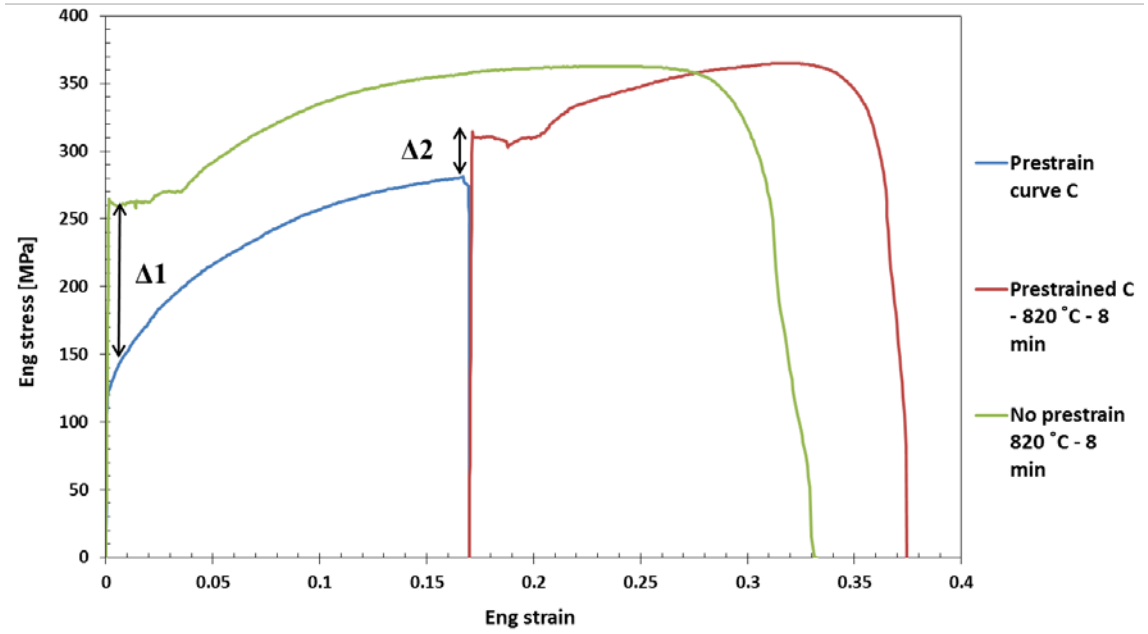

Figure 8-76 - Engineering stress-strain curves for 16.5% pre-strained coupon coated both side with 500 nm thick FeC film and induction heated at 1100 ºC – 1150 ºC for 1 second and then at 820 ˚C – 8 min (C)

Sample	$(\sigma_F - \sigma_{YS})$ [MPa]	$\Delta 2$ $(\sigma_{YS\ Upper} - \sigma_F)$ [MPa]	$\Delta 1$ [MPa]	$(L1 - \sigma_F)$ [MPa]	$(L1 - \sigma_{YS})$ [MPa]	$(\sigma_{YS\ Upper} - \sigma_{YS})$ [MPa]
820 ˚C-2 min A	164	43	258	36	201	207
820 ˚C-4 min B	174	48	110	45	219	222
820 ˚C-8 min C	163	34	146	28	191	197

Table 8-12 - Numerical values of mechanical properties of prestrained coupons induction heated at 1100 ºC – 1150 ºC for 1 second and then at 820 ˚C for different times

According to the values reported in Table 8-12, by comparing the values of *Δ2* and *Δ1*, one can see that the strengthening due to carbon diffusion in pre-strained coupons is much lower than the strengthening caused by the same amount of carbon diffused into a not-prestrained steel. Pre-strain increases the density of dislocations and when carbon is diffused, it will have more dislocations to saturate and this will result in less carbon dense Cottrell atmospheres. The result is that locally inside the grains and or even at dislocations, the concentration of carbon will not be high enough to cause precipitation as was obtained, for example, for a not-prestrained coupon after 2 minutes of induction heating. However, if for pre-strained coupons, the total strengthening due to pre-strain and carbon diffusion (column $(\sigma_{YS\ Upper} - \sigma_{YS})$ of Table 8-12) is compared with *Δ1*, one can see that pre-strain plus carbon diffusion will give a final strengthening which is higher than what was obtained just with carbon diffusion, except for the specimen induction heated for 2 minutes. Furthermore, while for the not-prestrained coupons there is a high difference in the strengthening due to carbon diffusion for the different times (column *Δ1* in Table 8-12), the same behaviour is not obtained for pre-strained coupons (column *Δ2* in Table 8-12) and this could be justified by the carbon at dislocations being "diluted" enough to not cause any precipitation.

8.5. Discussion and Conclusions

The first consideration must be done concerning the austenitization of the IF substrate. In the first part of the induction heating, the specimen is brought in 10 seconds to 1150 ˚C and according to literature; the start temperature for austenite formation is a function of heating rate, initial microstructure and carbon content [194]. Usually, Orlich's curves are used to determine the critical austenitic transformation temperatures. In literature [194] the formula

to evaluate the start temperature for austenite formation for a steel SAE 1045 is reported. In particular, if the heating rate is lower than 150 ˚C/s, the start temperature for austenite formation is given by:

$$A_{C1} = (4.84)\log^3\left(\dot{T}\right) + (3.33)\log^2\left(\dot{T}\right) + (8.23)\log\left(\dot{T}\right) + 735.91 \qquad \text{(eq. 8-5)}$$

while, if the heating rate is ≥ 150 ˚C/s, then A_{C1} (the austenite start temperature) is equal to 790 ˚C. If eq. 8-6 is used considering the heating rate of 115 ºC/s used for the Gracos coupons, the temperature A_{C1} is equal to 810 ºC. For the steel used in this PhD, the microstructure is fully ferritic before starting the induction heat treatment and the carbon content is low and all the carbon is supposed to be combined to the titanium which is added in the composition for this purpose. When this IF steel is brought to 1150 ˚C in 10 s, the microstructure is supposed to transform completely into austenite even if the specimen stays at that temperature just for 1s. According to the Fe-Fe_3C equilibrium phase diagram, a specimen containing no carbon or only 3 x 10^{-3} wt% of carbon (as the IF steel used in this work) will be fully austenitic for temperatures above 912 ˚C [152]. Since the temperature reached by the specimen during the heating rate of the induction heating is well above 912 ˚C, it is believed that the specimen is fully austenitic. One should also note that 1150 ˚C is very close to the temperature 1153 ˚C, which corresponds to the maximum solubility limit of carbon into austenite equal to 2.14 wt% (9.23 at%) [152].

When the temperature is lowered to 820 ˚C, depending on how long the heat treatment is performed, the final microstructure and mechanical properties will be different. It is important to consider the influence played by the magnetic field. In literature [195] it was reported that the transformation of austenite into ferrite is accelerated under the influence of an external magnetic field. Indeed, the magnetic field enhances the difference in total Gibbs free energy between the product ferrite and the parent austenite phase and as a consequence, the nucleation rate and quantity of ferrite is increased [195]. Moreover, it was also reported that the α/α+γ and the γ/α+γ boundaries in the Fe-Fe_3C phase diagram shift under the magnetic field towards higher carbon contents or high temperatures [195].

The following discussion will be divided in two subsections; the first will explain the mechanism occurring for one side coated coupons, while the second section will discuss the results for the both sides coated coupons. It must be pointed out that the physical

mechanisms of microstructure transformation which take place during induction heating are exactly the same for one side and both sides coated coupons. However, there is always a 2 factor of difference between the mechanical properties of one side and both sides coated coupons, since the amount of diffused carbon is higher for the second one. For this reason, the increase of yield stress for both sides coated coupons is twice the increase of yield stress obtained for one side coated coupons.

8.5.1. One side coated coupons

For the one side coated coupons, the main results obtained from mechanical testing are the following:

- After only 30 seconds of heat treatment at 820 ˚C the yield stress is increased by 54 MPa compared to the yield stress of an uncoated and not-annealed IF steel (see Figure 8-26). Moreover this specimen showed a gradient of hardness through thickness with a Vickers hardness of 240 MPa close to the coated surface and of 160 MPa close to the uncoated surface (see Figure 8-21). From metallographic analyses it was shown that the grains close to the coated surface show some features, while the remaining area of the thickness is quite homogeneous. EBSD analyses confirmed that the microstructure is mainly ferritic in the middle of the specimen. From the value of hardness measured close to the coated surface, it is believed that in those grains carbides are present. The evolution of the microstructure for these coupons is shown schematically in Figure 8-77, where the microstructure is fully austenitic at 1150 ºC for 1s, then once the specimen is brought to 820 ºC, the amount of diffused carbon is not sufficient to stabilize any austenite (except in the grains which are up to 20 µm from the coated surface as predicted by Table 8-3 considering 1 second of induction heating at 1150 ºC and 30 seconds at 820 ºC). For this reason, when the temperature is lowered to 820 ºC, the microstructure becomes fully ferritic.

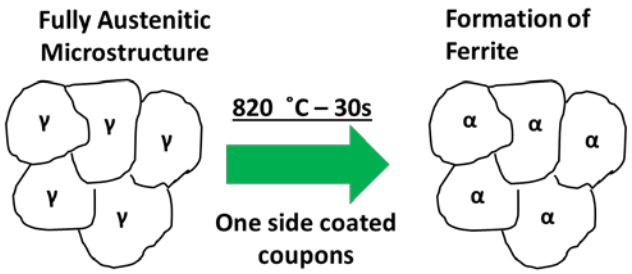

Figure 8-77 - Schematic view of microstructure evolution for one-side coated coupon during induction heating at 1100 ºC – 1150 ºC for 1 second and then induction heated at 820 ºC – 30 seconds

- After 2 minutes of induction heating at 820 ˚C, the highest yield stress among all one side coated coupons is obtained (see Figure 8-26). The increase in yield stress compared to an uncoated and not-annealed IF steel is 134 MPa. More details of the mechanism of microstructure transformation for this time and temperature will be given in the next paragraph when the results for both sides coated coupons will be explained. However, it is believed that after 2 minutes, the maximum amount of carbon has diffused from the FeC film, which is crystallized after these 2 minutes. The diffused carbon can cover the whole thickness of the coupon and the amount is high enough to stabilize some austenite (mainly at grain boundaries and in the grains close to the coated surface). At 820 ˚C the steel is in the ferrite/austenite intercritical region, so only the grains which contain enough carbon will be stabilized as austenite, while the others will transform into ferrite. Precipitation of carbides can occur in the carbon rich austenite and this might explain the high strength found for this annealing condition.
- An increase of yield stress of 128 MPa is obtained for one side coated coupons after induction heating at 1100 ˚C for 4 minutes. This increase of yield stress can be considered to be the same as the strengthening obtained for induction heating at 820 ˚C for 2 minutes, however, the transformation of the microstructure is different. At 1100 ˚C the microstructure is considered to be fully austenitic. The amount of carbon diffused is the same as the one diffused after 2 minutes of heat treatment, however, the diffusion proceeds slower in austenite compared to ferrite since its activation energy is higher than the one for diffusion of carbon into ferrite. For this reason, even

if the treatment was prolonged for 4 minutes, the final strengthening was found to be the same.

- If the heat treatment is done at 820 ˚C for 4 minutes, the Lüders plateau is suppressed, even if a decrease in the yield stress is obtained compared to the specimen annealed at 2 minutes since the yield stress is only 51 MPa higher than an uncoated and not heat treated IF steel. It is believed that Lüdering is suppressed due to full precipitation of carbon (further details are reported in the next section where results of both sides coated coupons are summarized).

8.5.2. Both sides coated coupons

For the both sides coated coupons, the main results obtained from tensile tests are the following:

- After 1 minute of heat treatment at 820 ˚C, the increase of yield stress was 144 MPa. From SEM images, it was revealed that the specimen had two different phases, one at grain boundaries which was not attacked by Nital solution and one inside the grains. In just one minute, the diffusion of carbon at the grain boundaries is fast enough to cover the whole thickness of the specimen since as reported in literature [18], diffusion at grain boundaries can be 3 or 4 orders of magnitude faster than through the bulk of the grains, As shown in Table 8-4, in 1 minute of heat treatment at 820 ºC, the depth covered by carbon at grain boundaries is 108 µm considering diffusion just from one side of the IF steel. This means that if carbon diffusion occurs from both sides, then the whole thickness of 200 µm will be affected. It is believed that retained austenite might be present only at grain boundaries and during quenching in water, carbide precipitation can occur only in those zones but not inside the bulk of the grains. The pattern highlighted by SEM images resembles epitaxial ferrite which is formed during cooling from austenite stabilized at grain boundaries. The schematic evolution of the microstructure is reported in Figure 8-78, where the microstructure is initially fully austenitic, then, when the temperature is lowered at 820 ºC for 1 minute, the carbon is mainly at the grain boundaries and during quenching, carbides are probably formed in those zones, while the bulk of the grains is ferrite.

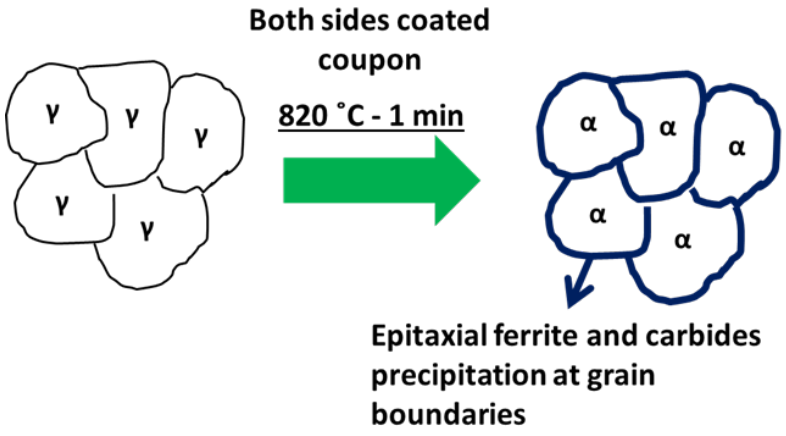

Figure 8-78 - Schematic view of microstructure evolution for both-sides coated coupon during induction heating at 1100 ºC – 1150 ºC for 1 second and then induction heated at 820 ºC – 1 minute

- Both sides coated specimens induction heated at 820 ˚C for 2 minutes show the highest increase of yield stress of 261 MPa. When these specimens are heated up to 1150 ˚C for 1 s, the microstructure is fully transformed into austenite. When the temperature is lowered to 820 ˚C – 2 minutes, the amount of diffused carbon is high enough to stabilize austenite not only at the grain boundaries but also inside the grains for the temperature of 820 ºC. At this temperature, however, the steel is in the ferrite/austenite region of the Fe-Fe_3C diagram so ferrite will start nucleating from the austenite grains. The nucleation of ferrite is favoured at the triple points of austenitic grains. In literature [196], [197] it was reported that the magnetic field can influence the growth of ferrite. Indeed, ferrite will grow following the direction of the lines of the magnetic field since this phase is magnetic compared to the parent austenite which is non-magnetic. However, this does not explain the elongated features that are highlighted after the microstructure is etched with Nital solution. First of all, in literature all the magnetic fields used for experiments are above 5T of intensity; moreover, when ferrite is growing aligned to the magnetic field, a grain boundary is clearly distinguished between this ferrite and the surrounding material (see microstructures reported in [196], [198]). This is not the case, for the specimen presented in this chapter. So the lines found for specimens induction heated for 2 minutes are most probably due to an etching effect since carbides might have precipitated preferentially in some zones compared to others, causing different levels of etching.

Garcin [199] has calculated the variation of the difference in Gibbs free energy between ferrite and austenite as function of the magnetic field intensity. The results shown in Figure 8-79 prove that to have a marked change of the difference in Gibbs free energy, it is necessary to have magnetic fields of several Tesla of intensity. For a given temperature, the driving force for the transformation of austenite into ferrite increases as the intensity of the magnetic field is increased [199]. In the same work, Garcin [199] stated that the influence of the magnetic field on the kinetics of transformation is negligible.

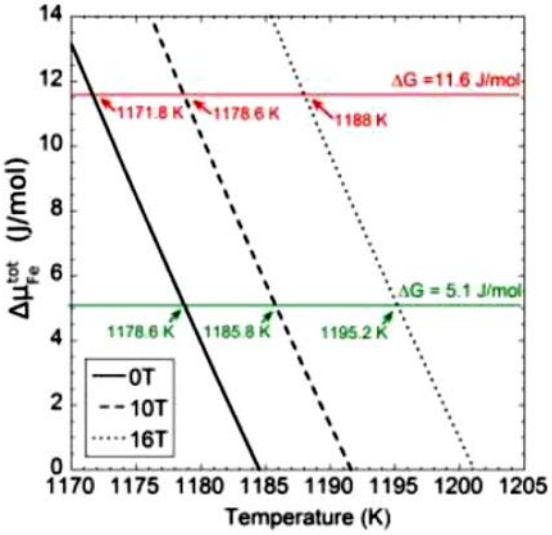

Figure 8-79 - Variation in the difference of Gibbs free energy between ferrite and austenite as function of temperature and magnetic field intensity (calculated from molecular field model and [200]) [199]

In the same work, Garcin [199] studied several ferrite plus pearlite microstructures obtained with and without magnetic field. In some microstructures obtained without the magnetic field, pearlite seemed still arranged in some lines. These difference in microstructure between ferrite and pearlite was highlighted with Nital solution etch. The image is shown in Figure 8-80. Based on these results, the lines found for the specimen induction heated for 2 minutes are not caused by the magnetic field since its intensity is in the range of few mT. These lines are caused by different levels of etching between zones of the grains containing more carbides compared to other zones where less carbides are present.

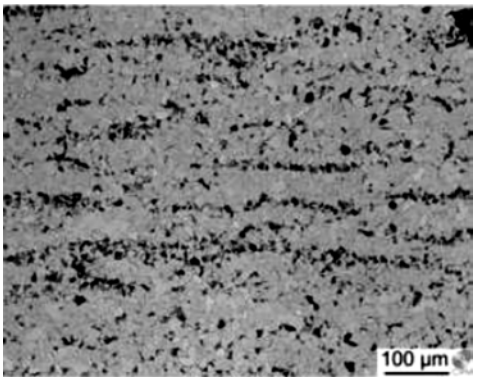

Figure 8-80 - Ferrite plus pearlite microstructure obtained after continuous cooling in absence of magnetic field (microstructure revealed after etching with Nital solution) [199]

It was reported in literature [201] that in pure Fe-C alloys containing 0.02 – 0.8 wt% of carbon, the pile-up of carbon at the austenite/ferrite interface in the range of temperatures 1000-1040 K (727 – 767 ˚C) can lead to the precipitation of non–equilibrium carbides. According to the same paper, the mobility of the austenite/ferrite interface is determined by the diffusion of carbon into austenite. Based on the TEM results obtained for this specimen, its strength can be due to the presence of nanosize TiC inside the ferrite matrix. According to the calculations shown in chapter 5, there is still 0.018 wt% of "free" Ti that can be combined with the diffusing carbon to form TiC. In literature [202], it has been shown that nanoscale precipitates can enhance the strength of the steel. In particular, Xu et al. [202] found a yield strength of 420 MPa for a steel containing 0.034 wt% of Ti. According to the same paper, these nanoscale TiC precipitates would strengthen the steel by impeding dislocation motion during deformation of the sample. Hong et al. [203] reported that the precipitation of TiC carbides with diameter lower than 20 nm promotes grain refinement in the ferrite obtained from austenite. It is interesting to note that in their experiments [203], they obtained a yield stress of 372 MPa (very close to the value found for the coupon induction heated for 2 minutes in this PhD thesis) after the precipitation of TiC into ferrite. Hong et al. [203] specified that TiC are dissolved at 1150 ºC but they are precipitated during cooling and during the transformation of austenite into ferrite and preferentially in the range of temperatures between 800 ºC – 920 ºC. Other papers reported the precipitation of nanosized TiC at the

austenite/ferrite interface at 750 ºC [204]. Wang et al. [204] specified in their paper that "carbides can precipitate through different processes, such as nucleation in austenite, formation of rows of carbides during the austenite/ferrite phase transformation and precipitation of fine carbides from supersaturated ferrite".

From grazing X-ray diffraction experiments, peaks of a crystalline phase were found in the film after 1 minute and 4 minutes of induction heating and some of them have been identified as cementite, while others are due to the formation of iron oxides during quenching. The same analysis should be repeated when the film has undergone only a heating ramp of 10 seconds and the austenitization of 1 s, in order to see if its structure is still amorphous or fully crystalline. From the mechanical properties, it seems that the maximum amount of carbon that is diffused during induction heating is 0.064 at%. This amount is double of what could be diffused inside a vacuum furnace and it could be due to the very fast heating rate which could promote a faster diffusion of carbon towards the IF steel and a delay in film crystallization.

- If the time of heating at 820 ˚C is increased to 4 minutes, Lüdering is suppressed and the yield stress is lowered as seen for one side coated coupons. From TEM analyses and EBSD analyses, no clear difference between this specimen and the one induction heated for 2 minutes could be discerned. However, the suppression of Lüdering is the result of two main mechanisms: full precipitation of carbon, with a coarsening of the TiC precipitates and formation of several mobile dislocations. When carbides coarsen, they will not be able to impede dislocation movement and this could explain the decrease of yield stress found for this specimen. At the same time, the increase of the number of mobile dislocations will prevent Lüdering.

  It was reported in literature by Ramazani [205] that for dual phase steels, " the volume expansion due to austenite transforming into martensite can create geometrically inhomogeneous dislocations (GNDs) at the ferrite martensite interfaces". These dislocations are mobile and can suppress Lüdering. However, it is believed that the amount of carbon diffused in these experiments might not be enough to cause any relevant volume expansion. Moreover, in another study related to Lüdering [83], it was shown that if the carbon instead of being in solid solution is

present as fine dispersed cementite particles in a ferrite matrix, the Lüders plateau can be reduced. This reduction of Lüdering was explained with the generation of "geometrically necessary dislocations", which are defined as Orowan loops formed close to the particles. These dislocations increase the work hardening of the material.

- If the heat treatment time at 820 ˚C is further increased up to 8 minutes, an increase of 40 MPa of yield stress is found compared to the 4 minutes specimens and Lüdering appears again, while the UTS are comparable for both specimens. The reappearance of Lüdering proves that some carbon is diffused back to dislocations, compared to the 4 minutes specimen. The microstructure does not show anymore the typical lines found in the specimen annealed for 2 minutes. It. It is not yet clear why this happens. Moreover, it was also noticed that the engineering stress-strain curves for this heat treatment is very similar to the one obtained after 1 minute of induction heating.
- Another important aspect that was reported in literature and that should be considered for the experiments presented above is decarburization occurring in vacuum at high temperature. It was reported that heating of low-carbon steel in vacuum can lead to the evolution of CO and CO_2 which are formed on the surface of the specimen, where carbon and oxygen diffuse from the base metal [156]. In particular, the experiment performed in literature was measuring decarburization at a vacuum level of $5x10^{-5}$ Torr (which is higher than the vacuum of 10^{-6} Torr used in the quartz ampoules of the induction heated specimens) and for various temperature. They recorded an increase of decarburization for temperatures above 900 ˚C, however, decarburization was occurring also at temperatures between 700 ˚C and 900 ˚C but from their results, the decarburized layers seems to be around 10 micron after 5 hours of heat treatment at 800 ºC [156]. Using this information to do a linear interpolation to calculate the decarburization caused by induction heating at 820 ºC for 1 minute, 2 minutes, 4 minutes and 8 minutes, it can be found that the depth of decarburization would be respectively 0.03 µm, 0.07 µm, 0.13 µm and 0.27 µm. According to these calculations, the decarburization should not be playing a significant role in the induction heating experiments, especially considering that the specimen is left at high temperature only for few minutes, and that the level of

vacuum in the quartz ampoules is lower. However, it must be kept in mind that an oxide layer is still present at the interface between FeC film and IF substrate and it contains oxygen which could react with some of the diffusing carbon at these higher temperatures. In Chapter 5, it was found that this oxide layer was not influencing carbon diffusion, however those experiments were run at temperatures up to 710 ºC, while with the induction heating the temperatures are always above 800 ºC.

- If the induction heating treatment is performed on coupons coated on both sides after having undergone 15% of pre-strain, the strengthening due to carbon diffusion is lower compared to unstrained specimens. This confirms the results already presented in Chapter 7 according to which, if the number of dislocations inside the specimen is increased, then the Cottrell atmosphere will be less carbon dense. Moreover, the diffusing carbon will be “more diluted” between the higher density of dislocations and this will not stabilize any martensite or bainite nor will allow for any carbon precipitation to occur.

Chapter 9 : Fracture Studies on Carbon Graded Interstitial Free Steel

The literature review revealed a lack of experimental studies related to the influence of compositional gradient on fracture. Most of the studies present in literature involve crack propagation in materials containing a gradient of Young modulus obtained with ceramic-metallic FGMs. Only one FEM study was reported describing void growth and void coalescence for a material having a gradient of yield stress [122]. The influence of carbon gradient on void growth inside an IF steel is investigated in this thesis. All fracture tests were carried out using specimens containing cylindrical voids. Two graded configurations were studied. The first configuration had a carbon gradient along the gauge length of the specimen, while the second series of specimens had a gradient along the gauge width.

9.1. Carbon gradient along gauge length

9.1.1. Prediction of carbon diffusion for half coated gauge length

The specimens identified as ECD5H-Q have been coated only on one side with a 500 nm thick FeC film (30 at% as carbon content) and the film was applied only on half of the gauge length. A schematic view of the starting coupon configuration is shown in Figure 9-1.

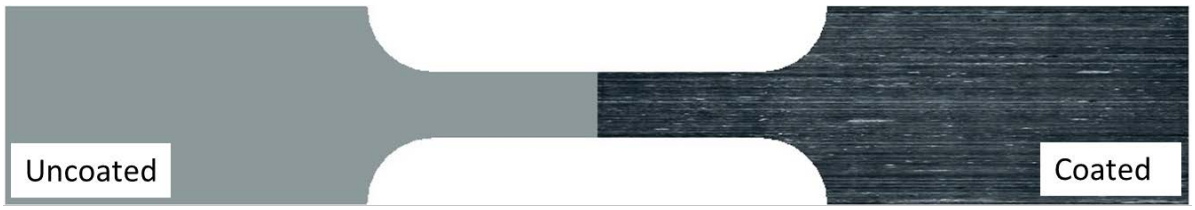

Figure 9-1 - Schematic view of a tensile coupon having the gauge length half coated with a FeC film (500 nm – 30 at%) on one side

In order to maximize the slope of the carbon gradient obtained along the gauge length, the carbon coating was applied only on half the gauge length and only on one side of the tensile coupon, which means that the back side of the coupon in Figure 9-1 is not coated with FeC film. In order to limit the carbon gradient through thickness it was decided to perform annealing at a temperature and time that would give a uniform carbon concentration through thickness, so that the final carbon gradient would be only along the gauge length. For this

reason the annealing temperature and time have been set to 630 ˚C – 1h and the annealing was performed in high vacuum furnace with vacuum levels of 10^{-6} – 10^{-7} Torr. In order to predict the carbon gradient along the gauge length, the diffusion program used in chapter 5 and based on a 1D solution of second Fick's law was used considering the coating only on one side of the tensile coupon and for only half of the gauge length. Considering the interface between the coated side and the not coated side of the gauge length, it can be assumed that the carbon will diffuse first through thickness (path 1 in Figure 9-2) until the solubility limit of carbon into ferrite is reached (for 630 ˚C -1h the amount of diffused carbon is considered limited to (0.0334/2 = 0.0170 at%) due to the crystallization of the film (as explained in Chapter 5) and due to the FeC film being present only on one side of the coupon). Successively, this amount of carbon, which is considered uniform through thickness, will diffuse along the gauge length to cover 2000 μm (path 2 in Figure 9-2). This approximation can be considered acceptable since the length along "path 1" is ten times smaller than "path 2" and therefore carbon diffusion along "path 2" is negligible before "path 1" is saturated. Carbon diffusion along path 1 was simulated for annealing temperatures of 530 ˚C – 1h and 630 ˚C – 1h to ensure a uniform carbon concentration through thickness. In Table 9-1 the calculated concentrations through thickness are reported, with AV1 indicating the carbon concentration at the coordinate 0 in Figure 9-3 (not coated surface) and AV10 is giving the carbon concentration at the coordinate 197 in Figure 9-3, while "AVfull" gives an average carbon content through the whole thickness. Figure 9-4 gives the plot of carbon concentration through thickness. It is clear that for the annealing at 630 ˚C – 1h, the carbon concentration through thickness is more uniform than the 1h annealing at 530 ˚C. For this reason, in order to limit the gradient of carbon only along the gauge length, the annealings were all performed at 630 ˚C.

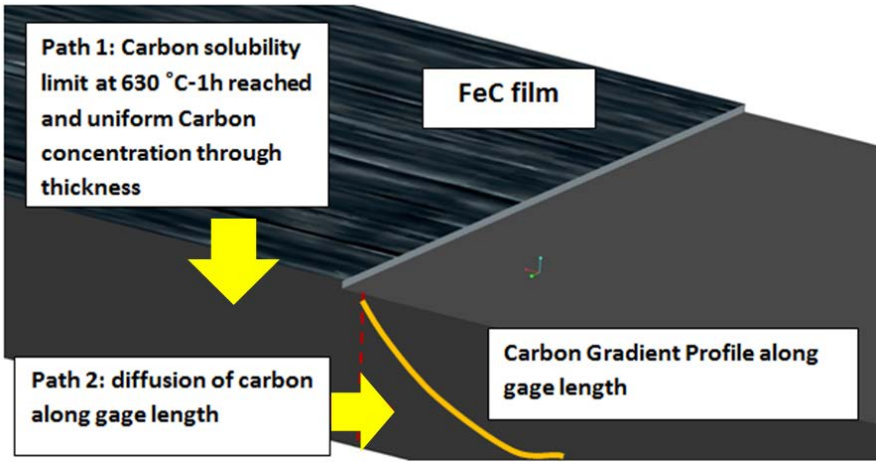

Figure 9-2 - Assumption made in order to simulate carbon diffusion for half masked tensile coupons

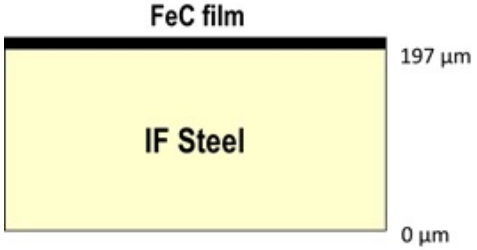

Figure 9-3 - Schematic view through thickness of the one side coated portion of the gauge length

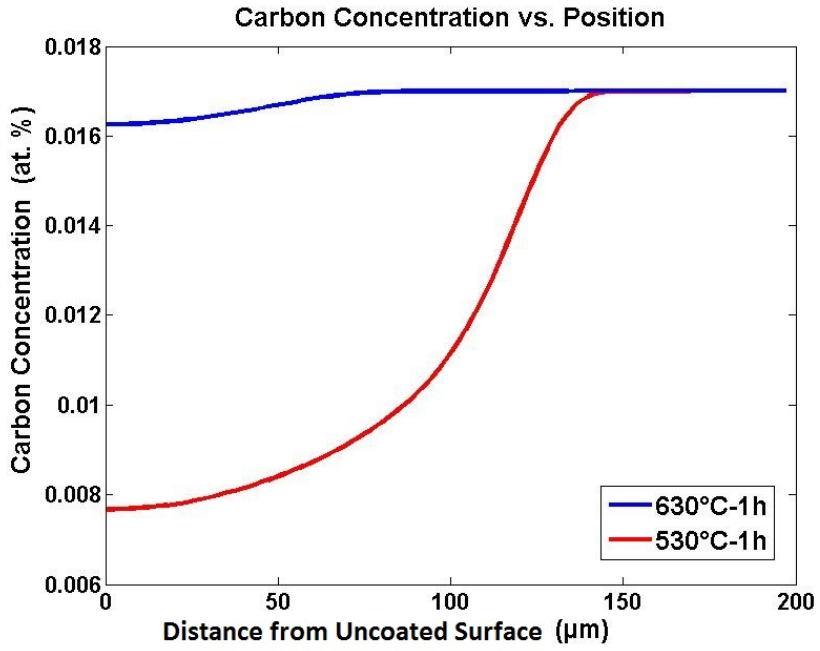

Figure 9-4 - Carbon concentration through thickness for tensile coupon coated one side and annealed at 630 ˚C and 530 ˚C for 1h

Concentration	530 ˚C-1h (at%)	630 ˚C-1h (at%)
AV1	0.0077	0.0163
AV2	0.0079	0.0164
AV3	0.0084	0.0167
AV4	0.0091	0.0169
AV5	0.0102	0.0170
AV6	0.0123	0.0170
AV7	0.0156	0.0170
AV8	0.0170	0.0170
AV9	0.0170	0.0170
AV10	0.0170	0.0170
AVfull	0.0122	0.0168

Table 9-1 - Carbon concentration through thickness considering only one side coated coupon

From the results listed in Table 9-1, the carbon profile through thickness will be close to uniform if the heat treatment is performed at 630 ˚C for 1h and this will be the parameters used for annealing.

In order to obtain only part of the gauge length coated with FeC film, during the PVD deposition, a portion of the gauge length was masked with aluminium foil. Since the mask was applied manually using tweezers, the interface between coated and not-coated side was not always placed exactly in the center of the gauge length. For this reason, it was necessary to characterize the exact position of the interface between coated and uncoated zones before placing the holes with the femtosecond laser. Optical microscope images of the interface between coated and not-coated zones taken after annealing in high vacuum at 630 ˚C – 1h are shown in Figure 9-5.

(a) Interface between coated and not-coated zone after annealing in high vacuum (magnification 5X)

(b) Interface between coated and not-coated zone after annealing in high vacuum (magnification 10X)

Figure 9-5 - Optical microscope pictures of the interface between coated and not-coated zone of the gauge length of a tensile coupon: (a) magnification 5X and (b) magnification 10X

In order to analyze the influence of carbon gradient on void growth, it was chosen to place holes along the gauge length. In particular the following specimens were prepared:

- Two specimens having a carbon gradient along the gauge length (specimens designated as 5 and 6);
- One specimen having a uniform carbon profile along the gauge length (specimen designated as 10);
- Two specimens of IF steel without carbon gradient and without annealing (specimens designated as 7 and 8);

All the half masked coupons have been characterized with the optical microscope in order to detect exactly the position of the interface between the coated and not-coated zone before performing Vickers hardness measurements to identify the dimension of the carbon gradient and before placing holes. A schematic view of the dimensions measured along the gauge

length with the aid of the optical microscope is shown in Figure 9-6. For all the specimens the distance BC was approximately 4081 μm.

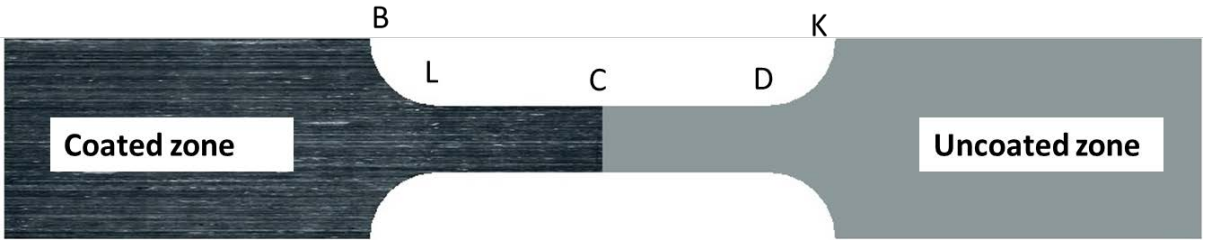

Figure 9-6 - Schematic view of the measurements taken on a tensile coupon having half gauge length coated and half not coated. B indicates the upper corner, L the end of the first fillet radii, C is the interface, D is the start of the second fillet radii and K is the other upper corner

Successively, a diffusion simulation was performed considering the above geometrical values to find out the shape of the expected gradient through the interface. The maximum amount of carbon that can be diffused at 630 ˚C - 1h is (0.0334/2 = 0.0170 at%) (considering transformation of the FeC film into cementite and considering the specimen coated with FeC film only on half of the gauge length). Figure 9-7 shows the expected gradient at the interface between coated and not-coated zones of the gauge length.

The distance considered for diffusion in the X axis of Figure 9-7 is defined as CD in Figure 9-6. The graded zone is expected to be around 800 - 1000 μm long.

After the heat treatment, in order to see if the C-gradient has the shape predicted by the simulations, Vickers indents were performed along the gauge length of the specimens and close to the edges so that they would not influence the mechanical behaviour during the tensile tests. The hardness was done using 25 g load for 10 s and no polishing was performed before the hardness test.

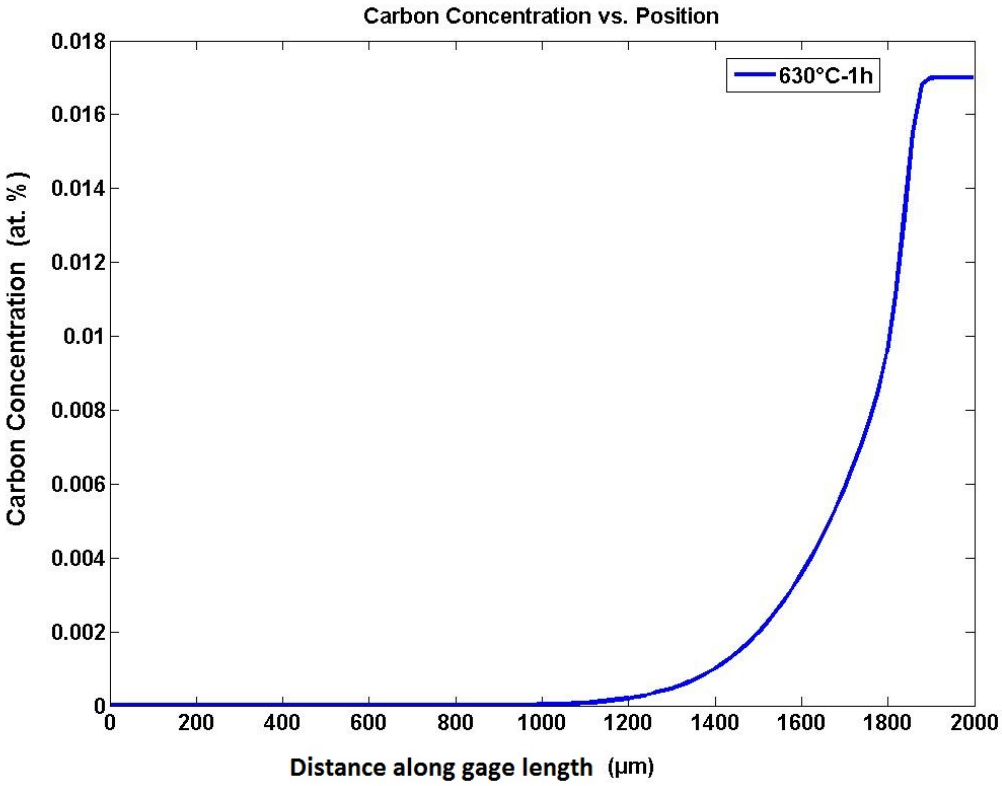

Figure 9-7 - Expected carbon gradient along the gauge length– annealing at 630 ˚C – 1h in high vacuum

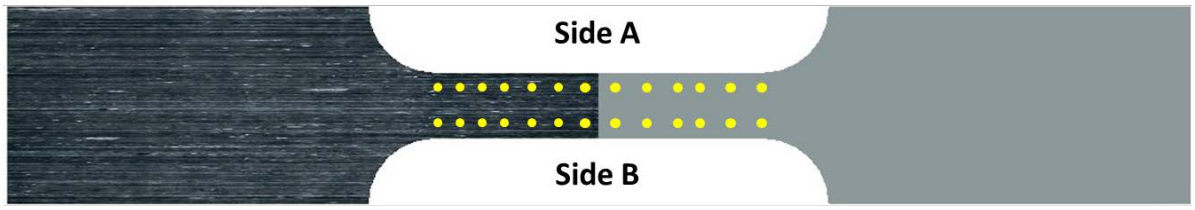

Figure 9-8 - Schematic view of how Vickers hardness has been performed to assess the shape of the gradient

Vickers hardness of the half coated and annealed specimens was measured before and after polishing to obtain the shape of the carbon gradient. The hardness measurements were taken at a load of 25 g applied for 10 s. Before polishing, the hardness was taken on at least two lines along the gauge length of the half coated face of the tensile coupon and successively the tensile coupon was flipped and Vickers hardness measurements were taken on at least two lines on the not coated face of the specimen. In the zone coated with FeC film, the Vickers hardness is expected to be high because the FeC amorphous film transforms into cementite (Fe_3C) during the heat treatment, so it is important also to take hardness after

performing a slight polishing with 1 μm diamond solution to remove the film in order to fully assess the real carbon gradient in the diffused IF steel. For the flipped side of the tensile coupon which has no FeC film in its entire length, the hardness was taken only once without polishing.

9.1.2. Vickers Hardness Measurements

For specimen number 5, after the heat treatment performed at 630 ˚C for 1h in high vacuum, two sets of Vickers hardness measurements were taken on the half coated surface without performing any polishing. The distance reported in the X axis was measured from the end of the first fillet radii (point L in Figure 9-6). Vickers measurements were performed applying 25 g load for 10 seconds and in the half coated face, two measurements were taken and are identified as A and B in Figure 9-8, while the results are shown in Figure 9-9. Successively, the specimen was flipped and four Vickers hardness measurements were taken along the gauge length of this uncoated side. Two measurements A and B were taken closer to the edges of the tensile coupon, while two other measurements were taken in the middle of the tensile coupon. The results are shown in Figure 9-10. The carbon gradient is present on both sides, however, on the side which is coated with FeC film, the hardness is higher (between 220 MPa and 240 MPa) than on the side which is uncoated (between 190 MPa and 220 MPa) since the FeC film has transformed into cementite during annealing. Moreover, the fact that the carbon gradient along the gauge length was detected even in the uncoated side (Figure 9-10) means that the carbon concentration through thickness is uniform so the gradient will be mainly along the gauge length. However, in order to assess the “true” carbon gradient on the half coated side without FeC film, the specimen needed to be polished on the half coated side. Successively, fours Vickers hardness measurements were taken on the polished surface. Two measurements were done closer to the tensile coupon edges (A and B) and two measurements were taken in the middle of the specimen. The graph of the obtained hardness is shown in Figure 9-11. The same procedure was repeated for specimen number 6.

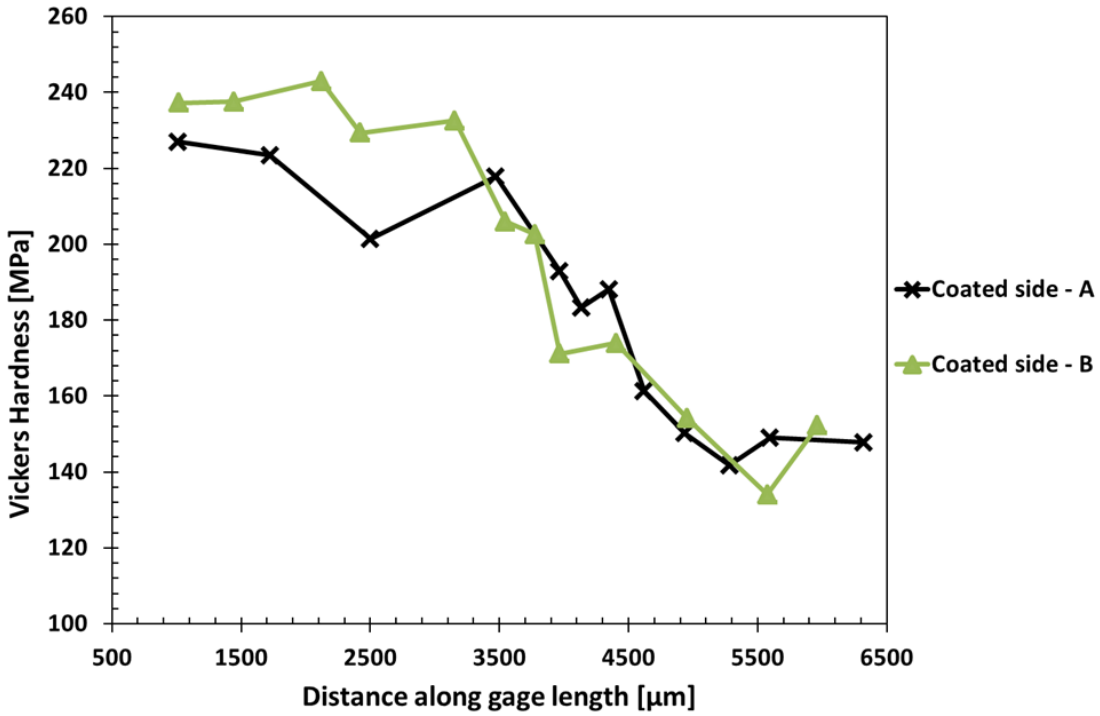

Figure 9-9 - Vickers measurements along the half coated gauge length for specimen 5 after heat treatment at 630 ˚C – 1h in high vacuum without polishing

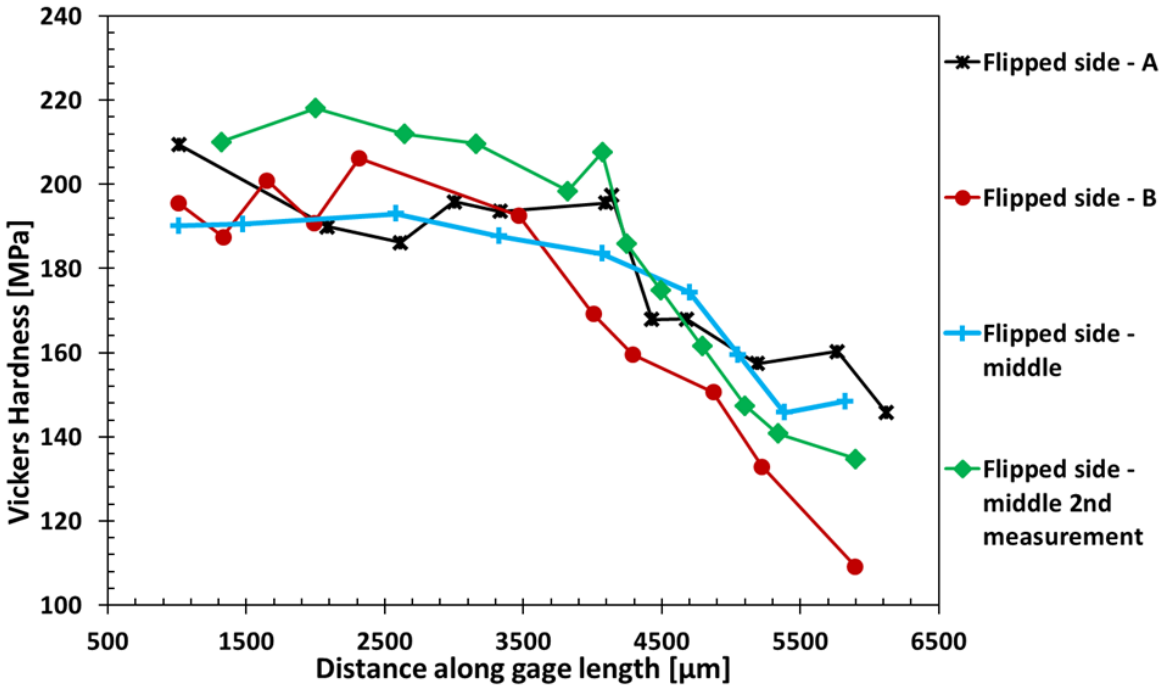

Figure 9-10 - Vickers measurements along the uncoated gauge length on the uncoated side for specimen 5 after heat treatment at 630 ˚C – 1h in high vacuum: two measurements were taken close to the edges (A and B) and two measurements were taken in the center of the gauge width

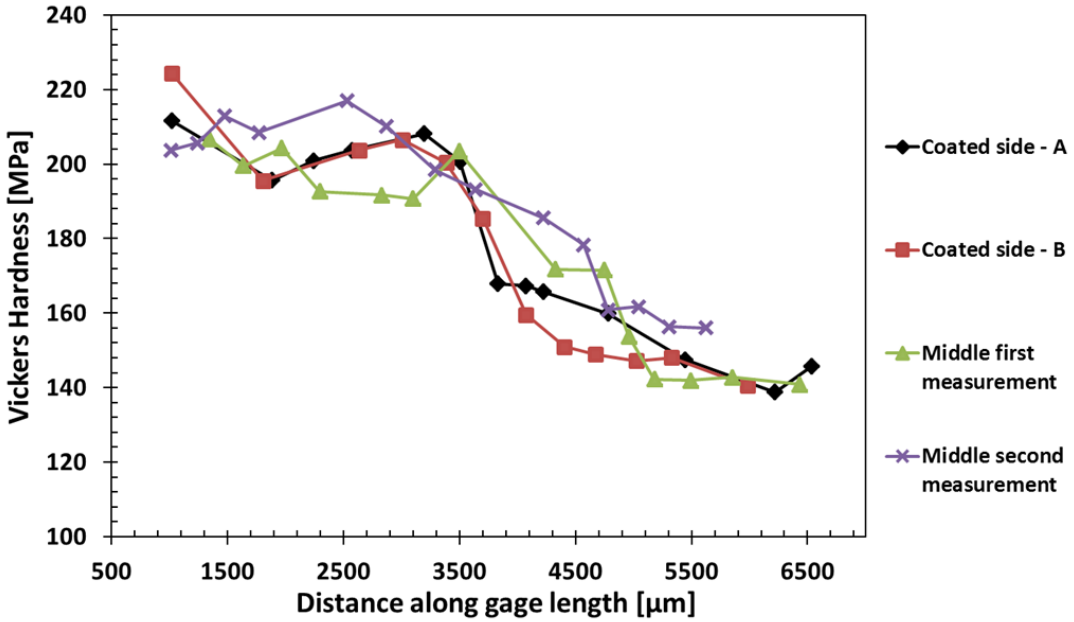

Figure 9-11 - Vickers measurements after polishing along the half coated gauge length for specimen 5 after heat treatment at 630 ˚C – 1h in high vacuum: two measurements (A and B) were taken close to the edges of the coupon, while two measurements were taken in the center of the coupon

From Figure 9-11, the hardness in the zone which was coated with FeC film has dropped after polishing since the formed cementite was removed. Figures 9-12, 9-13 and 9-14 show the obtained results for specimen 6.

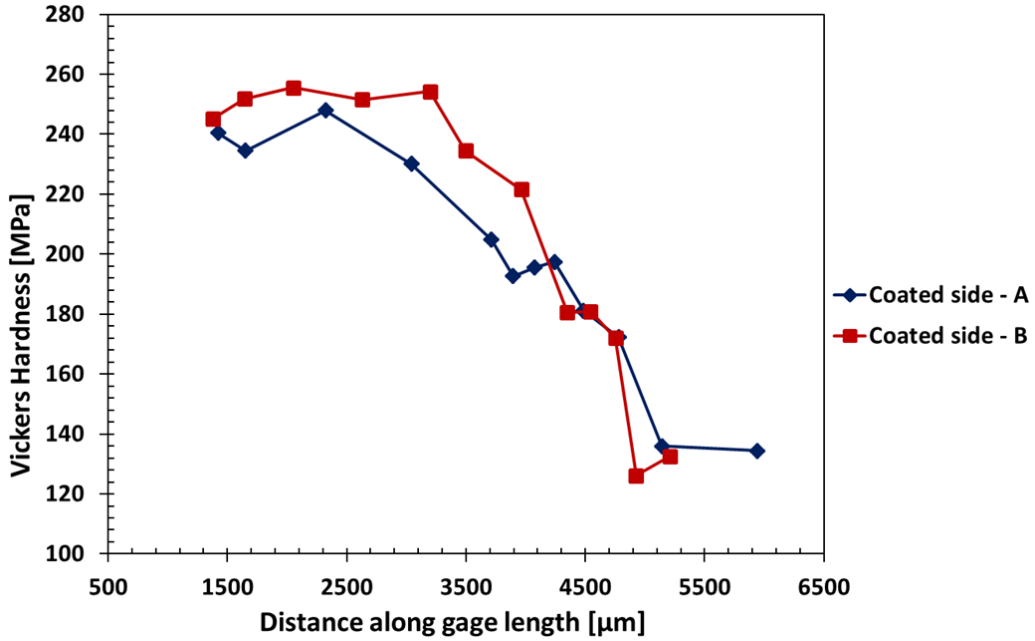

Figure 9-12 - Vickers measurements along the half coated gauge length for specimen 6 after heat treatment at 630 ˚C – 1h in high vacuum without polishing

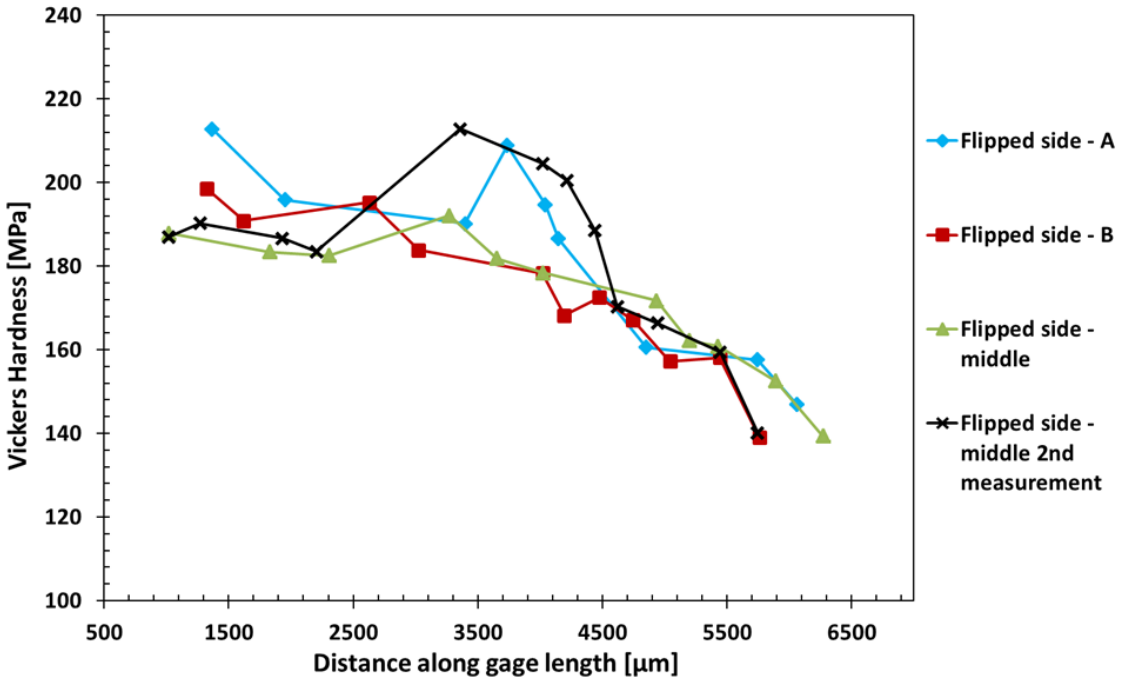

Figure 9-13 - Vickers measurements along the uncoated gauge length for specimen 6 after heat treatment at 630 ˚C – 1h in high vacuum

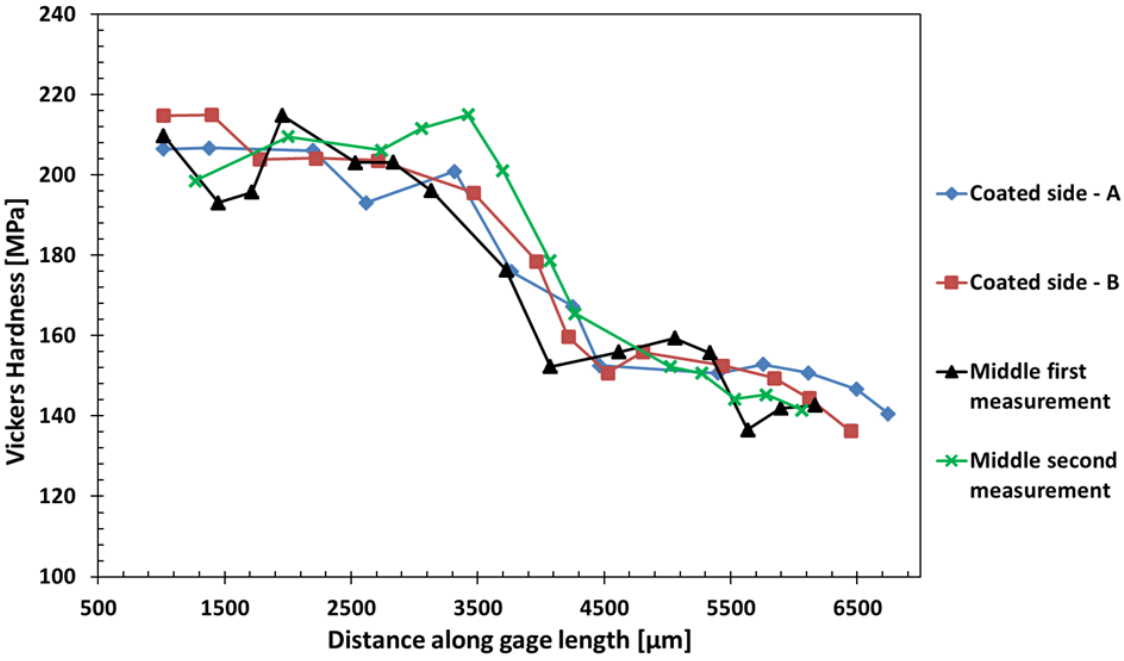

Figure 9-14 - Vickers measurements after polishing along the half coated gauge length for specimen 6 after heat treatment at 630 ˚C – 1h in high vacuum

From the graph of Vickers hardness obtained on the polished surfaces, specimens number 5 and 6 show a gradient of 70 MPa between the coated and uncoated side of the gauge length. In order to obtain a uniform carbon content through the gauge length, specimen 10 was annealed at 630 ˚C -1h in high vacuum and the face having the FeC carbon film was polished before taking Vickers hardness measurements. In Figure 9-15 the Vickers hardness measurements obtained for this specimen are shown.

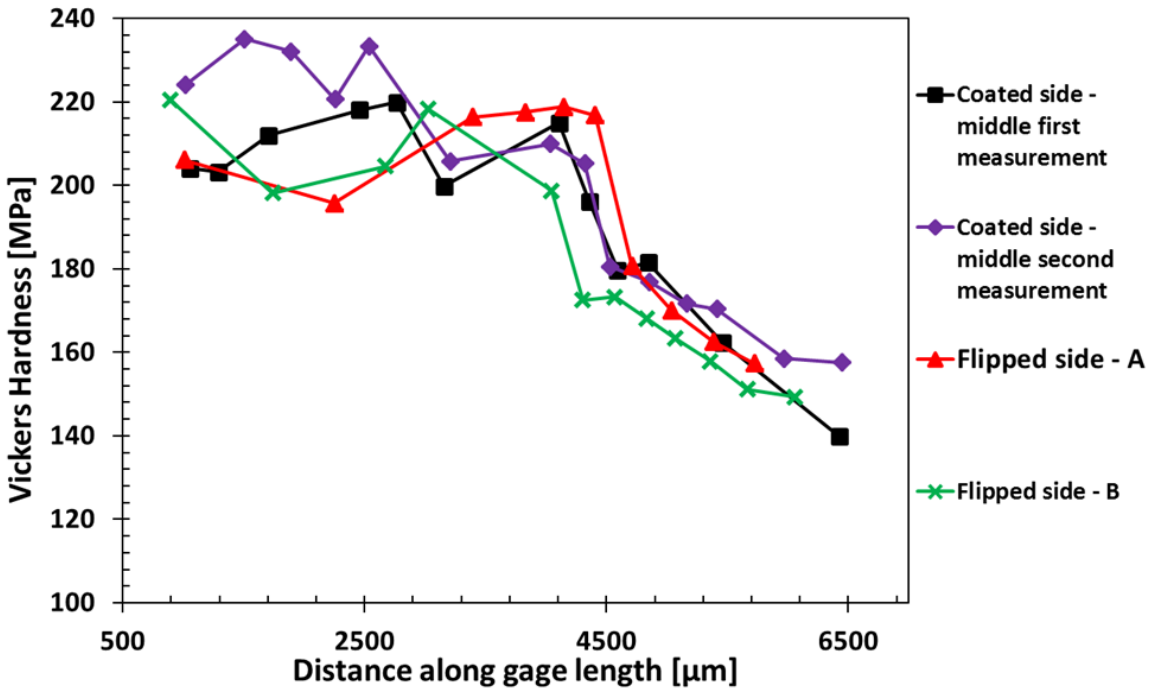

Figure 9-15 - Vickers measurements along the half coated gauge length and the uncoated side for specimen 10 after heat treatment at 630 ˚C – 1h in high vacuum after polishing

Successively, by using the 1D solution to second Fick's law, it was predicted that to obtain a linear profile, an annealing of 5 days at 630 ˚C was necessary. For this reason, specimen number 10 was then annealed at 630 ˚C for 5 days in high vacuum. The Vickers hardness of the specimen along the gauge length was measured again in order to assess if the hardness profile was linear. Figure 9-16 and Figure 9-17 show the obtained results. It can be seen that for both faces of the tensile coupon, the hardness has a linear profile compared to the graded specimens.

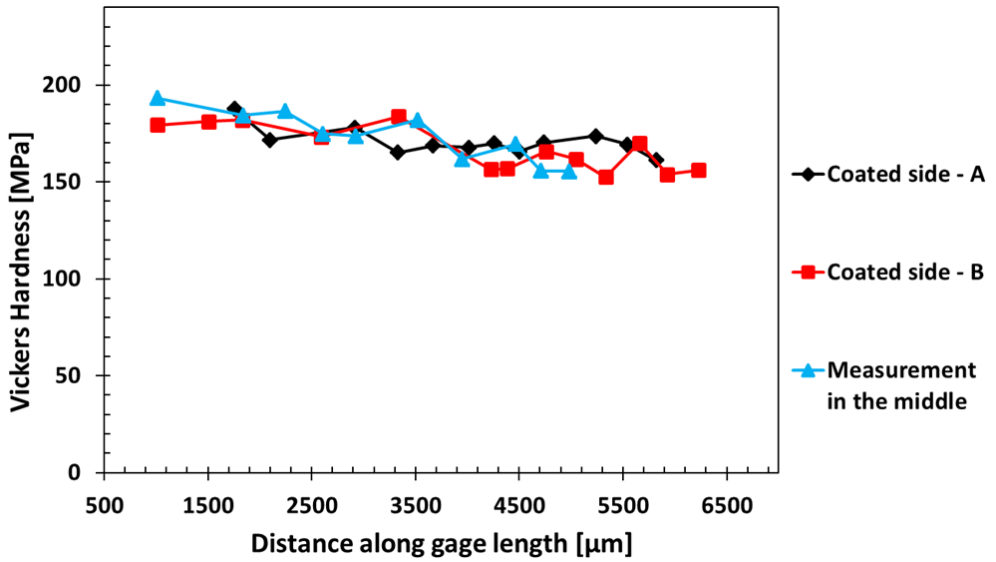

Figure 9-16 - Vickers measurements after polishing along the half coated gauge length for specimen 10 after heat treatment at 630 ˚C for 5 days in high vacuum

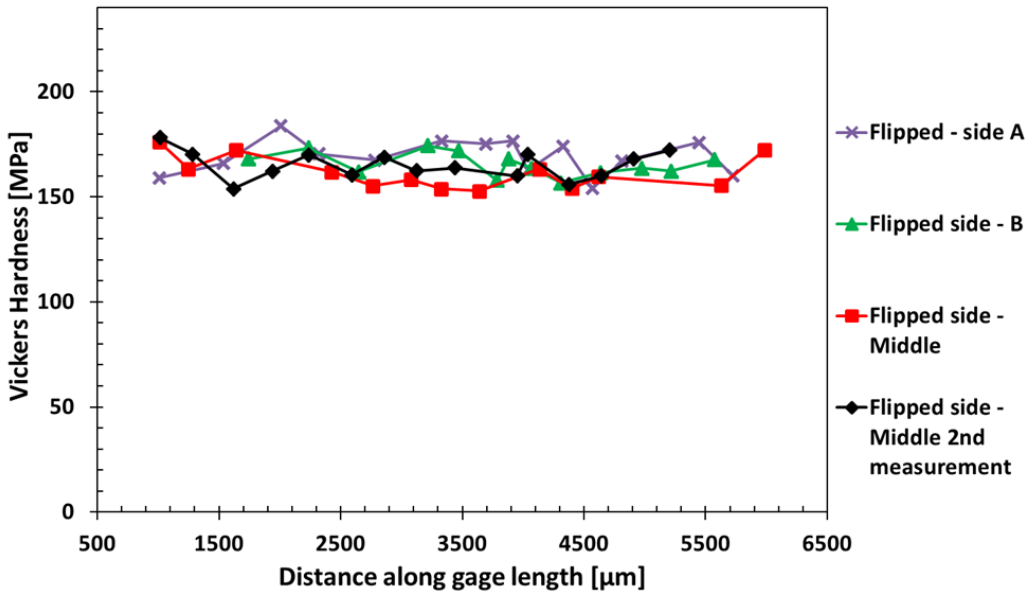

Figure 9-17 - Vickers measurements after polishing along the uncoated gauge length for specimen 10 after heat treatment at 630 ˚C for 5 days in high vacuum

Another specimen identified as “specimen 11” was annealed in high vacuum at 630 ºC – 1h and it was tested without voids. Its engineering stress-strain curve was compared with the curves obtained for specimens having a carbon gradient along the gauge length and voids. The hardness measurements before polishing and after polishing for specimen 11 are shown in Figure 9-18 and Figure 9-19 respectively.

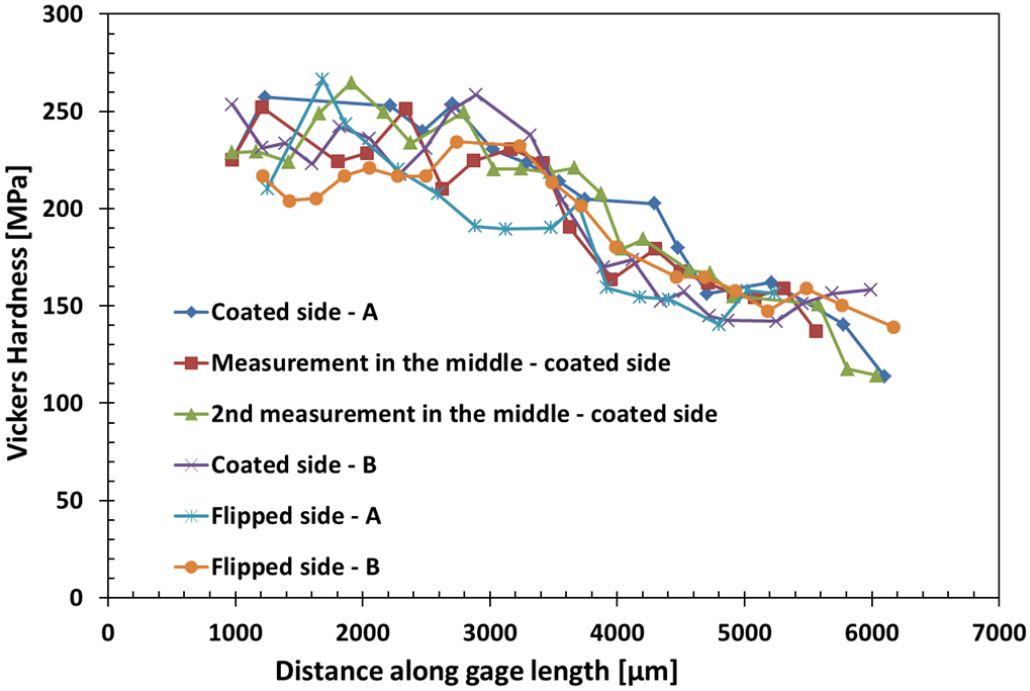

Figure 9-18 - Vickers measurements along the half coated gauge length and the uncoated side (flipped side) for specimen 11 after heat treatment at 630 ˚C – 1h in high vacuum without polishing

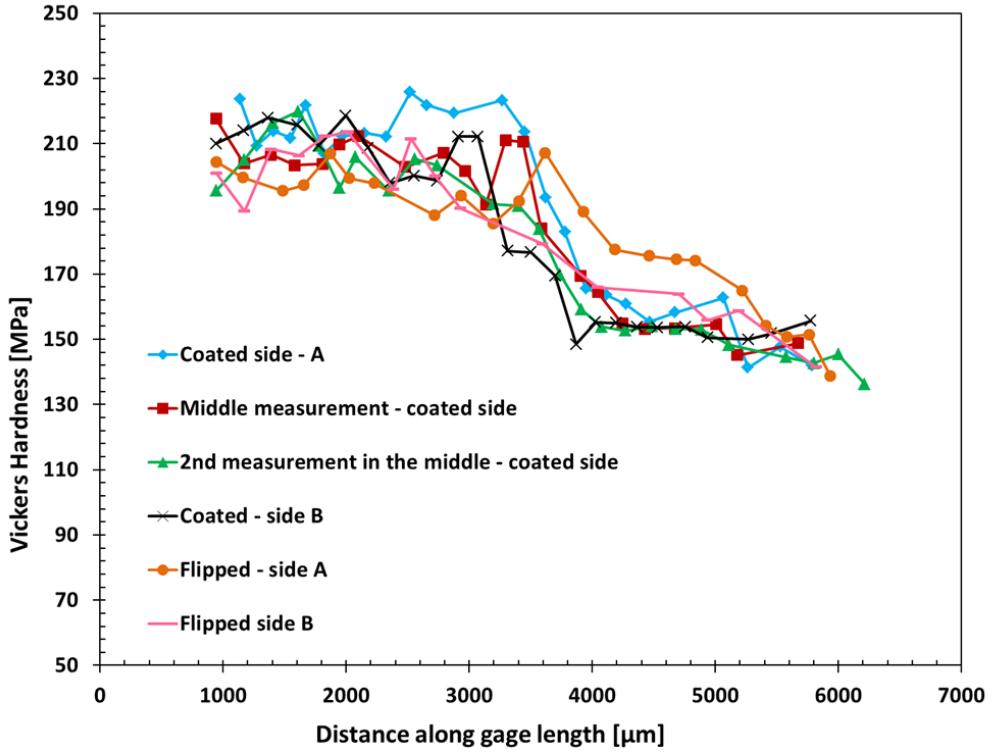

Figure 9-19 - Vickers measurements along the half coated gauge length and the uncoated side (flipped side) for specimen 11 after heat treatment at 630 ˚C – 1h in high vacuum after polishing

The gradients of hardness obtained for the half coated coupons are summarized in Table 9-2.

Specimen	Length of the gradient [µm]	Theoretical yield stress gradient [MPa]	Theoretical hardness gradient [MPa]	Experimental hardness gradient [MPa]	Experimental length of the gradient [µm]
5	1000	136	45	64	1500
6	1000	136	45	62	1200
11	1000	136	45	63	755

Table 9-2 - Size and steepness of the obtained carbon gradient for one side half coated coupons

In Table 9-2 the gradient expected theoretically is compared with the gradient obtained experimentally. The gradient of yield stress was calculated considering that in the coated zone, the amount of diffused carbon is equal to 0.017 at% (considering a nominal content of 30 at% in the FeC film), while the amount of carbon at 1000 µm from the interface will be zero. The corresponding increase of yield stress can be calculated using the equation $\Delta\sigma = M(0.051 \times \mu) \times (X_C)^{1/2}$ which gives an increase of 136 MPa for the coated zone and no increase in the zone where carbon has not diffused. For this reason, the expected gradient of yield stress is 136 MPa. However, experimentally, the gradient of hardness was assessed, for this reason it is necessary to find a relation that can allow to evaluate the theoretical gradient of hardness which is expected from the theoretical gradient of yield stress. From coupon 10, which had uniform carbon distribution, it was found experimentally that the increase of yield stress is around 136 MPa (considering that its yield stress was 250 MPa and that the yield stress of an uncoated IF steel is 114 MPa). This value is in agreement with the increase of yield stress predicted considering the theoretical amount of diffused carbon. For the same coupon an hardness of 175 MPa in average was measured, while the Vickers hardness of an uncoated IF steel is around 130-140 MPa. So, the increase in hardness is around 45 MPa. It is expected that this value will be also the gradient of hardness in coupons having a carbon gradient at the interface between the coated and uncoated zone. From Table 9-2, the measured hardness gradient are higher than the expected theoretical values. It is possible that since the amount of carbon 0.0170 at% is not enough to saturate the thickness of the IF steel, the diffusion of carbon along the gauge length is lower than what would be expected theoretically, since the carbon will prefer to saturate first the thickness.

9.2. Femtosecond Laser Drilling of Holes

Once the hardness profiles along the gauge length were characterized for each tensile coupon, holes were placed along the gauge length by using a femtosecond laser (Pharos from LightConversion). The femtosecond laser was chosen since it creates a negligible heat affected zone around the machined voids. This is particularly important since it is not possible to anneal the coupons after the laser machining, otherwise it would compromise the carbon gradient. It was chosen to drill holes having diameters on the order of 30 μm since this falls within the range of voids found in commercial materials during ductile fracture. In Table 9-3, the laser parameters used to drill the holes are reported. The main parameters which were considered in order to obtain the required void dimension include the laser repetition rate, energy, time during which the shutter is left open (number of pulses) and the Z position (or how much out of focus the sample surface is). On each specimen two rows of holes were placed along the gauge length and each row had 14 holes. The distance between the holes along the gauge length was 200 μm, while the distance between the two lines was set to 90 μm as shown schematically in Figure 9-20 for all the specimens except for the "uncoated number 8" for which the drilled holes were bigger than the other specimens and in order to have a ligament length of at least a void, then the distance between the two lines needed to be set to 130 μm. Table 9-4 lists the geometrical dimensions of the voids. The surface of the specimens was then prepared to perform digital image correlation (DIC).

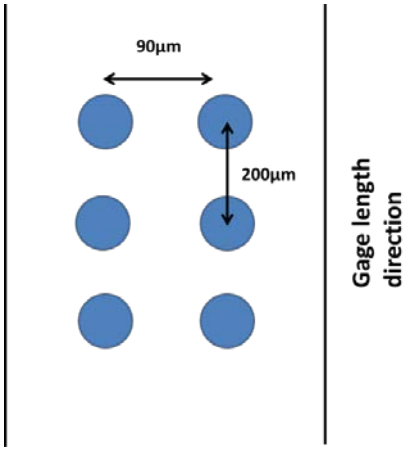

Figure 9-20 - Sketch of the holes configuration drilled along the gauge length

For the DIC it is necessary to have features on the surface to track during the tensile test. Random marks (300 holes with a minimum spacing of 30μm in an area of 300 μm x 900

μm) have been generated with the laser on the surface of the coupon. The laser parameters used to create these marks are as follows:

- power measured with the power meter before the objective lens was 0.003/0.004 W, which corresponds to an energy of $3 \times 10^{-3} - 4 \times 10^{-3}$ μJ of energy by considering a repetition rate of 1 kHz;
- Dwell time before opening the shutter 0.01s;
- Dwell time before closing the shutter 0.03s;

Pictures of the obtained pattern for specimen 5 and 6 (with carbon gradient) and for specimen 7 (uncoated) are shown in Figure 9-22.

Specimen	**Repetition Rate [kHz]**	**Energy [W]**	**Z position [mm]**	**Time open shutter [s]**
5 – C gradient	1	0.088	0.28	20.5
6 – C gradient	1	0.088	0.28	20.5
10 – C uniform	1	0.071	0.03	22
7 - uncoated	1	0.088	0.28	20.5
8 - uncoated	1	0.088	0.18	20.5

Table 9-3 – Femtosecond laser parameters used to machine holes along the gauge length of tensile coupons

Specimen	**Diameter of the holes [μm]**	**Distance between holes from center to center [μm]**	**Ligament length [μm]**	**Distance from center to center along gauge length [μm]**
5 – C gradient	33	94	60	200
6 – C gradient	33	90	52	200
10 – C uniform	25	90	57	200
7 – uncoated	28	90	56	200
8 – uncoated	55	130	70	200

Table 9-4 - Dimensions of the holes measured by optical microscope after laser machining and polishing

An image of the set-up used for lasing of the holes and application of DIC features is shown in Figure 9-21. The line indicates the path followed by the laser beam. The power meter to measure the energy is placed on the top of the microscope objective.

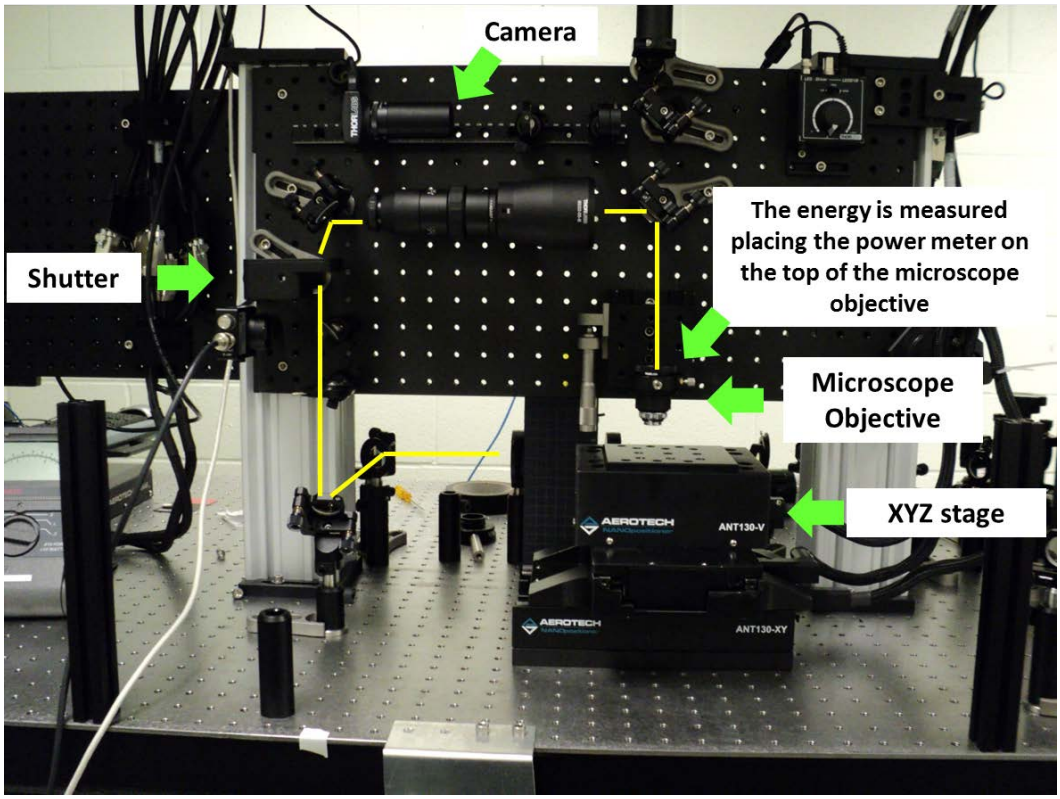

Figure 9-21 - Laser set-up used for lasing of holes and DIC features on tensile coupons. The yellow line shows the path followed by the laser beam up to the top of the microscope objective

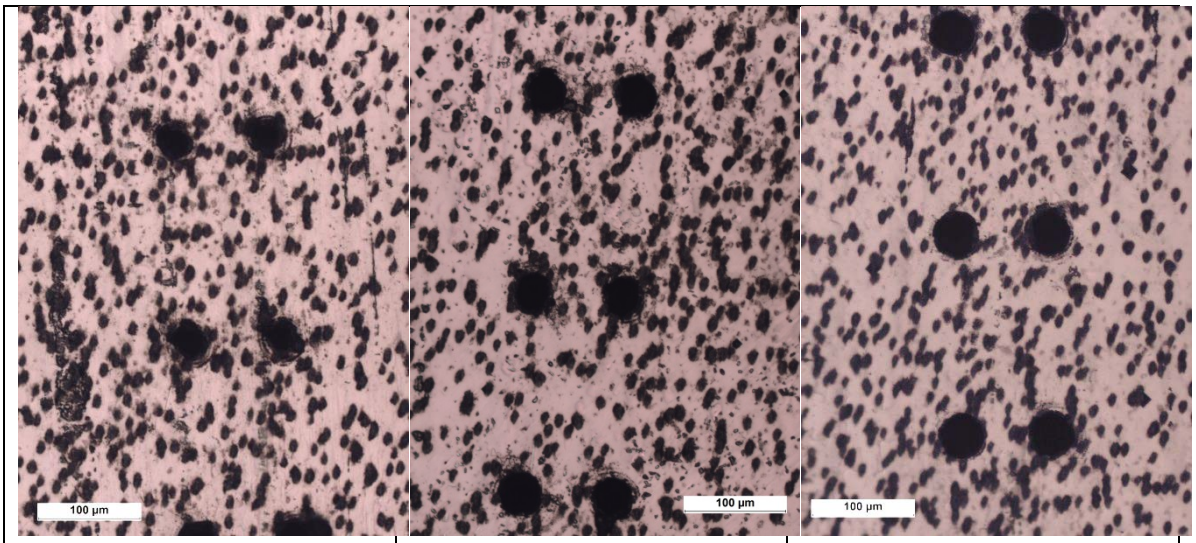

Specimen 7 uncoated (magnification 20X)	Specimen 5 half coated with carbon gradient (magnification 20X)	Specimen 6 half coated with carbon gradient (magnification 20X)

Figure 9-22 - Examples of features for DIC analyses applied with laser on tensile coupons

9.3. Tensile tests

Tensile tests were carried out at a speed of 2.5 µm/s (strain rate of 5 x 10^{-4} s^{-1}) and DIC analyses were then performed. Pictures have been taken with the optical microscope at a magnification of 5X every 10 ms during the tensile test. A summary of engineering stress-strain curves obtained for the tested specimens is shown in Figure 9-23. For comparison, a coupon (specimen 11) having carbon gradient but without voids was also tested. The dimensions of the specimens are reported in Table H- 1 of Appendix H, while numerical values of mechanical properties are listed in Table H- 2 of Appendix H.

It is interesting to note that the Lüders plateau stress for uniform carbon content and for graded carbon content is the same; however, having one part of the tensile coupon which has no carbon causes a lower yield stress and a change in slope before reaching the upper yield stress of the Lüders plateau. On the other hand, if the carbon content along the gauge length is uniform, this change in slope is not obvious.

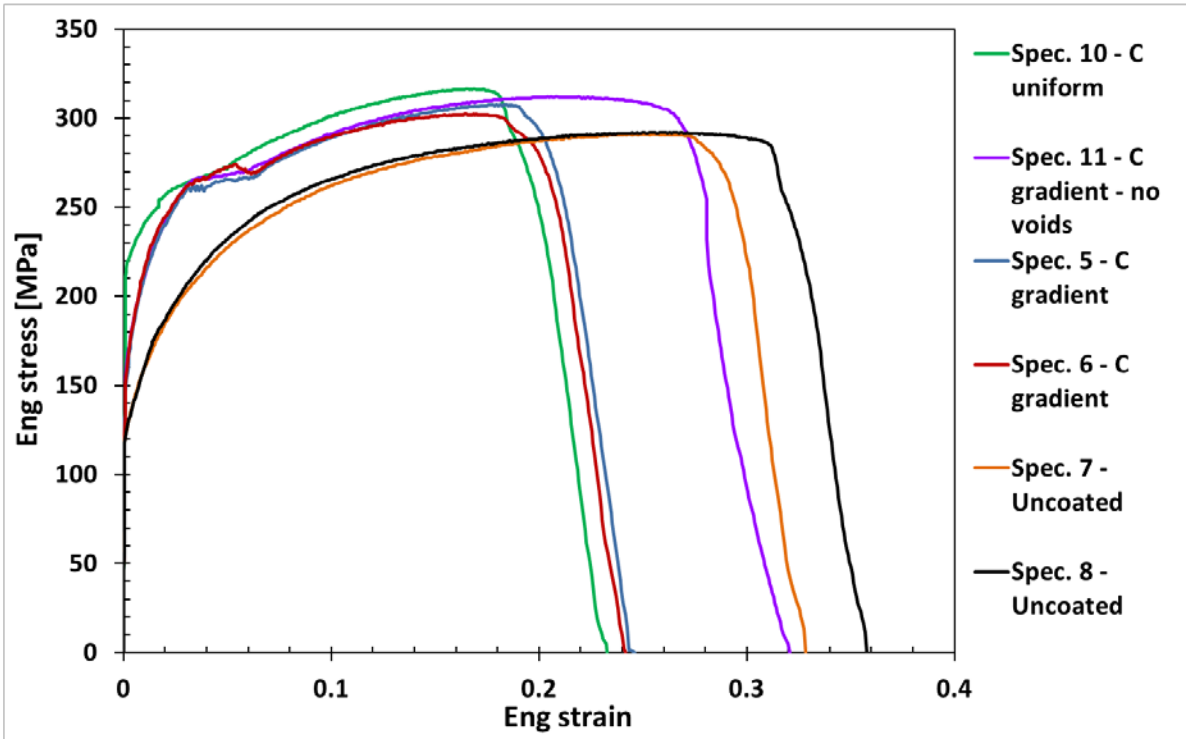

Figure 9-23 - Engineering stress-strain curves for specimen having holes along the axis of the gauge length

The yield stress of the curves shown in Figure 9-23 can be predicted using the rule of mixture. Details of the calculations are shown in section H.1.1 of Appendix H.

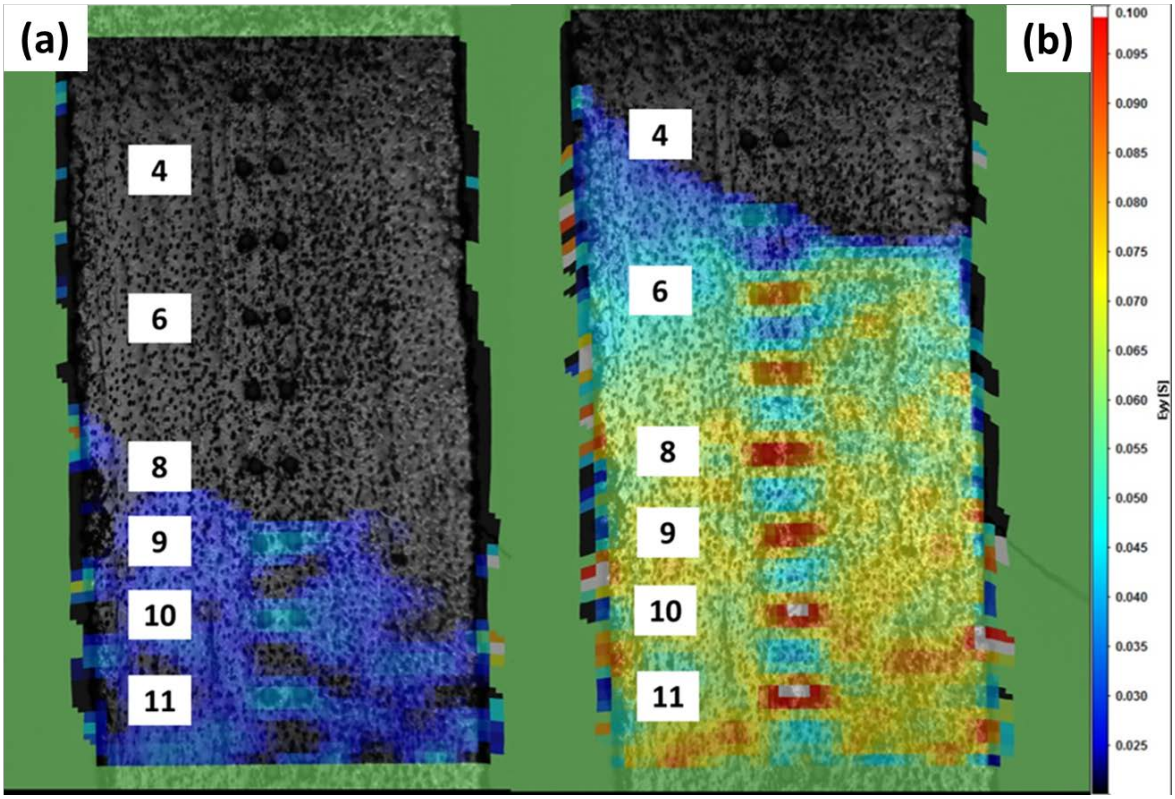

Figure 9-24 - Lüders band propagation during tensile test of carbon graded specimen number 5: (a) starting of the nucleation of the Lüders band along the gauge length (couple of holes 9 and 10 are at the end of the graded zone, while couple 11 is in a no carbon zone); (b) progressing of the Lüders band in the graded zone from couple of hole number 10 until couple of hole number 6. (Couple of holes 6 was at the interface between FeC coated zone and uncoated zone)

The results of the Lüders bands propagation are shown in Figure 9-24 and Figure 9-25. For specimens 5 and 6, it was found that a single Lüders front starts to propagate at the interface between the graded zone and the no carbon containing zone as expected. For specimen 10 having a uniform carbon gradient, the Lüders front starts to propagate uniformly from the zone which was uncoated before diffusion. For the uncoated specimens number 7 and 8, no Lüdering was found and the strain was homogeneous in the whole gauge length.

During testing of specimen 5, the Lüders bands started to propagate at voids couple number 9 and 10 which are located at the end of the graded zone and close to the no carbon zone Figure 9-24 (a). Successively, the band will keep propagating along the graded zone and the coated zone as shown in Figure 9-24 (b). For specimen number 6, the Lüders band also nucleated at the end of the graded zone at the couple of voids numbered as 9 and 10 in Figure 9-25 (a). The band is then progressing in the carbon graded zone as shown in Figure 9-25 (b).

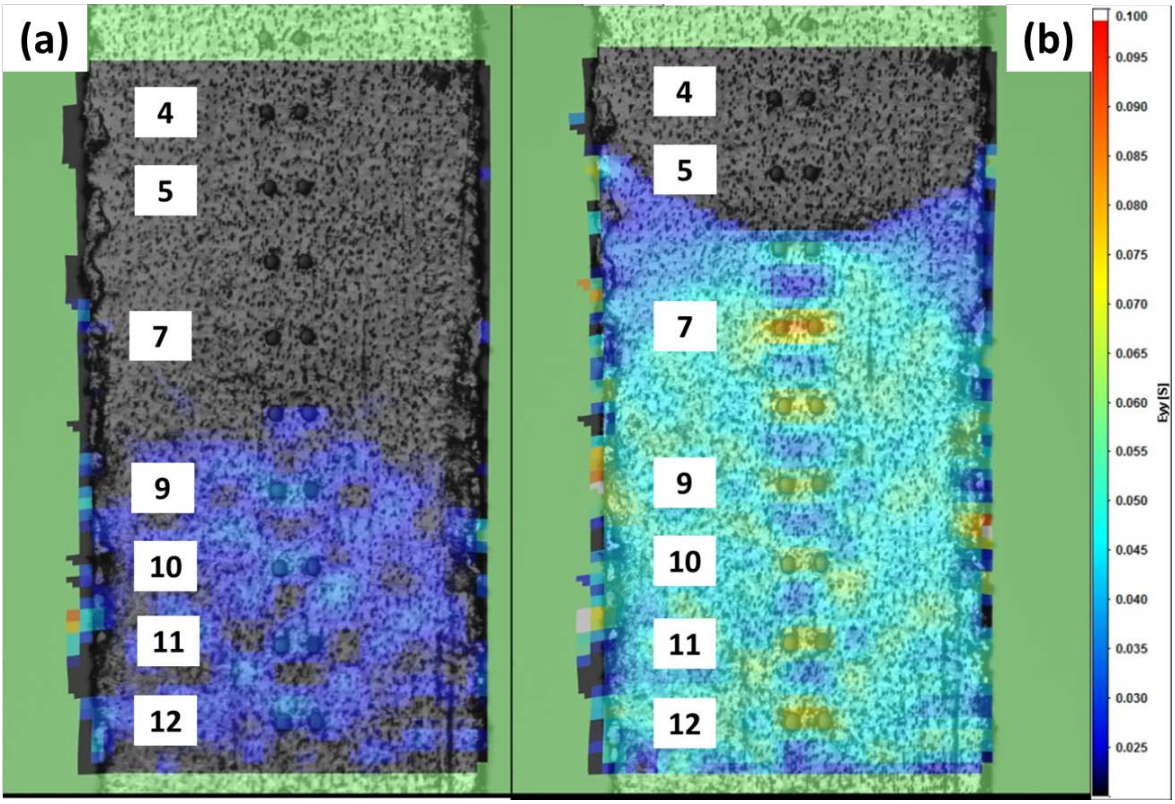

Figure 9-25 - Lüders band propagation during tensile test of carbon graded specimen number 6: Starting of the nucleation of the Lüders band (a). Couple of holes 9 and 10 are inside the graded zone, while couple 11 and 12 are inside the uncoated zone. (b) progressing of the Lüders band in the graded zone of specimen 6 from couple of holes number 9 until couple of holes number 6, which is at the end of the graded zone and the voids above this couple are in the FeC coated zone.

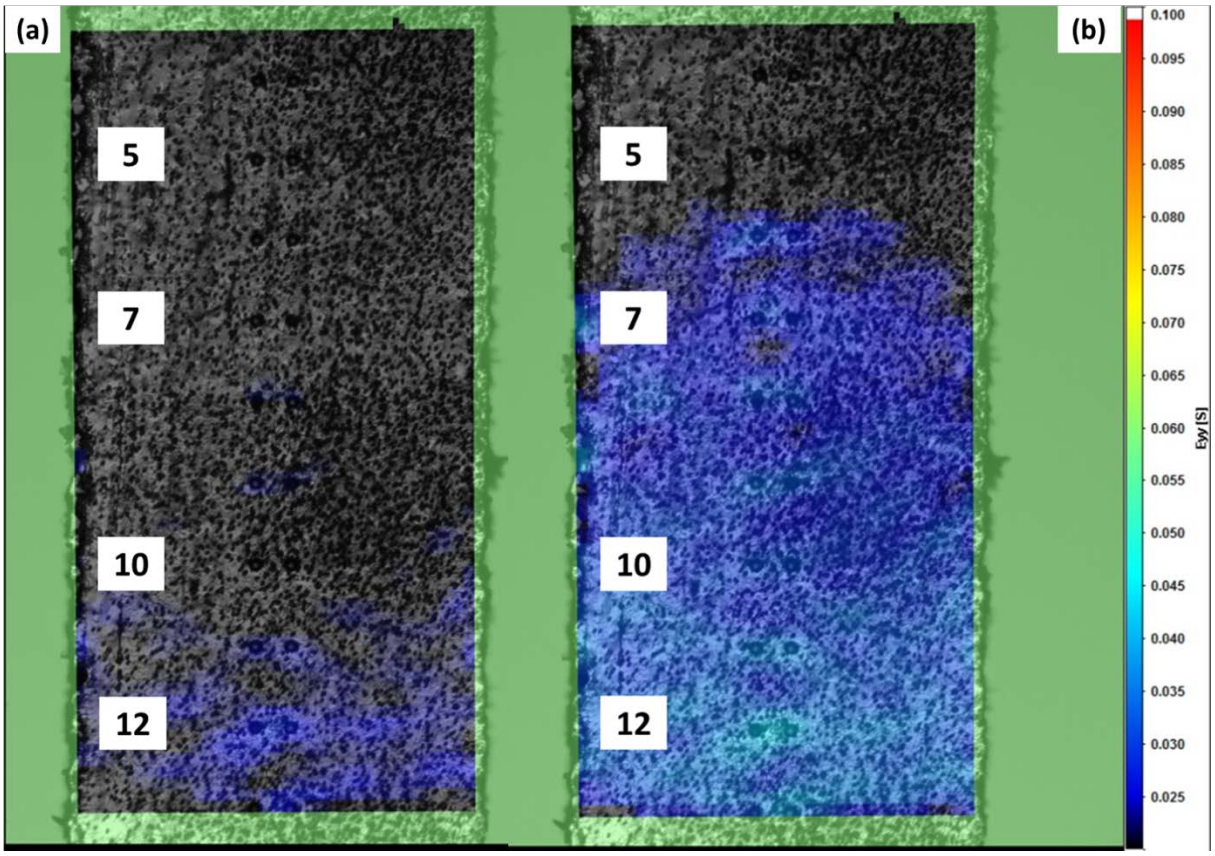

Figure 9-26 - Lüders band propagation during tensile test of carbon graded specimen number 10: Starting of the nucleation of the Lüders band during tensile testing of specimen 10 having uniform carbon content along the gauge length (a) Couple of voids 5 is at the interface of the coated FeC zone and the uncoated zone. (b) progressing of the Lüders band in the uniform zone of specimen 10

Figure 9-26 (a) shows the nucleation of Lüders bands on a specimen having uniform carbon distribution along the gauge length. The front of Lüdering nucleated at the couple 12 which was inserted in the uncoated zone of the gauge length, meaning that the carbon has diffused in the whole gauge length and then the front propagates uniformly for the whole length as shown in Figure 9-26 (b).

As shown in Figure 9-27, if the specimen has no carbon, there is no nucleation of Lüders bands and there is a uniform strain occurring in the whole gauge length of the tensile coupon.

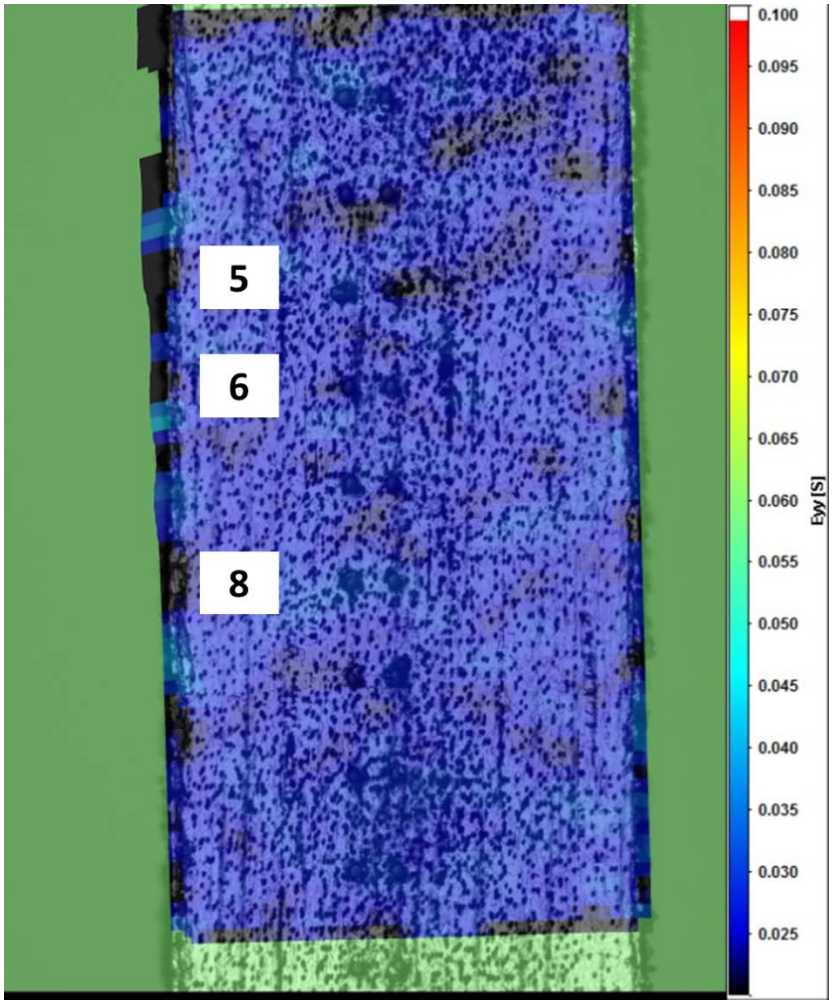

Figure 9-27 - Uniform deformation of specimen 7 without carbon

9.4. Void Growth Analyses

For the specimens presented in the previous paragraph and having a carbon gradient along the gauge length, two rows of holes were machined along the length of the tensile coupon. However, during the tensile tests it was not possible to follow the growth of all the voids since, even with a magnification of 5X in the optical microscope (which is the smallest available), the maximum window size which remains available to follow the deformation of the specimen covers an area of 2 mm x 1.5 mm. For this reason some holes are out of the field of view of the microscope camera. In Figure 9-28, Figure 9-29, Figure 9-30, Figure 9-31 and Figure 9-32, the positions of the voids are shown for the different tested samples. The couple of voids were numbered considering also the voids that are outside the field of view.

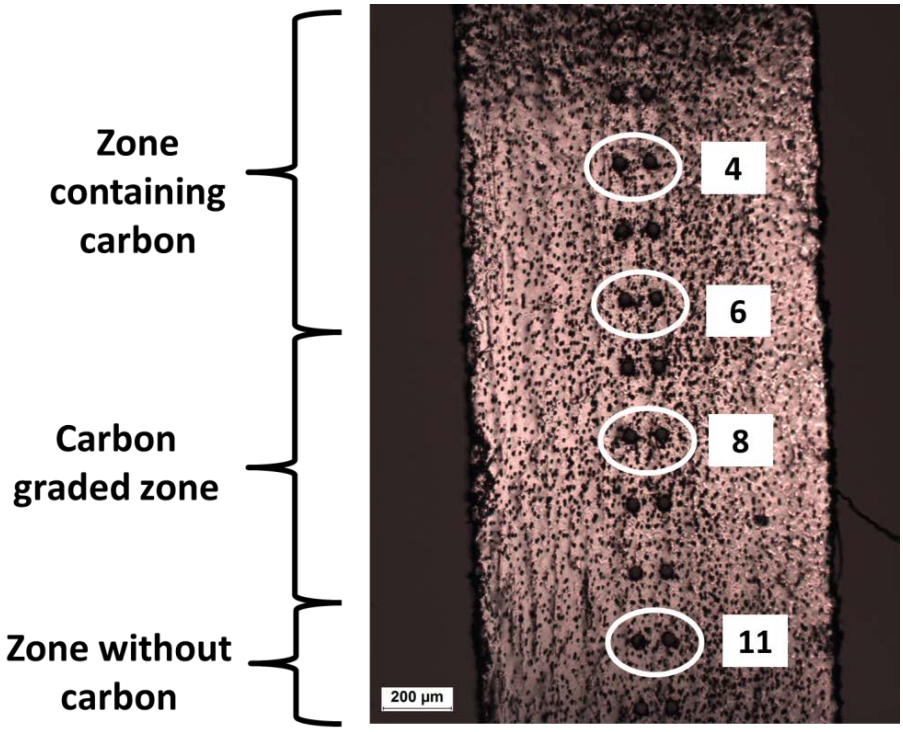

Figure 9-28 - Hole configuration at the starting of the tensile test for specimen number 5 showing carbon gradient along the gauge length

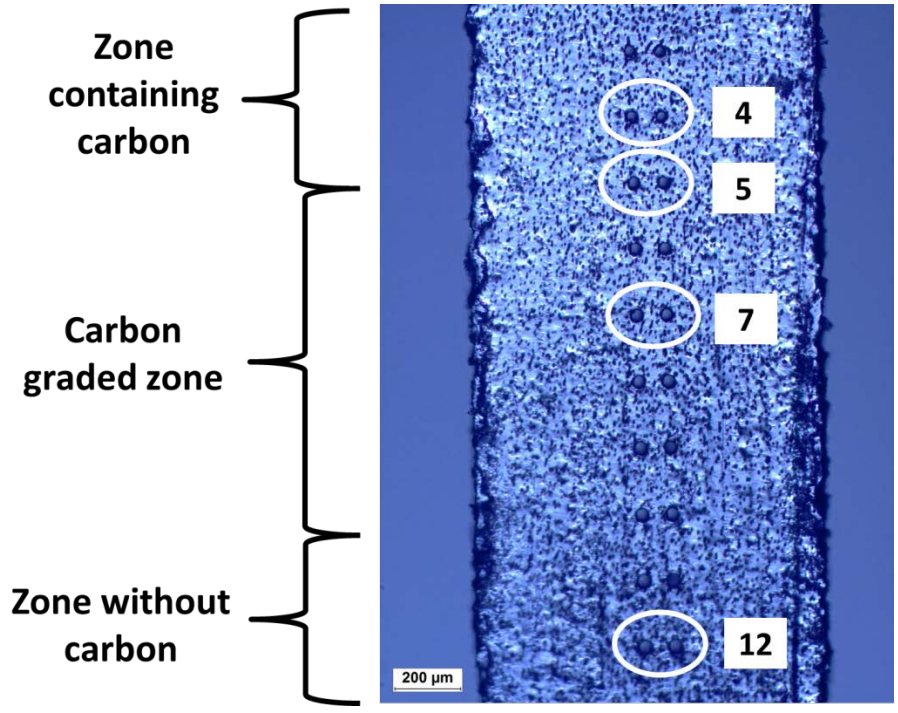

Figure 9-29 - Hole configuration at the starting of the tensile test for specimen number 6 showing carbon gradient along the gauge length

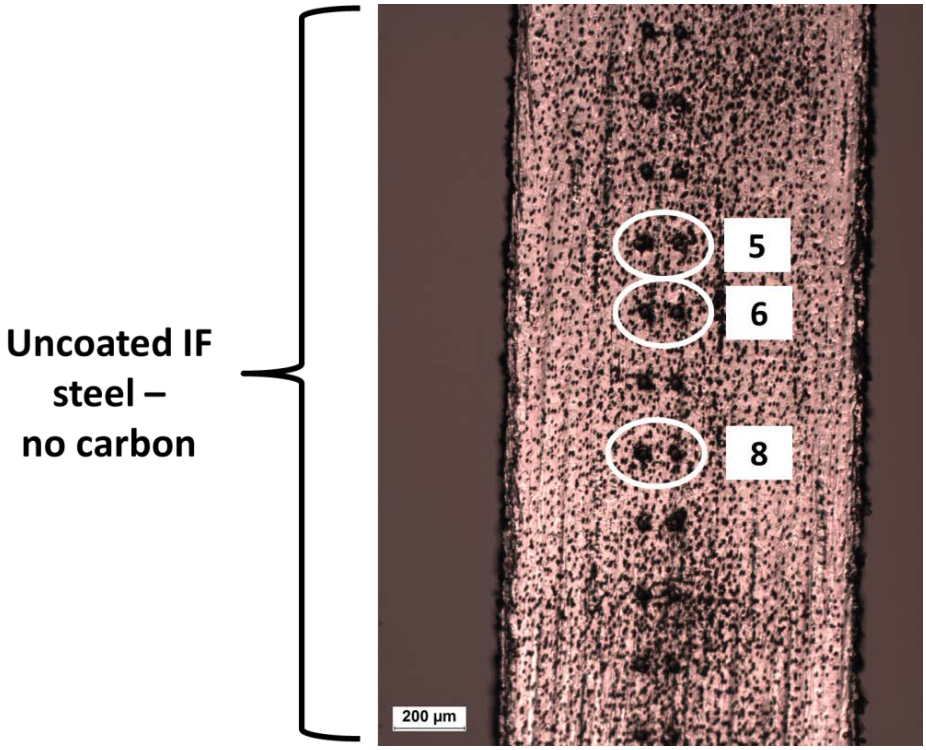

Figure 9-30 - Hole configuration at the starting of the tensile test for uncoated IF steel (specimen 7)

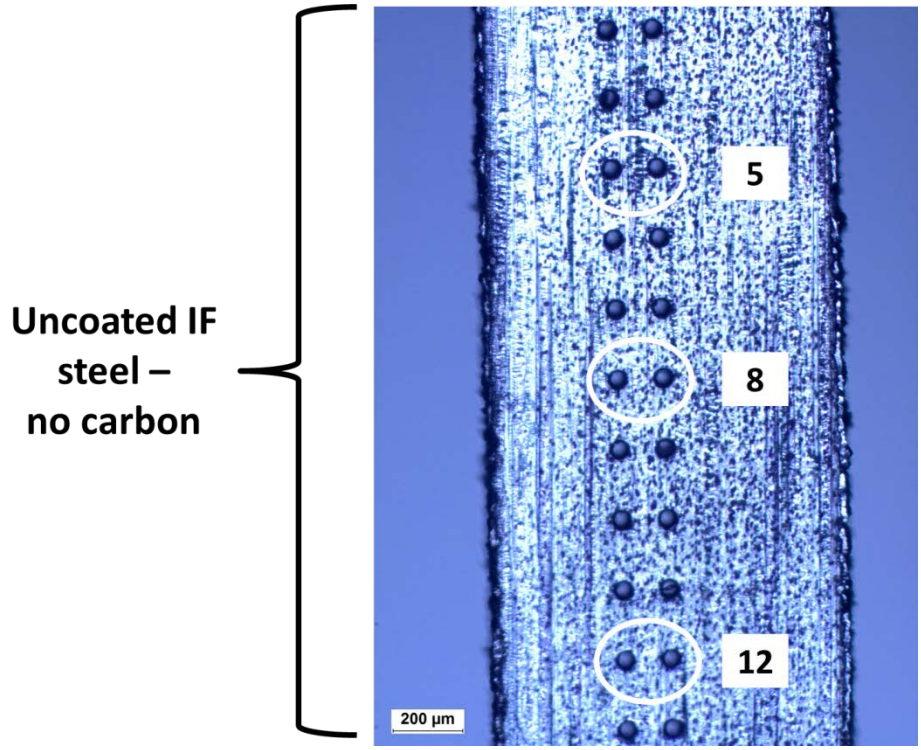

Figure 9-31 - Hole configuration at the starting of the tensile test for uncoated IF steel (specimen 8)

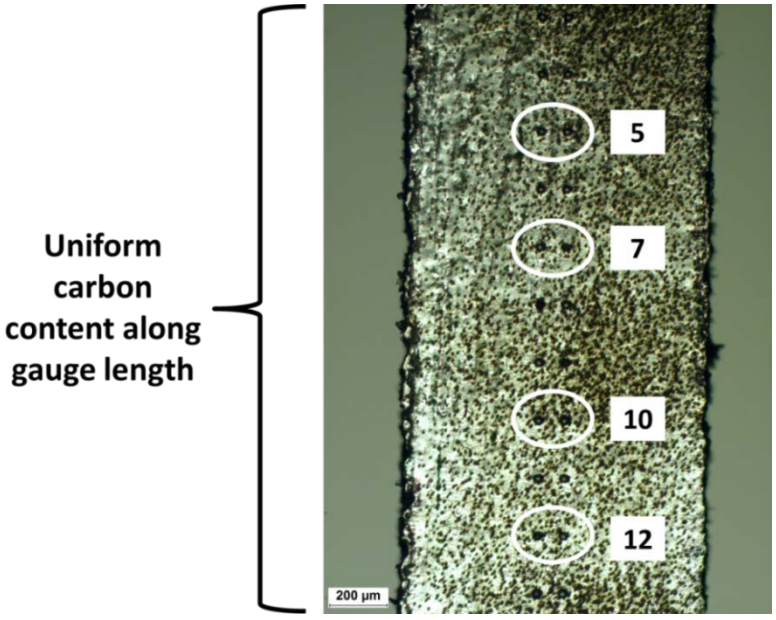

Figure 9-32 - Hole configuration at the starting of the tensile test for specimen number 10 having uniform carbon distribution along the gauge length

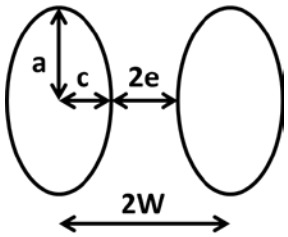

Figure 9-33 - Schematic view of evolution of voids dimensions during a uniaxial tensile test **[206]**

From Figure 9-28 to Figure 9-32, several parameters can be extracted in order to assess the deformation of the voids. These parameters include the major diameter of the void "2a", the ligament length "2e" and the intervoid spacing from center to center "2W' of the couple of voids. As already done by Weck. [206] for 2D fracture studies, in order to be consistent, the minor diameter of the voids "2c" was not measured directly but it is calculated by using:

$$c = W - e$$

The parameters are written as a, c, W and e when they correspond to the current void dimensions during the tensile test, while they are written as a_0, c_0, e_0, W_0, when they refer to the initial void dimensions. The local strain at the scale of voids is defined as $\ln(a/a_0)$ and it is plotted as function of the far field strain. The variation of the main diameter of the voids (2a) is obtained by measuring the dimension of the voids using the free source software

Image J [207]. In particular, a measurement every 10 pictures was taken for these specimens. The fracture analysis was focused only on the study of the evolution of the major diameter since it is the most indicative parameter of the void growth evolution. For some specimens it is also possible to measure automatically the change of the dimensions of the voids by converting the picture in 8 bit format in Image J (Figure 9-34 (a)) and by adjusting the threshold of the image (Figure 9-34 (b)). Successively, the dimension of the voids can be measured by using the "analyse particles" option of Image J. However, this method can only be applied when the surface is clean enough and not too many laser features for DIC are present on the surface, otherwise changes in void dimensions have to be extracted manually.

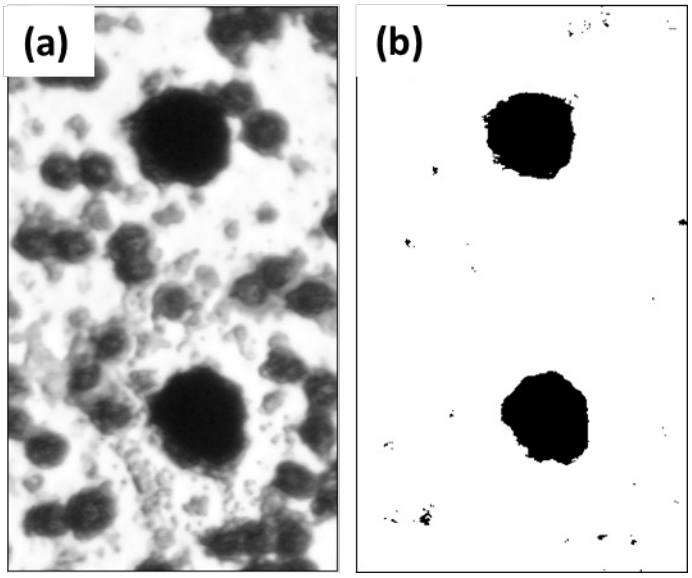

Figure 9-34 - Example of thresholding of an image of voids: (a) 8-bit image of couple of voids; (b) thresholded image of couple of voids

The change in dimension of the main diameter is then plotted as function of the true far field strain extracted from digital image correlation (DIC). For the uncoated and not-annealed IF steel, the true strain was extracted as an average of the strain along the whole gauge length since there is no gradient and for this reason, the specimen is supposed to deform uniformly. For this reason, for the uncoated specimen 7, the true far field strain was extracted taking the average true strain in the tensile direction in a rectangular area as schematically shown in Figure 9-35 for specimen 7. For the same specimen, other graphs were made to plot void growth as function of the local true strain (taken as average on a rectangular area at the sides of the analyzed couple of voids). However, as expected, there was a negligible difference in

the strain levels since the specimen is uncoated, its composition is supposed to be uniform in the whole coupon.

For the half-coated and graded specimens, three analyses were performed. The first analysis shows void growth as function of true far field strain extracted from the whole gauge length as already shown in Figure 9-35 for the uncoated specimen 7. However, for the specimens which have a carbon gradient along the gauge length, since the voids are placed in "series", they will experience the same stress but different strains. For this reason, the average true strain in the tensile direction was extracted for each zone, namely, the coated zone, the graded zone of the gauge length and the uncoated and no carbon zone. For these zones, the strain will be called as "local true far field strain" in the corresponding graphs. The extraction of the true strain from these different areas is shown schematically in Figure 9-36 for specimen number 5. Successively, the void growth for each couple of voids will be plotted both for the true far field strain taken along the whole gauge length and for the "local" true far field strain, in order to assess the different void growth caused by the carbon gradient.

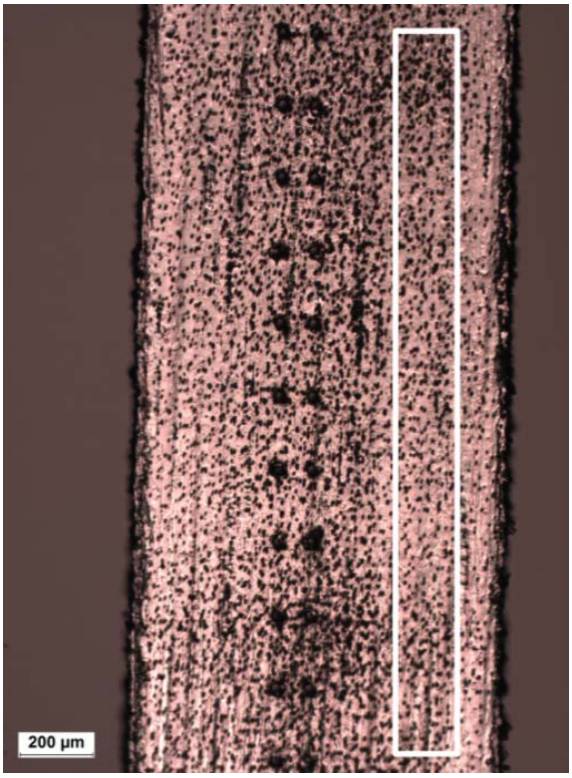

Figure 9-35 - Schematic view of extraction of the average true far field strain for uncoated and not-annealed IF steel (specimen 7)

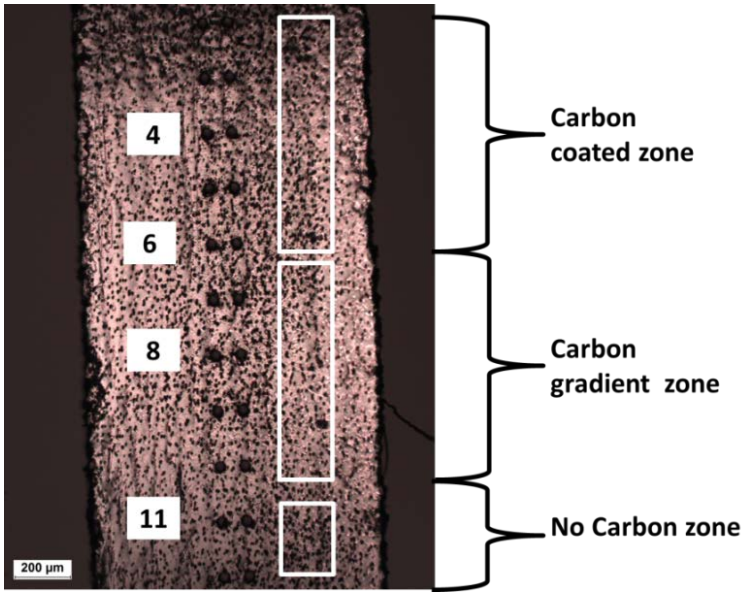

Figure 9-36 - Schematic view of the extraction of the true far field strain for coupons having a carbon gradient along the gauge length. The number of analyzed couple is also reported for specimen number 5

A third analyses of void growth was performed on the same specimens considering the local far field strain extracted at the side of the couple of voids as shown for specimen 5 in Figure 9-37.

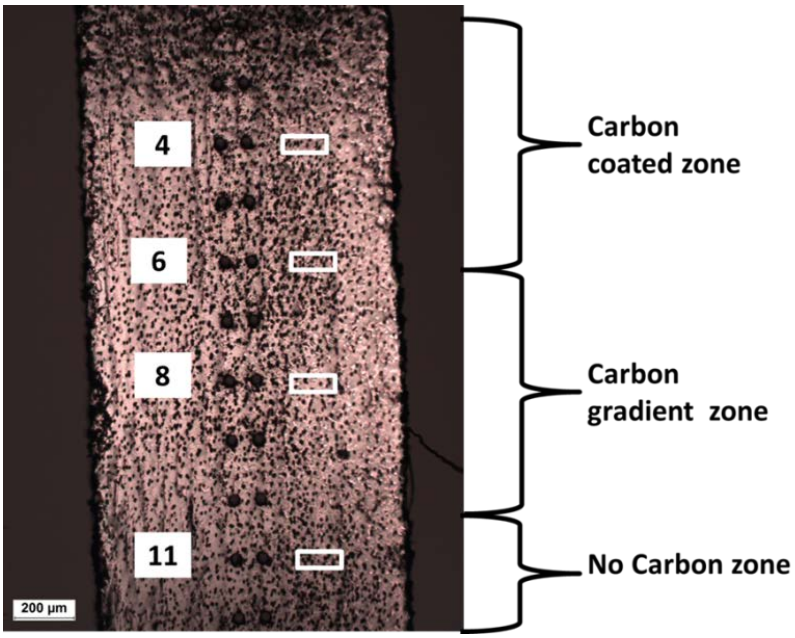

Figure 9-37 - Schematic view of the extraction of the local true far field strain at the side of the voids for coupons having a carbon gradient along the gauge length. The number of analyzed couple is also reported for specimen number 5

9.4.1. Void Growth Analyses for coupons with holes along the gauge length

In this section, the void growth as function of the true far field strain extracted in the whole gauge length (Figure 9-35) is reported togheter with the void growth obtained as function of the local true far field strain extracted considering the zones having different carbon content (Figure 9-36). In particular, one example of the void growth extracted for each coupon is reported. All the other curves are reported in section H.2 (Appendix H). The graphs of the slopes representing the speed of the void growth are also reported for both the far field strain along the whole gauge length and the local far field strain. Again, in this section, these graphs are reported only for some coupons while, all the remaining graphs are shown in section H.2 of Appendix H. Table 9-5 summarizes the void growth for all the couple of voids analyzed for each specimen, both considering the true far field in the whole gauge length or the local true far field strain.

- **Specimen 7 uncoated and not-annealed IF steel**

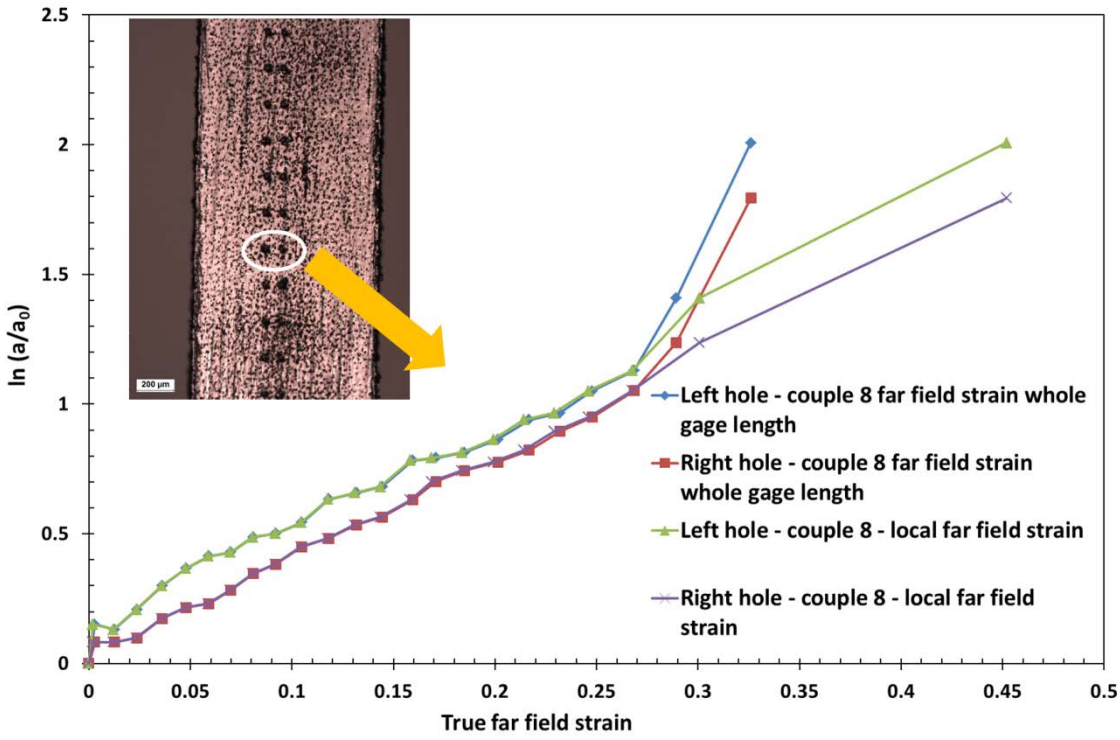

Figure 9-38 - Local true strain versus true far field strain for couple 8 of holes on uncoated and not-annealed IF steel (specimen 7)

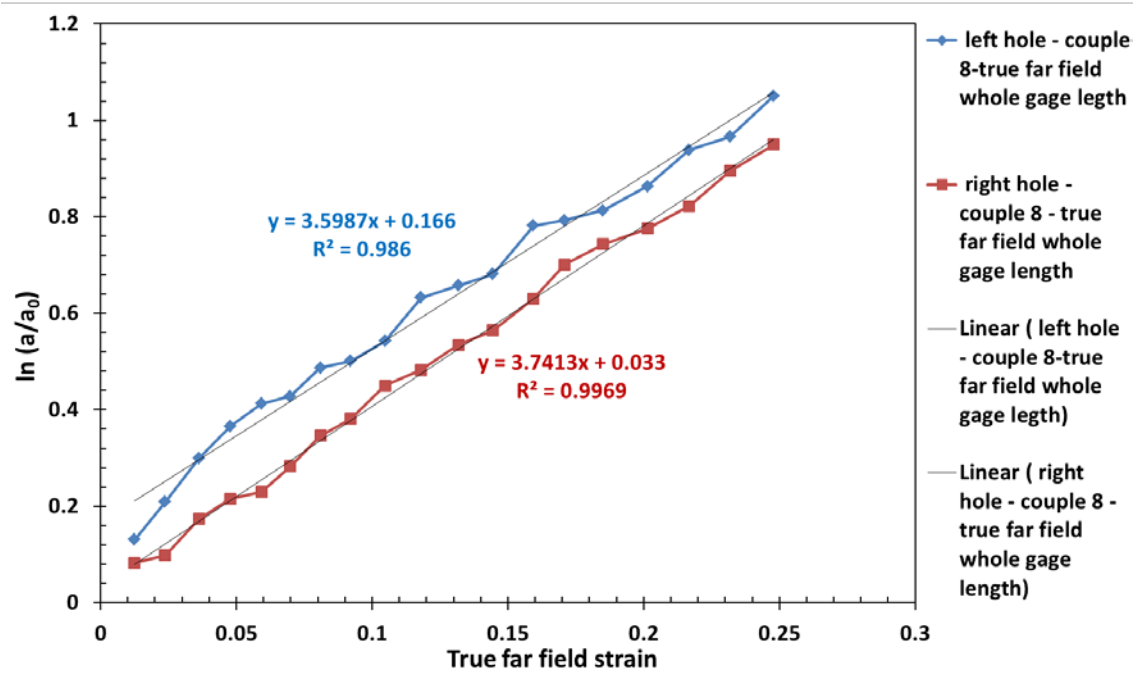

Figure 9-39 - Slope of the local true strain versus true far field strain for couple 8 of holes on uncoated and not-annealed IF steel (specimen 7)

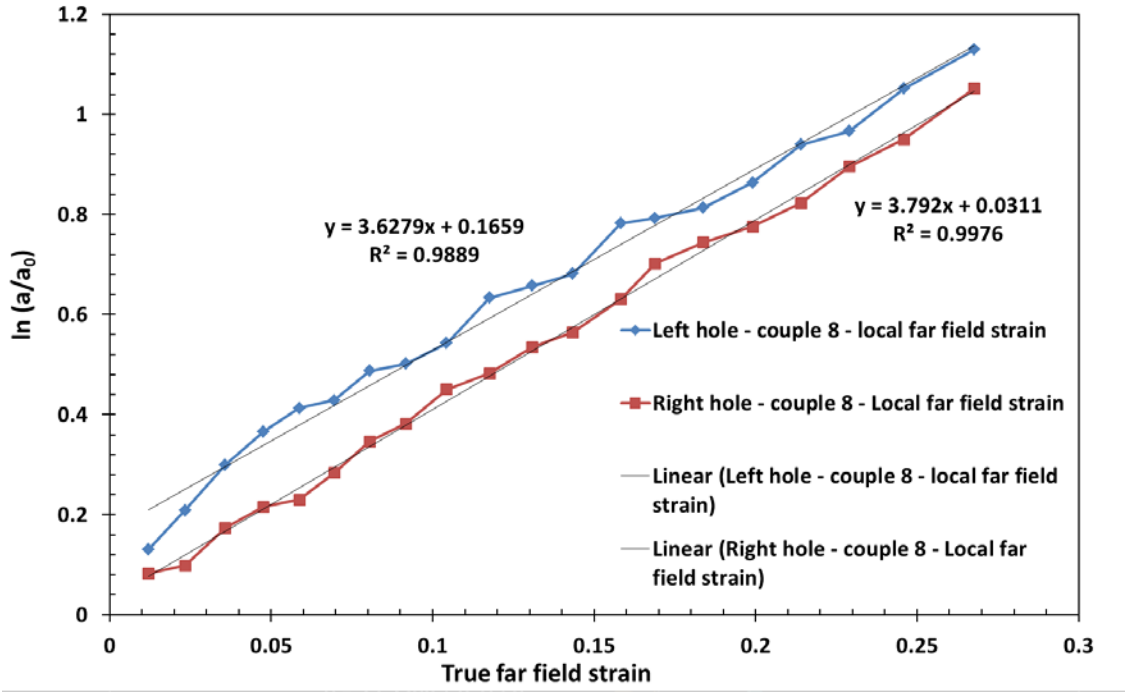

Figure 9-40 - Slope of the local true strain versus the local true far field strain for couple 8 of holes on specimen number 7 having carbon gradient along the gauge length

- **Specimen 5 carbon gradient: couple of holes 4 (coated zone)**

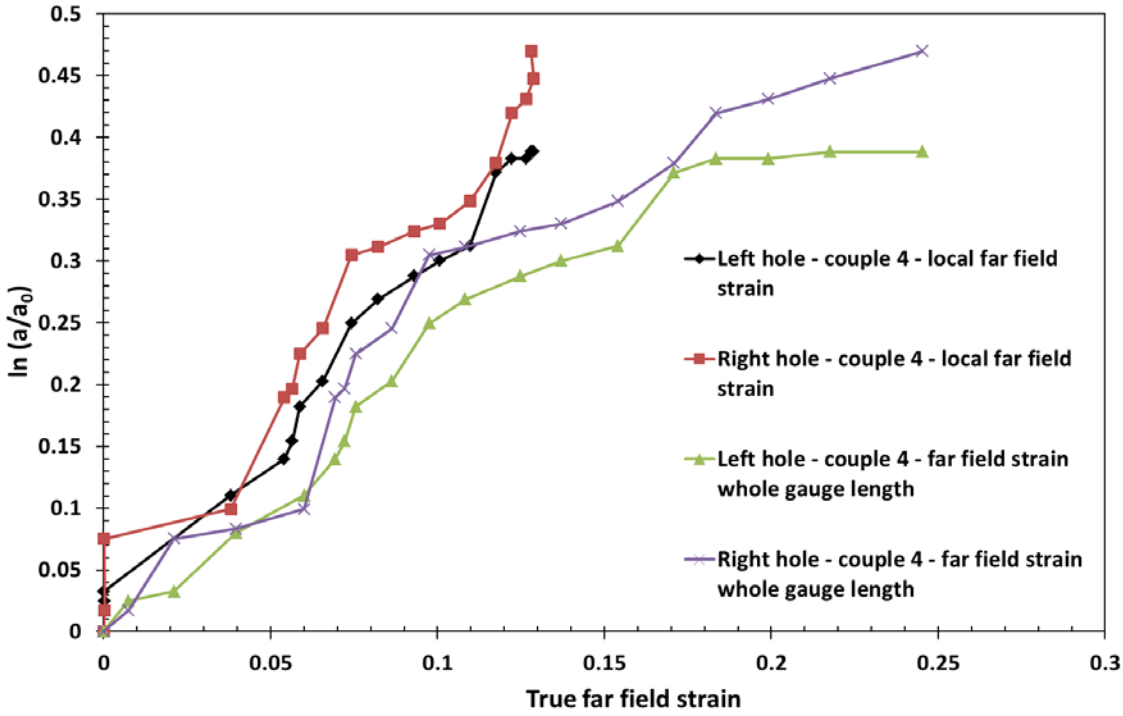

Figure 9-41 - Local true strain versus true far field strain for couple number 4 of voids for specimen number 5 having carbon gradient along the gauge length

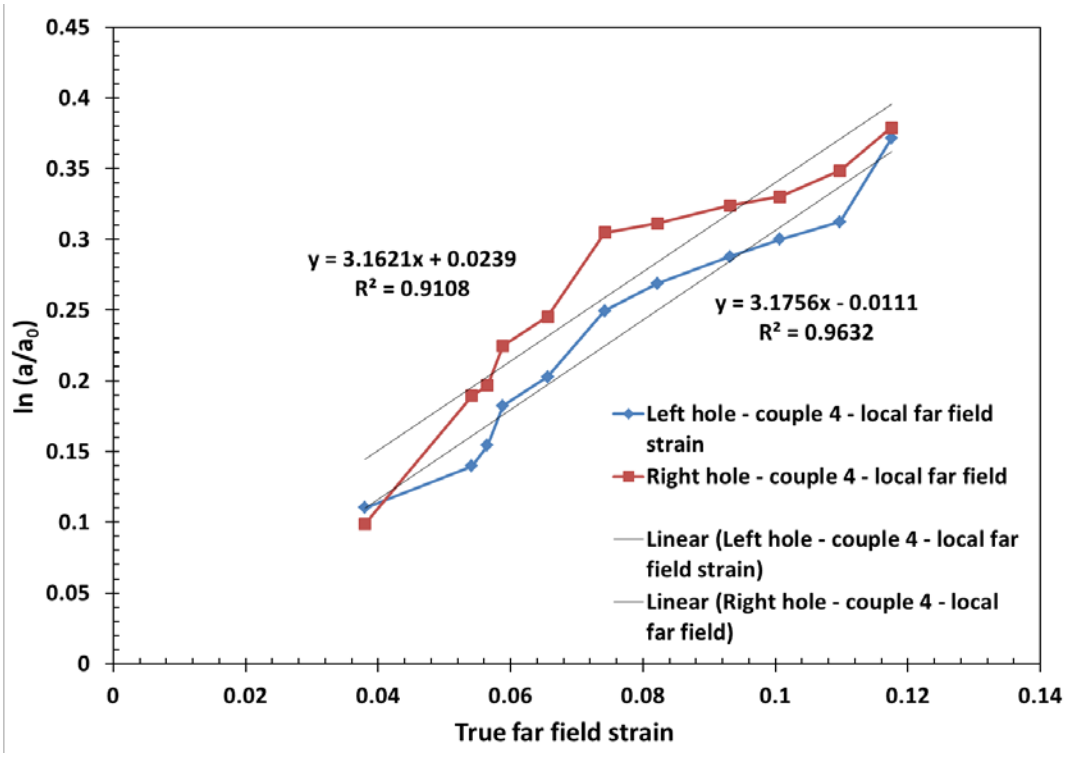

Figure 9-42 - Slope of the local true strain versus the local true far field strain for couple 4 of holes on specimen number 5 having carbon gradient along the gauge length

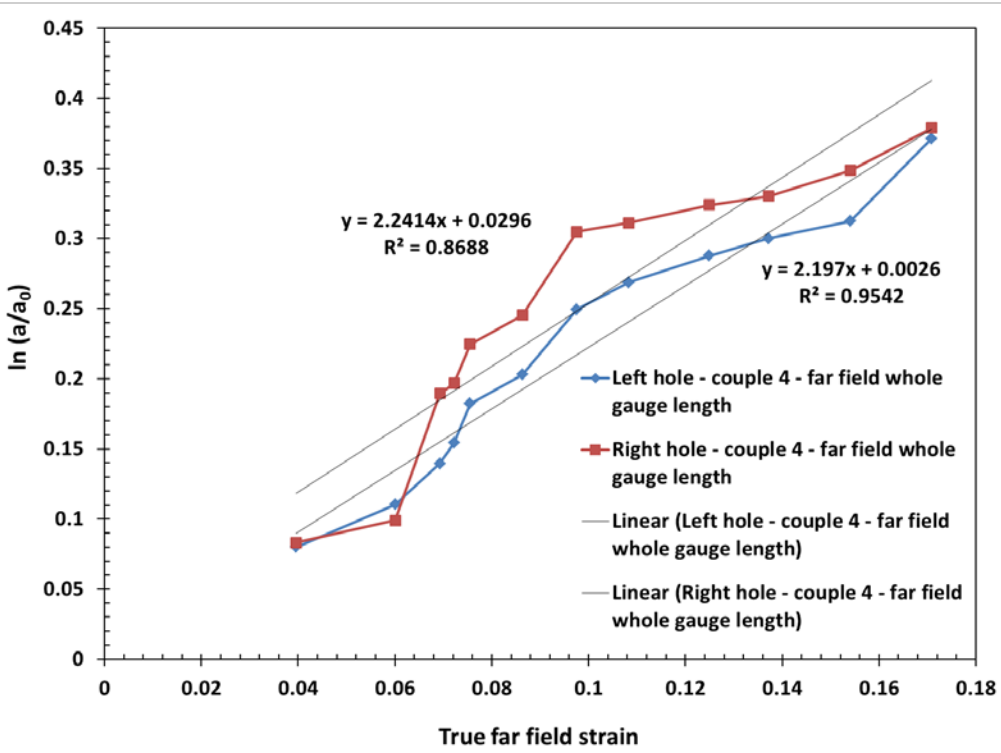

Figure 9-43 - Slope of the local true strain versus the true far field strain taken along the whole gauge length for couple 4 of holes on specimen number 5

- **<u>Specimen 6 carbon gradient: couple of holes 4 (coated zone)</u>**

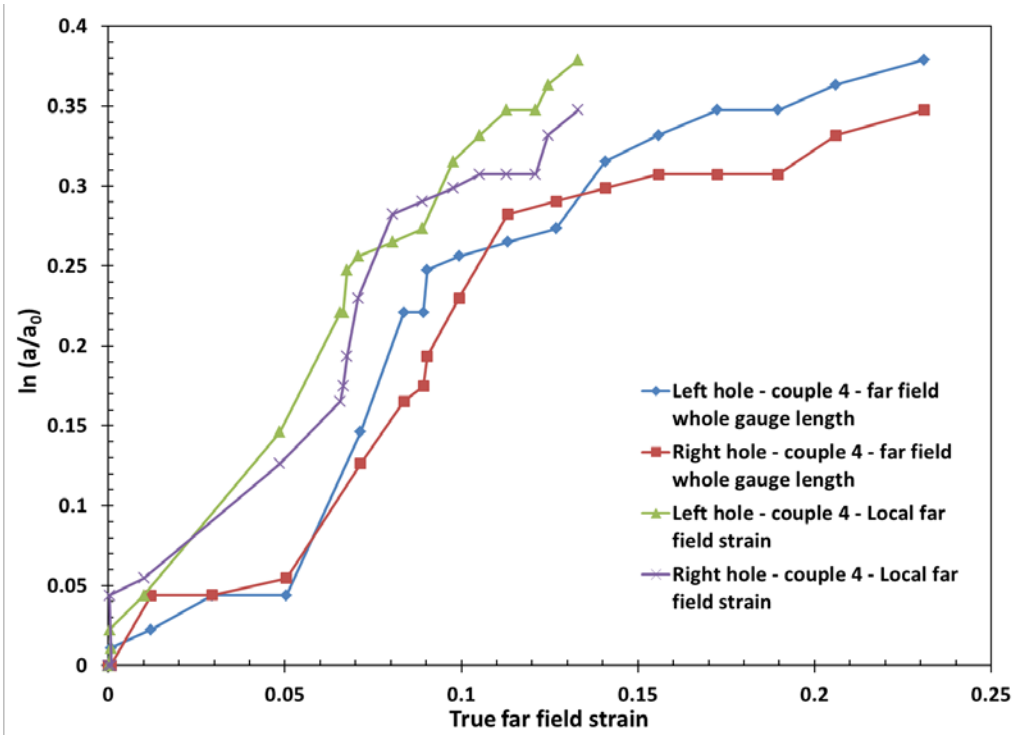

Figure 9-44 - Local true strain versus true far field strain for couple number 4 of voids for specimen number 6 having carbon gradient along the gauge length

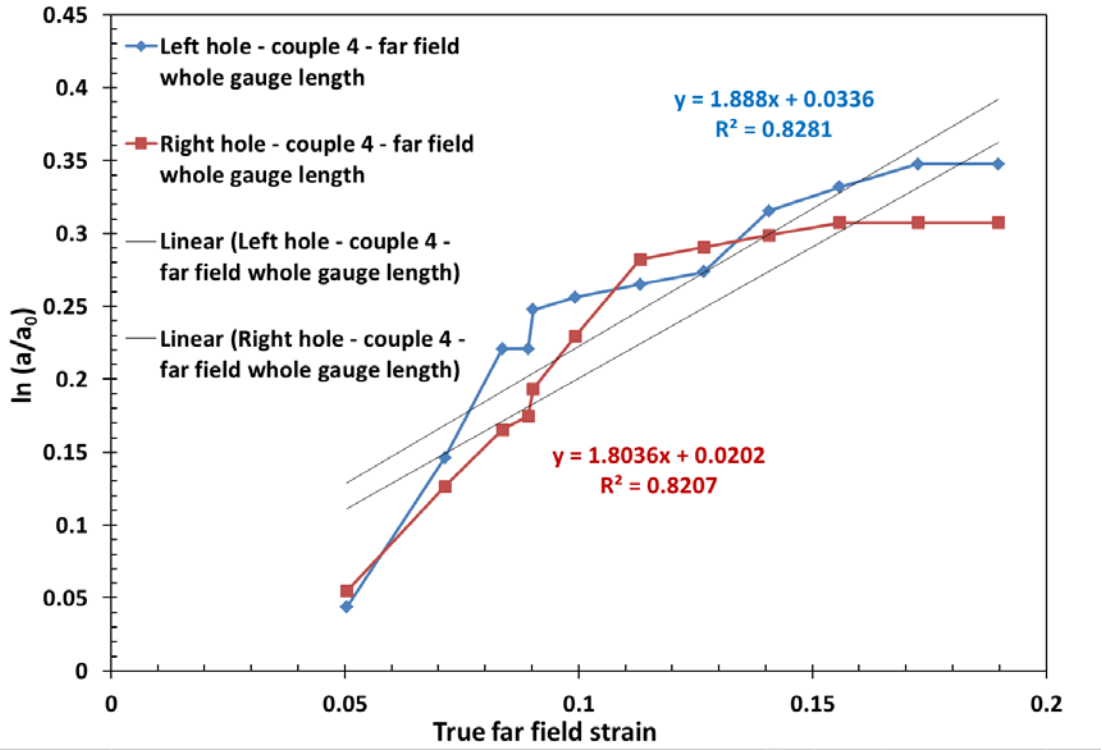

Figure 9-45 - Slope of the local true strain versus the true far field strain taken in the whole gauge length for couple 4 of holes on specimen number 6 having carbon gradient along the gauge length

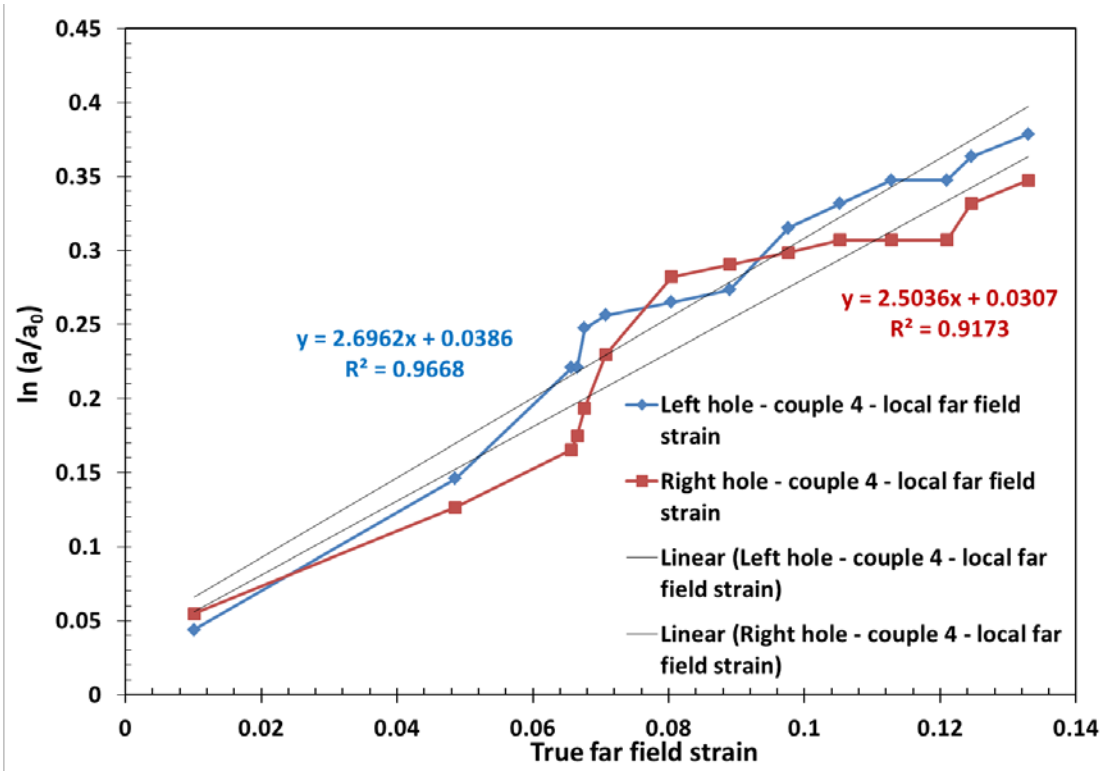

Figure 9-46 - Slope of the local true strain versus the local true far field strain for couple 4 of holes on specimen number 6 having carbon gradient along the gauge length

- **Specimen 10 uniform carbon distribution: couple of holes 5 (coated zone/interface coated-uncoated zone)**

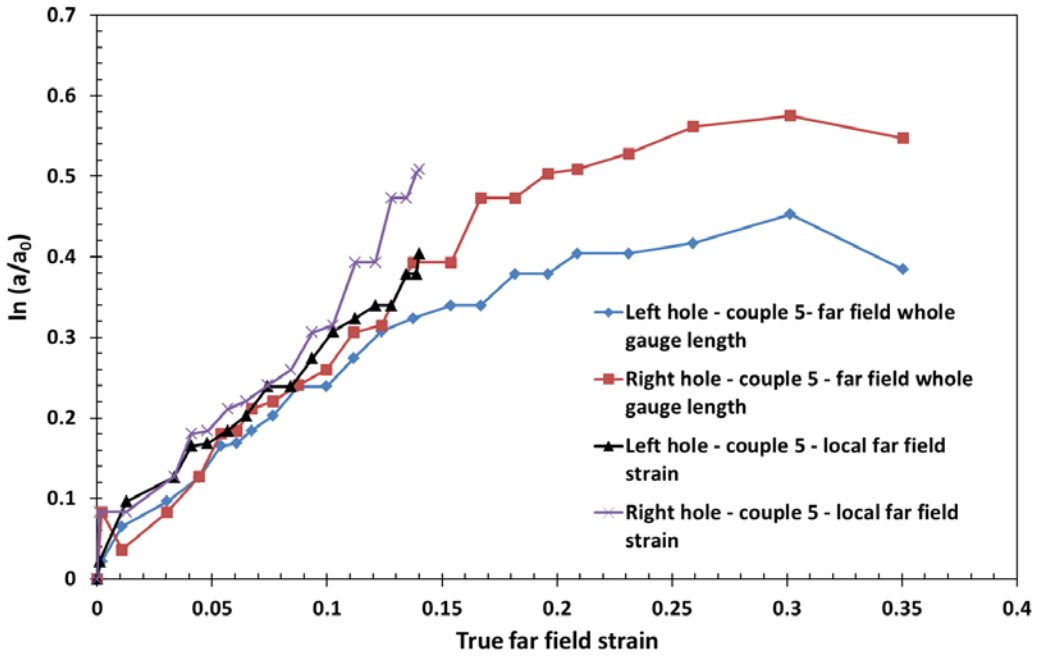

Figure 9-47 - Local true strain versus true far field strain for couple number 5 of voids for specimen number 10 having uniform carbon distribution along the gauge length

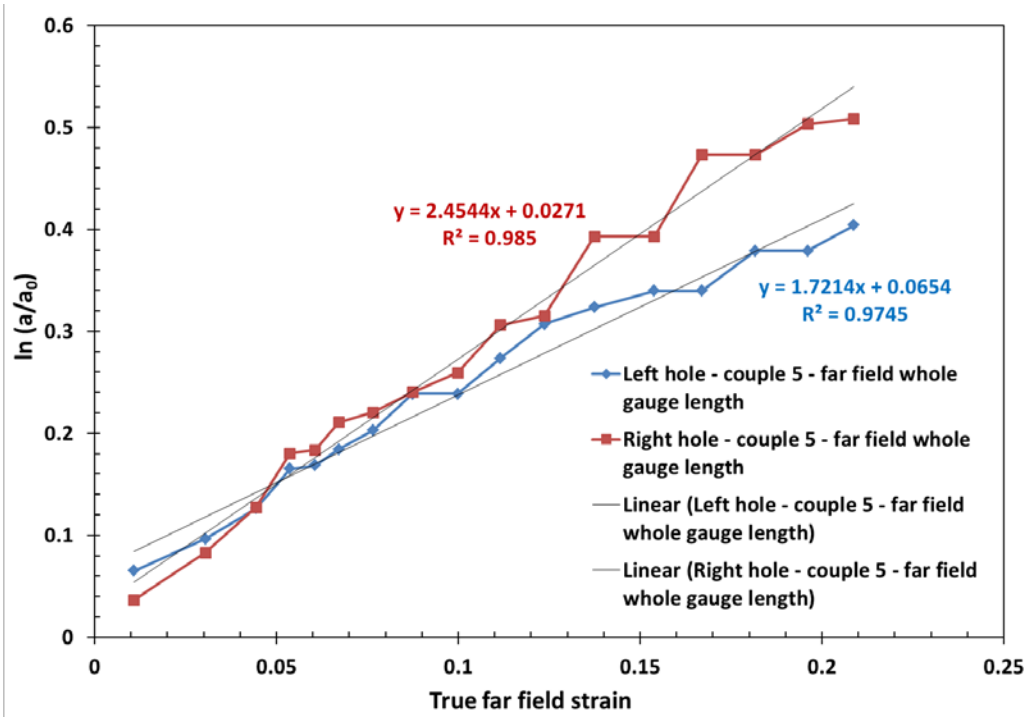

Figure 9-48 - Slope of the local true strain versus the true far field strain taken in the whole gauge length for couple 5 of holes on specimen number 10 having uniform carbon distribution along the gauge length

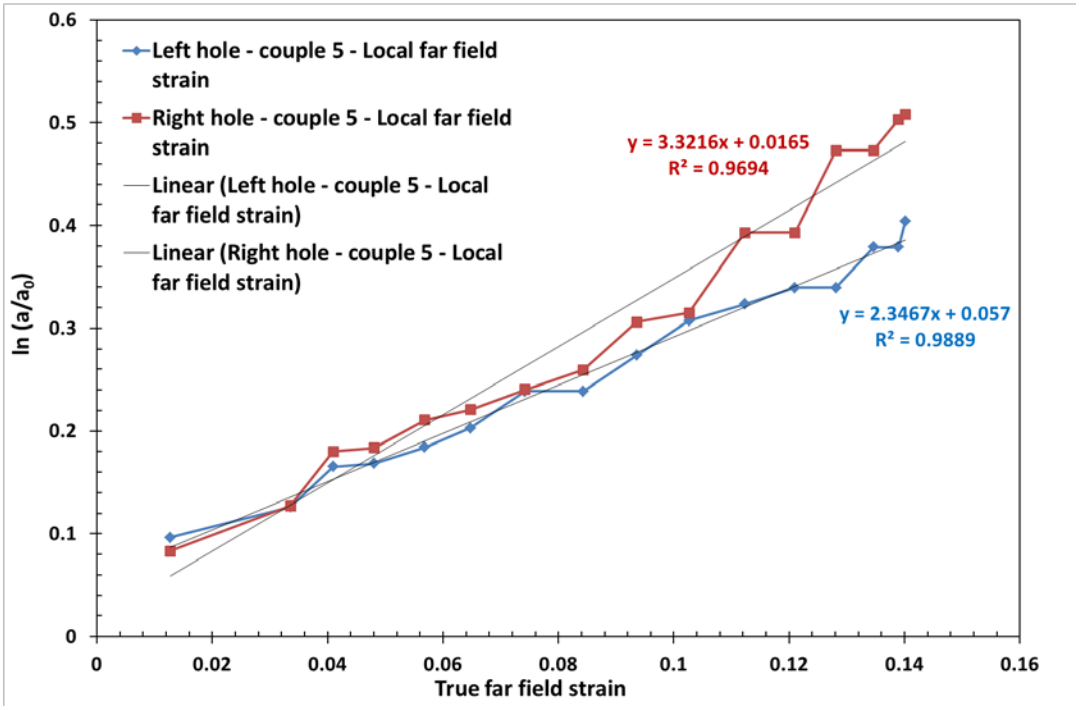

Figure 9-49 - Slope of the local true strain versus the local true far field strain for couple 5 of holes on specimen number 10 having uniform carbon distribution along the gauge length

Void growth was extracted for the same coupons considering the local strain extracted at the sides of the voids as shown in Figure 9-37. In this section only one graph for coupon 5 will be shown. All the detailed graphs for the remaining couple of voids of specimen 5 and for the other specimens are included in Appendix H (section H.2.2). The numerical values obtained for void growth are reported in Table 9-5. Figure 9-50 shows the void growth for couples of voids 4 and 6 in specimen 5 as a function of the true strain extracted at the sides of the voids. The void growth is irregular due to the propagation of Lüders bands. The slopes of the curves obtained by removing the initial "jump" in strain caused by the bands is shown in Figure 9-51.

- **Specimen 5 carbon gradient along the gauge length: void growth as function of the local true strain at the sides of the voids**

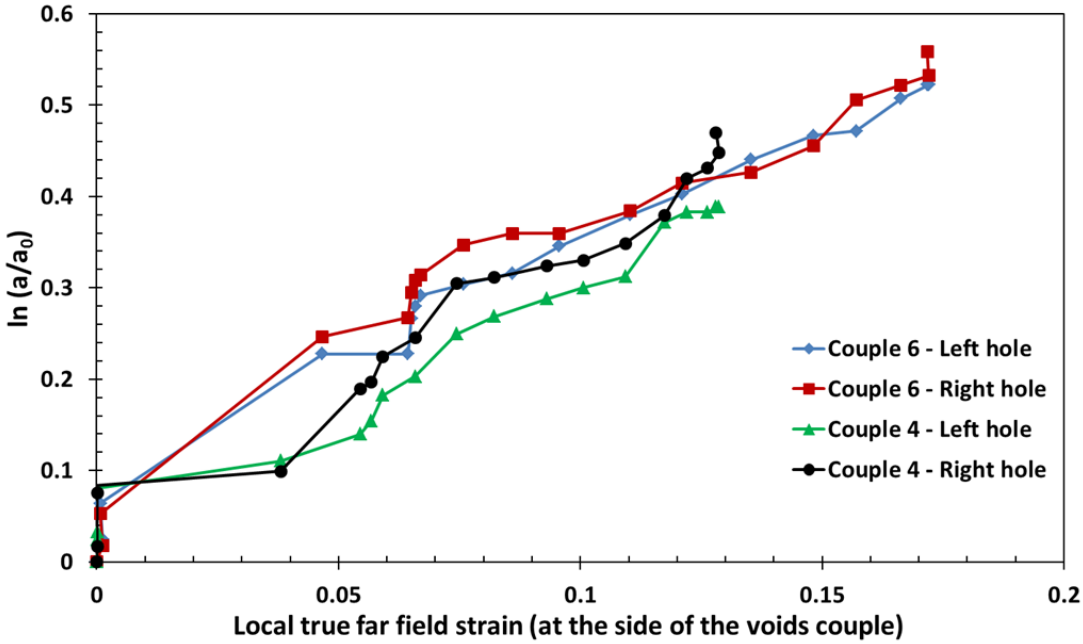

Figure 9-50 - Local true strain as function of the local true far field strain extracted at the side of the voids for couples 4 and 6 of specimen 5 having carbon gradient along the gauge length

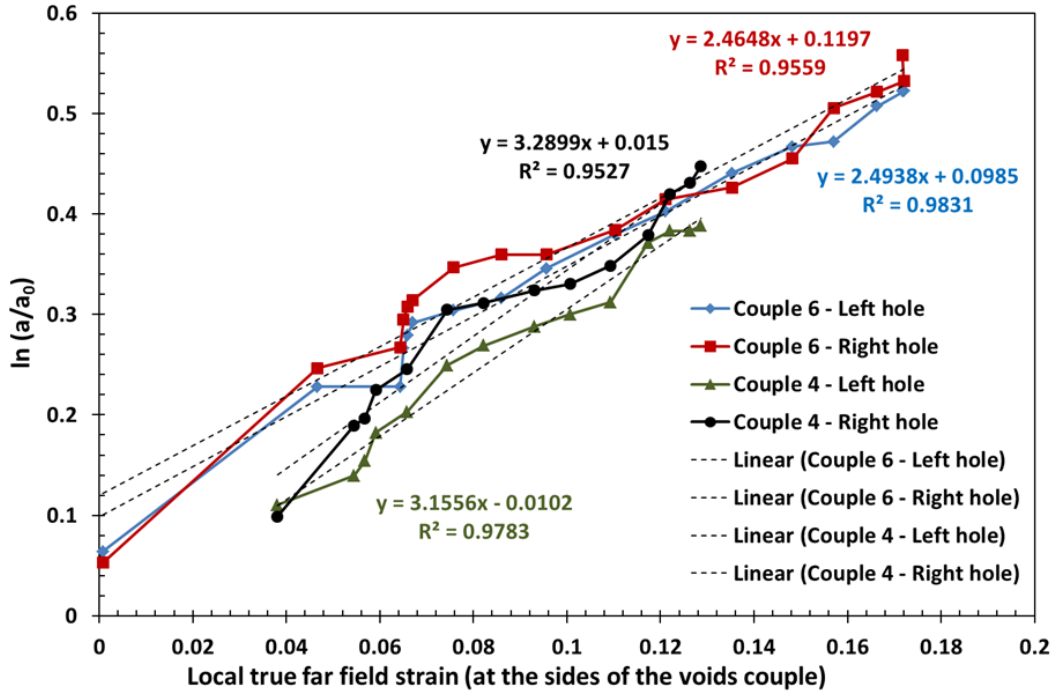

Figure 9-51 - Slope of the local true strain versus the local true far field strain at the sides of the voids for couples 4 and 6 on specimen number 5 having carbon gradient along the gauge length

Couple of voids	Void growth for local true far field strain		Average void growth for local strain	Void growth for strain along the whole gauge length		Average void growth for strain in the whole gauge length	Void growth for local strain at the sides of the voids		Average void growth for strain at the sides of the voids
	Left hole	Right hole		Left hole	Right hole		Left hole	Right hole	
Specimen 7 – uncoated and not-annealed IF steel									
5	1.8	3.3	3.4 (*)	1.8	3.3	3.4 (*)	1.8	3.3	3.4 (*)
6	3	3.1		3.1	3.3		3	3.1	
8	3.6	3.8		3.6	3.7		3.6	3.8	
Specimen 5 – carbon gradient along gauge length									
4	3.2	3.2	2.9	2.2	2.2	2.7	3.2	3.3	2.9
6	2.6	2.9		1.7	1.9		2.5	2.5	
8	2.8	3.1		3.2	3.4		3	3.2	
11	2.5	2.6		3.4	3.4		2.6	2.7	
Specimen 6 – carbon gradient along gauge length									
4	2.7	2.5	2.6	1.9	1.8	2.5	2.6	2.6	2.7
5	2.7	3.2		1.9	2.4		2.5	3.2	
7	2.3	2.2		2.6	2.7		2.7	2.5	
12	2.7	2.5		3.4	2.9		2.9	2.7	
Specimen 10 –Uniform carbon content along gauge length									
5	2.3	3.3	2.5	1.7	2.5	2.5	2.4	3.5	2.4
7	2	2.1		1.9	2.1		2.2	2.4	
10	2.4	2		2.3	1.9		2	1.6	
12	2.4	3.3		3.4	4		2.5	2.8	

Table 9-5 - Summary of void growth obtained for all the specimens having holes along the gauge length. (*) for the average of this specimens, the value of 1.8 has been discarded

According to the results shown in Table 9-5, no clear trend can be discerned if void growth is extracted considering the local strain. The values of void growth obtained considering the local strain extracted from different carbon zones is similar to the void growth obtained considering the local strain extracted at the sides of the voids couple. On the other hand, a difference in void growth is detected if the far field strain in the whole gauge length is considered. The assumption is that void growth is controlled by the local strain ; so for a same local strain, the voids are expected to grow at the same rate. However, the local strain is different from the far field strain in the whole gauge length, since this is an average of the

strain in the whole gauge length and it is not the strain that the voids see locally, which is why it is possible to discern the difference due to the gradient.

For these coupons, the holes where placed in series, which means they will experience the same load but different strains. For this configuration of holes in serie, the coated zone will stop deforming at some point because the uncoated zone can deform more before reaching an earlier failure. It is like having two different materials in serie, for example steel and rubber. When this "composite" is tested in tension, the material will fail in the rubber zone since this will be the zone which will accumulate most of the deformation. The same reasoning can be applied to the coupons tested in this section, where the coated zone deforms less than the uncoated zone and it yields later than the uncoated zone. For this reason, the failure is expected to occur in voids placed in no-carbon zones since the critical strain for failure will be reached earlier. In particular, the voids placed in the carbon containing zones will stop growing at some point, while the voids placed in the uncoated zone will continue to grow until failure.

9.4.1.1. Fitting of void growth with McClintok

McClintok [208] developed a void growth model for 2D cylindrical voids which accounts for uniaxial or biaxial states of stress and for the strain-hardening exponent of the material. The model expresses the ratio between the mean radius (R) of the elliptical void and the initial radius (R_0) using the following relation:

$$\frac{R}{R_0} = \exp\left[\frac{\bar{\varepsilon}\sqrt{3}}{2(1-n)}\sinh\left(\frac{\sqrt{3}(1-n)}{2}\,\frac{\sigma_1+\sigma_2}{Y}\right)+\frac{\varepsilon_1+\varepsilon_2}{2}\right] \qquad \text{(eq. 9-1)}$$

In the above equation, n is the strain-hardening exponent, while σ_1 and σ_2 are the principal stresses in the x and y directions and ε_1 and ε_2 are the main principal strains.

In the case of a uniaxial tensile test, σ_2 is equal to zero and σ_1 is equal to Y (equivalent stress). Moreover, for a uniaxial tensile test, $\varepsilon_2 = -\varepsilon_1/2$, so the above equation becomes:

$$\frac{R}{R_0} = \exp\left[\frac{\bar{\varepsilon}\sqrt{3}}{2(1-n)}\sinh\left(\frac{\sqrt{3}(1-n)}{2}\right)+\frac{\bar{\varepsilon}}{4}\right] \qquad \text{(eq. 9-2)}$$

However, in order to easily compare the model with the experimental results, it is necessary to manipulate the above relations in order to obtain the ratio (a/a_0) and (b/b_0) which represent the evolution of the major diameter and minor diameter respectively. This is

obtained by using an eccentricity parameter *m = (a-b)/(a+b).* For an uniaxial tensile test and for an initial eccentricity equal to zero (since before the test, the major and minor diameters have the same dimensions), the parameter *m* is expressed as:

$$\boldsymbol{m = 1 - \exp\left[\frac{-\bar{\varepsilon}\sqrt{3}}{(1-n)}\sinh\left(\frac{\sqrt{3}(1-n)}{2}\right)\right]} \qquad \text{(eq. 9-3)}$$

The evolution of the major diameter is then related to the ratio R/R_0 and to *m* by the following equation:

$$\frac{\mathbf{a}}{\mathbf{a_0}} = \frac{\mathbf{R}}{\mathbf{R_0}}(\mathbf{1} + \mathbf{m}) \qquad \text{(eq. 9-4)}$$

By combining eq. 9-2 and eq. 9-3 into eq. 9-4, the evolution of the major diameter is obtained as a function of the true strain ε and of the strain hardening exponent *n* and it is given by:

$$\boldsymbol{\frac{a}{a_0} = \exp\left[\frac{\bar{\varepsilon}\sqrt{3}}{2(1-n)}\sinh\left(\frac{\sqrt{3}(1-n)}{2}\right) + \frac{\bar{\epsilon}}{4}\right] \times \left[2 - exp\left(\left(\frac{-\bar{\varepsilon}\sqrt{3}}{(1-n)}\right) sinh\ \left(\frac{\sqrt{3}(1-n)}{2}\right)\right)\right]} \qquad \text{(eq. 9-5)}$$

The calculations shown above are also reported in other studies related to void growth in aluminium [209].

This expression was used to fit the void growth for all specimens having holes placed along the gauge width. For fitting the specimens having holes along the gauge length, the strain used in McClintok equation is the local true far field strain extracted at the sides of the couple of voids, while the strain hardening exponent was extracted by the engineering stress-strain curves of each coupon and the values are reported in Table 9-6.

Specimen	Strain hardening exponent
Specimen 7 (uncoated)	0.25
Specimen 5 (carbon gradient)	0.25
Specimen 6 (carbon gradient)	0.22
Specimen 10 (uniform carbon distribution)	0.23

Table 9-6 - Values of strain hardening exponent extracted from stress-strain curves of coupons having holes along the gauge length

The results of the fitting are reported in Figure 9-52 for specimen 7 which was uncoated and in Figure 9-53 for specimen 5 which had carbon gradient along the gauge length.

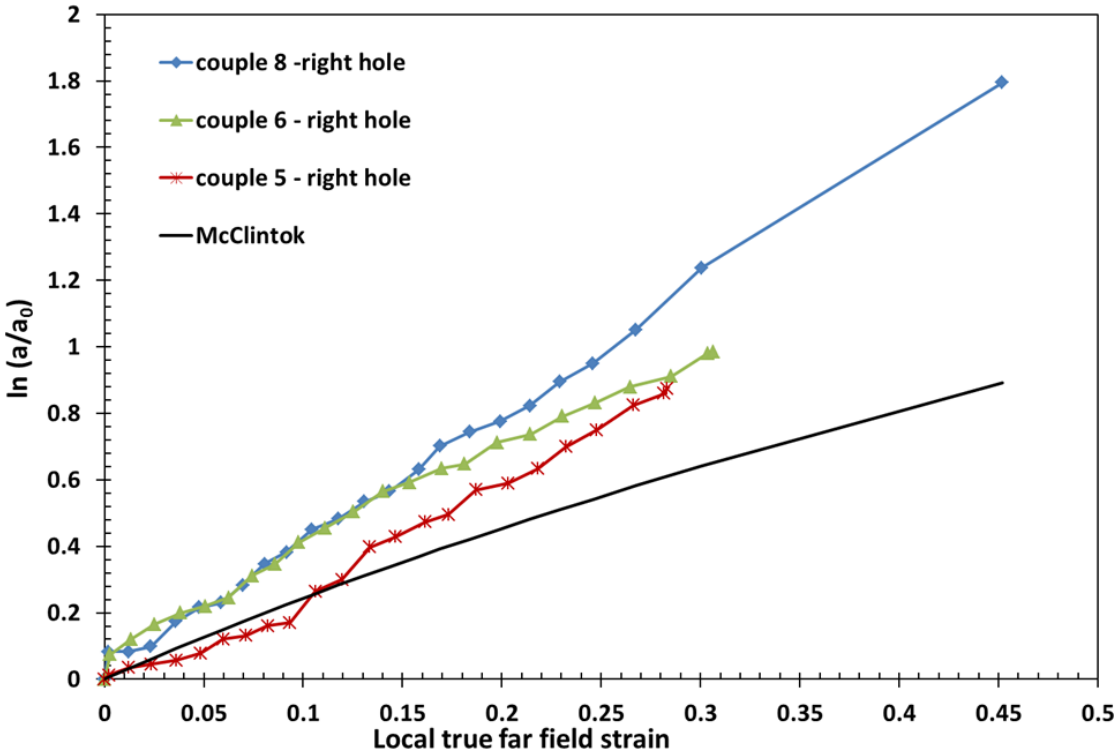

Figure 9-52 - McClintok fitting of the void growth of uncoated specimen 7

From Figure 9-52, the McClintok model seems to fit well the void growth for strains lower than 0.1, however, the couple of voids 6 and 8 depart early from the McClintok model. In Figure 9-53, McClintok was used to fit the void growth for specimen 5 which has a gradient of carbon along the gauge length. From the graph, one can see that again McClintok fits reasonably well the void growth for true strains lower than 0.1, except for the couple of holes 6 which was placed at the interface between the coated and not-coated zone and whose growth is influence by Lüders propagation. However, it seems that even the couple of holes 11 in the uncoated zone tends to depart early from the McClintok model even if no marked Lüdering is affecting these voids. This can be explained considering that the couples inserted in the uncoated zone will accumulate more deformation than the couples of voids placed in the coated zone or in the carbon graded zone. For this reason, the voids in the uncoated zone will start to interact earlier and coalescence will occur. McClintok model does not take into account coalescence which could explain why the prediction deviates from the experimental results.

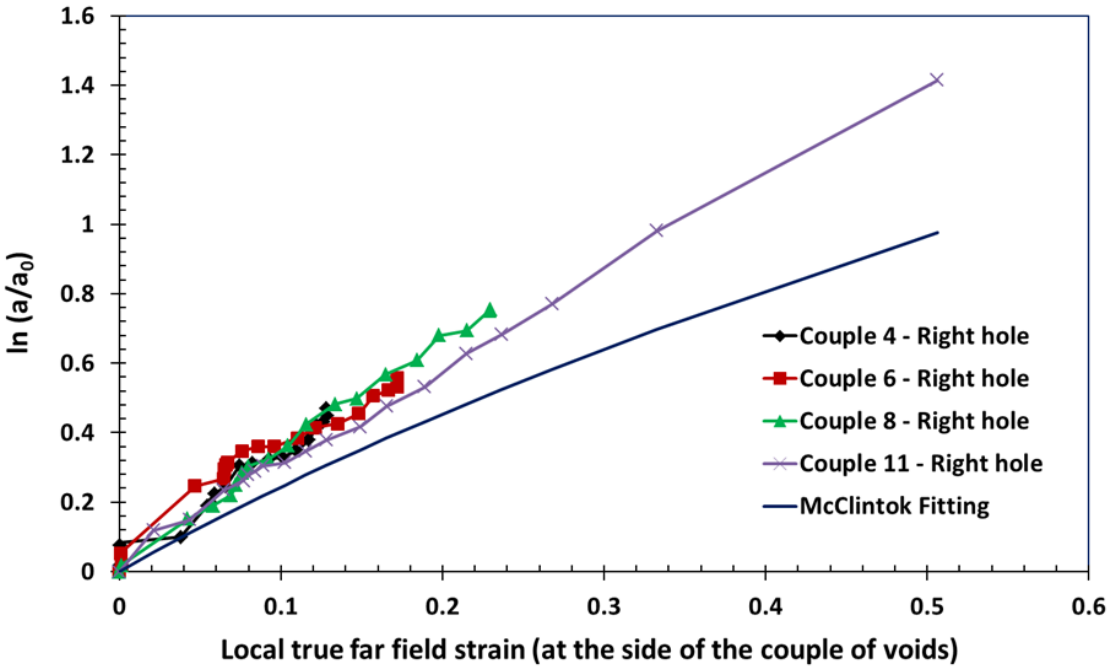

Figure 9-53 - McClintok fitting of the void growth of specimen 5 having carbon gradient along gauge length

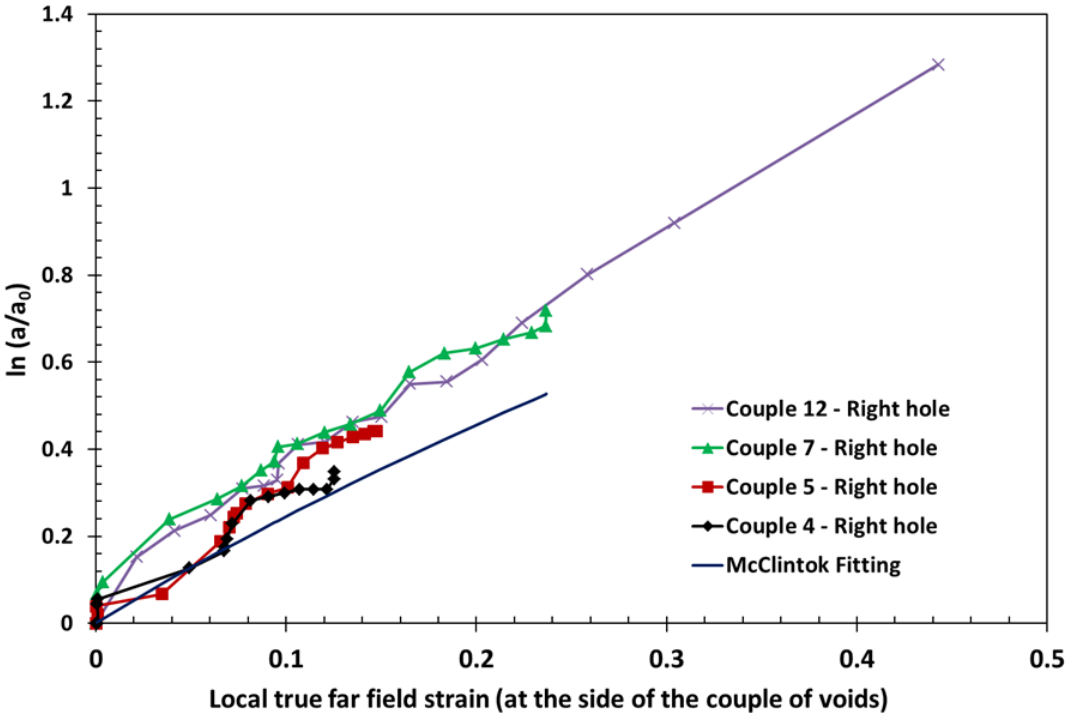

Figure 9-54 - McClintok fitting of the void growth of specimen 6 having carbon gradient along gauge length

Figure 9-54 shows the McClintok fitting for specimen 6 and one can see that for this specimen, the fitting fails even at low strain, most probably because of the propagation of Lüders bands, which cause a local increase of strain. Moreover, as already seen in coupon 5, it was noticed that the voids which are placed in the uncoated zone tend to deform more than the voids placed inside the coated zone and for this reason they deviate more from the McClintok curve (curves “couple 12 and 7” in Figure 9-54). Moreover from both Figure 9-53 and Figure 9-54, one can clearly see that the voids placed in the coated zone (couple 4 Figure 9-53 and Figure 9-54) will stop growing earlier than the voids placed in the carbon graded zone (couple 8 in Figure 9-53 and couple 7 in Figure 9-54) and these voids will stop growing ealier than the holes placed in the no-carbon zone (couple 11 in Figure 9-53 and couple 12 in Figure 9-54).

On the other hand, McClintok seems to fit well the void growth for coupon 10 (Figure 9-55), probably because of the more uniform Lüders bands propagation and for the uniform carbon distribution. Indeed, one must remember that the stress-strain curves of specimens 5 and 6 showed a yielding before the upper yield stress for the bands propagation was reached. This first yielding is a result of the localization of deformation in the uncoated zone. This could explain why the void growth of couples placed in the uncoated zone in carbon graded material (specimen 5 and 6) departs from McClintok even at low strains.

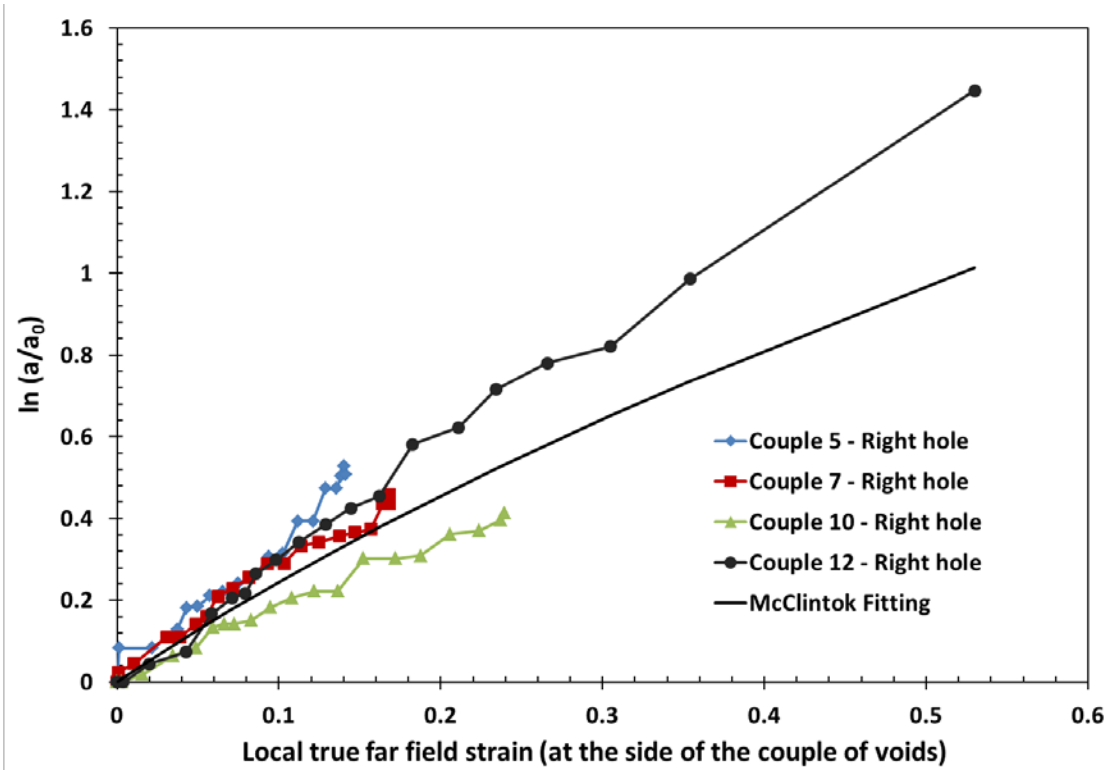

Figure 9-55 - McClintok fitting of the void growth of specimen 10 having uniform carbon distribution along gauge length

9.4.2. Carbon gradient along gauge width

In the previous paragraphs, results on tensile coupons having the carbon gradient along the gauge length were presented. For that configuration, the holes act as if they were in series, which means they experience the same stress but different strains.

In this paragraph, a carbon gradient is created along the gauge width and holes are also placed along the gauge width resulting in a parallel configuration, so they will experience the same strain but different levels of stress.

9.4.2.1. Preparation of specimens having carbon gradient through width

For these tests, both sides coated tensile coupons will be used and the carbon gradient will be created by selectively ablating the FeC film with the femtosecond laser before performing the heat treatment in high vacuum. In this paragraph, it will be shown that in order to obtain a significant carbon gradient, annealing temperatures lower than 630 ˚C and annealing times even shorter than 1h will have to be used. However, decreasing the annealing temperature and the annealing time simultaneously can cause a non-uniform carbon concentration

through the thickness of the coupon and in order to prevent this, the specimen will be coated on both sides. The FeC film will therefore be removed selectively on both sides of the tensile coupon in selected areas. Two symmetric gradient configurations are studied as shown in Figure 9-56 (a) and (b). The first configuration has the FeC film removed at the centre of the coupon in order to obtain higher yield strength and hardness close to the edges of the sample after heat treatment. On the contrary, the second configuration will have the FeC film removed in zones close to the edges which results in higher yield strength and hardness at the centre of the specimen.

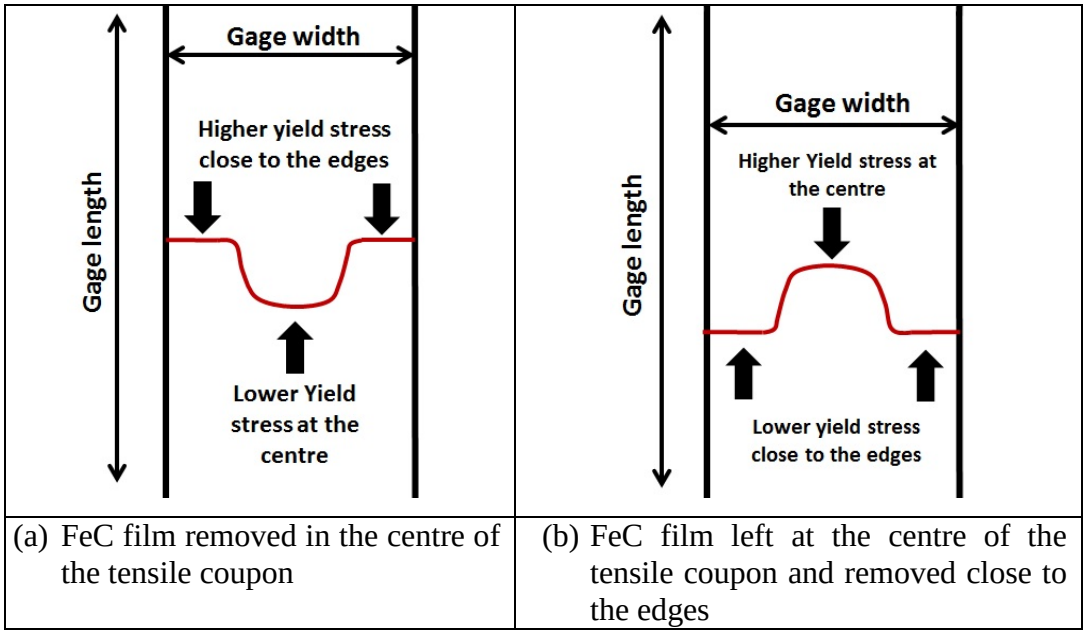

(a) FeC film removed in the centre of the tensile coupon	(b) FeC film left at the centre of the tensile coupon and removed close to the edges

Figure 9-56 - Ablation configurations to obtain carbon gradient along the gauge width of tensile coupons after annealing

9.4.2.2. Theoretical Prediction of carbon gradient

Using the 1D solution to Fick's second law, different configurations of ablations and heat treatment were evaluated to find the best conditions to obtain the highest carbon gradient. The configurations summarized in Table 9-7 were simulated for annealing temperatures of 530 ˚C and 630 ˚C -1h considering both heating and cooling steps of the high vacuum furnace.

530 ˚C-1h	630 ˚C-1h
333 µm removed in the center	333 µm removed in the center
500 µm removed in the center	500 µm removed in the center
600 µm removed in the center	600 µm removed in the center
500 µm removed completely on one side of the width	500 µm removed completely on one side of the width

Table 9-7 - Simulation of ablated configurations

The FeC film will have to be removed on both sides as shown in Figure 9-57 to avoid carbon diffusion in the center of the specimen, or it can be removed on the sides as shown in Figure 9-58.

Figure 9-57 - 500 µm removal of the FeC film in the center of the tensile coupon

Figure 9-58 – 500 µm of FeC film left at the center of the gauge width

Also in this case, it is assumed that carbon diffusion follows path 1 (Figure 9-59) and then, once the solubility limit is reached in the thickness of the coated zones, the diffusion involves path 2 causing a carbon gradient in the gauge length. This approximation was implemented since along path 1, the carbon coming from each coated side will have to cover 100 µm, while along path 2 the carbon coming from each side covers 250 µm. The solubility limit is 0.0264 at% for 530 ˚C - 1h and 0.0334 at% for 630 ˚C - 1h.

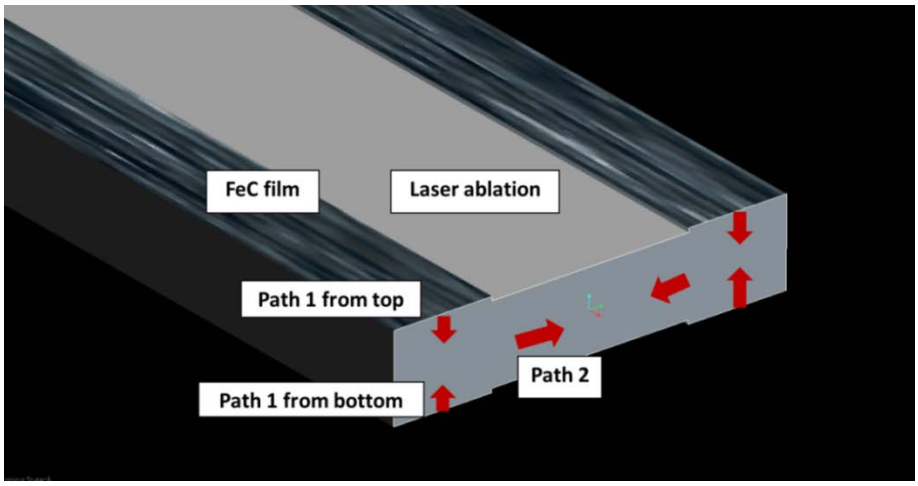

Figure 9-59 - Diffusion paths followed by carbon in coupons which have undergone laser ablation of FeC film

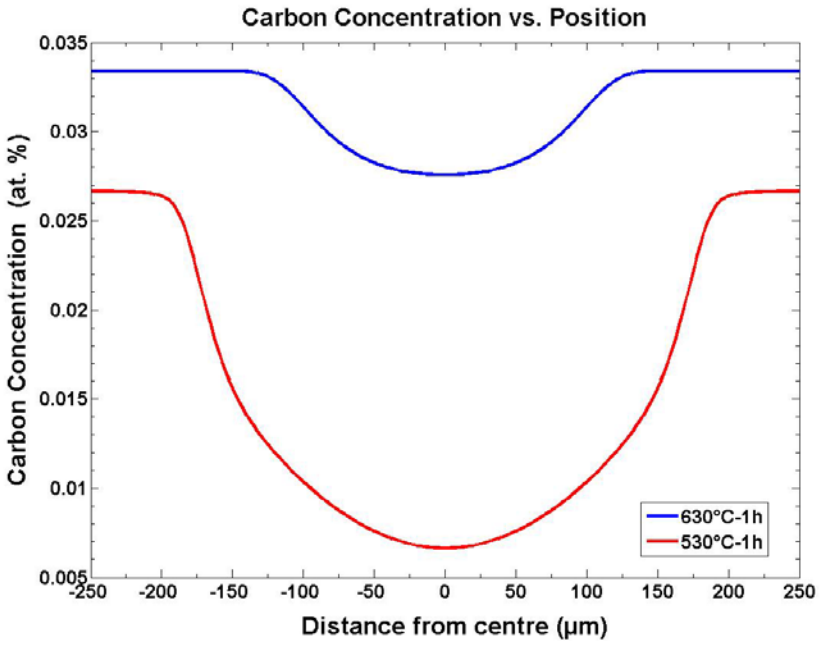

Figure 9-60 - Carbon gradient obtained along a gauge width in a zone where 500 µm coating was removed

In Figure 9-60 the carbon diffusion profile obtained along the width in a tensile coupon where 500 µm of FeC film was ablated from the centre is shown for both annealing at 530 ˚C – 1h and 630 ˚C – 1h.

In order to estimate the yield stress gradient from the interface between the ablated and not-ablated zones to the center of the specimen, the carbon concentrations were obtained from the above graph and they were used to calculate the yield stress. The concentrations were extracted for half of the thickness since the carbon concentration is mirrored due to the diffusion occurring on both sides. In Table H- 4 of Appendix H, the values of carbon concentration and the corresponding yield stresses for both 530 ˚C – 1h and 630 ˚C – 1h annealing are reported. Other configurations of ablations were studied (Table 9-8) and the corresponding diffusion profiles and obtained yield stress gradients are reported in Appendix H (section H.2).

Annealing temperature and time	Ablated width [µm]	Yield stress gradient [MPa]
530 ºC – 1h	333 (in the center)	38
630 ºC – 1h	333 (in the center)	1
530 ºC – 1h	500 (in the center)	86
630 ºC – 1h	500 (in the center)	17
530 ºC – 1h	600 (in the center)	108
630 ºC – 1h	600 (in the center)	34
530 ºC – 1h	500 (removed completely on one side of the width)	158 (*)
630 ºC – 1h	500 (removed completely on one side of the width)	99 (*)

Table 9-8 - Summary of the simulated ablated configurations – (*) details reported in Appendix H

Considerations for coupons which have to be selectively uncoated using laser ablation:

- Considering that ideally an isothermal heat treatment of 1h would be preferable to keep the carbon concentration constant through thickness and in order to have a high gradient in mechanical properties in the gauge width, it is necessary to remove 600 µm of FeC film in the center of the tensile coupon and to perform the annealing at 530 ˚C - 1h.
- A high gradient of mechanical properties can also be obtained if 500 µm of the FeC coating is removed with the laser on one side of the gauge width and annealing performed at 530 ˚C - 1h or 630 ˚C - 1h. However, this will not allow to study two symmetric configuration as shown in Figure 9-56.
- If 500 µm coating has to be removed in the middle of the tensile coupon, then in order to have a satisfactory gradient, it is necessary to anneal at 530 ˚C -1h or even shorter annealing times (25 minutes or 30 minutes) have to be considered.

At the end, it was decided to implement the 500 µm configuration of ablation in order to have more FeC film left so that the results would be more reproducible, in case the carbon distribution inside the deposited film would not be uniform. For annealing at 530 ˚C for less than 1 h, the carbon profile through thickness could become non uniform. For this reason, the evolution of carbon gradient through thickness for times shorter than 1h was assessed and the diffusion profiles are shown in Figure 9-61.

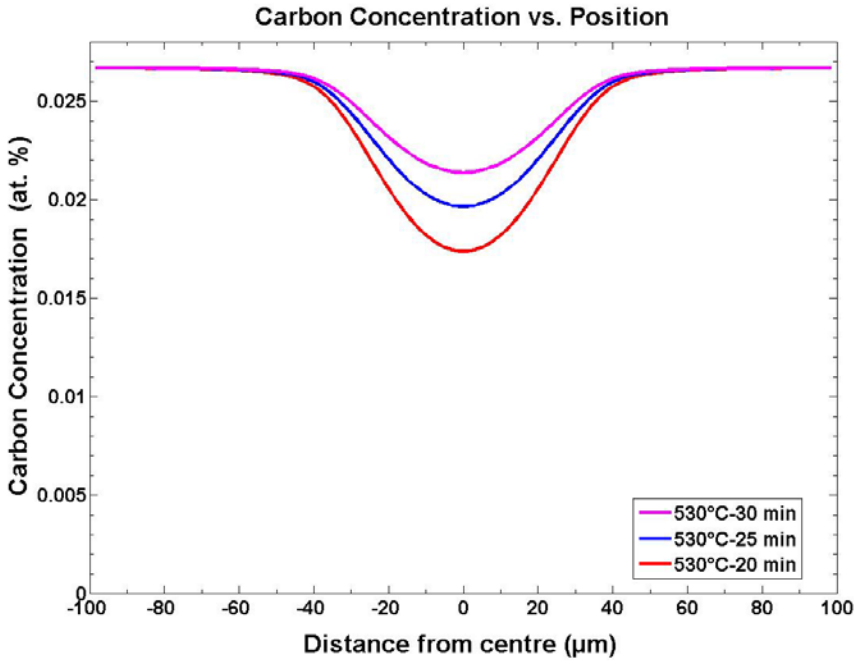

Figure 9-61 - Change in carbon concentration profile through thickness for annealing at 530 ˚C for different times

Since, the carbon gradient through thickness has to be kept at low level; no heat treatment was performed below 25 minutes. In Figure 9-62, the diffusion of carbon through the width of a sample where 500 μm was ablated from its centre was simulated for heat treatments of 530 ˚C -25 minutes and 530 ˚C – 30 minutes. The gradient of yield stress between the center of the specimen and the interface between coated and not-coated zone was calculated after obtaining the carbon concentration from Figure 9-62 and it was found to be 138 MPa for annealing at 530 ºC – 25 min and 128 MPa for annealing at 530 ºC- 30 min.

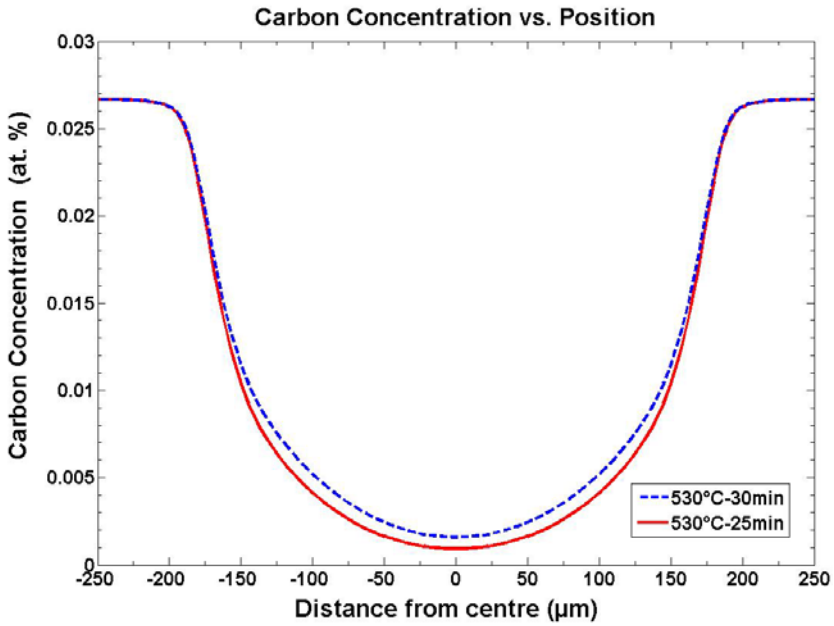

Figure 9-62 - Carbon gradient obtained along a gauge width in a zone where 500 µm coating was removed for annealing times shorter than 1h

Finally, another configuration was simulated where 500 µm of FeC was left at the centre of the tensile coupons, while 250 µm were ablated on each edge. The simulation for the diffusion inside one edge is shown in Figure 9-63, where one can see that a higher gradient is obtained if the annealing is performed at 530 ºC – 1h.

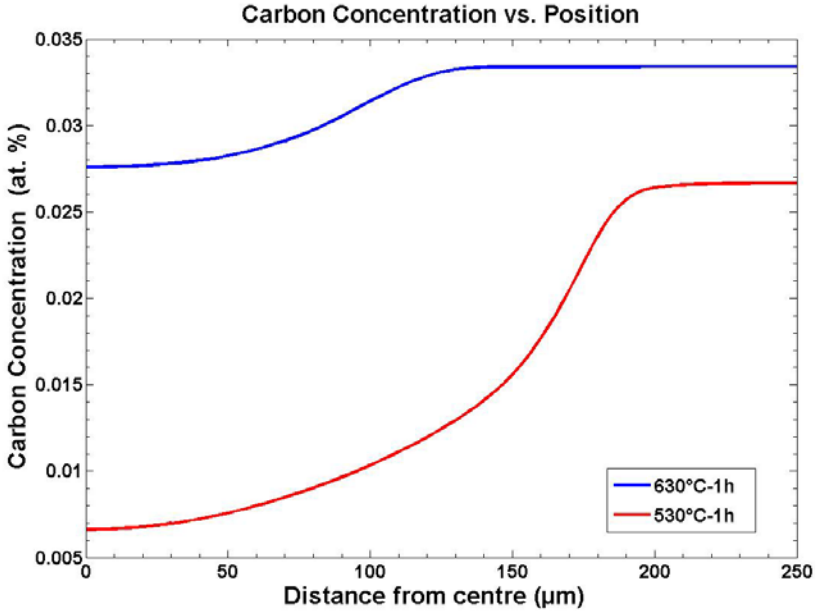

Figure 9-63 - Carbon gradient obtained along a gauge width in a zone where 250 µm coating was removed on the side of the gauge width

9.5. Laser Ablation

In order to perform the ablation of the FeC film, it was necessary to find the proper parameters, to remove the film without removing too much of the IF substrate. The film itself is 500 nm thick, so in order to be sure that it is completely removed, from 1 up to 2 μm from the surface were ablated. A G-code program was written to perform ablation by creating rectangular zones as shown schematically in Figure 9-64. In the program, the parameters, which were implemented in order to control the amount of ablation for a given laser energy, were the following:

- Feed rate: speed of the stage under the laser beam;
- Steps size: distance between one pass and the next pass (Y displacement);
- Height of the ablation zone;
- Length of the ablation zone;
- Number of passes: number of times the whole zone is ablated;

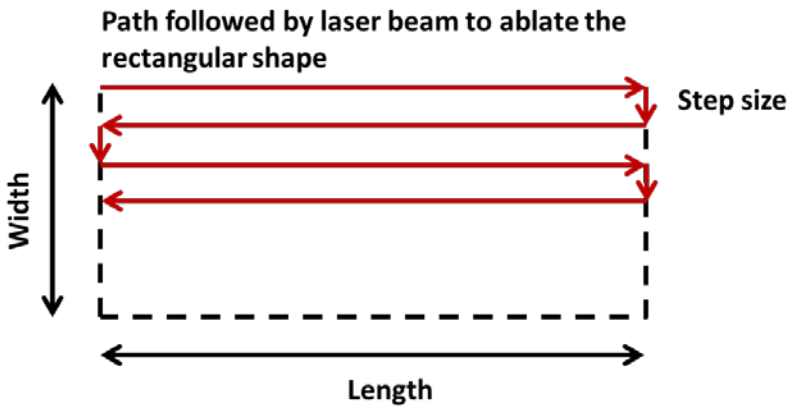

Figure 9-64 - Path followed by the laser beam to create the rectangular ablated zone

A piece of IF steel coated with 500 nm of FeC film was used to analyze the effect of the different parameters described above. The ablated zones where squares with dimensions of 0.1 mm x 0.1 mm. The repetition rate of the laser was 100 kHz and the power was 6000 mW, which gives an energy per pulse of 0.06 mJ. The values of the parameters used to obtain different levels of ablation are listed in Table 9-9. The energy measurements were taken with the power meter before the microscope objective (as previously shown in Figure 9-21).

Ablated zone name	Energy measured with power meter [W]	Energy per pulse[µJ]	Feed rate [mm/s]	Step [µm]	Passes
E1	0.007(0.008)	0.07 (0.08)	0.01	2	1
E2	0.007 (0.008)	0.07 (0.08)	0.04	2	1
E3	0.007 (0.008)	0.07 (0.08)	0.1	2	1
E4	0.007	0.07	0.1	5	1
E5	0.007	0.07	0.1	2	2
E6	0.004	0.04	0.01	2	1
E7	0.004	0.04	0.01	2	3
E8	0.009 (0.010)	0.09 (0.10)	0.05	2	1
E9	0.009 (0.010)	0.09 (0.10)	0.15	2	1
E10	0.009 (0.010)	0.09 (0.10)	0.25	2	1
E11	0.016	0.16	0.5	2	1
E12	0.016	0.16	0.5	2	2

Table 9-9 - Summary of the laser parameters used to perform ablation

An example of optical microscope pictures of the ablated zones is shown in Figure 9-65.

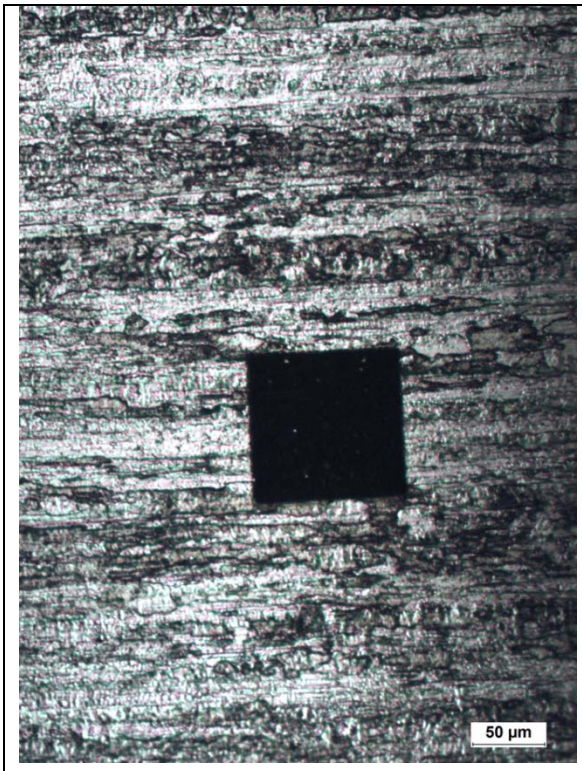

E3 (energy per pulse 0.07-0.08 µJ, feedrate 0.1 mm/s, step 2 µm and 1 pass)

E4 (energy per pulse 0.07 µJ, feedrate 0.1 mm/s, step 5 µm and 1 pass)

Figure 9-65 - Optical microscope pictures of the ablated zone E 3 and E 4

As it can be seen from Figure 9-65 given the same energy, same federate and same pass, changing the step will have a high influence on the uniformity of the ablated zone. The surface obtained for the spot "E4" would not be acceptable for the diffusion tests.

In order to properly characterize the depth of the material removed in the ablated zones, a 3D confocal laser microscope (LEXT 3D Measuring Laser Microscope OLS 4000) was used. The measurements were performed by the department of mechanical engineering at the École de technologie supérieure in Montreal. By using the "STEP" mode of operation of the microscope, a line is scanning the whole zone and going through the ablated square by measuring its depth in different point. Successively, an average of the measurements is done. An image of the line scanning the surface of the specimen is shown in Figure 9-66 (a) while in Figure 9-66 (b) an example of the measuring points obtained by scanning the square "E1" is shown. It is important to point out that during the ablation; there is redeposition of the ablated material. Some of this material can be removed by placing the specimen in the ultrasonic bath for just 1 minute, however, most of this material will remain on the surface and this causes some variation in the depth measurements. Moreover, the IF substrate itself has some lines on the surface due to the "skin pass" performed during the production of the sheet and in order to remove these lines it would be necessary to remove 10 μm of material from the surface. The average depth measurements for each ablated zone and their standard deviation are reported in Table 9-10.

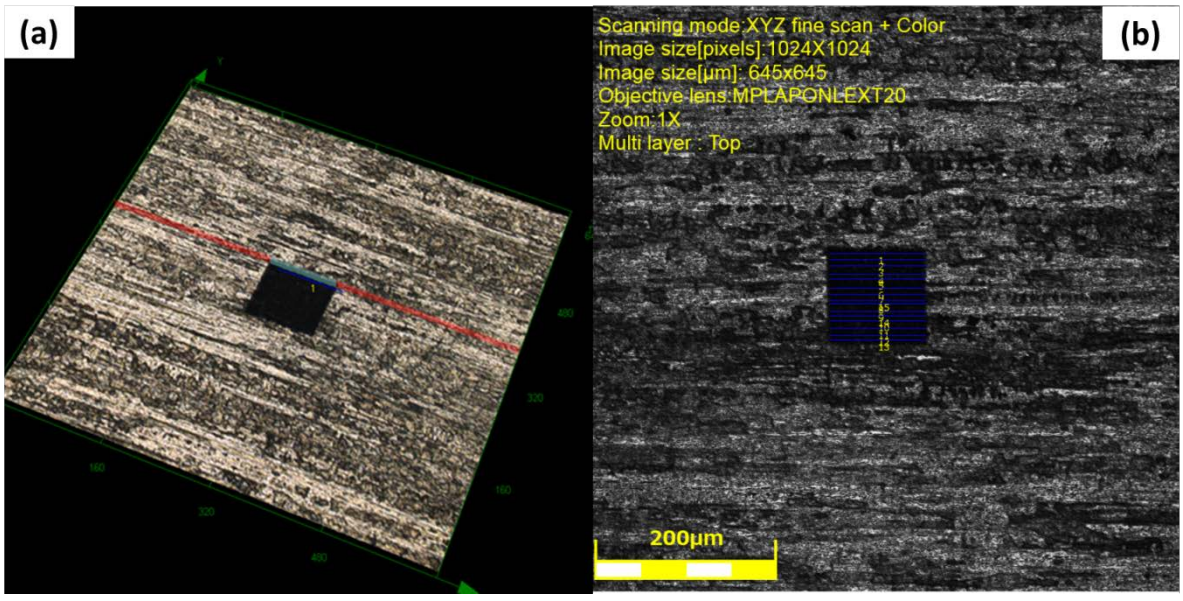

Figure 9-66 - (a) Scanning of the ablated square with a 3D confocal laser microscope; (b) scanning of the ablated surface showing the points where the measurements were taken

The relative high standard deviation is due to the measurements being influenced by the roughness left by the ablation of the surface. However, the measurements are still able to give a trend when compared with the laser parameters used to perfom the ablation.

Ablated zone	Average depth [μm]	Standard deviation [μm]
E1 (*)	1.3	0.4
E2	0.7	0.2
E3 (*)	1.6	0.3
E4	0.5	0.3
E5	1.3	0.6
E6	1.2	0.7
E7	0.9	0.6
E8	0.5	0.3
E9	0.8	0.5
E10	0.6	0.3
E11 (*)	1.2	0.6
E12 (*)	1.2	0.5

Table 9-10 - Average depth and corresponding standard deviation for the different ablated zones: (*) indicates ablations which are acceptable for the creation of graded coupons

From the above measurements, the acceptable ablations could be E1, E3, E11 and E12 since the standard deviation is small enough to ensure that at least 0.5 mm was removed. However, E1 and E3 were discarded since the feed rate was only 0.1 mm/s so quite small and it would require several hours to ablate an area of 9 mm x 0.5 mm on each side of the tensile coupon. E12 was discarded because it also required several hours due to the 2 passes. So, the parameters associated to E11 were chosen concerning feed rate, step and number of passes. During ablation, the power measured with the power meter was raised from 0.016 W to 0.018 W so that the energy per pulse was 0.18 μJ, while the feed rate was left at 0.5 mm/s, the step size was still 2 μm and the number of passes was 1. These parameters ensured that at least 1.2 μm were removed from the surface. Before starting the ablation of the specimens, an ablation trial was performed with these parameters on a piece of coated IF steel and with the optical microscope it was measured how much material was removed by measuring the Z variation which was necessary to focus on the ablated area compared to the not ablated area. It was found that the removed material ranged from 1.5 μm to 2 μm, which is acceptable to remove the FeC film completely. Pictures taken with a camera after ablation are reported in Figure 9-67 and in Figure 9-68, while pictures taken with the optical microscope are shown in Figure 9-69 (a) and Figure 9-69 (b).

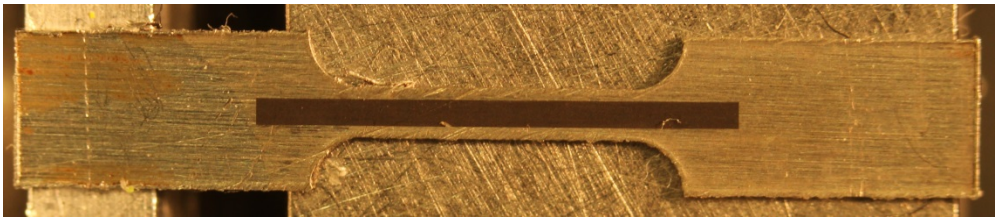

Figure 9-67 - Tensile coupon with ablated zone in the centre of the gauge width (area of the ablated zone is 9 mm x 0.5 mm)

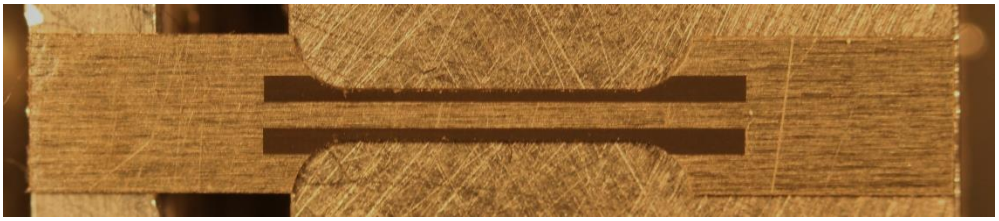

Figure 9-68 - Tensile coupon with ablated zone in the outer sides of the gauge width (area of the ablated zone is 9 mm x 0.5 mm). 0.5 mm of coated width left in the centre of the specimen

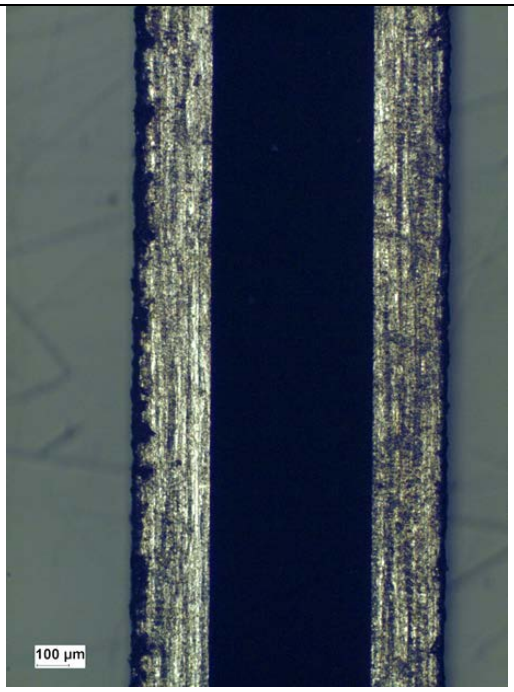

(a) 500 µm ablated in the centre of the width of the tensile coupon

(b) 500 µm left in the centre of the width of the tensile coupon

Figure 9-69 - Optical microscope picture of tensile coupons ablated with femtosecond laser

In Table 9-11 a summary of all the prepared specimens with their ablation configuration is reported. Once the specimens were ablated, they were annealed in high vacuum (10^{-6} -10^{-7} Torr) at 530 ˚C for different times in order to create the proper carbon gradient. Table 9-11 summarizes the annealing times. For specimens EC 9, EC 10 and EC 12, a uniform carbon

profile is sought and for this reason the heat treatment was performed in two steps. The first step of 1 h was performed in order to diffuse the same amount of carbon diffused in other coupons. The hardness of the specimens was measured before and after removal of the FeC film by polishing. The polished specimens then underwent a heat treatment of 12 h in vacuum in order to redistribute uniformly the carbon through the width of the sample as shown in Figure 9-70.

Name of the specimen	Annealing time	Expected carbon configuration	Ablated configuration
EC 1	1h	Graded	
EC 2	1h	Graded	
EC 3	1h	Graded	
EC 4	1h	Graded	
EC 5	1h	Graded	
EC 6	25 min	Graded	
EC 7	25 min	Graded	
EC 9	1h and then 12 h	Uniform	
EC 10	1h and then 12 h	Uniform	
EC 11	30 min	Graded	
EC 12	1h and then 12 h	Uniform	
EC 13	1h	Graded	

Table 9-11 - Summary of the performed ablation configurations and heat treatments

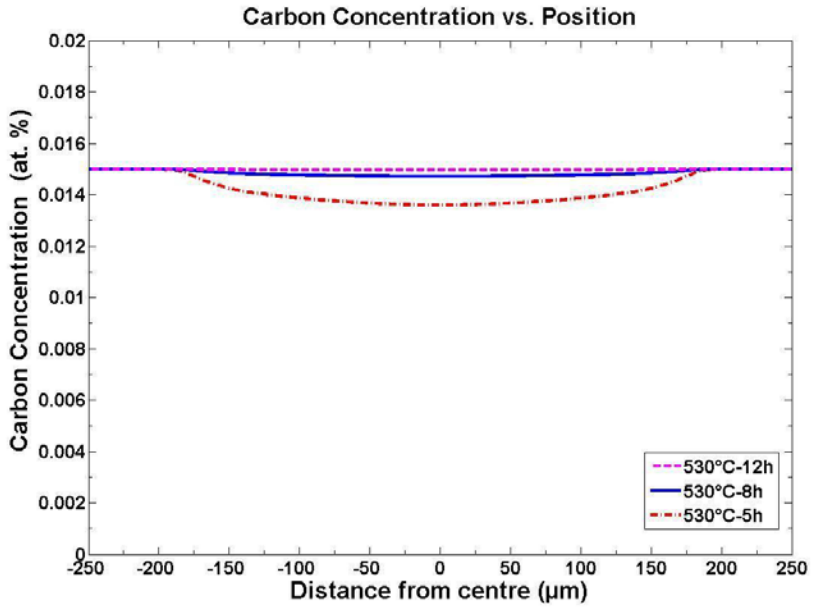

Figure 9-70 - Annealing time required to obtain a uniform carbon content in a specimen having an ablated zone of 500 µm width which was previously diffused at 530 ˚C for 1h

9.6. Characterization of carbon gradient

In order to characterize the carbon gradient, Vickers microhardness measurements were performed on the surface of each specimen right after the heat treatment and after removal of the FeC film. At least 4 measurements were taken along the gauge width for each specimen as schematically shown in Figure 9-71 (where the dots represent schematically four examples of hardness measurements).

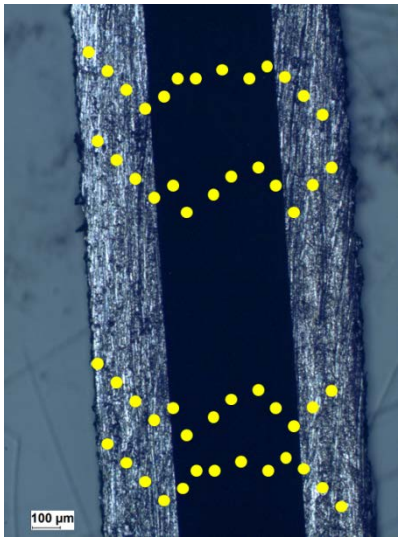

Figure 9-71 - Specimen with 500 µm ablated zone in the middle of the gauge width with hardness patterns schematically shown by dots

Vickers hardness measurements were taken by applying 25 g load for 10 seconds. In this section, the graph showing the hardness behaviour along the gauge width after heat treatment and after polishing is shown, while all the graphs showing hardness before polishing are reported in section H.4 of Appendix H for all the specimens. In this section only one example of hardness plot for each specimen configuration is reported, while the hardness of all other specimens is reported in section H.4 of Appendix H. First the hardness measured for a specimen having 500 µm of ablated zone in the centre of the gauge length is provided (Figure 9-72). The hardness of a specimen having 250 µm of FeC removed on each side of the width is reported in Figure 9-73. The film and the ablated zone were polished by performing 10 minutes of polishing with 4000 SiC paper, followed by a polishing with 1 µm diamond solution for 30 minutes and then by using OPS solution for another 20 minutes in order to have a uniform surface. During the experimental procedure, it was noticed that it was hard to remove the debris in the ablated zone. It is believed that this zone could have influenced slightly the hardness measurements in some specimens, causing a higher hardness measurement in the ablated zone, which could reduce the detected gradient.

- **Specimen EC 1:**

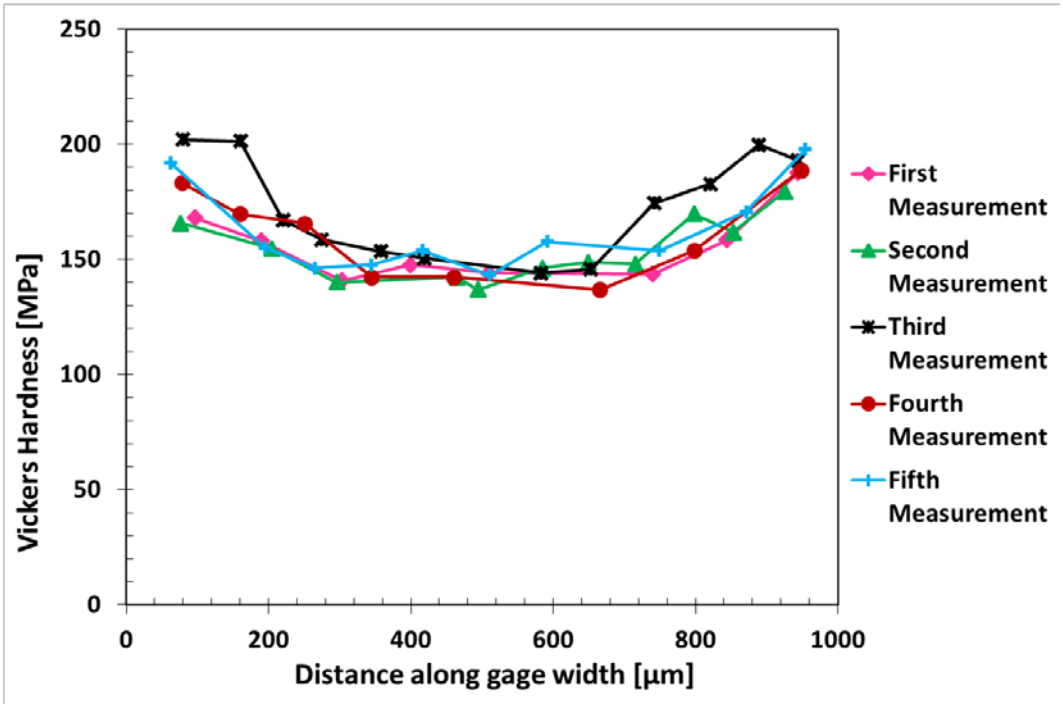

Figure 9-72 - Vickers hardness through width for specimen EC 1 where 500 µm were ablated in the centre of the gauge width

In the following figures, the gradient obtained for specimens ablated at the edges and preserving 500 μm of FeC film at the centre of the tensile coupon will be shown.

- **Specimen EC 2:**

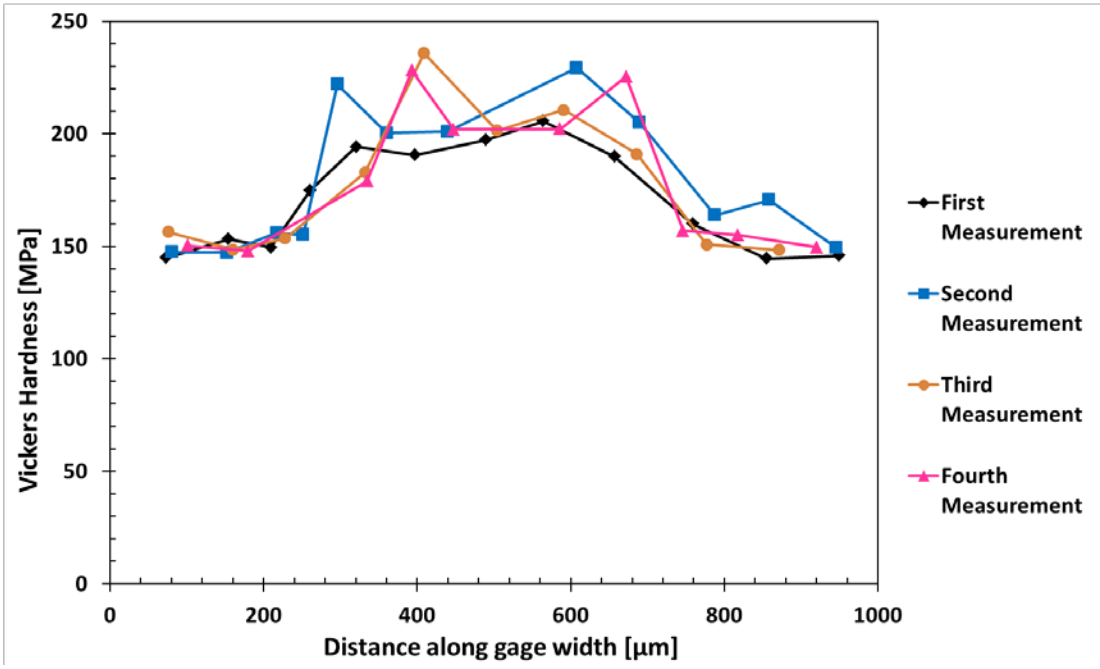

Figure 9-73 - Vickers hardness of specimen EC 2 after polishing of the surface

It was noticed that the trend of the hardness profile is more difficult to discern when the surface is not polished since it was difficult to properly measure the dimensions of the Vickers indent in the ablated zone. After polishing, the hardness gradient is usually lower since the FeC film crystallized into cementite has been removed.

Three specimens were prepared to have a uniform carbon content along the gauge width. The carbon content was still the same as in the specimens having a gradient along the gauge width, however, it was uniformly distributed along the width. In order to diffuse the same amount of carbon, the specimen was first annealed in high vacuum at 530 ˚C – 1h and then the Vickers hardness of the unpolished specimen was measured. The specimen was then polished, its hardness was measured to assess the presence of a gradient, and it was placed again in high vacuum for a further annealing at 530 ˚C for 12h which was predicted to spread uniformly the previously diffused carbon amount. After this heat treatment, the hardness of the tensile coupons through width was probed again The results after 12 hours of annealing for the specimens EC 9, EC 10 and EC 12 are shown from Figure 9-74 to Figure

9-76, while values of hardness before and after polishing for annealing at 530 ºC – 1h are shown in section H.4 of Appendix H.

- **Specimen EC 9:**

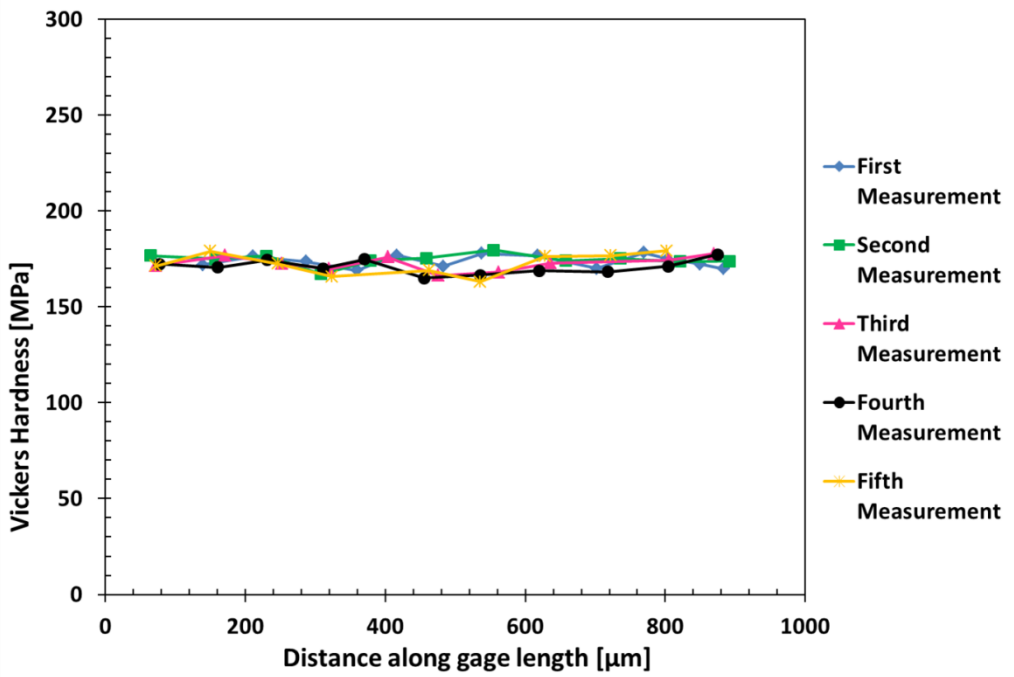

Figure 9-74 - Vickers hardness of specimen EC 9 after annealing in high vacuum at 530 ˚C for 12h

- **Specimen EC 10:**

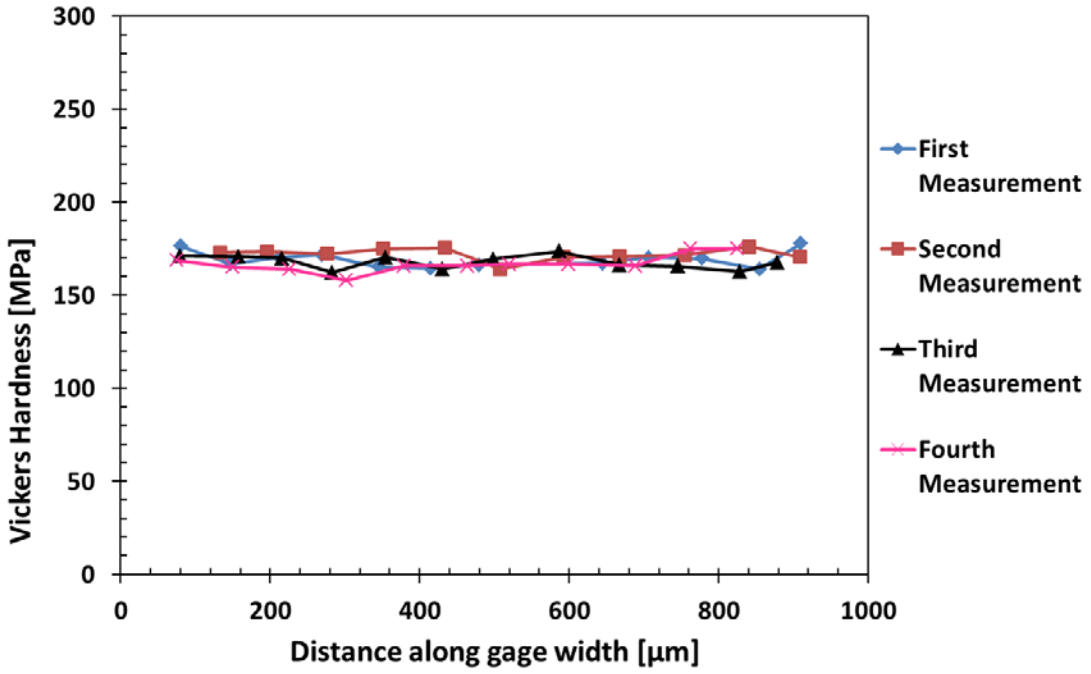

Figure 9-75 - Vickers hardness of specimen EC 10 after annealing in high vacuum at 530 ˚C for 12h

- **Specimen EC 12:**

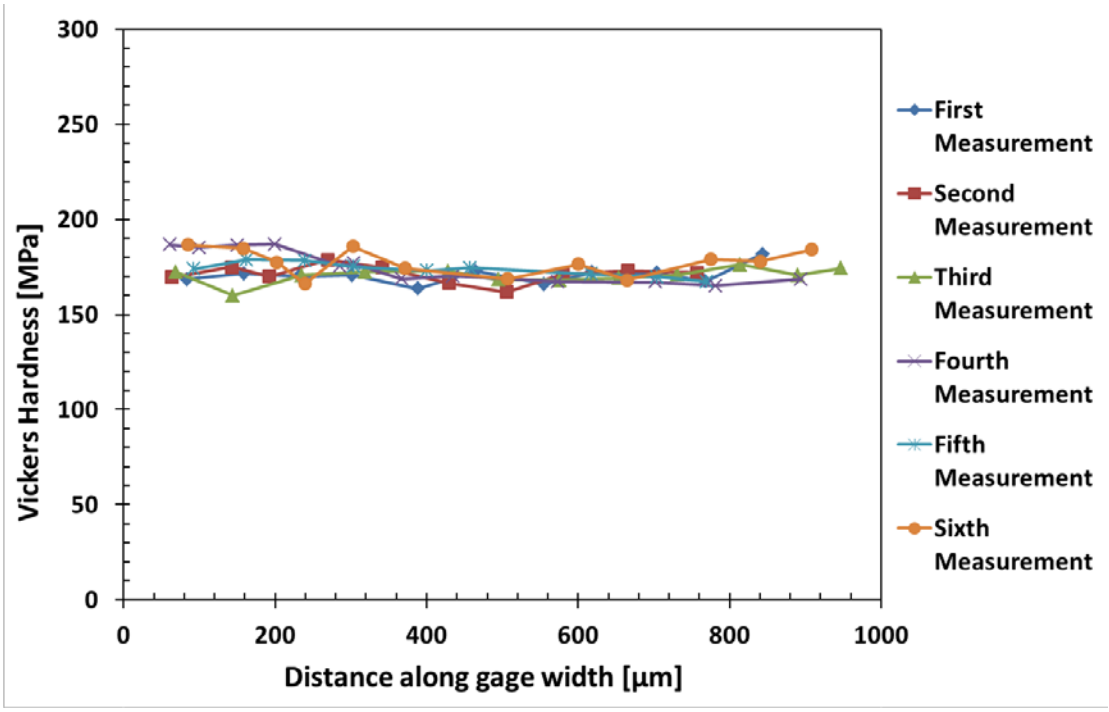

Figure 9-76 - Vickers hardness of specimen EC 12 after annealing in high vacuum at 530 ˚C for 12h

From Figure 9-74, Figure 9-75 and Figure 9-76 it is evident that after 12 hours of heat treatment at 530 ˚C, the carbon profile became uniform through the width.

Finally, two tensile coupons of uncoated and not-annealed IF steel were also prepared in order to be used as comparison for the fracture studies. The hardness of the two uncoated and not-annealed specimens was also assessed using Vickers testing after polishing the surface to a mirror finish. The results of the measurements for these two specimens are shown in Figure 9-77 and Figure 9-78. The specimens will be identified with the names GW 1 and GW 2.

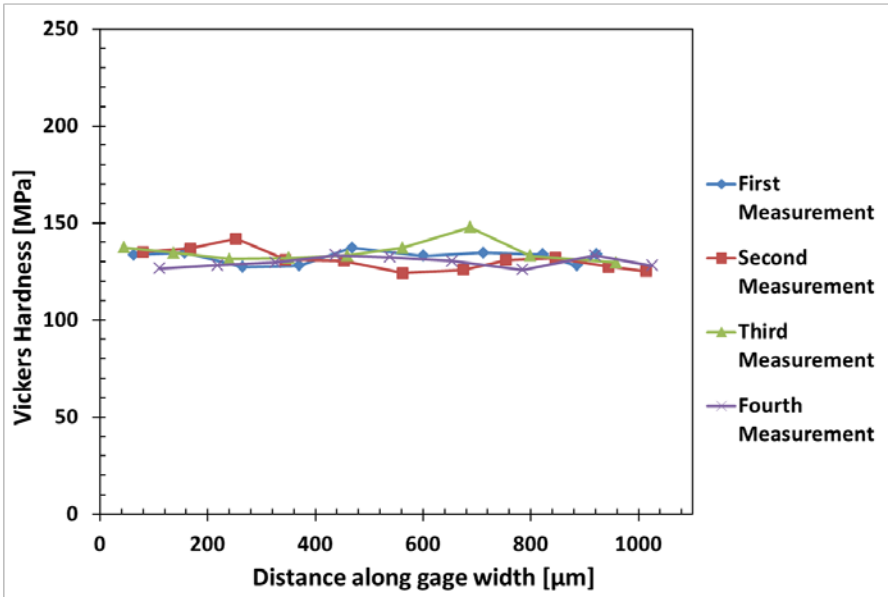

Figure 9-77 - Hardness measurements of an uncoated not-annealed coupon of IF steel (specimen GW1)

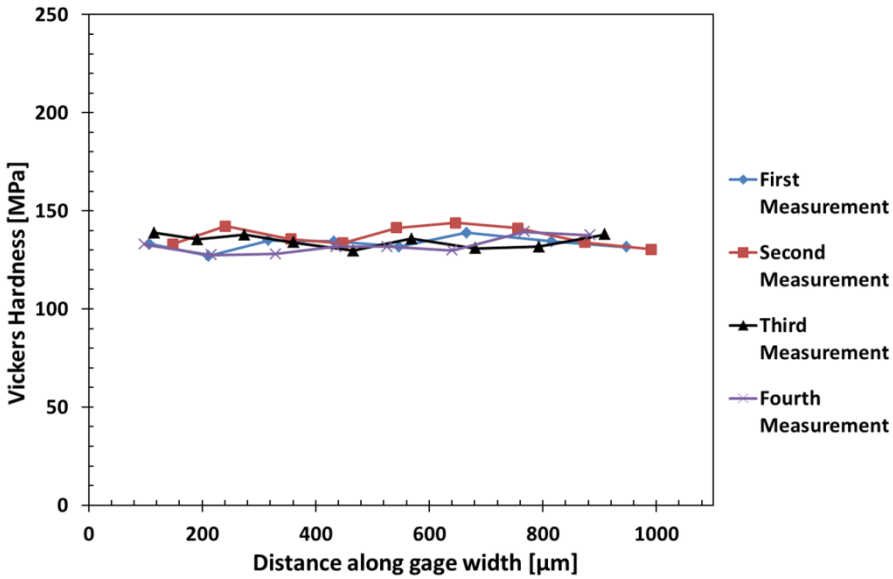

Figure 9-78 - Hardness measurements of an uncoated not-annealed coupon of IF steel (specimen GW2)

The gradient of hardness had to be converted into gradient of yield stress. From the diffusion modelling, the diffusing carbon content can be predicted and from these values, the corresponding yield stresses can be calculated. However, experimentally, the gradient or the uniform carbon profiles were assessed by using microhardness tests, so the gradient detected with hardness had to be related to the yield stress. In order to find a relation between yield stress and hardness, the values of hardness for an uncoated and not-annealed IF steel were

related to its yield stress obtained with tensile test and the same ratio of yield stress (YS) over Vickers Hardness (VH) was used for the carbon diffused specimens. From the hardness plot in Figure 9-77 and Figure 9-78, the hardness of the uncoated and not-annealed IF steel is around 130 MPa, while the yield stress of an uncoated IF steel is around 114 – 115 MPa, which means that the ratio between yield stress (YS) and Vickers Hardness (VH) is (115/130) = 0.9. This value will be used to evaluate the yield stress for the other specimens having a gradient of carbon or a uniform carbon content through the width. Table 9-12 summarizes what would be expected from a theoretical point of view and what was obtained experimentally.

Specimen	**Experimental gradient of hardness [MPa]**	**Gradient of yield stress calculated from hardness [MPa]**	**Expected yield stress gradient [MPa]**
EC 1 Graded	65	59	85
EC 2 Graded	75	68	85
EC 3 Graded	115	104	85
EC 4 Graded (*)	48	43	85
EC 5 Graded	82	74	85
EC 6 Graded (*)	92	83	138
EC 7 Graded (*)	60	54	138
EC 9 Uniform	7	6	0
EC 10 Uniform	3	2.7	0
EC 11 Graded (*)	85	77	128
EC 12 Uniform	7	6	0
EC 13 Graded	51	46	85

Table 9-12 - Comparison between theoretical and experimentally obtained carbon gradient; (*) indicates specimens showing high difference between expected and obtained gradient

From Table 9-12, one can see that some specimens show a lower steepness of the gradient compared to what would be expected theoretically. These specimens have been marked with

a (*) in the table. This can be caused by several factors. First of all, it was noticed that the debris of the ablated film were redepositing on the surface during the ablation (black deposit shown in the images reported in Table 9-11). This deposit could not be removed even using the ultrasonic bath. For this reason, it is possible that still some carbon diffusion could occur from the ablated zone causing a smoothening of the expected gradient. Another source of error is due to the positioning of the specimen under the laser beam before performing laser ablation. When the specimen was flipped in order to ablate both its surfaces, it was sometimes difficult to be sure that the interfaces between ablated and not-ablated zones are perfectly aligned with the interfaces on the other side of the specimen. Usually the difference of alignment was around 5 µm, however, this can cause a smoothening of carbon diffusion.
Another important point is the assumption that was made to simulate carbon diffusion. It was supposed that the solubility limit of carbon into ferrite had to be reached first through thickness before any carbon starts to diffuse through the width. However, this could not be the case, since at 530 ºC, carbon has enough mobility to start some diffusion along the width before the solubility limit in the thickness has been reached. Other important parameters that can affect the obtained carbon gradient are the variation of ± 3 at% of carbon in the FeC film and the ± 20 nm variation in its thickness. Finally, for some specimens after annealing, it was difficult to completely remove the black traces left by laser in the ablated zone and this could as well affect the experimental values recorded for hardness.

9.7. Laser parameters and hole configuration

In order to study the influence of carbon gradient along the width on void growth, six voids were machined in the width of the samples with the femtosecond laser. One couple of voids was drilled in each zone as shown in Figure 9-80. The power of the laser was 200 mW and the repetition rate was 1 kHz for all specimens, except for specimen EC 12 for which the power of the laser was 186 mW, since the laser could not reach 200 mW. This means that for all the specimens the energy per pulse was 0.2 mJ, while for specimen EC 12 the energy per pulse was 0.186 mJ. All the parameters used to machine the holes for the different specimens are summarized in Table 9-13. Specimen EC 6 is not listed in the table since it was used to study Lüders bands propagation performing digital image correlation in the whole gauge length without the presence of any void.

Specimen	Power [W]	Energy [µJ]	Z position [mm]	Time [s]	Intervoid spacing (2W) [mm]
EC 1	0.072	0.072	0.03	24	0.080
EC 2	0.072	0.072	0.03	24	0.080
EC 3	0.072	0.072	0.03	24	0.080
EC 4	0.072	0.072	0.03	24	0.080
EC 5	0.068	0.068	0.08	23	0.084
EC 7	0.068	0.068	0.03	24	0.080
EC 9	0.068	0.068	0.03	24	0.082
EC10	0.068	0.068	0.03	24	0.082
EC11	0.068	0.068	0.03	24	0.082
EC12	0.081	0.081	0.08	26.5	0.082
GW 1	0.072	0.072	0.03	24	0.065
GW 2	0.072	0.072	0.03	24	0.080

Table 9-13 - Femtosecond laser parameters used to machine holes along the gauge width of tensile coupons

The dimensions of the holes obtained for each specimen are listed in Table 9-14 while Figure 9-79 shows schematically the quantities of interest for the voids.

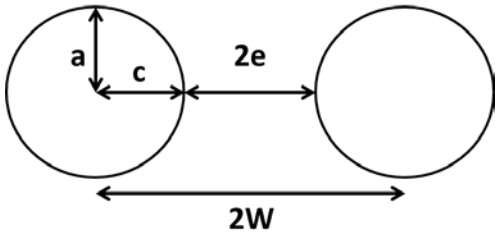

Figure 9-79 - Sketch of the quantities measured for the voids

	Top couple of voids			Central couple of voids			Bottom couple of voids		
Specimen	**2a [μm]**	**2e [μm]**	**2W [μm]**	**2a [μm]**	**2e [μm]**	**2W [μm]**	**2a [μm]**	**2e [μm]**	**2W [μm]**
EC 1	30-33	43	84	30-33	40.5	82	32-34	43	83
EC 2	32-34	44	82	30-33	43.5	82	31-33	42	80.5
EC 3	30-32	46	82	32-33	46	83	30-32	46	82
EC 4	31-32	41-42	81	30-32	42	80	31-32	40	80
EC 5	30-33	43	80	29-30	43	83	29-30	42	83
EC 7	26-28	50	81	28-31	47	81	29-31	53	84
EC 9	25-27	58	82	26-28	58	83	26-28	58	82
EC10	26-27	60	88	26-27	57	87	25-28	55	86
EC11	25-26	58	84	25-26	60	86	25-27	60	84
EC12	26-28	52	85	27-29	52	88	27-28	53	85
GW 1	28-30	32	65	28-31	37	68	32-33	33	73
GW 2	28-30	51	85	27-31	44	83	31-33	44	83

Table 9-14 - Voids dimensions measured from pictures taken with optical microscope

The measure of the ligament between the voids (2e) can be obtained as (2W – 2a), where 2W is the spacing from centre to centre of the voids, while 2a is the major diameter of the voids, which before deformation and void growth is equal to 2c (small diameter of the voids). However, from Table 9-14 it can be seen that "2e" for the specimens from EC1 up to EC 5 is lower than the expected 50 μm, this is due to the presence of a dark halo around the lased voids, which makes measurements of the ligament length less precise (2e). This measure was easily taken for specimens from EC7 to GW2 since their surface was more polished, however, polishing more the specimens will cause a decrease of the void diameters, since there is always a bit of conicality associated to the voids.

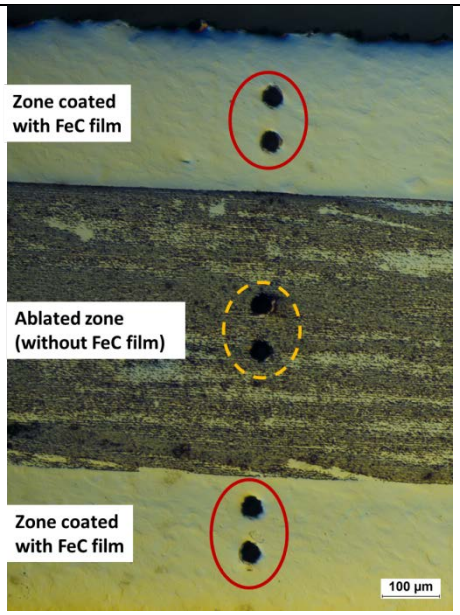

(a) Void configuration along the gauge width of a specimen where 500 µm of FeC film were ablated in the centre (specimen EC 3)

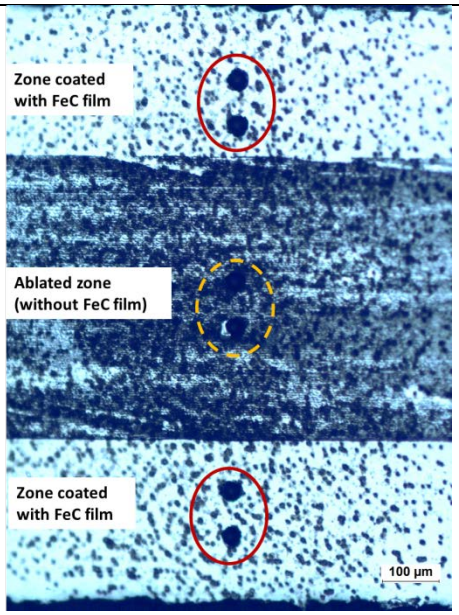

(b) Void configuration along the gauge width of a specimen where 500 µm of FeC film were ablated in the centre. Application of the DIC features with the laser (specimen EC 3)

Figure 9-80 - Void configuration along the gauge width of a specimen where 500 µm of FeC film were ablated in the centre (specimen EC 3)

Once the hole were machined, the surface of the specimen was polished with a 1 µm diamond polishing suspension and with a 0.05 µm OPS solution to remove the redeposited material around the holes. However, in the ablated zone, traces left by the laser ablation are still visible. Features then had to be placed on the surface of the specimen in order to perform digital image correlation. These features were placed randomly on the surface using the laser as described in section 9.2. Images of the surface before and after the application of the DIC features are show in Figure 9-80 (a) and (b) respectively.

9.8. Results of specimens containing voids and having carbon gradient along the gauge width

9.8.1. Results of tensile tests and Digital Image Correlation (DIC)

In the present paragraph, the engineering stress-strain curves obtained for the specimens described in the previous paragraph will be shown. The table listing the dimensions of the specimens before tensile tests is included in section H.5 of Appendix H. During the tensile

tests, pictures of the surface of the tensile coupons were taken at a magnification of 5X or 10X and at a rate of 1 picture every 10 ms. These pictures were then uploaded in the LaVision-Davis software to perform DIC analyses in order to extract true strain levels. The values of mechanical properties extracted from the engineering stress-strain curves in Figure 9-81 for specimens which were ablated 500 µm in the center of the width are reported in Table H- 11 included in section H.5 of Appendix H. From these curves, one can see that the highest strain at failure is obtained as expected for the coupon without voids (EC 6). The coupons EC 3, EC 5 and EC 1 have similar results, while coupon EC 11 shows a higher strain at failure compared to them despite its gradient of mechanical properties is the same as the one of specimen EC 5. This is justified by different void geometry for specimen EC 11. Indeed, coupons EC 1, EC 3 and EC 5 had voids of 33 µm diameter with a ligament (2e) over major diameter (2a) ratio of 1.30, while coupon EC 11 had voids of 28-30 µm diameter, but the ratio between ligament and major diameter was 2, which means that the voids are initially more far apart and their coalescence is delayed, which explains a higher strain at failure.

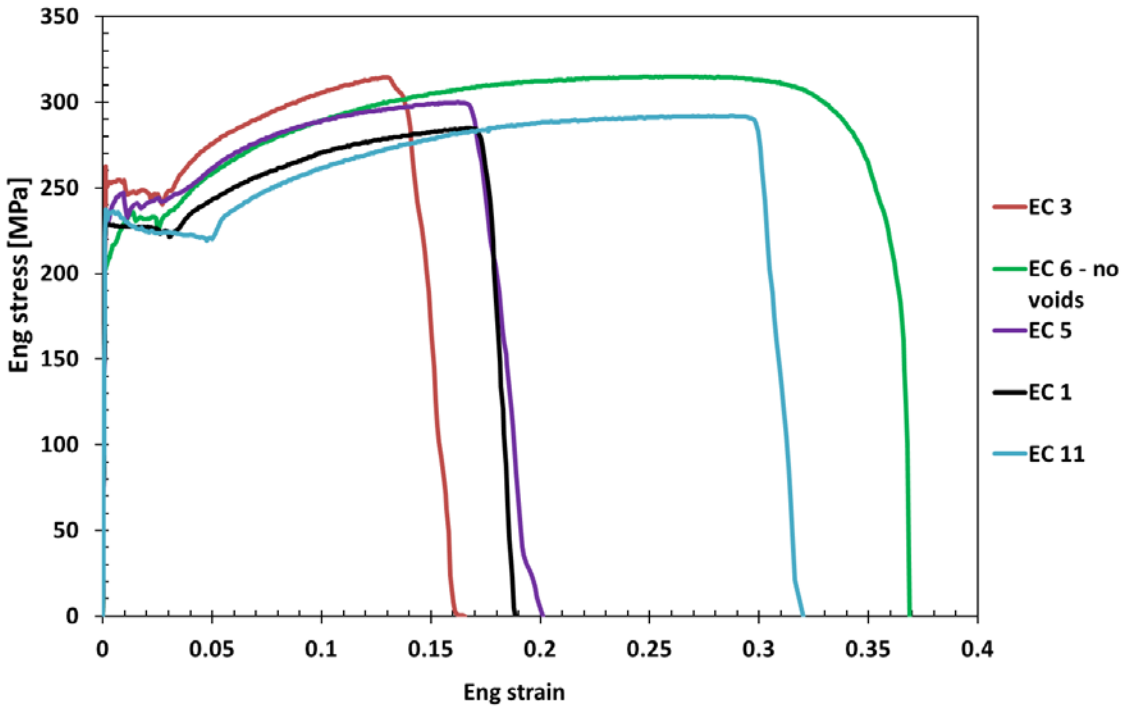

Figure 9-81 - Engineering stress-strain curves for tensile coupons having a gradient of carbon obtained by removing 500 µm of FeC film at the centre of the coupon

The yield stress for the coupons shown in Figure 9-81 can be predicted using a rule of mixture. Details of the calculations are shown in section H.5.1 of Appendix H for specimens EC5 and EC11.

The Lüders bands pattern obtained for each specimens are reported. In Figure 9-82 the bands in specimen EC 1 nucleated far from the voids and then one band front crosses the voids as the test proceeds.

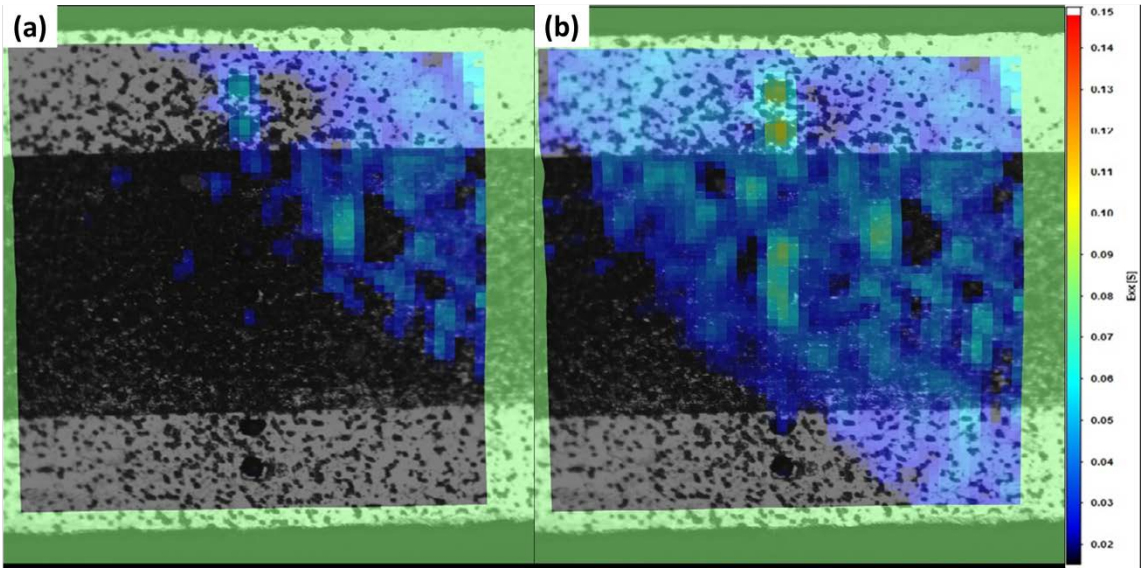

Figure 9-82 - Specimen EC 1: (a) starting of Lüders bands nucleation far from voids; (b) propagation of the band

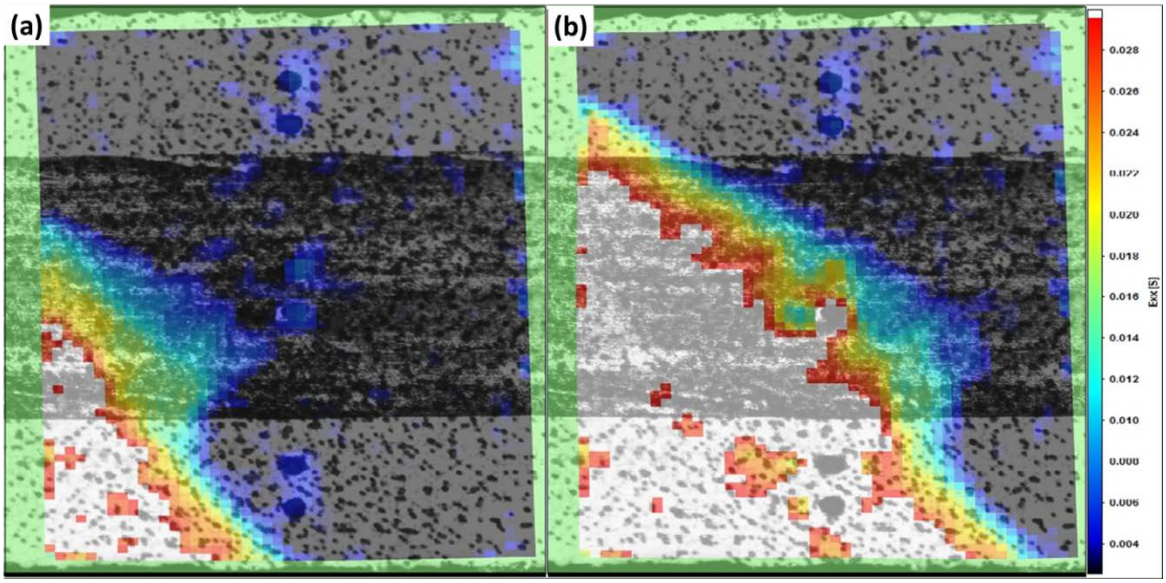

Figure 9-83 - Specimen EC 3: (a) starting of Lüders bands nucleation far from voids; (b) propagation of the bands in the voids zone

In Figure 9-83, for specimen EC 3, Lüders bands are nucleated far from the voids and one front crosses the voids during the tensile test, while for specimen EC 5 (Figure 9-84) the bands nucleated at the voids , while for specimen EC 11 (Figure 9-86) the bands coalesce at the voids.

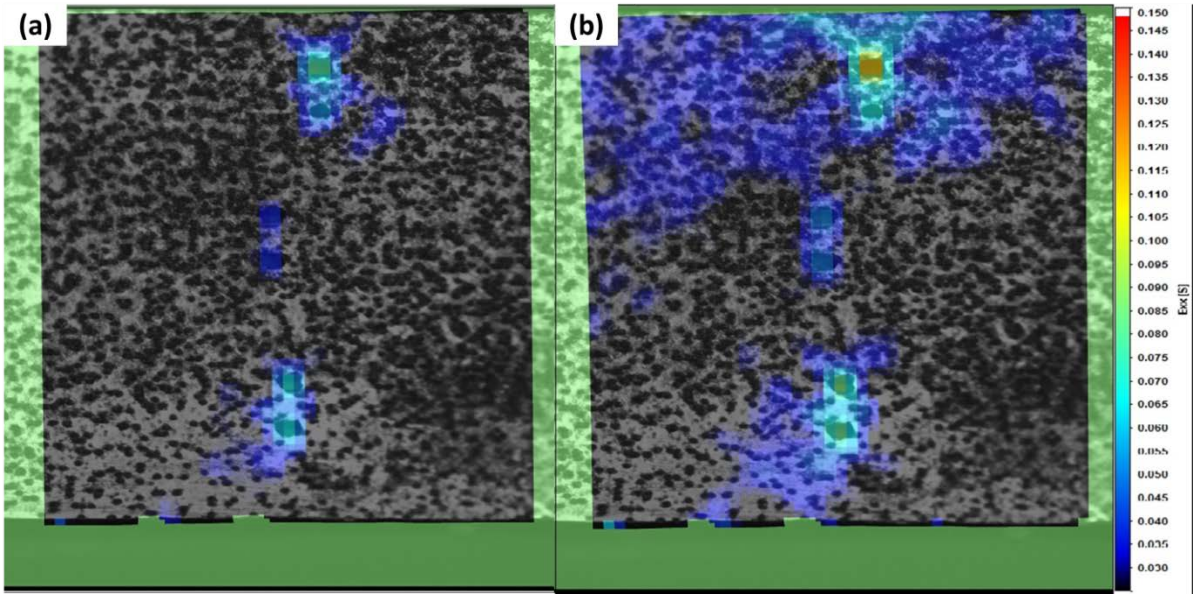

Figure 9-84 - Specimen EC 5: (a) starting of Lüders bands nucleation at voids; (b) propagation of the bands

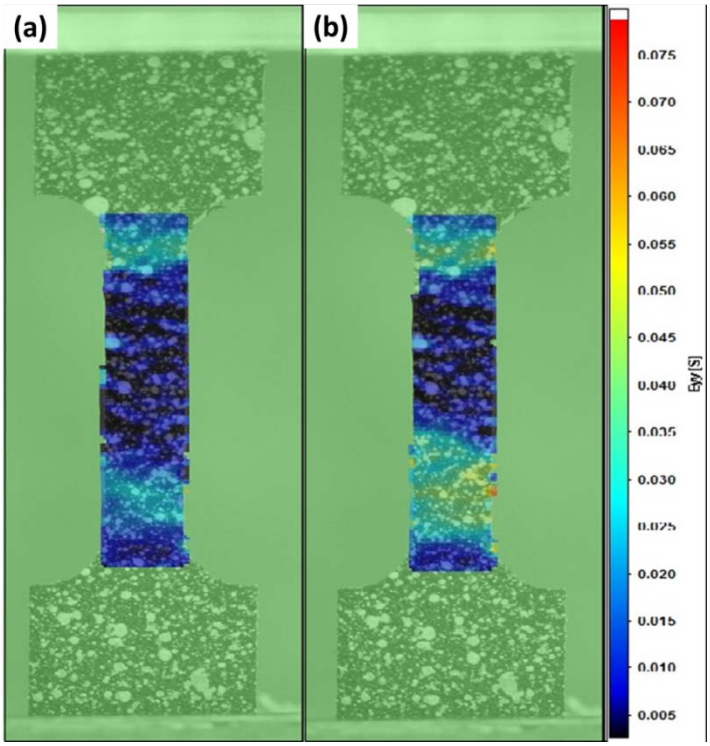

Figure 9-85 - Lüders bands propagation for specimen EC 6: (a) nucleation of the bands at the fillet radii; (b) bottom band propagating along the gauge length

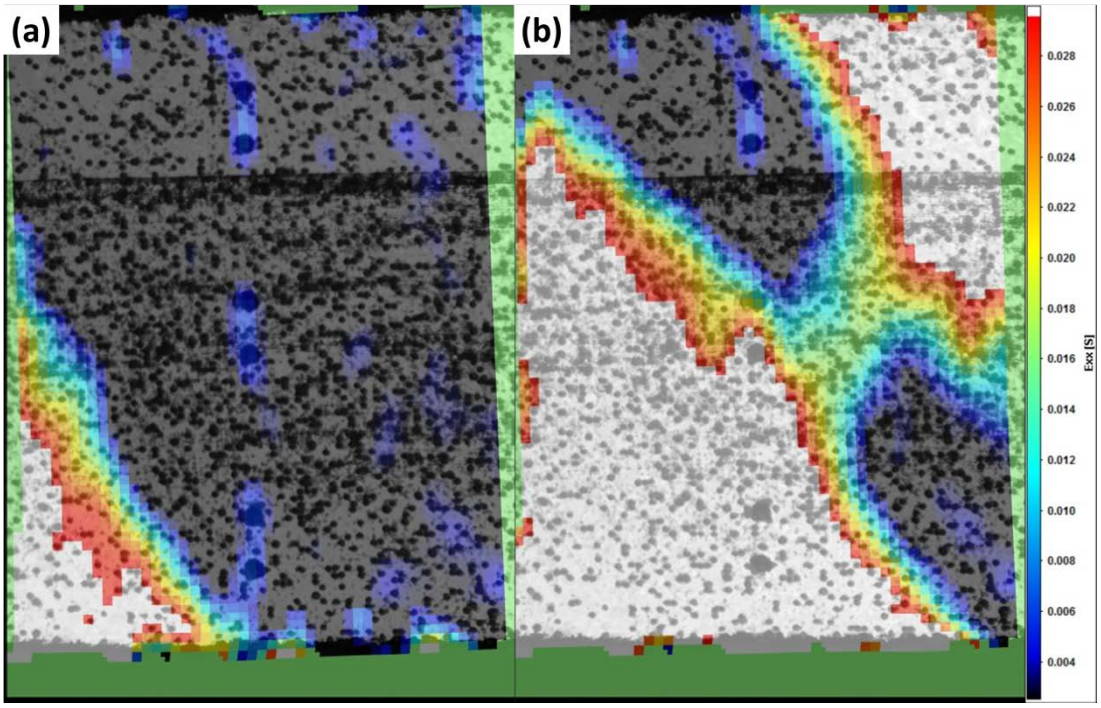

Figure 9-86 - Specimen EC 11: (a) starting of Lüders bands far from the voids; (b) coalescence of Lüders bands close to the voids

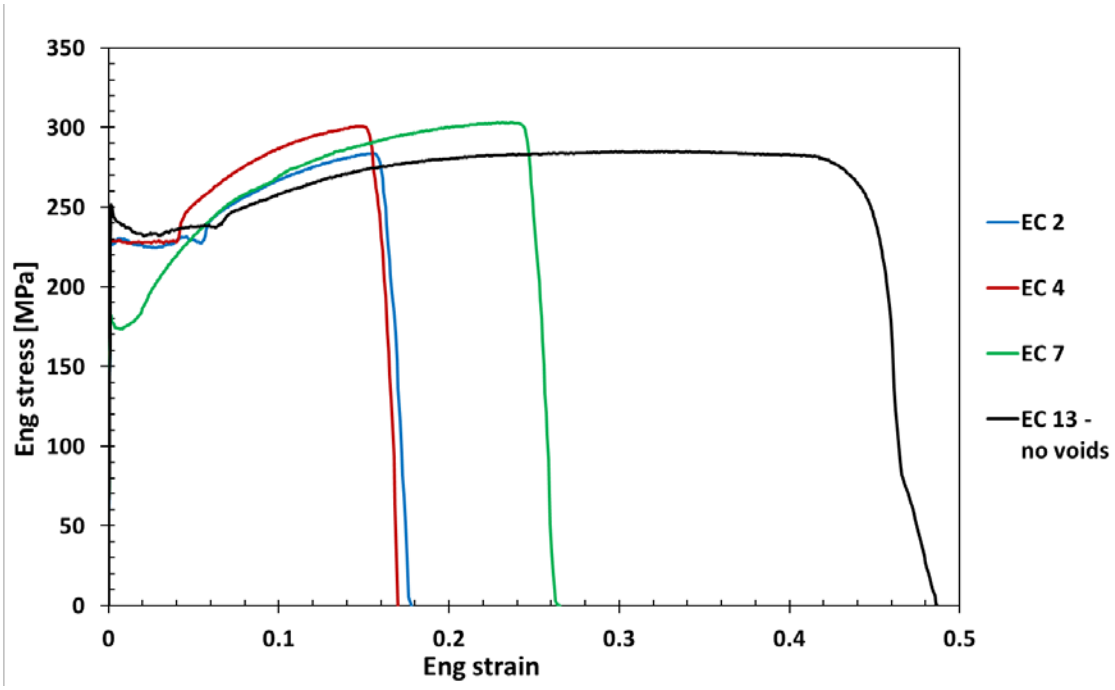

Figure 9-87 - Engineering stress-strain curves for tensile coupons having a gradient of carbon obtained by leaving 500 μm of FeC film at the centre of the coupon

Figure 9-87 shows the engineering stress-strain curves obtained for coupons ablated on the sides. From the curves in Figure 9-87, specimen EC 7 shows a very low yield stress

compared to EC 2 and EC 4. It is possible that less carbon diffused into the IF substrate even if the heat treatment was the same. The hardness gradient of specimen EC 7 was also not higher than 30 – 40 MPa which means that not much carbon diffused in the coated zones compared to the uncoated zones. It is believed that either the specimen was not properly coated or the amount of carbon in the FeC film was not uniform or was very low. For this reason, the void growth analysis of this specimen was not performed. Specimen EC 13 was ablated on the sides but had no voids and as expected has the highest strain at failure.

The DIC pattern of Lüders bands for coupons EC 2 and EC 4 are shown in Figure 9-88 and Figure 9-89 respectively. For EC 2 the bands nucleated at the voids, while for EC 4, two band fronts nucleated far from the voids and then coalesced at the voids.

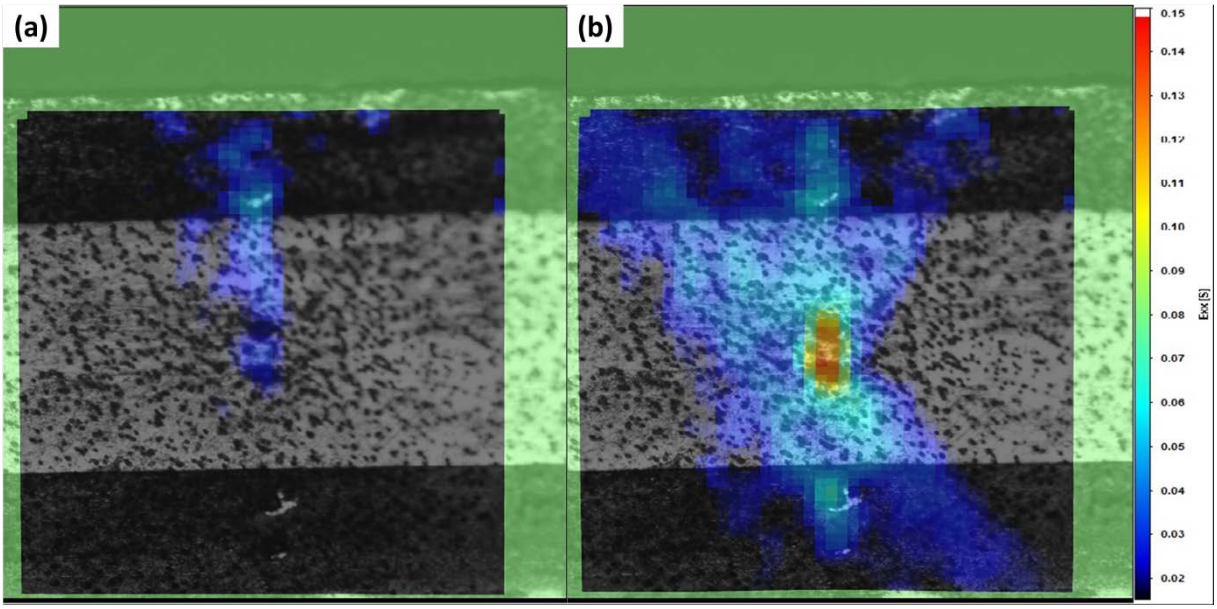

Figure 9-88 - Specimen EC 2: (a) starting of Lüders bands nucleation at voids; (b) propagation of the bands in the voids zone

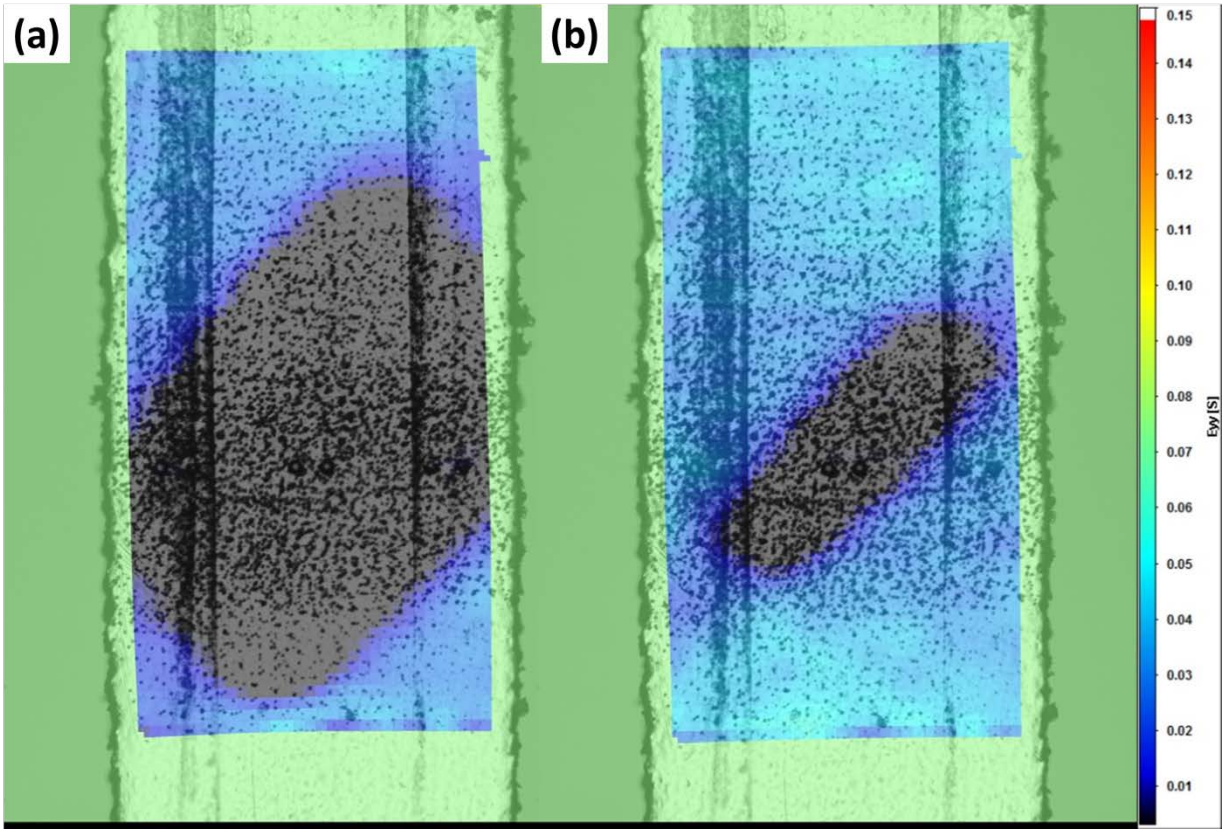

Figure 9-89 - Specimen EC 4: (a) starting of Lüders bands nucleation far from voids; (b) propagation of the bands in the voids zone

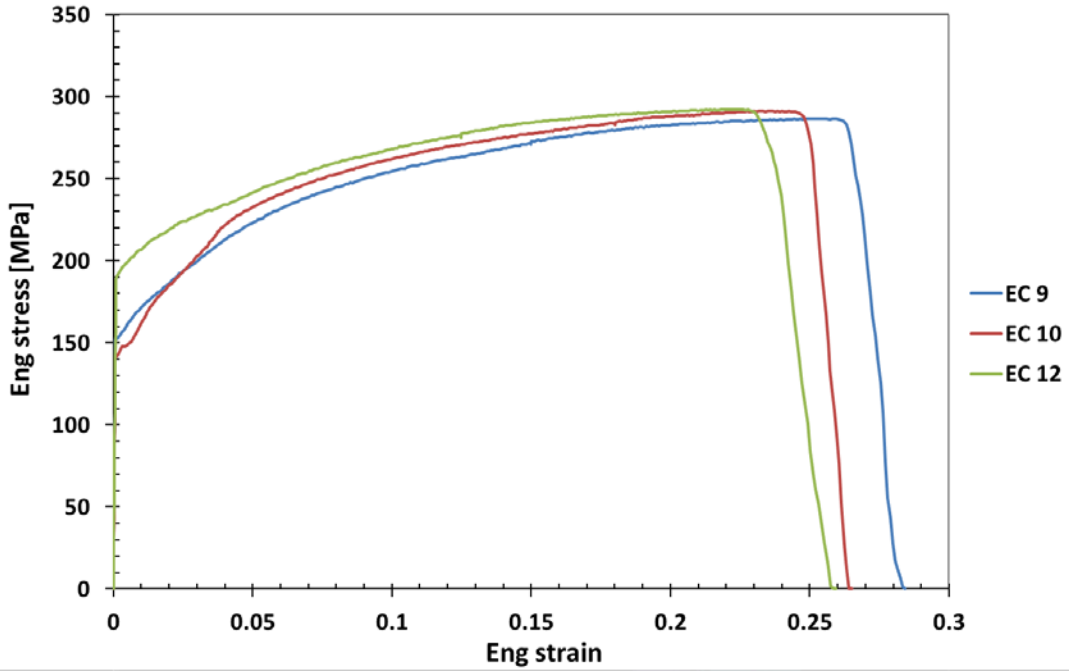

Figure 9-90 - Engineering stress-strain curves for tensile coupons having a uniform distribution of carbon along the gauge width

The yield stress of coupons shown in Figure 9-90 can be theoretically predicted by using a rule of mixture as shown in section H.5.1 in Appendix H.

From the curves shown in Figure 9-90, it is interesting to note that if the amount of carbon from a graded configuration is uniformly distributed along the gauge width, there is only a slight Lüders plateau. This can be justified by the fact that the same amount of carbon will be redistributed to more dislocations resulting in less carbon dense Cottrell atmospheres. This will make easier the unlocking of dislocations, which will result in the absence of the peak of stress at the starting of the Lüders plateau. Moreover, the lower density of carbon atoms around a dislocation could also cause the disappearance of the Lüders plateau from the stress-strain curve (as shown for specimen 12). However, when the DIC pattern where extracted, bands where still detected at the surface, even if for specimen EC 9 and EC 10 the propagation seems to be fast and it seems that they nucleate at lower strain compared to the bands obtained for the previously graded configurations. Indeed, for the carbon graded configurations, the Lüders bands were detectable from the DIC by setting the strain range from 0.0025 to 0.150, while for specimen EC 9 in order to detect visually some bands from DIC, the strain range had to be set to 0.002 up to 0.028. Figure 9-91 shows the nucleation and propagation of the bands in specimen EC 9.

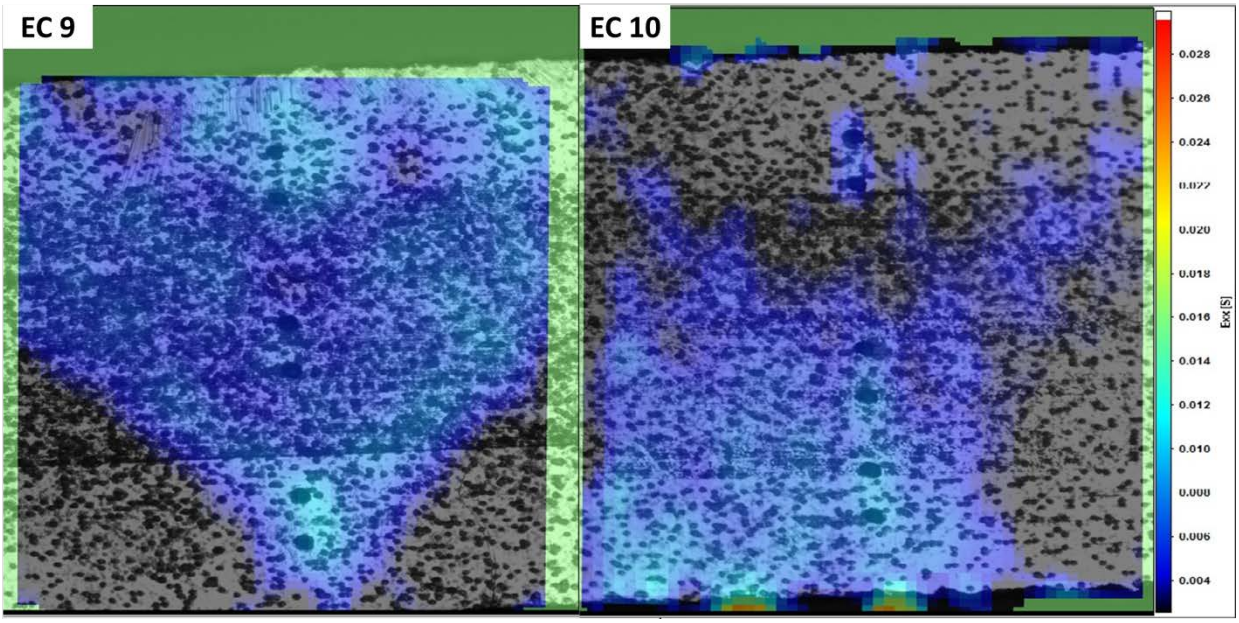

Figure 9-91 - Lüders bands nucleation for specimen EC 9 Lüders bands nucleation for specimen EC 10

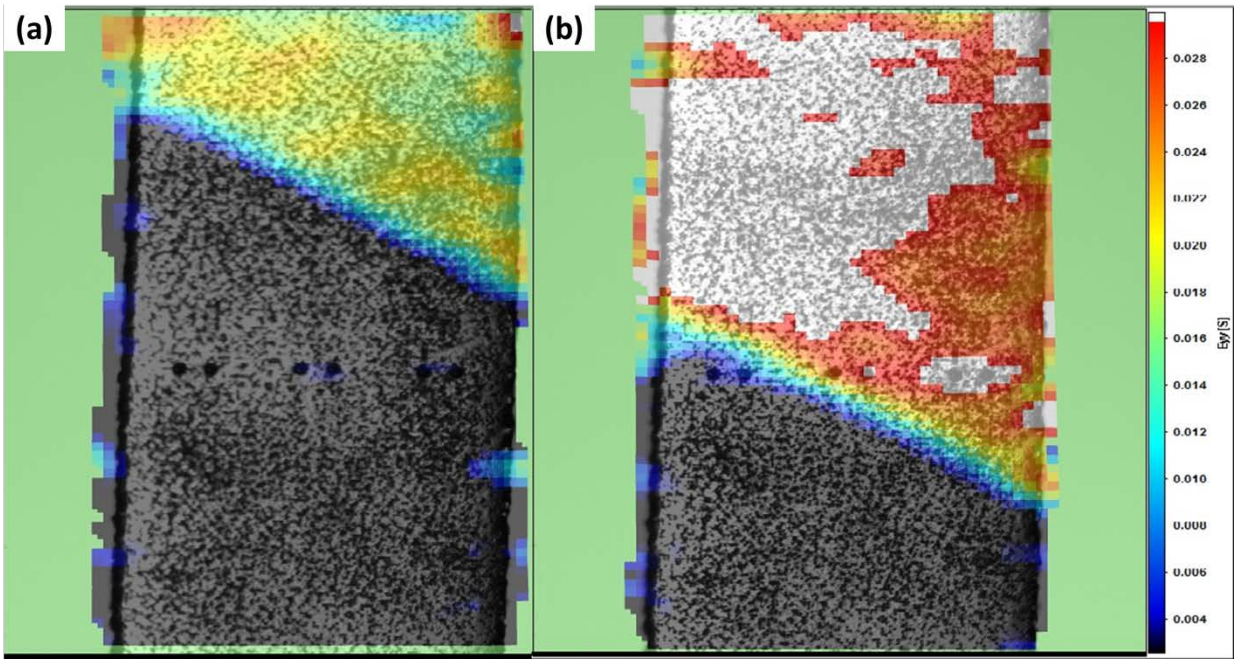

Figure 9-92 – (a) Lüders bands propagation for specimen EC 12; (b) bands crossing the voids

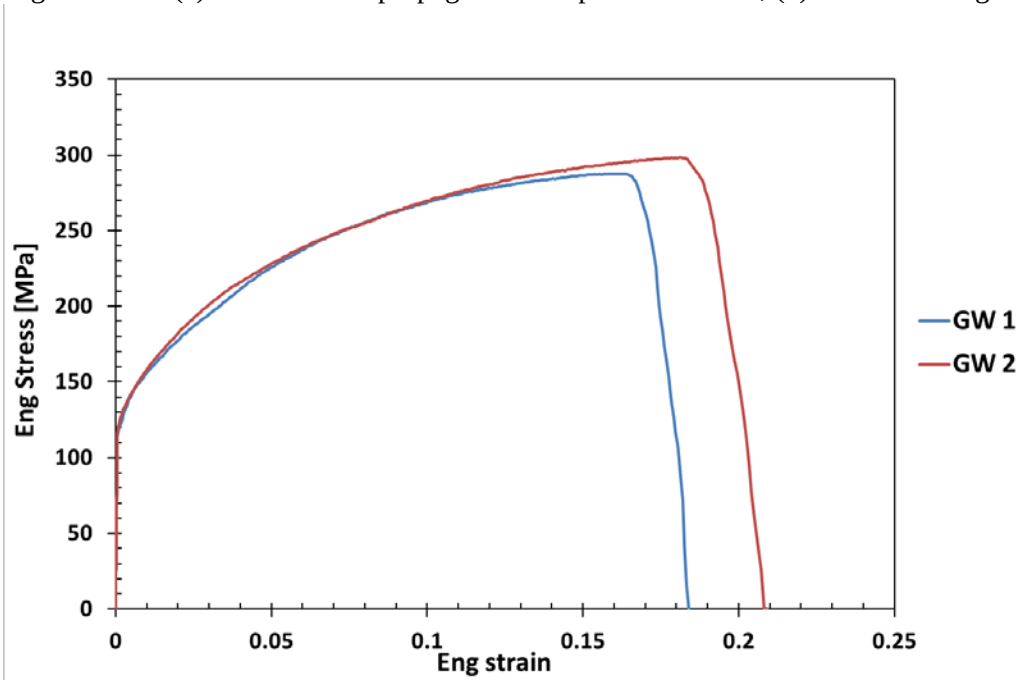

Figure 9-93 - Engineering stress-strain curves for uncoated and not-annealed tensile coupons

Mechanical properties are listed in Table H- 14 of Appendix H and the pictures showing the starting and progressing of the deformation are shown in Figure H. 70 for specimen GW 1 and Figure H. 71 for specimen GW 2 in Appendix H. As expected, no Lüders bands are propagating for both specimens.

9.8.2. Extraction of void growth from tensile tests

During the tensile tests, optical microscope pictures were taken at a rate of 1 picture every 10 ms. Depending on the density of the DIC features, the magnification of the pictures was set to 5X or 10X. If the features were not too dense, then it was easy to follow the deformation with 5X magnification and this would allow following the deformation on a larger part of the gauge length. On the other hand, if the density of the features was high, in order to better discern the features, a magnification of 10X was chosen. Void growth was extracted following the same procedure described in section 9.4. The true far field strain was extracted from digital image correlation (DIC) analyses by selecting an area far from the voids. DIC will give an average true strain in this area as a function of the number of pictures used to run the analysis. For each specimen, three couple of voids where analyzed and for each couple the local strain at the voids ($\ln(a/a_0)$) was plotted as function of the far field strain. The slope of this curve will give an indication of the speed of void growth and the scope will be to see if the carbon distribution has an effect on this growth. In particular, in the presence of a carbon gradient, it is expected that some void will grow faster compared to other voids.

9.9. Results of void growth for specimens having carbon gradient along the gauge width

9.9.1. Results for specimens having a 500 μm ablation in the centre

In the present paragraph, the results of void growth (local strain versus true far field strain) will be first presented for specimens having a carbon gradient through the width which was obtained by ablating a 500 μm wide section of FeC film from the middle of the tensile coupon.

- **Specimen EC 1: bottom couple**

In Figure 9-94 void growth for the specimen EC 1 is shown for the bottom couple of voids. At the beginning, the local strain is zero and the voids are not growing since a Lüders band has localized in another region of the sample (see Figure 9-82 for reference on Lüders propagation). However, once the band reaches the bottom couple of voids, there is a sudden increase in the local strain and a sudden increase in void growth which results in a step in the

curve shown in Figure 9-94. After the band has crossed the couple of voids, their growth follows a linear behaviour. The slope of the void growth curve was extracted after the "jump" caused by the Lüders propagation (Figure 9-95). All graphs showing the change in major void diameter and of the linear slopes are reported in Appendix H for the specimens.

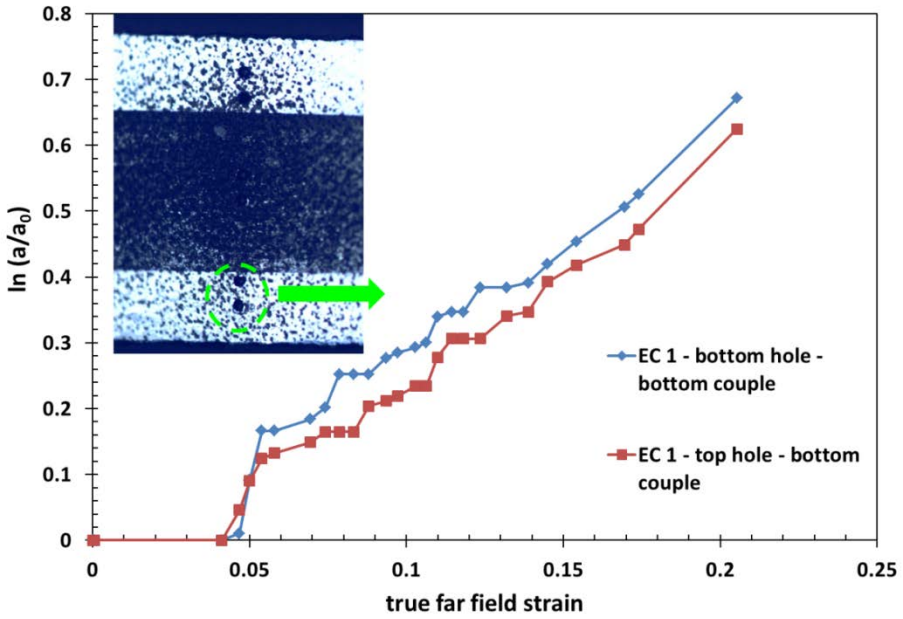

Figure 9-94 - Local true strain versus true far field strain for bottom couple of holes of specimen EC 1

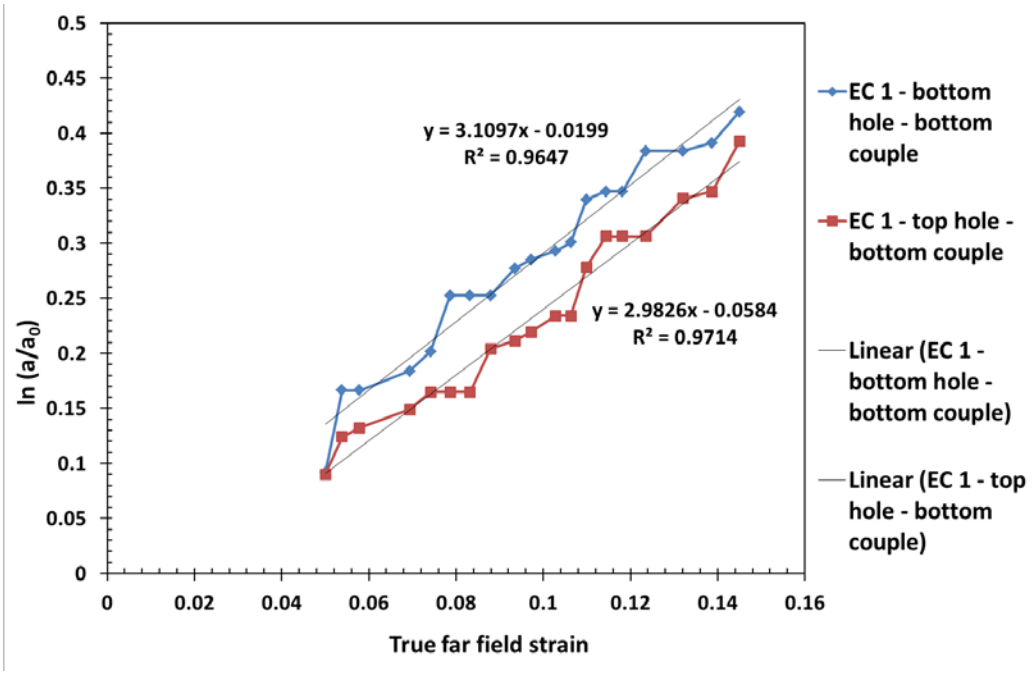

Figure 9-95 - Linear slope of local true strain versus true far field strain of the bottom couple of holes for specimen EC 1

Specimen	**Bottom couple**		**Central couple**		**Top couple**	
	Bottom hole	Top Hole	Bottom Hole	Top hole	Bottom Hole	Top Hole
EC 1	3	3	2.3	2.6	3.2	3.6
Average EC 1	3		2.5		3.4	
Lüders pattern EC 1	For EC 1 the Lüders band nucleated far from the voids and then a single front crosses the voids, starting to affect first the top couple, then the central couple and then the bottom couple					
EC 3	5	4.7	3	2	2.9	3.1
Average EC 3	4.9		2.5		3	
Lüders pattern EC 3	For EC 3 the Lüders band nucleated far from the voids and then a single front crosses the voids, starting to affect first the bottom couple, then the central couple and then the top couple					
EC 5	3.3	3.6	3.2	2.9	3.5	4.3
Average EC 5	3.5		3.1		3.9	
Lüders pattern EC 5	For EC 5, the Lüders bands nucleated at the holes. They start in the zones containing carbon (bottom and top couple of holes) and then they propagate on the central couple of holes					
EC 11	2.8	3.2	2.6	2.8	3	3.2
Average EC 11	3		2.7		3.1	
Lüders pattern EC 11	For EC 11 two Lüders bands nucleated far from the voids and then the two fronts coalesce close to the voids affecting the top couple					

Table 9-15 – Summary of the void growth obtained for specimen ablated 500 μm at the center of the gauge width

Table 9-15 summarizes all the slopes obtained for the specimens having 500 μm of FeC film ablated in the centre of the tensile coupon. The average void growth was calculated for each couple of voids in order to easily compare them.

For specimens EC 1 and EC 3, the bottom and top couple of voids which were placed in the zones with higher carbon content grow faster than the central couple of voids where no carbon is present. For the specimen EC 11, this consideration is still valid, however the difference of growth between the top couple and the central couple or between the bottom couple and the central couple is less marked. The gradient of yield stress calculated from the hardness was 59 MPa for EC 1, 104 MPa for EC 3 and 77 MPa for EC 11. According to these values, it would be expected that also EC 11 should show a marked difference in void growth, but this is not what was found. Looking at the Lüders bands pattern, it was noticed

that they are different in each specimen and it is believed that this could justify the differences in void growth. In the curves of the local strain versus the true far field strain, every time a band crosses a void, it causes a sudden increase in the strain and as a consequence an increase in void growth.

For the specimen EC 1 there is a single Lüders band crossing the void zone and it affects first the top couple, which could justify why this couple is the one growing faster. However, the influence of the carbon gradient is preserved since there is only one Lüders front crossing the voids zone and that originated far from them.

For specimen EC 3, again there is only one Lüders front propagating and it starts to affect first the bottom couple, which is the one that grows faster compared to the central and top couple, but again since there is only one front crossing the voids and since the band originated far from them, the difference in void growth is still due to the carbon gradient. However, looking at specimen EC 5 which had a gradient of yield stress of 74 MPa (obtained from the measured Vickers hardness), void growth seems to be almost the same for each couple of voids. This is due to the nucleation of the Lüders bands at the voids. In specimen EC 11, the difference in void growth is not so marked and it was noticed that there are two fronts propagating and they coalesce at the voids. This could explain why there is less difference in the void growth for the different couple of voids compared to specimens EC 1 and EC 3.

In the next graphs, the results of void growth for specimens EC 2 and EC 4 will be presented. These specimens had a carbon gradient through width obtained by ablating 250 μm of FeC film on each side of the width and leaving 500 μm of FeC film on the centre of the tensile coupon. Specimen EC 7 was not analyzed since its mechanical properties were lower than the one found for EC 2 and EC 4. Once again, in section 9.9.2, an example of void growth extracted for one couple of voids in one specimen is reported, while all the void growth curves for the other couple of voids and coupons are included in Appendix H.

9.9.2. Results for specimens having 500 µm of film left in the centre

- **Specimen EC 2: bottom couple**

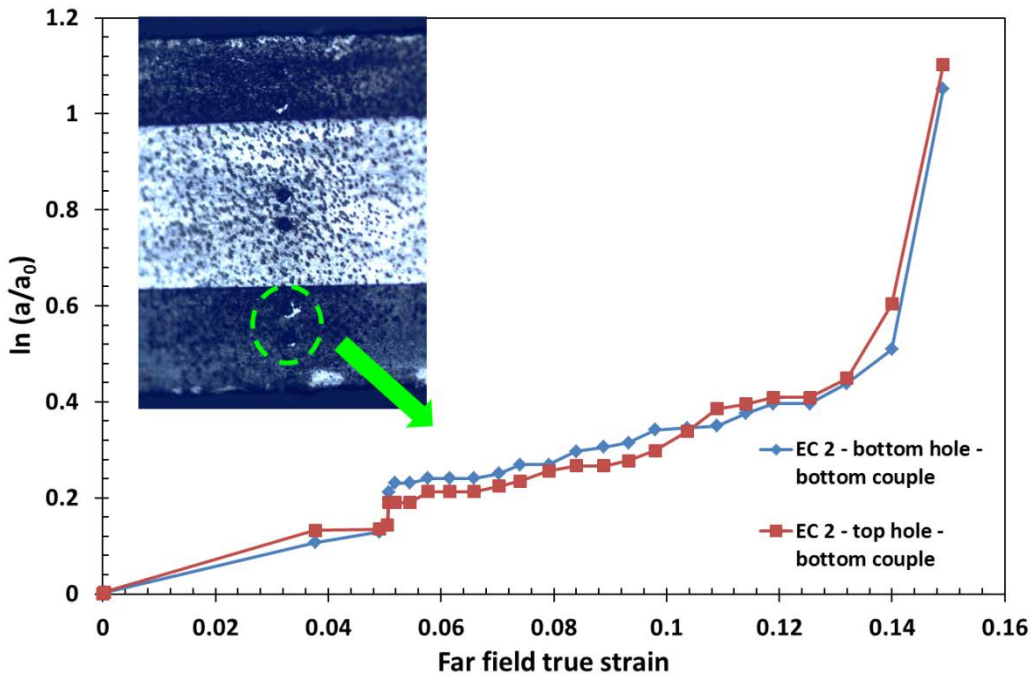

Figure 9-96 - Local true strain versus true far field strain for bottom couple of holes of specimen EC 2

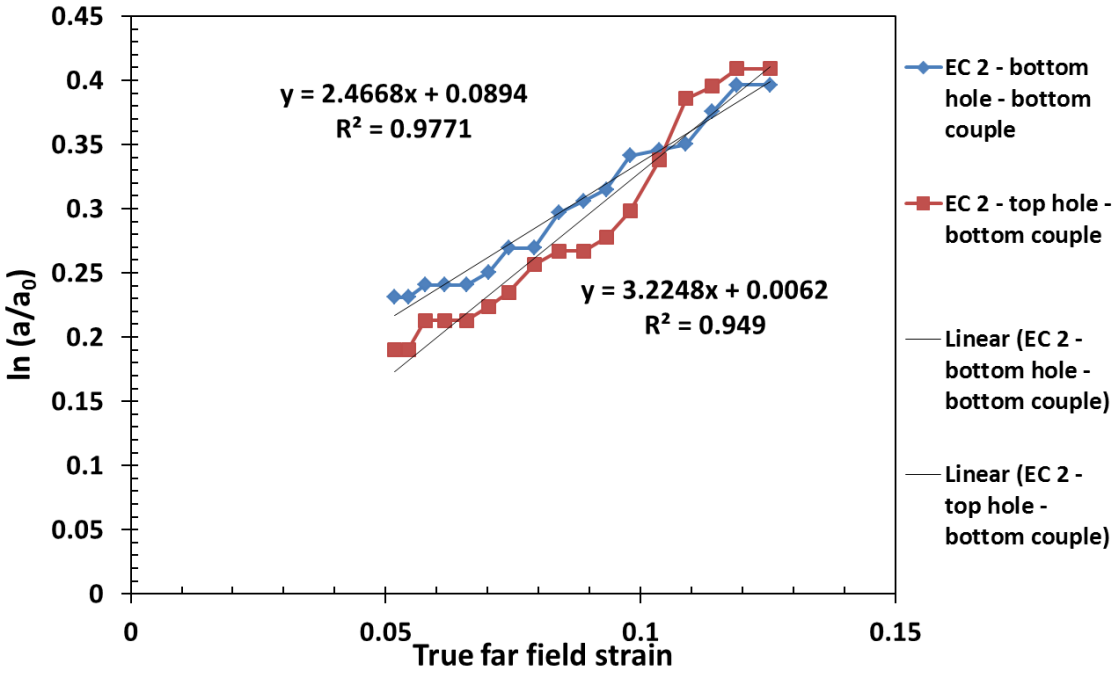

Figure 9-97 - Linear slope of local true strain versus true far field strain of the bottom couple of holes for specimen EC 2

Specimen	**Bottom couple**		**Central couple**		**Top couple**	
	Bottom hole	Top Hole	Bottom Hole	Top hole	Bottom Hole	Top Hole
EC 2	2.5	3.2	3.4	3.1	3.7	4
Average EC 2	2.9		3.3		3.9	
Lüders pattern EC 2	The Lüders bands nucleate at the holes, starting from the top couple and then involving the central couple and finally the bottom couple. This could justify the higher void growth of the top couple compared to the central couple and to the bottom couple					
Specimen	**Left couple**		**Central couple**		**Right couple**	
	Left hole	Right hole	Left hole	Right hole	Left hole	Right hole
EC 4	3.3	3.4	3.8	3.4	3.1	2.7
Average EC 4	3.4		3.6		2.9	
Lüders pattern EC 4	Two bands are propagating. One propagates crossing the left couple, the other propagates crossing the right couple and they coalesce close to the central couple.					

Table 9-16 - Summary of the void growth obtained for specimens having 500 μm of FeC film left at the center of the gauge width

For specimens EC 2 and EC 4, the gradient of yield stress calculated from the Vickers hardness was 68 MPa and 43 MPa respectively, however, no marked difference on the growth of the different void couples was recorded. It was again noticed that for EC 2 the Lüders bands nucleate at the voids and especially at the top couple of voids and this justifies the higher void growth shown by this couple of voids. For the specimen EC 4, the uniform void growth is due to the presence of two fronts propagating which coalesce at the central couple of voids. The central couple where the bands coalesce shows the highest void growth. From the results presented so far, it can be inferred that if only one Lüders bands is propagating and if it is originated far from the voids, then a gradient of void growth is occurring in the specimens due to the gradient of yield stress. However, if the Lüders bands start at the voids or if two fronts are propagating and coalesce at the voids, then the

difference in void growth is cancelled out by the bands. Moreover, the voids where the bands originated first or the voids at which the bands coalesced show higher void growth due to the high stress field associated to the band front.

9.9.3. Results for specimens having uniform carbon content along gauge width

As already explained in the previous paragraphs, these specimens were obtained from coupons having 500 μm of FeC film ablated in the center and then they were annealed for 12 hours in order to distribute uniformly the carbon through the width. For this reason, it is expected that there will be no difference in void growth between the different couple of holes. An example of void growth extraction is reported for specimen EC 9 in this section, while all the other graphs related to other couples of voids and other coupons are included in Appendix H.

- **Specimen EC 9: bottom couple of holes**

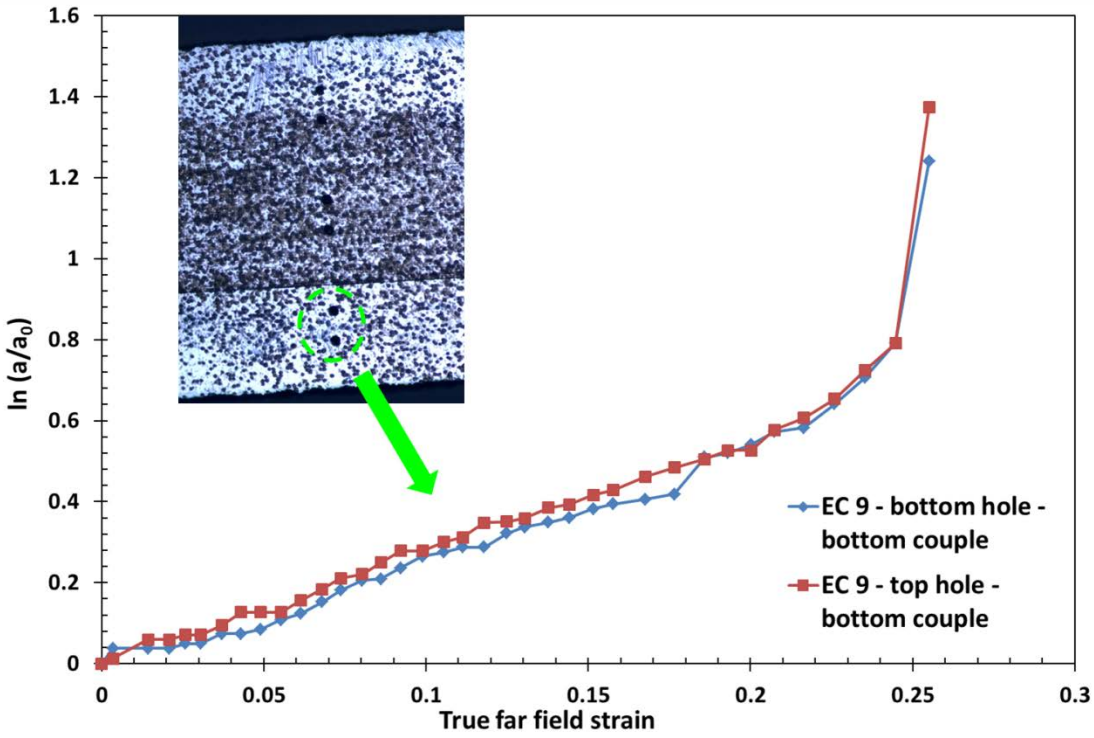

Figure 9-98 - Local true strain versus true far field strain for bottom couple of holes of specimen EC 9

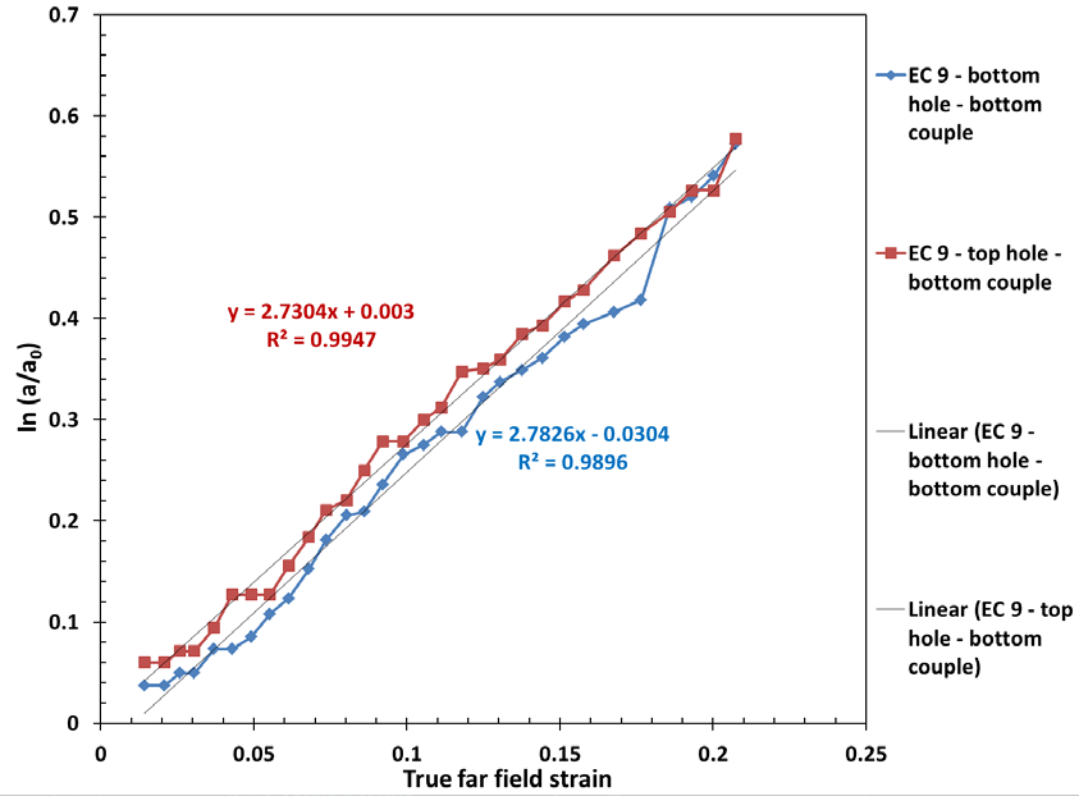

Figure 9-99 - Linear slope of local true strain versus true far field strain of the bottom couple of holes for specimen EC 9

Specimen	**Bottom couple**		**Central couple**		**Top couple**	
	Bottom hole	Top Hole	Bottom Hole	Top hole	Bottom Hole	Top Hole
EC 9	2.7	2.8	2.7	2.9	2.9	2.9
Average EC 9	2.75		2.8		2.9	
Lüders pattern EC 9	Two Lüders band fronts start at the holes					
EC 10	2.9	2.9	2.6	2.4	2.9	2.9
Average EC 10	2.9		2.5		2.9	
Lüders pattern EC 10	Two Lüders band fronts start at the holes					
	Left couple		**Central couple**		**Right couple**	
	Left hole	**Right hole**	**Left hole**	**Right hole**	**Left hole**	**Right hole**
EC 12	2.5	2.5	1.5	1.9	2.4	2.4
Average EC 12	2.5		1.7		2.4	
Lüders pattern EC 12	A Lüders band front propagates along the gauge length and it has originated far from the voids					

Table 9-17 - Summary of the void growth obtained for specimens having uniform carbon distribution along the gauge width

From the results shown in Table 9-17, for specimens having uniform carbon content along the width, no void growth gradient was recorded. However, specimens EC 9 and EC 10 have the Lüders bands nucleating at the voids and this smooths out the difference in void growth. For this reason, it is difficult to state if the void growth is the same for all the couples of voids because no carbon gradient is present or because the Lüders bands are nucleating at the voids. For specimen EC 12, the left and the right couples have similar void growth, while the central couple grows slower than the other two couples. This could be due to a bad lasing of that couple of holes. Indeed, the conicality of the voids for this specimen was higher than what found for other coupons.

9.9.4. Results for uncoated and not-annealed specimens of IF steel

- **Specimen GW 1: left couple of holes**

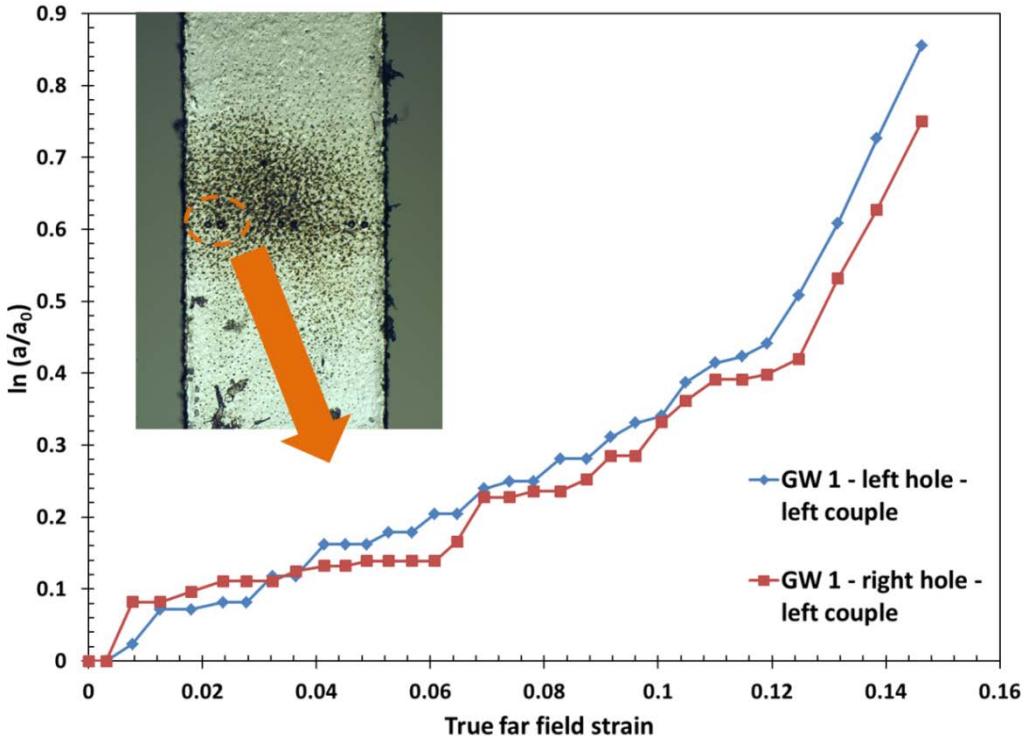

Figure 9-100 - Local true strain versus true far field strain for left couple of holes of specimen GW 1

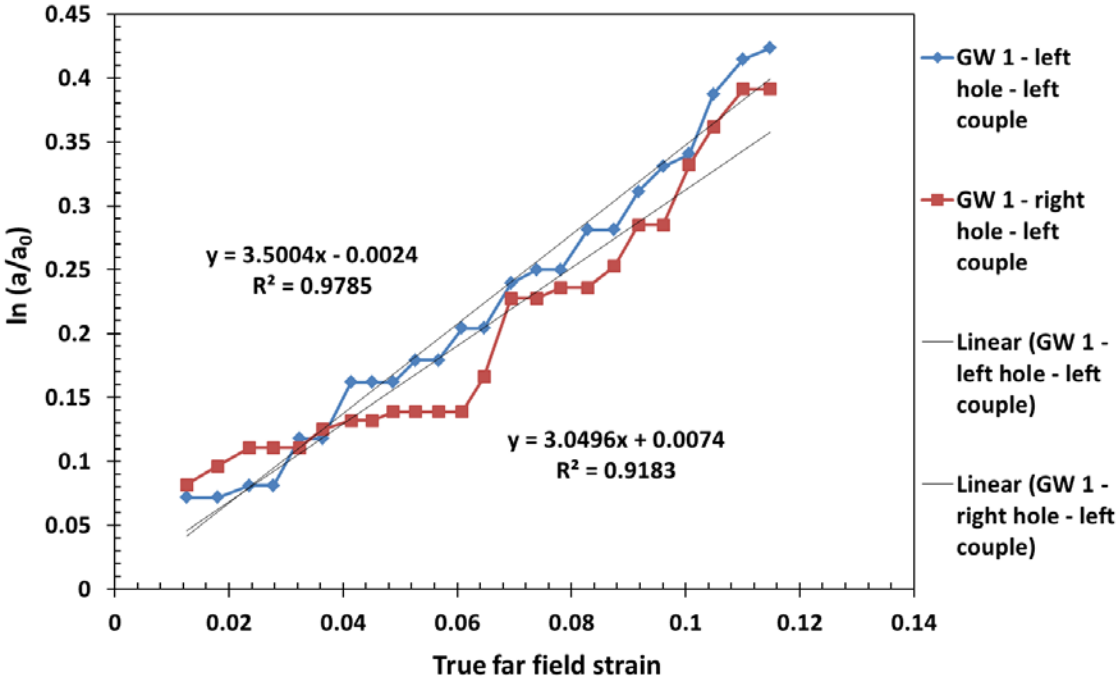

Figure 9-101 - Linear slope of local true strain versus true far field strain of the left couple of holes for uncoated and not-annealed specimen GW 1

Specimen	Left couple		Central couple		Right couple	
	Left hole	Right Hole	Left Hole	Right hole	Left Hole	Right Hole
GW 1	3.50	3.1	3.2	3.4	3.3	3.3
Average GW 1	3.3		3.3		3.3	
	Bottom couple		Central couple		Top couple	
	Bottom hole	Top hole	Bottom hole	Top hole	Bottom hole	Top hole
GW 2	4	3.1	3.2	3.2	3.5	3.2
Average GW 2	3.6		3.2		3.4	

Table 9-18 - Summary of the void growth obtained for uncoated and not-annealed specimens

From the above table, it is clear that for uncoated and not-annealed coupons, the void growth is fairly uniform through the whole width.

9.10. Void Growth fitting with theoretical models

McClintok model has been already presented in section 9.4.1.1 and the same model is used also for these coupons to fit the void growth. The strain used in the equation was the far field strain obtained from the DIC analysis, while the strain hardening exponent was obtained from the true stress-strain curve of each specimen by applying the Hollomon equation. In particular, the slope of the graph ln (σ_{True}) versus ln (ε_{True}) will give the value of the strain-hardening exponent. The graph was fitted with a line taking the points from the yield stress up to the ultimate tensile strength (UTS) for specimens without Lüdering, while for coupons having Lüders plateau, the slope was taken from the end of the plateau up to the UTS. The values of strain-hardening exponent obtained for the specimens are reported in Table 9-19.

Specimen	Strain hardening exponent
EC 1 (carbon gradient)	0.23
EC 2 (carbon gradient)	0.28
EC 3 (carbon gradient)	0.23
EC 4 (carbon gradient)	0.27
EC 5 (carbon gradient)	0.21
EC 9 (uniform carbon distribution)	0.24
EC 10 (uniform carbon distribution)	0.26
EC 11 (carbon gradient)	0.28
EC 12 (uniform carbon distribution)	0.17
GW 1 (uncoated not-annealed)	0.25
GW 2 (uncoated not-annealed)	0.26

Table 9-19 – Strain-hardening exponent for specimens having holes along the gauge width

In the next graphs, the $ln\ (a/a_0)$ obtained experimentally will be fitted with McClintok model. However, for clarity, only the evolution of the top hole or of the bottom hole for each couple of holes in each specimen will be shown. In this section one fitting for one specimen of each type is reported, while the McClintok fittings for other specimens are shown in section H.7 of Appendix H.

- **McClintok fitting of specimen EC 1 (500 µm of FeC film removed in the middle)**

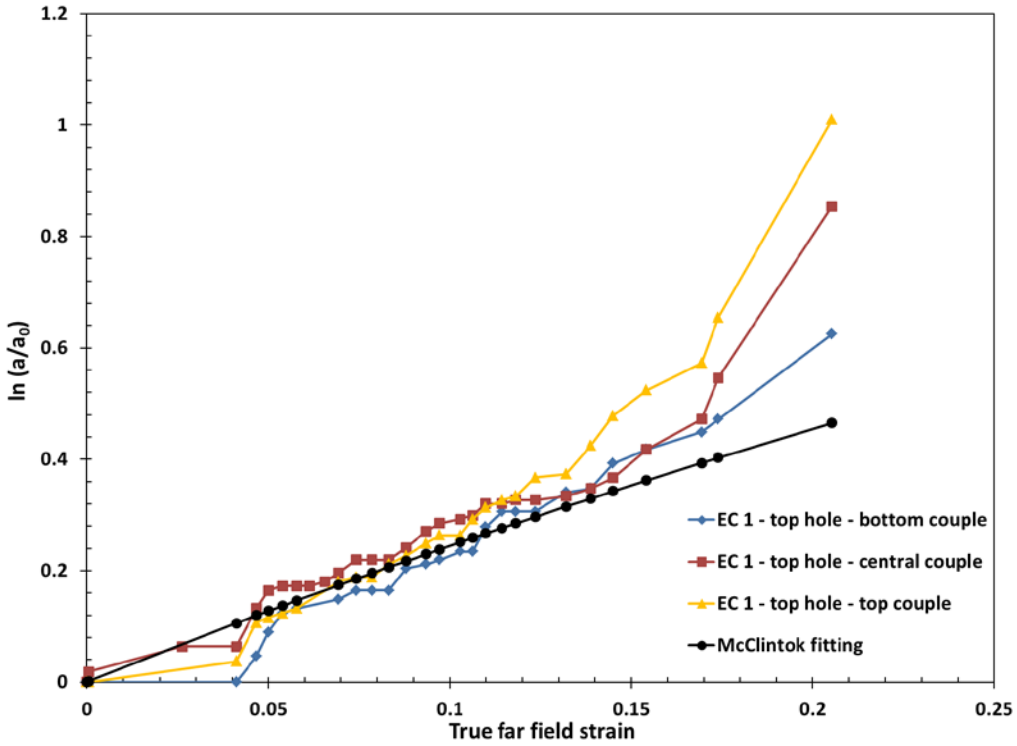

Figure 9-102 - McClintok fitting of the void growth for top holes in specimen EC 1 having 500 µm FeC film removed in the center of the tensile coupon

- **McClintok fitting of specimen EC 2 (FeC film removed on the sides)**

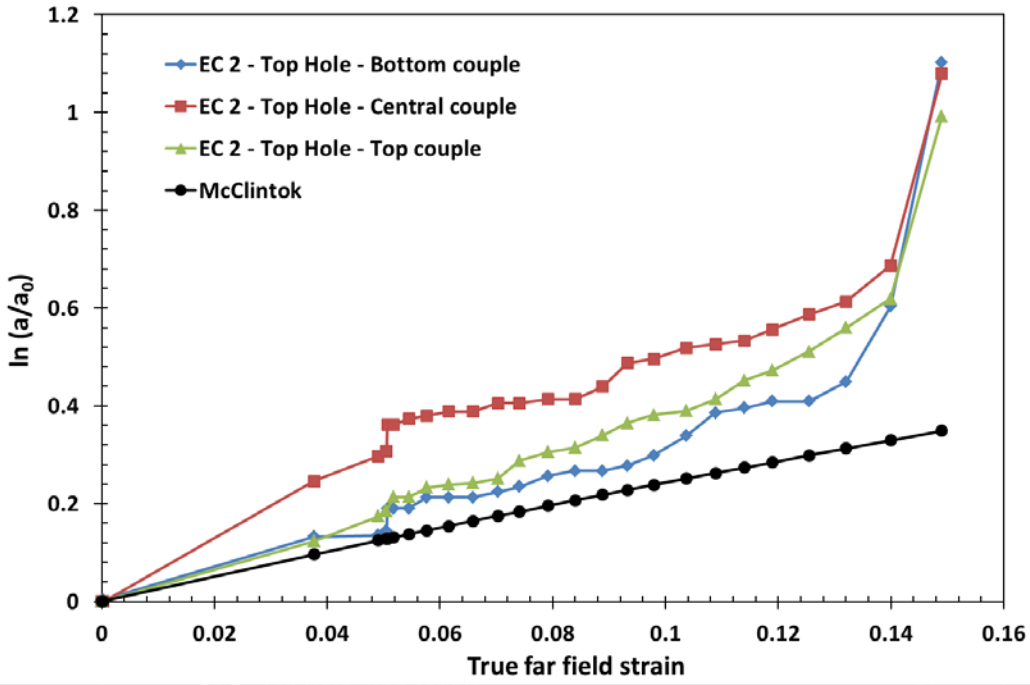

Figure 9-103 - McClintok fitting of the void growth for top holes in specimen EC 2

- **McClintok fitting of specimen EC 9 (FeC film removed in the center – uniform carbon distribution)**

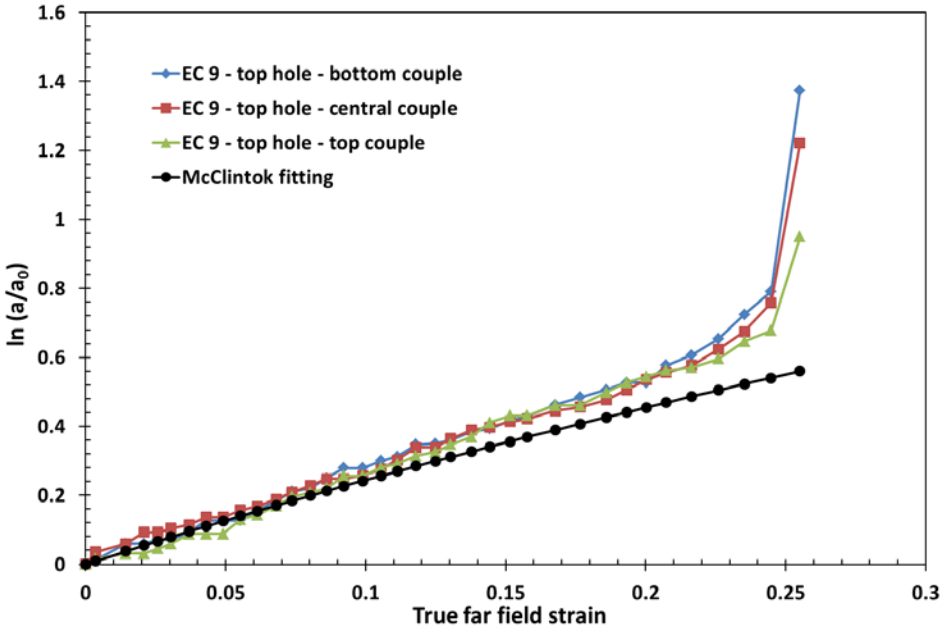

Figure 9-104 - McClintok fitting of the void growth for top holes in specimen EC 9

- **McClintok fitting of specimen GW 1 (uncoated)**

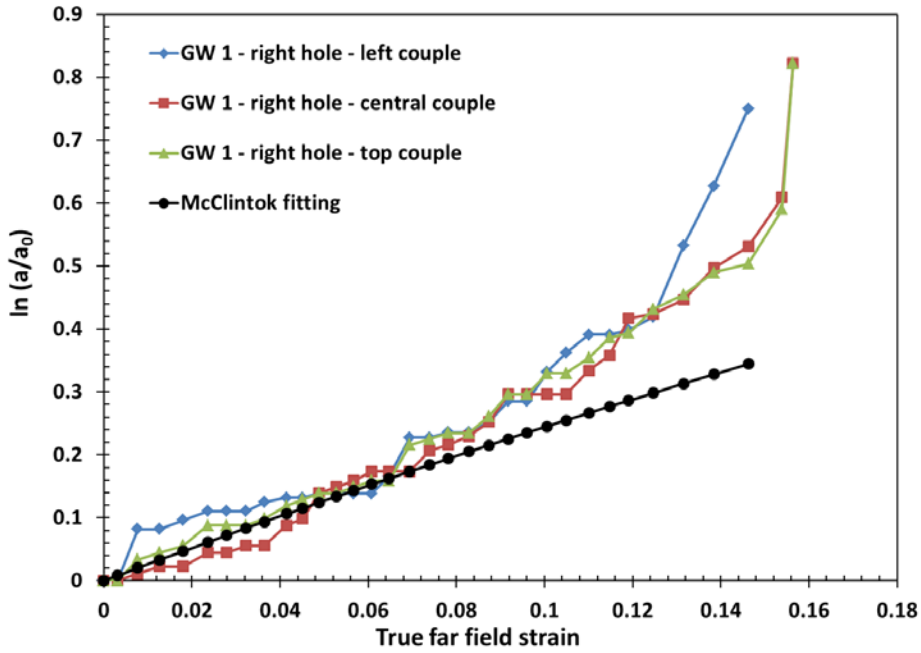

Figure 9-105 - McClintok fitting of the void growth for right holes in specimen GW 1

McClintok model is supposed to fit well void growth at low strains before the voids start to interact and to approach the coalescence phase. From the fitting performed on the experiments presented in this section, it was noticed that coupons having no Lüdering (or very fast Lüders bands propagating) as in the case of uniform carbon distribution through width; the model fits the void growth well in a range of true strain up to 0.1 (see Figure 9-104, or Figure H. 134 and Figure H. 135 in section H.7.3). The same holds for uncoated coupons, where McClintok fits well the void growth for true strains up to 0.07 (see Figure 9-105 or Figure H. 136 in section H.7.4). On the other hand, for specimens having carbon gradient and propagation of Lüders bands, the fitting is not good due to the sudden increase of strain and of void growth caused by the bands propagation. Indeed, McClintok cannot predict void growth when Lüders bands are nucleated at the voids or when they coalesce at the voids. It was however noticed that if the void growth curves are shifted to remove the "jump" in void growth caused by the Lüdering, then McClintok can still predict the growth very well. In Figure 9-106 the McClintok fitting excluding Lüdering is shown for specimen EC 3 (having the FeC film removed in the center), while in Figure 9-107 the fitting is reported for specimen EC 2 (having the FeC film removed on the sides).The same fitting with the void growth curves shifted to neglect Lüdering was performed also for specimens EC1, EC4, EC5 and EC11 and their curves are reported in section H.8 of Appendix H.

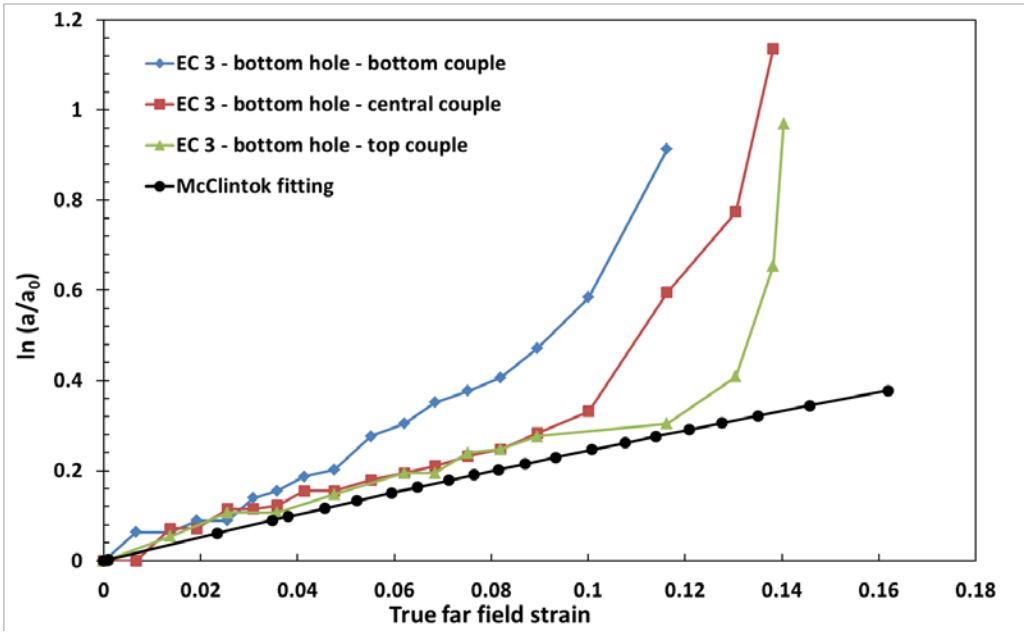

Figure 9-106 - McClintok fitting of specimen EC 3 after Lüdering removal in the curves describing void growth

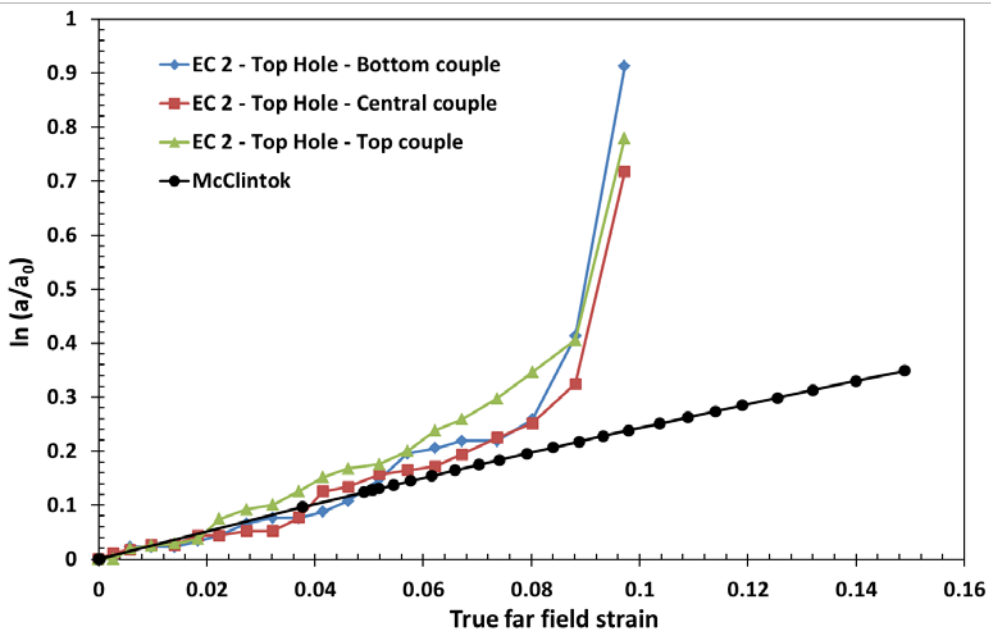

Figure 9-107 - McClintok fitting of specimen EC 2 after Lüdering removal in the curves describing void growth

9.11. Conclusions

In this chapter, the influence of carbon gradient on the growth of 2D cylindrical voids was experimentally studied. In order to obtain the carbon gradient, two procedures were presented. The first procedure required masking the tensile coupon during the PVD deposition, to only partially coat the gauge length. The second procedure showed the removal of the FeC film by laser ablation in selected zones of the gauge width in order to create carbon gradient along this direction. Following these two procedures, two categories of specimens were produced, the first had a gradient of carbon along the gauge length and the second one had a gradient along the gauge width. Coupons containing a uniform distribution of carbon as well as uncoated and not-annealed IF steel were also tested as comparison.

From the tests performed on specimens having carbon gradient (i.e. yield strength gradient) along the gauge length, the following results were obtained:

- For coupons having a gradient of carbon, the fracture always occurred in a zone containing no carbon;

- By plotting the change of the main diameter of the voids versus the true far field strain ($\ln(a/a_0)$ versus true far field strain taken in the whole gauge length), it is evident that the voids placed in zones containing carbon were growing more slowly than voids inserted in zones without carbon. Moreover, the voids inserted in the FeC coated zones were growing more slowly than the voids inserted in the graded zone.
- By plotting the change of main diameter of the voids versus the local far field strain (taken in each zone which has a different carbon content), no clear difference in void growth could be discerned.
- For uncoated and not-annealed IF coupons, void growth was homogeneous for all couples of voids and higher for the couple which failed first. Similar behaviour was obtained for the coupon having a uniform carbon content along the gauge length.
- For the specimens having carbon gradient along the gauge length, the Lüders band nucleated at the interface between the graded zone and the no-carbon zone. As the bands propagate, when it reaches the voids, it causes a sudden increase in the void growth, which is recorded as a "step" in the graph of $ln(a/a_0)$ versus the true far field strain.

From the tests performed on specimens having carbon gradient along the gauge width, the following results were obtained:

- Fracture occurred always in the couple of voids placed in a zone containing carbon (which was coated with FeC film). In these configurations, the voids are placed in isostrain condition, which mean they experience the same strain but different stress. For this reason, failure is determined by reaching a critical level of stress and since the stress is higher in zones containing more carbon, these are the one where failure takes place.
- For the specimens which were obtained by ablating 500 μm of FeC film in the centre of the tensile coupon, high yield strength gradient were present after annealing. It was noticed that void growth was higher for holes inserted in the coated zones and it was low for voids placed in the uncoated zone (specimens EC 1 and EC 3 in Table 9-15). This holds true if the Lüders bands nucleated far from the voids and coalesced far from the voids. On the other hand, if the bands nucleate at the holes (specimen EC 5) or coalesce at the voids (specimen EC 11), then the difference in void growth

which would be caused by the different carbon amounts, will be smoothen by the bands. If the tensile curves of specimens with carbon ablated in the center of the gauge width are compared with uncoated IF steel having the same void size and intervoids spacing, it is seen that the strain at failure is lower for the carbon diffused coupons (Figure 9-108). This can be explained considering that the specimens diffused with carbon are stronger than the uncoated IF steel and for this reason will reach earlier the critical stress to cause failure.

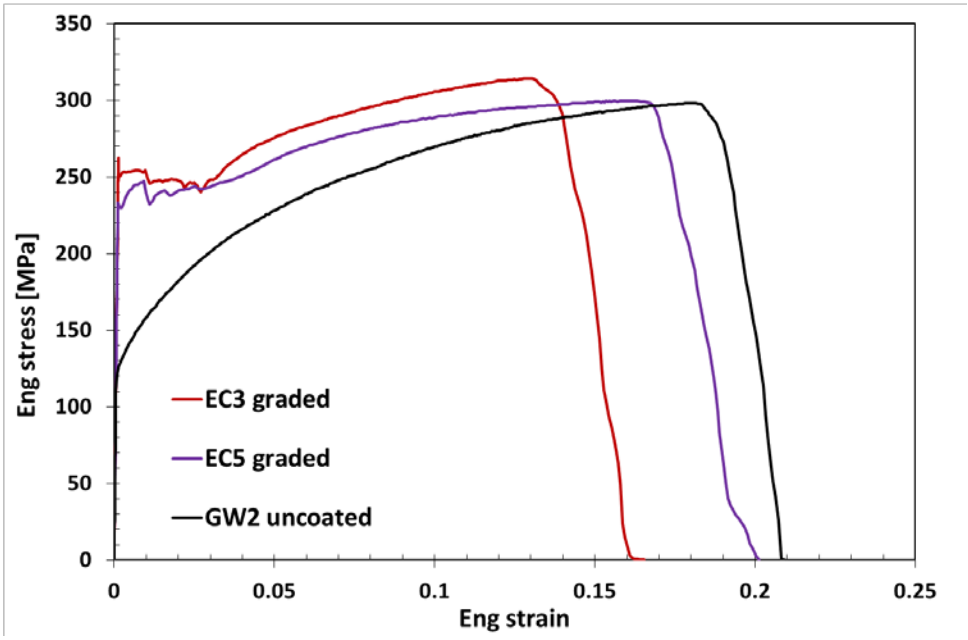

Figure 9-108 - Comparison of engineering stress-strain curves of coupons with carbon ablated in the center of the gauge width and uncoated IF steel

- Given the same void size and intervoid spacing, graded coupons obtained by ablating carbon at the center of the gauge width have the same strain at failure of graded coupons which have carbon left only at the center of the gauge width. This is drawn by comparing stress-strain curves of specimens EC 1, EC 3, EC 5 in Figure 9-81 with the curves EC 2 and EC 4 in Figure 9-87.
- For specimens which were obtained leaving 500 μm of FeC film in the centre of the tensile coupon, moderate yield stress gradients along the gauge width were present after annealing. In these specimens, failure occurred still in the FeC coated zone, however, void growth was very uniform in each zone. This could be caused by the Lüders bands, since for specimen EC 2 they are nucleating at the voids, while for

specimen EC 4 they coalesced at the voids. This smoothens the gradient of void growth which would be expected because of the carbon gradient (i.e. yield strength gradient);

- For specimens having uniform carbon content (i.e. uniform yield strength) along the gauge width, all couples of holes showed similar growth as expected, except the central couple for specimen EC 12. However, it is believed that this couple was probably not well machined with the laser.
- If the engineering stress-strain curve of a coupon having carbon gradient is compared with the curve of a coupon with uniform carbon distribution, it is seen that the strains at failure are very close (Figure 9-109). The higher strain at failure detected for the graded configuration is due to Lüders plateau. If Lüdering is removed and the curve is shifted, the strains at failure would be the same for both coupons. This means that having a graded carbon configuration is better than having a uniform carbon distribution because the strain at failure is the same in both situations but the carbon gradient shows higher strength.

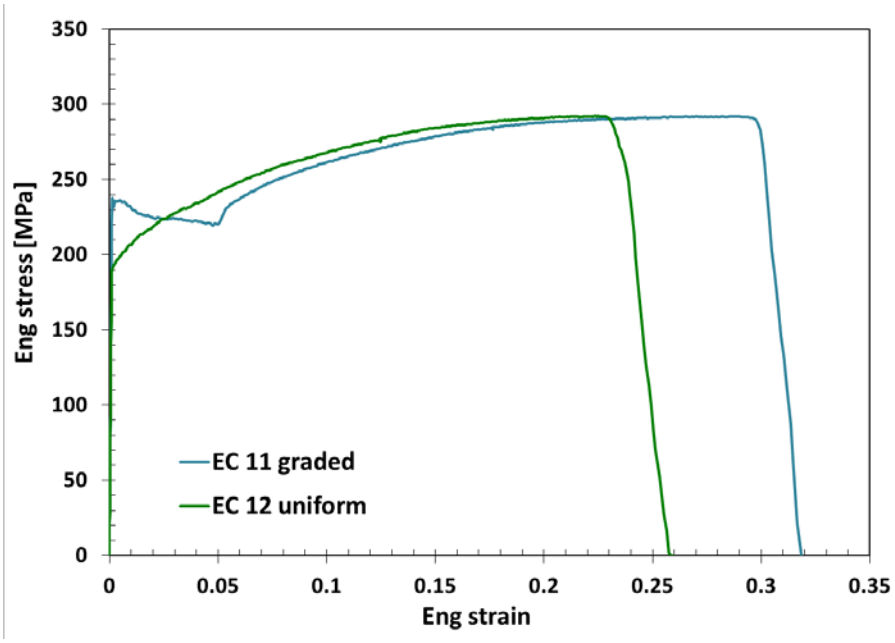

Figure 9-109 – Comparison of engineering stress-strain curves of a coupon having carbon gradient and a coupon having a uniform carbon distribution

- For uncoated and not-annealed IF coupons, the void growth was uniform for all the couples along the gauge width and it was higher than the growth recorded for specimens having a uniform carbon content along the width;
- McClintok model was used to predict void growth for these specimens. For the category of specimens having 500 μm of FeC film removed in the center of the tensile coupon, the fitting was good for specimen EC 1, specimen EC 3 (except the bottom couple) and EC 11. However, the fitting was not good for specimen EC 5 where Lüdering was starting at the voids. McClintok model cannot take into account the complex strain field associated with Lüders bands and the sudden and irregular void growth caused by these bands;
- For the category of specimens having 500 μm of FeC film left in the center of the tensile coupon, McClintok model fits well growth of voids in specimen EC 4, but it does not fit accurately the growth of voids in specimen EC 2. Once again, this is due to the bands since in coupon EC 2 the bands were nucleating at the voids.
- It was noticed that if the curves for the void growth are shifted to remove the "jump" in strain caused by Lüdering, then McClintok predicts well the void growth before the start of coalescence.
- For all coupons having uniform carbon amount along the gauge width, McClintok fitted the experimental data well even at higher strains before coalescence between the voids started;
- For the uncoated and not-annealed IF steel coupons, McClintok fitted the growth well for both specimens GW 1 and GW 2 before the voids started to coalesce.

Chapter 10 : Use of different films as reservoir for diffusion

During the development of this PhD work, other aspects were partially investigated. In particular it was interesting to show if films having three elements could be used for diffusion into steel. In the preliminary investigations performed in this work, FeMnC films were used to diffuse carbon and manganese into the IF steel substrate. The FeMnC films are still applied using PVD technology.

Another aspect that was partially investigated is the diffusion of carbon from films which contain 100% carbon without any iron. This could allow diffusion of carbon even in air and potentially more carbon could be diffused towards the IF steel since the transformation of the film into cementite would not happen. However, the preliminary work of Dr. Colin Scott indicates that, when a 500 nm thick film containing only carbon is used, its adhesion to the IF substrate is poor and hinders diffusion. In particular, PVD films with a carbon content above 50 at% and a thickness of 500 nm seem to be not adherent to the IF substrate compromising diffusion. In the next paragraphs, the preliminary results concerning these topics will be presented.

10.1. Diffusion of Carbon and Manganese into IF steel from FeMnC films

10.1.1. Importance of Manganese for steels

Manganese is considered a very important third element to be included for diffusion into IF steel from PVD coating since it is the main element used for twinning-induced plasticity (TWIP) steels, which combine high strength with good ductility. In general, manganese is used to increase strength and toughness and it can combine with sulphur to form MnS precipitates which have the benefit of limiting hot tearing [210]. Furthermore, manganese is an austenite stabilizer and the addition of manganese to steels containing carbon lowers the temperature at which formation of martensite starts [175]. However manganese became

particularly attractive when TWIP steels started to be developed for the automotive industry. TWIP steels are very important for their good combination of tensile strength (600 – 1100 MPa) and ductility (50% - 100%) which ensures high formability [211], [212]. It was reported that steelmaking consumes 93% of the total production of manganese, out of which 72% is used for the production of low carbon steels and High Strength Low Alloy (HSLA) steels [211]. Manganese is therefore an important element to consider for the development of highly performing microstructures and this is the reason why manganese was used in FeMnC films deposited by PVD. Theoretically it is believed that if manganese could diffuse towards the IF substrate it could stabilize austenite whose carbon solubility is higher than ferrite. If more carbon can be diffused into austenite then, with slow equilibrium cooling, a microstructure of pearlite can be formed, while bainite or martensite could be obtained by quenching. Preliminary tests performed in this PhD work aimed to show if it was feasible to diffuse solute elements (such as manganese) from PVD films and what would be the final mechanical properties after isothermal annealing performed in high vacuum.

As first attempt, the following annealing conditions were chosen:

- 530 ˚C – 1h and 630 ˚C – 1h in high vacuum using the same furnace used to diffuse carbon (results presented in Chapter 5). This annealing was chosen to compare the results with the one presented in Chapter 5 where only carbon was diffusing from the FeC film;
- 1000 ˚C – 1h and 1000 ˚C – 10h in high vacuum, in order to increase the diffusion coefficient of manganese and transform the whole IF substrate into austenite.

It is important to point out that manganese is a substitutional atom and its diffusion will be slower compared to interstitial atoms, such as carbon, since it will diffuse mainly through vacancy mechanism. For this reason, an increase in temperature could be beneficial to improve the diffusion of manganese towards the IF substrate.

For PVD deposition the target was a TWIP steel (used as source of manganese), while the carbon was obtained from graphoil and methane atmosphere as done for the FeC films. The final concentration of carbon into the FeMnC film was measured to be 15 at% for 10% voltage maintained by tuning the flow rate of methane during the deposition and 30 at% for 40% voltage again maintained by tuning the flow rate of methane as for FeC films used in chapter 5. However, it was quite difficult to measure the content of manganese both with

Auger Electron Spectroscopy (AES) and Atom Probe Tomography (APT) since the peak of manganese is overlapped with the one of iron. The amount of manganese in the film was measured at UBC by performing Energy Dispersive x-ray Spectrometry (EDX) measurements and it was found that the manganese to iron ratio was 19.9% Mn in the 40% voltage samples and 19.7% Mn in the 10% voltage sample. This level of manganese is close to that found for a base TWIP steel (Fe22Mn0.6C). A ratio of manganese to iron close to what is present in a TWIP steel was expected since the sputter yield of both atoms is very similar.

10.1.2. Experimental Results

Table 10-1 lists the dimensions of all the tested coupons:

Tensile coupon	Width [mm]	Thickness [mm]	Gauge length [mm]	Annealing treatment	Speed set on the tensile machine [µm/s]
A	1	0.185	5	530 ºC, 1h-High Vacuum	2.5
B	1	0.183	5	530 ºC, 1h-High Vacuum	2.5
C	1	0.166 (*)	5	530 ºC, 1h-High Vacuum	2.5
A	1	0.182	5	630 ºC, 1h-High Vacuum	2.5
B	1	0.182	5	630 ºC, 1h-High Vacuum	2.5
C	1	0.167 (*)	5	630 ºC, 1h-High Vacuum	2.5
A	1	0.182	5	1000 ºC, 1h-High Vacuum	2.5
B	1	0.182	5	1000 ºC, 1h-High Vacuum	2.5
C	1	0.169 (*)	5	1000 ºC, 1h-High Vacuum	2.5
A	1	0.182	5	1000 ºC, 10h-High Vacuum	2.5
B	1	0.182	5	1000 ºC, 10h-High Vacuum	2.5

Table 10-1 - Dimensions of tensile coupons coated both sides with 500 nm thick FeMnC films. (*) indicates specimens which were DIC tested and the thickness was measured before the application of the DIC coating

The engineering stress-strain curves are shown in Figure 10-1 for the coupons annealed at 530 ˚C – 1h.

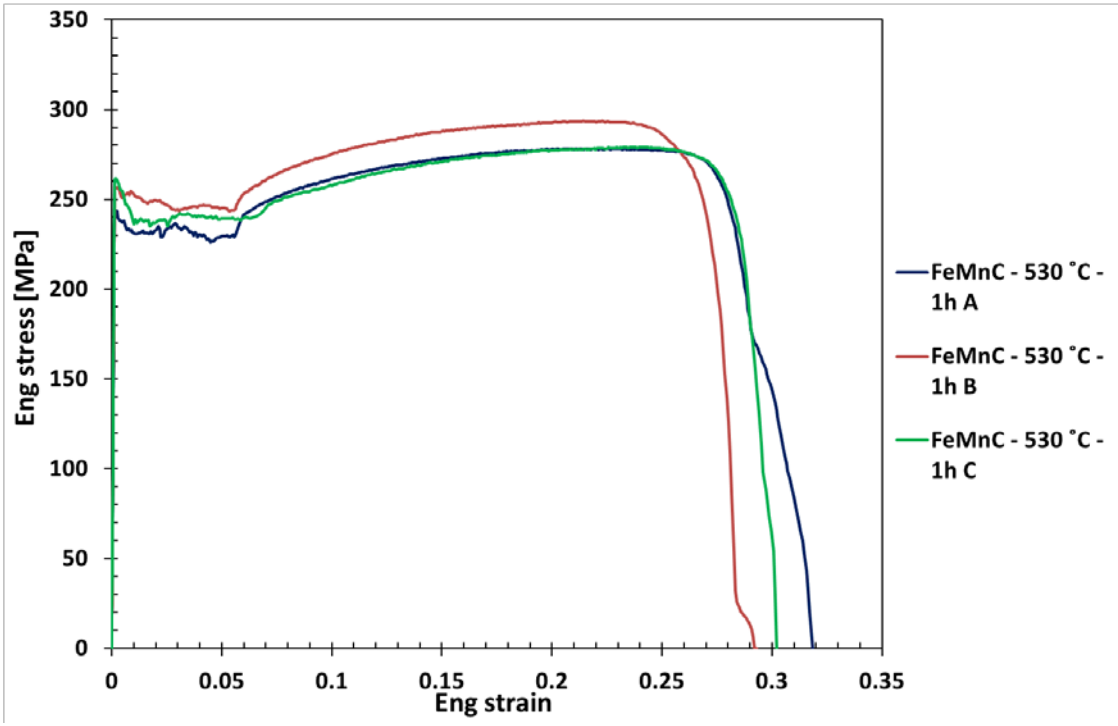

Figure 10-1 - Engineering stress-strain curves of coupons coated both sides with 500 nm thick FeMnC film and annealed at 530 ˚C – 1h in high vacuum

Optical microscope images were recorded during the tensile test of the coupon B annealed at 530 ˚C for 1h in high vacuum and are reported in Figure I. 1 of Appendix I, while a list of mechanical properties extracted from the engineering stress-strain curves are reported in Table I- 1 of Appendix I. For annealing at 530 ºC – 1h in high vacuum (Figure 10-1), an increase of yield stress is recorded with appearance of Lüdering. Figure 10-2 shows the engineering stress-strain curves for coupons annealed in high vacuum at 630 ˚C – 1h, where an increase of yield stress has been obtained; even if this increase of yield strength is at the same level of what was obtained with annealing at 530 ºC. For these specimens, optical microscope images were taken during the tensile test and are reported in Appendix I (Figure I. 2), while the relevant values for the mechanical properties are listed in Table I- 2.

In Appendix I, the mechanical properties of specimens annealed at 1000 ˚C -1 h and the images acquired during the tensile tests are reported in Figure I. 3. The engineering stress-strain curves of specimens annealed at 1000 ˚C – 1h and 1000 ˚C – 10 h are reported in

Figure 10-3 and Figure 10-4 respectively, while the values of mechanical properties for the coupons annealed for 10 h are reported in Table I- 4 of Appendix I.

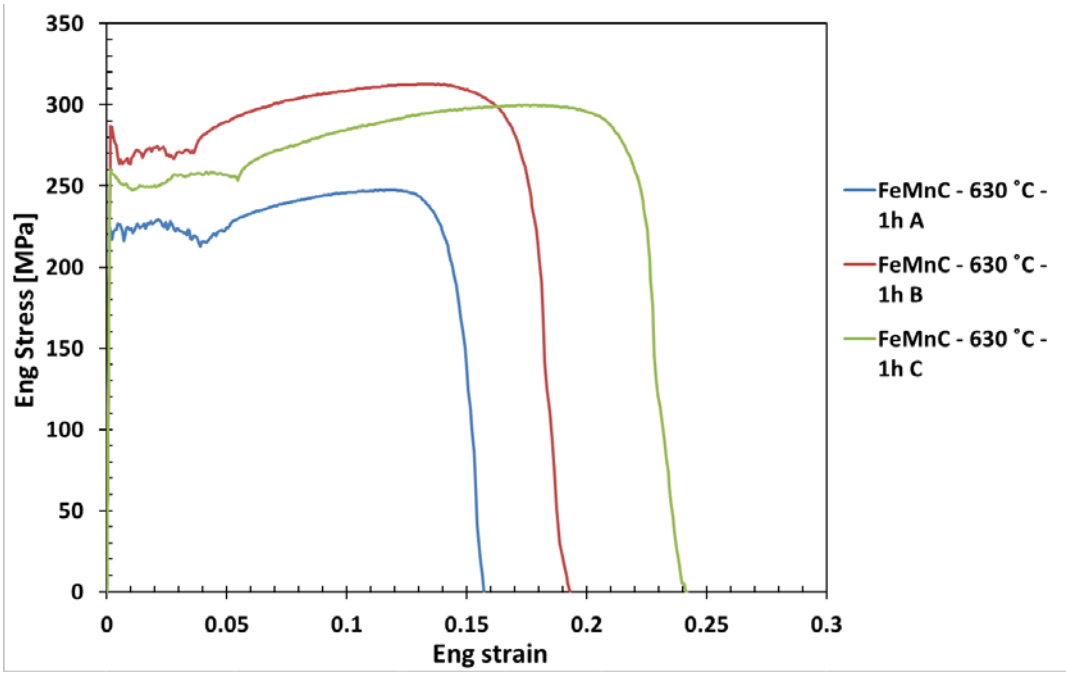

Figure 10-2 - Engineering stress-strain curves of coupons coated both sides with 500 nm thick FeMnC film and annealed at 630 ˚C – 1h in high vacuum

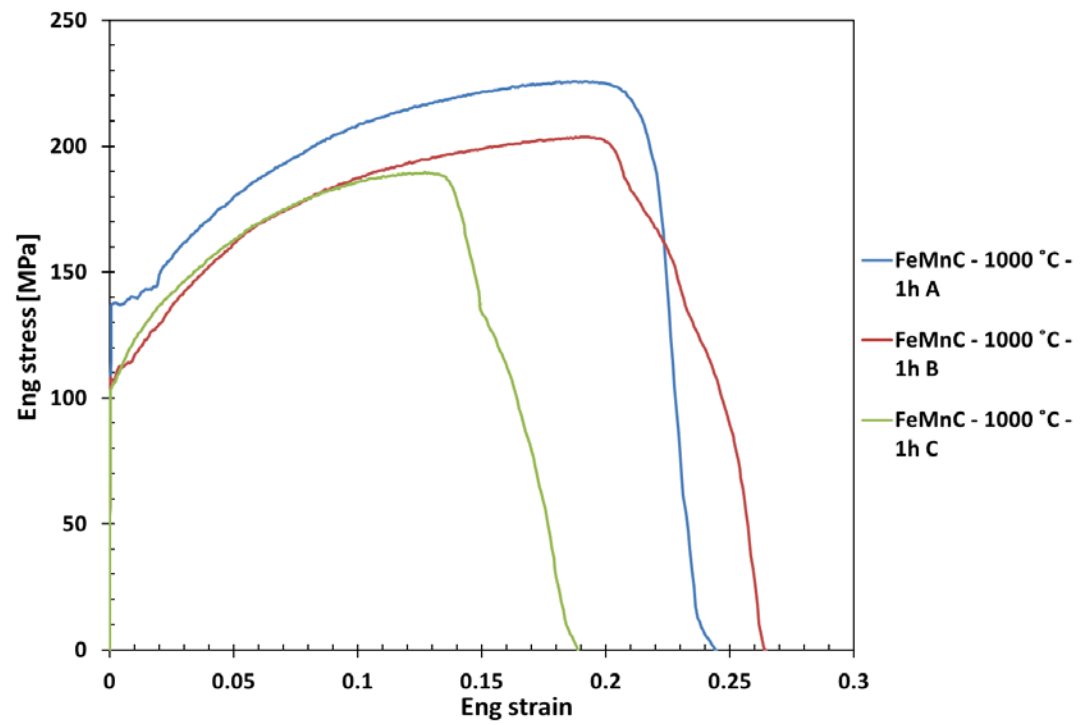

Figure 10-3 - Engineering stress-strain curves of coupons coated both sides with 500 nm thick FeMnC film and annealed at 1000 ˚C – 1h in high vacuum

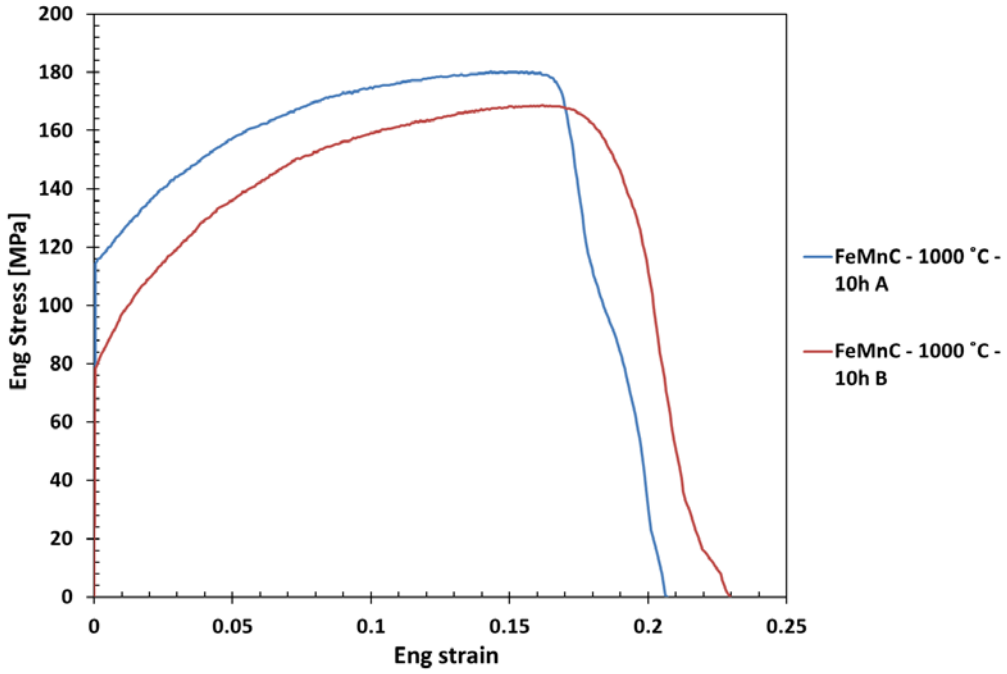

Figure 10-4 - Engineering stress-strain curves of coupons coated both sides with 500 nm thick FeMnC film and annealed at 1000 ˚C – 10h in high vacuum

From Figure 10-3 and Figure 10-4, one can see that annealing at 1000 ºC for 1h or 10h increases only slightly the yield stress, but the ultimate tensile strength (UTS) is highly reduced compared to annealing performed at lower temperatures. The reduction in area was evaluated for one specimen for each condition and the results are reported in Table 10-2.

Annealing condition	Reduction in area (%)
530 ˚C – 1h (sample B)	94.78 %
630 ˚C – 1h (sample B)	92.93 %
1000 ˚C – 1h (sample B)	94.71 %
1000 ˚C – 10h	91%

Table 10-2 - Reduction in area for specimens annealed at different temperatures and time in high vacuum after coating on both sides with 500 nm FeMnC films

The microstructure of one specimen for each temperature was revealed after polishing to a mirror finish followed by etching with 4% vol. Nital solution.

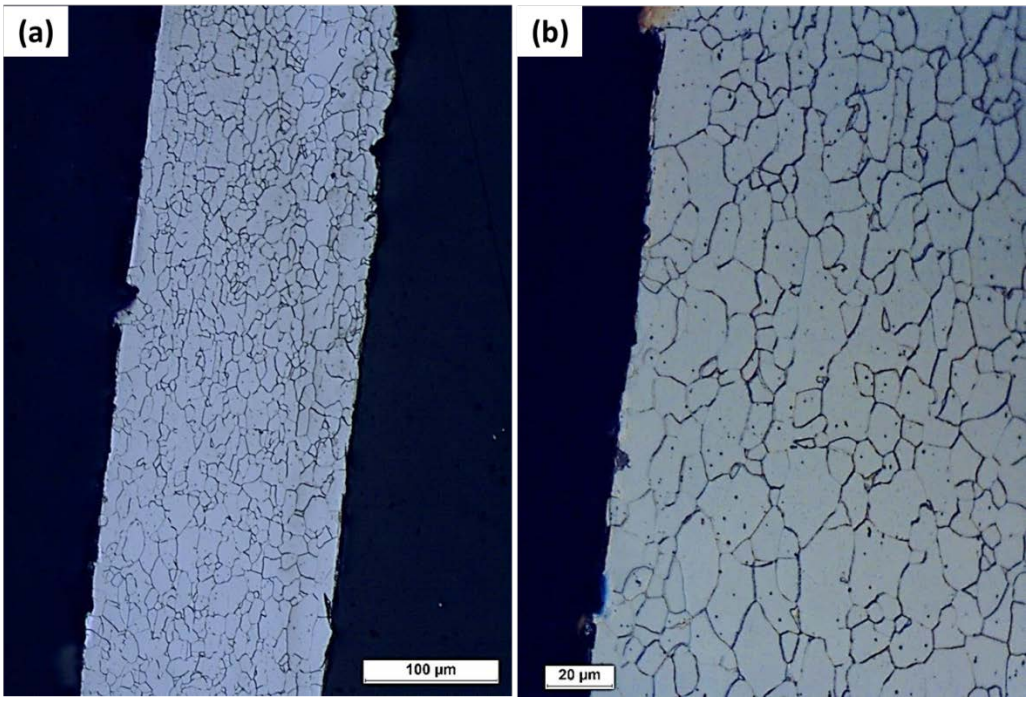

Figure 10-5 - Images of microstructure of tensile coupons A coated on both sides with 500 nm thick FeMnC film and annealed at 530 ˚C – 1h in high vacuum: (a) whole thickness (magnification 20X); (b) closer view at one edge (magnification 50X)

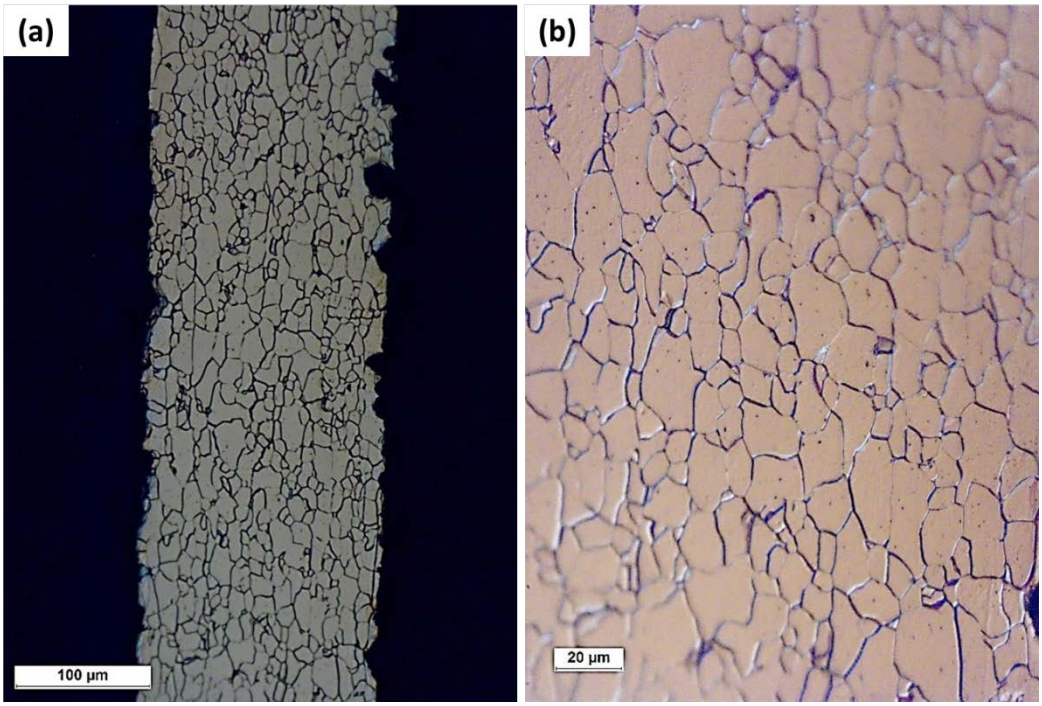

Figure 10-6 - Images of microstructure of tensile coupons B coated on both sides with 500 nm thick FeMnC film and annealed at 630 ˚C – 1h in high vacuum: (a) whole thickness (magnification 20X); (b) closer view (magnification 50X)

From the microstructures shown in Figure 10-5 and Figure 10-6, no grain size change occurs for annealing at 530 ºC and at 630 ºC. On the contrary, when the annealing temperature was raised to 1000 ºC, a significant grain growth was affecting the microstructure of the specimen (Figure 10-7 and Figure 10-8). This grain growth is the result of the specimen being austenitized at 1000 ºC and then transforming back to ferrite during cooling and it is responsible for the lower mechanical properties obtained for this temperature.

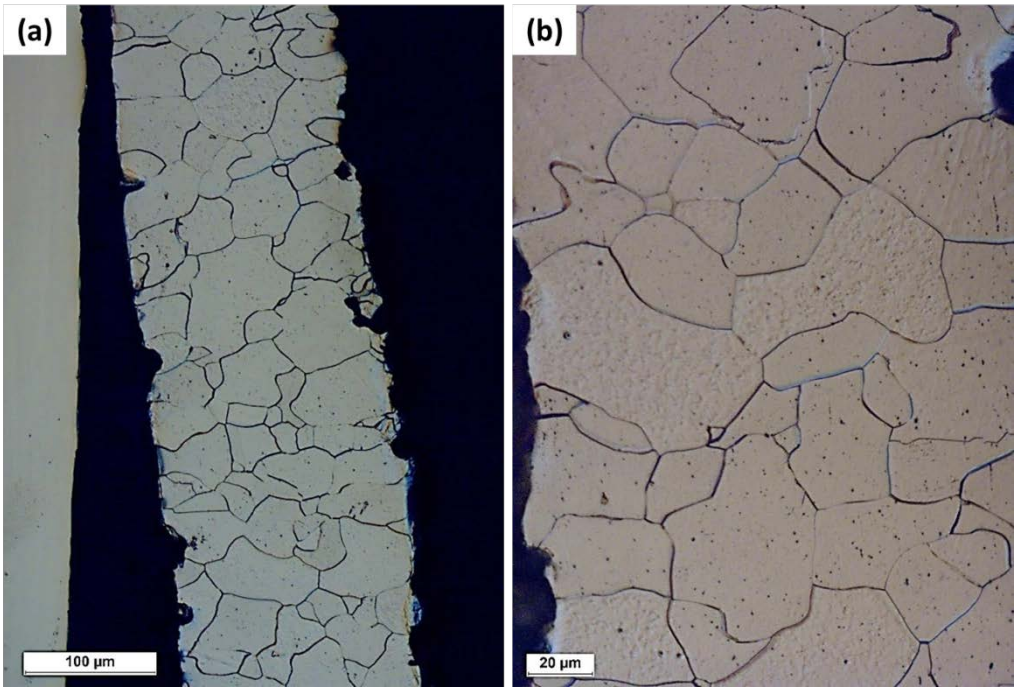

Figure 10-7 - Images of microstructure of tensile coupon B coated on both sides with 500 nm thick FeMnC film and annealed at 1000 ˚C – 1h in high vacuum: (a) whole thickness (magnification 20X); (b) closer view (magnification 50X)

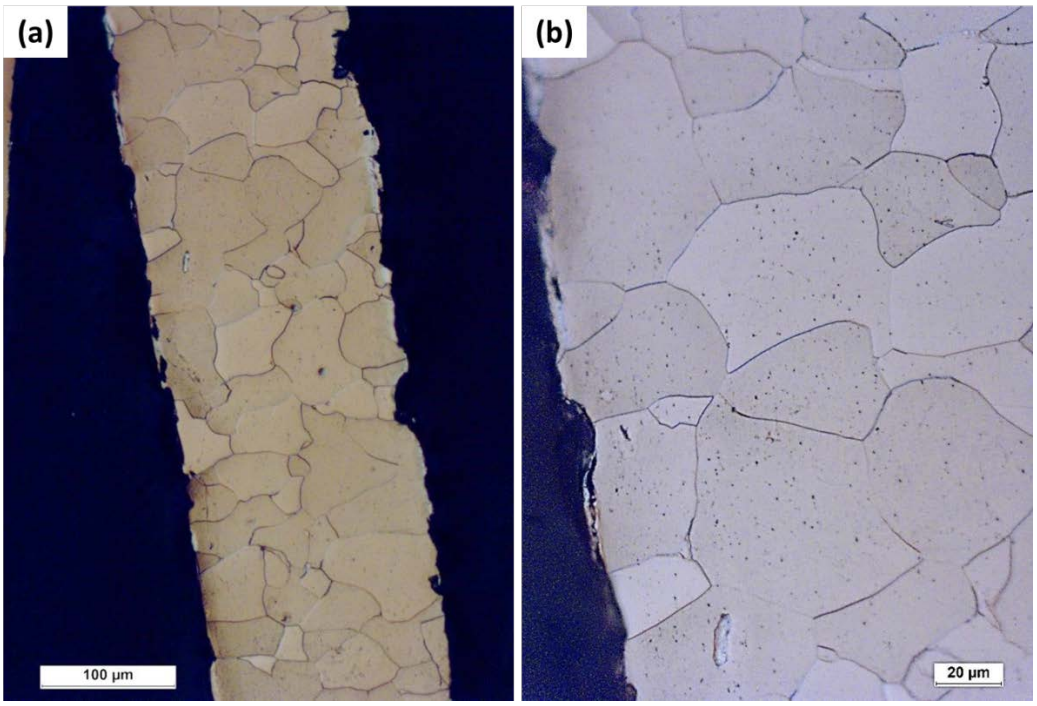

Figure 10-8 - Images of microstructure of tensile coupon A coated on both sides with 500 nm thick FeMnC film and annealed at 1000 ˚C – 10h in high vacuum: (a) whole thickness (magnification 20X); (b) closer view (magnification 50 X)

10.1.3. Discussion of experimental results on FeMnC coated coupons

From the tensile curves presented in the previous paragraph, it is evident that carbon diffusion is occurring at 530 ˚C and at 630 ˚C for 1h and partially also at 1000 ˚C for 1h since Lüders plateau is present on the curves. However, while the mechanical properties obtained for the annealing at 530 ˚C -1h are in the same range of the properties obtained for coupons coated with FeC films; yield stress and UTS of annealing at 630 ˚C -1h are lower than the properties of coupons coated with FeC films. Moreover, the coupon A annealed at 630 ˚C – 1h seems to have lower properties compared to the others, which could be justified by a non-uniform coating of the specimen or by a lower carbon content compared to the expected nominal content. Table 10-3 briefly summarizes the average values of mechanical properties obtained with FeC coatings and FeMnC coatings.

Annealing	FeC film		FeMnC film	
	Yield stress [MPa]	UTS [MPa]	Yield stress [MPa]	UTS [MPa]
530 ˚C – 1h	259	310	255	284
630 ˚C – 1h	306	337	257 (274 without specimen A)	287 (307 without specimen A)

Table 10-3 - Comparison of mechanical properties obtained from FeC films and FeMnC films

From the previous table, it is clear that mechanical properties using FeMnC films are lower than the one obtained using FeC films. From these first results it can be concluded that annealing at 500 or 600 ˚C for 1h is not enough to diffuse any manganese into the IF substrate. Moreover, the presence of manganese seems to limit even further the amount of carbon that can be diffused into the substrate.

The coefficient of diffusion of manganese into bcc iron is described by the following equation [213]:

$$D = \left(3.5\times10^{-5}\, m^2/s\right)\times\exp\left(-\frac{\left(52.5\times10^3\, cal/mol\right)}{\left(8.31\, J/mol\times K\right)\times\left(T\right)}\right) \qquad \text{(eq. 110-1)}$$

and converting cal into Joule (1 J = 0.239 cal):

$$D = \left(3.5\times10^{-5}\, m^2/s\right)\times\exp\left(-\frac{\left(219.67\times10^3\, J/mol\right)}{\left(8.31\, J/mol\times K\right)\times\left(T\right)}\right) \qquad \text{(eq. 110-2)}$$

Using this diffusion coefficient expression, the value of diffusion coefficient for Mn into bcc iron for annealing temperatures of 530 ˚C and 630 ˚C can be calculated and used to evaluate the penetration depth of Mn into the substrate of IF steel by using the equation $x = \sqrt{Dt}$ presented in Appendix G. In order to estimate the diffusion of Mn which could occur through grain boundaries, the diffusion coefficient will be increased by three orders of magnitude, since in literature it has been suggested that diffusion at grain boundaries is 3 or 4 order of magnitude faster than through the bulk, at least for interstitial elements such a carbon [18]. However, as first approximation, we could consider that the same holds for substitutional atoms.

Annealing	D [m^2/s]	Depth [µm]	D (grain boundary diffusion) [m^2/s]	Depth for diffusion of Mn through grain boundaries [µm]
530 ˚C – 1h	1.77×10^{-19}	0.025	1.77×10^{-16}	0.8
630 ˚C – 1h	6.77×10^{-18}	0.16	6.77×10^{-15}	4.94

Table 10-4 - Diffusion depth of manganese during annealing of FeMnC coated IF steel annealed at 530 ˚C and 630 ˚C for 1h in high vacuum

As it can be seen from the values reported in Table 10-4, the diffusion of manganese both through the bulk and through grain boundaries can be considered negligible for both annealing conditions.

For annealing at 1000 ˚C, the microstructure of IF steel is fully transformed into austenite during the heat treatment and the diffusion of both carbon and manganese will occur in austenite. Even if carbon has a higher solubility into austenite, its diffusion is slower in this phase and this is one reason justifying the lower mechanical properties obtained for high temperature annealing. Moreover, the substrate experiences a high grain growth suggesting that the few amount of diffused carbon at grain boundaries cannot limit grain growth and results in low UTS as shown in the engineering stress-strain curves. The diffusion depth of manganese after annealing at 1000 ˚C for 1h and at 1000 ˚C for 10h can be calculated using the diffusion coefficient of manganese into austenite. According to literature, the diffusion coefficient of Mn into austenite is given by the following equation [214]:

$$D = \left(0.16\, cm^2/s\right)\exp\left(-\frac{\left(261.7\times10^3\ J/mol\right)}{\left(8.31\, J/mol\times K\right)\times\left(T\right)}\right) \qquad \text{(eq. 110-3)}$$

which converted into m^2/s becomes:

$$D = \left(1.6\times10^{-5}\, m^2/s\right)\exp\left(-\frac{\left(261.7\times10^3\ J/mol\right)}{\left(8.31\, J/mol\times K\right)\times\left(T\right)}\right) \qquad \text{(eq. 110-4)}$$

Annealing	D [m^2/s]	Depth [µm]	D (grain boundary diffusion) [m^2/s]	Depth for diffusion of Mn through grain boundaries [µm]
1000 ˚C – 1h	2.89×10^{-16}	1	2.89×10^{-13}	32
1000 ˚C – 10h	2.89×10^{-16}	3.22	2.89×10^{-13}	102

Table 10-5 - Diffusion depth of manganese during annealing of FeMnC coated IF steel annealed at 1000 ˚C for 1h and for 10h in high vacuum

From Table 10-5 it can be seen that even the diffusion of manganese through austenite is quite slow and the annealing time to obtain a relevant concentration of Mn into the IF steel can become very long and not satisfactory for the production rates required by steel companies. The values of strain-hardening exponents were calculated for the different annealing temperatures and times and are reported in Table 10-6.

Sample	Strain hardening exponent (n)	Strain range (%)
IF steel – not annealed	0.29	2 - 28
530˚C-1h – FeMnC-A	0.81	5.4 – 5.8
	0.23	5.87 – 18.7
530˚C-1h – FeMnC-B	0.64	5.4 – 5.7
	0.23	5.7 – 19.4
530˚C-1h – FeMnC-C	0.34	6.1 – 7.1
	0.24	7.2 – 21
630˚C-1h – FeMnC-A	0.41	4.87 – 5.2
	0.18	5.3 – 11
630˚C-1h – FeMnC-B	0.51	3.5- 3.8
	0.16	3.87 – 12.2
630˚C-1h – FeMnC-C	0.5	5.3 – 5.8
	0.23	5.86 – 16
1000˚C-1h – FeMnC-A	0.27	1.9 – 17.5
1000˚C-1h – FeMnC-B	0.29	2.1 – 17.4
1000˚C-1h – FeMnC-C	0.23	0.5 – 12
1000˚C-10h – FeMnC-A	0.21	1 – 13.4
1000˚C-10h – FeMnC-B	0.28	0.81 15.1

Table 10-6 - Strain–hardening exponents values evaluated for FeMnC coated tensile coupons

From Table 10-6 it can be concluded that for specimens having a marked Lüders plateau (annealing at 530 ˚C and 630 ˚C for 1h), the strain hardening exponent has a “double-n behaviour”. In particular, n has a high value for the plastic deformation which occurs at the

end of the Lüders plateau due to the high density of dislocations created by the Lüders propagation. At higher strains, the n value decreases. For specimens with short Lüders plateau (specimens A and B annealed at 1000 ˚C for 1h) or without Lüders plateau (specimens A and B annealed at 1000 ˚C for 10h), there is only one n value which is close or equal to the strain-hardening exponent of an uncoated not-annealed IF steel. Specimens having a large grain size (annealing at 1000 ˚C – 1h and 1000 ˚C – 10h) have shorter plateau since the propagation of the dislocations is facilitated by the smaller amounts of grain boundaries present in the microstructure.

Moreover, the crystallization of the film plays an important role in the diffusion of the elements into the IF substrate (as was already shown in chapter 5 for the diffusion of carbon from FeC films). From preliminary TEM in-situ annealing experiments performed by the University of Rouen in collaboration with INSA Lyon, it was shown that the FeMnC film crystallizes already at 360 ˚C and after 5 minutes it is fully crystallized. Pictures of the as deposited film and of the film annealed in-situ in TEM are shown in Figure 10-9 and Figure 10-10 respectively.

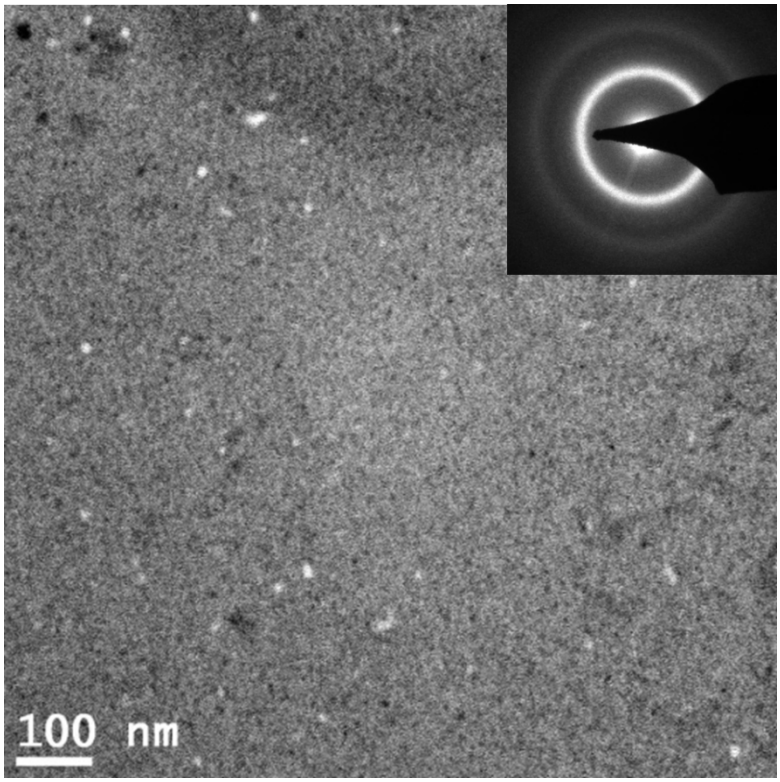

Figure 10-9 - TEM image and SAED pattern of as-deposited FeMnC film

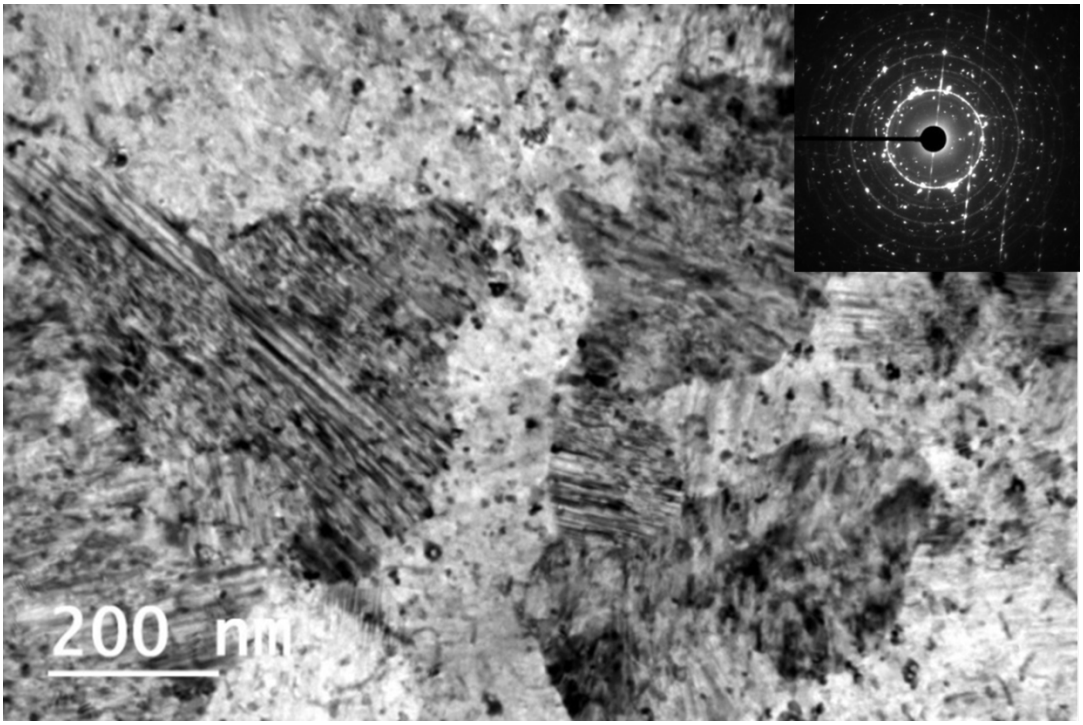

Figure 10-10 - TEM image and SAED pattern of FeMnC film at 360 ˚C after 5 minutes

In conclusion, this first attempt at diffusing a solute element, such as manganese, using PVD films was not successful. However, it is believed that other annealing technique (such as induction heating) would be worth investigating. The high heating rate of induction heating might promote diffusion of the elements before the film itself crystallizes.

10.2. Carbon films

As was shown in Chapter 5, the crystallization of FeC films limits the amount of carbon available to be diffused towards the IF substrate. For this reason, an investigation on whether higher carbon diffusion could be obtained using films containing only carbon was carried out.

FeC films with higher carbon content were tested, however, for carbon concentrations above 50% the 500 nm thick FeC films are no longer metallic in appearance and were not adherent to the IF substrate compromising carbon diffusion (discussion with Dr. C.P. Scott). However, it is believed that good mechanical properties could be obtained for thinner films containing 100% of carbon. A first trial was made during this PhD thesis.

One tensile coupon of IF steel was coated on one side with a 100-150 nm thick carbon film applied using an evaporator. The specimen was annealed in air at 530 ˚C -1h. Its mechanical properties were compared with the mechanical properties obtained for annealing in air at 530 ˚C-1h of a coupon coated both sides with 500 nm thick FeC film and with the mechanical properties of a one side coated coupon annealed at 530 ˚C -1h in high vacuum. The engineering stress-strain curves are reported in Figure 10-11.

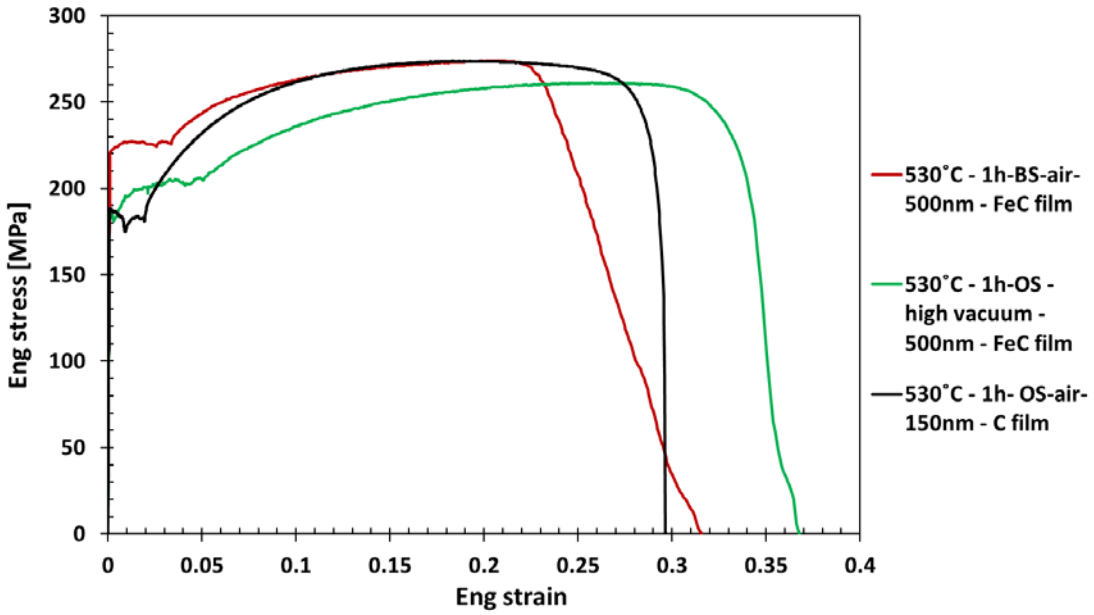

Figure 10-11 - Comparison of mechanical properties of a coupon coated one side (OS) with 150 nm amorphous carbon film with mechanical properties obtained for one side coated coupon (OS) with 500 nm FeC film and annealed in high vacuum. The curve for annealing in air at 530 ˚C – 1h of a both sides (BS) coated coupon with 500 nm thick FeC film is also reported

Sample	Upper Yield Stress [MPa]	Lower Yield Stress [MPa]	Average stress in Lüders plateau [MPa]	Lüders length	Ultimate Tensile Stress (UTS) [MPa]	Strain at fracture (ε_B)
530 ˚C – 1h air - 150 nm-OS 100% carbon	189	181	183	0.01852	274	0.3
530 ˚C – 1h high vacuum -500 nm-OS FeC (30at% carbon)	187	205	199	0.04974	261	0.37
530 ˚C – 1h air-500 nm-BS FeC (30at% carbon)	221	226	226	0.03237	274	0.31

Table 10-7 - Mechanical properties of tensile coupons coated one side with 150 nm thick carbon film annealed in air at 530 ˚C – 1h. Mechanical properties obtained with FeC films are reported for comparison

It can be seen from Figure 10-11, that with only a 150 nm thick film containing 100% of carbon, an increase of yield stress of up to 188.7 MPa after annealing in air at 530 ˚C for 1h can be obtained. This yield stress is close to what was obtained for a one side coated coupon annealed in high vacuum having a 500 nm FeC film with 30 at% of carbon. The advantage of having a film which could be 100% carbon should be further investigated. However, it should be verified that thicknesses higher than 150 nm would not compromise, the adhesion with the IF substrate.

It should be noted that only one tensile coupon was tested and that further tests should be performed to confirm the reproducibility of the results.

Another important aspect to take into consideration is the structure of a film containing 100% of carbon since it is very important that it is fully amorphous, otherwise if crystalline phases of carbons are formed during deposition, they may prevent carbon diffusion into the IF substrate.

Moreover, it should be considered that films containing 100% of carbon might not be suitable for packaging applications involving carbonated beverages and food in order to not alter their taste. However, 100% carbon films could be used to strengthen IF steels for automotive application so their research deserves some attention.

Chapter 11 : Conclusions and Future Work

11.1. Conclusions

The work presented in this thesis has investigated the use of FeC films as an alternative to traditional carburizing treatments and bake hardening processes used to strengthen Ultra Low Carbon (ULC) steel sheets. In chapters 5, 6 and 7, the influence of annealing temperature, annealing environment, film thickness and pre-strain was investigated. In chapter 6, FEM analyses related to Lüdering were reported with possible solutions to limit plastic instability. The main results presented in those chapters are summarized here:

- FeC films containing 30 at% of carbon can be effectively used to diffuse carbon at temperatures lower than 730 ˚C with an annealing time of 1h;
- At 330 ˚C – 1h no increase of yield stress was recorded since the diffusion of carbon is not fast enough. However above 400 ˚C the diffusion started to occur causing an increase of yield stress.
- Using a 1D solution to Fick's second law, it is possible to estimate the carbon diffused for a given annealing temperature and time and the theoretical yield stress can be calculated. However, these predictions are accurate only up to 530 ˚C -1h. Large deviations from the expected values were obtained for annealings at 630 ˚C and 710 ˚C – 1h. The deviation from the expected yield stress at 630 ˚C was related to the crystallization of the FeC film into Fe_3C, while the lower yield stress obtained for the temperature of 710 ˚C was related both to film crystallization and to precipitation of carbon causing a coarsening of TiC carbides or the transformation of TiS particles into $Ti_4C_2S_2$. Taking these effects into account in the model provided better agreement with the experimental results.
- The best mechanical properties in terms of yield strength and UTS were obtained for both sides coated coupons annealed in high vacuum;
- The minimum FeC film thickness to ensure some strengthening is 200 nm for films with 30 at% of carbon deposited on each side of the IF sheet and annealed in the vacuum furnace for 1h;
- If 500 nm thick FeC films are applied on 15% pre-strained IF steel, the increase of yield stress is lower than for not-prestrained coupons. This is due to Cottrell

atmospheres being less carbon dense which prevents the start of the precipitation stage close to the dislocations. All stress-strain curves have smooth Lüders plateau since dislocations are easier to unpin if the carbon atmosphere around them is less dense. It was also noticed that the IF sheet should be prestrained before applying the FeC film otherwise it will exfoliate from the coupon compromising carbon diffusion.

- From strain-ageing experiments it was possible to separate the contribution to strengthening coming from the formation of Cottrell atmosphere and from precipitation and grain boundary segregation. In particular, Cottrell atmosphere formation is giving high contribution to strengthening at 430 ºC since it represents 34% of the total strengthening obtained at this temperature. By increasing the annealing temperature, the contribution due to precipitation increases, while strengthening due to Cottrell atmosphere remains unchanged. So for annealing at 530 ºC or 710 ºC, strengthening due to Cottrell atmosphere represents 21% of the total strength, while 79% is due to precipitation and carbon segregation at grain boundaries. For annealing at 630 ºC, the contribution of Cottrell atmosphere represents only 16% of the total strength, while the remaining is due to precipitation.
- In chapter 6 it was shown that to limit Lüdering it is better to have a gradient of carbon instead of a uniform carbon content through thickness. Increasing the strain hardening also helps in reducing or even suppressing Lüdering. The same holds when the IF sheets with Lüdering are coupled with a central material having no plastic instability. Young's modulus of the central layer has a small influence on the Lüders plateau length, except if the elastic modulus of the central layer is lower than that of the outer layers since in this case, there is a delay in the start of the plastic instability;
- Void interspacing did not show any marked influence on the length of the Lüders plateau, however increasing the voids volume fraction will trigger the start of the Lüders bands at the voids.

In another section of this thesis, the possibility of obtaining a graded structure through the thickness of IF sheets was investigated. A gradient of microstructure ranging from martensite or bainite close to the coated side of the sheet to ferrite close to the uncoated side of the sheet would be ideal. To obtain these graded microstructure it was necessary to set-up

a “flash annealing” procedure which would ensure fast heating rates to limit FeC crystallization plus a rapid quenching in water to obtain eventually martensite or bainite. In chapter 8, the results obtained by using induction heating were presented. Induction heating is a very efficient heating process which turns out to be ideal for diffusing carbon from the FeC films. The main results obtained from induction heating coupled with rapid quenching in water are the following:

- For a one side coated coupon, it was possible to obtain a high hardness gradient through thickness. The hardness of the grains close to the coated surface is similar to the one found in the case of carbides precipitation, while the hardness of the uncoated side is at the same level of an uncoated IF steel;
- In just one minute of heat treatment at 820 ˚C for a both sides coated coupon after it has been austenitized at 1150 ˚C for 1 second, an increase of yield stress equal to the one obtained in the high vacuum furnace for annealing at 530 ˚C – 1h was achieved;
- For one side and both sides coated coupons, the maximum strength is obtained for induction heating of 2 minutes at 820 ˚C, while for 4 minutes, the increase of yield stress is lower than for the 2 minutes treatment but the Lüdering is fully suppressed. If the annealing time is raised up to 8 minutes, Lüdering reappears and the yield stress comes back to the same level found for the 1 minute heat treatment. From etching of the microstructure it was found that after 1 minute carbon is mainly at grain boundaries causing carbides precipitation during quenching. The high strength obtained for the 2 minutes annealing was related to the precipitation of fine lines of carbides inside the grains. These lines of carbides create different etching responses inside the grains and some lines were noticed after etching of the microstructure. However, it was excluded that these lines are due to the magnetic field since its intensity is not strong enough to change the Gibbs free energy for the transformation of austenite into ferrite. At 4 minutes the increase of yield strength compared to an uncoated IF steel is 110 MPa, which is lower than the increase of 257 MPa obtained for the 2 minutes of induction heating. However, the mechanical properties of the specimen induction heated for 4 minutes are of particular interest since Lüdering is suppressed. From EBSD and TEM analyses no clear difference could be discerned between the specimen induction heated for 2 minutes and the one induction heated

for 4 minutes. However, the suppression of Lüdering is caused by a full precipitation of carbon or by the presence of a higher density of mobile dislocations. If the heat treatment is prolonged for 8 minutes, Lüdering appears again and an increase of yield strength of 148 MPa compared to an uncoated IF steel is obtained. The appearance of Lüdering means that some carbon is again available at dislocations, however, no clear justification for this to happen was found.

In chapter 9 the influence of carbon gradient on void growth was studied to understand the influence of yield stress gradient on void growth. Two procedures to obtain a carbon gradient through the gauge length of a tensile coupon and through the width of a tensile coupon were established. From the results on void growth on specimens having a gradient along the gauge length, fracture always occurred on the zone having no carbon. If the change in the main diameter of the void is plotted against the true far field strain extracted from the whole gauge length, the voids placed in the carbon containing zone where shown to grow more slowly than voids placed in a no carbon-containing zone since the deformation was localized in the couple of voids that were in zones without carbon. This couple of voids will then be the one failing. McClintok was able to fit well void growth for uncoated specimens and for specimens having a uniform carbon distribution along the gauge length but it was not able to fit well the growth for specimens having a carbon gradient. This is mainly due to the fact that for these coupons, the deformation is not uniform along the gauge length, due to a double yielding behaviour, so the zone where no carbon has diffused will deform earlier than the zone where carbon has been diffused.

For specimens having a carbon gradient through the width, fracture occurred on the voids placed in the zones having high carbon gradient. If no Lüders bands was nucleating at the voids or coalescing at the voids, then there was a gradient in void growth. In particular, the voids placed in the carbon containing zones grew faster than the voids placed in the no carbon zones. However, if bands were nucleated or coalesced at the voids, then the high strain field associated to their front cancelled out void growth differences.

11.2. Future Work

Several aspects of this work deserving more research efforts are highlighted. First of all, the possibility of diffusing carbon from fully amorphous FeC films having carbon amounts

higher than 30 at% deserve some attention. The diffusion of carbon from amorphous films containing 100 at% of carbon is of particular interest. Indeed, films containing 100% of carbon would not undergo crystallization, leaving most of the carbon available for diffusion towards the IF substrate, moreover, they would not require the level of control which is required for the deposition of FeC films. However, it must be ensured that the adhesion between film and IF substrate is good enough to obtain diffusion, so probably only films thinner than 500 nm could be used, while still allowing enough carbon to diffuse.

Induction heating should also be further investigated, in particular, TEM on the specimens induction heated for 1 minute and 8 minutes could be performed to better relate mechanical properties with the microstructure. Moreover, the diffusion process could be modeled considering the transformation of austenite into ferrite to predict how much carbon can be diffused into the IF substrate during induction heating. It would be worth trying induction heating on coupons coated with 100 at% carbon coating since a lot of carbon could be diffused into the IF sheet and after quenching the whole structure could be martensitic; if the IF sheet is coated only on one side, then a high gradient of microstructure ranging from martensite to ferrite could be obtained. Induction heating could also be used on IF steels containing a high amount of silicon since additions of this element can suppress cementite precipitation and favour the formation of retained austenite [215].

Concerning the experimental study of yield stress and microstructure gradient on void growth, two main topics deserve investigation:

- The procedure of laser ablation presented in chapter 9 could be used to produce other coupons having the carbon coating only in selected zones of the gauge length. After ablation, the coupons could be induction heated and quenched to form bainite or martensite in the coated zones and ferrite in the uncoated zones. Voids can be placed in those zones and the growth is expected to be markedly influenced by the high difference in yield stress between the two phases;
- Void growth could be experimentally studied on specimens having a gradient of strain hardening;
- A further idea is the study of fracture on layered structures obtained using diffusion bonding techniques. In particular, the proposal is to couple titanium and alpha iron doing diffusion bonding to increase the adhesion between the two different materials

(this type of layered structures have already been obtained in literature [216], [217], [218], [219], [220], [221], [222] but no fracture study has been performed). A die can be used to diffusion bond sheets of titanium and IF steel or Armco Iron. This gradient will be present in the thickness of tensile coupons and then pattern of holes can be lased with femtosecond laser on the width. The main objective would be to understand how fracture propagation is influenced not only by the gradient of materials but also by the fact that the two materials will have different crystalline structures.

Bibliography

[1] Gasik, Michael M., "Industrial Applications of FGM solutions," *Material Science Forum,* Vols. 423-425, pp. 17-22, 2003.

[2] Shinohara, Yoshikazu, "Functionally Graded Materials", *Handbook of Advanced Ceramics Materials, Applications, Processing and Properties*, (Chapter 11.2.4), Copyright © 2013 Elsevier Inc. pp. 1179-1187.

[3] Lidong Chen, Takashi Goto, "Functionally Graded Materials," in *Handbook of Advanced Ceramics,* S. Sōmiya et al. (Eds) (2003) pp. 445-464 (Chapter 16).

[4] Nabih Cherradi, Akira Kawasaki, Michael Gasik, "Worldwide trends in functional gradient materials research and development," *Composites Engineering,* vol. 4, no. 8, pp. 883-894, 1994.

[5] Koizumi, M., "FGM Activities in Japan," *Composites Part B,* vol. 28B, pp. 1-4, 1997.

[6] Suresh S., Mortensen A., Fundamentals of Functionally Graded Materials: Processing and Thermomechanical behaviour of graded metals and Metal-Ceramic Composites, IOM Communications Ltd.

[7] Jerzy J. Sobczak, Ludmil Drenchev, "Metallic Functionally Graded Materials: a specific class of advanced composites," *J. Mater. Sci. Technol.,* vol. 29, no. 4, pp. 297-316, 2013.

[8] A.Mortensen, S.Suresh, "Functionally graded metals and metal-ceramic composites: Part 1 Processing," *International Materials Reviews,* vol. 40, no. 6, pp. 239-265, (1995), copyright © The Institute of Materials, Minerals and Mining.

[9] Limin Chen, Walter Lengauer, peter Ettmayer, Klaus Dreyer, Hans W. Daub, Dieter Kassel, "Fundamentals of liquid phase sintering for modern cermets and functionally graded cemeted carbonitrides (FGCC)," *International Journal of Refractory Metals and Hard Materials,* vol. 18, pp. 307-322, 2000.

[10] D. Asmi, I.M. Low, "Infiltration and physical characteristics of functionally graded alumina/calcium-hexaluminate composites," *Journal of Material Processing Technology,* vol. 118, pp. 225-230, 2001.

[11] Y. Zhang, J. Han, X. Zhang, X. He, Z. Li, S. Du, "Rapid prototyping and combustion synthesis of TiC/Ni functionally gradient materials," *Materials Science and Engineering A,* vol. 229, pp. 218-224, 2001.

[12] S. Eroglu, N.C. Birla, M. Demirci, T. Baykara, "Synthesis of functionally gradient NiCrAl/MgO-ZrO2ccoating by plasma spray technique," *Journal of Material Science Letters,* vol. 12, pp. 1099-1102, 1993.

[13] L.J. Baker, S.R. Daniel, J.D. Parker, "Metallurgy and processing of ultralow carbon bake hardening steels," *Materials Science and Technology,* vol. 18, pp. 355-368, April 2002.

[14] Campbell, F.C., Elements of Metallurgy and Engineering Alloys, ASM International-The Materials Information Society.

[15] Callister, W., "Materials Science and engineering: a introduction", NewYork, John Wiley and Sons, 2007.

[16] Wilkinson, David S., Mass Transport in Solids and Fluids, Cambridge University Press.

[17] Homan, C.G., "Diffusion of carbon in Alpha Iron," *Acta Metallurgica,* vol. 12, September 1964.

[18] S.Z. Bokshtein, M.A. Gubareva, I.E. Kontorovich, L.M. Moroz, "Peculiarities of the Diffusion of Carbon in Iron", *Metal Science and Heat Treatment of Metals,* Vol. 3(1), pp 6-9, 1961.

[19] Wert, C.A., "Diffusion Coefficient of C in alpha-iron," *Physical Review,* vol. 79, no. 4, pp. 601-605.

[20] C. Wert, C. Zener, "Interstitial Atomic Diffusion Coefficients," *Physical Review,* vol. 76, no. 8, pp. 1169-1175.

[21] R.H. Doremus,, "The Diffusion of Carbon during Precipitation in alpha-iron," *Acta Metallurgica,* vol. 7, pp. 399-402, June 1959.

[22] A.E. Lord, Jr., "Ultrasonic Determination of the Diffusion Coefficient of Carbon in alpha-iron at 408C and 430C," *The Journal of the Acoustical Society of America,* vol. 45, no. 6, pp. 1382-1384, 1969.

[23] R.B. McLellan, M.L. Wasz, "Carbon Diffusivity in BCC Iron," *J. Phys. Chem. Solids,* vol. 54, no. 5, pp. 583-586, 1993.

[24] Bhadeshia, H.K.D.H., "Carbon-carbon interactions in iron," *Journal of Materials Science,* vol. 39, pp. 3949-3955, 2004.

[25] D.E. Jang, Emily A. Carter, "Carbon dissolution and diffusion in ferrite and austenite from first principles," *Physical Review B,* vol. 67, 2003.

[26] Agren, J., "Computer Simulations of the Austenite/Ferrite diffusional transformations in low

alloyed steels," *Acta Metallurgica,* vol. 30, pp. 841-851, 1982.

[27] V. Rebischung, C. Scott, "Durcissement des Toles Minces par Revetements Carburisantes," USINOR Reserche et developpement (CMC-IRSID).

[28] Rex B. McLellan, Pavel Chraska, "Thermodynamics of Iron-Carbon Solid Solutions," *Mater. Sci. Eng.,* vol. 7, pp. 305-317, (1971).

[29] P.R. Wilson, Z. Chen, "TEM characterization of iron titanium sulphide in titanium- and niobium- containing low manganese steel," *Scripta Materialia,* vol. 56, pp. 753-756, 2007.

[30] J. Merlin, P. Merle, S. Garnier, M. Bouzekri, M. Soler, "Experimental Determination of the Carbon Solubility Limit in Ferritic Steels," *Metallurgical and Materials Transactions A,* vol. 35A, pp. 1655-1661, June 2004.

[31] Hajime Saitoh, Kohsaku Ushioda, Naoki Yoshinaga, Wataru Yamada, "Influence of substitutional atoms on the solubility limit of carbon in bcc iron," *Scripta Materialia,* vol. 65, pp. 887-890, 2011.

[32] N. Lavaire, Veronique Massardier, J. Merlin, "Quantitative evaluation of the interstitial content (C and/or N) in solid solution in extra-mild steels by thermoelectric power measurements," *Scripta Materialia,* vol. 50, pp. 131-135, 2004.

[33] Gladman, T., The Physical Metallurgy of Microalloyed Steels, ©The Institute of Materials (1997).

[34] Shyi-Chin Wang,, "The effect of Titanium and Nitrogen contents on the microstructure and mechanical properties of plain carbon steels," *Materials Science and Engineering A,* vol. 145, pp. 87-94, 1991.

[35] M.Hua, C.I. Garcia, A.J. DeArdo, "Precipitation behavior in Ultra-Low-Carbon Steels containing Titanium and Niobium," *Metallurgical and Materials Transactions A,* vol. 28A, pp. 1769-1780, September 1997.

[36] S. Carabajar, J. Merlin, V. Massardier, S. Chabanet, "Precipitation evolution during the annealing of an interstitial-free steel," *Materials Science and Engineering A,* vol. 281, pp. 132-142, 2000.

[37] R. Rodriguez, I. Gutierrez, "Correlation between nanoindentation and tensile properties influence of the indentation size effect," *Materials Science and Engineering A,* vol. 361, pp. 377-384, 2003.

[38] J.A. Ruud, T.R. Jervis, F. Spaepen, "Nanoindentation of Ag/Ni multilayered thin films," *J. Appl.*

Phys., vol. 75, no. 10, pp. 4969-4974, 15 May 1994.

[39] Linmao Qian, Mong Li, Zhongrong Zhou, Hui Yang, Xinyu Shi, "Comparison of nanoindentation hardness to microhardness," *Surface and Coatings Technology,* vol. 195, pp. 264-271, 2005.

[40] B. Yang, H. Vehoff, "Dependence of nanohardness upon indentation size and grain size-A local examination of the interaction between dislocations and grain boundaries," *Acta Materialia,* vol. 55, pp. 849-856, 2007.

[41] E. Rayon, V. Bonache, M.D. Salvador, J.J. Roa, E. Sanchez, "Hardness and Young's Modulus distributions in atmospheric plasma sprayed WC-Co coatings using nanoindentation," *Surface & Coatings Technology,* vol. 205, pp. 4192-4197, 2011.

[42] P. Lemoine, J.P. Quinn, P. Maguire, J.A. McLaughlin, "Comparing hardness and wear data for tetrahedral amorphous carbon and hydrogenated amorphous carbon thin films," *Wear,* vol. 257, pp. 509-522, 2004.

[43] Ali Nazari, Jamshid Aghazadeh Mohandesi Saeed Tavareh, "Microhardness profile prediction of a graded steel by strain gradient plasticity theory," *Computational Materials Science,* vol. 50, pp. 1781-1784, 2011.

[44] S. Suresh, A.E. Giannakopoulos, J. Alcala', "Spherical Indentation of Compositionally Graded Materials: Theory and Experiments," *Acta Materialia,* vol. 45, no. 4, pp. 1307-1321, 1997.

[45] Nathan A. Branch, Nagaraj K. Arakere, Ghatu Subhash, Michael A. Klecka, "Determination of constitutive response of plastically graded materials," *International Journal of Plasticity,* vol. 27, pp. 728-738, 2011.

[46] Michael A. Klecka, Ghatu Subhash, Nagaraj K. Arakere, "Determination of Subsurface Hardness Gradients in Plastically Graded Materials via Surface Indentation," *Journal of Tribology,* vol. 133, pp. 031403-1 - 031403-5, July 2011.

[47] A.K. Bhattacharya, W.D. Nix, "Analysis of Elastic and Plastic Deformatio associated with indentation testing of thin films on substrates," *Int. J. Solids Structures,* vol. 24, no. 12, pp. 1287-1298, 1988.

[48] A.Nayebi, R. El Abdi, O. Bartier, G. Mauvoisin, "Hardness profile analysis of elasto-plastic heat-treated steels with a gradient in yield strength," *Materials Science and Engineering A,* vol. 333, pp. 160-169, 2002.

[49] I.S. Choi, M. Dao, S. Suresh, "Mechanics of Indentation of plastically graded materials-I: Analysis," *Journal of the mechanics and Physics of Solids,* vol. 56, pp. 157-171, 2008.

[50] Caillard, D., "An in situ study of hardening and softening of iron by carbon interstitials," *Acta Materialia,* vol. 59, pp. 4974-4989, 2011.

[51] D.J. Quesnel, A. Sato, M. Meshii, "Solution softening and hardening in the Iron-Carbon system," *Materials Science and Engineering,* vol. 18, pp. 199-208, 1975.

[52] A.W. Cochardt, G. Schoek, H. Wiedersich, "Interaction between dislocations and interstitial atoms in body-centered cubic metals," *Acta Metallurgica,* vol. 3, pp. 533-537, November 1955.

[53] C. Krempaszky, u. Liedl, E.A. Werner, "A note on the diffusion of carbon atoms to dislocations," *Computational Materials Science,* vol. 38, pp. 90-97, 2006.

[54] A.S. Nandedkar, R.A. Johnson, "Carbon atmosphere near an edge dislocation in alpha-iron," *Acta Metallurgica,* vol. 30, pp. 2055-2059, 1982.

[55] A.K. De, K. De Blauwe, S. Vandeputte, B.C. De Cooman, "Effect of dislocation density on the low temperature aging behavior of an ultra-low carbon bake hardenig steel," *Journal of Alloys and Compounds,* vol. 310, pp. 405-410, 2000.

[56] George E. Dieter, Mechanical Metallurgy, McGrawHill Metric Editions Material Science and Metallurgy.

[57] M.J. Roberts, W.S. Owen, "Solid solution hardeing by carbon and nitrogen in ferrous martensites," *Physical properties of martensite and bainite,* vol. Special Report 93, pp. 171-178, 1965.

[58] D.F. Stein, J.R. Low, Jr., "Effects of orientation and Carbon on the Mechanical Properties of Iron Single Crystals," *Acta Metallurgica,* vol. 14, pp. 1183-1194, October 1966.

[59] Masaaki Itabashi, Kozo Kawata, "Carbon content effect on high-strain-rate tensile properties for carbon steels," *International Journal of Impact Engineering,* vol. 24, pp. 117-131, 2000.

[60] L.X. Chen, P. Bhandhubanyong, W. Vajragupta, C. Somsiri, "Plastic Properties of Low-Carbon Steel Sheets," *Journal of Materials Processing Technology,* vol. 63, pp. 95-99, 1997.

[61] V. Ballarin, M. Soler, A. Perlade, X. Lemoine, S. Forest, "Mechanisms and modeling of Bake-Hardening Steels: Part I. Uniaxial Tension," *Metallurgical and Materials Transactions A,* vol. 40A, pp. 1367-1374, June 2009.

[62] NIIR Board of Consultants and Engineers, The complete Technology Book on Hot Rolling of Steel.

[63] J. Aghazadeh Mohandesi, M.H. Shahosseinie, R. Parastar Namin, "Tensile Behavior of Functionally Graded Steels produced by Electroslag Remelting," *Metallurgical and Materials Transactions A,* vol. 37A, pp. 2125-2132, July 2006.

[64] S. Kyriakides, J.E. Miller, "On the Propagation of Lueders Bands in Steel Strips," *Journal of Applied Mechanics,* vol. 67, pp. 645-654, December 2000.

[65] Jixi Zhang, Yanyao Jiang, "Lueders bands propagation of 1045 steel under multiaxial stress state," *International Journal of Plasticity,* vol. 21, pp. 651-670, 2005.

[66] Alexey Lazarev, Alexei Vinogradov, "About Plastic Instabilities in Iron and Power Spectrum of Acoustic Emission," *J. Acoustic Emission,* vol. 27, pp. 144-156, 2009.

[67] Rooyen, G.T. Van, "Basic factors which influence the Lueders strain during discontinuous yielding," *Materials Science and Engineering,* vol. 7, pp. 37-48, 1971.

[68] V.M. Farber,, "Special Features of Metal Hardening on the Yield Plateau," *Metal Science and Heat Treatment,* vol. 49, pp. 132-134, 2007.

[69] L.P. Kubin, Y. Estrin, "Strain nonuniformities and plastic instabilities," *Revue Phys. Appl.,* vol. 23, pp. 573-583, 1988.

[70] Hahn, G.T., "A Model for yielding with special reference to the yield -point phenomena of iron and related bcc metals," *Acta Metallurgica,* vol. 10, pp. 727-738, August (1962).

[71] B.W. Christ, M.L. Picklesimer, "The relationship between Lueder's strain, testing system compliance and other phenomenological variables affecting serrated yielding of recrystallized iron," *Acta Metallurgica,* vol. 22, pp. 435-447, April 1974.

[72] H.B. Sun, F. Yoshida, M. Ohmori, X. Ma, "Effect of strain rate on Lueders band propagating velocity and Lueders strain for annealed mild steel under uniaxial tension," *Materials Letters,* vol. 57, pp. 4535-4539, 2003.

[73] R.Nogueira de Codes, O.S. Hopperstad, O. Engler, O.G. Lademo, J.D. Embury, A. Benallal, "Spatial and Temporal Characteristics of Propagating Deformation Bands in AA5182 Alloy at room temperature," *Metallurgical and Materials Transactions A,* vol. 42A, pp. 3358-3369, November 2011.

[74] Hart, E.W., "A uniaxial strain model for a Lueder's band," *Acta Metallurgica,* vol. 3, pp. 146-149, March 1955.

[75] Wilson, D.V., "Role of Grain Boundaries in the Discontinuous Yielding of Low-Carbon Steels," *Metal Science Journal,* vol. 1, pp. 40-47, 1967.

[76] V.S. Ananthan, E.O. Hall, "Macroscopic Aspects of Lueders Band Deformation in Mild Steel," *Acta Metallurgica Materialia,* vol. 39, no. 12, pp. 3153-3160, 1991.

[77] I. Gupta, F. Garofalo, "Effect of Grain Size and Free Interstitials on Yield Stress, Flow Stress and Lueders Strain in Iron and an Iron-Titanium Alloy," *Materials Science and Engineering,* vol. 5, pp. 271-278, May 1970.

[78] Roxana, Hutanu, Lynann Clapham, R.B. Rogge, "Intergranular strain and texture in steel Lueders bands," *Acta Materialia,* vol. 53, pp. 3517-3524, 2005.

[79] J.A. Shaw, S. Kyriakides, "Initiation and propagation of localized deformation in elasto-plastic strips under uniaxial tension," *International Journal of Plasticity,* vol. 13, no. 10, pp. 837-871, 1998.

[80] Lomer, W.M., "The Yield Phenomenon in Polycrystalline Mild Steel," *Journal of the Mechanics and Physics of Solids,* vol. 1, pp. 64-73, 1952.

[81] A.W. Sleeswyk, D.J. Verel, "The rate-determining process in Lueders band growth," *Scripta Metallurgica,* vol. 6, pp. 677-680, 1972.

[82] J.F. Butler,, "Lueders Front Propagation in Low Carbon Steels," *J. Mech. Phys. Solids,* vol. 10, pp. 313-334, 1962.

[83] R. Song, D. Ponge, D. Raabe, "Improvement of the work hardening rate of ultrafine grained steels through second phase particles," *Scripta Materialia,* vol. 52, pp. 1075-1080, 2005.

[84] J.C. Fisher, H.C. Rogers, "Propagation of Lueder's bands in steels wires," *Acta Metallurgica,* vol. 4, pp. 180-185, March 1956.

[85] H. Conrad,, "Effect of stress on the Lueders band velocity in low carbon steels," *J. Mech. Phys. Solids,* vol. 11, pp. 437-440, 1963.

[86] H. Conrad, G. Stone, "The effect of stress on the Lueders band velocity in niobium," *J.Mech. Phys. Solids,* vol. 12, pp. 139-148, 1964.

[87] D.E. Delwiche, D. W. Moon, "Orientation of Lueders Band Fronts," *Mater. Sci. Eng.,* vol. 7, pp. 203-207, 1971.

[88] J.F. Butler,, "Effect of Lueders front number on the yield point of iron," *Acta Metallurgica,* vol. 10, pp. 258-259, 1962.

[89] Wei Wen, J.G. Morris, "The effect of cold rolling and annealing on the serrated yielding phenomenon of AA5182 aluminum alloy," *Materials Science and Engineering A,* vol. 373, pp.

204-216, 2004.

[90] A.A. Shibkov, A.E. Zolotov, "Acoustic and Optical Monitoring of Lueder Band in Aluminum-Magnesium 5456 alloy," *Crystallography Reports,* vol. 56, no. 1, pp. 141-148.

[91] Herve Louche, Andre Chrysochoos, "Thermal and Dissipative effects accompanying Lueders band propagation," *Materials Science and Engineering A,* vol. 307, pp. 15-22, 2001.

[92] Fahmy M. Haggag, Glenn E. Lucas, "Determination of Lueders strains and Flow Properties in Steels from Hardness/Microhardness Tests," *Metallurgical Transaction A,* vol. 14A, pp. 1607-1613, August 1983.

[93] Julian F. Hallai, Stelios Kyriakides, "Underlying Material Response for Lueders-like instabilities," *International Journal of Plasticity,* 2013.

[94] Arnaud weck, Philippe Bisaillon, Lihang Nong, Trevor Meunier, Haiou Jin, Mark Gallerneault, "Mechanical Properties of the aluminum roll-bond laminate AA5005-AA5083-AA5005," *Materials Science and Engineering A,* vol. 528, pp. 6186-6193, 2011.

[95] Edmundo Corona, John A. Shaw, Mark A. Iadicola, "Buckling of Steel Bars with Lueders Bands," *International Journal of Solids and Structures,* vol. 39, pp. 3313-3336, 2002.

[96] Julian F. Hallai, Stelios Kyriakides, "On the effect of Lueders bands on the bending of steel tubes. Part I: experiments," *International Journal of Solids and Structures,* vol. 48, pp. 3275-3284, 2011.

[97] Stelios Kyriakides, Ali Ok, Edmundo Corona, "Localization and propagation of curvature under pure bending in steel tubes with Lueders bands," *International Journal of Solids and Structures,* vol. 45, pp. 3074-3087, 2008.

[98] Varvara Romanova, Ruslan Balokhonov, Siegfried Schmauder, "Three-dimensional analysis of mesoscale deformation phenomena in welded low carbon steel," *Materials Science and Engineering A,* vol. 528, pp. 5271-5277, 2011.

[99] Henri Tsukahara, Thierry Iung, "Finite element simulation of the Piobert-Lueders behavior in and uniaxial tensile test," *Materials Science and Engineering A,* vol. 248, pp. 304-308, 1998.

[100] J. Belotteau, C. Berdin, S. Forest, A. Parrot, C. Prioul, "Mechanical behavior modeling in the presence of strain aging," in *Fracture of Nano and Engineering Materials and Structures - Proceedings of th 16th European Conference of Fracture*, Alexandroupolis, Greece, July 3-7, 2006.

[101] H.B. Sun, F. Yoshida, X. Ma, t. Kamei, M. Ohmori, "Finite element simulation on the

propagation of Lueders band and effect of stress concentration," *Materials Letters,* vol. 57, pp. 3206-3210, 2003.

[102] Nikzad Nourpanah, Farid Taheri, "Effect of Lueders plateau on fracture response and toughness of pipelines subject to extreme plastic bending," *Journal of Pressure Vessel Technology,* vol. 133, pp. 051701-1 - 051701-9, October 2011.

[103] Robert A. Elliot, Ergon Orowan, Teruyoshi Udoguchi, Ali S. Argon, "Absence of yield points in iron on strain reversal after aging, and the Bauschinger overshoot," *Mechanics of Materials,* vol. 36, pp. 1143-1153, 2004.

[104] G.H. Paulino, Z.H. Jin, R.H. Dodds, Jr., "Failure of Functionally Graded Materials," in *"Comprehensive Structural Integrity"*, vol. 2, E. Science, Ed., Karihaloo B. and Knauss WG. Editors,, 2003.

[105] Reiter Thomas, Dvorak George J., "Micromechanical Models for Graded Composite Materials," *J. Mech. Phys. Solids,* vol. 45, no. 8, pp. 1281-1302, 1997.

[106] Jin Zhi-He, paulino Glaucio H., Dodds Robert H. Jr, "Cohesive Fracture Modelling of elastic-plastic crack growth in Functionally Graded Materials," *Engineering Fracture Mechanics,* vol. 70, pp. 1885-1912, 2003.

[107] Anlas G., Santare M.H.,Lambros J., "Numerical Calculation of Stress Intensity Factors in Functionally Graded Materials," *International Journal of Fracture,* vol. 104, pp. 131-143, 2000.

[108] C.E., Rousseau; V.B., Chalivendra; H.V., Tippur; A., Shukla, "Experimental Fracture Mechanics of Functionally Graded Materials: An Overview of optical investigations," *Experimental Mechanics,* vol. 50, pp. 845-865, 2010.

[109] Jin Z.H., Batra R.C.,, "Some Basic Fracture Mechanics Concepts in Functionally Graded Materials," *J. Mech. Phys. Solids,* vol. 44, no. 8, pp. 1221-1235, 1996.

[110] Lambros H.Li J., Cheeseman B.A., Santare M.H.,, "Experimental Investigation of the quasi-static fracture of Functionally Graded Materials," *International Journal of Solids and Structures,* vol. 37, pp. 3715-3732, 2000.

[111] Hill Michael R., Carpenter R. Doug, Paulino Glaucio H., Zuhair A. Munir, Gibeling Jeffery C.,, Fracture testing of a layered Functionally Graded Material, West Conshohocken, PA: ASTM STP 1409, J.A. Salem, G.D. Quinn, and M.G. Jenkins, Eds., American Society for Testing and Materials, 2002.

[112] Rousseau C.E., Tippur H.V.,, "Evaluation of crack tip fields and stress intensity factors in

Functionally Graded Elastic Materials: cracks parallel to elastic gradient," *Int. J. Fracture,* vol. 114, no. 1, pp. 87-111, 2002.

[113] Yang X.B., Qin Y.P., Zhuang Z., and You X.C.,, "Investigation of dynamic fracture behaviour in functionally graded materials," *Modelling and Simulation in Materials Science and Engineering,* vol. 16, 2008.

[114] Wang Zhiqiang, Nakamura Toshio,, "Simulations of crack propagation in elastic-plastic graded materials," *Mechanics of Materials,* vol. 36, pp. 601-622, 2004.

[115] Kolednik O., "The Yield Stress Gradient effect in inhomogeneous materials," *International Journal of Solid and Structures,* vol. 37, pp. 781-808, 2000.

[116] A. Shukla, N. Janin, R. Chona, "A review of dynamic fracture studies in functionally graded materials," *Strain,* vol. 43, pp. 76-95, 2007.

[117] J. Aghazadeh Mohandesi, A. Nazari, Mehdi Hamid Vishkasogheh, Mohammad Abedi,, "Modeling fracture toughness of functionally graded steels in crack divider configuration," *Modelling and Simulation in Materials Science and Engineering,* vol. 18, pp. 1-13, 2010.

[118] Ali Nazari, Jamshid Aghazadeh Mohandesi, Shadi Riahi,, "Fracture toughness of functionally graded steels," *Journal of Materials Engineering and Performance,* vol. 21, no. 4, pp. 558-563, April 2012.

[119] C.E. Rousseau, H.V. Tippur, "Compositionally graded materials with cracks normal to the elastic gradient," *Acta Materialia,* vol. 48, pp. 4021-4033, 2000.

[120] G. Bao, L. Wang,, "Multiple cracking in functionally graded ceramic/metal coatings," *Int. J. Solids Structures,* vol. 32, no. 19, pp. 2853-2871, 1995.

[121] G. Bao, H. Cai,, "Delamination cracking in functionally graded coating/metal substrate systems," *Acta Materialia,* vol. 45, no. 3, pp. 1055-1066, 1997.

[122] Zhenhuan Li, Chen Wang, Chuanyao Chen,, "The Influence of Matrix Yield Stress Gradient on the growth and coalescence of spheroidal voids," *International Journal of Solids and Structures,* vol. 39, no. 3, pp. 601-616, 2002.

[123] "Iron-carbon phase diagram," [Online]. Available: http://www.sv.vt.edu/classes/MSE2094 NoteBook/96ClassProj/examples/kimcon.html.

[124] I. Jouanny, V. Demange, J. Ghanbaja, E. Bauer-Grosse,, "Structural characterization of FeC coatings prepared by reactive triode-magnetron sputtering," *J. Mater. Res.,* vol. 25, no. 9, pp. 1859-1869, Sep 2012.

[125] E. Bauer-Grosse, "Thermal Stability and crystallization studies of amorphous TM-C films," *Thin Solid Films,* Vols. 447-448, pp. 311-315, 2004.

[126] E. Bauer-Grosse, G. Le Caer, "Crystallisation of amorphous Fe1-xCx alloys (0.30..x..0.32) and chemical twinning," *J.Phys.F: Met. Phys.,* vol. 16, pp. 399-406, 1986.

[127] Ben Lawrence, "Methods of Fe1-x Cx Thin Film Deposition," Internal Report GraCOS Project, March 30, 2011.

[128] M. Ohring, Materials Science of Thin Films, Academic Press, 2002.

[129] Ben Lawrence, "Using Far-From-Equilibrium Coatings to Produce Graded Steel Sheet," PhD Thesis Proposal, October 9, 2012.

[130] E. Reinhold, J. Richter, U. Seyfert, and C. Steuer, "Metal strip coating by electron beam PVD - industrial requirements and customized solutions," *Surface Coatings and Technology,* Vols. 188-189, pp. 708-713, 2004.

[131] H. Tsukahara, T. Iung,, "Piobert-Lueders and Portevin-Le Chatelier Instabilities. Finite element modelling with ABAQUS," *J. Phys. France,* vol. 9, pp. Pr9-157-Pr9-164, 1999.

[132] A. Weck, D.S. Wilkinson,, "Experimental investigation of void coalescence in metallic sheets containing laser drilled holes," *Acta Materialia,* vol. 56, pp. 1774-1784, 2008.

[133] L.B. Freund and S. Suresh, Thin Film Materials Stress, Defect Formation and Surface Evolution, Cambridge University Press.

[134] Krar, Steve, Electrical Discharge Machining.

[135] SME-Society of Manufacturing Engineers,, Electrical Discharge Machining, http://manufacturing.stanford.edu/processes/EDM.pdf.

[136] Elman C. Jameson,, Electrical Discharge Machining, Dearborn, Michigan: Society of Manufacturing Engineers-Machining technology Association/SME.

[137] http://www1.uwindsor.ca/chemicalcontrol/system/files/chemical%20stores/Linde_Scientific_Catalogue.pdf, [Online].

[138] Raymond A. Higgins,, Engineering Metallurgy, Arnold - A member of the Hodder Headline Group.

[139] Samuels, L.E., Metallographic Polishing by Mechanical Methods, New York: American Elsevier Publishing Company Inc..

[140] Wilson Hardness,, Poduct Manual Tukon 1102/1202.

[141] Y. Barranger, P. Doumalin, J.C. Dupre, A. Germaneau,, "Digital Image Correlation accuracy: influence of kind of speckle and recording setup," *EPJ Web of Conferences,* vol. 6, no. 31002, 2010.

[142] Zili Sun, Jed S. Lyons and Stephen R. McNeill, "Measuring Microscopic Deformations with Digital Image Correlation," *Optics and Lasers in Engineering - Elseviewer Science Limited, ,* vol. 27, pp. 409-428, 1997.

[143] "Product Manual "LaVision"".

[144] http://rsbweb.nih.gov/ij/.

[145] Rasband, W.S., "ImageJ," http://imagej.nih.gov/ij/, U.S. National Institutes of Health, Bethesda, Maryland, USA, 1997-2014.

[146] Joseph Goldstein, Dale Newbury, David Joy, Charles Lyman, Patrick Echlin, Eric Lifshin, Linda Sawyer, Joseph Michael, Scanning Electron Microscopy and X-Ray Microanalysis, Springer.

[147] R.C. Thomson, "Characterization of Carbides in Steels using Atom Probe Field-Ion Microscopy," *Materials Characterization,* vol. 44, pp. 219-233, 2000.

[148] Baptiste Gault, Michael P. Moody, Julie M. Cairney, Simon P. Ringer, Atom Probe Microscopy, Springer series in Materials Science.

[149] M.Perez, V.Massardier, X.Kleber, "Thermoelectric power applied to metallurgy: principle and recent applications," *Int.J.Mat.Res.,* vol. 100, no. 10, pp. 1461-1465, 2009.

[150] C. Capdevila, T. De Cock, F.G. Caballero, D. San Martin, C. Garcia de Andres, "Application of thermoelectric power measurements to the study of cold rolled austenitic stainless steels," *J. Mater. Sci.,* vol. 44, pp. 4499-4502, 2009.

[151] V.Massardier, N.Lavaire, M.Soler, J.Merlin, "Comparison of the evaluation of the carbon content in solid solution in extra-mild steels by thermoelectric power and by internal friction," *Scripta Materialia,* vol. 50, pp. 1435-1439, (2004).

[152] Okamoto, H., "The C-Fe (Carbon-Iron) System," *Journal of Phase Equilibria - ASM International,* vol. 13, no. 5, pp. 543-565, 1992.

[153] C.P. Scott, C. Sinclair and A. Weck, "Amorphous Fe1-xCx coatings as carbon reservoirs for diffusion strengthening of steel sheets," *Scripta Materialia,* vol. 65, pp. 763-766, 2011.

[154] ASTM: E384-11,, "Standard Test Method for Knoop and Vickers hardness of materials".

[155] Tabor, D., "The Physical Meaning of Indentation and Scratch Hardness," *British Journal of Applied Physics,* vol. 7, no. 5, pp. 159-166, 1956.

[156] Kraft, V.V., "Effect of Vacuum annealing on decarburizing of low-carbon steel," *Translated from Metallovedenie Termicheskaya Obrabotka Metallov,* vol. 8, pp. 61-63, August 1971.

[157] S.R.Elmi Hosseini,, "Simulation of Case Depth of Cementation Steels According to Fick's Laws," *Journal of Iron and Steel research International,* vol. 19, no. 11, pp. 71-78, 2012.

[158] A. Fillon, X. Sauvage, B. Lawrence, C. Sinclair, M. Perez, A. Weck, E. Cantergiani, T. Epicier and C.P. Scott, "On the direct nucleation and growth of ferrite and cementite without austenite," *Scripta Materialia,* vol. 95, pp. 35-38, 2015.

[159] P. Klugkist, Chr. Herzig, "Tracer Diffusion of Titanium in alpha-Iron," *Phys. Stat. Sol (a),* no. 148, pp. 413-421, 1995.

[160] J. Shi, X. wang, "Comparison of precipitate behaviors in Ultra-Low Carbon Titanium stabilized Interstitial free steel sheets under different annealing processes"," *Journal of Materials Engineering and Performances,* vol. 8, pp. 641-648, 1999.

[161] Xiang-dong Huo, Xin-Ping Mao, Sheng-Xia Lu, "Effect of annealing temperature on recrystallization behavior of cold rolled Ti-microalloyed Steel," *Journal of Iron and Steel Research, International,* vol. 2013, no. 20(9), pp. 105-110.

[162] Jae-Young Choi, Baek-Seok Seong, Seung Chul Baik and Hu-Chul Lee, "Precipitation and Recrystallization Behavior in Extra-Low Carbon Steels," *ISIJ International,* vol. 42, no. 8, pp. 889-893, 2002.

[163] Hall, E.O., Yield point phenomena in Metals and Alloys, New York: Plenum Press.

[164] Setsuo Takaki, Daichi Akama, Nobuo Nakada and Toshihiro Tsuchiyama, "Effect of Grain Boundary Segregation of Interstitial Elements on Hall-Petch Coefficient in Steels," *Materials Transactions,* vol. 55, no. 1, p. 28.34, 2014.

[165] http://mashayekhi.iut.ac.ir/sites/mashayekhi.iut.ac.ir/files/u32/presentation10.pdf.

[166] 6.7, ABAQUS Manual Version, http://www.egr.msu.edu/software/abaqus/Documentation/docs/v6.7/books/usb/default.htm?startat=pt02ch04s02xbv01.html.

[167] Mohamed Harhash, Olga Sokolova, Adele Carrado, Heinz Palkowski, "Mechanical Properties

and forming behaviour of laminated steel/polymer sandwich systems with local inlays - Part 1," *Composite Structures,* vol. 118, pp. 112 - 120, (2014).

[168] A.K. De, S. Vandeputte, B.C. De Cooman, "Static strain-aging behavior of ULC bake hardening steel," *Scripta Materialia,* vol. 41, no. 8, pp. 831-837, 1999.

[169] S. Lou, D.O. Northwood, "Effect of Temperature in the lower yield strength and static strain ageing in low carbon steels," *Journal of Materials Science,* vol. 30, pp. 1434-1438, 1995.

[170] Guenduez, Sueleyman, "Static strain ageing behaviour of dual phase steels," *Materials Science and Engineering A,* vol. 486, pp. 63-71, 2008.

[171] D. Hull, D.J. Bacon, Introduction to Dislocations, Butterworth-Heinemann, Fourth edition 2001.

[172] B. Soenen, A.K. De, S. Vandeputte, B.C. De Cooman, "Competition between grain boundary segregation and Cottrell atmosphere formation during static strain aging in ultra low carbon bake hardening steels," *Acta Materialia,* vol. 52, pp. 3483-3492, 2004.

[173] A.K. De, S. Vandeputte and B.C. De Cooman, "Kinetics of strain aging in Bake Hardening Ultra Low Carbon Steel - a comparison with Low Carbon Steel," *Journal of Materials Engineering and Performance,* vol. 10, no. 5, pp. 567-575, October 2001.

[174] O. Bouaziz, D. Barbier, J.D. Embury and G. Badinier, "An extension of the Kocks-Mecking model of work hardening to include kinematic hardening and its application to solutes in ferrite," *Philosophical magazine,* vol. 93, no. 1-3, pp. 247-255.

[175] Reed-Hill, Robert E., Physical Metallurgy Principles, D. VAN NOSTRAND COMPANY.

[176] Bramfitt, B. L., Metallographer's Guide: Practice and Procedures for Irons and Steels".

[177] George F. Van der Voort,, Etching Isothermally Treated Steels, Heat Treating Progress - Fellow of ASM International,, April/May 2001.

[178] Khzouz, Erik, Grain Growth Kinetics in Steels, Worcester Polytechnic Institute, April 28, 2011.

[179] Soon Tae Ahn, Dae Sung Kim, Won Jong Nam, "Microstructural evolution and mechanial properties of low alloy steel tempered by induction heating," *Journal of Materials Processing Technology,* vol. 160, pp. 54-58, 2005.

[180] Induction, EFD ®, Induction heating applications: the processes, the equipment, the benefits.

[181] Yuichiro Koizumi, Takeshi Otsuka, Yoritoshi Minamino, Takemori Takayama, Masanori Ueyama, Takeshi Daio, Satoshi Hata, "Microstructure developed by super-rapid induction

heating-and-quenching (SRIHQ) of Fe-1.4%Cr-1%C pearlitic steel," *Materials Science and Engineering A,* vol. 577, pp. 29-35, 2013.

[182] Dr. Valery Rudnev, Doug Brown, Dr. Chester J. Van Tyne, Dr. Kester D. Clarke, "Intricacies for the successfull induction heating of steels in modern forge shops".

[183] Valery Rudnev, Don Loveless, Raymond Cook, Micah Black, Handbook of Induction Heating.

[184] M. Atkinson,, "Strain Hardening Behavior of Polycrystalline Iron and Low-Carbon steels - a Statistical Analysis," *Metallurgical Transactions A,* vol. 15A, pp. 1185-1192, June 1984.

[185] S.R. Mediratta, V. Ramaswamy, V. Singh, P. Ramarao, "Dependence of strain hardening exponent on the volume fraction and carbon content of martensite in dual phae steels during multistage work hardening," *Journal of Materials Science Letters,* vol. 9, pp. 205-206, 1990.

[186] T.C. Huang, P.K. Predecki, "Grazing-incidence X-Ray technique for surface, interface, and thin-film analysis," *JCPDS - International Centre for Diffraction Data,* 1997.

[187] Bob Downs, Ranjini Swaminathan and Kurt Bartelmehs, *American Mineralogist,* vol. 78, pp. 1104-1107, 1993.

[188] Hendricks, S., *Z. Kristallogr., Kristallgeom., Kristallphys., Kristallchem.,* vol. 74, p. 534, (1930).

[189] Natl. Bur. Stand. (U.S.)Monogr., 25, *Natl. Bur. Stand. (U.S.)Monogr., 25,* vol. volume 21, p. page 72, (1985).

[190] Julian Richard Tolchard, Astri SØmme, Jan Ketil Solberg, Karl Gunnar Solheim, "On the measurement of austenite in supermartensitic stainless steel by x-ray diffraction," *Materials Characterization,* vol. 99, pp. 238-242, (2015).

[191] Swanson et al.,, *Natl. Bur. Stand. (U.S.),* vol. volume IV, no. Circ. 539, p. 3, (1955).

[192] Arne Kromm, Thomas Kannengiesser, "In-situ-phase analysis using synchrotron radiation of low transformation temperature (LTT) welding material," *Soldagem Insp. Sao Paulo,* vol. 14, no. 1, pp. 082-088, Jan/Mar 2009.

[193] http://www.rigaku.com/en/products/xrd/smartlab/app028, ""High-speed identification and quantification of Hematite and Magnetite"".

[194] B.J. Yang, A. Hattiangadi, W.Z. Li, G.F. Zhou, T.E. McGreevy, "Simulation of steel microstructure evolution during induction heating," *Materials Science and Engineering A,* vol. 527, pp. 2978-2984, 2010.

[195] Yudong Zhang, Changshu He, Xiang Zhao, Liang Zuo, Claude Esling, "Thermodynamic and kinetic characteristics of the austenite-to-ferrite transformation under high magnetic field in medium carbon steel," *Journal of Magnetism and Magnetic Materials,* vol. 294, pp. 267-272, 2005.

[196] Yudong Zhang, Changshu He, Xiang Zhao, Liang Zuo, Claude Esling, Jicheng He, "New microstructural features occurring during transformation from austenite to ferrite under the kinetic influence of magnetic field in a medium carbon steel," *Journal of Magnetism and Magnetic Materials,* vol. 284, pp. 287-293, 2004.

[197] M. Shimotomai, K. Maruta, K. Mine, M. Matsui, "Formation of aligned two-phase microstructures by applying a magnetic field during the austenite to ferrite transformation in steels," *Acta Materialia,* vol. 51, pp. 2921-2932, 2003.

[198] Michio Shimotomai, Kei-ichi Maruta, "Aligned two-phasestructures in Fe-C alloys," *Scripta Materialia,* vol. 42, pp. 499-503, 2000.

[199] Thomas Garcin, "Thermodynamics and kinetic effects of static magnetic field on phase transformation in low alloy steels," English. https://tel.archives-ouvertes.fr/tel-00519996, Engineering Sciences. Université Joseph-Fourier-Grenoble I, 2009.

[200] A.T. dinsdale, "SGTE data for pure elements," *Calphad,* vol. 15, no. 4, pp. 317-425, (1991).

[201] M. Onink, C.M. Brakman, J.H. Root, F.D. Tichelaar, E.J. Mittemeijer and S. van der Zwaag, "Redistribution of Carbon during the austenite to ferrite transformation in pure Fe-C alloys," *Materials Science Forum,* Vols. 163-165, pp. 63-68, 1994.

[202] Guang Xu, Xiaolong Gan, Guojun Ma, Feng Luo, Hang Zou, "The development of Ti-alloyed high strength microalloy steel," *Materials and Design,* vol. 31, pp. 2891-2896, 2010.

[203] Sung-Mo Hong, Eun-Kwang Park, Jin-Ju Park, Min-Ku Lee, Jung Gu Lee, ""Effect of nano-sized TiC particle addition on microstructure and mechanical properties of SA-106B Carbon steel," *Materials Science and Engineering A,* vol. 643, pp. 37-46, 2015.

[204] Tzu-Pin Wang, Fang-Hsin Kao, Shing-Hoa Wang, Jer-Ren Yang, Ching-Yuan Huang, Hsueh-Ren Chen, "Isothermal treatment influence on nanometer-size carbide precipitation of titanium-bearing low carbon steel," *Materials Letters,* vol. 65, pp. 396-399, 2011.

[205] A. Ramazani, S. Bruehl, T. Gerber, W. Bleck, U. Prahl, "Quantification of bake hardening effect in DP600 and TRIP700 steels," *Materials and Design,* no. 57, pp. 479-486, 2014.

[206] Arnaud Weck, David Wilkinson, "Experimental investigation of void coalescence in metallic sheets containing laser drilled holes," *Acta Materalia,* vol. 56, pp. 1774-1784, 2008.

[207] http://imagej.nih.gov/ij/, [Online].

[208] McClintok, F.,, "Criterion for Ductile Fracture by the Growth of Holes," *Journal of Applied Mechanics,* vol. 35, pp. 363-371.

[209] Yaser Alinaghian, Mahyar Asadi, Arnaud Weck, "Effect of pre-strain and work hardening rate on void growth and coalescence in AA5052," *International Journal of Plasticity,* no. http://dx.doi.org/10.1016/j.ijplas.2013.08.007, 2013.

[210] D. Senk, H. Emmerich, J.Rezende and R. Siquieri, "Estimation of segregation in Iron-Maganese Steels," *Advanced Engineering Materials,* vol. 9, no. 8, pp. 695-702, 2007.

[211] O. Bouaziz, S. Allain, C.P. Scott, P. Cugy, D. Barbier, "High manganese austenitic twinning induced plasticity steels: A review of the microstructure properties relationship," *Current Opinion in Solid State and Materials Science,* vol. 15, pp. 141-168, 2011.

[212] Zhang Li, Liu Xiang-hai, Shu Kang-ying, "Microstructure and Mechanical Properties of Hot-Rolled Fe-Mn-C-Si TWIP Steel," *Journal of Iron and Steel Research International,* vol. 18, no. 12, pp. 45-48, 2011.

[213] McNallan, J.M. Oh and M.J., "Kinetics of Oxidation Induced Transformations in Iron-Manganese-Nickel-Silicon Alloys," *J. Electrochem. Soc.: Solid-state science and technology,* vol. 134, no. 4, pp. 1010-1015, April 1987.

[214] Shoujin Sun, Martin Pugh, "Manganese partitioning in dual-phase steel during annealing," *Materials Science and Engineering A,* vol. 276, pp. 167-174, 2000.

[215] Furuhara, T., "Carbide-containing bainite in steels," in *Phase Transformations in Steels - Volume 1: Funamentals diffusion - controlled transformations*, vol. Chapter 11, E. P. a. D. V. Edmonds, Ed., Woodhead Publishing Limited, 2012.

[216] Bulent Kurt, Nuri Orhan, Ertan Evin, Adnan Calik,, "Diffusion boding between Ti-6Al-4V alloy and ferritic stainless steel," *Materials Letters,* vol. 61, pp. 1747-1750, 2007.

[217] B. Qin, G.M. Sheng, J.W. Huang, B. Zhou, S.Y. Qiu, C. Li,, "Phase transformation diffusion bonding of titanium alloy with stainless steel," *Materials Characterization,* vol. 56, pp. 32-38, 2006.

[218] M. Ghosh, K. Bhanumurthy, G.B. Kale, J. Krishnan, S. Chatterjee,, "Diffusion bonding of titanium to 304 stainless steel," *Journal of Nuclear Materials,* vol. 322, pp. 235-241, 2003.

[219] S. Kundu, S. Chatterjee,, "Diffusion bonding between commercially pure titanium and micro-duplex stainless steel," *Materials Science and Engineering A,* vol. 480, pp. 316-322, 2008.

[220] Evren Atasoy, Nizamettin Kahraman,, "Diffusion bonding of commercially pure titanium to low carbon steel using a silver interlayer," *Materials Characterization,* vol. 59, pp. 1481-1490, 2008.

[221] A. Elrefaey, W. Tillmann,, "Solid state diffusion bonding of titanium to steel using a copper base alloy as interlayer," *Journal of Materials Processing Technology,* vol. 209, pp. 2746-2752, 2009.

[222] Peng Li, Jinglong Li, Jiangtao Xiong, Fusheng Zhang, Syed Hamid Raza,, "Diffusion bonding titanium to stainless steel using Nb/Cu/Ni multi-interlayer," *Materials Characterization,* vol. 68, pp. 82-87, 2012.

[223] Didier Blavette, "Lectures APT school 2013".

[224] Pareige, C., "Time of Flight Mass Spectrometry for Atom Probes," Presentation at the atom probe tomography school, Universite de Rouen, 2013.

[225] Gerald da Costa, "3D data processing for Atom Probe," 2013.

[226] http://www.nims.go.jp/apfim/FIM_tip.html.

[227] N.Lavaire, J.Merlin, V.Sardoy, "Study of ageing in strained ultra and extra low carbon steels by thermoelectric power measurement," *Scripta Materialia,* vol. 44, pp. 553-559, 2001.

[228] M. Nash and P. Singleton,, "The C-Ni (Carbon-Nickel) System," *Bulletin of Alloy Phase Diagrams,* vol. Vol.10, no. No.2, pp. 121-126, 1989.

[229] ASTM International, "Standard Test Methods for Determining Average Grain Size," Vols. E112-10.

[230] http://www.gh-ia.com/induction_heating.html, [Online].

[231] http://www.richieburnett.co.uk/indheat.html, [Online].

[232] ASM International,, Practical Induction Heat Treating, 2001.

[233] S. Morito, H. Tanaka, R. Konishi, T. Furuhara, T. Maki, "The morphology and crystallography of lath martensite in Fe-C alloys," *Acta Materialia,* vol. 51, pp. 1789-1799, 2003.

[234] T. Furuhara, H. Kawata, S. Morito, G. Miyamoto, and T. Maki, "Variant Selection in Grain Boundary Nucleation of Upper Bainite," *Metallurgical and Materials Transactions A,* vol. 39A, pp. 1003-1013, May 2008.

[235] L. Koll, E. Werner, "Quantification of the martensite fraction in dual phase-steel by the use of electron backscatter diffraction (EBSD)," TUM Lehrstuhl fuer Werkstoffkunde und Werkstoffmechanik (MPA).

Appendices

Appendix A : Vickers and Knoop Microhardness

According to the definition included in the operation manual [140], "the Vickers indenter is a regular square-based pyramid with facial angles of 136˚ and the depth of the produced indent is around 1/7 of the length of the diagonal of the indent" (see Figure A. 1).

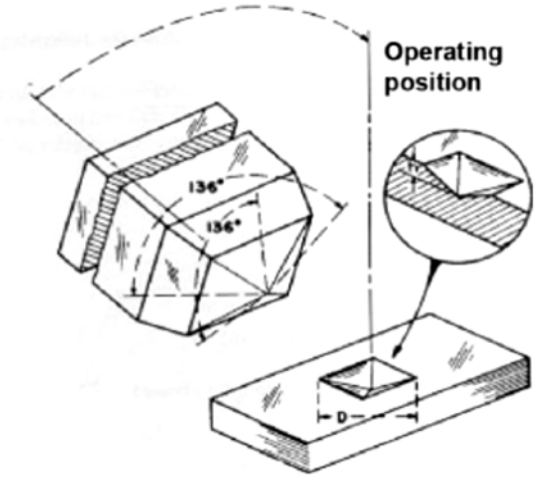

Figure A. 1 - Vickers indenter [140]

Vickers hardness values are calculated using the following expression:

$$HV = 0.102\frac{F}{S} = 0.102\frac{2F * \sin\left(\frac{\theta}{2}\right)}{D^2} = 0.1891\frac{F}{D^2} \qquad \text{(eq. A- 1)}$$

where,

HV is the values of Vickers hardness;

F is the force applied by loading the sample [N];

S is the surface area of the indent [mm^2];

Θ is the angle between the faces of the indenter (for Vickers 136˚);

D is the average length of the two Vickers diagonal [mm];

The Knoop indenter has also a pyramidal geometry but its diagonals have different lengths, in particular the relative ratio between the two diagonals is about 7:1; moreover two different angles can be defined between its faces, the first is the longitudinal internal angle which is around 172˚ and the other is the transverse internal angle of 130˚ (see Figure A. 2) [140]. The depth of a Knoop indent is around 1/30 of the length of the longer diagonal.

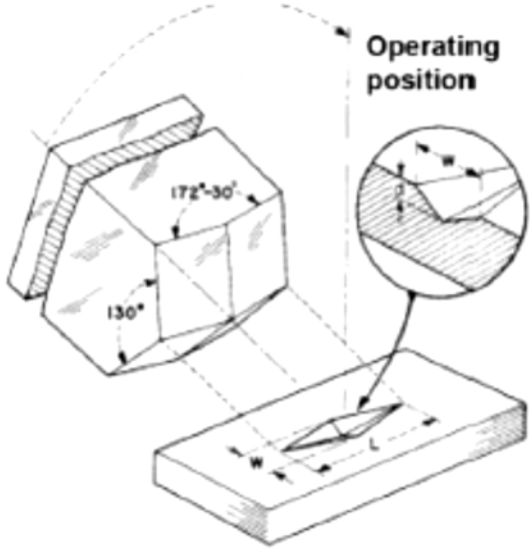

Figure A. 2 - Knoop indenter [140]

The Knoop hardness values are calculated using the following equation:

$$HK = 0.102\frac{F}{S} = 0.102\frac{F}{CD^2} = 1.451\frac{F}{D^2} \qquad \text{(eq. A- 2)}$$

where:

HK is the Knoop hardness value;

F is the force applied by loading the sample [N];

S is the projected area of indentation [mm^2];

C is a constant of the indenter which is calculated using the longitudinal and transverse angles;

D is the length of the longer diagonal [mm];

Appendix B : Atom Probe Tomography

B.1 Introduction to Atom Probe Tomography

The precursor of APT is the Field Ion Microscopy (FIM), which provides atomic-resolution imaging of the surface of a specimen. FIM is based on the field ionisation theory which requires the application of a high positive voltage at the tip of the material which needs to be analyzed. The high voltage will induce an electric field at the apex of the tip. The magnitude of the induced electric field depends on the geometrical shape of the tip. The tip is usually modelled as a truncated cone with a sphere on the top and the radius of this hemisphere on the top is considered to be responsible for the intensity of the generated electric field [148]. The chamber of the tip is filled with a rare gas whose atoms are ionised very close to the tip surface. "Once the ionization occurs, these new positively charged gas ions are repelled from the tip surface due to the intense electric field and they are accelerated towards a phosphor screen following a trajectory which is close to normal to the tangent of the specimen surface" [148]. A schematic view of the ionization process and of the FIM is shown in Figure B. 1.

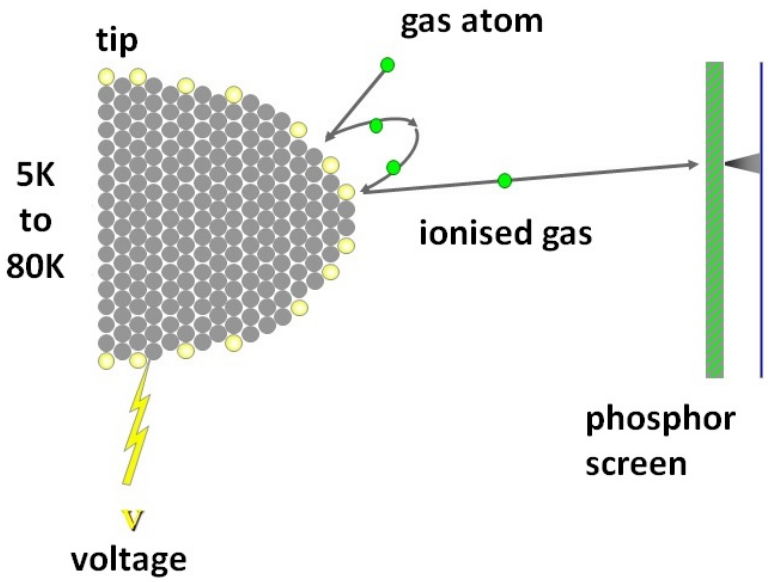

Figure B. 1 - Schematic view of the field ion microscopy (FIM) process [223]

As already mentioned above, the intensity of the electric field is strongly dependent on the radius of the tip. The following relation describes the relation between electric field and tip shape:

$$F = \frac{V}{\beta * R} \qquad \text{(eq. B. 1)}$$

where V is the voltage applied at the tip, R is the radius of the tip (around 20 nm or 50 nm as order of magnitude) and β is a correction factor (also known as field factor) whose value ranges between 3 and, which is necessary since the tip can be approximated as a cone with a sphere on the top.

Another important aspect of the analyses is to keep the specimen at cryogenic temperatures to reduce the thermal vibrations of the surface atoms, to minimise the diffusion of atoms inside the tip due to the electric field so that the surface atoms are really imaged in their original positions. Moreover, cryogenic temperatures reduce the thermal energy of the imaging-gas atoms lowering their lateral velocity at the instant of the evaporation, thereby ensuring a better spatial resolution [148].

B.2 Atom Probe Tomography

Atom Probe Tomography (APT) is a good technique to measure the small amount of carbon concentration which is diffused through the thickness of the IF sheet. APT measurements were performed in the center of the diffused IF sheet and at the interface between FeC coating and the IF substrate. The basic principles of atom probe tomography are illustrated in this paragraph, while the methods used to prepare specimens suitable for this technique are described in section B.3.

“APT is based on the field evaporation mechanism, which is defined as the removal of an atom from its own lattice due to a strong electric field. The intense electric field polarizes the surface atoms and once this is polarized, the surface atom can be pulled away from the surface of the tip while one of its electrons is drained into the surface of the tip causing the ionization of the atom” [148]. The created ion is then accelerated by the electric field far from the tip. The electric field depends on the radius of the tip according to (eq. B. 1)) as for the field ion microscopy. In APT the electric field penetration for metallic material is very small, therefore, only the atoms at the very surface of the specimen are affected by the field evaporation process which will take place almost atom by atom and

evaporating atomic layer after atomic layer. If a specimen is subjected to a certain direct current (DC) at a given base temperature, then there are two mechanisms that can be used to cause evaporation. The first method, which is called high-voltage pulsing (HV pulsing) and that is mainly used for conductive materials such as metals, is to increase the electric field at constant temperature, while the second method, known as laser-pulsing mode, will keep the electric field constant but it will increase the temperature locally (mainly implemented for semiconductors or non-conductive materials) [148]. By plotting the ratio between the electrical field acting on a specimen (F) and the field of evaporation (F_e) versus the temperature as shown in Figure B. 2, a decreasing linear relationship is found. The graph is shown in the following figure. So at point A in Figure B. 2 the electrical field is lower than the field required to evaporate the atoms. To start the evaporation process, it is possible to keep constant the temperature but then it is necessary to increase the electrical field of the tip by increasing the voltage (high-voltage pulsing method). Another method is to keep constant the field but to increase the temperature to lower the field of evaporation (F_e). This is usually obtained by using laser pulses and for this reason this approach is called laser-pulsing mode.

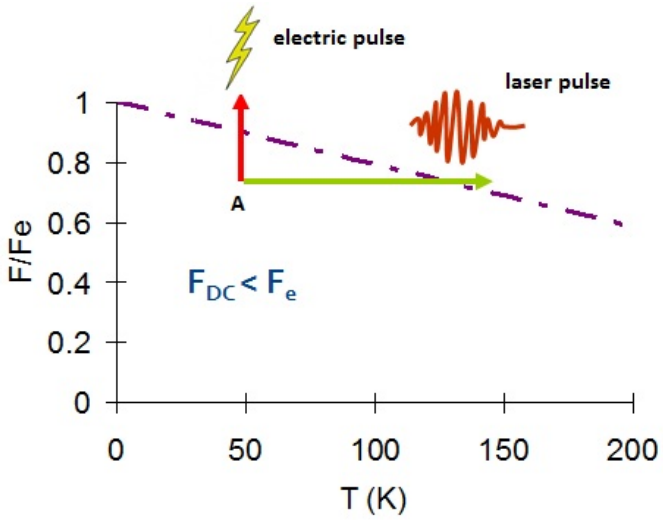

Figure B. 2 - Ratio between the field applied to the specimen (F) and the evaporation field (F_e) versus the temperature. The two modes, high-voltage pulse method and laser method, used to obtain evaporation are illustrated [224]

During the analyses of the specimens used in the Gracos project, the high-voltage method has been used to evaporate the specimens since the specimen is electrically conductive. In order to characterize the process, the evaporation rate can be defined as the number of atoms that can be evaporated per second and it can be calculated by using the following expression:

$$\Phi_{evap} = \nu_0 \exp\left(\frac{-Q(F)}{k_B T}\right) \qquad \text{(eq. B. 2)}$$

where, ν_0 is the frequency of the component of the atoms thermal vibrations which is normal to the surface of the tip, *Q (F)* is the height of the potential barrier that has to be overcome to evaporate the atom. *Q* is dependent on the applied electric field. K_B the Boltzmann constant and T is the absolute temperature [148].

In reality, what will influence the APT analyses is the detection rate which is not necessarily proportional to the evaporation rate since not all the evaporated atoms striking the detector will be detected due to the efficiency of the detector itself. In the case of the DC evaporation, the time for evaporation to take place is infinite, unlike in pulsed evaporation, where the evaporation happens only during the laser pulse, which will last for less than few ns. In the high voltage pulsing mode, the pulse fraction is defined as the ratio between the amplitude of the high voltage pulses and the DC voltage applied at the tip as shown schematically in Figure B. 3. Voltage pulses are applied on a certain time to evaporate the atomic species. However, the atoms will not exactly evaporate when the peak of the voltage is reached and there is an uncertainty δt_0 on the starting time t_0 of the evaporation. During the APT analysis, an increasing larger voltage will be required to produce the proper electric field to evaporate the atomic species since the radius of curvature of the tip changes during the evaporation. Moreover, in order to keep the pulse fraction constant, the amplitude of the high voltage pulse must continually increase in proportion to the DC voltage [148]. The pulse fraction is a parameter that can be adjusted during the analysis and it should be optimized in order to avoid preferential evaporation of the species with the lowest evaporation field [148].

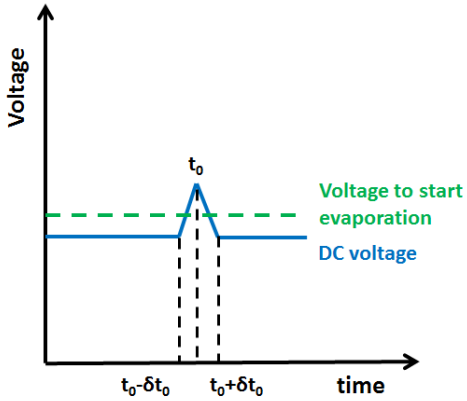

Figure B. 3 - Schematic view of the pulse behaviour during time for the high-pulse method

B.2.1 Set-up of an Atom Probe chamber

The general set-up of an atom probe is shown in Figure B. 4 and it includes an ultra-high vacuum chamber with a pressure below 10^{-8} Pa. The specimen is mounted on a stage that can be translated in the xyz directions to position the specimen in front of the counter-electrode. In some set-up like the one used for the Gracos project, a goniometric stage is also included to allow tilting and rotation of the sample in order to position it in the best way respect to the detector.

The temperature of the stage and specimen is kept low between 20K and 80K and a DC high-voltage power supply is connected to the specimen to generate the required electrostatic field. A counter electrode is also positioned in front of the specimen and it is connected to a high-voltage pulser. In the case of laser-assisted atom probes, there is the beam of the pulsed laser which is focused on the tip's apex [148]. In the same chamber there is also the detector to determine position and charge of the evaporated species.

However, "the field evaporation process is a probabilistic phenomenon and not all the atoms will be field evaporated at the same instant t_0 during a high-voltage pulse" [148]. "This uncertainty on the starting of the ions is detrimental for the determination of the mass to charge ration which is necessary to determine the type of atomic specie" [148], [224]. Depending on the instant at which the ion is created, it will be accelerated by a different stage of the varying electronic field so they will not acquire the full energy during the pulse [148]. This is known as energy deficit and it depends on the velocity of the ion and thus on the mass of the evaporated atom. The energy deficit is responsible for the tails in the peaks of the mass spectra obtained during the APT analysis. Techniques have been developed to limit this energy deficit. It has been considered that ions entering in an electrostatic field with a lower energy will be deflected first and for this reason they will have a shorter flight path than ions having higher energy. So, reflectrons which act as electrostatic mirrors have been designed to limit this energy deficiency so that the ions with a higher energy will travel farther into the reflectron before being deflected increasing their time of flight, while the ions having lower energy will be deflected earlier having shorter time of flight [148]. This ensures that the ions of the same atomic specie even if they are not evaporated at the same time, they will reach the detector on the same time and they will be detected as the same

element. The use of these time-focusing devices reduces the size of the tail in the peaks of the mass spectra improving the resolution and the signal to background.

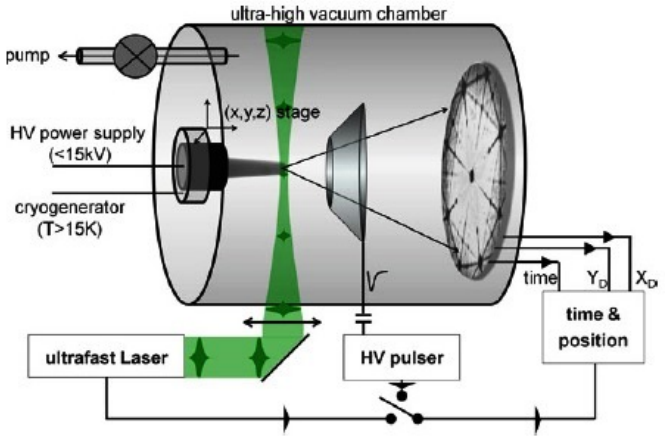

Figure B. 4 - Set-up of atom probe tomography **[148]**

B.2.2 Spectrum obtained from an Atom Probe Tomography analysis

The first information that can be obtained from the APT test is a mass spectrum which is calculated by measuring the time of flight (*ToF*) of the evaporated atoms. The time of flight is used to calculate the mass to charge ratio which will help in identifying the element and which will allow to identify the chemical composition of the analyzed material. The relation between the mass to charge ratio (*M*) and the time of flight (*ToF*) is obtained by writing an equation of energy conservation. The time of flight (*ToF*) of the ion is defined as the time between the application of the voltage pulse that triggers the evaporation and the moment when the impact of the ion is recorded on the detector. This time of flight is directly related to the kinetic energy of the ion. It is possible to write an equation of conservation of energy between the potential energy acquired by the ion in the electric field and its kinetic energy at the moment of the evaporation. The equation is shown below:

$$\frac{1}{2}mv^2 = neV \qquad \text{(eq. B. 3)}$$

where, *m* is the atomic mass of the ion, *v* is its velocity, *"ne"* is the charge of the ion (with *"e"* the charge of the electron) and *V* is the total voltage applied to trigger the evaporation. The velocity *"v"* of the ion can be calculated as the distance between tip of the analyzed material and detector (*L*) divided by the time of flight (*ToF*), so the previous equation can be rewritten as [148], [224]:

$$M = \frac{m}{n} = \frac{2eV}{v^2} = 2eV * \left(\frac{ToF}{L}\right)^2 \qquad \text{(eq. B. 4)}$$

A schematic view is shown in Figure B. 5.

The mass to charge ration is specific of the evaporated chemical element and of its isotopes, so from the analysis of the mass to charge ratio spectrum it is possible to identify the chemical composition of the tested material. However, as it can be seen schematically in Figure B. 5, the detector is a 2D detector and some ions will not be evaporated exactly perpendicular to the tip and therefore, they will not hit exactly the center of the detector which is identified in Figure B. 5 with the coordinates (X_0, Y_0). Those ions, which will not hit the center of the detector, will travel higher distance than the distance between the tip and the detector. So, their travelled distance is calculated by using the Pythagoras theorem once their coordinates (X, Y) are known.

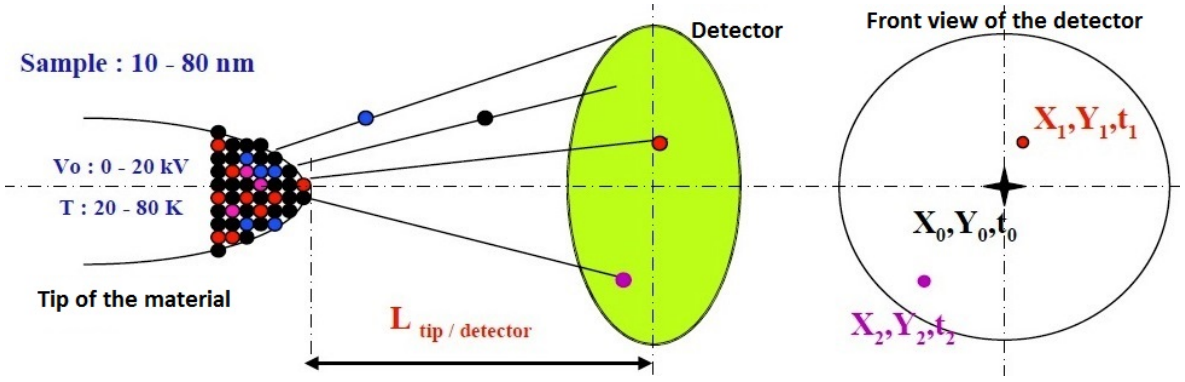

Figure B. 5 - Schematic view of field evaporation during atom probe tomography: L is the perpendicular direction between the tip and the center of the detector, however some ions will hit the detector not in the center, so L must be recalculated by using the Pythagore correction **[225]**

By applying the Pythagoras theorem, the flight distance can be written as:

$$L_{\text{flight}} = \sqrt{\left(L_{\text{tip/detector}}\right)^2 + \left(X - X_0\right)^2 + \left(Y - Y_0\right)^2} \qquad \text{(eq. B. 5)}$$

B.2.3 Three dimensional reconstruction of Atom Probe Tomography Data

From an APT analysis, the raw data obtained for each evaporated ion are the time of flight, the DC voltage, the position coordinate X and Y on the 2D detector and the sequence at which the ion has been evaporated. In the previous paragraph, it has been discussed how to use the time of flight and the position coordinates to identify the evaporated chemical

element. However, 3D reconstruction can also be performed from these raw data to map the positions of individual atoms in 3D to reveal their arrangement. In particular, there are algorithms where starting from the X and Y coordinates obtained with the detector; it is possible to calculate the projection of the ion to reconstruct its position in the z direction. In general, the calculation of the flight path followed by the ion during the evaporation would require accurate knowledge of the 3D electric field distribution both close and far from the tip surface. In Figure B. 6 a geometrical scheme of ion evaporation with the main dimensions necessary for the reconstruction is shown.

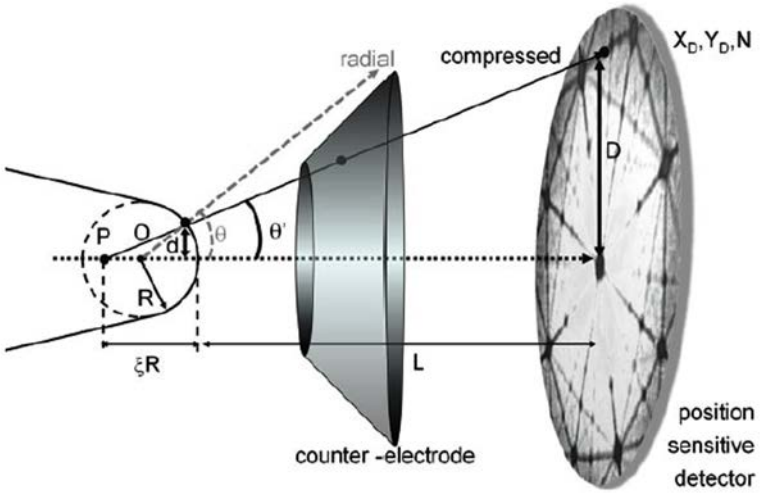

Figure B. 6 - Schematic view of the trajectory followed by an atom during its evaporation **[148]**

As shown in Figure B. 6, once emitted the ions should follow the lines of the electric field. As reported by Gault et al., [148] " Calculations have shown that the initial trajectories are radial so the ion leaves the surface of the tip almost normally. These trajectories are compressed after a certain distance. This is equivalent to consider the trajectories as straight but originated from a point which is located not in the center of the hemispherical cap but farther down along the specimen axis as shown by point P ". This approximation is at the origin of the point-projection model used for 3D reconstruction. The exact ion trajectory is difficult to determine since it requires having the exact electric field distribution, which might be difficult to determine considering that the shape of the tip also changes during the evaporation process.

It is supposed that the focal point "P" is located along the axis of the specimen at a distance ξR from the apex of the tip. The factor is called image compression factor and a relation can be written between the original launch angle Θ and he angle after compression Θ', which is:

$$\theta = \theta' + \arcsin\left(m * \sin\theta'\right) \qquad \text{(eq. B. 6)}$$

where, m is defined as: $m=(\xi-1)$.

Values for the image compression factor can be obtained considering that the image magnification of the ion at the detector corresponds to *D/d* and since the flight length *L* is bigger than the radius of curvature *R*, then it is possible to write [148]:

$$M_{proj} = \frac{D}{d} \cong \frac{L}{\xi R} \qquad \text{(eq. B. 7)}$$

In the above expression, *D* is the distance between the impact of the ion and the center of the detector, while *"d"* is the distance between the specimen axis and the projection of the ion into the plane tangent to the apex surface. The radius R of the tip can be obtained from the voltage *V* according to the equation $R = (V/\beta F)$ or it can be evaluated considering the evolution of the tip shape as the evaporation occurs.

The value of the image compression factor ranges between 1 (radial projection) and 2.

The 3D reconstruction process starts considering that the atoms that protrude most from the surface will be field evaporated more easily since they will experience a stronger electric field. In particular, the penetration depth of the electric field is in the range of picometres and, which is smaller than the interplanar spacing for most metals [148]. For this reason, the material is theoretically evaporated layer by layer, so the sequence in which ions are detected is directly related to the relative depth of the atoms within the original sample. The algorithm used for the 3D reconstruction supposes that the evaporated volume has the shape of a perfect cylinder and the lateral coordinates of an evaporated ion can be obtained using the point-projection method (since the quantity *"d"* can be obtained from (eq. B. 7) [148].

The depth *z*, which will give the third dimension, is deduced by the ion evaporation sequence and as ions are evaporated, the specimen surface becomes farther from the detector [148]. Details on the obtaining of the third dimension around z are reported in the work of Gault et al. [148]. The coordinate x and y of the position of the ion on the tip surface can be related to the coordinate X_D and Y_D of the detected ion by the following equations [148]:

$$x = \frac{X_D}{M_{proj}} \qquad y = \frac{Y_D}{M_{proj}} \qquad \text{(eq. B. 8)}$$

For each atom, the quantity M_{proj} can be calculated considering the evolution of R (radius of the tip) obtained from the applied voltage or by calculating the evolution of the shape of the tip [148]. Equations describing the evolution of the geometry of the evaporated volume are reported in detail in the work of Gault et al. [148].

During the reconstruction of the APT data, some discrepancies between the reconstructed data and the real structure of the tip might occur. These aberrations are caused by deflections in the flight of the ions. The first cause of deflection is the "roll-up" effect. This corresponds to a possible movement of an atom on the surface of tip before it actually evaporates. So the atom rolls along the edges of the terraces forming the apex of the tip as shown in Figure B. 7.

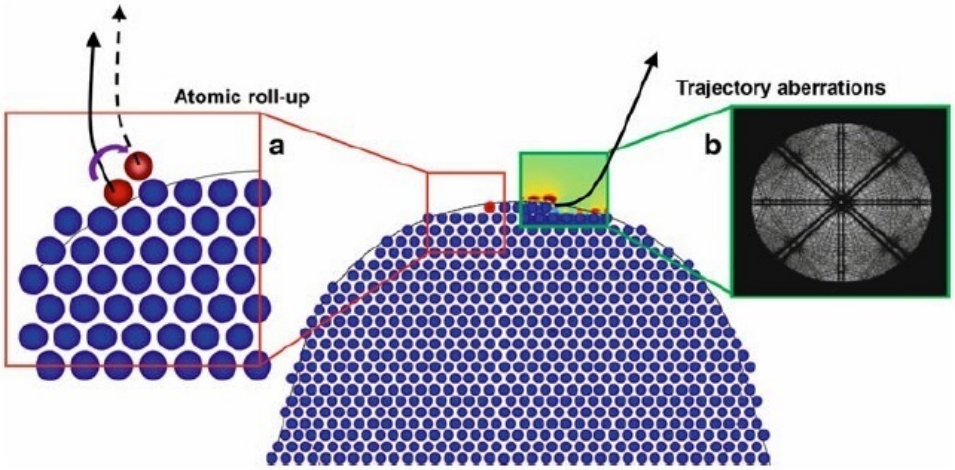

Figure B. 7 - View of the roll-up effect (a) and of its trajectory aberrations (b) **[148]**

Other trajectory aberrations are caused by the presence of precipitates having a big difference of evaporation field compared to the matrix where they are placed. When the field required to field evaporate the precipitate is lower than the one of the matrix, the term "low-field precipitate" is used; but if the field required to evaporate the precipitate is very high compared to the one of the matrix, then the precipitate is referred as "high-field precipitate". This difference of evaporation field between precipitates and matrix leads to the following aberrations:

- Flattening of the surface in the case of low-field precipitates which deflect the ion trajectories inwards as shown in Figure B. 8 causing an apparent increase in the density of hits;

- In the case of high-field precipitates, locally there is a higher field that repels the ions causing locally an apparent decrease in density in the detector (see Figure B. 8).

To avoid these aberrations in the reconstructions, specific protocols have been implemented. Further details are reported in the book of Gault et al. [148].

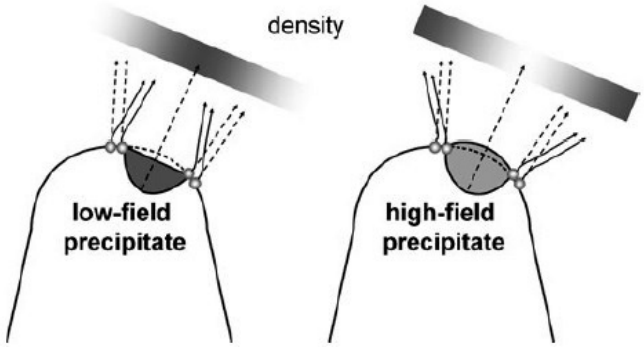

Figure B. 8 - Trajectory aberrations due to a change in surface curvature for the presence of low-field and high-field precipitates **[148]**

B.3 Specimen requirements for Atom Probe Tomography

In the previous section, it has been explained the importance of creating sharp needle-shaped tip of the material that needs to be analyzed using APT. Different techniques have been implemented depending on the geometry of the sample or whether a specific site within the sample has to be analyzed and if the specimen is electrically conductive or not.

If a specific feature inside the sample needs to be analyzed in APT, such as a grain boundary, it is necessary to consider the likelihood that this feature follows in the field of view of APT which is around 100nm.

The tip to be used for APT has to satisfy some requirements for the analysis to be successful; first of all, to reach the field strength required for field evaporation, the specimen has to be needle-shaped with an appropriate radius of curvature at the apex. According to literature [148], the radius of curvature at the apex is between 50 nm and 150 nm even if in some cases it can be also of 20 nm depending on the preparation method. The surface should be free from protrusion and cracks, which can cause stress concentration during the evaporation process bringing to rupture of the specimen. Moreover, the presence of cracks, protrusions or a non-circular cross section of the tip can cause artefacts in the 3D reconstruction since the algorithm is based on the assumption of a hemispherical cap as tip geometry.

During the needle-shaped tip preparation, a sufficient specimen length must be assured in order to avoid shielding of the tip from the supporting structure, moreover it is fundamental to avoid the presence of secondary sharp tips in proximity of the main specimen since they could also emit. If their presence cannot be avoided, they should be at least 100 µm distance from the main tip. However, 50nm seem to be sufficient for measurements conducted using with APT containing a microelectrode, since the use of the local electrode limits the area of field enhancement and hence the area that is field evaporated. For laser-pulsing experiments, secondary tips are of less importance unless they are very close to the area hit by the laser. Finally, the tip should have an appropriate shank angle. Based on the previous geometrical requirements, two main techniques to prepare the specimens will be presented in the next paragraph.

B.3.1 Methods to obtain specimens for Atom Probe Tomography

One of the simplest methods which is used for electrically conductive materials is the electropolishing technique. A power supply is applied to create an electrolytic cell where the specimen is the anode and a wire loop acts as cathode while both of them are immersed in an electrolyte. When a current is applied a corrosion reaction happens and the electrochemical reaction at the anode dissolves the metal. However, there is only a range of voltage where the polishing is effective as shown by Figure B. 9, since if the voltage is too low, etching will happen, while at high voltages, the specimen will be affected by pitting.

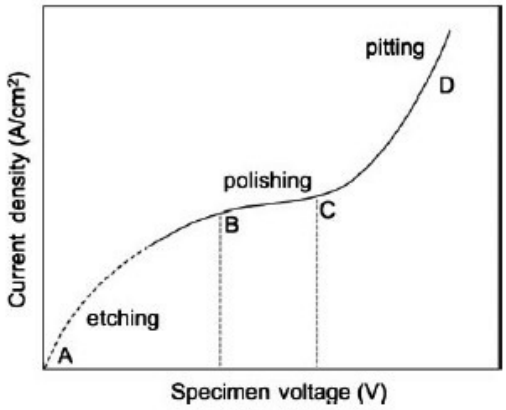

Figure B. 9 - Eectropolishing curve showing the current density between anode and cathode as function of the applied voltage. The optimal voltage range for polishing occurs between points B and C **[148]**

Before starting the electropolishing it is necessary to prepare square slices of the material which ideally should be 15/25 mm long and they should have a regular square cross-section

of 0.2/0.3 mm by 0.2/0.3 mm. It is very important that the initial cross-section is close to a square otherwise the specimen will not have a circular cross-section at the end of the polishing process; in alternative the slices can be of circular cross section. The slices are cut using precision saw or wire machining.

For the Gracos project, for the APT measurements which need to be performed in the center of the diffused IF sheet, the slices have been cut using a precision saw and their cross-section is (0.2x0.2 mm^2). A picture of the slices obtained from the IF steel of the Gracos project is shown in Figure B. 10.

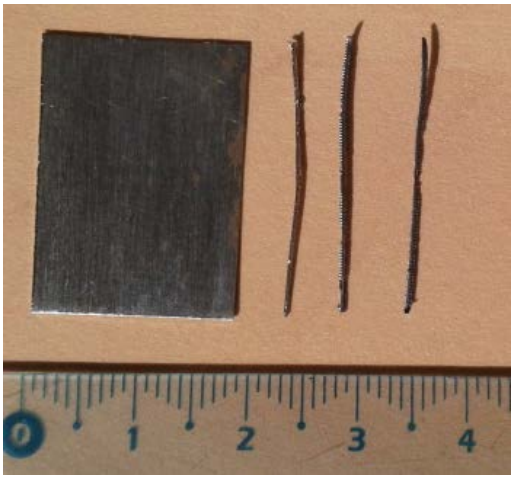

Figure B. 10 - Slices to be used to prepare tips for Atom Probe Tomography

When the slices have been cut, the electropolishing procedure can start. The first step involves a “rough” polishing which is performed to smooth the surface of the slice and to form a neck. When the neck is formed, the second step, which involves a “fine” polishing, is started. This second step is continued until the specimen breaks leaving a very fine tip.

For the Gracos project both steps are performed with a small test rig where the electrolyte is suspended within a wire loop, which is made of Pt and it is connected to a power supply. The raw slice of the specimen is repeatedly pushed through the loop and it is polished until it becomes sufficiently sharp to be used for APT analysis. The variation of geometry of the tip during the microelectropolishing is followed by using a high magnification optical microscope. A schematic view of the set-up is shown in Figure B. 11.

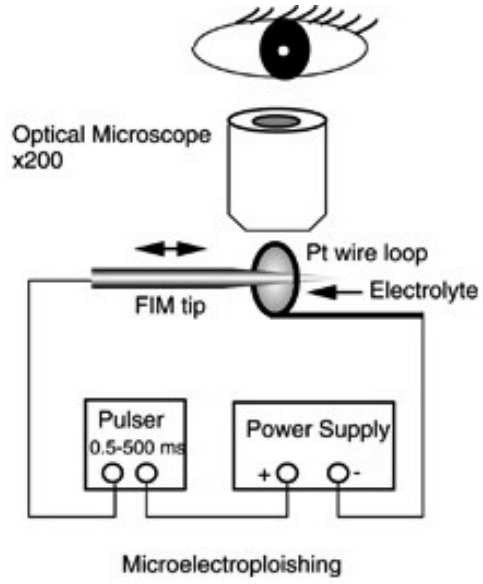

Figure B. 11 - Schematic view of experimental set-up for microelectropolishing [226]

For the Gracos project, in the initial stage a neck is created in the slice using a solution of 75% acetic acid and 25% percloric acid as electrolyte Figure B. 12 (a)), while in a second stage the neck is thinned removing the excess of metal using a solution of 98% monobutilique ether and 2% percholoric acid as electrolyte (Figure B. 12 (b)). For the micropolishing, it is important to replace frequently the electrolyte inside the loop in order to keep low its temperature to avoid heating effects which could modify the microstructure of the specimen.

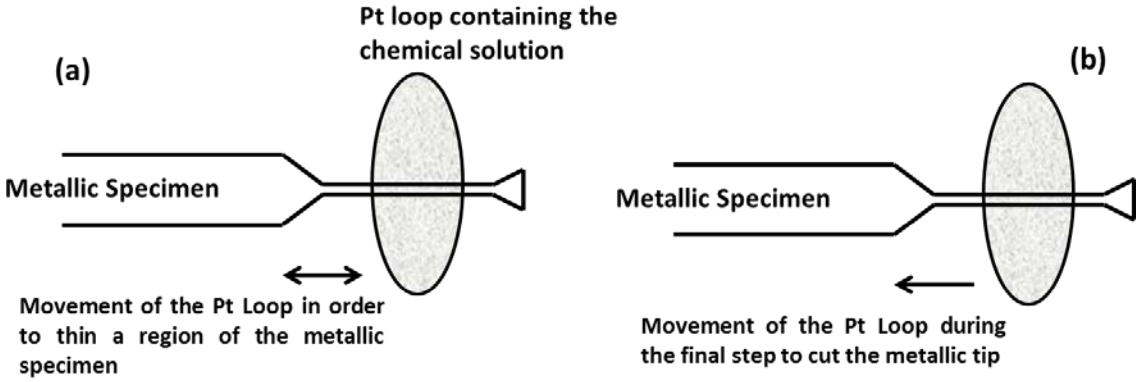

Figure B. 12 - Microelectropolishing schematic view

The polishing technique is quick, easy to apply, not expensive and it can be used to repolish analyzed samples. However, the main drawbacks are that this method is applicable only to

conductive materials and it is very difficult to prepare site-specific specimens. In Figure B. 13 a picture of a tip obtained by electropolishing method is shown.

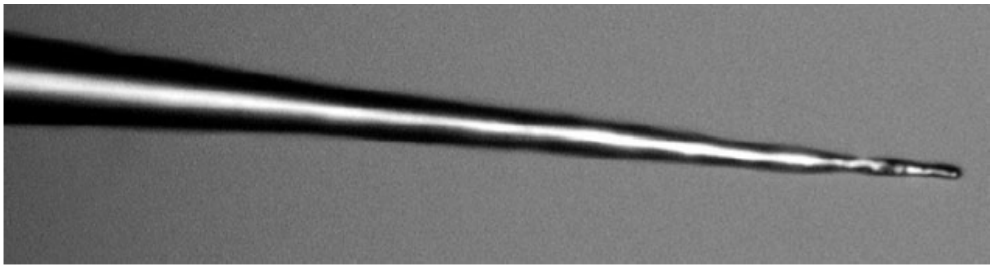

Figure B. 13 - Sharp tip obtained by electropolishing method (20X) [148]

B.3.2 Focused Ion Beam and Lift-Out Method

Focused Ion Beam (FIB) is a recent technique which is used to prepare needles for APT when site-specific specimens or tips from semiconductors have to be prepared. With this method, sharp needles can be prepared locating any interesting feature close to the apex which will be analyzed. One of the procedures to create the needles is called "lift-out" method. It involves cutting a specific site directly from the surface of the specimen by using the FIB; then the cut piece is lifted out by welding it to a micromanipulator and it is transferred to prefabricated posts. For the Gracos project, the preparation of prefabricated posts was made taking pins of steel and by doing a "rough" microelectropolishing using the loop test rig explained in section B.3.1; in alternative Silicon pillars can be used.

Before performing the cutting with the FIB, the specimen is inserted in the FIB-SEM chamber and the zone of interest is coated with a thin layer of W or Pt to protect the top-edge of the specimen from the damage caused by the Gallium ions used to cut the material. For the specimen prepared in the Gracos Project, the layer of deposited Pt applied on the FeC film had a width of 2 µm, a length of 20-30 µm and a thickness of 1.2 µm (Figure B. 14 and Figure B. 15). Successively, a rectangular bar of the specimen is isolated by milling trapezoidal zones around it as shown in Figure B. 15. Once these cuts are complete, another cut is made at one end of the bar to release it from the bulk. Successively, an in-situ micromanipulator is positioned adjacent to the free end of the wedge (Figure B. 16) and the tip of the micromanipulator is welded on this free end before cutting the other side of the wedge and releasing it completely from the bulk (Figure B. 17). The welding between micromanipulator and wedge is made deposition Pt.

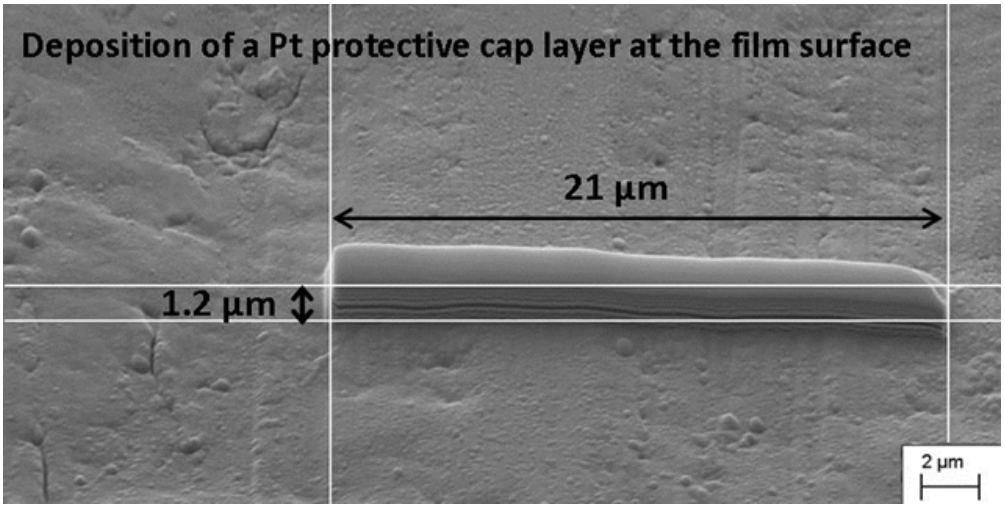

Figure B. 14 - Deposition of Pt protective layer on the IF steel

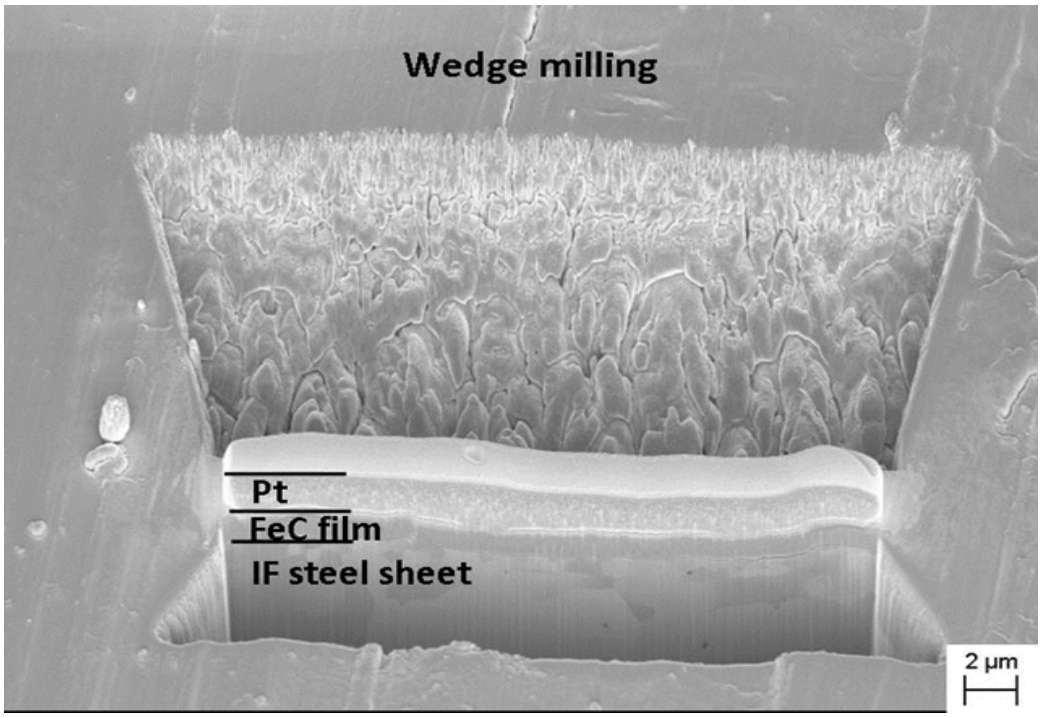

Figure B. 15 - Cross-section view of the milled wedge. The trapezoidal cuts are clearly visible while the wedge of interest is coated with the Pt protective layer

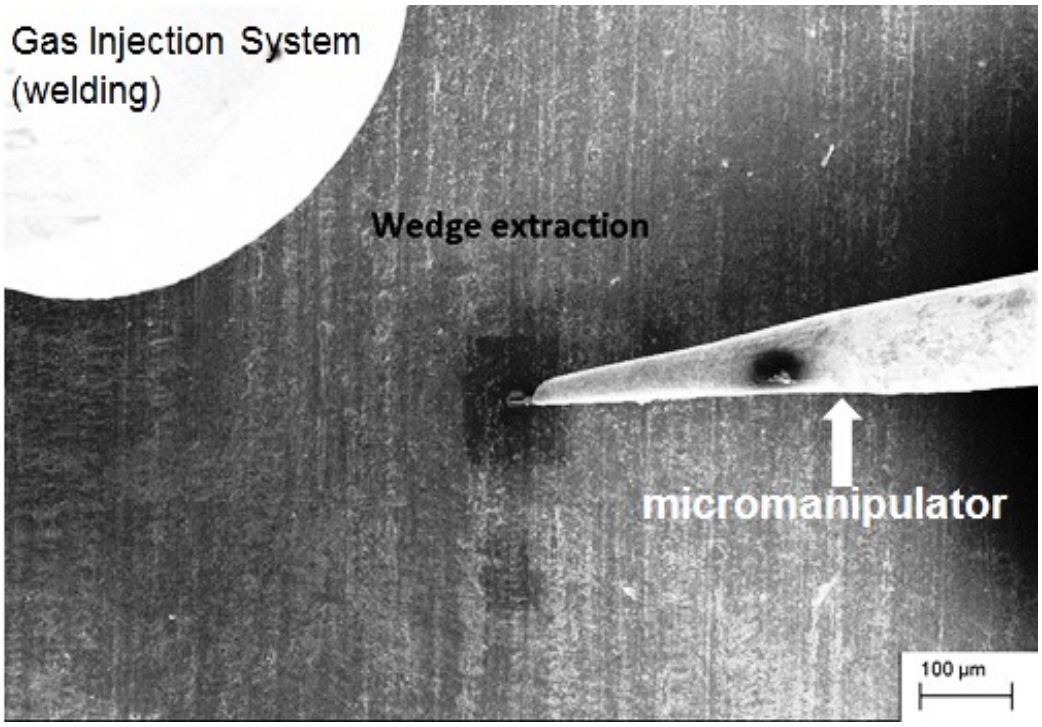

Figure B. 16 - Micromanipulator is placed adjacent to the free end of the wedge

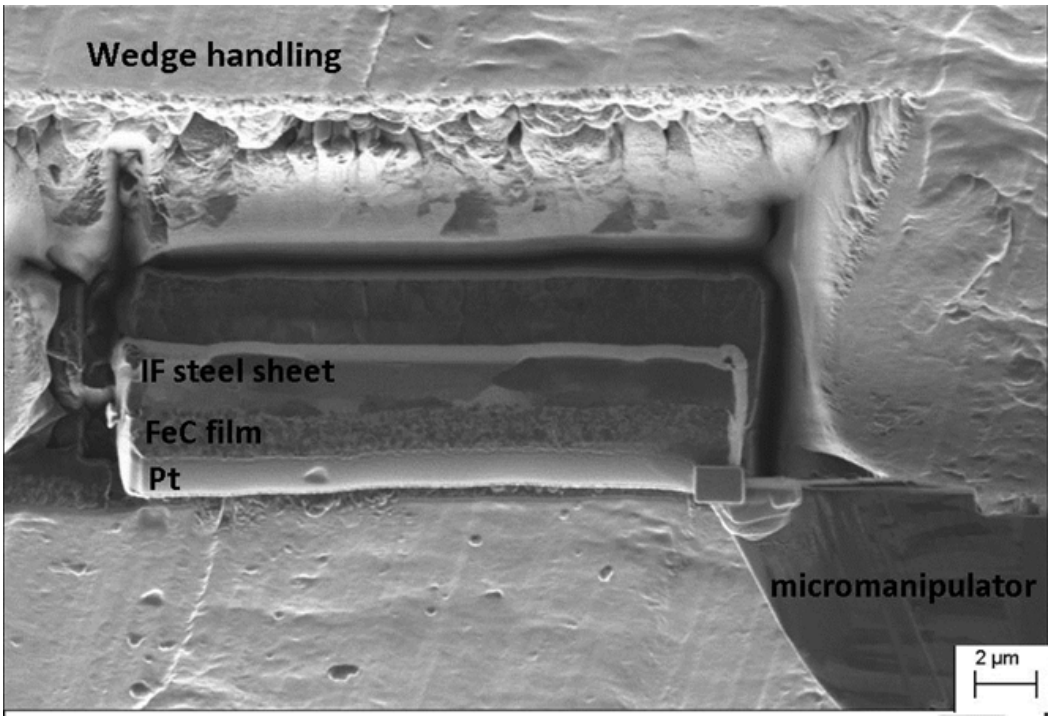

Figure B. 17 - Micromanipulator is welded on the free end of the wedge and the other end of the wedge is cut to completely extract the bar of material from the bulk

Sometimes it is preferably to pre-mill the end of the micromanipulator before welding it to the wedge in order to have a better flat surface to ensure a good contact with the material to be extracted. The wedge is then removed from the base material by lowering the FIB stage and the extracted material will be deposited on the posts which have been previously prepared (Figure B. 18 (a)). On each post a small slice of the extracted wedge will be welded (Figure B. 18 (a) and (b)) and later SEM annular milling is performed to obtain the final shape of a sharp tip for APT analysis (Figure B. 19).

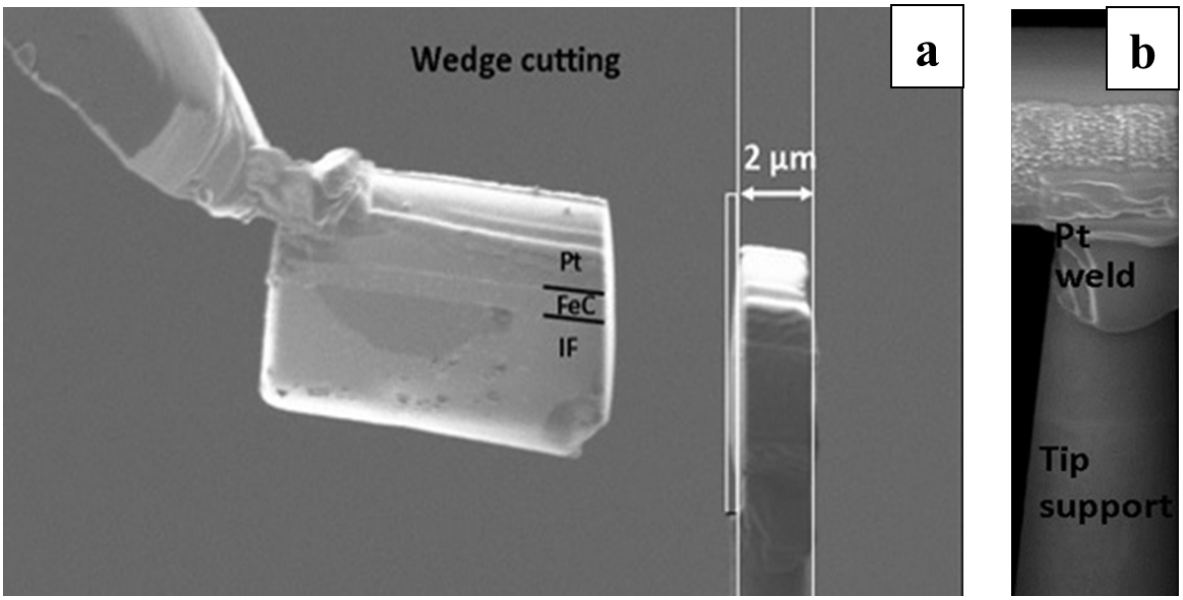

Figure B. 18 - Slices of the wedge are cut and welded on the posts before performing the final annular milling (a), detail of the deposited slice on the tip support (b)

"The final annular milling of the tip is a critical process to determine the final geometry of the apex of the tip, to position properly the region of interest when site-specific preparation are important and also to ensure minimization of the Gallium ions damage to the base material" [148]. In order to make thinner the slice of the wedge deposited on the support, *"successive annular mills are performed with progressively smaller beam currents and inner diameters to obtain the final tip shape"* [148]. The inner diameter and the current to use depend on the required final geometry and on the type of material. A schematic view of the process is reported in Figure B. 20. During all the stages of the FIB "Lift-out" procedure, the material is removed by using highly energetic Ga^+ ions which can cause damaging in the material to be analyzed. Ion-beam damage has the form of implantation of ion, amorphisation and creation of defects in the base material. Usually if there is a significant

implanatation of Ga^+ ions in the base material, they will be detected during APT analysis and they will be discarded, however, it is better to avoid Ga^+ damaging in order to avoid modification in the microstructure of the base material [148].

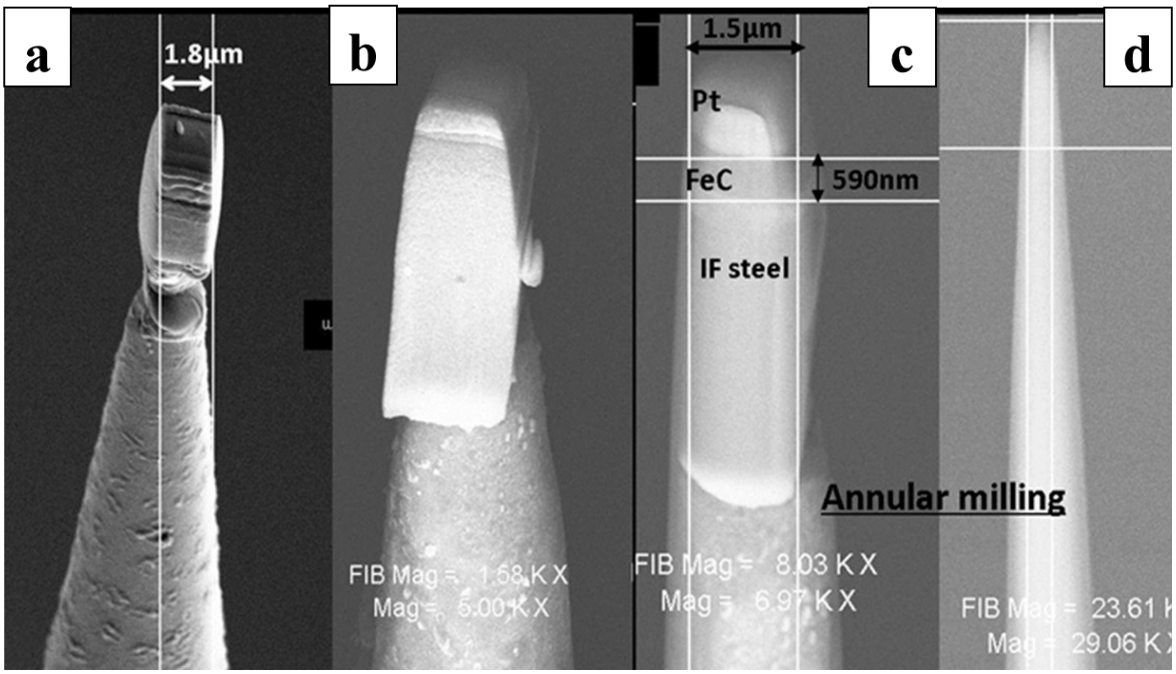

Figure B. 19 - Steps of FIB preparation of tips for Atom Probe Tomography: (a) the material to be analysed is placed on a metallic pre-tip, (b) and (c) SEM annular milling of the tip; (d) final shape of the tip that can be analyzed in APT

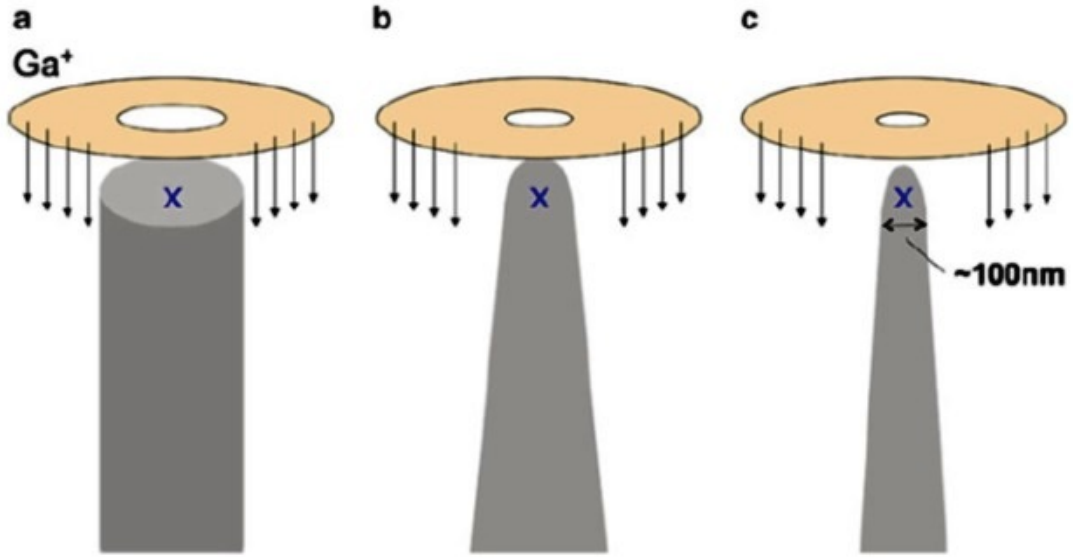

Figure B. 20 - Milling of a tip by using an annular milling pattern, where x represents a feature of interest to be kept in the final APT tip. The size of the inner diameter is progressively decreased from (a) to (c), while the beam current is decreased [148]

For this reason, the acceleration voltage of the Ga^+ ions is decreased so that also their energy is lowered and as a consequence, the depth of damage is reduced [148]. Furthermore, it is common practice to perform the final stage of the annular milling process at very low voltages to make a sort of "cleaning" to remove the highly damaged region produced from previous milling steps. According to literature [148], Ga^+ ions can penetrate deeper into the base material due to channeling along major crystallographic directions. "Ions penetration due to channeling can have penetration depths from two to six times higher than what expected and even if from APT analyses, the Ga^+ detected peaks corresponds to a low percentage of ions, the damage caused in the material can still be significant" [148]. For this reason, it is always better to use low voltages for the milling process since the beginning stages and not only in the final cleaning step even if the preparation of the specimen will require longer times.

Appendix C : Thermoelectric Power Measurements

C.1 Thermoelectric power measurements (TEP)

According to literature, the TEP value does not depend on the shape of the sample as long as the ratio between section *(S)* and length *(L)* is lower than *S/L*<0.5mm [150]. The technique is used quite often since it can be performed very quickly (< 1 min) and the resolution of the measurement is of the order of 1 nV/K [32]- [150]. Moreover, on the contrary of internal friction measurement, TEP is able to detect all the carbon atoms in solution whatever their environment may be, while the internal friction technique is not able to detect the carbon atoms which are in interaction with some substitutional atoms (especially manganese) [149]- [151]. According to the explanation given by Perez et al. [149] the absolute TEP of a pure metal (S_0^*) is the sum of two components S_d^x and S_g^x. The first term (S_d^x) is the diffusion component which is associated with the conduction electron scattering and which varies almost linearly with the absolute temperature, while the second term (S_g^x) is the lattice component which takes into account the interaction between phonons and electrons. However, the absolute TEP of pure metal at room temperature seems to be determined mainly by the diffusion component [149]. Moreover, the absolute value of TEP for a metallic material (S^x) is in reality the sum of different contributes and it is expressed as:

$$S^* = S_0^* + \Delta S_{SS} + \Delta S_d + \Delta S_{pp} \qquad \text{(eq. C. 1)}$$

where, S_0^x is the TEP of the pure metal, ΔS_{SS} is the variation of TEP caused by elements in solid solution, ΔS_d is due to dislocations and ΔS_{pp} is due to precipitates [32]- [149]. In particular, the contribution due to elements in solid solution is evaluated using the Gorter-Nordhein law which can be expressed as:

$$\Delta S_{SS} = \sum P_i * [i_{SS}] \qquad \text{(eq. C. 2)}$$

where, $[i_{SS}]$ is the content of the element "i" in solid solution (expressed in wt%) and P_i is a coefficient reflecting the contribution of the element "*i*" to the modification of the TEP of pure iron [151]. The coefficient P_i is related to the resistivity of the material according to the following relation:

$$\left|P_i\right| = \frac{\alpha_i * S_i}{\rho} \qquad \text{(eq. C. 3)}$$

where, α_i and S_i are the specific resistivity and the specific TEP of the element "*i*" in solution of the pure metal, whilst ρ is the resistivity of the material [151]. From this, it derives that the content in solution of the elements "*i*" can be obtained from the measured TEP value once that the coefficient $\left|P_i\right|$ is known applying the following equation [151]:

$$[i_{SS}](wt\%) = \frac{\Delta S_{SS}}{\left|P_i\right|} \qquad \text{(eq. C. 4)}$$

The elements in solid solution have strong influence in the modification of the TEP value because they create new diffusion centres for electrons and phonons and according to literature, if the concentration of the element "*i*" is low (<0.1at%), the interaction between elements can be neglected and the addition rule mentioned above can be applied [227].

It has been shown that TEP technique is very sensitive to the amount of atoms in solid solutions (for example variations caused by precipitation and dissolution processes) and to the dislocation state such as deformation and recovery [150]. In general, TEP measurements are very sensitive to modifications of the electronic or elastic properties of the iron lattice induced by defects [32]. Researchers have also shown that the introduction of dislocations causes a negative variation of the TEP measurement [32], [227]. Incoherent precipitates have no influence on the TEP value but coherent precipitates are able to modify the TEP because they induce elastic and electronic disturbances in the lattice [32], [227].

TEP measurements have been used to follow the kinetic of segregation of carbon atoms to dislocations in heavily deformed steel. During these analyses, the steel is deformed up to a given strain and then it is aged for different times and temperatures. After each treatment, the TEP variation of the steel is measured so that its change can be plotted as function of ageing time or aging temperature. If during this ageing treatment, no recovery and no precipitation phenomena are taking place, then the variation of the TEP value is due to the segregation of carbon atoms to the dislocations and it is proportional to the amount of interstitial atoms which are segregated [149].

A procedure to evaluate the concentration of interstitial atoms (carbon) in a ferrite matrix is described in detail in ref. [32]. This procedure is schematically shown in Figure C. 1 and it is

made by two steps. The first step consists in cold-working the material to introduce a sufficient density of dislocations to trap all the interstitial solutes. After this step, the TEP variation of the cold rolled specimen is measured compared to the initial state of the material. Successively, the second step is applied and it involves a static strain ageing treatment of 30min at 120˚C which will cause the segregation of all the interstitial atoms to the dislocations [31], [32]. After the TEP variation between the cold-rolled state and the aged state is measured to assess the concentration of interstitial elements [32]. However, this technique can be used only if the amount of interstitial atoms does not exceed $15x10^{-3}$ wt% [31], because above this concentration the dislocation density which can be introduced in the samples is not sufficient to trap all the interstitial atoms in solid solution [32]. In the same paper, Lavaire et al. [32] have proved that the variation of thermoelectric power ($\Delta S_{a,max}$) is directly proportional to the interstitial atoms in solid solution in the steel. This has been proven evaluating the variation of TEP ($\Delta S_{a,max}$) as function of precipitation of carbon, in particular the initial state of the steel has the carbon in solid solution and this state is named {ss}. Successively, the steel is treated at 270˚C for different times in order to cause precipitation of a certain fraction of carbon and the TEP of this state, which is named {p(t)}, is measured. The difference between the TEP of the two states is directly proportional to the carbon which is not precipitated [32]. In the same paper [32], a procedure to distinguish between the TEP variation caused by carbon in solid solution and nitrogen is described.

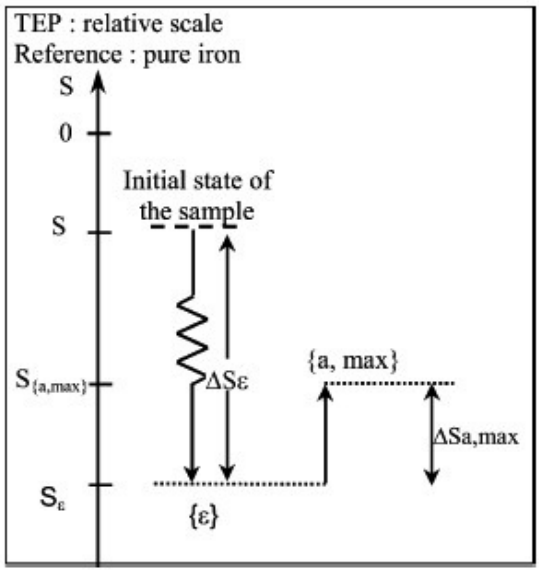

Figure C. 1 - Experimental procedure used for the quantitative evaluation of the amount of interstitial atoms in solid solution using TEP measurements **[32]**

Appendix D : Tensile Tests

D.1 Calibration of the tensile machine

Before performing the tensile tests reported in Chapter 5, a calibration of the tensile machine was performed in order to establish a correlation between the parameter written on the program for the speed of the test and the real speed of the movable arm of the tensile machine. Table D- 1 summarizes the obtained measures.

Calibration of the tensile machine (magnification of the microscope 10X)				
Speed set in the program	**time**	**space**	**total time in sec**	**real speed on the sample [µm/s]**
2	8 min, 55s	659.60µm	535	1.232897196
5	4min, 29s	659.60µm	269	2.45204461
10	2min, 27s	659.60µm	147	4.48707483
15	1min, 39s	659.60µm	99	6.662626263

Table D- 1 - Calibration of the tensile machine

To calibrate the machine, the time to cover a distance of 659.60 µm was measured setting different values for the speed inside the program of the tensile machine. After this, by simply dividing the distance by the time, the real speed at which the sample is pulled was calculated. This means that a speed of 2 in the program corresponds to 1.23 µm/s and a speed of 5 in the program corresponds to a speed of 2.45 µm/s and so on. The distance taken into account is 659.60 µm, because this is the maximum size of the sample on the screen of the microscope for a magnification of 10X. In our case, all the samples were tested using the speed of 5, which corresponds to 2.45 µm/s. Considering that the gauge length of the specimen is 5 mm, this speed will correspond to a strain rate of $5x10^{-4}$ s^{-1}.

D.2 Tensile Tests

D.2.1 Dimensions of tested coupons

In this section of Appendix D all the dimensions of the tensile coupons tested in section 5.3 are reported. From Table D- 6 to Table D- 13 the values of mechanical properties extracted from the engineering stress-strain curves are listed for the tested tensile coupons. If the tensile coupon did not show Lüdering, only one value of yield stress is reported, while if

Lüdering is present, then the value of the upper yield stress is reported and the value of the yield stress at the end of the plateau (lower yield stress) is listed as well. Lüders length was also extracted for coupons showing Lüdering. Ultimate Tensile Strength (UTS) with strain at fracture were also listed for each coupon. Table D- 2 lists dimensions for uncoated and not-annealed coupons, while Table D- 3 summarizes dimensions of coupons annealed at 330 ºC for 4 days or at 430 ºC and 530 ºC for 1h. Table D- 4 shows dimensions for specimens annealed at 630 ºC or 710 ºC for 1h and finally, Table D- 5 reports the dimensions of uncoated but annealed IF steel coupons.

Tensile coupon	**Width [mm]**	**Thickness [mm]**	**Gauge length [mm]**	**Annealing treatment**	**Speed set on the tensile machine [µm/s]**
NA 1	1	0.195	5	Not annealed-coated both sides	2.5
NA 2	1	0.192	5	Not annealed-coated both sides	2.5
NA 3	1	0.194	5	Not annealed-coated both sides	2.5
NA 4	1	0.195	5	Not annealed-coated both sides	2.5
A-1	1	0.200	5	330 ºC, 1h	2.5
A-2	1	0.194	5	330 ºC, 1h	2.5
A-3	1	0.198	5	330 ºC, 1h	2.5

Table D- 2 - Dimensions of tensile coupons coated both sides and not-annealed and of tensile coupons coated both sides and annealed at 330 ºC – 1h in high vacuum

Tensile coupon	Width [mm]	Thickness [mm]	Gauge length [mm]	Annealing treatment	Speed set on the tensile machine [µm/s]
B-1	1	0.199	5	330ºC, 4 days	2.5
B-2	1	0.198	5	330ºC, 4 days	2.5
B-3	1	0.197	5	330ºC, 4 days	2.5
C-1	1	0.204	5	430ºC, 1h	2.5
C-2	1	0.193	5	430ºC, 1h	2.5
C-3	1	0.195	5	430ºC, 1h	2.5
C-4	1	0.186	5	430ºC, 1h	2.5
C-5	1	0.187	5	430ºC, 1h	2.5
D-1	1	0.195	5	530ºC, 1h	2.5
D-2	1	0.200	5	530ºC, 1h	2.5
D-3	1	0.187	5	530ºC, 1h	2.5
D-4	1	0.189	5	530ºC, 1h	2.5

Table D- 3 - Dimensions of tensile coupons coated both sides and annealed at 330 ºC – 4 days or at 430 ºC or 530 ºC – 1h in high vacuum

Tensile coupon	Width [mm]	Thickness [mm]	Gauge length [mm]	Annealing treatment	Speed set on the tensile machine [µm/s]
E-1	1	0.2	5	630ºC, 1h	2.5
E-2	1	0.195	5	630ºC, 1h	2.5
E-3	1	0.200	5	630ºC, 1h	2.5
E-4	1	0.197	5	630ºC, 1h	2.5
E-5	1	0.193	5	630ºC, 1h	2.5
E-6	1	0.192	5	630ºC, 1h	2.5
E-7	1	0.187	5	630ºC, 1h	2.5
E-8	1	0.186	5	630ºC, 1h	2.5
E-9	1	0.186	5	630ºC, 1h	2.5
F-1	1	0.194	5	710ºC, 1h	2.5
F-2	1	0.197	5	710ºC, 1h	2.5
F-3	1	0.185	5	710ºC, 1h	2.5
F-4	1	0.185	5	710ºC, 1h	2.5
F-5	1	0.195	5	710ºC, 1h	2.5
F-6	1	0.197	5	710ºC, 1h	2.5
F-7	1	0.198	5	710ºC, 1h	2.5
F-8	1	0.192	5	710ºC, 1h	2.5
F-9	1	0.190	5	710ºC, 1h	2.5
F-10	1	0.194	5	710ºC, 1h	2.5
F-11	1	0.187	5	710ºC, 1h	2.5
F-12	1	0.187	5	710ºC, 1h	2.5

Table D- 4 - Dimensions of tensile coupons coated both sides and annealed at 630 ºC – 1h or at 710 ºC-1h in high vacuum

Tensile coupon	Width [mm]	Thickness [mm]	Gauge length [mm]	Annealing treatment	Speed set on the tensile machine [µm/s]
430˚C-1h – U1	1	0.205	5	430ºC, 1h	2.5
530˚C-1h – U2	1	0.200	5	530ºC, 1h	2.5
630˚C-1h – U3	1	0.191	5	630ºC, 1h	2.5
710˚C-1h – U4	1	0.200	5	710ºC, 1h	2.5

Table D- 5 - Dimensions of uncoated tensile coupons annealed at different temperatures for 1h in high vacuum

D.2.2 Values of Mechanical Properties obtained from Tensile Tests

sample	yield stress σ_{ys} [MPa]	Ultimate tensile stress (UTS) [MPa]	Strain at fracture (ε_B)
NA 1	108.75	265.71	0.5
NA 2	115.61	280.46	0.47
NA 3	120.86	280	0.51
NA 4	109.77	279	0.51
Average	113.75	276.3	0.5

Table D- 6 - Values of mechanical properties for both sides coated and not annealed samples tested at a speed of 2.5µm/s

sample	yield stress σ_{ys} [MPa]	Ultimate tensile stress (UTS) [MPa]	Strain at fracture (ε_B)
A-1	108.17	271.81	0.53
A-2	116.46	280.79	0.47
A-3	119.14	272.68	0.49
Average	114.6	275.1	0.50

Table D- 7 - Values of mechanical properties for both sides coated samples annealed at 330 ºC for 1h and tested at a speed of 2.5 µm/s

sample	yield stress σ_{ys} [MPa]	Ultimate tensile stress (UTS) [MPa]	Strain at fracture (ε_B)
B-1	118.27	270.65	0.53
B-2	140.53	268.65	0.49
B-3	156.8	279.7	0.46
Average	138.53	273	0.49
Average without B-1	148.7	274.2	0.48

Table D- 8 - Values of mechanical properties for both sides coated samples annealed at 330 ºC for 4 days and tested at a speed of 2.5 µm/s

sample	Upper Yield stress [MPa]	Lower Yield stress [MPa]	Average stress in Lüders plateau [MPa]	Lüders length	Ultimate tensile stress (UTS) [MPa]	Strain at fracture (ε_B)
C-1	178.3	185.98	185.48	0.02925	272.91	0.44
C-2	201.26	201.80	203.72	0.02949	292.48	0.41
C-3	179.04	193.54	189.66	0.03159	284.97	0.46
C-4	228.92	211	218	0.03391	295.8	0.47
C-5	218.92	210	213	0.03195	284	0.45
Average	201.3	200.46	201.97	0.03124	286	0.45

Table D- 9 - Values of mechanical properties for both sides coated samples annealed at 430 ºC for 1h and tested at a speed of 2.5 µm/s

sample	Upper Yield stress [MPa]	Lower Yield stress [MPa]	Average stress in Lüders plateau [MPa]	Lüders length	Ultimate tensile stress (UTS) [MPa]	Strain at fracture (ε_B)
D-1	277.64	257.49	266.56	0.04518	323.08	0.39
D-2	249.5	235.9	245	0.03559	305.9	0.39
D-3	261.2	233	244.3	0.04761	303.87	0.44
D-4	248.93	231.93	238.8	0.04183	305.93	0.40
Average	259.32	239.58	248.67	0.04255	309.7	0.41

Table D- 10 - Values of mechanical properties for both sides coated samples annealed at 530 ºC for 1h and tested at a speed of 2.5 µm/s

sample	Upper Yield stress [MPa]	Lower Yield stress [MPa]	Average stress in Lüders plateau [MPa]	Lüders length	Ultimate tensile stress (UTS) [MPa]	Strain at fracture (ε_B)
E-1	276.82	248.55	259.95	0.02217	302.94	0.39
E-2	286.65	258	262	0.05416	313.70	0.38
E-3	289.85	309	297.4	0.06276	347.92	0.22
E-4	334.44	326.43	332.6	0.03418	384	0.24
E-5	332.6	275	288.66	0.0451	340.72	0.33
E-6	296.24	274.94	281.75	0.04098	338.84	0.32
E-7	259.95	247	250.96	0.04363	321.47	0.38
E-8	318.73	282.67	288.45	0.04302	340.64	0.33
E-9	357.15	292.77	298.8	0.04850	343.5	0.34
Average	305.83	279.4	284.5	0.04383	337	0.33

Table D- 11 - Values of mechanical properties for both sides coated samples annealed at 630 ºC for 1h and tested at a speed of 2.5 µm/s

sample	Upper Yield stress [MPa]	Lower Yield stress [MPa]	Average stress in Lüders plateau [MPa]	Lüders length	Ultimate tensile stress (UTS) [MPa]	Strain at fracture (ε_B)
F-1	213.5	189.2	198.4	0.03753	280	0.45
F-2	253.8	202.1	212.6	0.04553	281	0.45
F-3	241.8	220.8	231.4	0.03186	289	0.3
F-4	236.4	221.9	231.2	0.03083	280	0.23
F-5	278.4	214.5	215	0.04416	282.8	0.49
F-6	149.8	158.3	151.8	0.01377	275.7	0.49
F-7	203.8	186.2	187.1	0.02618	277.7	0.46
F-8	276.45	245.35	252.7	0.04474	312.87	0.37
F-9	290.93	249.52	259.52	0.04593	312	0.44
F-10	286	267.84	261.44	0.052355	315	0.39
F-11	265	248.4	251.3	0.04055	308.65	0.39
F-12	258.85	235.6	244.5	0.04043	313	0.39
Average	246.23	220	224.75	0.03782	293.98	0.40
Average (without F-6 and F-7)	260.11	229.52	235.81	0.04139	297.43	0.39

Table D- 12 - Values of mechanical properties for both sides coated samples annealed at 710 ˚C for 1h and tested at a speed of 2.5 µm/s

sample	Upper Yield stress [MPa]	Lower Yield stress [MPa]	Average stress in Lüders plateau [MPa]	Lüders length	Ultimate tensile stress (UTS) [MPa]	Strain at fracture (ε_B)
430˚C-1h – U1	110.98	-	-	-	284	0.48
530˚C-1h – U2	110.31	-	-	-	291.4	0.48
630˚C-1h – U3	106.3	-	-	-	318	0.47
710˚C-1h – U4	114	-	-	-	294.6	0.46

Table D- 13 - Values of mechanical properties of not-coated IF coupons annealed at different temperatures for 1h in high vacuum

D.3 Tensile Tests on coupons coated both sides with FeC film and annealed in argon atmosphere

In Table D- 14 the dimensions of coupons annealed in argon are summarized. The specimens marked with a (*) were analyzed using digital image correlation (DIC) and the thickness written in this table is the thickness of the coupon after polishing but before the application

of the DIC coating. The polishing is performed to remove the FeC coating and to have a smooth surface.

Tensile coupon	Width [mm]	Thickness [mm]	Gauge length [mm]	Annealing treatment	Speed set on the tensile machine [µm/s]
Ar-1	1	0.193	5	430ºC, 1h-Argon	2.5
Ar-2	1	0.197	5	430ºC, 1h-Argon	2.5
Ar-3 (*)	1	0.196	5	430ºC, 1h-Argon	2.5
Ar-4	1	0.198	5	530ºC, 1h-Argon	2.5
Ar-5	1	0.200	5	530ºC, 1h-Argon	2.5
Ar-6 (*)	1	0.209	5	530ºC, 1h-Argon	2.5
Ar-7	1	0.199	5	630ºC, 1h-Argon	2.5
Ar-8	1	0.194	5	630ºC, 1h-Argon	2.5
Ar-9 (*)	1	0.210	5	630ºC, 1h-Argon	2.5
Ar-10	1	0.198	5	710ºC, 1h-Argon	2.5
Ar-11	1	0.192	5	710ºC, 1h-Argon	2.5
Ar-12 (*)	1	0.182	5	710ºC, 1h-Argon	2.5

Table D- 14 - Dimensions of tensile coupons coated both sides and annealed at different temperatures for 1h in argon atmosphere

From Table D- 15 to Table D- 18 the mechanical properties obtained for this series of coupons are shown.

sample	Upper Yield stress [MPa]	Lower Yield stress [MPa]	Average stress in Lüders plateau [MPa]	Lüders length	Ultimate tensile stress (UTS) [MPa]	Strain at fracture (ε_B)
Ar-1	220.35	221.42	219.1	0.00956	301.6	0.43
Ar-2	220.85	233.67	229.98	0.0269	281	0.31
Ar-3	210.67	224.65	218.94	0.0230	281.64	0.27
Average	217	227	223	0.0198	288	0.34

Table D- 15 - Mechanical properties obtained for annealing in argon at 430 ˚C-1h

sample	Upper Yield stress [MPa]	Lower Yield stress [MPa]	Average stress in Lüders plateau [MPa]	Lüders length	Ultimate tensile stress (UTS) [MPa]	Strain at fracture (ε_B)
Ar-4	265.47	258.35	261.63	0.04088	306.2	0.37
Ar-5	261.27	259.34	260.2	0.04969	300.7	0.33
Ar-6	254.90	244.52	253	0.0371	287.21	0.28
Average	261	254	258	0.04256	298	0.33

Table D- 16 - Mechanical properties obtained for annealing in argon at 530 ˚C-1h

sample	Upper Yield stress [MPa]	Lower Yield stress [MPa]	Average stress in Lüders plateau [MPa]	Lüders length	Ultimate tensile stress (UTS) [MPa]	Strain at fracture (ε_B)
Ar-7	265.82	261.80	263	0.05311	303.25	0.32
Ar-8	275.7	274.3	276.4	0.04132	322	0.33
Ar-9	277	243.2	258.4	0.0509	297.3	0.28
Average	273	260	266	0.04844	308	0.31

Table D- 17 - Mechanical properties obtained for annealing in argon at 630 ˚C-1h

sample	Upper Yield stress [MPa]	Lower Yield stress [MPa]	Average stress in Lüders plateau [MPa]	Lüders length	Ultimate tensile stress (UTS) [MPa]	Strain at fracture (ε_B)
Ar-10	203.33	-	-	-	318.84	0.34
Ar-11	280.7	272	273	0.04512	316	0.32
Ar-12	298	283.3	287	0.06775	331.7	0.33
Average	261	278	280	0.05644	322	0.33

Table D- 18 - Mechanical properties obtained for annealing in argon at 710 ˚C-1h

D.4 Tensile Tests on coupons coated both sides with FeC film and Nickel cap layer annealed in Argon atmosphere

Since the argon used for the annealing contained some oxygen, it was believed that it could possibly interfere with the C diffusion from the FeC film. For this reason, another series of tests was proposed where coupons were coated both sides with a 500 nm thick FeC amorphous film which was protected with 20 nm Nickel cap layer applied using a SEM sputter coater. A schematic view of the thickness of the coupons is shown in Figure D. 1. Successively, the coupons were annealed in argon atmosphere at the temperatures 430 ˚C, 530 ˚C, 630 ˚C and 710 ˚C for 1h. In some of the coupons, digital image correlation (DIC) was performed to reveal Lüders bands pattern. Table D- 19 lists a summary of all the tested coupons for each annealing temperature, while in Table D- 20 their dimensions are reported.

Figure D. 1 - Schematic view of the thickness of tensile coupons of IF steel coated both sides with a 500 nm thick amorphous FeC film protected from oxidation or decarburization with 20 nm Nickel cap layer on both sides

Sample Name	Coating Condition	Heat Treatment
NiAr-1, NiAr-2	Both sides	430 ºC – 1h – Argon – Ni cap layer
NiAr-3, NiAr-4, NiAr-5	Both sides	530 ºC – 1h – Argon – Ni cap layer
NiAr-6, NiAr-7, NiAr-8	Both sides	630 ºC – 1h – Argon – Ni cap layer
NiAr-9, NiAr-10, NiAr-11, NiAr-12	Both sides	710 ºC – 1h – Argon – Ni cap layer

Table D- 19 - Summary of tensile coupon coated both sides with FeC film and Nickel cap layer annealed at different temperatures in argon

Tensile coupon	Width [mm]	Thickness [mm]	Gauge length [mm]	Annealing treatment	Speed set on the tensile machine [µm/s]
NiAr-1	1	0.188	5	430ºC, 1h-Argon-Ni cap layer	2.5
NiAr-2	1	0.205	5	430ºC, 1h-Argon-Ni cap layer	2.5
NiAr-3	1	0.198	5	530ºC, 1h-Argon-Ni cap layer	2.5
NiAr-4	1	0.186	5	530ºC, 1h-Argon-Ni cap layer	2.5
NiAr-5	1	0.197	5	530ºC, 1h-Argon-Ni cap layer	2.5
NiAr-6	1	0.199	5	630ºC, 1h-Argon-Ni cap layer	2.5
NiAr-7	1	0.190	5	630ºC, 1h-Argon-Ni cap layer	2.5
NiAr-8	1	0.190	5	630ºC, 1h-Argon-Ni cap layer	2.5
NiAr-9	1	0.198	5	710ºC, 1h-Argon-Ni cap layer	2.5
NiAr-10	1	0.194	5	710ºC, 1h-Argon-Ni cap layer	2.5
NiAr-11	1	0.185	5	710ºC, 1h-Argon-Ni cap layer	2.5
NiAr-12	1	0.184	5	710ºC, 1h-Argon-Ni cap layer	2.5

Table D- 20 - Summary of the dimensions of the tensile coupons coated both sides with FeC film and Nickel cap layer

In Figure D. 2 the engineering stress-strain curves for the specimens annealed at 430 ˚C are shown, while in Table D- 21 their significant mechanical properties values are listed.

sample	Upper Yield stress [MPa]	Lower Yield stress [MPa]	Average stress in Lüders plateau [MPa]	Lüders length	Ultimate tensile stress (UTS) [MPa]	Strain at fracture (ε_B)
NiAr-1	109.22	-	-	-	245.18	0.49
NiAr-2	132.78	-	-	-	294.34	0.46
Average	121	-	-	-	270	0.48

Table D- 21 - Mechanical properties obtained for annealing in argon at 430 ˚C - 1h of coupons coated both sides with 500 nm thick FeC and 20 nm Nickel cap layer

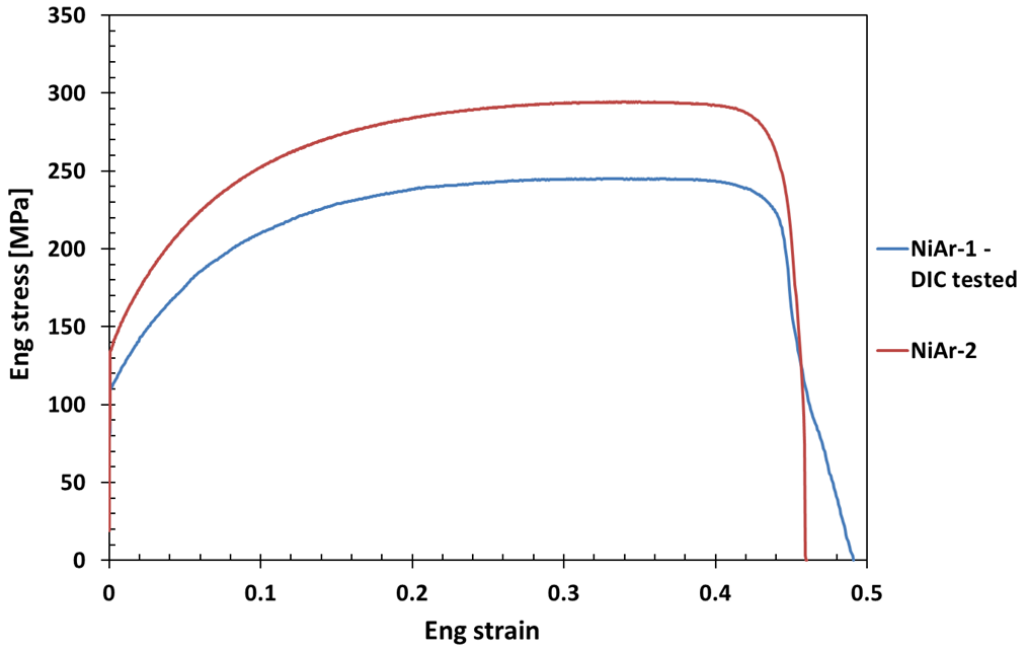

Figure D. 2 - Engineering stress-strain curves obtained for coupons coated both sides with a 500 nm thick FeC amorphous film and 20 nm Nickel cap layer annealed at 430 ˚C - 1h in argon

From Figure D. 2, it can be concluded that some diffusion occurred for the sample NiAr-2 since its yield stress is around 19 MPa higher than a not annealed-coated IF steel, however, no diffusion took place for the sample NiAr-1. Moreover, for both curves no plastic instability was recorded. For this reason, it is believed that the Nickel cap layer for the annealing at 430˚C-1h in argon is decreasing the carbon diffusion towards the IF steel compared to a situation where the coupon is coated only with the FeC amorphous film.

Annealing was then performed on coupons with FeC film and Nickel cap layer at 530 ˚C in argon atmosphere. Table D- 22 summarizes the mechanical properties obtained from the tests while engineering stress-strain curves are shown in Figure D. 4. Figure D. 3 shows the behaviour of the FeC film and of the nickel cap layer during the tensile test.

sample	Upper Yield stress [MPa]	Lower Yield stress [MPa]	Average stress in Lüders plateau [MPa]	Lüders length	Ultimate tensile stress (UTS) [MPa]	Strain at fracture (ε_B)
NiAr-3	249.13	226	235.5	0.05107	293.78	0.41
NiAr-4	255.44	237.33	243.87	0.05048	291.83	0.46
NiAr-5	251.12	232.63	236	0.04809	277.28	0.4
Average	252	232	238	0.04988	288	0.42

Table D- 22 - Mechanical properties obtained for annealing in argon at 530 ˚C - 1h of coupons coated both sides with 500 nm thick FeC and 20 nm Nickel cap layer

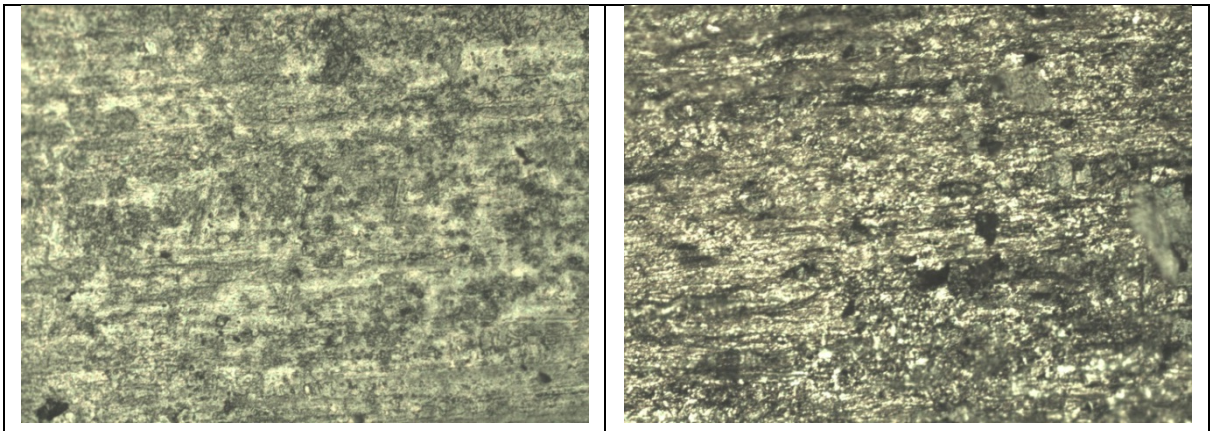

(a) Surface at the starting of the tensile test | (b) Surface at the end of the tensile test

Figure D. 3 - Surface of the tensile coupon coated with 500 nm thick FeC amorphous film and 20 nm Nickel cap layer after annealing in argon at 530 ˚C - 1h

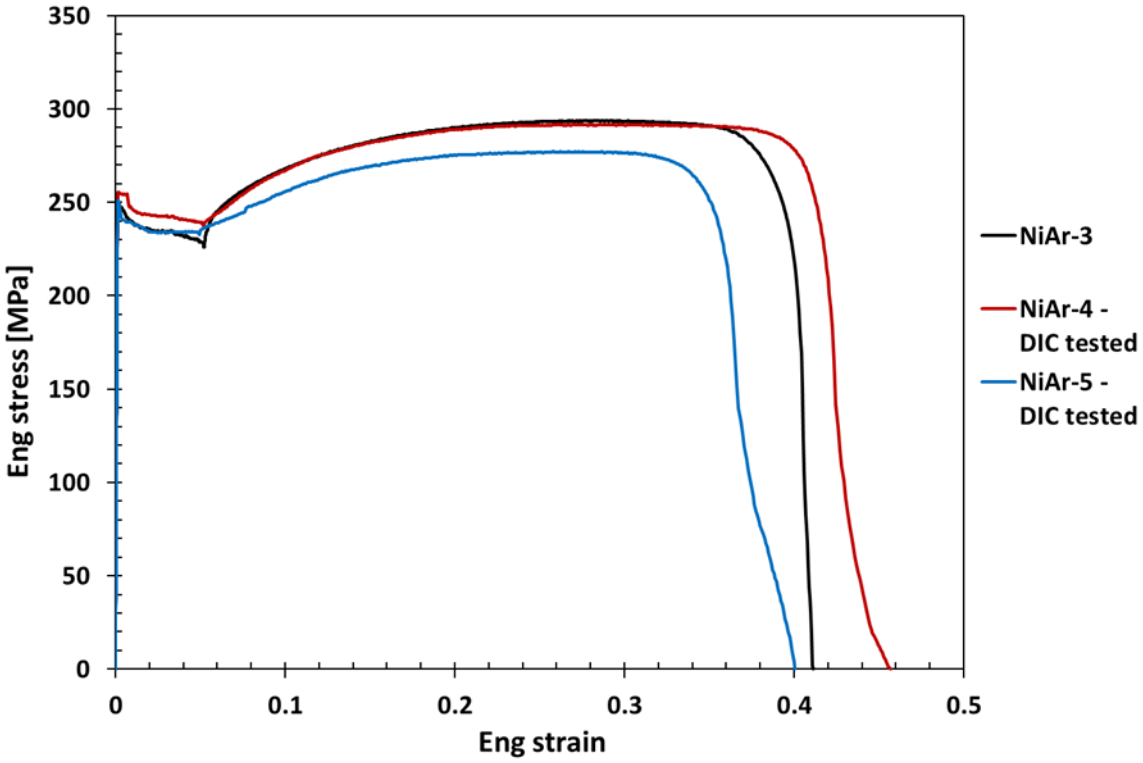

Figure D. 4 - Engineering stress-strain curves obtained for coupons coated both sides with a 500 nm thick FeC amorphous film and 20 nm Nickel cap layer annealed at 530 ˚C - 1h in argon

The values of mechanical properties reported in Table D- **22** show that the upper yield stress and the average plateau stress are lower then what obtained performing annealing in argon without Nickel cap layer, which could justify that some of the carbon could diffuse into the Nickel cap layer instead of diffusing towards the IF substrate. Pictures of the surface of

sample A having nickel cap layer and annealed at 530 ˚C - 1h in argon were taken using the optical microscope during the tensile test and they are reported in Figure D. 3. One can see that the surface shows no exfoliation confirming what was found also during annealing in high vacuum for the same temperature and time.

Another series of coupons was used to perform annealing at 630 ˚C - 1h in argon and a summary of the obtained mechanical properties is shown in Table D- 23, and even for this series of coupons, pictures of the surface during the tensile test have been taken and they are shown in Figure D. 6. The corresponding engineering stress-strain curves are shown in Figure D. 5.

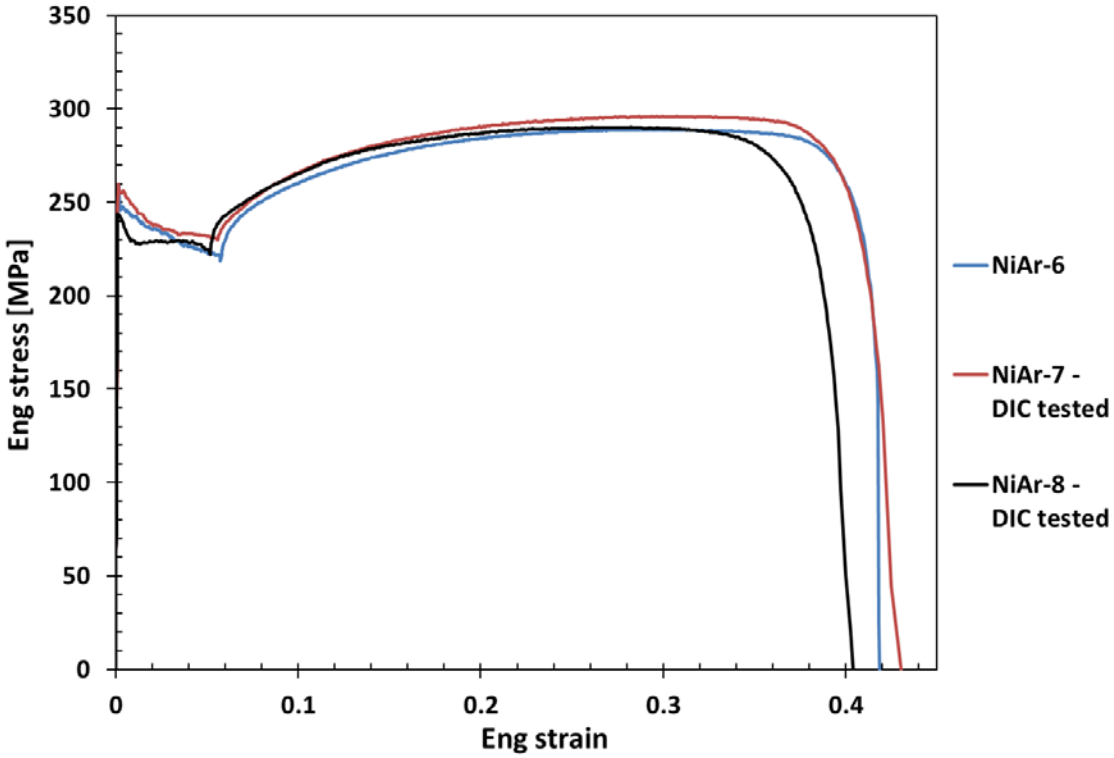

Figure D. 5 - Engineering stress-strain curves obtained for coupons coated both sides with a 500 nm thick FeC amorphous film and 20 nm Nickel cap layer annealed at 630 ˚C - 1h in argon

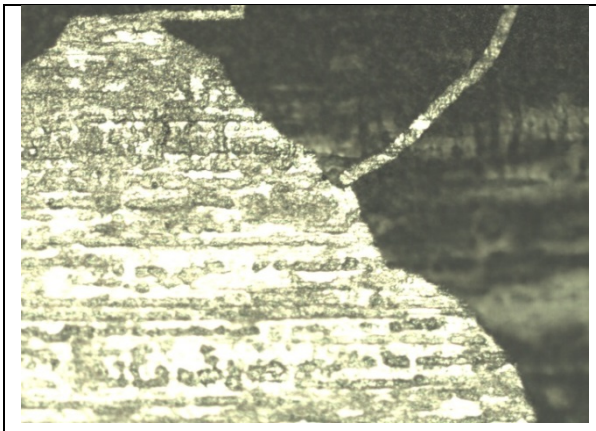

(a) Surface of the tensile coupon during the elastic part of the tensile test. The Nickel cap layer in black fractures markedly

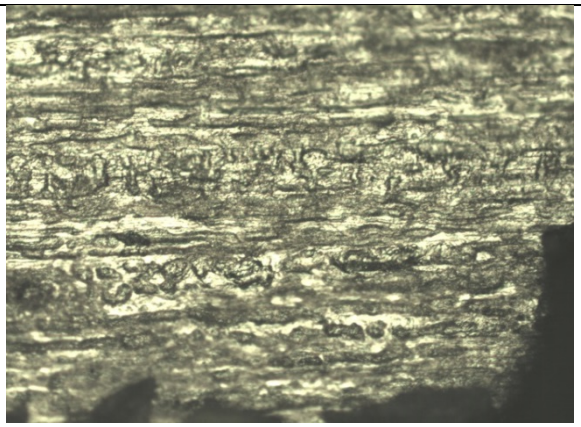

(b) Surface at the end of the tensile test where the Nickel cap layer is completely fractured and exfoliated while the FeC film has no exfoliation

Figure D. 6 - Surface of the tensile coupon NiAr-6 coated with 500 nm thick FeC amorphous film and 20 nm Nickel cap layer after annealing in argon at 630 ˚C - 1h

sample	Upper Yield stress [MPa]	Lower Yield stress [MPa]	Average stress in Lüders plateau [MPa]	Lüders length	Ultimate tensile stress (UTS) [MPa]	Strain at fracture (ε_B)
NiAr-6	259.6	218.7	232.8	0.05618	289	0.42
NiAr-7	259.6	230	238	0.05459	296.2	0.43
NiAr-8	244	222	229.5	0.05057	290	0.4
Average	254	224	233	0.05378	292	0.42

Table D- 23 - Mechanical properties obtained for annealing in argon at 630 ˚C - 1h of coupons coated both sides with 500 nm thick FeC and 20 nm Nickel cap layer

The annealing was also performed at 710 ˚C - 1h in argon and the corresponding engineering stress-strain curves are shown in Figure D. 7 while the values of the mechanical properties are reported in Table D- 24.

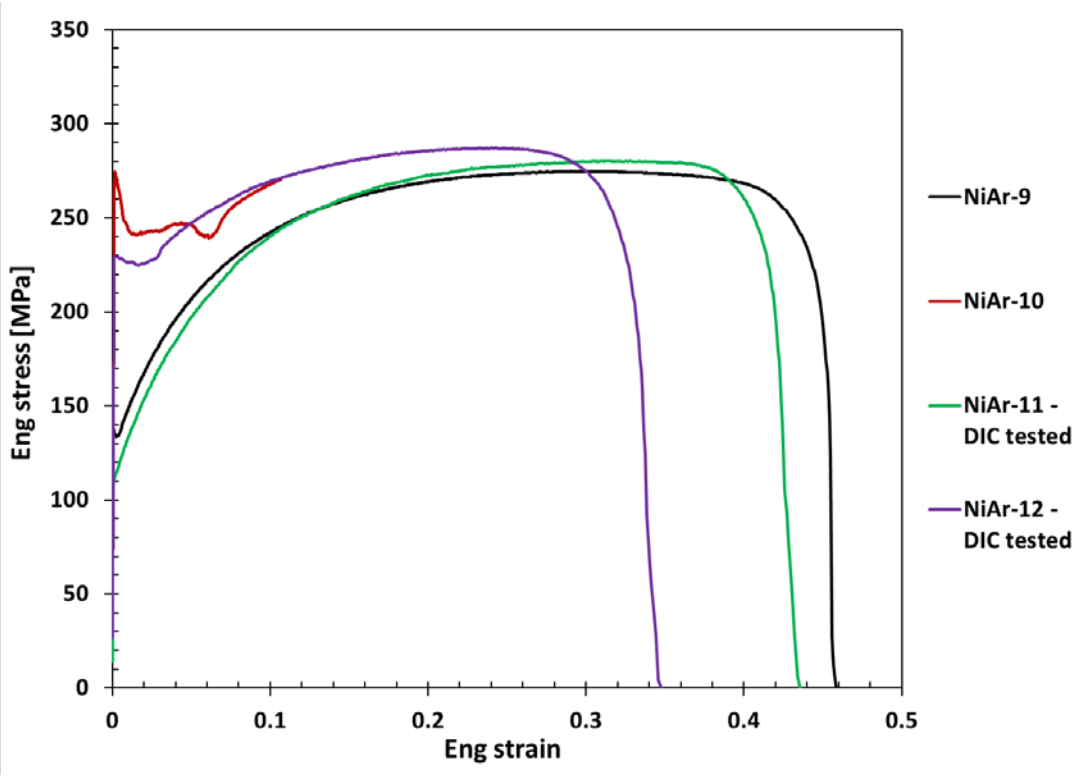

Figure D. 7 - Engineering stress-strain curves obtained for coupons coated both sides with a 500 nm thick FeC amorphous film and 20 nm Nickel cap layer annealed at 710 ˚C - 1h in argon

sample	Upper Yield stress [MPa]	Lower Yield stress [MPa]	Average stress in Lüders plateau [MPa]	Lüders length	Ultimate tensile stress (UTS) [MPa]	Strain at fracture (ε_B)
NiAr-9	137.7	134	135	0.002724	275	0.46
NiAr-10	274.5	239.5	245.7	0.06075	NA	NA
NiAr-11	109	-	-	-	280	0.44
NiAr-12	229	225	227	0.01780	287	0.35
Average	188	200	203	0.0271	281	0.42

Table D- 24 - Mechanical properties obtained for annealing in argon at 710 ˚C - 1h of coupons coated both sides with 500 nm thick FeC and 20 nm Nickel cap layer

Pictures were taken with the optical microscope during the testing of the specimen NiAr-10 annealed at 710 ˚C - 1h in argon and having the surface coated with the nickel cap layer (Figure D. 8).

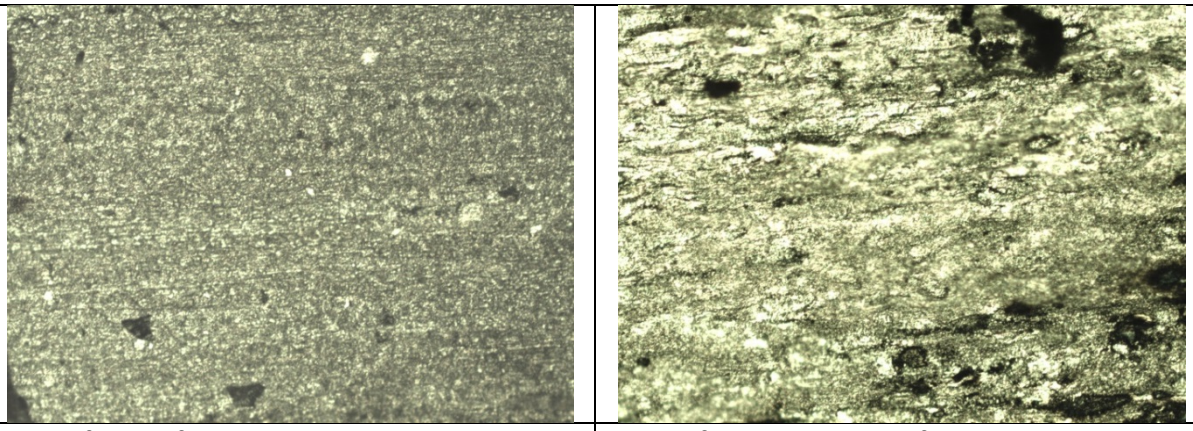

(a) Surface of the tensile coupon at the starting of the test

(b) Surface at the end of the test close to the necking zone. The film has some exfoliated zones

Figure D. 8 - Surface of the tensile coupon NiAr-10 coated with 500 nm thick FeC amorphous film and 20 nm Nickel cap layer after annealing in Argon at 710 ˚C - 1h

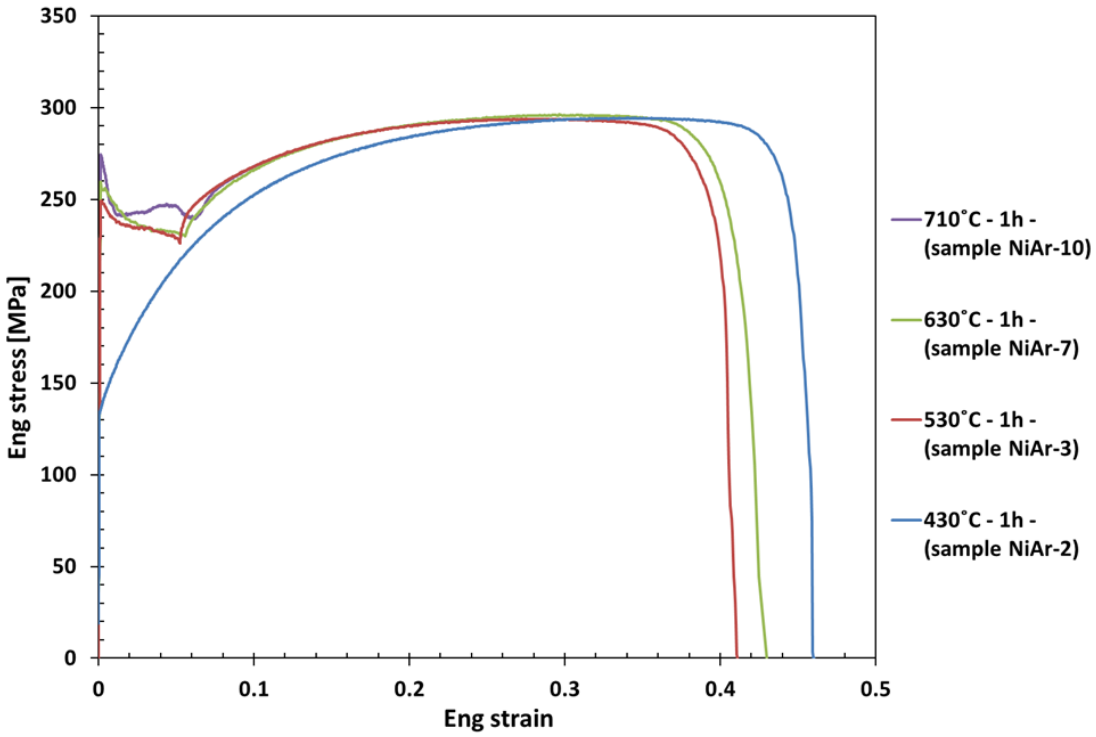

Figure D. 9 - Global comparison of engineering stress-strain curves for coupons coated both sides with 500 nm thick FeC film and 20 nm Ni cap layer after annealing in argon

From Figure D. 9, for annealing in argon at 430 ˚C there is only a slight increase in yield strength and no Lüdering in the curve, while the increase of strength is higher for annealing at 530 ˚C. However, annealing at 630 ˚C and 710 ˚C seem to cause no further increase in yield strength. Specimen 710 ˚C was interrupted because the LVDT stopped working,

however even for this specimen, the quantities of interest (upper yield stress, lower yield stress and Lüders length) were obtained. In Table D- 25 the comparison between the average yield stress obtained for annealing in argon without Ni cap layer and the average yield stress for annealing in argon with Ni cap layer is reported for all the temperatures. The values have been graphed in Figure D. 10.

Annealing	Upper Yield Stress (Argon without Ni cap layer) [MPa]	Upper Yield Stress (Argon with Ni cap layer) [MPa]
430 ˚C – 1h	217	121
530 ˚C – 1h	261	252
630 ˚C – 1h	273	254
710 ˚C – 1h	261	188

Table D- 25 - Comparison of upper yield stress for annealing in argon at different temperatures for 1h of coupons coated both sides with 500 nm FeC film and of coupons coated both sides with 500 nm FeC film and 20 nm Nickel cap layer

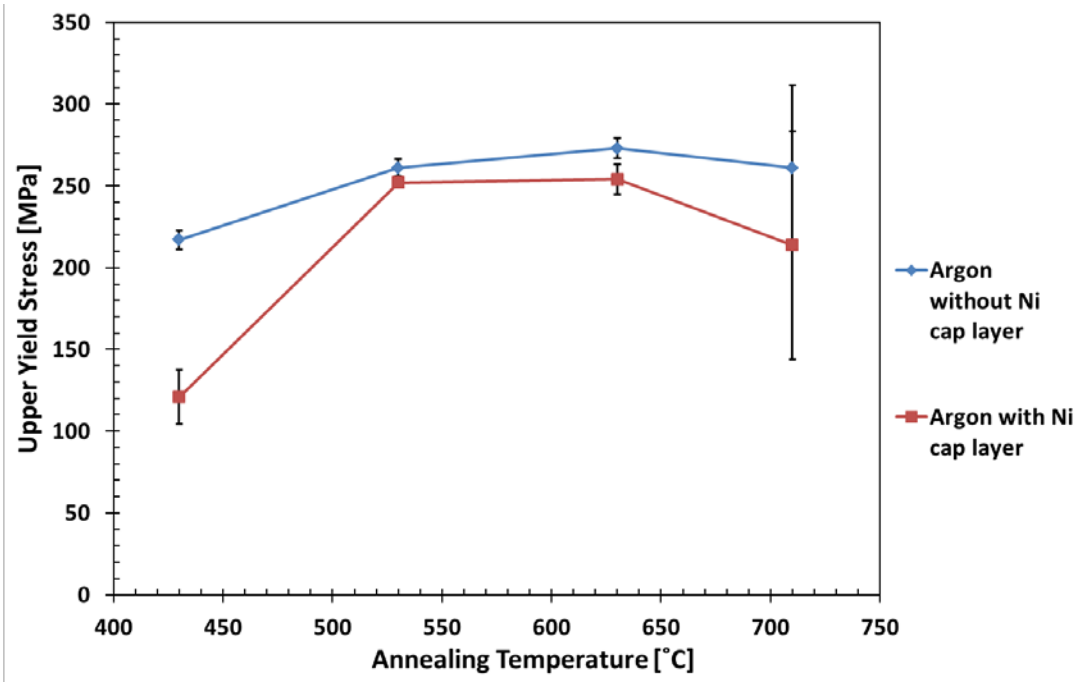

Figure D. 10 - Graph of the upper yield stress for annealing in argon at different temperatures for 1h of coupons coated both sides with 500 nm FeC film and of coupons coated both sides with 500 nm FeC film and 20 nm Nickel cap layer

From Figure D. 10, at 430 ˚C there is a high difference between the strengthening obtained without nickel cap layer and with nickel cap layer. At 530 ˚C – 1h and at 630 ˚C -1h the difference between the two conditions is not so strong, even if for both temperatures having a nickel cap layer on the surface reduces the increase of upper yield stress. At 710 ˚C the

difference between the two conditions is high. The standard deviation have been plot taking into account all the values used to calculate the averages. The standard deviation is very high for annealing at 710 ˚C. This temperature showed always higher variability of the upper yield stress compared to other temperatures, even for annealing in high vacuum and this was related to precipitations occurring inside the microstructure of the IF substrate. Indeed, at 710 ˚C not all the diffused carbon goes at dislocations or at grain boundaries, but instead, it is participating in a transformation of TiS precipitates or in a coarsening of TiC carbides. The results presented in Figure D. 10 can be also explained considering that above 500 ˚C carbon has some solubility in nickel [228], moreover at temperature above 500 ˚C, the diffusion of carbon into nickel is no more negligible. Table D- 26 compares the diffusion coefficient of carbon inside alpha iron and inside nickel for the different annealing temperatures. In literature [15], it was reported that the diffusion coefficient of carbon into nickel is 5.5 x 10^{-14} m^2/s at 600 ˚C and 3.9 x 10^{-13} m^2/s at 700 ˚C. If this two values are used to obtain the pre-exponential factor D_0 and the activation energy Q_d by using the Arrhenius equation, the following equation is obtained:

$$D = \left(1.04 \cdot 10^{-5}\right) \cdot e^{\left(\frac{-138000}{8.31 \cdot (T)}\right)} \left[m^2/s\right] \qquad \text{(eq. D- 1)}$$

Annealing Temperature [˚C]	**Diffusion coefficient of carbon in alpha iron [cm^2/s]**	**Diffusion coefficient of carbon in nickel [cm^2/s]**
430	6.6 x 10^{-9}	5.7 x 10^{-12}
530	3.7 x 10^{-8}	1.1 x 10^{-10}
630	1.4 x 10^{-7}	1.1 x 10^{-9}
710	3.3 x 10^{-7}	4.8 x 10^{-9}

Table D- 26 - Comparison of diffusion coefficient of carbon into ferrite and nickel for different annealing temperatures

At 430 ˚C the diffusion of carbon into nickel seems to be negligible compared to the diffusion into alpha iron since the diffusion into nickel is on the order of 10^{-12} cm^2/s. For this reason, the high difference in mechanical properties between the coupons without nickel cap layer and with nickel cap layer has to be attributed probably to a bad deposition of the FeC film (very low carbon content in the film).

At 530 ˚C the diffusion of carbon into nickel is on the order of 10^{-10} cm^2/s but this value is still not enough high to cause a difference in mechanical properties between the coupons having nickel cap layer and the one without nickel. However, above 600 ˚C, the diffusion coefficient of carbon into nickel is no more negligible. This means that some carbon will diffuse into the nickel cap layer instead of diffusing towards the IF substrate and as a consequence, this will result in lower yield strength for the coupons coated with nickel cap layer.

D.5 Tensile Tests on coupons cleaned using HCl and coated both sides with FeC amorphous film

During Transmission Electron Microscope (TEM) analyses performed by Dr. Amélie Fillon at the University of Rouen (France) in 2013, it was discovered that a layer of oxygen was present at the interface between the FeC amorphous film and the IF substrate. The thickness of this layer is around 15 nm and a picture of the interface between substrate and FeC film is shown in Figure D. 11. It was inferred that this oxide layer was caused by oxidation of the substrate after Nital cleaning; for this reason, it was decided to clean the surface with a stronger acidic solution and a series of coupons were produced where the IF substrate was cleaned with a chloridric acid 1 M/l solution instead of the usual 2% vol. Nital solution used for the results shown in the previous sections. The etching time in the chloridric acid solution was 20 s and this cleaning procedure reduced the oxygen content of the interface (as shown by XPS measurements performed at UBC) but still there was oxide present. In particular the thickness of the oxide layer at the interface was reduced from 15 nm to 8 nm. A series of tensile coupons was then cleaned with HCl and coated both sides with 500 nm thick FeC film containing 30 at% of carbon. The isothermal annealing treatments in high vacuum were repeated for these specimens in order to verify if more carbon could diffuse since the thickness of the oxide layer had been decreased. Table D- 27 reports the vacuum levels for the heat treatments performed on these coupons, while Table D- 28 lists all the dimensions of the specimens.

Annealing Parameters	Vacuum furnace on [torr]	Vacuum furnace off [torr]
430 ºC-1h	$1.2 \cdot 10^{-6}$	$1.0 \cdot 10^{-7}$
530 ºC-1h	$7 \cdot 10^{-7}$	$1.0 \cdot 10^{-7}$
630 ºC-1h	$5.0 \cdot 10^{-7}$	$1.0 \cdot 10^{-7}$
710˚C-1h	1.1×10^{-6}	1×10^{-7}

Table D- 27 - Vacuum levels during annealing in high vacuum of specimens cleaned with HCl before deposition of the FeC film

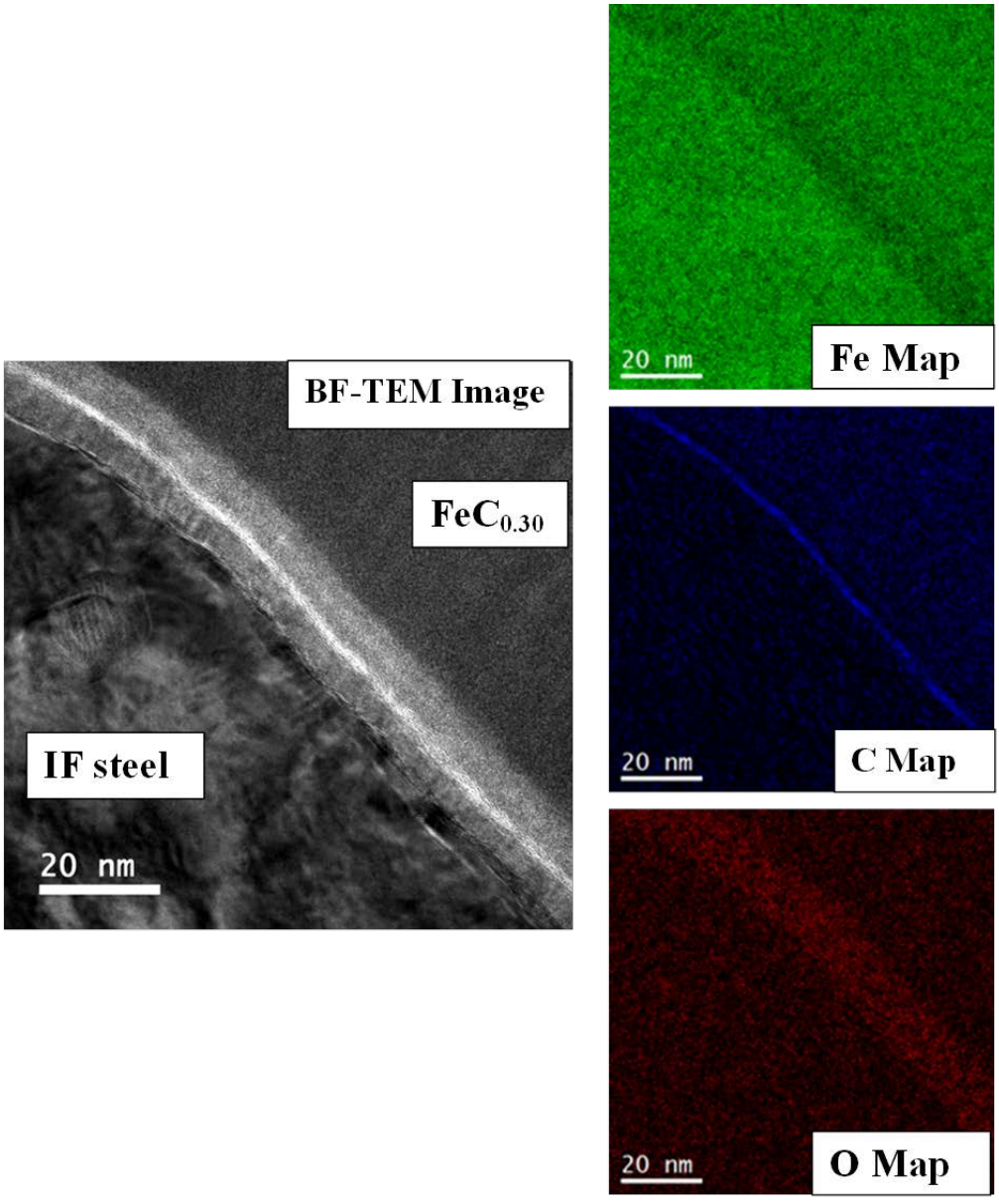

Figure D. 11 - Energy filtering TEM of the interface between IF substrate and as deposited FeC film (courtesy of Dr. Amélie Fillon)

Tensile coupon	Width [mm]	Thickness [mm]	Gauge length [mm]	Annealing treatment	Speed set on the tensile machine [µm/s]
HCl-A	1	0.197	5	430ºC, 1h-HCl cleaning	2.5
HCl-B	1	0.197	5	430ºC, 1h-HCl cleaning	2.5
HCl-C	1	0.186	5	430ºC, 1h-HCl cleaning	2.5
HCl-D	1	0.197	5	530ºC, 1h-HCl cleaning	2.5
HCl-E	1	0.198	5	530ºC, 1h-HCl cleaning	2.5
HCl-F	1	0.184	5	530ºC, 1h-HCl cleaning	2.5
HCl-G	1	0.196	5	630ºC, 1h-HCl cleaning	2.5
HCl-H	1	0.196	5	630ºC, 1h-HCl cleaning	2.5
HCl-I	1	0.185	5	630ºC, 1h-HCl cleaning	2.5
HCl-J	1	0.193	5	710ºC, 1h-HCl cleaning	2.5
HCl-K	1	0.185	5	710ºC, 1h-HCl cleaning	2.5

Table D- 28 - Dimensions of coupons coated with a 500 nm thick FeC film on both sides after a cleaning with HCl solution of the IF core and annealed at different temperatures for 1h in high vacuum

Figure D. 12 reports the tensile curves for the coupons annealed at 430˚C-1h, where clearly some carbon has diffused since an increase of the yield stress compared to the raw IF steel is recorded. Moreover, Lüdering is clearly present in all the tested coupons. Table D- 29 lists the numerical values of the main mechanical properties extracted from the curves in Figure D. 12.

sample	Upper Yield stress [MPa]	Lower Yield stress [MPa]	Average stress in Lüders plateau [MPa]	Lüders length	Ultimate tensile stress (UTS) [MPa]	Strain at fracture (ε_B)
HCl-A	175.84	178.8	178.7	0.02712	270.8	0.51
HCl-B	184.2	174	177.7	0.03022	263.76	0.5
HCl-C	190.3	184.3	188.7	0.02385	286.8	0.45
Average	183	179	182	0.02706	274	0.49

Table D- 29 - Mechanical properties obtained for annealing in high vacuum at 430 ˚C - 1h of coupons coted both sides with 500 nm thick FeC and cleaned using HCl solution

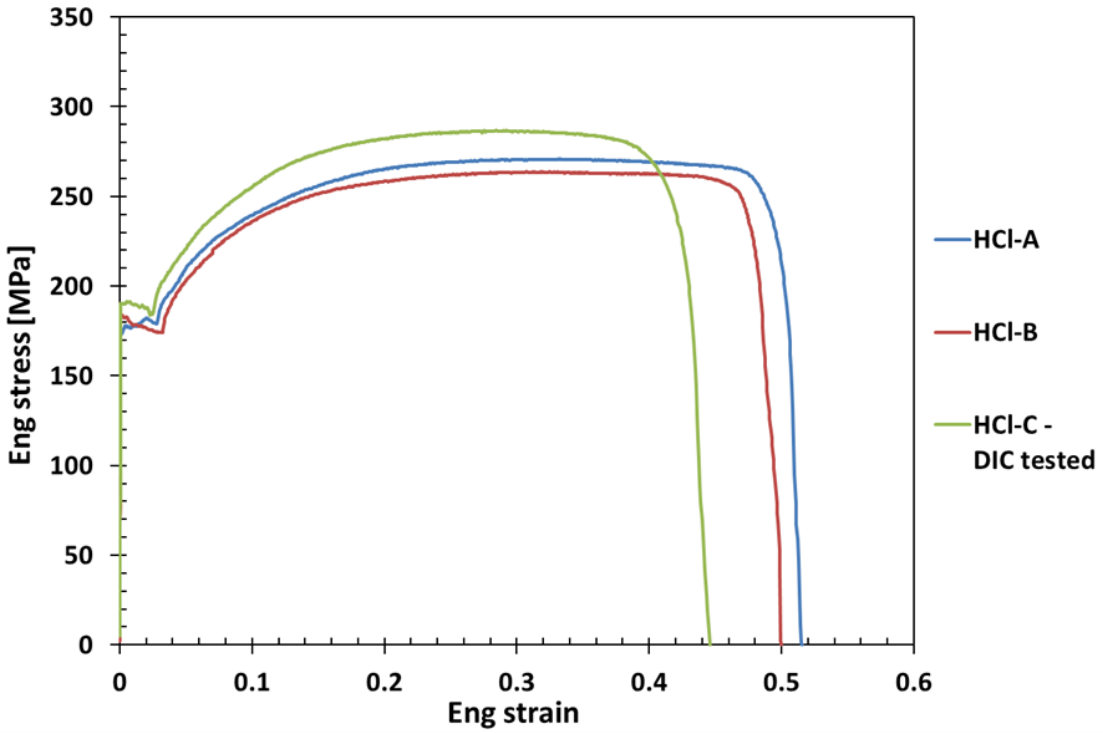

Figure D. 12 - Engineering stress-strain curves for coupons coated both sides with a 500 nm thick FeC amorphous film after cleaning with HCl solution. Annealing performed in high vacuum at 430˚C - 1h

Pictures of the FeC film were captured with the optical microscope during the tensile test. In particular, for coupon annealed at 430 ˚C - 1h the exfoliation of the film was following the pattern of the Lüders bands propagation as shown in Figure D. 13 (a, b, c, d).

After, other coupons were annealed at 530 ºC – 1h in high vacuum. The obtained engineering stress-strain curves are shown in Figure D. 14, while the values of the mechanical properties extracted from these curves are reported in Table D- 30.

(a) Surface of a coupon annealed at 430 ˚C - 1h at the starting of the tensile test (magnification 5X)

(b) Surface of a coupon annealed at 430 ˚C - 1h after that Lüders bands start propagate. The zone where the bands is propagating shows exfoliation of the film (magnification 5X)

(c) Complete propagation of the Lüders bands and film exfoliation (magnification 5X)

(d) Surface of the specimen completely exfoliated at the end of tensile test (magnification 5X)

Figure D. 13 - Lüders bands propagation and exfoliation of the film for a coupon annealed at 430 ˚C - 1h cleaned with HCl before applying the FeC film

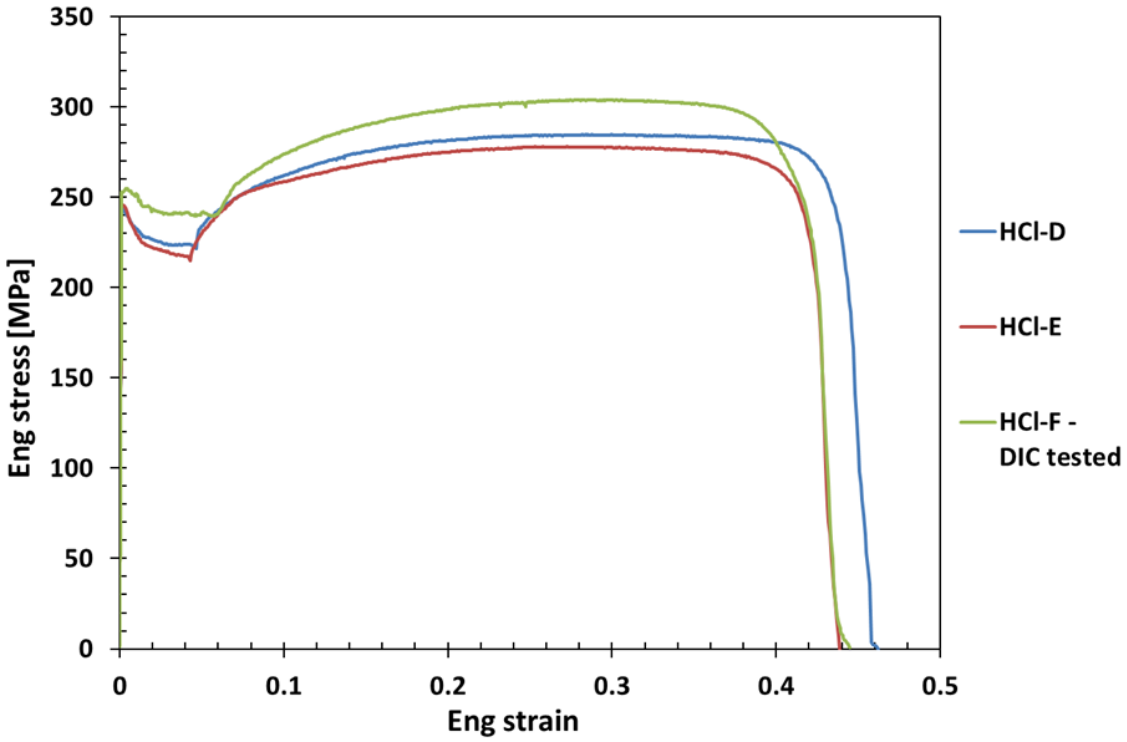

Figure D. 14 - Engineering stress-strain curves for coupons coated both sides with a 500 nm thick FeC amorphous film after cleaning with HCl solution. Annealing performed in high vacuum at 530˚C - 1h

sample	Upper Yield stress [MPa]	Lower Yield stress [MPa]	Average stress in Lüders plateau [MPa]	Lüders length	Ultimate tensile stress (UTS) [MPa]	Strain at fracture (ε_B)
HCl-D	245.3	223	228	0.04315	284.8	0.46
HCl-E	245.8	215	224.4	0.04172	278	0.44
HCl-F	253.2	239.8	244	0.05634	304	0.44
Average	248	226	232	0.0471	289	0.45

Table D- 30 - Mechanical properties obtained for annealing in high vacuum at 530 ˚C - 1h of coupons coted both sides with 500nm thick FeC and cleaned using HCl solution

Taking pictures with the optical microscope during tensile test of coupons annealed at 530˚C, it was noticed that the film does not exfoliates but it cracks slightly (Figure D. 15). This proves that the film itself is transforming during the annealing from amorphous to crystalline.

(a) Surface of the coupon annealed at 530˚C-1h at the starting of tensile test (magnification 5X)

(b) Lüders bands propagating (magnification 5X)

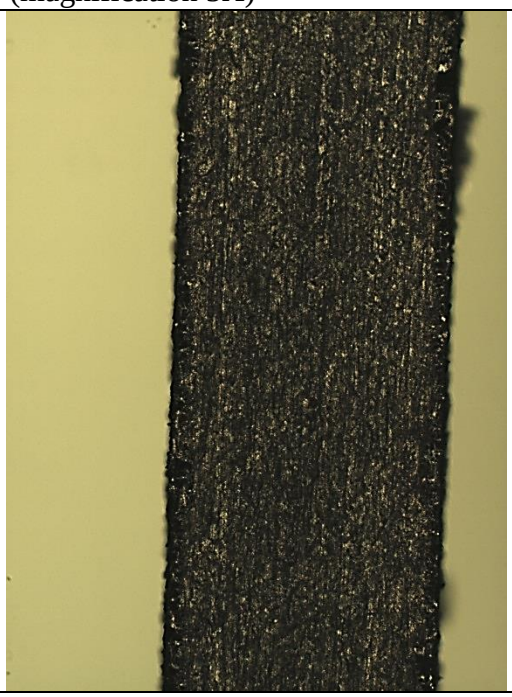

(c) Surface at the end of the tensile tests (magnification 5X)

(d) Surface at the end of tensile test showing mainly cracks of the film but no exfoliation (magnification 20X)

Figure D. 15 - Microscope pictures of the FeC film for a coupon annealed at 530 ˚C - 1h cleaned with HCl before applying the FeC film

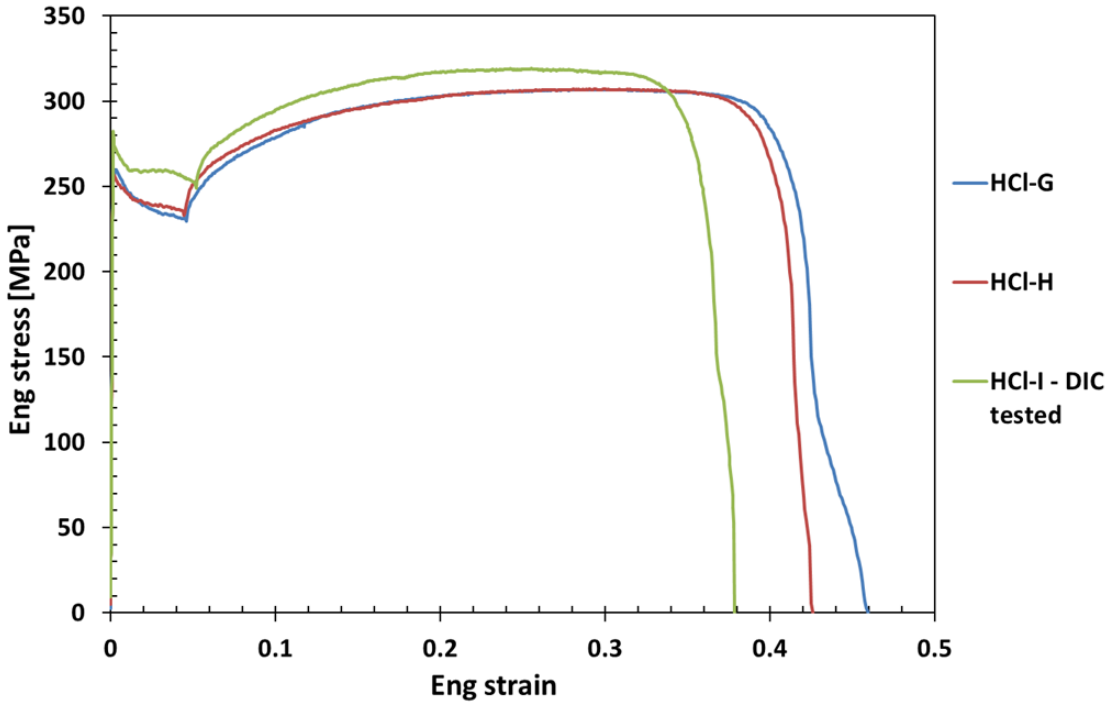

Figure D. 16 - Engineering stress-strain curves for coupons coated both sides with a 500 nm thick FeC amorphous film after cleaning with HCl solution. Annealing performed in high vacuum at 630 ˚C - 1h

sample	Upper Yield stress [MPa]	Lower Yield stress [MPa]	Average stress in Lüders plateau [MPa]	Lüders length	Ultimate tensile stress (UTS) [MPa]	Strain at fracture (ε_B)
HCl-G	259	229.7	240	0.04475	306.8	0.46
HCl-H	257	232.8	242	0.04325	307	0.42
HCl-I	282	249	260.5	0.0503	319	0.38
Average	266	237	248	0.0461	311	0.42

Table D- 31 - Mechanical properties obtained for annealing in high vacuum at 630 ˚C - 1h of coupons coted both sides with 500nm thick FeC and cleaned using HCl solution

During the tensile test of the specimen annealed at 630 ºC – 1h, optical microscope pictures of the surface were taken and the film did not show exfoliation.

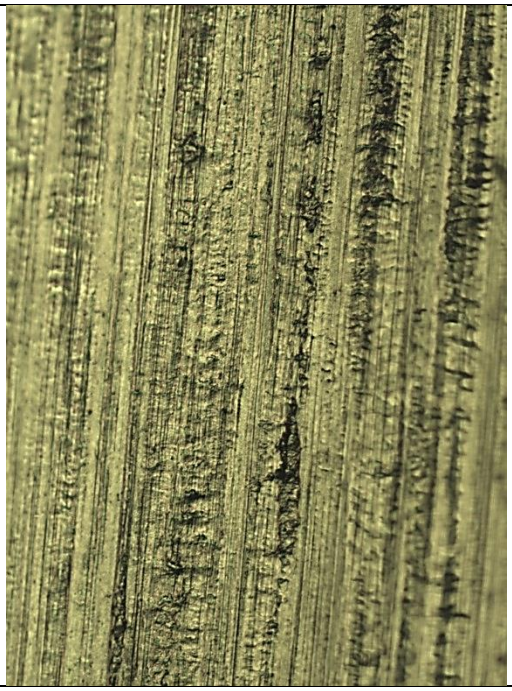

(a) Surface at the beginning of the tensile test (magnification 20X)

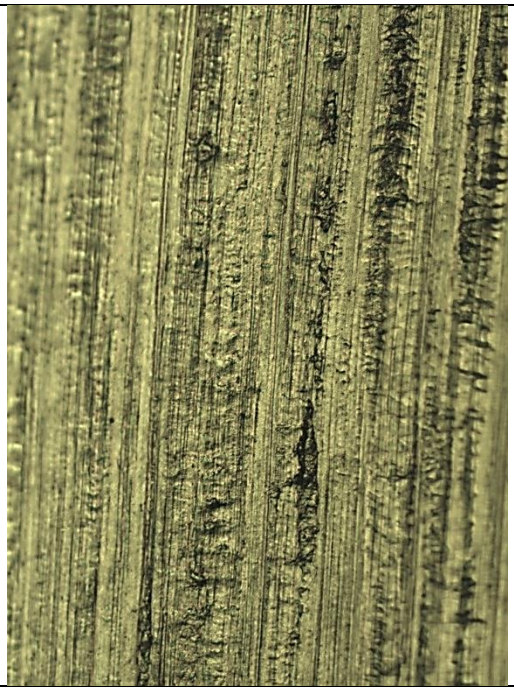

(b) Surface during propagation of the Lüders bands-no marked exfoliation of the coating (magnification 20X)

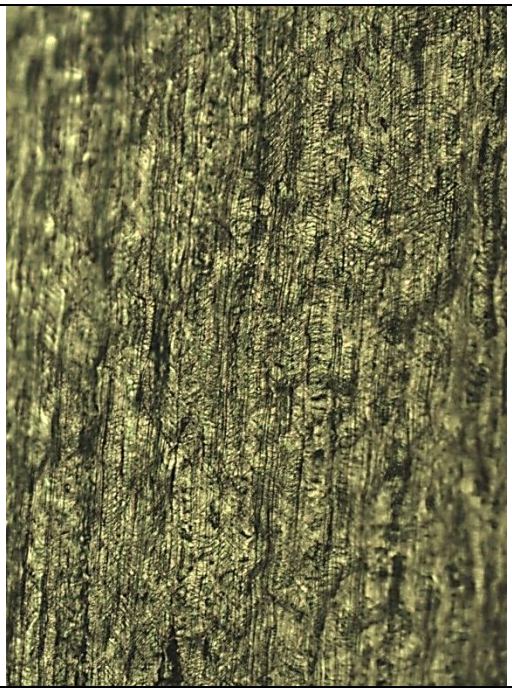

(c) Surface at the end of the tensile test-no exfoliation of the coating (magnification 20X)

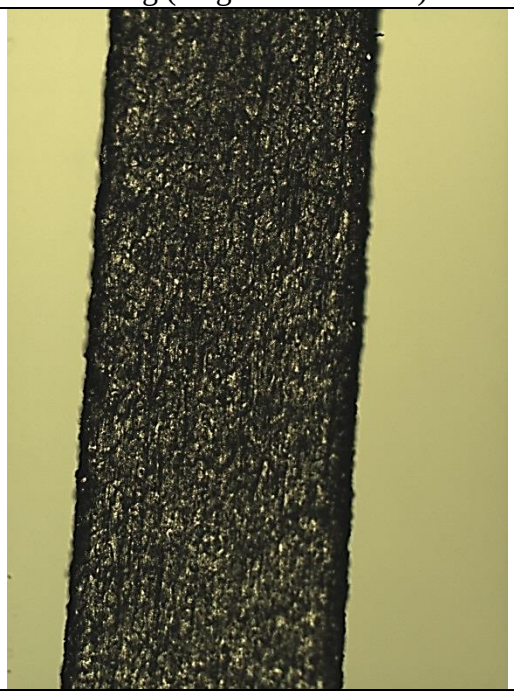

(d) Surface of the coupon after tensile test (magnification 5X)

Figure D. 17 - Microscope pictures of the FeC film for a coupon annealed at 630˚C-1h cleaned with HCl before applying the FeC film

Finally, the results for the annealing at 710 ˚C-1h are also reported. Figure D. 18 gives the engineering stress-strain for these specimens. In Table D- 32 the obtained mechanical properties are listed.

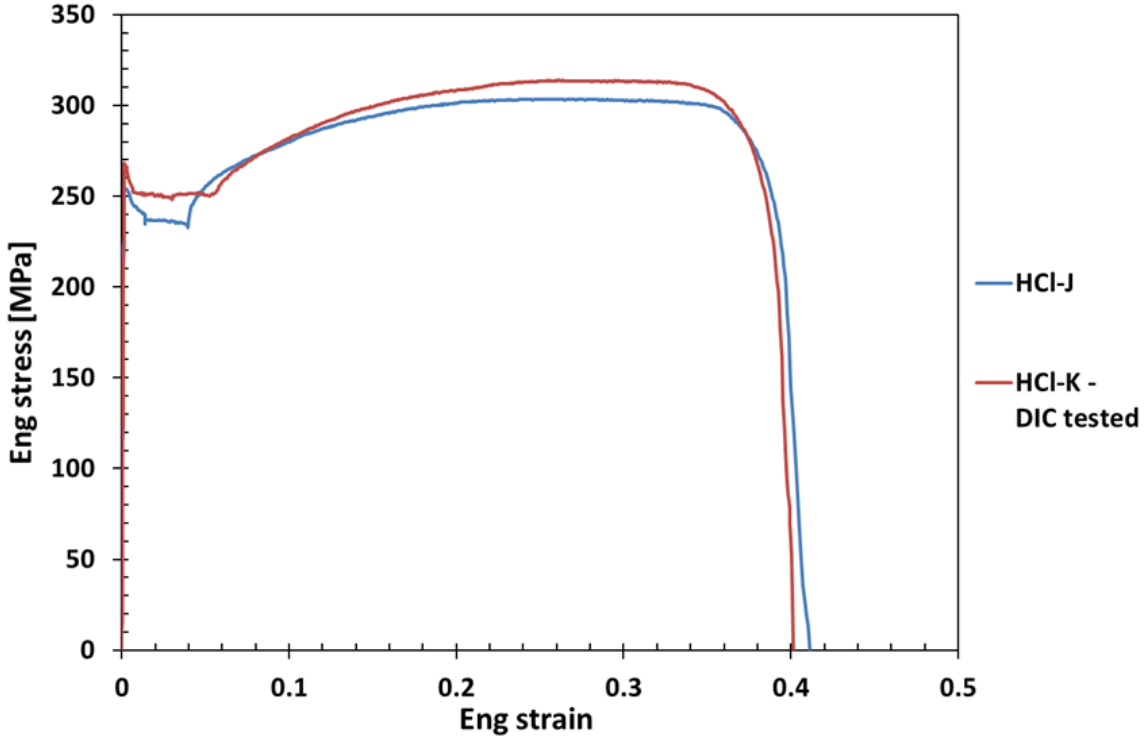

Figure D. 18 - Engineering stress-strain curves for coupons coated both sides with a 500 nm thick FeC amorphous film after cleaning with HCl solution. Annealing performed in high vacuum at 710 ˚C - 1h

sample	Upper Yield stress [MPa]	Lower Yield stress [MPa]	Average stress in Lüders plateau [MPa]	Lüders length	Ultimate tensile stress (UTS) [MPa]	Strain at fracture (ε_B)
HCl-J	254.5	232.6	239.5	0.03821	303.5	0.41
HCl-K	268	250.8	252	0.05338	313.8	0.4
Average	261	242	246	0.0458	309	0.41

Table D- 32 - Mechanical properties obtained for annealing in high vacuum at 710 ˚C - 1h of coupons coted both sides with 500 nm thick FeC and cleaned using HCl solution

In Figure D. 19 pictures of the behaviour of the FeC film during the tensile test for the coupons annealed at 710 ˚C - 1h are shown.

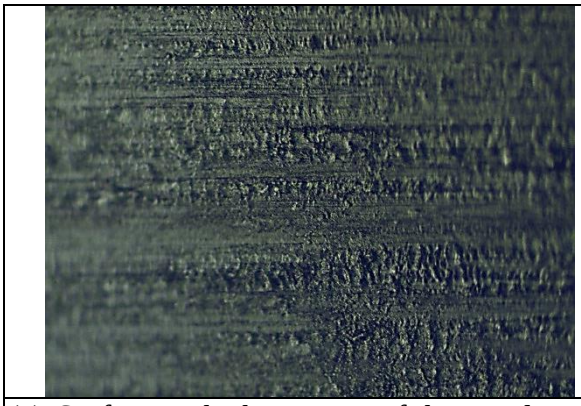

(a) Surface at the beginning of the tensile test (magnification 20X)

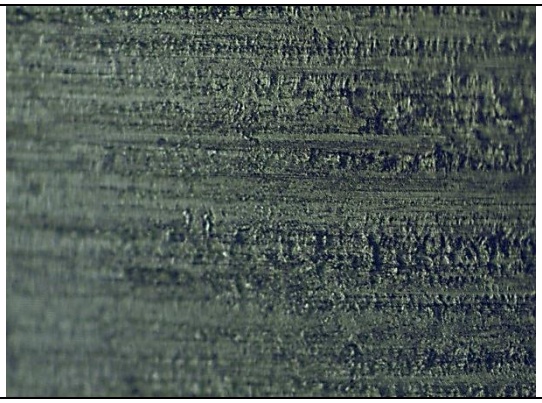

(b) Starting of the Lüders band propagation- no exfoliation of the film detected (magnification 20X)

(c) Surface when Lüders band have finished propagating

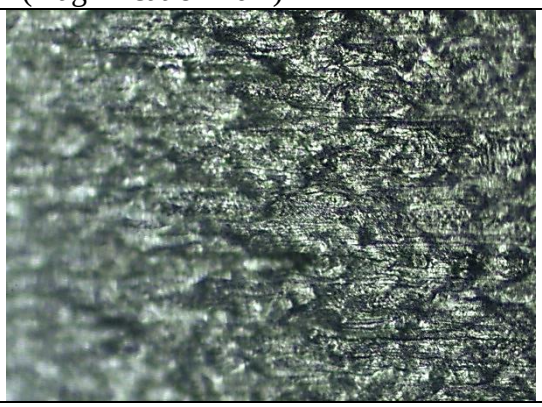

(d) End of the tensile test

Figure D. 19 - Microscope pictures of the FeC film for a coupon annealed at 710 ˚C - 1h cleaned with HCl before applying the FeC film

A summary of the best curves obtained for the cleaning of tensile coupons with HCl and annealing in high vacuum is shown in Figure D. 20, where it is evident that the strengthening increases by raising the annealing temperature, except for the annealing at 710 ˚C where the mechanical properties drop back at the same level of the mechanical properties encountered for the specimens annealed at 530 ˚C. When comparing the average upper yield stresses obtained for Nital cleaning and annealing in high vacuum with the average upper yield stresses obtained for HCl cleaning and annealing in high vacuum, the two curves shown in Figure D. 21 are obtained. The difference between the results obtained for the two different cleaning processes is negligible at 430 ˚C and 530 ˚C since the standard deviation overlap and the average values are very close, at 710 ˚C the values obtained coincide, while a high gap between the average values is recorded at 630 ˚C even if the standard deviation overlap.

A cleaning with HCl is probably too strong and locally it could eventually leave some pits. Moreover, there was no improvement of the mechanical properties even if the oxide layer became thinner, for this reason, the possibility of using HCl instead of Nital was abandoned.

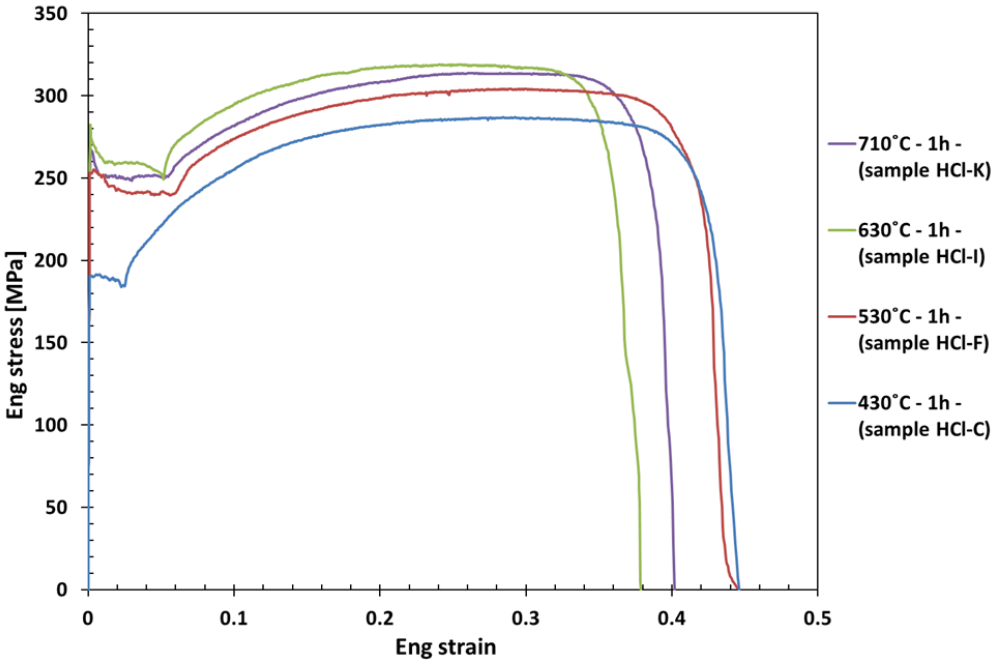

Figure D. 20 - Comparison of engineering stress-strain curves obtained at different temperatures on coupons cleaned with HCl and coated on both sides with 500 nm FeC film. Annealing was performed in high vacuum

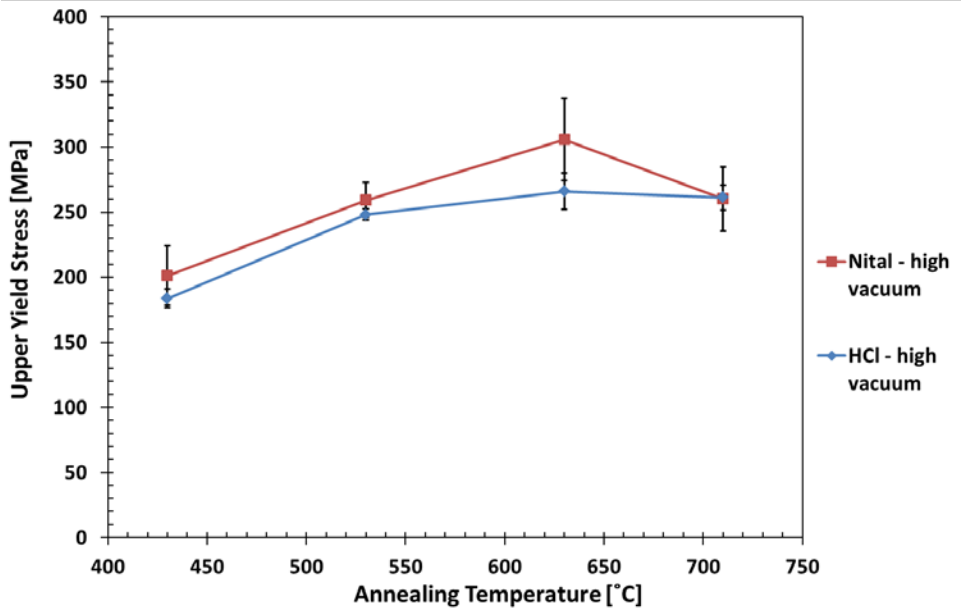

Figure D. 21 - Comparison of the upper yield stress obtained on coupon cleaned with Nital and on coupon cleaned with HCl

During the tensile tests of coupon cleaned with HCl, optical microscope pictures were captured and the behaviour of the film was the same shown for specimens cleaned with Nital, so exfoliation occurred at 430 ˚C, while the film was only cracking at 530 ˚C, 630 ˚C and 710 ˚C.

Before applying the FeC coating by PVD, the IF steel is cleaned with 2vol% Nital solution, however, from HRTEM analyses it has been seen that an oxide layer of 15 nm is present at the interface between the IF core and the FeC film. In order to reduce the thickness of this oxide which could potentially limit carbon diffusion, a series of IF steel coupons were cleaned with an HCl solution instead of 2vol% Nital. As consequence of this cleaning the thickness of the oxide layer had been reduced to 8 nm. However, the mechanical properties obtained after diffusion of coupons cleaned with HCl before applying the FeC film are lower than the mechanical properties obtained for specimens cleaned with Nital. For this reason, it can be concluded that for the range of temperatures between 400 ºC 1nd 710 ºC, the carbon diffusion is not significantly affected by this oxide layer. A graph showing the yield stresses of samples with different cleaning prior to film deposition are presented in Figure D. 22, where the error bars for Nital and HCl cleaning represent the experimental standard deviation. The error bars in the curves considering FeC crystallization are calculated considering ± 3 at% carbon content variation and ± 20 nm film thickness variation from the nominal values of 30 at% and 500 nm respectively.

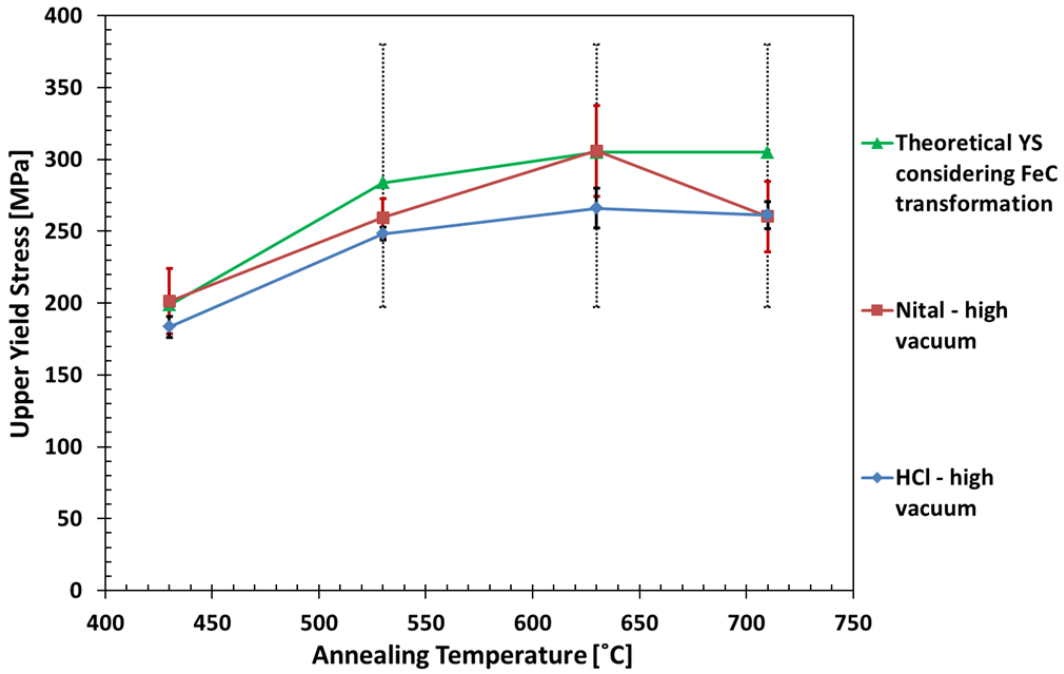

Figure D. 22 - Comparison between theoretical yield stress considering FeC transformation and yield stresses obtained with annealing in high vacuum with coupons cleaned with Nital before PVD deposition or cleaned with HCl before the PVD deposition

D.6 Annealing of both sides coated coupons in air

Tensile coupon	Width [mm]	Thickness [mm]	Gauge length [mm]	Annealing treatment	Speed set on the tensile machine [µm/s]
A	1	0.212	5	530ºC, 1h-Air	2.5
B	1	0.214	5	530ºC, 1h-Air	2.5
C	1	0.194	5	630ºC, 1h-Air	2.5

Table D- 33 - Dimensions of coupons coated with a 500 nm thick FeC film on both sides annealed at 530 ˚C - 1h in air

sample	Upper Yield stress [MPa]	Lower Yield stress [MPa]	Average stress in Lüders plateau [MPa]	Lüders length	Ultimate tensile stress (UTS) [MPa]	Strain at fracture (ε_B)
A	220.8	225.6	226	0.03237	274	0.31
B	213	220	219	0.03359	268	0.33
Average for specimens annealed at 530˚C-1h	217	223	222.5	0.03298	271	0.32
C	213	198	200	0.05502	245.6	0.36

Table D- 34 - Mechanical properties obtained for two coupons annealed in air at 530 ˚C - 1h and one coupon annealed in air at 630 ˚C - 1h. All coupons were coated both sides with 500 nm thick FeC amorphous film

D.7 Comparison between theoretical yield stresses and experimental yield stresses

Annealing Parameters	Theoretical Yield stress considering a yield stress of 113.7MPa for not coated IF steel [MPa]	Experimental Yield Stress [MPa]
330 ˚C - 1h	133	115
430 ˚C - 1h	199	201
530 ˚C - 1h	284	263 (*)
630 ˚C - 1h	353	306
710 ˚C - 1h	412	265 (*)

Table D- 35 - Expected theoretical yield stress and experimentally obtained yield stress. (*) indicates that for these temperatures, the coupons having lower yield stress were discarded to minimize the standard deviation

D.8 Stoichiometric calculation of FeC film crystallization

D.8.1 Stoichiometric calculation considering carbon concentration variation in the film

500nm	Fe	C
at%	73	27
mol%	73	27
Number of atoms	$(0.73 \times (6.022 \times 10^{23})) = 4.396 \times 10^{23}$	$(0.27 \times (6.022 \times 10^{23})) = 1.626 \times 10^{23}$

Table D- 36 - Carbon atoms and iron atoms in the FeC film considering 27 at% of carbon as nominal content

From the values shown in Table D- 36 it is possible to calculate how many carbon atoms remain available if the film transforms into cementite when the carbon concentration is 27 at%: $(4.396 \times 10^{23}/3) = 1.465 \times 10^{23}$ C atoms consumed to form cementite in the film;

So the remaining carbon is: $(1.626 \times 10^{23} - 1.465 \times 10^{23}) = 1.61 \times 10^{22}$

Mol of C atoms = $(1.61 \times 10^{22}/6.022 \times 10^{23}) = 0.0267$ mol in 500 nm^3

(0.0267/400) x 2 x 100 = 0.01337 mol% (which is lower than the solubility limit of C into ferrite at 530 ˚C - 1h of 0.0260 at%) and if we calculate the strengthening: $\Delta\sigma = (2.5) \times (0.051 \times 82000) \times (0.01337/100)^{1/2} = 121$ MPa that added to the 113.7 MPa of the uncoated IF steel gives 235 MPa. So the difference between the yield stress obtained at 530 ˚C, if the solubility limit of carbon into ferrite (0.0260 at%) for this temperature is diffused, and the value of 235 MPa will give the lower standard deviation. In order to find the upper standards deviation, the calculation above has to be repeated considering 33 at% of carbon in the film.

500nm	**Fe**	**C**
at%	67	33
mol%	67	33
Number of atoms	$(0.67 \times (6.022 \times 10^{23})) = 4.035 \times 10^{23}$	$(0.33 \times (6.022 \times 10^{23})) = 1.987 \times 10^{23}$

Table D- 37 - Carbon atoms and iron atoms in the FeC film considering 33 at% of carbon as nominal content

From the values shown in Table D- 37 it is possible to calculate how many carbon atoms remain available if the film transforms into cementite when the carbon concentration is 33 at%:

$(4.035 \times 10^{23}/3) = 1.345 \times 10^{23}$ C atoms consumed to form cementite in the film;

So the remaining carbon is: $(1.987 \times 10^{23} - 1.345 \times 10^{23}) = 6.42 \times 10^{22}$ atoms

Mol of C atoms = $(6.42 \times 10^{22}/6.022 \times 10^{23}) = 0.1066$ mol in 500 nm^3

(0.1066/400) x 2 x 100 = 0.0533 mol% (which is close to the solubility of carbon into ferrite at 630 ˚C) and if we calculate the strengthening:

$\Delta\sigma = (2.5) \times (0.051 \times 82000) \times (0.0533/100)^{1/2} = 241$ MPa that added to the 113.7 MPa of the uncoated IF steel gives 355 MPa, while experimentally the best value obtained for annealing at 630 ˚C was 357 MPa. The difference between 355 MPa and the yield stress corresponding to 0.0334 at% of carbon will give the upper part of the standard deviation, where, 0.0334 at% was the carbon left available to be diffused into the IF steel considering the nominal concentration of 30 at% of carbon in the film.

D.8.2 Stoichiometric calculation considering tolerance of film thickness

Considering a deposition rate of 12.2 nm/min and that the uncertainty is ± 0.50 nm/min, then the variation in film thickness respect to the nominal thickness will be ± 20 nm. In particular, we should start considering that in the "best scenario" there is 33 at% of carbon into 500 nm of film. This amount of carbon has to be calculated if the film is 520 nm thick. In order to do this, we have to calculate how much carbon there will be in a 520 nm thick FeC film if there is 33 at% carbon into 500 nm. This means that the number of carbon atoms corresponding to 33 at% in 500 nm will have to be divided by the ratio 500 nm/520 nm = 0.96. So, 33 at% of carbon in 500 nm will correspond to 34.3 at% of carbon into 520 nm. Table D- 38 summarizes the calculations.

520 nm (considering 33 at% carbon into 500 nm)	**Fe**	**C**
at%	65.7	34.3
mol%	65.7	34.3
Number of atoms	$(0.657 \times (6.022 \times 10^{23})) = 3.956 \times 10^{23}$	$(0.343 \times (6.022 \times 10^{23})) = 2.07 \times 10^{23}$

Table D- 38 - Carbon atoms and iron atoms in the FeC film considering a film thickness of 520 nm and a 34.3 at% of carbon content

Then, considering Fe_3C formation, the amount of carbon atoms consumed is given by $(3.956 \times 10^{23} / 3) = 1.32 \times 10^{23}$ atoms, which means that the carbon atoms which remain available in the film for diffusion are:

$(2.07 \times 10^{23} - 1.32 \times 10^{23}) = 7.51 \times 10^{22}$ corresponding to 0.12 mol in 520 nm^3. This quantity has then to be diluted into 200000 nm of IF steel, so the ratio between 200000 nm and 520 nm is 384.6 so:

$(0.12/384.6) \times 2 \times 100 = 0.065$ mol% (which is higher than the solubility of carbon into ferrite at 630 ˚C) and if we calculate the strengthening:

$\Delta\sigma = (2.5) \times (0.051 \times 82000) \times (0.065/100)^{1/2} = 266.6$ MPa that added to the 113.7 MPa of the uncoated IF steel gives 380 MPa, which is higher than the maximum obtained experimentally, which was 357 MPa.

Following the same approach, it is possible to calculate the 'worst condition" where the film contains 27 at% if it has 500 nm thickness but if the film is 480 nm thick, then 27 at% will have to be divided by the ratio between 500 nm and 480 nm (which is 1.04). So, the film will

contain only 26 at%. Table D- 39 summarizes the calculation of the initial carbon and iron atoms present in the film if its thickness is only 480 nm.

480nm (considering 27 at% carbon into 500 nm)	Fe	C
at%	74	26
mol%	74	26
Number of atoms	$(0.74 \times (6.022 \times 10^{23})) = 4.46 \times 10^{23}$	$(0.26 \times (6.022 \times 10^{23})) = 1.57 \times 10^{23}$

Table D- 39 - Carbon atoms and iron atoms in the FeC film considering a film thickness of 480 nm and a 26 at% of carbon content

Then, considering Fe_3C formation, the amount of carbon atoms consumed is given by $(4.46 \times 10^{23} / 3) = 1.49 \times 10^{23}$ atoms, which means that the carbon atoms which remain available in the film for diffusion are:

$(1.57 \times 10^{23} - 1.49 \times 10^{23}) = 8 \times 10^{21}$ corresponding to 0.013 mol in 480 nm^3. This quantity has then to be diluted into 200000 nm of IF steel, so the ratio between 200000 nm and 480 nm is 416.7 so:

$(0.013/416.7) \times 2 \times 100 = 6.38 \times 10^{-3}$ mol% and if we calculate the strengthening:

$\Delta\sigma = (2.5) \times (0.051 \times 82000) \times (6.38 \times 10^{-3}/100)^{1/2} = 83.5$ MPa that added to the 113.7 MPa of the uncoated IF steel gives 197 MPa. So the error bars can be recalculated considering 380 MPa as the maximum strengthening and 197 MPa as the minimum strengthening.

D.9 Coupons having different FeC film thickness

D.9.1 Tensile tests on coupons having different film thicknesses

Table D- 40 lists all the dimensions for the coupons having different film thicknesses, while from Table D- 41 to Table D- 45 the numerical values of the obtained mechanical properties are reported.

Tensile coupon	Film thickness [nm]	Width [mm]	Thickness [mm]	Gauge length [mm]	Annealing treatment	Speed set on the tensile machine [µm/s]
50 - A	50	1	0.205	5	Not annealed	2.5
50 – B	50	1	0.203	5	530ºC, 1h	2.5
50 – C	50	1	0.214	5	530ºC, 1h	2.5
100 – A	100	1	0.200	5	Not annealed	2.5
100 - B	100	1	0.194	5	530ºC, 1h	2.5
200 - A	200	1	0.199	5	Not annealed	2.5
200 - B	200	1	0.198	5	530ºC, 1h	2.5
200 - C	200	1	0.194	5	530ºC, 1h	2.5
300 - A	300	1	0.203	5	530ºC, 1h	2.5
300 - B	300	1	0.202	5	530ºC, 1h	2.5
300 - C	300	1	0.184	5	530ºC, 1h	2.5
300 - D	300	1	0.183	5	530ºC, 1h	2.5
400 - A	400	1	0.197	5	530ºC, 1h	2.5
400 - B	400	1	0.200	5	530ºC, 1h	2.5
400 - C	400	1	0.185	5	530ºC, 1h	2.5
400 - D	400	1	0.187	5	530ºC, 1h	2.5

Table D- 40 - Dimensions of coupons coated both sides with different FeC film thicknesses

sample	Upper Yield stress [MPa]	Ultimate tensile stress (UTS) [MPa]	Strain at fracture (ε_B)
50 - A (not annealed)	110	262	0.5
50 - B	108	260	0.47
50 - C	116	254	0.52
Average (annealed coupons)	112	257	0.5

Table D- 41 - Mechanical properties obtained for coupons coated both sides with 50 nm thick FeC amorphous film: specimen 50 - A (not annealed), specimen 50 - B and 50 - C (annealed in high vacuum at 530 ˚C-1h)

sample	Upper Yield stress [MPa]	Ultimate tensile stress (UTS) [MPa]	Strain at fracture (ε_B)
100 - A (not annealed)	107	269	0.5
100 - B (annealed)	110	277	0.5

Table D- 42 - Mechanical properties obtained for coupons coated both sides with 100 nm thick FeC amorphous film: specimen 100 - A (not annealed), specimen 100 - B (annealed in high vacuum at 530 ˚C-1h)

sample	Upper Yield stress [MPa]	Lower Yield stress [MPa]	Average stress in Lüders plateau [MPa]	Lüders length	Ultimate tensile stress (UTS) [MPa]	Strain at fracture (ε_B)
200 - A (not annealed)	116	-	-	-	271	0.47
200 - B	175	170	171	0.02894	269	0.46
200 - C	188	187	189	0.02522	280	0.49
Average (annealed coupons)	182	180	180	0.02708	275	0.48

Table D- 43 - Mechanical properties obtained for coupons coated both sides with 200 nm thick FeC amorphous film: specimen 200 - A (not annealed), specimen 200 - B and 200 - C (annealed in high vacuum at 530 ˚C-1h)

sample	Upper Yield stress [MPa]	Lower Yield stress [MPa]	Average stress in Lüders plateau [MPa]	Lüders length	Ultimate tensile stress (UTS) [MPa]	Strain at fracture (ε_B)
300 - A	249	216	226	0.04723	285	0.41
300 - B	234	222	225	0.03371	285	0.42
300 - C	245	225	232	0.03938	298	0.43
300 - D	248	235	239	0.04671	305	0.44
Average	244	225	230	0.04176	293	0.43

Table D- 44 - Mechanical properties obtained for coupons coated both sides with 300 nm thick FeC amorphous film, specimen 300 - C and 300 - D were DIC tested

sample	Upper Yield stress [MPa]	Lower Yield stress [MPa]	Average stress in Lüders plateau [MPa]	Lüders length	Ultimate tensile stress (UTS) [MPa]	Strain at fracture (ε_B)
400 - A	262	242	244	0.0494	298	0.43
400 - B	233	233	230	0.04815	286	0.41
400 - C	253	239	238	0.04409	300	0.41
400 - D	258	249	251	0.04608	303	0.44
Average	251	241	240	0.04693	297	0.42

Table D- 45 - Mechanical properties obtained for coupons coated both sides with 400 nm thick FeC amorphous film, specimen 400 - C and 400 - D were DIC tested

D.9.2 Stoichiometric calculation considering variation of film thickness

The carbon available after the crystallization of the FeC film can be calculated also for coupons coated with less than 500 nm of film. For example for 400 nm thick FeC film, the amounts of Fe and C atoms are calculated by dividing the numbers of atoms by the ratio

between the nominal thickness and the actual thickness (500 nm/400 nm = 1.25). In this section, the calculation will be done considering the nominal carbon content of 30 at% in a film of 500 nm. In section D.9.3 the variation of film thickness and carbon concentration will be taken into account for coupons coated with different thicknesses of the FeC film.

400 nm	**Fe**	**C**
at%	70	30
mol%	70	30
Number of atoms	$4.215x10^{23}/1.25 = 3.37x10^{23}$	$1.807x10^{23}/1.25 = 1.45x10^{23}$

Table D- 46 - Iron and carbon atoms for FeC film of 400 nm thickness

The carbon atoms necessary to form cementite in the 400 nm thick FeC film are given by: $(3.37x10^{23}/3) = 1.12x10^{23}$ C atoms consumed to form cementite in the film. The carbon atoms which remain available for diffusion are: $(1.45x10^{23} – 1.12x10^{23}) = 3.3x10^{22}$, which corresponds to $(3.3x10^{22}/6.022x10^{23}) = 0.0548$ mol of carbon atoms in 400 nm. This concentration has to be "diluted" into 200 µm and the ratio between 200 $x10^3$ nm / 400 nm is equal to 500, so: (0.0548/500) x 2 x 100 = 0.0219 mol%. This carbon amount is lower than the solubility limit of carbon into ferrite at 530 ˚C so it can all diffuse into the IF substrate. The expected strengthening is given by: $\Delta\sigma = (2.5) \times (0.051 \times 82000) \times (0.0219/100)^{1/2} =$ 155 MPa that added to the 113.7 MPa of the uncoated IF steel gives 269 MPa, while experimentally the average is around 249 MPa.

The same procedure has been applied for the 300 nm considering that the ratio between 500 nm and 300 nm is equal to 1.7.

300 nm	**Fe**	**C**
at%	70	30
mol%	70	30
Number of atoms	$4.215x10^{23}/1.7=2.48x10^{23}$	$1.807x10^{23}/1.7=1.06x10^{23}$

Table D- 47 - Iron and carbon atoms for FeC film of 300 nm thickness

The carbon atoms necessary to form cementite in the 300 nm thick FeC film are given by: $(2.48x10^{23}/3) = 8.26x10^{22}$ C atoms consumed to form cementite in the film. The carbon atoms which remain available for diffusion are: $(1.06x10^{23} – 8.26x10^{22}) = 2.34x10^{22}$, which corresponds to $(2.34x10^{22}/6.022x10^{23}) = 0.03886$ mol of carbon atoms in 300 nm. This concentration has to be "diluted" into 200 µm and the ratio between 200 x 10^3 nm / 300 nm

is equal to 667, so: (0.03886/667) x 2 x 100 = 0.0117 mol%. This carbon amount is lower than the solubility limit of carbon into ferrite at 530 ˚C so it can all diffuse into the IF substrate. The expected strengthening is given by: $\Delta\sigma$ = (2.5) x (0.051 x 82000) x $(0.0117/100)^{1/2}$ = 113 MPa that added to the 113.7 MPa of the uncoated IF steel gives 227 MPa, while experimentally the average is around 243 MPa.

In case of the film 200 nm thick, the ratio between 500 nm/200 nm is equal to 2.5 and the carbon and iron atoms initially present in the film are given in the following table.

200 nm	**Fe**	**C**
at%	70	30
mol%	70	30
Number of atoms	$4.215x10^{23}/2.5=1.686x10^{23}$	$1.807x10^{23}/2.5=7.228x10^{22}$

Table D- 48 - Iron and carbon atoms for FeC film of 200 nm thickness

The carbon atoms necessary to form cementite in the 200 nm thick FeC film are given by: $(1.686 \times 10^{23}/3) = 5.62x10^{22}$ C atoms consumed to form cementite in the film. The carbon atoms which remain available for diffusion are: $(7.228x10^{22} - 5.62x10^{22}) = 1.608x10^{22}$, which corresponds to $(1.608x10^{22}/6.022x10^{23}) = 0.0267$ mol of carbon atoms in 200 nm. This concentration has to be "diluted" into 200 µm and the ratio between $200x10^{3}$ nm / 200 nm is equal to 1000, so: (0.0267/1000) x 2 x 100 = $5.34x10^{-3}$ mol%. The strengthening is calculated as: $\Delta\sigma$ = (2.5) x (0.051 x 82000) x $(5.34 \times 10^{-3}/100)^{1/2}$ = 76 MPa that summed with 113.7 MPa gives 190 MPa, while experimentally an average yield stress of 182 MPa has been obtained. Finally the same calculations are performed for FeC 50 nm and 100 nm thick. The ratio between 500 nm and 100 nm is equal to 5 so the amount of iron atoms and carbon atoms initially present in the film is obtained as shown in Table D- 49.

100 nm	**Fe**	**C**
at%	70	30
mol%	70	30
Number of atoms	$4.215x10^{23}/5=8.43x10^{22}$	$1.807x10^{23}/5=3.614x10^{22}$

Table D- 49 - Iron and carbon atoms for FeC film of 100 nm thickness

The carbon atoms necessary to form cementite in the 100 nm thick FeC film are given by: $(8.43x10^{22}/3) = 2.81x10^{22}$ C atoms consumed to form cementite in the film. The carbon atoms which remain available for diffusion are: $(3.614x10^{22} - 2.81x10^{22}) = 8.04 \times 10^{21}$, which corresponds to $(8.04x10^{21}/6.022x10^{23}) = 0.01335$ mol of carbon atoms in 100 nm.

Successively, this concentration has to be "diluted" into 200 μm and it has to be considered that the coupons are coated both sides, so: (0.01335/2000) x 2 x 100 = $1.335x10^{-3}$ mol% and the strengthening is calculated as: $\Delta\sigma = (2.5) \times (0.051 \times 82000) \times (1.335 \times 10^{-3}/100)^{1/2} = 38$ MPa that added to the 113.7 MPa of the uncoated IF steel gives 152 MPa, while experimentally we are close to 110 MPa.

For the 50 nm thick FeC film the ratio between 500 nm/50 nm is equal to 10 and the number of iron and carbon atoms initially present is reported in Table D- 50.

50 nm	**Fe**	**C**
at%	70	30
mol%	70	30
Number of atoms	$4.215x10^{23}/10=4.215x10^{22}$	$1.807x10^{23}/10=1.807x10^{22}$

Table D- 50 - Iron and carbon atoms for FeC film of 50 nm thickness

The carbon atoms necessary to form cementite in the 50 nm thick FeC film are given by: $(4.215x10^{22}/3) = 1.405x10^{22}$ C atoms consumed to form cementite in the film. The carbon atoms which remain available for diffusion are: $(1.807x10^{22} - 1.405x10^{22}) = 4.02x10^{21}$, which corresponds to $(4.02x10^{21}/6.022x10^{23}) = 6.68x10^{-3}$ mol of carbon atoms in 50 nm. Successively, this concentration has to be "diluted" into 200 μm and it has to be considered that the coupons are coated both sides, so: $(6.68x10^{-3}/4000) \times 2 \times 100 = 3.34x10^{-4}$ mol% and the strengthening is calculated as: $\Delta\sigma = (2.5) \times (0.051 \times 82000) \times (3.34 \times 10^{-4}/100)^{1/2} = 19$ MPa that added to the 113.7 MPa of the uncoated IF steel gives 133 MPa, while experimentally we are close to 110 MPa.

In Table D- 51 it is also reported the maximum and minimum yield stress considering that during the deposition of the FeC film, the carbon content can differ ± 3 at% from the nominal value of 30 at%. The detailed calculations considering different film thicknesses with 27at % carbon or 33 at% of carbon are reported in section D.9.2.1.

Thickness of the coating	YS (27at% of carbon) [MPa]	YS (33at% of carbon) [MPa]	YS (30at% of carbon) [MPa]	YS obtained experimentally [MPa]
50nm	126	138	133	112
100nm	138	162	152	110
200nm	162	210	190	182
300nm	198	258	227	244
400nm	211	307(x)	268	251
500nm	235	355(x)	282(xx)	259

Table D- 51 - Comparison between calculated yield stress and experimental yield stress considering different film thicknesses. The values marked as (x) are calculated considering that all the carbon available can be diffused even if its amount is higher than the solubility limit at 530 ˚C - 1h (which is equal to 0.0260 at%). The value marked as (xx) is calculated considering that only the solubility limit of carbon at 530 ˚C can be effectively diffused

D.9.2.1 Stoichiometric calculation considering carbon variation for different nominal film thicknesses

Following the same procedure shown in section D.9.2, the amount of carbon after crystallization of the FeC film can be calculated considering 27 at% of carbon and 33 at% of carbon as lower and upper limit respectively. The results of the final strengthening for these limits are shown in Table D- 51, while in this section the details of the calculations are reported.

- **Calculation of strengthening due to 27 at% of carbon for different nominal film thicknesses**

It was shown in Table D- 36 that for 500 nm of nominal film thickness having 27 at% of carbon content, the iron atoms in the film are 4.396×10^{23}, while the number of carbon atoms is 1.626×10^{23}. These numbers of atoms can be recalculated for a film having a nominal thickness of 400 nm. The ratio between 500nm and 400nm is 1.25, so to obtain the carbon and iron atoms into 400 nm of film, it is necessary to divide the numbers of atoms corresponding to 500 nm by 1.25 as shown in Table D- 52.

400nm	Fe	C
at%	73	27
mol%	73	27
Number of atoms	$4.396*10^{23}/1.25 = 3.517*10^{23}$	$1.626*10^{23}/1.25 = 1.301*10^{23}$

Table D- 52 - Iron and carbon atoms for FeC film of 400 nm thickness and 27 at % of carbon

$(3.517x10^{23}/3) = 1.172x10^{23}$ C atoms consumed to form cementite in the film;

So the remaining carbon is: $(1.301x10^{23} – 1.172x10^{23})=1.29x10^{22}$

Mol of C atoms = $(1.29x10^{22}/6.022x10^{23})$ = 0.02142 in $400nm^3$

(0.02142/500)x2x100 = 0.00857 mol% and if we calculate the strengthening:

$\Delta\sigma=(2.5)x\ (0.051x82000)x(0.00857/100)^{1/2}$ = 97 MPa that added to the 113.7 MPa of the uncoated IF steel gives 211 MPa, while experimentally we are around 251 MPa. The same procedure was done for the other nominal thicknesses.

300nm	**Fe**	**C**
at%	73	27
mol%	73	27
Number of atoms	$4.396x10^{23}/1.7 = 2.586x10^{23}$	$1.626x10^{23}/1.7 = 9.56x10^{22}$

Table D- 53 - Iron and carbon atoms for FeC film of 300 nm thickness and 27 at % of carbon

$(2.586x10^{23}/3) = 8.62x10^{22}$ C atoms consumed to form cementite in the film;

So the remaining carbon is: $(9.56x10^{22} – 8.26x10^{22}) = 1.3x10^{22}$

Mol of C atoms = $(1.3x10^{22}/6.022x10^{23})$ = 0.02159 in $300nm^3$

(0.02159/667)x2x100 = 0.00647 mol% and if we calculate the strengthening:

$\Delta\sigma=(2.5)x(0.051x82000)x(0.00647/100)^{1/2}$=84 MPa that added to the 113.7MPa of the uncoated IF steel gives 198 MPa, while experimentally we are around 244 MPa.

200nm	**Fe**	**C**
at%	73	27
mol%	73	27
Number of atoms	$4.396x10^{23}/2.5=1.758x10^{23}$	$1.626x10^{23}/2.5=6.504x10^{22}$

Table D- 54 - Iron and carbon atoms for FeC film of 200 nm thickness and 27 at % of carbon

In the 200nm we have $1.758x10^{23}$ atoms of iron and supposing that all of them take part to cementite transformation, we have $(1.758x10^{23}/3)=5.86x10^{22}$ carbon atoms which are necessary to form cementite, so $(6.504x10^{22} – 5.86x10^{22}) = 6.44x10^{21}$ are the carbon atoms which can diffuse towards the IF core.

Supposing that all this carbon atoms diffuse into the IF core and considering we have:

mol of C atoms = $(6.44x10^{21}/6.022x10^{23})$ = 0.0107 in $200nm^3$ of volume (considering $1nm^2$ of area and 200nm of thickness). Now this mol of C atoms will diffuse in a volume of $100000nm^3$ of atoms (considering again $1nm^2$ of area but a thickness of the core of 200µm and considering the film on both sides). So divide the mol C concentration by 500 and we obtain:

(0.0107/500)x100=2.14x10^{-3}mol%, this is equal to the at% so if we calculate the strengthening:

$\Delta\sigma=(2.5)x(0.051x82000)x(2.14x10^{-3}/100)^{1/2}$ = 48 MPa that summed with 113.7 MPa we get 162 MPa, while experimentally we got 182 MPa.

100nm	**Fe**	**C**
at%	73	27
mol%	73	27
Number of atoms	$4.396*10^{23}/5=8.792*10^{22}$	$1.626*10^{23}/5=3.252*10^{22}$

Table D- 55 - Iron and carbon atoms for FeC film of 100 nm thickness and 27 at % of carbon

If we repeat the calculation for the 100nm:

$(8.792x10^{22}/3)= 2.93x10^{22}$ C atoms consumed to form cementite in the film;

So the remaining carbon is: $(3.252x10^{22} - 2.93x10^{22}) = 3.22x10^{21}$

Mol of C atoms = $(3.22x10^{21}/6.022x10^{23}) = 0.00535$ in 100nm^3

$(0.00535/2000)x2x100 = 5.35x10^{-4}$mol% and if we calculate the strengthening:

$\Delta\sigma=(2.5)x(0.051x82000)x(5.35x10^{-4}/100)^{1/2}$ = 24 MPa that added to the 113.7 MPa of the uncoated IF steel gives 138 MPa, while experimentally we are close to 110 MPa.

50nm	**Fe**	**C**
at%	73	27
mol%	73	27
Number of atoms	$4.396*10^{23}/10=4.396*10^{22}$	$1.626*10^{23}/10=1.626*10^{22}$

Table D- 56 - Iron and carbon atoms for FeC film of 50 nm thickness and 27 at % of carbon

If we repeat the calculation for the 50nm:

$(4.396x10^{22}/3)= 1.465x10^{22}$ C atoms consumed to form cementite in the film;

So the remaining carbon is: $(1.626x10^{22} – 1.465x10^{22}) = 1.61x10^{21}$

Mol of C atoms = $(1.61x10^{21}/6.022x10^{23}) = 2.67x10^{-3}$ in 50nm^3

$(2.67x10^{-3}/4000$ x 2 x 100 = $1.34x10^{-4}$mol% and if we calculate the strengthening:

$\Delta\sigma=(2.5)x(0.051x82000)x(1.34x10^{-4}/100)^{1/2}$ = 12MPa that added to the 113.7 MPa of the uncoated IF steel gives126 MPa, while experimentally we are close to 112 MPa.

- **Calculation of strengthening due to 33 at% of carbon for different nominal film thicknesses**

It was shown in Table D- 37 that for 500 nm of nominal film thickness having 27 at% of carbon content, the iron atoms in the film are 4.035 x 10^{23}, while the number of carbon atoms is 1.987 x 10^{23}. These numbers of atoms can be recalculated for a film having a nominal thickness of 400 nm. The ratio between 500 nm and 400 nm is 1.25, so to obtain the carbon and iron atoms into 400 nm of film, it is necessary to divide the numbers of atoms corresponding to 500 nm by 1.25 as shown in Table D- 57.

400nm	**Fe**	**C**
at%	67	33
mol%	67	33
Number of atoms	$4.035*10^{23}/1.25=3.228*10^{23}$	$1.987*10^{23}/1.25=1.59*10^{23}$

Table D- 57 - Iron and carbon atoms for FeC film of 400 nm thickness and 33 at % of carbon

$(3.228*10^{23}/3) = 1.076*10^{23}$ C atoms consumed to form cementite in the film;

So the remaining carbon is: $(1.59*10^{23} – 1.076*10^{23})=5.14*10^{22}$

Mol of C atoms = $(5.14*10^{22}/6.022*10^{23}) = 0.08535$ in $400nm^3$

$(0.08535/500)*2*100 = 0.0341$ mol% and if we calculate the strengthening:

$\Delta\sigma=(2.5) \times (0.051 \times 82000) \times (0.0341/100)^{1/2} = 193$ MPa that added to the 113.7 MPa of the uncoated IF steel gives 306 MPa, while experimentally we are around 236MPa.

The calculation can be repeated for the film having 300 nm of thickness by considering that the ratio between 500 nm and 300 nm is 1.7.

300nm	**Fe**	**C**
at%	67	33
mol%	67	33
Number of atoms	$4.035*10^{23}/1.7=2.37*10^{23}$	$1.987*10^{23}/1.7=1.17*10^{23}$

Table D- 58 - Iron and carbon atoms for FeC film of 300 nm thickness and 33 at % of carbon

$(2.37 \times 10^{23}/3) = 7.9 \times 10^{22}$ C atoms consumed to form cementite in the film;

So the remaining carbon is: $(1.17 \times 10^{23} – 7.9 \times 10^{22}) = 3.8 \times 10^{22}$

Mol of C atoms = $(3.8 \times 10^{22}/6.022 \times 10^{23}) = 0.06310$ in $300nm^3$

$(0.06310/667) \times 2 \times 100 = 0.0189$ mol% and if we calculate the strengthening:

$\Delta\sigma = (2.5) \times (0.051 \times 82000) \times (0.0189/100)^{1/2} = 144$ MPa that added to the 113.7 MPa of the uncoated IF steel gives 258 MPa, while experimentally we are around 230MPa

The calculation can be repeated for the film having 200 nm of thickness by considering that the ratio between 500 nm and 200 nm is 2.5.

200nm	**Fe**	**C**
at%	67	33
mol%	67	33
Number of atoms	$4.035*10^{23}/2.5=1.614*10^{23}$	$1.987*10^{23}/2.5=7.948*10^{22}$

Table D- 59 - Iron and carbon atoms for FeC film of 200 nm thickness and 33 at % of carbon

$(1.614 \times 10^{23}/3) = 5.38 \times 10^{22}$ carbon atoms which are necessary to form cementite;

$(7.948 \times 10^{22} - 5.38 \times 10^{22}) = 2.568 \times 10^{22}$ are the carbon atoms which can diffuse towards the IF core.

mol of C atoms = $(2.568 \times 10^{22}/6.022 \times 10^{23}) = 0.0426$ in $200nm^3$ of volume

$(0.0426/1000) \times 2 \times 100 = 8.52 \times 10^{-3}$ mol% and if we calculate the strengthening:

$\Delta\sigma = (2.5) \times (0.051 \times 82000) \times (8.52 \times 10^{-3}/100)^{1/2} = 96.5$ MPa that added to the 113.7 MPa of the uncoated IF steel gives 210 MPa, while experimentally we are around 182 MPa

The calculation can be repeated for the film having 100 nm of thickness by considering that the ratio between 500 nm and 100 nm is 5.

100nm	**Fe**	**C**
at%	67	33
mol%	67	33
Number of atoms	$4.035 \times 10^{23}/5 = 8.07 \times 10^{22}$	$1.987 \times 10^{23}/5 = 3.974 \times 10^{22}$

Table D- 60 - Iron and carbon atoms for FeC film of 100 nm thickness and 33 at % of carbon

$(8.07 \times 10^{22}/3) = 2.69 \times 10^{22}$ C atoms consumed to form cementite in the film;

So the remaining carbon is: $(3.974 \times 10^{22} - 2.69 \times 10^{22}) = 1.284 \times 10^{22}$

Mol of C atoms = $(1.284 \times 10^{22}/6.022 \times 10^{23}) = 0.02132$ in $100nm^3$

$(0.02132/2000) \times 2 \times 100 = 2.132 \times 10^{-3}$ mol% and if we calculate the strengthening:

$\Delta\sigma = (2.5) \times (0.051 \times 82000) \times (2.132 \times 10^{-3}/100)^{1/2} = 48.27$ MPa that added to the 113.7 MPa of the uncoated IF steel gives 162 MPa, while experimentally we are close to 110MPa.

Finally, the calculation can be repeated for a film thickness of 50 nm by considering that the ratio between 500 nm and 50 nm is 10.

50nm	Fe	C
at%	67	33
mol%	67	33
Number of atoms	$4.035*10^{23}/10=4.035*10^{22}$	$1.987*10^{23}/10=1.987*10^{22}$

Table D- 61 - Iron and carbon atoms for FeC film of 50 nm thickness and 33 at % of carbon

$(4.035 \times 10^{22}/3)= 1.345 \times 10^{22}$ C atoms consumed to form cementite in the film;

So the remaining carbon is: $(1.987 \times 10^{22} – 1.345 \times 10^{22}) = 6.42 \times 10^{21}$

Mol of C atoms = $(6.42 \times 10^{21}/6.022 \times 10^{23}) = 0.0107$ in $50nm^3$

$(0.0107/4000) \times 2 \times 100 = 5.33 \times 10^{-4}$mol% and if we calculate the strengthening:

$\Delta\sigma=(2.5) \times (0.051 \times 82000) \times (5.33 \times 10^{-4}/100)^{1/2} = 24.14$ MPa that added to the 113.7 MPa of the uncoated IF steel gives 138 MPa, while experimentally we are close to 110MPa.

D.9.3 Stoichiometric calculations considering carbon concentration and film thickness variations for coupons having different nominal FeC film thicknesses

It was already discussed in the thesis that the deposition rate is 12.2 nm/min and the uncertainty associated to this rate is ±0.5 nm/min, so the film thickness uncertainty can be calculated for each nominal thickness as shown in Table D- 62.

Nominal thickness [nm]	Deposition time [min]	Film thickness uncertainty [nm]
400	(400/12.2) = 33	17
300	(300/12.2) = 24.6	12
200	(200/12.2) = 16.4	8
100	(100/12.2) = 8.2	4
50	(50/12.2) = 4	2

Table D- 62 - Uncertainty associated to the film thickness for different nominal values of FeC film thicknesses

For each film thickness two extremes were considered. The “worst condition” where the film is thinner than the nominal dimension (for example instead of 400 nm, it is 383 nm) and in the same time, the carbon content would be 27 at% at 400 nm. The upper part of the error bars is calculated considering instead the “best condition” where the film is thicker than the nominal value (for example 417 nm instead of 400 nm) and the carbon content would be 33 at% in 400 nm. In Table D- 63 an example of the atoms concentration considering film

thickness and carbon concentration in a 400 nm nominal film are shown. The number of iron atoms and carbon atoms for a nominal film thickness of 400 nm and concentration of 33 at% of carbon are used as reference to calculate the number of atoms present in a film which had 417 nm of thickness. The ratio between 400 nm and 417 nm is 0.96 and this factor has been used to calculate the number of carbon atoms inside the film which is 417 nm thick (as shown in Table D- 63). The percentage corresponding to this number of atoms was calculated (which is 34.4 at%) and then it was considered that the remaining percentage (100 – 34.4 = 65.6 at%) is of iron. Then, the number of iron atoms was calculated.

The same procedure was repeated for the "worst condition" of 383 nm thickness.

Nominal thickness	**Atoms of Fe**	**Atoms of C**
400 nm (33 at% of carbon)	3.228×10^{23} (67 at% of Fe)	1.59×10^{23} (33 at% of C)
417 nm	$(3.228 \times 10^{23}) \times (65.6/67) =$ 3.16×10^{23} (65.6 at % of Fe)	$(1.59 \times 10^{23}/0.96) =$ 1.66×10^{23} (34.4 at% of C)
400 nm (27 at% of carbon)	3.517×10^{23} (73 at% of Fe)	1.301×10^{23} (27 at% C)
383 nm	$(3.517 \times 10^{23}) \times (74/73) =$ 3.57×10^{23} (74 at% of Fe)	$(1.301 \times 10^{23}/1.04) =$ 1.25×10^{23} (26 at% of C)

Table D- 63 - Iron and carbon atoms considering film thickness variation of ± 17 nm on a nominal thickness of 400 nm

Then, considering the crystallization of the 417 nm thick FeC film into Fe_3C, we obtain that: $(3.16 \times 10^{23}/3) = 1.05 \times 10^{23}$ atoms which are consumed to form cementite. So, the remaining carbon available for diffusion is given by:

$(1.66 \times 10^{23}) - (1.05 \times 10^{23}) = 6.1 \times 10^{22}$ atoms, which correspond to $(6.1 \times 10^{22}/6.022 \times 10^{23}) = 0.101$ mol. This amount has then to be "diluted" in 200 µm of IF substrate so it has to be divided by a factor of (200000/417) = 480, which will give 2.10×10^{-4} mol in 200 µm. After, considering that the coupons are coated both sides, the total carbon that remains available to be diffused is given by: $(2.10 \times 10^{-4} \times 2 \times 100) = 0.042$ at %. Using this amount to calculate the strengthening, we get: $\Delta\sigma = (2.5)\ (0.051 \times 82000) \times (0.042/100)^{1/2} = 214$ MPa, which added to the yield stress of an uncoated IF steel (113.7 MPa), will give 328 MPa. The difference between this value and the value of yield stress calculated considering

400 nm of film thickness with the nominal carbon content of 30 at%, will give the upper portion of the standard deviation bars shown in Figure 5-69 of section 5.7

Then, considering the crystallization of the 383 nm thick FeC film into Fe_3C, we obtain that: $(3.57 \times 10^{23}/3) = 1.19 \times 10^{23}$ atoms which are consumed to form cementite. So, the remaining carbon available for diffusion is given by:

$(1.25 \times 10^{23}) - (1.19 \times 10^{23}) = 6 \times 10^{21}$ atoms, which correspond to $(6 \times 10^{21}/6.022 \times 10^{23}) = 9.96 \times 10^{-3}$ mol. This amount has then to be "diluted" in 200 µm of IF substrate so it has to be divided by a factor of (200000/383) = 522, which will give 1.91×10^{-5} mol in 200 µm. After, considering that the coupons are coated both sides, the total carbon that remains available to be diffused is given by: $(1.91 \times 10^{-5} \times 2 \times 100) = 3.82 \times 10^{-3}$ at %. Using this amount to calculate the strengthening, we get: $\Delta\sigma = (2.5)\ (0.051 \times 82000) \times (3.82 \times 10^{-3}/100)^{1/2} = 64.6$ MPa, which added to the yield stress of an uncoated IF steel (113.7 MPa), will give 178 MPa. The difference between this value and the value of yield stress calculated considering 400 nm of film thickness with the nominal carbon content, will give the lower portion of the standard deviation bars shown in Figure 5-69 of section 5.7

Similar calculations have been performed also for the other film thicknesses (300 nm, 200 nm, 100 nm and 50 nm). In Table D- 64 the calculation of the number of iron and carbon atoms in 312 nm of film and in 288 nm of film are shown considering that the ratio between 300 nm and 312 nm is 0.96, while the ratio between 300 nm and 288 nm will be 1.04.

Nominal thickness	**Atoms of Fe**	**Atoms of C**
300 nm (33 at% of carbon)	2.37×10^{23} (67 at% of Fe)	1.17×10^{23} (33 at% of C)
312 nm	$(2.37 \times 10^{23}) \times (65.6/67) =$ 2.32×10^{23} (65.6 at % of Fe)	$(1.17 \times 10^{23}/0.96) =$ 1.22×10^{23} (34.4 at% of C)
300 nm (27 at% of carbon)	2.586×10^{23} (73 at% of Fe)	9.56×10^{22} (27 at% C)
288 nm	$(2.586 \times 10^{23}) \times (74/73) =$ 2.62×10^{23} (74 at% of Fe)	$(9.56 \times 10^{22}/1.04) =$ 9.2×10^{22} (26 at% of C)

Table D- 64 - Iron and carbon atoms considering film thickness variation of ± 12 nm on a nominal thickness of 300 nm

In 312 nm thick: $(2.32 \times 10^{23}/3) = 7.73 \times 10^{22}$ atoms which are consumed to form cementite. So, the remaining carbon available for diffusion is given by:

$(1.22 \times 10^{23}) - (7.73 \times 10^{22}) = 4.47 \times 10^{22}$ atoms, which correspond to $(4.47 \times 10^{22}/6.022 \times 10^{23}) = 0.074$ mol. This amount has then to be "diluted" in 200 µm of IF substrate so it has to be divided by a factor of (200000/312) = 641, which will give 1.15×10^{-4} mol in 200 µm. After, considering that the coupons are coated both sides, the total carbon that remains available to be diffused is given by: $(1.15 \times 10^{-4} \times 2 \times 100) = 0.023$ at %. Using this amount to calculate the strengthening, we get: $\Delta\sigma = (2.5)\ (0.051 \times 82000) \times (0.023/100)^{1/2} = 159$ MPa, which added to the yield stress of an uncoated IF steel (113.7 MPa), will give 273 MPa. The difference between this value and the value of yield stress calculated considering 300 nm of film thickness with the nominal carbon content, will give the upper portion of the standard deviation bars shown in Figure 5-69 in section 5.7. Same calculations can be performed for 288 nm thickness, where:

$(2.62 \times 10^{23}/3) = 8.7 \times 10^{22}$ atoms which are consumed to form cementite.

$(9.2 \times 10^{22}) - (8.7 \times 10^{22}) = 5 \times 10^{21}$ atoms, which correspond to $(5 \times 10^{21}/6.022 \times 10^{23}) = 8.3 \times 10^{-3}$ mol.

$(8.3 \times 10^{-3} / (200000/288)) = 1.2 \times 10^{-5}$ mol in 200 µm.

$(1.2 \times 10^{-5} \times 2 \times 100) = 2.4 \times 10^{-3}$ at % (total carbon available for diffusion)

$\Delta\sigma = (2.5)\ (0.051 \times 82000) \times (2.4 \times 10^{-3}/100)^{1/2} = 51$ MPa, which added to 113.7 MPa gives a total yield stress of 165 MPa.

Nominal thickness	**Atoms of Fe**	**Atoms of C**
200 nm (33 at% of carbon)	1.614×10^{23} (67 at% of Fe)	7.948×10^{22} (33 at% of C)
208 nm	$(1.614 \times 10^{23}) \times (65.6/67) =$ 1.58×10^{23} (65.6 at % of Fe)	$(7.948 \times 10^{22}/0.96) =$ 8.28×10^{22} (34.4 at% of C)
200 nm (27 at% of carbon)	1.758×10^{23} (73 at% of Fe)	6.504×10^{22} (27 at% C)
192 nm	$(1.758 \times 10^{23}) \times (74/73) =$ 1.78×10^{23} (74 at% of Fe)	$(6.504 \times 10^{22}/1.04) =$ 6.25×10^{22} (26 at% of C)

Table D- 65 - Iron and carbon atoms considering film thickness variation of ± 8 nm on a nominal thickness of 200 nm

Same calculations can be performed for 208 nm thickness, where:

$(1.58 \times 10^{23}/3) = 5.3 \times 10^{22}$ atoms which are consumed to form cementite.

$(8.28 \times 10^{22}) - (5.3 \times 10^{22}) = 2.98 \times 10^{22}$ atoms, which correspond to $(2.98 \times 10^{22}/6.022 \times 10^{23}) = 0.049$ mol.

$(0.049/(200000/208)) = 5.1 \times 10^{-5}$ mol in 200 µm.

$(5.1 \times 10^{-5} \times 2 \times 100) = 0.0102$ at % (total carbon available for diffusion)

$\Delta\sigma = (2.5)\ (0.051 \times 82000) \times (0.0102/100)^{1/2} = 106$ MPa, which added to 113.7 MPa gives a total yield stress of 220 MPa.

Same calculations can be performed for 192 nm thickness, where:

$(1.78 \times 10^{23}/3) = 5.9 \times 10^{22}$ atoms which are consumed to form cementite.

$(6.25 \times 10^{22}) - (5.9 \times 10^{22}) = 3.2 \times 10^{21}$ atoms, which correspond to $(3.2 \times 10^{21}/6.022 \times 10^{23}) = 5.26 \times 10^{-3}$ mol.

$(5.26 \times 10^{-3}/(200000/192)) = 5.05 \times 10^{-6}$ mol in 200 µm.

$(5.05 \times 10^{-6} \times 2 \times 100) = 1 \times 10^{-3}$ at % (total carbon available for diffusion)

$\Delta\sigma = (2.5)\ (0.051 \times 82000) \times (1 \times 10^{-3}/100)^{1/2} = 33$ MPa, which added to 113.7 MPa gives a total yield stress of 147 MPa.

Nominal thickness	**Atoms of Fe**	**Atoms of C**
100 nm (33 at% of carbon)	8.07×10^{22} (67 at% of Fe)	3.974×10^{22} (33 at% of C)
104 nm	$(8.07 \times 10^{22}) \times (65.6/67) =$ 7.90×10^{22} (65.6 at % of Fe)	$(3.974 \times 10^{22}/0.96) =$ 4.1×10^{22} (34.4 at% of C)
100 nm (27 at% of carbon)	8.792×10^{22} (73 at% of Fe)	3.252×10^{22} (27 at% C)
96 nm	$(8.792 \times 10^{22}) \times (74/73) =$ 8.91×10^{22} (74 at% of Fe)	$(3.252 \times 10^{22}/1.04) =$ 3.13×10^{22} (26 at% of C)

Table D- 66 - Iron and carbon atoms considering film thickness variation of ± 4 nm on a nominal thickness of 100 nm

Same calculations can be performed for 104 nm thickness, where:

$(7.90 \times 10^{22}/3) = 2.63 \times 10^{22}$ atoms which are consumed to form cementite.

$(4.1 \times 10^{22}) - (2.63 \times 10^{22}) = 1.47 \times 10^{22}$ atoms, which correspond to $(1.47 \times 10^{22}/6.022 \times 10^{23}) = 0.024$ mol.

$(0.024/(200000/104)) = 1.25 \times 10^{-5}$ mol in 200 µm.

$(1.25 \times 10^{-5} \times 2 \times 100) = 2.5 \times 10^{-3}$ at % (total carbon available for diffusion)

$\Delta\sigma = (2.5)\ (0.051 \times 82000) \times (2.5 \times 10^{-3}/100)^{1/2} = 52$ MPa, which added to 113.7 MPa gives a total yield stress of 166 MPa.

Same calculations can be performed for 96 nm thickness, where:

$(8.91 \times 10^{22}/3) = 2.97 \times 10^{22}$ atoms which are consumed to form cementite.

$(3.13 \times 10^{22}) - (2.97 \times 10^{22}) = 1.6 \times 10^{21}$ atoms, which correspond to $(1.6 \times 10^{21}/6.022 \times 10^{23}) = 2.66 \times 10^{-3}$ mol.

$(2.66 \times 10^{-3}/(200000/96)) = 1.28 \times 10^{-6}$ mol in 200 µm.

$(1.28 \times 10^{-6} \times 2 \times 100) = 2.55 \times 10^{-4}$ at % (total carbon available for diffusion)

$\Delta\sigma = (2.5)\ (0.051 \times 82000) \times (2.55 \times 10^{-4}/100)^{1/2} = 16.7$ MPa, which added to 113.7 MPa gives a total yield stress of 130 MPa.

Nominal thickness	**Atoms of Fe**	**Atoms of C**
50 nm (33 at% of carbon)	4.035×10^{22} (67 at% of Fe)	1.987×10^{22} (33 at% of C)
52 nm	$(4.035 \times 10^{22}) \times (65.6/67) =$ 3.95×10^{22} (65.6 at % of Fe)	$(1.987 \times 10^{22}/0.96) =$ 2.1×10^{22} (34.4 at% of C)
50 nm (27 at% of carbon)	4.396×10^{22} (73 at% of Fe)	1.626×10^{22} (27 at% C)
48 nm	$(4.396 \times 10^{22}) \times (74/73) =$ 4.46×10^{22} (74 at% of Fe)	$(1.626 \times 10^{22}/1.04) =$ 1.56×10^{22} (26 at% of C)

Table D- 67 - Iron and carbon atoms considering film thickness variation of ± 2 nm on a nominal thickness of 50 nm

Same calculations can be performed for 52 nm thickness, where:

$(3.95 \times 10^{22}/3) = 1.32 \times 10^{22}$ atoms which are consumed to form cementite.

$(2.1 \times 10^{22}) - (1.32 \times 10^{22}) = 7.8 \times 10^{21}$ atoms, which correspond to $(7.8 \times 10^{21}/6.022 \times 10^{23}) = 0.013$ mol.

$(0.013/(200000/52)) = 3.38 \times 10^{-6}$ mol in 200 µm.

$(3.38 \times 10^{-6} \times 2 \times 100) = 6.76 \times 10^{-4}$ at % (total carbon available for diffusion)

$\Delta\sigma = (2.5)\ (0.051 \times 82000) \times (6.76 \times 10^{-4}/100)^{1/2} = 27$ MPa, which added to 113.7 MPa gives a total yield stress of 141 MPa.

Same calculations can be performed for 48 nm thickness, where:

$(4.46 \times 10^{22}/3) = 1.49 \times 10^{22}$ atoms which are consumed to form cementite.

$(1.56 \times 10^{22}) - (1.49 \times 10^{22}) = 7 \times 10^{20}$ atoms, which correspond to $(7 \times 10^{20}/6.022 \times 10^{23}) = 1.16 \times 10^{-3}$ mol.

$(1.16 \times 10^{-3}/(200000/48)) = 2.78 \times 10^{-7}$ mol in 200 µm.

$(2.78 \times 10^{-7} \times 2 \times 100) = 5.57 \times 10^{-5}$ at % (total carbon available for diffusion)

$\Delta\sigma = (2.5)\ (0.051 \times 82000) \times (5.57 \times 10^{-5}/100)^{1/2} = 7.8$ MPa, which added to 113.7 MPa gives a total yield stress of 122 MPa.

D.10 Annealing in high vacuum at 630 ºC of both sides coated coupons for times longer than 1h

The dimensions of the two specimens annealed at 630 ºC for 5h are shown in Table D- 68.

Tensile coupon	Width [mm]	Thickness [mm]	Gauge length [mm]	Annealing treatment	Speed set on the tensile machine [µm/s]
A	1	0.195	5	630ºC, 5h-High Vacuum	2.5
B	1	0.195	5	630ºC, 5h-High Vacuum	2.5

Table D- 68 - Dimensions of coupons coated both sides with 500 nm FeC film and annealed at 630˚C - 5h in high vacuum

Values of the mechanical properties obtained for the same coupons are reported in Table D-69.

sample	Upper Yield stress [MPa]	Lower Yield stress [MPa]	Average stress in Lüders plateau [MPa]	Lüders length	Ultimate tensile stress (UTS) [MPa]	Strain at fracture (ε_B)
A	274	239	252	0.048374	307	0.41
B	308	234	250	0.049674	308	0.37
Average	291	237	251	0.049024	307.5	0.39

Table D- 69 - Mechanical properties of coupons coated both sides with 500 nm FeC film and annealed at 630 ˚C - 5h in high vacuum

From Table D- 69, the average yield stress is 291 MPa and the standard deviation is ± 23.6 MPa, while for the heat treatment of 1 h, the average was 306 MPa with a standard deviation

of ± 31.6 MPa. The two ranges of yield stress overlap proving that the amount of carbon which is diffused seems to be the same even if the time of heat treatment is prolonged to 5 h.

D.11 Annealing in high vacuum at 430 ºC for several hours

The dimensions of the coupons annealed at 430 ˚C for 10h are listed in Table D- 70, while mechanical properties obtained during the tensile test are reported in Table D- 71.

Tensile coupon	Width [mm]	Thickness [mm]	Gauge length [mm]	Annealing treatment	Speed set on the tensile machine [µm/s]
A	1	0.195	5	430ºC, 10h-High Vacuum	2.5
B	1	0.195	5	430ºC, 10h-High Vacuum	2.5

Table D- 70 - Geometrical dimensions of coupons coated both sides with 500 nm FeC film and annealed at 430 ˚C - 10h in high vacuum

sample	Upper Yield stress [MPa]	Lower Yield stress [MPa]	Average stress in Lüders plateau [MPa]	Lüders length	Ultimate tensile stress (UTS) [MPa]	Strain at fracture (ε_B)
A	236	230	229	0.04805	292	0.43
B	233	211	219	0.04591	289	0.41
Average	234.5	220.5	224	0.04698	290.5	0.42

Table D- 71 - Mechanical properties obtained during tensile test of tensile coupons coated both sides with 500 nm FeC film annealed at 430 ˚C - 10h in high vacuum

D.12 Annealing of one side coated coupons

Table D- 72 shows their geometrical dimensions

Tensile coupon	Width [mm]	Thickness [mm]	Gauge length [mm]	Annealing treatment	Speed set on the tensile machine [µm/s]
A	1	0.191	5	530ºC, 1h-High Vacuum-one side coated	2.5
B	1	0.188	5	530ºC, 1h-High Vacuum-one side coated	2.5
A	1	0.185	5	630ºC, 1h-High Vacuum-one side coated	2.5
B	1	0.184	5	630ºC, 1h-High Vacuum-one side coated	2.5

Table D- 72 - Dimensions of coupons coated on one side with 500 nm FeC film and annealed at 530 ˚C - 1h or 630 ºC – 1h in high vacuum

The obtained mechanical properties are listed in Table D- 73.

sample	Upper Yield stress [MPa]	Lower Yield stress [MPa]	Average stress in Lüders plateau [MPa]	Lüders length	Ultimate tensile stress (UTS) [MPa]	Strain at fracture (ε_B)
A	187	205	199	0.04974	261	0.37
B	198	182	189	0.03584	242	0.3
Average	192.5	193.5	194	0.04279	251.5	0.34

Table D- 73 - Mechanical properties obtained for specimens coated on one side with 500 nm thick FeC film and annealed at 530 ˚C - 1h in high vacuum

Table D- 74 lists the mechanical properties of one side coated coupons annealed at 630 ºC – 1h.

sample	Upper Yield stress [MPa]	Lower Yield stress [MPa]	Average stress in Lüders plateau [MPa]	Lüders length	Ultimate tensile stress (UTS) [MPa]	Strain at fracture (ε_B)
A	221.6	208	215	0.04288	264	0.25
B	257	219	238	0.04578	292	0.24
Average	239	214	227	0.04433	278	0.25

Table D- 74 - Mechanical properties of a coupon coated only on one side with 500 nm thick FeC film and annealed at 630 ˚C - 1h in high vacuum

D.13 Digital Image Correlation on specimens annealed in high vacuum

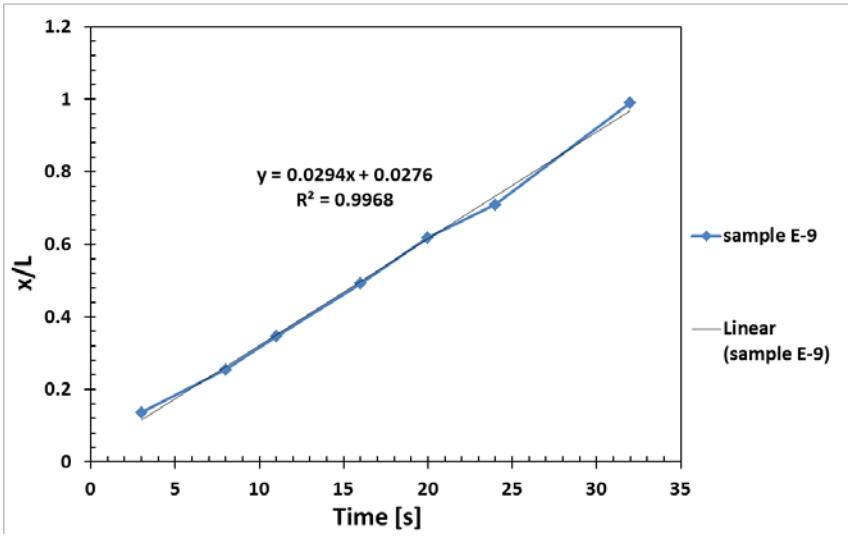

Figure D. 23 - Velocity profile of Lüders bands in sample E-9 coated both sides with 500 nm FeC film and annealed at 630 ˚C - 1h

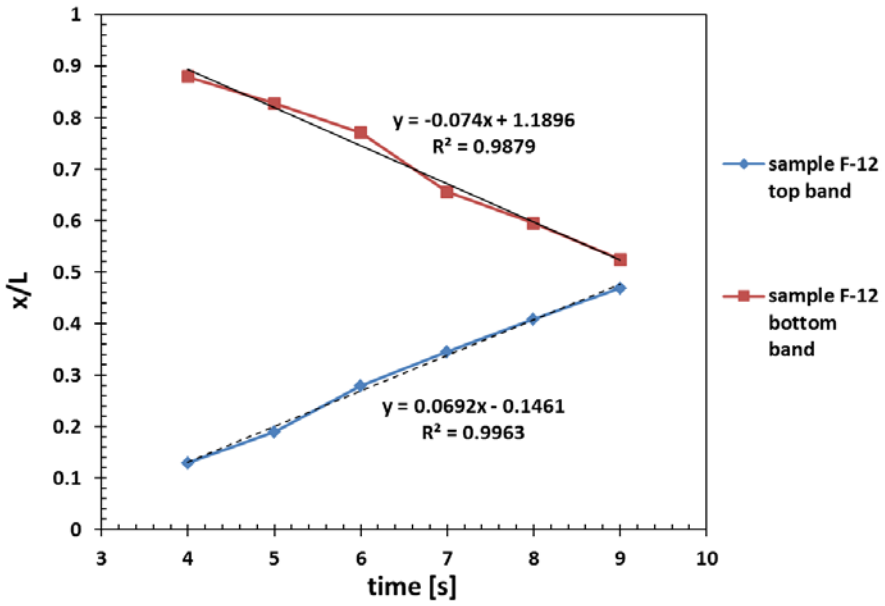

Figure D. 24 - Velocity profile of Lüders bands in sample F-12 coated both sides with 500 nm FeC film and annealed at 710 ˚C - 1h

D.14 Grain size analyses on diffusion annealed coupons

The grain size of coupons coated both sides with 500 nm FeC film and annealed at different temperatures in the furnace in argon atmosphere was measured. The images of the microstructures after etching with 4% Nital solution for 20 seconds are shown in Figure D. 25. Similar microstructure were found also on specimens annealed in high vacuum for 1h at different temperatures. For each specimen, analyses on one image taken at 10X magnification and on one image taken at 20X magnification were performed by using the method of the lineal intercept as described in the norm ASTM E112-10 [229]. For each image, 5 vertical lines, 9 horizontal lines and 10 oblique lines were drawn and the intercepts of this lines with the grain boundaries were calculated for each of them. The average grain size was found to be 14 µm for all the annealing temperatures.

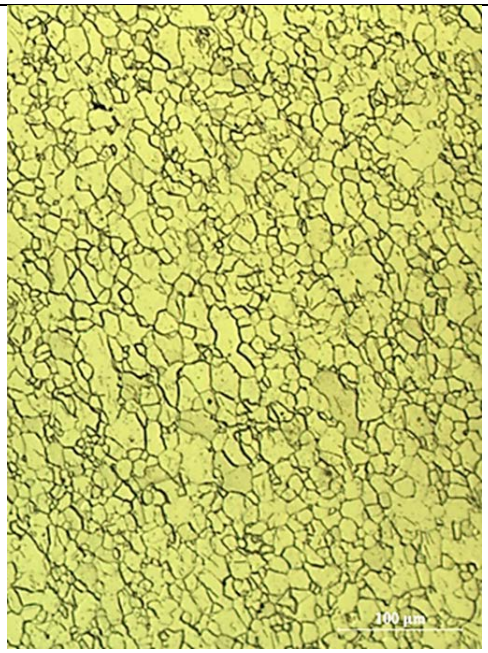

(a) Microstructure after annealing in furnace at 430 ºC – 1h

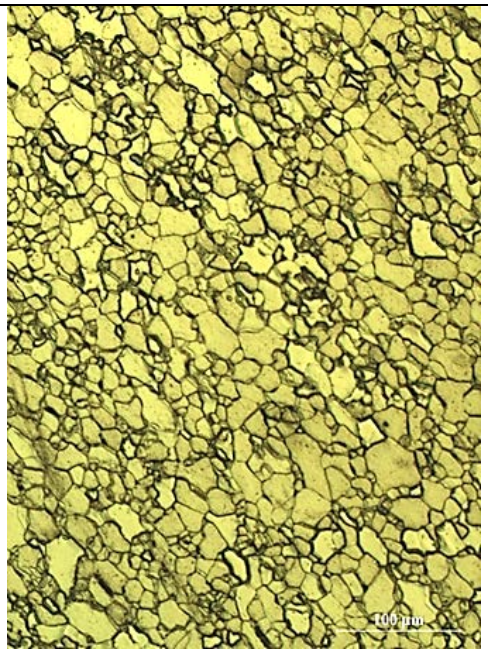

(b) Microstructure after annealing in furnace at 530 ºC – 1h

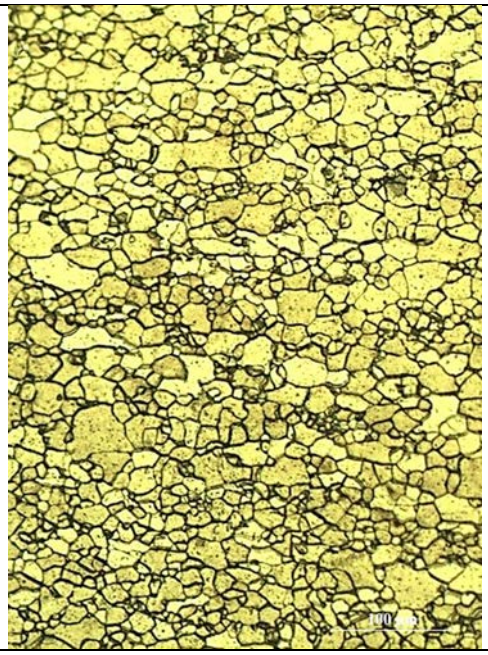

(c) Microstructure after annealing in furnace at 630 ºC – 1h

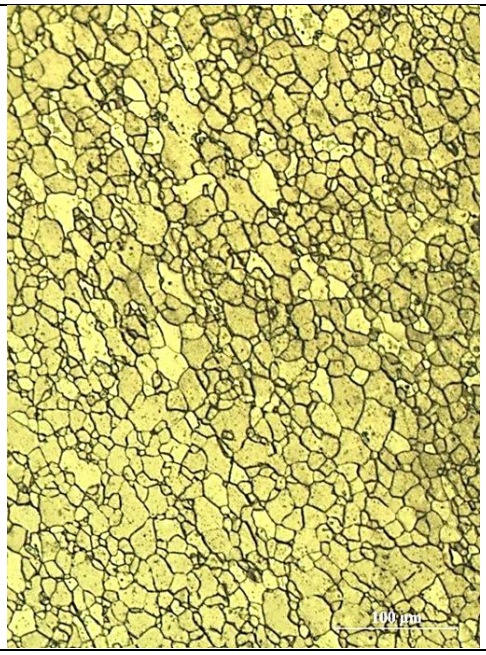

(d) Microstructure after annealing in furnace at 710 ºC – 1h

Figure D. 25 - Microstructures of both sides coated coupons annealed in the furnace in argon at different temperatures for 1h

D.15 Scanning Electron Microscope Images of specimens annealed in high vacuum in the furnace

Images of tensile coupons coated on both sides with 500 nm FeC film and annealed at different temperatures in high vacuum for 1h were taken using SEM after a light etching (30 seconds) of the surfaces with 4% Nital solution (Figure D. 26). The grain boundaries look highlighted compared to a not-coated and not-annealed IF steel (shown in Figure 8-41) and they appear easily revealed after the etching. No change in grain boundary morphology is detected as function of annealing temperature.

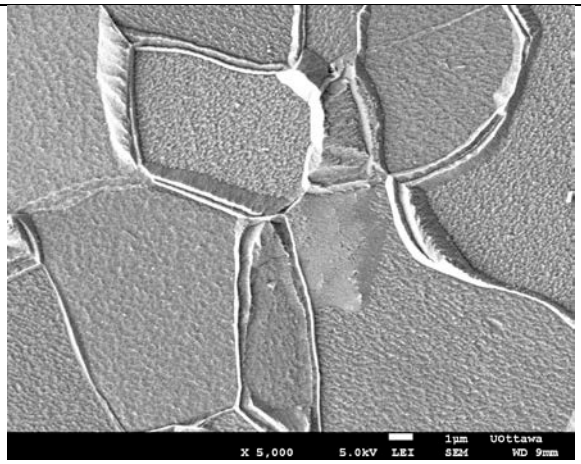

(a) Coupon annealed at 430 ºC – 1h in high vacuum

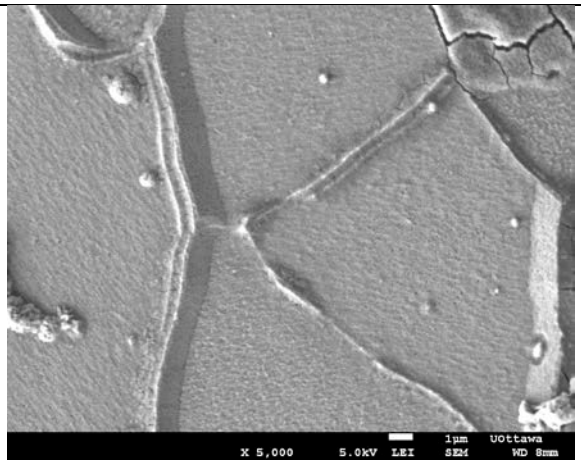

(b) Coupon annealed at 530 ºC – 1h in high vacuum

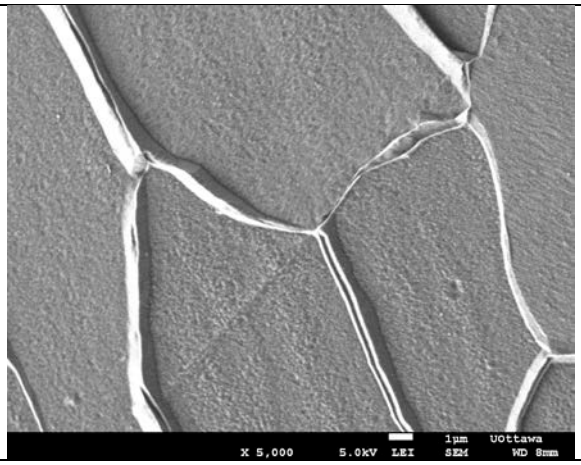

(c) Coupon annealed at 630 ºC – 1h in high vacuum

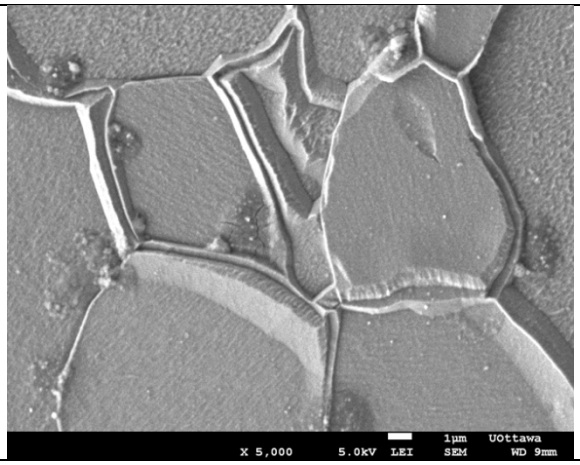

(d) Coupon annealed at 710 ºC – 1h in high vacuum

Figure D. 26 - SEM images of grain boundaries in both sides coated coupons annealed in high vacuum at different temperatures for 1h.

The specimen annealed at 530 ºC – 1h (Figure D. 26 (b)) has the grain boundaries less revealed due to the poor etching caused by a poor cleaning of the surface after the polishing. Some residues of polishing and etching solutions are revealed inside the grains.

Appendix E : Finite Element Method

E.1 Mesh Influence on Lüders bands simulation

In Figure E. 1, the results of the influence of the number of elements used for the mesh are shown. It can be seen that for meshed close to 70000 of elements or above, the length of Lüders plateau becomes stable.

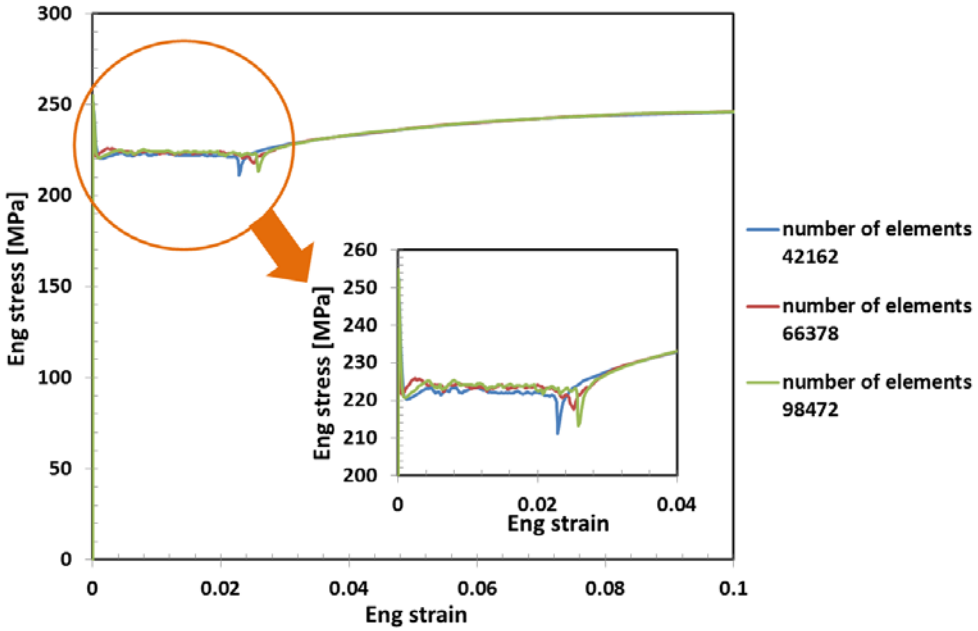

Figure E. 1 - Study of mesh influence on Lüders bands propagation

E.2 Evolution of artificial energy and internal energy for FEM simulations of Lüdering

In the following appendix, all the percentage ratio of the artificial energy over the internal energy for the finite elements simulations performed in Chapter 6 are reported.

- **Simulation of change in yield stress of the linear softening**

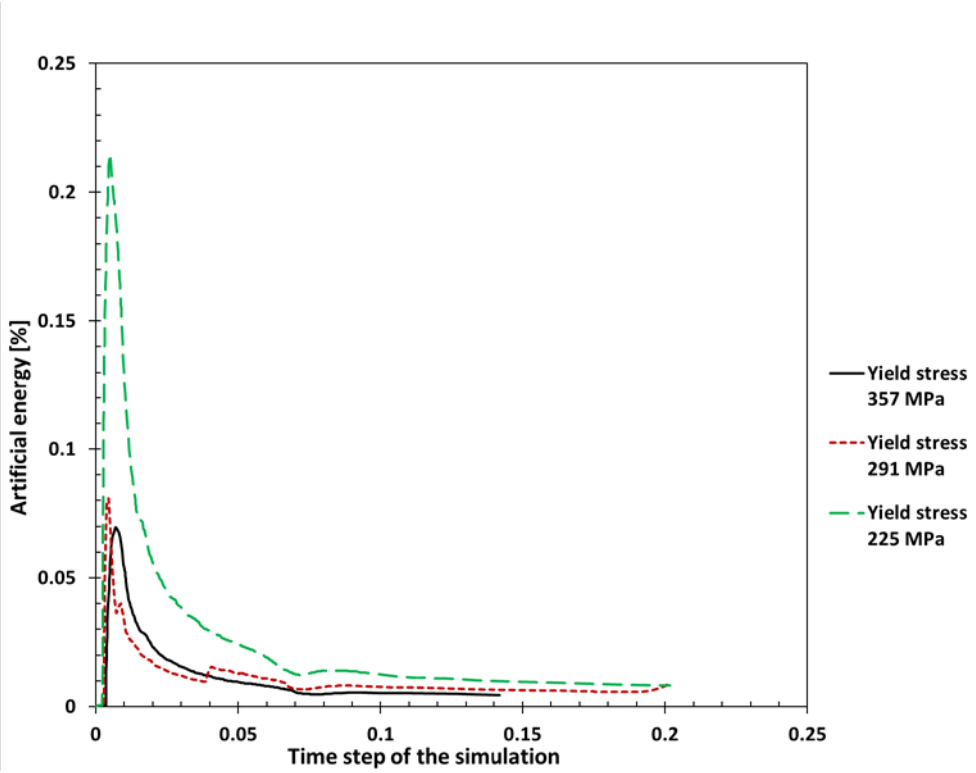

Figure E. 2 - Artificial energy evolution expressed as percentage of the internal energy during the simulation of change in yield stress under the same slope of the linear softening

- **Simulation of change in yield stress of the linear softening**

Figure E. 3 shows the evolution of the internal energy and artificial energy as function of the time step of the simulation for both graded and uniform carbon distribution though thickness. Figure E. 4 shows the evolution of the percentage ratio of the artificial energy over the internal energy. Even at the last time step of 0.2, the internal energy is close to 42 J while the artificial energy is only 19 x 10^{-4} J, which represents only the 4.5 x 10^{-3} % of the internal energy.

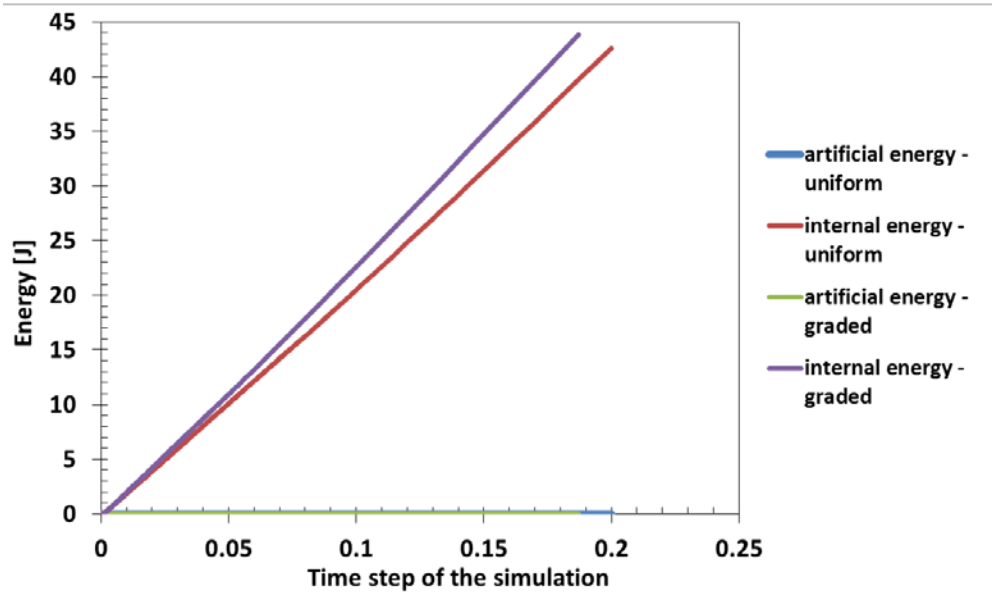

Figure E. 3 - Comparison of internal energy and artificial energy evolution for simulations of graded mechanical properties and uniform mechanical properties

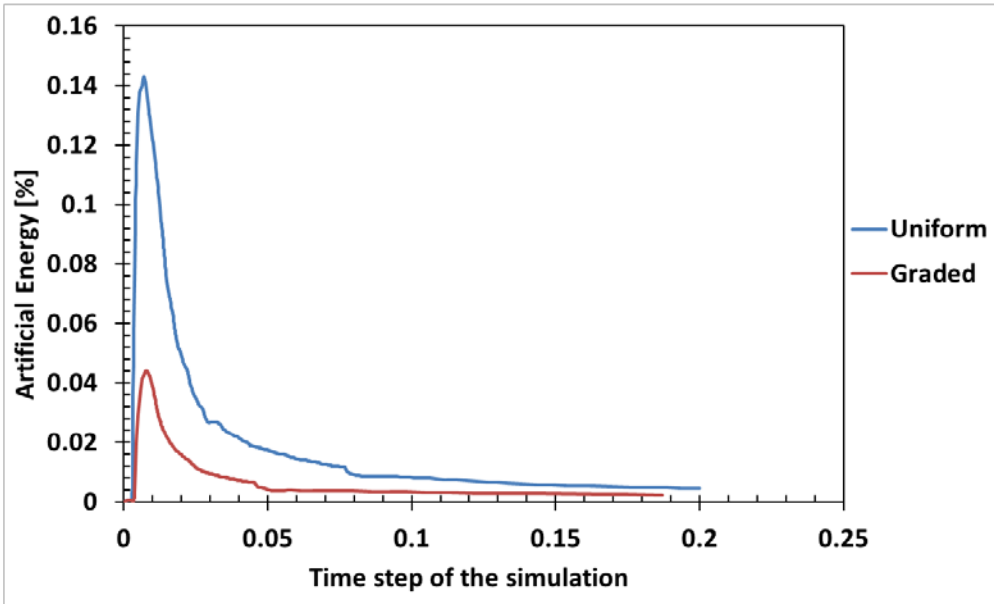

Figure E. 4 - Artificial energy evolution during the simulation of graded mechanical properties and uniform mechanical properties through thickness, expressed as percentage of the internal energy

- **Simulation of change in Young's modulus of the central layer**

The percentage of the ratio between artificial energy over the internal energy was extracted for each simulation and it was found that the ratio is below 1% for all the simulations, meaning that no hourglass problem is affecting the results due to the meshing being done with reduced elements. The results are shown in Figure E. 5.

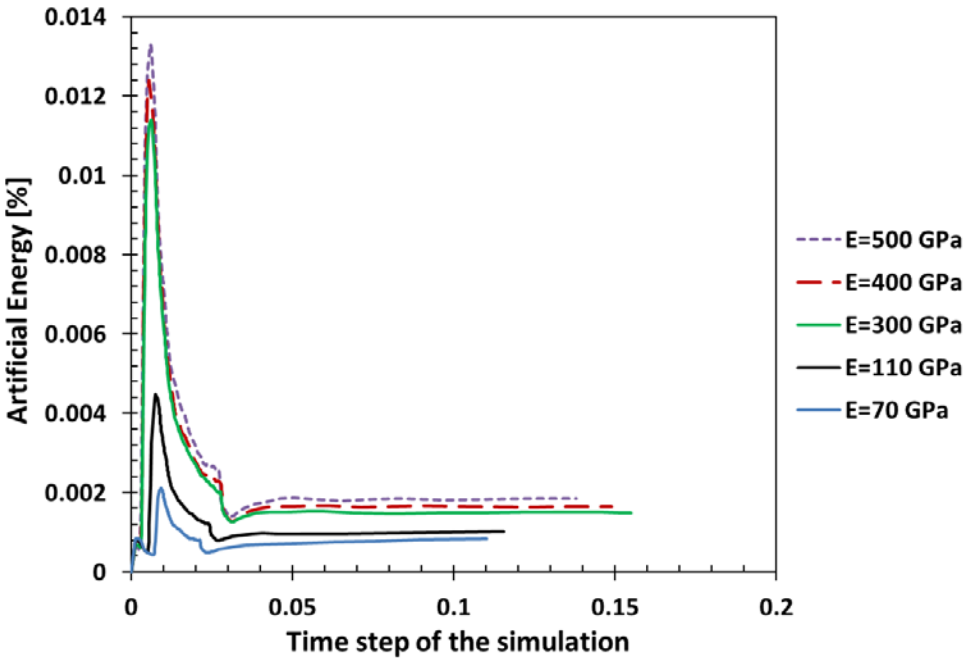

Figure E. 5 - Artificial energy evolution expressed as percentage of the internal energy during the simulation of change of Young's modulus of a central layer having no Lüdering

- **Simulation of change in thickness of the central layer**

The evolution of the energy for the simulations related to the change in thickness of the central layer is shown in Figure E. 6 for the 1:1 ratio and for the 1.5:1 ratio, while it is reported in Figure E. 7 for the 2:1 ratio and for the 2.5:1 ratio.

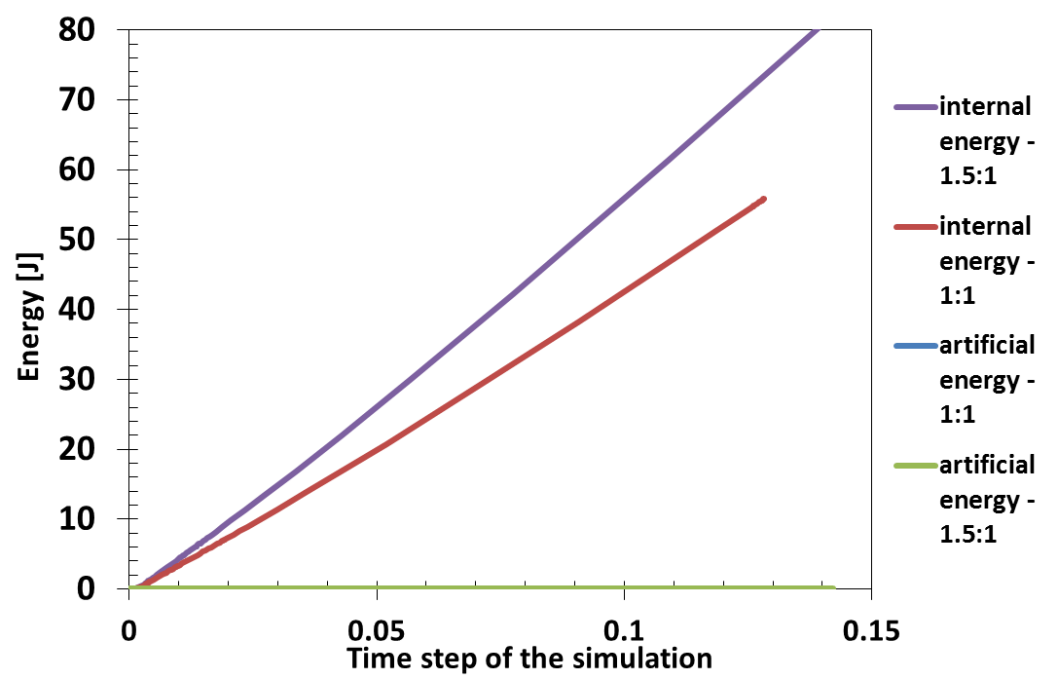

Figure E. 6 - Comparison of internal energy and artificial energy evolution for simulations having changes of thickness of the central layer (ratio 1:1 and ratio 1.5:1) and uniform mechanical properties in the outer layers

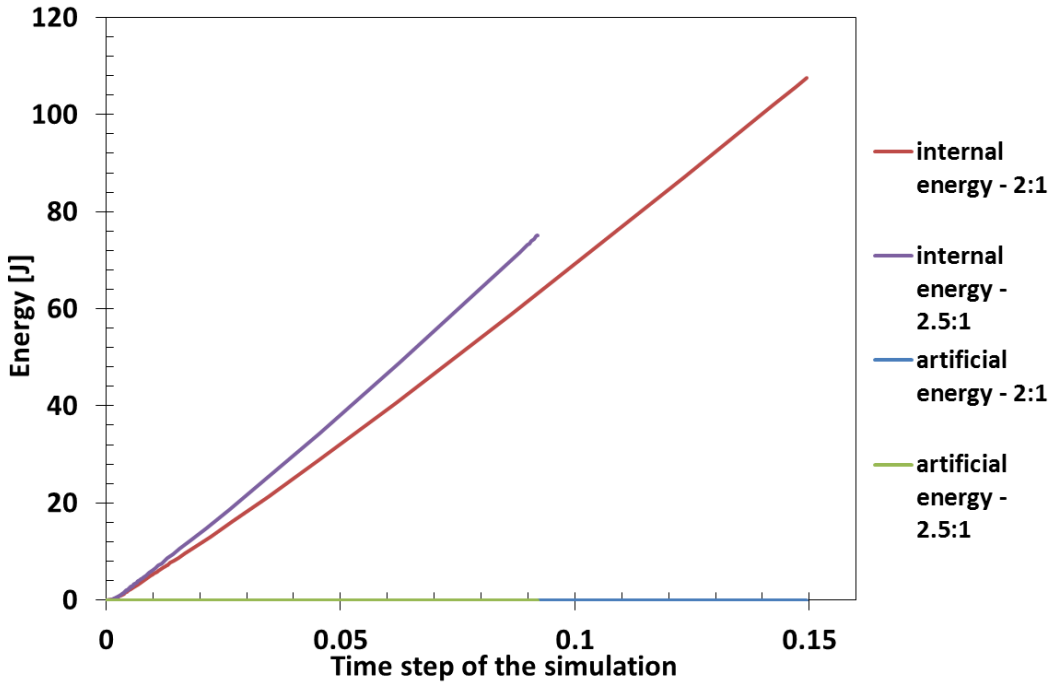

Figure E. 7 - Comparison of internal energy and artificial energy evolution for simulations having changes of thickness of the central layer (ratio 2:1 and ratio 2.5:1) and uniform mechanical properties in the outer layers

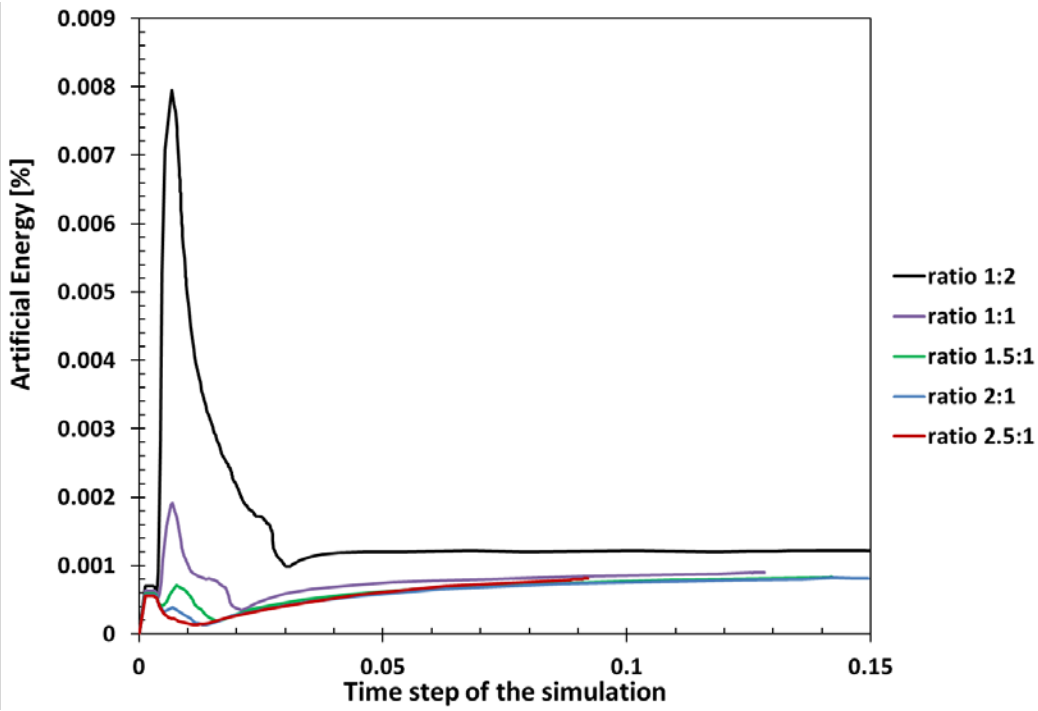

Figure E. 8 - Artificial energy evolution during the simulation expressed as percentage of the internal energy for change of thickness of the central layer and uniform material properties in the outer layers

In Figure E. 8, the evolution of the artificial energy as percentage of the internal energy during the simulation is reported. It can be clearly seen that the artificial energy remains lower than 1% for the whole simulation meaning that no hourglass instability is compromising the results.

- **Simulation of change in thickness of the central layer for graded outer layers**

The evolution of the energy to check if the simulations show hourglass problems is shown in Figure E. 9 for the 1:1 ratio and for the 1.5:1 ratio, while it is reported in Figure E. 10 for the 2:1 ratio and for the 2.5:1 ratio. The percentage evolution of the two energies is reported in Figure E. 11, where it is evident that remains lower than 1% so no hourglass problem is affecting the results.

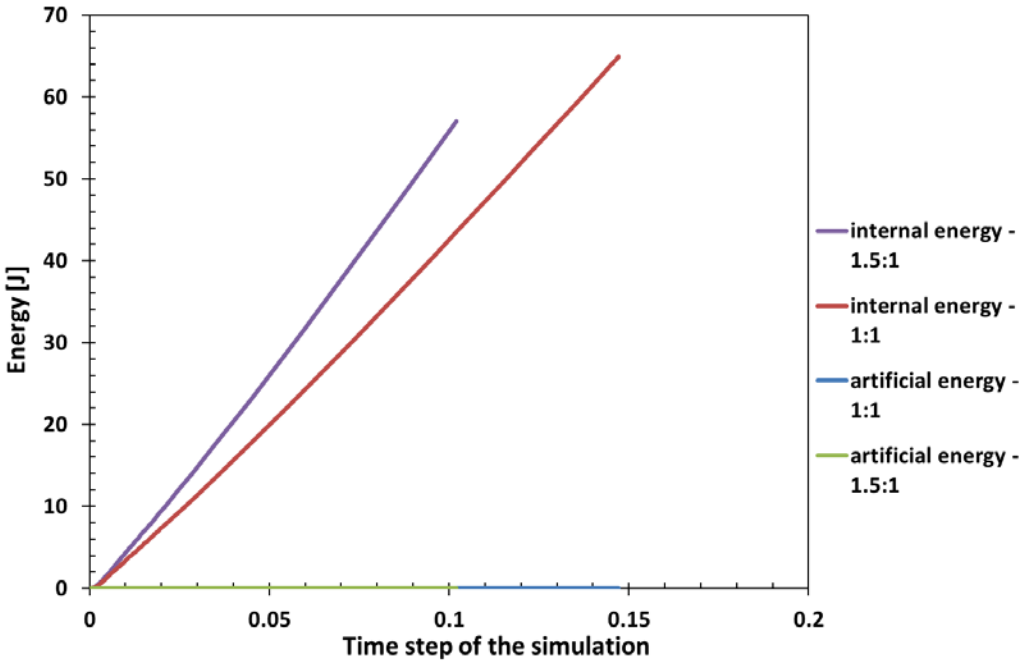

Figure E. 9 - Comparison of internal energy and artificial energy evolution for simulations having changes of thickness of the central layer (ratio 1:1 and ratio 1.5:1) and graded mechanical properties in the outer layers

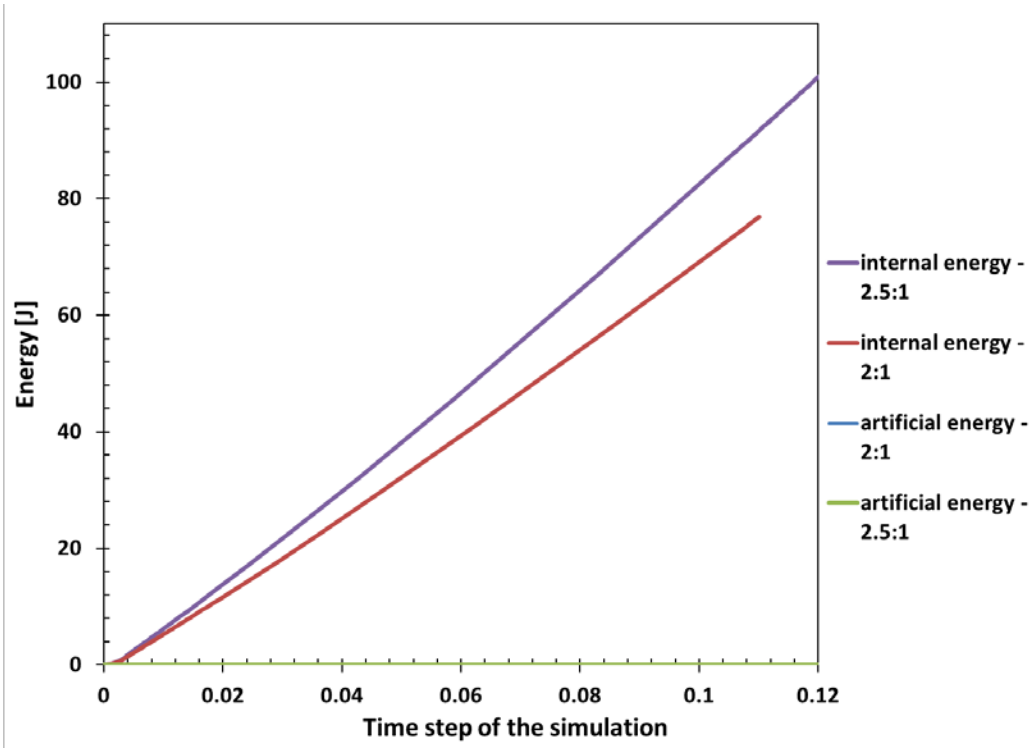

Figure E. 10 - Comparison of internal energy and artificial energy evolution for simulations having changes of thickness of the central layer (ratio 2:1 and ratio 2.5:1) and graded mechanical properties in the outer layers

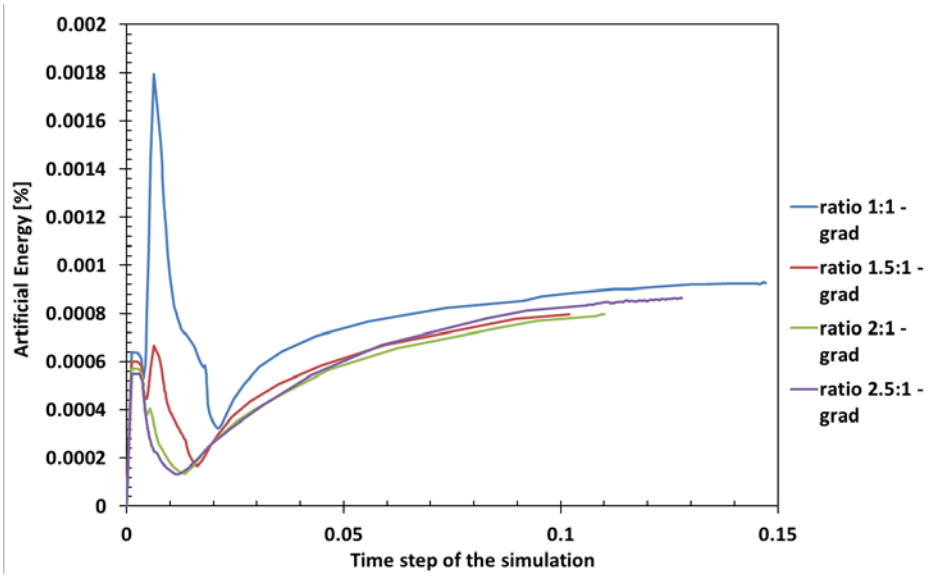

Figure E. 11 - Artificial energy evolution during the simulation expressed as percentage of the internal energy for change of thickness of the central layer and gradient of material properties in the outer layers

- **<u>Simulation of change in strain-hardening behaviour</u>**

Even for these simulations the ratio of artificial energy over the internal energy was checked to see if hourglass problems were affecting the results (Figure E. 12), however the ratio was found below 1% so the results are not affected by instability of the mesh.

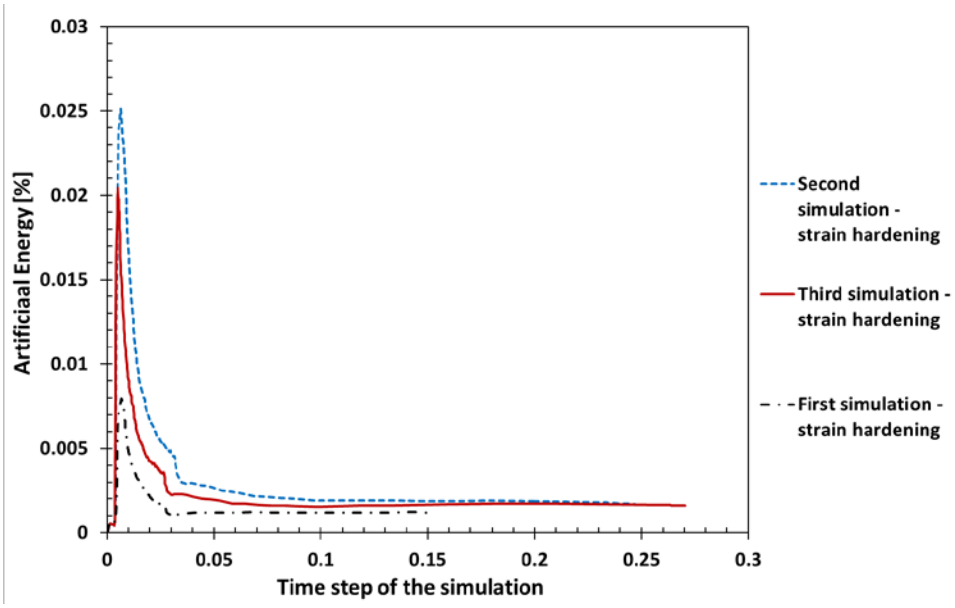

Figure E. 12 - Artificial energy evolution during the simulation expressed as percentage of the internal energy for change of strain hardening

- **Simulation of change in void interspacing on Lüders bands propagation**

The evolution of the ratio between the artificial energy and the internal energy during the simulation is shown in Figure E. 13. The simulations have no hourglass problems even if the element C3D8R was used for the meshing.

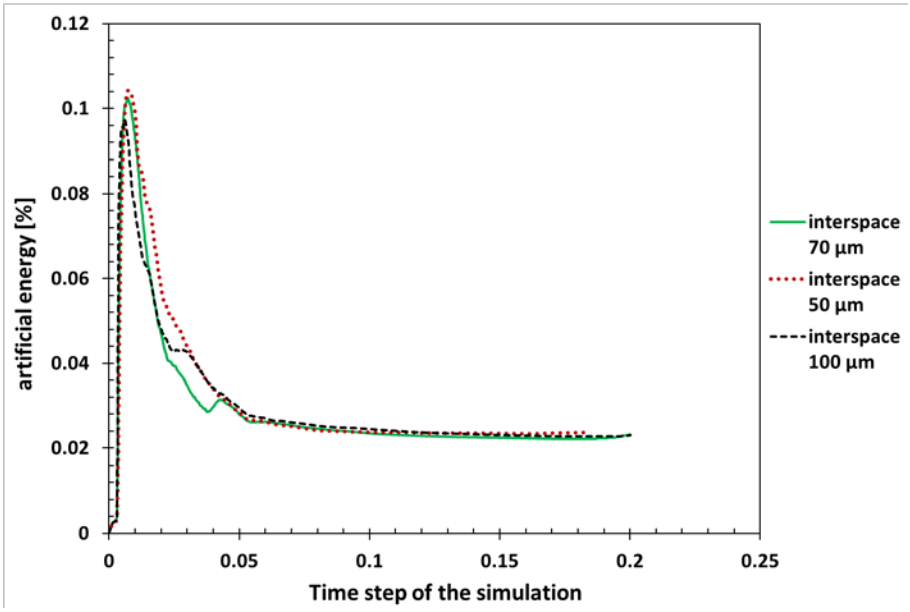

Figure E. 13 - Artificial energy evolution during the simulation expressed as percentage of the internal energy for change of voids interspacing

- **Influence of void volume fraction on Lüders propagation**

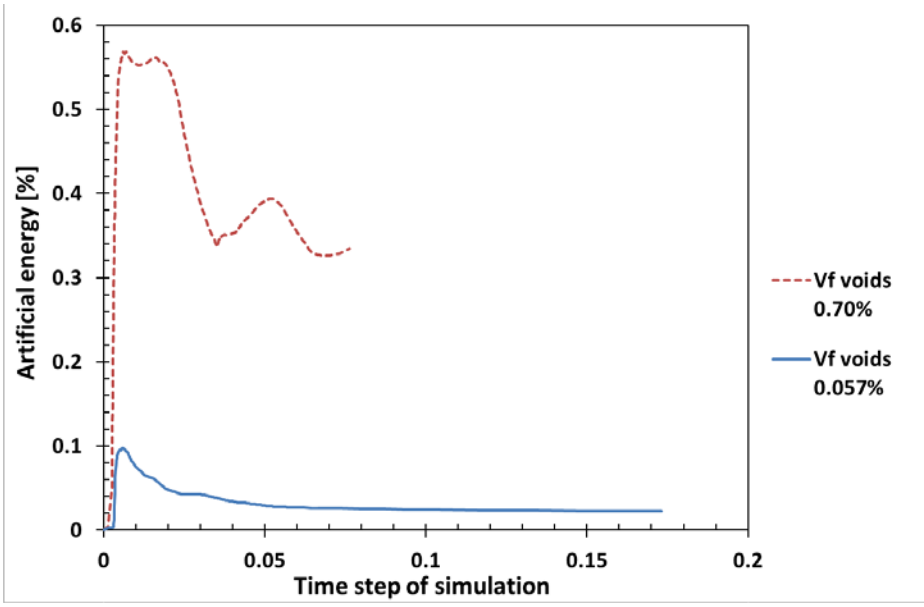

Figure E. 14 - Artificial energy evolution during the simulation expressed as percentage of the internal energy for change of voids volume fraction

Appendix F : Pre-strain Results

In this appendix, all the engineering stress-strain curves obtained during pre-strain of uncoated IF steel coupons are reported. The stress-strain curves obtained after heat treatment in high vacuum of these uncoated coupons for the different temperatures are also shown.

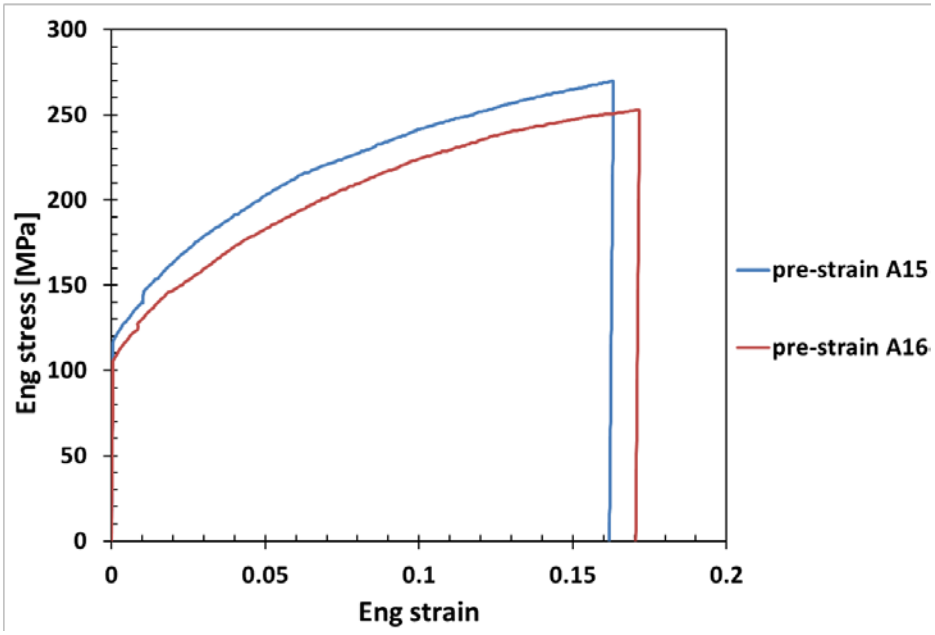

Figure F. 1 - Pre-strain engineering stress-strain curves of specimens A15 and A16 which will be annealed at 430 ˚C - 1h in high vacuum

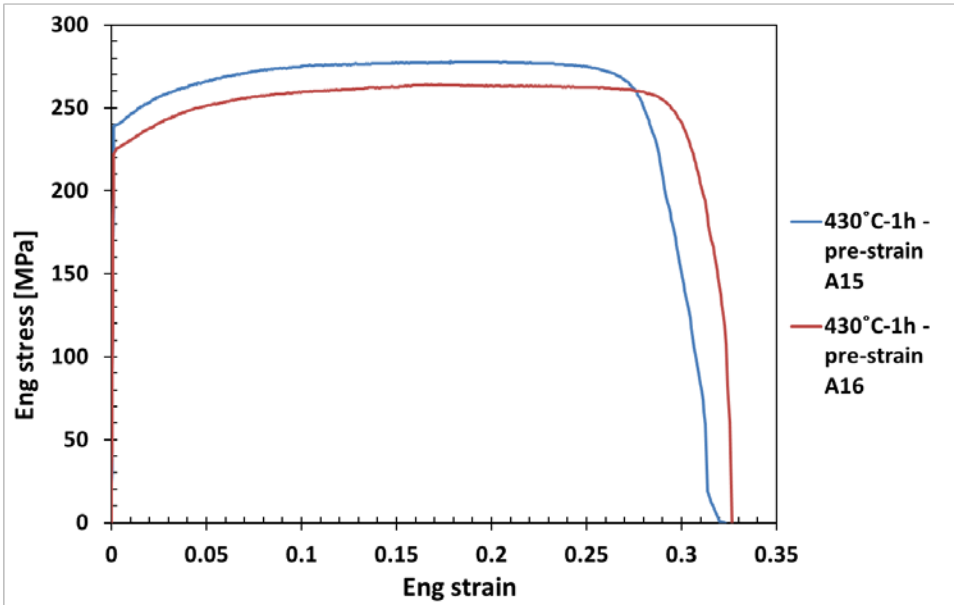

Figure F. 2 - Engineering stress-strain curves of specimens A15 and A16 after pre-strain and annealing at 430 ˚C - 1h in high vacuum

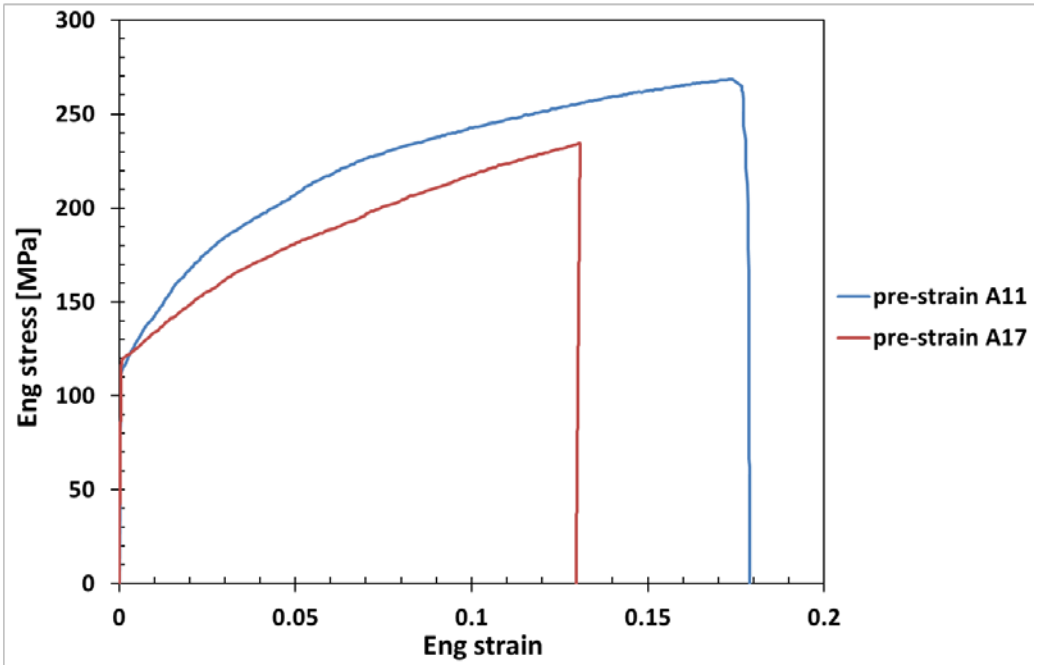

Figure F. 3 - Pre-strain engineering stress-strain curves of specimens A11 and A17 which will be annealed at 530 ˚C - 1h in high vacuum

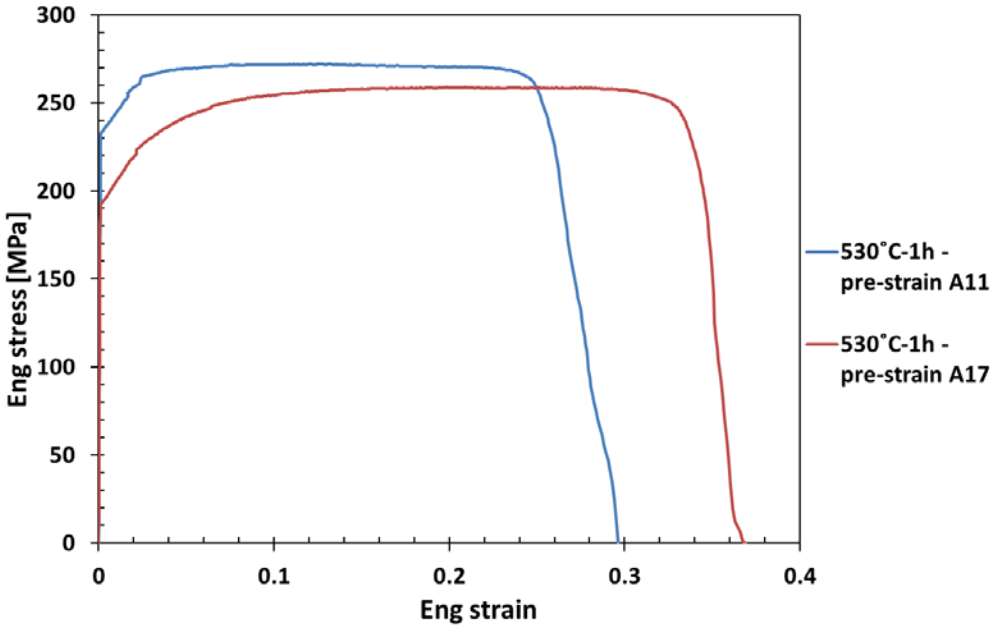

Figure F. 4 - Engineering stress-strain curves of specimens A11 and A17 after pre-strain and annealing at 530 ˚C - 1h in high vacuum

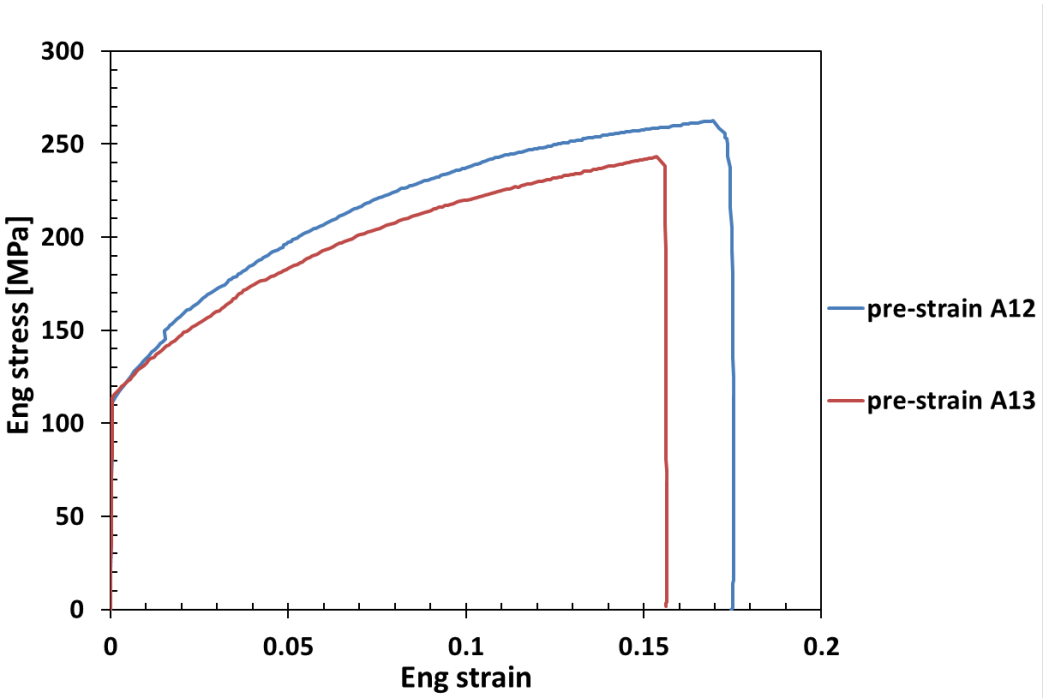

Figure F. 5 - Pre-strain engineering stress-strain curves of specimens A12 and A13 which will be annealed at 630 ˚C - 1h in high vacuum

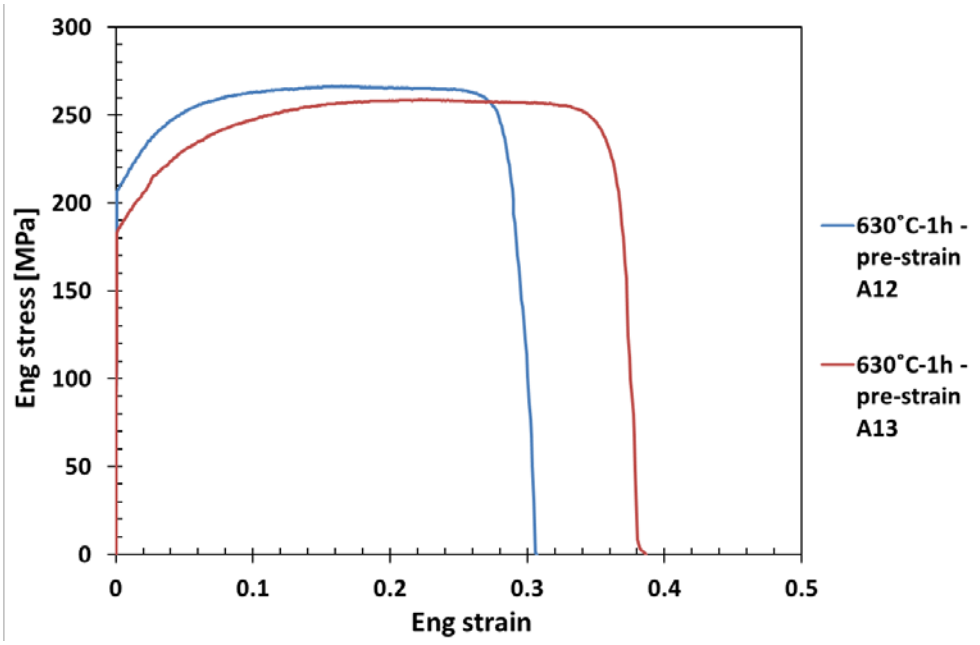

Figure F. 6 - Engineering stress-strain curves of specimens A12 and A13 after pre-strain and annealing at 630 ˚C - 1h in high vacuum

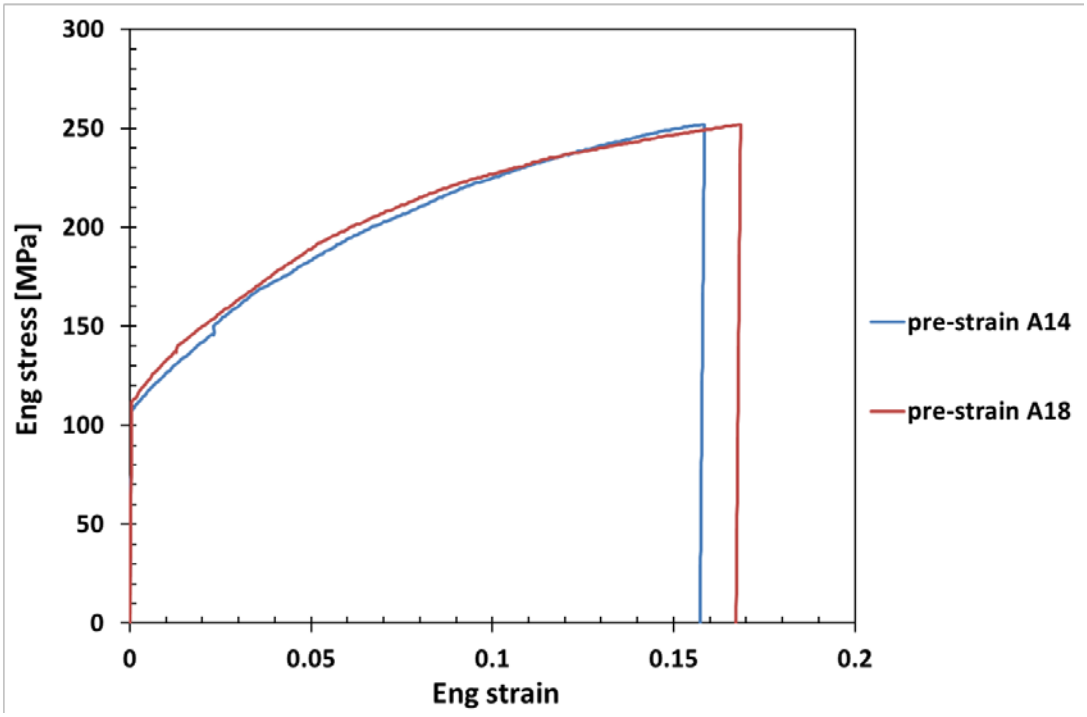

Figure F. 7 - Pre-strain engineering stress-strain curves of specimens A14 and A18 which will be annealed at 710 ˚C - 1h in high vacuum

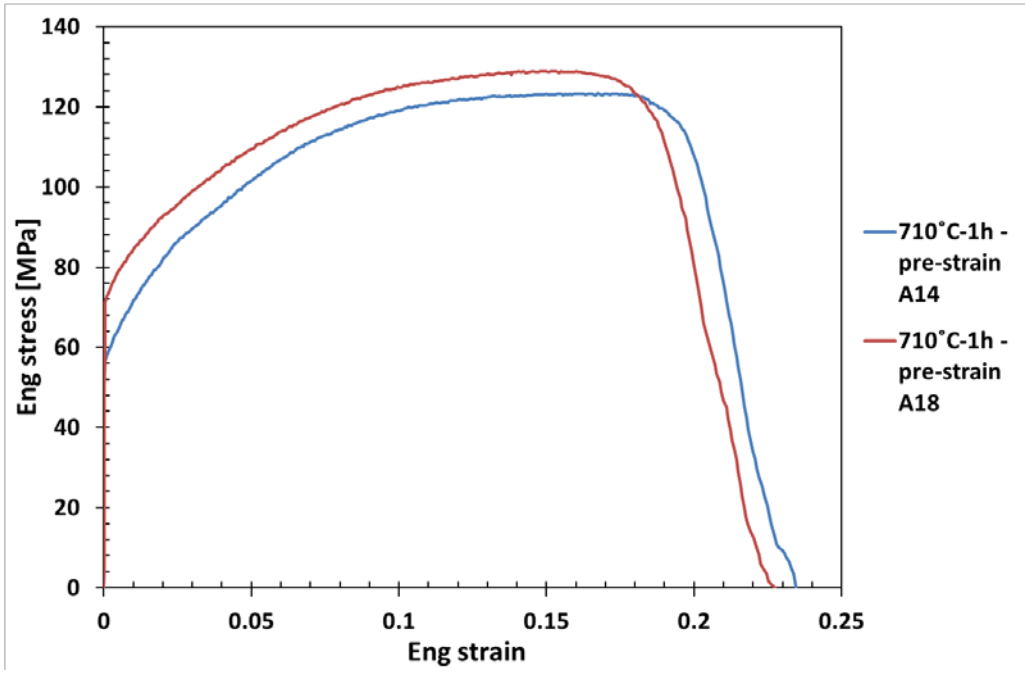

Figure F. 8 - Engineering stress-strain curves of specimens A14 and A18 after pre-strain and annealing at 710 ˚C - 1h in high vacuum

Appendix G : Flash Annealing

G.1 Sealing of quartz ampoules

(a) Quartz ampoule connected to the turbopump. The level of vacuum is recorded and the sealing of the ampoule starts only when the vacuum is at least $5x10^{-6}$ Torr. The quartz is heated only in the zone of the flame and it is completely cold on the other end where the specimen sits. In this way, the specimen is not affected by the sealing process

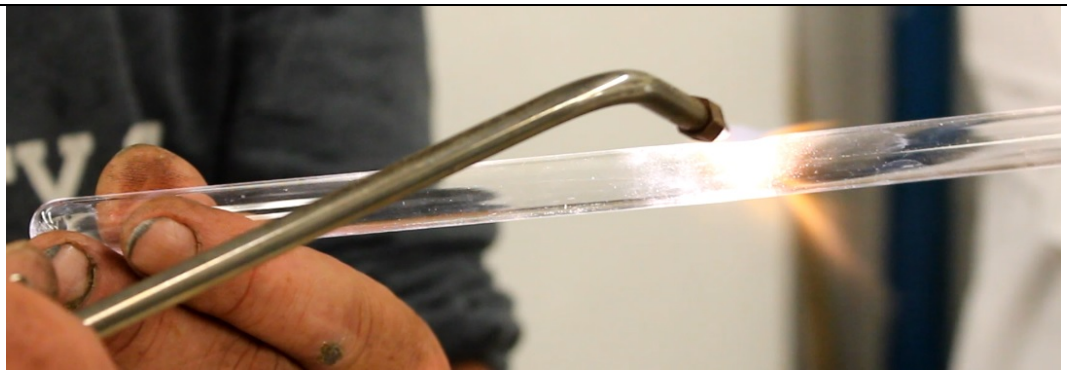

(b) The flame is applied all around the glass ampoule and a necking zone starts to form where the glass is starting to become more soft, while the other end is hold.

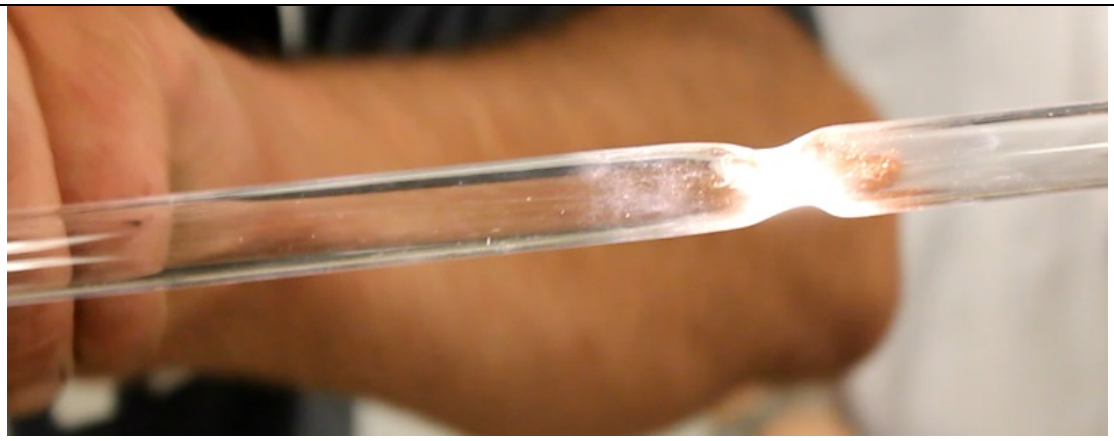

(c) The necking zone is clearly visible in the glass ampoule

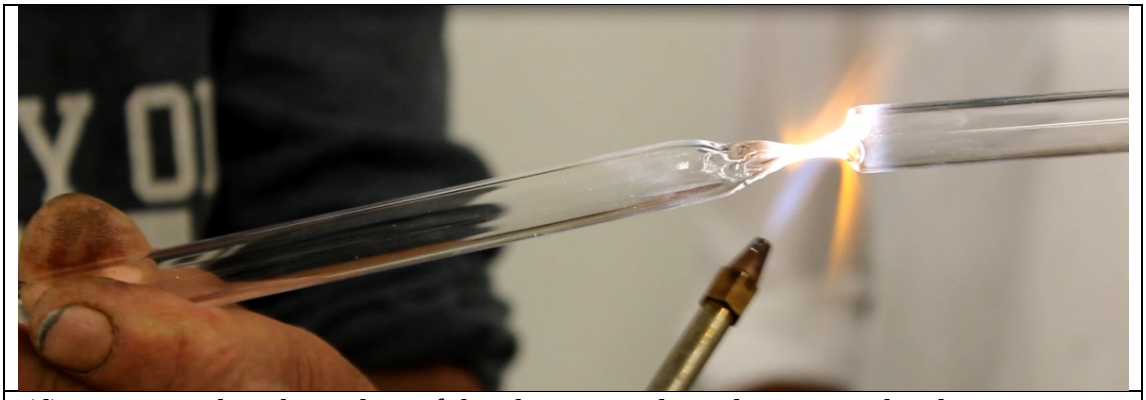

(d) Last step when the sealing of the glass ampoule is almost completed

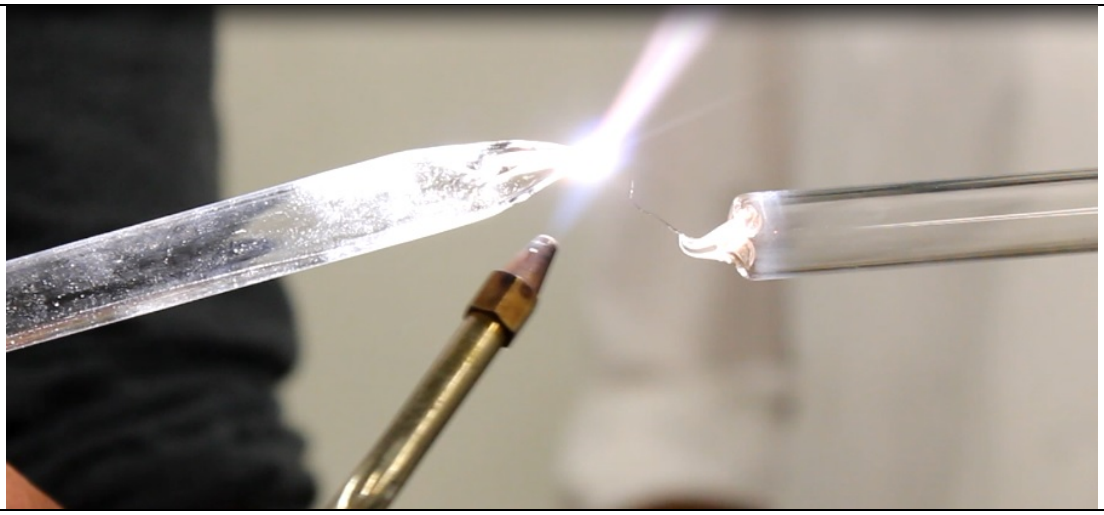

(e) After that the glass ampoule has been sealed, its tip is heated for few seconds to be sure that there is no air bubble trapped at the tip which could compromise the sealing

Figure G. 1 - Sequence of steps showing the sealing of the quartz ampoule containing the IF steel specimen

G.2 Calculation of time required for flash annealing in the furnace

The time required to heat the quartz ampoule at 900 ˚C inside the furnace can be calculated in first approximation by using the equation for conduction in variable regime for semi-infinite solids, which is the following:

$$\frac{(T - T_S)}{(T_i - T_S)} = 1 - erfc(\eta) \qquad \text{(eq. G. 1)}$$

where:

T = temperature of the quartz after a certain time t;

T_i = initial temperature of the quartz ampoule (which can be considered 25 ˚C);

T_S = temperature inside the furnace (which is set to 950˚C);

erfc(η) is the complementary error function, which is defined as (1-erf(η)), where erf(η) is the Gaussian error function.

The parameter η is defined by the following equation.

$$\eta = \frac{x}{\sqrt{4\alpha t}} \qquad \text{(eq. G. 2)}$$

x = thickness of the glass ampoule equal to 2.25 mm;

α = thermal diffusivity for quartz (values range between 1.4 mm^2/s to 3 mm^2/s) (for the calculation an average between the two values will be taken, which is equal to 2.2 mm^2/s);

t = time to reach temperature T_S.

$$\frac{(T-950)}{(25-950)} = 1 - erfc\left(\frac{2.25mm}{\sqrt{4*\left(2.2\,mm^2/s\right)*90s}}\right) = 1 - erfc(0.079950) \qquad \text{(eq. G. 3)}$$

From the table of the complementary error function:

x	**erfc(x)**
0.07	0.921142
0.08	0.909922

By doing a linear interpolation between the values shown above, the value of the erfc for x = 0.079950 can be obtained:

$$\left(\frac{0.079950 - 0.07}{0.08 - 0.07}\right) = \left(\frac{x - 0.921142}{0.909922 - 0.921142}\right)$$

From which x = 0.90998, so substituting in eq. G. 3:

$$T = (950) + \left[(25-950)\times(1-0.90998)\right] = 866.73^{\circ}C$$

The heating rate was also verified experimentally by placing a thermocouple inside the quartz glass ampoule to verify if after 90 seconds the reached temperature was effectively close to 900˚C. The values recorded by the thermocouple placed inside the quartz ampoule are reported in Table G- 1. The temperature inside the quartz ampoule at 90 s was recorded to be 910˚C. The heating rate experienced by the quartz ampoule and by the sample of steel sealed in it, is around (910 ˚C/90 s = 10.1 ˚C/s).

Time [s]	Temperature [˚C]
0	20.4
15	327
30	598
45	768
60	855
75	894
90	910
105	919
120	924.5
135	927.7
150	930

Table G- 1 - Values recorded by the thermocouple inserted in the furnace inside the quartz ampoule

G.3 Theory of Induction Heating

"An induction heater is made by a source of high frequency, an induction coil and a cooling system. In a basic induction heating set-up, a solid state RF power supply sends an alternate current (AC) through the induction coil" [230]. The passage of this current though the working coil will produce a very intense magnetic field and since the current is alternate; the magnetic field will also be changing its direction of flow inside the working coil [231]. "The piece to be heated is placed inside the zone surrounded by the coil and it will experience the alternate magnetic field. This alternating magnetic field will induce currents (*eddy currents*) inside the conductive material that needs to be annealed" [231]. The rate of heating is dependent on the frequency and intensity of the induced current, and on materials properties such as specific heat, magnetic permeability, and its resistance to the flow of current [232]. Moreover, the specific heat, the magnetic permeability and the resistivity of the metals are temperature dependent [232]. " The *eddy currents* generated in the piece will flow against the electrical resistivity of the metal generating heat without any direct contact between the part and the inductor. This heating occurs both with magnetic metals and non-magnetic metals and it is known as *Joule effect* " [230]. "All metals are capable of conducing electricity but they offer some resistance to this flow". "This resistance causes loss of power and the generation of heat, which can be calculated as $P = i^2 \cdot R$, where "i" is the amount of current flowing in the metal and "R" is its resistance" [232].

"The high frequency used in induction heating can cause a phenomenon called "skin effect" which forces the alternating currents created in the workpiece to flow in a thin layer towards the surface. The skin effect increases the effective resistance of the metal so it can increase greatly the heating effect caused by the current flowing in the workpiece" [231].

"For ferrous materials, the heat is not only caused by Eddy currents but also by hysteresis effect. The alternate magnetic field that is generated inside the coil magnetizes and de-magnetizes repeatedly the magnetic dipoles of iron" [232]. This high variation of the magnetic domains causes a high friction and heating inside the material. However, "the hysteresis effect is occurring only if the material is heated below the Curie temperature (760 ˚C); above this temperature the heating is due only to *eddy currents*" [232] since above this temperature the material is paramagnetic while below the Curie temperature the material is ferromagnetic.

The hysteresis behaviour shown by ferromagnetic materials below the Curie temperature can be explained as follow. Any ferromagnetic material below the Curie temperature is made of magnetic domains which are zones where there is an alignment in the same direction of all the magnetic dipole moments [15]. Each domain can have different magnetization orientation. These domains have transition zones which separate them as boundaries, across which the direction of magnetization gradually changes. Usually a grain inside a polycrystalline material can be made of several microscopic magnetic domains [15]. The magnetic flux density B induced inside a ferromagnetic material by an external magnetic field H is not proportional; instead it follows the shape shown in Figure G. 1. "As the intensity of the external magnetic field H increases, the magnetic flux B created inside the material starts to increase slowly at the beginning of the curve, then it increases rapidly and then it reaches a saturation point (plateau zone) where it does not depend anymore on the intensity of H" [15]. "Initially the domains are randomly oriented, and then when an external magnetic field is applied, the domains whose orientation is favorable to the external magnetic field grow at expenses of the others" [15]. The process continues until the material becomes a single domain completely oriented with the external magnetic field.

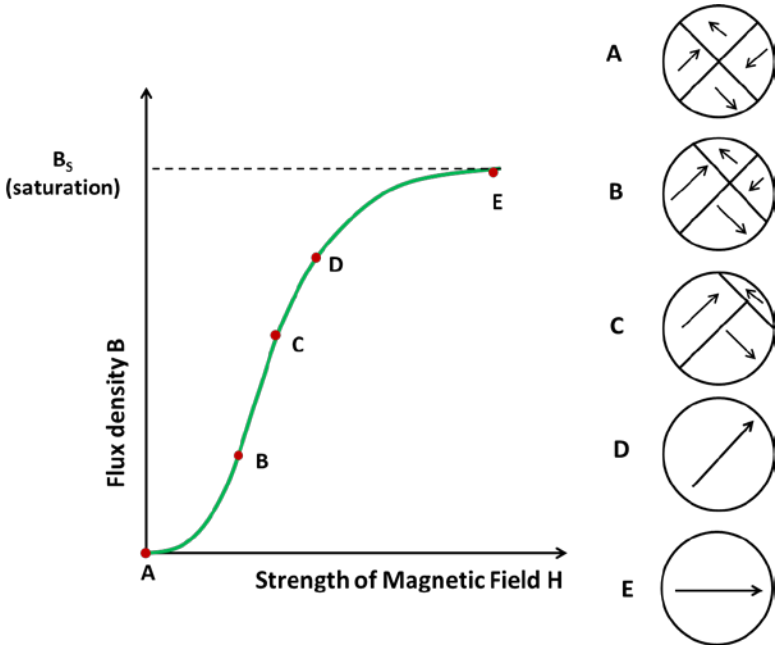

Figure G. 2 - Magnetic domain configurations during the magnetization of a ferromagnetic material (redrawn from a figure published in ref. **[15]**)

If the external field is reversed the internal magnetic flux of the material (B) does not follow the same path so that even when H is zero, there is still a remanence of $B_{residual}$ inside the material, which means that the material remains magnetized even in the absence of the external magnetic field H [15]. In order to remove $B_{residual}$ it is necessary to apply a further external magnetic field in a direction opposite to the one of the original field [15]. A hysteresis cycle is created in the diagram of B versus H and this is responsible also for heat generation in the ferromagnetic materials such as ferrite for the present project.

Moreover, the depth of heating during induction treatment depends on the frequency of the AC field, on the electrical resistivity of the material to be treated and on its relative magnetic permeability. The reference depth decreases with higher frequency and increases with higher temperature [232]. Higher operating frequencies have a shallow skin depth, while lower operating frequencies have a thicker skin depth and greater depth of penetration [230].

G.4 Mechanical Properties of induction heated one side coated coupons

Table G- 2 reports the values of hardness measured through the thickness of uncoated and one-side coated IF steel coupons after induction heating at 820 ºC for different times. Each value is the average of 10 measurements and the corresponding standard deviation is as well listed in the table.

Specimen	Distance from Edge [µm]	Vickers Hardness [MPa]	Standard Deviation [MPa]
One-side coated coupon induction heated at 820 ˚C for 30s	24.52142857	246.8332411	4.321425283
	29.221	242.7940079	11.87151618
	57.04	205.7187886	4.669192985
	77.28857143	202.2157454	7.604567532
	80.7075	194.2509686	3.392829921
	89.10571429	191.9587379	6.631849183
	119.162	180.2839521	6.035496942
	153.805	161.1811265	9.53490969
One-side coated coupon induction heated at 820 ˚C for 4 minutes	23.63222222	207.7398097	7.667005941
	50.353	201.7437642	5.407253666
	88.885	193.7458077	7.714055996
	137.4811111	185.2414478	9.885223768
	155.5	183.8112144	10.23631524
Uncoated coupon induction heated at 820 ˚C for 30s	21.155	151.177862	5.855231728
	54.338	138.5922814	5.658566723
	73.03727273	135.1678718	4.79834566
	83.892	145.9970127	5.859677115
	124.052	141.8373515	7.46689051
	147.635	145.9428572	0.154795528
Uncoated coupon induction heated at 820 ˚C for 1 minute	23.02909091	150.845494	7.879838594
	73.783	147.2633988	7.195287778
	105.161	144.3913279	3.996358281
	141.735	151.2575526	7.19749085
	159.912	145.0664413	6.882784797
Uncoated coupon induction heated at 820 ˚C for 4 minutes	27.343	138.6821833	6.072372959
	49.64	140.2079587	5.52845928
	86.094	143.3152906	4.96079127
	120.589	140.4519882	5.85866733
	150.495	138.3545382	7.204487388
IF steel uncoated and not annealed	14.955	143.0118248	6.006666086
	33.63555556	153.5008195	3.332516448
	82.066	146.5083733	2.74190872
	115.732	144.3214165	5.149650317
	145.406	148.0801123	4.327003099

Table G- 2 - Vickers hardness values through thickness for one side coated coupons and for uncoated coupons induction heated at 1100 ºC – 1150 ºC for 1 seconds and then at 820 ˚C for different times. Vickers hardness of an uncoated and not-annealed IF steel is reported as reference

Table G- 3 lists the dimensions of coupons coated one side and induction heated at 820 ºC for different times, while Table G- 4 lists the obtained mechanical properties.

Sample	Annealing Treatment	Heat Treatment environment	Width [mm]	Thickness [mm]	Gauge length [mm]	Speed set on the tensile machine [µm/s]
IF not annealed	IF steel not annealed	-	1	0.195	5	2.5
HV - A	530 ˚C-1h	High vacuum furnace	1	0.188	5	2.5
IH - A	820 ˚C – 30s	Induction Heating	1	0.188	5	2.5
IH - B	820 ˚C - 2 min	Induction Heating	1	0.195	5	2.5
IH - C	820 ˚C – 4 min	Induction Heating	1	0.195	5	2.5
IH - D	1100 ˚C – 4 min	Induction Heating	1	0.203	5	2.5
IH - E	1100 ˚C – 4 min	Induction Heating	1	0.204	5	2.5

Table G- 3 - Dimensions of tensile coupons coated only on one side with 500 nm FeC film and annealed in high vacuum (HV) using furnace or induction heating (IH) for different temperatures and times

sample	Upper YS [MPa]	Lower YS [MPa]	Average stress in Lüders plateau [MPa]	Lüders length	UTS [MPa]	Strain at fracture (ε_B)
IF steel – not annealed	117	-	-	-	266	0.5
530˚C-1h-HV-A	198	182	189	0.03584	242	0.3
820˚C-30s–IH-A	171	192	184	0.02692	268	0.26
820˚C-2min–IH-B	251	255	252	0.03352	336	0.35
820˚C-4min-IH-C	168	-	-	-	319	0.41
1100˚C-4min–IH-D	255	250	252	0.03504	333	0.38
1100˚C-4min–IH-E	235	240	239	0.03036	327	0.35
Average 1100˚C - 4min - IH	245	245	246	0.0327	330	0.37

Table G- 4 - Mechanical properties obtained for one side coated coupons annealed in furnace or induction heated at different temperatures and times (YS means yield stress, while UTS is the ultimate tensile strength)

G.4.1 Calculation of strain-hardening exponent for one side coated coupons

If the natural logarithm is applied on both sides of the Hollomon's equation, the following expression is obtained:

$$\ln(\sigma_{true}) = \ln(K) + n \times \ln(\varepsilon_{true}) \qquad \text{(eq. G. 4)}$$

So, *n* (which represents the strain-hardening exponent) will be the slope of the graph of logarithm of the true stress versus the logarithm of the true strain. For curves that do not show Lüders plateau, the graph was plot from the yield stress until the ultimate tensile stress; while for curves showing Lüders plateau, the log-log graph was calculated considering the values from the stress at the end of the plateau until the ultimate tensile stress. The curves shown in Figure G. 3 represent the natural logarithm of the true stress versus the natural logarithm of true strain for all the tensile tests shown in Figure 8-26 (section 8.2.4.1).

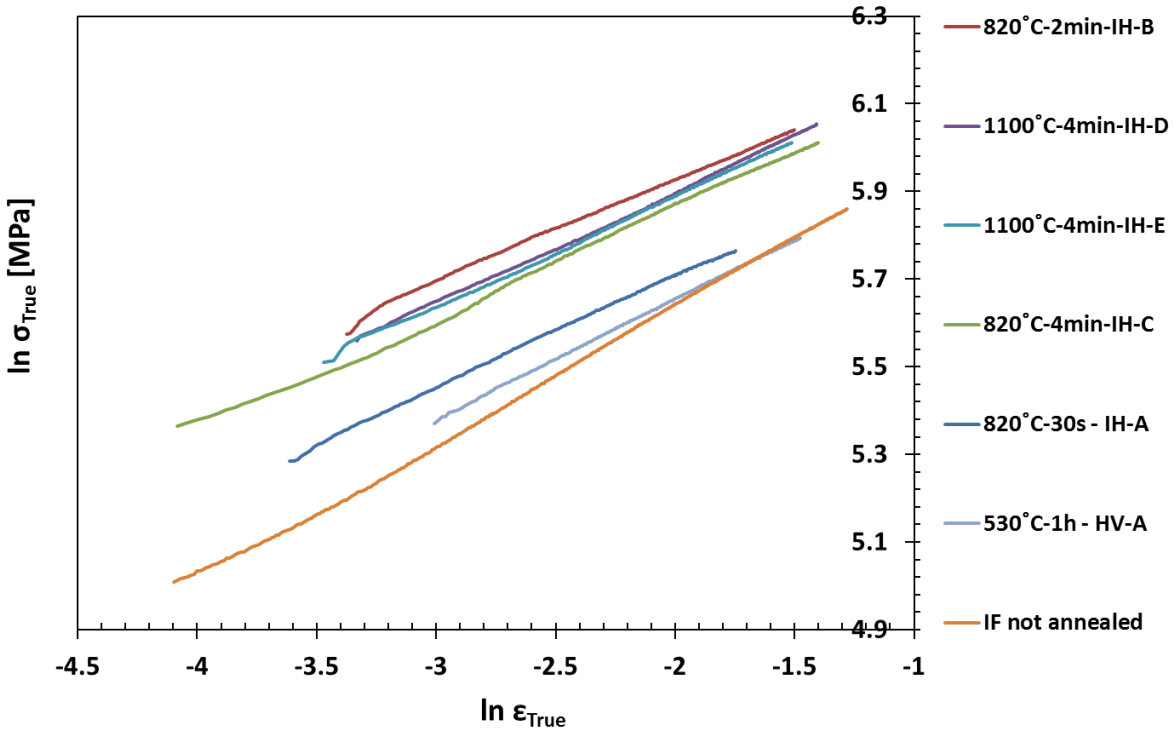

Figure G. 3 - ln (σ_{True}) versus ln (ε_{True}) for tensile coupons coated on one side with 500 nm thick FeC film and annealed using furnace and induction heating at different times and temperatures. IH means induction heating.

G.5 Mechanical Properties of induction heated both sides coated coupons

Annealing Treatment	Width [mm]	Thickness [mm]	Gauge length [mm]	Speed set on the tensile machine [µm/s]
IF steel not annealed	1	0.195	5	2.5
530 ˚C-1h – High vacuum – furnace annealing	1	0.195	5	2.5
820 ˚C – 2 min – High vacuum – furnace annealing	1	0.198	5	2.5
820 ˚C – 1 min – Induction heated	1	0.205	5	2.5
820 ˚C – 2 min – Induction heated (specimen ECD 1L-O)	1	0.199	5	2.5
820 ˚C – 2 min – Induction heated (specimen ECD 1C-K)	1	0.198	5	2.5
820 ˚C – 4 min – Induction heated	1	0.197	5	2.5
820 ˚C – 8 min – Induction heated	1	0.198	5	2.5

Table G- 5 - Dimensions of tensile coupons coated on both sides with 500 nm FeC film and annealed in high vacuum (HV) using furnace or induction heating (IH) for different temperatures and times

sample	Upper YS [MPa]	Lower YS [MPa]	Average stress in Lüders plateau [MPa]	Lüders length	UTS [MPa]	Strain at fracture (ε_B)
IF steel – not annealed	117	-	-	-	266	0.5
530˚C-1h HV - A	278	258	267	0.04518	323	0.39
820˚C-2min HV - B	274	288	284	0.02727	322	0.26
820˚C-1min –IH-BS-A	261	253	256	0.03090	350	0.31
820˚C-2min –IH ECD1 L-O	370	374	378.5	0.03391	446	0.21
820˚C-2min –IH ECD1 C-K	379	383	381	0.03074	452	0.19
820˚C-4min –IH-BS-B	227	-	-	-	340	0.33
820˚C-8min –IH – BS-C	265	270	264	0.03405	363	0.33

Table G- 6 - Mechanical properties obtained for both sides coated coupons annealed in furnace or induction heated at different temperatures and times (YS means yield stress, while UTS is the ultimate tensile stress)

G.5.1 Calculation of strain-hardening exponent for both sides coated coupons

In Figure G. 4 the curves of the natural logarithm of the true stress versus the natural logarithm of the true strain are shown for coupons coated both sides. The slope of these curves corresponds to the strain-hardening exponent.

Table G- 7 lists the values of Vickers hardness obtained for both sides coated coupons. Each value represents an average of 10 measurements and the corresponding standard deviation is also indicated.

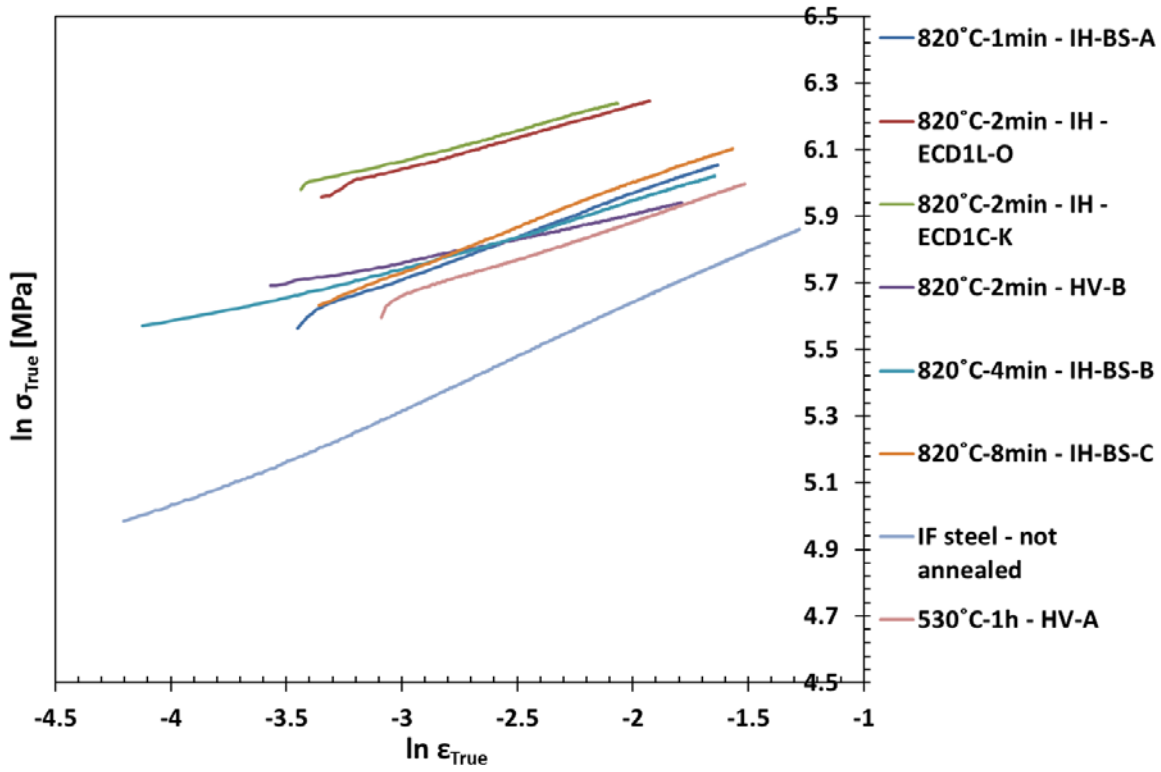

Figure G. 4 - ln (σ_{True}) versus ln (ε_{True}) for tensile coupons coated on both sides with 500 nm thick FeC film and annealed using furnace and induction heating at different times and temperatures. IH means induction heating

Specimen	Distance from Edge [µm]	Vickers Hardness [MPa]	Standard Deviation [MPa]
IF steel uncoated and not annealed	14.955	143.0118248	6.006666086
	33.63555556	153.5008195	3.332516448
	82.066	146.5083733	2.74190872
	115.732	144.3214165	5.149650317
	145.406	148.0801123	4.327003099
One-side coated coupon induction heated at 820 ˚C for 4 minutes	23.63222222	207.7398097	7.667005941
	50.353	201.7437642	5.407253666
	88.885	193.7458077	7.714055996
	137.4811111	185.2414478	9.885223768
	155.5	183.8112144	10.23631524
Both sides coated coupon induction heated at 820 ˚C for 4 minutes	22.89888889	197.1592271	5.903002177
	55.265	184.3767617	3.948755156
	84.19	185.258455	4.681923632
	129.0675	191.2905981	4.21177156
	158.6922222	198.7815877	8.392577673
Both sides coated coupon induction heated at 820 ˚C for 1 minute	24.068	207.5557554	5.086315264
	49.38625	200.9487041	6.313420491
	86.75555556	197.6816654	5.363420479
	126.6177778	193.8407866	5.261092941
	167.634	217.7647382	4.968222323
Both sides coated coupon induction heated at 820 ˚C for 2 minutes	20.086	275.2809461	7.719970912
	48.98166667	272.3573748	10.64178267
	81.57142857	252.7656388	6.870334173
	115.8811111	250.038169	4.955530335
	147.42	258.7806111	6.714688467
	161.96	270.9871626	7.928525986

Table G- 7 - Vickers microhardness of one side and both sides coated coupons induction heated at 1100 ºC – 1150 ºC for 1 seconds and then at 820 ˚C for different times

G.5.2 EDS and BSE on induction heated specimens

From the previous section, the most important mechanical properties for an industrial application are represented by both sides coated specimens induction heated at 820 ˚C for 2 minutes and 4 minutes. The specimen induction heated for 2 minutes shows high strength and high hardness, while the one induction heated for 4 minutes is important because Lüders plateau is suppressed.

In order to relate the mechanical properties with the microstructure of these specimens, it was proposed to analyze how carbon is distributed between grain boundaries and the core of the grains. To satisfy this purpose, energy dispersive spectrometry (EDS) was run for both specimens. Moreover, to confirm the presence of different phases (ferrite/bainite or martensite) in the microstructures, the surface of the specimen was analyzed using the back scattering detector inside the SEM (BSE).

For EDS, the specimen was polished to a mirror surface and was then etched for 30s with 4% vol. Nital solution. For the BSE analyses, the specimens were polished to mirror finish without applying any etching since this would compromise the detection. The contrast mechanism obtained by collecting backscattered electrons is arising from difference in chemical composition and it is expressed as different levels of grays in the picture of the specimen. In the BSE pictures, the regions of high average atomic number will appear bright compared to regions made of low atomic number elements. This happens because the number of back scattered electron is higher for elements having high atomic number.

G.4.2.1 Energy Dispersive Spectrometry (EDS) Results

- **EDS for both sides coated specimen induction heated at 820 ˚C for 1 minute**

Spectra 1, 3, 4 and 7 were taken inside grains. The position of the points is shown in Figure G. 5 and Figure G. 6, while spectra 2, 5 and 6 were taken at the grain boundaries and their position is shown in Figure G. 7 and Figure G. 8, while Table G- 8 lists the corresponding concentrations.

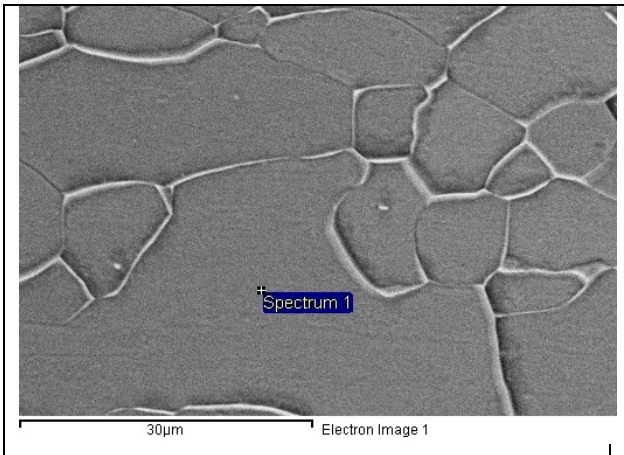

(a) spectrum 1 – composition measured inside a grain

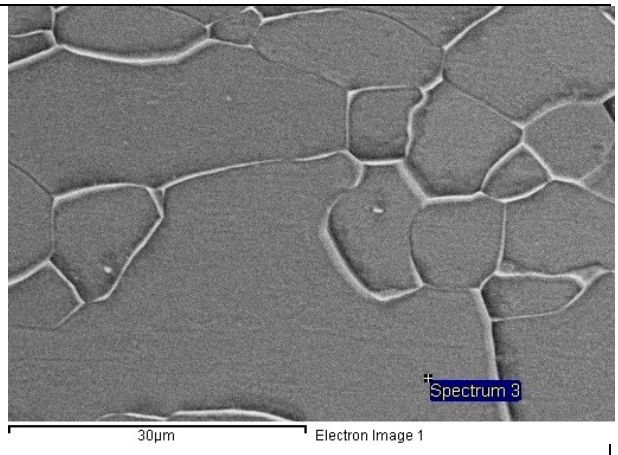

(b) spectrum 3 – composition measured inside another grain

Figure G. 5 - EDS performed inside a grain of a specimen induction heated at 1100 ºC – 1150 ºC for 1 seconds and then at 820 ˚C – 1 minute

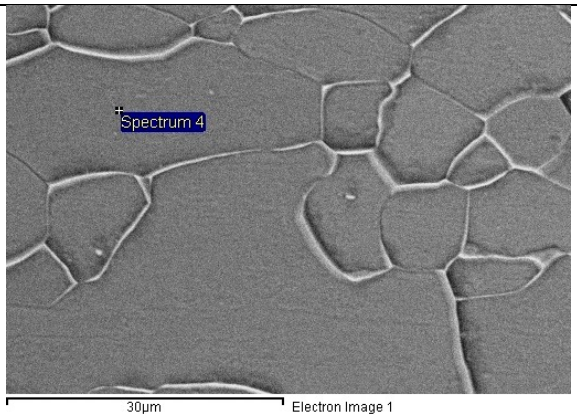

(c) spectrum 4 – composition measured inside a grain

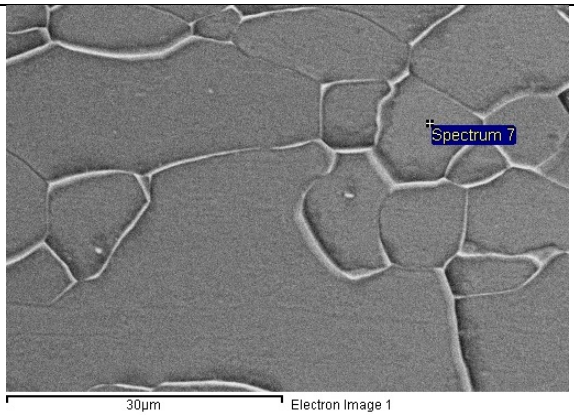

(d) spectrum 7 – composition measured inside a grain

Figure G. 6 - EDS performed inside grains of a specimen induction heated at 1100 ºC – 1150 ºC for 1 seconds and then at 820 ˚C – 1 minute

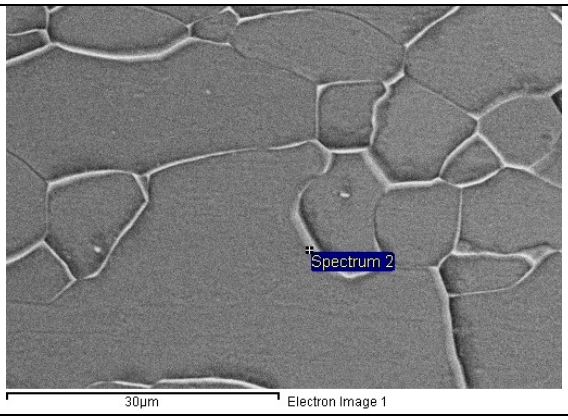

(a) spectrum 2 – composition measured at a grain boundary

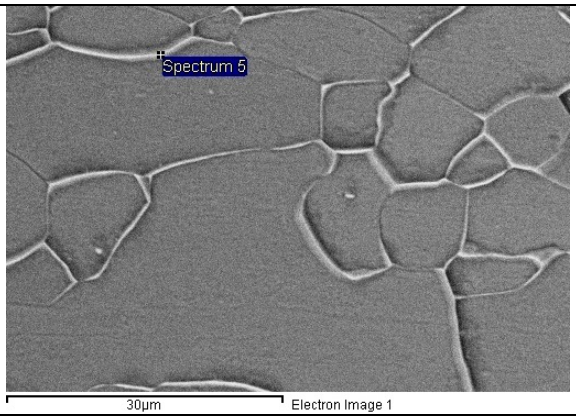

(b) spectrum 5 – composition measured at another grain boundary

Figure G. 7 - EDS performed at grain boundaries of a specimen induction heated at 1100 ºC – 1150 ºC for 1 seconds and then at 820 ˚C – 1 minute

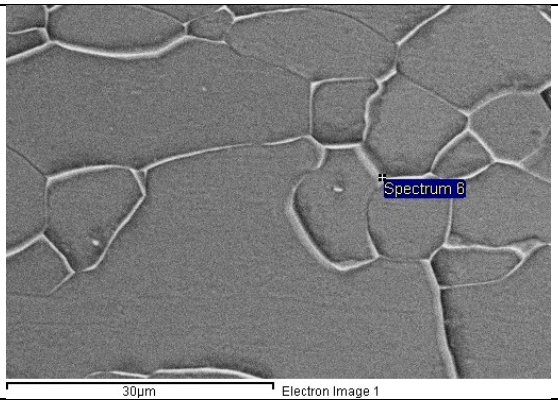

(c) spectrum 6 – composition measured at another grain boundary

Figure G. 8 - EDS performed at grain boundaries of a specimen induction heated at 1100 ºC – 1150 ºC for 1 seconds and then at 820 ˚C – 1 minute

Spectrum	C [wt%]	Fe [wt%]
1 – inside a grain	7.5	92.5
3 – inside a grain	7.7	92.3
4 – inside a grain	7	93
7 – inside a grain	7.5	92.5
2 – at grain boundary	11.5	87.4
5 – at grain boundary	7	93
6 – at grain boundary	9	91

Table G- 8 - Carbon concentration obtained during EDS performed in a specimen induction heated at 1100 ºC – 1150 ºC for 1 seconds and then at 820 ˚C for 1 minute

- **EDS for both sides coated specimen induction heated at 820 ˚C for 2 minutes**

Spectra 1 and 4 were taken in a point inside a grain. The points are shown in Figure G. 9.

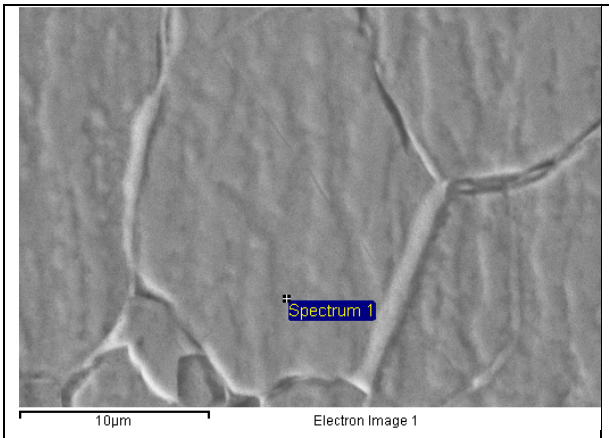

(a) spectrum 1 – composition measured inside a grain

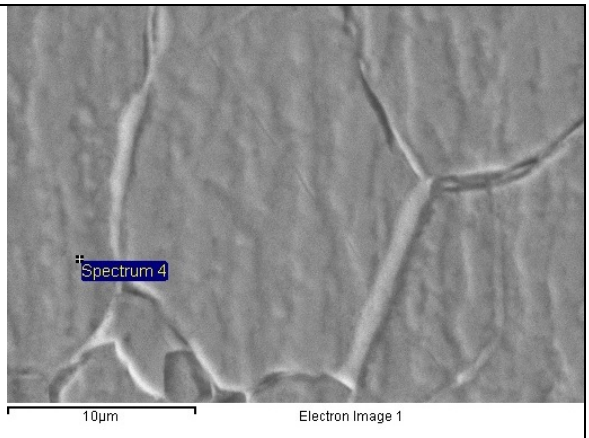

(b) spectrum 4 – composition measured inside another grain

Figure G. 9 - EDS performed inside two grains of a specimen induction heated at 1100 ºC – 1150 ºC for 1 seconds and then at 820 ˚C – 2 minutes

Spectrum 2 and 3 were taken at the grain boundaries (Figure G. 10 (a) and (b) respectively).

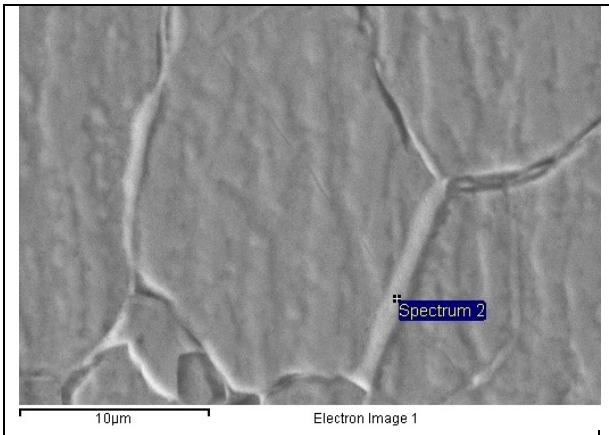

(a) Spectrum 2 – composition measured on a grain boundary

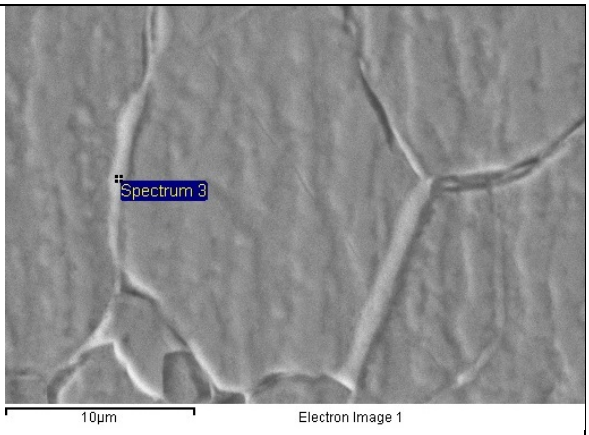

(b) Spectrum 3 – Composition measured on another grain boundary

Figure G. 10 - EDS performed at grain boundaries for a specimen induction heated at 1100 ºC – 1150 ºC for 1 seconds and then at 820 ˚C – 2 minutes

Spectrum	C [wt%]	Fe [wt%]
1 – inside a grain	15.15	84.85
2 – at grain boundary	16.07	83.93
3 – at grain boundary	18.31	81.69
4 – inside a grain	15.25	84.75

Table G- 9 - Carbon content measured by EDS inside grains and at grain boundaries for a specimen induction heated at 1100 ºC – 1150 ºC for 1 seconds and then at 820 ˚C for 2 minutes

From the results shown in Table G- 9, there is not a high difference in carbon content between grain boundaries and the grains; however, it seems that at grain boundaries, the carbon amount is 1 or 2 % higher than inside the grains.

- **EDS for both sides coated specimen induction heated at 1100 ºC – 1150 ºC for 1 seconds anf then at 820 ˚C for 4 minutes**

Spectra 1, 2 and 3 were taken inside three different grains, while spectrum 4 was taken at a thick grain boundary.

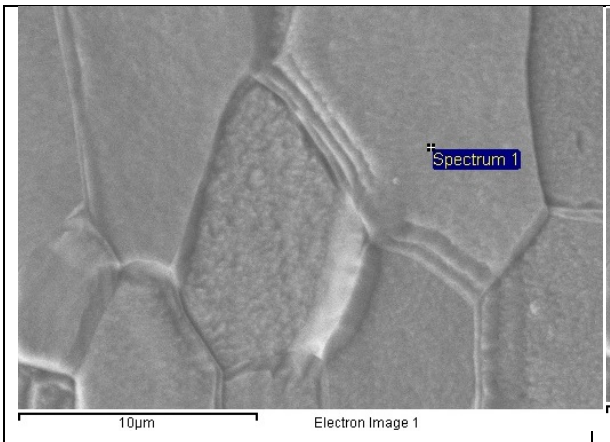

(a) spectrum 1 – composition measured inside a grain

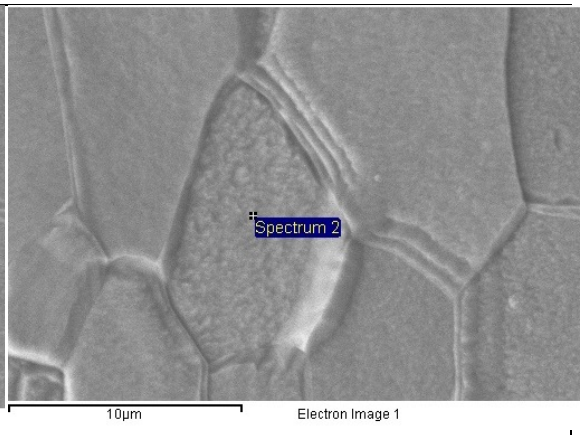

(b) spectrum 2 – composition measured inside a grain

Figure G. 11 - EDS performed inside grains for a specimen induction heated at 1100 ºC – 1150 ºC for 1 seconds and then at 820 ˚C – 4 minutes

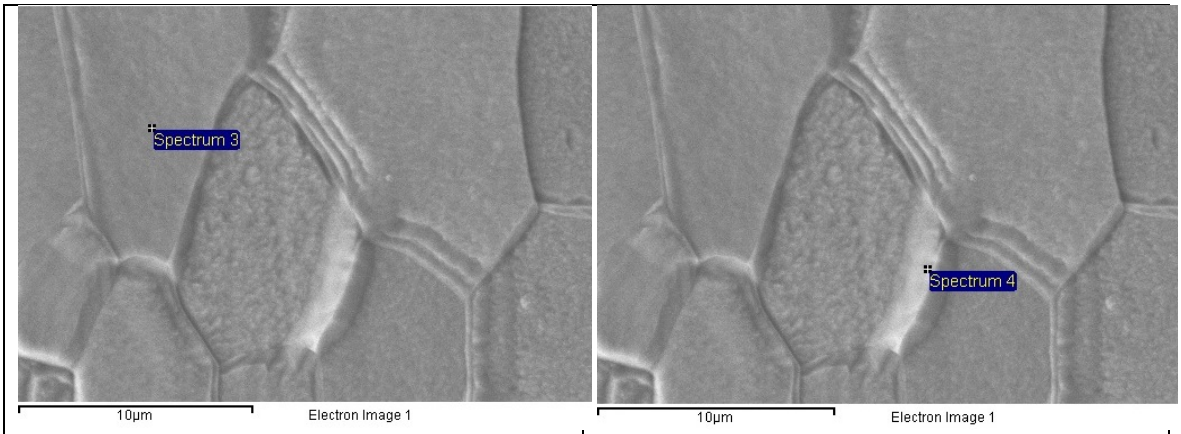

(a) spectrum 3 – composition measured inside a grain	(b) spectrum 4 – composition measured at a grain boundary

Figure G. 12 - EDS performed inside a grain and at a grain boundary for a specimen induction heated at 1100 ºC – 1150 ºC for 1 seconds and then at 820 ˚C – 4 minutes

Table G- 10 lists the amount of carbon atoms obtained for the spectra in the different zones.

Spectrum	C [wt%]	Fe [wt%]
1 – inside a grain	11	89
2 – inside a grain	9	91
3 – inside a grain	13.3	86.7
1 – in another zone - inside a grain	10.3	89.7
2 – in another zone - inside a grain	8	92
3 – in another zone - inside a grain	9.5	90.5
4 – in another zone – inside a grain	8.8.	91.2
1 – in another zone – at grain boundary	7.8	92.2
2 – in another zone – at grain boundary	8.3	91.7
4 – at grain boundary	11.2	88.8

Table G- 10 - Carbon content measured by EDS inside grains and at grain boundaries for a specimen induction heated at 1100 ºC – 1150 ºC for 1 seconds and then at 820 ˚C for 4 minutes

For the specimen induction heated for 4 minutes, there is no difference of carbon content between core of the grains and grain boundaries, however, in this specimen; the amount of detected carbon was lower than what was found in the specimen induction heated for 2

minutes, but in average higher than the carbon amount measured in the specimen induction heated for 1 minute.

G.4.2.2 Back Scattered Electrons (BSE) Results

- **BSE Images for both sides coated specimen induction heated at 820 ˚C for 2 minutes**

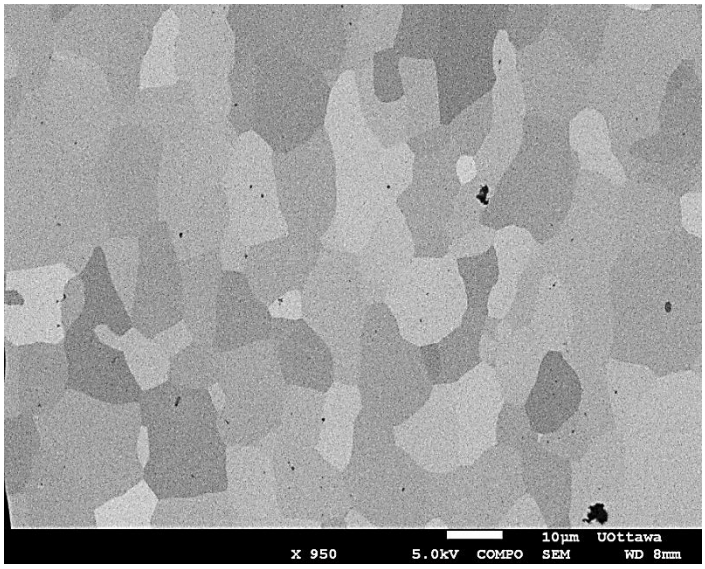

Figure G. 13 - BSE image obtained in one zone close to one edge of a both sides coated coupon induction heated at 1100 ºC – 1150 ºC for 1 seconds and then at 820 ˚C for 2 minutes

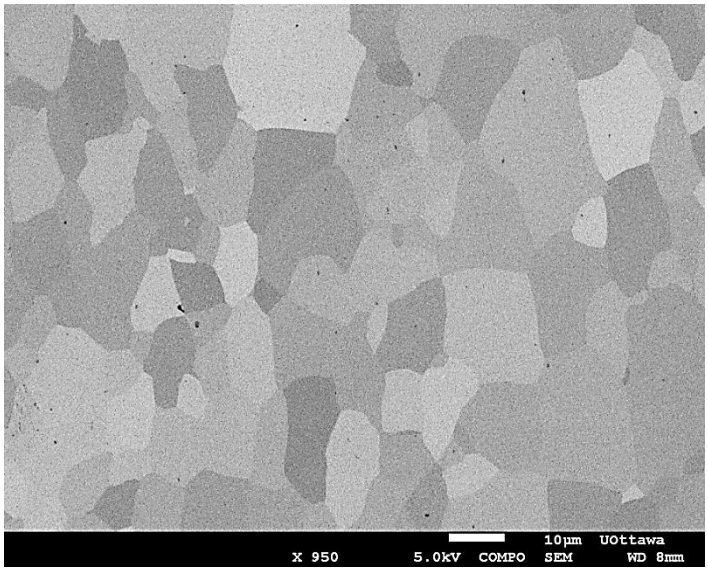

Figure G. 14 - BSE image obtained in another zone of a both sides coated coupon induction heated at 1100 ºC – 1150 ºC for 1 seconds and then at 820 ˚C for 2 minutes

In Figure G. 13 and Figure G. 14, the white grains or the light gray grains are probably the one containing more carbon atoms than the darkest grains.

- **BSE Images for both sides coated specimen induction heated at 1100 ºC – 1150 ºC for 1 seconds and then at 820 ˚C for 4 minutes**

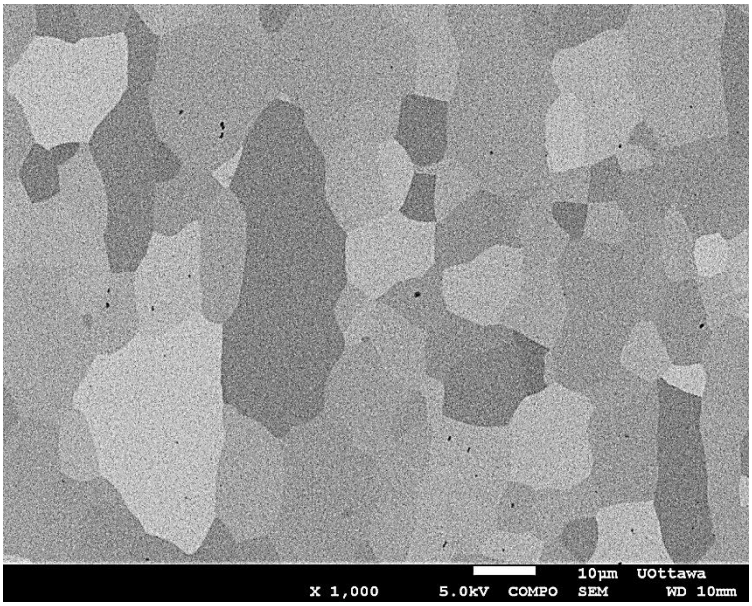

Figure G. 15 - BSE image obtained in a zone close to the edge of a both sides coated coupon induction heated at 1100 ºC – 1150 ºC for 1 seconds and then at 820 ˚C for 4 minutes

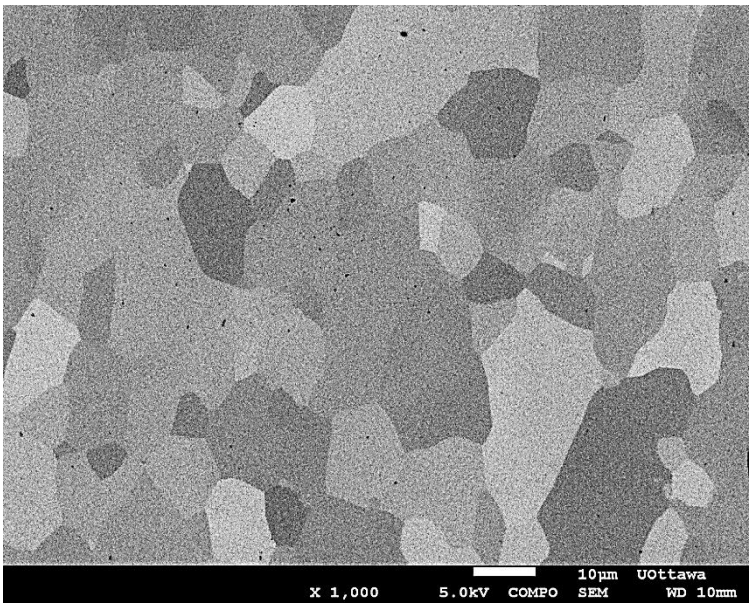

Figure G. 16 - BSE image obtained in another zone of a both sides coated coupon induction heated at 1100 ºC – 1150 ºC for 1 seconds and then at 820 ˚C for 4 minutes

BSE images can be elaborated with Image J software by setting the threshold and calculating the volume fraction of grains having the same level of gray. However, this would not help identifying the phase, i.e. if bainite or martensite is formed and if there is any retained austenite. For this reason, EBSD and TEM analyses are preferred and necessary to fully characterize the microstructure of the above specimens.

G.4.2.3 EBSD on Induction Heated Specimens

EBSD was performed on one specimen induction heated at 820 ˚C for 2 minutes and one specimen induction heated at 820 ˚C for 4 minutes after they were polished to a mirror finish. In order to remove the damaged layer caused by the mechanical polishing, the OPS polishing step was alternated with etching in 4% vol. Nital and the procedure was repeated for at least 5 times before the specimen was analyzed with EBSD. For both specimens an area of 65 x 65 μm was analyzed using a step of 0.1 μm and producing a phase map and band slope map. For both specimens, at first a phase map was obtained to see if the microstructure had retained austenite present. In literature EBSD analyses on lath martensite were performed by doing variant analyses considering that for both martensite and bainite the Kurdjumov-Sachs (K-S) orientation relationship respects the previous austenite grain holds [233], [234]. However, this type of analysis is quite time consuming and it is usually coupled with TEM imaging to clearly identify the analyzed laths inside the single packets of the formed martensite. Another approach that has been used in literature [235] to identify the fraction of low carbon martensite in dual-phase steels is the band slope parameter. This parameter is sensitive to lattice distortion and it characterizes the average intensity of Kikuchi lines compared to the intensity of all the Kikuchi lines in the range of 0-255. If martensite is present, the quality of the band slope will be lower since the microstructure is more distorted due to the high density of dislocations. In Figure G. 17 (a) the phase maps for specimen induction heated at 820 ˚C for 2 minutes and (b) the for the specimen induction heated at 820 ˚C for 4 minutes are reported.

(a) Specimen coated both sides and induction heated at 820 ˚C for 2 minutes

(b) Specimen coated both sides and induction heated at 820 ˚C for 4 minutes

Figure G. 17 - Phase maps obtained on coupons induction heated at 1100 ºC – 1150 ºC for 1 seconds and then at 820 ˚C for 2 minutes (a) and 4 minutes (b)

From the phase maps, it seems that the grain boundaries are more highlighted in the specimen induction heated for 4 minutes, however, this could be due also to a difficulty indexing some points in zone boundaries. For this reason, it is hard to conclude if any retained austenite is present at the boundaries.

Successively, the local misorientation and the band contrast maps where extracted for both specimens and they are reported in Figure G. 18 (a) and Figure G. 18 (b) for the specimen induction heated at 820 ˚C for 2 minutes and at 820 ˚C for 4 minutes respectively. The two specimens look very similar and no conclusion can be drawn from these maps. At the grain boundary the pattern is poor but this can be due to the patterns from two unit cells differently oriented which are overlapping . This can also cause local misorientations to appear higher. Moreover, these patterns are influenced by surface topography, oxidation, deformation of the surface and beam conditions, so unless the microstructure is made by two phases which can easily be distinguished with SEM, then it is not possible to draw any conclusion from these maps.

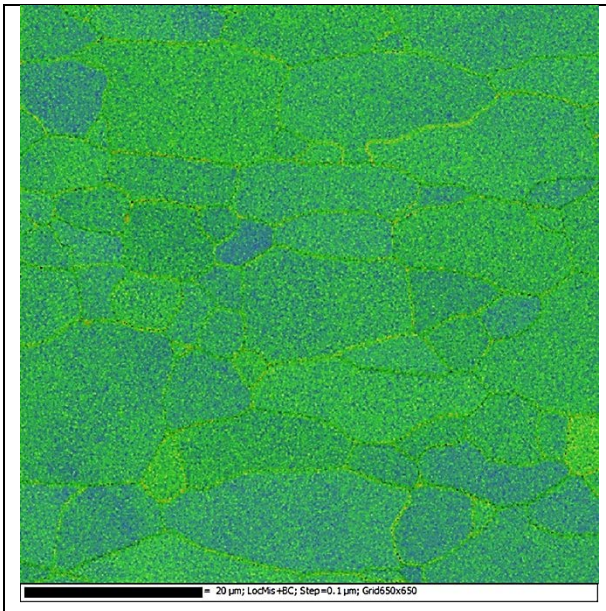

(a) Specimen coated both sides and induction heated at 820 ˚C for 2 minutes

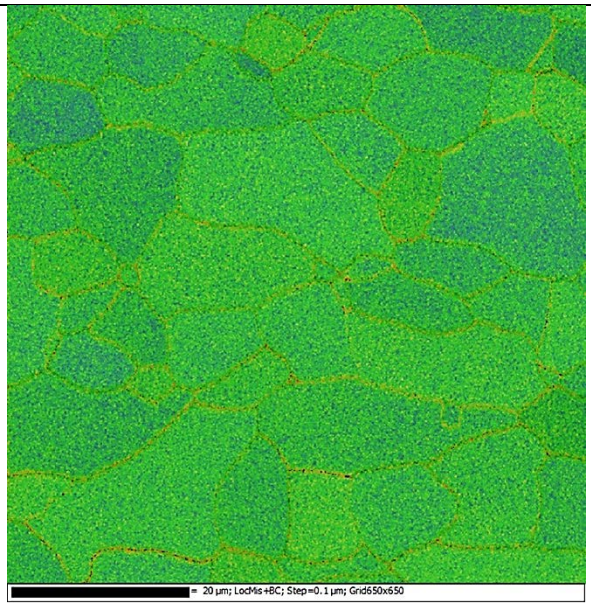

(b) Specimen coated both sides and induction heated at 820 ˚C for 4 minutes

Figure G. 18 - Local misorientation and band contrast maps on coupons induction heated at 1100 ºC – 1150 ºC for 1 seconds and then at 820 ˚C for 2 minutes (a) and 4 minutes (b)

G.4.3 Tensile Test of pre-strained and induction heated coupons

Table G- 11 lists the dimensions of coupons which were prestrained before being coated and induction heated.

Annealing Treatment	Width [mm]	Thickness [mm]	Gauge length [mm]	Speed set on the tensile machine [µm/s]
A	1	0.211	5	2.5
B	1	0.202	5	2.5
C	1	0.206	5	2.5

Table G- 11 - Dimension of specimens before performing 16-17% pre-strain

Appendix H : Fracture Studies Results

H.1 Tensile tests of coupons having carbon gradient along the gauge length

Table H- 1 lists the dimensions of the coupons having holes and carbon gradient along the gauge length, while Table H- 2 lists the values of the mechanical properties obtained for the same coupons.

Tensile coupon	Width [mm]	Thickness [mm]	Gauge length [mm]	Speed set on the tensile machine [µm/s]
5 – C gradient	1	0.189	5	2.5
6 – C gradient	1	0.188	5	2.5
10 – C uniform	1	0.184	5	2.5
7 – uncoated	1	0.188	5	2.5
8 - uncoated	1	0.193	5	2.5
C gradient – no voids	1	0.184	5	2.5

Table H- 1 - Dimensions of tensile coupons having holes lased along the gauge length

Specimen	Yield stress [MPa]	Upper yield stress [MPa]	Average stress Lueder plateau [MPa]	Maximum stress before failure [MPa]	Strain at fracture
5 – C gradient	147	261	264	308	0.24
6 – C gradient	139	263	269	302	0.24
10 – C uniform	216	251	263	316	0.23
7 – uncoated	119	-	-	291	0.33
8 - uncoated	118	-	-	292	0.36
C gradient – no voids	154	266	268	312	0.32

Table H- 2 - Mechanical properties of specimens having holes along the gauge length

H.1.1 Theoretical calculation of yield stress for coupons having half-coated gauge length

For coupons having carbon gradient along the gauge length, the yield stress can be theoretically predicted by using the rule of mixture as shown by the following equation:

$$YS_{specimen} = \left(YS_{carbon} \times V_{fcarbon}\right) + \left(YS_{graded} \times V_{fgraded}\right) + \left(YS_{noc} \times V_{fnoc}\right) \qquad \text{(eq. H- 1)}$$

where:

$YS_{specimen}$ is the theoretical yield stress for the whole coupons;

YS_{carbon} is the yield stress of the carbon coated zone;

$V_{fcarbon}$ is the volume fraction of the gauge length which is fully covered by carbon;

YS_{graded} is the yield stress corresponding to the graded zone;

$V_{fgraded}$ is the volume fraction of the graded zone;

YS_{fnoc} is the yield stress of the uncoated zone of the gauge length;

V_{fnoc} is the volume fraction of the uncoated zone of the gauge length;

The carbon coated zone will have an amount of carbon corresponding to 0.017 at% since the surface is coated only on one side. This corresponds to a yield stress of 249 MPa (calculated using eq. 5-2). The extent of the carbon coated zone is 3100 µm, which represent the 62% of the gauge length of 5000 µm. The theoretical carbon content in the graded zone can be extracted from Figure 9-7 and it corresponds to 7.05×10^{-3} at%. The yield stress corresponding to this amount of carbon is 201 MPa and the extent of the graded zone accoding to Figure 9-7 is 900 µm, which corresponds to 18% of the gauge length. Finally for the no carbon zone, the yield stress will be the same of an IF steel (113 MPa) and this zone is 1000 µm long, which represents 20% of the total gauge length. Substituting these values in eq. H- 1 the theoretical yield stress for coupons having carbon gradient along the gauge length is expected to be 213 MPa.

$$YS_{specimen} = (249 \times 0.62) + (201 \times 0.18) + (113 \times 0.20) = 213 MPa$$

This value of 213 MPa is in agreement with the experimental yield stress found for specimens 5 and 6, which showed a yield stress of 204 MPa and 201 MPa respectively. These two yield stresses were calculated by doing an average of the two yield stresses (yield stress and upper yield stress) shown in Table H- 2.

The same approach can be used to theoretically predict the yield stress for the coupon having a uniform carbon distribution (sample 10 - C uniform). For this specimen, the amount of carbon diffused from the FeC film is 0.017 at%. This concentration is then diluted in the whole gauge length. Considering that the coated zone of the gauge length covers a length of 3000 µm and the whole gauge length is 5000 µm, then the carbon concentration has to be divided by the ratio (5000/3000) = 1.7, which means (0.017/1.7) = 0.010 at%. Using eq. 5-2,

the yield stress corresponding to this carbon concentration is 219 MPa, while experimentally, the yield stress equal to 216 MPa was obtained.

H.2 Void Growth analyses of coupons with holes along the gauge length

H.2.1 Void growth as function of true strain extracted in the gauge length

From Figure H. 1 to Figure H. 9, the graphs for the void growth of an uncoated and not-annealed IF steel (specimen 7) are shown. The graphs plot the void growth as function of the true far field strain extracted in the whole gauge length as shown in Figure 9-35 of Chapter 9 and as function of the true local field strain extracted considering the different zones of the gauge length as shown in Figure 9-34 of Chapter 9.

- **Specimen 7 uncoated and not-annealed IF steel**

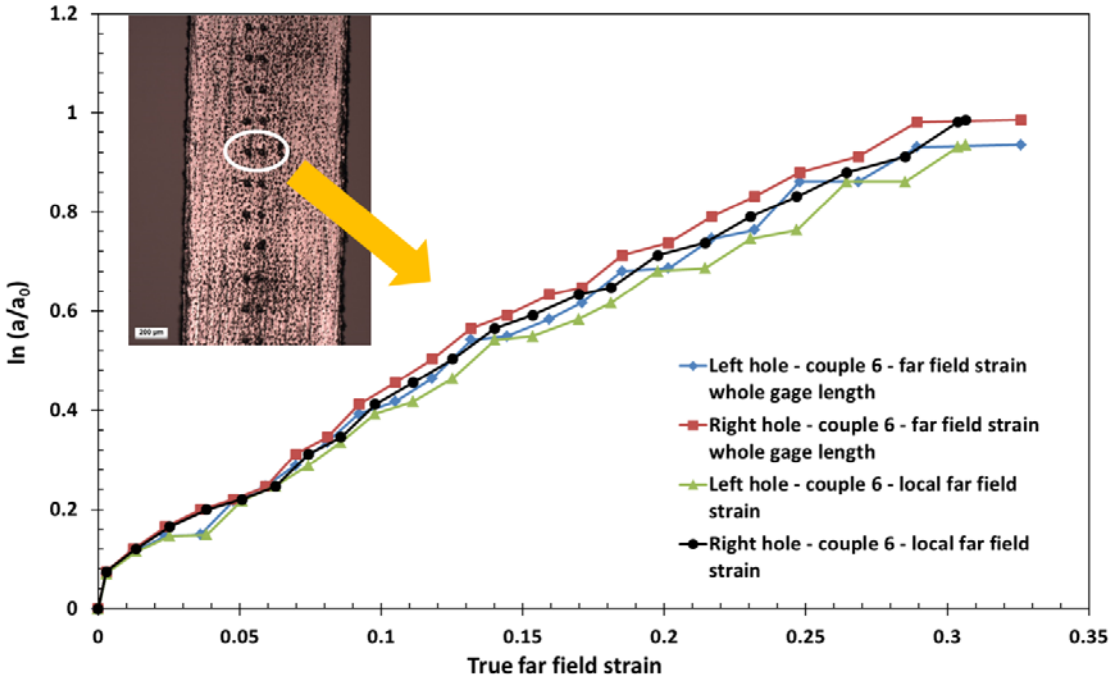

Figure H. 1 - Local true strain versus true far field strain for couple of holes number 6 on uncoated and not-annealed IF steel (specimen 7)

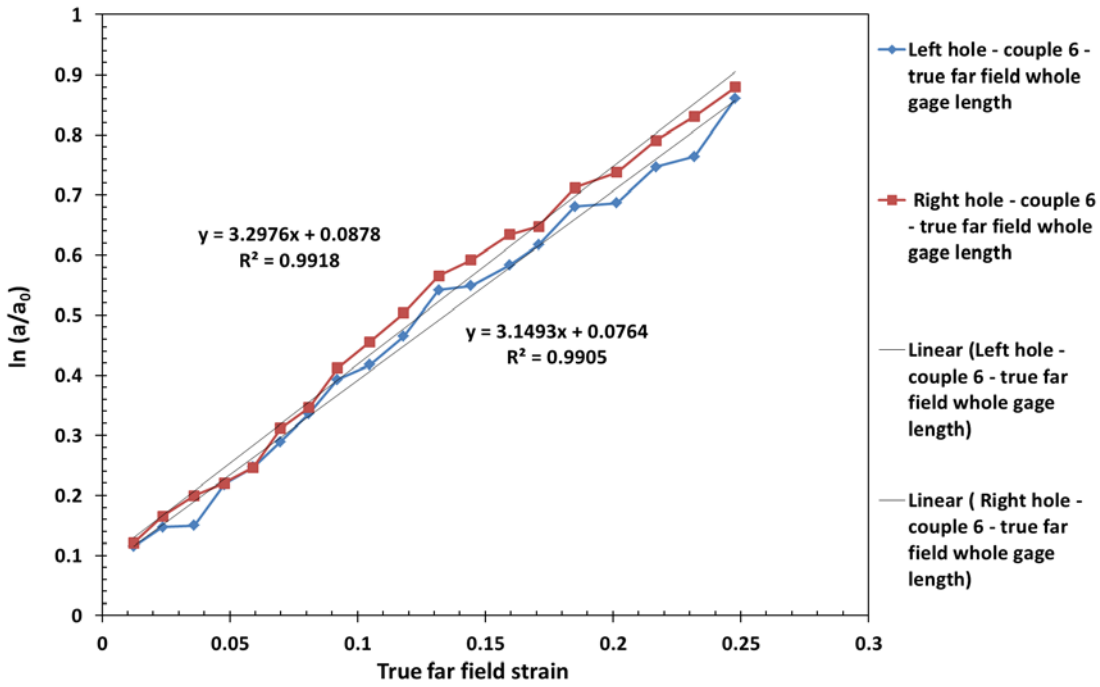

Figure H. 2 - Slope of the local true strain versus true far field strain extracted in the whole gauge length for couple of holes number 6 on uncoated and not-annealed IF steel (specimen 7)

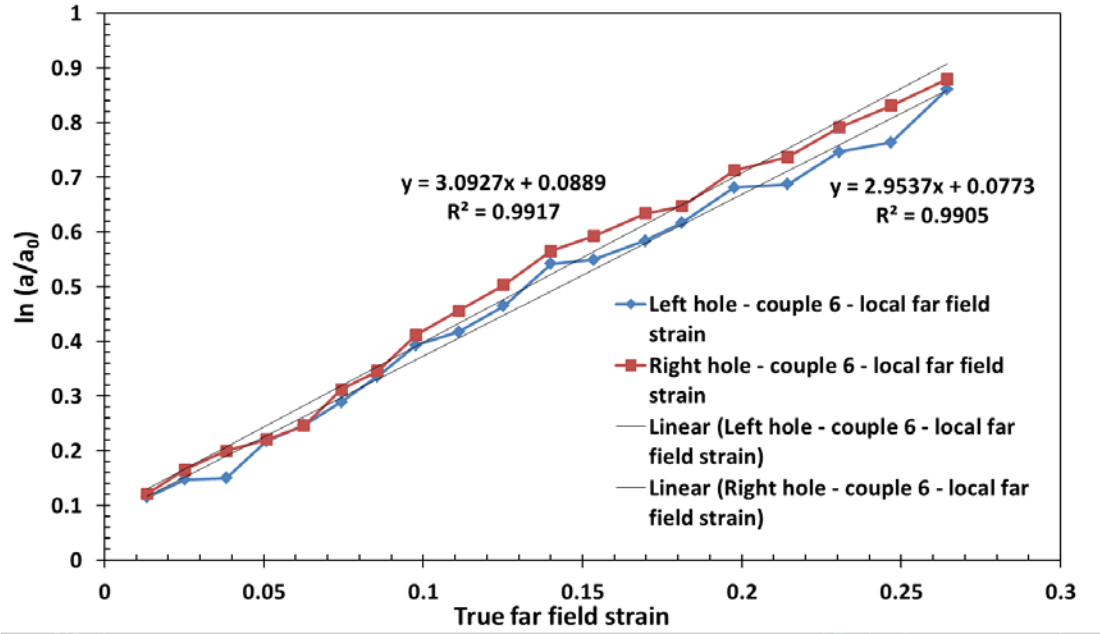

Figure H. 3 - Slope of the local true strain versus the local true far field strain for couple of holes number 6 on specimen number 7 having carbon gradient along the gauge length

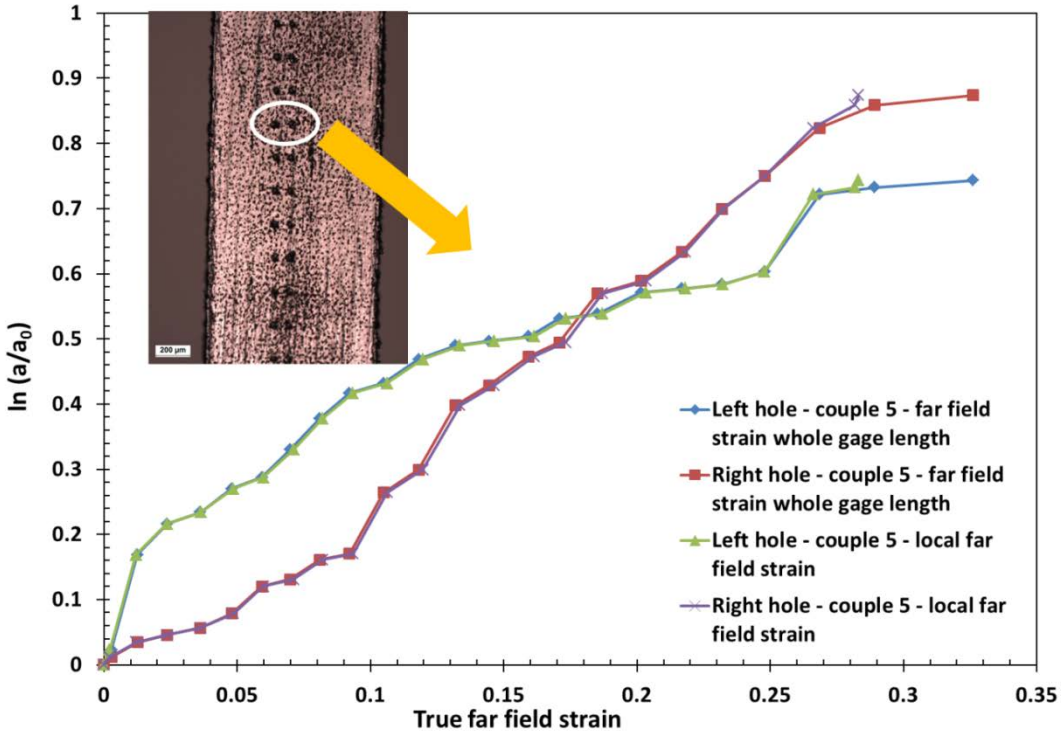

Figure H. 4 - Local true strain versus true far field strain for couple of holes number 5 on uncoated and not-annealed IF steel (specimen 7)

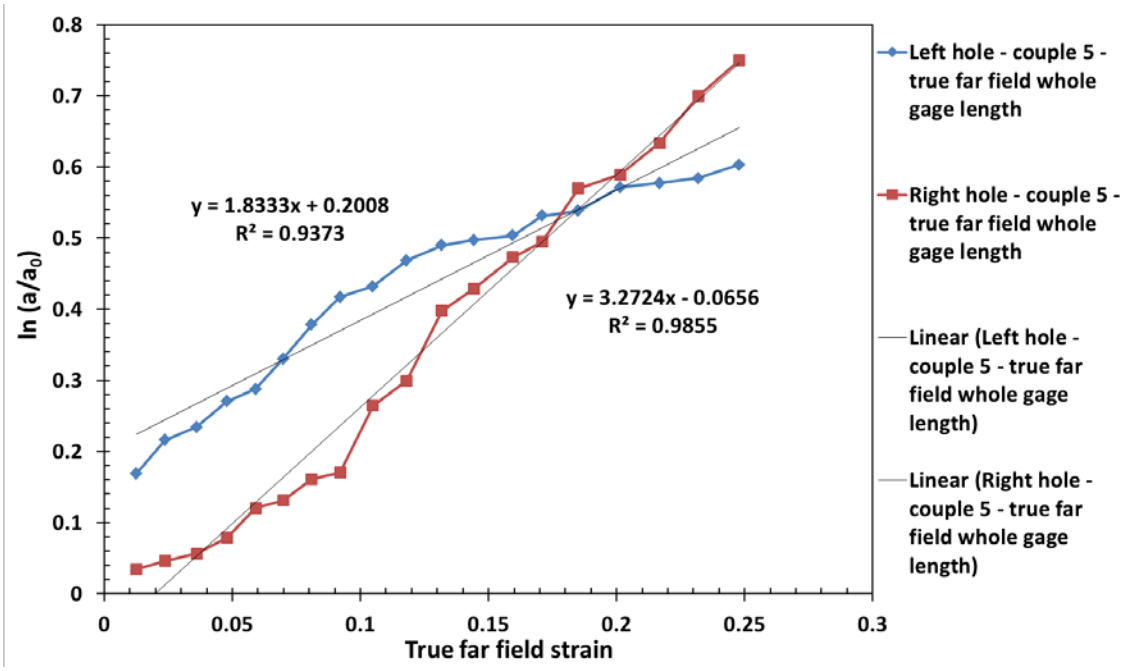

Figure H. 5 - Slope of the local true strain versus true far field strain extracted in the whole gauge length for couple of holes number 5 on uncoated and not-annealed IF steel (specimen 7)

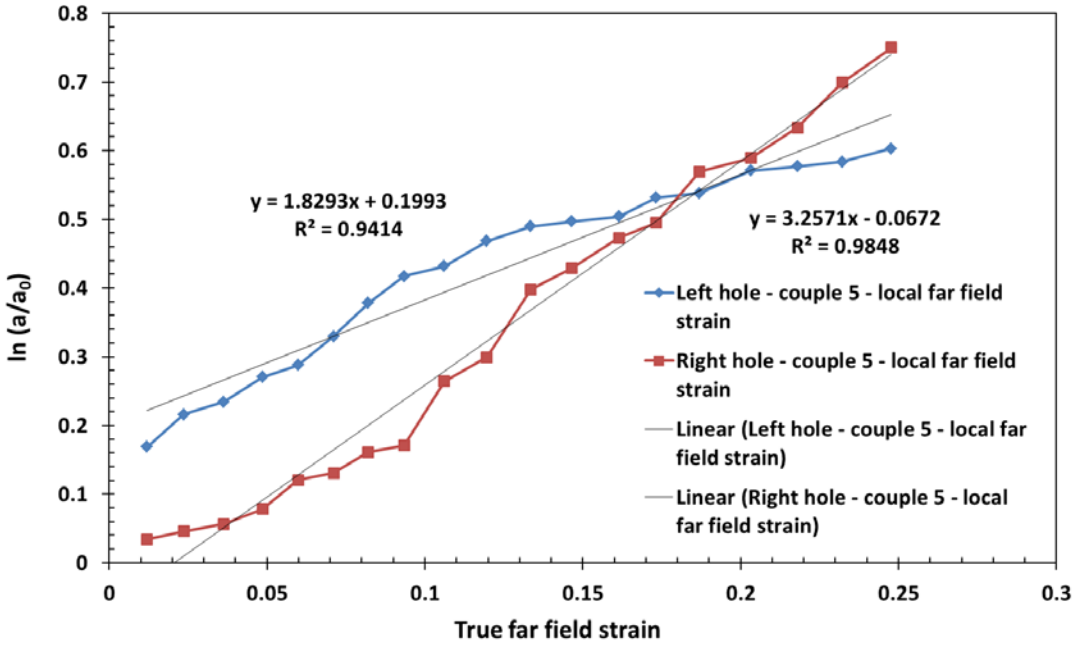

Figure H. 6 - Slope of the local true strain versus the local true far field strain for couple of holes number 6 on specimen number 7 having carbon gradient along the gauge length

- **<u>Specimen 5 carbon gradient: couple of holes 6 (interface between coated and not-coated zone)</u>**

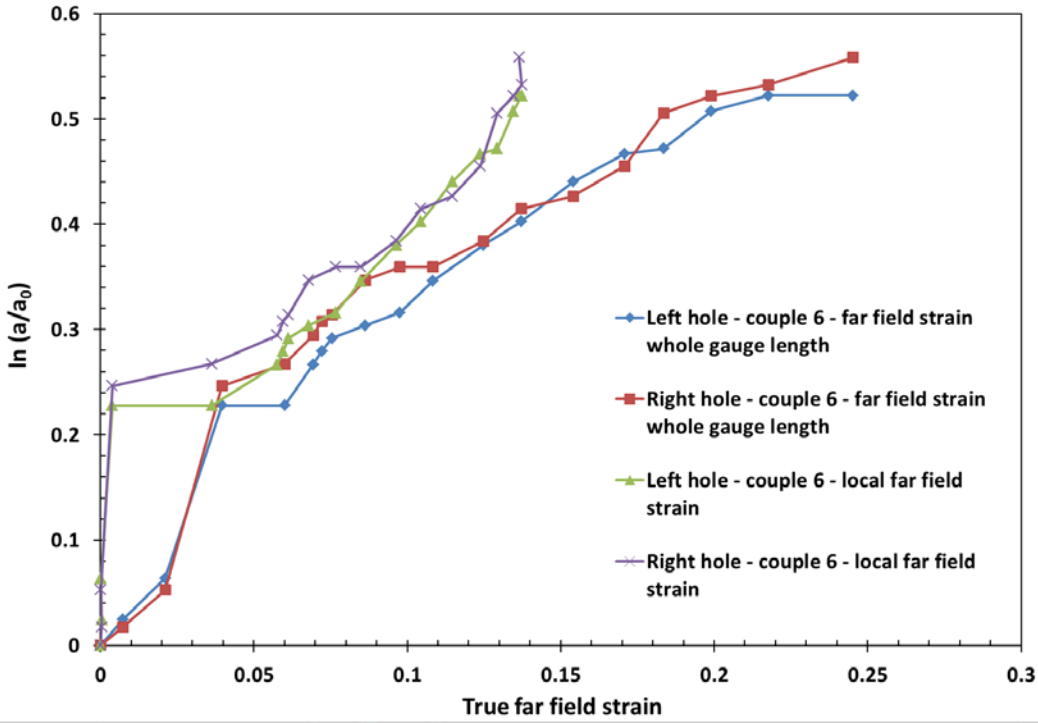

Figure H. 7 - Local true strain versus true far field strain for couple of holes number 6 for specimen number 5 having carbon gradient along the gauge length

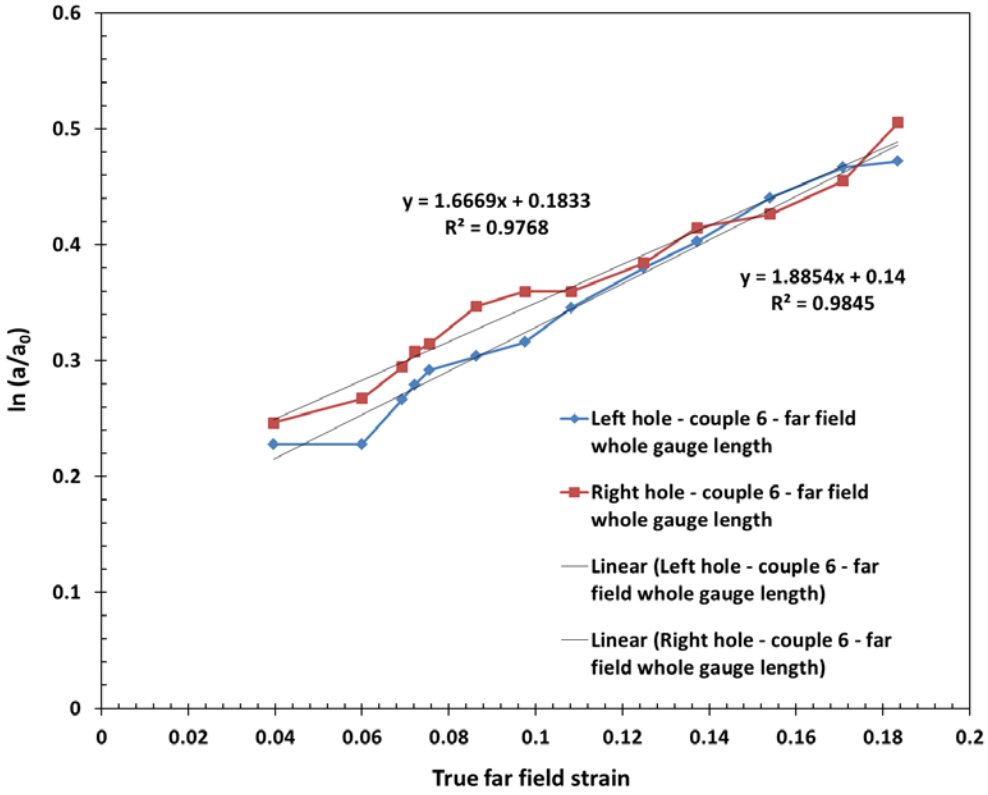

Figure H. 8 - Slope of the local true strain versus the true far field strain extracted in the whole gauge length for couple of holes number 6 on specimen number 5 having carbon gradient along the gauge length

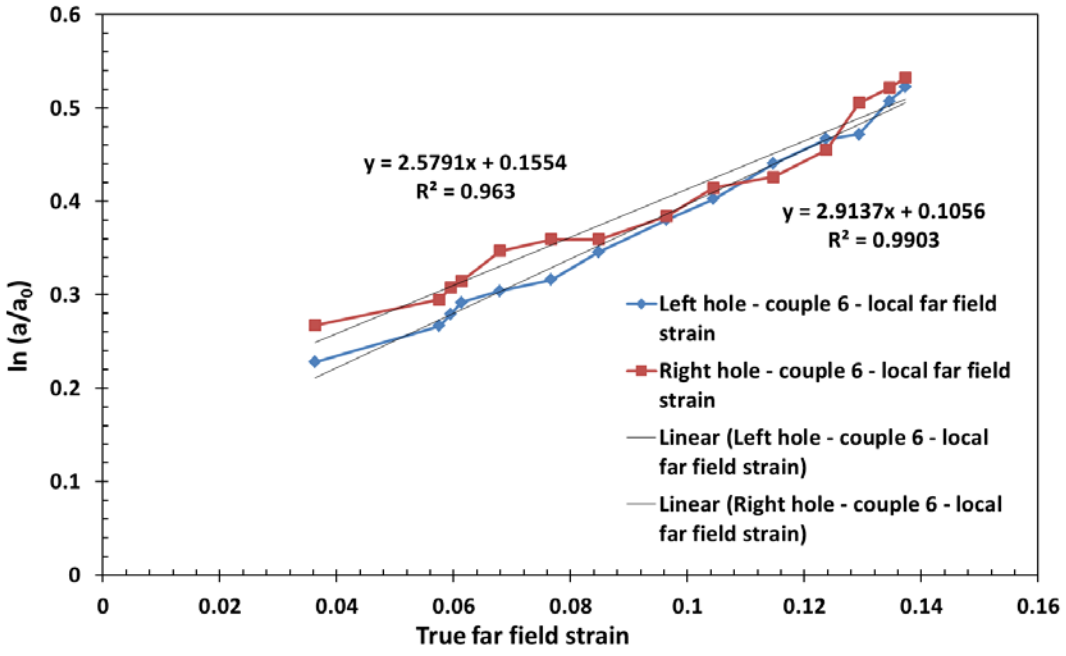

Figure H. 9 - Slope of the local true strain versus the local true far field strain for couple of holes number 6 on specimen number 5 having carbon gradient along the gauge length

From Figure H. 10 to Figure H. 15, the graphs plotting the void growth for coupon 5 having carbon gradient along the gauge length are shown. The graphs consider the void growth as function of the true strain extracted in the whole gauge length or as the true strain extracted in the zones having different carbon content as already explained for specimen 7.

- **Specimen 5 carbon gradient: couple of holes 8 (inside graded zone)**

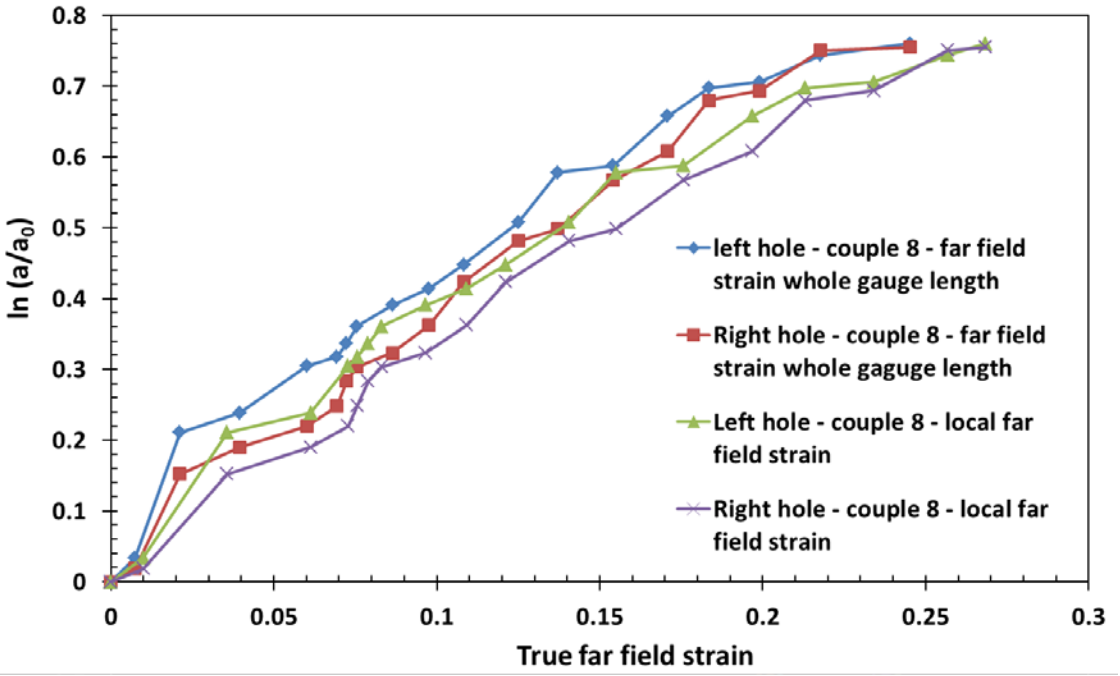

Figure H. 10 - Local true strain versus true far field strain for couple of holes number 8 for specimen number 5 having carbon gradient along the gauge length

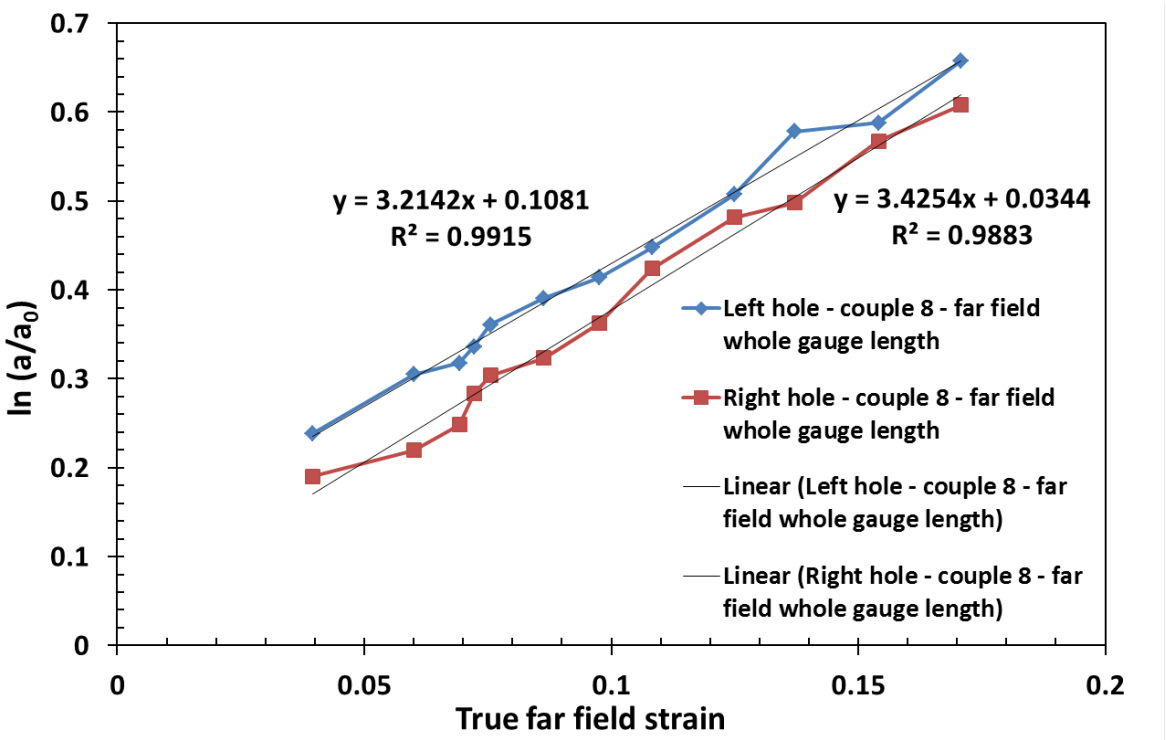

Figure H. 11 - Slope of the local true strain versus the true far field strain extracted in the whole gauge length for couple of holes number 8 on specimen number 5 having carbon gradient along the gauge length

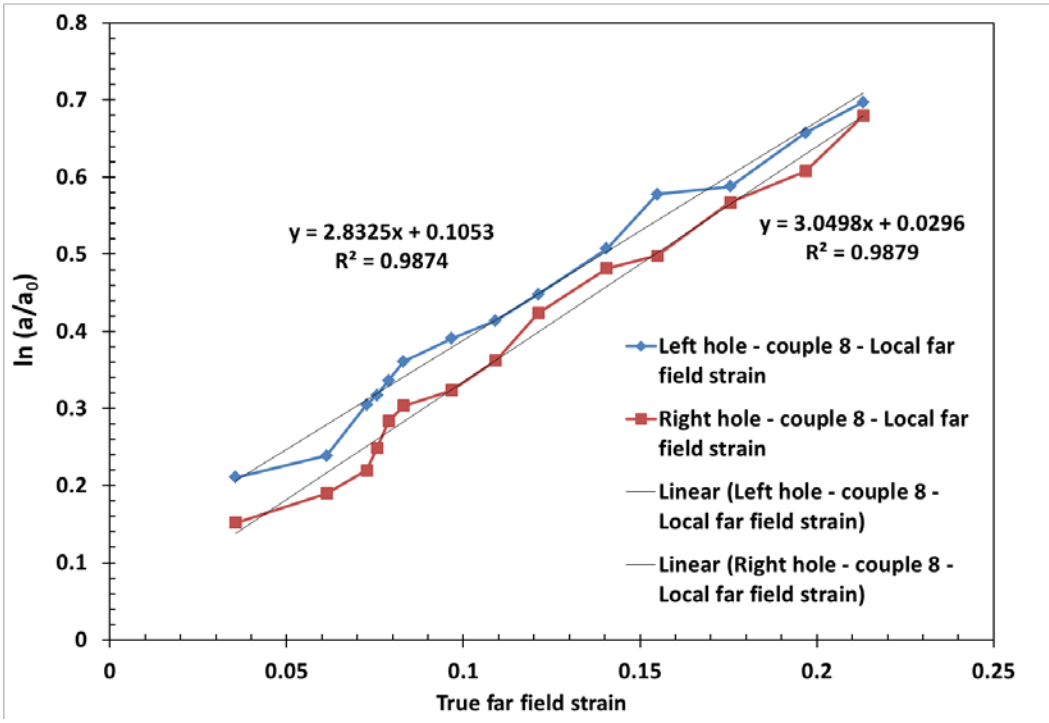

Figure H. 12 - Slope of the local true strain versus the local true far field strain for couple of holes number 8 on specimen number 5 having carbon gradient along the gauge length

- **Specimen 5 carbon gradient: couple of holes 11 (inside no carbon zone)**

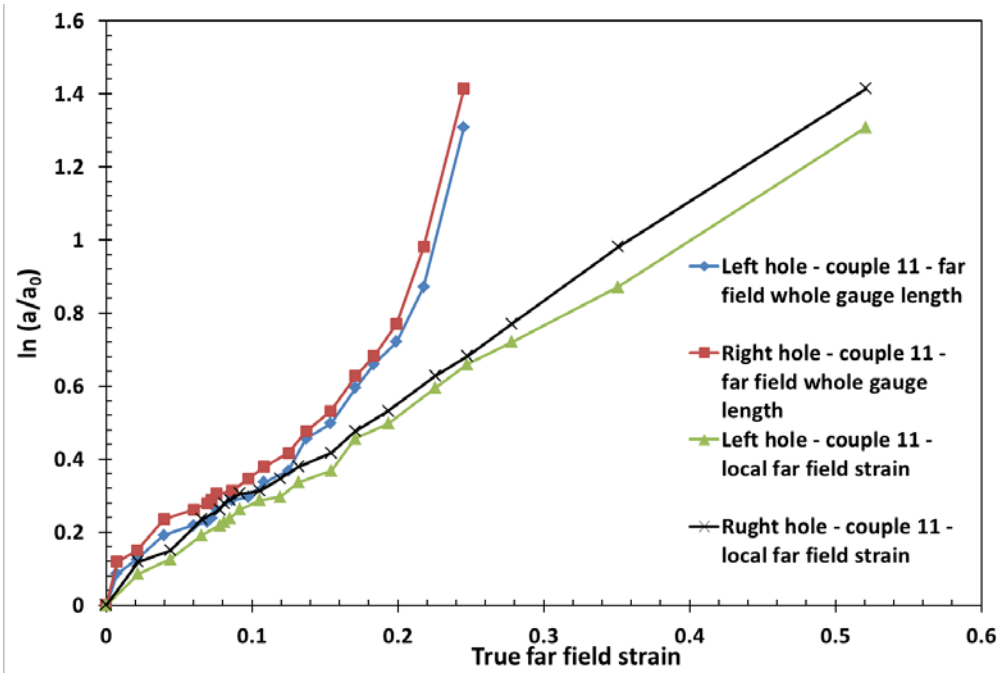

Figure H. 13 - Local true strain versus true far field strain for couple of holes number 11 for specimen number 5 having carbon gradient along the gauge length

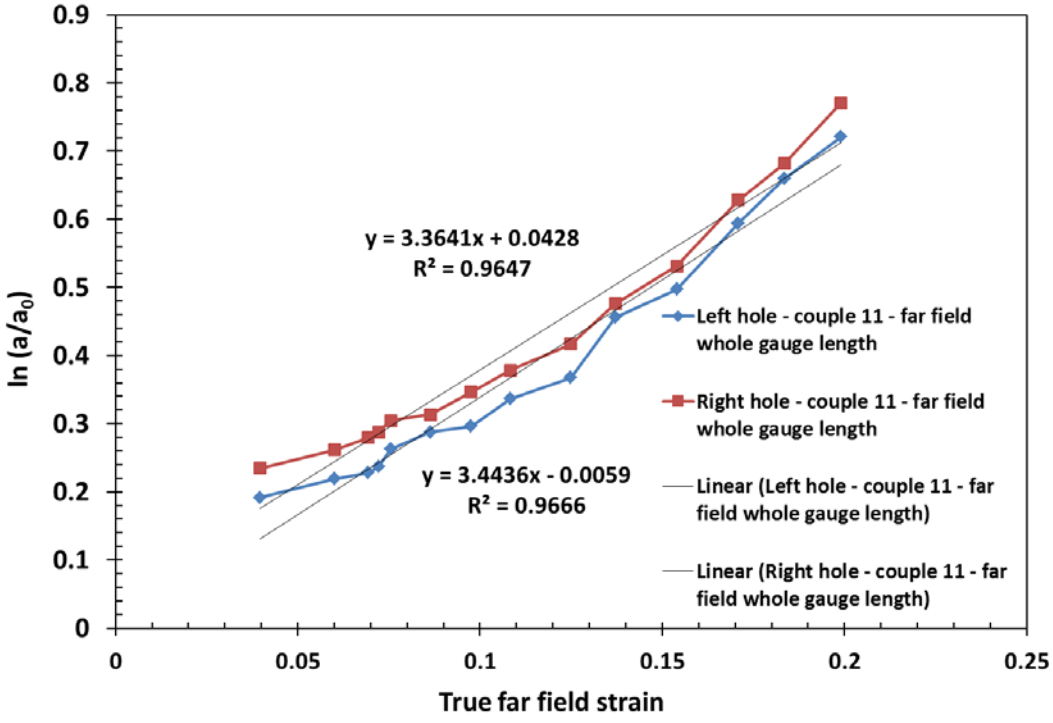

Figure H. 14 - Slope of the local true strain versus the true far field strain extracted in the whole gauge length for couple of holes number 11 on specimen number 5 having carbon gradient along the gauge length

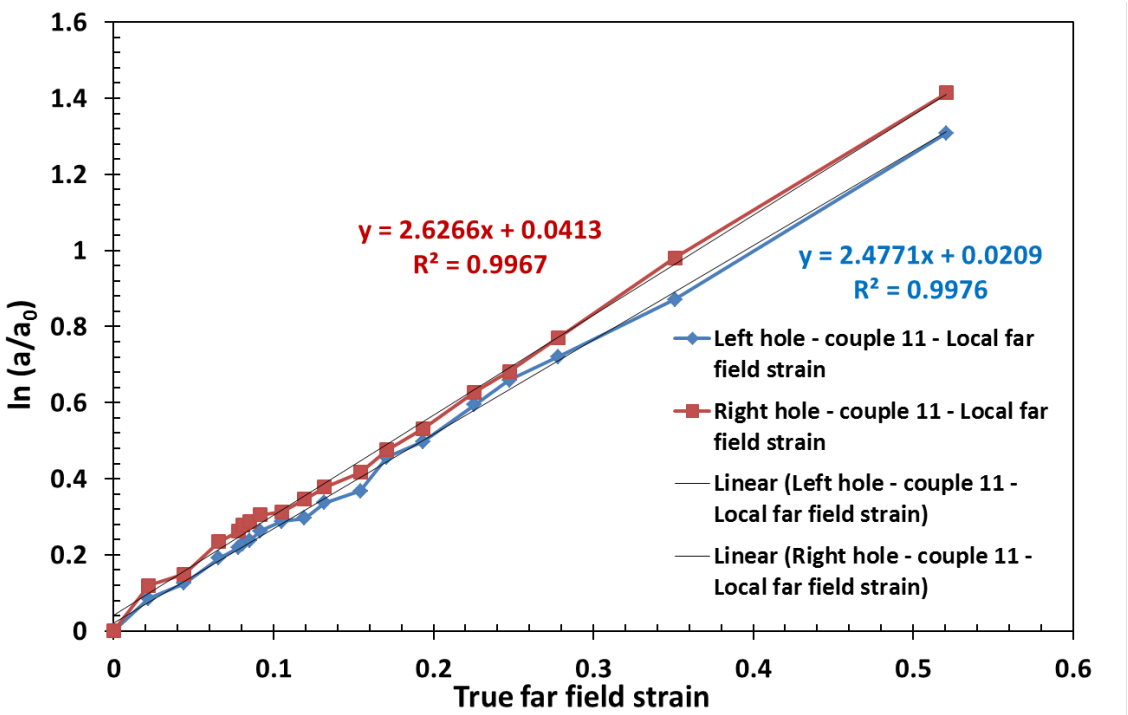

Figure H. 15 - Slope of the local true strain versus the local true far field strain for couple of holes number 11 on specimen number 5 having carbon gradient along the gauge length

From Figure H. 16 to Figure H. 24 the void growth for the voids of specimen 6 having a carbon gradient along the gauge length are plot. The graphs report the void growth as function of the true strain extracted in the whole gauge length and as function of the local true strain extracted considering different zones in the gauge length as shown in Figure 9-36 in Chapter 9.

- **Specimen 6 carbon gradient: couple of holes 5 (interface of coated and uncoated zone)**

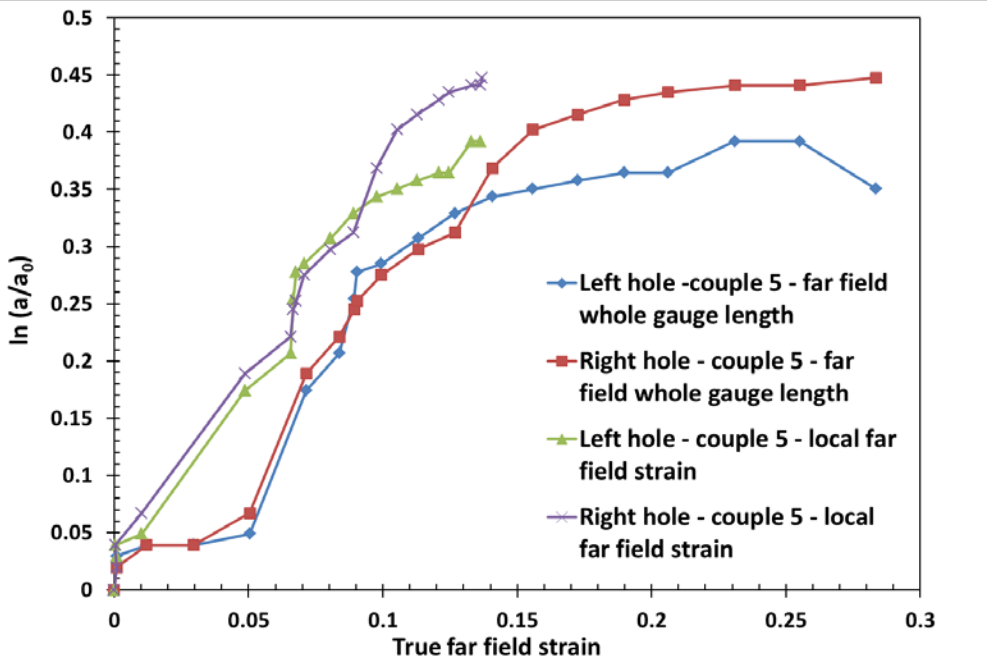

Figure H. 16 - Local true strain versus true far field strain for couple of holes number 5 for specimen number 6 having carbon gradient along the gauge length

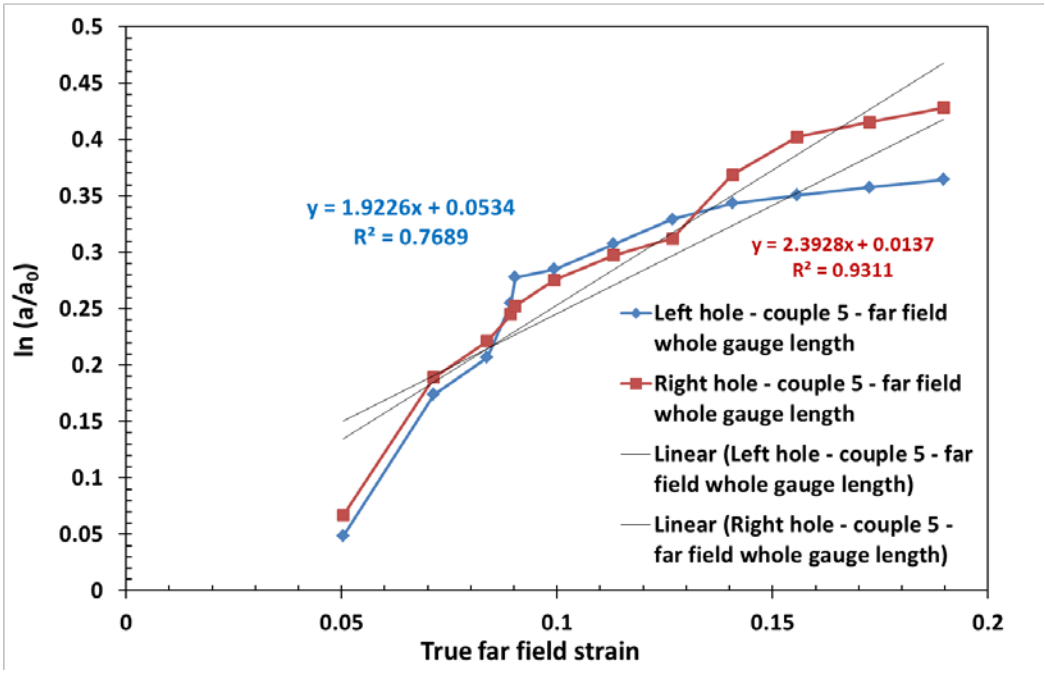

Figure H. 17 - Slope of the local true strain versus the true far field strain extracted in the whole gauge length for couple of holes number 5 on specimen number 6 having carbon gradient along the gauge length

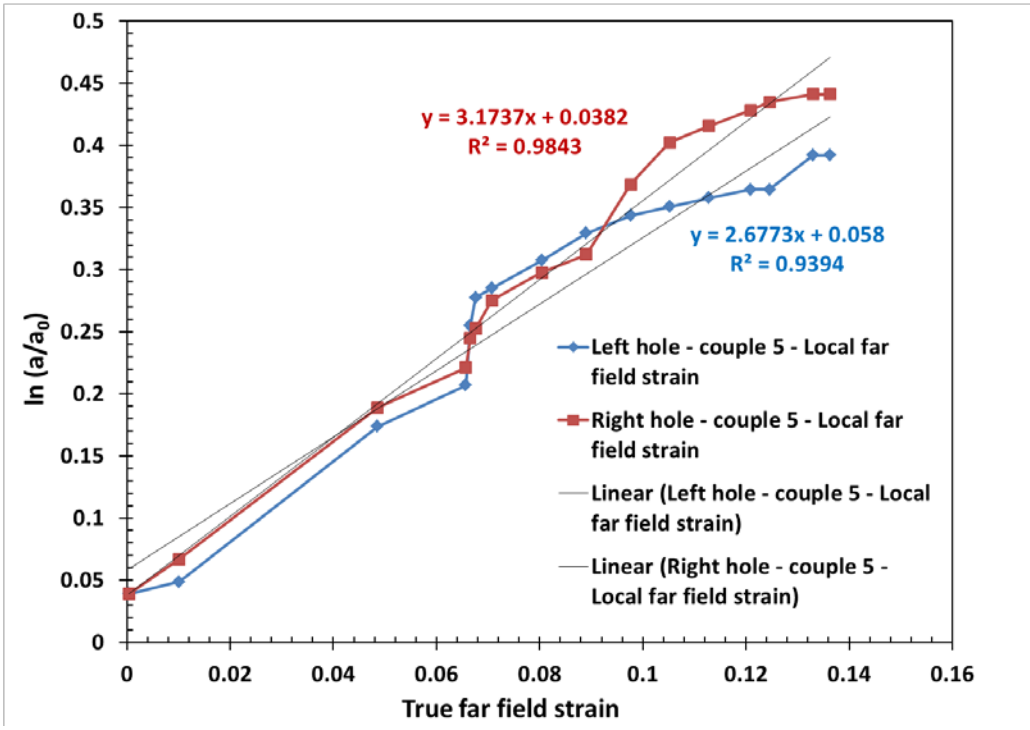

Figure H. 18 - Slope of the local true strain versus the local true far field strain for couple of holes 5 on specimen number 6 having carbon gradient along the gauge length

- **<u>Specimen 6 carbon gradient: couple of holes 7 (inside the graded zone)</u>**

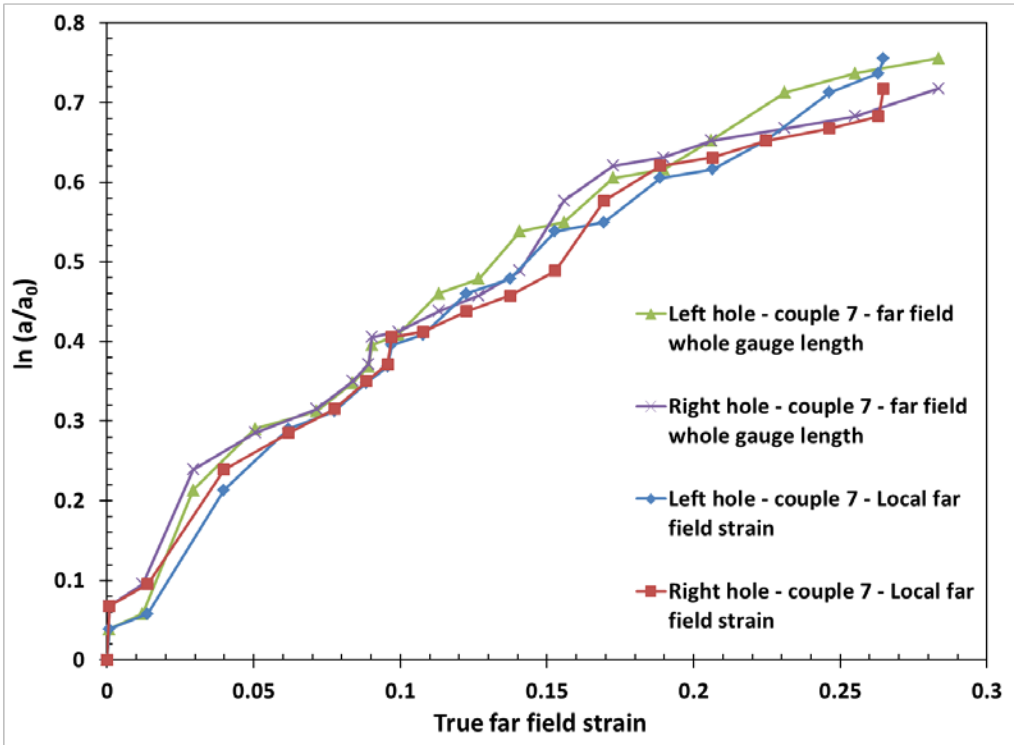

Figure H. 19 - Local true strain versus true far field strain for couple of holes number 7 for specimen number 6 having carbon gradient along the gauge length

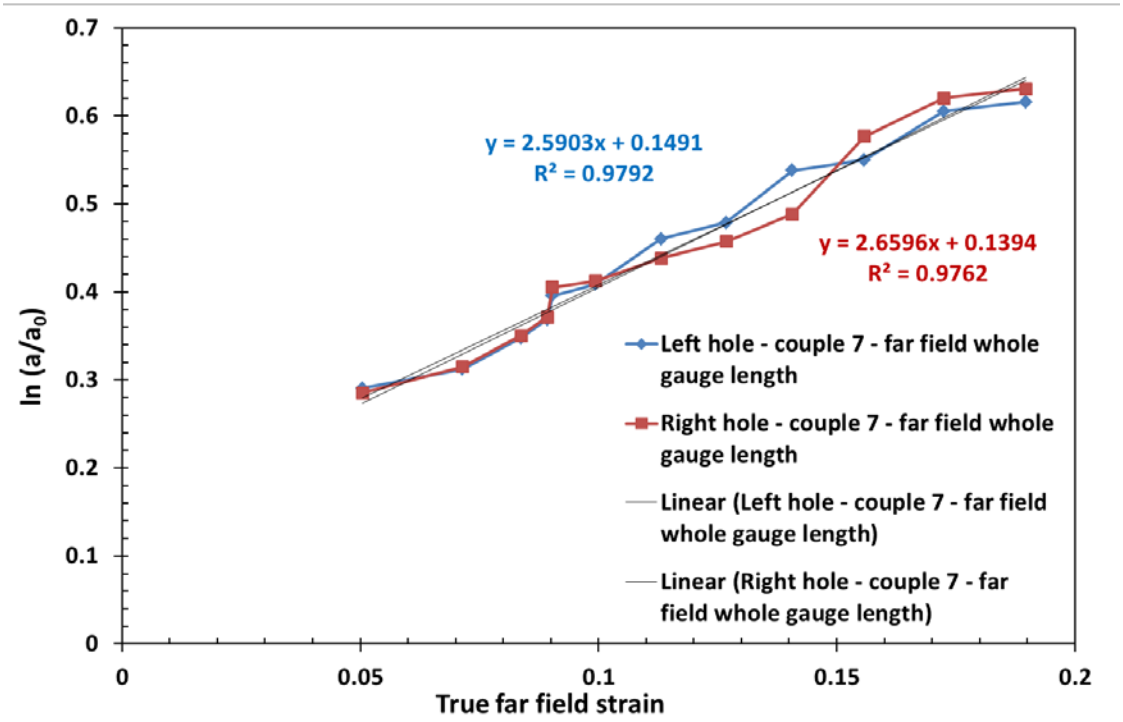

Figure H. 20 - Slope of the local true strain versus the true far field strain extracted in the whole gauge length for couple of holes number 7 on specimen number 6 having carbon gradient along the gauge length

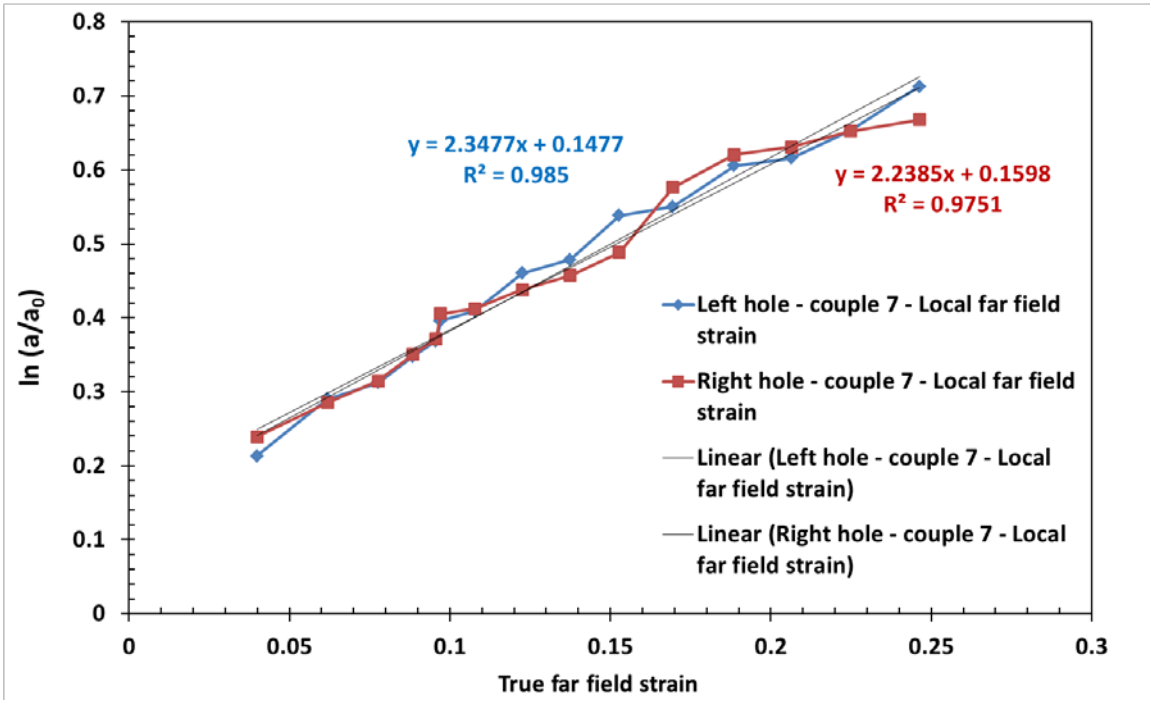

Figure H. 21 - Slope of the local true strain versus the local true far field strain for couple of holes number 7 on specimen number 6 having carbon gradient along the gauge length

- **Specimen 6 carbon gradient: couple of holes 12 (inside the no carbon zone)**

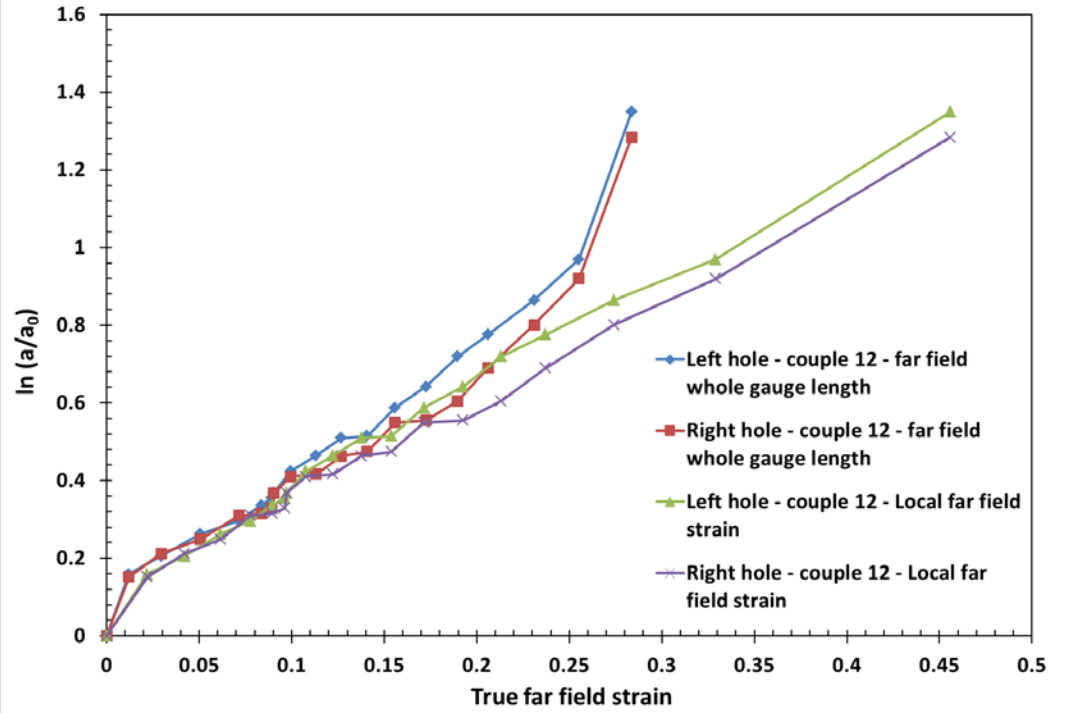

Figure H. 22 - Local true strain versus true far field strain for couple of holes number 12 for specimen number 6 having carbon gradient along the gauge length

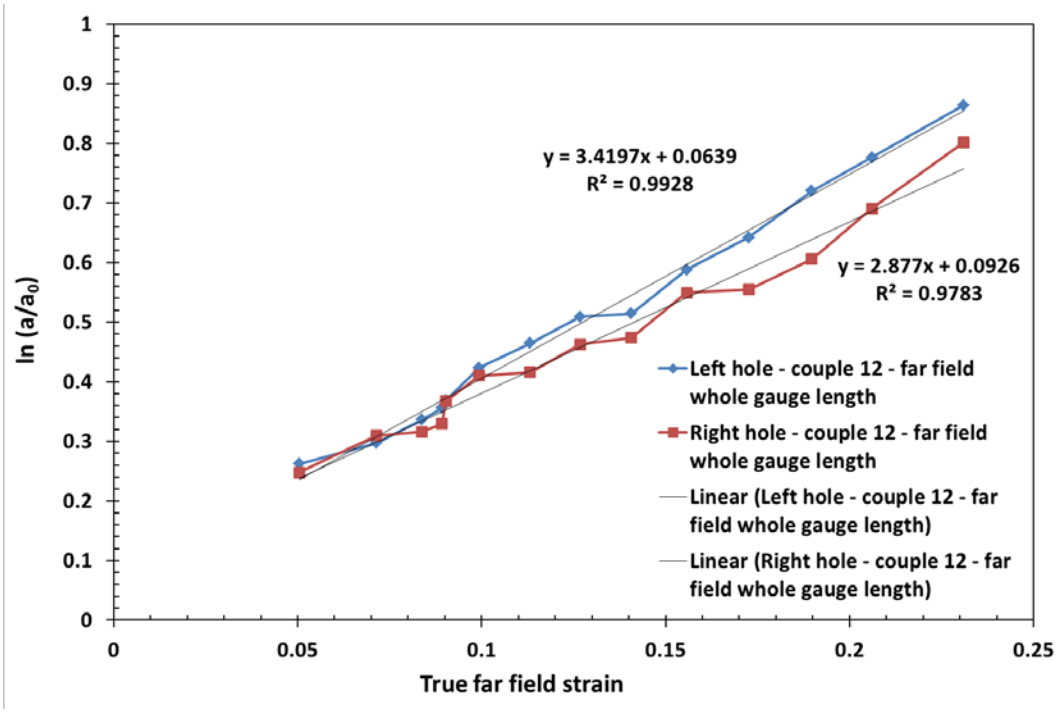

Figure H. 23 - Slope of the local true strain versus the true far field strain extracted in the whole gauge length for couple of holes number 12 on specimen number 6 having carbon gradient along the gauge length

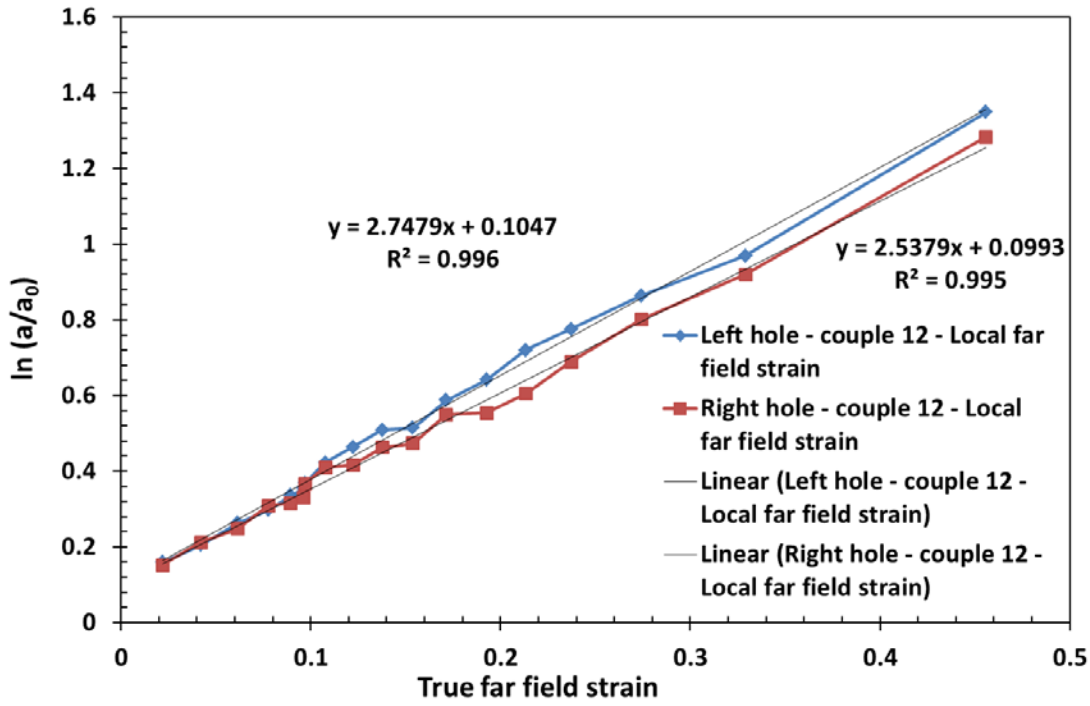

Figure H. 24 - Slope of the local true strain versus the local true far field strain for couple of holes number 12 on specimen number 6 having carbon gradient along the gauge length

From Figure H. 25 to Figure H. 33 the void growth for the voids of specimen 10 having a uniform carbon distribution along the gauge length are plot. The graphs report the void growth as function of the true strain extracted in the whole gauge length and as function of the local true strain extracted considering different zones in the gauge length as shown in Figure 9-36 in Chapter 9.

- **Specimen 10 uniform carbon distribution: couple of holes 7 (uncoated zone)**

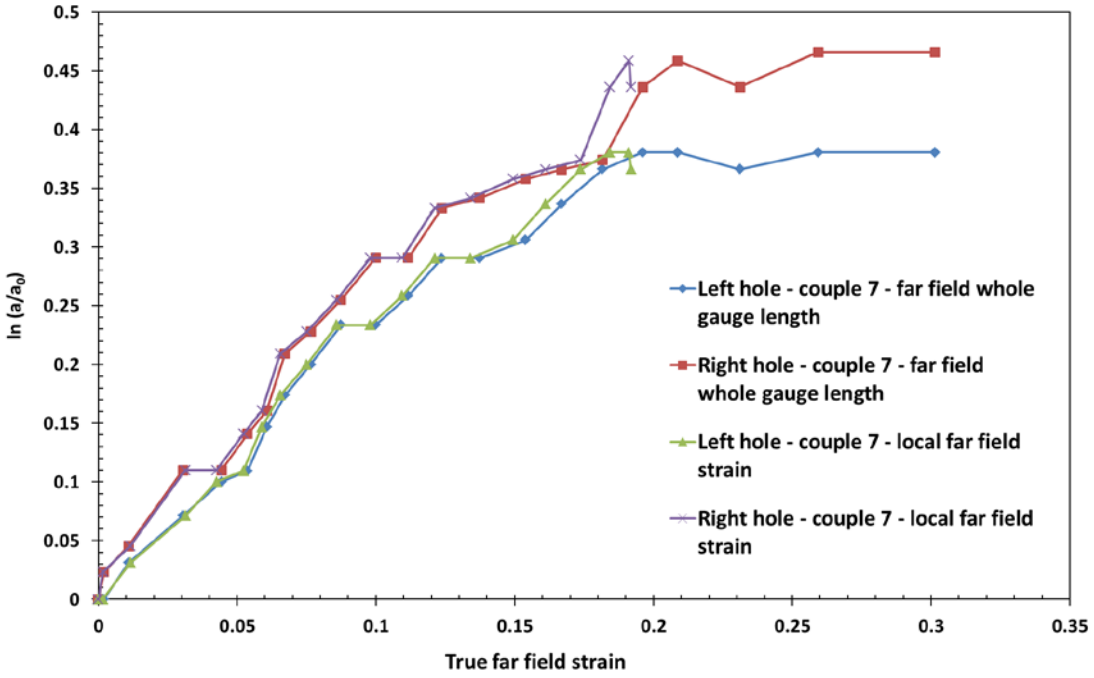

Figure H. 25 - Local true strain versus true far field strain for couple of holes number 7 for specimen number 10 having uniform carbon distribution along the gauge length

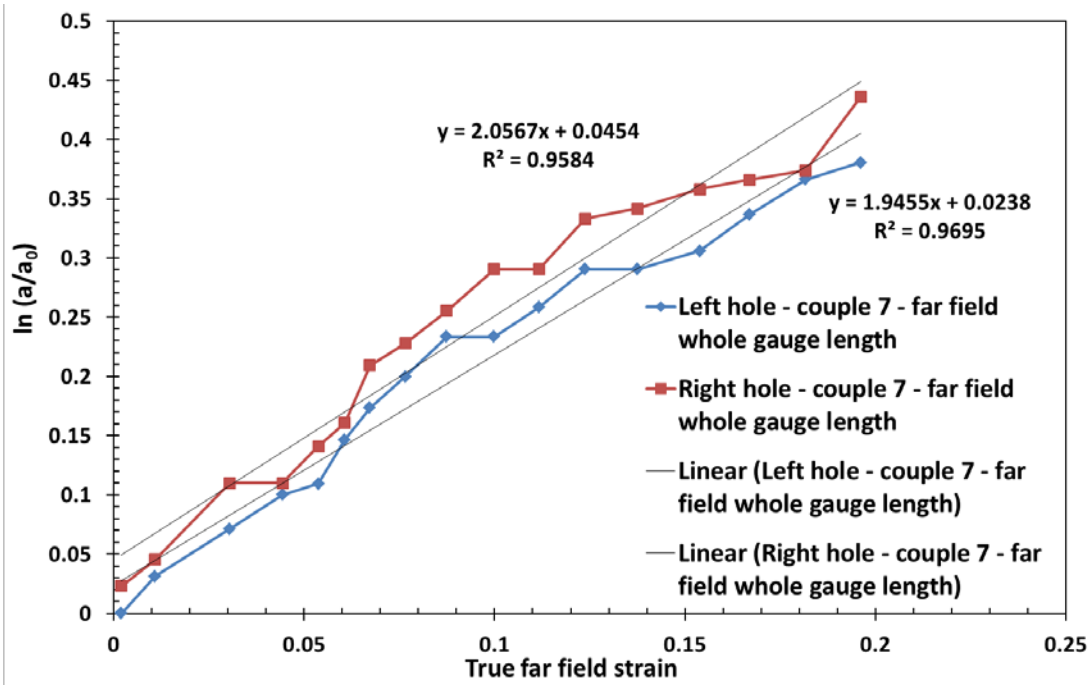

Figure H. 26 - Slope of the local true strain versus the true far field strain extracted in the whole gauge length for couple of holes number 7 on specimen number 10 having uniform carbon distribution along the gauge length

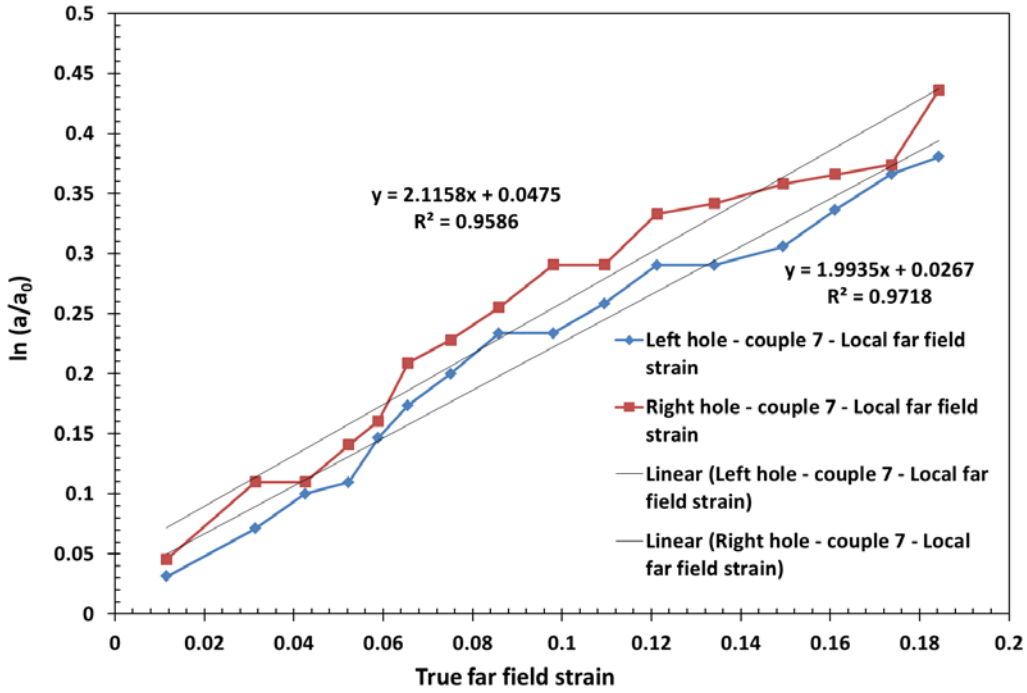

Figure H. 27 - Slope of the local true strain versus the local true far field strain for couple of holes number 7 on specimen number 10 having uniform carbon distribution along the gauge length

- **<u>Specimen 10 uniform carbon distribution: couple of holes 10 (uncoated zone)</u>**

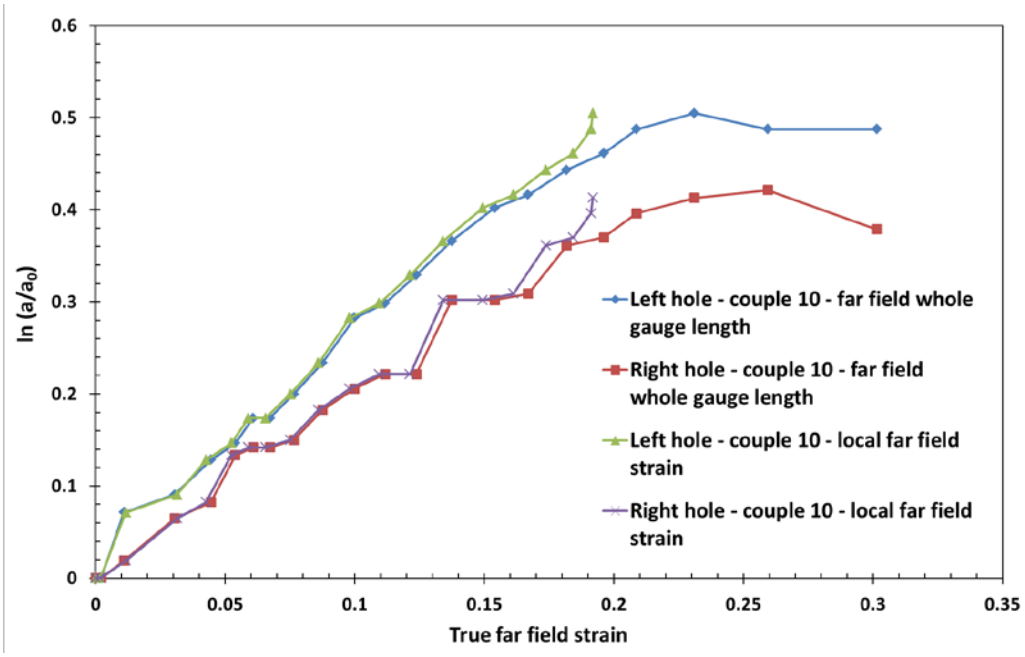

Figure H. 28 - Local true strain versus true far field strain for couple of holes number 10 for specimen number 10 having uniform carbon distribution along the gauge length

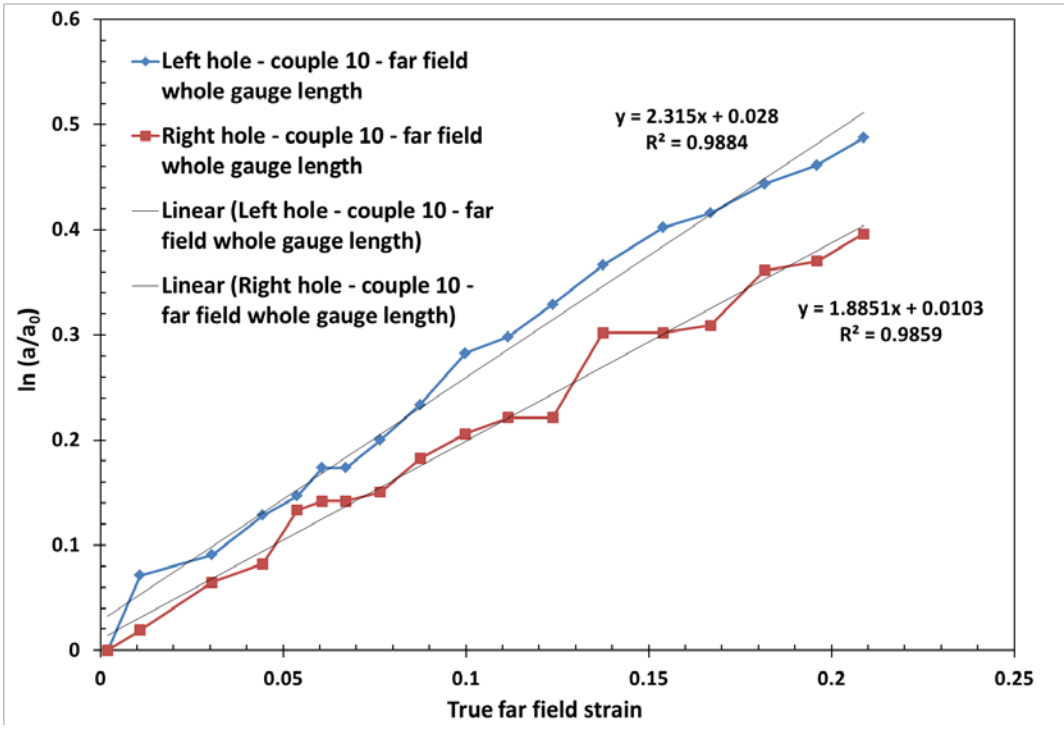

Figure H. 29 - Slope of the local true strain versus the true far field strain taken in the whole gauge length for couple of holes number 10 on specimen number 10 having uniform carbon distribution along the gauge length

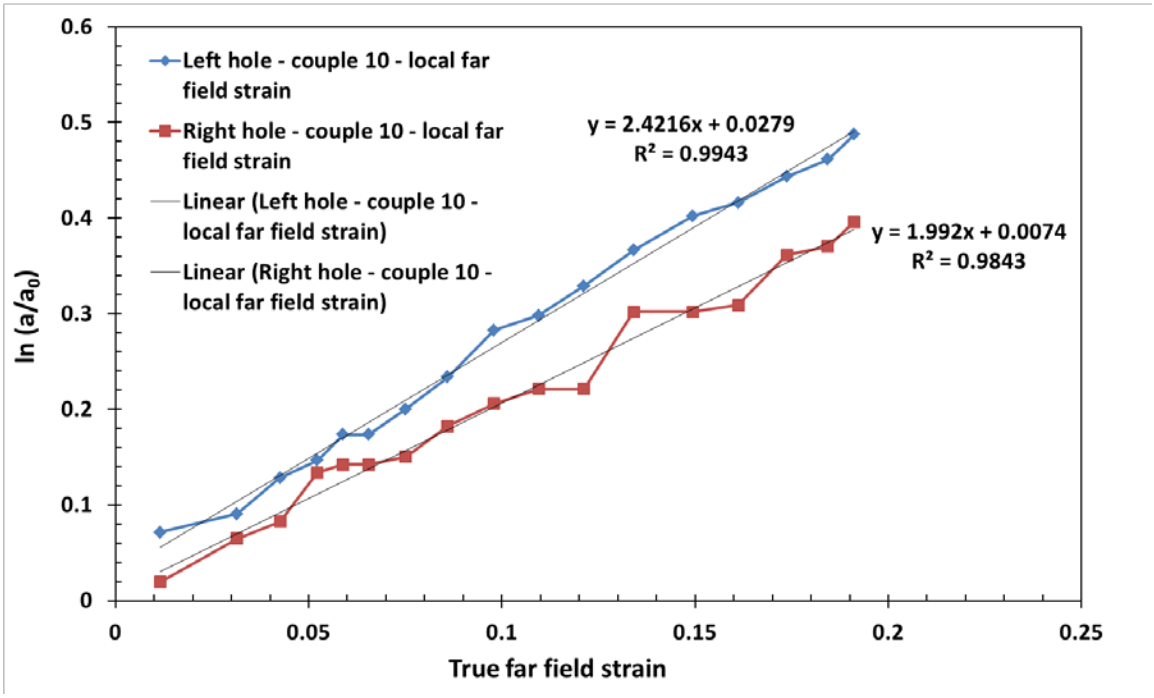

Figure H. 30 - Slope of the local true strain versus the local true far field strain for couple of holes number 10 on specimen number 10 having uniform carbon distribution along the gauge length

- **Specimen 10 uniform carbon distribution: couple of holes 12 (uncoated zone)**

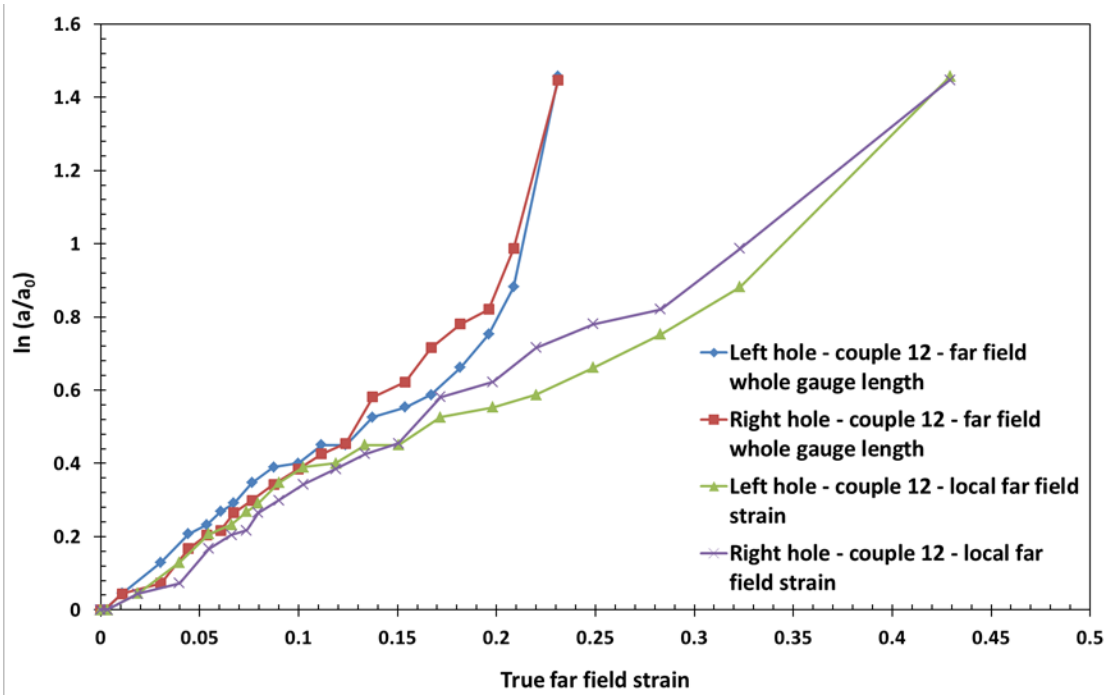

Figure H. 31 - Local true strain versus true far field strain for couple number of holes number 12 for specimen number 10 having uniform carbon distribution along the gauge length

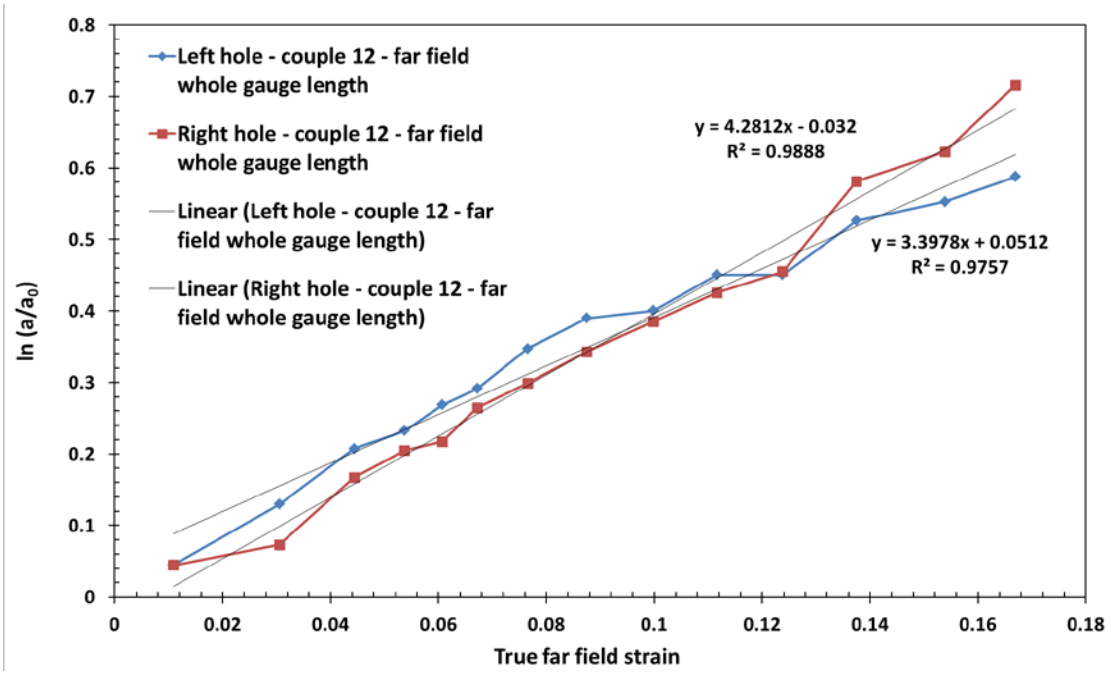

Figure H. 32 - Slope of the local true strain versus the true far field strain taken in the whole gauge length for couple of holes number 12 on specimen number 10 having uniform carbon distribution along the gauge length

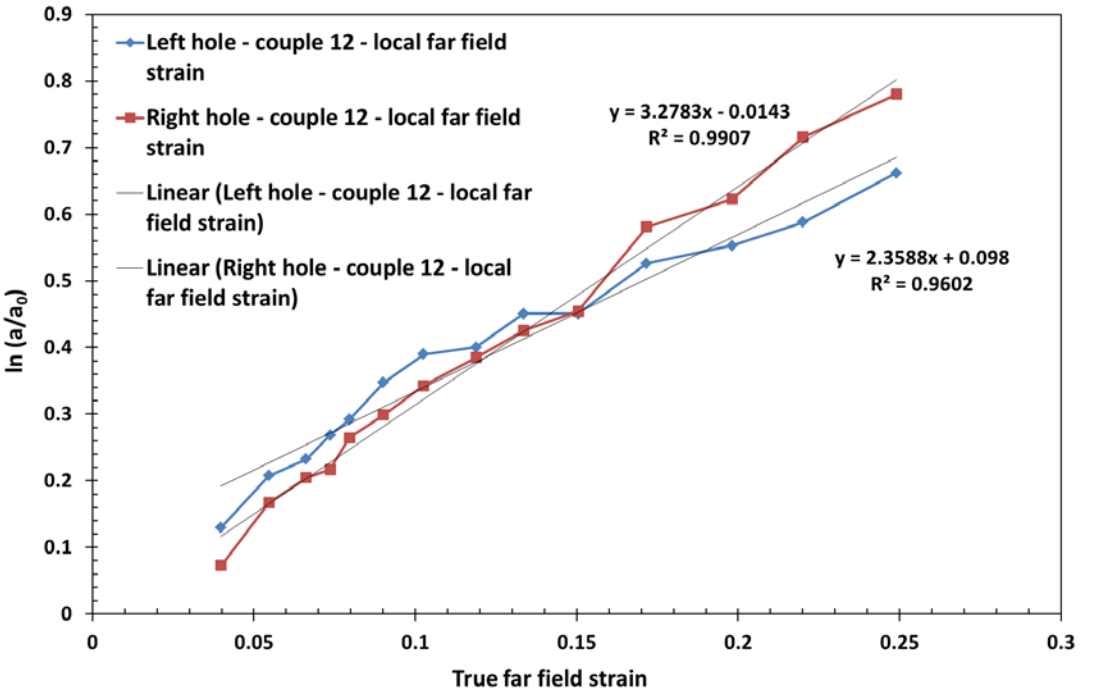

Figure H. 33 - Slope of the local true strain versus the local true far field strain for couple of holes number 12 on specimen number 10 having uniform carbon distribution along the gauge length

H.2.2 Void Growth as function of the local true strain at the sides of the voids

The void growth for coupons having voids along the gauge length was also plot as function of the local true far field strain extracted exactly on the side of the studied voids couple as shown in Figure 9-37 of Chapter 9. From Figure H. 34 to Figure H. 39 the graphs corresponding to coupon 5 and 6 (having carbon gradient) are plot, while from Figure H. 40 to Figure H. 43 the graphs corresponding to coupon 10 having uniform carbon distribution are shown.

- **Specimen 5 carbon gradient along the gauge length: void growth as function of the local true strain at the sides of the voids**

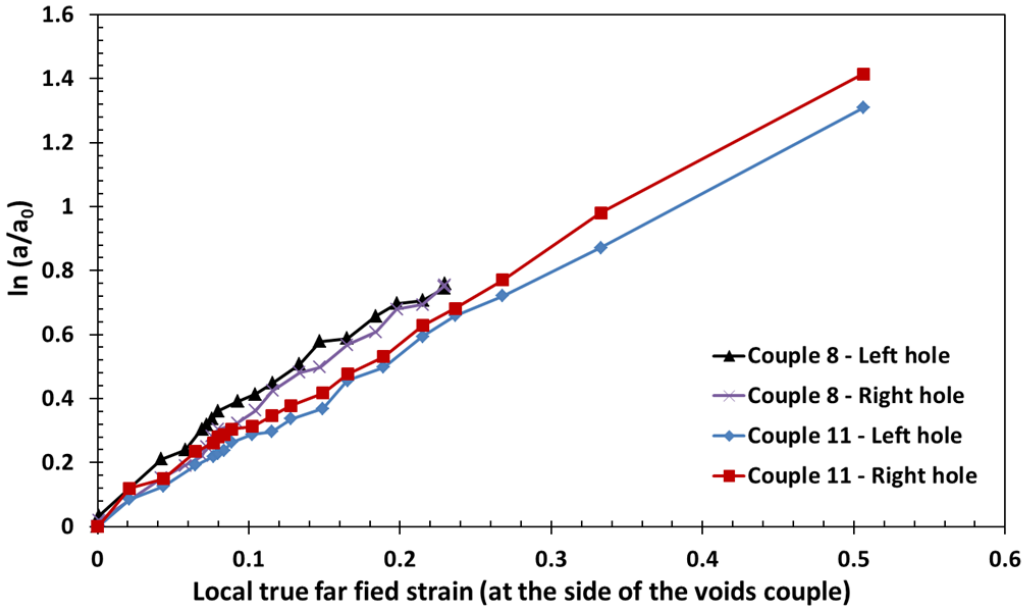

Figure H. 34 - Local true strain as function of the local true far field strain extracted at the side of the voids for couples 8 and 11 of specimen 5 having carbon gradient along the gauge length

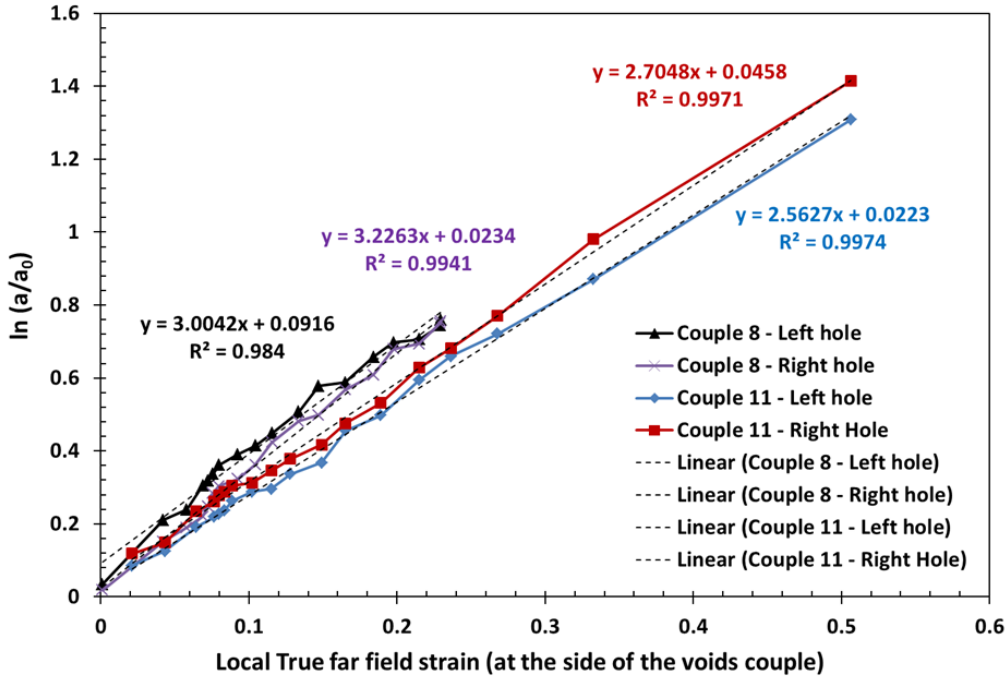

Figure H. 35 - Slope of the local true strain versus the local true far field strain at the sides of the voids for couples 8 and 11 on specimen number 5 having carbon gradient along the gauge length

- **Specimen 6 carbon gradient along the gauge length: void growth as function of the local true strain at the sides of the voids**

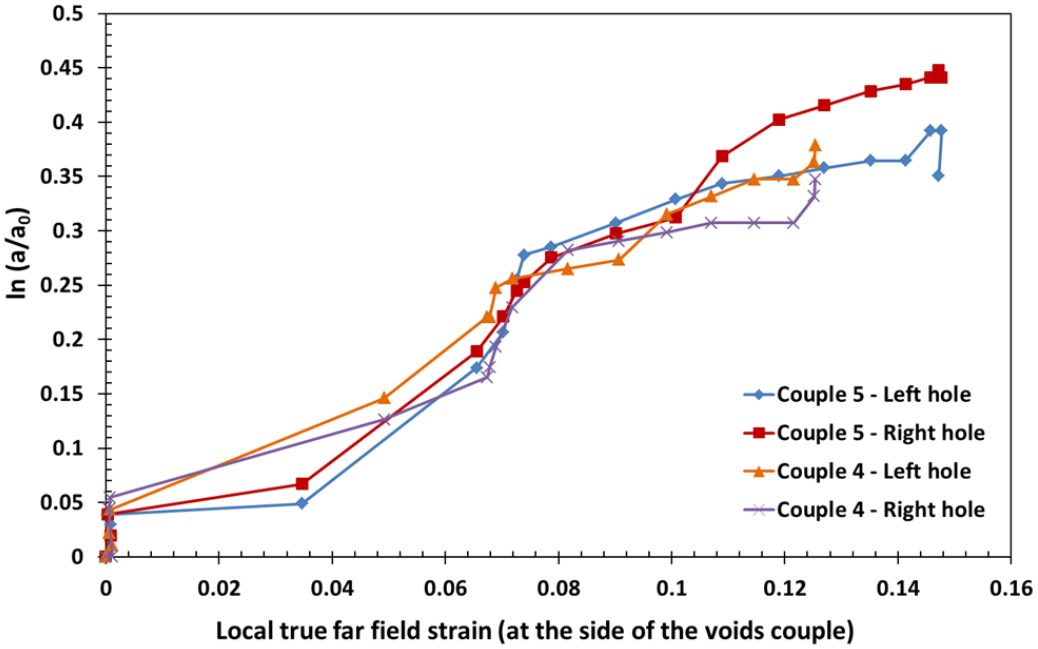

Figure H. 36 - Local true strain as function of the local true far field strain extracted at the side of the voids for couples 4 and 5 of specimen 6 having carbon gradient along the gauge length

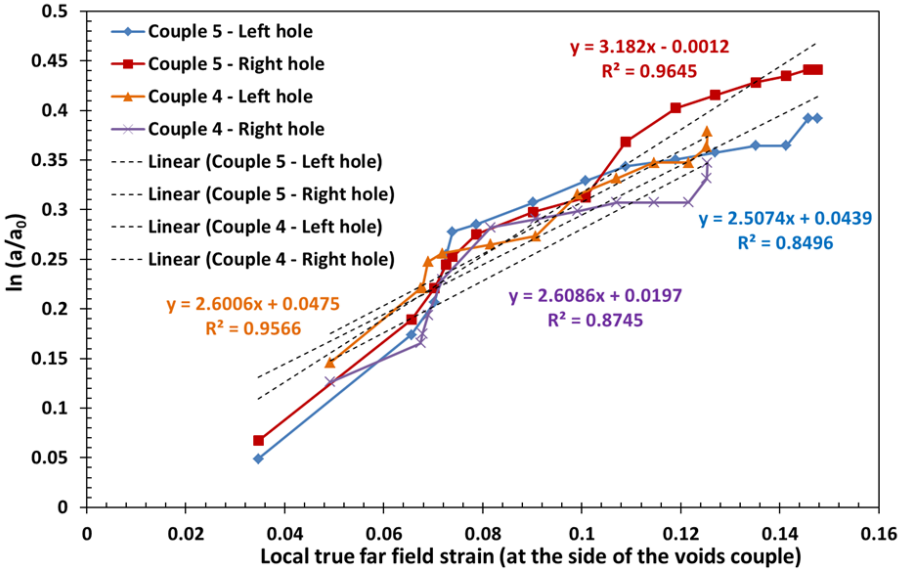

Figure H. 37 - Slope of the local true strain versus the local true far field strain at the sides of the voids for couples 4 and 5 on specimen number 6 having carbon gradient along the gauge length

In Figure H. 36, the void growth of couples 4 and 5 in specimen 6 is shown. As obtained for specimen 5, the void growth appears highly irregular due to Lüdering. Even for this coupon,

the speed fo void growth was extracted as slope of the curves neglecting the initial “jump” in strain caused by the bands.

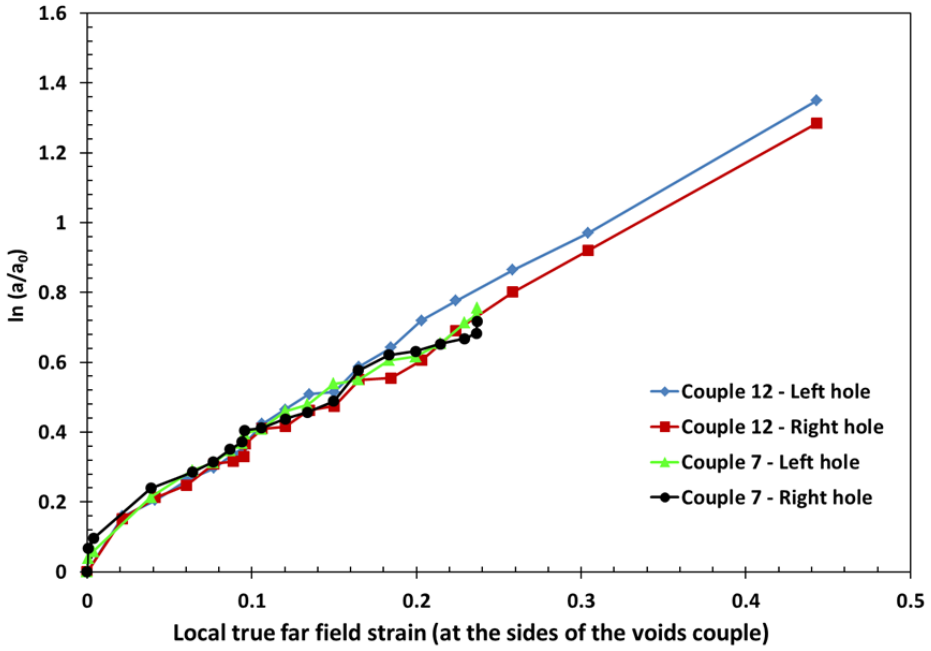

Figure H. 38 - Local true strain as function of the local true far field strain extracted at the side of the voids for couples 7 and 12 of specimen 6 having carbon gradient along the gauge length

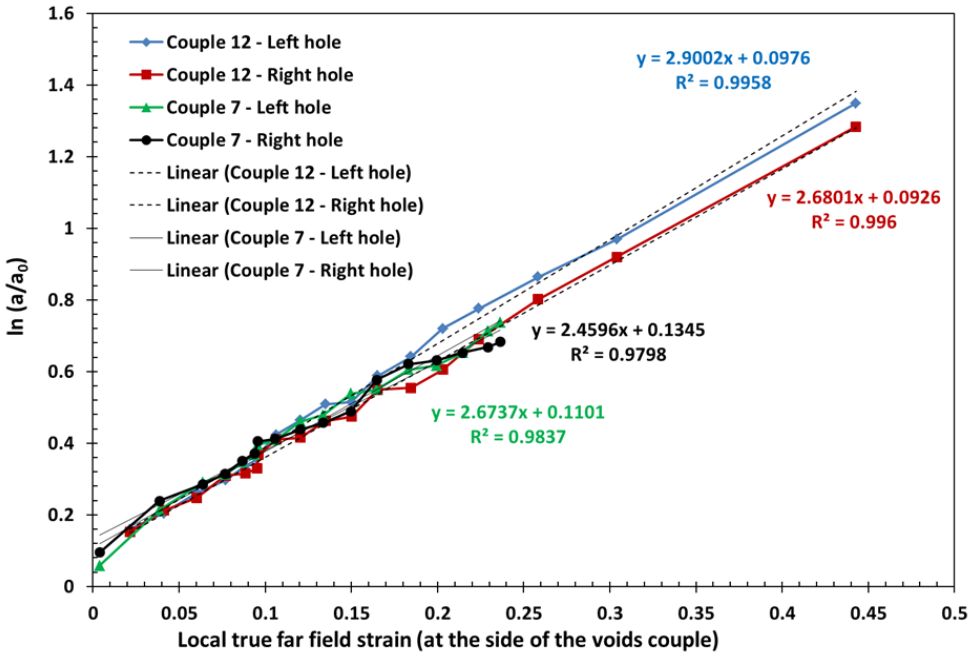

Figure H. 39 - Slope of the local true strain versus the local true far field strain at the sides of the voids for couples 7 and 12 on specimen number 6 having carbon gradient along the gauge length

- **Specimen 10 uniform carbon distribution along the gauge length: void growth as function of the local true strain at the sides of the voids**

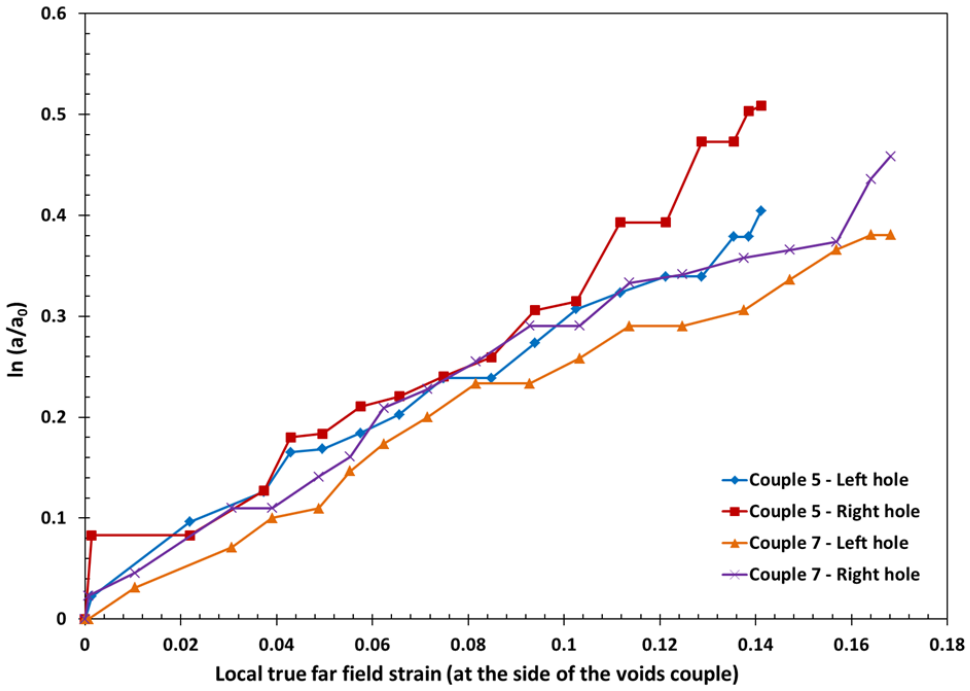

Figure H. 40 - Local true strain as function of the local true far field strain extracted at the side of the voids for couples 5 and 7 of specimen 10 having uniform carbon distribution along the gauge length

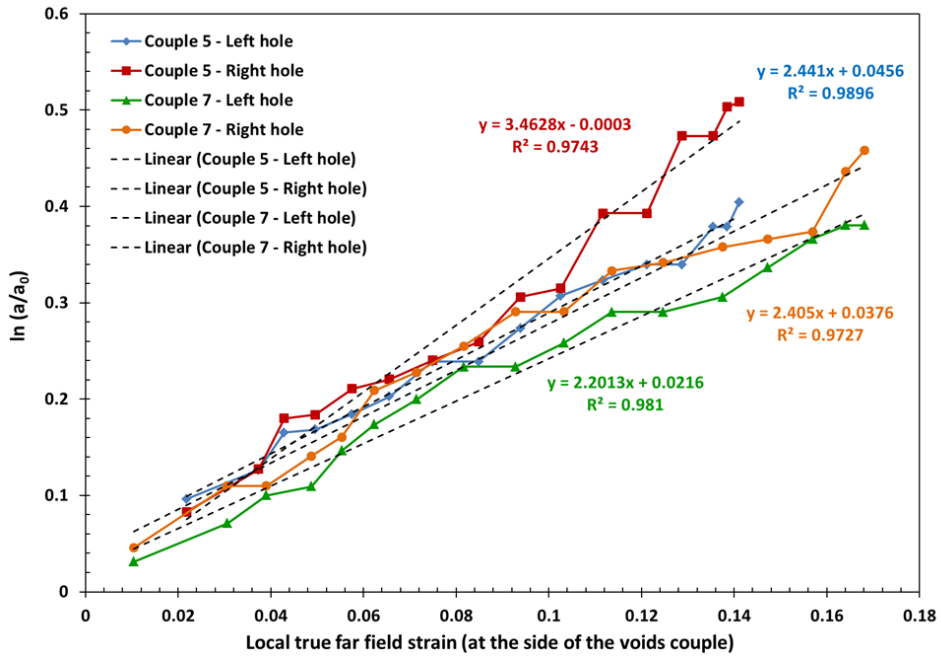

Figure H. 41 - Slope of the local true strain versus the local true far field strain at the sides of the voids for couples 5 and 7 on specimen number 10 having uniform carbon distribution along the gauge length

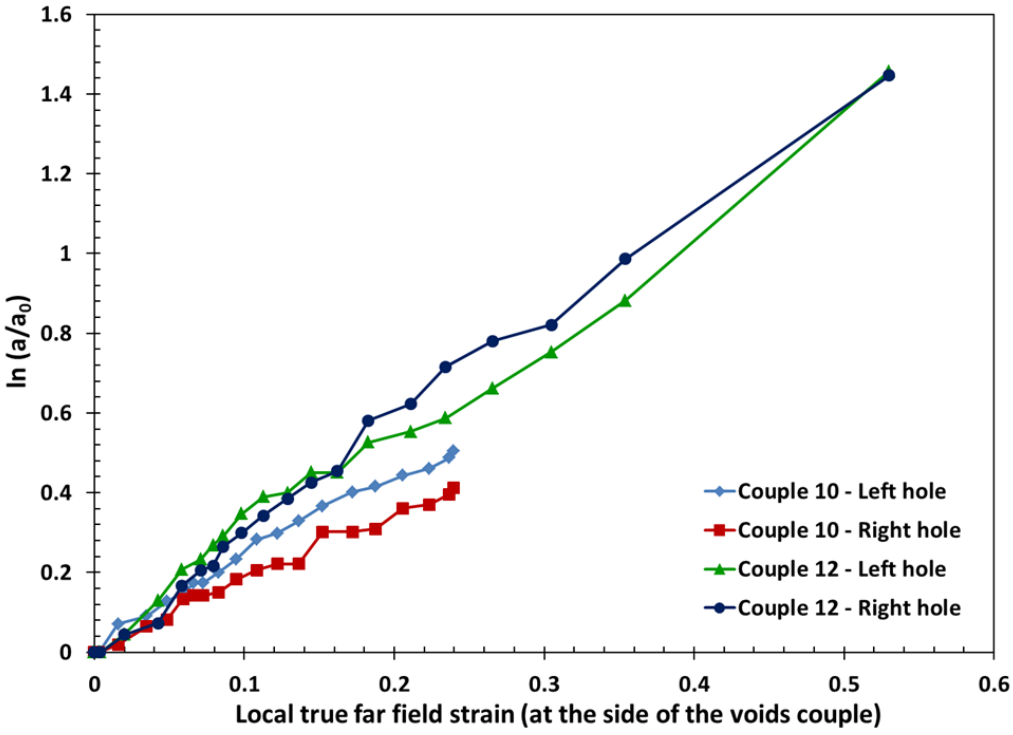

Figure H. 42 - Local true strain as function of the local true far field strain extracted at the side of the voids for couples 10 and 12 of specimen 10 having uniform carbon distribution along the gauge length

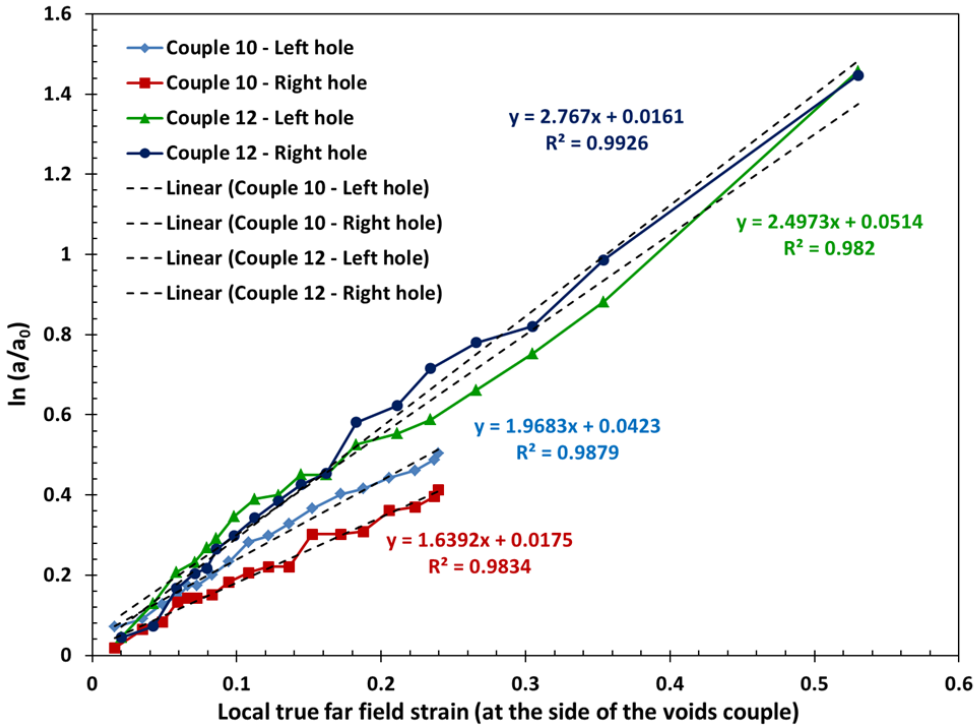

Figure H. 43 - Slope of the local true strain versus the local true far field strain at the sides of the voids for couples 10 and 12 on specimen number 10 having uniform carbon distribution along the gauge length

H.3 Theoretical prediction of carbon gradient through width

In this section, simulations showing the carbon profiles obtained by different ablation configurations are shown. In Figure H. 44, the carbon diffusion profile in a tensile coupon where 333 µm of FeC film was ablated from the centre is shown for both annealing at 530 ˚C – 1h and 630 ˚C – 1h.

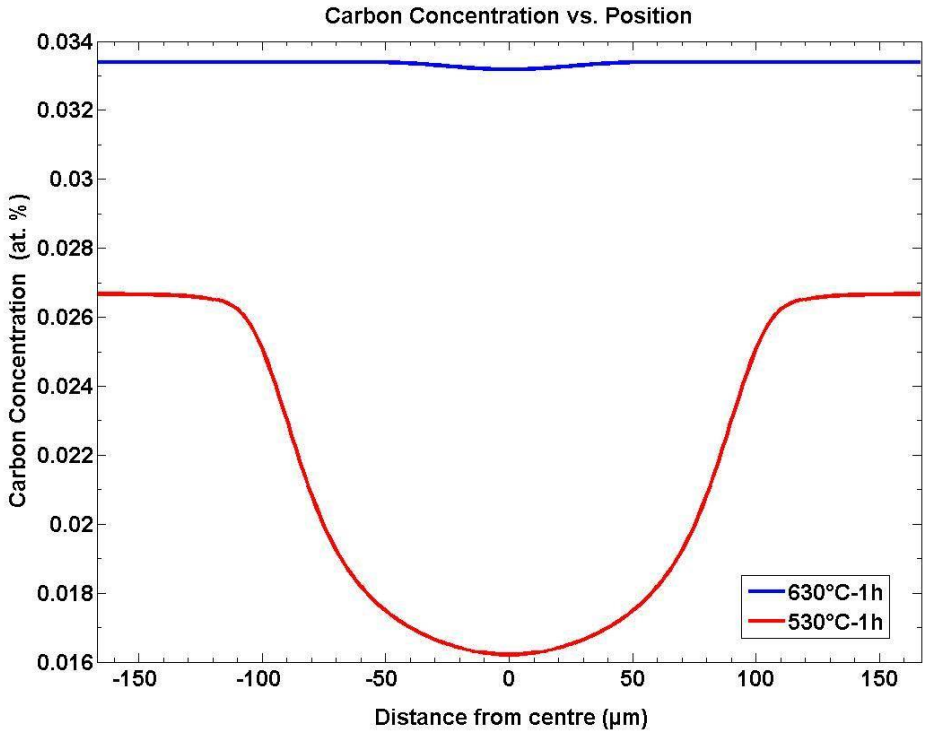

Figure H. 44 - Carbon gradient obtained along a gauge width in a zone where 333 µm coating was removed

In order to estimate the yield stress gradient from the edge to the center of the specimen, the carbon concentrations were obtained from the above graph and they were used to calculate the yield stress. The concentration where extracted for half of the thickness since the carbon concentration is mirrored due to the diffusion occurring on both sides. In Table H- 3 the values of carbon concentration and the corresponding yield stresses for both 530 ˚C – 1h and 630 ˚C – 1h annealings are reported. The zone "AV" is close to the centre of the specimen (coordinate 0 in Figure H. 44), while zone "AV 10" is close to the edge (coordinate 167 in Figure H. 44). This interval from 0 to 167 µm was divided in 10 subintervals each having a width of 16.7 µm and inside this interval the concentration is calculated every 0.6 µm and then the average for the whole subinterval is obtained.

Zone	Carbon concentration for 530 ˚C – 1h [at%]	Carbon concentration for 630 ˚C – 1h [at%]	Yield stress for 530 ˚C – 1h [MPa]	Yield stress for 630 ˚C – 1h [MPa]
AV	0.0163	0.0332	247	304
AV 2	0.0165	0.0333	248	305
AV 3	0.0171	0.0334	251	305
AV 4	0.0181	0.0334	255	305
AV 5	0.0200	0.0334	262	305
AV 6	0.0233	0.0334	273	305
AV 7	0.0260	0.0334	282	305
AV 8	0.0266	0.0334	284	305
AV 9	0.0266	0.0334	284	305
AV 10	0.0267	0.0334	285	305
Gradient of Yield stress [MPa]			**38**	**1**

Table H- 3 - Carbon concentration and yield stress gradient created by ablating 333 μm in the centre of the tensile coupon. AV indicates the concentration in the center of the width, while AV 10 reports the concentration at the interface between ablated and not-ablated zones

From the values reported in Table H- 3 it is evident that ablating a zone of 333 μm (so 1/3 of the gauge width) is not enough to create a marked carbon gradient through the width of the specimen. For this reason, different ablation patterns were studied. The above simulations were repeated considering an ablation of 500 μm in the centre of the specimen. In Figure H. 45 the carbon profile through width obtained for annealing at 530 ˚C – 1h and 630 ˚C – 1h is shown, while in Table H- 4 the concentration and the respective yield stresses are reported. For this simulation, the interval from 0 to 250 μm was divided in 10 subintervals, each 25 μm thick. Inside each subinterval, a value of concentration was extracted every 0.8 μm and the average of all the readings was obtained.

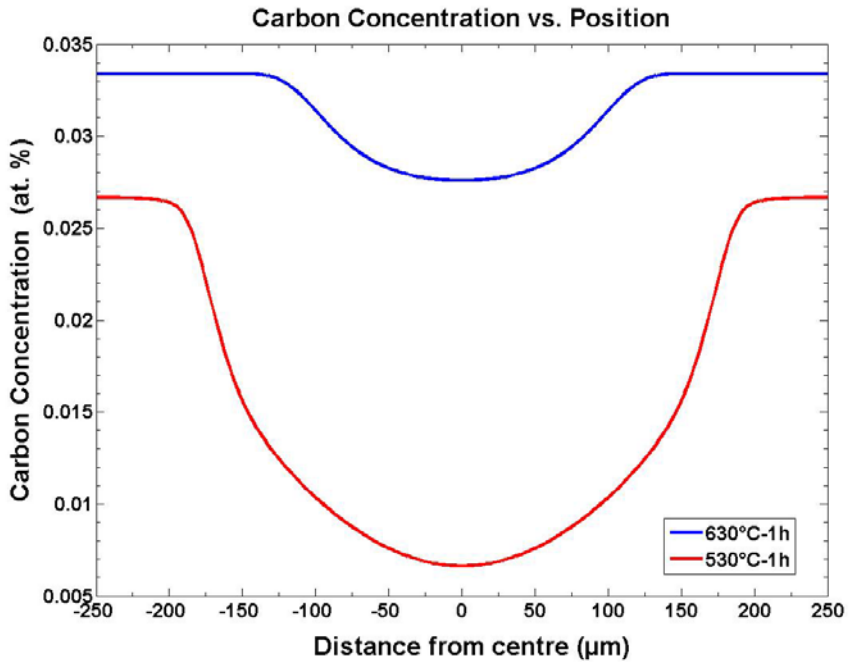

Figure H. 45 - Carbon gradient obtained along a gauge width in a zone where 500 µm coating was removed

Zone	Carbon concentration for 530 ˚C – 1h [at%]	Carbon concentration for 630 ˚C – 1h [at%]	Yield stress for 530 ˚C – 1h [MPa]	Yield stress for 630 ˚C – 1h [MPa]
AV	0.0067	0.0276	199	288
AV 2	0.0072	0.0279	203	288
AV 3	0.0081	0.0288	208	291
AV 4	0.0095	0.0304	216	296
AV 5	0.0113	0.0323	225	302
AV 6	0.0139	0.0333	237	305
AV 7	0.0185	0.0334	256	305
AV 8	0.0249	0.0334	279	305
AV 9	0.0266	0.0334	284	305
AV 10	0.0267	0.0334	285	305
Gradient of Yield stress [MPa]			**86**	**17**

Table H- 4 - Carbon concentration and yield stress gradient created by ablating 500 µm in the centre of the tensile coupon

From Table H- 4, it can be seen that the gradient of yield stress obtained for annealing at 530 ˚C – 1h on a coupon which was ablated removing 500 µm in the centre is expected to be high enough to perform fracture studies. Again, the gradient of mechanical properties obtained at 630 ˚C -1h is too low. Another configuration where 600 µm of width were ablated was simulated and the results are shown in Figure H. 46 and in Table H- 5.

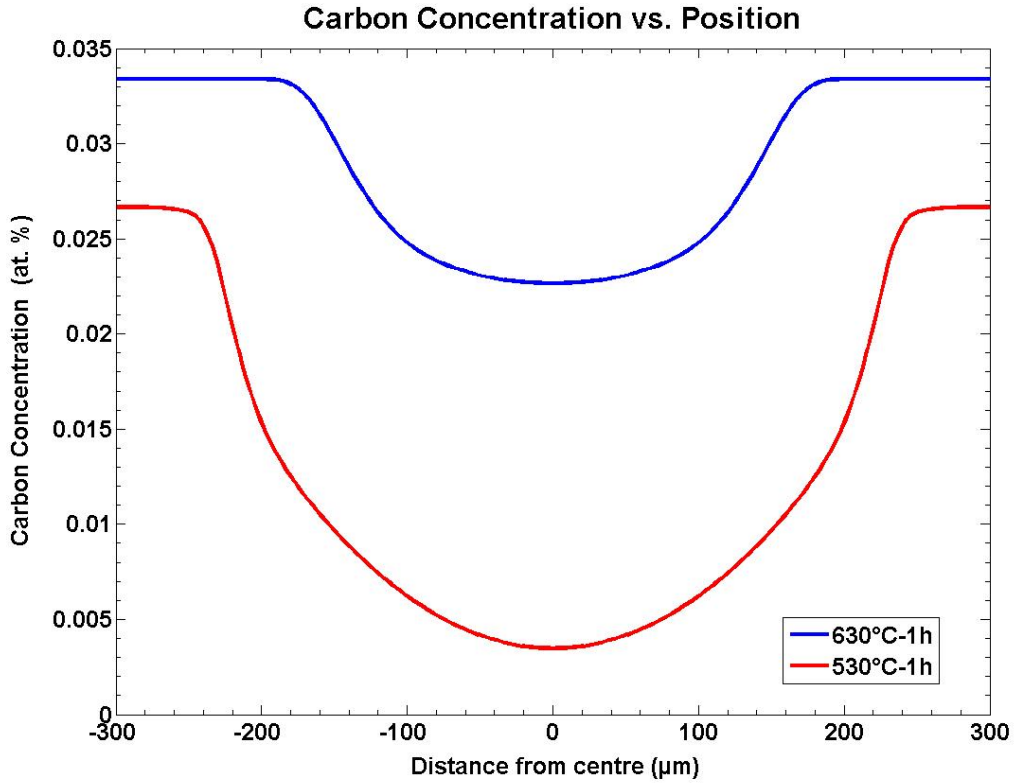

Figure H. 46 - Carbon gradient obtained along a gauge width in a zone where 600 µm coating was removed

Zone	Carbon concentration for 530 ˚C – 1h [at%]	Carbon concentration for 630 ˚C – 1h [at%]	Yield stress for 530 ˚C – 1h [MPa]	Yield stress for 630 ˚C – 1h [MPa]
AV	0.0036	0.0227	177	271
AV 2	0.0040	0.0230	180	272
AV 3	0.0050	0.0237	188	275
AV 4	0.0065	0.0252	198	280
AV 5	0.0085	0.0282	210	289
AV 6	0.0110	0.0319	224	301
AV 7	0.0146	0.0333	240	305
AV 8	0.0218	0.0334	268	305
AV 9	0.0264	0.0334	284	305
AV 10	0.0267	0.0334	285	305
Gradient of Yield stress [MPa]			**108**	**34**

Table H- 5 - Carbon concentration and yield stress gradient created by ablating 600 μm in the centre of the tensile coupon

According to Table H- 5, the gradient of mechanical properties obtained by ablating 600 μm of film in the centre of the tensile coupon is also acceptable for studying fracture in graded material; however, it is acceptable only if the heat treatment is performed at 530 ˚C – 1h. Finally, another configuration where 500 μm of film were ablated close to one edge of the width was also simulated. The results of the diffusion profiles are shown in Figure H. 47 and the numerical values reported in Table H- 6.

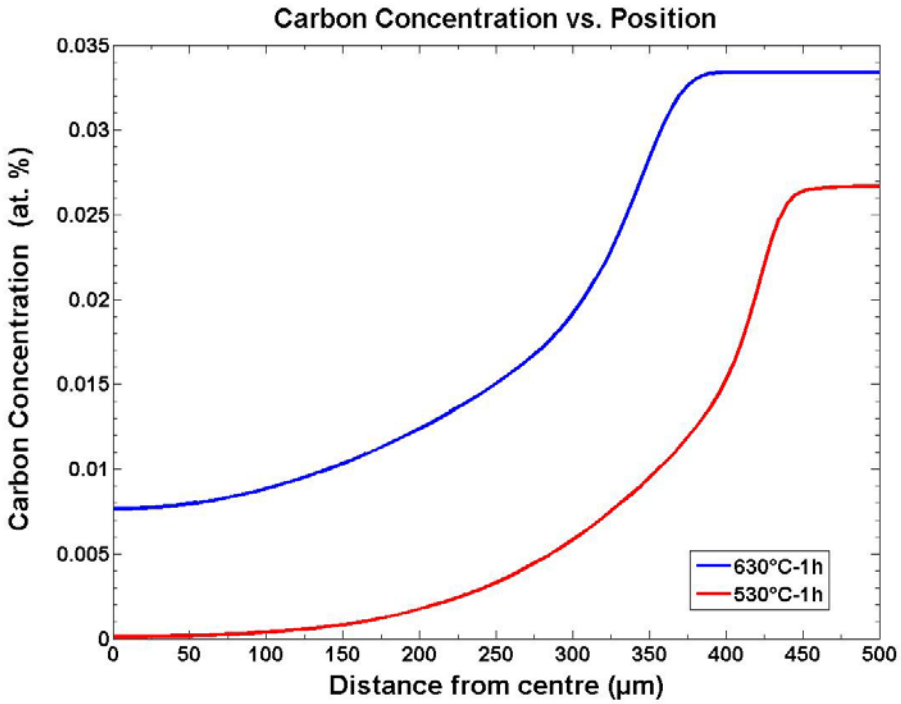

Figure H. 47 - Carbon gradient obtained along a gauge width in a zone where 500 µm coating was removed close to one edge of the width

Zone	Carbon concentration for 530 ˚C – 1h [at%]	Carbon concentration for 630 ˚C – 1h [at%]	Yield stress for 530 ˚C – 1h [MPa]	Yield stress for 630 ˚C – 1h [MPa]
AV	$1.32x10^{-4}$	0.0078	126	206
AV 2	$2.6x10^{-4}$	0.0084	131	210
AV 3	$5.8x10^{-4}$	0.0095	139	215.7
AV 4	0.0012	0.0113	150	225
AV 5	0.0025	0.0137	166	236
AV 6	0.0045	0.0169	184	250
AV 7	0.0076	0.0232	205	273
AV 8	0.0120	0.0319	228	300.5
AV 9	0.0216	0.0334	267	305
AV 10	0.0266	0.0334	284	305
Gradient of Yield stress [MPa]			**158**	**99**

Table H- 6 - Carbon concentration and yield stress gradient created by ablating 500 µm close to one edge of the tensile coupon

This configuration is expected to create a high gradient but it would not allow the study of symmetric configurations as shown in Figure 9-56 of Chapter 9 and for this reason it was discarded.

H.3.1 Carbon Gradient obtained for annealing times shorter than 1h

In order to create steeper gradients, annealing times shorter than 1h were evaluated. The values of carbon concentration through thickness for the above profiles were extracted and they are reported in Table H- 7 to verify that the concentration remains uniform even if the time is shortened. Half of the interval was divided in 10 subintervals, each one of 10 μm thickness and inside each subinterval, the concentration was measured in 30 points and the average value of the concentration in these points was obtained. In Table H- 7 "AV" indicates the concentration at the centre of the thickness (so coordinate 0 in Figure 9-61), while "AV 10" indicates the concentration close to the coated surfaces (so coordinate +100 μm and -100 μm in Figure 9-61). In Table H- 8, the carbon gradient and the corresponding yield stress gradient for annealing times shorter than 1h are shown. The simulated specimen has 500 μm of FeC film removed in the center of the width. Table H- 9 lists the expected gradient for annealing at 530 ºC or 630 ºC for 1h of coupons having 500 μm of FeC film left in the center of the width and ablated on the sides.

Zone	Carbon concentration for 530 ˚C – 20 min [at%]	Carbon concentration for 530 ˚C – 25 min [at%]	Carbon concentration for 530 ˚C – 30 min [at%]
AV	0.0176	0.0198	0.0215
AV 2	0.0192	0.0210	0.0224
AV 3	0.0220	0.0231	0.0240
AV 4	0.0247	0.0252	0.0255
AV 5	0.0261	0.0262	0.0263
AV 6	0.0265	0.0265	0.0265
AV 7	0.0266	0.0266	0.0266
AV 8	0.0266	0.0266	0.0266
AV 9	0.0267	0.0267	0.0267
AV 10	0.0267	0.0267	0.0267
Carbon gradient	9.1×10^{-3}	7×10^{-3}	5×10^{-3}

Table H- 7 - Values of diffused carbon for heat treatments performed at 530 ˚C for 20 min, 25 min and 30 min

Zone	Carbon concentration for 530 ˚C – 25 min [at%]	Carbon concentration for 530 ˚C – 30 min [at%]	Yield stress for 530 ˚C – 25 min [MPa]	Yield stress for 530 ˚C – 30 min [MPa]
AV	9.80×10^{-4}	0.0017	146.5	157
AV 2	0.0013	0.0021	151.5	162
AV 3	0.0021	0.0029	162	170
AV 4	0.0033	0.0043	174	182
AV 5	0.0052	0.0063	189	197
AV 6	0.0081	0.0093	208	214.6
AV 7	0.0145	0.0154	240	243.5
AV 8	0.0240	0.0242	276	276.4
AV 9	0.0265	0.0265	284	284
AV 10	0.0267	0.0267	284.6	285
Gradient of Yield stress [MPa]			**138**	**128**

Table H- 8 - Carbon concentration and yield stress gradient created by ablating 500 μm in the centre of the specimen and by performing annealing at 530 ˚C for 25 minutes and 30 minutes

Zone	Carbon concentration for 530 ˚C – 1h [at%]	Carbon concentration for 630 ˚C – 1h [at%]	Yield stress for 530 ˚C – 1h [MPa]	Yield stress for 630 ˚C – 1h [MPa]
AV	0.0067	0.0276	199.4	287.5
AV 2	0.0072	0.0279	202.5	288
AV 3	0.0081	0.0288	208	291
AV 4	0.0095	0.0304	215.7	296
AV 5	0.0113	0.0323	225	302
AV 6	0.0139	0.0333	237	304.6
AV 7	0.0185	0.0334	256	305
AV 8	0.0249	0.0334	278.8	305
AV 9	0.0266	0.0334	284	305
AV 10	0.0267	0.0334	284.6	305
Gradient of Yield stress [MPa]			**85**	**18**

Table H- 9 - Gradient of yield stress obtained by removing 250 µm of FeC film on the sides of the tensile coupon and leaving 500 µm at the centre of the coupon

H.4 Vickers Hardness for coupons having carbon gradient along the width

- **Specimen EC 1:**

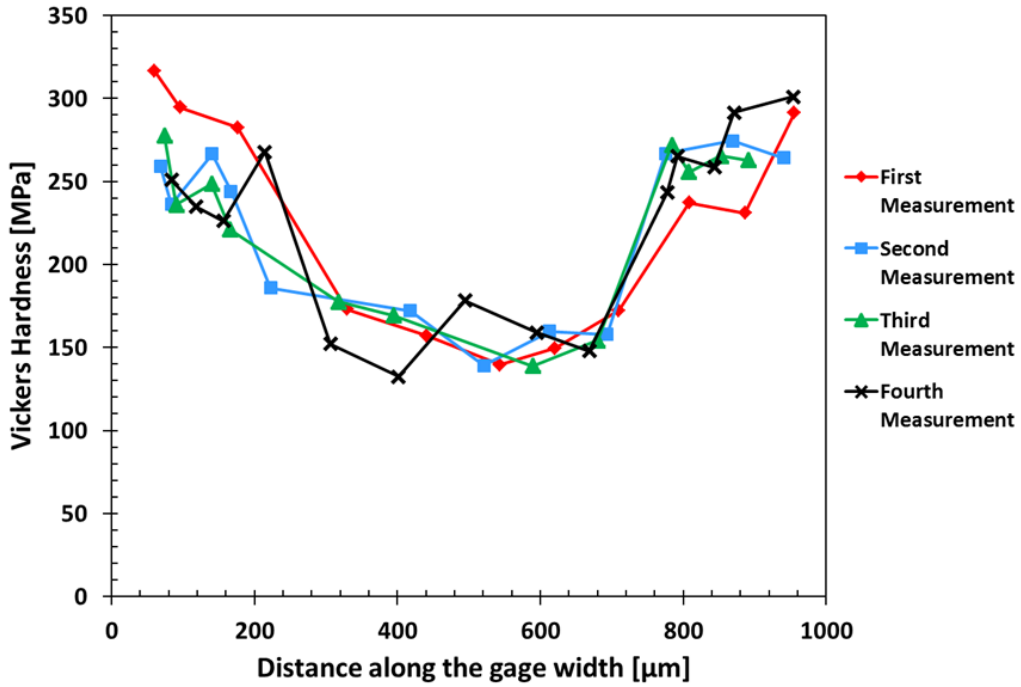

Figure H. 48 - Hardness through with for specimen EC 1 before polishing

From the graph shown in Figure H. 48 it can be seen that the hardness is around 270 in the coated zones and around 140 in the ablated zone. However, it is known that the FeC film will form cementite during the heat treatment, so it is important to remove the film and to take again hardness measurements in order to assess the real gradient of mechanical properties.

- **Specimen EC 3:**

For coupon EC 3, when the hardness was performed without any polishing, it was hard to discern any gradient as it can be seen from Figure H. 49. This could be due to the presence of the debris of the ablated zone which makes difficult a precise measurement of the Vickers indent. Plus the zone is affected by the heat caused by the laser, for this reason the hardness of this zone can result sometimes high. However, when the specimen was polished following the procedure described in section 9.6, the gradient of hardness was much easier to discern as it can be seen from Figure H. 50.

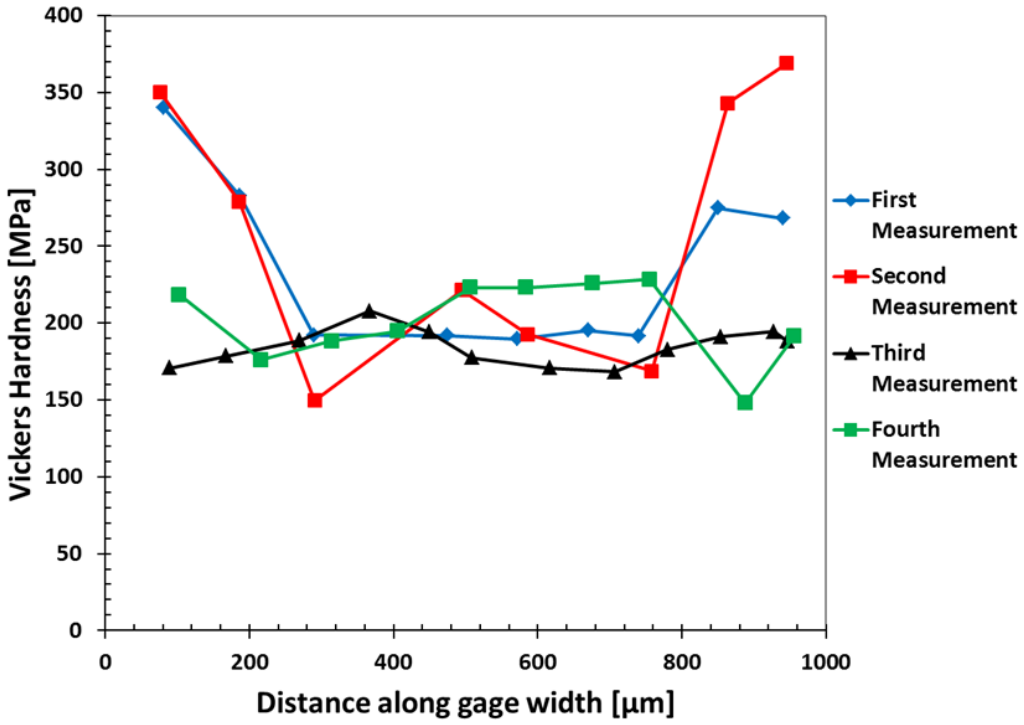

Figure H. 49 - Vickers hardness of specimen EC 3 without polishing of the surface

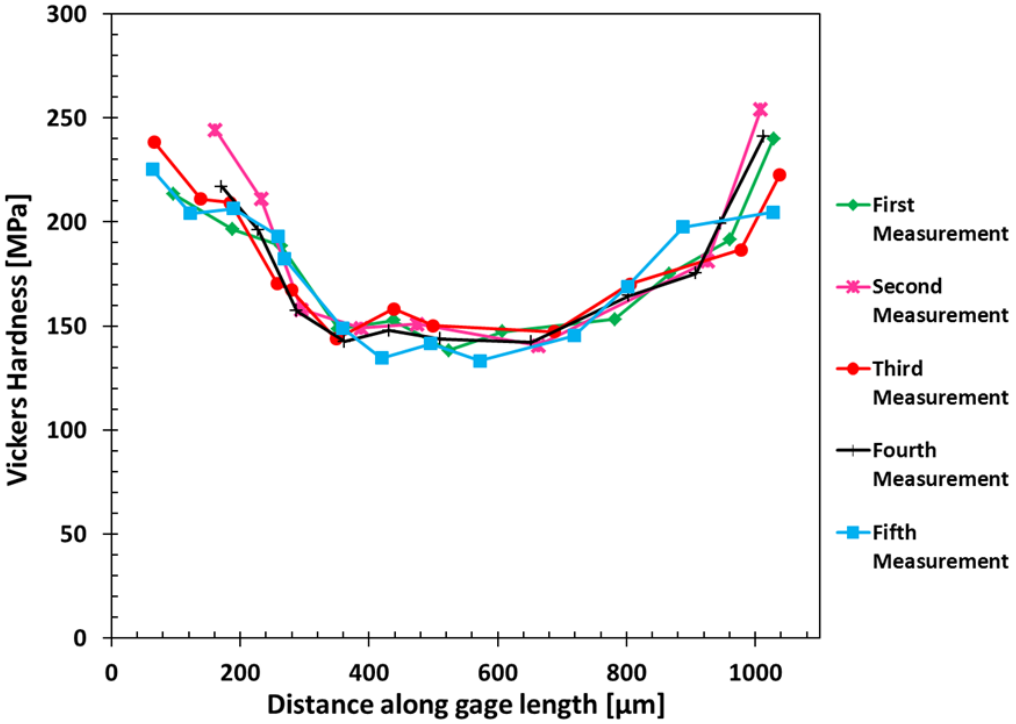

Figure H. 50 - Vickers hardness of specimen EC 3 after polishing of the surface

- **Specimen EC 5:**

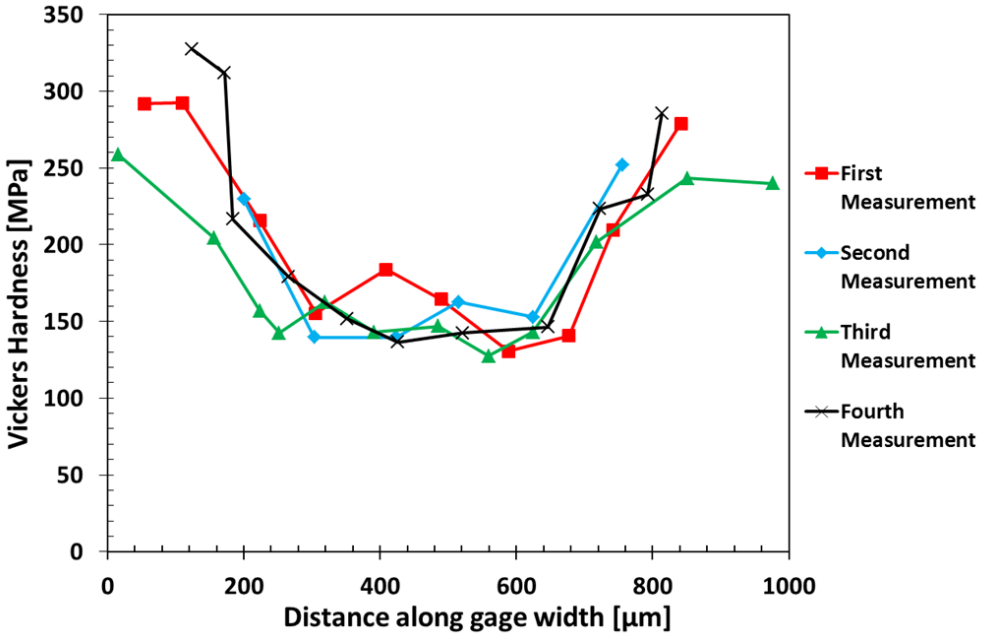

Figure H. 51 - Vickers hardness of specimen EC 5 without polishing of the surface

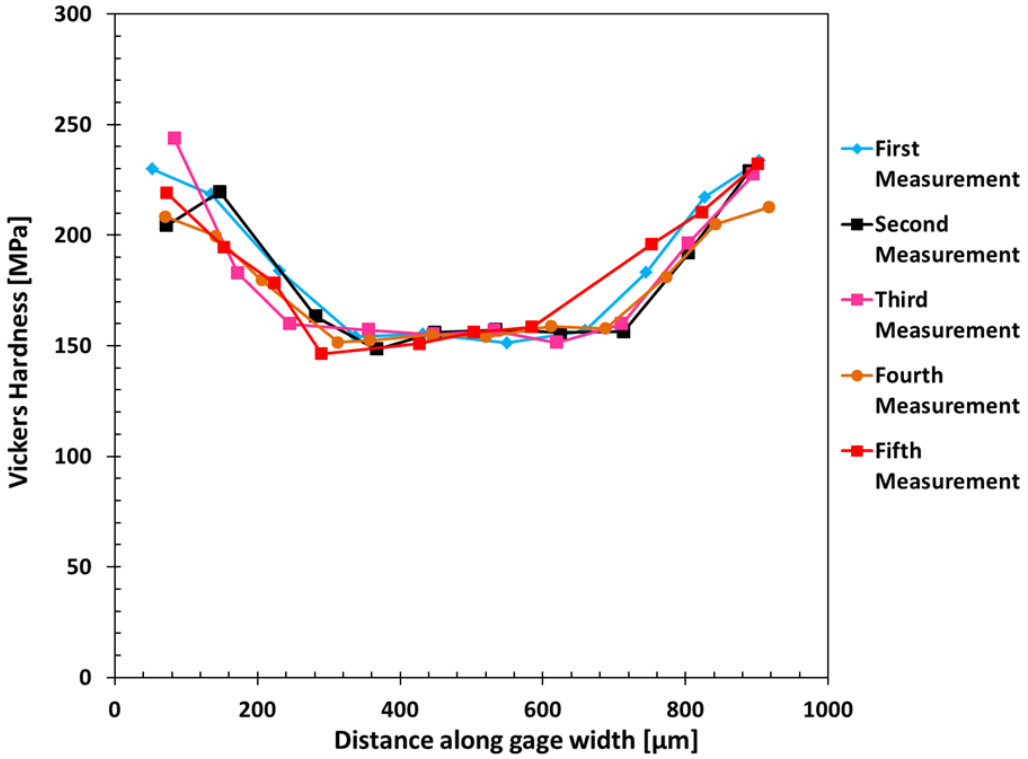

Figure H. 52 - Vickers hardness of specimen EC 5 after polishing of the surface

- **Specimen EC 6:**

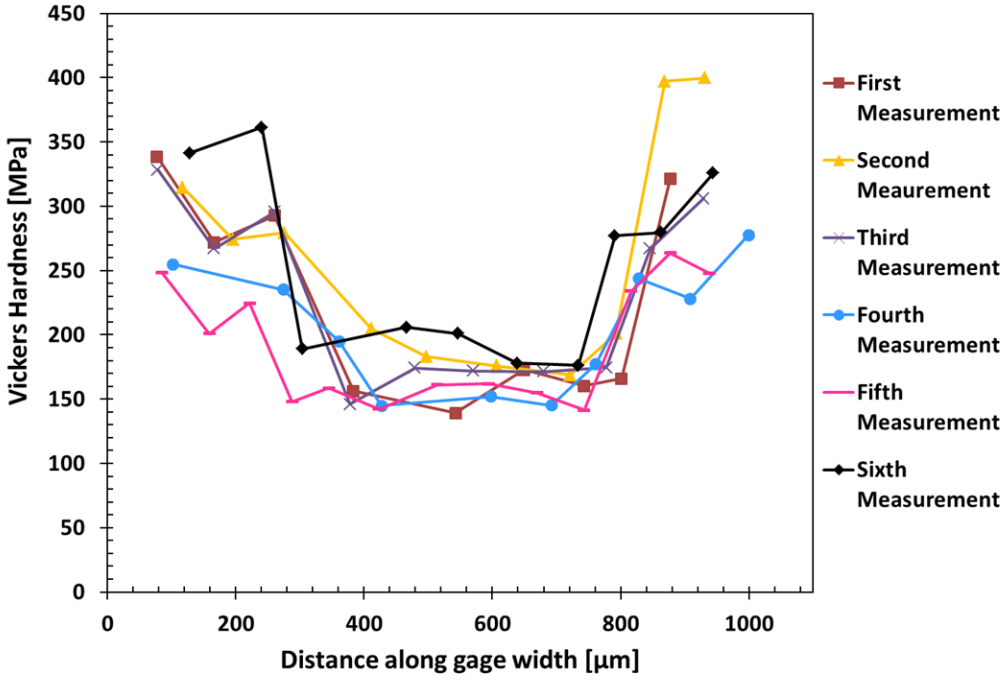

Figure H. 53 - Vickers hardness of specimen EC 6 without polishing of the surface

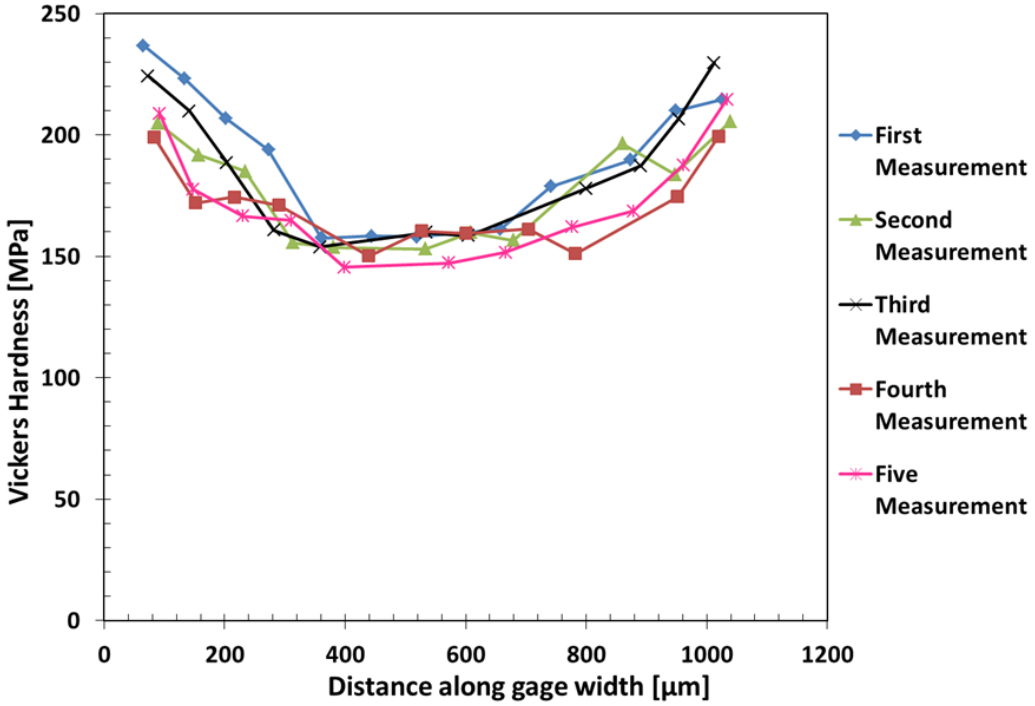

Figure H. 54 - Vickers hardness of specimen EC 6 after polishing of the surface

- **Specimen EC 11:**

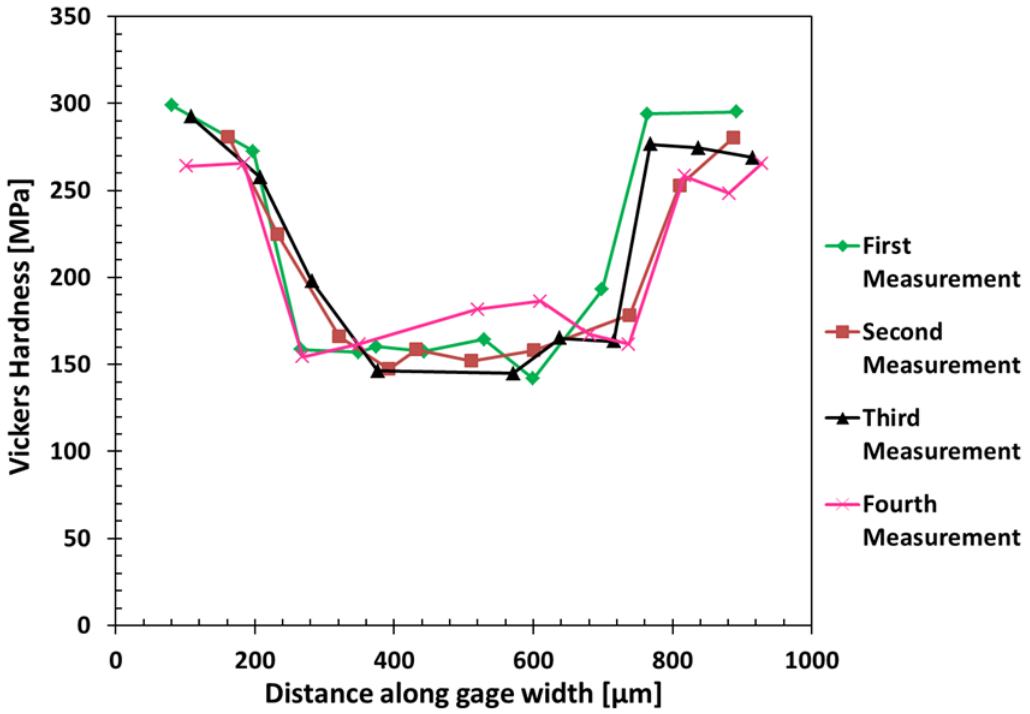

Figure H. 55 - Vickers hardness of specimen EC 11 without polishing of the surface

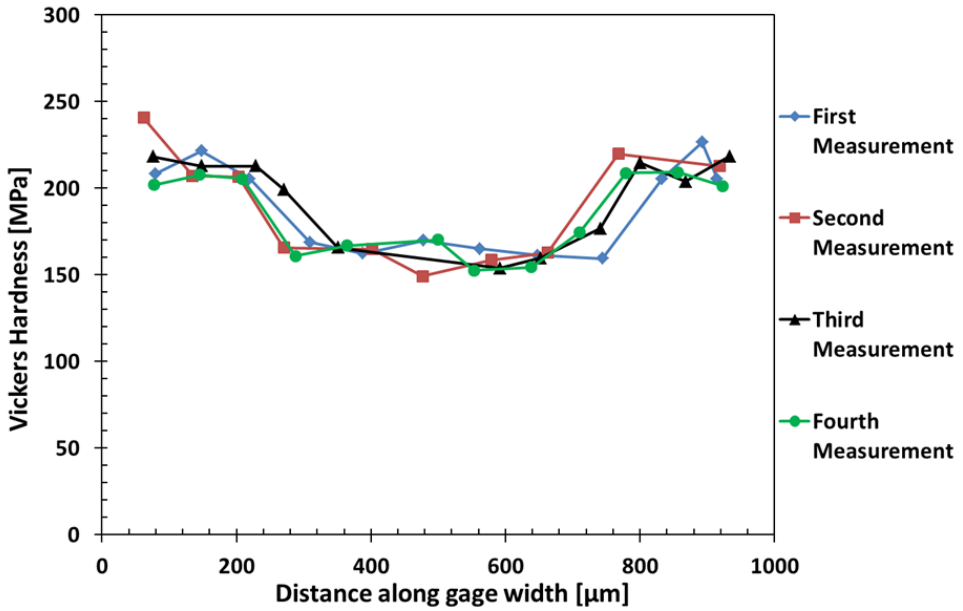

Figure H. 56 - Vickers hardness of specimen EC 11 after polishing of the surface

From Figure H. 57 to Figure H. 63, the hardness gradients of unpolished and polished surfaces of coupons having only 500 µm of FeC film left at the center of the width are plot.

- **Specimen EC 2:**

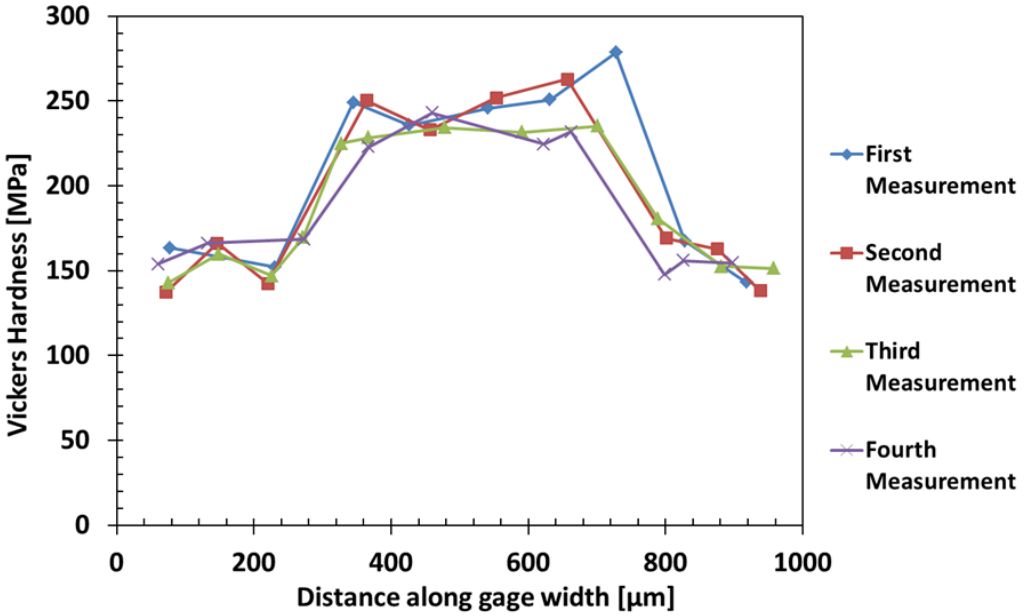

Figure H. 57 - Vickers hardness of specimen EC 2 without polishing of the surface

- **Specimen EC 4:**

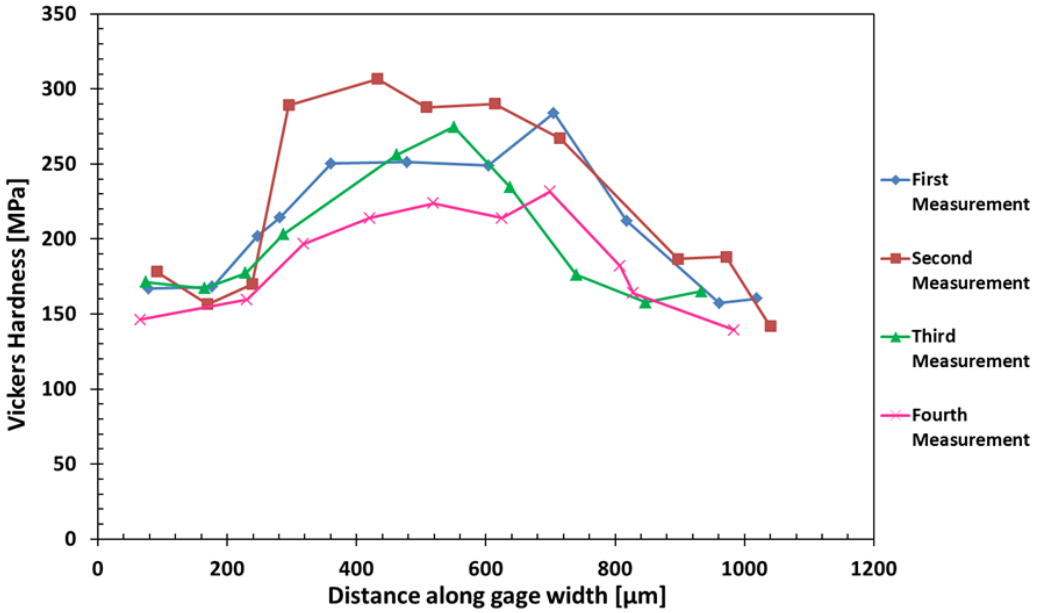

Figure H. 58 - Vickers hardness of specimen EC 4 without polishing of the surface

- **Specimen EC 4:**

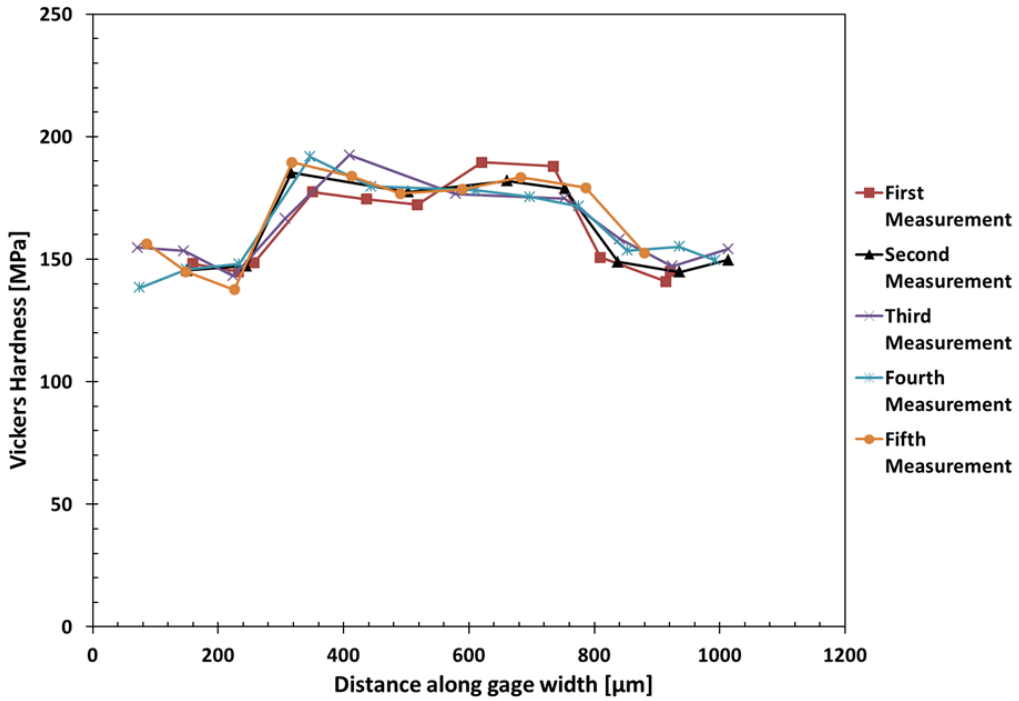

Figure H. 59 - Vickers hardness of specimen EC 4 after polishing of the surface

- **Specimen EC 7:**

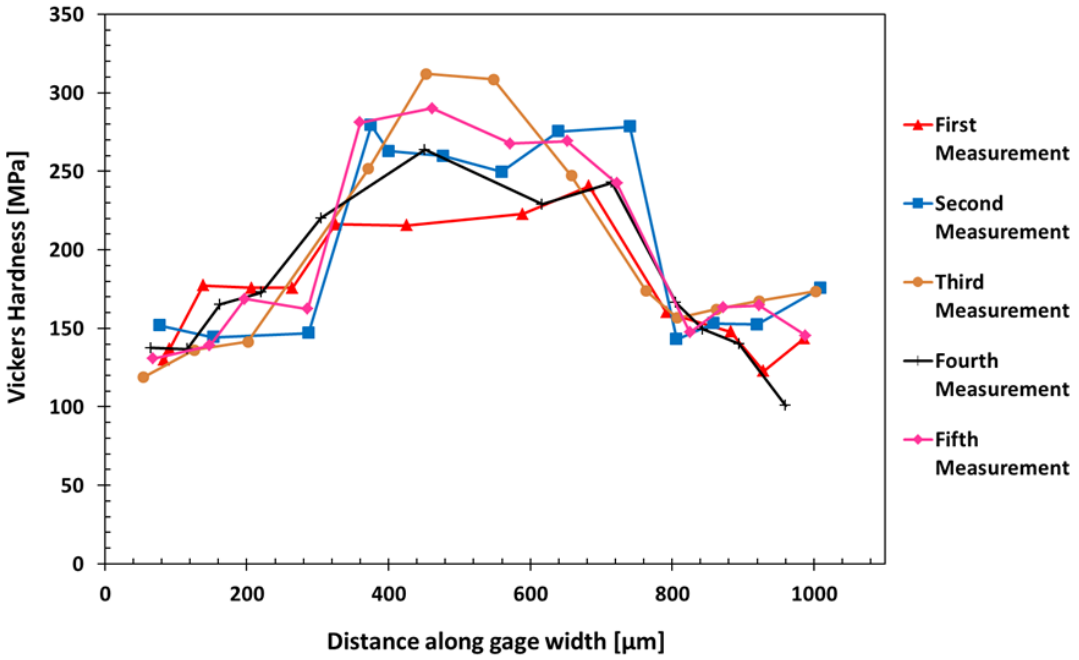

Figure H. 60 - Vickers hardness of specimen EC 7 without polishing of the surface

- **Specimen EC 7:**

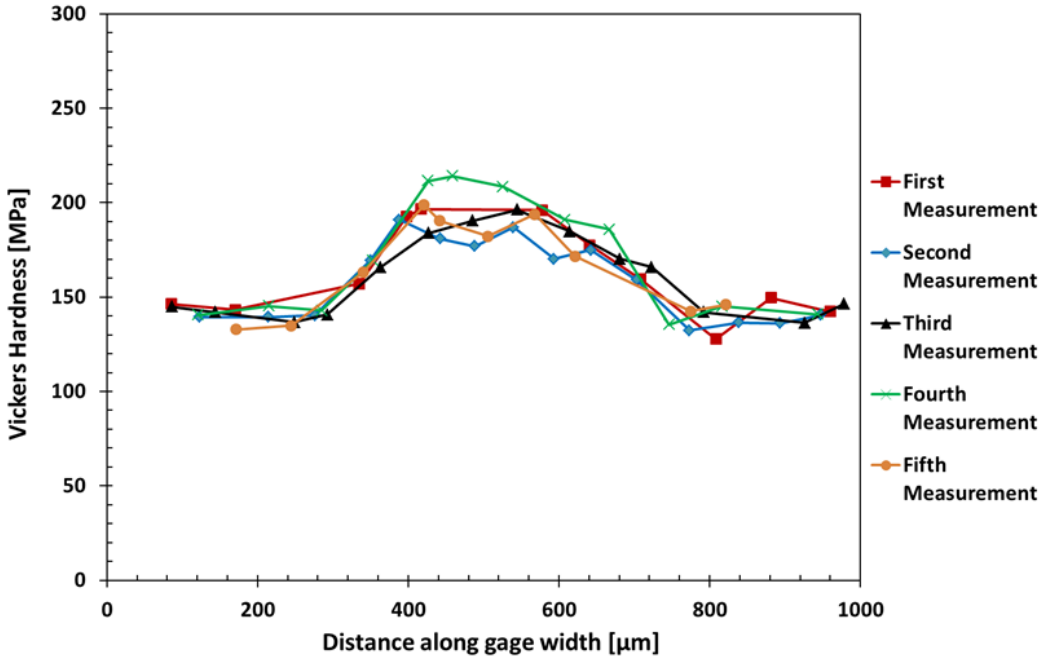

Figure H. 61 - Vickers hardness of specimen EC 7 after polishing of the surface

- **Specimen EC 13:**

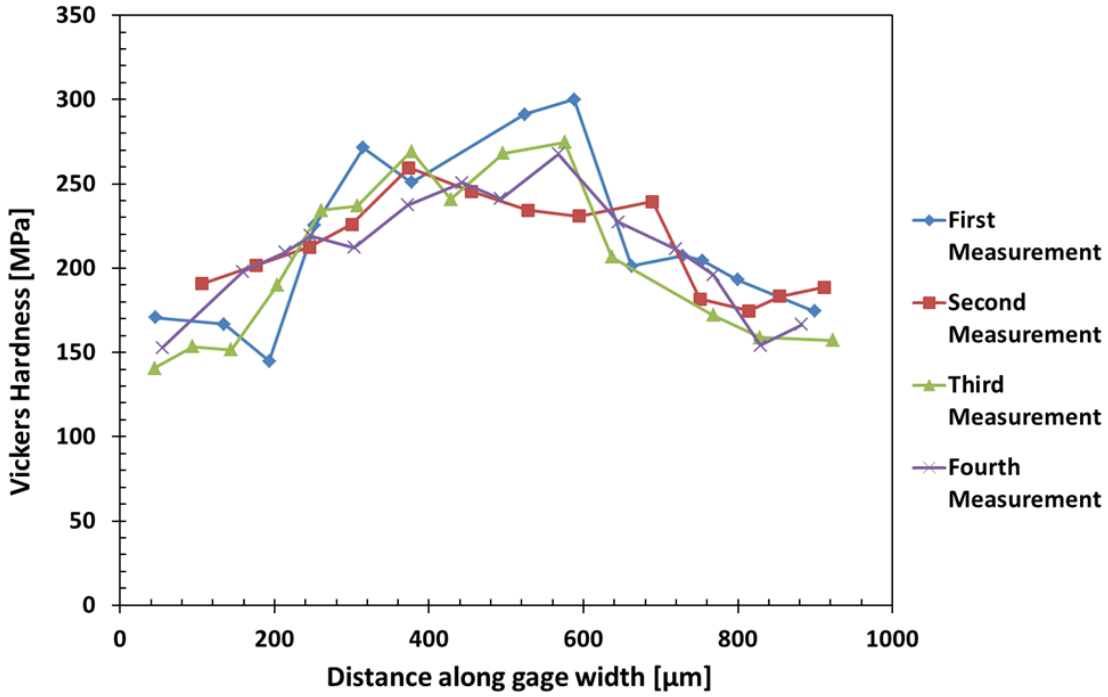

Figure H. 62 - Vickers hardness of specimen EC 13 without polishing of the surface

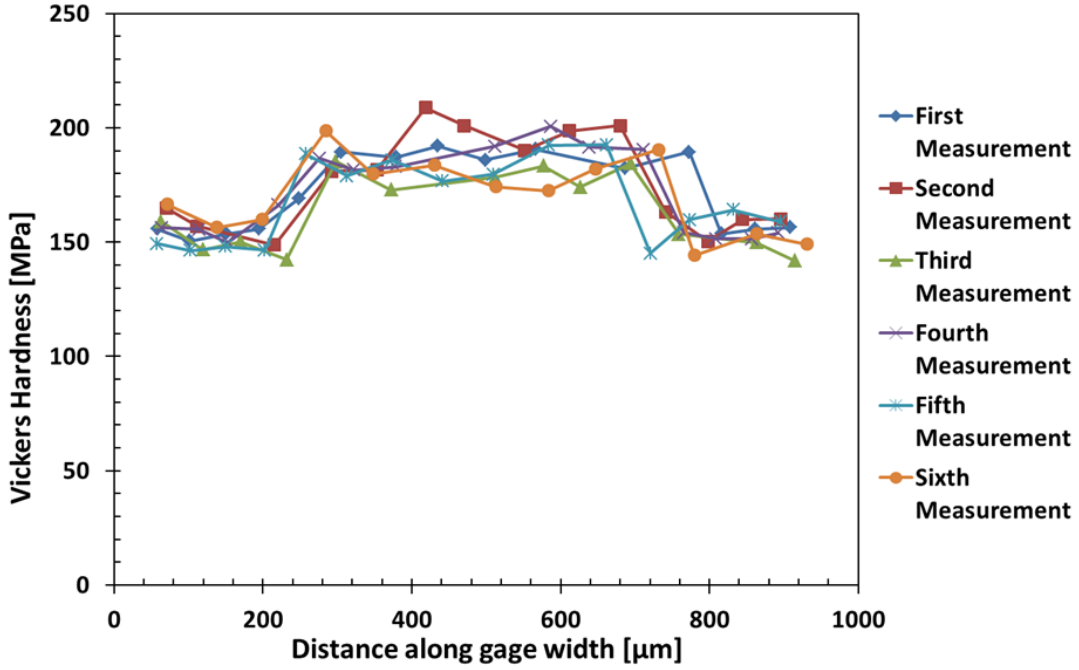

Figure H. 63 - Vickers hardness of specimen EC 13 after polishing of the surface

From Figure H. 64 to Figure H. 69, the graph of the hardness gradient for coupons EC 9, EC 10 and EC 12 are shown. These specimens will then undergo a heat treatment of 12 hours to uniformly distribute the carbon content along the gauge width, however, before these treatments, the show clearly a graded distribution of carbon.

- **Specimen EC 9:**

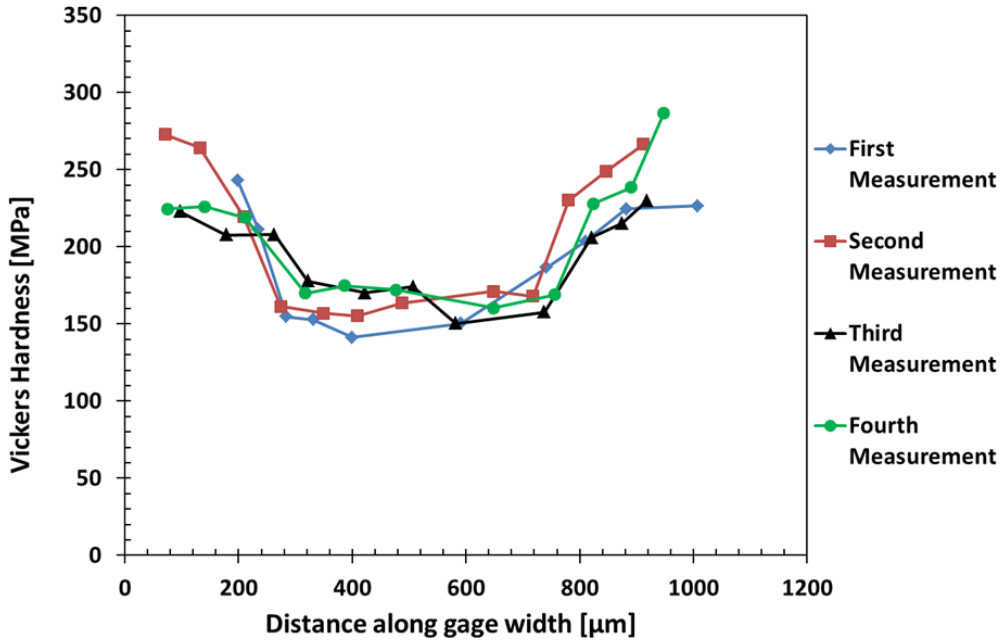

Figure H. 64 - Vickers hardness of specimen EC 9 without polishing of the surface after annealing in high vacuum at 530 ˚C – 1h

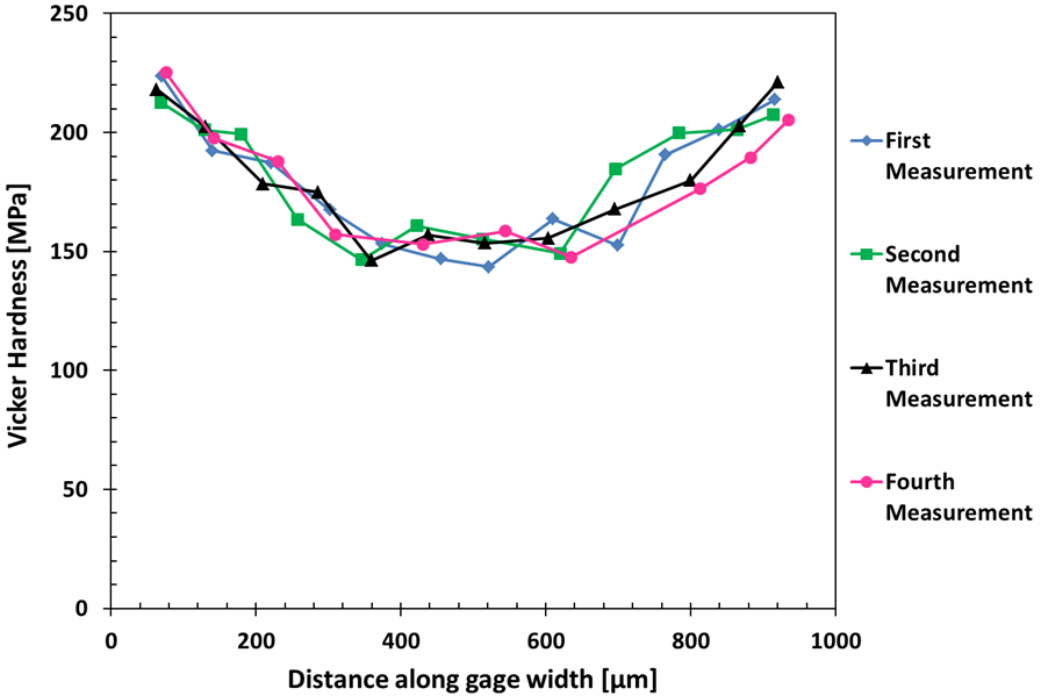

Figure H. 65 - Vickers hardness of specimen EC 9 after polishing of the surface and annealing at 530 ˚C -1h in high vacuum

- **Specimen EC 10:**

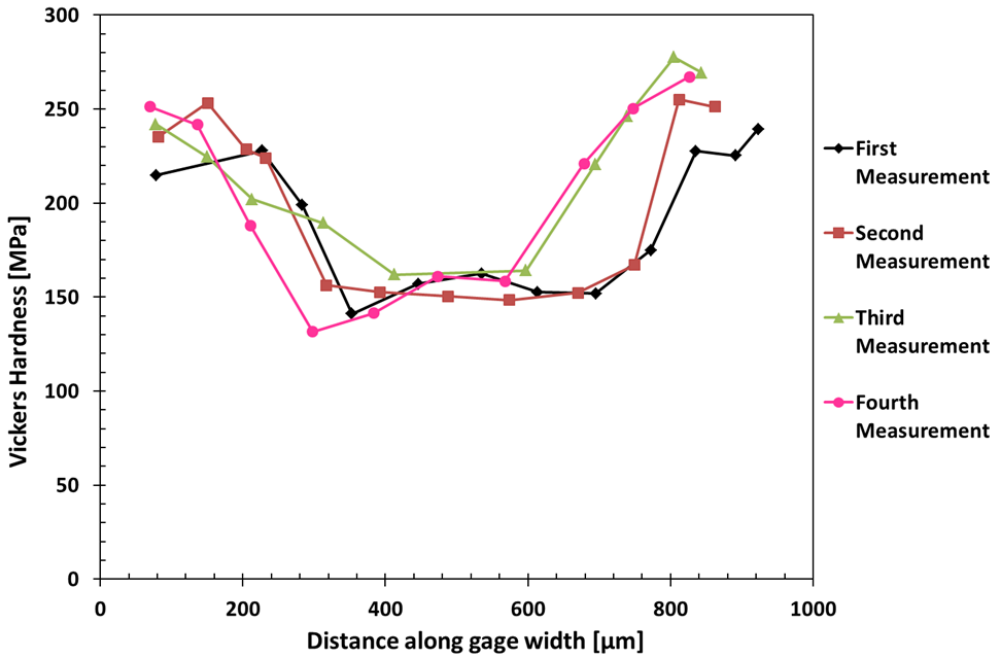

Figure H. 66 - Vickers hardness of specimen EC 10 without polishing of the surface after annealing in high vacuum at 530 ˚C – 1h

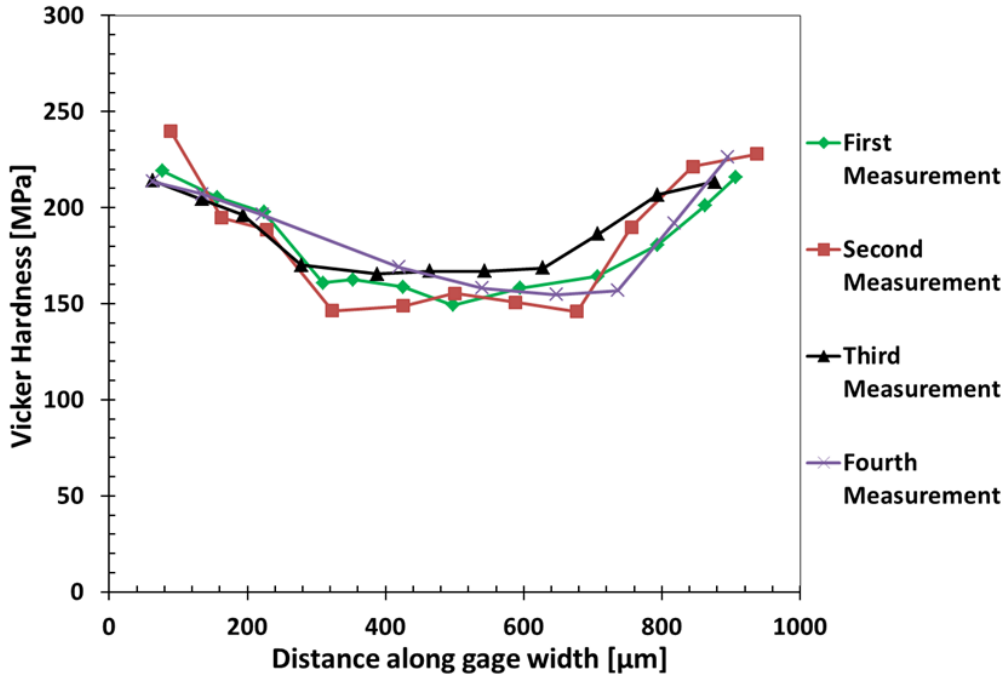

Figure H. 67 - Vickers hardness of specimen EC 10 after polishing of the surface and annealing at 530 ˚C -1h in high vacuum

- **Specimen EC 12:**

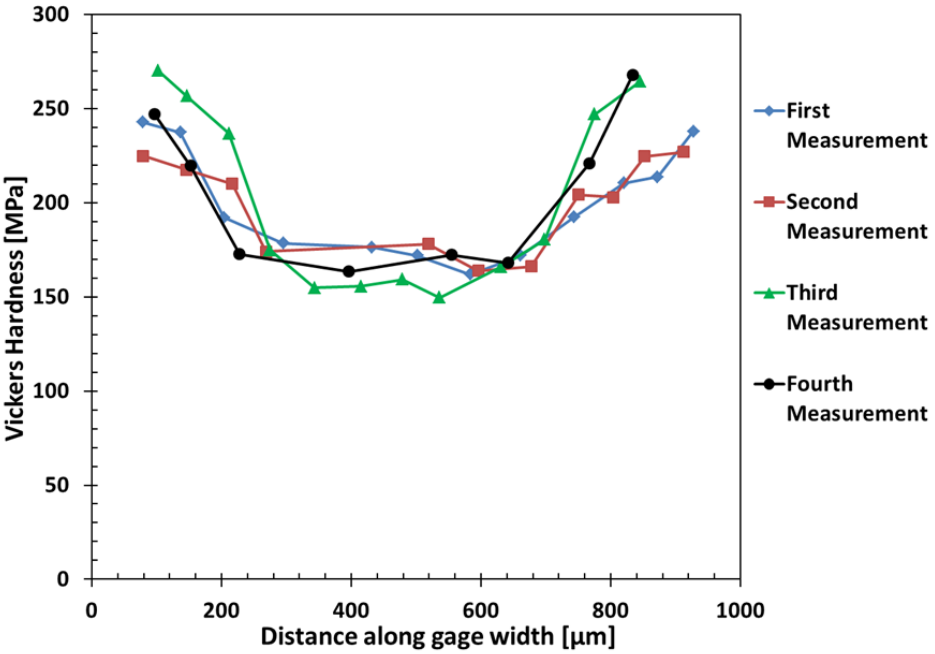

Figure H. 68 - Vickers hardness of specimen EC 12 without polishing of the surface after annealing in high vacuum at 530 ˚C – 1h

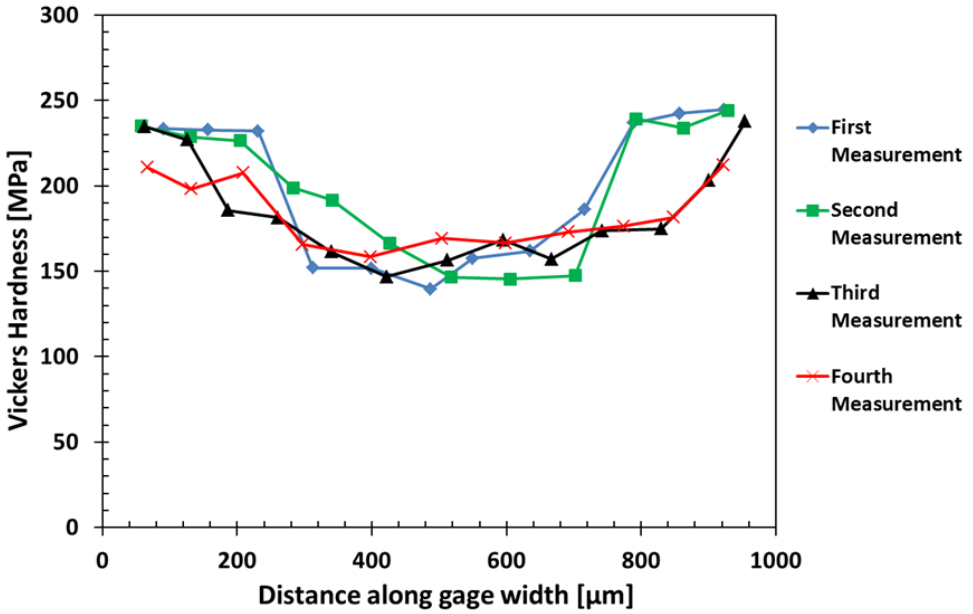

Figure H. 69 - Vickers hardness of specimen EC 12 after polishing of the surface and annealing at 530 ˚C -1h in high vacuum

H.5 Tensile tests of coupons having carbon gradient on the width

Table H- 10 summarizes the dimensions of all the tested coupons.

Specimen	Carbon configuration	Gauge length [mm]	Width [mm]	Thickness [mm]	Speed of tensile test [µm/s]
EC 1	Gradient	5	1	0.178	2.5
EC 2	Gradient	5	1	0.175	2.5
EC 3	Gradient	5	1	0.181	2.5
EC 4	Gradient	5	1	0.184	2.5
EC 5	Gradient	5	1	0.184	2.5
EC 6	Gradient	5	1	0.184	2.5
EC 7	Gradient	5	1	0.179	2.5
EC 9	Uniform	5	1	0.181	2.5
EC 10	Uniform	5	1	0.180	2.5
EC 11	Gradient	5	1	0.186	2.5
EC 12	Uniform	5	1	0.175	2.5
EC 13	Gradient	5	1	0.186	2.5
GW 1	Uncoated	5	1	0.186	2.5
GW 2	Uncoated	5	1	0.185	2.5

Table H- 10 - Dimensions of tested specimens having holes on the gauge width (EC 6 and EC 13 had no voids)

Table H- 11 and Table H- 12 list mechanical properties obtained for the graded configurations. In Table H- 13 values of the mechanical properties for uniform carbon

distribution are listed, while Table H- 14 shows the relevant mechanical properties for uncoated and not-annealed coupons.

Specimen	Upper yield stress [MPa]	Average stress Lueder plateau [MPa]	Lüders length [MPa]	Maximum stress before failure [MPa]	Strain at fracture
EC 1	228	227	0.02927	285	0.19
EC 3	262	249	0.02586	314	0.17
EC 5	233	240	0.02571	300	0.20
EC 6 (no voids)	202 (YS upper Lüders = 236)	232	0.01174	315	0.37
EC 11	237	226	0.04631	292	0.32

Table H- 11 - Summary mechanical properties for tensile coupons having a gradient of carbon obtained by removing 500 μm of FeC film at the centre of the coupon

Specimen	Upper yield stress [MPa]	Average stress Lueder plateau [MPa]	Lüders length [MPa]	Maximum stress before failure [MPa]	Strain at fracture
EC 2	229	228	0.0527	284	0.18
EC 4	229	228	0.0388	301	0.17
EC 7	182	176	0.0072	303	0.27
EC 13 (no voids)	251	236	0.06163	285	0.49

Table H- 12 - Summary mechanical properties for tensile coupons having a gradient of carbon obtained by leaving 500 μm of FeC film at the centre of the coupon

Specimen	Upper yield stress [MPa]	Average stress Lueder plateau [MPa]	Lüders length [MPa]	Maximum stress before failure [MPa]	Strain at fracture
EC 9	153	153	0.0015	287	0.28
EC 10	141	145	0.0031	291	0.27
EC 12	188	-	-	292	0.26

Table H- 13 - Summary mechanical properties for tensile coupons having a uniform distribution of carbon along the gauge width

Specimen	Upper yield stress [MPa]	Maximum stress before failure [MPa]	Strain at fracture
GW 1	114	288	0.18
GW 2	116	298	0.21

Table H- 14 - Summary mechanical properties for uncoated and not-annealed tensile coupons

Figure H. 70 and Figure H. 71 show the DIC results of uncoated coupons.

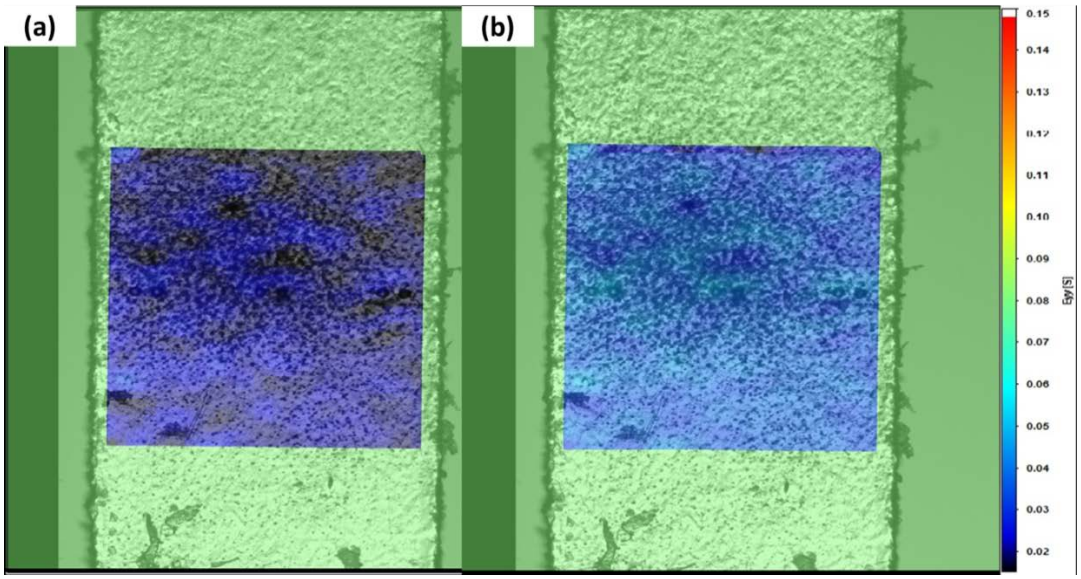

Figure H. 70 - Starting of the deformation for uncoated and not-annealed specimen (GW 1); progressing of the deformation for uncoated and not-annealed specimen (GW 1)

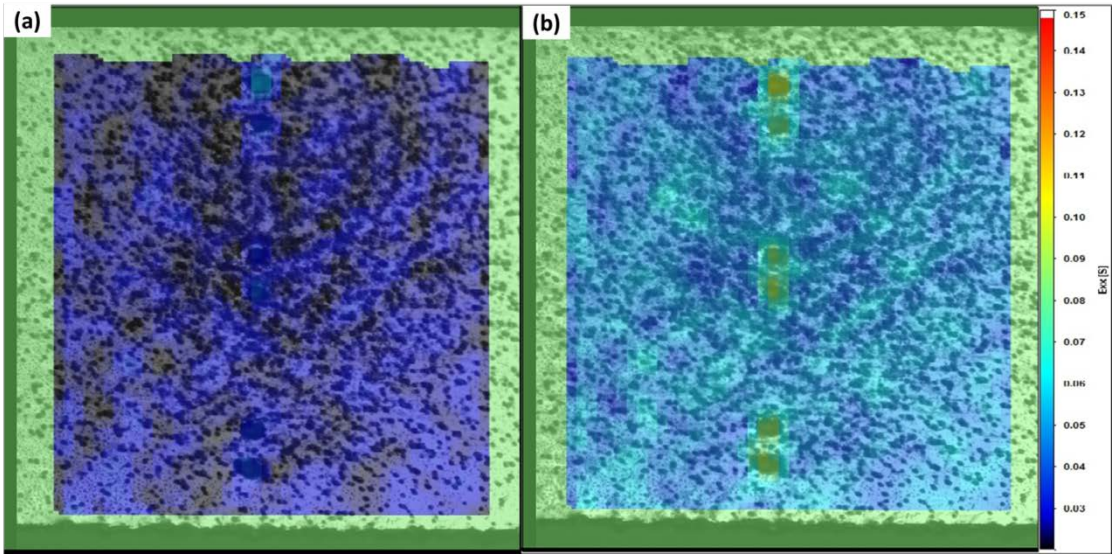

Figure H. 71 - Starting of the deformation for uncoated and not-annealed specimen (GW 2) progressing of the deformation for uncoated and not-annealed specimen (GW 2)

H.5.1 Theoretical yield stress calculation for coupons having gradient along the gauge width

The yield stress of coupons having gradient along the gauge width can be predicted by using a rule of mixture. Indeed, the yield stress can be expressed as:

$$YS_{specimen} = \left(YS_{coated} \times V_{f,coated}\right) + \left(YS_{graded} \times V_{f,graded}\right) \qquad \text{(eq. H- 2)}$$

where:

$YS_{specimen}$ is the yield stress for the whole coupon;

YS_{coated} is the yield stress corresponding to the coated zones of the gauge width;

YS_{graded} is the yield stress of the carbon graded zone;

$V_{f,\,coated}$ is the volume fraction of the coated zones of the gauge width;

$V_{f,\,graded}$ is the volume fraction of the carbon graded zone.

This calculation was first performed for specimens having 500 µm film removed from the center of the width and annealed at 530 ºC for 1h. In the coated zones, the amount of carbon which has been diffused is supposed to be equal to the solubility limit at 530 ºC (i.e. 0.026 at%). Again, using eq. 5-2, the corresponding yield stress can be calculated and it is 284.5 MPa. Then, the central zone of the gauge width has a carbon gradient and the corresponding yield stress can be obtained from the carbon distribution predicted by Fick`s law (see values reported in Table H- 4). The yield stress for the graded zone is 228 MPa and it is calculated by doing an average of the yield stresses from AV to AV8 reported in Table H- 4 for annealing at 530 ºC. Concerning the volume fractions, even if the FeC film has been ablated in 500 µm, in reality the graded zone is expected to cover only 400 µm since at the interface between the coated zone and the ablated zone, there will be a uniform carbon distribution due to heating and cooling ramps of the heat treatment. For this reason, the volume fraction of the graded zone is 40% and the volume fraction of the coated zone is 60%. Substituting the numerical values in eq. H- 2:

$$YS_{specimen} = \left(228 \times 0.4\right) + \left(284.5 \times 0.6\right) = 261.9 MPa$$

This value is in good agreement with the experimental yield stresses obtained for coupons EC1, EC3 and EC5, whose yield stresses were 228 MPa, 262 MPa, 233 MPa respectively.

The same calculation holds for the configurations where 500 µm film have been left in the center (i.e. coupons EC2 and EC4).

Yield stress can be predicted also for coupons having annealing at 530 ºC for times shorter then 1h (for example coupon EC 11 annealed for 30 min). In this case, the coated zones will have a yield stress of 284.5 MPa, while the yield stress of the graded zone can be obtained from the carbon distribution given by the Fick`s law (see Table H- 8). This yield stress is 200 MPa, which is calculated by doing an average of the yield stresses from AV to AV8 reported in Table H- 8 for annealing at 530 ºC for 30 minutes. Substituting these values in the rule of mixture:

$$YS_{specimen} = (200 \times 0.4) + (284.5 \times 0.6) = 250.7 MPa$$

This theoretical value of the yield stress is in good agreement with the yield stress (237.4 MPa) obtained experimentally for coupon EC11.

The same procedure can be applied to predict the yield stress for coupons having uniform carbon distribution (EC9, EC10, EC12). From the 500 µm of coated width, the amount of carbon that will be diffused is supposed to be equal to the solubility limit at 530 ºC (i.e. 0.026 at%). This carbon concentration has then to be diluted in the other 500 µm of width that have been ablated. Based on this, the final carbon concentration in the coupon shold be (0.026/2) = 0.013 at%, which corresponds to 232 MPa of yield stress. However, the yield stresses found experimentally were all lower then this value; in particular, EC9 had a yield stress of 153 MPa, EC10 of 141 MPa and EC 12 of 188 MPa. The discrepancy could be due to low carbon concentration in the FeC film. If the film contains only 27 at% of carbon, then the maximum amount of carbon that can be diffused after its crystallization would be 0.01337 at%, which diluted in the whole width would give (0.01337/2) = 6.68×10^{-3} at%. This wold correspond to a yield stress of 198 MPa, which is very close to the value obtained for EC12. The amount of carbon that can be diffused could be even lower if the thickness of the film is below the nominal value of 500 nm. Moreover, for these coupons, an old batch of specimens deposited in 2013 was used while the fracture tests had been performed in 2015.

H.6 Void growth analyses

H.6.1 Void growth of specimens having FeC film removed in the center

From Figure H. 72 until Figure H. 93 the graphs related to the extraction of the void growth for coupons having 500 µm of FeC film ablated in the center of the width are shown.

- **Specimen EC 1: central couple**

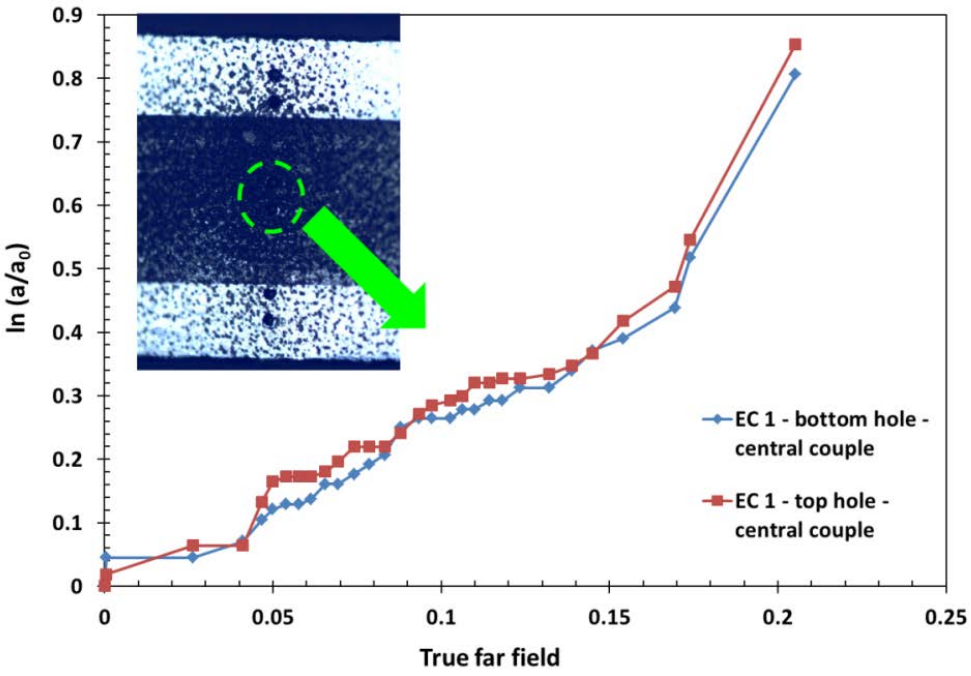

Figure H. 72 - Local true strain versus true far field strain for central couple of holes of specimen EC 1

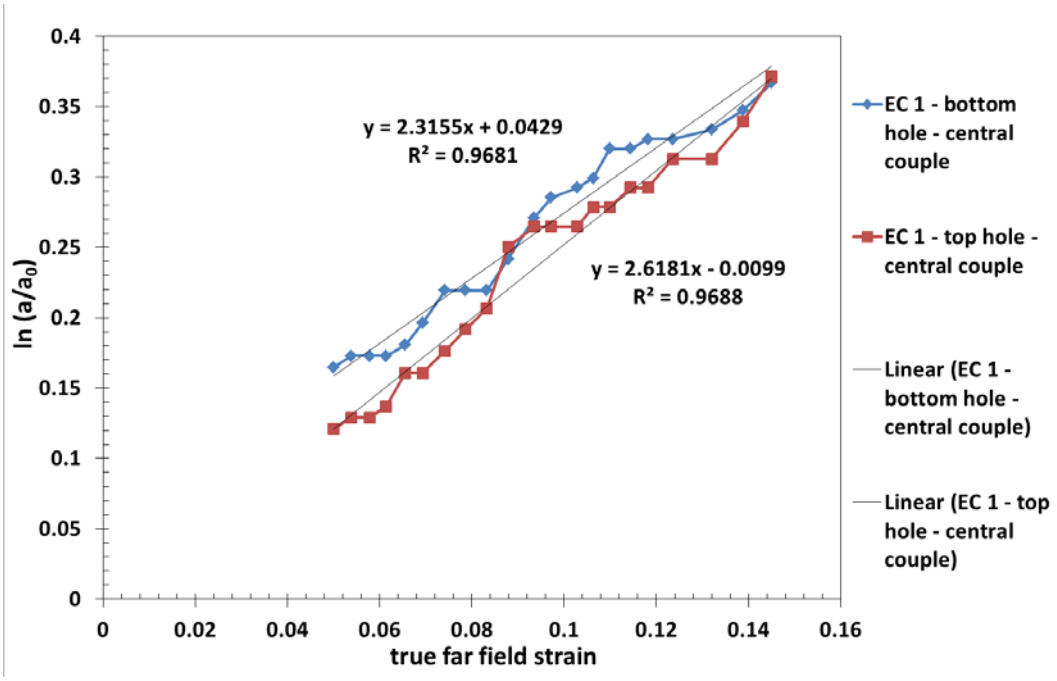

Figure H. 73 - Linear slope of local true strain versus true far field strain of the central couple of holes for specimen EC 1

- **Specimen EC 1: top couple**

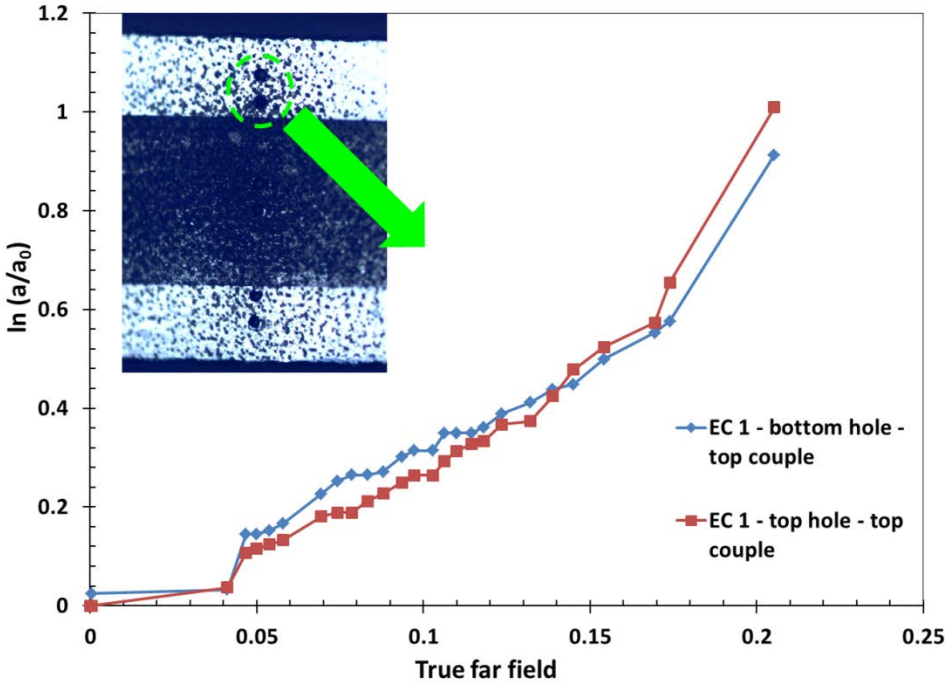

Figure H. 74 - Local true strain versus true far field strain for top couple of holes of specimen EC 1

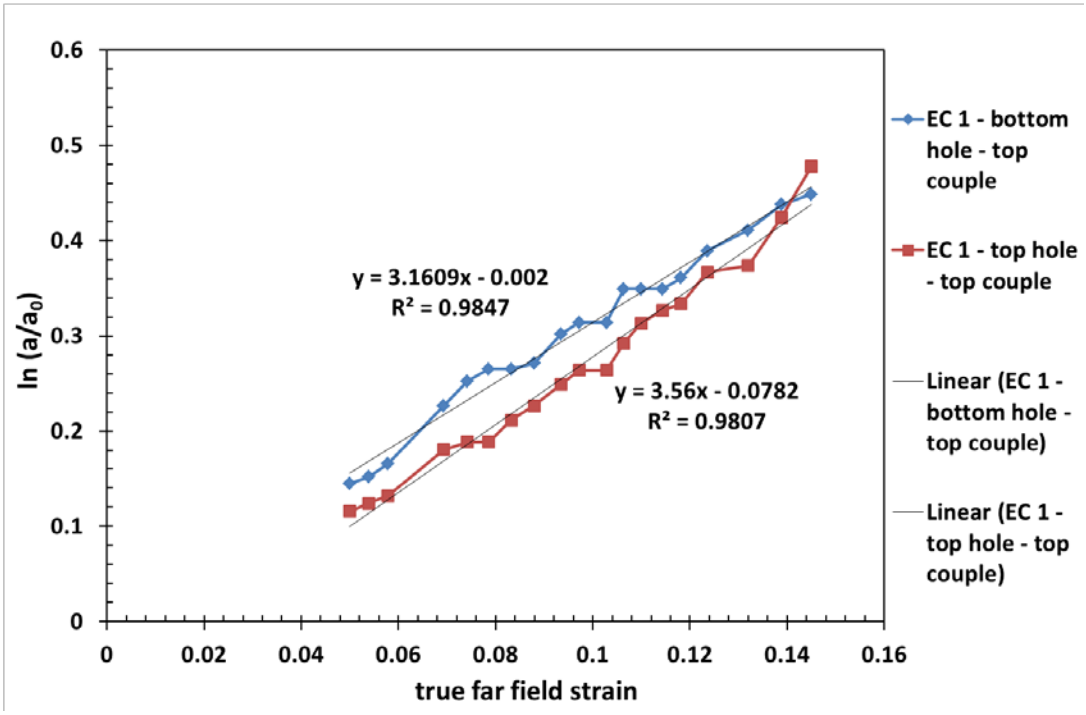

Figure H. 75 - Linear slope of local true strain versus true far field strain of the top couple of holes for specimen EC 1

- **Specimen EC 3: bottom couple**

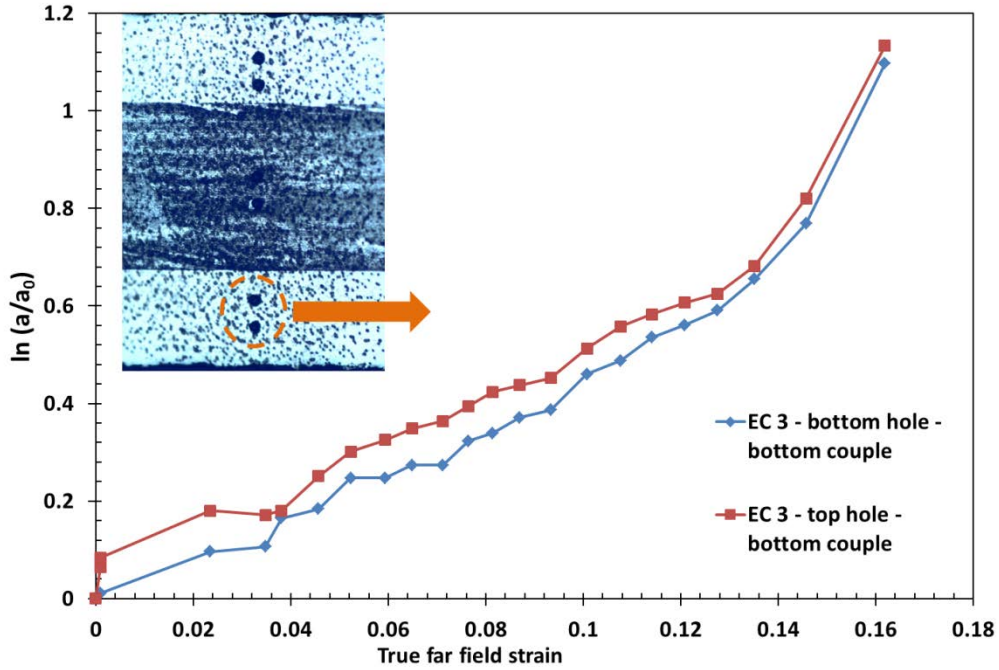

Figure H. 76 - Local true strain versus true far field strain for bottom couple of holes of specimen EC 3

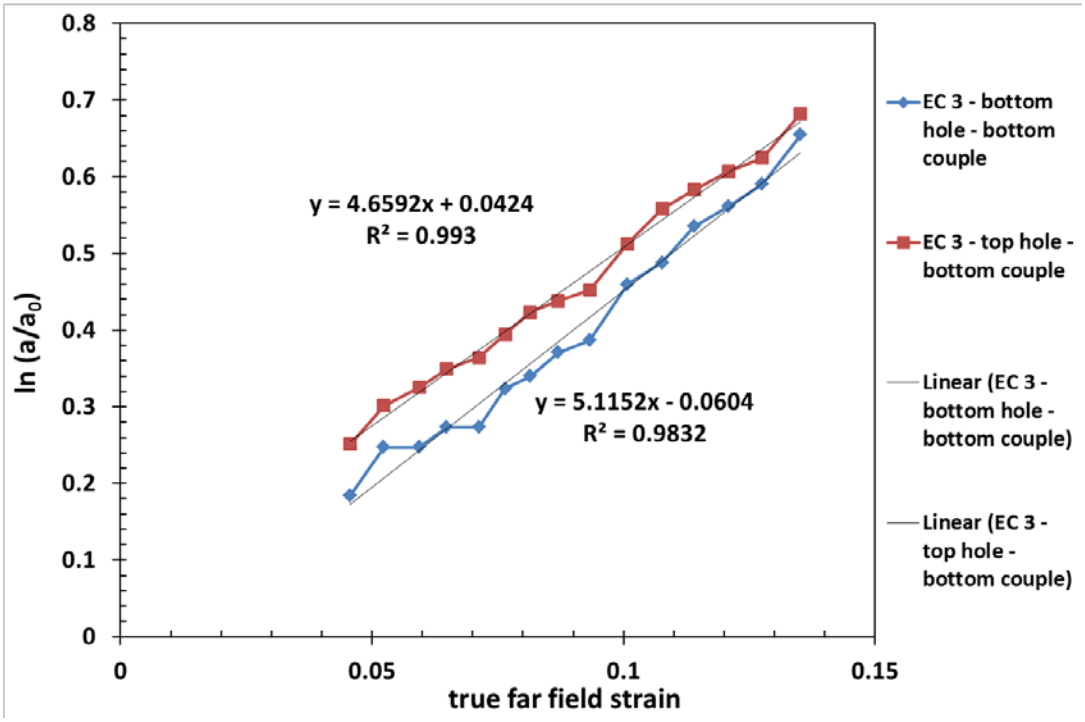

Figure H. 77 - Linear slope of local true strain versus true far field strain of the bottom couple of holes for specimen EC 3

- **Specimen EC 3: central couple**

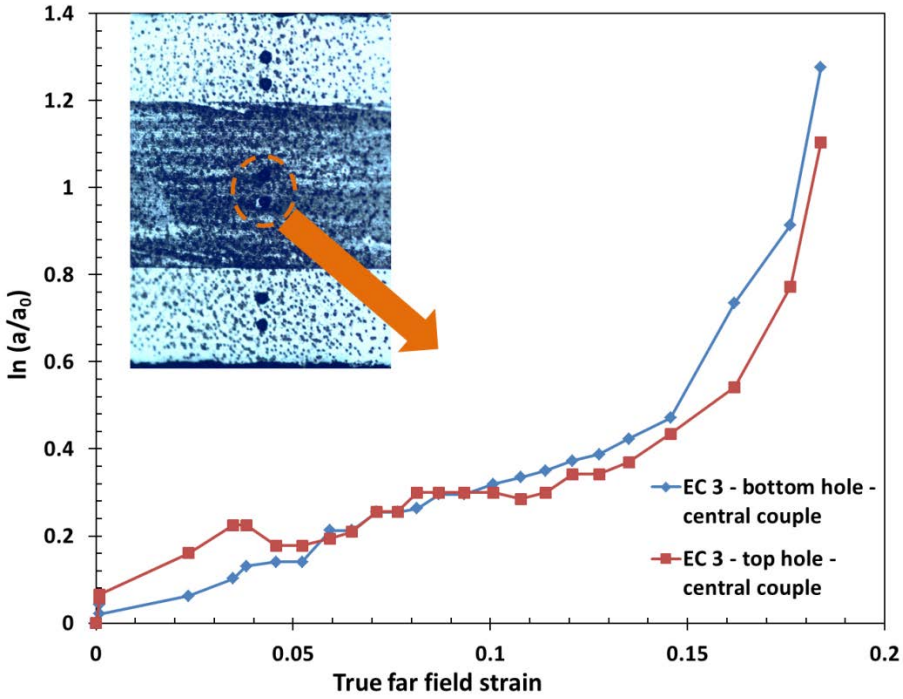

Figure H. 78 - Local true strain versus true far field strain for central couple of holes of specimen EC 3

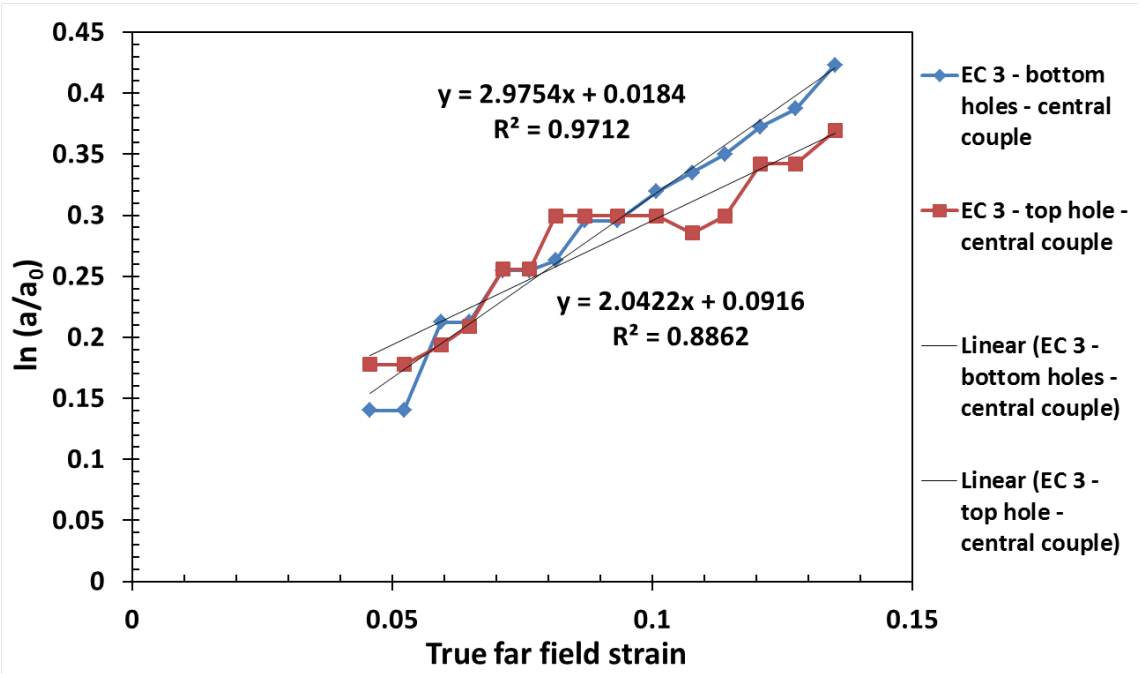

Figure H. 79 - Linear slope of local true strain versus true far field strain of the central couple of holes for specimen EC 3

- **Specimen EC 3: top couple**

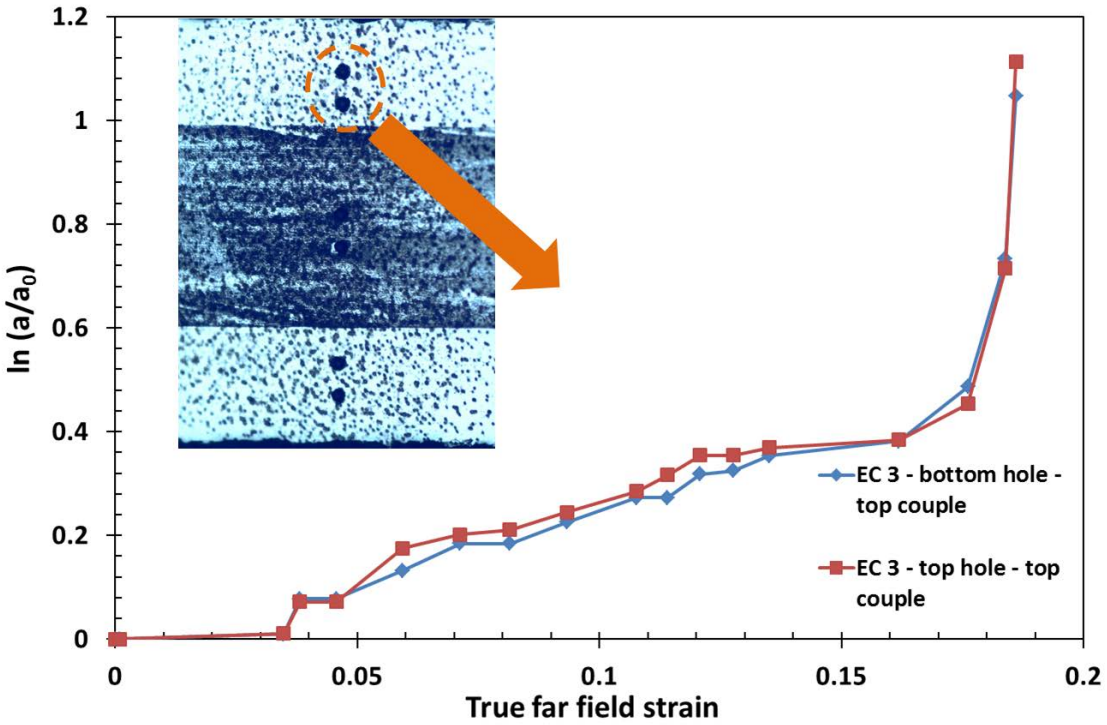

Figure H. 80 - Local true strain versus true far field strain for top couple of holes of specimen EC 3

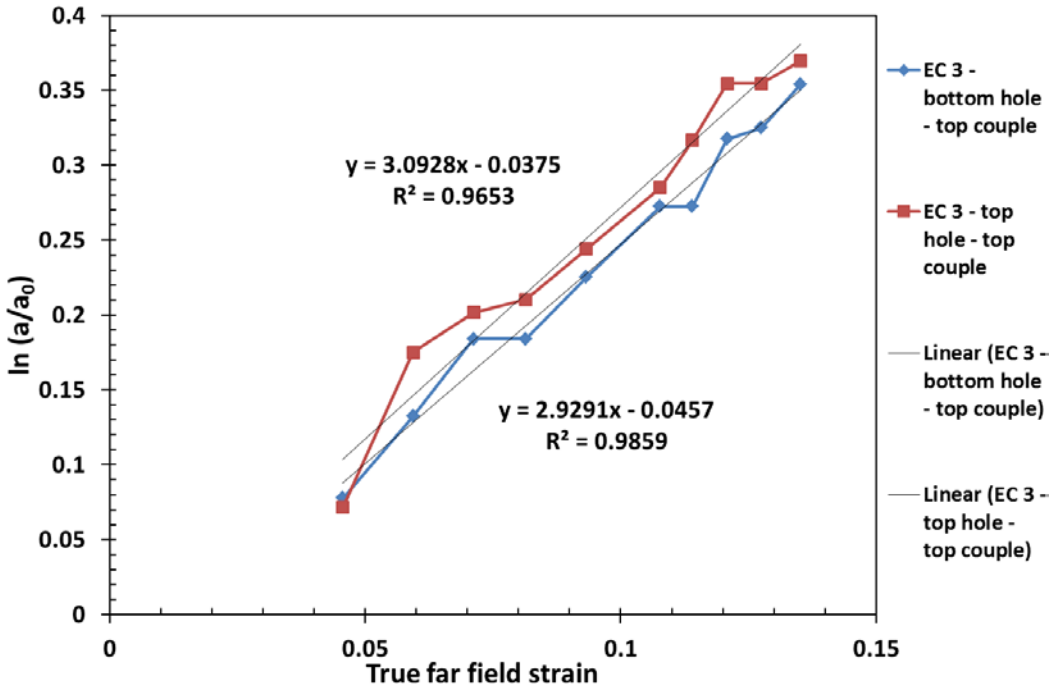

Figure H. 81 - Linear slope of local true strain versus true far field strain of the top couple of holes for specimen EC 3

- **Specimen EC 5: bottom couple**

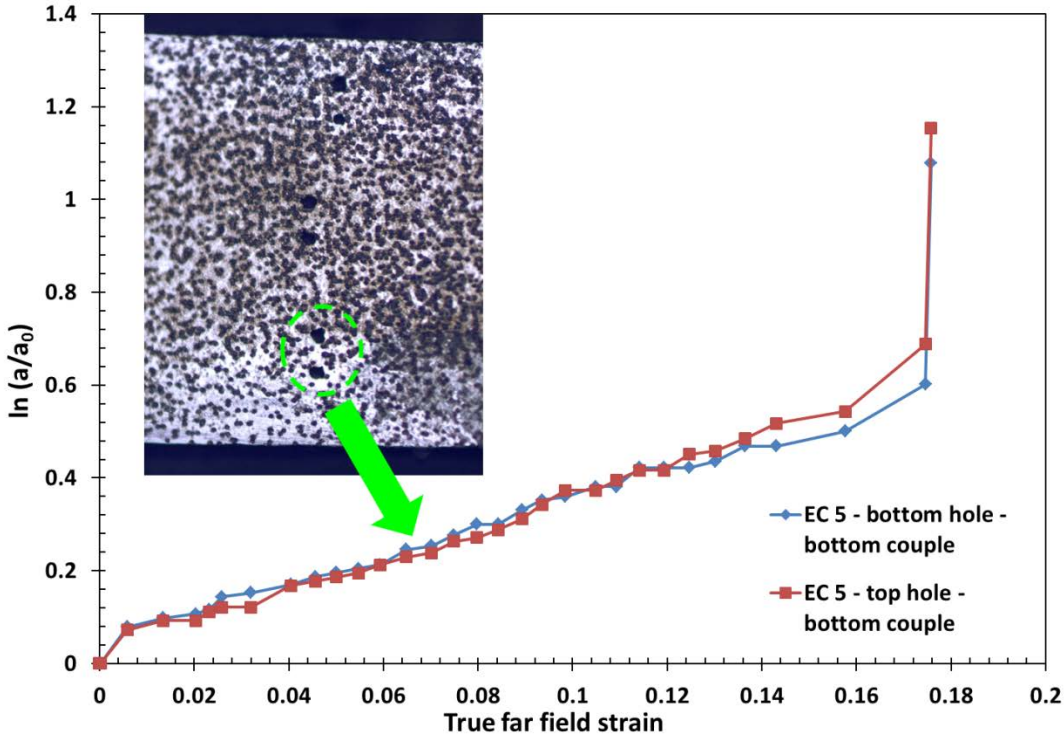

Figure H. 82 - Local true strain versus true far field strain for bottom couple of holes of specimen EC 5

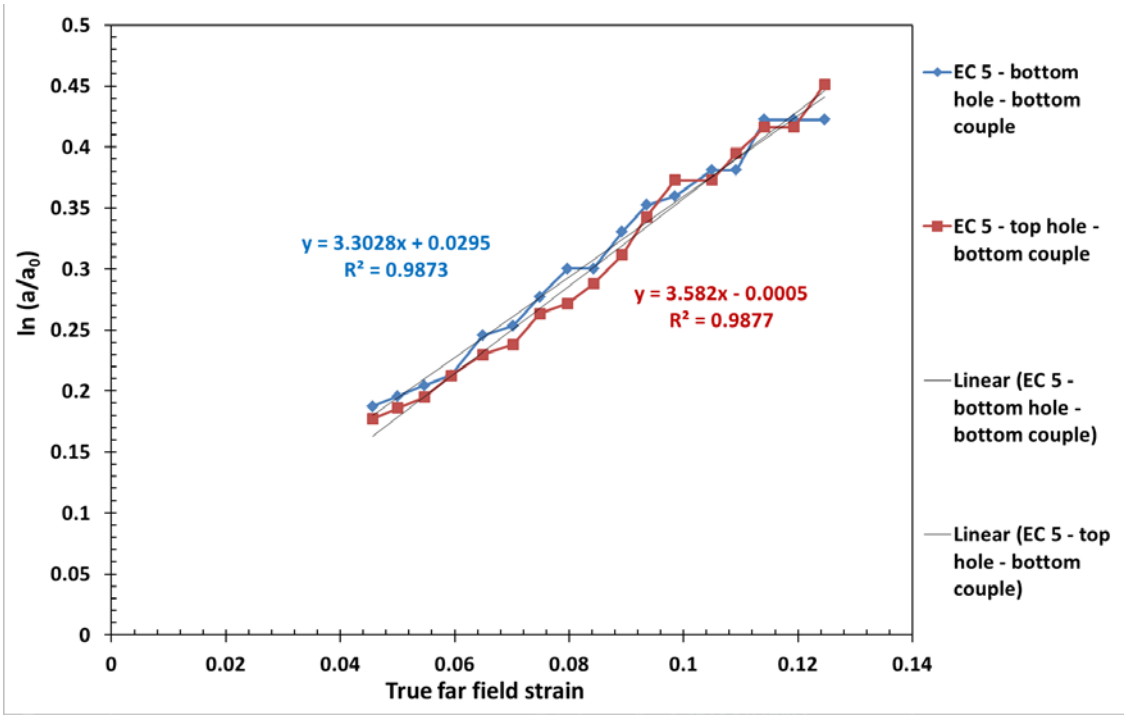

Figure H. 83 - Linear slope of local true strain versus true far field strain of the bottom couple of holes for specimen EC 5

- **Specimen EC 5: central couple**

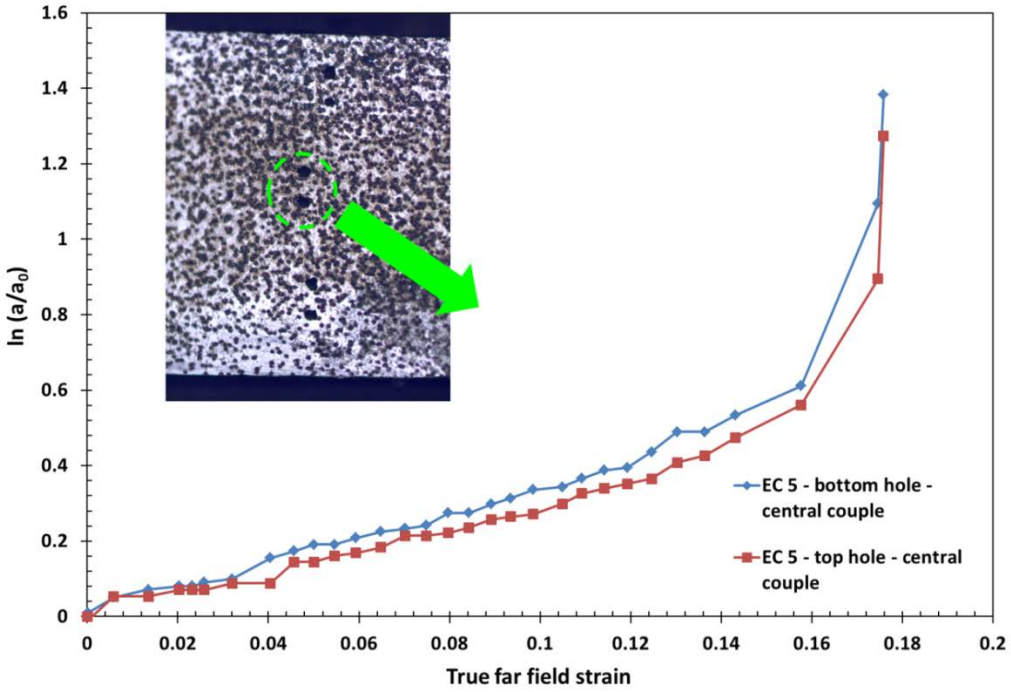

Figure H. 84 - Local true strain versus true far field strain for central couple of holes of specimen EC 5

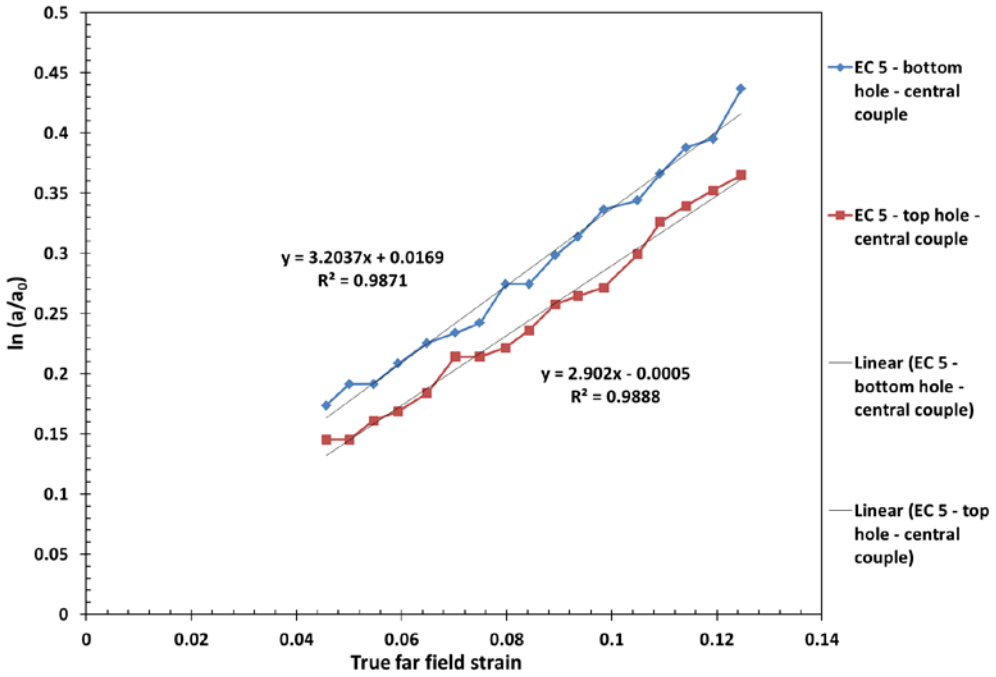

Figure H. 85 - Linear slope of local true strain versus true far field strain of the central couple of holes for specimen EC 5

- **Specimen EC 5: top couple**

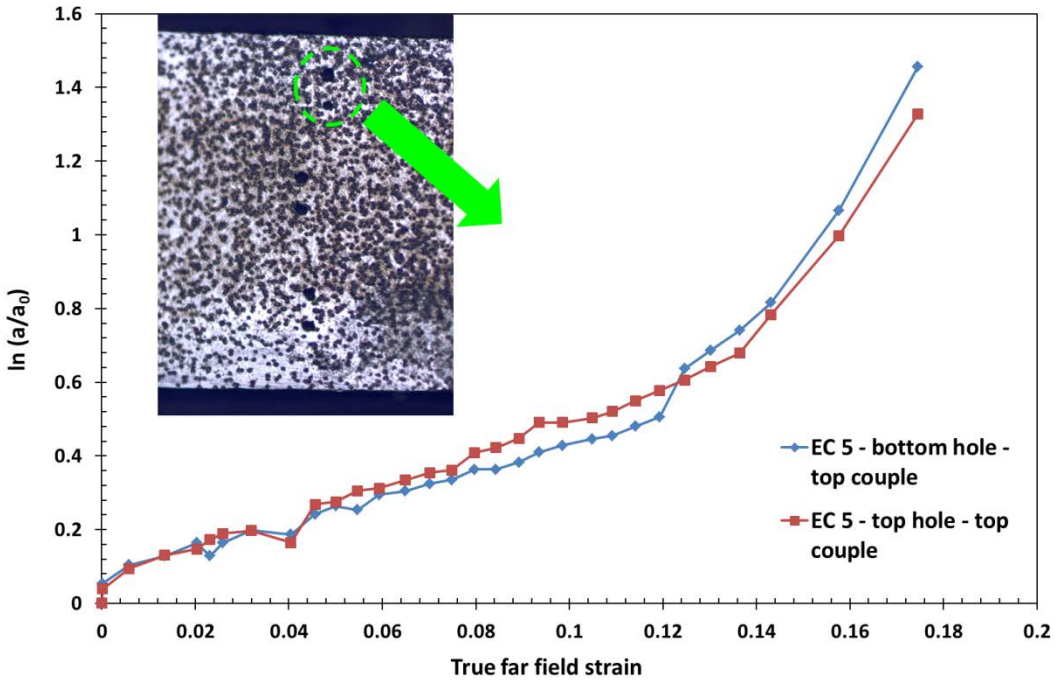

Figure H. 86 - Local true strain versus true far field strain for top couple of holes of specimen EC 5

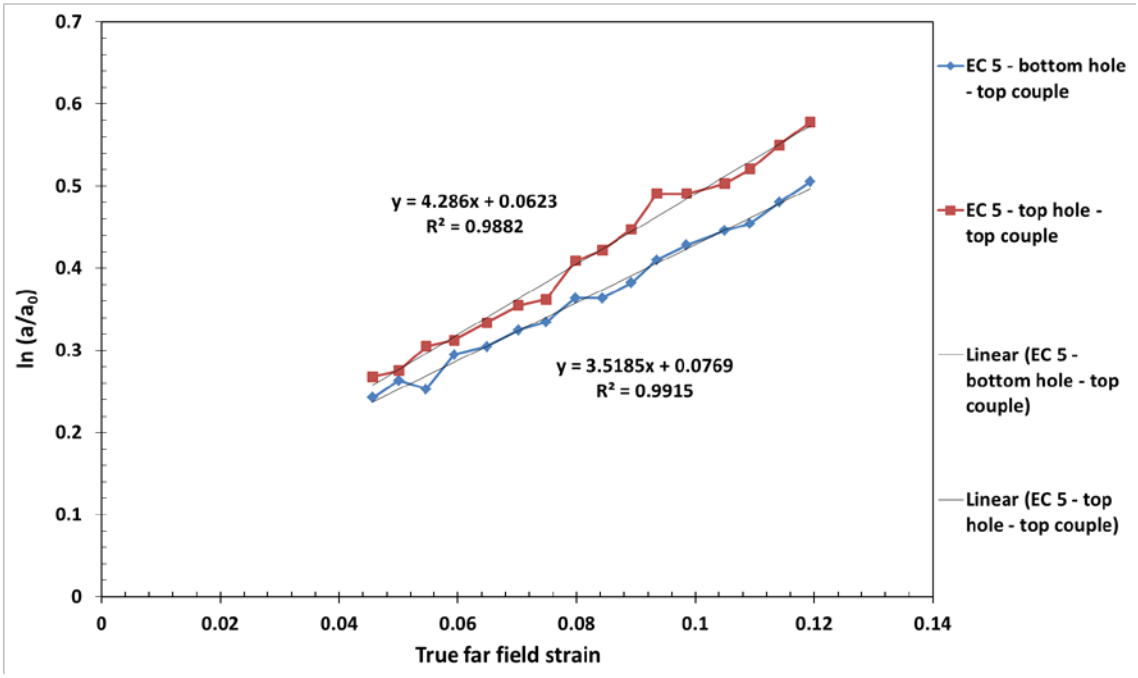

Figure H. 87 - Linear slope of local true strain versus true far field strain of the top couple of holes for specimen EC 5

- **Specimen EC 11: bottom couple**

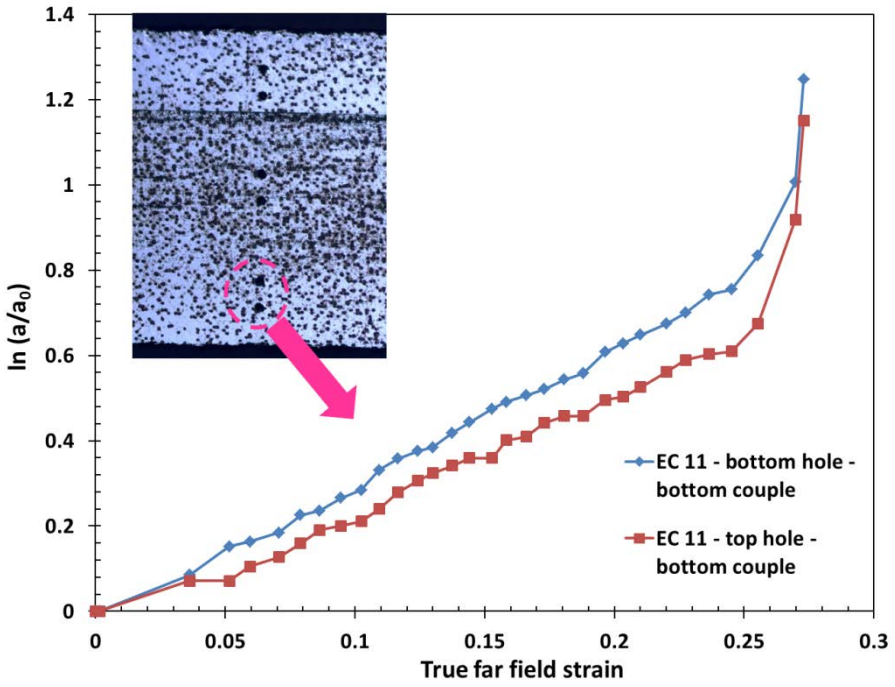

Figure H. 88 - Local true strain versus true far field strain for bottom couple of holes of specimen EC 11

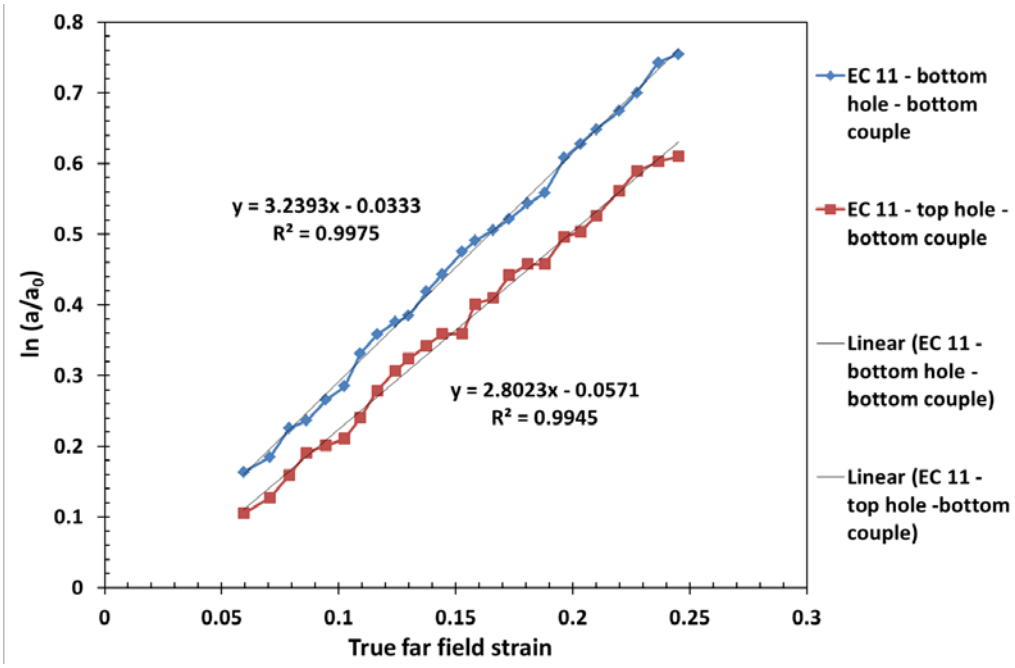

Figure H. 89 - Linear slope of local true strain versus true far field strain of the bottom couple of holes for specimen EC 11

- **Specimen EC 11: central couple**

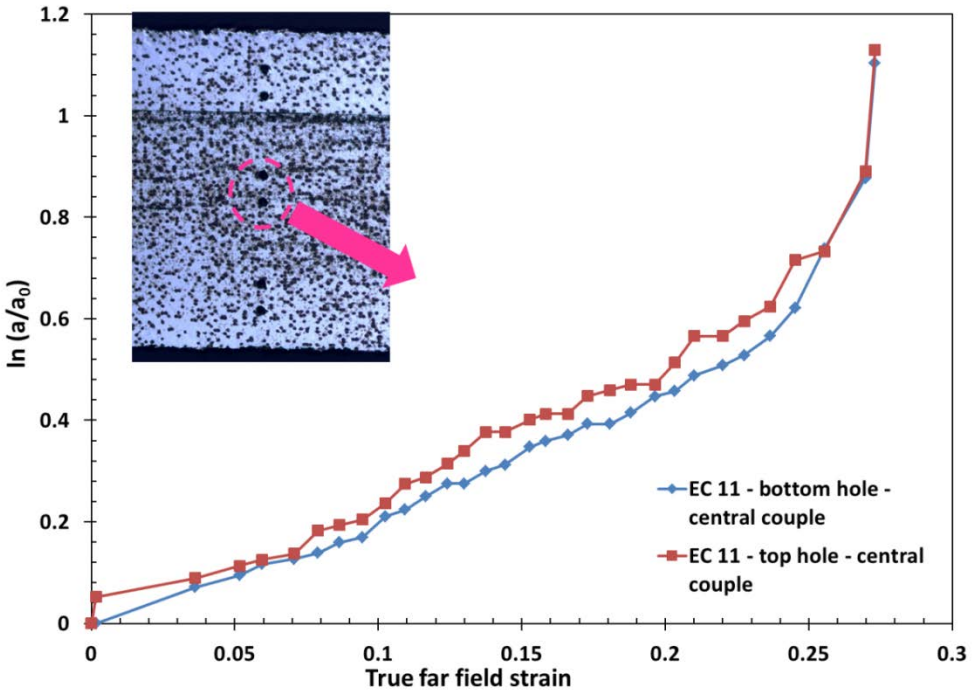

Figure H. 90 - Local true strain versus true far field strain for central couple of holes of specimen EC 11

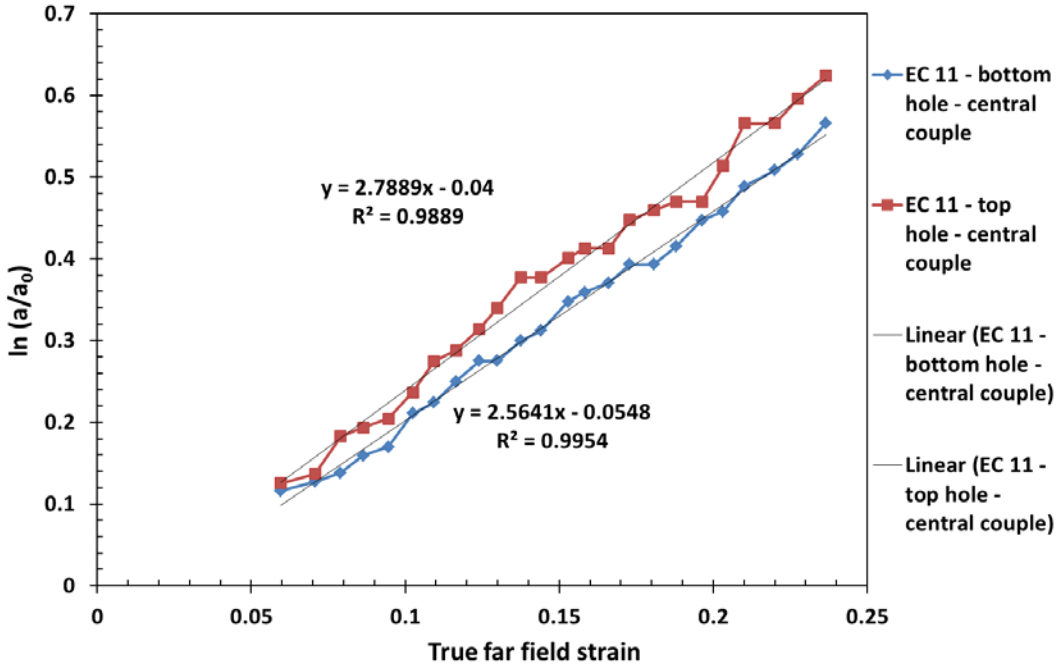

Figure H. 91 - Linear slope of local true strain versus true far field strain of the central couple of holes for specimen EC 11

- **Specimen EC 11: top couple**

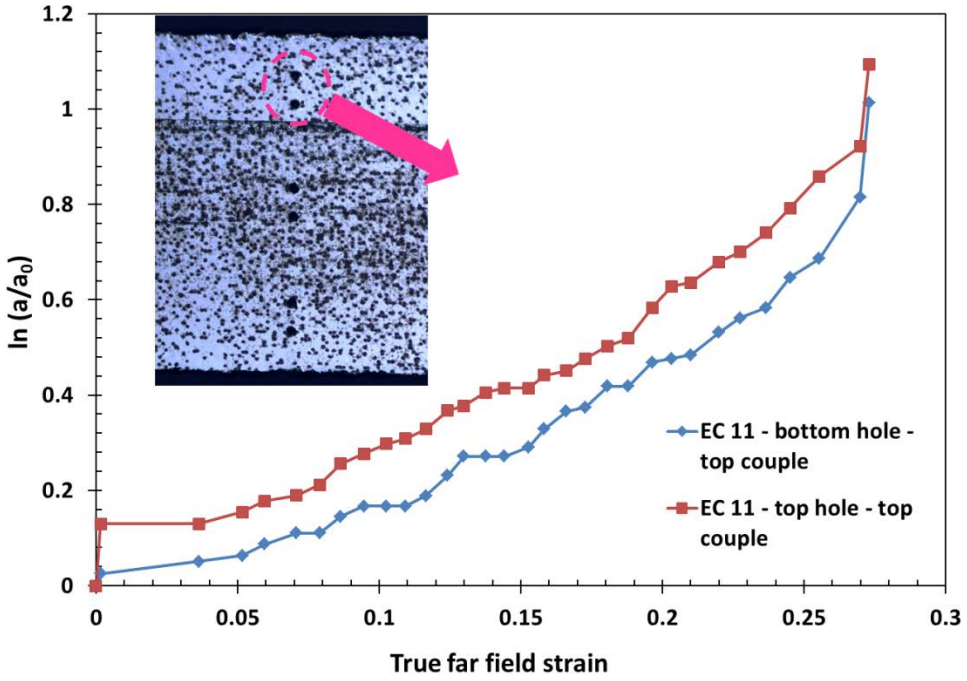

Figure H. 92 - Local true strain versus true far field strain for top couple of holes of specimen EC 11

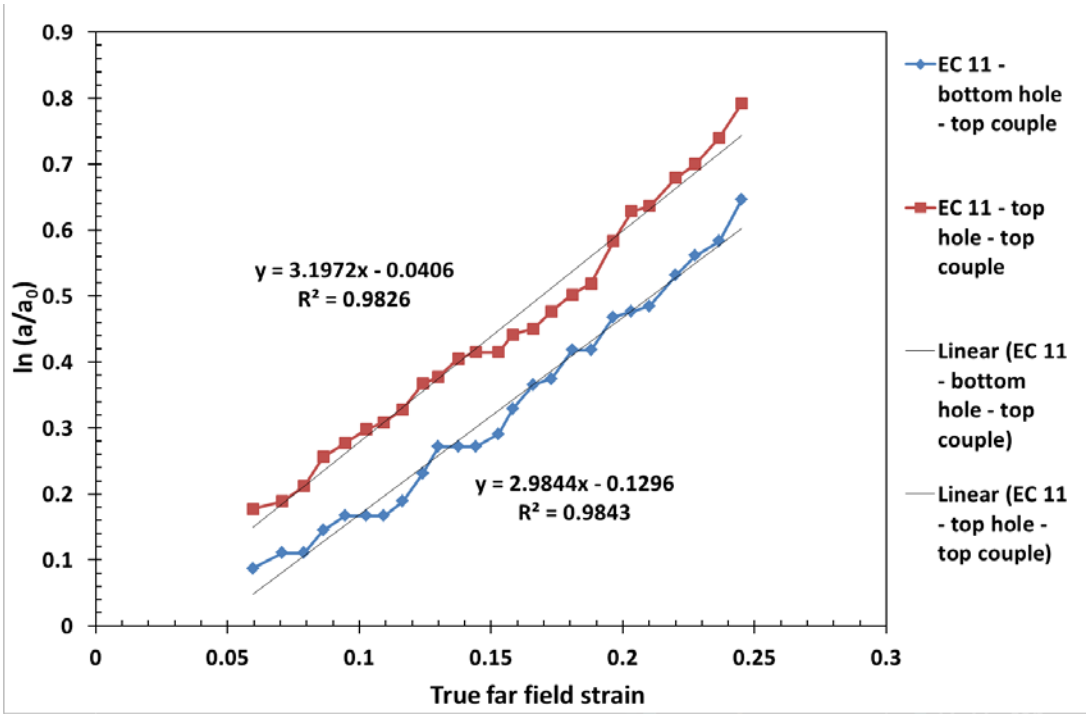

Figure H. 93 - Linear slope of local true strain versus true far field strain of the central couple of holes for specimen EC 11

H.6.2 Void growth of specimens having FeC film removed on the sides

From Figure H. 94 until Figure H. 103, the void growths for coupons having 500 µm FeC film left in the center are plot.

- **Specimen EC 2: central couple**

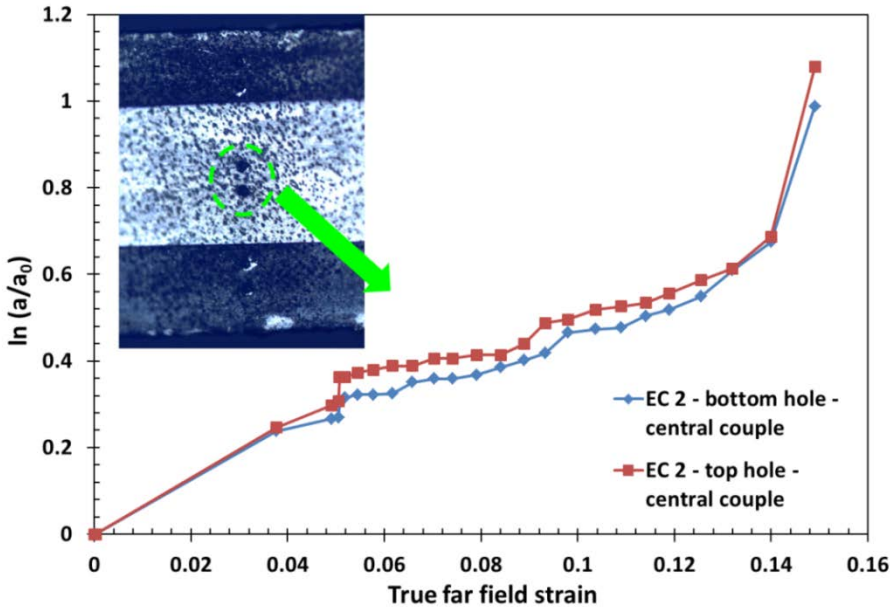

Figure H. 94 - Local true strain versus true far field strain for central couple of holes of specimen EC 2

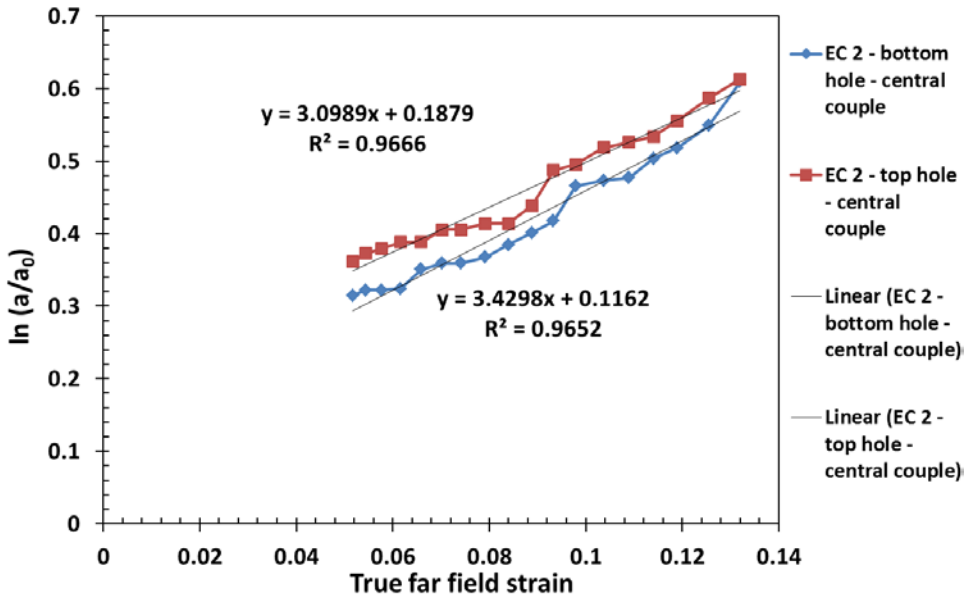

Figure H. 95 - Linear slope of local true strain versus true far field strain of the central couple of holes for specimen EC 2

- **Specimen EC 2: top couple**

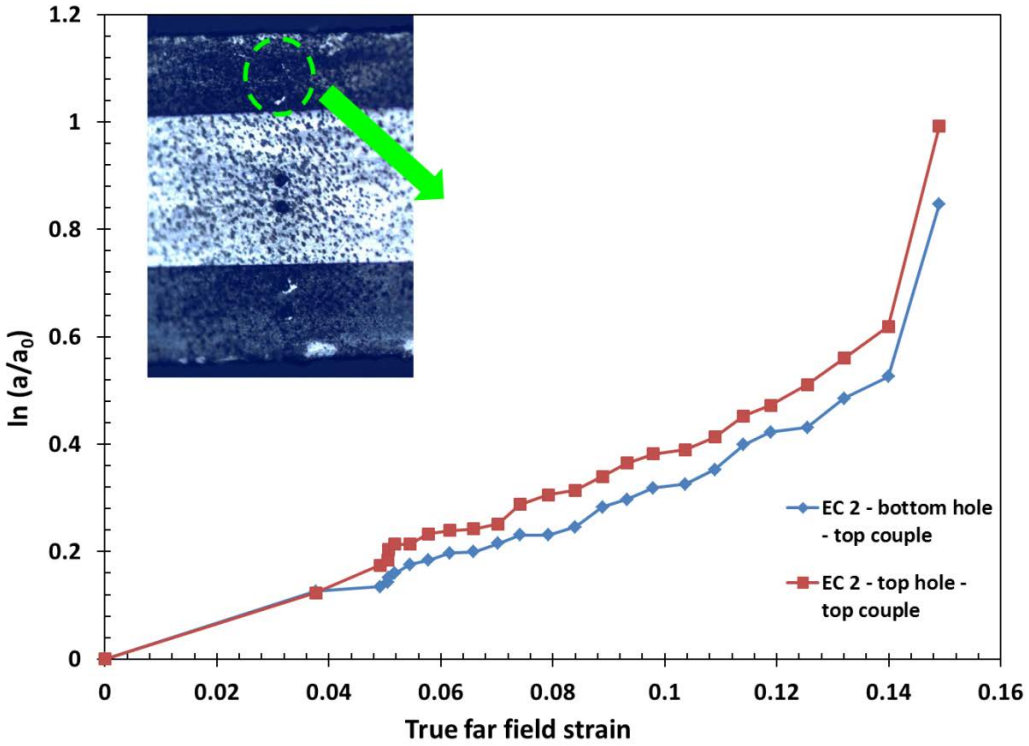

Figure H. 96 - Local true strain versus true far field strain for top couple of holes of specimen EC 2

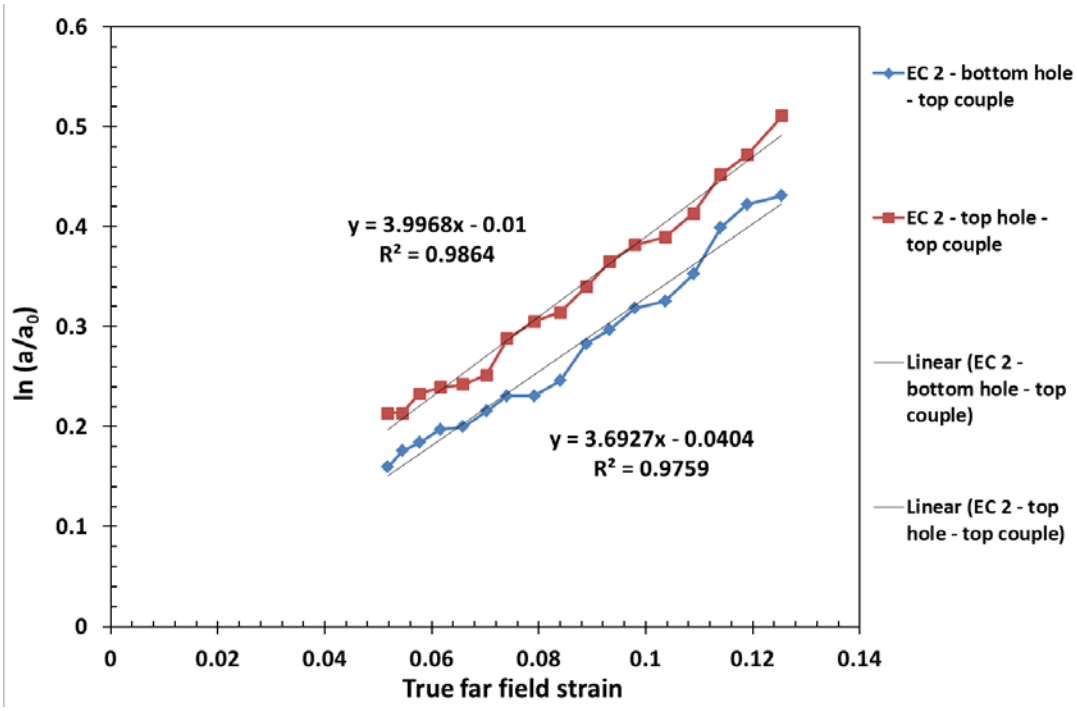

Figure H. 97 - Linear slope of local true strain versus true far field strain of the top couple of holes for specimen EC 2

- **Specimen EC 4: left couple**

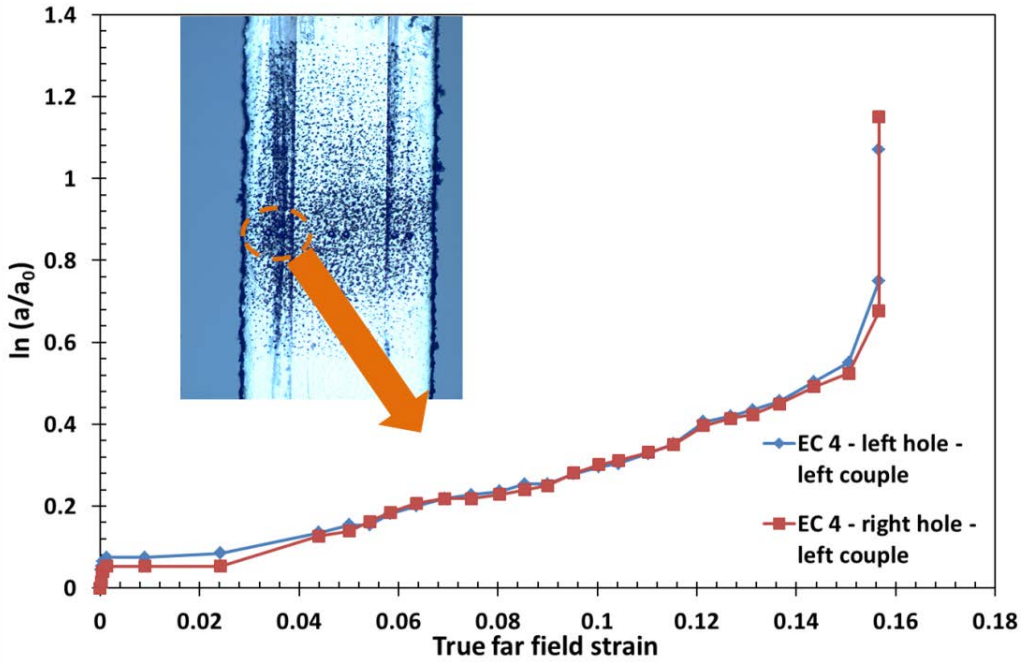

Figure H. 98 - Local true strain versus true far field strain for left couple of holes of specimen EC 4

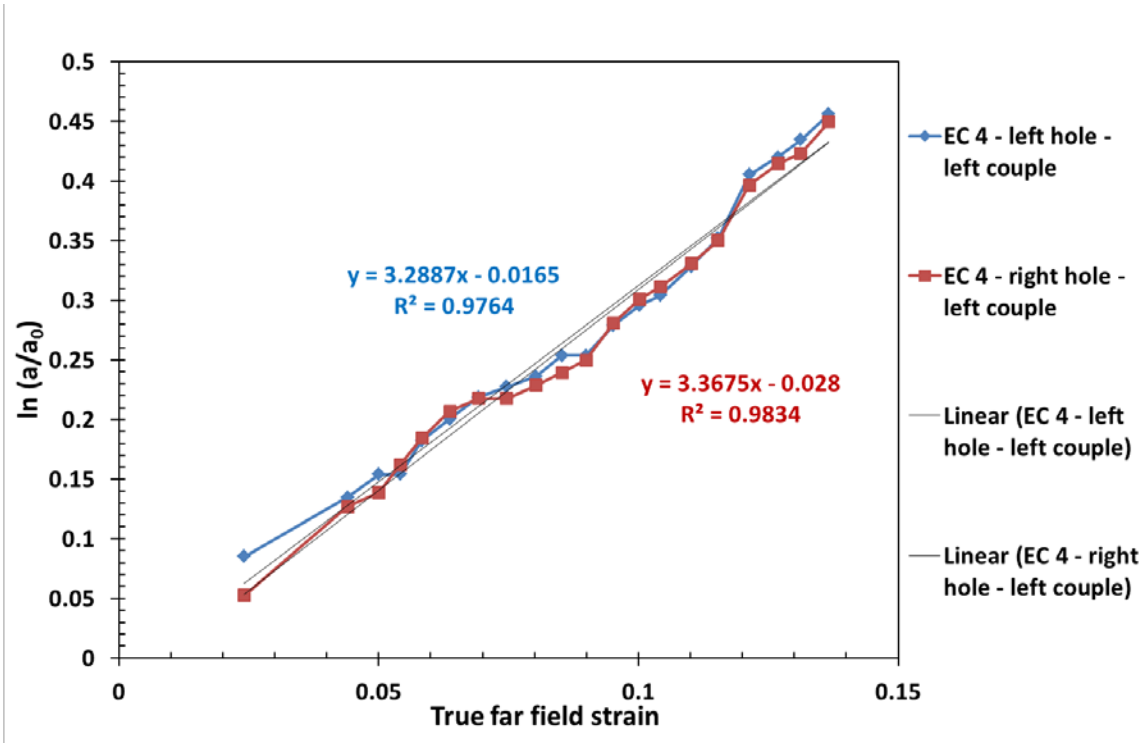

Figure H. 99 - Linear slope of local true strain versus true far field strain of the left couple of holes for specimen EC 4

- **Specimen EC 4: central couple**

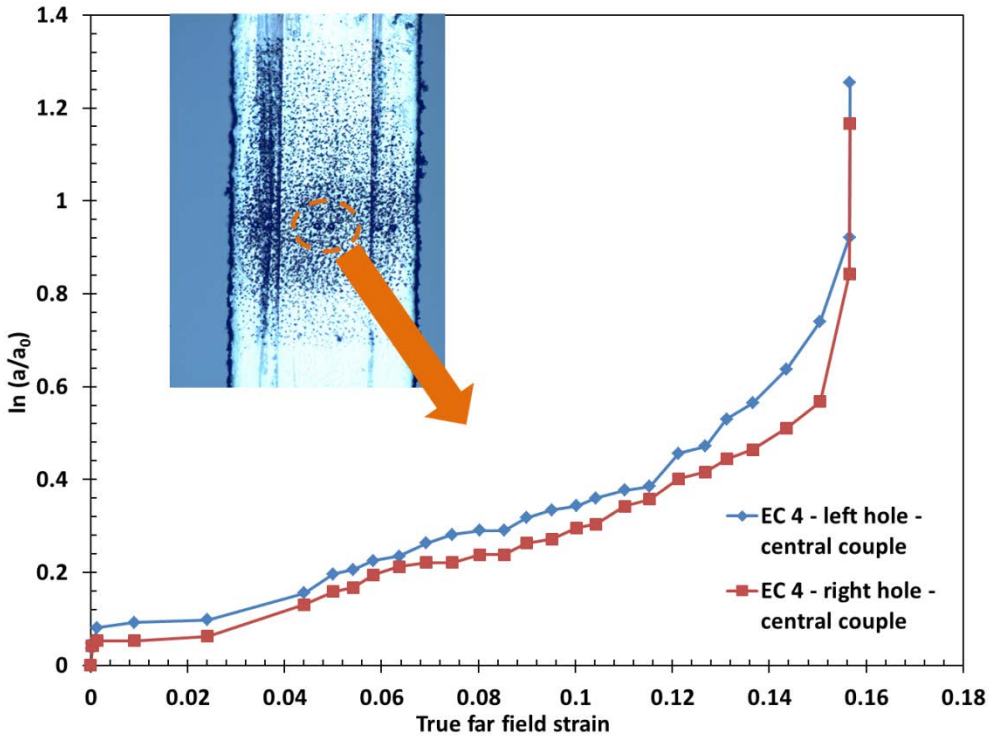

Figure H. 100 - Local true strain versus true far field strain for central couple of holes of specimen EC 4

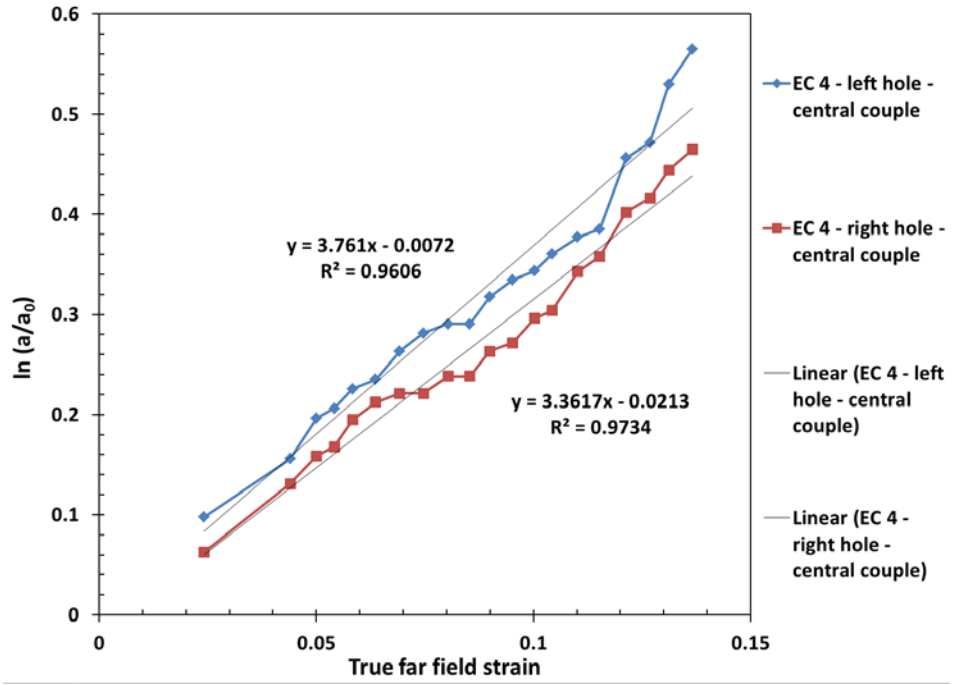

Figure H. 101 - Linear slope of local true strain versus true far field strain of the central couple of holes for specimen EC 4

- **Specimen EC 4: right couple**

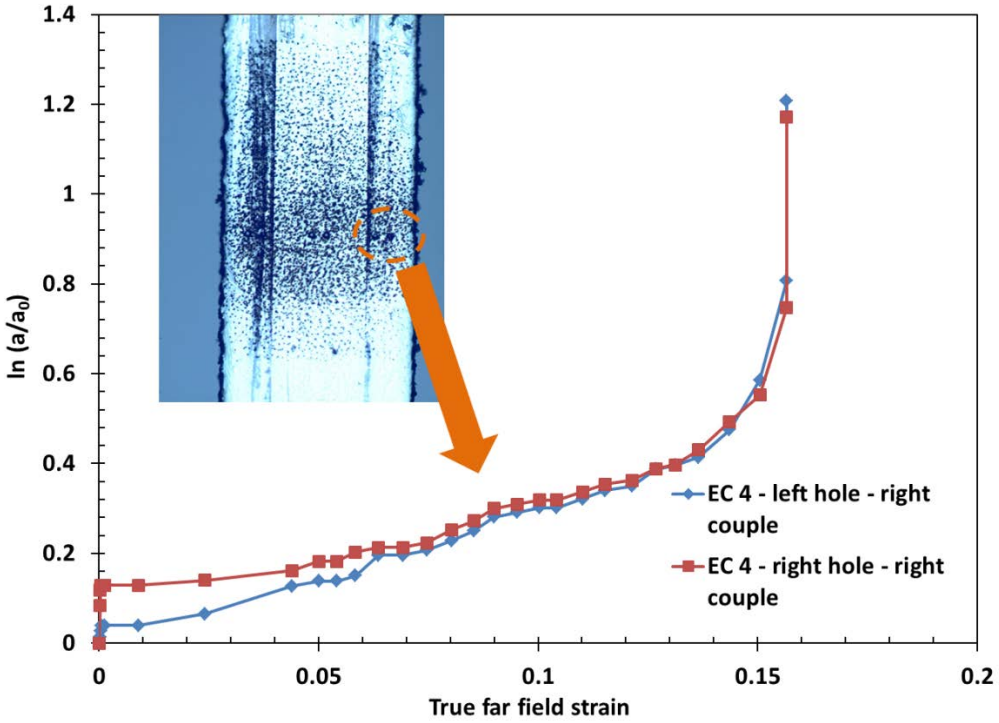

Figure H. 102 - Local true strain versus true far field strain for right couple of holes of specimen EC 4

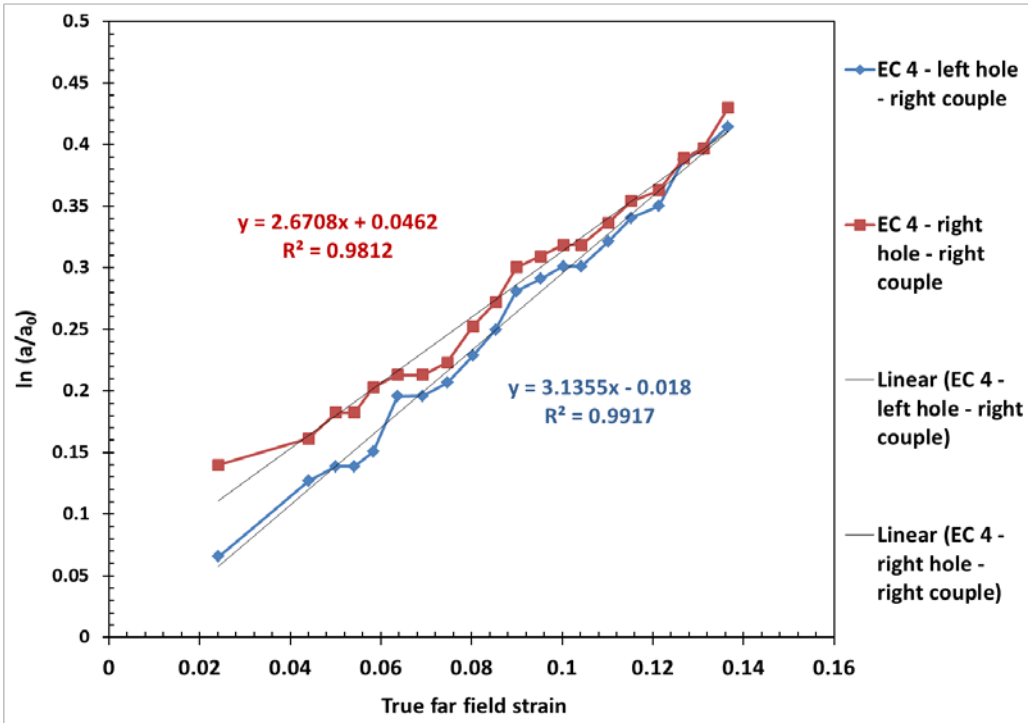

Figure H. 103 - Linear slope of local true strain versus true far field strain of the right couple of holes for specimen EC 4

H.6.3 Void growth of specimens having FeC film removed in the center and uniform carbon distribution

From Figure H. 104 until Figure H. 119 the void growths obtained in coupons having uniform carbon content are shown.

- **Specimen EC 9: central couple of holes**

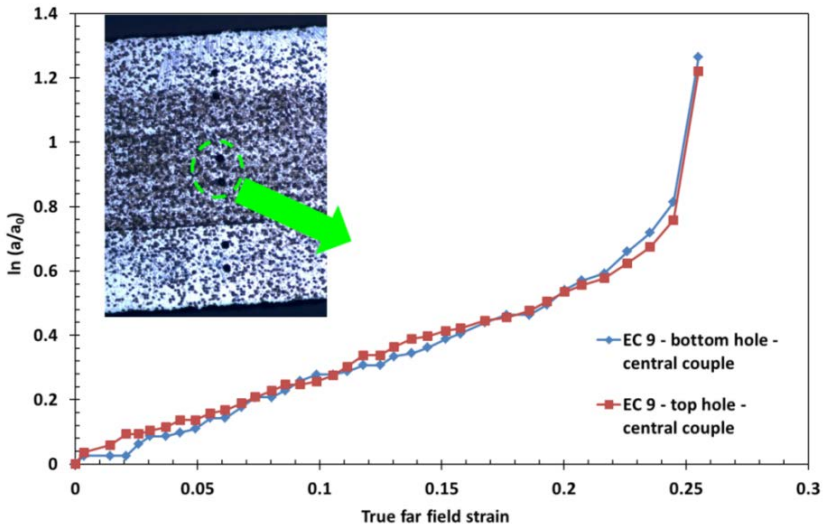

Figure H. 104 - Local true strain versus true far field strain for central couple of holes of specimen EC 9

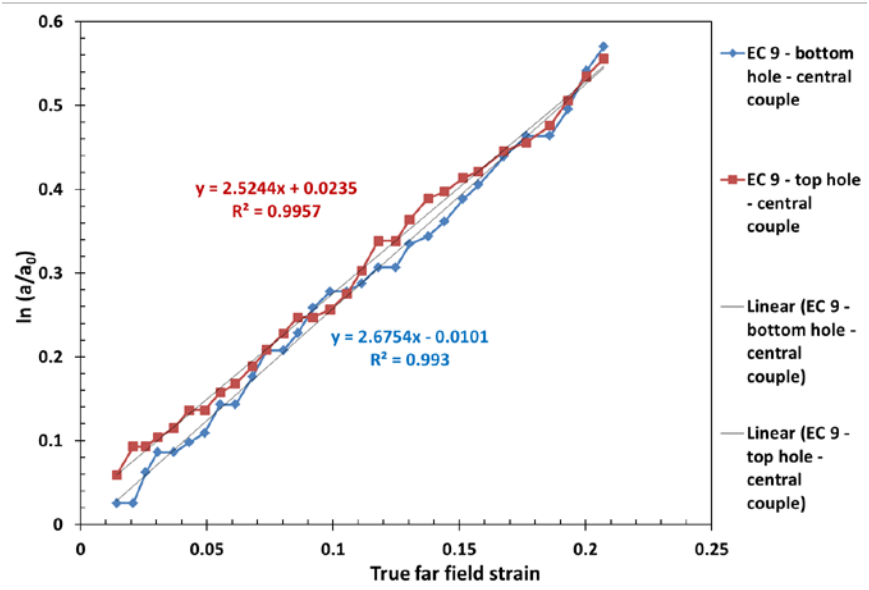

Figure H. 105 - Linear slope of local true strain versus true far field strain of the central couple of holes for specimen EC 9

- **Specimen EC 9: top couple of holes**

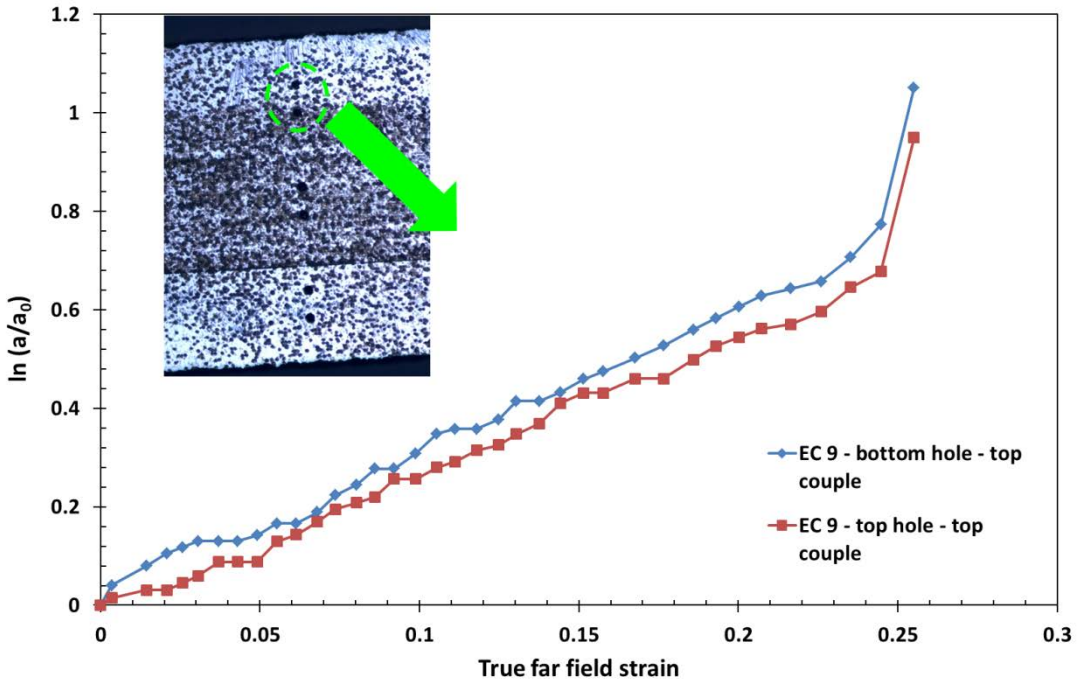

Figure H. 106 - Local true strain versus true far field strain for top couple of holes of specimen EC 9

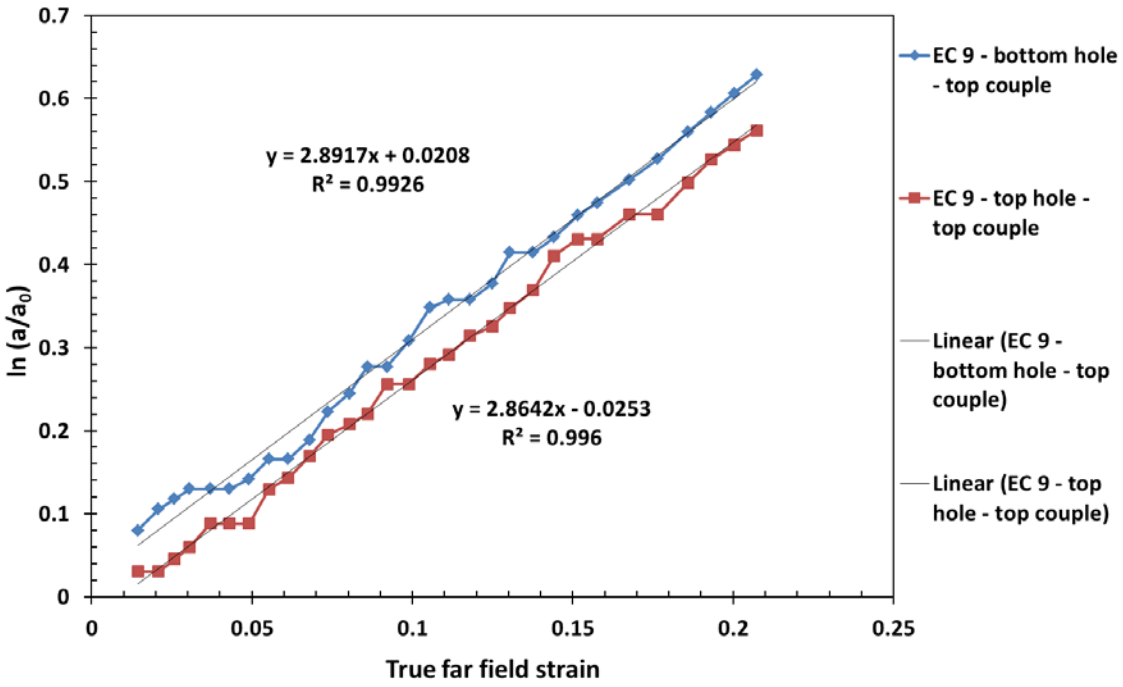

Figure H. 107 - Linear slope of local true strain versus true far field strain of the top couple of holes for specimen EC 9

- **Specimen EC 10: bottom couple of holes**

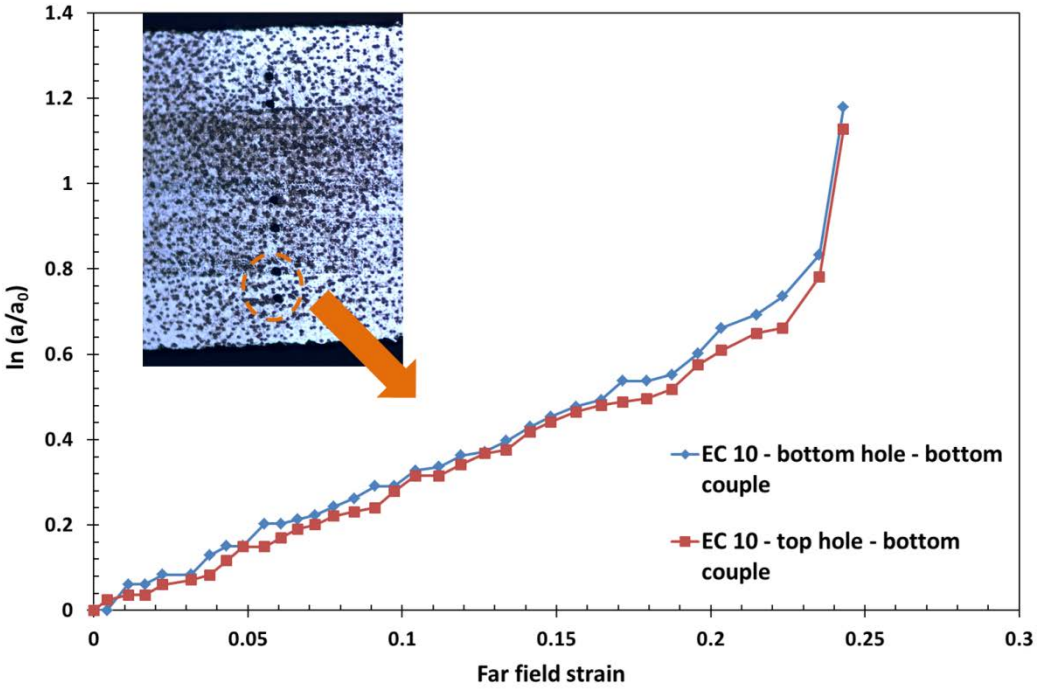

Figure H. 108 - Local true strain versus true far field strain for bottom couple of holes of specimen EC 10

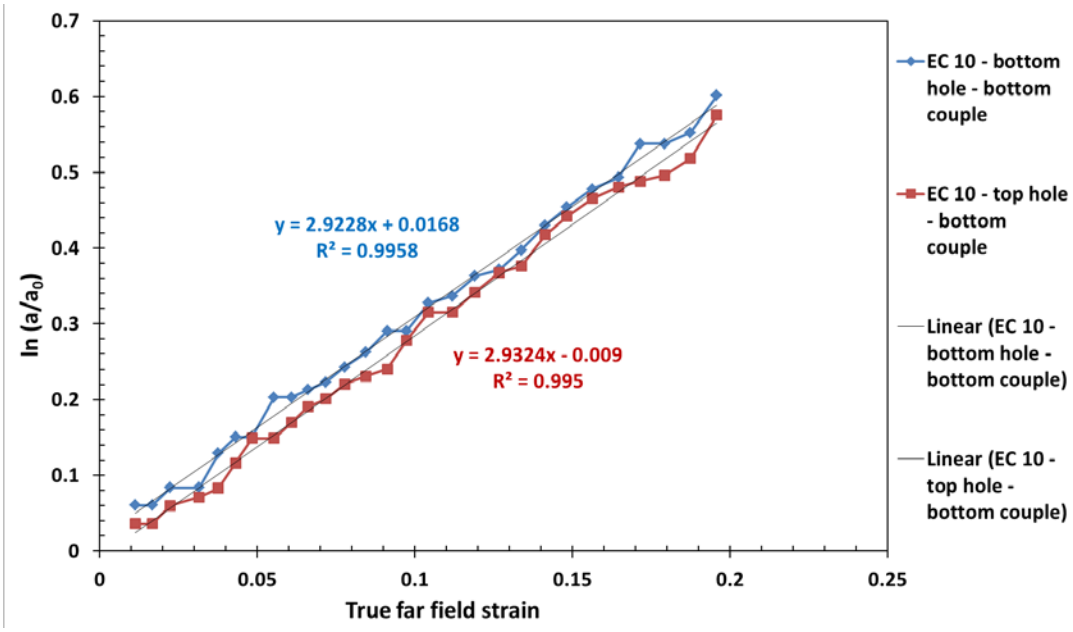

Figure H. 109 - Linear slope of local true strain versus true far field strain of the bottom couple of holes for specimen EC 10

- **Specimen EC 10: central couple of holes**

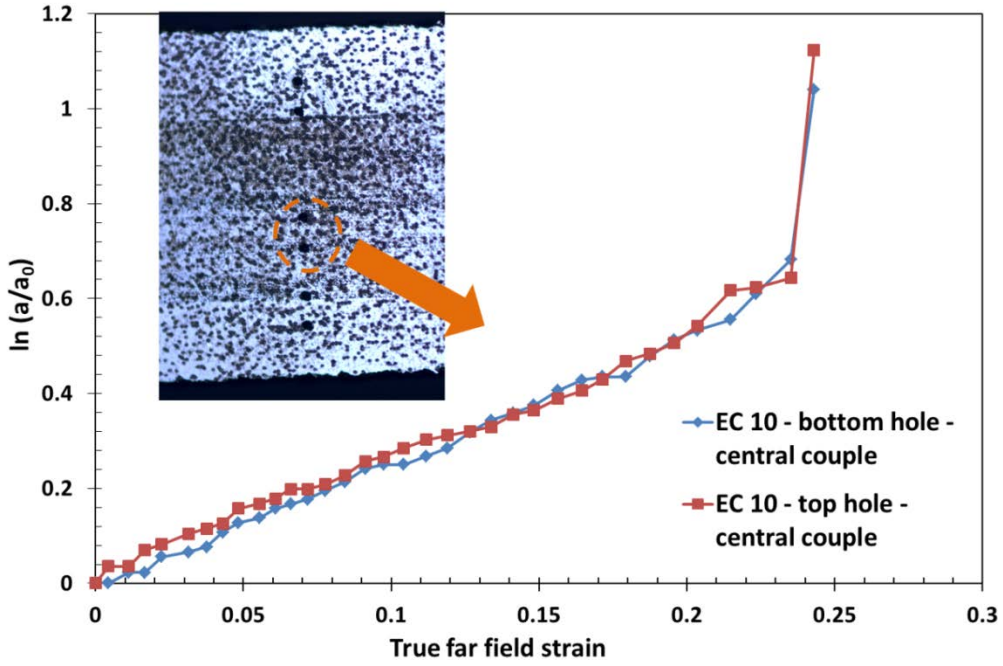

Figure H. 110 - Local true strain versus true far field strain for central couple of holes of specimen EC 10

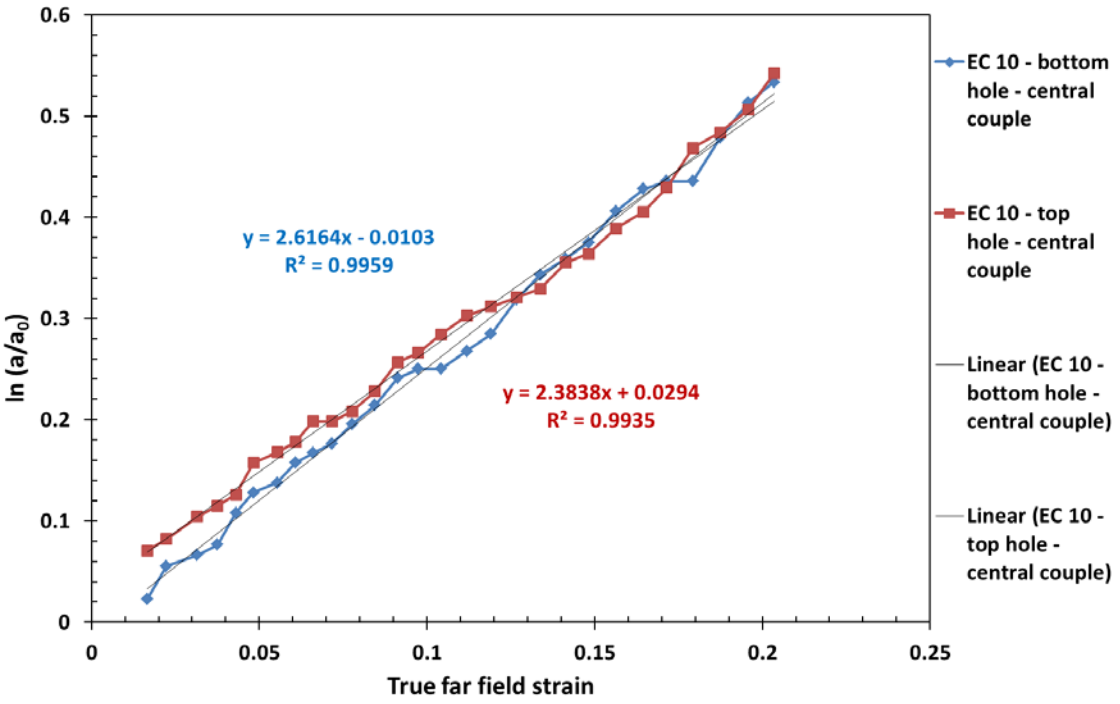

Figure H. 111 - Linear slope of local true strain versus true far field strain of the central couple of holes for specimen EC 10

- **Specimen EC 10: top couple of holes**

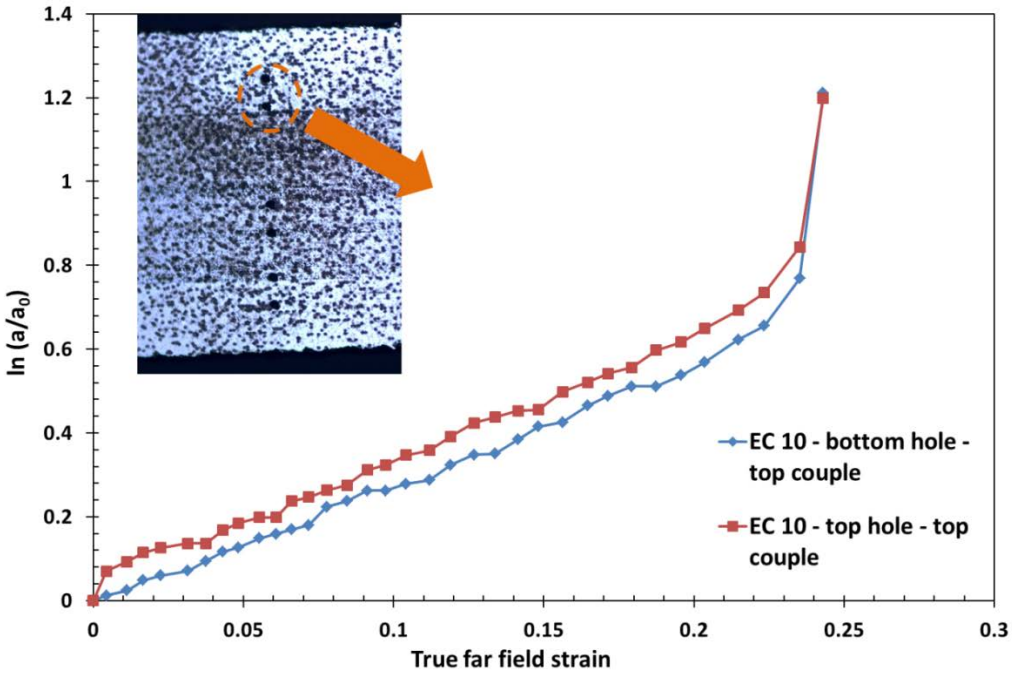

Figure H. 112 - Local true strain versus true far field strain for top couple of holes of specimen EC 10

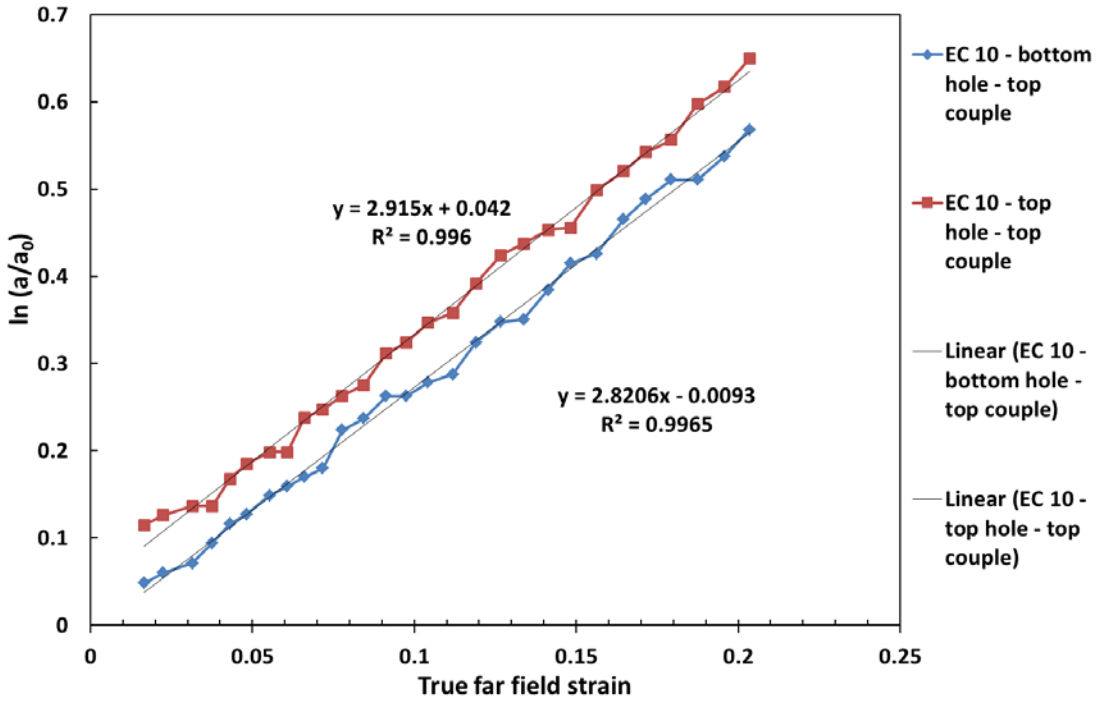

Figure H. 113 - Linear slope of local true strain versus true far field strain of the top couple of holes for specimen EC 10

- **Specimen EC 12: left couple of holes**

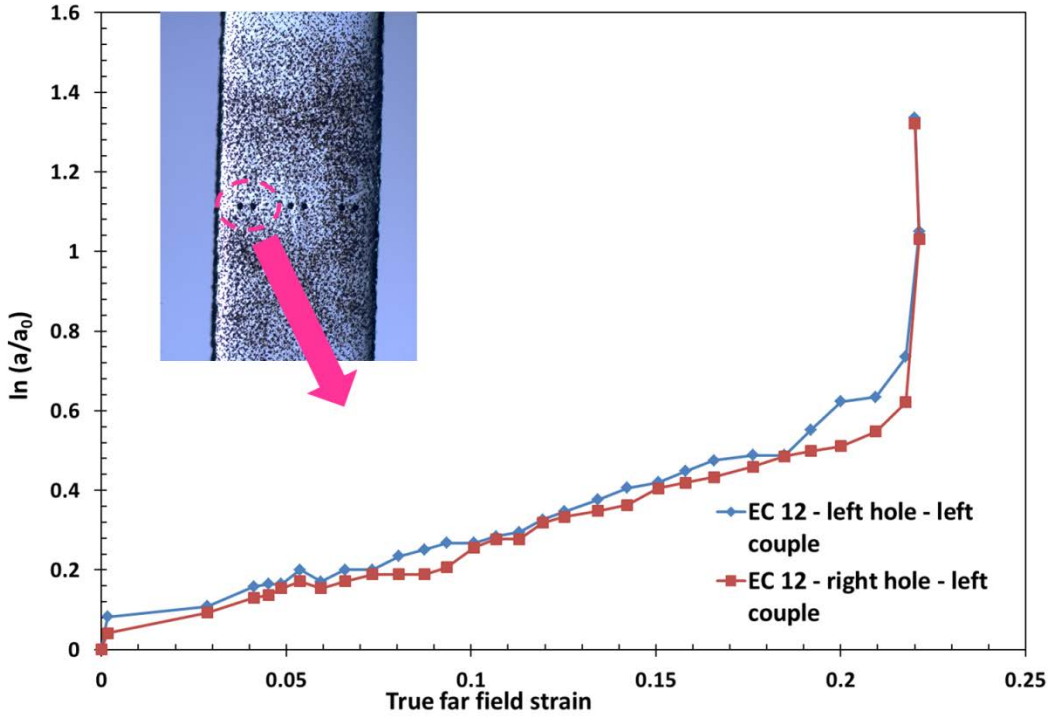

Figure H. 114 - Local true strain versus true far field strain for left couple of holes of specimen EC 12

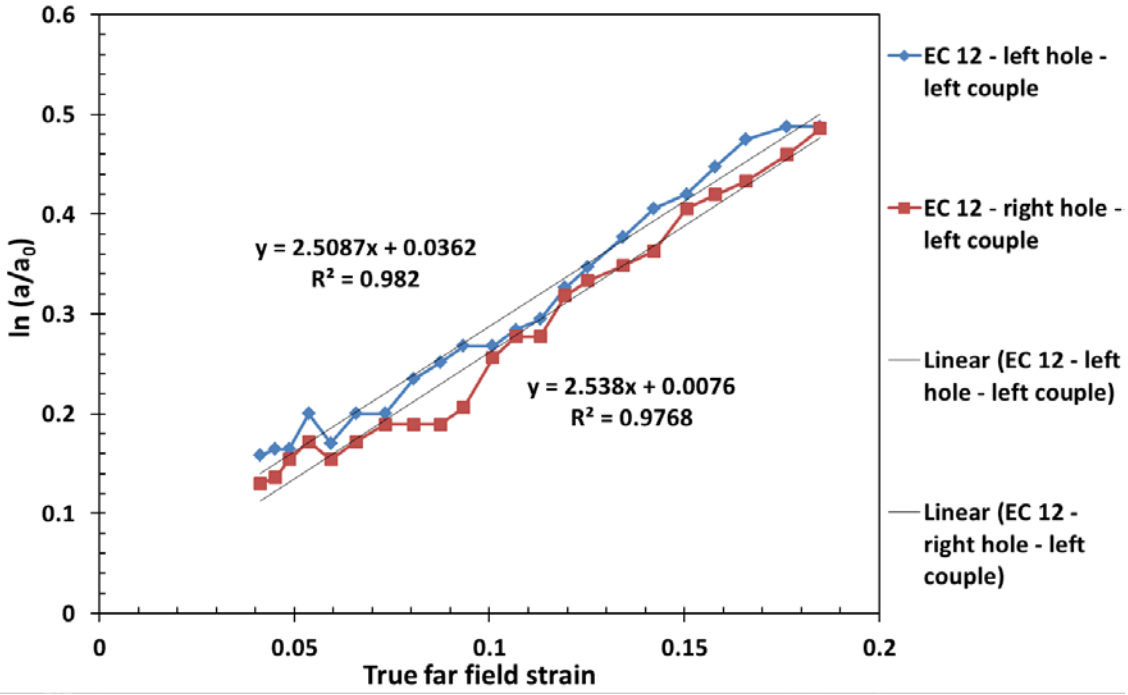

Figure H. 115 - Linear slope of local true strain versus true far field strain of the left couple of holes for specimen EC 12

- **Specimen EC 12: central couple of holes**

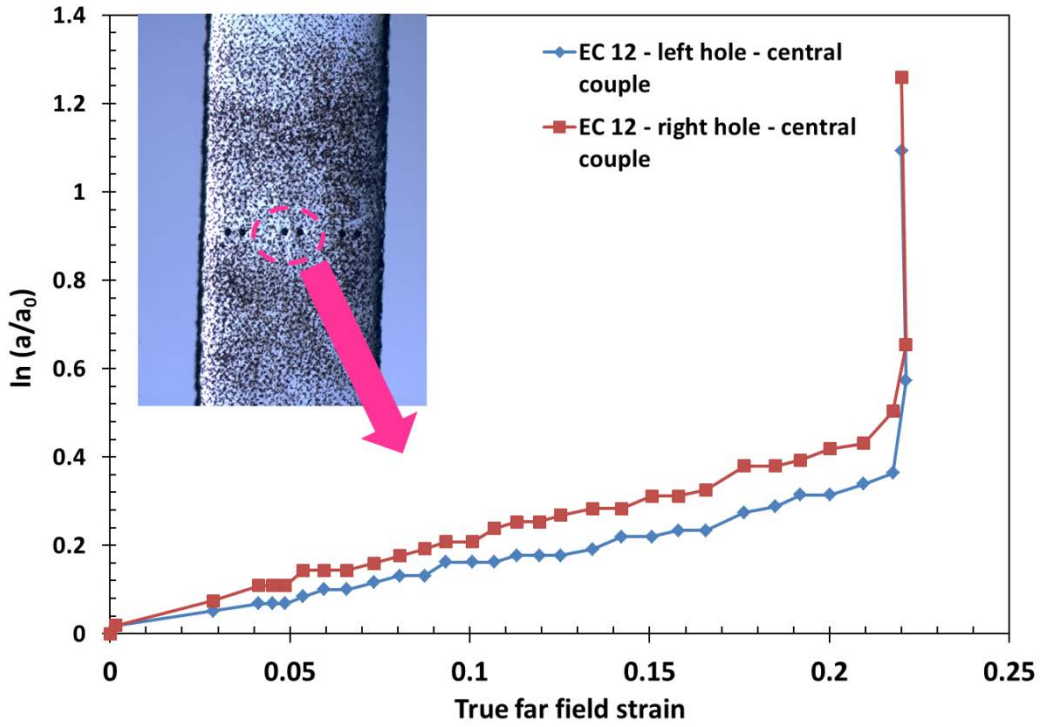

Figure H. 116 - Local true strain versus true far field strain for central couple of holes of specimen EC 12

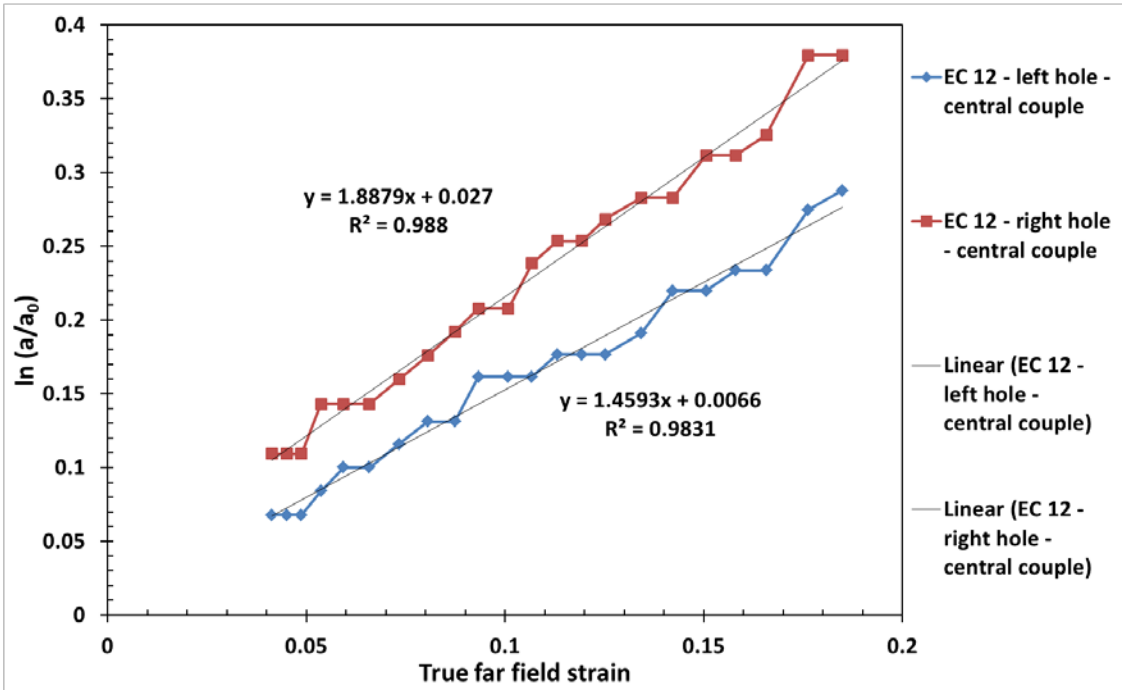

Figure H. 117 - Linear slope of local true strain versus true far field strain of the central couple of holes for specimen EC 12

- **Specimen EC 12: right couple of holes**

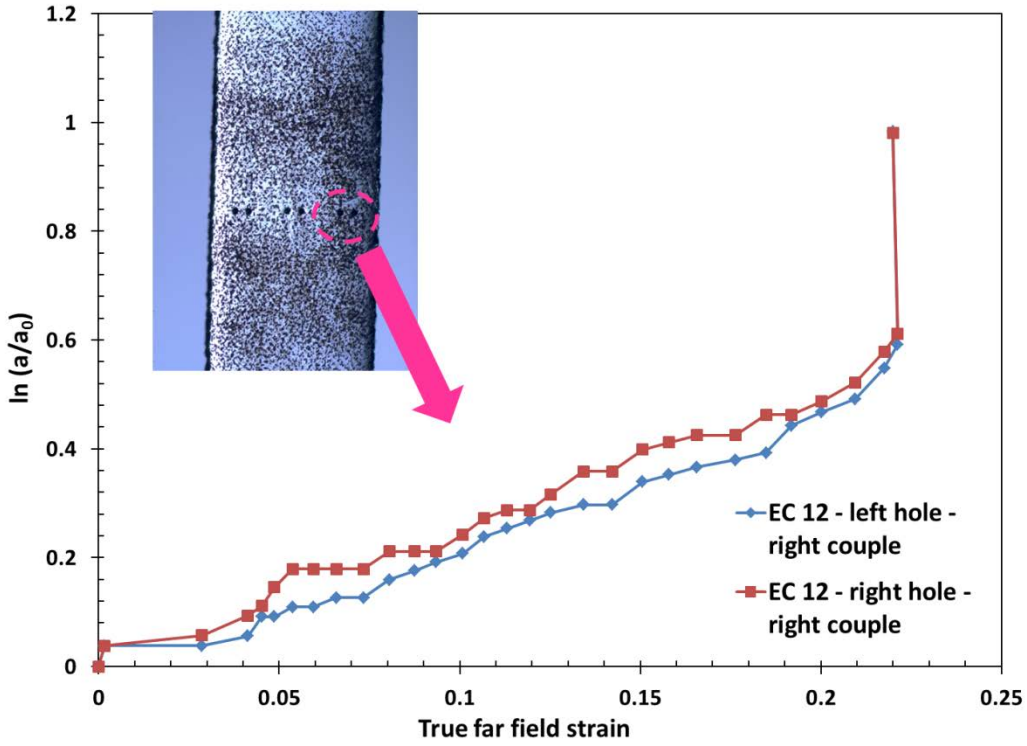

Figure H. 118 - Local true strain versus true far field strain for right couple of holes of specimen EC 12

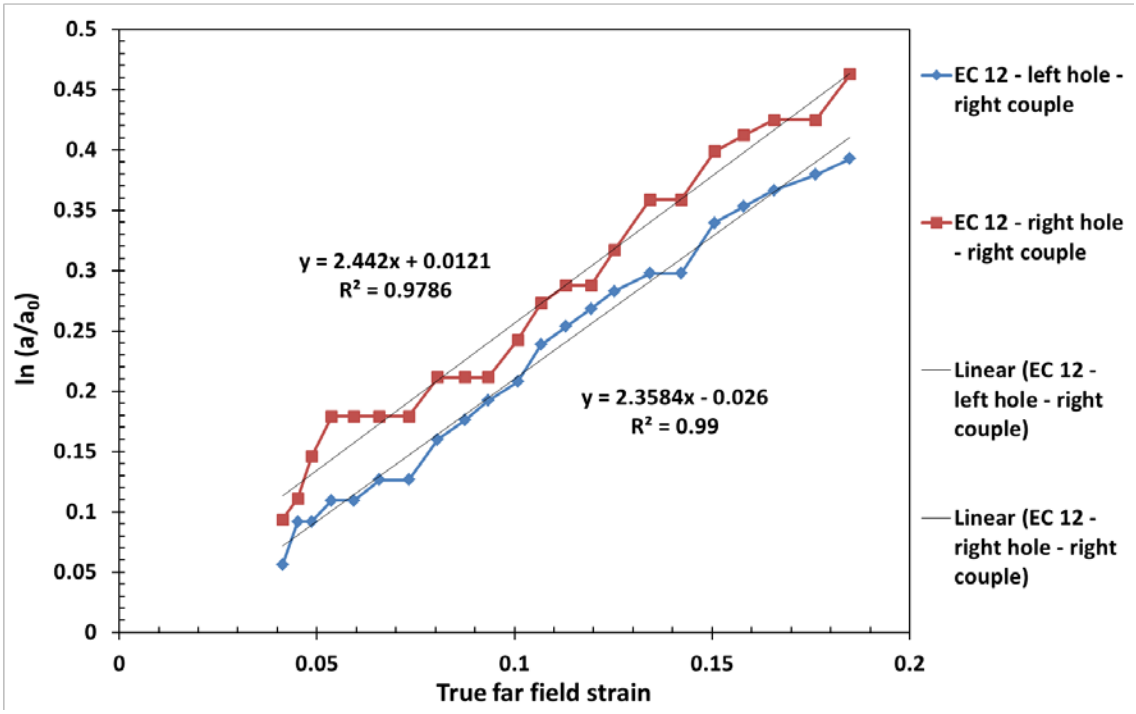

Figure H. 119 - Linear slope of local true strain versus true far field strain of the right couple of holes for specimen EC 12

H.6.4 Void growth of uncoated specimens

From Figure H. 120 to Figure H. 129 void growths obtained for uncoated and not-annealed tensile coupons are summarized.

- **Specimen GW 1: central couple of holes**

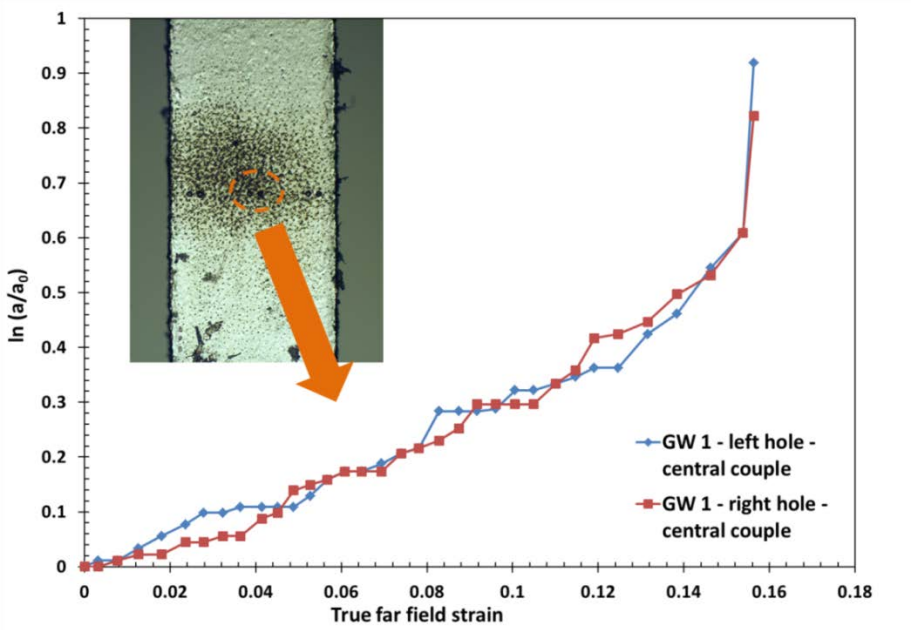

Figure H. 120 - Local true strain versus true far field strain for central couple of holes for uncoated and not annealed specimen GW 1

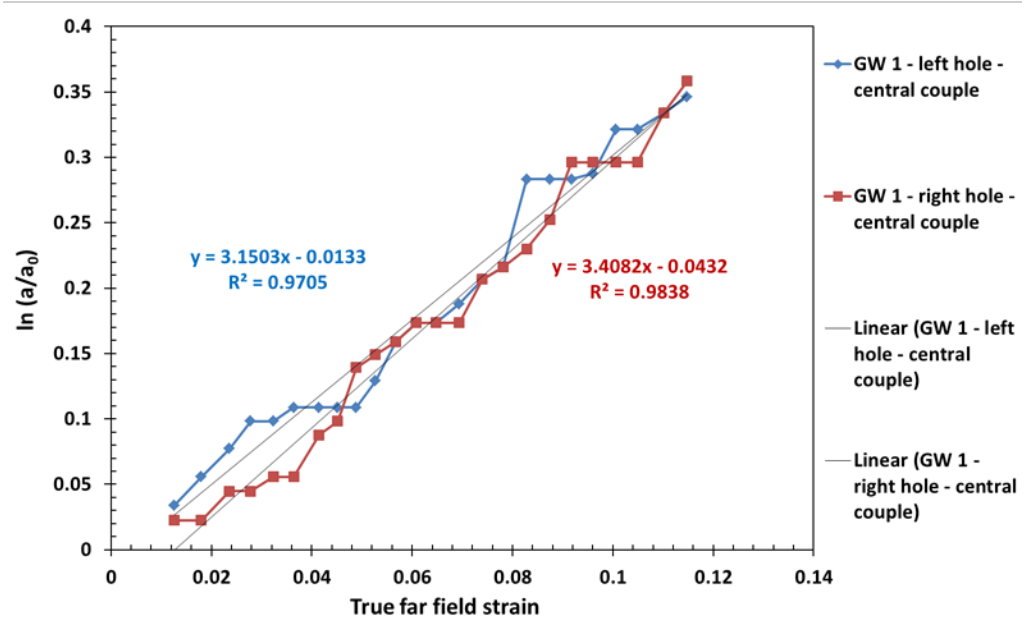

Figure H. 121 - Linear slope of local true strain versus true far field strain of the central couple of holes for uncoated and not-annealed specimen GW 1

- **Specimen GW 1: right couple of holes**

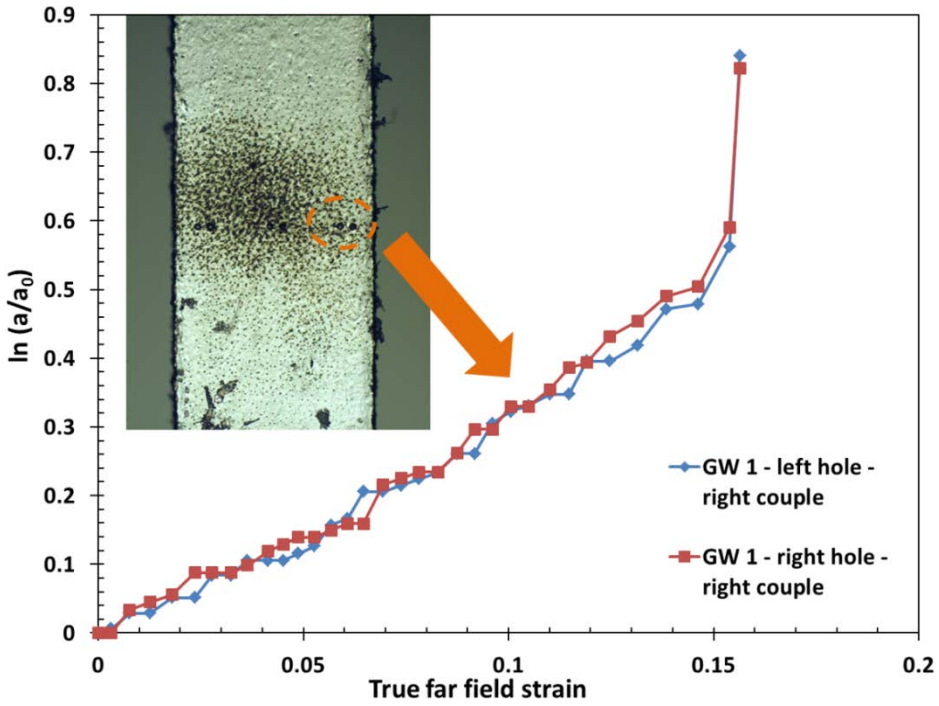

Figure H. 122 - Local true strain versus true far field strain for right couple of holes for uncoated and not annealed specimen GW 1

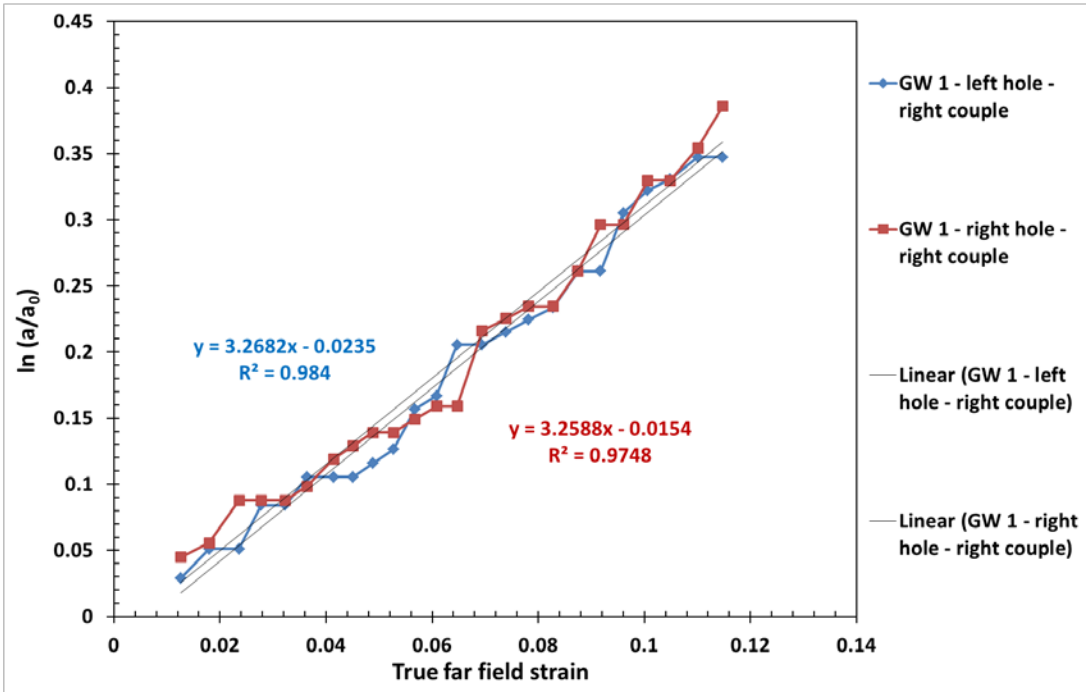

Figure H. 123 - Linear slope of local true strain versus true far field strain of the right couple of holes for uncoated and not-annealed specimen GW 1

- **Specimen GW 2: bottom couple of holes**

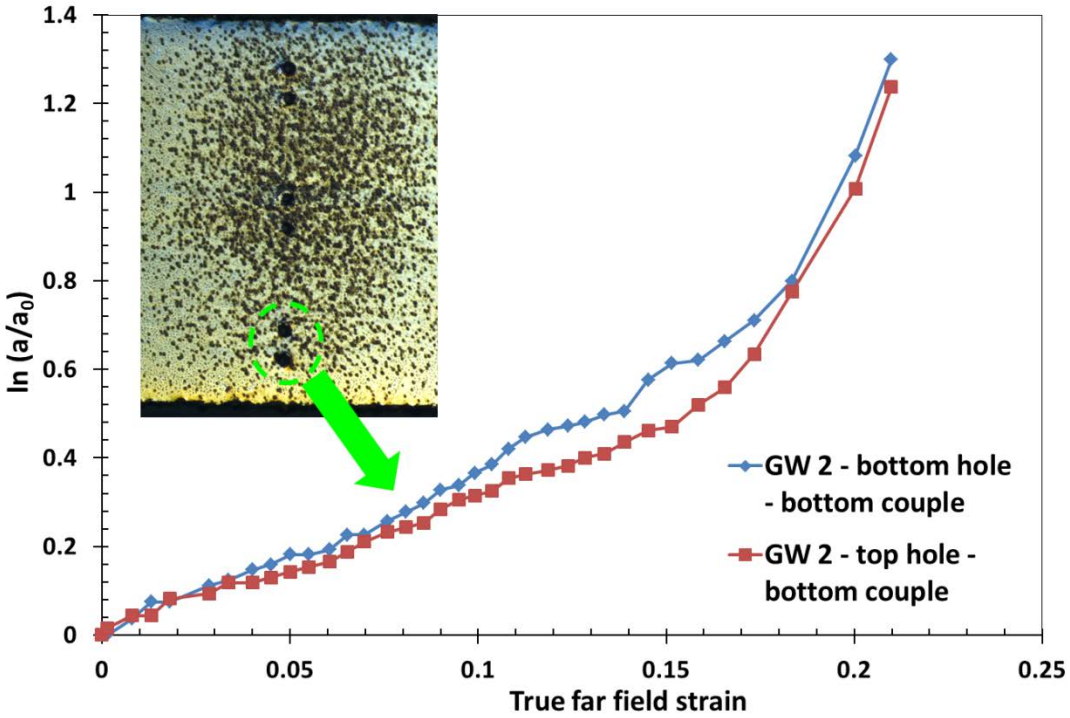

Figure H. 124 - Local true strain versus true far field strain for bottom couple of holes of specimen GW 2

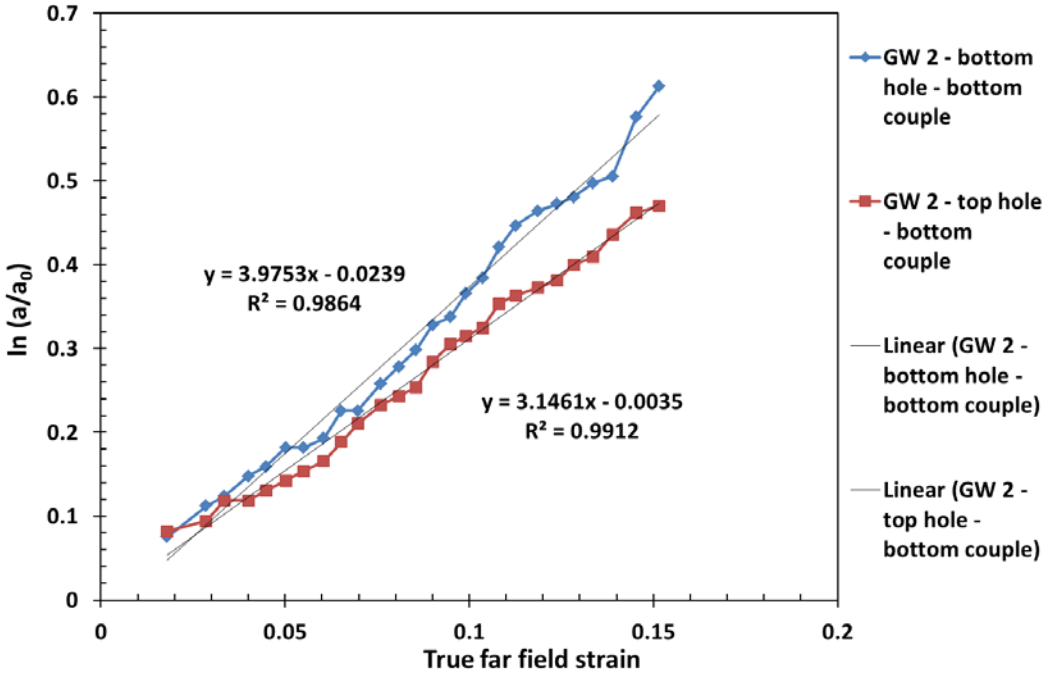

Figure H. 125 - Linear slope of local true strain versus true far field strain of the bottom couple of holes for specimen GW 2

- **Specimen GW 2: central couple of holes**

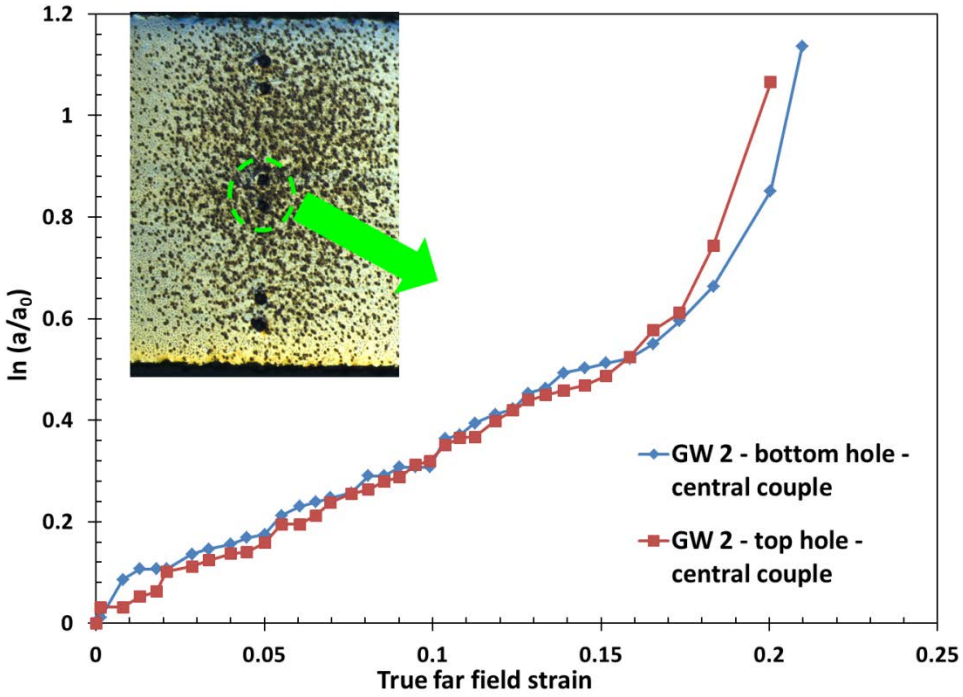

Figure H. 126 - Local true strain versus true far field strain for central couple of holes of specimen GW 2

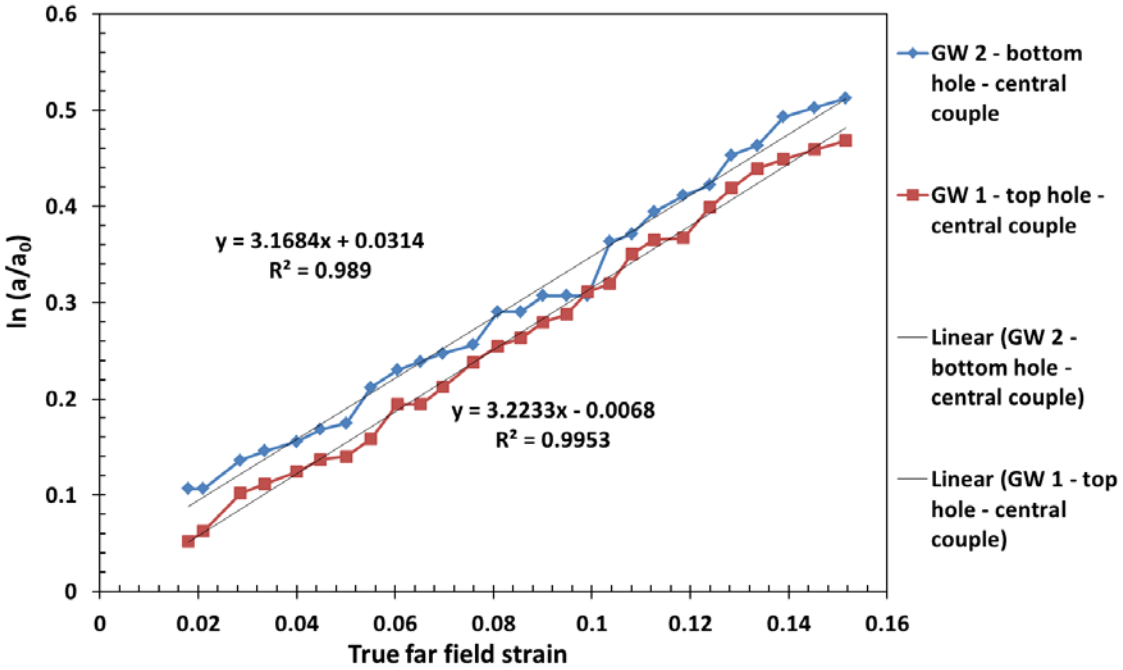

Figure H. 127 - Linear slope of local true strain versus true far field strain of the central couple of holes for specimen GW 2

- **Specimen GW 2: top couple of holes**

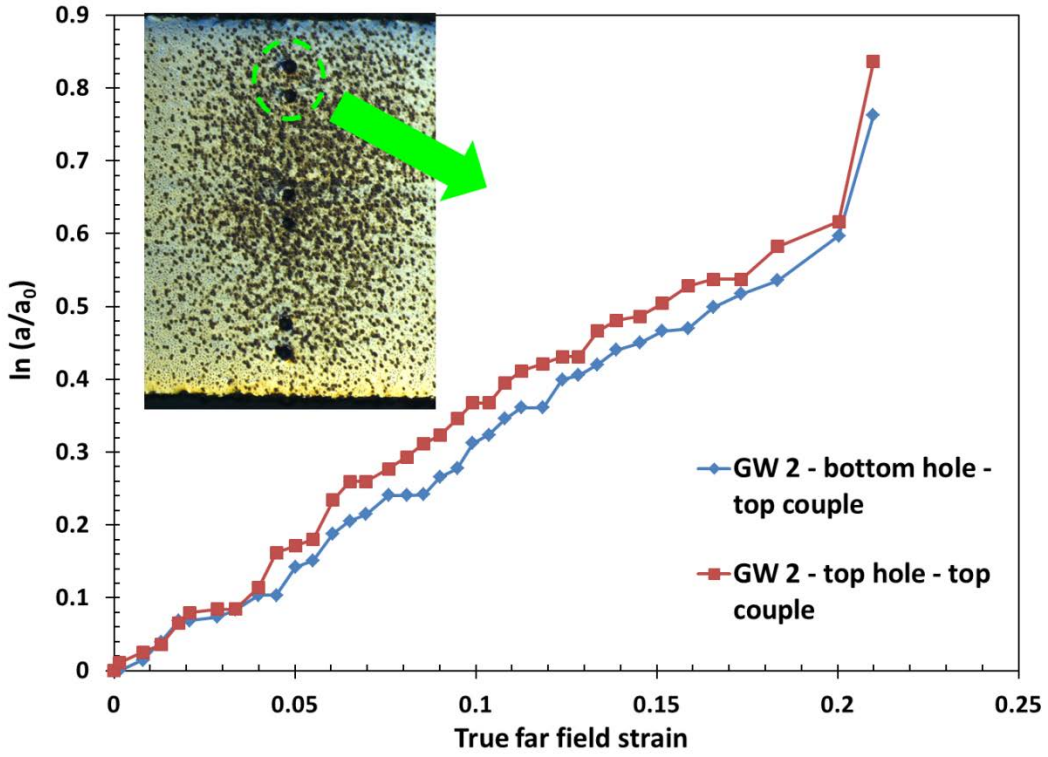

Figure H. 128 - Local true strain versus true far field strain for top couple of holes of specimen GW 2

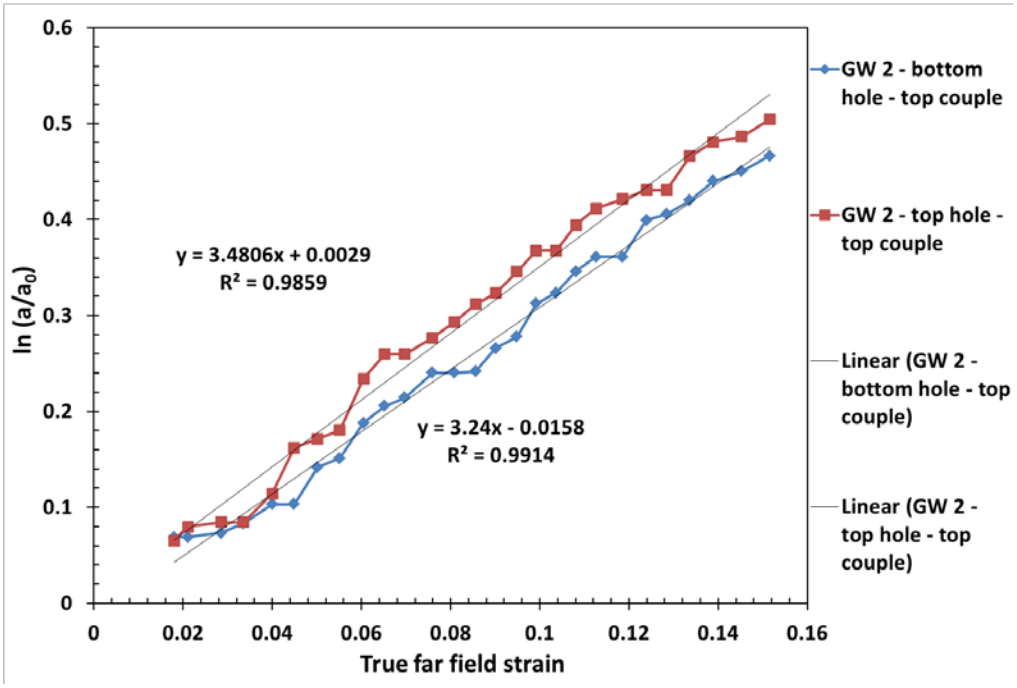

Figure H. 129 - Linear slope of local true strain versus true far field strain of the top couple of holes for specimen GW 2

H.7 McClintok Fitting

H.7.1 McClintok fitting for specimens having FeC film removed in the center

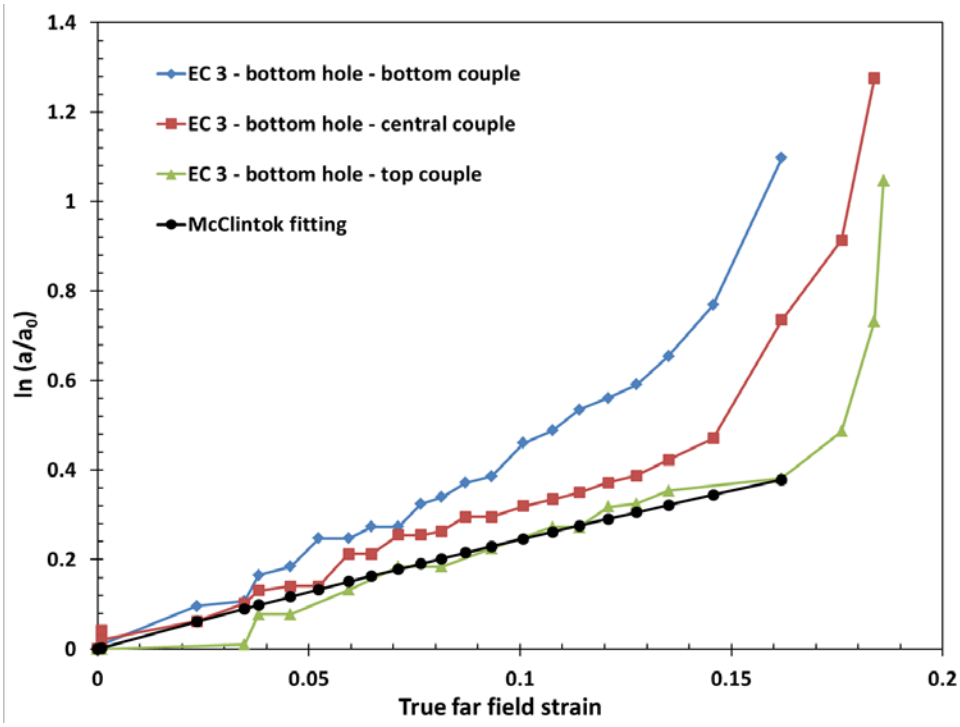

Figure H. 130 - McClintok fitting of the void growth for top holes in specimen EC 3

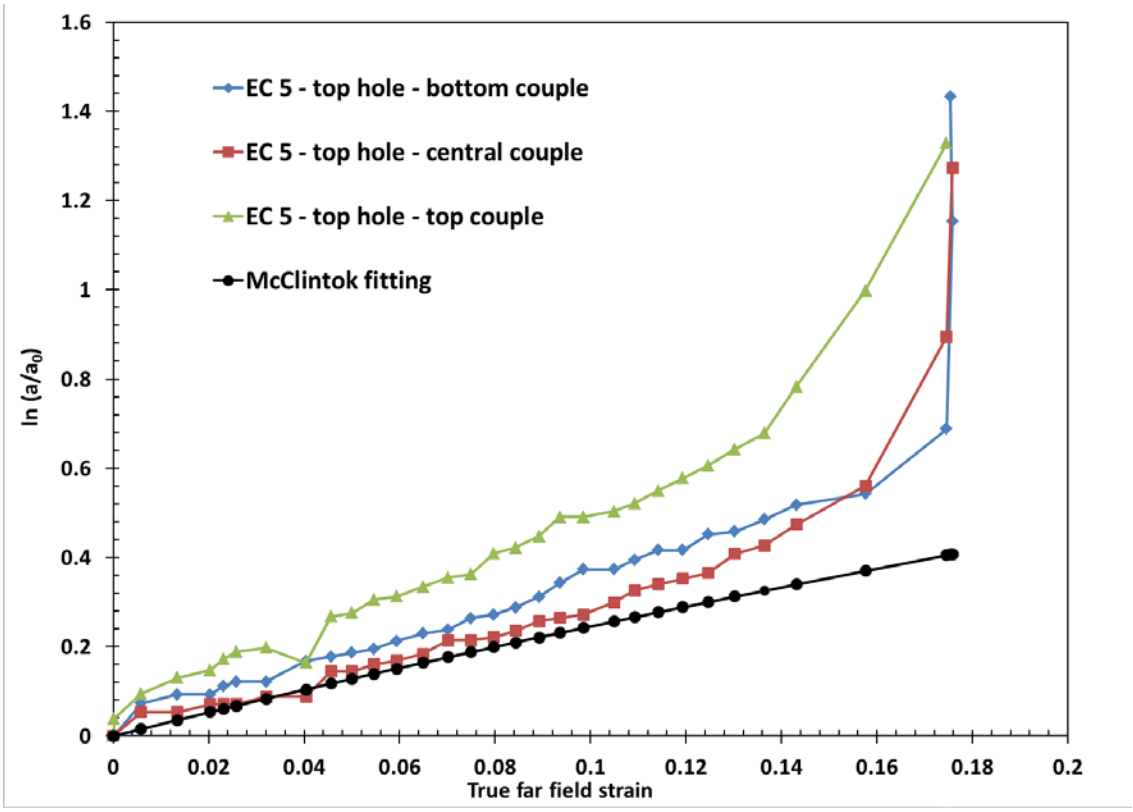

Figure H. 131 - McClintok fitting of the void growth for top holes in specimen EC 5

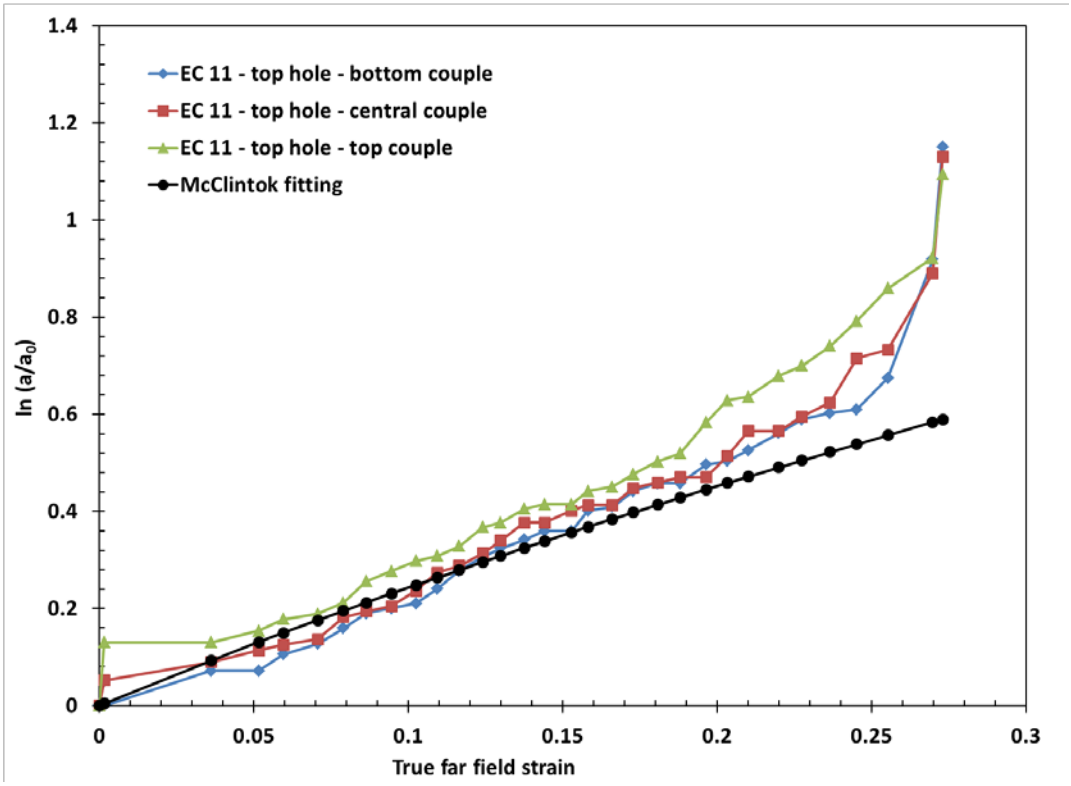

Figure H. 132 - McClintok fitting of the void growth for top holes in specimen EC 11

H.7.2 McClintok fitting for specimens having FeC film removed on the sides

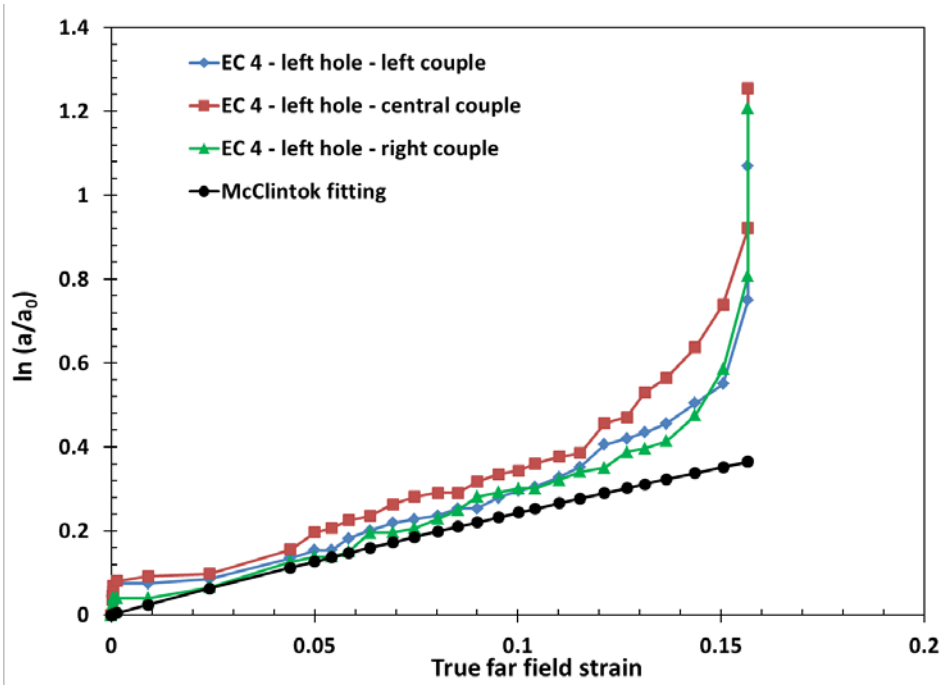

Figure H. 133 - McClintok fitting of the void growth for top holes in specimen EC 4

H.7.3 McClintok fitting for specimens having FeC film removed in the center and uniform carbon distribution

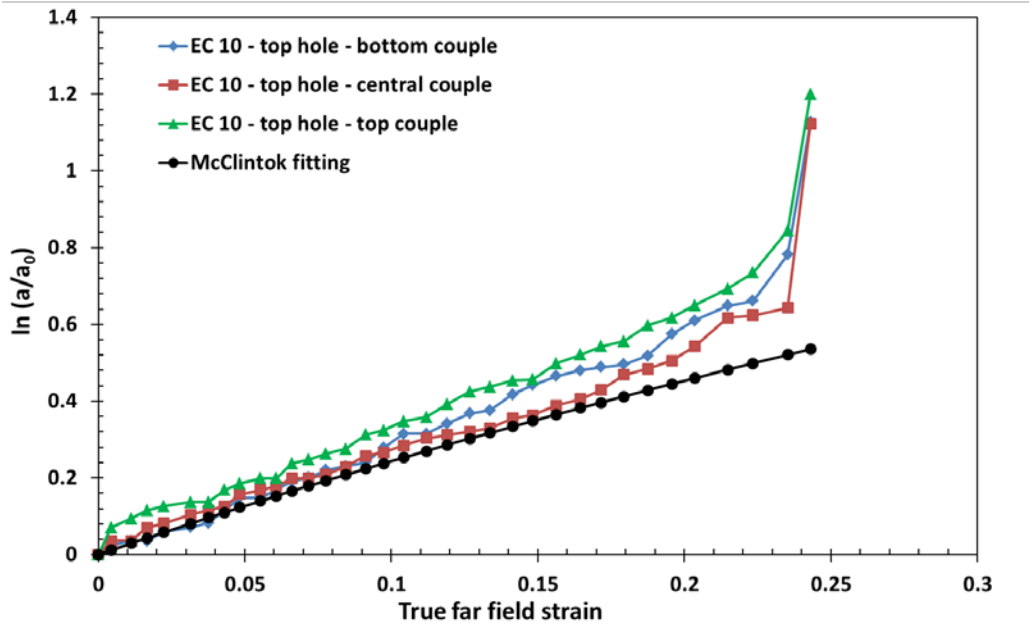

Figure H. 134 - McClintok fitting of the void growth for top holes in specimen EC 10

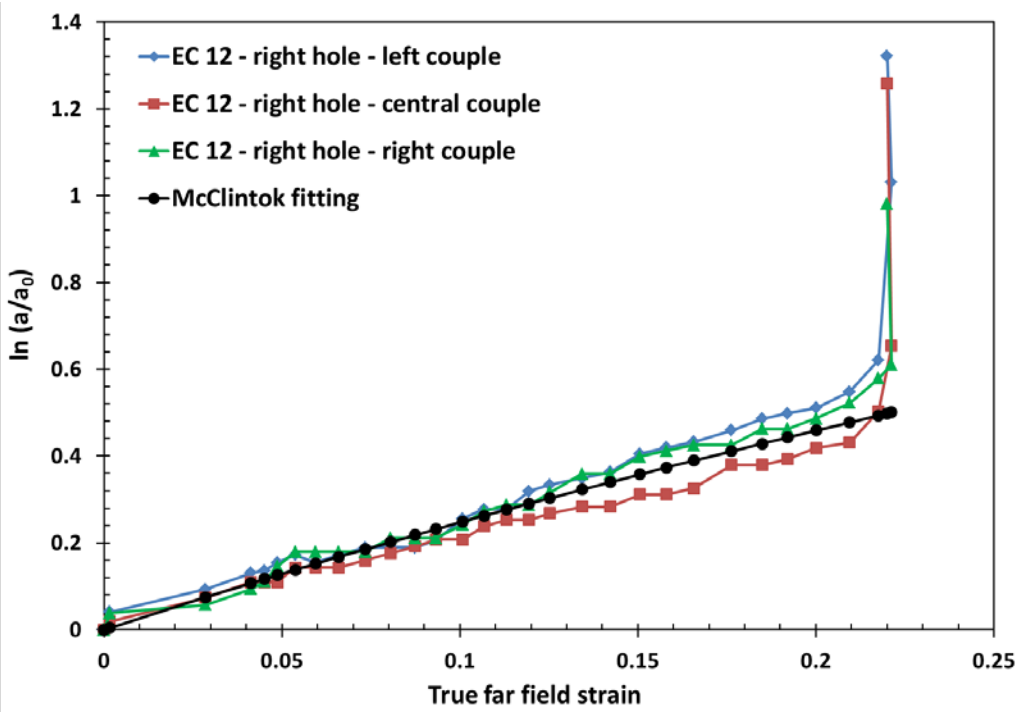

Figure H. 135 - McClintok fitting of the void growth for right holes in specimen EC 12

H.7.4 McClintok fitting for uncoated coupons

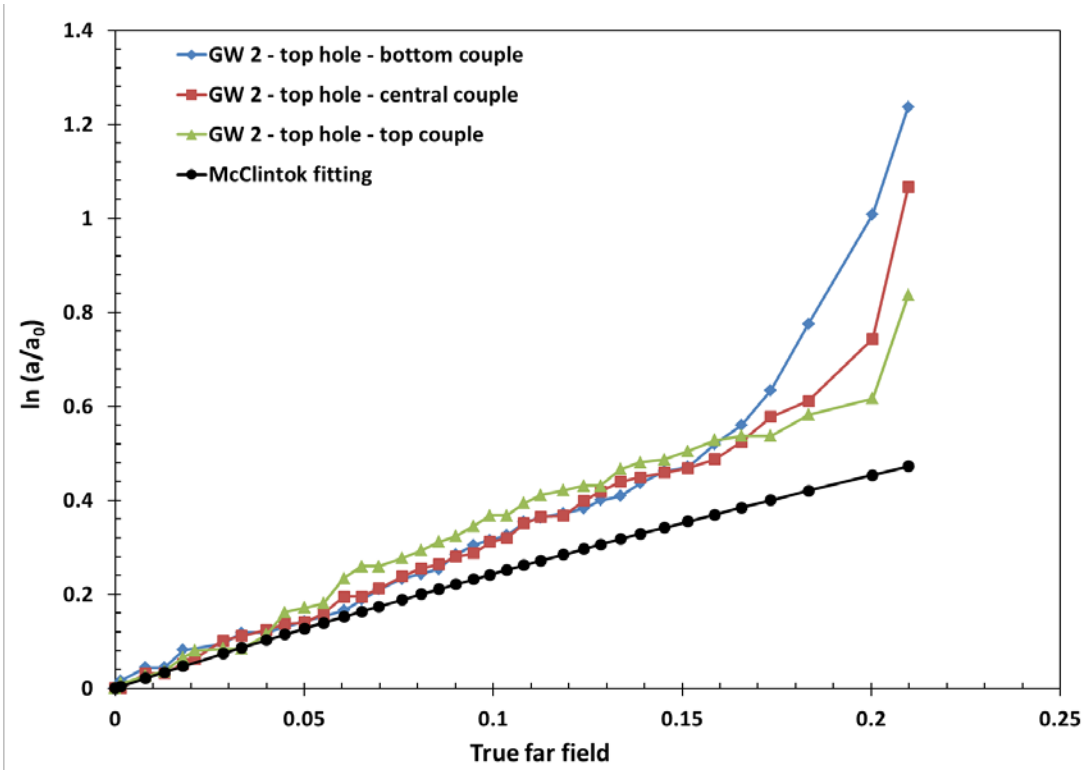

Figure H. 136 - McClintok fitting of the void growth for top holes in specimen GW 2

H.8 McClintok fitting neglecting Lüdering

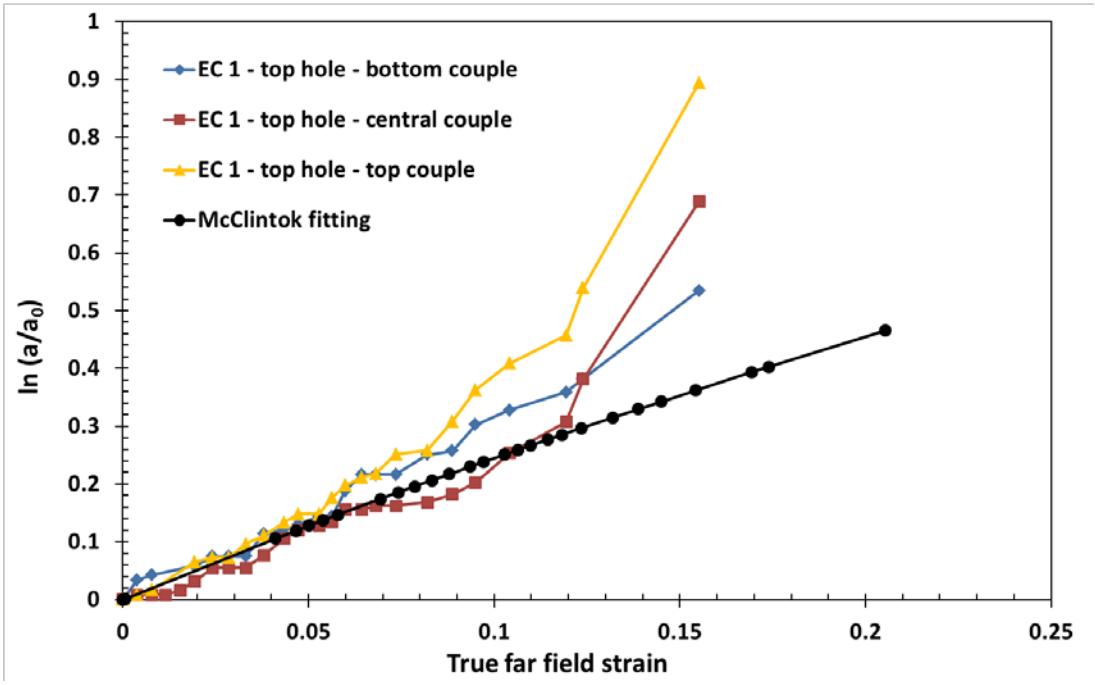

Figure H. 137 - McClintok fitting of specimen EC 1 after Lüdering removal in the curves describing void growth

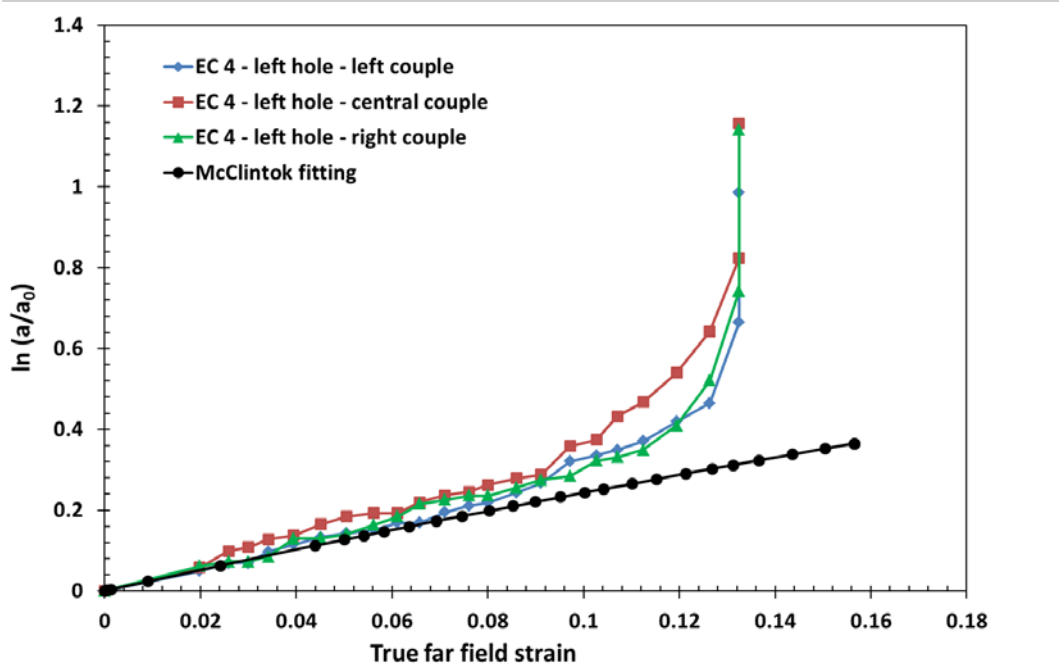

Figure H. 138 - McClintok fitting of specimen EC 4 after Lüdering removal in the curves describing void growth

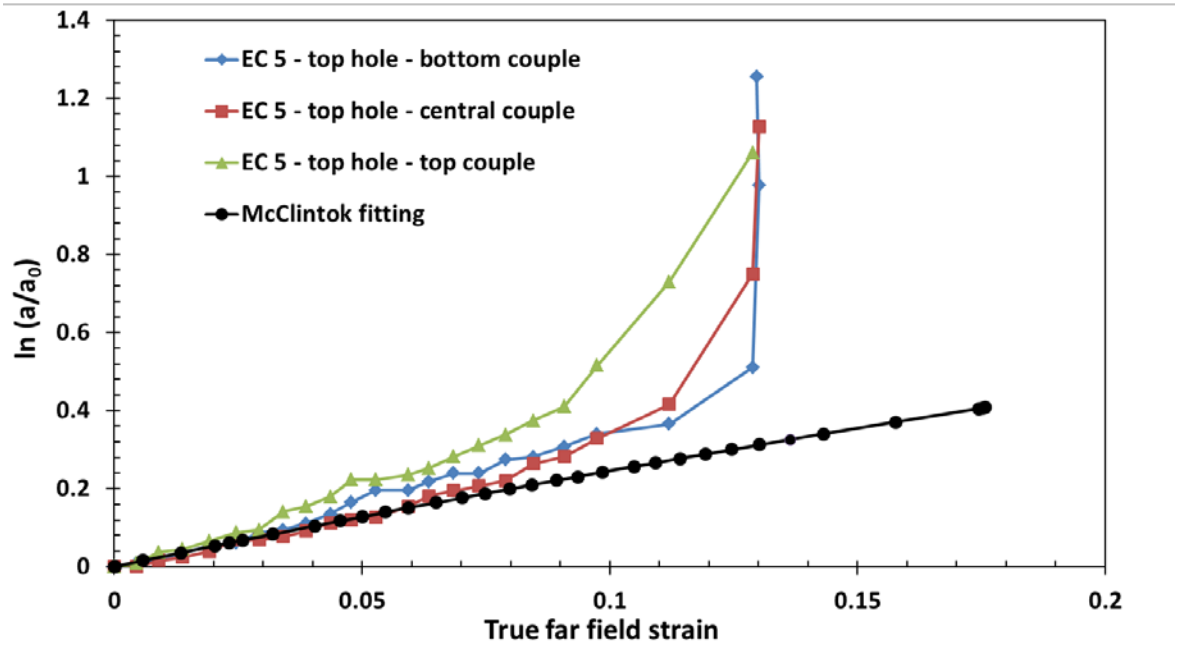

Figure H. 139 - McClintok fitting of specimen EC 5 after Lüdering removal in the curves describing void growth

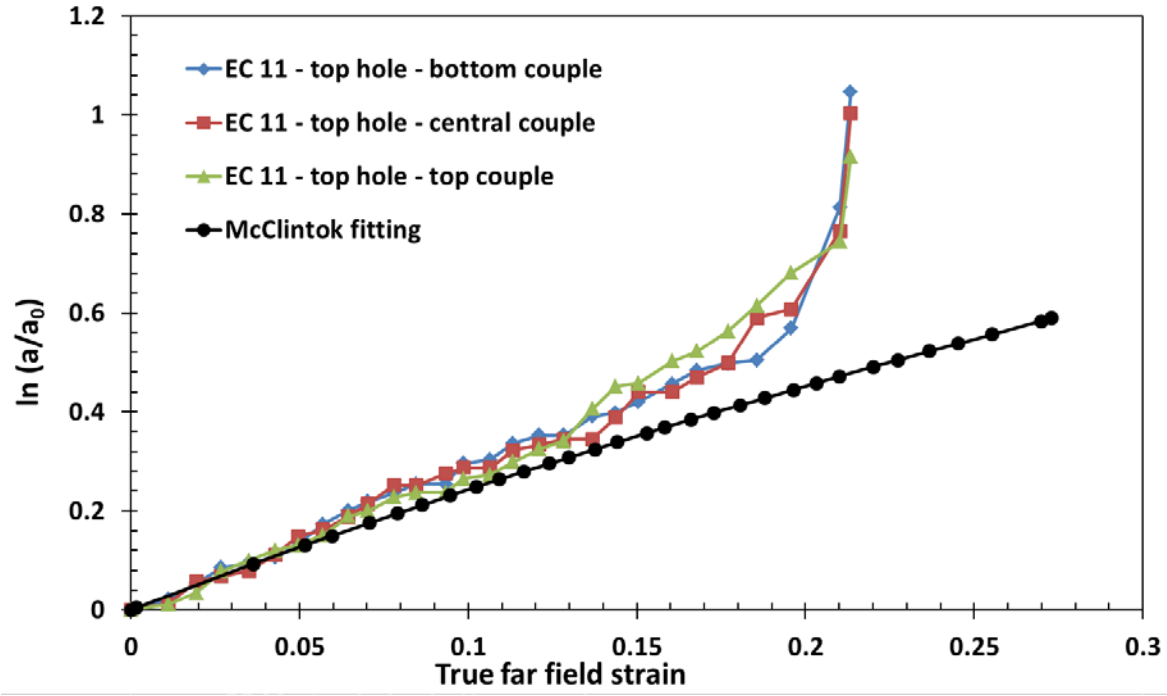

Figure H. 140 - McClintok fitting of specimen EC 11 after Lüdering removal in the curves describing void growth

Appendix I : IF steel coated with FeMnC Films

Sample	Upper Yield Stress [MPa]	Lower Yield Stress [MPa]	Average stress in Lueder plateau [MPa]	Lüders length	Ultimate Tensile Stress (UTS) [MPa]	Strain at fracture (ε_B)
530 ˚C – 1h A	247	229	233	0.05062	278	0.32
530 ˚C – 1h B	257	244	248	0.05423	294	0.29
530 ˚C – 1h C	262	239	241	0.06153	279	0.30
Average	255	237	241	0.05546	284	0.30

Table I- 1 - Mechanical properties of tensile coupons coated both sides with 500 nm thick FeMnC film and annealed at 530 ˚C – 1h in high vacuum

Optical microscope images were recorded during the tensile test of the coupon B annealed at 530 ˚C for 1h in high vacuum.

Table I- 2 lists the mechanical properties obtained for coupons annealed at 630 ˚C – 1h.

Sample	Upper Yield Stress [MPa]	Lower Yield Stress [MPa]	Average stress in Lueder plateau [MPa]	Lüders length	Ultimate Tensile Stress (UTS) [MPa]	Strain at fracture (ε_B)
630 ˚C – 1h A	225	215	223	0.04032	247.6	0.16
630 ˚C – 1h B	287	270	271	0.03457	313	0.19
630 ˚C – 1h C	260	253	254	0.05323	300	0.24
Average	257	246	249	0.04271	287	0.20

Table I- 2 - Mechanical properties of tensile coupons coated both sides with 500 nm thick FeMnC film and annealed at 630 ˚C – 1h in high vacuum

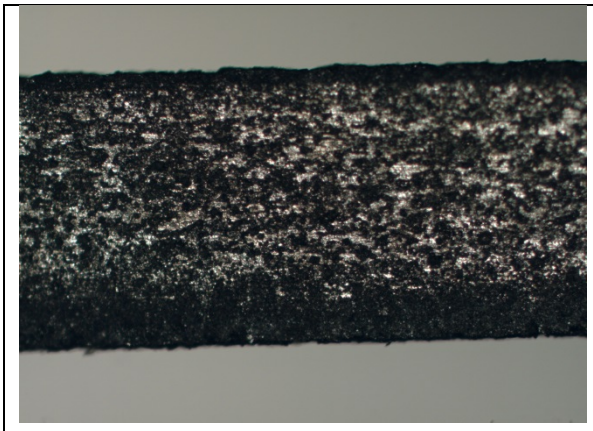

(a) Starting of the tensile test

(b) Propagation of Lüders plateau: the film shows no exfoliation even if the band is propagating

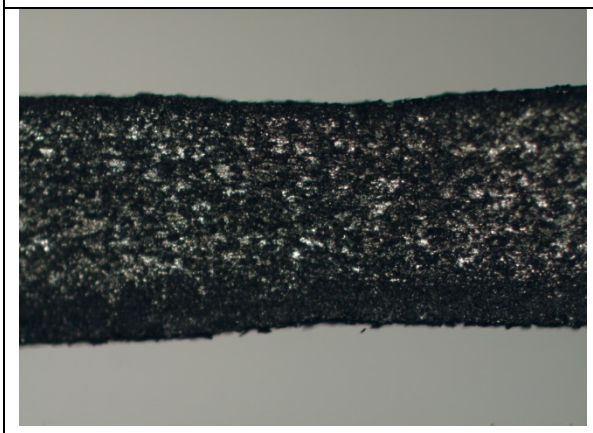

(c) Surface of the tensile coupon approaching end of the test

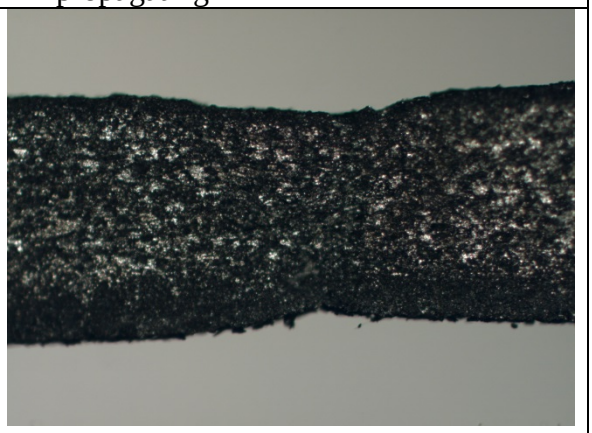

(d) Surface of the tensile coupon approaching fracture

Figure I. 1 - Optical microscope pictures of the surface of the film for a coupon annealed at 530 ˚C – 1h in high vacuum and coated with 500 nm thick FeMnC film on both sides

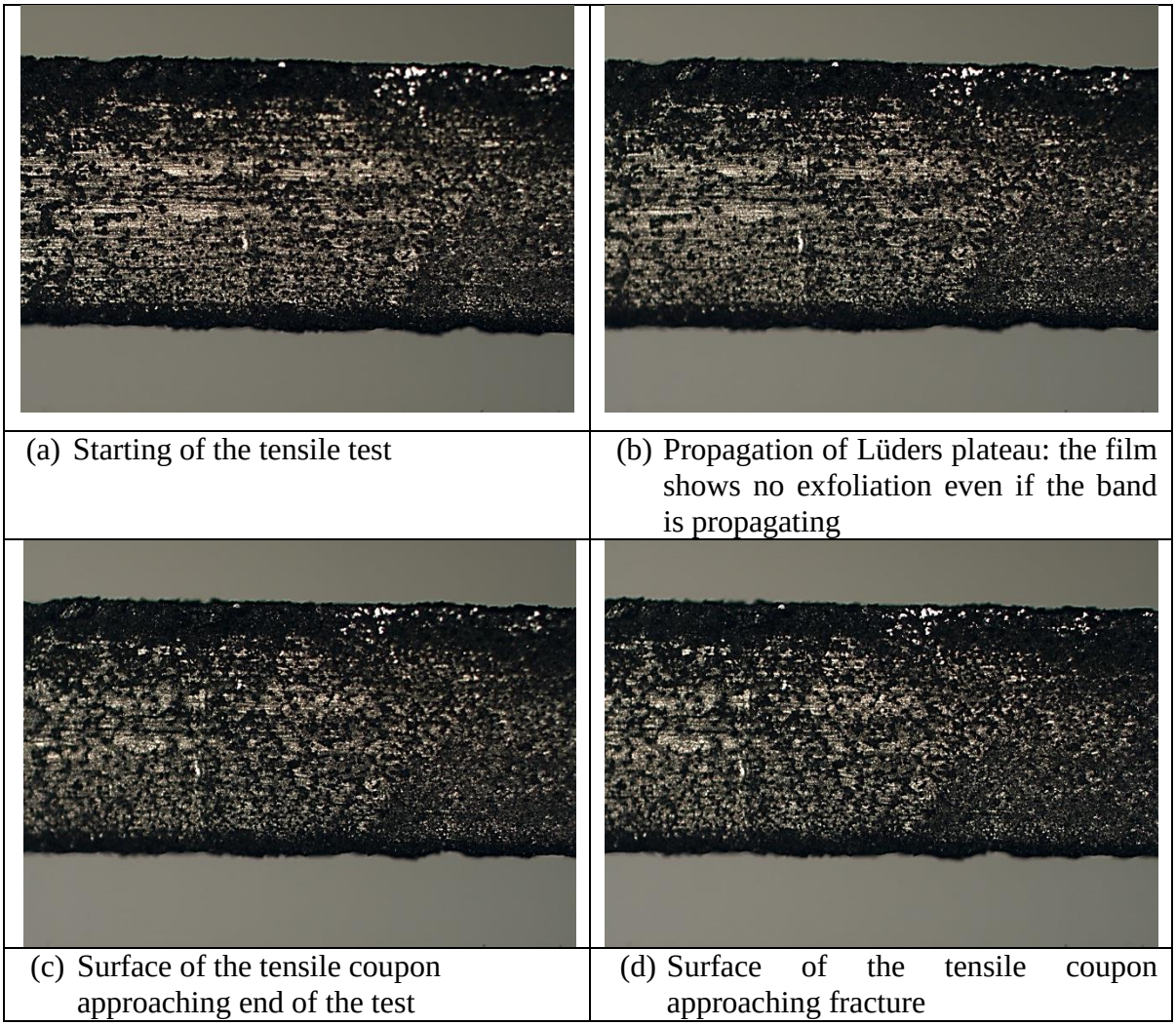

(a) Starting of the tensile test

(b) Propagation of Lüders plateau: the film shows no exfoliation even if the band is propagating

(c) Surface of the tensile coupon approaching end of the test

(d) Surface of the tensile coupon approaching fracture

Figure I. 2 - Optical microscope pictures of the surface of the film for a coupon annealed at 630 ˚C – 1h in high vacuum and coated with 500 nm thick FeMnC film on both sides

In Table I- 3 mechanical properties of specimens annealed at 1000 ˚C for 1h are reported

Sample	Upper Yield Stress [MPa]	Lower Yield Stress [MPa]	Average stress in Lüders plateau [MPa]	Lüders length	Ultimate Tensile Stress (UTS) [MPa]	Strain at fracture (ε_B)
1000 ˚C – 1h A	137	143	140	0.01623	226	0.24
1000 ˚C – 1h B	108	116.4	112	0.00921	204	0.26
1000 ˚C – 1h C	103	-	-	-	189.6	0.19
Average	116	129.7	126	0.01272	206.5	0.23

Table I- 3 - Mechanical properties of tensile coupons coated both sides with 500 nm thick FeMnC film and annealed at 1000 ˚C – 1h in high vacuum

In Table I- 4 mechanical properties of specimens annealed at 1000 ˚C for 10h.

Sample	Upper Yield Stress [MPa]	Lower Yield Stress [MPa]	Average stress in Lüders plateau [MPa]	Lüders length	Ultimate Tensile Stress (UTS) [MPa]	Strain at fracture (ε_B)
1000 ˚C – 10h A	114.6	-	-	-	180	0.21
1000 ˚C – 10h B	78	-	-	-	169	0.23
Average	96.3	-	-	-	174.5	0.22

Table I- 4 - Mechanical properties of tensile coupons coated both sides with 500 nm thick FeMnC film and annealed at 1000 ˚C – 10h in high vacuum

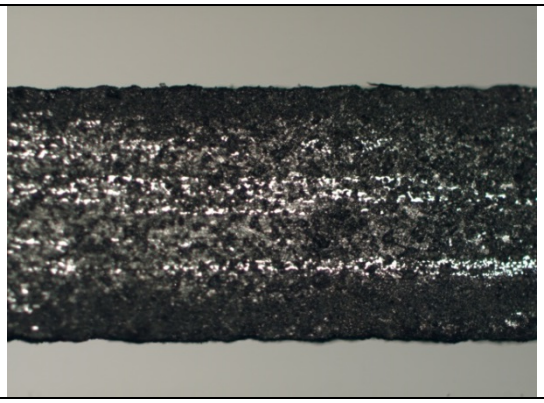

(a) Starting of the tensile test

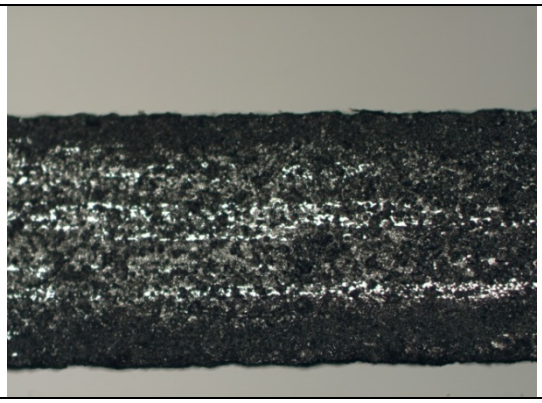

(b) Propagation of Lüders plateau: the film shows no exfoliation even if the band is propagating

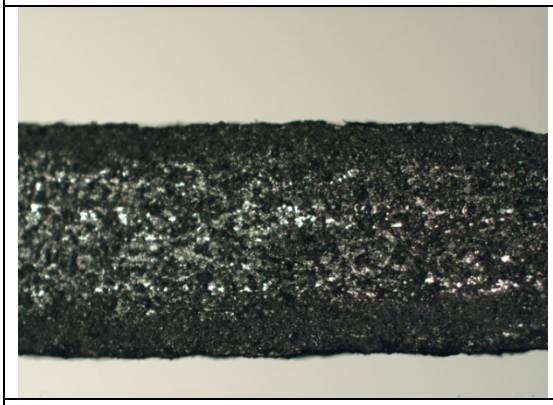

(c) Surface of the tensile coupon approaching end of the test

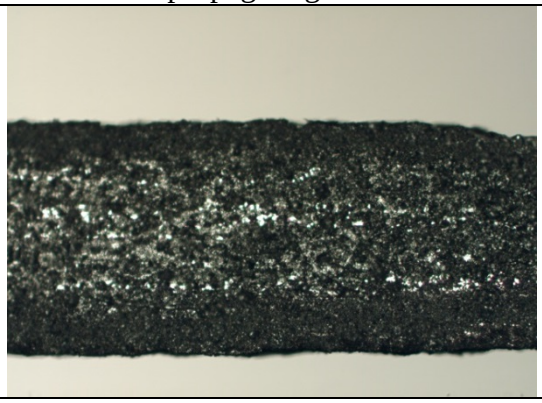

(d) Surface of the tensile coupon approaching fracture

Figure I. 3 - Optical microscope pictures of the surface of the film for a coupon annealed at 1000 ˚C – 1h in high vacuum and coated with 500 nm thick FeMnC film on both sides